# CISPR TR 16-3

Edition 4.0 2020-10
REDLINE VERSION

# TECHNICAL REPORT

colour inside

IECNORM.COM : Click to view the full PDF of CISPR TR 16-3:2020 RLV

INTERNATIONAL SPECIAL COMMITTEE ON RADIO INTERFERENCE

## Specification for radio disturbance and immunity measuring apparatus and methods –
## Part 3: CISPR technical reports



**THIS PUBLICATION IS COPYRIGHT PROTECTED**
**Copyright © 2020 IEC, Geneva, Switzerland**

All rights reserved. Unless otherwise specified, no part of this publication may be reproduced or utilized in any form or by any means, electronic or mechanical, including photocopying and microfilm, without permission in writing from either IEC or IEC's member National Committee in the country of the requester. If you have any questions about IEC copyright or have an enquiry about obtaining additional rights to this publication, please contact the address below or your local IEC member National Committee for further information.

IEC Central Office
3, rue de Varembé
CH-1211 Geneva 20
Switzerland

Tel.: +41 22 919 02 11
info@iec.ch
www.iec.ch

**About the IEC**
The International Electrotechnical Commission (IEC) is the leading global organization that prepares and publishes International Standards for all electrical, electronic and related technologies.

**About IEC publications**
The technical content of IEC publications is kept under constant review by the IEC. Please make sure that you have the latest edition, a corrigendum or an amendment might have been published.

**IEC publications search - webstore.iec.ch/advsearchform**
The advanced search enables to find IEC publications by a variety of criteria (reference number, text, technical committee,…). It also gives information on projects, replaced and withdrawn publications.

**IEC Just Published - webstore.iec.ch/justpublished**
Stay up to date on all new IEC publications. Just Published details all new publications released. Available online and once a month by email.

**IEC Customer Service Centre - webstore.iec.ch/csc**
If you wish to give us your feedback on this publication or need further assistance, please contact the Customer Service Centre: sales@iec.ch.

**Electropedia - www.electropedia.org**
The world's leading online dictionary on electrotechnology, containing more than 22 000 terminological entries in English and French, with equivalent terms in 16 additional languages. Also known as the International Electrotechnical Vocabulary (IEV) online.

**IEC Glossary - std.iec.ch/glossary**
67 000 electrotechnical terminology entries in English and French extracted from the Terms and Definitions clause of IEC publications issued since 2002. Some entries have been collected from earlier publications of IEC TC 37, 77, 86 and CISPR.

IECNORM.COM : Click to view the full PDF of CISPR TR 16-3:2020 RLV

# CISPR TR 16-3

Edition 4.0 2020-10
REDLINE VERSION

# TECHNICAL REPORT

colour inside

IECNORM.COM : Click to view the full PDF of CISPR TR 16-3:2020 RLV

INTERNATIONAL SPECIAL COMMITTEE ON RADIO INTERFERENCE

## Specification for radio disturbance and immunity measuring apparatus and methods –
## Part 3: CISPR technical reports

INTERNATIONAL
ELECTROTECHNICAL
COMMISSION

ICS 33.100.10; 33.100.20

ISBN 978-2-8322-8985-3

**Warning! Make sure that you obtained this publication from an authorized distributor.**

® Registered trademark of the International Electrotechnical Commission

CONTENTS

FOREWORD ..... 16
1 Scope ..... 18
2 Normative references ..... 18
3 Terms, definitions and abbreviated terms ..... 19
3.1 Terms and definitions ..... 19
3.2 Abbreviated terms ..... 23
4 Technical reports ..... 24
4.1 Correlation between measurements made with apparatus having characteristics differing from CISPR characteristics and measurements made with CISPR apparatus ..... 24
4.1.1 General ..... 24
4.1.2 Critical interference-measuring instrument parameters ..... 24
4.1.3 Impulse interference – correlation factors ..... 26
4.1.4 Random noise ..... 28
4.1.5 The root mean square (RMS) detector ..... 28
4.1.6 Discussion ..... 28
4.1.7 Application to typical noise sources ..... 28
4.1.8 Conclusions ..... 29
4.2 Interference simulators ..... 30
4.2.1 General ..... 30
4.2.2 Types of interference signals ..... 30
4.2.3 Circuits for simulating broadband interference ..... 31
4.3 Relationship between limits for open-area test site and the reverberation chamber ..... 35
4.3.1 General ..... 35
4.3.2 Correlation between measurement results of the reverberation chamber and OATS ..... 35
4.3.3 Limits for use with the reverberation chamber method ..... 36
4.3.4 Procedure for the determination of the reverberation chamber limit ..... 36
4.4 Characterization and classification of the asymmetrical disturbance source induced in telephone subscriber lines by AM broadcasting transmitters in the LW, MW and SW bands ..... 37
4.4.1 General ..... 37
4.4.2 Experimental characterization ..... 37
4.4.3 Prediction models and classification ..... 47
4.4.4 Characterization of the immunity-test disturbance source ..... 51
4.5 Predictability of radiation in vertical directions at frequencies above 30 MHz ..... 58
4.5.1 Summary ..... 58
4.5.2 Range of application ..... 59
4.5.3 General ..... 59
4.5.4 Method used to calculate field patterns in the vertical plane ..... 61
4.5.5 Limitations of predictability of radiation at elevated angles ..... 62
4.5.6 Differences between the fields over a real ground and the fields over a perfect conductor ..... 90
4.5.7 Uncertainty ranges ..... 96
4.5.8 Conclusions ..... 98

IECNORM.COM : Click to view the full PDF of CISPR TR 16-3:2020 RLV

4.6 The predictability of radiation in vertical directions at frequencies up to 30 MHz ..... 99
4.6.1 Range of application ..... 99
4.6.2 General ..... 100
4.6.3 Method of calculation of the vertical radiation patterns ..... 101
4.6.4 The source models ..... 101
4.6.5 Electrical constants of the ground ..... 103
4.6.6 Predictability of radiation in vertical directions ..... 103
4.6.7 Conclusions ..... 111
4.6.8 Figures associated with predictability of radiation in vertical directions ..... 112
4.7 Correlation between amplitude probability distribution (APD) characteristics of disturbance and performance of digital communication systems ..... 147
4.7.1 General ..... 147
4.7.2 Influence on a wireless LAN system ..... 147
4.7.3 Influence on a Bluetooth system ..... 150
4.7.4 Influence on a W-CDMA system ..... 154
4.7.5 Influence on Personal Handy Phone System (PHS) ..... 157
4.7.6 Quantitative correlation between noise parameters and system performance ..... 161
4.7.7 Quantitative correlation between noise parameters of repetition pulse and system performance of PHS and W-CDMA (BER) ..... 164
4.8 Background material on the definition of the RMS-average weighting detector for measuring receivers ..... 167
4.8.1 General – purpose of weighted measurement of disturbance ..... 167
4.8.2 General principle of weighting – the CISPR quasi-peak detector ..... 168
4.8.3 Other detectors defined in CISPR 16-1-1 ..... 168
4.8.4 Procedures for measuring pulse weighting characteristics of digital radiocommunications services ..... 169
4.8.5 Theoretical studies ..... 172
4.8.6 Experimental results ..... 174
4.8.7 Effects of spread-spectrum clock interference on wideband radiocommunication signal reception ..... 192
4.8.8 Analysis of the various weighting characteristics and proposal of a weighting detector ..... 193
4.8.9 Properties of the RMS-average weighting detector ..... 195
4.9 Common mode absorption devices (CMAD) ..... 197
4.9.1 General ..... 197
4.9.2 CMAD as a two-port device ..... 199
4.9.3 Measurement of CMAD ..... 203
4.10 Background on the definition of the FFT-based receiver ..... 213
4.10.1 General ..... 213
4.10.2 Tuned selective voltmeters and spectrum analyzers ..... 214
4.10.3 General principle of a tuned selective voltmeter ..... 214
4.10.4 FFT-based receivers – digital signal processing ..... 215
4.10.5 Measurement errors specific to FFT processing ..... 219
4.10.6 FFT-based receivers – examples ..... 221
4.11 Parameters of signals at telecommunication ports ..... 234
4.11.1 General ..... 234
4.11.2 Estimation of common mode disturbance levels ..... 235
4.12 Background on CDNE equipment and measurement method ..... 236

IECNORM.COM : Click to view the full PDF of CISPR TR 16-3:2020 RLV

4.12.1 General ..... 236
4.12.2 Historical overview ..... 237
4.12.3 From CDN to CDNE ..... 241
4.13 Background on LLAS, validation and measurement method ..... 244
4.13.1 General ..... 244
4.13.2 Historical overview ..... 244
4.13.3 Models and equations for the LLAS method ..... 245
5 Background and history of CISPR ..... 245
5.1 The history of CISPR ..... 245
5.1.1 The early years: 1934-1984 ..... 245
5.1.2 The division of work ..... 247
5.1.3 The computer years: 1984 to 1998 ..... 248
5.1.4 The people in CISPR ..... 248
5.2 Historical background to the method of measurement of the interference power produced by electrical household and similar appliances in the VHF range ..... 249
5.2.1 Historical detail ..... 249
5.2.2 Development of the method ..... 250
Annex A (informative) Derivation of the formula ..... 252
Annex B (informative) The field-strength distribution ..... 256
B.1 General ..... 256
B.2 $H_o$-field expressions ..... 256
B.3 $H_i$ field expressions ..... 258
B.4 $E_o$-field expressions ..... 259
Annex C (informative) The induced asymmetrical open-circuit voltage distribution ..... 260
C.1 General ..... 260
C.2 $H$-field-based relations ..... 260
C.3 $E$-field-based relations ..... 262
Annex D (informative) The outlet-voltage distribution ..... 263
D.1 General ..... 263
D.2 $H$-field-based relations ..... 263
D.3 $E$-field-based relations ..... 264
Annex E (informative) Some mathematical relations ..... 265
E.1 General ..... 265
E.2 The error function ..... 265
E.3 Application to the lognormal distribution ..... 266
Annex F (informative) Harmonic fields radiated at elevated angles from 27 MHz ISM equipment over real ground ..... 267
Annex G (informative) Models and equations associated with the LLAS method ..... 273
G.1 General ..... 273
G.2 Response of an LAS to a magnetic field dipole ..... 273
G.2.1 Magnetic field strength model of a disturbance source ..... 273
G.2.2 Response of an LAS to a magnetic field dipole ..... 274
G.2.3 Sensitivity of an LLAS for different diameters ..... 278
G.2.4 Limitation of application of the relative sensitivity curves ..... 279
G.3 Response of LLAS to the LLAS verification dipole ..... 280
G.3.1 Relation of LLA current and voltage applied to the LLAS verification dipole ..... 280

IECNORM.COM : Click to view the full PDF of CISPR TR 16-3:2020 RLV

G.3.2 Calculation of mutual inductance: the original method ..... 281
G.3.3 Calculation of mutual inductance: the improved method ..... 281
G.3.4 Derivation of the equation for the reference validation factor ..... 281
G.3.5 Replication of the original version of the reference validation factor ..... 284
G.3.6 Calculation of the improved reference validation factor ..... 284
G.3.7 NEC2 method ..... 286
G.4 Magnetic field strength of a magnetic field dipole above a ground plane ..... 287
G.4.1 Model ..... 287
G.4.2 Replication of Figure C.10 ..... 288
G.4.3 Conversion factors for calculating magnetic field strength at other distances ..... 290
G.5 LLAS validation criterion ..... 291
Bibliography ..... 292

Figure 1 – Relative response of various detectors to impulse interference ..... 25
Figure 2 – Pulse rectification coefficient $P(\alpha)$ ..... 26
Figure 3 – Pulse repetition frequency ..... 27
Figure 4 – Block diagram and waveforms of a simulator generating noise bursts ..... 33
Figure 5 – Block diagram of a simulator generating noise bursts according to the pulse principle ..... 34
Figure 6 – Details of a typical output stage ..... 35
Figure 7 – Scatter plot of the measured outdoor magnetic field strength $H_o$ (dBμA/m) versus the calculated outdoor magnetic field strength $H_c$ dB(μA/m) ..... 39
Figure 8 – Measured outdoor magnetic versus distance, and probability of the building-effect parameter ..... 40
Figure 9 – Normal probability plot of the building-effect parameter $A_b$ dB ..... 41
Figure 10 – Scatter plot of the outdoor antenna factor $G_o$ dB(Ωm) versus the indoor antenna factor $G_i$ ..... 42
Figure 11 – Normal probability plots of the antenna factors ..... 43
Figure 12 – Normal probability plot of the equivalent asymmetrical resistance $R_a$ dB(Ω) ..... 46
Figure 13 – Examples of the frequency dependence of some parameters ..... 47
Figure 14 – Example of the frequency histogram $\Delta N(E_o,\Delta E_o)$ ..... 52
Figure 15 – Example of $n_m(E_o)$, i.e. the distribution of the outlets experiencing a maximum field strength $E_o$ resulting from a given number of transmitters in (or near) the respective geographical region ..... 53
Figure 16 – Example of the number of outlets with an induced asymmetrical open-circuit voltage $U_L \leq U_h \leq U_{max}$ = 79 V (see Table 10) ..... 55
Figure 17 – Examples of number (left-hand scale) and relative number (right-hand scale) of outlets with $U_L \leq U_h \leq U_{max}$ ..... 56
Figure 18 – Vertical polar patterns of horizontally polarized $E_x$ field strengths emitted around small vertical loop (horizontal magnetic dipole) over three different types of real ground ..... 64
Figure 19 – Height scan patterns of vertically oriented $E_z$ field strengths emitted from small vertical loop (horizontal magnetic dipole) over three different types of real ground ..... 64
Figure 20 – Vertical polar patterns of horizontally polarized $E_x$ field strengths emitted around small vertical loop (horizontal magnetic dipole), over three different types of real ground ..... 66

IECNORM.COM : Click to view the full PDF of CISPR TR 16-3:2020 RLV

Figure 21 – Vertical polar patterns of vertically oriented $E_z$ field strengths emitted around small vertical loop (horizontal magnetic dipole) over three different types of real ground ..... 66

Figure 22 – Height scan patterns of vertically oriented $E_z$ field strengths emitted at 1 000 MHz from the small vertical loop (horizontal magnetic dipole), at horizontal distance of 10 m, 30 m and 300 m in the Z-X plane over three different types of real ground ..... 67

Figure 23 – Vertical polar patterns of horizontally polarized $E_x$ and vertically oriented $E_z$ field strengths emitted around small horizontal electric dipole, in Y-Z and Z-X planes respectively ..... 69

Figure 24 – Height scan patterns of horizontally polarized $E_x$ field strengths emitted from small horizontal electric dipole ..... 69

Figure 25 – Vertical polar patterns of horizontally polarized $E_x$ and vertically oriented $E_z$ field strengths emitted around small horizontal electric dipole in Y-Z and Z-X planes respectively ..... 72

Figure 26 – Height scan patterns of horizontally polarized $E_x$ field strengths emitted small horizontal electric dipole ..... 72

Figure 27 – Vertical polar patterns of horizontally polarized $E_x$ and vertically oriented $E_z$ field strengths emitted around small vertical loop (horizontal magnetic dipole) in Y-Z and Z-X planes respectively ..... 73

Figure 28 – Height scan patterns of vertically oriented $E_z$ and horizontally oriented $E_x$ field strengths emitted from small vertical loop (horizontal magnetic dipole) ..... 73

Figure 29 – Vertical polar patterns of vertically oriented $E_z$ and horizontally oriented $E_x$ field strengths emitted around small vertical electric dipole ..... 76

Figure 30 – Height scan patterns of vertically oriented $E_z$ and horizontally oriented $E_x$ field strengths emitted from small vertical electric dipole ..... 76

Figure 31 – Vertical polar patterns of horizontally polarized $E_x$ and vertically oriented $E_z$ field strengths emitted around small vertical loop (horizontal magnetic dipole) in Y-Z and Z-X planes respectively ..... 77

Figure 32 – Height scan patterns of vertically oriented $E_z$ and horizontally oriented $E_x$ field strengths emitted from small vertical loop (horizontal magnetic dipole) ..... 77

Figure 33 – Vertical polar patterns of horizontally polarized $E$-field strength emitted around small horizontal loop (vertical magnetic dipole) ..... 78

Figure 34 – Height scan patterns of horizontally polarized $E$-field strength emitted from small horizontal loop (vertical magnetic dipole) ..... 78

Figure 35 – Vertical polar patterns of vertically oriented $E_z$ and horizontally oriented $E_x$ field strengths emitted around small vertical electric dipole ..... 81

Figure 36 – Height scan patterns of vertically oriented $E_z$ and horizontally oriented $E_x$ field strengths emitted from the small vertical electric dipole ..... 81

Figure 37 – Vertical polar patterns of horizontally polarized $E_x$ and vertically oriented $E_z$ field strengths emitted around small vertical loop (horizontal magnetic dipole) in Y-Z and Z-X planes respectively ..... 82

Figure 38 – Height scan patterns of vertically oriented $E_z$ and horizontally oriented $E_x$ field strengths emitted from small vertical loop (horizontal magnetic dipole) ..... 82

Figure 39 – Vertical polar patterns of horizontally polarized $E$-field strength emitted around small horizontal loop (vertical magnetic dipole) ..... 83

Figure 40 – Height scan patterns of horizontally polarized $E$-field strength emitted from small horizontal loop (vertical magnetic dipole) ..... 83

Figure 41 – Vertical polar patterns of horizontally polarized $E$-field strength emitted around the small horizontal loop (vertical magnetic dipole) ..... 86

Figure 42 – Height scan patterns of horizontally polarized $E$-field strength emitted from small horizontal loop (vertical magnetic dipole) ..... 86

IECNORM.COM : Click to view the full PDF of CISPR TR 16-3:2020 RLV

Figure 43 – Height scan patterns of horizontally polarized $E$-field strength emitted from small horizontal loop (vertical magnetic dipole) ..... 90
Figure 44 – Height scan patterns of the vertical component of the $E$-fields emitted from a small vertical electric dipole ..... 93
Figure 45 – Height scan patterns of the vertical component of the $E$-fields emitted from a small vertical electric dipole ..... 93
Figure 46 – Height scan patterns of the horizontally polarized $E$-fields emitted in the vertical plane normal to the axis of a small horizontal electric dipole ..... 95
Figure 47 – Height scan patterns of the horizontally polarized $E$-fields emitted in the vertical plane normal to the axis of a small horizontal electric dipole ..... 95
Figure 48 – Ranges of uncertainties in the predictability of radiation in vertical directions from electrically small sources located at a height of 1 m or 2 m above ground ..... 97
Figure 49 – Ranges of uncertainties in the predictability of radiation in vertical directions from electrically small sources located at a height of 1 m or 2 m above ground ..... 97
Figure 50 – Ranges of uncertainties in the predictability of radiation in vertical directions from electrically small sources located at a height of 1 m or 2 m above ground ..... 98
Figure 51 – Geometry of the small vertical electric dipole model ..... 102
Figure 52 – Geometry of the small horizontal electrical dipole model ..... 102
Figure 53 – Geometry of the small horizontal magnetic dipole model (small vertical loop) ..... 102
Figure 54 – Geometry of the small vertical magnetic dipole model (small horizontal loop) ..... 102
Figure 55 – Ranges of errors in the predictability of radiation in vertical directions from electrically small sources located close to the ground, based on measurements of the horizontally oriented $H$-field near ground at a distance of 30 m from the sources ..... 110
Figure 56 – Ranges of errors in the predictability of radiation in vertical directions from electrically small sources located close to the ground, based on measurements of the horizontally oriented $H$-field at the ground supplemented with measurements of the vertically oriented $H$-field in a height scan up to 6 m at a distance of 30 m from the sources ..... 111
Figure 57 – Vertical radiation patterns of horizontally oriented $H$-fields emitted by a small vertical electric dipole located close to the ground ..... 113
Figure 58 – Vertical radiation patterns of horizontally oriented $H$-fields emitted by a small vertical electric dipole located close to the ground ..... 113
Figure 59 – Vertical radiation patterns of $E$-fields emitted by a small vertical electric dipole located close to the ground ..... 114
Figure 60 – Vertical radiation patterns of the $E$-fields emitted by a small vertical electric dipole located close to the ground ..... 114
Figure 61 – Vertical radiation patterns of the $H$-fields emitted by a small horizontal electric dipole located close to the ground ..... 116
Figure 62 – Influence of a wide range of values of the electrical constants of the ground on the vertical radiation patterns of the horizontally oriented $H$-fields emitted by a small horizontal electric dipole located close to the ground ..... 116
Figure 63 – Vertical radiation patterns of the horizontally oriented $H$-fields emitted by a small horizontal electric dipole located close to the ground ..... 117
Figure 64 – Vertical radiation patterns of the $E$-fields emitted by a small horizontal electric dipole located close to the ground ..... 117

IECNORM.COM : Click to view the full PDF of CISPR TR 16-3:2020 RLV

Figure 65 – Vertical radiation patterns of the $E$-fields emitted by a small horizontal electric dipole located close to the ground ..... 118
Figure 66 – Vertical radiation patterns of $H$-fields emitted by small horizontal magnetic dipole (vertical loop) located close to ground ..... 118
Figure 67 – Vertical radiation patterns of the horizontally oriented $H$-fields emitted by a small horizontal magnetic dipole (vertical loop) located close to the ground ..... 119
Figure 68 – Vertical radiation patterns of the horizontally oriented $H$-fields emitted by a small horizontal magnetic dipole (vertical loop) located close to the ground ..... 119
Figure 69 – Vertical radiation patterns of the $E$-fields emitted by a small horizontal magnetic dipole (vertical loop) located close to the ground ..... 120
Figure 70 – Vertical radiation patterns of the $E$-fields emitted by a small horizontal magnetic dipole (vertical loop) located close to the ground ..... 120
Figure 71 – Vertical radiation patterns of the $H$-fields emitted by a small vertical magnetic dipole (horizontal loop) located close to the ground ..... 122
Figure 72 – Vertical radiation patterns of the $H$-fields emitted by a small vertical magnetic dipole (horizontal loop) located close to the ground ..... 122
Figure 73 – Vertical radiation patterns of the $H$-fields emitted by a small vertical magnetic dipole (horizontal loop) located close to the ground ..... 123
Figure 74 – Vertical radiation patterns of the $H$-fields emitted by a small vertical magnetic dipole (horizontal loop) located close to the ground ..... 123
Figure 75 – Vertical radiation pattern of the $E$-field emitted by a small vertical magnetic dipole (horizontal loop) located close to the ground ..... 124
Figure 76 – Vertical radiation patterns of the $E$-fields emitted by a small vertical magnetic dipole (horizontal loop) located close to the ground ..... 124
Figure 77 – Vertical radiation patterns of the horizontally oriented $H$-fields emitted by a small vertical electric dipole located close to the ground ..... 125
Figure 78 – Vertical radiation patterns of the $E$-fields emitted by a small vertical electric dipole located close to the ground ..... 125
Figure 79 – Vertical radiation patterns of the $E$-fields emitted by a small vertical electric dipole located close to the ground ..... 126
Figure 80 – Vertical radiation patterns of the $H$-fields emitted by a small horizontal electric dipole located close to the ground ..... 126
Figure 81 – Vertical radiation patterns of the horizontally oriented $H$-fields emitted by a small horizontal electric dipole located close to the ground ..... 127
Figure 82 – Vertical radiation patterns of the $E$-fields emitted by a small horizontal electric dipole located close to the ground ..... 127
Figure 83 – Vertical radiation patterns of the $E$-fields emitted by a small horizontal electric dipole located close to the ground ..... 129
Figure 84 – Vertical radiation patterns of the $H$-fields emitted by a small horizontal magnetic dipole (vertical loop) located close to the ground ..... 129
Figure 85 – Vertical radiation patterns of the horizontally oriented $H$-fields emitted by a small horizontal magnetic dipole (vertical loop) located close to the ground ..... 130
Figure 86 – Vertical radiation patterns of the horizontally oriented $H$-fields emitted by a small horizontal magnetic dipole (vertical loop) located close to the ground ..... 130
Figure 87 – Vertical radiation patterns of the $E$-fields emitted by a small horizontal magnetic dipole (vertical loop) located close to the ground ..... 131
Figure 88 – Vertical radiation patterns of the $E$-fields emitted by a small horizontal magnetic dipole (vertical loop) located close to the ground ..... 131
Figure 89 – Vertical radiation patterns of the $H$-fields emitted by a small vertical magnetic dipole (horizontal loop) located close to the ground ..... 132

IECNORM.COM : Click to view the full PDF of CISPR TR 16-3:2020 RLV

Figure 90 – Vertical radiation patterns of the $H$-fields emitted by a small vertical magnetic dipole (horizontal loop) located close to the ground ..... 132
Figure 91 – Vertical radiation patterns of the $H$-fields emitted by a small vertical magnetic dipole (horizontal loop) located close to the ground ..... 133
Figure 92 – Vertical radiation patterns of the $E$-fields emitted by a small vertical magnetic dipole (horizontal loop) located close to the ground ..... 133
Figure 93 – Vertical radiation patterns of the horizontally oriented $H$-fields emitted by a small vertical electric dipole located close to the ground ..... 134
Figure 94 – Vertical radiation patterns of the $E$-fields emitted by a small vertical electric dipole located close to the ground ..... 134
Figure 95 – Vertical radiation patterns of the $E$-fields emitted by a small vertical electric dipole located close to the ground ..... 136
Figure 96 – Vertical radiation patterns of the $H$-fields emitted by a small horizontal electric dipole located close to the ground ..... 136
Figure 97 – Vertical radiation patterns of the $E$-fields emitted by a small horizontal electric dipole located close to the ground ..... 137
Figure 98 – Vertical radiation patterns of the $E$-fields emitted by a small horizontal electric dipole located close to the ground ..... 137
Figure 99 – Vertical radiation patterns of the $H$-field emitted by a small horizontal magnetic dipole (vertical loop) located close to the ground ..... 139
Figure 100 – Vertical radiation patterns of the vertically polarized $E$-fields emitted by a small horizontal magnetic dipole (vertical loop) located close to the ground ..... 139
Figure 101 – Vertical radiation patterns of the $H$-field emitted by a small vertical magnetic dipole (horizontal loop) located close to the ground ..... 140
Figure 102 – Vertical radiation patterns of the $E$-fields emitted by a small vertical magnetic dipole (horizontal loop) located close to the ground ..... 140
Figure 103 – Vertical radiation patterns of the horizontally oriented $H$-fields emitted by a small vertical electric dipole located close to the ground ..... 141
Figure 104 – Vertical radiation patterns of the vertically polarized $E$-fields emitted by a small vertical electric dipole located close to the ground ..... 141
Figure 105 – Vertical radiation patterns of the $H$-fields emitted by a small horizontal electric dipole located close to the ground ..... 142
Figure 106 – Vertical radiation patterns of the horizontally oriented $H$-fields emitted by a small horizontal electric dipole located close to the ground ..... 142
Figure 107 – Influence of a wide range of values of the electrical constants of the ground on the vertical radiation patterns of the horizontally oriented $H$-fields emitted by a small horizontal electric dipole located close to the ground ..... 143
Figure 108 – Vertical radiation patterns of the vertically polarized $E$-fields emitted by a small horizontal electric dipole located close to the ground ..... 143
Figure 109 – Vertical radiation patterns of the $H$-fields emitted by a small horizontal magnetic dipole (vertical loop) located close to the ground ..... 145
Figure 110 – Vertical radiation patterns of the vertically polarized $E$-fields emitted by a small horizontal magnetic dipole (vertical loop) located close to the ground ..... 145
Figure 111 – Vertical radiation patterns of the $H$-fields emitted by a small vertical magnetic dipole (horizontal loop) located close to the ground ..... 146
Figure 112 – Vertical radiation patterns of the $E$-fields emitted by a small vertical magnetic dipole (horizontal loop) located close to the ground ..... 146
Figure 113 – Set-up for measuring communication quality degradation of a wireless LAN .. 147
Figure 114 – APD characteristics of disturbance ..... 149
Figure 115 – Wireless LAN throughput influenced by noise ..... 150

IECNORM.COM : Click to view the full PDF of CISPR TR 16-3:2020 RLV

Figure 116 – Set-up for measuring the communication quality degradation of Bluetooth ..... 151
Figure 117 – APD of disturbance of actual MWO (2 441MHz) ..... 151
Figure 118 – APD characteristics of disturbance (2 460 MHz) ..... 152
Figure 119 – Throughput of Bluetooth influenced by noise ..... 154
Figure 120 – Set-up for measuring the BER of W-CDMA ..... 155
Figure 121 – APD characteristics of disturbance ..... 156
Figure 122 – BER of W-CDMA caused by radiation noise ..... 157
Figure 123 – Set-up for measuring the PHS throughput ..... 158
Figure 124 – Set-up for measuring the BER of PHS ..... 158
Figure 125 – APD characteristics of disturbance ..... 159
Figure 126 – PHS throughput caused by radiation ..... 160
Figure 127 – BER of PHS caused by radiation noise ..... 161
Figure 128 – Correlation of the disturbance voltages with the system performance ($C/N_0$) ..... 162
Figure 129 – Correlation of the disturbance voltages with the system performance ..... 162
Figure 130 – Correlation of the disturbance voltages with the system performance ..... 163
Figure 131 – Correlation of the disturbance voltages with the system performance ($C/N_0$) ..... 163
Figure 132 – Correlation of the disturbance voltages with the system performance ($C/N_0$) ..... 164
Figure 133 – Experimental set-up for measuring communication quality degradation of a PHS or W-CDMA ..... 164
Figure 134 – Simulation set-up for estimating communication quality degradation of a PHS or W-CDMA ..... 165
Figure 135 – APD of pulse disturbance ..... 165
Figure 136 – BER degradation of PHS and W-CDMA caused by repetition pulse (Carrier power, –35 dBm) ..... 166
Figure 137 – Evaluation method of the correlation between BER and APD ..... 166
Figure 138 – Correlation between measured $\Delta L_{BER}$ and $\Delta L_{APD}$ ..... 167
Figure 139 – Correlation between measured $p_{BER}$ and $p_{APD}$ ..... 167
Figure 140 – Weighting curves of quasi-peak measuring receivers for the different frequency ranges as defined in CISPR 16-1-1 ..... 168
Figure 141 – Weighting curves for peak, quasi-peak, RMS and linear average detectors for CISPR bands C and D ..... 169
Figure 142 – Test setup for the measurement of the pulse weighting characteristics of a digital radiocommunication system ..... 170
Figure 143 – Example of an interference spectrum: pulse modulated carrier with a pulse duration of 0,2 μs and a PRF < 10 kHz ..... 171
Figure 144 – The RMS and peak levels for constant BEP for three $K$ = 3, convolutional codes of different rate ..... 173
Figure 145 – The RMS and peak levels for constant BEP for two rate ½, convolutional code ..... 174
Figure 146 – Test setup for the measurement of weighting curves for Digital Radio Mondiale (DRM) ..... 176
Figure 147 – Weighting characteristics for DRM signals for various pulse widths of the pulse-modulated carrier ..... 177

IECNORM.COM : Click to view the full PDF of CISPR TR 16-3:2020 RLV

Figure 148 – Weighting characteristics for DRM protection level 0: average of results for two receivers ..... 178
Figure 149 – Weighting characteristics for DRM protection level 1: average of results for two receivers ..... 178
Figure 150 – Weighting characteristics for DVB-T with 64 QAM 2k, $CR$ 3/4 (as used in France and UK) ..... 180
Figure 151 – Weighting characteristics for DVB-T with 64 QAM 8k, $CR$ 3/4 (as used in Spain) ..... 181
Figure 152 – Weighting characteristics for DVB-T with 16 QAM 8k, $CR$ 2/3 (as used in Germany) ..... 181
Figure 153 – Average weighting characteristics of 6 receiver types for DVB-T with 16QAM ..... 182
Figure 154 – Average weighting characteristics of 6 receiver types for DVB-T with 64QAM ..... 182
Figure 155 – Weighting characteristics for DAB (signal level -71 dBm) with a flat response down to approximately 1 kHz ..... 183
Figure 156 – Weighting characteristics for DAB: average of two different commercial receiver types ..... 184
Figure 157 – Weighting characteristics for TETRA (signal level –80 dBm) for a code rate of 1 ..... 185
Figure 158 – Weighting characteristics for RBER 1b of GSM (signal level –90 dBm) ..... 186
Figure 159 – Weighting characteristics for RBER 2 of GSM ..... 186
Figure 160 – Carrier-to-interference improvements with decreasing PRF in dB computed for GSM using COSSAP ..... 187
Figure 161 – RMS and quasi-peak values of pulse level for constant effect on FM radio reception ..... 187
Figure 162 – Weighting characteristics for RBER 1b of GSM (signal level –90 dBm) ..... 188
Figure 163 – Weighting characteristics for DECT (signal level –83 dBm) ..... 189
Figure 164 – Weighting characteristics for IS-95 (signal level -97 dBm) with comparatively high immunity to interference ..... 190
Figure 165 – Weighting characteristics for J-STD 008 (signal level –97 dBm) ..... 190
Figure 166 – Weighting characteristics for the Frame Error Ratio (FER) of CDMA2000 (measured at a receive signal level of –112 dBm) for a low data rate of 9,6 kb/s ..... 191
Figure 167 – Weighting characteristics for the Frame Error Ratio (FER) of CDMA2000 (measured at a receive signal level of –106 dBm) for two different data rates (9,6 kb/s and 76,8 kb/s) ..... 191
Figure 168 – The proposed RMS-average detector for CISPR Bands C and D with a corner frequency of 100 Hz ..... 194
Figure 169 – RMS-average detector function by using an RMS detector followed by a linear average detector and peak reading ..... 194
Figure 170 – RMS-average weighting functions for CISPR Bands A, B, C/D and E for the shortest pulse widths allowed by the measurement bandwidths ..... 195
Figure 171 – Shift of the RMS-average weighting function for CISPR band C/D by using a bandwidth of 1 MHz instead of 120 kHz, if the shortest possible pulse widths are applied ..... 196
Figure 172 – Example of a simple EUT model ..... 198
Figure 173 – Representation of a CMAD as a two-port device ..... 199
Figure 174 – Conformal mapping between $z$-plane and $f$-plane ..... 202

IECNORM.COM : Click to view the full PDF of CISPR TR 16-3:2020 RLV

Figure 175 – Conversion from 50 Ω coaxial system to the geometry of the two-port device-under-test ..... 204
Figure 176 – Basic model for the TRL calibration ..... 205
Figure 177 – The four calibration configurations necessary for the TRL calibration ..... 206
Figure 178 – Measurement of CMAD characteristics ..... 210
Figure 179 – Preliminary measurements of the test set-up ..... 212
Figure 180 – Position of the reference planes for the measurement with SOLT calibration and $ABCD$ transformation to $Z_{ref}$ level ..... 213
Figure 181 – Superheterodyne EMI receiver ..... 215
Figure 182 – An example spectrogram $Z[m,k]$ ..... 217
Figure 183 – Sidelobe effect due to the finite length of window ..... 219
Figure 184 – Measurement error for a single pulse ..... 220
Figure 185 – IF signal for different overlapping factors for the same sequence of pulses ..... 221
Figure 186 – FFT-based baseband system ..... 222
Figure 187 – Real-time FFT-based measuring instrument ..... 223
Figure 188 – Digital down-converter ..... 223
Figure 189 – Short time fast Fourier transform – An example of implementation ..... 224
Figure 190 – Floating-point analogue-to-digital conversion ..... 224
Figure 191 – Example of a 120 kHz Gaussian filter ..... 225
Figure 192 – Essential parts of an FFT-based heterodyne receiver ..... 226
Figure 193 – Dynamic range for broadband emission as measured with the peak detector ..... 228
Figure 194 – Set-up of FFT-based system type 2 ..... 228
Figure 195 – FFT Software (“FFTemi”) screen shot ..... 231
Figure 196 – Example of pulse generator measurement with antenna ..... 232
Figure 197 – Radiated emission measurement of a motor – peak detector ..... 232
Figure 198 – Angular characterization of a PC ..... 233
Figure 199 – Example FFT IF analysis display ..... 234
Figure 200 – Equivalent radiated measurement methods (30 MHz to 300 MHz) ..... 238
Figure 201 – Measured relationship between field strength $E_z$ and CM current $I_{cm}$ for various termination resistances $R$ ..... 238
Figure 202 – Modelled relationship between field strength $E_z$ and CM current $I_{cm}$ using EUT height 0,8 m, measurement distance 3 m, receive antenna height 1 m ..... 240
Figure 203 – Limit for the terminal voltage at the CDN ..... 240
Figure 204 – Results of a Philips 11-lab internal CDN RRT using an artificial class 1 EUT – expanded uncertainty nearly 10 dB ..... 242
Figure 205 – Block diagram for CDNE-measurement method ..... 243
Figure A.1 – Example plot using the expression $P_t + G = P_q + 2$ ..... 253
Figure A.2 – Examples of a number of microwaves measured for $P_q$ and $P_t$ ..... 255
Figure B.1 – Definition of the ring-shaped area round the transmitter $T$ ..... 257
Figure C.1 – The permissible ranges of $U_h$ and $G$ are within the polygon $\{G_L,U_a\}$, $\{G_L,U_b\}$, $\{G_U,U_d\}$, $\{G_l,U_c\}$ and $\{G_L,U_a\}$. For the given value $U_L$ the double-shaded area represents $pr\{U_h \geq U_L\}$ ..... 261

IECNORM.COM : Click to view the full PDF of CISPR TR 16-3:2020 RLV

Figure F.1 – Vertical radiation patterns of horizontally polarized fields, 109 MHz, 300 m scan radius (adapted from [34]) ..... 269
Figure F.2 – Vertical radiation patterns of horizontally polarized fields, 109 MHz, 300 m scan radius (adapted from [34]) ..... 270
Figure F.3 – Vertical radiation patterns of horizontally polarized fields, 109 MHz, 300 m scan radius (adapted from [34]) ..... 271
Figure F.4 – Vertical radiation patterns of horizontally polarized fields, 109 MHz, 300 m scan radius (adapted from [34]) ..... 272
Figure G.1 – Geometry and coordination system for a single magnetic field dipole ..... 273
Figure G.2 – Configuration of measurement of an EUT in an LLA with two slits ..... 274
Figure G.3 – Transformer model representation of a disturbance source inside an LLA ..... 275
Figure G.4 – Transfer functions $f_c(\omega)$, $g_c(\omega)$ and their product (expressed in dB) as a function of frequency for a 2 m LLAS ..... 278
Figure G.5 – Sensitivity $S_D$ of an LLAS with diameter $D$ relative to an LLAS with 2 m diameter (Figure C.11 of CISPR 16-1-4:2019 [102]) ..... 279
Figure G.6 – Setup of the LLAS verification dipole for verification of an LLAS ..... 280
Figure G.7 – Geometry model of LLA for numerical computation of Neumann integral [113] ..... 283
Figure G.8 – LLAS verification dipole excluding the coupling effect from the LLAS loops ..... 283
Figure G.9 – Network model representation of the LLAS verification dipole fed by a generator source and the LLA ..... 284
Figure G.10 – First version of the reference validation factor for an LLA of 2 m diameter (Figure C.8 of CISPR 16-1-4:2010 [102]) ..... 284
Figure G.11 – Reference validation factors for an LLA of 2 m, 3 m and 4 m diameter (Figure C.8 of CISPR 16-1-4:2019 and CISPR 16-1-4:2019/AMD1:2020 [102]) ..... 285
Figure G.12 – Relative sensitivities of the LLAS verification dipole for an LLAS with different diameters (relative to an LLAS of 2 m diameter) ..... 286
Figure G.13 – Comparison of analytical and numerical (NEC2) calculations of the reference validation factors ..... 286
Figure G.14 – Magnetic field dipole moment of a small loop radiator in free space ..... 288
Figure G.15 – EUT above a ground plane and the coordinate system and possible magnetic field dipole orientations ..... 288
Figure G.16 – Magnetic field strength resulting from a source and its image below the ground plane (side view) ..... 288
Figure G.17 – Magnetic field strength expressed in dB(µA/m) of three magnetic field dipole orientations at three distances ..... 289
Figure G.18 – Conversion factors $C_{dA}$ [for conversion into dB(µA/m)] for three standard measurement distances $d$ (replicated Figure C.10 of CISPR 16-1-4:2010; exclusive the 30 m curve [102]) ..... 290
Figure G.19 – Conversion factors for calculating magnetic field strength at 10 m or 30 m ..... 290

Table 1 – Comparative response of slideback peak, quasi-peak and average detectors to sine wave, periodic pulse and Gaussian waveform ..... 25
Table 2 – Characteristics of gate generator and modulator to simulate various types of broadband interference ..... 31
Table 3 – Summary results of building-effect, $A_b$, analysis ..... 41
Table 4 – Summary of results of $G$-factor analysis ..... 44
Table 5 – Summary of $L_o$ factors (far-field) ..... 44

IECNORM.COM : Click to view the full PDF of CISPR TR 16-3:2020 RLV

Table 6 – Summary of truncation parameters of $f(G)$ ..... 45
Table 7 – Summary results of equivalent-resistance analysis ..... 46
Table 8 – Example of field-strength classification ..... 49
Table 9 – Example of voltage classification assuming for the outdoor field strength: $E_{max}$ = 60 V/m and $E_{min}$ = 0,01 V/m ..... 50
Table 10 – Summary of the parameters used in the numerical examples presented in Figure 16 and Figure 17 ..... 54
Table 11 – Frequencies of interest in ITU designated bands from Table 9 of CISPR 11:2009 ..... 61
Table 12 – Electrical constants for “medium dry ground” [31] (CCIR: medium dry ground; rocks; sand; medium sized towns[32]) ..... 62
Table 13 – Electrical constants for “wet ground” [31] (CCIR: marshes (fresh water); cultivated land [24]) and “very dry ground” [31] (CCIR: very dry ground; granite mountains in cold regions; industrial areas [32]) ..... 62
Table 14 – Estimates of the errors in prediction of radiation in vertical directions based on a measurement height scan from 1 m to 4 m at known distances, $d$; frequency = 75 MHz (adapted from [39]) ..... 70
Table 15 – Estimates of the errors in prediction of radiation in vertical directions based on a measurement height scan from 1 m to 4 m at known distances, $d$; frequency = 110 MHz (adapted from [39]) ..... 74
Table 16 – Estimates of the errors in prediction of radiation in vertical directions based on a measurement height scan from 1 m to 4 m at known distances, $d$; frequency = 243 MHz (adapted from [39]) ..... 79
Table 17 – Estimates of the errors in prediction of radiation in vertical directions based on a measurement height scan from 1 m to 4 m at known distances, $d$; frequency = 330 MHz (adapted from [39]) ..... 84
Table 18 – Estimates of the errors in prediction of radiation in vertical directions based on a measurement height scan from 1 m to 4 m at known distances, $d$; frequency = 1 000 MHz (adapted from [39]) ..... 87
Table 19 – Predictability of radiation in vertical directions at 100 kHz, using ground-based measurements of horizontally oriented $H$-field at distances up to 3 km from the source (figures are located in 4.6.8) ..... 104
Table 20 – Predictability of radiation in vertical directions at 1 MHz, using ground-based measurements of horizontally oriented $H$-field at distances up to 300 m from the source (figures are located in 4.6.8) ..... 105
Table 21 – Predictability of radiation in vertical directions at 10 MHz, using ground-based measurements of horizontally oriented $H$-field at distances up to 300 m from the source (figures are located in 4.6.8) ..... 106
Table 22 – Predictability of radiation in vertical directions at 30 MHz, using ground-based measurements of horizontally oriented $H$-field at distances up to 300 m from the source (figures are located in 4.6.8) ..... 107
Table 23 – Conditions for measuring communication quality degradation ..... 148
Table 24 – Average and RMS values of noise level normalized by $N_0$ ..... 149
Table 25 – Conditions for measuring communication quality degradation of Bluetooth ..... 151
Table 26 – Average and RMS values of noise level normalized by $N_0$ ..... 152
Table 27 – Average and RMS values of noise level normalized by $N_0$ ..... 153
Table 28 – Conditions for measuring communication quality degradation of W-CDMA ..... 155
Table 29 – Average and RMS values of noise level normalized by $N_0$ ..... 156
Table 30 – Conditions for measuring the PHS throughput ..... 158
Table 31 – Conditions for measuring the BER of PHS ..... 158

IECNORM.COM : Click to view the full PDF of CISPR TR 16-3:2020 RLV

Table 32 – Average and RMS values of noise level normalized by $N_0$ ..... 159
Table 33 – Overview of types of interference used in the experimental study of weighting characteristics ..... 171
Table 34 – DRM radio stations received for the measurement of the weighting characteristics ..... 175
Table 35 – Comparison of BER values for the same interference level ..... 179
Table 36 – Transmission parameters of DVB-T systems used in various countries ..... 180
Table 37 – Example of measurement results in dB(μV) of unmodulated and FM modulated carriers for various detectors (bandwidth 120 kHz) ..... 192
Table 38 – Survey of the corner frequencies found in the various measurement results ..... 193
Table 39 – Measurement results for broadband disturbance sources (measurements with RMS-average and quasi-peak detectors are normalized to average detector values) ..... 197
Table 40 – Expected deviations between different laboratories for small EUTs due to variations of the impedance $Z_{apparent}$ at point B ..... 198
Table 41 – Calibration measurement results format ..... 207
Table 42 – Scan times ..... 225
Table 43 – Sampling rates for different $B_{WIF}$ ..... 229
Table 44 – Scan times for a scan 30 MHz to 1 GHz ..... 230

IECNORM.COM : Click to view the full PDF of CISPR TR 16-3:2020 RLV

INTERNATIONAL ELECTROTECHNICAL COMMISSION

_____

# SPECIFICATION FOR RADIO DISTURBANCE AND IMMUNITY MEASURING APPARATUS AND METHODS –

## Part 3: CISPR technical reports

## FOREWORD

1) The International Electrotechnical Commission (IEC) is a worldwide organization for standardization comprising all national electrotechnical committees (IEC National Committees). The object of IEC is to promote international co-operation on all questions concerning standardization in the electrical and electronic fields. To this end and in addition to other activities, IEC publishes International Standards, Technical Specifications, Technical Reports, Publicly Available Specifications (PAS) and Guides (hereafter referred to as "IEC Publication(s)"). Their preparation is entrusted to technical committees; any IEC National Committee interested in the subject dealt with may participate in this preparatory work. International, governmental and non-governmental organizations liaising with the IEC also participate in this preparation. IEC collaborates closely with the International Organization for Standardization (ISO) in accordance with conditions determined by agreement between the two organizations.
2) The formal decisions or agreements of IEC on technical matters express, as nearly as possible, an international consensus of opinion on the relevant subjects since each technical committee has representation from all interested IEC National Committees.
3) IEC Publications have the form of recommendations for international use and are accepted by IEC National Committees in that sense. While all reasonable efforts are made to ensure that the technical content of IEC Publications is accurate, IEC cannot be held responsible for the way in which they are used or for any misinterpretation by any end user.
4) In order to promote international uniformity, IEC National Committees undertake to apply IEC Publications transparently to the maximum extent possible in their national and regional publications. Any divergence between any IEC Publication and the corresponding national or regional publication shall be clearly indicated in the latter.
5) IEC itself does not provide any attestation of conformity. Independent certification bodies provide conformity assessment services and, in some areas, access to IEC marks of conformity. IEC is not responsible for any services carried out by independent certification bodies.
6) All users should ensure that they have the latest edition of this publication.
7) No liability shall attach to IEC or its directors, employees, servants or agents including individual experts and members of its technical committees and IEC National Committees for any personal injury, property damage or other damage of any nature whatsoever, whether direct or indirect, or for costs (including legal fees) and expenses arising out of the publication, use of, or reliance upon, this IEC Publication or any other IEC Publications.
8) Attention is drawn to the Normative references cited in this publication. Use of the referenced publications is indispensable for the correct application of this publication.
9) Attention is drawn to the possibility that some of the elements of this IEC Publication may be the subject of patent rights. IEC shall not be held responsible for identifying any or all such patent rights.

**This redline version of the official IEC Standard allows the user to identify the changes made to the previous edition. A vertical bar appears in the margin wherever a change has been made. Additions are in green text, deletions are in strikethrough red text.**

IECNORM.COM : Click to view the full PDF of CISPR TR 16-3:2020 RLV

The main task of IEC technical committees is to prepare International Standards. However, a technical committee may propose the publication of a technical report when it has collected data of a different kind from that which is normally published as an International Standard, for example "state of the art."

CISPR 16-3, which is a Technical Report, has been prepared by CISPR subcommittee A: Radio-interference measurements and statistical methods.

This fourth edition cancels and replaces the third edition published in 2015. This edition constitutes a technical revision.

The main technical change with respect to the previous edition consists of the addition of detailed background information on the large loop antenna system (LLAS) and its measurement method in general and on the models and equations which apply to calculate the reference validation factor and conversion factor curves.

The text of this Technical Report is based on the following documents:

| Draft TR | Report on voting |
|---|---|
| CIS/A/1298/DTR | CIS/A/1310/RVDTR |

Full information on the voting for the approval of this Technical Report can be found in the report on voting indicated in the above table.

This publication has been drafted in accordance with the ISO/IEC Directives, Part 2.

A list of all parts of the CISPR 16 series can be found, under the general title *Specification for radio disturbance and immunity measuring apparatus and methods*, on the IEC website.

The committee has decided that the contents of the base publication and its amendments will remain unchanged until the stability date indicated on the IEC web site under "http://webstore.iec.ch" in the data related to the specific publication. At this date, the publication will be

- reconfirmed,
- withdrawn,
- replaced by a revised edition, or
- amended.

IECNORM.COM : Click to view the full PDF of CISPR TR 16-3:2020 RLV

**IMPORTANT – The 'colour inside' logo on the cover page of this publication indicates that it contains colours which are considered to be useful for the correct understanding of its contents. Users should therefore print this document using a colour printer.**

# SPECIFICATION FOR RADIO DISTURBANCE AND IMMUNITY MEASURING APPARATUS AND METHODS –

## Part 3: CISPR technical reports

## 1 Scope

This part of CISPR 16 is a collection of technical reports (Clause 4) that serve as background and supporting information for the various other standards and technical reports in CISPR 16 series. In addition, background information is provided on the history of CISPR, as well as a historical reference on the measurement of interference power from household and similar appliances in the VHF range (Clause 5).

Over the years, CISPR prepared a number of recommendations and reports that have significant technical merit but were not generally available. Reports and recommendations were for some time published in CISPR 7 and CISPR 8.

At its meeting in Campinas, Brazil, in 1988, CISPR subcommittee A agreed on the table of contents of CISPR 16-3, and to publish the reports for posterity by giving the reports a permanent place in CISPR 16-3.

With the reorganization of CISPR 16 in 2003, the significance of CISPR limits material was moved to CISPR 16-4-3, whereas recommendations on statistics of disturbance complaints and on the report on the determination of limits were moved to CISPR 16-4-4:2007. The contents of Amendment 1 (2002) of CISPR 16-3:2000 were moved to CISPR 16-4-1.

NOTE As a consolidated collection of independent technical reports, this document ~~may~~ can contain symbols that have differing meanings from one clause to the next. Attempts have been made to minimize this to the extent possible at the time of editing.

## 2 Normative references

The following documents are referred to in the text in such a way that some or all of their content constitutes requirements of this document. For dated references, only the edition cited applies. For undated references, the latest edition of the referenced document (including any amendments) applies.

CISPR 11:2009, *Industrial, scientific and medical equipment – Radio-frequency disturbance characteristics – Limits and methods of measurement*[1]

CISPR 16-1-1, *Specification for radio disturbance and immunity measuring apparatus and methods – Part 1-1: Radio disturbance and immunity measuring apparatus – Measuring apparatus*

IEC 60050-161:1990, *International Electrotechnical Vocabulary (IEV) – Part 161: Electromagnetic compatibility*

IECNORM.COM : Click to view the full PDF of CISPR TR 16-3:2020 RLV

[1] 5th edition (2009). This 5th edition has been replaced in 2016 by a 6th Edition CISPR 11, Industrial, scientific and medical equipment – Radio-frequency disturbance characteristics – Limits and methods of measurement.

IEC 60050-300:2001, *International Electrotechnical Vocabulary (IEV) – Electrical and electronic measurements and measuring instruments – Part 311: General terms relating to measurements – Part 312: General terms relating to electrical measurements – Part 313: Types of electrical measuring instruments – Part 314: Specific terms according to the type of instrument*

ISO/IEC Guide 99:2007, *International vocabulary of metrology – Basic and general concepts and associated terms (VIM)*

## 3 Terms, definitions and abbreviated terms

### 3.1 Terms and definitions

For the purposes of this document, the terms and definitions given in IEC 60050-161, IEC 60050-300, ISO/IEC Guide 99, as well as the following apply.

NOTE While the symbol $U$ is commonly used in CISPR publications to represent uncertainty, in this technical report the symbols $U$ and $V$ are used interchangeably to represent "voltage" in order to accommodate the legacy diagrams contained herein.

**3.1.1**
**asymmetric voltage**
radio-frequency disturbance voltage appearing between the electrical mid-point of the mains terminals and earth

Note 1 to entry: It is sometimes called the common-mode voltage and is half the vector sum of $V_a$ and $V_b$, i.e. $(V_a + V_b)/2$

Note 2 to entry: $V_a$ is the vector voltage between one of the mains terminals and earth, and $V_b$ is the vector voltage between the other mains terminal and earth.

**3.1.2**
**bandwidth**
$B_n$
width of the overall selectivity curve of the receiver between two points at a stated attenuation, below the mid-band response

Note 1 to entry: The bandwidth is represented by the symbol $B_n$, where $n$ is the stated attenuation in decibels.

~~**3.1.3**~~
~~**CISPR indicating range**~~
~~range specified by the manufacturer which gives the maximum and the minimum meter indications within which the receiver meets the requirements of CISPR 16-1-1~~

**3.1.3**
**electrical charge time constant**
$T_C$
time needed after the instantaneous application of a constant sine-wave voltage to the stage immediately preceding the input of the detector for the output voltage of the detector to reach 63 % of its final value

Note 1 to entry: This time constant is determined as follows. A sine-wave signal of constant amplitude and having a frequency equal to the mid-band frequency of the IF amplifier is applied to the input of the stage immediately preceding the detector. The indication $\alpha_{max}$ of an instrument having no inertia (for example, a cathode-ray oscilloscope) connected to a terminal in the DC amplifier circuit so as not to affect the behaviour of the detector, is noted. The level of the signal is chosen such that the response of the stages concerned remains within the linear operating range. A sine-wave signal of this level, applied for a limited time only and having a wave train of rectangular envelope is gated such that the deflection registered is $0{,}63\alpha_{max}$. The duration of this signal is equal to the charge time of the detector.

IECNORM.COM : Click to view the full PDF of CISPR TR 16-3:2020 RLV

**3.1.4**
**electrical discharge time constant**
$T_D$
time needed after the instantaneous removal of a constant sine-wave voltage applied to the stage immediately preceding the input of the detector for the output of the detector to fall to 37 % of its initial value

Note 1 to entry: The method of measurement is analogous to that for the charge time constant, but instead of a signal being applied for a limited time, the signal is interrupted for a definite time. The time taken for the deflection to fall to 0,37$D$ is the discharge time constant of the detector.

**3.1.5**
**impulse bandwidth**
$B_{imp}$

$$B_{imp} = \frac{A(t)_{max}}{2G_o \times A_{imp}} \quad (1)$$

where

$A(t)_{max}$ is the peak of the envelope at the IF output of the receiver with an impulse area $A_{imp}$ applied at the receiver input;

$G_o$ is the gain of the circuit at the centre frequency;

specifically, for two critically coupled tuned transformers,

$$B_{imp} = 1{,}05 \times B_6 = 1{,}31 \times B_3 \quad (2)$$

where $B_6$ and $B_3$ are respectively the bandwidths at the –6 dB and –3 dB points (see CISPR 16-1-1 for further information)

**3.1.6**
**impulse area**
~~(sometimes called~~ impulse strength~~)~~
$A_{imp}$
voltage-time area of a pulse defined by the integral:

$$A_{imp} = \int_{-\infty}^{+\infty} V(t)dt \text{ expressed in } \mu Vs \text{ or } dB(\mu Vs) \quad (3)$$

Note 1 to entry: Spectral density $D$ is related to impulse area and is expressed in μV/MHz or dB(μV)/MHz. For rectangular impulses of pulse duration $T$ at frequencies $f << 1/T$, the relationship $D = 2 \times 10^6 / A_{imp}$ applies because $D$ is calibrated in RMS values of a corresponding sine wave.

**3.1.7**
**mechanical time constant of a critically damped indicating instrument**
$T_M$

$$T_M = \frac{T_L}{2\pi} \quad (4)$$

where $T_L$ is the period of free oscillation of the instrument with all damping removed

Note 1 to entry: For a critically damped instrument, the equation of motion of the system may be written as

$$T_M^2\left(\frac{d^2\alpha}{dt^2}\right) + 2T_M\frac{d\alpha}{dt} + \alpha = ki \quad (5)$$

where

IECNORM.COM : Click to view the full PDF of CISPR TR 16-3:2020 RLV

$\alpha$ is the deflection;

$i$ is the current through the instrument;

$k$ is a constant.

It can be deduced from this relation that this time constant is also equal to the duration of a rectangular pulse (of constant amplitude) that produces a deflection equal to 35 % of the steady deflection produced by a continuous current having the same amplitude as that of the rectangular pulse.

Note 2 to entry: The methods of measurement and adjustment are deduced from one of the following:

a) The period of free oscillation having been adjusted to $2\pi T_M$, damping is added so that $\alpha_{TM}$ = 0,35 $\alpha_{max}$.

b) When the period of oscillation cannot be measured, the damping is adjusted to be just below critical such that the over-swing is not greater than 5 % and the moment of inertia of the movement is such that $\alpha_{TM}$ = 0,35 $\alpha_{max}$.

**3.1.8**
**overload factor**
ratio of the level that corresponds to the range of practical linear function of a circuit (or a group of circuits) to the level that corresponds to full-scale deflection of the indicating instrument

Note 1 to entry: The maximum level at which the steady-state response of a circuit (or group of circuits) does not depart by more than 1 dB from ideal linearity defines the range of practical linear function of the circuit (or group of circuits).

**3.1.9**
**symmetric voltage**
radio-frequency disturbance voltage appearing between the wires of a two-wire circuit, such as a single-phase mains supply

Note 1 to entry: Symmetric voltage is sometimes called the differential mode voltage and is the vector difference between $V_a$ and $V_b$, i.e. ($V_a$ – $V_b$). Refer to the NOTE in 3.1.1 for definition of $V_a$ and $V_b$.

**3.1.10**
**unsymmetric voltage**
amplitude of the vector voltage, $V_a$ or $V_b$

Note 1 to entry: Unsymmetric voltage is the voltage measured by the use of an artificial mains V-network. Refer to the NOTE in 3.1.1 for definition of $V_a$ and $V_b$.

**3.1.11**
**weighting** (of e.g. impulsive disturbance)
pulse-repetition-frequency (PRF) dependent conversion (mostly reduction) of a peak-detected impulse voltage level to an indication that corresponds to the interference effect on radio reception

Note 1 to entry: For the analogue receiver, the psychophysical annoyance of the interference is a subjective quantity (audible or visual, usually not a certain number of misunderstandings of a spoken text).

Note 2 to entry: For the digital receiver, the interference effect is an objective quantity that may be defined by the critical bit error ratio (BER) or bit error probability (BEP) for which perfect error correction can still occur, or by another objective and reproducible parameter.

**3.1.11.1**
**weighted disturbance measurement**
measurement of disturbance using a weighting detector

**3.1.11.2**
**weighting characteristic**
peak voltage level as a function of PRF for a constant effect on a specific radiocommunication system, i.e. the disturbance is weighted by the radiocommunication system itself

IECNORM.COM : Click to view the full PDF of CISPR TR 16-3:2020 RLV

**3.1.11.3**
**weighting detector**
detector which provides an agreed weighting function

**3.1.11.4**
**weighting factor**
value of the weighting function relative to a reference PRF or relative to the peak value

Note 1 to entry: Weighting factor is expressed in dB.

**3.1.11.5**
**weighting function**
**weighting curve**
relationship between input peak voltage level and PRF for constant level indication of a measuring receiver with a weighting detector, i.e. the curve of response of a measuring receiver to repeated pulses

IECNORM.COM : Click to view the full PDF of CISPR TR 16-3:2020 RLV

### 3.2 Abbreviated terms

| | |
|---|---|
| ADPCM | Adaptive differential pulse code modulation |
| AGC | Automatic gain control |
| AM | Amplitude modulation |
| AMN | Artificial mains network |
| APD | Amplitude probability distribution |
| BEP | Bit error probability |
| BER | Bit error rate |
| CDN | Coupling decoupling network |
| CDNE | CDN for emission measurement |
| CM | Common mode |
| CMAD | Common mode absorption device |
| COFDM | Coded orthogonal frequency division multiplex |
| DAB | Digital audio broadcasting |
| DDC | Digital down-conversion |
| DECT | Digitally enhanced cordless telephone |
| DIF | Decimated in frequency |
| DIT | Decimated in time |
| DM | Differential mode |
| DPCH | Dedicated physical channel |
| DPDCH | Dedicated physical data channel |
| DQPSK | Digital QPSK |
| DRM | Digital radio mondiale |
| DVB-T | Digital video broadcasting – terrestrial |
| EMC | Electromagnetic compatibility |
| EMI | Electromagnetic emissions |
| ERP | Equivalent radiating power |
| EUT | Equipment under test |
| FER | Frame error rate |
| FFT | Fast Fourier transform |
| FM | Frequency modulation |
| GSM | Global system for mobile communications |
| GMSK | Gaussian minimum shift keying |
| GTEM | Gighertz TEM |
| IF | Intermediate frequency |
| ILS | Instrument landing system |
| ISM | Industrial, scientific and medical |
| ITU | International Telecommunications Union |
| LAN | Local area network |
| LAS | Loop antenna system |
| LCL | Longitudinal conversion loss |
| LISN | Line-impedance stabilization network |
| LLA | Large loop antenna |
| LLAS | Large loop antenna system |
| LW | Long wave |
| MPEG | Moving picture expert group |
| MW | Medium wave |
| MWO | Microwave oven |
| OATS | Open-area test site |
| OFDM | Orthogonal frequency division multiplex |
| PC | Personal computer |
| PHS | Personal handy phone system |
| PRBS | Pseudo random binary sequence |
| PRF | Pulse-repetition frequency |
| QAM | Quadrature amplitude modulation |
| QPSK | Quadrature phase-shift keying |
| RAM | Random access memory |
| RBER | Residual bit error rate |
| RF | Radio frequency |
| RMS | Root-mean square |
| RRT | Round robin test |
| RSA | Ring-shaped area |
| SAC | Semi-anechoic chamber |
| SOLT | Short-open-load-through |
| STFFT | Short-time FFT |
| SW | Short wave |
| TEM | Transverse electromagnetic |
| TETRA | Terrestrial trunked radio |
| TRL | Through-reflect-line |
| TTE | Telephone terminal equipment |
| VNA | Vector network analyzer |
| W-CDMA | Wideband code division multiple access |

IECNORM.COM : Click to view the full PDF of CISPR TR 16-3:2020 RLV

# 4 Technical reports

## 4.1 Correlation between measurements made with apparatus having characteristics differing from CISPR characteristics and measurements made with CISPR apparatus

### 4.1.1 General

CISPR standards for instrumentation and methods of measurement have been established to provide a common basis for controlling radio interference from electrical and electronic equipment in international trade.

The basis for establishing limits is that of providing a reasonably good correlation between measured values of the interference and the degradation it produces in a given communications system. The acceptable value of signal-to-noise ratio in any given communication system is a function of its parameters, including bandwidth, type of modulation, and other design factors. As a consequence, various types of measurements are used in the laboratory in research and development work in order to carry out the required investigations.

The purpose of this subclause is to analyse the dependence of the measured values on the parameters of the measuring equipment and on the waveform of the measured interference.

### 4.1.2 Critical interference-measuring instrument parameters

The most critical factors in determining the response of an instrument for measuring interference are the following: the bandwidth, the detector, and the type of interference being measured. Considered to be of secondary importance, but, nevertheless, quite significant in correlating instruments under particular circumstances, are: overload factor, AGC design (if used), image and other spurious responses, and meter time constant and damping.

For purposes of discussion, reference is made to three fundamental types of radio noise: impulse, random and sine wave. The dependence of the response to each of these on the bandwidth and the type of detector is given in Table 1. In Table 1, $\delta$ is the magnitude of the impulse strength, $\Delta f_{\text{imp}}$ is the impulse bandwidth, $\Delta f_{\text{rn}}$ is the random noise bandwidth, $P(\alpha)$ is the pulse response for the quasi-peak detector, $f_{\text{PR}}$ is the pulse repetition frequency, and $E'$ is the spectral amplitude of the random noise. The relative responses of various detectors to impulse interference for one instrument are shown in Figure 1.

Table 1 shows that the dependence of the noise meter response on bandwidth is different for all three types of interference. If the waveform being measured can be defined as being any of the three types listed in Table 1, and if a standard source provides that type of waveform, then by using the substitution method, a satisfactory calibration can be obtained for any instrument with adequate overload factor independent of its bandwidth. Thus, with a purely random interference or a purely impulsive interference of known repetition rate, calibration can be made using a corresponding source, or a correlation factor calculated on the basis of known circuit parameters.

If a particular interference waveform is of an intermediate type between these three types, then the correction or correlation factors will also be intermediate. In any given case, it will be necessary to classify the noise waveform in such a manner that a significant correlation factor can be established. Hence, in order to develop this subject to any significant extent, it will be necessary to examine typical interference sources and to determine the extent to which they are of impulsive, random, or sine-wave type.

If an interference measuring set with several types of detectors is available, for example, peak, quasi-peak and average, the type of interference can be assessed by measuring the

IECNORM.COM : Click to view the full PDF of CISPR TR 16-3:2020 RLV

ratios of the readings obtained with these detectors. These ratios will, of course, depend upon the bandwidth and other characteristics of the instrument being used for the measurement.

**Table 1 – Comparative response of slideback peak, quasi-peak and average detectors to sine wave, periodic pulse and Gaussian waveform**

| Input waveform | Detector type | | | |
|---|---|---|---|---|
| | Slideback peak (sb) | Quasi-peak:1/600 (qp) | Field intensity (average) | RMS |
| CW sine wave | $e$ | $e$ | $e$ | $e$ |
| Periodic pulse (no overlap) | $1{,}41\ \delta\ \Delta f_{imp}$ | $1{,}41\ \delta\ \Delta f_{imp}\ P(\alpha)$ | $1{,}41\ \delta f_{PR}$ | $1{,}41\ \delta\ \sqrt{f_{PR}\ \Delta f_{imp}}$ |
| Random | – | $1{,}85\ \sqrt{\Delta f_{rn}\ E'}$ | $0{,}88\ \sqrt{\Delta f_{rn}\ E'}$ | $\sqrt{\Delta f_{rn}\ E'}$ |

**Key**

$e$ is the RMS value of the applied sine wave.

$P(\alpha)$ is given in Figure 2.

$E'$ is the spectral strength in RMS V/Hz bandwidth.

$\delta$ is the impulse strength. It is assumed the instrument is calibrated in terms of the RMS value of a sine wave. It is assumed that characteristics of the envelope are measured by the detector on random noise.

$\Delta f_{imp}$ is the impulse bandwidth.

$\Delta f_{rn}$ is the random noise bandwidth.

$f_{PR}$ is the pulse repetition frequency.

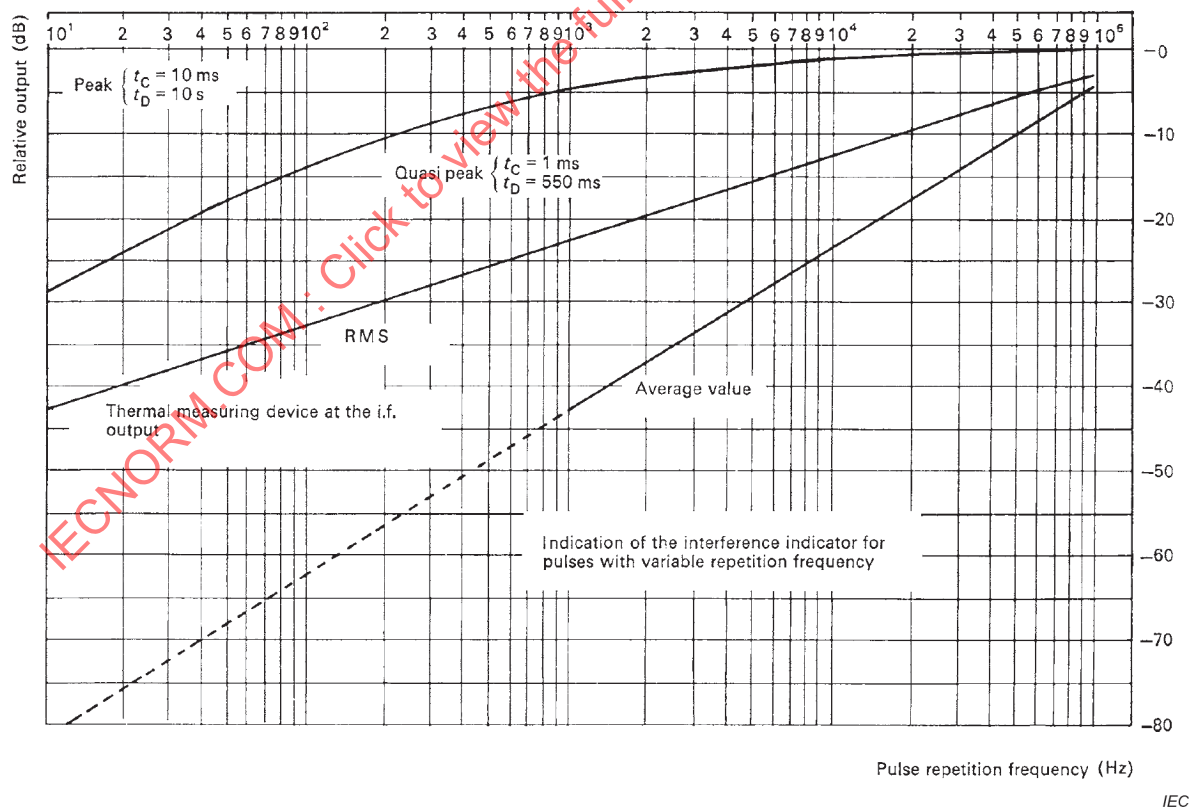


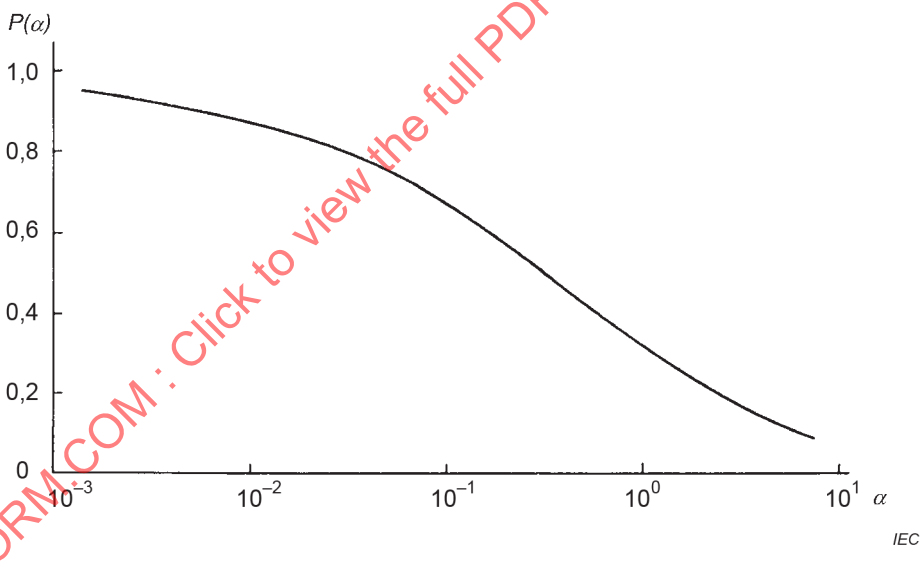

**Figure 1 – Relative response of various detectors to impulse interference**

IECNORM.COM : Click to view the full PDF of CISPR TR 16-3:2020 RLV

### 4.1.3 Impulse interference – correlation factors

The quasi-peak detector response of any interference measuring set to regularly repeated impulses of uniform amplitude can be determined by the use of the "pulse response curve" which is shown in Figure 2. This figure shows the response of the detector in percentage of peak response for any given bandwidth and value of charge resistance and discharge resistance. Applying this curve, it should be noted that the peak itself is dependent upon the bandwidth, so that as the bandwidth increases, the peak value increases, but the percentage of peak, which is read by the detector, decreases; over a narrow range of bandwidth, these effects tend to counteract each other. The bandwidth used in this curve is the 6 dB bandwidth, which for the passband characteristics typical of most interference measuring equipment, is about 5 % less than the so-called impulse bandwidth. A theoretical comparison of instruments having various bandwidths and detector parameters with the CISPR instrument is shown in Figure 3.

The response of the average detector to impulsive noise is an interesting case. The reading of an average detector for impulsive noise is independent of the bandwidth of the pre-detector stages. It is, of course, directly proportional to the repetition rate. In most cases, the reading obtained with an average detector for impulsive noise is so low as to be of no practical value unless the noise meter bandwidth is exceedingly narrow, such as of the order of a few hundred hertz. For a repetition rate of 100 Hz and a bandwidth of the order of 10 kHz, the average value would be approximately 1 % of the peak value. Such a value is too low to measure with any degree of precision. Furthermore, for many communication systems, the annoyance effect may be well above the reading obtained with the average meter. This, of course, is one of the justifications for the use of the quasi-peak instrument.



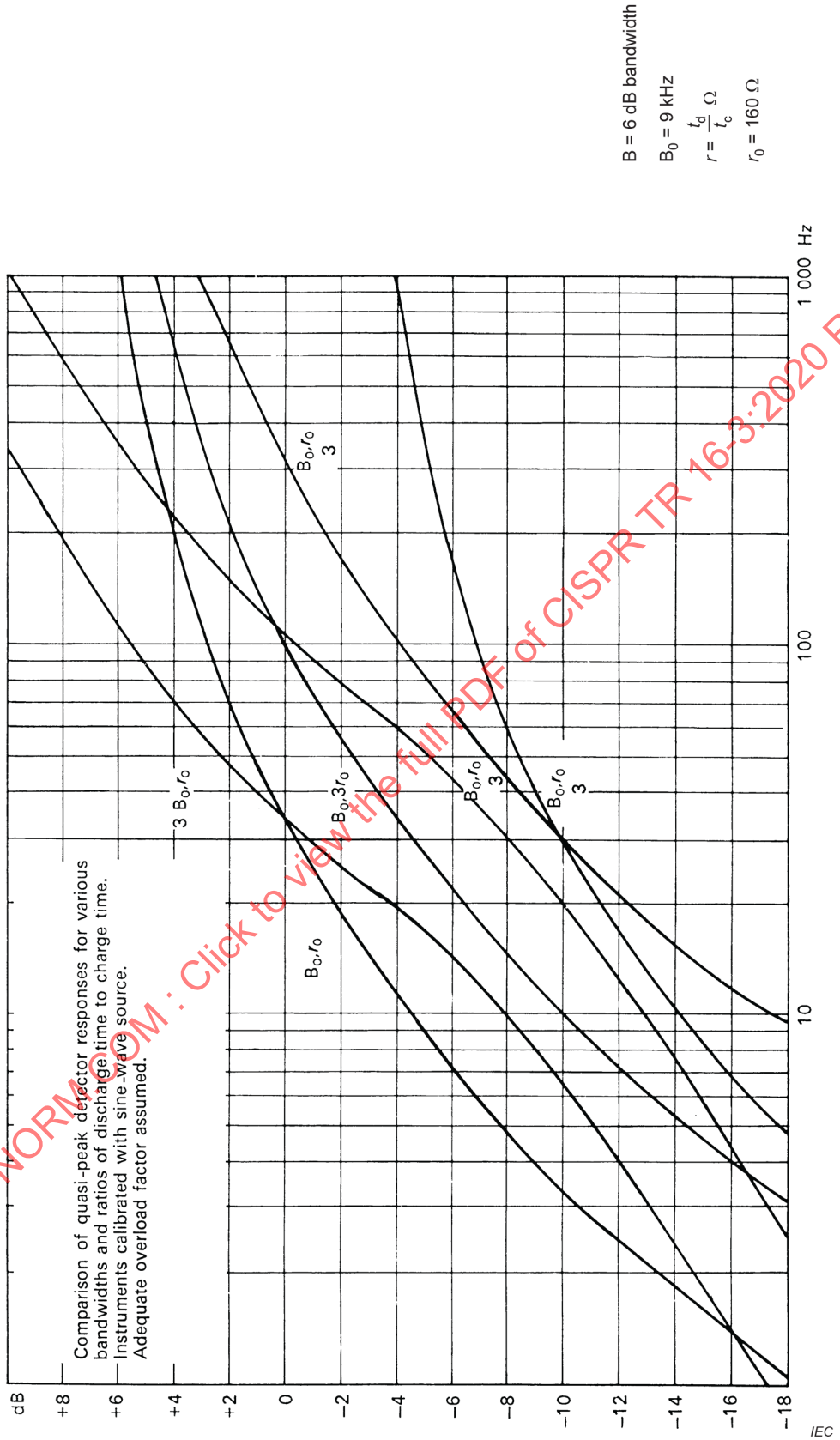

$$\alpha = \frac{(\pi R_c \Delta F)}{(R_d f_{PR})}$$

**Key**

| | |
|---|---|
| $R_c$ | charging resistance, in Ω |
| $R_d$ | discharging resistance, in Ω |
| $\Delta F$ | 6 dB bandwidth, in Hz |
| $f_{PR}$ | pulse repetition frequency, in Hz |

**Figure 2 – Pulse rectification coefficient $P(\alpha)$**

IECNORM.COM : Click to view the full PDF of CISPR TR 16-3:2020 RLV




IECNORM.COM : Click to view the full PDF of CISPR TR 16-3:2020 RLV

**Figure 3 – Pulse repetition frequency**

#### 4.1.4 Random noise

The response of a noise meter to random noise is proportional to the square root of the bandwidth. This result is independent of the type of detector used. The ratio of the random noise bandwidth to the 3-dB bandwidth is a function of the type of filter circuit. On the other hand, it has been shown that for many circuits typical of those used in interference measuring equipment, a value of about 1,04 for the ratio of effective random noise bandwidth to the 3 dB bandwidth is a reasonable figure.

#### 4.1.5 The root mean square (RMS) detector

One of the advantages of the RMS detector in correlation work is that for broadband noise the output obtained from it will be proportional to the square root of the bandwidth, i.e. the noise power is directly proportional to the bandwidth. This feature makes the RMS detector particularly desirable and is one of the main reasons for adopting the RMS detector to measure atmospheric noise. Another advantage is that the RMS detector makes a correct addition of the noise power produced by different sources, for example, impulsive noise and random noise, thus for instance allowing a high degree of background noise.

The RMS values of noise often give a good assessment of the subjective effect of interference to AM sound and television reception. However, the very wide dynamic range needed when using very wide-band instruments for measuring impulsive noise, limits the use of RMS detectors to narrow-band instruments.

#### 4.1.6 Discussion

The preceding paragraphs have indicated the theoretical basis for comparing measurements obtained with different instruments. As mentioned previously, the possibility of establishing significant correlation factors depends upon the extent to which noise can be classified and identified so that the proper correlation factors may be used. In many frequency ranges, impulsive interference appears to be the most serious; however, for power lines where corona interference is the primary concern, random interference would be expected to be more characteristic. Additional quantitative data are needed on typical interference characteristics. Another important parameter is the overload factor.

#### 4.1.7 Application to typical noise sources

##### 4.1.7.1 Commutator motors

The noise generated by commutator motors is usually a combination of impulse and random noise. The random noise originates in the varying brush contact resistance, while the impulse noise is generated from the switching action at the commutator bars. For optimum adjustment of commutation, the impulse noise can be minimized. However, where variable loading is possible, measurements have confirmed that for the peak and quasi-peak detectors, the dominant noise is of impulse type and the random component may be neglected. While the repetition rate may be of the order of 4 kHz, the effective rate is lower because the amplitude of the impulses is usually modulated at twice the line frequency. Hence, experimental results have shown that quasi-peak readings are consistent with bandwidth variations if the repetition rate of the impulse is assumed to be twice the line frequency.

Peak measurements show fluctuating levels on such noise because of the irregular nature of the commutator switching action.

The quasi-peak to average ratio is lower than would be obtained for pure impulse noise for two reasons:

1) the modulation of the commutator switching transients by line frequency produces many pulses below the measured quasi-peak level. These pulses do not contribute to the quasi-peak value but do contribute to the average.

IECNORM.COM : Click to view the full PDF of CISPR TR 16-3:2020 RLV

2) the relatively low level, but continuous, random noise can likewise contribute substantially only to the average value. Experimental values of quasi-peak to average ratio ranged from 13 dB to 23 dB with the highest ratios for the widest bandwidths (120 kHz).

#### 4.1.7.2 Impulsive sources

Tests on an ignition model, commutator motor appliances, and appliances using vibrating regulators showed reasonable agreement on instruments with the same nominal bandwidth, but with time constant ratios of the order of 3:1 on restricted portions of the output indicator scale. Deviations at higher scale values are without explanation. Relatively poor correlation was obtained on sources producing very low repetition rate pulses.

#### 4.1.7.3 Ignition interference

"CISPR Recommendation 35" recognizes that correlation between quasi-peak and peak detectors can be established as a practical matter. The conversion factor of 20 dB is explained partly on the basis of theory for uniform repeated impulses, and partly on the basis of the actual irregularity of the amplitude and wave shape of such impulses.

NOTE "CISPR Recommendation 35", from CISPR 7:1969, *Recommendations of the CISPR*, is quoted for reference:

" RECOMMENDATION No. 35
THE CORRELATION BETWEEN PEAK AND QUASI-PEAK MEASUREMENTS OF INTERFERENCE FROM IGNITION SYSTEMS
(This Recommendation closes Study Question No. 45 of 1961)
(Stockholm, 1964)

The C.I.S.P.R.,
CONSIDERING
that for the measurement of interference from the ignition systems of internal combustion engines there will, in general, be two types of detector, namely, peak and quasi-peak;

RECOMMENDS
that a correlation factor of 20 dB between peak and quasi-peak measurements of interference from ignition systems be adopted for frequencies in the range covered by C.I.S.P.R. Publication 2, i.e. when peak measurements are made the acceptable limits are 20 dB above the corresponding quasi-peak measurements; for peak measurements the engine may be operated at any speed above idling speed but for quasi-peak measurements the speed should be set as near as possible to 1 500 rev/min for multi-cylinder engines and 2 500 rev/min for single cylinder engines."

#### 4.1.7.4 Dependence on bandwidth

Comparisons of measurements made in the UK with two instruments having bandwidths of 90 kHz and 9 kHz respectively have been reported to show that for most interference sources, the values obtained are in the ratio 14 dB to 18 dB. This figure is consistent with the concept that the interference is dominated by impulse type noise but that some random components are present.

### 4.1.8 Conclusions

Analysis of data comparing the responses of various instruments shows that, in almost every case, it is possible to explain the differences in measured values on the basis of theoretical and practical considerations. In many instances, it is indicated that waveform characteristics are known to predict correlation factors adequately with an accuracy of 2 dB to 4 dB.

Further studies are needed:

a) to characterize in some detail the waveforms of various sources of interference, and

b) to correlate these waveform characteristics with measured values and the instrument parameters.

IECNORM.COM : Click to view the full PDF of CISPR TR 16-3:2020 RLV

## 4.2 Interference simulators

### 4.2.1 General

Interference simulators can be used for various applications, in particular to study signal processing in systems and equipment in the presence of interference (for example, overloading of receivers, synchronization of TV receivers, error rate of data signals, etc.) and for assessment of the annoyance caused by disturbances in broadcast and communication services.

A simulator should produce a stable and reproducible output signal, which requirement is normally not fulfilled by an actual interference source, and the simulator output waveform should show a good resemblance to the actual interference signal.

### 4.2.2 Types of interference signals

The following interference sources can be simulated.

a) Narrowband interference sources generating sine-wave signals, for example receiver oscillators and ISM equipment. An appropriate RF standard signal generator can be used to simulate these sources. ISM interference is often modulated by the mains voltage, which can be simulated by modulating the RF signal with a full-wave rectified mains signal.

b) Broadband interference sources producing continuous broadband noise, for example, gaseous discharges and corona. For simulating purposes a standard broadband noise source (saturated vacuum tube diode, zener diode or gas tube followed by a suitable broadband amplifier) can be used. In mains-fed sources of this type, mains modulation is present, but because of the non-linear behaviour of gaseous discharges the envelope of the actual noise signal can deviate appreciably from the normal full-wave rectified mains waveform. In this case, gating the noise of the simulator at a repetition frequency of twice the mains frequency can yield a good correspondence with the actual interference signal.

c) Thyristor controlled regulators with phase control generate narrow pulses of constant amplitude in an RF-channel at a repetition frequency equal to twice the mains frequency. Standard pulse generators with narrow output pulses ($10^{-7}$ s to $10^{-9}$ s width) of the same repetition frequency can be used to easily simulate these sources.

d) Ignition systems, mechanical contacts and commutator motors generate short periods (bursts) of quasi-impulsive noise. This type of noise is caused by very short pulses of regular or irregular height at random time intervals; if the average interval between adjacent pulses is less than the reciprocal of the channel bandwidth under test ($\tau_{av} < 1/B$), the pulses overlap, and because of the random phase conditions, a random fluctuating output signal (noise) results. Therefore, bursts of quasi-impulsive interference of this type can be simulated by a gated broadband noise signal.

The duration and the repetition frequency of the bursts depend on the type of interference source (see Table 2).

Ignition interference is characterized by burst durations between 20 µs and 200 µs and repetition frequencies between 30 bursts/s and 300 bursts/s depending on the number of cylinders and revolutions/min of the engine.

Mechanical contacts produce bursts (clicks) which can vary between some milliseconds (snap-off switches) and more than 200 ms. In the case of a contact device in a mains-fed circuit, the noise during the burst is modulated with the full-wave rectified mains voltage.

Commutator motors produce much shorter bursts with durations between 20 µs and 200 µs at repetition frequencies between $10^3$ bursts/s and $10^4$ bursts/s, depending on the number of commutator bars and revolutions per minute of the rotor. Also in this case, the mains supply causes a similar envelope modulation of the noise bursts.

IECNORM.COM : Click to view the full PDF of CISPR TR 16-3:2020 RLV

### 4.2.3 Circuits for simulating broadband interference

Simulators of this type should generate gated noise bursts with or without mains modulation according to the characteristics specified in Table 2. Figure 4 shows a straightforward design with a noise source followed by an appropriate amplifier of 70 dB to 80 dB gain, a gating circuit to simulate the bursts, a mains envelope modulator and an output attenuator to adjust the required output level.

**Table 2 – Characteristics of gate generator and modulator to simulate various types of broadband interference**

| Simulator signal | Burst duration | Burst repetition frequency | Mains modulation [a] |
|---|---|---|---|
| Gaseous discharge | | Continuous | Yes/no [b] |
| Ignition | 20 μs to 200 μs | 30 bursts/s to 300 bursts/s | No |
| Switches | 5 ms to 500 ms | 0,2 bursts/min to 30 bursts/min, or single | Yes/no |
| Commutator motors | 30 μs to 300 μs | $10^3$ bursts/s to $10^4$ bursts/s | Yes/no |

[a] Depending on AC or DC supply.

[b] In the case of mains modulation, gating at a repetition frequency $2f_{mains}$ and gate width of 1 ms to 2 ms may be more appropriate.

The disadvantage of this layout is that a wide usable frequency range requires a broad bandwidth for the entire circuit between noise source and output terminal. The most critical part in this respect is the high-gain amplifier. For applications in a wide frequency range (for example, 0 MHz to 1 000 MHz) such a range can be split up in several smaller ranges or a tunable amplifier may be used. Such a design complicates the construction of the simulator appreciably.

Another way to produce a gated wideband noise signal is given in the diagram of Figure 5. In this design, nanosecond pulses are generated in the output stage, for example, a step recovery diode or similar device. These pulses of constant height are triggered at random time intervals and at a sufficiently high repetition rate to cause overlap in the RF channel under test in order to result in quasi-impulsive noise in the output of the channel. Average repetition rates of a few megahertz are required for measurements in a TV channel of at least 100 kHz for measurements in an FM channel and of at least 10 kHz in an AM channel. The random occurrence of the trigger pulses is obtained from the zero crossings of a broadband signal. For this purpose the output of a noise source is fed to an appropriate amplifier which is followed by a gating circuit for burst simulation. The gated noise signal is fed to a bistable multivibrator which converts the zero crossings into pulses of random varying width from which narrow trigger pulses at random distances are generated by the monostable multivibrator.

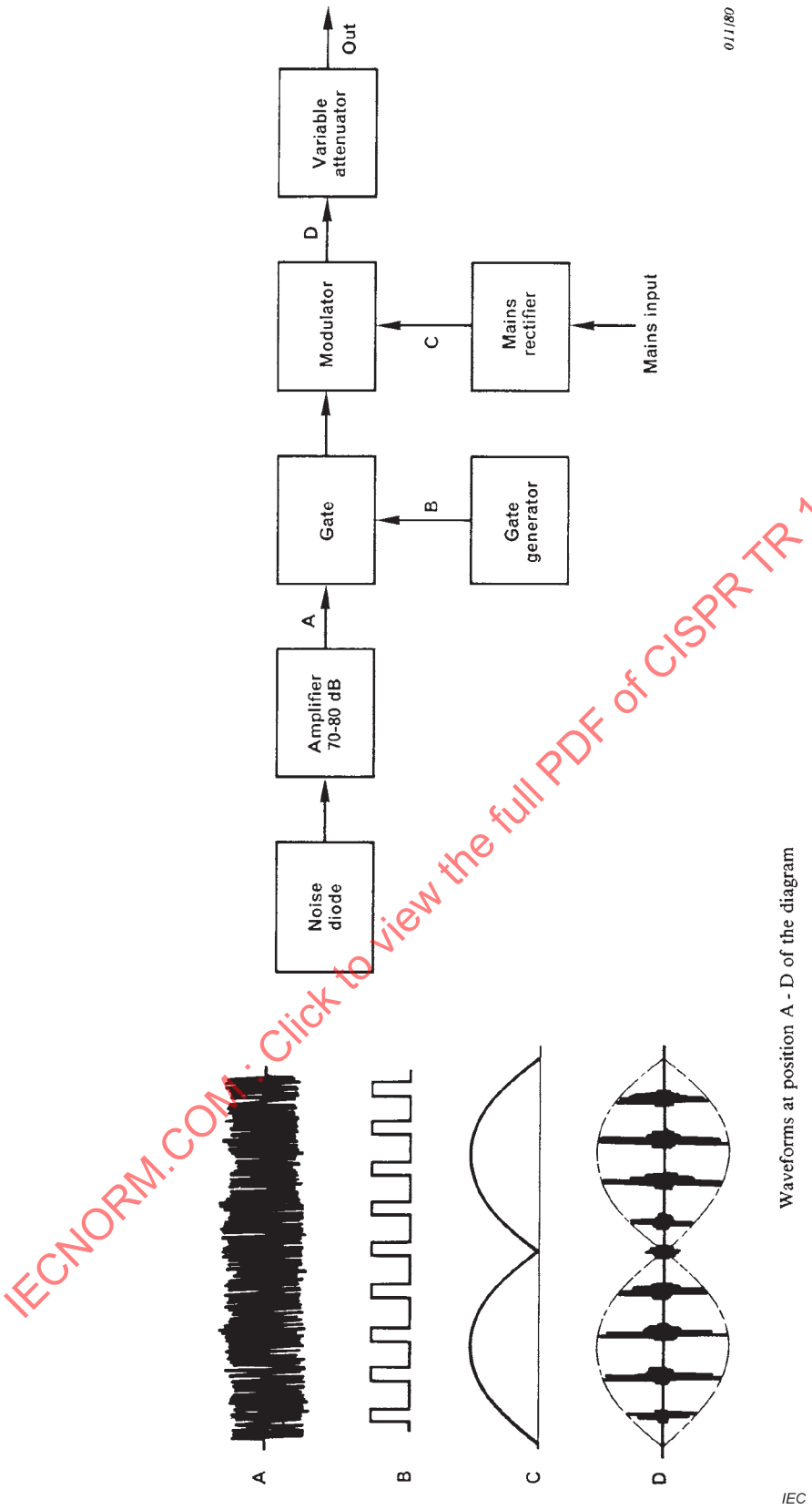
The advantage of this system over the circuit of Figure 4 is that the usable frequency range is determined by the output pulses of the step-recovery diode only. An example of such a circuit is given in Figure 6, in which circuit output pulses are generated by the step recovery diode HP0102, the pulse width is determined by the length of a short-circuited coaxial cable $L$. Ringing effects are suppressed by the fast switch diode HP2301, and mains modulation can be effected simply by modulating the supply voltage of the step recovery diode with a full-wave rectified mains voltage. Pulses of 1 ns duration and 5 V amplitude are generated and offer an output spectrum flat to about 500 MHz. Such a single pulse causes a 50 mV pulse in a TV channel and a 1 mV pulse in an FM channel; overlapping pulses add up, and the peak and quasi-peak value of the resulting signal is considerably higher.

IECNORM.COM : Click to view the full PDF of CISPR TR 16-3:2020 RLV

The bandwidth of the preceding stages which generate the trigger signal (noise source, amplifier and gating circuit) should be sufficient for the required pulse repetition rate, so for measurements in a TV channel a bandwidth of 5 MHz to 10 MHz is quite satisfactory. Moreover, the linearity of these stages is not critical because only the position of the zero crossings is important. The multivibrators have to generate steep pulses of short duration (about 0,1 μs) to drive the step-recovery diode.

In summary, the circuit according to Figure 4 is very useful for broadband interference simulators to be operated in a limited frequency range, whereas the circuit of Figure 5 is more suitable for simulators intended for wideband use.

IECNORM.COM : Click to view the full PDF of CISPR TR 16-3:2020 RLV




IECNORM.COM : Click to view the full PDF of CISPR TR 16-3:2020 RLV

**Figure 4 – Block diagram and waveforms of a simulator generating noise bursts**

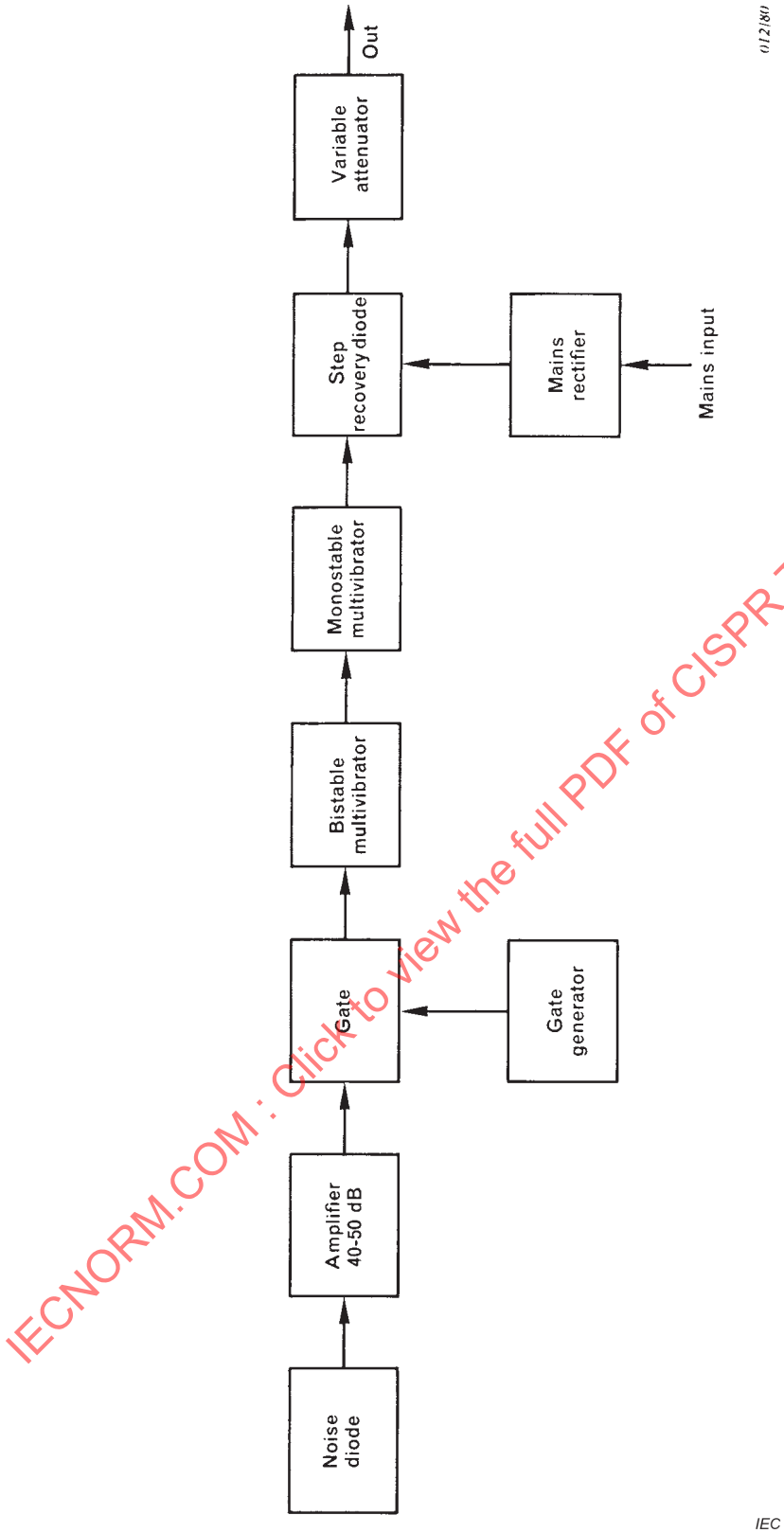



**Figure 5 – Block diagram of a simulator generating noise bursts according to the pulse principle**

IECNORM.COM : Click to view the full PDF of CISPR TR 16-3:2020 RLV

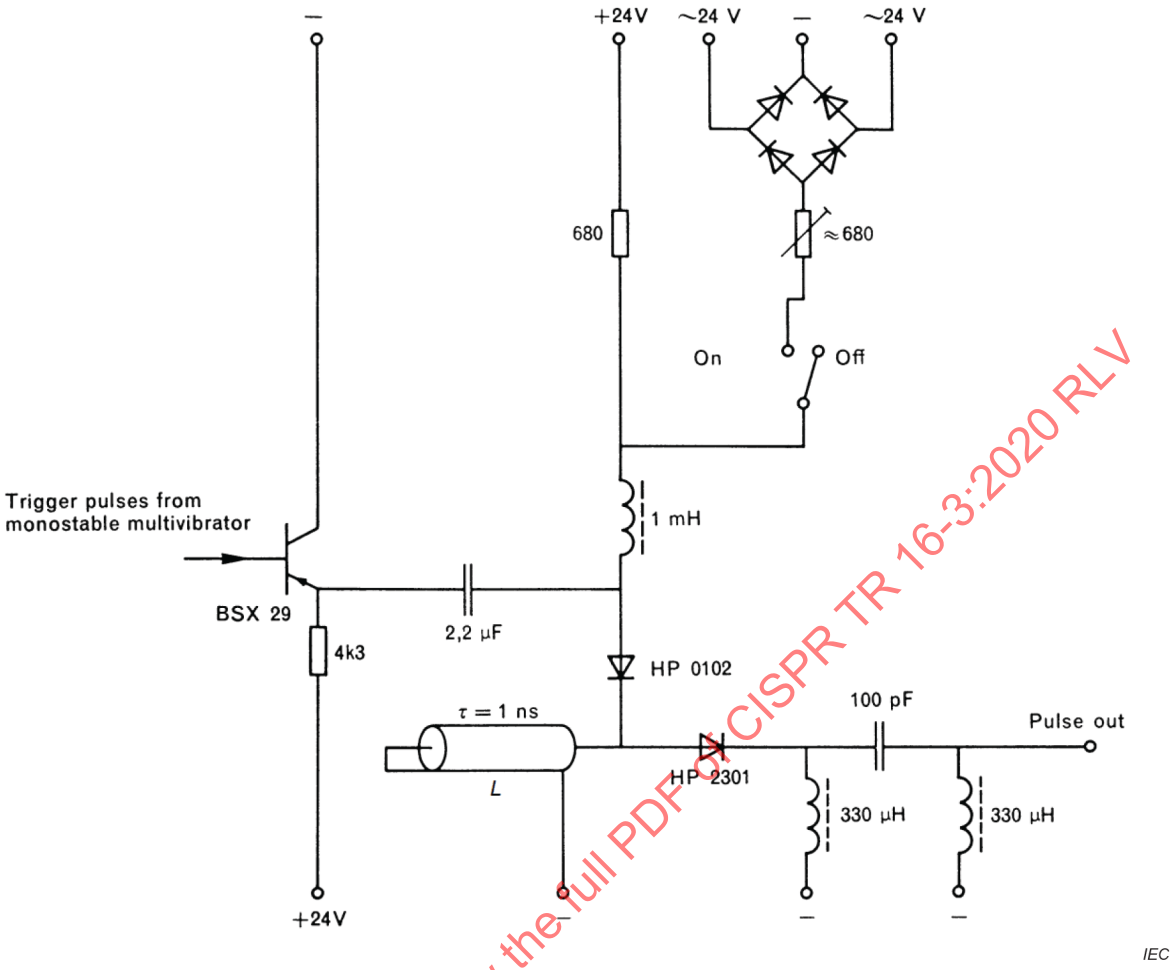



**Figure 6 – Details of a typical output stage**

## 4.3 Relationship between limits for open-area test site and the reverberation chamber

### 4.3.1 General

At present there are limits for use with the open-area test site method of measurement specified in several CISPR publications. For equipment that can be measured using the reverberation chamber method, a procedure is required to relate the limit to be used with that of the open-area test site (OATS) limit. The procedure is described in this subclause.

### 4.3.2 Correlation between measurement results of the reverberation chamber and OATS

The OATS measurement sets out to find the maximum level of radiation of an EUT (equipment under test). Whether the measurement is of the field strength or of power density at the measurement antenna, or of the power into an antenna in substitution of an EUT, the measured results can be expressed in terms of the equivalent radiated power from a half-wave dipole. Let this equivalent radiated power be $P_q$ in dB(pW).

The reverberation chamber measures the total radiated power of the EUT. Let the measured power be $P_t$ in dB(pW).

The two measurements are related to each other by the gain of the EUT as a radiator with respect to an isotropic radiator. Let this EUT gain be $G$ in dB. The relationship is given by Equation (6). The equation is derived in Annex A.

IECNORM.COM : Click to view the full PDF of CISPR TR 16-3:2020 RLV

$$P_t + G = P_q + 2 \quad (6)$$

### 4.3.3 Limits for use with the reverberation chamber method

Consider the case of an EUT which is exactly on the limit, $L_o$, when measured in the open area test site, i.e. $P_q = L_o$.

This EUT should also be exactly on the corresponding limit, $L_r$, when it is measured in the reverberating chamber, i.e. $P_t = L_r$.

From Equation (6), we can relate the two limits as in Equation (7).

$$L_r = L_o + 2 - G \quad (7)$$

The value of $L_r$ is dependent not only on $L_o$, but also on $G$. Because $G$ will not be the same for all EUTs, it is not possible to set $L_r$ to treat all EUTs in a manner identical to the effect of $L_o$. If say $L_r = L_o$, then it is correct only for EUTs with $G = 2$. EUTs with a $G$ greater than 2 will find it easier to pass the reverberation chamber limit, and vice versa.

It is necessary to determine the value of $G$. This can be done from measurements of $P_q$ and $P_t$. Figure A.1 shows the curves of ~~$P_w$~~ $P_q$ versus $P_t$ for various values of $G$. The shaded region is for negative values of $G$. (Experimental points appearing in this region are caused by failure to locate the maximum open-site radiation, probably due to the maximum radiation lying outside of the horizontal plane).

An example is given in Figure A.2. A number of microwave ovens were measured for $P_q$ and $P_t$. It can be seen that:

– for points lying in the positive $G$ region, the majority have values around 2;

– more points lying in the positive $G$ region as the frequency goes up, indicating that the radiation pattern is becoming more directional in the vertical direction.

Based on this evidence, the reverberation chamber results can be related to those of an OATS. In fact, use of a reverberation chamber appears to be a more effective method in the ability to measure a quantity representative of the maximum radiation.

### 4.3.4 Procedure for the determination of the reverberation chamber limit

The procedure to determine the reverberation chamber limit is as follows.

i) Measure a sample of equipment for the maximum radiation on an OATS. Convert the measured quantities to the equivalent power from a half-wave dipole. Call this quantity $P_q$, in dB(pW).

ii) Measure the same sample in the reverberating chamber for total radiated power. Call this quantity $P_t$, in dB(pW).

iii) The relationship between the reverberation chamber limit and the OATS limit can be found by the graphical method of Figure A.1, or by calculating the gain of each equipment, obtaining a representative value of $G$ for the equivalent type using statistical methods, and applying Equation (7).

IECNORM.COM : Click to view the full PDF of CISPR TR 16-3:2020 RLV

## 4.4 Characterization and classification of the asymmetrical disturbance source induced in telephone subscriber lines by AM broadcasting transmitters in the LW, MW and SW bands

### 4.4.1 General

The use of semiconductor devices in telephone terminal equipment (TTE) has created the need to verify the immunity to RF fields of this equipment, as non-linear semiconductor devices demodulate the induced RF signals [1], [17], [18], [19], [20].[2] The latter effect gives rise to a DC shift which may alter the operating point of such a device, thus, for example, reducing the noise margin of digital devices. In the case of amplitude-modulated RF fields, the non-linearity gives rise to a baseband signal that may become audible in the telephony system. AM broadcasting transmitters in the LW, MW and SW bands form an important class of RF-field sources.

Because of the relatively small dimensions of TTE (compared to the wavelength of the disturbance signal) the asymmetrical (common-mode) source induced in telecommunication lines is expected to be the dominant disturbance source. Therefore, a conducted-immunity test (current-injection test) is relevant for this equipment. In this test, the disturbance signal is applied via the telecommunication lines. As a consequence, this subclause deals with the characterization of the unwanted antenna properties of telecommunication lines and with prediction models supplying information about the probability that certain parameter values will be met in practice. Moreover, it discusses the parameters that are of relevance when specifying the disturbance source used in the immunity test. The various considerations will be limited to parameters relevant at the subscriber end of the telephone lines.

In 4.4.2 the antenna properties will be expressed in terms of an antenna factor of the subscriber lines i.e. the induced asymmetrical open-circuit voltage normalized to the RF field strength, and an equivalent resistance of the induced asymmetrical source. The prediction models are needed in the classification of the RF fields and the induced asymmetrical disturbances, i.e. 4.4.3, and when setting immunity limits, i.e. 4.4.4. This subclause takes the view that the disturbance source in the immunity test is to be specified by an open-circuit voltage and a source impedance.

All mathematical relations associated with the derivation of the models and those needed by the user of this subclause when applying the models to the respective geographical area are given in Annex B, Annex C, Annex D, and Annex E.

This subclause is based on results of experimental investigations carried out on buried telephone-subscriber lines in Germany [21], [22] and in the Netherlands [23]. In these investigations induced-voltage and current data and magnetic-field-strength data were recorded at a large number of locations, permitting a statistical evaluation of the parameter values. A statistical approach was needed, because the telephone lines have random routing in the buildings and, consequently, random orientation with respect to the RF field makes for random coupling with nearby metal objects, while the buildings cause a random scattering of the RF fields.

It is to be expected that the contents of this subclause will also be applicable to other types of lines running through buildings in a similar manner to telephone-subscriber lines, for example, bus-system lines and signal and control lines.

### 4.4.2 Experimental characterization

#### 4.4.2.1 General

A full description of the experimental characterization is presented in [22] and [23]. Therefore, this subclause contains only a summary of this method with regard to the parameters needed.

---

2 Numbers in square brackets refer to the bibliography.

IECNORM.COM : Click to view the full PDF of CISPR TR 16-3:2020 RLV

The induced asymmetrical voltage was measured at the outlet of a telephone-subscriber line using a modified T-network [24] and [25]. As a result of this modification, a voltage $U_h$ could be measured across a 10 kΩ resistor and a voltage $U_l$ across a 150 Ω resistor. The investigations showed that $U_h$ could be considered as the induced open-circuit voltage. In practice, the reference for this voltage is generally unknown. During the measurements that reference was a special metal measuring cart connected via a copper strap to the central heating system. The equivalent resistance $R_a$ of the induced source is estimated from data pairs $\{U_h, U_l\}$.

At each location two magnetic-field-strength data of the broadcasting transmitter were measured using a loop antenna positioned in a vertical plane and rotated about its vertical axis to find the maximum reading. One datum, $H_i$, was measured near the outlet under investigation inside the building, and one datum, $H_o$, was measured outside the building at a distance of about 10 m from that building. In order to obtain a sufficiently high induced-signal-to-ambient-noise ratio, the measurements were carried out in areas with a relatively high value of the RF field strength. This is not expected to influence the applicability of the results, as the presence of a broadcasting transmitter is not taken into account in the layout of telephone-subscriber lines. Moreover, as mentioned in 4.4.1, the induced voltage will be normalized to the field strength and the resulting "antenna factor" will represent a property of the subscriber lines measured.

#### 4.4.2.2 Field strength and building effect

Although the RF field is not a characteristic of the subscriber lines, it forms the origin of the induced disturbances. Two aspects of the RF field will be considered in this subclause:

a) The measured field strength $H_o$ outside the buildings compared to the field strength $H_c$ calculated from the simple far-field relation for a half-wave dipole (in its main direction):

$$H_c = \frac{7\sqrt{P}}{Z_0 r} \tag{8}$$

where

$P$ is the transmitter power;

$Z_0$ is free-space wave impedance (377 Ω) and

$r$ the distance between the transmitter and the point of observation.

In the calculations, the values of $P$ as given in [28] are used.

NOTE Although broadcast transmitter antennas usually are monopoles (in the frequencies of interest), the half-wave dipole formula in Equation (8) has been used for convenience.

b) The effect of the building on the field strength, which can be expressed in a building-effect parameter $A_b$ defined by:

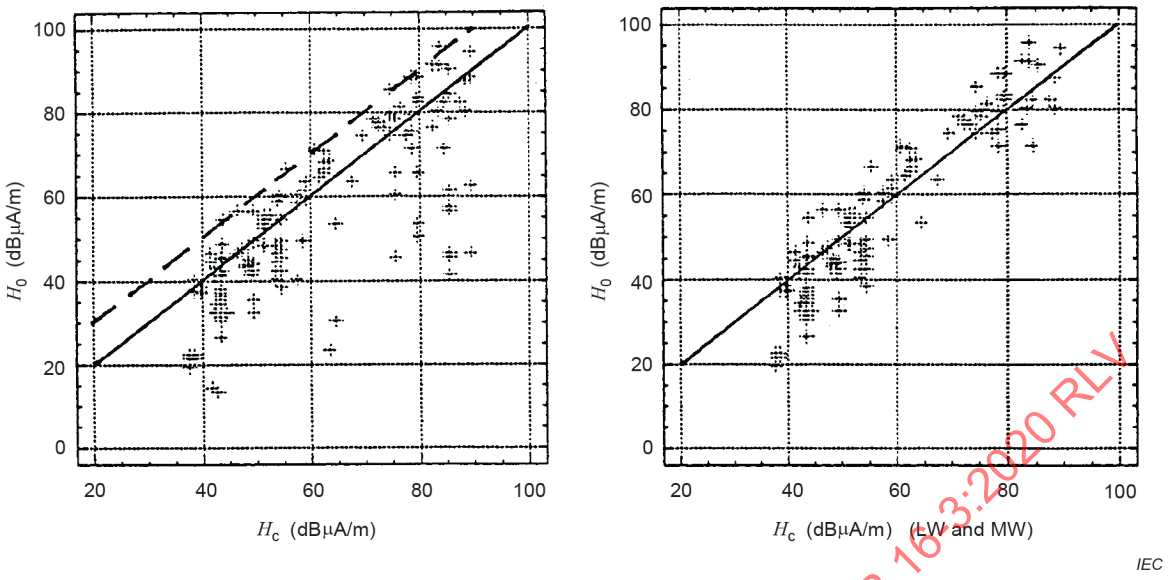
$$A_b = H_o - H_i \tag{9}$$

where $H_o$ and $H_i$ are in dB(μA/m).

This factor is often called the building attenuation. However, this factor not only depends on the attenuation properties of the building material itself, but also on the re-radiation properties of metallic structures in and near the building, and on the height above ground at which $H_o$ and $H_i$ were measured. Therefore the term building effect is used in this subclause.

A consideration of these two aspects is needed in view of the antenna factors to be discussed in 4.4.2.3 and in view of the prediction models to be discussed in 4.4.2.4.

IECNORM.COM : Click to view the full PDF of CISPR TR 16-3:2020 RLV



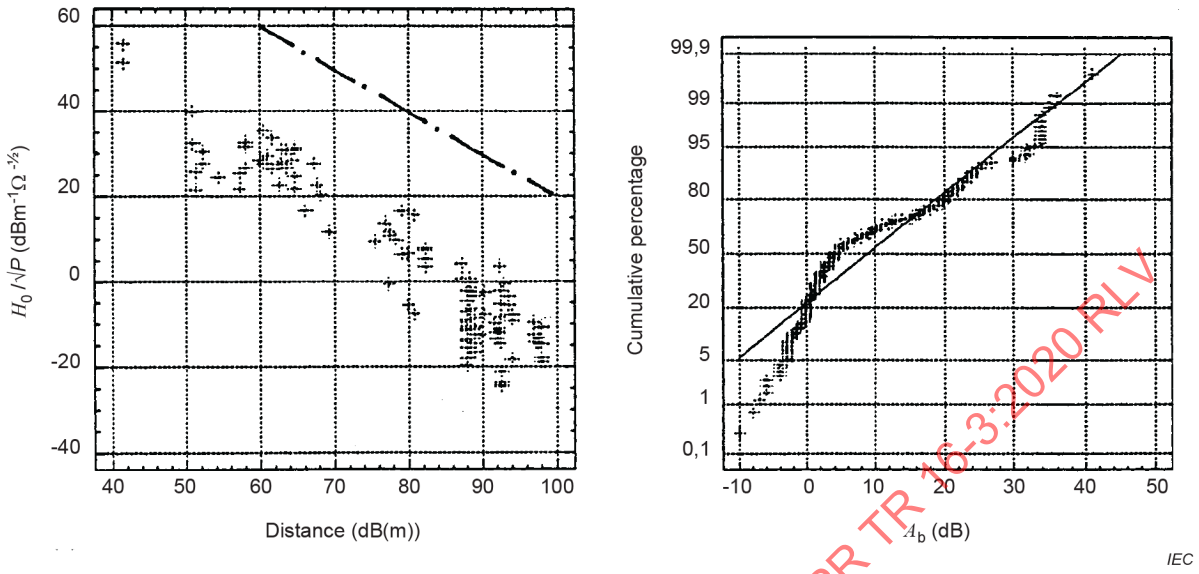

a) All data

b) Data of SW transmitters rejected

**Figure 7 – Scatter plot of the measured outdoor magnetic field strength $H_o$ (dBμA/m) versus the calculated outdoor magnetic field strength $H_c$ dB(μA/m)**

The results of $H_o(H_c)$ given in Figure 7a) show that large deviations from $H_o = H_c$ are possible (solid line), but that $H_o \leq (H_c + 10)$ dB(μA/m) (dashed line), hence the measured value is at most a factor of 3 higher than the value calculated from Equation (8). The largest deviations concern data of SW transmitters. This is understandable, because SW transmitters normally have a beamed antenna pattern, whereas the antenna patterns of the LW and MW transmitters are generally close to circular. Figure 7b) gives the scatter plot $H_o(H_c)$ after rejection of the SW transmitter data.

IECNORM.COM : Click to view the full PDF of CISPR TR 16-3:2020 RLV




**a) Scatter plot of the measured outdoor magnetic field strength $H_o$ normalized to the square root of the reported power [26] versus the distance $d$ (m) to the transmitter**

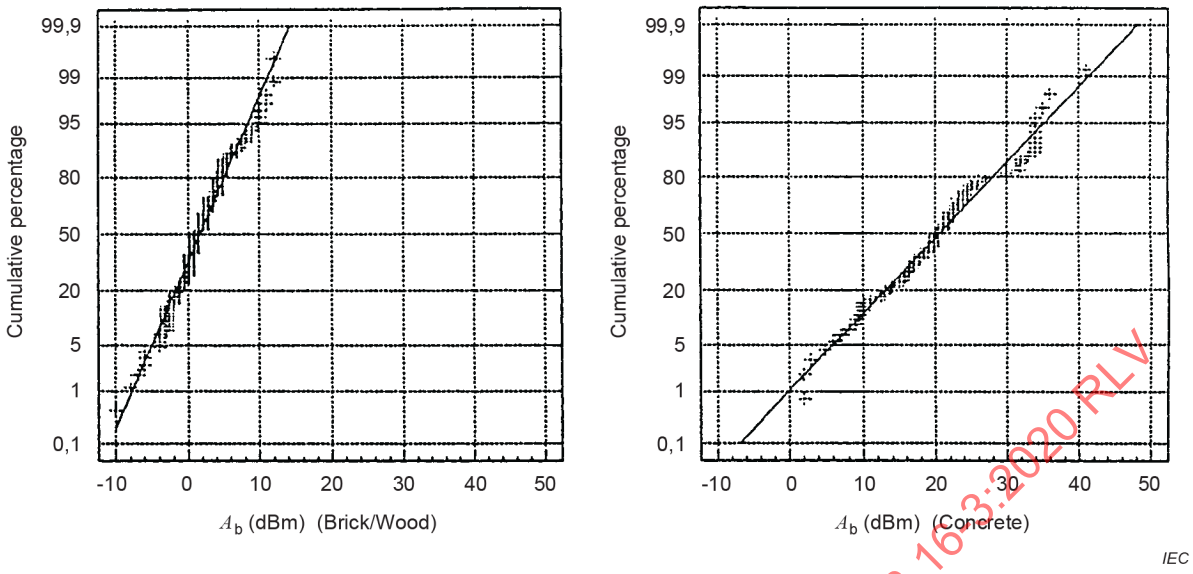
**b) Normal probability plot of the building-effect parameter $A_b$ dB, all data**

**Figure 8 – Measured outdoor magnetic versus distance, and probability of the building-effect parameter**

Figure 8a) shows the ratio $H_o/\sqrt{P}$ versus the distance between the point of observation and the transmitter, and the dash-dot line indicates a slope –1. It can be concluded that, on average, the data follow this slope fairly well. The associated intercept is higher than that expected from Equation (8), which is in agreement with the ($H_c$ + 10) dBμA/m limit observed in Figure 7.

Figure 8b) shows the normal probability plot of all building-effect data. If these data were normally distributed, a straight line would have resulted. This is not the case, and the data suggest that, in a first-order approximation, two distributions are superimposed. The two distributions are found when distinguishing between data associated with buildings constructed from brick and/or wood (B/W) and data associated with buildings constructed from reinforced concrete (C). The normal probability plots of these distributions are given in Figure 9a) and Figure 9b). The negative values of $A_b$ predominantly stem from measurements where $H_i$ was measured on an upper floor of the building, whereas $H_o$ was already measured at about 1,5 m above ground level outside the building. Effects of re-radiation also influence the actual field-strength data.

IECNORM.COM : Click to view the full PDF of CISPR TR 16-3:2020 RLV




**a) Buildings constructed from brick and/or wood** **b) Buildings constructed from reinforced concrete**

**Figure 9 – Normal probability plot of the building-effect parameter $A_b$ dB**

The numerical results have been summarized in Table 3. No clear frequency dependence of the $A_b$ data could be observed (see 4.4.2.5).

**Table 3 – Summary results of building-effect, $A_b$, analysis**

| Building material | Average<br>dB | Standard deviation<br>dB | Median<br>dB | Number of data |
|---|---|---|---|---|
| Brick and/or wood | 1,6 | 4,0 | 1,0 | 138 |
| Reinforced concrete | 20,6 | 8,7 | 20,1 | 84 |

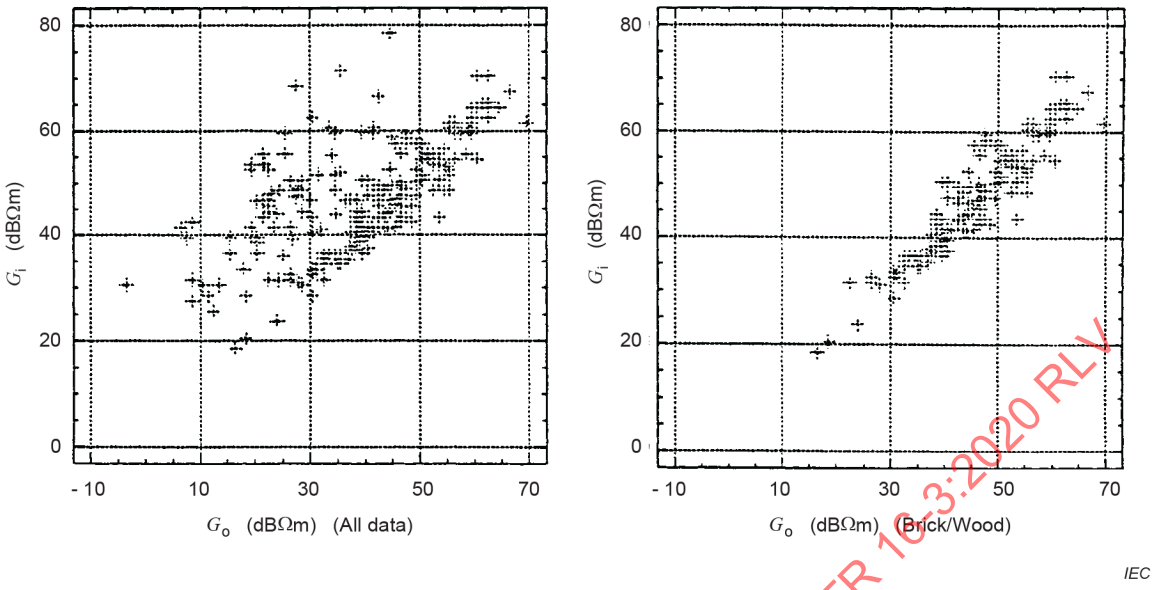
#### 4.4.2.3 The asymmetrical open-circuit voltage normalized to the field strength

##### 4.4.2.3.1 General

The interface for the voltage measurements was the outlet to which the telephone set was connected during the measurements. The investigations showed that the influence on the measured voltages of the telephone set and its standard lead (4 m long) could be neglected.

The measured voltage will be normalized to the measured magnetic field strength in 4.4.2.3.2, and assuming far-field conditions, to the electric field strength in 4.4.2.3.3. After that, 4.4.2.3.4 deals with truncation of the distributions found in 4.4.2.3.2 and 4.4.2.3.3.

IECNORM.COM : Click to view the full PDF of CISPR TR 16-3:2020 RLV




**a) All data**

**b) Data associated with buildings constructed from brick and/or wood**

**Figure 10 – Scatter plot of the outdoor antenna factor $G_o$ dB(Ωm) versus the indoor antenna factor $G_i$**

#### 4.4.2.3.2 *G* factors

To obtain an antenna property of the subscriber lines, the open-circuit voltage $U_h$ is normalized to the field strength ($H_i$ or $H_o$), yielding the antenna factors $G_i$ and $G_o$ defined by

$$G_{i,o} = \frac{U_h}{H_{ino}} \tag{10}$$

where

$G_{i,o}$ is in Ωm,

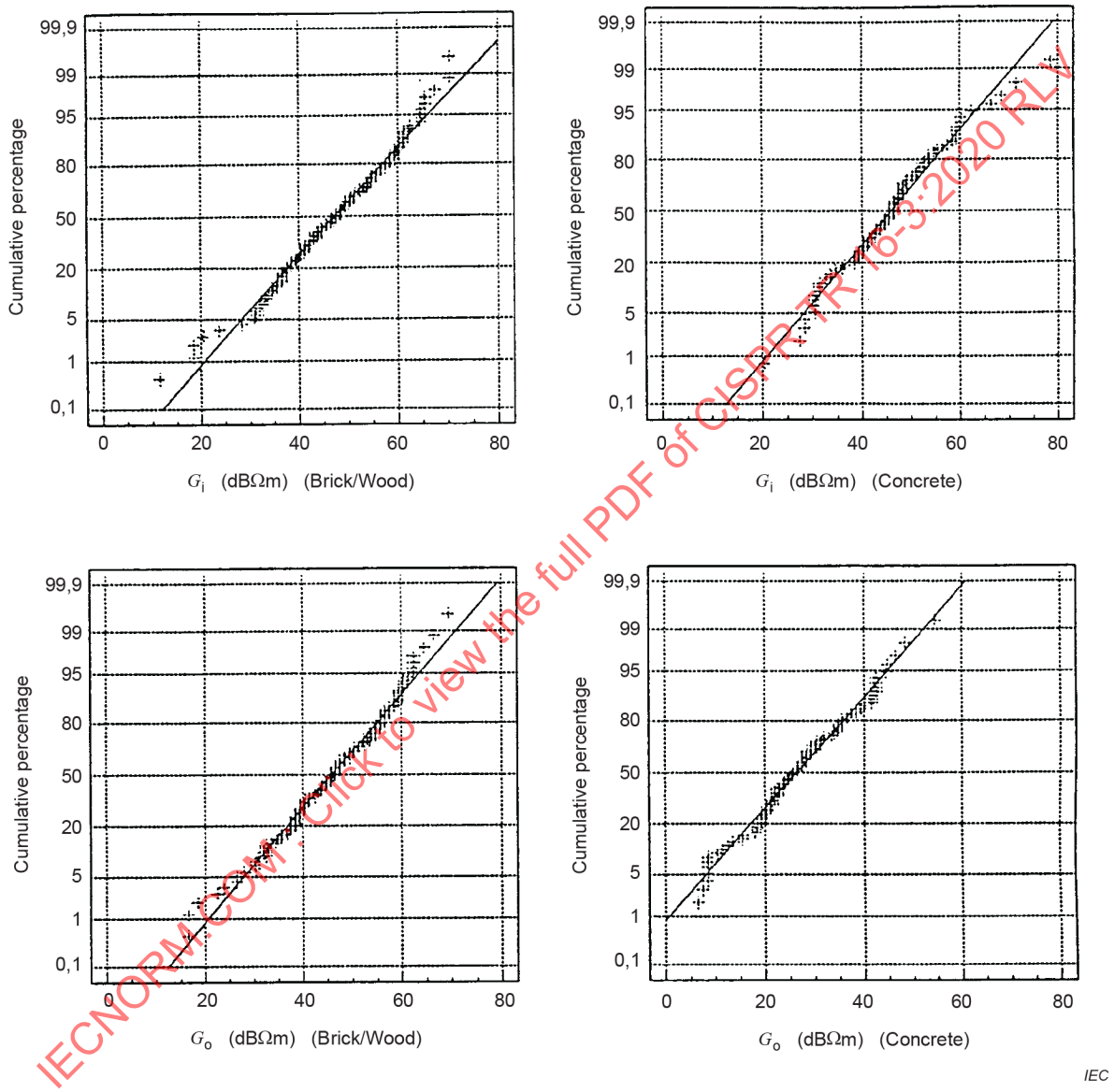
$U_h$ is in μV, and

$H_{ino}$ is in μA/m.

Figure 10a) shows the scatter plot $G_i(G_o)$ using all data. The plot suggests that there is one dominant "cloud" of data with a limited scattering and a second "cloud" with much more scattering. Further investigation revealed that the first cloud stems from data measured in buildings constructed from brick and/or wood, see Figure 10b), while the other cloud is associated with buildings constructed (predominantly) from reinforced concrete. Consequently, the building effect discussed in 4.4.2.2 is of importance.

IECNORM.COM : Click to view the full PDF of CISPR TR 16-3:2020 RLV

The normal probability plots of $G_i$ dB(Ωm) and $G_o$ dB(Ωm) associated with the two types of building material considered, are given in Figure 11. It can be concluded that the data follow a normal distribution, which means lognormal distributions of the $G$ factors in Ωm. The numerical results have been summarized in Table 4, where $G_U$ and $G_L$ are the upper and lower limit of the range of experimental $G$ data (see 4.4.2.3.4). The differences between $G_i$ and $G_o$ of the two classes of building material considered are consistent with the building-effect data for these buildings (see Table 3). No clear frequency dependence could be observed (see 4.4.2.5).




**a) $G_i$ dB(Ωm) and c) $G_o$ dB(Ωm), associated with buildings constructed from brick and/or wood**

**b) $G_i$ dB(Ωm) and d) $G_o$ dB(Ωm), associated with buildings constructed from reinforced concrete**

**Figure 11 – Normal probability plots of the antenna factors**

IECNORM.COM : Click to view the full PDF of CISPR TR 16-3:2020 RLV

**Table 4 – Summary of results of $G$-factor analysis**

| $G$ factor | Building material | Average<br>dB(Ωm) | Standard deviation<br>dB | Median<br>dB(Ωm) | Number of data points |
|---|---|---|---|---|---|
| $G_i$ | B/W | 47,3 | 11,2 | 47,5 | 135 |
| $G_i$ | C | 45,9 | 10,5 | 46,5 | 88 |
| $G_o$ | B/W | 45,8 | 10,6 | 46,4 | 134 |
| $G_o$ | C | 26,5 | 10,9 | 26,0 | 90 |

#### 4.4.2.3.3 $L$ factors

In 4.4.2.3.2, $U_h$ was normalized to the measured magnetic field strength, thus yielding the $G$ factors. Assuming far-field conditions, the electric field strength follows from $E = Hz_0$ with $Z_0 = 377\ \Omega$. If the outdoor field strength is considered, this assumption seems to be reasonable and the $G_o$ factor can be converted into an $L_o$ factor defined by

$$L_o = \frac{G_o}{Z_0} = \frac{U_h}{H_o Z_0} = \frac{U_h}{E_o} \tag{11}$$

where $U_h$ is in µV and $E_o$ is in µV/m.

The $L$ factor can be considered as the effective length or effective height of the subscriber line acting as an antenna. The results for $L_o$ have been summarized in Table 5, where $L_U$ and $L_L$ are the upper and lower limit of the range of experimental $L$ factors (see 4.4.2.3.4).

**Table 5 – Summary of $L_o$ factors (far-field)**

| $L$ factor | Building material | Average[a]<br>dB(m) | Standard deviation<br>dB | $L_U$<br>dB(m) | $L_L$<br>dB(m) |
|---|---|---|---|---|---|
| $L_o$ | B/W | –5,7 | 10,6 | 18,0 | –35,0 |
| $L_o$ | C | –25,0 | 10,9 | 3,0 | –55,0 |

[a] Note that dB(m) refers to dB with respect to 1 m.

In the literature an $L$ factor of –3,0 dB(m) average (standard deviation 10 dB, number of data points = 10) has been reported [27] for a cable running 1 300 m underground and 1 000 m to 3 000 m overhead (aerial cable) towards the subscriber. Broadcasting frequencies were 594 kHz and 1 242 kHz. No details were given about the field-strength measurements, the reference for the asymmetrical voltage and the properties of the building material. The results reported in [27] are in line with the results for $L_o$ (B/W), as given in Table 5. However, more recent investigations by the same team [29] indicate an average $L$-factor of 0 dB(m).

$L_i$ factors might be derived from the $G_i$ factors in a similar way as the $L_o$ factors. However, it is to be expected that inside the buildings the far-field conditions are not satisfied and it has to be decided which wave impedance has to be taken. Therefore, no $L_i$ data have been presented in Table 5. See also NOTE 2 at the end of 4.4.4.2.

#### 4.4.2.3.4 Truncation

In 4.4.2.3.2 it was concluded that the distribution $f(G)$ of the $G$ factors (antenna factors) is lognormal or in mathematical form

IECNORM.COM : Click to view the full PDF of CISPR TR 16-3:2020 RLV

$$f(g)dG = \frac{1}{G\sigma\sqrt{2\pi}} e^{(\ln G-\mu)/2\sigma^2}\, dG \tag{12}$$

However, by adopting this lognormal distribution it is automatically assumed that a $G$ factor may range from zero to infinitely large. In practice, infinitely large will never occur as wavelength effects and effects of coupling with nearby structures create an upper limit ($G_U$ or $L_U$) of the antenna factors [28]. Consequently, for correct use in the prediction models (4.4.3 and 4.4.4) $f(G)$ has to be truncated. Similarly, truncation has to be applied to the distribution of the building-effect parameters.

Unfortunately, no theoretical study is known which predicts the upper limit of $G$ (or $L$) of an actual telephone-subscriber line taking into account the length and the routing of a line inside the building and, buried, outside the building. However, it has to be expected that such a limit exists and the best approach is to use the experimental upper limit ($G_U$ or $L_U$).

In addition to the upper limit, one may also consider a lower limit ($G_L$ or $L_L$) and truncate $f(G)$ at the lower end. It is found that in the range of parameter values to be considered in 4.4.3 and 4.4.4, the influence of $G_L$ (or $L_L$) is negligible.

The truncated probability density function reads

$$f_t(G)dG = \frac{f(G)dG}{\int_{G_L}^{G_U} f(G)dG} = \frac{f(G)dG}{F(G_U) - F(G_L)} = \alpha_t f(G)dG \tag{13}$$

The mathematical form of the cumulative distributions $F(G_U)$ and $F(G_L)$ is given in Annex E. Table 6 summarizes the truncation data of the $G$ factors and the building-effect parameter $A_b$. Note that $\alpha t$ differs very little from 1, that is from the value of $\alpha t$ if $-\infty \le G$ dB(Ωm) $\le \infty$ or $-\infty \le A_b$ (dB) $\le \infty$ because $F(\infty) = 0{,}5$ and $F(-\infty) = -0{,}5$. The upper and lower limit in dB(m) of the $L$ factor range are found by subtracting 51,5 dB(Ω) from the corresponding $G$ factors in dB(Ωm).

**Table 6 – Summary of truncation parameters of $f(G)$**

| $G$ factor or $A_b$ | Building material | $G_U$ dB(Ωm) $A_{bu}$ (dB) | $G_L$ dB(Ωm) $A_{bl}$ (dB) | $F(G_U)$ $F(A_{bu})$ | $F(G_L)$ $F(A_{bl})$ | $\alpha t_G$ $\alpha t_A$ |
|---|---|---|---|---|---|---|
| $G_i$ | B/W | 70,5 | 11,5 | 0,480 5 | –0,499 3 | 1,021 |
| $G_i$ | C | 78,5 | 20,5 | 0,498 5 | –0,492 2 | 1,009 |
| $G_o$ | B/W | 69,5 | 16,5 | 0,487 3 | –0,497 1 | 1,016 |
| $G_o$ | C | 54,5 | –3,5 | 0,495 0 | –0,497 1 | 1,008 |
| $A_b$ | B/W | 12,0 | –10,0 | 0,495 3 | –0,498 1 | 1,007 |
| $A_b$ | C | 41,0 | 2,0 | 0,490 5 | –0,483 7 | 1,026 |

#### 4.4.2.4 The equivalent asymmetrical-source resistance

The equivalent resistance of the induced asymmetrical source can be determined from data pairs $\{U_h, U_l\}$, where $U_h$ is the open-circuit voltage and $U_l$ the voltage measured across 150 Ω, using the simple relation:

IECNORM.COM : Click to view the full PDF of CISPR TR 16-3:2020 RLV

$$R_a = \frac{U_h - U_l}{U_l} 150\ (\Omega) \qquad (14)$$

The normal probability plot of $R_a$ dB(Ω) is given in Figure 12. It can be concluded that $R_a$ in dB(Ω) follows a normal distribution and, hence, $R_a$ in Ω follows a lognormal distribution. The numerical results have been summarized in Table 7. The average value found is close to the value 150 Ω used in existing immunity tests [24], [14]. In Table 7, $R_{au}$ and $R_{al}$ are the upper and lower limit of the range of experimental $R_a$ data. The relatively large and small values of $R_{au}$ and $R_{al}$ compared to the average value of $R_a$ stem from resonances and anti-resonances in the common mode circuit of the subscriber line. No clear frequency dependence of $R_a$ could be observed (see 4.4.2.5), and no influence of the building material was observed.

**Table 7 – Summary results of equivalent-resistance analysis**

| $R_a$ (average) | Standard deviation | Median | $R_a$ (average) | Number of data points | $R_{au}$ | $R_{al}$ | $R_{au}$ | $R_{al}$ |
|---|---|---|---|---|---|---|---|---|
| dB(Ω) | dB | dB(Ω) | Ω | | dB(Ω) | dB(Ω) | Ω | Ω |
| 44,2 | 6,8 | 43,5 | 162 | 204 | 63,7 | 25,2 | 1 531 | 18 |

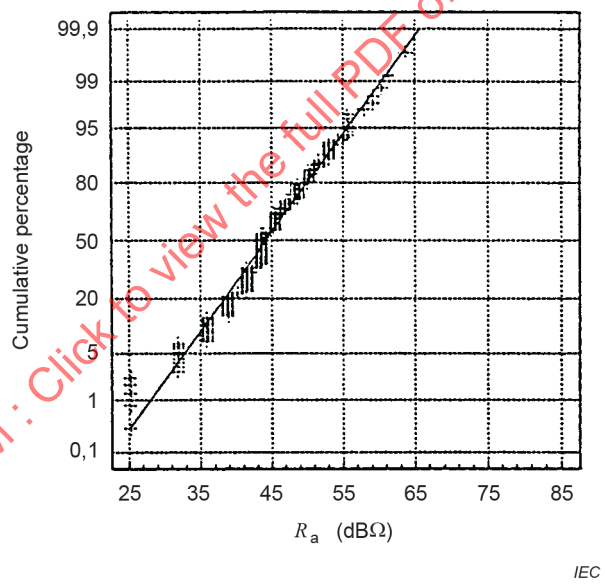


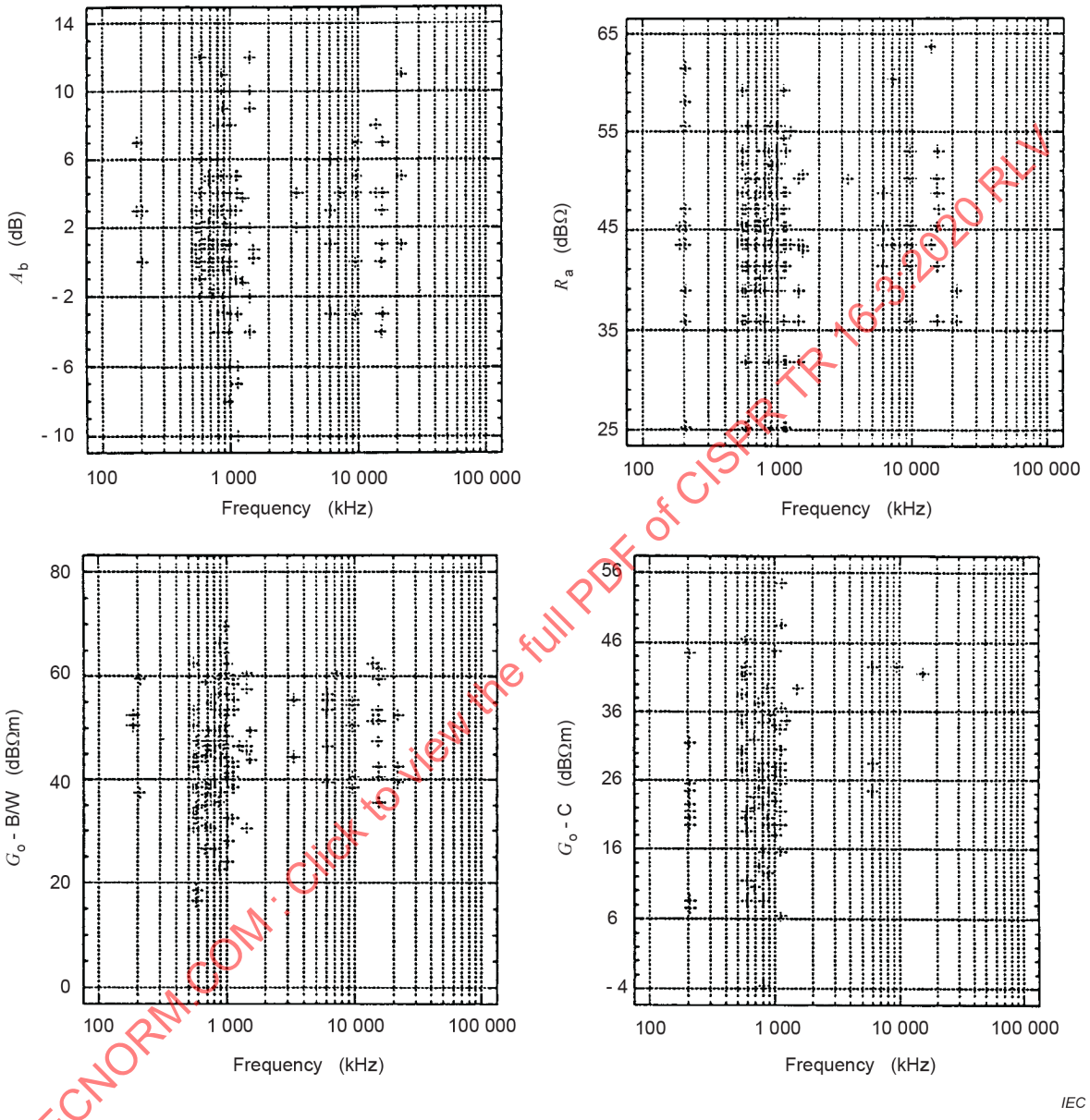

**Figure 12 – Normal probability plot of the equivalent asymmetrical resistance $R_a$ dB(Ω)**

IECNORM.COM : Click to view the full PDF of CISPR TR 16-3:2020 RLV

#### 4.4.2.5 Frequency dependence of the parameters

In the frequency range determined by the measurements in the LW, MW and SW bands, no clear frequency dependence of the building effect $A_b$, the $G$ factors $G_o$ and $G_i$, and the equivalent resistance $R_a$ could be observed. This is illustrated in Figure 13a) and Figure 13b) the $A_b$ data for brick/wood buildings, the $R_a$ data, the $G_o$ data for brick/wood buildings, and for reinforced concrete buildings.

Because no clear frequency dependence of the various quantities could be observed, it will be assumed in 4.4.3 and 4.4.4 that the building effect, the $G$ and the $L$ factors and the equivalent resistance are independent of the frequency in the frequency range of the LW, MW and SW bands. A possible frequency dependence is then incorporated in the standard deviation of the respective distributions.




a) Building effect $A_b$ in the case of brick/wood buildings

b) Equivalent resistance $R_a$

c) $G_o$ factor for brick/wood buildings

d) $G_o$ factor for reinforced concrete buildings

**Figure 13 – Examples of the frequency dependence of some parameters**

### 4.4.3 Prediction models and classification

#### 4.4.3.1 General

This subclause presents some simple prediction models for fields and voltages needed in the process of classification of the electromagnetic environment and when setting immunity limits for the telephone sets to be connected to the subscriber lines.

IECNORM.COM : Click to view the full PDF of CISPR TR 16-3:2020 RLV

Because the measuring locations were not chosen randomly in order to obtain a sufficiently high induced signal-to-ambient noise ratio, the basic data from which the parameters reported in 4.4.2 were derived cannot be used directly because they form a non-random sample from their actual distributions. The models to be discussed permit an estimate to be made of the complete distributions of the field strength and induced voltage. In addition, the complete distributions allow for a classification of these quantities. This subclause gives only the procedure for this classification. The actual class limits are outside its scope.

#### 4.4.3.2 Field-strength classification

As mentioned in 4.4.2.2, the field strength is not a property of the subscriber line. Nevertheless, information about the field strength is needed in order to make a prediction of the induced voltages.

From the results given in 4.4.2.2, it follows that in a first-order approximation the outdoor field strength, to be indicated by $E_o$ and $H_o$ for the electric and magnetic field component respectively, is inversely proportional to the distance $r$ between the point of observation and the transmitter, and proportional to the square root of the transmitter power. From the results summarized in 4.4.2.2 it follows that, in the worst case, the constant of proportionality is a factor of 3 (≡ 10 dB) larger than the constant of proportionality in the case of a half-wave dipole.

A classification of the outdoor electric or magnetic field strength may be based on the probability $pr\{E_o \geq E_L\}$ or $pr\{H_o \geq H_L\}$ that the outdoor field strength is greater than or equal to a given limit value, indicated by the subscript $L$. As explained in Annex B, this probability can be written as

$$pr\{H_o \geq H_L\} = \int_{R_L}^{H_{max}} f_n(H)dH \quad \text{or} \quad pr\{E_o \geq E_L\} = \int_{E_L}^{E_{max}} f_n(E)dH \tag{15}$$

where

$f(H)$ and $f(E)$ are the normalized field-strength distribution, and

$H_{max}$ and $E_{max}$ are the maximum field strength in the geographical region in which the probability has to be estimated.

Under far-field conditions both relations in Equation (15) are equivalent.

Considering a ring-shaped area (RSA) around a transmitter having a circular antenna pattern, it follows (see Annex B) that

$$pr\{E_o \geq E_L\} = \frac{\left(E_{max}^2 - E_L^2\right)E_{min}^2}{\left(E_{max}^2 - E_{min}^2\right)E_L^2} \approx \frac{E_{min}^2}{E_L^2} \tag{16}$$

where

$E_{max}$ is the field strength at the inner boundary of the RSA, and

$E_{min}$ is the field strength at the outer boundary of the RSA.

A similar expression is valid for the magnetic field strength (see Annex B).

IECNORM.COM : Click to view the full PDF of CISPR TR 16-3:2020 RLV

The inner boundary of the RSA has to be specified, as the relation between $E_o$ and $r$ derived from the measuring data will not be valid arbitrarily close to the transmitter, i.e. in the near-field region of the transmitter. A non-zero outer boundary field strength is needed, as $E_{min}$ = 0 would mean that $pr\{E_o \geq E_L\}$ = 0 for all values of $E_L$. Note that by definition $pr\{E_o \geq E_L\}$ = 0 and that $pr\{E_o \geq E_{min}\}$ = 1 (= 100 %). The approximation given in Equation (16) is valid if $E_{max} >> \{E_{min}, E_L\}$, which is normally the case. Hence, it can be concluded that in the present model the value of $E_{min}$ to be specified is very important. The choice of $E_{min}$ and $E_{max}$ will be discussed further in 4.4.4.

As an example, Table 8 gives the values of $E_L$ for a number of probability values, assuming $E_{max}$ = 60 V/m, which is an example of a radiation-hazard limit in the MW band of frequencies, and $E_{min}$ = 0,01 V/m [= 80 dB(μV/m)]. The latter value is of the order of magnitude of the minimum field strength in the service area of a broadcasting transmitter. Note that the probability values are almost completely determined by $E_{min}$.

**Table 8 – Example of field-strength classification**

| $pr\{E_o \geq E_L\}$ | $E_L$ | $\frac{E_{min}}{\sqrt{pr\{E_o \geq E_L\}}}$ | $P$ = 500 kW | |
|---|---|---|---|---|
| | | | $k$ = 7<br>$R_L$ | $k$ = 22<br>$R_L$ |
| % | V/m | | m | m |
| 0 | 60 | – | (80) | (260) |
| 100 | 0,01 | – | 495 000 | 1 550 000 |
| $10^{-1}$ | 0,32 | 0,33 | 15 652 | 49 193 |
| $10^{-2}$ | 1,00 | 1,00 | 4 950 | 11 556 |
| $10^{-3}$ | 3,16 | 3,16 | 1 565 | 4 919 |
| $10^{-4}$ | 9,86 | 10,00 | 495 | 1 556 |

By expressing the RSA boundaries in terms of a field strength, and not, for example, in terms of the distance between the transmitter and the point of observation, Equation (15) is applicable to any transmitter producing a field strength which is inversely proportional to the distance. However, after the classes have been established, a certain transmitter will have a certain value of the constant of proportionality $k$. Then class boundaries can be associated with distances $R_L = (k/P)/E_L$ between transmitter and point of observation. In Table 8 examples of $R_L$ are given, assuming $k$ = 7 (as in the case of a half-wave dipole) and $k$ = 22 (the worst-case value found in 4.4.2.2), while the transmitter power $P$ = 500 kW. The $R_L$ values for $E_L$ = 60 V/m have been put in between brackets, because, in the considered frequency range, the far-field condition is not valid at these distances.

The advantage of choosing the field-strength boundaries first is that the classes are the same for all kinds of transmitter, while the choice of a class is then determined by the probability that victim equipment will be at a certain distance from the chosen class of transmitters. In general, an estimate of the latter probability is easier than an estimate of the field-strength probability.

#### 4.4.3.3 Asymmetrical-voltage classification

A classification of the induced open-circuit common-mode voltage $U_h$ may be based on the probability $pr\{U_h \geq U_L\}$ that $U_h$ is equal to or larger than a given limit value $U_L$. If $f_t(G)$ describes the truncated distribution of $G$ factors (see 4.4.2.3.4), $f_n(H_o)$ the normalized field-strength distribution and use is made of the relation $U_h = G_o \times H_o$, in Annex C it is shown that this probability can formally be written as

IECNORM.COM : Click to view the full PDF of CISPR TR 16-3:2020 RLV

$$pr\{U_h \geq U_L\} = \int_{G_1}^{G_2} dG_o \int_{U_1}^{U_2} dU_h \frac{1}{G_o} f\left(\frac{U_h}{G_o}\right) f_t(G_o) \quad (17)$$

where $G_1$, $G_2$, $U_1$ and $U_2$ are suitably chosen boundaries (see Annex C). In Equation (17) the product of the two distributions, i.e. the joint distribution, is needed because $pr\{U_h \geq U_L\}$ depends on simultaneously meeting a certain field-strength value $H_o = (U_h/G_o)$ and a certain value of $G_o$. In Equation (17) the factor $1/G_o$ stems from the transformation of $f(H_o)$ into $f(U_h/G_o)$.

Note that Equation (17) is not an explicit function of the distance between the transmitter and the point of observation as a consequence of the fact that the boundaries of the RSA have been defined by field-strength values. A similar remark was made in connection with Equation (15), and similar conclusions are possible here.

Considering again the ring-shaped area as introduced in 4.4.3.2, examples of the classification of $U_h$, i.e. $U_L$ values corresponding with chosen values $pr\{U_h \geq U_L\}$, are given in classification of Table 9. The relations used can be found in Annex C. As in 4.4.3.1, it was assumed that the outdoor field strengths $E_{max}$ = 60 V/m ($H_{max}$ = 0,16 A/m) and $E_{min}$ = 0,01 V/m ($H_{min}$ = 27 µA/m) have been specified. When using $G_i$ and specifying the outdoor field strength, the building effect has to be taken into account, as is explained in Annex C.

**Table 9 – Example of voltage classification assuming for the outdoor field strength: $E_{max}$ = 60 V/m and $E_{min}$ = 0,01 V/m**

| | $G_i$ | | $G_o$ | |
|---|---|---|---|---|
| **Building material** | **B/W** | **C** | **B/W** | **C** |
| $A_b$ dB | 1,6 | 20,6 | – | – |
| $S_b$ dB | 4,0 | 8,7 | – | – |
| $A_{bu}$ dB | 12,0 | 41,0 | – | – |
| $A_{bl}$ dB | –10,0 | 2,0 | – | – |
| $G_{i,o}$ dB(Ωm) | 47,3 | 45,9 | 45,8 | 26,5 |
| $S$ dB | 11,2 | 10,5 | 10,6 | 10,9 |
| $G_U$ dB(Ωm) | 70,5 | 78,5 | 69,5 | 54,5 |
| $G_L$ dB(Ωm) | 11,5 | 20,5 | 16,5 | –3,5 |
| $pr\{U_h \geq U_L\}$ | $U_L$ dB(µV) | $U_L$ dB(µV) | $U_L$ dB(µV) | $U_L$ dB(µV) |
| $10^{-1}$ | 115 | 101 | 114 | 96 |
| $10^{-2}$ | 125 | 111 | 124 | 106 |
| $10^{-3}$ | 135 | 121 | 134 | 116 |
| $19^{-4}$ | 145 | 131 | 143 | 125 |

**Key**

B/W is brick and/or wood

C is concrete

IECNORM.COM : Click to view the full PDF of CISPR TR 16-3:2020 RLV

### 4.4.4 Characterization of the immunity-test disturbance source

#### 4.4.4.1 General

The results presented in 4.4.2 and 4.4.3 may be used to specify the open-circuit voltage and the internal impedance of the disturbance source in a conducted-immunity test that would be needed to achieve a sufficiently high probability that TTE to be connected to the subscriber lines will be electromagnetically compatible.

The specification of the open-circuit voltage $U_h$ should be based on the distribution of the voltages over all telephone outlets to be considered. Therefore, this distribution is calculated first, using models and parameter values derived in the preceding subclauses. Once the distribution is known it is possible to calculate $N_o(U_h \geq U_L)$, i.e. the number of outlets in the respective geographical region showing a voltage $U_h \geq U_L$, where $U_L$ may be considered as the open-circuit voltage in the immunity test. The internal impedance may be chosen directly using the results given in Table 5. After that, the relevant parameters for the specification of the disturbance source in the immunity test will be summarized in 4.4.4.3.

This subclause gives only the procedures to arrive at a specification of the parameters needed. The assignment of actual values is the prerogative of the Product Committees.

#### 4.4.4.2 Outlet-voltage distribution

The derivation of the outlet-voltage distribution is described in detail in Annex C and Annex D. In this derivation, the following steps have been taken.

(1) Determine the total probability density $n(H_o)$ of the telephone outlets experiencing an outdoor magnetic field strength $H_o$ in ring-shaped areas around the $N$ transmitters to be considered, where the inner boundary of the areas is specified by a maximum field strength $H_{max}$ and the outer boundary by a minimum field strength $H_{min}$.

(Again, the magnetic field strength is considered first, because this field strength was measured in the experimental characterization procedure. If far-field conditions are valid, so that the magnetic and electric field strength have a constant ratio, the results can be converted directly in terms of the electric field strength.)

(2) Determine the joint probability density $f(H_o,G_o) = f(H_o) \times f(G_o)$ describing the density of outlets where the field strength has a magnitude $H_o$ and, simultaneously, the antenna factor of the subscriber lines has the magnitude $G_o$, then and convert the result into the joint probability density $f(U_h,G_o)$, by using the relation $U_h = H_o G_o$.

(3) Calculate the probability $pr\{U_h \geq U_L\}$. If $N_T$ is the total number of outlets in the respective geographical region, and the boundary conditions are taken into account such that $N_o(U_h \geq U_L) \leq N_T$ (or = 0) if $pf\{U_h \geq U_L\} = 1$ (or = 0), then the number of outlets $N_o(U_h \geq U_L)$ equals $N_T \times pr\{U_h \geq U_L\}$.

It is the prerogative of a product committee to choose a value of $N_o$ $(U_h \geq U_L)$ from which $U_L$ follows, and hence the open-circuit voltage of the disturbance source in the immunity test.

Assuming the field strength to be inversely proportional to the distance between the outlet and the transmitter, and assuming constant densities of outlets around the transmitters, it is shown in Annex D that the field-strength distribution $n(H_o)$ can be written as

$$n(H_o) = \frac{2\pi \sum_{j=1}^{N} \mu_j k_j^2 P_j}{E_o^3} = \frac{-C_{Eo}}{E_o^3} \tag{18}$$

IECNORM.COM : Click to view the full PDF of CISPR TR 16-3:2020 RLV

where

$\mu_j$ is the outlet density,

$k_j$ is the constant of proportionality of the $j$-th transmitter and

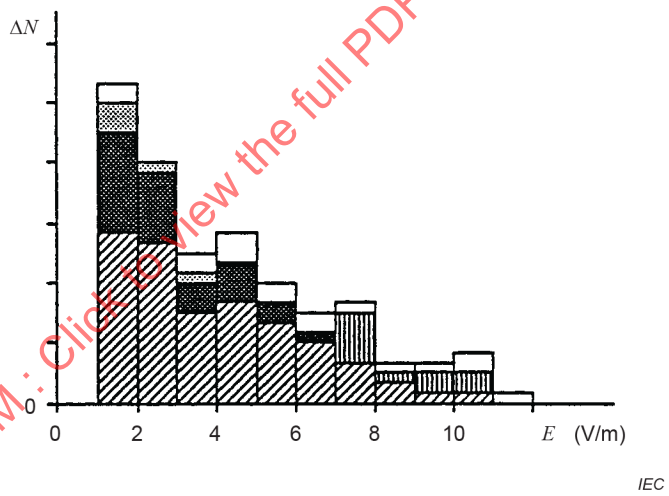
$N$ is the total number of transmitters considered.

If the density $\mu$ is the same around all transmitters and all transmitters have the same constant of proportionality $k$, $CH_o$ is simply a constant times the sum over all transistor powers.

When considering the electric field strength $E_o = (k/P)/r$, the distribution $n(E_o)$ reads

$$n(E_o) = \frac{2\pi \sum_{j=1}^{N} \mu_j k_j^2 P_j}{E_o^3} = \frac{-C_{Eo}}{E_o^3} \tag{19}$$

so that $C_{Eo} = C_{Ho} Z_o^2$. In Annex B and Annex C it is explained how the various relations change when the indoor field strength $H_i$ or $E_i$ is to be used.




NOTE The various shadings indicate schematically the contributions from various transmitters and non-homogeneous outlet densities; in this example the field-strength increment is $\Delta E_o$ = 1 V/m.

**Figure 14 – Example of the frequency histogram $\Delta N(E_o,\Delta E_o)$**

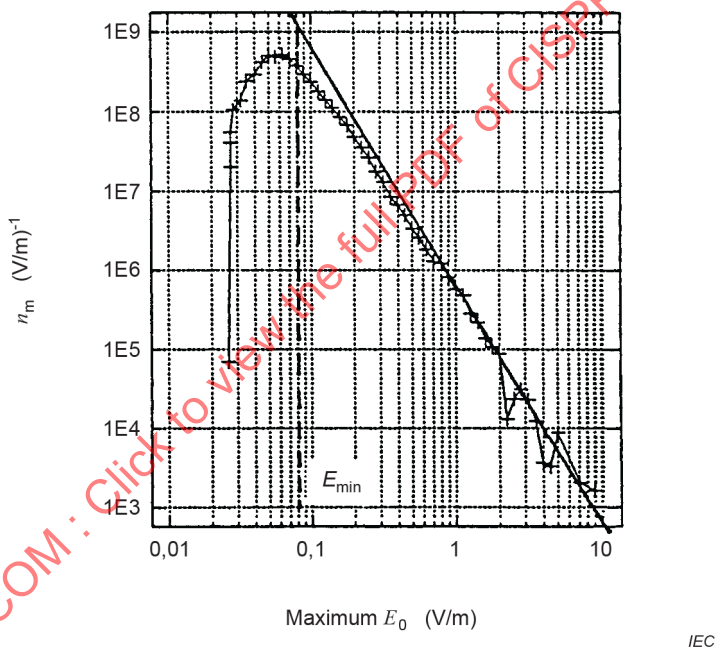
The outlet density, in general, will not be homogeneous around a transmitter. To derive $n(H_o)$ in that case, a possible procedure is to determine a frequency histogram $\Delta N(H_o,\Delta H_o)$ so that $n(H_o)$ is approximated by $n(H_o) = \Delta N(H_o,\Delta H_o) / \Delta H_o$.

In practice, the magnitude of the electric field strength is mostly considered, so $n(E_o)$ may be determined first, after which $n(H_o)$ follows after assuming far-field conditions. An example of $\Delta N(E_o,\Delta E_o)$ is given in Figure 14, where the different shadings indicate the various contributions resulting from various transmitters and non-homogeneous outlet densities around these transmitters.

IECNORM.COM : Click to view the full PDF of CISPR TR 16-3:2020 RLV

A drawback of the method leading to Figure 14 and a drawback of the model leading to Equations (18) and (19), is that the fields of the various transmitters overlap, particularly in the lower field strength regions. As a result, the same outlets in these regions are counted more than once if no discrimination is made with respect to the broadcast frequency. In 4.4.2.5 it was explained that no real frequency dependence could be observed, so this discrimination is not possible, which leads to an over-estimate of $\Delta N(E_o,\Delta E_o)$ at the lower field-strength values.

A procedure which might be followed is then to determine $n_m(E_o)$, i.e. the distribution of the maximum field strength in the respective geographical region resulting from the $N$ relevant transmitters in (and in the direct vicinity of) that region. An example of such a distribution is given in Figure 15. This distribution is a result for a part of Germany (having an area of $2{,}5 \times 10^5$ km and $42 \times 10^6$ outlets) by calculating the maximum field strength in each node at a 1 km by 1 km grid over this region as caused by one of the seventy-nine actual broadcasting transmitters in the respective frequency range, with a total ERP of 12,2 MW. The resolution of the field strength, i.e. $\Delta E_o$ was taken to be 0,1 dB(μV/m). It was assumed that the density $\mu$ was a constant ($42 \times 10^6/2{,}5 \times 10^5 = 168$ km$^{-2}$) throughout the region. When performing these calculations it was found that $n_m(E_o)$ does not vary much beyond a certain number (fifty in this case, with a total power of 7,5 MW) of transmitters taken into account.




NOTE The solid line represents $n(E_o) = -C_{Eo}/E_o^3$ with $n(E_o$ = 1 V/m) = $n_m(E_o$ = 1 V/m) × $E_{min}$ chosen such that the integral over the field strength of $n_m(E_o)$ and $n(E_o)$ both yield the total number of outlets in that region.

**Figure 15 – Example of $n_m(E_o)$, i.e. the distribution of the outlets experiencing a maximum field strength $E_o$ resulting from a given number of transmitters in (or near) the respective geographical region**

The solid line in Figure 15 represents $n(E_o) = -C_{Eo}/E_o^3$ with $C_{Eo}$ taken such that $n_m(E_o) = n(E_o)$ when $E_o$ = 1 V/m. This value is somewhat smaller than $C_{Eo}$ calculated from Equation (19), due to the aforementioned fact that $n_m(E_o)$ seems to "saturate" when the number of transmitters is increased.

When integrating the distributions over the entire respective region, the total number of outlets $N_T$ shall follow the equation

IECNORM.COM : Click to view the full PDF of CISPR TR 16-3:2020 RLV

$$N_T = \int_{E\,\min}^{E\,\max} n(E_o)\,d_{Eo} = \frac{C_{Eo}}{2}\left\{\frac{1}{E_{\min}^2} - \frac{1}{E_{\max}^2}\right\} \quad (20)$$

where the right-hand side of Equation (20) follows when Equation (19) is used. Equation (20) indicates that for a given or agreed maximum field strength $E_{max}$, the value of $E_{min}$ follows when $C_{Eo}$ is given or that $C_{Eo}$ follows when $E_{min}$ is given. The former approach was used to calculate $E_{min}$ = 0,08 V/m, as indicated in Figure 15, assuming $n_m(E_o$ = 1 V/m) = $C_{Eo}/E_o^3$ = $C_{Eo}$) 5,4 × $10^5$ $V^2/m^2$.

**Table 10 – Summary of the parameters used in the numerical examples presented in Figure 16 and Figure 17**

| **Figure** | | **16** | **17 a)** | | | **17 b)** | | |
|---|---|---|---|---|---|---|---|---|
| **Curve** | | **–** | **1** | **3** | **4** | **2** | **3** | **4** |
| ***L*-factor** | | $L_o$ | $L_o$ | $L_o$ | $L_o$ | $L_i$ [a] | $L_o$ | $L_i$ [a] |
| **Building material** | | **B/W** | **B/W** | **B/W** | **B/W** | **B/W** | **C** | **C** |
| $M_L$ | dB(m) | –5,7 | –5,7 | –5,7 | –5,7 | –4,2 | –25,0 | –5,6 |
| $S_L$ | dB | 10,6 | 10,6 | 10,6 | 10,6 | 11,2 | 10,9 | 10,5 |
| $L_u$ | dB(m) | 18,0 | +∞ | 18,0 | 18,0 | 19,0 | 3,0 | 27,0 |
| $L_u$ | m | 7,9 | +∞ | 7,9 | 7,9 | 8,9 | 1,4 | 22,4 |
| $L_i$ | dB(m) | –35,0 | –∞ | –35,0 | –35,0 | –40,0 | –55,0 | –31,0 |
| $L_i$ | m | 0,02 | –∞ | 0,02 | 0,02 | 0,01 | 0,002 | 0,03 |
| $M_A$ | dB | – | – | – | – | 1,6 | – | 20,6 |
| $S_A$ | dB | – | – | – | – | 4,0 | – | 8,7 |
| $A_{bu}$ | dB | – | – | – | – | 12,0 | – | 41,0 |
| $A_{bl}$ | dB | – | – | – | – | –10,0 | – | 0,0 |
| $N_T$ | millions | 42 | 42 | 42 | 42 | 42 | 42 | 42 |
| $C_{Eo}$ | $V^2/m^2$ | 5,4 × $10^5$ | 5,4 × $10^5$ | 5,4 × $10^5$ | 5,4 × $10^5$ | – | 5,4 × $10^5$ | – |
| $C_{Ei}$ | $V^2/m^2$ | – | – | – | – | 3,3 × $10^4$ | – | – |
| $E_{max}$ | V/m | 10,0 | 10,0 | 3,0 | 10,0 | 3,0 | 3,0 | 3,0 |
| $E_{i,max}$ | V/m | – | – | – | – | 9,5 | – | 2,4 |
| $E_{min}$ | V/m | 0,08 | 0,08 | 0,08 | 0,008 | 0,08 | 0,08 | 0,08 |
| $E_{i,min}$ | V/m | – | – | – | – | 0,02 | – | 0,000 7 |
| $U_{max}$ | V | 79 | +∞ | 24 | 79 | 85 | 42 | 53 |

[a] See NOTE 3 at the end of 4.4.4.2.

NOTE Some curves have the same parameter values: Figure 17 a) curve 2 and Figure 16, and Figure 17 b) curve 1 and Figure 17 a) curve 3.

**Key**

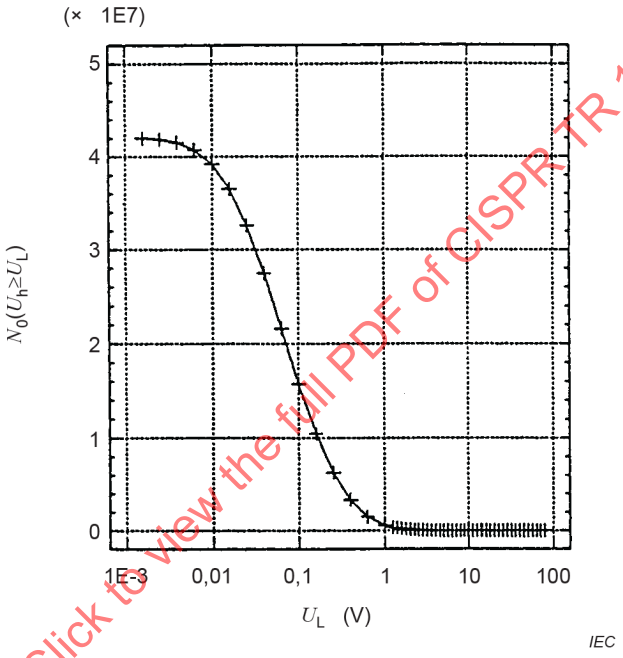
B/W is brick and/or wood

C is concrete

IECNORM.COM : Click to view the full PDF of CISPR TR 16-3:2020 RLV

This subclause is concluded by giving several numerical examples of $N_o(U_h \geq U_L)$, i.e. of the number of outlets in the respective geographical region showing an induced open-circuit voltage $U_h \geq U_L$, where $U_L$ may be considered as the open-circuit voltage in the immunity test. The region in these examples is the aforementioned part of Germany. The relations used in the calculation of $N_o(U_h \geq U_L)$ can be found in Annex C and Annex D. The values of the various parameters used in these calculations are summarized in Table 10.

Figure 15 shows an example of $N_o(U_h \geq U_L)$ in the voltage range $U_L \leq U_{max}$ = 79 V, based on $L_o$ data for buildings constructed from brick and/or wood (B/W) and assuming that all 42 million outlets are in these types of building. $U_{max}$ (see also Table 10) is given by $U_{max} = E_{max} L_U$, where $E_{max}$ is the maximum outdoor field strength in the respective geographical region, and $L_U$ the upper limit of the range of $L_o$(B/W) data (see 4.4.2.3.3). $U_{max}$ is quite large in this case. The maximum value measured in the experimental investigations is 22 V.




NOTE The total number of outlets $N_T = 42 \times 10^6$ .

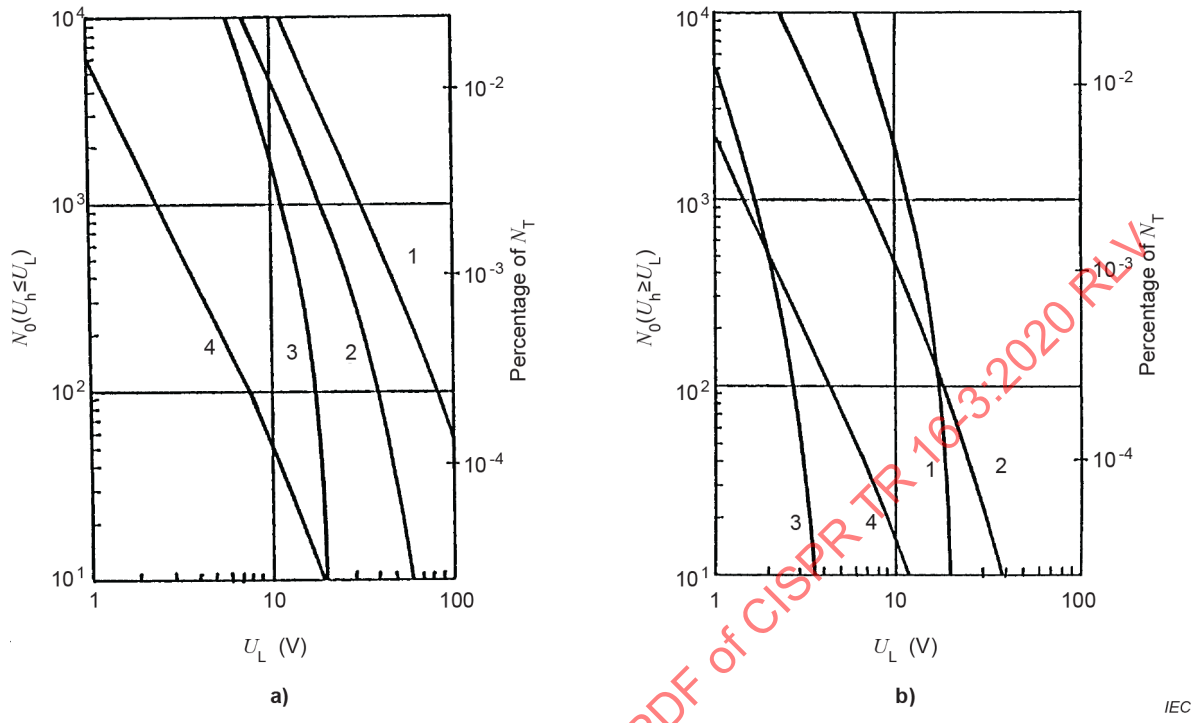
**Figure 16 – Example of the number of outlets with an induced asymmetrical open-circuit voltage $U_L \leq U_h \leq U_{max}$ = 79 V (see Table 10)**

To set the specifications for an immunity test, the higher range of $U_L$ values is of interest. Therefore, the results given in Figure 16 have been replotted as curve 2 in Figure 17a). Curve 1 in Figure 17a) gives $N_o(U_h \geq U_L)$ for the same situation as in Figure 16 but neglecting the truncation of the $L$ factor distribution. In that case $U_{max}$ is infinitely large, which is not very realistic. Curve 3 in Figure 17a) demonstrates how the results represented by curve 2 are modified when $E_{max}$ is reduced from 10 V/m to 3 V/m; then $U_{max}$ = 24 V. Finally, curve 4 in Figure 17a demonstrates how the results represented by curve 2 are modified when $E_{min}$ is reduced from 0,08 V/m to 0,008 V/m. The latter curve clearly demonstrates the importance of the minimum field strength in the geographical region.

In Figure 17b) the influence of the building material (B/W or reinforced concrete, C) and the choice of $L$ factor ($L_o$ or $L_i$) on the results can be observed. Curve 1 in that figure is identical to curve 3 in Figure 17 a), so it concerns $L_o$ data for B/W-buildings. When using $L_i$ data the building effect has to be taken into account because there is no direct model to predict the indoor field-strength distribution. By doing so, the results represented by curve 2 are found. As for curve 1 the maximum outdoor field-strength $E_{max}$ = 3 V/m, but due to the building effect the maximum indoor field strength $E_{i,max} = E_{max} A_{bi}$, where $A_{bi}$ is the lowest building effect as

IECNORM.COM : Click to view the full PDF of CISPR TR 16-3:2020 RLV

determined from the experimental data. In this case $A_{bi}$ = −10 dB, so that $E_{i,max}$ = 9,5 V/m, hence there is an amplification of the outdoor field strength.




NOTE See Table 10 for the various parameter values used, and below for key. Total number of outlets 42 × 106, homogeneous density of the outlets: $\mu$ = 168 km$^{-2}$.

**Figure 17 – Examples of number (left-hand scale) and relative number (right-hand scale) of outlets with $U_L \leq U_h \leq U_{max}$**

Key to Figure 17 curves:

a) B/W buildings

| | | | |
|---|---|---|---|
| Curve 1: | nontruncated $L_o$ factor, | $E_{max}$ = 10 V/m, | $E_{min}$ = 0,08 V/m |
| Curve 2: | truncated $L_o$ factor, | $E_{max}$ = 10 V/m, | $E_{min}$ = 0,08 V/m |
| Curve 3: | truncated $L_o$ factor, | $E_{max}$ = 3 V/m, | $E_{min}$ = 0,008 V/m |
| Curve 4: | truncated $L_o$ factor, | $E_{max}$ = 10 V/m, | $E_{min}$ = 0,08 V/m |

b) Truncated $L$ factors, maximum outdoor field strength 3 V/m

| | |
|---|---|
| Curve 1: | B/W buildings, $L_o$ factor |
| Curve 2: | B/W buildings, $L_i$ factor |
| Curve 1: | C buildings, $L_o$ factor |
| Curve 2: | C buildings, $L_i$ factor |

One might argue that a negative value of $A_{bi}$ is not realistic. As mentioned in 4.4.2.2, the negative values predominantly originated from measurements where the indoor field strength was measured at an upper floor of the building, and the outdoor field strength at 1,5 m above ground level. Furthermore, re-radiation effects also influenced the actual field-strength data. One may decide to truncate the building-effect distribution at the lower end at 0 dB. In that case, $E_{i,max}$ and $U_{max}$ reduce from 85 V to $L_u E_{max}$ = 8,9 × 3 = 27 V.

IECNORM.COM : Click to view the full PDF of CISPR TR 16-3:2020 RLV

Assuming that all 42 million outlets are located in reinforced concrete buildings, the results represented by curve 1 in Figure 17 b) are modified into those represented by curve 3, while curve 4 follows if the $L_i$ data are used. In practice, the outlets will be distributed over the B/W and C buildings. Then $N_T$ in the calculations is the total number of outlets in a given type of building, and the results for both types of building have to be added.

NOTE 1 Although the number of outlets $N_o(U_h \geq U_L)$ as given in Figure 17 may have non-negligible values, the relative number is very low. This stresses the importance of the "tails" of the various distributions used and of the applied truncation. In addition, if the analytical expressions given in the annexes are not used, but a full-numerical calculation is made [for example, one starting with $n_m(E_o)$], care has to be taken that the accuracy of the numerical calculations is sufficiently high. The very low values of the relative number $N_o(U_h \geq U_L)/N_T$ form an indication of the accuracy needed. The relative number is identical to $pr\{U_h \geq U_L\}$ in %.

NOTE 2 In all calculations the density of the outlets $\mu$ was considered to be a constant over the entire respective region. The results can be improved, for example, when the calculations leading to $n_m(E_o)$ (see Figure 15), take a location-dependent $\mu$ into account.

NOTE 3 Curves 2 and 4 in Figure 17b) are based on $L_i$ and $A_b$ data, and a warning has to be given here. As mentioned in 4.4.2, it is not very likely that inside the buildings the far-field condition will be satisfied and, formally speaking $L_i$ cannot be derived from $G_i$. In addition, $A_b$ was determined from magnetic field-strength data and $A_b$ for the electric field need not be the same. In the calculations leading to curves 2 and 4, it was tacitly assumed that $L_i = G_i/Z_0$ ($Z_0$ = 377 Ω). However, the same curves for $N_o(U_h \geq U_L)$ would have been found when correctly using the $G_i$ and $A_b$, but quoting rows 15 and 16 of Table 10 means the magnetic field quantities $H_{max} = E_{max}/Z_0$ etc., and replacing $C_{Ei}$ by $C_{Hi} = C_{Ei}/Z_0^2$ (see B.4).

#### 4.4.4.3 Summary of disturbance source parameters

##### 4.4.4.3.1 General

Assuming that the disturbance source in the conducted-immunity test is sufficiently described by an open-circuit voltage and internal impedance, the following parameters are of importance.

##### 4.4.4.3.2 The internal impedance

The internal impedance may be specified as a purely resistive quantity, for which the magnitude is chosen on the basis of the results for the equivalent asymmetrical resistance $R_a$, as given in 4.4.2.4. The choice depends on the reference for the asymmetrical disturbance source considered to be relevant in the situations where interference problems have to be prevented. An often used value is $R_a$ = 150 Ω [24], [25], [14] which is not in conflict with the $R_a$ results presented in 4.4.2.4.

##### 4.4.4.3.3 The open-circuit voltage

Because the induced asymmetrical voltage has been measured at non-random locations in order to have a sufficiently large induced-signal-to-ambient-noise ratio, the raw $U_h$ data cannot be used and the procedure described in 4.4.4.2 has to be followed. From that procedure, described in more detail in Annex C and Annex D, it can be concluded that the following parameters have to be considered (see also Table 10).

a) $N_T$ — The total number of outlets in the geographical region (country) to be considered. $N_T$ is either the grand total of outlets or the total number of outlets in a certain type of building (brick/wood or reinforced concrete).

b) $M_G$ or $M_L$ — The average value of the $G$ or $L$ factor, in dB(Ωm) or dB(m) (see Table 4 and Table 5). If the $G_i$ or $L_i$ factors are used, the following building effect parameters shall be known (see Table 3 and Table 6):

$M_A$: the average building effect $A_b$ in dB

$S_A$: the standard deviation of $A_b$ in dB

$A_{bu}$: the maximum building effect

IECNORM.COM : Click to view the full PDF of CISPR TR 16-3:2020 RLV

$A_{BI}$: the minimum building effect

c) $S_G$ or $S_L$ — The standard deviation (in dB) associated with $M_G$ or $M_L$

d) $G_U$, $G_L$ — The upper and lower limit of the $G$-factor range or the $L$-factor range

$L_U$, $L_L$

e) $H_{max}$ or $E_{max}$ — The upper boundary of the outdoor field strength, in A/m or V/m, which determines the inner boundary of the areas around the transmitters to be considered.

This value may be chosen after considering radiation hazards. However, in particular in the case of mass-produced appliances, the following consideration seems to be relevant. Choose (or agree on) a maximum field strength of $X$ (A/m or V/m) such that there is a high probability that all equipment will be electromagnetically compatible when the field strength is equal to or smaller than $X$ (A/m or V/m), and agree that special EMC hardening measures are to be taken in that part of the region where the field strength is larger than $X$ (A/m or V/m) and (simultaneously) a complaint occurs.

f) $H_{min}$ or $E_{min}$ — The minimum field strength determining the outer boundary of the areas around the transmitters (see 4.4.4.2).

This value needs to be chosen only when the field-strength distribution $n(H)$ or $n(E)$ is unknown. If this distribution is known, $H_{min}$ or $E_{min}$ is calculated from an equation like Equation (20).

g) $n(H)$ or $n(E)$ — The field-strength distribution, as discussed in 4.4.4.2 and Annex B.

## 4.5 Predictability of radiation in vertical directions at frequencies above 30 MHz

### 4.5.1 Summary

CISPR 11 sets limits for the electromagnetic disturbances emitted *in situ* near the ground from industrial, scientific and medical (ISM) radio-frequency equipment. In CISPR 11:2003 with Amendment 1 (2004) [5], referring to protection of safety of life services, it was stated, "Many aeronautical communications require the limitation of vertically radiated electromagnetic disturbances. Work is continuing to determine what provisions may be necessary to provide protection for such systems."

This subclause considers the calculated vertical radiation patterns of the $E$-field which will be emitted at frequencies above 30 MHz from electrically small sources physically located close to the surface of real homogeneous plane ground. Its purpose is the study of the predictability of radiation in vertical directions based on *in situ* measurements of the strength of the $E$-field near the ground. The sources considered are electrically small balanced electric and magnetic dipoles excited in the frequency range from 30 MHz to 1 000 MHz.

The effects on the vertical radiation patterns caused by a wide range of the electrical properties of the ground, varying from wet ground to very dry ground – and the special case of a ground that behaves like a near-perfect conductor – have also been considered.

These studies show the limitations of the predictability of radiation at elevated angles when based on measurements near the ground. The subclause identifies some of the factors to be considered when developing and specifying limits of radiated electromagnetic disturbances and methods of measurement which are intended to protect aeronautical radionavigation and communication systems operating at frequencies above 30 MHz. For example, it shows that vertical patterns of the fields over good conductors do not represent the field patterns over real grounds. Moreover, the subclause shows that for good predictability of the field strengths at elevated angles, the *in situ* measurements near the ground shall not be made at fixed heights but instead they shall use height scans and, in particular shall be made at a known distance from the equipment which is the source of the radiation.

IECNORM.COM : Click to view the full PDF of CISPR TR 16-3:2020 RLV

### 4.5.2 Range of application

This subclause considers the predictability of radiation in vertical directions based on measurements of the strength of the electric ($E$) fields emitted by electrical equipment near the ground. It is intended to give guidance about the predictability of radiation emitted at elevated angles by electrical equipment *in situ*, in particular industrial, scientific, and medical (ISM) radio-frequency equipment. For that purpose, it studies the calculated vertical radiation patterns of the $E$-fields which will be emitted at frequencies above 30 MHz from electrically small sources located close to the surface of real homogeneous plane ground.

The vertical radiation patterns of the horizontally and vertically polarized $E$-fields, including the surface waves, have been calculated at distances of 10 m, 30 m and 300 m from various electrically small sources, so that the field variations with distance can be quantified. In this way, a general knowledge has been obtained of the shapes of the vertical radiation patterns, showing the magnitudes of the $E$-field strengths near ground compared with the magnitudes of the $E$-field components at elevated angles, and the ways in which the relative magnitudes can be expected to vary with distance over a plane ground.

The sources considered were electrically small balanced electric and magnetic dipoles excited in the frequency range from 30 MHz to 1 000 MHz. For the purposes of the study, an electrically small source is defined as one whose largest linear dimension is one-tenth or less of the free-space wavelength at the frequency of interest.

Subclause 4.5 also considers the effects on the vertical radiation patterns caused by a range of electrical properties of the ground, varying from electrical conductivities and dielectric constants of wet ground to those of very dry ground [31], [32], and the special case of a ground that behaves like a near-perfect conductor.

The effects on wave propagation near the ground of walls, buildings, terrain irregularities, watercourses, vegetation cover, and so on, are not within the scope of this subclause. It is important to note, therefore, that the additional uncertainties in wave propagation caused by the presence of such discontinuities, and their effects on predictability based on measurements *in situ*, have not been considered.

### 4.5.3 General

Table E.1 of CISPR 11:2009 provides radiation limits for the protection of specific safety-related radio services. The limits apply to ground level measurements of the electromagnetic disturbances emitted by ISM radio-frequency (RF) equipment *in situ*, not on a test site. Above 30 MHz the five frequency bands listed in Table ~~9~~ E.1 of CISPR 11:2009 are all used for aeronautical services, including the instrument landing system (ILS) or instrument low-approach system marker beacon, localizer, and glide path frequencies, as well as a survival frequency and other radio-navigation and communication frequencies bands.

The *in situ* measuring distance specified in Table ~~9~~ E.1 of CISPR 11:2009, for all five frequency bands above 30 MHz, is 10 m "from the outer face of the exterior wall outside the building in which the equipment is situated." It is important to note that the precise measuring distance from the ISM apparatus itself is not specified.

IECNORM.COM : Click to view the full PDF of CISPR TR 16-3:2020 RLV

The heights at which measurements of horizontally and vertically polarized $E$-fields in the frequency range from 30 MHz to 1 000 MHz are made using a balanced dipole, and are specified in 7.3.4 of CISPR 11:2009. “The nearest point of the antenna to ground shall be not less than 0,2 m. For measurements *in situ* the centre of the antenna shall be fixed at 2,0 m ± 0,2 m height above the ground. For measurements on a test site the centre of the antenna shall be varied between 1 m and 4 m height for maximum indication at each test frequency”. CISPR 11:2009 specifies that “Class A equipment may be measured on a test site or *in situ*, as preferred by the manufacturer” and notes that “Due to size, complexity or operating conditions, some equipment may have to be measured *in situ* in order to show compliance with the radiation disturbance limits”. It goes on to say that “Class B equipment shall be measured on a test site.”

After considering the methods of specifying *in situ* measurement distance and measuring antenna height in CISPR 11, it is useful to address the following questions:

a) How well do measurements of the vertically and horizontally polarized $E$-fields, in a height scan of 1 m to 4 m at a horizontal distance of 10 m from the source over real ground, predict the field strengths emitted at elevated angles? (See 4.5.5.2)

b) How predictable are the field strengths at elevated angles when the horizontal measuring distance is greater than 10 m but, beyond that fact, the actual distance is not known (not specified)? (See 4.5.5.3)

c) How is the predictability affected when the height above ground to the centre of the measuring antenna is fixed, for example at a nominal 3 m? (See 4.5.5.4)

d) What errors in judgement of the predictability of the vertical patterns may arise if calculations are made using the common approximation that the influence of the real ground can be simulated by replacing it with a perfect conductor? (See 4.5.6)

To provide some answers, in the frequency range 30 MHz to 1 000 MHz a number of vertical polar patterns and linear height scan patterns have been calculated for the $E$-field radiation emitted by four kinds of electrically small sources located close to the surface of real homogeneous plane ground. Predictability has been assessed by judging how well, or how badly, the calculated patterns show that ground-based measurements of the vertically and horizontally polarized $E$-fields emitted from the various sources will correlate with the maximum strengths of either vertically or horizontally polarized $E$-fields (whichever are greater) at elevated angles. The patterns have been calculated for the simplest of sources radiating into the half-space above ground. If these patterns identify problems of predictability, it is unlikely that predictability will be improved when real ISM devices, like plastics welders or RF diathermy machines, are the sources.

Vertical polar patterns and linear height scan patterns have also been calculated for the $E$-field radiation emitted from the small sources over a copper ground plane. A copper ground plane provides boundary conditions which distinguish, in effect, a perfect conductor from a real ground, and allows identification of the differences between the vertical radiation patterns that will exist close to the surface of a real ground when compared with those calculated close to the surface of a perfect conductor. The differences determine how large the errors will be if predictability is judged by considering vertical patterns calculated over a perfectly conducting ground plane.

The four kinds of sources considered were electrically small vertical and horizontal balanced electric and magnetic dipoles. There is justification for the use of small dipole sources as models in the study of the predictability of radiation at elevated angles from real ISM equipment. Airborne measurements of the fourth harmonic field radiated from 27 MHz ISM apparatus over real ground reported in [33] have been studied further in [34]. In [34] it is shown that the vertical distribution of horizontally polarized fields at approximately 109 MHz, encountered by an aircraft during any single flight pass over the ISM apparatus, can be well matched with a field distribution produced at elevated angles by a simple small electric or magnetic dipole source. Some of the work in [34] is summarized in Annex F.

IECNORM.COM : Click to view the full PDF of CISPR TR 16-3:2020 RLV

### 4.5.4 Method used to calculate field patterns in the vertical plane

#### 4.5.4.1 General

The $E$-field vertical polar patterns and linear height scan patterns have been calculated using a double precision version of the method of moments computer code known as the Numerical Electromagnetics Code (NEC) [35]. NEC2 with the companion code SOMNEC allows the Sommerfeld integral evaluation of the field interactions at the air-ground interface [36], and so includes the contribution of the Sommerfeld-Norton surface wave when calculating the total $E$-fields above real grounds (discussed in 4.5.6.4). The near fields were also included in the calculations for results in this subclause.

The small vertical and horizontal balanced electric dipoles, and vertical and horizontal balanced loops (magnetic dipoles) used as the models for the calculations each had a unit dipole moment [i.e. a dipole (current) moment of 1 A·m for the electric dipoles and a dipole moment of 1 A·m$^2$ for the loops]. All were positioned with their centres at a height above ground of either 1 m or 2 m in order to show the effects of variations in the source height on the vertical radiation patterns. The effects include the appearance of additional major lobes of radiation – called grating lobes – as the spacing between the source and its image in the ground increases beyond $\lambda/2$ with increasing frequency [37].

The geometries of the models, and the paths of the scans in vertical planes at constant radius about each source for the vertical polar pattern computations, are shown in the top right corner of each polar pattern plot.

The planes in which the linear height scan patterns were calculated are shown in the diagrams accompanying each linear height scan pattern plot.

#### 4.5.4.2 Frequencies of interest and the electrical constants of the ground

The five frequencies of interest at which the models were excited, in the five ITU designated bands [38] listed in Table E.1 of CISPR 11:2009, are shown here in Table 11.

**Table 11 – Frequencies of interest in ITU designated bands from Table 9 of CISPR 11:2009**

| Excitation frequency MHz | ITU designated bands |
|---|---|
| 75 | 74,8 MHz to 75,2 MHz, Aeronautical Radionavigation (Instrument Landing System (ILS) marker beacons, horizontal polarization) |
| 110 | 108 MHz to 137 MHz, Aeronautical Radionavigation and Aeronautical Mobile (R) (including ILS localizers (108 MHz to 112 MHz), horizontal polarization) |
| 243 | 243 MHz is for use by survival craft stations and equipment used for survival purposes |
| 330 | 328,6 MHz to 335,4 MHz, limited to ILS (glide path, horizontal polarization) |
| 1 000 | 960 MHz to 1 215 MHz, reserved on a worldwide basis for the use and development of airborne electronic aids to air navigation |

Most attention has been devoted to the small sources placed above a “medium dry ground” [31] (CCIR: medium dry ground; rocks; sand; medium sized towns [32]). The electrical constants, the relative permittivity $\varepsilon_r$ and the conductivity $\sigma$ (mS/m), for “medium dry ground” at 30 MHz and the other five frequencies of interest are listed in Table 12.

IECNORM.COM : Click to view the full PDF of CISPR TR 16-3:2020 RLV

**Table 12 – Electrical constants for "medium dry ground" [31] (CCIR: medium dry ground; rocks; sand; medium sized towns[32])**

| Frequency<br>MHz | $\varepsilon_r$ | $\sigma$<br>mS/m |
|---|---|---|
| 30 | 15 | 1 |
| 75 | 15 | 1,5 |
| 110 | 15 | 2 |
| 243 | 15 | 4,5 |
| 330 | 15 | 7,5 |
| 1 000 | 15 | 35 |

Near the lower and upper ends of the frequency range, at frequencies of 75 MHz and 1 000 MHz, examples of two other types of grounds have been used with the electrically small vertical loop model (horizontal magnetic dipole) to illustrate the influence of differing values of the ground constants on the vertical radiation patterns (see 4.5.6.2). The electrical constants for "wet ground" and "very dry ground" at 30 MHz, 75 MHz and 1 000 MHz, are listed in Table 13.

**Table 13 – Electrical constants for "wet ground" [31] (CCIR: marshes (fresh water); cultivated land [24]) and "very dry ground" [31] (CCIR: very dry ground; granite mountains in cold regions; industrial areas [32])**

| Frequency | Wet ground | | Very dry ground | |
|---|---|---|---|---|
| MHz | $\varepsilon_r$ | $\sigma$<br>mS/m | $\varepsilon_r$ | $\sigma$<br>mS/m |
| 30 | 30 | 10 | 3 | 0,1 |
| 75 | 30 | 13 | 3 | 0,1 |
| 1 000 | 30 | 140 | 3 | 0,15 |

IECNORM.COM : Click to view the full PDF of CISPR TR 16-3:2020 RLV

### 4.5.5 Limitations of predictability of radiation at elevated angles

#### 4.5.5.1 Influence of the electrical constants of the ground

##### 4.5.5.1.1 General

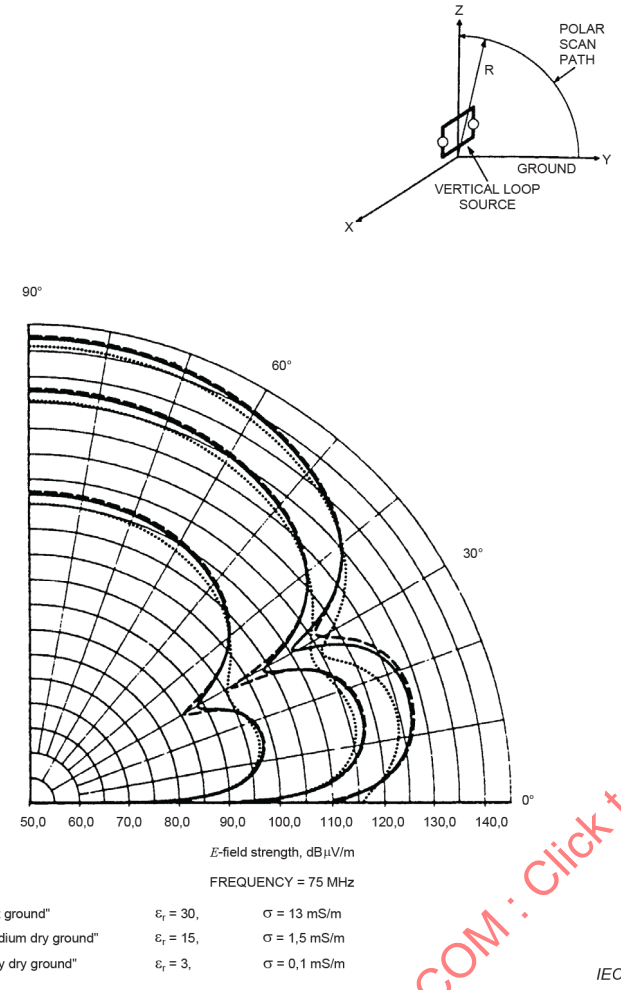
It is useful to observe the relatively small influence of widely differing values of the ground constants on the predictability of the field strengths at elevated angles. A small vertical loop (horizontal magnetic dipole) at a centre height of 2 m above ground was chosen as the source model. The geometry of the model is shown in Figure 18. For this source, the best predictability is obtained when the vertical $E_z$ field component is measured near the ground to estimate the maximum strength of either the horizontally oriented $E_x$ field or the vertically oriented $E_z$ field at elevated angles.

##### 4.5.5.1.2 Influence of the ground constants at 75 MHz

In Figure 18, the vertical polar patterns at 75 MHz show the horizontally polarized $E_x$ field strengths in the Y-Z plane at scan radii $R$ of 10 m, 30 m, and 300 m, over real grounds having the electrical constants in Table 12 and Table 13. It can be seen that at each of the three scan radii, the total *spread* in the maximum $E_x$ fields in the vertical direction is less than 3 dB.

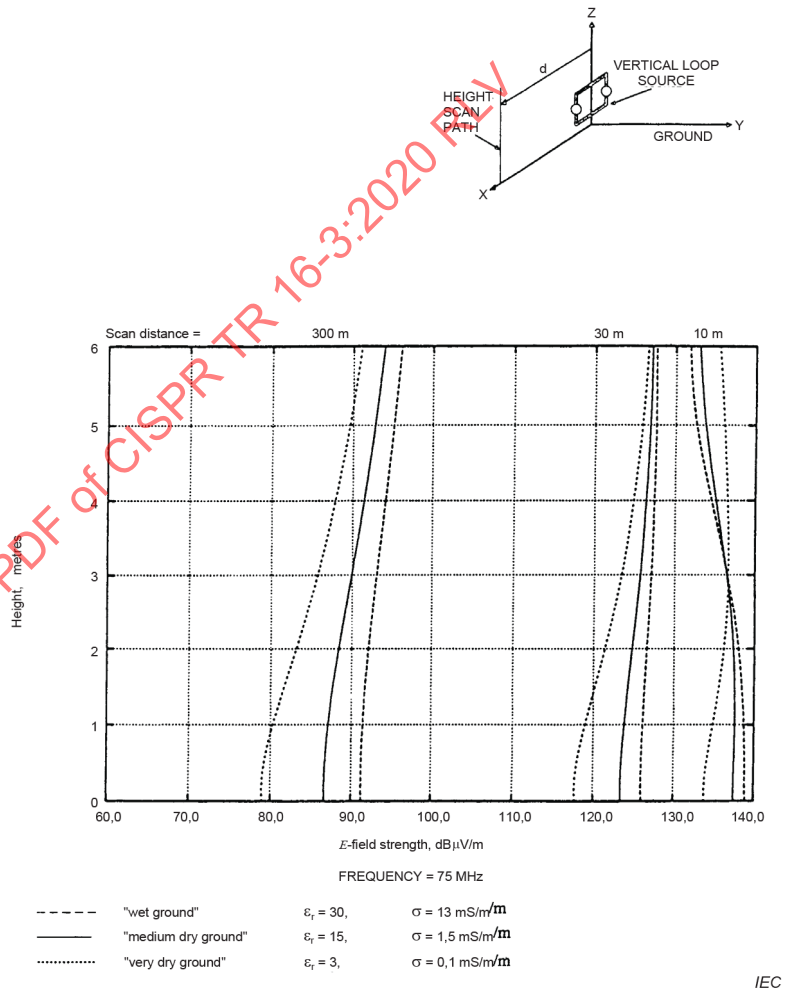
In Figure 19, the height scan patterns calculated up to a height of 6 m at 75 MHz show the $E_z$ field strengths in the Z-X plane at the three corresponding horizontal distances over the same three types of real ground. It can be seen that the *spread* in magnitudes of the $E_z$ field strengths at ground level for the three ground types is much greater than 3 dB. However, if measurements of $E_z$ are made at heights from 1 m to 4 m, then at a horizontal distance of 10 m the underestimates of the maximum $E_x$ field strengths in the vertical direction vary from about 3,9 dB to about 4,7 dB (a *spread* of only 0,8 dB), at a horizontal distance of 30 m, the underestimates vary from about 5,1 dB to about 5,7 dB (a *spread* of only 0,6 dB), and at 300 m, the underestimates vary from about 18,4 dB to about 22,1 dB (a *spread* of 3,7 dB). Thus, for the range of values of the ground constants and measuring distances considered here, the worst case *spread* or *variation* in the underestimates of maximum field strengths in the vertical direction is only 3,7 dB, and this occurs at the largest measuring distance of 300 m.

IECNORM.COM : Click to view the full PDF of CISPR TR 16-3:2020 RLV




NOTE Loop dimensions 0,1 m × 0,1 m; loop centre height 2 m; dipole moment 1 A·m$^2$; scan radii of 10 m, 30 m and 300 m; 75 MHz; Y-Z plane (Reproduced from [39]).

**Figure 18 – Vertical polar patterns of horizontally polarized $E_x$ field strengths emitted around small vertical loop (horizontal magnetic dipole) over three different types of real ground**




NOTE Loop dimensions 0,1 m × 0,1 m; loop centre height 2 m; dipole moment 1 A·m$^2$; horizontal distances 10 m, 30 m and 300 m; 75 MHz; Z-X plane (Reproduced from [39]).

**Figure 19 – Height scan patterns of vertically oriented $E_z$ field strengths emitted from small vertical loop (horizontal magnetic dipole) over three different types of real ground**

IECNORM.COM : Click to view the full PDF of CISPR TR 16-3:2020 RLV

#### 4.5.5.1.3 Influence of the ground constants at 1 000 MHz

In Figure 20, the vertical polar patterns at 1 000 MHz show the horizontally polarized $E_x$ field strength in the Y-Z plane at the same three scan radii $R$ around the small vertical loop over the same three types of real ground with the electrical constants at 1 000 MHz given in Table 12 and Table 13. It can be seen that for a source height of 2 m at this frequency, multiple grating lobes are established.

Figure 21 shows the vertical polar patterns of the vertically oriented $E_z$ field strengths in the Z-X plane, and Figure 22 shows the height scan patterns of the $E_z$ field strengths calculated up to a height of 6 m in the Z-X plane, at the three scan distances and over the three types of real ground.

Figure 20 shows that the maximum strength of the $E_x$ field occurs at an elevation angle between 77° and 78° at all three scan radii. A comparison of Figure 21 with Figure 20 also shows, in the case of a "very dry ground", that the maximum field strength is contributed by $E_z$ at the scan radii of 30 m and 300 m at an elevation angle of 2° (that is, at heights of approximately 1,1 m and 10,5 m at the two radii respectively).

Inspection of Figure 20 through Figure 22 reveals the following information. If a vertically polarized antenna measures maximum $E_z$ in height scans from 1 m to 4 m, then at 10 m horizontal distance the resulting underestimates of the maximum $E_x$ field strengths range from about 1,8 dB to about 3,2 dB, a *spread* of only 1,4 dB. At 30 m horizontal distance, with "medium dry ground" or "wet ground," a 1 m to 4 m $E_z$ height scan measurement underestimates the maximum $E_x$ field strengths by about 1,4 dB ("medium dry ground") or about 2,9 dB ("wet ground"), a *spread* of only 1,5 dB. Over "very dry ground," the maximum field strength, $E_z$, is reached at a height of about 1,1 m, and will therefore be measured within the height scan from 1 m to 4 m.

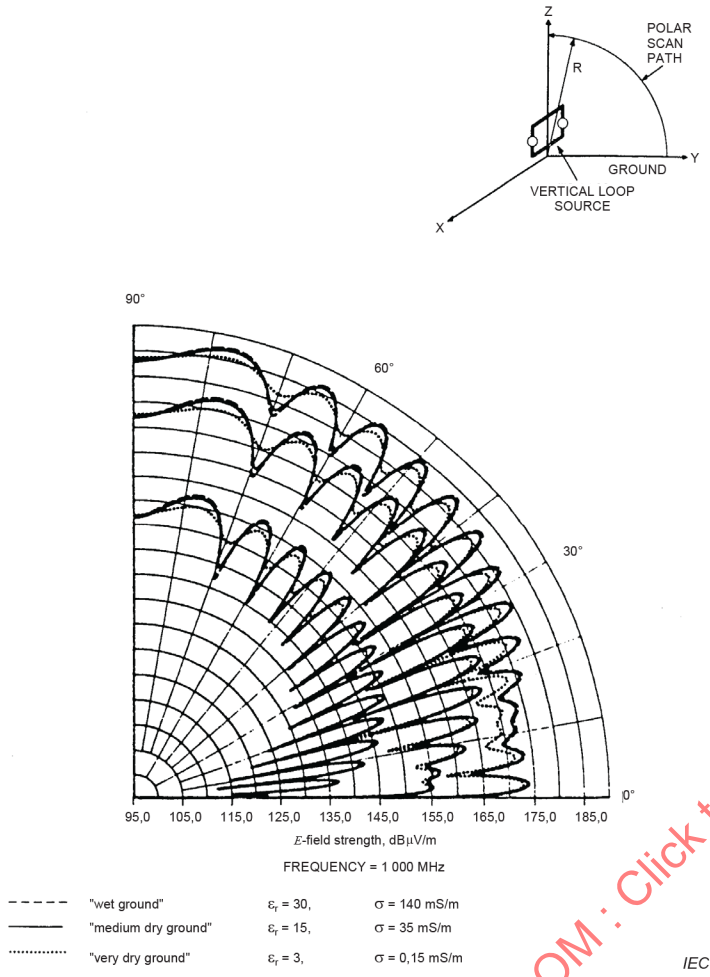
At 300 m horizontal distance, over "medium dry ground" and "wet ground", a 1 m to 4 m height scan of $E_z$ underestimates the maximum $E_x$ field strengths (at about 77° elevation) by about 4,4 dB ("medium dry ground") or about 5,2 dB ("wet ground") a *spread* of only 0,8 dB. Over "very dry ground" a measurement of $E_z$ at a height of 4 m underestimates the maximum field strength (maximum $E_z$ at an elevation angle of 2°, height approximately 10,5 m) by about 5,1 dB. The overall *spread* in the underestimates at 300 m distance therefore remains only 0,8 dB.

Thus, at 1 000 MHz, the calculations show that the differing values of the electrical constants of the ground we have considered here produce a worst-case *variation* or *spread* of only 1,5 dB in the underestimates of the maximum $E$-field strengths at elevated angles, when the estimates are based on 1 m to 4 m height scan measurements of $E_z$ at horizontal distances ranging from 10 m to 300 m.

#### 4.5.5.1.4 Predictability estimated over a "medium dry ground"

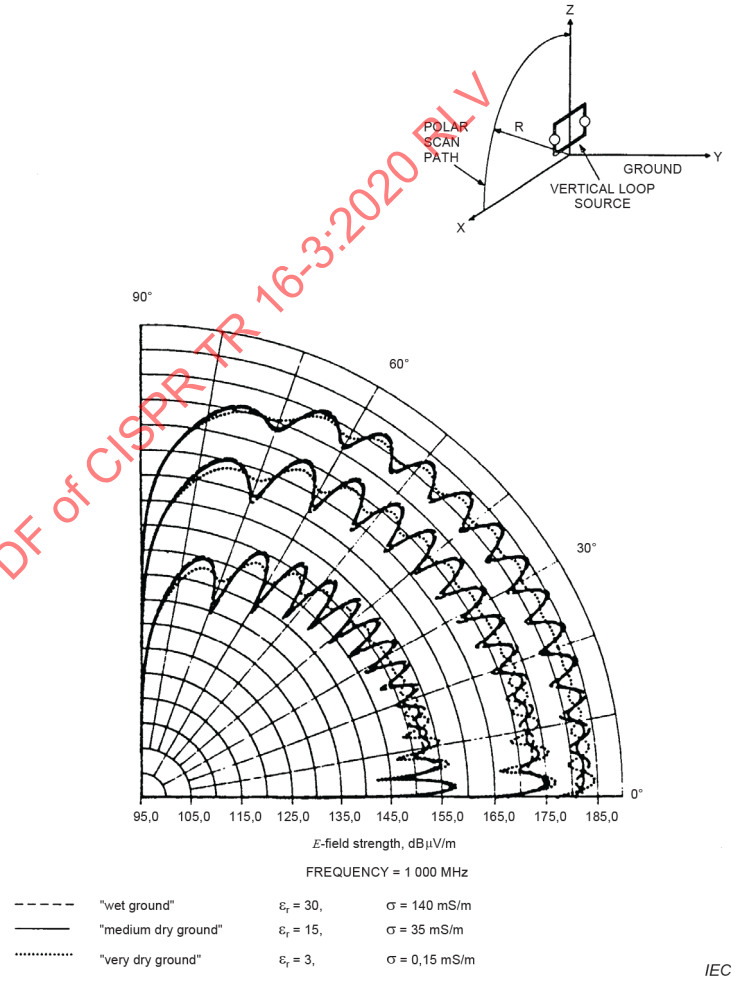
The foregoing shows that in the frequency range from 75 MHz to 1 000 MHz it is justifiable to make general judgements of the predictability of the strength of radiation in vertical directions above ground by considering the $E$-field patterns calculated over a real ground having the electrical constants of a "medium dry ground."

IECNORM.COM : Click to view the full PDF of CISPR TR 16-3:2020 RLV




NOTE Loop dimensions 0,02 m × 0,02 m; loop centre height 2 m; dipole moment 1 A·m$^2$; scan radii of 10 m, 30 m and 300 m; 1 000 MHz; Y-Z plane (Reproduced from [39]).

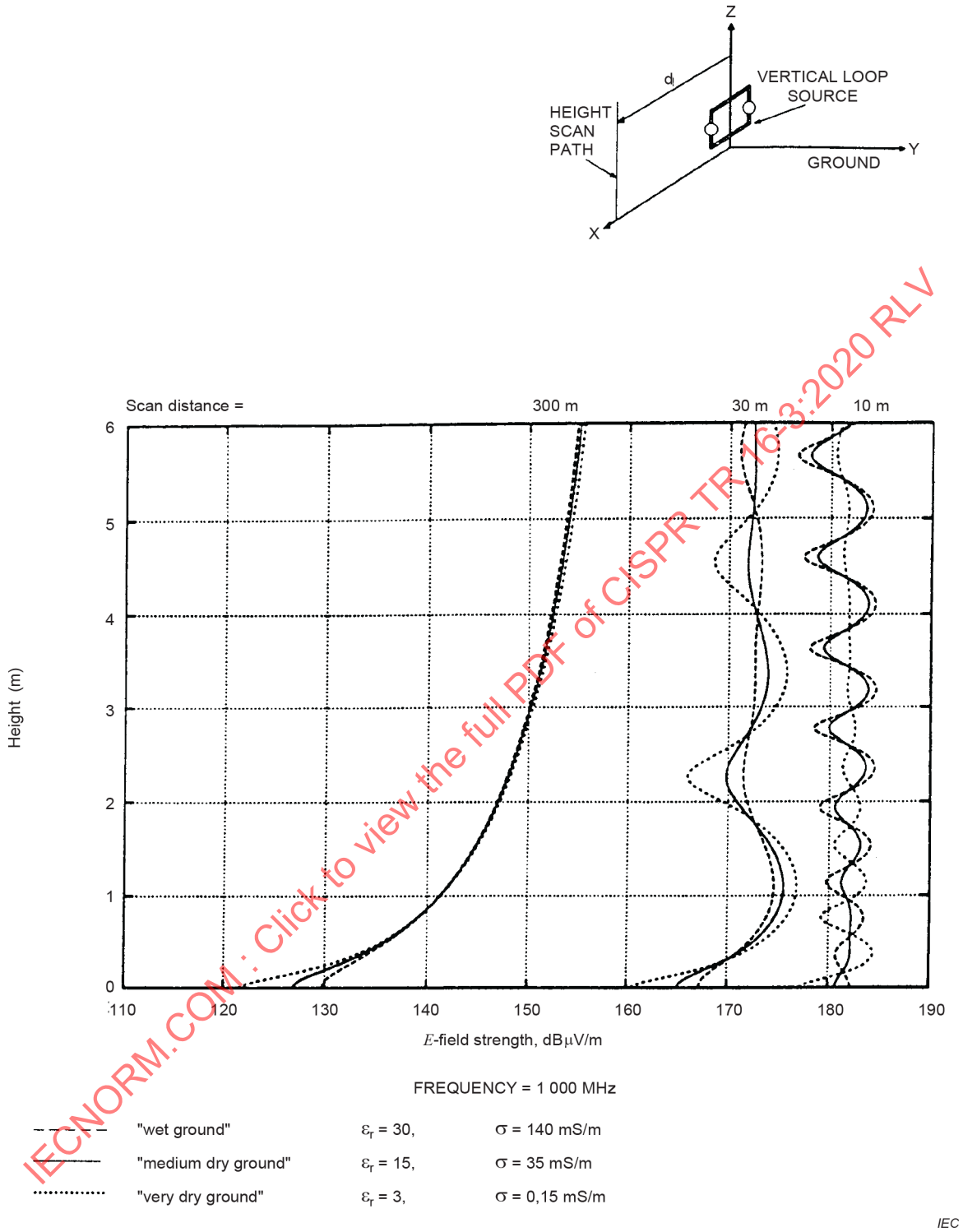
**Figure 20 – Vertical polar patterns of horizontally polarized $E_x$ field strengths emitted around small vertical loop (horizontal magnetic dipole), over three different types of real ground**




NOTE Loop dimensions 0,02 m × 0,02 m; loop centre height 2 m; dipole moment 1 A·m$^2$; scan radii of 10 m, 30 m and 300 m; 75 MHz; Z-X plane (Reproduced from [39]).

**Figure 21 – Vertical polar patterns of vertically oriented $E_z$ field strengths emitted around small vertical loop (horizontal magnetic dipole) over three different types of real ground**

IECNORM.COM : Click to view the full PDF of CISPR TR 16-3:2020 RLV




IECNORM.COM : Click to view the full PDF of CISPR TR 16-3:2020 RLV

NOTE Loop dimensions 0,02 m × 0,02 m. Loop centre height 2 m. Dipole moment 1 A·m$^2$. (Reproduced from [39]).

**Figure 22 – Height scan patterns of vertically oriented $E_z$ field strengths emitted at 1 000 MHz from the small vertical loop (horizontal magnetic dipole), at horizontal distance of 10 m, 30 m and 300 m in the Z-X plane over three different types of real ground**

#### 4.5.5.2 Predictability based on height scan measurements near real ground at 10 m distance from the source

##### 4.5.5.2.1 General

Here we can provide an answer to the first question raised in 4.5.3.

In summary, the answer is that the predictability of the maximum $E$-field strengths at elevated angles by means of 1 m to 4 m height scan measurements at a horizontal distance of 10 m, for all four types of sources placed either 1 m or 2 m above a “medium dry ground” is very good. Underestimates at all five of the frequencies used for aeronautical services are less than 6 dB.

At the two lower frequencies of 75 MHz and 110 MHz, the larger underestimates occur when the source is either a small horizontal electric dipole 1 m above the ground or a small vertical loop (horizontal magnetic dipole) with a centre height 2 m above ground.

At the frequencies of 243 MHz and 330 MHz, the larger underestimates occur when the source is either a small vertical electric dipole or a small vertical loop with a centre height 1 m above ground.

At 1 000 MHz, the larger underestimate occurs when the source is a small vertical loop with a centre height 2 m above ground.

##### 4.5.5.2.2 Predictability at 75 MHz

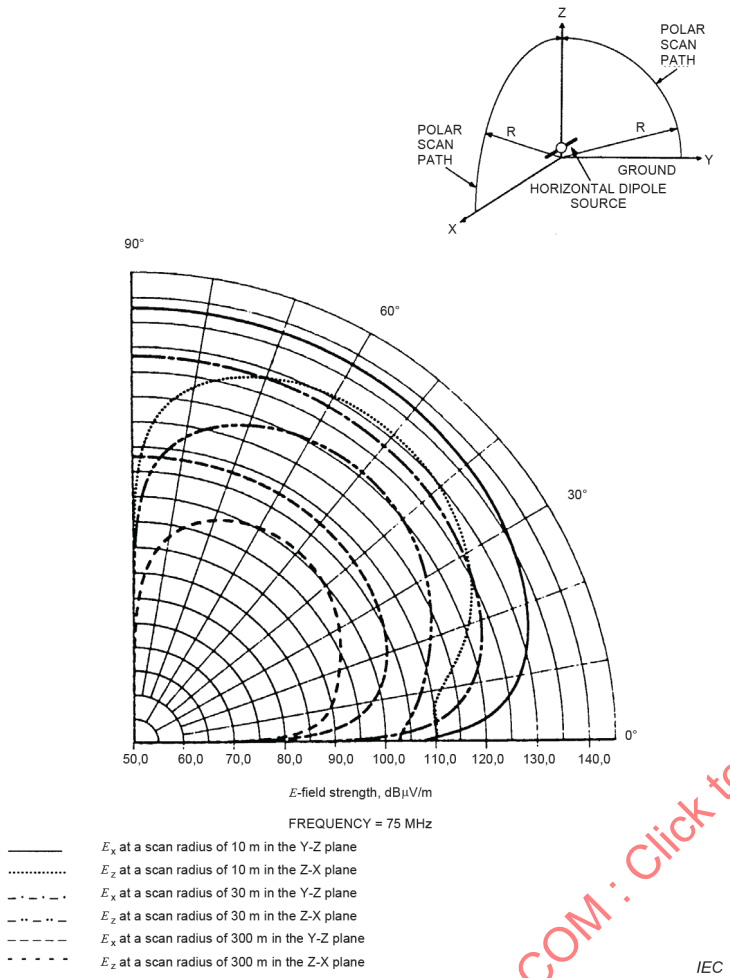
Figure 23 shows polar plots of $E_x$ in the Y-Z plane and $E_z$ in the Z-X plane, at 75 MHz, around the horizontal electric dipole placed 1 m above ground. At a scan radius of 10 m, $E_x$ reaches maximum field strength of almost 138 dBμV/m at an elevation angle near 73°. The polar plots of $E_z$ in the Z-X plane – the vertically polarized radiation emitted from the tips of a horizontal electric dipole over real ground [36] – show that vertically polarized measurements near the ground do not give the best predictions of field strength at high elevation angles. Therefore, Figure 24 shows the height scan calculations of horizontally polarized $E_x$ in the Y-Z plane, reaching an $E_x$ magnitude of almost 133 dB(μV/m) at a horizontal distance of 10 m and a height of 4 m. In consequence, 1 m to 4 m height scan measurements of $E_x$ at a distance of 10 m will underestimate the maximum $E_x$ at 73° elevation by almost 5 dB.

The vertical polar plots in Figure 18 show that measurement of $E_x$ at a distance of 10 m near the ground will not give a good prediction of the maximum field strength emitted at 75 MHz by a small vertical loop placed at a height of 2 m above a “medium dry ground.”

$E_x$ field strength reaches a maximum of over 142 dB(μV/m) in the vertical Y-Z plane. The calculated height scan patterns in Figure 19 show that a vertically polarized measurement of $E_z$ at a horizontal distance of 10 m in the Z-X plane will reach a maximum of almost 138 dB(μV/m) at 1,2 m height. This underestimates by less than 5 dB the maximum strength of the radiation in the vertical direction.

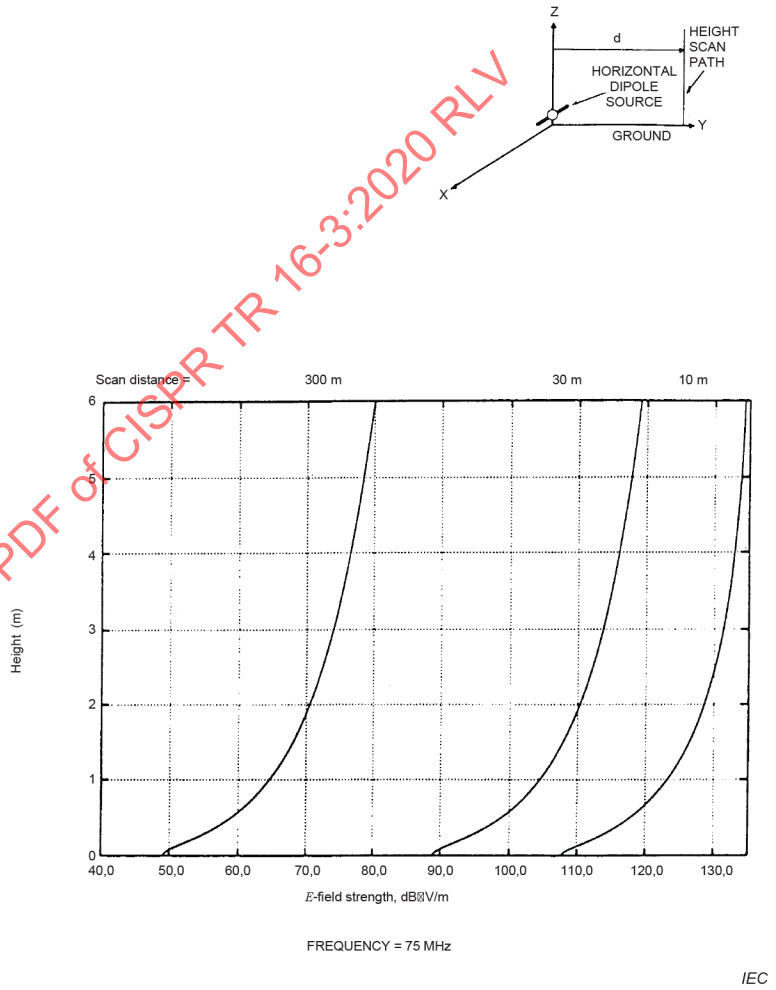
Column (4) of Table 14 summarizes the estimated errors to be expected in the predictability of radiation in vertical directions when based on measurements in height scans from 1 m to 4 m at a horizontal distance of 10 m from each of the four sources operating at 75 MHz. Column (1) lists the radiation sources and their heights. Column (2) lists the field components that contribute the maximum field strengths in the vertical polar patterns, and the elevation angles at which the maximum field strengths occur. Column (3) lists the field component that should be measured in a linear height scan at a horizontal distance of 10 m to provide the best estimates of the maximum field strengths.

IECNORM.COM : Click to view the full PDF of CISPR TR 16-3:2020 RLV




NOTE Dipole length 0,2 m; dipole height 1 m; dipole moment 1 A·m; scan radii of 10 m, 30 m and 300 m; 75 MHz; ground constants: $\varepsilon_r$ = 15, $\sigma$ = 1,5 mS/m (Reproduced from [39]).

**Figure 23 – Vertical polar patterns of horizontally polarized $E_x$ and vertically oriented $E_z$ field strengths emitted around small horizontal electric dipole, in Y-Z and Z-X planes respectively**




NOTE Dipole length 0,2 m; dipole height 1 m; dipole moment 1 A·m; horizontal distances 10 m, 30 m and 300 m; 75 MHz; ground constants: $\varepsilon_r$ = 15, $\sigma$ = 1,5 mS/m, Y-Z plane (Reproduced from [39]).

**Figure 24 – Height scan patterns of horizontally polarized $E_x$ field strengths emitted from small horizontal electric dipole**

IECNORM.COM : Click to view the full PDF of CISPR TR 16-3:2020 RLV

**Table 14 – Estimates of the errors in prediction of radiation in vertical directions based on a measurement height scan from 1 m to 4 m at known distances, $d$; frequency = 75 MHz (adapted from [39])**

| (1) Source of radiation at height | (2) Max. $E$, at angle, in 10 m polar plot | (3) At hor. $d$ = 10 m, measure this field | (4) Estimated prediction n error, at $d$ = 10 m | (5) Max. $E$, at angle, in 30 m polar plot | (6) At hor. $d$ = 30 m, measure this field | (7) Estimated prediction n error, at $d$ = 30 m | (8) Max. $E$, at angle, in 300 m polar plot | (9) At hor. $d$ = 300 m, measure this field | (10) Estimated prediction error, at $d$ = 300 m |
|---|---|---|---|---|---|---|---|---|---|
| Vertical electric dipole at 1 m | $E_z$ at 15,25° | $E_z$ $z$ | 0 dB | $E_z$ at 17,75° | $E_z$ | –2 dB | $E_z$ at 18° | $E_z$ | –17,5 dB |
| Vertical electric dipole at 2 m | $E_z$ at 8° | $E_z$ | 0 dB | $E_z$ at 12,75° | $E_z$ | –1 dB | $E_z$ at 13° | $E_z$ | –16 dB |
| Horizontal electric dipole at 1 m | $E_x$ at 72,5° in Y-Z plane | $E_x$ in Y-Z plane | –5 dB | $E_x$ at 67,5° in Y-Z plane | $E_x$ in Y-Z plane | –12 dB | $E_x$ at 66° in Y-Z plane | $E_x$ in Y-Z plane | –31,5 dB |
| Horizontal electric dipole at 2 m | $E_x$ at 30° in Y-Z plane | $E_x$ in Y-Z plane | –1,5 dB | $E_x$ at 28,75° in Y-Z plane | $E_x$ in Y-Z plane | –7 dB | $E_x$ at 28,5° in Y-Z plane | $E_x$ in Y-Z plane | –26,5 dB |
| Vertical loop (horizontal magnetic dipole) at 1 m | $E_z$ at 17,5° in Z-X plane | $E_z$ in Z-X plane | –0,5 dB | $E_z$ at 19,75° in Z-X plane | $E_z$ in Z-X plane | –2,5 dB | $E_z$ at 20° in Z-X plane | $E_z$ in Z-X plane | –18 dB |
| Vertical loop (horizontal magnetic dipole at 2 m | $E_x$ at 90° | $E_x$ in Z-X plane | –4,5 dB | $E_x$ at 90° | $E_z$ in X-Z plane | –5,5 dB | $E_x$ at 90° | $E_z$ in Z-X plane | –20,5 dB |
| Horizontal loop (vertical magnetic dipole at 1 m | $E_y$ at 37,5° in Z-X plane | $E_y$ in Z-X plane | –2,5 dB | $E_y$ at 36,75° in Z-X plane | $E_y$ in Z-X plane | –9 dB | $E_y$ at 36,5° in Z-X plane | $E_y$ in Z-X plane | –28,5 dB |
| Horizontal loop (vertical magnetic dipole) at 2 m | $E_y$ at 27° in Z-X plane | $E_y$ in Z-X plane | –1 dB | $E_y$ at 25,5° in Z-X plane | $E_y$ in Z-X plane | –6,5 dB | $E_y$ at 25° in Z-X plane | $E_y$ in Z-X plane | –25,5 dB |

IECNORM.COM : Click to view the full PDF of CISPR TR 16-3:2020 RLV

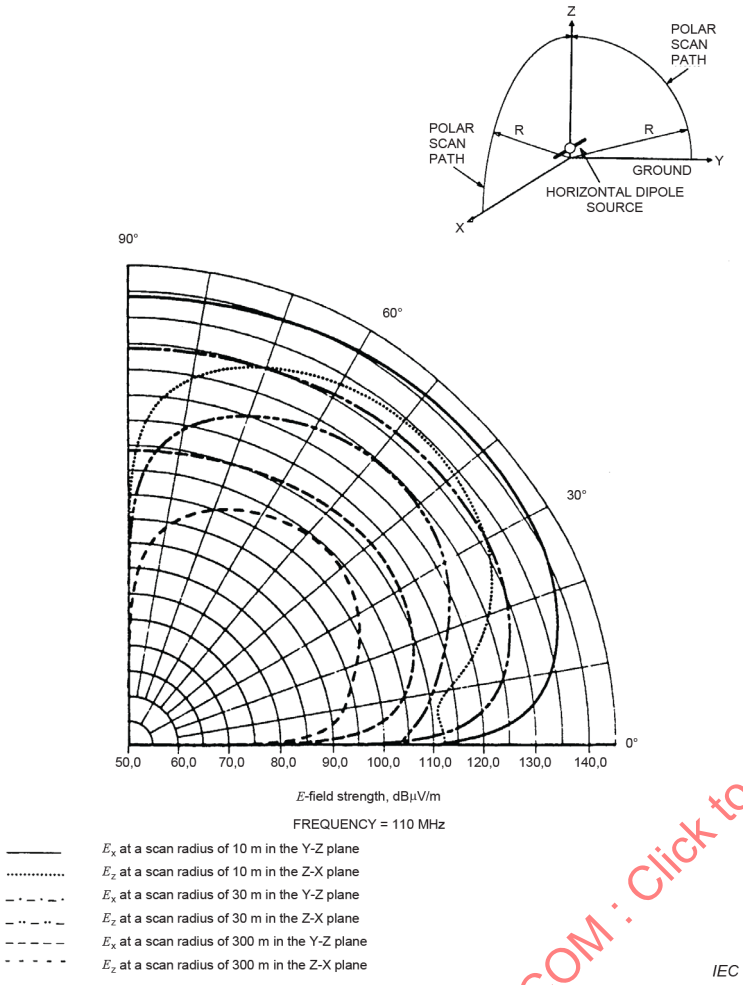
#### 4.5.5.2.3 Predictability at 110 MHz

Figure 25 shows vertical polar plots of $E_x$ in the Y-Z plane and $E_z$ in the Z-X plane, at 110 MHz, around a small horizontal electric dipole placed 1 m above the ground. At a scan radius of 10 m, $E_x$ reaches a maximum field strength of over 141 dB(μV/m) at an elevation angle of 41°. The polar plots of $E_z$ in the Z-X plane show that vertically polarized measurements near the ground will not give good guidance to high-angle field strength. Figure 26 shows height scan calculations of $E_x$ in the Y-Z plane. At a horizontal distance of 10 m the magnitude of $E_x$ reaches almost 139 dB(μV/m) at a height of 4 m, and a height scan measurement of horizontally polarized $E_x$ therefore underestimates the maximum strength of $E_x$ at 41° elevation by less than 3 dB.

Figure 27 shows vertical polar plots of $E_x$ in the Y-Z plane and $E_z$ in the Z-X plane, around a small vertical loop (horizontal magnetic dipole) placed at a centre height of 2 m above ground and excited at 110 MHz. The maximum field strength reached at a scan radius of 10 m is the vertical $E_z$ component, 146 dB(μV/m) at an elevation angle of 40°. The height scan plots of $E_z$ in Figure 28 show that at a horizontal distance of 10 m the magnitude of $E_z$ is almost 144 dB(μV/m) at a height of 1 m, which underestimates the strength of $E_z$ at 40° elevation by less than 2,5 dB.

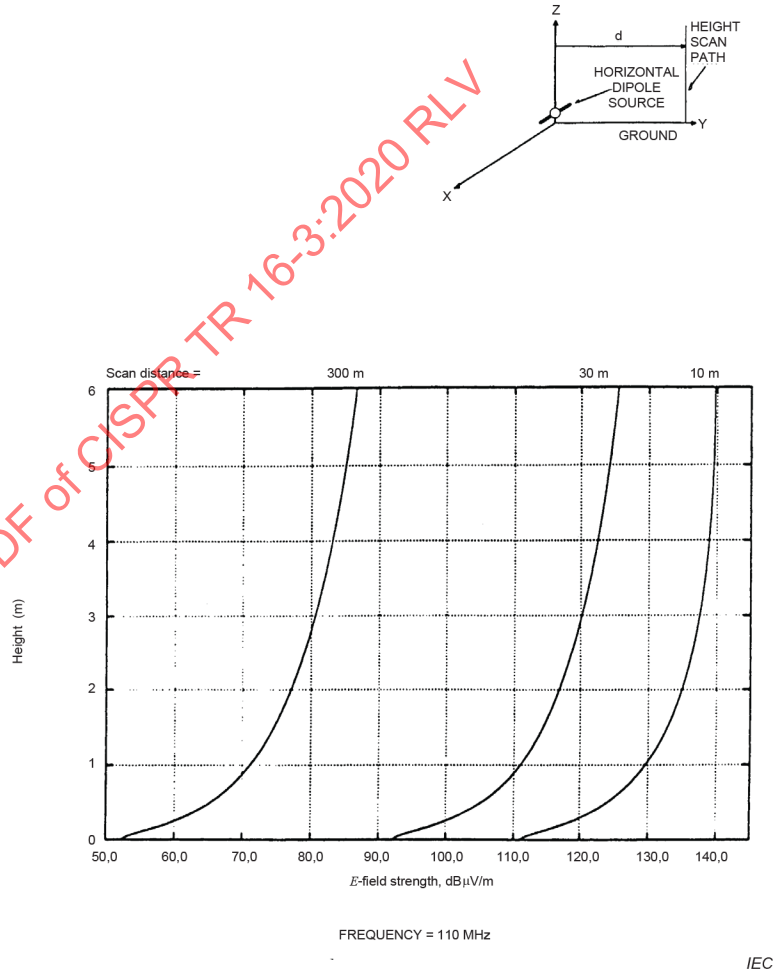
Column (4) of Table 15 summarizes the errors expected in the predictability of radiation in vertical directions based on measurements in height scans from 1 m to 4 m at a horizontal distance of 10 m from each of the four sources operating at 110 MHz.

IECNORM.COM : Click to view the full PDF of CISPR TR 16-3:2020 RLV




NOTE Dipole length 0,2 m; dipole height 1 m; dipole moment 1 A·m; scan radii of 10 m, 30 m and 300 m; 110 MHz; ground constants: $\varepsilon_r$ = 15, $\sigma$ = 2 mS/m (Reproduced from [39]).

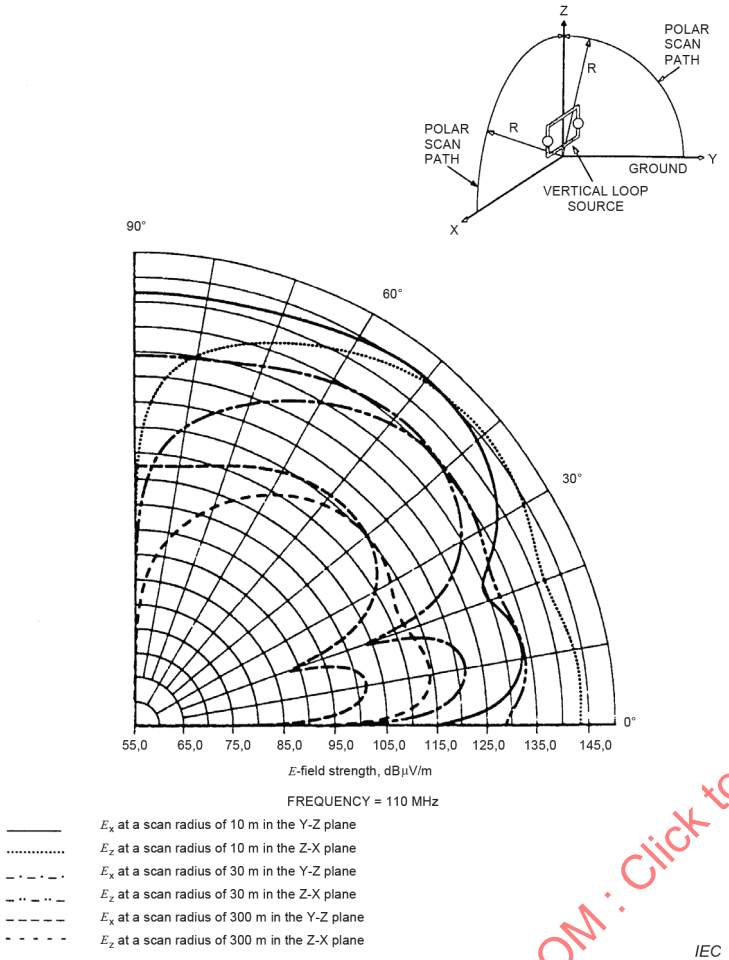
**Figure 25 – Vertical polar patterns of horizontally polarized $E_x$ and vertically oriented $E_z$ field strengths emitted around small horizontal electric dipole in Y-Z and Z-X planes respectively**




NOTE Dipole length 0,2 m; dipole height 1 m; dipole moment 1 A·m; horizontal distances 10 m, 30 m and 300 m; 110 MHz; ground constants: $\varepsilon_r$ = 15, $\sigma$ = 2 mS/m, Y-Z plane (Reproduced from [39]).

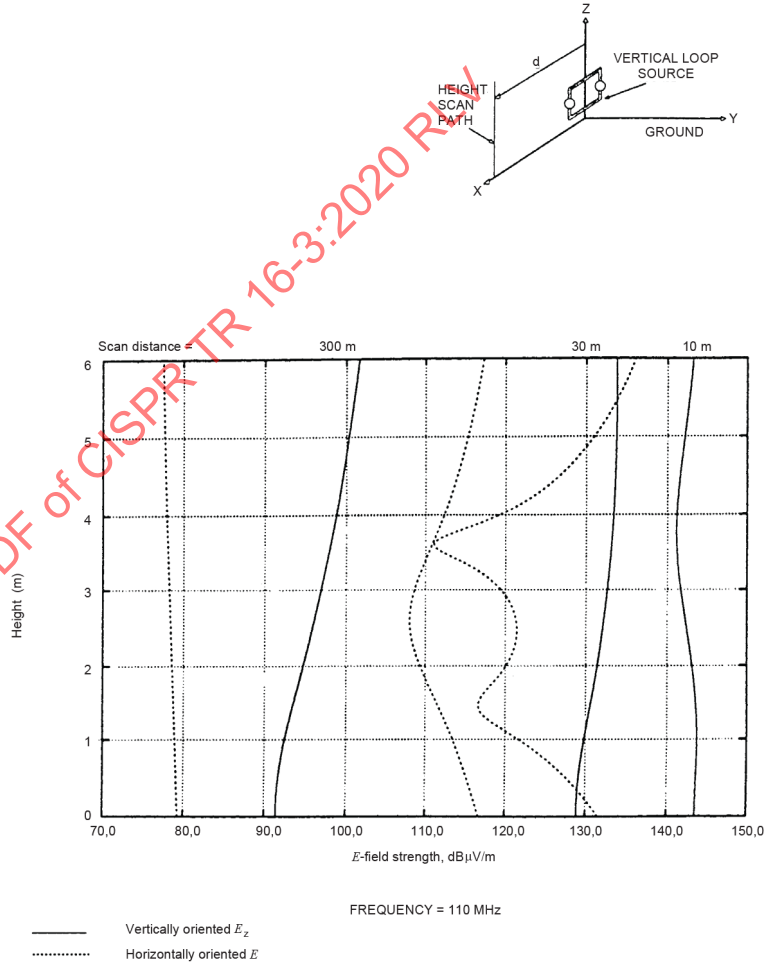
**Figure 26 – Height scan patterns of horizontally polarized $E_x$ field strengths emitted small horizontal electric dipole**

IECNORM.COM : Click to view the full PDF of CISPR TR 16-3:2020 RLV




NOTE Loop dimensions 0,1 m × 0,1 m; loop centre height 2 m; dipole moment 1 A·m$^2$; scan radii of 10 m, 30 m and 300 m; 110 MHz; ground constants: $\varepsilon_r$ = 15, $\sigma$ = 2 mS/m (Reproduced from [39]).

**Figure 27 – Vertical polar patterns of horizontally polarized $E_x$ and vertically oriented $E_z$ field strengths emitted around small vertical loop (horizontal magnetic dipole) in Y-Z and Z-X planes respectively**




NOTE Loop dimensions 0,1 m × 0,1 m; loop centre height 2 m; dipole moment 1 A·m$^2$; horizontal distances 10 m, 30 m and 300 m; ground constants: $\varepsilon_r$ = 15, $\sigma$ = 2 mS/m; 110 MHz; Z-X plane (Reproduced from [39]).

**Figure 28 – Height scan patterns of vertically oriented $E_z$ and horizontally oriented $E_x$ field strengths emitted from small vertical loop (horizontal magnetic dipole)**

IECNORM.COM : Click to view the full PDF of CISPR TR 16-3:2020 RLV

**Table 15 – Estimates of the errors in prediction of radiation in vertical directions based on a measurement height scan from 1 m to 4 m at known distances, $d$; frequency = 110 MHz (adapted from [39])**

| (1) Source of radiation at height | (2) Max. $E$, at angle, in 10 m polar plot | (3) At hor. $d$ = 10 m, measure this field | (4) Estimated prediction error, at $d$ = 10 m | (5) Max. $E$, at angle, in 30 m polar plot | (6) At hor. $d$ = 30 m, measure this field | (7) Estimated prediction error, at $d$ = 30 m | (8) Max. $E$, at angle, in 300 m polar plot | (9) At hor. $d$ = 300 m, measure this field | (10) Estimated prediction error, at $d$ = 300 m |
|---|---|---|---|---|---|---|---|---|---|
| Vertical electric dipole at 1 m | $E_z$ at 13,5° | $E_z$ | 0 dB | $E_z$ at 15,25° | $E_z$ | –1,5 dB | $E_z$ at 15,25° | $E_z$ | –17,5 dB |
| Vertical electric dipole at 2 m | $E_z$ at 36,5° | *1* | –1 dB | $E_z$ at 10,75° | $E_z$ | –0,5 dB | $E_z$ at 11° | $E_z$ | –15,5 dB |
| Horizontal electric dipole at 1 m | $E_x$ at 41° in Y-Z plane | $E_y$ in Y-Z plane | –2,5 dB | $E_x$ at 40° in Y-Z plane | $E_y$ in Y-Z plane | –9,5 dB | $E_x$ at 39,75° in Y-Z plane | $E_y$ in Y-Z plane | –29 dB |
| Horizontal electric dipole at 2 m | $E_x$ at 20° in Y-Z plane | $E_y$ in Y-Z plane | –0,5 dB | $E_x$ at 19,25° in Y-Z plane | $E_y$ in Y-Z plane | –4,5 dB | $E_x$ at 19,25° in Y-Z plane | $E_y$ in Y-Z plane | –23,5 dB |
| Vertical loop (horizontal magnetic dipole) at 1 m | $E_x$ at 90° | $E_z$ in Z-X plane | –2 dB | $E_y$ at 90° | $E_z$ in Z-X plane | –3,5 dB | $E_y$ at 90° | $E_z$ in Z-X plane | –19 dB |
| Vertical loop (horizontal magnetic dipole) at 2 m | $E_y$ at 40° in Z-X plane | $E_z$ in Z-X plane | –2,5 dB | $E_x$ at 48° in Y-Z plane | $E_z$ in Z-X plane | –2,5 dB | $E_x$ at 47,5° in Y-Z plane | $E_z$ in Z-X plane | –17,5 dB |
| Horizontal loop (vertical magnetic dipole) at 1 m | $E_y$ at 31,75° in Z-X plane | $E_y$ in Z-X plane | –1,5 dB | $E_y$ at 31° in Z-X plane | $E_y$ in Z-X plane | –8 dB | $E_y$ at 31° in Z-X plane | $E_y$ in Z-X plane | –27 dB |
| Horizontal loop (vertical magnetic dipole) at 2 m | $E_y$ at 19,25° in Z-X plane | $E_y$ in Z-X plane | –0,5 dB | $E_y$ at 18,5° in Z-X plane | $E_y$ in Z-X plane | –4 dB | $E_y$ at 18,25° in Z-X plane | $E_y$ in Z-X plane | –23 dB |

IECNORM.COM : Click to view the full PDF of CISPR TR 16-3:2020 RLV

#### 4.5.5.2.4 Predictability at 243 MHz

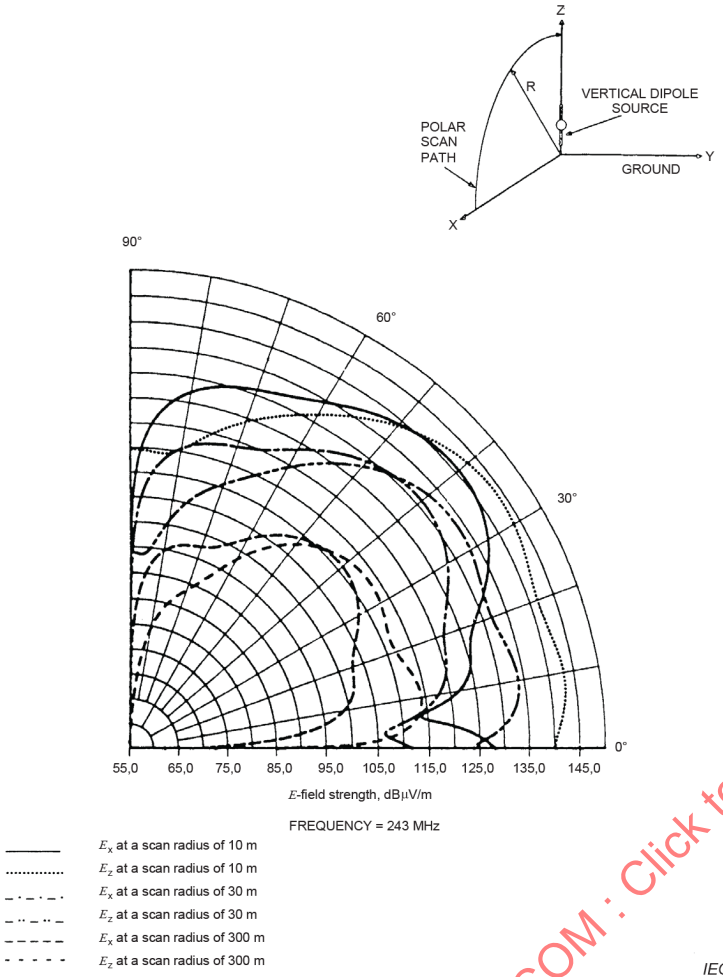
Figure 29 shows vertical polar plots of $E_z$ and $E_x$ in the Z-X plane, at 243 MHz, around the small vertical electric dipole placed at a centre height of 1 m above ground. At a scan radius of 10 m the maximum field strength of almost 144 dB(μV/m) is contributed by $E_z$ at an elevation angle of 33,75°. Calculations of the vertical field component $E_z$ in a height scan from 1 m to 4 m at a horizontal distance of 10 m produce a peak magnitude of almost 143 dB(μV/m) at a measuring height of 1,65 m, as shown in Figure 30. This underestimates the maximum field strength by only 1 dB.

Figure 31 shows vertical polar plots of $E_x$ in the Y-Z plane and $E_z$ in the Z-X plane, around the small vertical loop placed at a centre height of 1 m above a “medium dry ground.” It can be seen that, at a scan radius of 10 m, the maximum field strength of more than 159 dB(μV/m) is reached by $E_z$ at an elevation angle of 36,25° in the Z-X plane. The calculated $E_z$ height scan patterns shown in Figure 32 produce a peak field strength of 157 dB(μV/m), at 10 m horizontal distance and a height of 1,65 m. This underestimates the maximum $E_z$ by approximately 2,5 dB.

The vertical polar plots of horizontally polarized $E$-field emitted at 243 MHz by a small horizontal loop placed at a height of 1 m above a “medium dry ground” are shown in Figure 33. The peak of the major lobe, nearest the ground, occurs at an elevation angle of 17° and is therefore reached at a height of 2,9 m at a horizontal distance of 10 m. The height scan plot at a horizontal distance of 10 m in Figure 34, which is of $E_y$ in the Z-X plane in this example, underestimates the maximum field strength in a vertical polar scan by less than 0,5 dB.

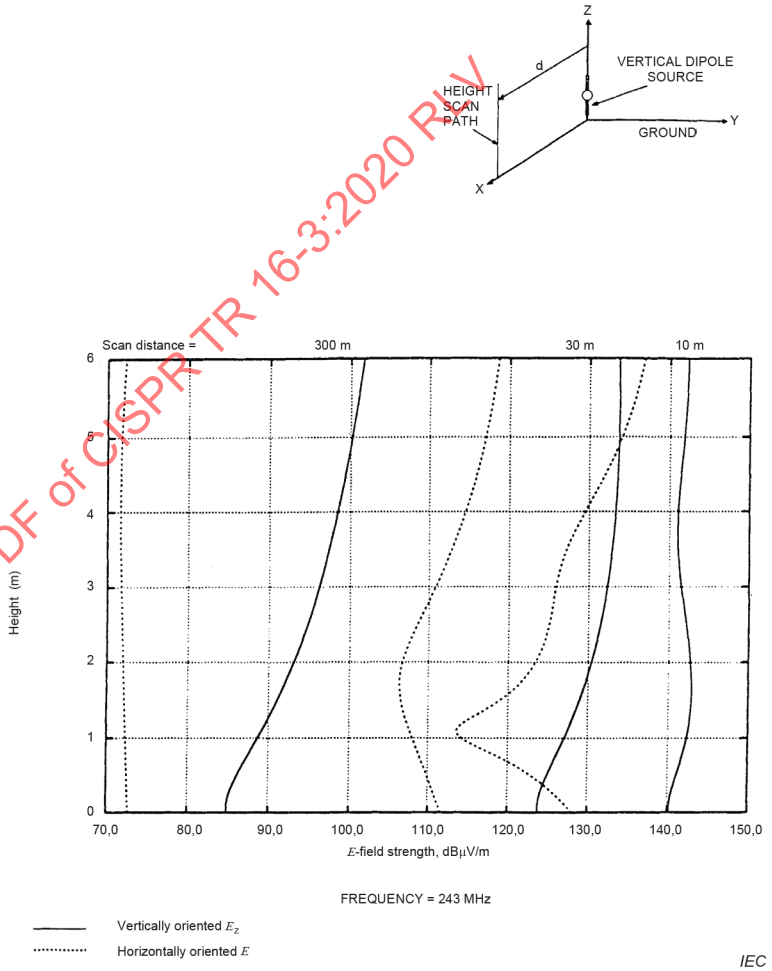
Column (4) of Table 16 summarizes the errors expected in the predictability of radiation in vertical directions based on measurements in height scans from 1 m to 4 m at a horizontal distance of 10 m from each of the four sources operating at 243 MHz.

IECNORM.COM : Click to view the full PDF of CISPR TR 16-3:2020 RLV




NOTE Dipole length 0,05 m; dipole centre height 1 m; dipole moment 1 A·m; scan radii of 10 m, 30 m and 300 m; 243 MHz; ground constants: $\varepsilon_r$ = 15, $\sigma$ = 4,5 mS/m; Z-X plane (Reproduced from [39]).

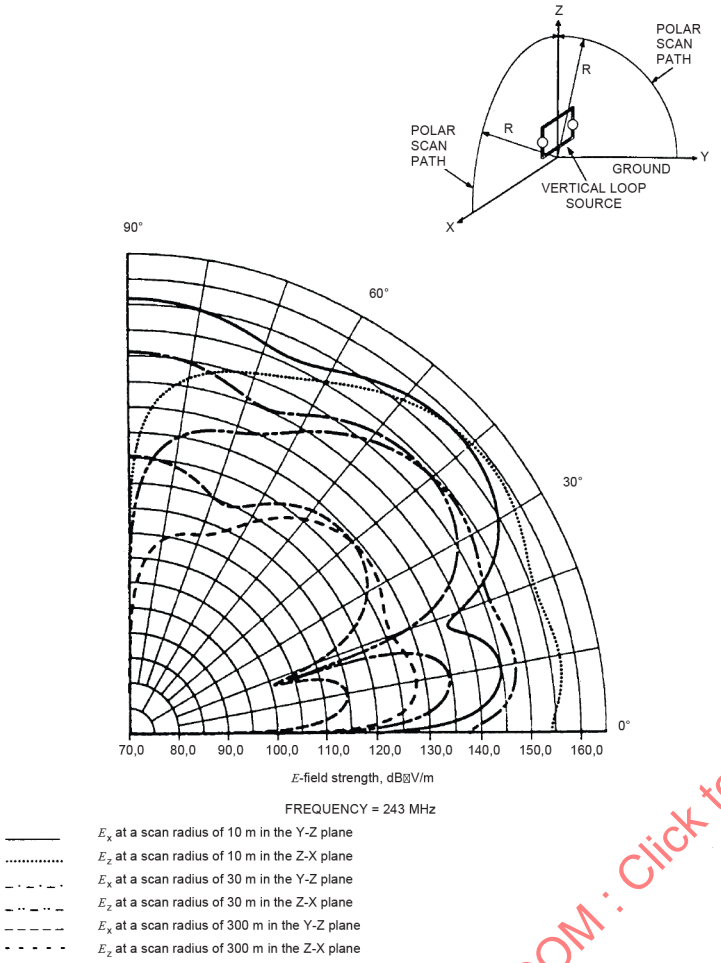
**Figure 29 – Vertical polar patterns of vertically oriented $E_z$ and horizontally oriented $E_x$ field strengths emitted around small vertical electric dipole**




NOTE Dipole length 0,05 m; dipole centre height 1 m; dipole moment 1 A·m; horizontal distance 10 m, 30 m and 300 m; 243 MHz; ground constants: $\varepsilon_r$ = 15, $\sigma$ = 4,5 mS/m; Z-X plane (Reproduced from [39]).

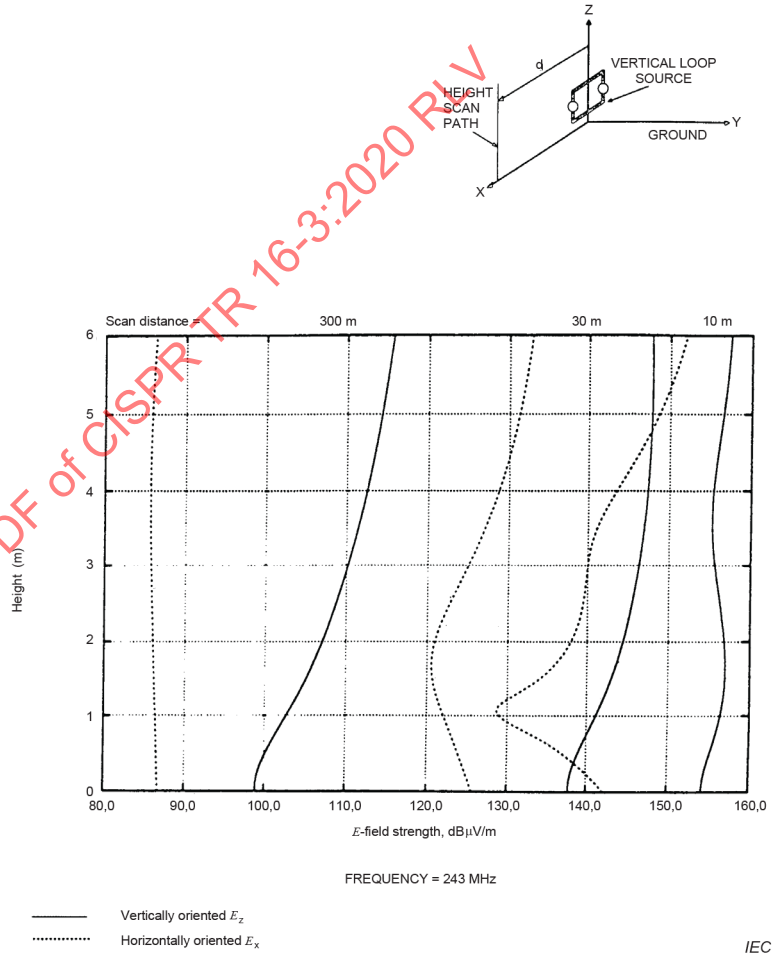
**Figure 30 – Height scan patterns of vertically oriented $E_z$ and horizontally oriented $E_x$ field strengths emitted from small vertical electric dipole**

IECNORM.COM : Click to view the full PDF of CISPR TR 16-3:2020 RLV




NOTE Loop dimensions 0,05 m × 0,05 m; loop centre height 1 m; dipole moment 1 A·m$^2$; scan radii of 10 m, 30 m and 300 m; 243 MHz; ground constants: $\varepsilon_r$ = 15, $\sigma$ = 4,5 mS/m (Reproduced from [39]).

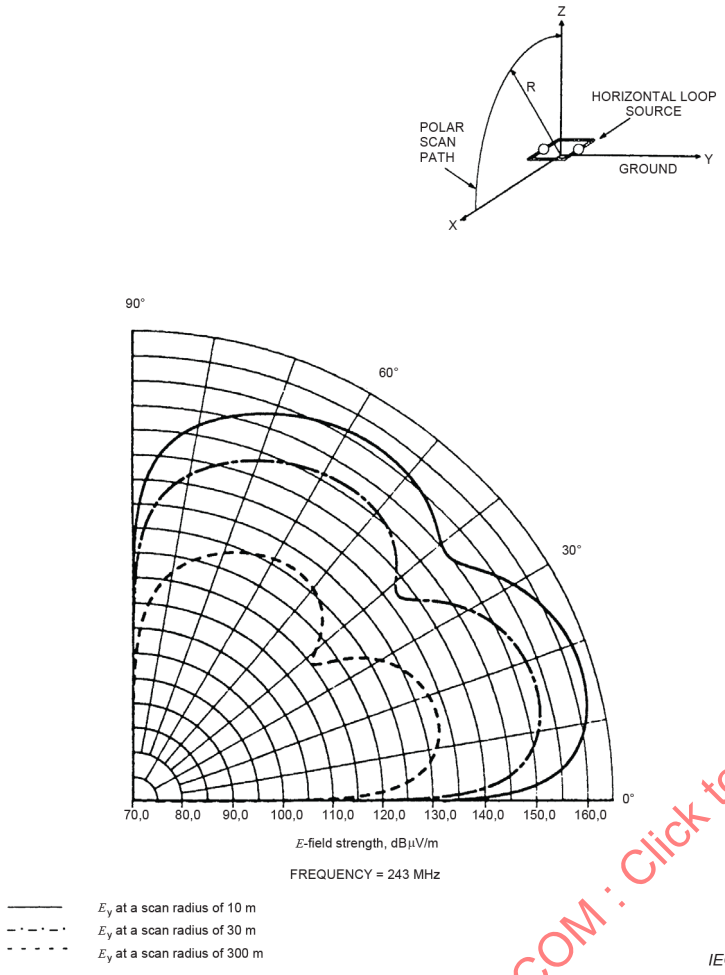
**Figure 31 – Vertical polar patterns of horizontally polarized $E_x$ and vertically oriented $E_z$ field strengths emitted around small vertical loop (horizontal magnetic dipole) in Y-Z and Z-X planes respectively**




NOTE Loop dimensions 0,05 m × 0,05 m; loop centre height 1 m; dipole moment 1 A·m$^2$; horizontal distance 10 m, 30 m and 300 m; 243 MHz; ground constants: $\varepsilon_r$ = 15, $\sigma$ = 4,5 mS/m; Z-X plane (Reproduced from [39]).

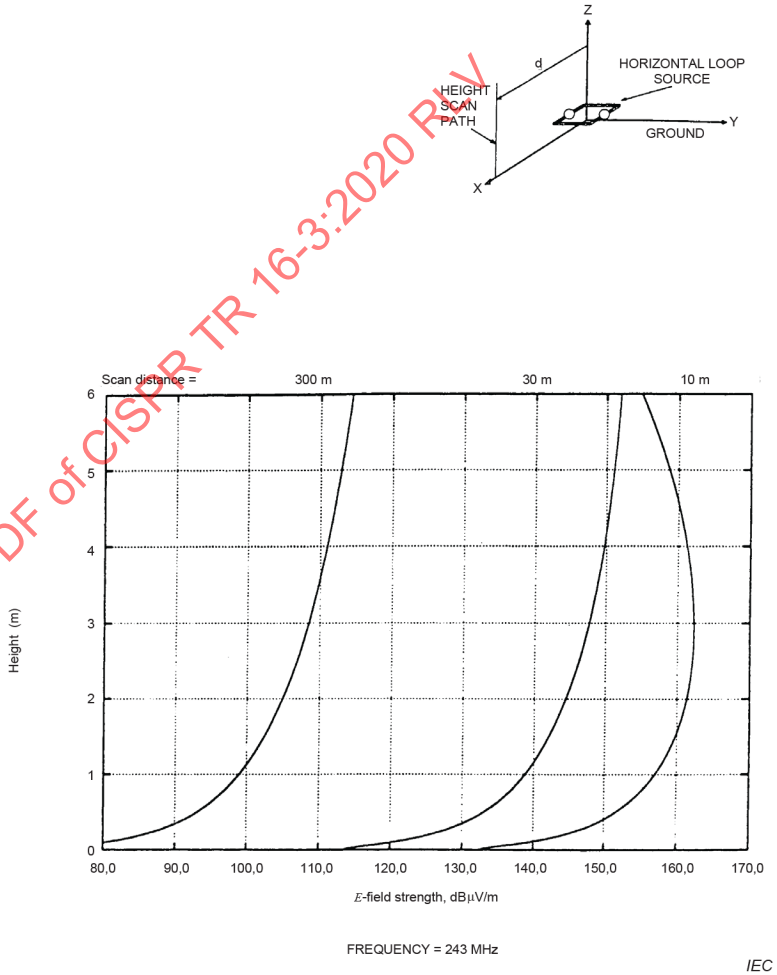
**Figure 32 – Height scan patterns of vertically oriented $E_z$ and horizontally oriented $E_x$ field strengths emitted from small vertical loop (horizontal magnetic dipole)**

IECNORM.COM : Click to view the full PDF of CISPR TR 16-3:2020 RLV




NOTE Loop dimensions 0,05 m × 0,05 m; loop height 1 m; dipole moment 1 A·m$^2$; scan radii of 10 m, 30 m and 300 m; 243 MHz; ground constants: $\varepsilon_r$ = 15, $\sigma$ = 4,5 mS/m; Z-X plane (Reproduced from [39]).

**Figure 33 – Vertical polar patterns of horizontally polarized *E*-field strength emitted around small horizontal loop (vertical magnetic dipole)**




NOTE Loop dimensions 0,05 m × 0,05 m; loop height 1 m; dipole moment 1 A·m$^2$; horizontal distance 10 m, 30 m and 300 m; 243 MHz; ground constants: $\varepsilon_r$ = 15, $\sigma$ = 4,5 mS/m; Z-X plane (Reproduced from [39]).

**Figure 34 – Height scan patterns of horizontally polarized *E*-field strength emitted from small horizontal loop (vertical magnetic dipole)**

IECNORM.COM : Click to view the full PDF of CISPR TR 16-3:2020 RLV

**Table 16 – Estimates of the errors in prediction of radiation in vertical directions based on a measurement height scan from 1 m to 4 m at known distances, $d$; frequency = 243 MHz (adapted from [39])**

| (1) Source of radiation at height | (2) Max. $E$, at angle, in 10 m polar plot | (3) At hor. $d$ = 10 m, measure this field | (4) Estimated prediction error, at $d$ = 10 m | (5) Max. $E$, at angle, in 30 m polar plot | (6) At hor. $d$ = 30 m, measure this field | (7) Estimated prediction error, at $d$ = 30 m | (8) Max. $E$, at angle, in 300 m polar plot | (9) At hor. $d$ = 300 m, measure this field | (10) Estimated prediction error, at $d$ = 300 m |
|---|---|---|---|---|---|---|---|---|---|
| Vertical electric dipole at 1 m | $E_z$ at 33,75° | $E_z$ | –1 dB | $E_z$ at 10,5° | $E_z$ | –0,5 dB | $E_z$ at 10,5° | $E_z$ | –16 dB |
| Vertical electric dipole at 2 m | $E_z$ at 18,25° | $E_z$ | –0,5 dB | $E_z$ at 18,25° | $E_z$ | –0,5 dB | $E_z$ at 7° | $E_z$ | –13 dB |
| Horizontal electric dipole at 1 m | $E_x$ at 17,5° in Y-Z plane | $E_x$ in Y-Z plane | –0,5 dB | $E_x$ at 17,5° in Y-Z plane | $E_x$ in Y-Z plane | –4 dB | $E_x$ at 17,5° in Y-Z plane | $E_x$ in Y-Z plane | –22,5 dB |
| Horizontal electric dipole at 2 m | $E_x$ at 9° in Y-Z plane | $E_x$ in Y-Z plane | 0 dB | $E_x$ at 8,75° in Y-Z plane | $E_x$ in Y-Z plane | –0,5 dB | $E_x$ at 8,75° in Y-Z plane | $E_x$ in Y-Z plane | –17 dB |
| Vertical loop (horizontal magnetic dipole) at 1 m | $E_z$ at 36,25° in Z-X plane | $E_z$ in Z-X plane | –2,5 dB | $E_z$ at 36,5° in Z-X plane | $E_z$ in Z-X plane | –2 dB | $E_z$ at 36,5° in Z-X plane | $E_z$ in Z-X plane | –17 dB |
| Vertical loop (horizontal magnetic dipole at 2 m | $E_x$ at 70,5° in Y-Z plane | $E_z$ in Z-X plane | –2,5 dB | $E_x$ at 69,25° in Y-Z plane | $E_z$ in Z-X plane | –3 dB | $E_x$ at 69° in Y-Z plane | $E_z$ in Z-X plane | –15 dB |
| Horizontal loop (vertical magnetic dipole) at 1 m | $E_y$ at 17° in Z-X plane | $E_y$ in Z-X plane | –0,5 dB | $E_y$ at 16,75° in Z-X plane | $E_y$ in Z-X plane | –3,5 dB | $E_y$ at 16,75° in Z-X plane | $E_y$ in Z-X plane | –22,5 dB |
| Horizontal loop (vertical magnetic dipole) at 2 m | $E_y$ at 9° in Z-X plane | $E_y$ in Z-X plane | 0 dB | $E_y$ at 8,75° in Z-X plane | $E_y$ in Z-X plane | 0 dB | $E_y$ at 8,75° in Z-X plane | $E_y$ in Z-X plane | –17 dB |

IECNORM.COM : Click to view the full PDF of CISPR TR 16-3:2020 RLV

#### 4.5.5.2.5 Predictability at 330 MHz

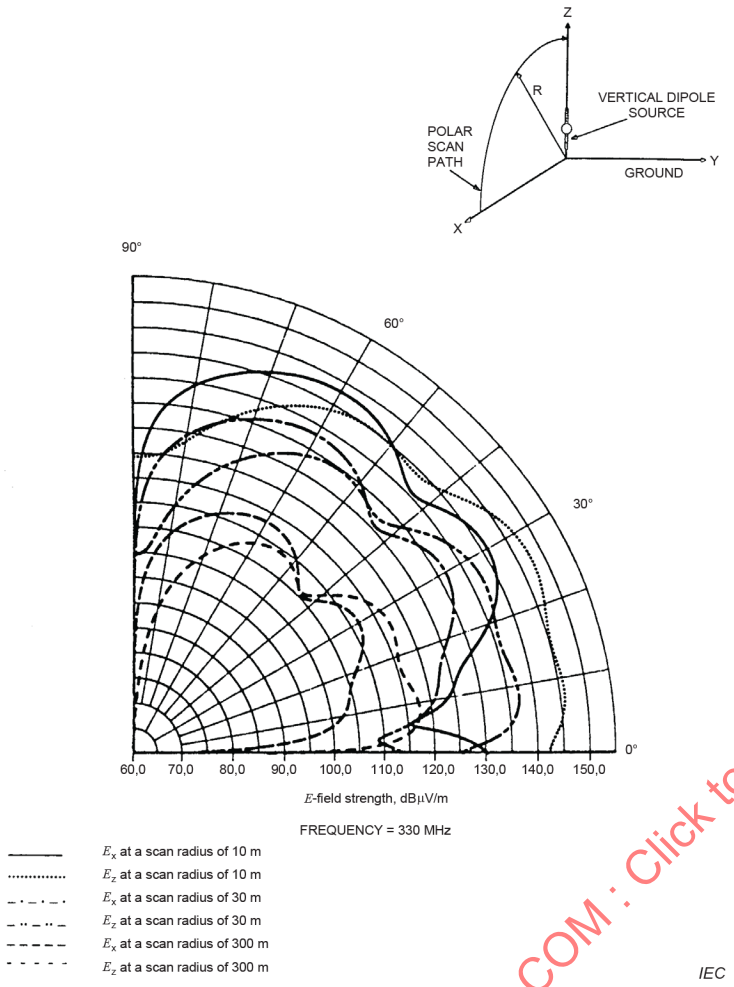
Figure 35 shows vertical polar plots of $E_z$ and $E_x$ in the Z-X plane, at 330 MHz, around the small vertical electric dipole placed at a centre height of 1 m above ground. At a scan radius of 10 m the maximum field strength of almost 148 dB(μV/m) is contributed by $E_z$ at an elevation angle of 26°. Calculations of the vertically oriented $E_z$ field in a height scan from 1 m to 4 m at 10 m horizontal distance produce a peak magnitude of almost 146 dB(μV/m) at a measuring height of 1,45 m, as shown in Figure 36. This underestimates the maximum field strength by less than 2 dB.

Figure 37 shows vertical polar plots of $E_x$ in the Y-Z plane and $E_z$ in the Z-X plane, around the small vertical loop placed at a centre height of 1 m above a “medium dry ground.” It can be seen that, at a scan radius of 10 m, the maximum field strength of almost 167 dB(μV/m) is reached by $E_x$ at an elevation angle of 69° in the Y-Z plane. The calculated $E_z$ height scan patterns in the Z-X plane shown in Figure 38 produce a peak magnitude greater than 162 dB(μV/m) at 10 m horizontal distance, measured at a height of 1,45 m. A height scan measurement of the vertical $E_z$ field therefore underestimates the maximum strength of the radiation in vertical directions, the horizontal polarized $E_x$ at an elevation angle of 69°, by approximately 4,5 dB.

It is interesting to observe the vertical polar plots of horizontally polarized $E$-field emitted at 330 MHz by a small horizontal loop placed at a height of 1 m above a “medium dry ground,” shown in Figure 39. The peak of the major lobe, nearest the ground, occurs at an elevation angle of only 12,75°. It is therefore measured at a height of only 2,2 m at a horizontal distance of 10 m, see Figure 40. Thus, there is virtually no error in this example of the estimation of maximum field strength at elevated angles.

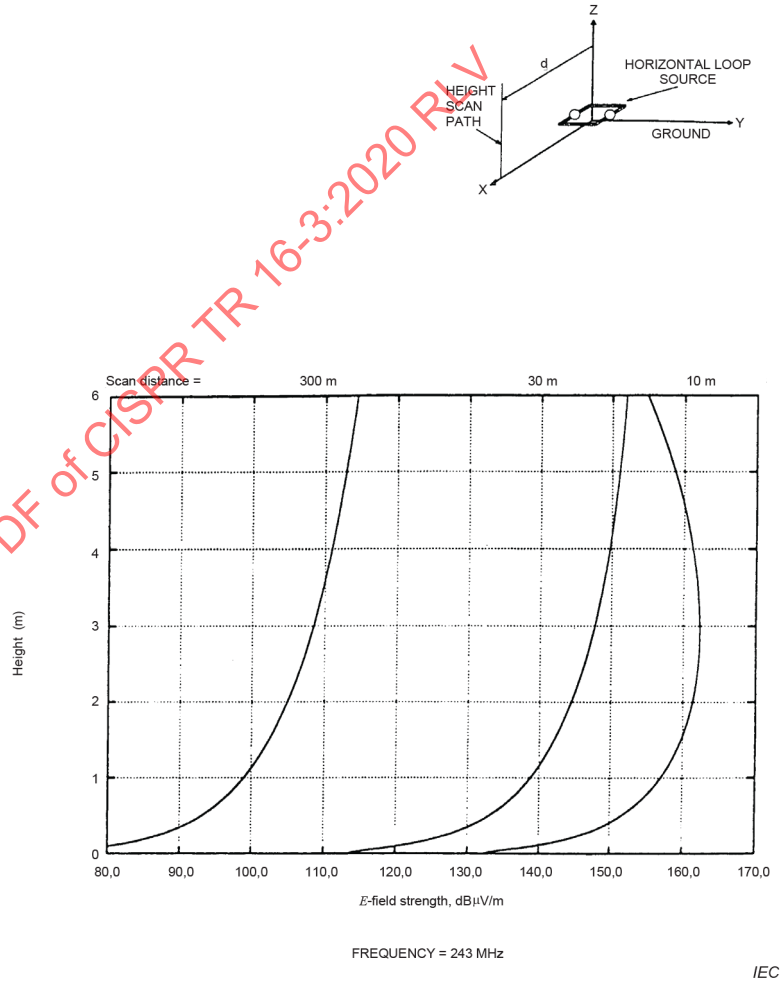
Column (4) of Table 17 summarizes the estimated errors in the predictability of radiation in vertical directions based on measurements in height scans from 1 m to 4 m at a horizontal distance of 10 m from each of the four sources operating at 330 MHz.

IECNORM.COM : Click to view the full PDF of CISPR TR 16-3:2020 RLV




NOTE Dipole length 0,05 m; dipole centre height 1 m; dipole moment 1 A·m; scan radii of 10 m, 30 m and 300 m; 330 MHz; ground constants: $\varepsilon_r$ = 15, $\sigma$ = 7,5 mS/m; Z-X plane (Reproduced from [39]).

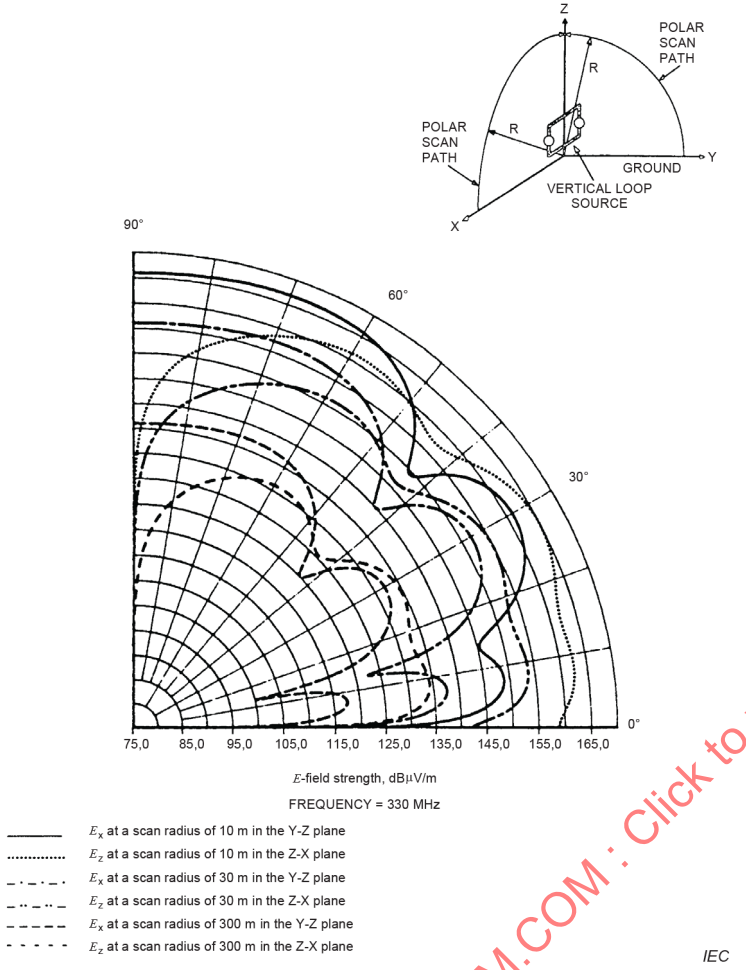
**Figure 35 – Vertical polar patterns of vertically oriented $E_z$ and horizontally oriented $E_x$ field strengths emitted around small vertical electric dipole**




NOTE Loop dimensions 0,05 m × 0,05 m; loop height 1 m; dipole moment 1 A·m$^2$; horizontal distance 10 m, 30 m and 300 m; 243 MHz; ground constants: $\varepsilon_r$ = 15, $\sigma$ = 4,5 mS/m; Z-X plane (Reproduced from [39]).

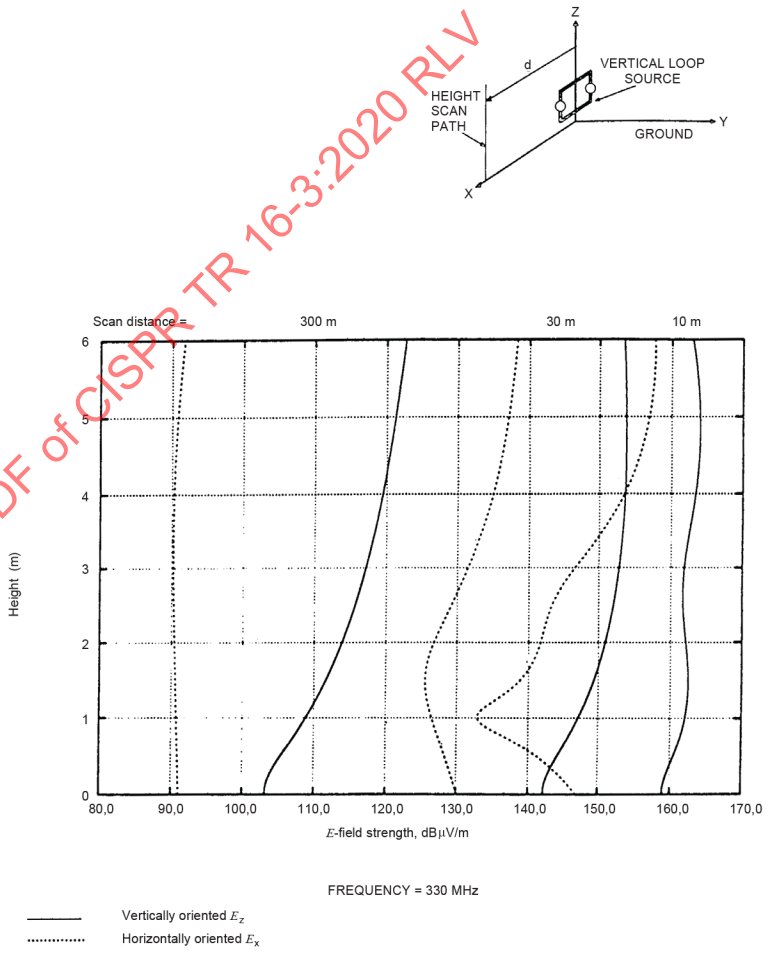
**Figure 36 – Height scan patterns of vertically oriented $E_z$ and horizontally oriented $E_x$ field strengths emitted from the small vertical electric dipole**

IECNORM.COM : Click to view the full PDF of CISPR TR 16-3:2020 RLV




NOTE Loop dimensions 0,05 m × 0,05 m; loop centre height 1 m; dipole moment 1 A·m$^2$; scan radii of 10 m, 30 m and 300 m; 330 MHz; ground constants: $\varepsilon_r$ = 15, $\sigma$ = 7,5 mS/m (Reproduced from [39]).

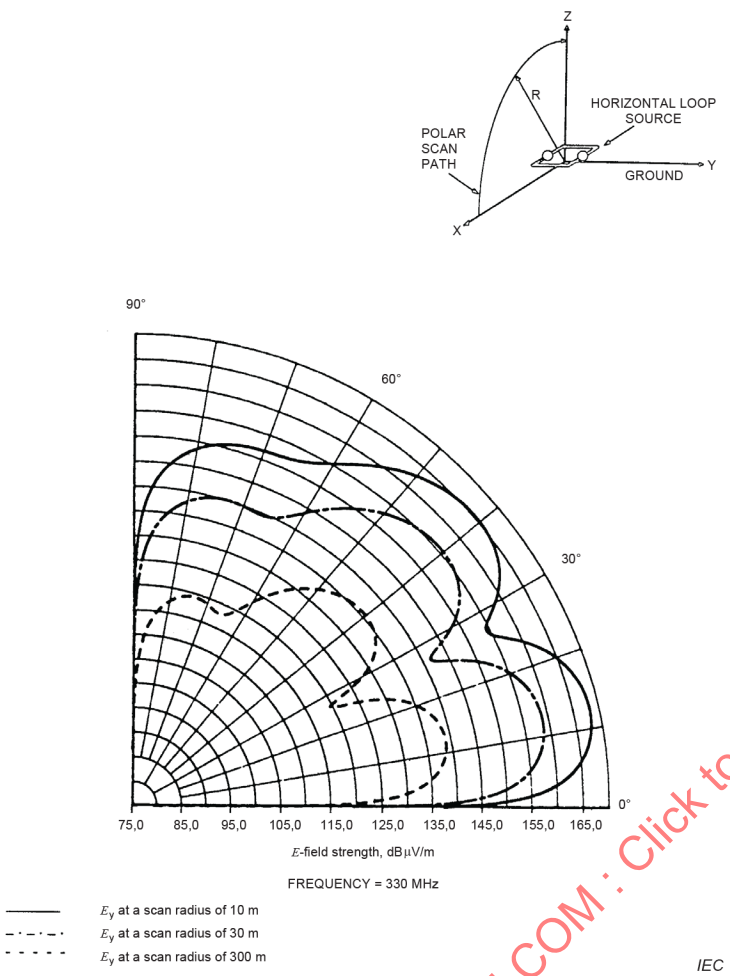
**Figure 37 – Vertical polar patterns of horizontally polarized $E_x$ and vertically oriented $E_z$ field strengths emitted around small vertical loop (horizontal magnetic dipole) in Y-Z and Z-X planes respectively**




NOTE Loop dimensions 0,05 m × 0,05 m; loop centre height 1 m; dipole moment 1 A·m$^2$; horizontal distance 10 m, 30 m and 300 m; 330 MHz; ground constants: $\varepsilon_r$ = 15, $\sigma$ = 7,5 mS/m; Z-X plane (Reproduced from [39]).

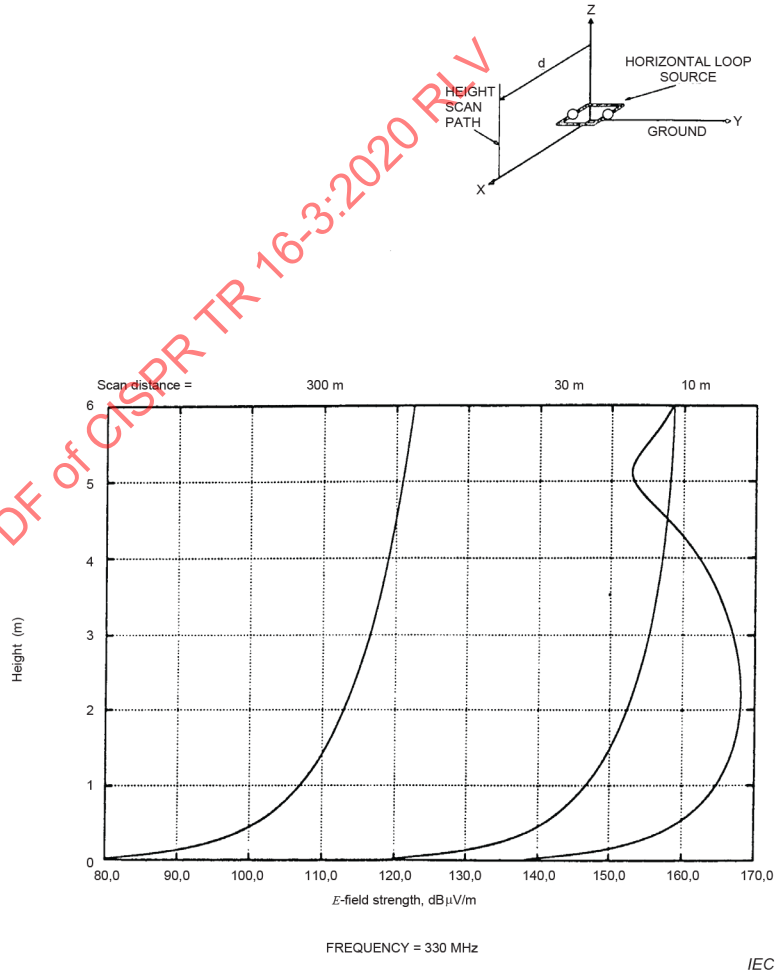
**Figure 38 – Height scan patterns of vertically oriented $E_z$ and horizontally oriented $E_x$ field strengths emitted from small vertical loop (horizontal magnetic dipole)**

IECNORM.COM : Click to view the full PDF of CISPR TR 16-3:2020 RLV




NOTE Loop dimensions 0,05 m × 0,05 m; loop height 1 m; dipole moment 1 A·m$^2$; scan radii of 10 m, 30 m and 300 m; 330 MHz; ground constants: $\varepsilon_r$ = 15, $\sigma$ = 7,5 mS/m; Z-X plane (Reproduced from [39]).

**Figure 39 – Vertical polar patterns of horizontally polarized *E*-field strength emitted around small horizontal loop (vertical magnetic dipole)**




NOTE Loop dimensions 0,05 m × 0,05 m; loop height 1 m; dipole moment 1 A·m$^2$; horizontal distance 10 m, 30 m and 300 m; 330 MHz; ground constants: $\varepsilon_r$ = 15, $\sigma$ = 4,5 mS/m; Z-X plane (Reproduced from [39]).

**Figure 40 – Height scan patterns of horizontally polarized *E*-field strength emitted from small horizontal loop (vertical magnetic dipole)**

IECNORM.COM : Click to view the full PDF of CISPR TR 16-3:2020 RLV

**Table 17 – Estimates of the errors in prediction of radiation in vertical directions based on a measurement height scan from 1 m to 4 m at known distances, $d$; frequency = 330 MHz (adapted from [39])**

| (1) Source of radiation at height | (2) Max. $E$, at angle, in 10 m polar plot | (3) At hor. $d$ = 10 m, measure this field | (4) Estimated prediction error, at $d$ = 10 m | (5) Max. $E$, at angle, in 30 m polar plot | (6) At hor. $d$ = 30 m, measure this field | (7) Estimated prediction error, at $d$ = 30 m | (8) Max. $E$, at angle, in 300 m polar plot | (9) At hor. $d$ = 300 m, measure this field | (10) Estimated prediction error, at $d$ = 300 m |
|---|---|---|---|---|---|---|---|---|---|
| Vertical electric dipole at 1 m | $E_z$ at 26° | $E_z$ | –2 dB | $E_z$ at 26° | $E_z$ | –0,5 dB | $E_z$ at 9° | $E_z$ | –15 dB |
| Vertical electric dipole at 2 m | $E_z$ at 27,25° | $E_z$ | –0,5 dB | $E_z$ at 5,75° | $E_z$ | 0 dB | $E_z$ at 5,5° | $E_z$ | –11,5 dB |
| Horizontal electric dipole at 1 m | $E_x$ at 13° in Y-Z plane | $E_y$ in Y-Z plane | 0 dB | $E_x$ at 12,75° in Y-Z plane | $E_y$ in Y-Z plane | –2 dB | $E_x$ at 12,75° in Y-Z plane | $E_y$ in Y-Z plane | –20 dB |
| Horizontal electric dipole at 2 m | $E_x$ at 6,5° in Y-Z plane | $E_y$ in Y-Z plane | 0 dB | $E_x$ at 6,5° in Y-Z plane | $E_y$ in Y-Z plane | 0 dB | $E_x$ at 6,5° in Y-Z plane | $E_y$ in Y-Z plane | –14,5 dB |
| Vertical loop (horizontal magnetic dipole) at 1 m | $E_x$ at 69° in Y-Z plane | $E_z$ in Z-X plane | –4,5 dB | $E_x$ at 68,25° in Y-Z plane | $E_z$ in Z-X plane | –3,5 dB | $E_x$ at 68° in Y-Z plane | $E_z$ in Z-X plane | –17,5dB |
| Vertical loop (horizontal magnetic dipole) at 2 m | $E_x$ at 66,75° in Y-Z plane | $E_z$ in Z-X plane | –2,5 dB | $E_x$ at 66° in Y-Z plane | $E_z$ in Z-X plane | –2,5 dB | $E_x$ at 66° in Y-Z plane | $E_z$ in Z-X plane | –12,5 dB |
| Horizontal loop (vertical magnetic dipole) at 1 m | $E_y$ at 12,75° in Z-X plane | $E_y$ in Z-X plane | 0 dB | $E_y$ at 12,5° in Z-X plane | $E_y$ in Z-X plane | –2 dB | $E_y$ at 12,5° in Z-X plane | $E_y$ in Z-X plane | –20 dB |
| Horizontal loop (vertical magnetic dipole) at 2 m | $E_y$ at 6,5° in Z-X plane | $E_y$ in Z-X plane | 0 dB | $E_y$ at 6,5° in Z-X plane | $E_y$ in Z-X plane | 0 dB | $E_y$ at 6,5° in Z-X plane | $E_y$ in Z-X plane | –14,5 dB |

IECNORM.COM : Click to view the full PDF of CISPR TR 16-3:2020 RLV

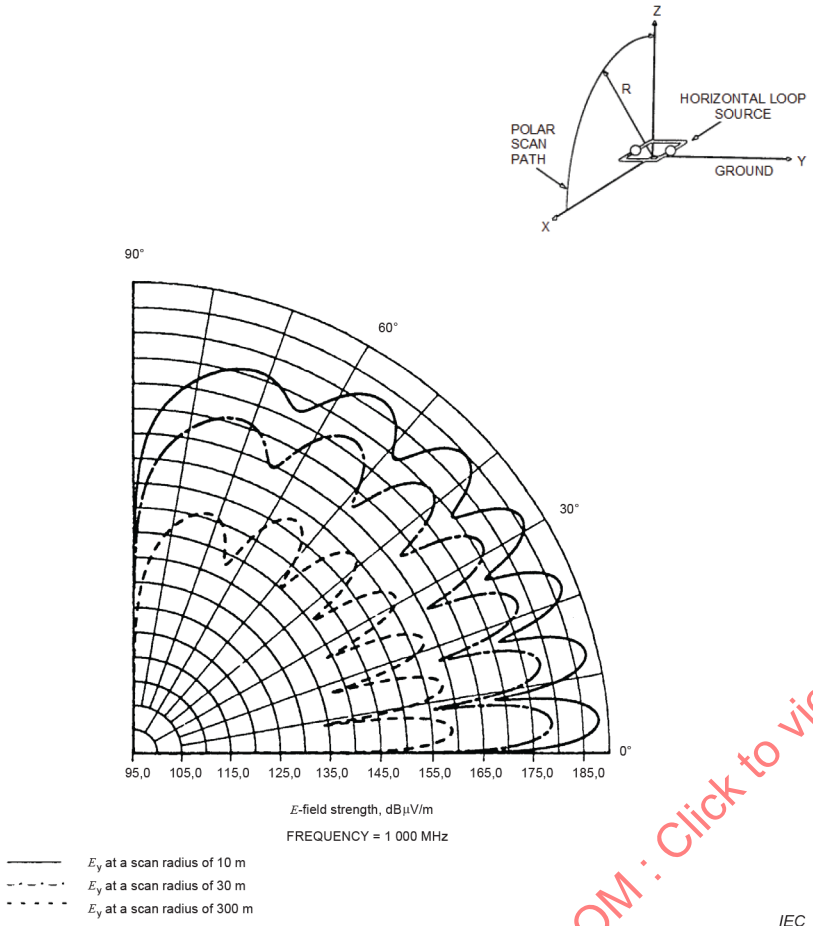
#### 4.5.5.2.6 Predictability at 1 000 MHz

Figure 20 to Figure 22 show vertical polar plots of $E_z$ and $E_x$, at 1 000 MHz, around a small vertical loop placed at a centre height of 2 m above ground. At a scan radius of 10 m over a "medium dry ground" the maximum field strength of 187 dB(μV/m) is contributed by the horizontally polarized $E_x$ at an elevation angle of 77,5° in the Y-Z plane. Calculations of the vertically oriented $E_z$ field in a height scan from 1 m to 4 m at 10 m horizontal distance in the Z-X plane produce a peak field of almost 184 dB(μV/m) at a height of 3,2 m, as shown in Figure 22. A vertically polarized height scan measurement therefore underestimates the maximum field strength by approximately 3 dB.

It is interesting to observe the vertical polar plots of horizontally polarized $E$-field emitted at 1 000 MHz by a small horizontal loop placed at a height of 1 m above a “medium dry ground,” shown in Figure 41. The peak of the major lobe, nearest the ground, occurs at an elevation angle of only 4,25°. Shown again in Figure 42, it occurs at a height of 0,74 m at a horizontal distance of 10 m, and therefore will *not* be measured in a 1 m to 4 m height scan measurement. The next grating lobe is encountered at a height of 2,3 m, and its measurement contributes to an underestimate of less than 0,5 dB to the prediction of maximum field strength of the major (lower) lobe.

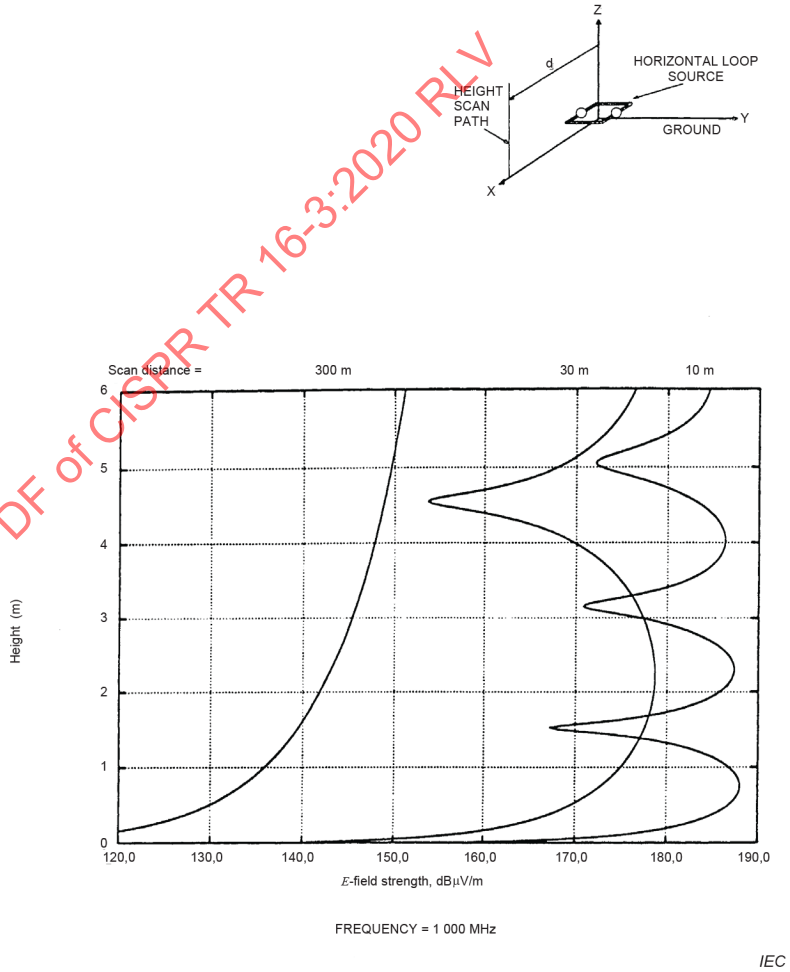
Column (4) of Table 18 summarizes the errors estimated for the predictability of radiation in vertical directions based on measurements in height scans from 1 m to 4 m at a horizontal distance of 10 m from each of the four sources operating at 1 000 MHz.

IECNORM.COM : Click to view the full PDF of CISPR TR 16-3:2020 RLV




NOTE Loop dimensions 0,02 m × 0,02 m; loop height 1 m; dipole moment 1 A·m$^2$; scan radii of 10 m, 30 m and 300 m; 1 000 MHz; ground constants: $\varepsilon_r$ = 15, $\sigma$ = 35 mS/m; Z-X plane (Reproduced from [39]).

**Figure 41 – Vertical polar patterns of horizontally polarized *E*-field strength emitted around the small horizontal loop (vertical magnetic dipole)**




NOTE Loop dimensions 0,02 m × 0,02 m; loop height 1 m; dipole moment 1 A·m$^2$; horizontal distance 10 m, 30 m and 300 m; 1 000 MHz; ground constants: $\varepsilon_r$ = 15, $\sigma$ = 35 mS/m; Z-X plane (Reproduced from [39]).

**Figure 42 – Height scan patterns of horizontally polarized *E*-field strength emitted from small horizontal loop (vertical magnetic dipole)**

IECNORM.COM : Click to view the full PDF of CISPR TR 16-3:2020 RLV

**Table 18 – Estimates of the errors in prediction of radiation in vertical directions based on a measurement height scan from 1 m to 4 m at known distances, $d$; frequency = 1 000 MHz (adapted from [39])**

| (1) Source of radiation at height | (2) Max. $E$, at angle, in 10 m polar plot | (3) At hor. $d$ = 10 m, measure this field | (4) Estimated prediction n error, at $d$ = 10 m | (5) Max. $E$, at angle, in 30 m polar plot | (6) At hor. $d$ = 30 m, measure this field | (7) Estimated prediction n error, at $d$ = 30 m | (8) Max. $E$, at angle, in 300 m polar plot | (9) At hor. $d$ = 300 m, measure this field | (10) Estimated prediction error, at $d$ = 300 m |
|---|---|---|---|---|---|---|---|---|---|
| Vertical electric dipole at 1 m | $E_z$ at 17,5° | $E_z$ | –0,5 dB | $E_z$ at 4° | $E_z$ | 0 dB | $E_z$ at 3,75° | $E_z$ | –9,5 dB |
| Vertical electric dipole at 2 m | $E_z$ at 17,75° | $E_z$ | –0,5 dB | $E_z$ at 2° | $E_z$ | 0 dB | $E_z$ at 2° | $E_z$ | –5 dB |
| Horizontal electric dipole at 1 m | $E_x$ at 4,25° in Y-Z plane | $E_y$ in Y-Z plane | –0,5 dB | $E_x$ at 4,25° in Y-Z plane | $E_y$ in Y-Z plane | 0 dB | $E_x$ at 4,25° in Y-Z plane | $E_y$ in Y-Z plane | –11 dB |
| Horizontal electric dipole at 2 m | $E_x$ at 2,25° in Y-Z plane | $E_y$ in Y-Z plane | 0 dB | $E_x$ at 2,25° in Y-Z plane | $E_y$ in Y-Z plane | 0 dB | $E_x$ at 2,25° in Y-Z plane | $E_y$ in Y-Z plane | –5,5 dB |
| Vertical loop (horizontal magnetic dipole) at 1 m | $E_x$ at 64,5° in Y-Z plane | $E_z$ in Z-X plane | –2,5 dB | $E_x$ at 64,25° in Y-Z plane | $E_z$ in Z-X plane | –1 dB | $E_z$ at 4° in Z-X plane | $E_z$ in Z-X plane | –9,5 dB |
| Vertical loop (horizontal magnetic dipole) at 2 m | $E_x$ at 77,5° in Y-Z plane | $E_z$ in Z-X plane | –3 dB | $E_x$ at 77,25° in Y-Z plane | $E_z$ in Z-X plane | –1,5 dB | $E_z$ at 2° in Z-X plane | $E_z$ in Z-X plane | –5 dB |
| Horizontal loop (vertical magnetic dipole) at 1 m | $E_y$ at 4,25° in Z-X plane | $E_y$ in Z-X plane | –0,5 dB | $E_y$ at 4,25° in Z-X plane | $E_y$ in Z-X plane | 0 dB | $E_y$ at 4,25° in Z-X plane | $E_y$ in Z-X plane | –11 dB |
| Horizontal loop (vertical magnetic dipole) at 2 m | $E_y$ at 2,25° in Z-X plane | $E_y$ in Z-X plane | 0 dB | $E_y$ at 2,25° in Z-X plane | $E_y$ in Z-X plane | 0 dB | $E_y$ at 2,25° in Z-X plane | $E_y$ in Z-X plane | –5,5 dB |

IECNORM.COM : Click to view the full PDF of CISPR TR 16-3:2020 RLV

#### 4.5.5.3 Predictability based on height scan measurements near real ground at an unknown distance, greater than 10 m, from the radiation source

Here we can answer the second question posed in 4.5.3. This measurement situation is analogous to making measurements *in situ* at a distance of 10 m from the wall outside a building containing ISM equipment that is located at an unknown distance inside the building. As mentioned earlier, we do not consider here the attenuation that may be introduced by intervening building materials.

Calculations have been made of vertical polar patterns and linear height scan patterns at distances of 30 m and 300 m. The reader will have already seen that patterns for those distances have also been included in the figures.

The figures, together with the comprehensive summaries presented in columns (7) and (10) of Table 14 to Table 18, show that the predictability of fields at elevated angles based on height scan measurements near real ground becomes more prone to underestimation as the horizontal measuring distance increases beyond 10 m, especially at the lower frequencies. Underestimation can become very large at a distance of 300 m. At the lower frequencies underestimates can reach more than 30 dB at that distance when the source behaves as a small horizontal electric dipole. The underestimates for both horizontally and vertically polarized fields occur in spite of the significant contributions that can be made by surface waves at the lower frequencies near 30 MHz [40]. Predictability improves as the frequency increases, primarily because at higher frequencies, the surface wave contributions decrease and the maximum field strength measured in the height scan is created by the sum of the direct and reflected space wave components (the sum is sometimes called, somewhat misleadingly, the “ground wave”). The contributions of the space wave signals increase at lower elevation angles as more grating lobes form with increasing frequency.

It is particularly important to recognize that, at horizontal distances of 30 m and more, the worst-case underestimations of the maximum levels of field strengths at elevated angles will generally occur when the fields are horizontally polarized. This is very unfortunate, because the signals for the ILS (marker beacons, localizer, and glide path, see Table 11) are all horizontally polarized transmissions and therefore require the maximum protection from horizontally polarized disturbances.

The figures also provide guidance to the rates of change of the fields with distance. Calculations and measurements made at a constant height, avoiding nulls, show that the maximum rate of change of the fields with distance can approach a rate that is inversely proportional to distance squared. When surface wave contributions are negligible, then for grazing incidence in the far field a field strength inversely proportional to distance squared is to be expected at a constant measuring height [40], [41]. However, the space wave field strengths along radial paths at constant elevation angles vary in simple proportion with inverse distance, which is to be expected of such far fields propagating freely in space. Therefore, it is to be expected that the fields measured near the ground (the so-called “ground waves”), in general, will attenuate more rapidly with increasing distance than do the fields from the same source which are propagating radially up into space.

If the horizontal distances at which height scan measurements are made *in situ* are not known, very large errors can arise – all of them underestimates – in the predictability of the strength of radiation in vertical directions from all four types of source and at all frequencies from 75 MHz to 1 000 MHz.

#### 4.5.5.4 Predictability based on measurement at a fixed height

In its measurement procedures relating to the ways in which measuring antennas are to be used, CISPR 11 does not distinguish between measurements made *in situ* for the protection of specific safety-related radio services and those made for the protection of other services. Thus, if a measurement of emissions is made *in situ* from a Group 2 Class A ISM equipment in accordance with the specification, the measuring antenna is placed at a height of 2,0 m ± 0,2 m (7.3.4 of CISPR 11:2009); no height scan is specified.

The obvious risk with fixed height measurements is that a measurement will be made at a null in the field strength pattern. The risk of this happening is increased if the electrical height above ground of the radiation centre of the source increases – for example with increasing frequency – which contributes to the formation of an increasing number of grating lobes, and hence nulls. A few examples of the effects these nulls can have on a measurement made at a height near 3 m (or any other *fixed* height) are shown in several of the figures.

IECNORM.COM : Click to view the full PDF of CISPR TR 16-3:2020 RLV

For example, Figure 22 shows that, depending on the type of ground over which the measurements are made, at a horizontal distance of 10 m from a small vertical loop source located at a height of 2 m, the measured vertically polarized field strength at 1 000 MHz might vary by more than 6 dB for measurements made somewhere in the height tolerance range of 2,8 m to 3,2 m, and that at 30 m horizontal distance a measurement made at 3 m height is also close to a null.

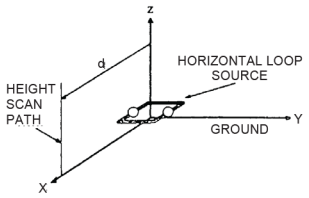
Figure 40 shows that a horizontal distance of 10 m from a small horizontal loop source located 1 m above ground with the measured horizontally polarized field strength at 1 000 MHz might vary by more than 12 dB in the CISPR measurement height tolerance range from 2,8 m to 3,2 m. It also shows how the field strength can vary with distance in an apparently anomalous manner when measurements are made at a fixed height. Note that at a height of 3 m, the field strength at 30 m distance is the same as the field strength at 10 m distance. At other heights, the field strength at 30 m distance becomes greater than that at 10 m distance.

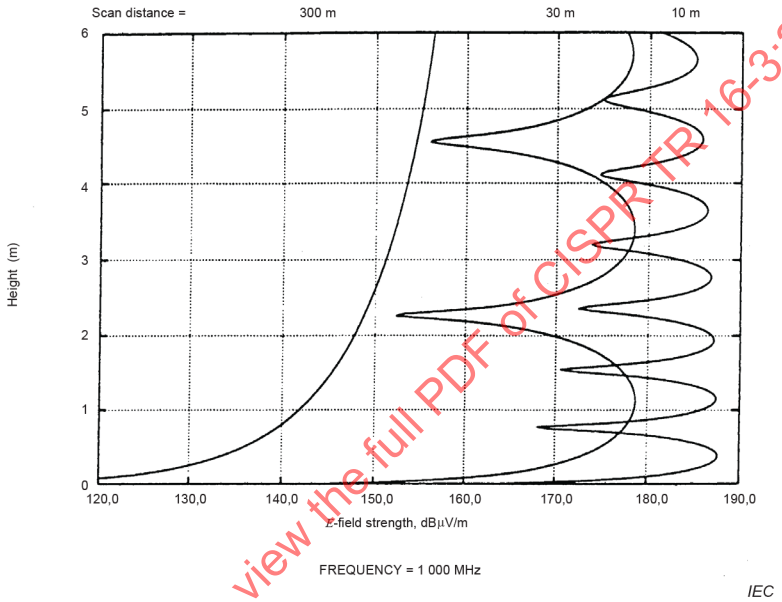
Comparison of the height scan curves in Figure 43 with those in Figure 40, at 1 000 MHz, shows that as the small horizontal loop source height varies between 1 m and 2 m, deep nulls will pass through the measuring height of 3 m at horizontal measuring distance of 10 m and 30 m. These effects can be encountered at *greater horizontal measuring distances* and *lower frequencies* if the height of the radiating source is increased.

We are now in a position to answer the third question posed in 4.5.3. The answer is that predictability is degraded by fixed height measurements. Measurements at a fixed height should not be permitted, especially if they are being made to determine protection for specific safety services.

Height scans shall be specified or, for measuring convenience, the measuring height *in situ* could be specified in the manner of [42], so that at a horizontal distance of 10 m, the measuring height would be specified as 4 m above the immediate terrain *or at such lower height at which the field strengths may exceed that at 4 m.*

IECNORM.COM : Click to view the full PDF of CISPR TR 16-3:2020 RLV




NOTE Loop dimensions 0,02 m × 0,02 m; loop height 2 m; dipole moment 1 A·m$^2$; horizontal distance 10 m, 30 m and 300 m; 1 000 MHz; ground constants: $\varepsilon_r$ = 15, $\sigma$ = 35 mS/m; Z-X plane (Reproduced from [39]).

**Figure 43 – Height scan patterns of horizontally polarized *E*-field strength emitted from small horizontal loop (vertical magnetic dipole)**

IECNORM.COM : Click to view the full PDF of CISPR TR 16-3:2020 RLV

### 4.5.6 Differences between the fields over a real ground and the fields over a perfect conductor

#### 4.5.6.1 General

There are significant differences between the field distributions above a real earth plane and over a perfect conductor. There are several reasons for the differences, not the least being that the reflection factors for both polarizations over a perfect conductor always have a magnitude of unity at all angles of incidence, whereas over real ground they have a magnitude less than unity except at grazing incidence. In addition, for vertically polarized waves over a perfect conductor there is no Brewster's angle, or expressed in another way, at all reflection angles a vertically polarized image in a perfect conductor is always in phase with the vertically polarized source above the conductor. This contrasts with the situation of vertically polarized waves impinging upon a lossy dielectric such as real ground, where reflections taking place below Brewster's angle experience a large phase change, and the image can be visualized as being in approximate anti-phase with the source. It should also be observed that the reflection factor for a vertically polarized wave reflecting at Brewster's angle has a very small magnitude for most types of real ground encountered in practice.

The behaviour of the fields above a metal ground plane compared with the fields over an earthen ground plane is discussed at length in [40]. The brief discussion below, derived from [40], serves to provide an answer to the fourth question posed in 4.5.3.

#### 4.5.6.2 Vertically polarized fields over a perfect conductor

The contribution of the vertically polarized surface wave over real ground can be significant. However, it cannot increase the total field strength created by a small vertical electric dipole over real ground to equal the strength of the fields created by the same vertical dipole moment over a perfect conductor. Figure 44 displays the vertical components of the fields emitted at 30 MHz from a small vertical electric dipole situated 1 m above a “medium dry ground,” calculated using NEC and SOMNEC to include the surface wave, compared with the fields calculated over an almost perfect conductor (in this case annealed copper).

Comparisons of the fields over real ground with those over the good conductor show why vertically polarized measurements at 30 MHz on a measuring site with a metal ground plane are not comparable with measurements made on sites with earthen ground planes. Specifically, they show why measurements of vertically polarized disturbances made on a metal ground place for comparison with field strength disturbance limits developed for earth sites may penalize the equipment under test (EUT). The fields measured over a metal ground plane can exceed the limits, even when the fields from the same EUT over an earthen ground plane are comfortably below the limits. The comparisons also show why calculations of the vertically polarized fields created at 30 MHz over a perfect conductor or a metal ground plane, for a given dipole moment, are a bad guide to the predictability achievable for the fields created at elevated angles by that dipole moment over a real ground. If the fields over the good conductor are mistakenly believed to resemble those over a real ground, they will encourage a false sense of confidence that ground based measurements over real ground will give good guidance to the field strengths to be expected at elevated angles.

In Figure 45, the height scan patterns of the vertical components of the $E$-fields emitted from the small vertical dipole show that at 1 000 MHz, just as was the case at 30 MHz, the vertically polarized fields developed near a metal ground plane at 1 000 MHz are much stronger than those developed near a “medium dry ground.” The same conclusions which were reached at a frequency of 30 MHz regarding the possible penalties imposed on an EUT, when the disturbances measured on a metal ground plane site are compared with field strength disturbance limits developed for earth sites, also apply at a frequency of 1 000 MHz. Similarly, it can be seen in Figure 45 that at 1 000 MHz the patterns of the vertically polarized fields over a metal ground plane are a bad guide to the predictability of the fields created at elevated angles by the same dipole moment over a real ground.

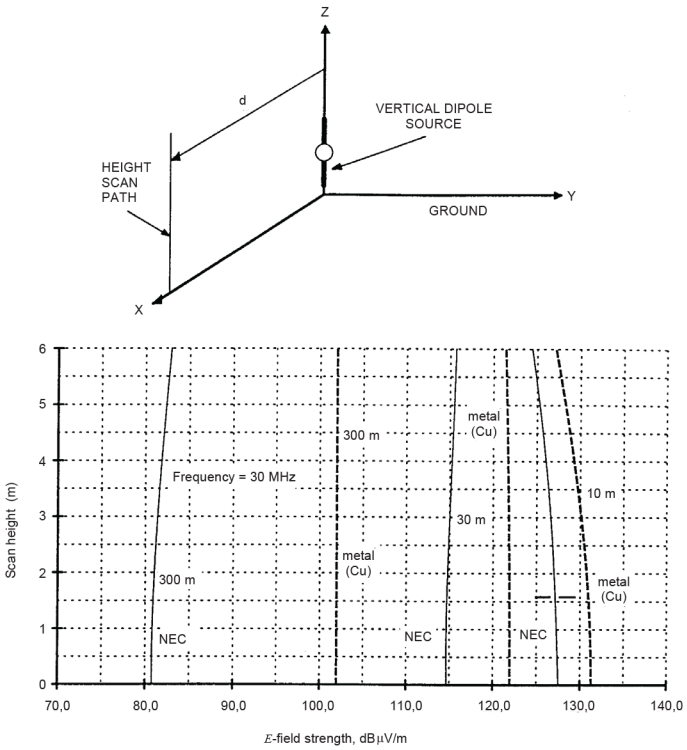
The height scan patterns in Figure 45 also clearly illustrate the effect of the phase reversal of the vertical dipole image in a lossy dielectric when reflection take place below Brewster's angle. The dashed horizontal line across the height scan pattern for 10 m distance shows the height to the field point, approximately 1,6 m, which corresponds with a reflection taking place at Brewster's angle when the source is 1 m above the “medium dry ground.”

In Figure 45 it is quite clear that at 10 m distance the field nulls and maxima at heights greater than 1,6 m above both the copper ground plane and the “medium dry ground” are in phase, signifying that the images in the two kinds of ground planes have similar phases when reflection from the real ground takes place at elevation angles above Brewster's angle. However, it is also quite clear that vertically polarized waves reflected below Brewster's angle over the “medium dry ground” are reversed in phase with respect to the corresponding reflected waves over the copper ground plane. In other words, the vertical image in the lossy dielectric is reversed, producing destructive interference (a null) at the surface of the “medium dry ground” whereas constructive interference (a maximum) occurs at the surface of the copper ground plane (the direct and reflected path lengths being the same in both cases). With the vertical dipole source at a height of 1 m, a maximum occurs in the field at 10 m distance at a height of 0,75 m above the “medium dry ground”, whereas a very deep null occurs at that height over the copper ground plane (the direct and reflected path lengths differ by $\lambda/2$ in both cases).

IECNORM.COM : Click to view the full PDF of CISPR TR 16-3:2020 RLV

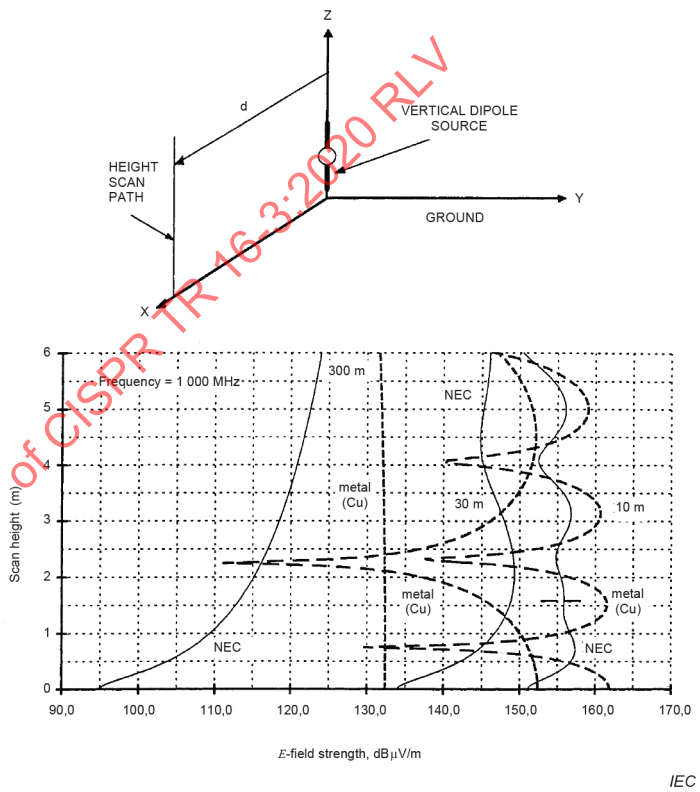
The height scans at 30 m and 300 m, up to a height of 6 m, take place below Brewster's angle. Maxima in the height-scanned fields over the metal ground plane therefore coincide with minima in the fields over real ground in both those height scans. This is largely the reason why it shall not be believed that the height scanned vertically polarized fields calculated over a good conductor will resemble those over real ground, especially at the larger horizontal distances. Such a belief will create false confidence that measurements made near real ground, without regard for the horizontal distance from the source, can give good guidance to the field strengths to be expected at elevated angles.

IECNORM.COM : Click to view the full PDF of CISPR TR 16-3:2020 RLV




NOTE NEC dipole length 0,2 m; dipole centre height 1 m; dipole moment 1 A·m; horizontal distance 10 m, 30 m and 300 m; 30 MHz; ground constants: real ground ("medium dry ground") $\varepsilon_r$ = 15, $\sigma$ = 1 mS/m, copper $\varepsilon_r$ = 1, $\sigma$ = 5,81 × $10^7$ S/m; Z-X plane (Adapted from [40]). Fields calculated in NEC (solid lines) include the surface wave over real ground. The dashed curves were calculated geometrically to include the direct and reflected space waves from an infinitesimal vertical electric dipole over a metal (copper) ground plane.

**Figure 44 – Height scan patterns of the vertical component of the *E*-fields emitted from a small vertical electric dipole**




NOTE NEC dipole length 0,02 m; dipole centre height 1 m; dipole moment 1 A·m; horizontal distance 10 m, 30 m and 300 m; 30 MHz; ground constants: real ground $\varepsilon_r$ = 15, $\sigma$ = 35 mS/m, copper $\varepsilon_r$ = 1, $\sigma$ = 5,81 × $10^7$ S/m; Z-X plane (Adapted from [40]). Fields calculated in NEC (solid lines) include the surface wave over real ground. The dashed curves were calculated geometrically to include the direct and reflected space waves from an infinitesimal vertical electric dipole over a metal (copper) ground plane.

**Figure 45 – Height scan patterns of the vertical component of the *E*-fields emitted from a small vertical electric dipole**

IECNORM.COM : Click to view the full PDF of CISPR TR 16-3:2020 RLV

#### 4.5.6.3 Horizontally polarized fields over a perfect conductor

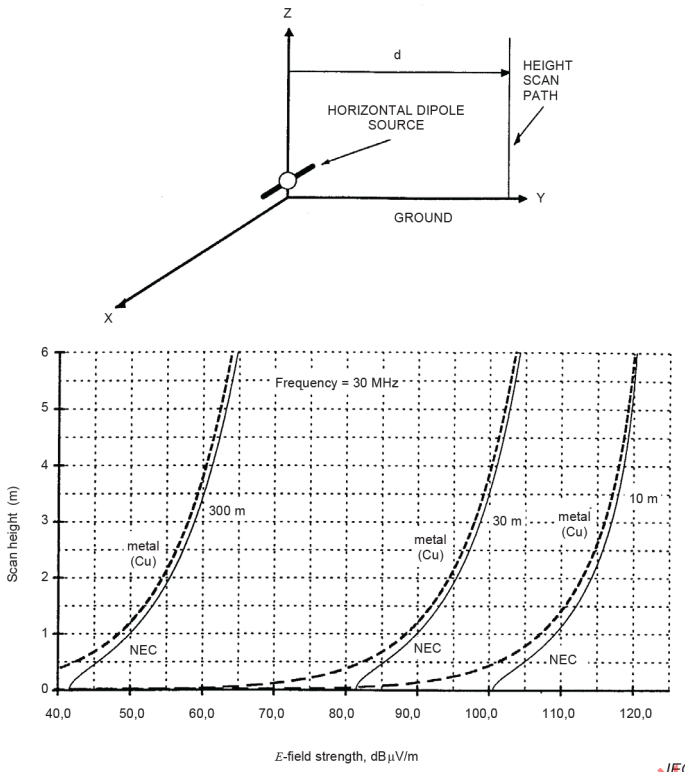
Although the contribution of the horizontally polarized surface wave over real ground at 30 MHz is small, nevertheless the height scan patterns in Figure 46 show that the horizontally polarized fields near the “medium dry ground” are stronger in this case than the corresponding fields near the copper ground plane.

In both cases a null is required in the vertical field pattern at the ground, to satisfy the boundary conditions, and the null is deeper in the copper ground plane example. This example shows, in contrast with vertically polarized measurements, that it is possible that measurements of horizontally polarized fields made on a metal ground plane for comparison with radiated disturbance limits developed for earth sites may slightly favour the EUT when measuring for compliance with the limits.

In Figure 47, the height scan patterns of the horizontally polarized $E$-fields emitted at 1 000 MHz from the small horizontal electric dipole show that at height scan distance of 30 m and more, with no useful contribution from the surface wave, the maximum horizontally polarized fields over a “medium dry ground” are very similar to those over a copper ground plane. The similarity of magnitude in regions of constructive interference is caused by the similar reflection factors (magnitudes close to unity) over both surfaces at low angles of reflection. At higher reflection angles, and a shorter measurement distance of 10 m, the maximum horizontally polarized fields over a metal ground plane exceed those over an earthen ground plane because the magnitude of the reflection factor over the earth plane becomes significantly less than unity. The reflected wave then contributes less to the constructive interference occurring at the field maxima.

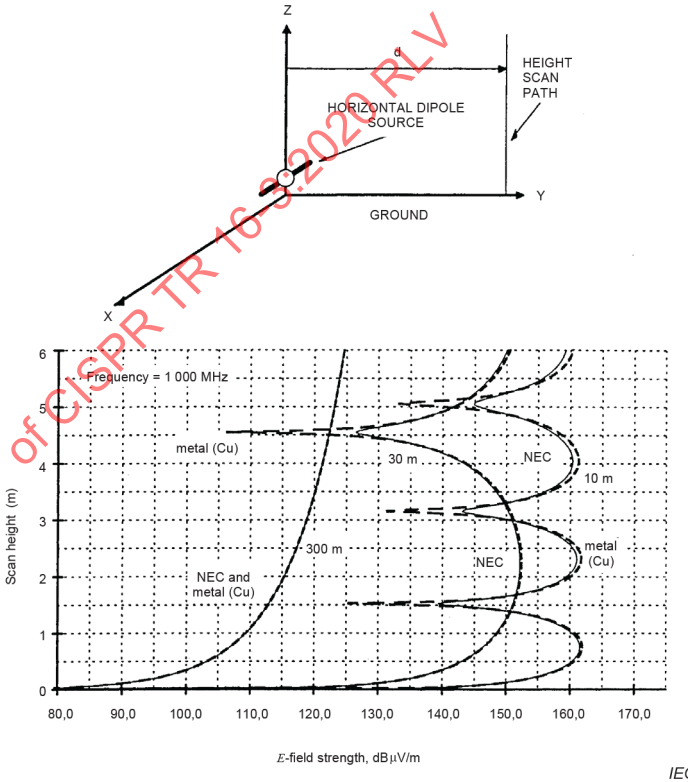
The behaviour of the horizontally polarized fields over an earthen ground plane is not complicated by a Brewster's angle phenomenon. In general, at frequencies of 30 MHz and above, the horizontally polarized field patterns over a real ground resemble the shapes of the corresponding patterns over a metal ground plane. Some small differences in field strengths are created over real ground compared with those over a metal ground plane at the lower frequencies by the presence of the surface wave over a real ground. Differences are also created at short horizontal distances, and higher frequencies at which the surface wave is insignificant, because the magnitude of the horizontal reflection factor decreases below unity as the waves reflect at higher angles from the earth plane.

IECNORM.COM : Click to view the full PDF of CISPR TR 16-3:2020 RLV




NOTE NEC dipole length 0,2 m; dipole height 1 m; dipole moment 1 A·m; horizontal distance 10 m, 30 m and 300 m; 30 MHz; ground constants: real ground ("medium dry ground") $\varepsilon_r$ = 15, $\sigma$ = 1 mS/m, copper $\varepsilon_r$ = 1, $\sigma$ = 5,81 × $10^7$ S/m; Z-X plane. Fields calculated in NEC (solid lines) include the surface wave over real ground. The dashed curves were calculated geometrically to include the direct and reflected space waves from an infinitesimal horizontal electric dipole over a metal (copper) ground plane. (Adapted from [40])

**Figure 46 – Height scan patterns of the horizontally polarized *E*-fields emitted in the vertical plane normal to the axis of a small horizontal electric dipole**




NOTE NEC dipole length 0,02 m; dipole height 1 m; dipole moment 1 A·m; horizontal distance 10 m, 30 m and 300 m; 1 000 MHz; ground constants: real ground ("medium dry ground") $\varepsilon_r$ = 15, $\sigma$ = 35 mS/m, copper $\varepsilon_r$ = 1, $\sigma$ = 5,81 × $10^7$ S/m; Z-X plane. Fields calculated in NEC (solid lines) include the surface wave over real ground. The dashed curves were calculated geometrically to include the direct and reflected space waves from an infinitesimal horizontal electric dipole over a metal (copper) ground plane. (Adapted from [40])

**Figure 47 – Height scan patterns of the horizontally polarized *E*-fields emitted in the vertical plane normal to the axis of a small horizontal electric dipole**

IECNORM.COM : Click to view the full PDF of CISPR TR 16-3:2020 RLV

#### 4.5.6.4 Fields over a perfect conductor as guides to the fields over real ground

We can now answer the fourth question raised in 4.5.3.

In summary, the horizontal polarized field patterns created over real ground at frequencies of 30 MHz and above resemble the corresponding patterns over a metal ground plane. There are some differences of a few decibels in field magnitudes. At the lower frequencies some small differences are also created by the existence of the surface wave over a real ground. At the higher frequencies, the field strength differences at short measuring distances are caused by the decrease below unity of the magnitude of the horizontal reflection factor for real ground when reflection takes place at angles significantly above grazing incidence. Constructive interference of direct and reflected waves over real ground then produces field strength maxima of somewhat smaller magnitudes than those produced over a good conductor which has a reflection factor close to unity at all reflection angles.

However, very large differences are found when comparing the patterns of vertically polarized fields over a metal ground plane with those over a real ground. The differences are primarily created by the existence of Brewster's angle for the reflections of vertically polarized waves from a lossy dielectric like real ground. When reflections from real ground take place below Brewster's angle the minima in the fields occur at the same heights at which the maxima are produced with the same measuring geometry over the metal ground plane, most notably at the surface of the ground plane. This contrapositioning of minima and maxima is the main reason why the height scanned vertically polarized fields calculated over a good conductor shall not be assumed to resemble those over real ground, especially at the larger horizontal distances when reflection takes place near grazing incidence. An assumption that there is a resemblance encourages false confidence that measurements near real ground, without regard for the horizontal distance from the source, can give good guidance to the field strengths to be expected at elevated angles.

Vertically polarized field patterns over a metal ground plane do not resemble the shapes and magnitudes of the vertically polarized field patterns to be expected from the same sources over a real ground.

### 4.5.7 Uncertainty ranges

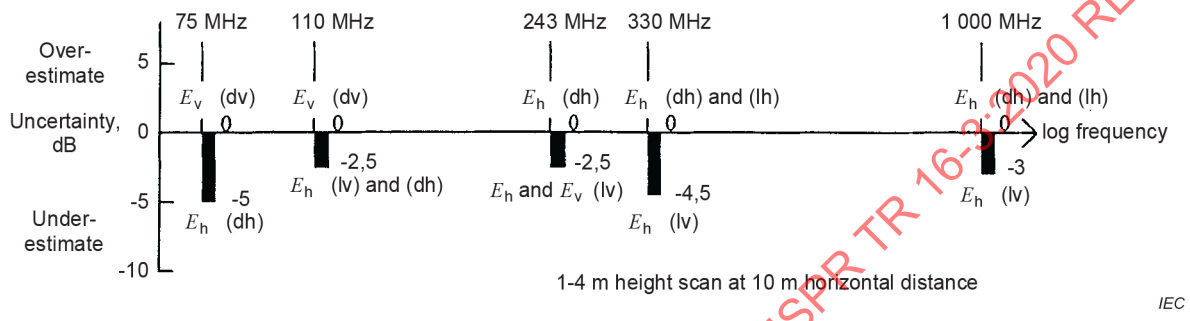
The information summarized in Table 14 to Table 18 can also be used to show pictorially the ranges of uncertainties in the predictability of the radiation emitted at elevated angles at frequencies above 30 MHz. The information has been used to construct bar charts illustrating the uncertainties for electrically small sources located 1 m or 2 m above ground when predictions of the field strengths at elevated angles are based on $E$-field measurements in 1 m to 4 m height scans at horizontal distances of 10 m, 30 m and 300 m.

Figure 48 illustrates the uncertainties in predictability based on measurements made at a horizontal distance of 10 m. The bar for the uncertainty range at 330 MHz shows that the best predictability at 330 MHz is obtained when the source behaves as either a small horizontal dipole (dh) or as a small horizontal loop (lh). There is nominally zero error predicting the maximum strength of the horizontally polarized $E_{\mathrm{h}}$ fields. The poorest predictability at 330 MHz results in an underestimate of approximately 4,5 dB for the maximum horizontally polarized field $E_{\mathrm{h}}$ emitted at elevated angles from a small vertical loop (lv).

When measurements are made in a height scan at a horizontal distance of 30 m, the bar for the uncertainty range at 110 MHz in Figure 49 shows that the best predictability at 110 MHz occurs when the source behaves as a small vertical dipole (dv). There is a negligible underestimate, by 0,5 dB, predicting the $E_z$ vertical component of the vertically polarized field. The poorest predictability at 110 MHz produces a greater underestimate, by 9,5 dB, of the horizontally polarized $E_{\mathrm{h}}$ field emitted at elevated angles from a small horizontal dipole source (dh).

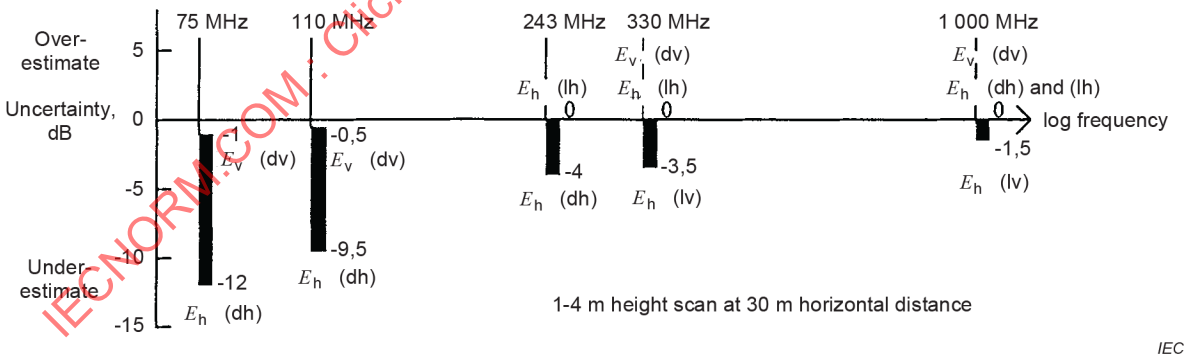
IECNORM.COM : Click to view the full PDF of CISPR TR 16-3:2020 RLV

Figure 50 graphically illustrates the very large uncertainties in predictability that occur if the horizontal measuring distance is as great as 300 m. At 243 MHz, the bar illustrating the uncertainty range shows that the poorest predictability at 243 MHz introduces a very large underestimate by 22,5 dB for the horizontally polarized $E_h$ fields emitted at elevated angles from a small horizontal dipole (dh) and from a small horizontal loop (lh). The best predictability at 243 MHz also produces a large underestimate, by 13 dB, of the vertical $E_z$ component of the vertically polarized field emitted at elevated angles from a small vertical dipole (dv). Figure 49 and Figure 50, in particular, graphically illustrate the very large underestimates which can occur when attempts are made to predict the strength of radiation in vertical directions based on measurements near the ground at unknown horizontal distances greater than 10 m from the sources.




NOTE The predictability is based on measurements of the horizontally and vertically polarized $E$-fields in a height scan from 1 m to 4 m at a horizontal distance of 10 m from the sources. The following example shows how the bar chart can be interpreted. At 243 MHz, the bar shows that the best predictability, with nominally zero error, is obtained when estimating the maximum strength of the horizontally polarized $E_h$ field emitted at elevated angles from a source behaving as a small horizontal dipole (dh). The poorest predictability at 243 MHz, an underestimate by as much as 2,5 dB, can occur when predicting the maximum strengths of the horizontally polarized $E_h$ fields and the $E_z$ vertical component of the vertically polarized fields emitted at elevated angles from a source behaving as a small vertical loop (lv). (Reproduced from [39])

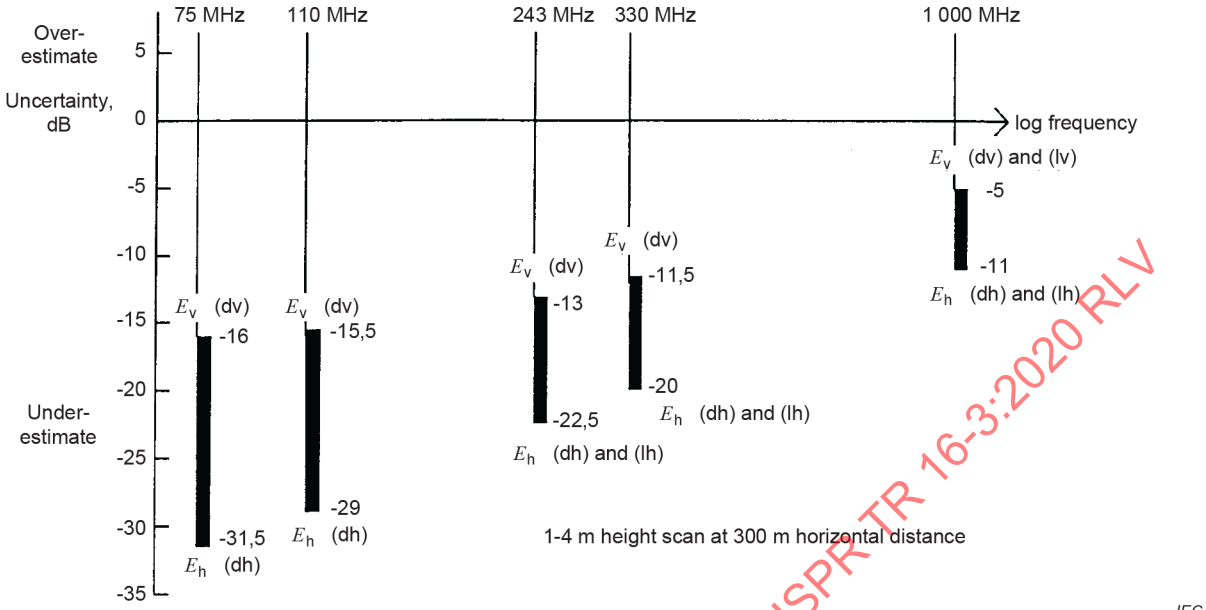
**Figure 48 – Ranges of uncertainties in the predictability of radiation in vertical directions from electrically small sources located at a height of 1 m or 2 m above ground**




NOTE The predictability is based on measurements of the horizontally and vertically polarized $E$-fields in a height scan from 1 m to 4 m at a horizontal distance of 30 m from the sources. The following example shows how the bar chart can be interpreted. At 330 MHz, the bar shows that the best predictability, with nominally zero error, is obtained when estimating the maximum strength of either the horizontally polarized $E_h$ field emitted at elevated angles from a small horizontal loop (lh) or the $E_z$ vertical component of the vertically polarized field emitted at elevated angles from a small vertical dipole (dv). But at 330 MHz the height scan measurements ~~may~~ can provide an underestimate by as much as 3,5 dB when predicting the strength of the horizontally polarized $E_h$ field, which is the maximum field emitted at elevated angles from a source behaving as a small vertical loop (lv) (Reproduced from [39])

**Figure 49 – Ranges of uncertainties in the predictability of radiation in vertical directions from electrically small sources located at a height of 1 m or 2 m above ground**

IECNORM.COM : Click to view the full PDF of CISPR TR 16-3:2020 RLV




NOTE The predictability is based on measurements of the horizontally and vertically polarized $E$-fields in a height scan from 1 m to 4 m at a horizontal distance of 300 m from the sources. The following example shows how the bar chart can be interpreted. The bar at 1 000 MHz shows that the best predictability at that frequency, which is an underestimate by as much as 5 dB, will be obtained when predicting the maximum strength of the $E_z$ vertical component of the vertically polarized field emitted at elevated angles from a source behaving as a small vertical loop (lv) or a small vertical dipole (dv). However, an underestimate by as much as 11 dB can occur at 1 000 MHz when predicting the maximum strength of the horizontally polarized $E_h$ field emitted at elevated angles from a source behaving as a small horizontal loop (lh) or a small horizontal dipole (dh). (Reproduced from [39])

**Figure 50 – Ranges of uncertainties in the predictability of radiation in vertical directions from electrically small sources located at a height of 1 m or 2 m above ground**

### 4.5.8 Conclusions

The *in situ* measurement procedures at frequencies above 30 MHz which are specified in CISPR 11 can lead to significant underestimates of the field strengths emitted at elevated angles from ISM equipment. The underestimates can arise due to the ill-defined measurement distance; the measuring distance from the radiating ISM equipment is not defined.

The largest underestimates of the fields at elevated angles will generally occur for horizontally polarized fields. This is a cause for concern, because the aeronautical safety of life services requiring greatest protection from disturbances originating at the ground are those provided by the horizontally polarized marker beacon, localizer, and glide path signals of the aeronautical ILS.

Under some conditions, measurements are specified in CISPR 11 at a fixed height of 2,0 m. Measurements at a fixed height should not be specified if they are being made to determine protection for specific safety services. There is a risk that fixed height measurements will be made in, or close to, a null. The risk increases at the higher frequencies and when the height to the radiation centre of the source is unknown. Fixed height measurements can seriously underestimate the true field strength near the ground and, in consequence, the maximum field strength at elevated angles.

IECNORM.COM : Click to view the full PDF of CISPR TR 16-3:2020 RLV

Calculations or measurements of the field strength patterns of vertically polarized fields over a perfect conductor or metal ground plane do not provide good guidance to the fields to be expected over a real ground. At reflection angles below Brewster's angle over real ground the field minima and maxima are contraposed with those created by the same source over a metal ground plane.

To provide protection for aeronautical safety of life services, and other communication systems, height scan measurements and limits for radiated disturbances from *in situ* ISM equipment located near the ground shall be *specified at a known horizontal distance from the equipment*. Height scan measurements at a horizontal distance of 10 m from an ISM equipment *in situ* allow accurate estimates to be made of the fields emitted at elevated angles. If for practical reasons the *in situ* measurements shall be made at a distance greater than 10 m from the equipment which is the source of the radiation then the limits at the larger distance, particularly if it is more than 30 m, shall be derived from the 10 m limits by adjusting them in inverse proportion with increasing distance squared. This shall be so in order to prevent relaxation of the protection when limits are intended to provide for communication or radionavigation systems that are operated high above ground.

### 4.6 The predictability of radiation in vertical directions at frequencies up to 30 MHz

#### 4.6.1 Range of application

This subclause considers the vertical radiation patterns of the magnetic ($H$) fields and electric ($E$) fields emitted at frequencies up to 30 MHz from electrically small sources located close to the surface of real homogeneous plane ground, for the purpose of studying the predictability of radiation in vertical directions based on measurements of the strength of the $H$-field near the ground.

The vertical radiation patterns of the fields have been calculated at a distance of 30 m from various electrically small sources, and then the patterns of the fields at greater distances have been calculated so that the field variations with distance can be quantified. In this way, a general knowledge has been obtained of the shapes of the vertical radiation patterns, showing the magnitudes of the field strengths near ground compared with the magnitudes of the field components at elevated angles, and the ways in which the relative magnitudes can be expected to vary with distance over a plane ground.

The sources considered are electrically small balanced electric and magnetic dipoles excited in the frequency range 100 kHz to 30 MHz. For the purposes of the subclause, an electrically small source is defined as one whose largest linear dimension is one-tenth or less of the free space wavelength at the frequency of interest.

This subclause also considers the effects on the vertical radiation patterns of locating the electrically small sources close to real grounds having several different values of electrical conductivity and dielectric constants [43], [44], and includes the special case of a ground that behaves as a perfect conductor.

The possible effects on the vertical radiation patterns produced by walls, buildings, reinforced concrete structures, and the like, in the vicinity of the sources, and the effects on wave propagation near the ground that could be produced by changes with distance of the electrical constants of the ground, caused by intervening roads, watercourses, buried metallic pipes, and so on, are not within the scope of this subclause. It is important to note, therefore, that the errors in predictability that may be produced by such effects have not been considered.

IECNORM.COM : Click to view the full PDF of CISPR TR 16-3:2020 RLV

### 4.6.2 General

CISPR 11 sets limits for the electromagnetic disturbances emitted near the ground from industrial, scientific and medical (ISM) radio-frequency equipment. The limits are intended to provide protection of the reception of radio services. At frequencies below 30 MHz the limits apply to the horizontally oriented components of the $H$-fields emitted by the ISM apparatus. For measurements on a test site, the limits apply at a distance of 30 m from the source. When measurements are made *in situ* the distance to the measurement point is defined as 30 m from the exterior wall outside the building in which the ISM equipment is situated; the distance from the source is not defined. Measurements are to be made with a vertically oriented loop, the base of which shall be 1 m above the ground.

It is acknowledged in CISPR 11 that many aeronautical communications require the limitation of vertically radiated electromagnetic disturbances, and that work is necessary to determine what provisions may be required to provide protection of such systems.

The aeronautical radio services to be protected may be either horizontally or vertically polarized transmissions. Thus, the field components at elevated angles, emitted from potential interference sources located near the ground, that are of interest in a study of field strength predictability include the vertically and horizontally oriented $H$- and $E$-field components.

In this subclause the judgements of predictability of radiation in vertical directions are based on the accuracy with which ground-based measurements of the horizontally oriented $H$-fields emitted from a variety of sources will indicate the maximum strengths of the horizontally or vertically oriented $H$-fields at elevated angles.

As might be expected, at a distance of 30 m from an electrically small source there are significant changes in the field behaviour with changing wavelength as the frequency is varied from 100 kHz to 30 MHz. The subclause, therefore, concentrates attention at four frequencies, namely 100 kHz, 1 MHz, 10 MHz and 30 MHz. At 100 kHz the distance of 30 m lies well within the electrostatic or inductive near-field region close to the source. At 1 MHz the distance of 30 m is within $\lambda/10$ of an electrically small source, and places the measurement position in what might be called the radiating near-field region. At 10 MHz, a distance of 30 m represents approximately one wavelength from the source, a region where the far field has become established. At 30 MHz, a distance of 30 m represents approximately three wavelengths from the source and places the measurement position well into the far field.

In addition to the variations in field behaviour produced by changes from near-field to far-field conditions as the wavelength is varied, in the frequency range 100 kHz to 30 MHz the electrical behaviour of real ground varies. In general, real ground has the characteristics of a lossy conductor at low frequencies, and the characteristics of a lossy dielectric at the higher frequencies. Moreover, the values of the electrical constants of real ground can vary widely; they may range typically from a conductivity of $10^{-4}$ S/m and relative permittivity of 3 to a conductivity of $10^{-2}$ S/m and relative permittivity of 30 [43], [44]. Even this wide range of values of the ground constants does not encompass all of the values that may be encountered in some localities.

The subclause shows the limitations of the predictability of radiation in vertical directions. In particular, it identifies the critical importance of a knowledge of the precise measurement distance – the actual distance between the source and the field measuring point near the ground – if it is to be possible to make predictions of the radiated field strengths at elevated angles with a known margin of error.

IECNORM.COM : Click to view the full PDF of CISPR TR 16-3:2020 RLV

Subclause 4.6 indicates the ranges of magnitude of the significant errors in predictability that can still occur when the precise measurement distance over real ground is 30 m from the sources, and the large errors that can arise from the approximation that the influence of real ground can be determined by assuming it behaves like a perfect conductor. It also shows how magnitudes of the errors in predictability above real ground may be reduced, although they remain significant, by supplementing measurements of horizontally oriented $H$-fields near ground with height scan measurements of vertically oriented $H$-fields at heights up to 6 m, when the measurements are made at a distance of 30 m from the sources.

### 4.6.3 Method of calculation of the vertical radiation patterns

The $H$- and $E$-field vertical radiation patterns in this subclause were calculated using a Method of Moments computer code known as the Numerical Electromagnetics Code (NEC) [35]. A double precision version, NEC2D, with the companion code SOMNEC2D, was used. NEC with SOMNEC allows the Sommerfeld integral evaluation of the field interactions at the air-ground interface [36] to be included in the determination of the $E$-fields above real grounds.

In the version of the NEC codes that were first released for public use, a section of code for calculation of the near $H$-field in the presence of real ground was omitted, which can lead to large errors in the $H$-field calculations [45], [46]. In the version of NEC2D used to calculate the radiation patterns in this subclause the missing code has been restored, allowing calculation of all the $H$-field components close to the surface of a real ground. The restored section of code calculates the $H$-field components by using a six-point finite-difference approximation of the curl of the $E$-field obtained by the Sommerfeld method.

The spatial sampling interval used in the finite-difference calculation of $H$-field in NEC is normally fixed at $10^{-3}\ \lambda$. For the $H$-field radiation patterns calculated at the frequencies of 100 kHz and 1 MHz the spatial sampling interval has to be altered to $10^{-5}\ \lambda$ and $10^{-4}\ \lambda$, respectively, in order to obtain accurate calculations of the near $H$-field [46], [47].

Some remaining problems of numerical stability, arising from the finite-difference approximation of the $H$-fields from $E$-fields, which in some cases have components whose curl is mathematically zero but which have become numerically non-zero due to small numerical inaccuracies [48], have required smoothing of some of the calculated $H$-field radiation patterns.

### 4.6.4 The source models

The electrically small sources that form the basis of this subclause consist of small vertical and horizontal balanced electric dipoles, and vertical and horizontal balanced magnetic dipoles (horizontally and vertically oriented loops respectively), each having a unit dipole moment [i.e. a dipole (current) moment of 1 A·m for the electric dipoles and a dipole moment of 1 A·m$^2$ for the magnetic dipoles]. All were located very close electrically to the air-ground interface (within a small fraction of a wavelength); the height above ground of the base of each dipole was varied between either 7 cm or 15 cm and a maximum of 1 m to determine the sensitivity of the shape of the field-strength patterns to changes in the source height. The patterns considered in this subclause are those that exhibited the greatest variation in shape with height.

The geometries of the models used for the field-pattern computations are shown in Figure 51 to Figure 52, including the paths of the radial scans about each source; advantage has been taken of the verified azimuthal symmetry of the fields around the vertical magnetic and vertical electric dipoles to confine attention to the radial scans around those sources in only the Z-X plane.

IECNORM.COM : Click to view the full PDF of CISPR TR 16-3:2020 RLV

It is seen in Figure 53 and Figure 54 that two generators drive each loop. Although the loops used in the models were electrically small, it was found that when driven by one generator only, each displayed sufficient current asymmetry to produce a significant electric dipole contribution to the electromagnetic fields – because of their finite size the small loops did not behave as electrically infinitesimal magnetic dipole sources. In the models used here, therefore, each loop was driven by two identical aiding generators located as shown, and the electric dipole contribution produced by current asymmetry arising from the use of a single generator was reduced to insignificance. Of course, in the case of the horizontal magnetic dipole (vertical loop), there is always a loop current asymmetry (and a resultant electric dipole moment) caused by proximity to the ground and this effect also occurs in the models used in this subclause.

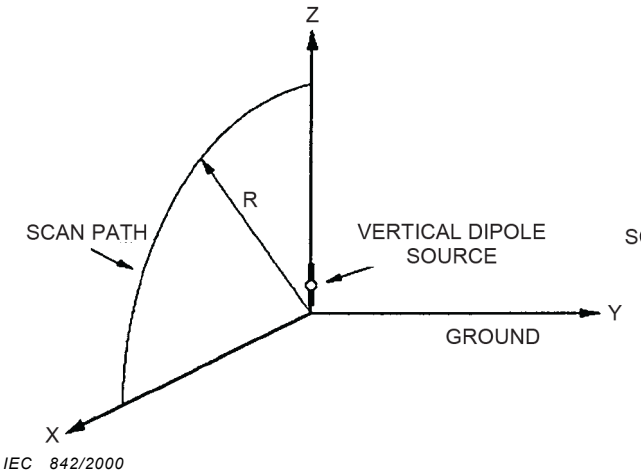



**Figure 51 – Geometry of the small vertical electric dipole model**

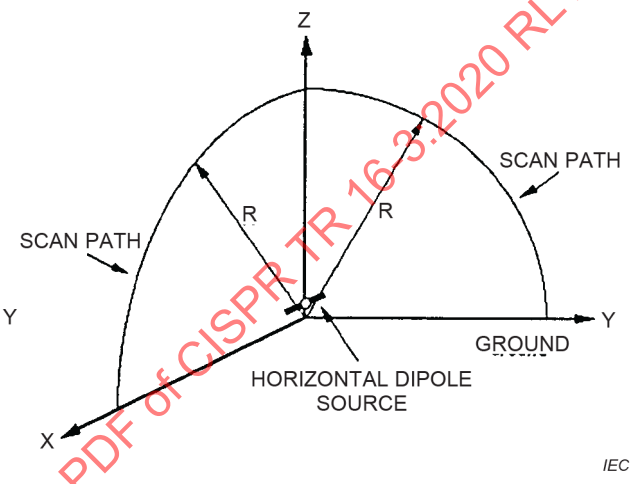



**Figure 52 – Geometry of the small horizontal electrical dipole model**

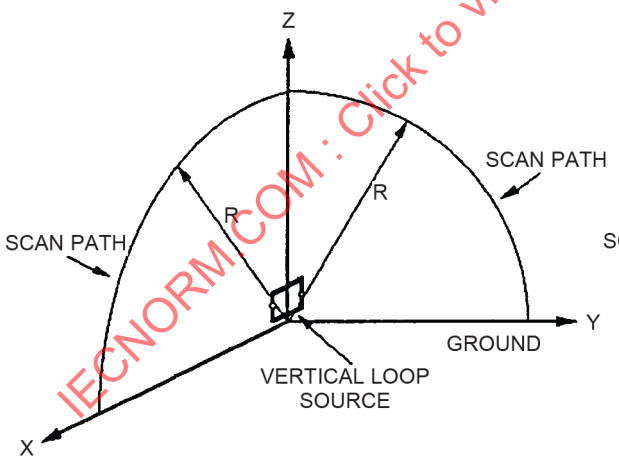



**Figure 53 – Geometry of the small horizontal magnetic dipole model (small vertical loop)**

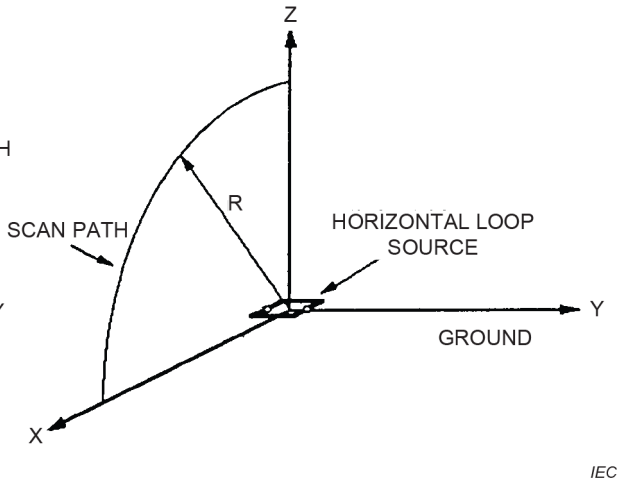



**Figure 54 – Geometry of the small vertical magnetic dipole model (small horizontal loop)**

IECNORM.COM : Click to view the full PDF of CISPR TR 16-3:2020 RLV

### 4.6.5 Electrical constants of the ground

Most attention in this subclause has been devoted to radiation sources located close to a ground having a conductivity, $\sigma$ = $10^{-3}$ S/m and a relative dielectric constant, $\varepsilon_r$ of 15; these electrical constants are in the CCIR category of a medium dry ground [43], [44].

At the upper and lower extremes of the frequency range, i.e. 30 MHz and 100 kHz, examples of two other sets of values of ground constants were used with the small horizontal electric dipole model to illustrate the influence of differing values of the ground constants on the vertical radiation patterns. The electrical constants mentioned in 4.6.2, with the numerical values of $\sigma$ = $10^{-2}$ S/m and $\varepsilon_r$ = 30 (ITU-R – cultivated land and fresh water marshes) and $\sigma$ = $10^{-4}$ S/m and $\varepsilon_r$ = 3 (ITU-R – very dry ground and granite mountains in cold regions), were chosen as the examples [43], [44].

For each type of source, the field patterns above a perfectly conducting ground were also been compared with the patterns generated above real grounds, to identify the errors that can arise from the approximation which is sometimes made so that the influence of real ground can be determined by assuming it behaves as a perfect conductor.

In general, it is necessary to recall that specific boundary conditions apply to the fields at the surface of a perfect conductor that do not necessarily apply at the surface of a real ground. In particular, the $H$-field component normal to the surface of a perfect conductor shall go to zero at the surface, as shall the tangential $E$-field component at the surface, and it will be recalled that this is why a horizontally polarized surface wave cannot exist at the surface of a perfect conductor. Further, a vertically polarized surface wave travelling on a perfectly conducting ground plane experiences no ohmic loss – it merely attenuates with distance at the free space rate. Those boundary conditions, however, certainly do not apply at the surface of a real ground; thus the boundary conditions identify the most general set of differences between the vertical radiation patterns that will exist close to the surface of a real ground when compared with those calculated close to the surface of a perfectly conducting ground.

### 4.6.6 Predictability of radiation in vertical directions

#### 4.6.6.1 Tabular summaries of predictability

The vertical radiation patterns on which the judgements of predictability are based are presented in Figure 55 to Figure 112 (see 4.6.8), which are polar patterns showing field strength plotted against elevation angle above the ground. To summarize the information presented in those figures, the summary information of Table 19 through Table 22 were prepared, one for each frequency considered in this subclause.

IECNORM.COM : Click to view the full PDF of CISPR TR 16-3:2020 RLV

**Table 19 – Predictability of radiation in vertical directions at 100 kHz, using ground-based measurements of horizontally oriented *H*-field at distances up to 3 km from the source (figures are located in 4.6.8)**

| Type of source | Predictability based on measurements near real ground at 30 m distance from the source | Predictability based on *in situ* measurements near real ground when the measurement distance from the source is not precisely known | Predictability based on vertical radiation patterns calculated at a known distance from the source, assuming the ground behaves as a perfect conductor |
|---|---|---|---|
| Electrically small vertical electric dipole | Excellent (see Figure 57, Figure 59) | Excellent (see Figure 57 to Figure 60) | Excellent (see Figure 57) |
| Electrically small horizontal electric dipole | Excellent (see Figure 61 to Figure 63) Notes 1, 2 | Very good (see Figure 49, Figure 63 to Figure 65) | Poor (see Figure 61) Note 3 |
| Electrically small horizontal magnetic dipole (vertical loop) | Excellent (see Figure 66, Figure 68) Note 4 | Very good (see Figure 66, Figure 68 to Figure 70) | Very good (see Figure 66, Figure 67) Note 5 |
| Electrically small vertical magnetic dipole (horizontal loop) | Poor (see Figure 71, Figure 81) Note 6 | Impossible (see Figure 71, Figure 73 to Figure 76) Note 7 | Impossible (see Figure 71, Figure 72) Note 8 |

NOTE 1 The measurement of the horizontally oriented *H*-field emitted by the small horizontal electric dipole near the ground can overestimate the maximum vertically oriented *H*-field strength emitted at an elevated angle by approximately 1 dB (see Figure 61). Note, however, that the measurement overestimates the strength of the horizontally oriented *H*-field emitted in the vertical direction by 5 dB.

NOTE 2 The small influence exerted on the small horizontal electric dipole vertical radiation patterns at 100 kHz by a wide range of the electrical constants of the ground is shown in Figure 62.

NOTE 3 The horizontal electric dipole's *H*-field pattern calculated assuming a perfectly conducting ground shows that such an assumption causes an underestimate of more than 20 dB in the absolute field strength, and falsely indicates that the ground-based measurement underestimates the maximum field strength by 6 dB (refer to NOTE 1) (see Figure 61).

NOTE 4 The measurement of horizontally oriented *H*-field emitted by the small horizontal magnetic dipole (vertical loop) near the ground can overestimate the maximum vertically oriented *H*-field strength at elevated angles by less than 1 dB (see Figure 66). Note, however, that the measurement overestimates the strength of the horizontally oriented *H*-field emitted in the vertical direction by more than 3 dB.

NOTE 5 Vertical patterns of the horizontally oriented *H*-fields emitted by the small horizontal magnetic dipole (vertical loop), calculated assuming a perfectly conducting ground, can overestimate absolute values of field strength over real ground by 6 dB, but the shapes of the patterns are a good guide to those over real ground. However, boundary conditions are such that the vertically oriented *H*-field goes to zero at the surface of the perfectly conducting ground which is not the case at the surface of a real ground. See Figure 66 and Figure 67.

NOTE 6 The measurement of horizontally oriented *H*-field emitted by the small vertical magnetic dipole (horizontal loop) near the ground at a distance of 30 m underestimates the *H*-field strengths at elevated angles by more than 16 dB (see Figure 71). However, measurement of the vertically oriented *H*-field, in Hz, near the ground improves predictability; it provides an underestimate of the vertically oriented *H*-field emitted in the vertical direction by approximately 6 dB, and an underestimate of the maximum horizontally oriented *H*-field emitted at elevated angles by about 3 dB.

NOTE 7 The relative magnitudes of the *H*-field components near the ground and at elevated angles are strongly dependent on the actual distance from the small horizontal loop. See Figure 71, Figure 73 and Figure 74.

NOTE 8 The small horizontal loop field patterns calculated close to the ground assuming a perfectly conducting ground have no resemblance, in shape and absolute magnitude, to the field patterns calculated close to a real ground. See Figure 71 and Figure 72.

IECNORM.COM : Click to view the full PDF of CISPR TR 16-3:2020 RLV

**Table 20 – Predictability of radiation in vertical directions at 1 MHz, using ground-based measurements of horizontally oriented *H*-field at distances up to 300 m from the source (figures are located in 4.6.8)**

| Type of source | Predictability based on measurements near real ground at 30 m distance from the source | Predictability based on *in situ* measurements near real ground when the measurement distance from the source is not precisely known | Predictability based on vertical radiation patterns calculated at a known distance from the source, assuming the ground behaves as a perfect conductor |
|---|---|---|---|
| Electrically small vertical electric dipole | Excellent (see Figure 77, Figure 78) | Excellent (see Figure 77 to Figure 79) | Excellent (see Figure 77) |
| Electrically small horizontal electric dipole | Very good (see Figure 80, Figure 82) Note 1 | Good (see Figure 80 to Figure 83) | Poor (see Figure 80) Note 2 |
| Electrically small horizontal magnetic dipole (vertical loop) | Excellent (see Figure 82, Figure 87) Note 3 | Good (see Figure 82, Figure 86 to Figure 88) | Fair (see Figure 84, Figure 85) Note 4 |
| Electrically small vertical magnetic dipole (horizontal loop) | Excellent (see Figure 89, Figure 92) Note 5 | Impossible (see Figure 89, Figure 91 to Figure 92) Note 6 | Poor (see Figure 90) Note 7 |

NOTE 1 The measurement of the horizontally oriented $H$-field emitted by the horizontal electric dipole near the ground can overestimate the maximum vertically oriented $H$-field strength emitted at elevated angles by approximately 3 dB (see Figure 80). Note, however, that the measurement can overestimate the strength of the horizontally oriented $H$-field emitted in the vertical direction by more than 9 dB.

NOTE 2 The $H$-field patterns calculated at a distance of 30 m from the horizontal electric dipole assuming a perfectly conducting ground show that such an assumption causes an underestimate of 20 dB in the absolute field strength at 1 MHz, and falsely indicates that the ground-based measurement underestimates the maximum field strength emitted in vertical directions by 5 dB. See Figure 80.

NOTE 3 The measurement of the horizontally oriented $H$-field emitted by the small vertical loop near the ground can overestimate the maximum field strength emitted at elevated angles by less than 3 dB (see Figure 84).

NOTE 4 The patterns of horizontally oriented $H$-field calculated at 30 m from the small vertical loop assuming perfectly conducting ground are very similar to the $H$-field patterns over a real ground. See Figure 84 and Figure 85.

NOTE 5 The measurement of the horizontally oriented $H$-field emitted by the small horizontal loop near the ground at 30 m distance can underestimate the maximum vertically oriented $H$-field strength emitted in the vertical direction by more than 2 dB, and the maximum horizontally oriented $H$-field emitted at elevated angles by less than 1 dB (see Figure 89). A measurement of the vertically oriented $H$-field, Hz, near ground reduces the underestimate of the strength of the vertically oriented $H$-field emitted in the vertical direction to about 1 dB, and overestimates the maximum horizontally oriented $H$-field strength by more than 1 dB.

NOTE 6 The relative magnitudes of the $H$-field components near the ground and at elevated angles are strongly dependent on the actual distance from the horizontal loop source. The horizontally oriented $H$-field near the ground is a radially directed component which attenuates more rapidly with increasing distance than does the horizontally oriented $H$-field at elevated angles. The vertically oriented $H$-field near the ground is a component of the horizontally polarized ground wave launched by the horizontal loop and attenuates very rapidly with increasing distance from the source at 1 MHz. See Figure 89 and Figure 91.

NOTE 7 At 1 MHz, the vertical radiation pattern of the horizontally oriented $H$-field emitted by the small horizontal loop above a perfectly conducting ground has an absolute value more than 15 dB less than the field strength calculated above a real ground. The shape of the vertical pattern of the vertically oriented $H$-field calculated close to a perfectly conducting ground bears no resemblance to the vertical pattern calculated close to the real ground. Compare Figure 89 and Figure 90. In general, the boundary condition which requires the vertically oriented $H$-field strength to be zero at the surface of a perfectly conducting ground means that the pattern of vertically oriented $H$-field at the real ground, which is non-zero, does not resemble the corresponding pattern at the perfect ground.

IECNORM.COM : Click to view the full PDF of CISPR TR 16-3:2020 RLV

**Table 21 – Predictability of radiation in vertical directions at 10 MHz, using ground-based measurements of horizontally oriented *H*-field at distances up to 300 m from the source (figures are located in 4.6.8)** *(1 of 2)*

| Type of source | Predictability based on measurements near real ground at 30 m distance from the source | Predictability based on *in situ* measurements near real ground when the measurement distance from the source is not precisely known | Predictability based on vertical radiation patterns calculated at a known distance from the source, assuming the ground behaves as a perfect conductor |
|---|---|---|---|
| Electrically small vertical electric dipole | Excellent (see Figure 93, Figure 94) | Excellent (see Figure 93 to Figure 95) Note 1 | Impossible (see Figure 93) Note 2 |
| Electrically small horizontal electric dipole | Poor (see Figure 96, Figure 97) Note 3 | Good (see Figure 96 to Figure 98) Note 4 | Impossible (see Figure 96) Note 5 |
| Electrically small horizontal magnetic dipole (vertical loop) | Very good (see Figure 99, Figure 100) Note 6 | Impossible (see Figure 99, Figure 100) Note 7 | Impossible (see Figure 99) Note 8 |
| Electrically small vertical magnetic dipole (horizontal loop) | Poor (see Figure 101, Figure 102) Note 9 | Impossible (see Figure 101, Figure 102) Note 10 | Fair (see Figure 101) Note 11 |

NOTE 1 The horizontally oriented $H$-field near the ground is a component of the vertically polarized ground wave emitted from the vertical electric dipole. At 10 MHz the vertically polarized wave near the ground attenuates rapidly with increasing distance, such that there is an excess 8 dB ground-wave attenuation in addition to the 20 dB sky-wave attenuation over the distance from 30 m to 300 m. See Figure 93.

NOTE 2 At a distance of 30 m from the vertical electric dipole over a perfectly conducting ground the vertical radiation pattern of the horizontally oriented $H$-field is within about 3 dB of the pattern of the $H$-field over a real ground. However, the vertically polarized wave near a perfectly conducting ground attenuates with increasing distance at the free space rate and therefore does not attenuate with distance in the way it does over a real ground at 10 MHz (see NOTE ~~16~~ 11). It is thus misleading as a guide to the vertical radiation patterns over real ground at distances much beyond 30 m.

NOTE 3 The measurement of the horizontally oriented $H$-field near the real ground at 30 m from the small horizontal electric dipole can underestimate the field strength of the horizontally oriented $H$-field emitted in the vertical direction by approximately 8 dB, and the vertically oriented $H$-field strength emitted at elevated angles by about 3 dB. Measurements of vertically oriented Hz near ground cannot improve the predictability in this case. See Figure 96.

NOTE 4 At 10 MHz, the horizontally oriented $H$-field components near real ground attenuate more rapidly with increasing distance from the horizontal electric dipole than do the sky-wave components. The excess attenuation is approximately 7 dB over the distance from 30 m to 300 m. See Figure 96.

NOTE 5 The horizontally oriented $H$-field near a perfectly conducting ground attenuates by 40 dB as the distance from the small horizontal electric dipole increases from 30 m to 300 m, an excess attenuation of 20 dB more than the sky-wave attenuation over the same distance. Near a real ground the excess attenuation is about 7 dB over the same distance at 10 MHz. The vertical radiation patterns over real and perfectly conducting grounds therefore differ significantly in that range of measuring distances. See Figure 96.

NOTE 6 The measurement of the horizontally oriented $H$-field near the real ground at 30 m distance from the small vertical loop can underestimate the horizontally oriented $H$-field strength emitted in the vertical direction by less than 3 dB, but it overestimates the strength of the vertically oriented $H$-field emitted at elevated angles by approximately 3 dB. See Figure 99.

NOTE 7 The horizontally oriented $H$-field components near real ground attenuate much more rapidly with increasing distance from the small vertical loop than do the sky-wave components, at 10 MHz. The excess attenuation is approximately 8 dB over the distance from 30 m to 300 m. See Figure 99.

NOTE 8 At a distance of 30 m from the small vertical loop over a perfectly conducting ground the vertical radiation pattern of the horizontally oriented $H$-field is within about 4 dB of the pattern of the $H$-field over a real ground. However, the vertically polarized wave near a perfectly conducting ground attenuates with increasing distance at the free space rate, unlike a vertically polarized wave over a real ground which attenuates more rapidly with distance at 10 MHz – see NOTE ~~22~~ 11 and Figure 99 and Figure 100. Vertical radiation patterns calculated over a perfectly conducting ground can therefore be very misleading as guidance to the patterns to be expected over real ground at distances much beyond 30 m at 10 MHz.

IECNORM.COM : Click to view the full PDF of CISPR TR 16-3:2020 RLV

**Table 21** *(2 of 2)*

NOTE 9 The measurement of the horizontally oriented $H$-field components near the real ground at 30 m distance from the small horizontal loop can underestimate the maximum horizontally and vertically oriented $H$-field strengths at elevated angles by more than 6 dB. Note, however, that a measurement of the vertically oriented $H$-field, Hz, at a height of 6 m underestimates the maximum $H$-field, the vertically oriented $H$-field, at elevated angles by approximately 5 dB at 10 MHz. See Figure 101.

NOTE 10 The relative magnitudes of the $H$-field components near the ground and at elevated angles are strongly dependent on the actual distance from the horizontal loop source at 10 MHz. The horizontally oriented $H$-field near the ground is a radially directed component which attenuates more rapidly with increasing distance than does the horizontally oriented $H$-field at elevated angles. The vertically oriented $H$-field near the ground is a component of the horizontally polarized ground wave launched by the horizontal loop and attenuates very rapidly with increasing distance from the source. See Figure 101.

NOTE 11 The shape of the vertical radiation pattern of the horizontally oriented $H$-field calculated at a distance of 30 m from the small horizontal loop over perfectly conducting ground is very similar to that calculated over a real ground at 10 MHz. The absolute value of the field strength calculated over perfectly conducting ground is about 5 dB less than the field strength calculated over real ground. Both calculated vertical radiation patterns at 30 m distance indicate that ground-based measurement of horizontally oriented $H$-field underestimates the maximum field strength at elevated angles by more than 6 dB. The measurable horizontally oriented $H$-field components near the ground in both cases are the remnants of radially directed near-field components, not a part of propagating waves, and they attenuate more rapidly with increasing distance from the source than do the fields at elevated angles. See Figure 101. ~~It must also be recalled that,~~ In general, the boundary condition which requires the vertically oriented $H$-field strength to be zero at the surface of a perfectly conducting ground means that at all frequencies up to 30 MHz the patterns of vertically oriented $H$-field which are non-zero at the real ground do not resemble the corresponding vertically oriented $H$-field patterns which go to zero at the perfectly conducting ground.

**Table 22 – Predictability of radiation in vertical directions at 30 MHz, using ground-based measurements of horizontally oriented $H$-field at distances up to 300 m from the source (figures are located in 4.6.8)** *(1 of 3)*

| Type of source | Predictability based on measurements near real ground at 30 m distance from the source | Predictability based on *in situ* measurements near real ground when the measurement distance from the source is not precisely known | Predictability based on vertical radiation patterns calculated at a known distance from the source, assuming the ground behaves as a perfect conductor |
|---|---|---|---|
| Electrically small vertical electric dipole | Very good (see Figure 103, Figure 104) Note 1 | Impossible (see Figure 103, Figure 104) Note 2 | Impossible (see Figure 103) Note 3 |
| Electrically small horizontal electric dipole | Poor (see Figure 105, Figure 106, Figure 108) Notes 4, 5 | Impossible (see Figure 105, Figure 106, Figure 108) Note 6 | Impossible (see Figure 105, Figure 106) Note 7 |
| Electrically small horizontal magnetic dipole (vertical loop) | Good (see Figure 109, Figure 110) Note 8 | Impossible (see Figure 109, Figure 110) Note 9 | Impossible (see Figure 109) Note 10 |
| Electrically small vertical magnetic dipole (horizontal loop) | Poor (see Figure 111, Figure 112) Note 11 | Impossible (see Figure 111, Figure 112) Note 12 | Good (see Figure 111) Note 13 |

NOTE 1 The measurement of the horizontally oriented $H$-field near the real ground at 30 m distance from the small vertical electric dipole underestimates the maximum field strength at elevated angles by about 3 dB at 30 MHz.

NOTE 2 The horizontally oriented $H$-field near ground is a component of the vertically polarized ground wave emitted from the vertical electric dipole. At 30 MHz the vertically polarized wave attenuates rapidly with increasing distance near ground, such that there is an excess 13 dB attenuation of the ground wave in addition to the 20 dB sky-wave attenuation over the distance from 30 m to 300 m. See Figure 103 and Figure 105.

IECNORM.COM : Click to view the full PDF of CISPR TR 16-3:2020 RLV

**Table 22** *(2 of 3)*

NOTE 3 At a distance of 30 m from the small vertical electric dipole over a perfectly conducting ground, the vertical radiation pattern of the horizontally oriented $H$-field is within about 8 dB of the pattern of the $H$-field over real ground. However, the very high rate of attenuation with a distance of a vertically polarized ground wave over real ground at 30 MHz is apparent even at the short range of 30 m (see Figure 103). Moreover, at 30 MHz there is an excess 13 dB attenuation of the ground wave in addition to the 20 dB sky-wave attenuation over the distance from 30 m to 300 m. Over a perfectly conducting ground the excess ground-wave attenuation does not occur, so that the vertical radiation patterns over perfectly conducting ground cannot give guidance to the patterns over real ground at the distances from the small vertical electric dipole that are considered in this subclause.

NOTE 4 The measurement of horizontally oriented $H$-field emitted by the small horizontal electric dipole near the ground can underestimate the maximum horizontally oriented $H$-field strength in the vertical direction by more than 16 dB at 30 MHz (see Figure 105). Note, however, that a measurement of the vertically oriented $H$-field, Hz, at a height of 6 m improves predictability and underestimates the magnitude of the horizontally oriented $H$-field in the vertical direction by approximately 12 dB. The height scan measurement of Hz underestimates the magnitude of the vertically oriented $H$-field at elevated angles by approximately 7 dB.

NOTE 5 The small influence exerted by a wide range of the electrical constants of the real ground on the shape and magnitude of the small horizontal electric dipole vertical radiation pattern at 30 MHz is shown in Figure 107.

NOTE 6 Excess attenuation of the horizontally oriented $H$-field component of the vertically polarized ground wave emitted by the small horizontal electric dipole at the real ground is almost 12 dB more than the sky-wave attenuation over the distance from 30 m to 300 m from the source. If the true measurement distance is not known, the amount of excess attenuation suffered by the ground wave cannot be known when making predictions of the strength of radiation in vertical directions based on measurements at the ground.

NOTE 7 The horizontally oriented $H$-field near a perfectly conducting ground attenuates by 40 dB as the distance from the small horizontal electric dipole increases from 30 m to 300 m, an excess attenuation of 20 dB more than the sky-wave attenuation, as the far-field radiation pattern becomes established over that distance. On the other hand, the excess attenuation of the $H$-field component of the vertically polarized ground wave is about 12 dB near a real ground over the 30 m to 300 m distance. The vertical radiation patterns over real and perfectly conducting grounds therefore differ significantly at 30 MHz in that range of measuring distances. See Figure 105 and Figure 106.

NOTE 8 Measurement of the horizontally oriented $H$-field near real ground at 30 m distance from the small vertical loop can underestimate the maximum horizontally oriented $H$-field strength emitted in the vertical direction by less than 6 dB. It gives an exact indication of the strength of the vertically oriented $H$-field emitted at elevated angles. See Figure 109.

NOTE 9 The horizontally oriented $H$-field components near real ground attenuate more rapidly with increasing distance from the small vertical loop than do the sky-wave components, at 30 MHz. The excess attenuation is approximately 13 dB over the distance from 30 m to 300 m. See Figure 109.

NOTE 10 At a distance of 30 m from the small vertical loop over a perfectly conducting ground the vertical radiation pattern of the horizontally oriented $H$-field is within about 8 dB of the pattern of the $H$-field over a real ground. However, the vertically polarized wave near a perfectly conducting ground attenuates with distance at the free space rate, unlike the vertically polarized wave over a real ground which attenuates more rapidly with distance at 30 MHz (see Figure 109 and Figure 110). Vertical radiation patterns calculated over a perfectly conducting ground can therefore be very misleading as guidance to the patterns over real ground at a distance of 30 m and beyond.

NOTE 11 Measurement of the horizontally oriented $H$-field components near the real ground at 30 m distance from the small horizontal loop can underestimate the $H$-field strengths emitted at elevated angles by more than 16 dB. Note, however, that a measurement of the vertically oriented $H$-field, in Hz, at a height of 6 m underestimates the maximum $H$-field strengths at elevated angles by less than 6 dB. See Figure 111.

NOTE 12 The relative magnitudes of the $H$-field components near the ground and at elevated angles are strongly dependent on the actual distance from the horizontal loop source. The horizontally oriented $H$-field near the ground is a radially directed component which attenuates more rapidly with increasing distance than does the horizontally oriented $H$-field at elevated angles. The vertically oriented $H$-field near the ground is a component of the horizontally polarized ground wave launched by the horizontal loop and at 30 MHz it attenuates very rapidly with increasing distance from the source. See Figure 111 and Figure 112.

IECNORM.COM : Click to view the full PDF of CISPR TR 16-3:2020 RLV

**Table 22** *(3 of 3)*

| |
|---|
| NOTE 13 The shape and magnitude of the vertical radiation pattern of the horizontally oriented $H$-field calculated at a distance of 30 m from the small horizontal loop over perfectly conducting ground at 30 MHz are very similar to the shape and magnitude of the pattern calculated over real ground. Both the calculated patterns indicate that ground-based measurement of horizontally oriented $H$-field will underestimate the maximum field strength at elevated angles by 16 dB or 17 dB. However, the measurable horizontally oriented $H$-field components near the ground in both cases are the remnants of radially directed near-field components, not a part of propagating waves, and they attenuate more rapidly with increasing distance from the small horizontal loop than do the fields at elevated angles. See Figure 100. In general, the boundary condition which requires the vertically oriented $H$-field strength to be zero at the surface of a perfectly conducting ground means that at all frequencies up to 30 MHz the patterns of vertically oriented $H$-field which are non-zero at the real ground do not resemble the corresponding vertically oriented $H$-field patterns which go to zero at the perfectly conducting ground. |

#### 4.6.6.2 Error ranges

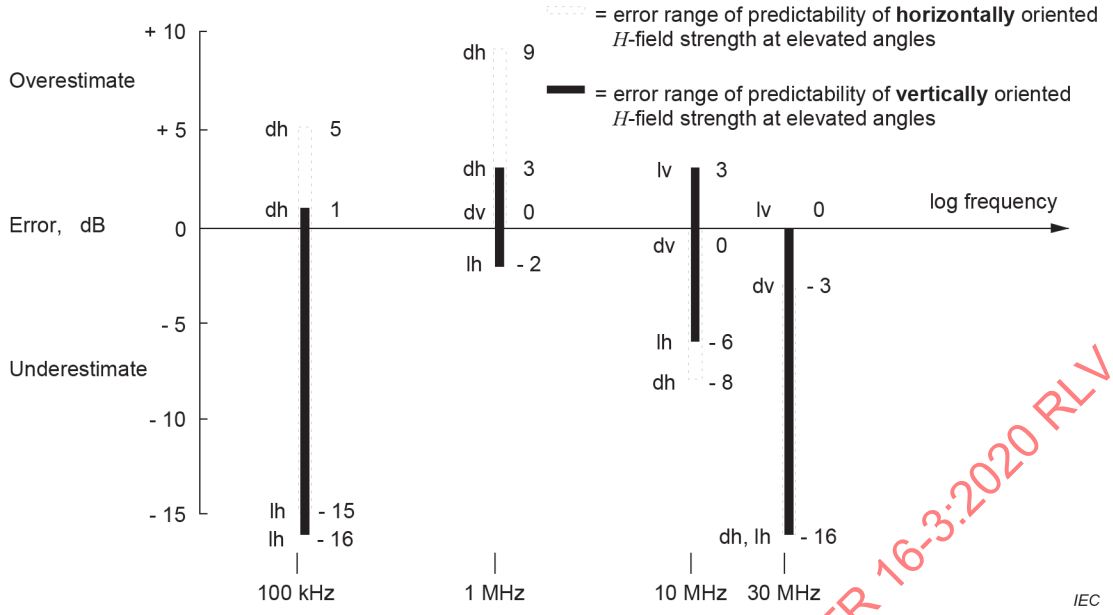
It is possible to present pictorially the ranges of errors of the predictability of radiation in vertical directions at different frequencies, when the precise horizontal measurement distance from the sources is known to be 30 m. Figure 55 and Figure 56 show in bar chart form the error ranges to be expected; Figure 55 is for measurements of the horizontally oriented $H$-field near the ground at 30 m distance from the sources, and Figure 56 is for the measurements of horizontally oriented $H$-field supplemented with measurements of vertically oriented $H$-field in a 6 m height scan near the ground at 30 m distance from the sources.

The error range bar charts summarize the information presented in the various notes to the tables and in the radiation pattern diagrams. The following examples serve to illustrate the ways in which the error range bar charts can be interpreted.

In Figure 55, which is used when predictability of radiation in vertical directions is to be based only on measurements near ground of the horizontally oriented $H$-field components at 30 m horizontal distance from the sources, the charts show that at 100 kHz the largest over-estimation of the strength of radiation in vertical directions occurs in the case of a source behaving as a small horizontal electric dipole, and the error is an overestimate by 5 dB of the maximum strength of the horizontally oriented $H$-field. The largest error in overestimating the maximum vertically oriented $H$-field strength at 100 kHz is an overestimate of only 1 dB, as indicated in the chart by the solid bar, again for the case of a source behaving as a small horizontal electric dipole. At 100 kHz, Figure 55 shows that the largest error in prediction of the strength of radiation in vertical directions occurs in the case of a source behaving as a small vertical magnetic dipole (horizontal loop) and the error is an underestimate by 16 dB of the maximum vertically oriented $H$-field. The largest error at 100 kHz in predicting the maximum horizontally oriented $H$-field strength emitted in vertical directions is an under-estimate by 15 dB, again in the case of a source behaving as a small vertical magnetic dipole (horizontal loop).

In Figure 56, which is used when predictability of radiation in vertical directions is to be based on measurements near ground of the horizontally oriented $H$-field components supplemented with 6 m height-scan measurements of the vertically oriented $H$-field components at 30 m distance, the charts show that at 100 kHz the worst error in the prediction of the strength of radiation in vertical directions still occurs for the vertically oriented $H$-field components emitted from a source behaving as a small vertical magnetic dipole (horizontal loop), but that the magnitude of the error has been reduced to an underestimate by 6 dB (solid bar). The magnitude of the largest underestimate at 100 kHz of the maximum strength of the horizontally oriented $H$-field emitted in vertical directions has been reduced to 3 dB, and this also occurs for the case of a source behaving as a small vertical magnetic dipole (horizontal loop).

IECNORM.COM : Click to view the full PDF of CISPR TR 16-3:2020 RLV




Electrical constants of the ground: $\sigma$ = 1 mS/m, $\varepsilon_r$ = 15.

Source identification:

dh = horizontal electric dipole

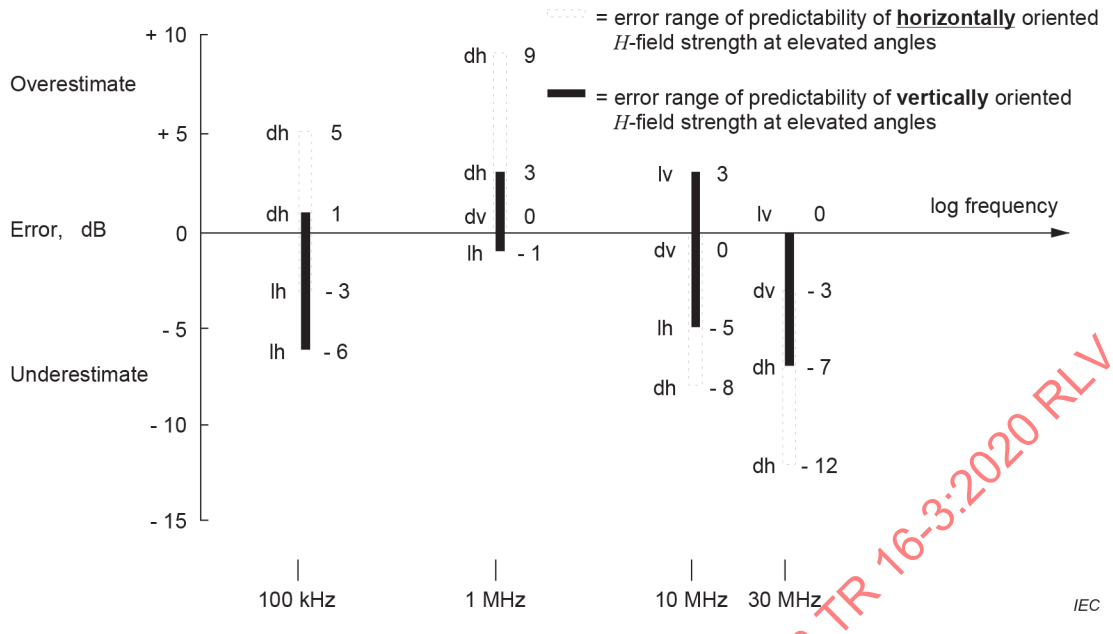
dv = vertical electric dipole

lh = vertical magnetic dipole (horizontal loop)

lv = horizontal magnetic dipole (vertical loop)

**Figure 55 – Ranges of errors in the predictability of radiation in vertical directions from electrically small sources located close to the ground, based on measurements of the horizontally oriented *H*-field near ground at a distance of 30 m from the sources**

IECNORM.COM : Click to view the full PDF of CISPR TR 16-3:2020 RLV




Electrical constants of the ground: $\sigma$ = 1 mS/m, $\varepsilon_r$ = 15.

Source identification:

dh = horizontal electric dipole

dv = vertical electric dipole

lh = vertical magnetic dipole (horizontal loop)

lv = horizontal magnetic dipole (vertical loop)

**Figure 56 – Ranges of errors in the predictability of radiation in vertical directions from electrically small sources located close to the ground, based on measurements of the horizontally oriented *H*-field at the ground supplemented with measurements of the vertically oriented *H*-field in a height scan up to 6 m at a distance of 30 m from the sources**

### 4.6.7 Conclusions

Vertical radiation patterns have been calculated for electrically small sources located close to real homogeneous plane ground, ignoring the possible contributions to pattern distortion that might arise from the presence of nearby buildings or other field disturbing objects, or from discontinuities in the electrical constants of the ground. Nevertheless, even with such a simplification, the studies still show that in the case of solitary electrically small sources located close to a plane homogeneous ground the predictability of radiation in vertical directions can be subject to large errors, when the predictions are to be based on measurements of the strength of the horizontally oriented *H*-field at the ground in the manner presently described in CISPR 11.

In particular, this subclause has identified many examples of the impossibility of making predictions of field strength at elevated angles with a known margin of error, using ground-based measurements, when the measuring distances from the sources are not precisely known. The limits and methods of measurement of radiation *in situ* for which the precise measurement distance from the ISM equipment is not defined in CISPR 11 cannot provide a known level of protection of aeronautical communication services. For example, this limitation applies over the entire frequency range from 100 kHz to 30 MHz if the radiation source behaves like an electrically small vertical magnetic dipole (horizontal loop).

IECNORM.COM : Click to view the full PDF of CISPR TR 16-3:2020 RLV

The large errors in calculation of the vertical radiation patterns that can arise from the approximation, which is sometimes made, that the influence of real ground can be determined by assuming it behaves like a perfect conductor have also been indicated. Apart from the more complex interaction between the source and its image in a real ground, two more obvious reasons for the errors are: that the boundary condition that requires the vertically oriented $H$-field strength and the horizontally oriented $E$-field strength to be zero at the surface of a perfectly conducting ground does not apply at the surface of a real ground, and the vertically polarized ground wave attenuation with distance over real ground is greater than the attenuation with distance over a perfectly conducting ground, especially at the higher frequencies.

Subclause 4.6 has also shown, even when the measurement distance over real ground is precisely known, that predictability of the strength of radiation in vertical directions based on measurements near the ground at a distance of 30 m remains subject to significant errors.

Figure 55 depicts the error ranges that can apply when predictability is based solely on measurement of the horizontally oriented $H$-field near ground at 30 m distance. It can be seen that over the frequency range from 100 kHz to 30 MHz the margin for error can be as much as +9 dB (overestimate) at 1 MHz, or as much as –16 dB (underestimate) at the extremes of the frequency range, i.e. 100 kHz and 30 MHz.

Figure 56 illustrates the reduced error ranges obtained for predictability of radiation in vertical directions when measurements of horizontally oriented $H$-field near the ground are supplemented with measurements of vertically oriented $H$-field at heights up to 6 m above the ground. It can be seen that the potential overestimate of 9 dB at 1 MHz remains a possibility, but the potential underestimate of 16 dB at 100 kHz and 30 MHz has become a possible underestimate of 6 dB at 100 kHz and of 12 dB at 30 MHz.

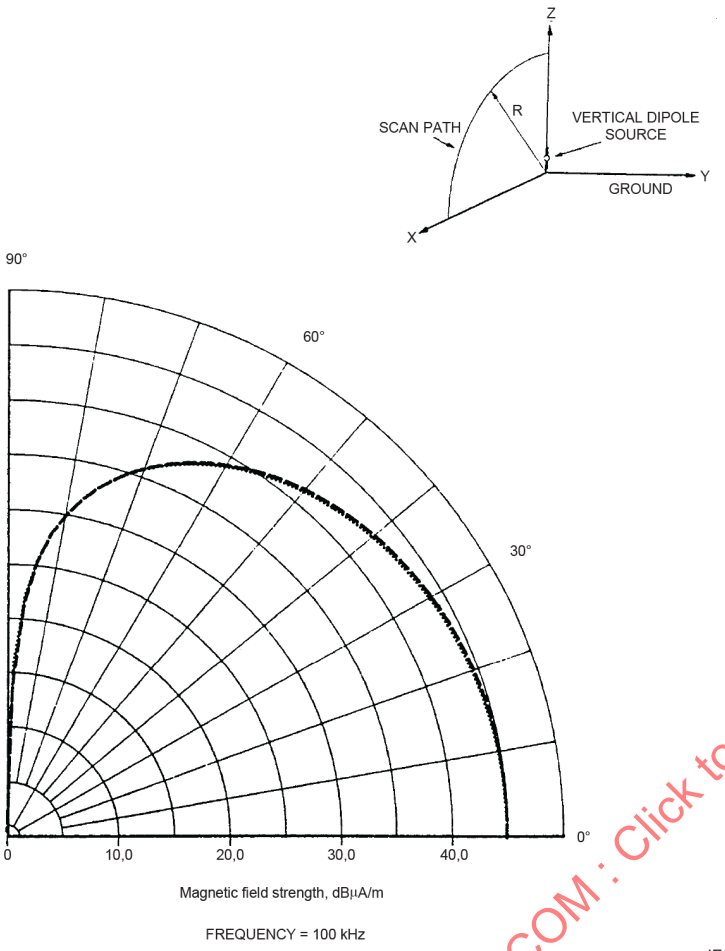
The studies described in 4.6 have identified some of the factors that shall be taken into account when determining limits and methods of measurement of radiated electromagnetic disturbances from ISM apparatus to ensure the protection of aeronautical communication services operating below 30 MHz.

In addition, the comparisons of the vertical radiation patterns over real ground with those over perfectly conducting ground have also shown the large differences that can occur in the assessments of the potential for interference made by measurements on a test site having a conducting metal ground plane compared with assessments using measurements made on a test site having a real ground reference plane.

### 4.6.8 Figures associated with predictability of radiation in vertical directions

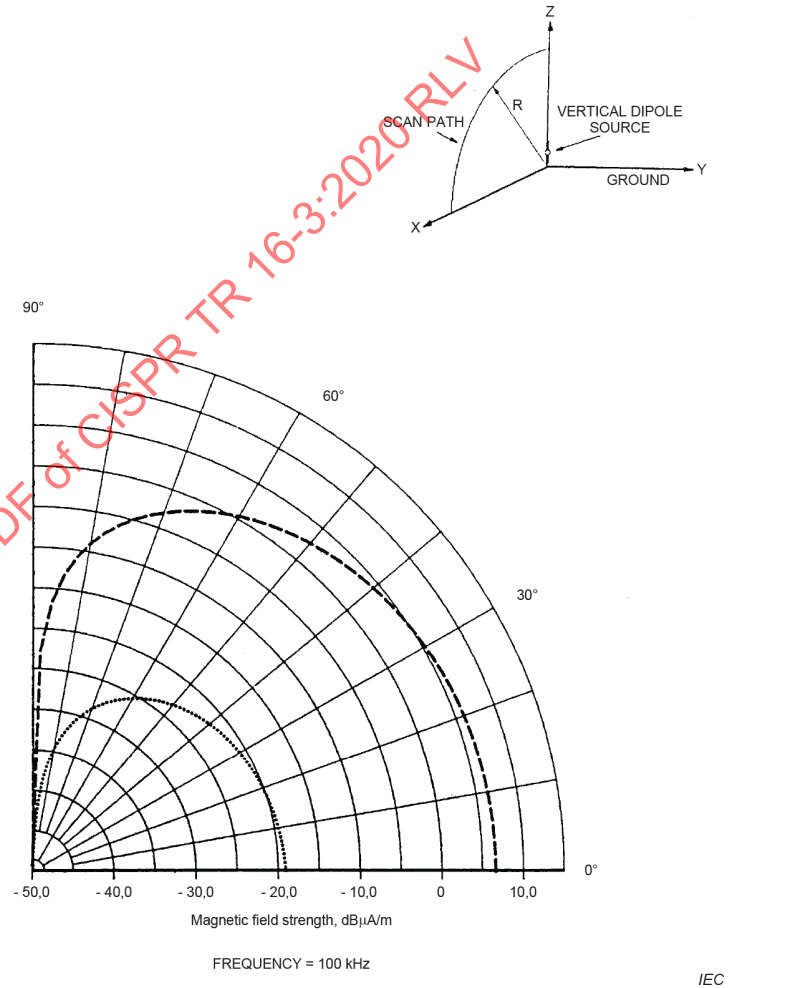
Figures referenced in 4.6.6.1 are provided in this subclause.

IECNORM.COM : Click to view the full PDF of CISPR TR 16-3:2020 RLV




Dipole length 3 m; dipole base at a height above ground of 0,15 m; dipole moment 1 A·m. Dashed line curve – $H_y$ at a scan distance of 30 m. Dotted line curve – $H_y$ at a scan distance of 30 m. Electrical constants of the ground: $\sigma$ = 1 mS/m, $\varepsilon_r$ = 15. Perfectly conducting ground.

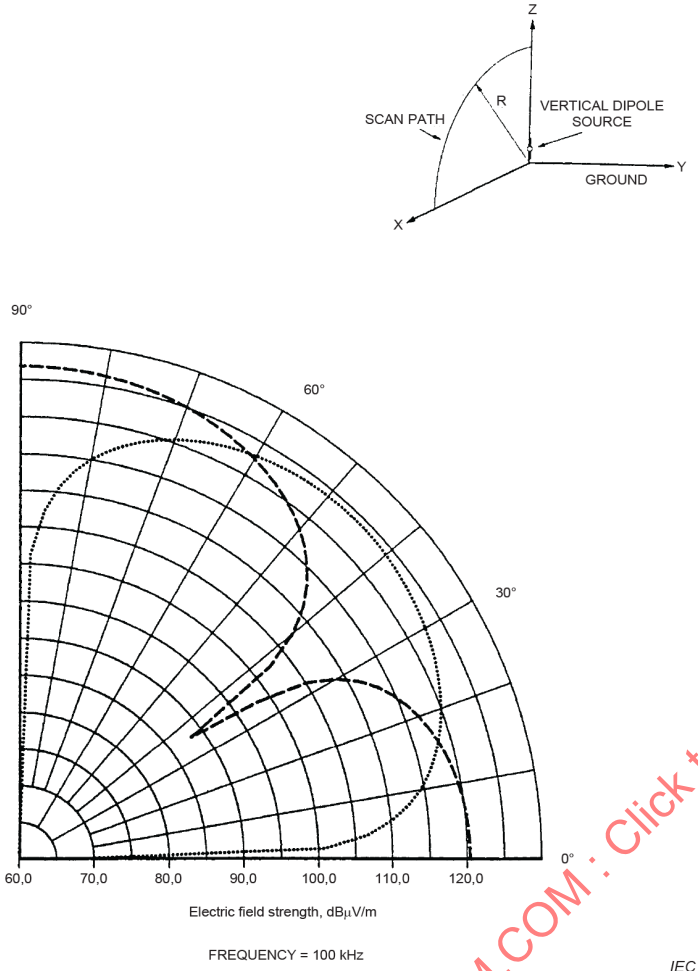
**Figure 57 – Vertical radiation patterns of horizontally oriented *H*-fields emitted by a small vertical electric dipole located close to the ground**




Dipole length 3 m; dipole base at a height above ground of 0,15 m; dipole moment 1 A·m. Dashed line curve – $H_y$ at a scan distance of 300 m. Dotted line curve – $H_y$ at a scan distance of 3 000 m. Electrical constants of the ground: $\sigma$ = 1 mS/m, $\varepsilon_r$ = 15.

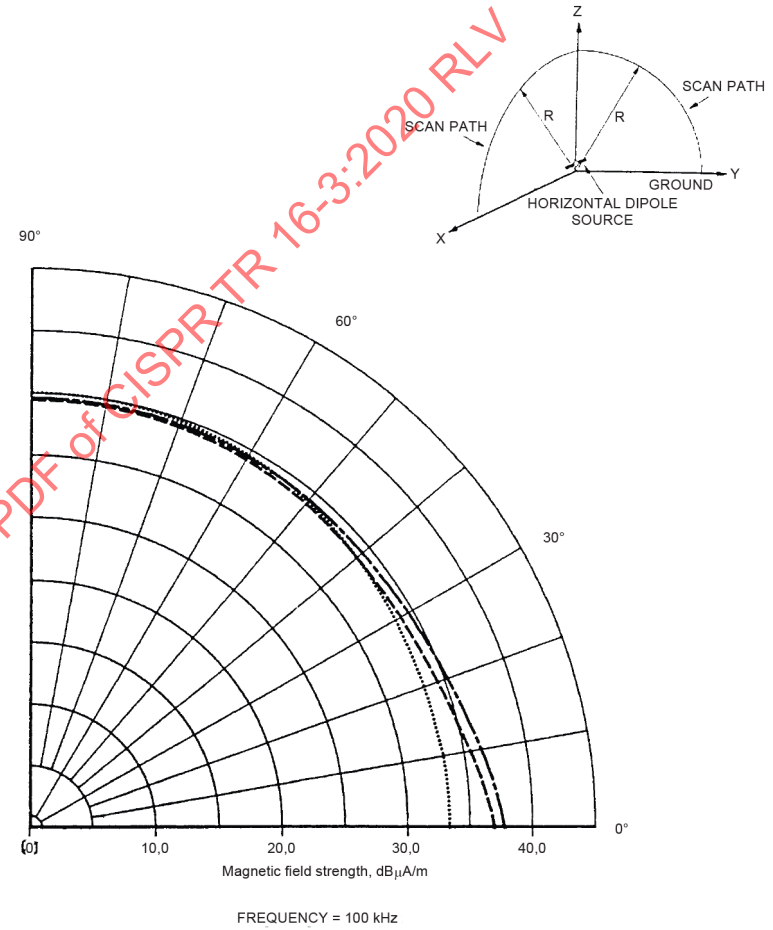
**Figure 58 – Vertical radiation patterns of horizontally oriented *H*-fields emitted by a small vertical electric dipole located close to the ground**

IECNORM.COM : Click to view the full PDF of CISPR TR 16-3:2020 RLV




Dipole length 3 m; dipole base at a height above ground of 0,15 m; dipole moment 1 A·m. Dashed line curve – vertically oriented $E_z$ at a scan distance of 30 m. Dotted line curve – horizontally oriented $E_x$ at a scan distance of 30 m. Electrical constants of the ground: $\sigma$ = 1 mS/m, $\varepsilon_r$ = 15.

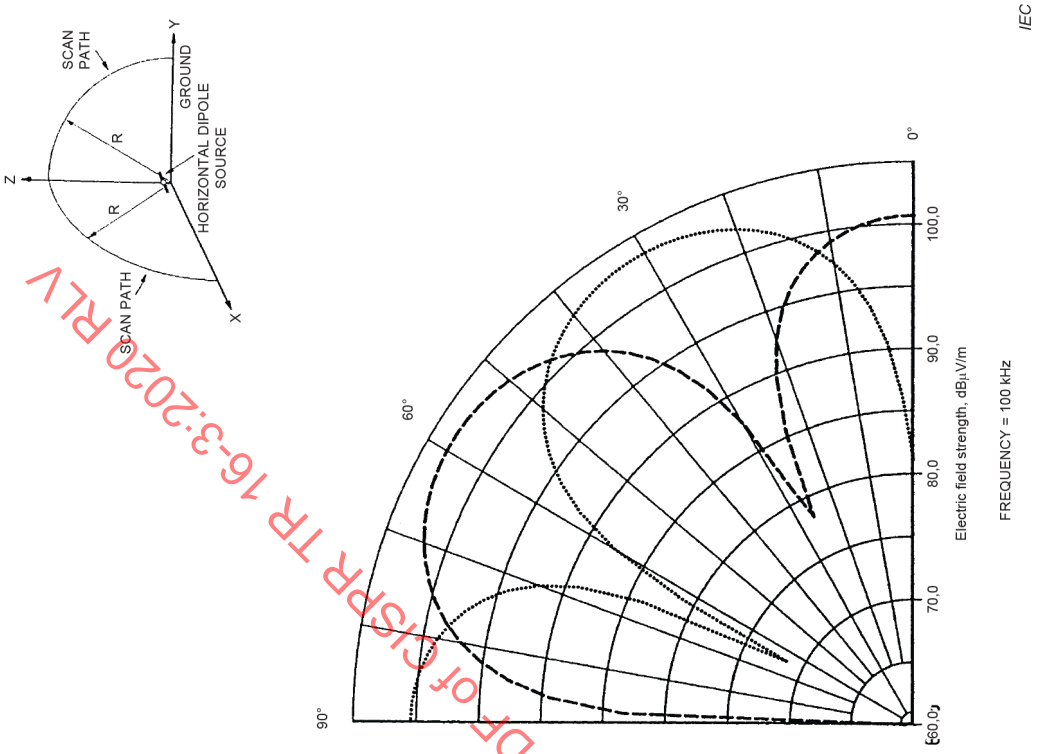
**Figure 59 – Vertical radiation patterns of $E$-fields emitted by a small vertical electric dipole located close to the ground**

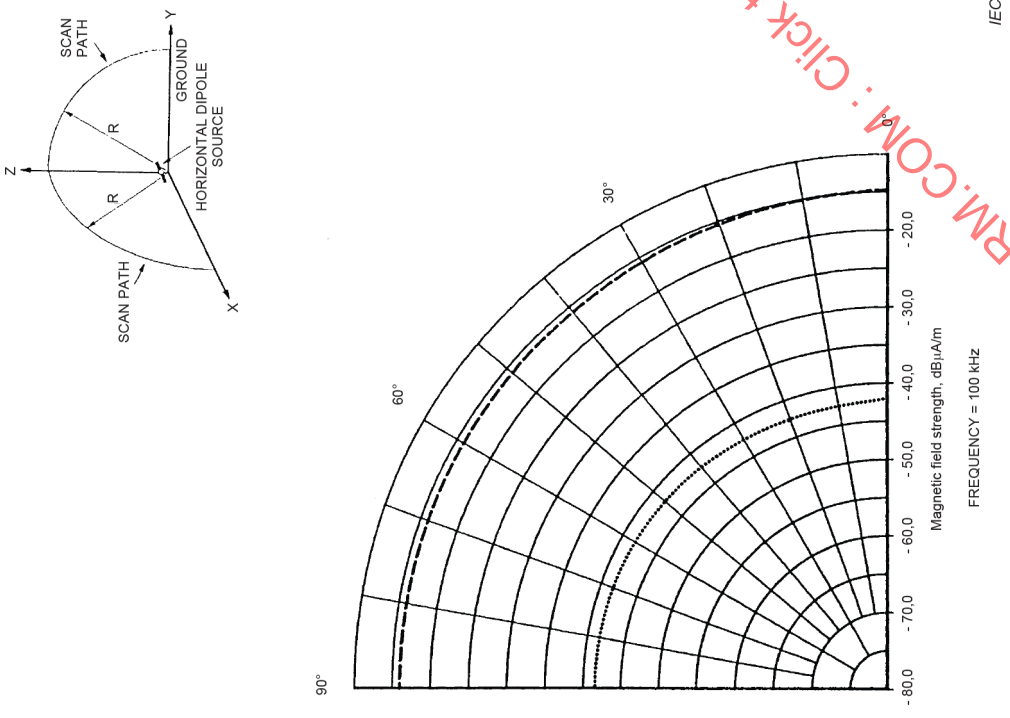



Dipole length 3 m; dipole base at a height above ground of 0,15 m; dipole moment 1 A·m. Dashed line curve – vertically oriented $E_z$ at a scan distance of 3 000 m. Dotted line curve – horizontally oriented $E_x$ at a scan distance of 3 000 m. Dash-dot line curve – total vector/phasor sum of $E_z$ and $E_x$ at a scan distance of 3 000 m, the vertically polarized $E$-field. Electrical constants of the ground: $\sigma$ = 1 mS/m, $\varepsilon_r$ = 15.

**Figure 60 – Vertical radiation patterns of the $E$-fields emitted by a small vertical electric dipole located close to the ground**

IECNORM.COM : Click to view the full PDF of CISPR TR 16-3:2020 RLV




IECNORM.COM : Click to view the full PDF of CISPR TR 16-3:2020 RLV

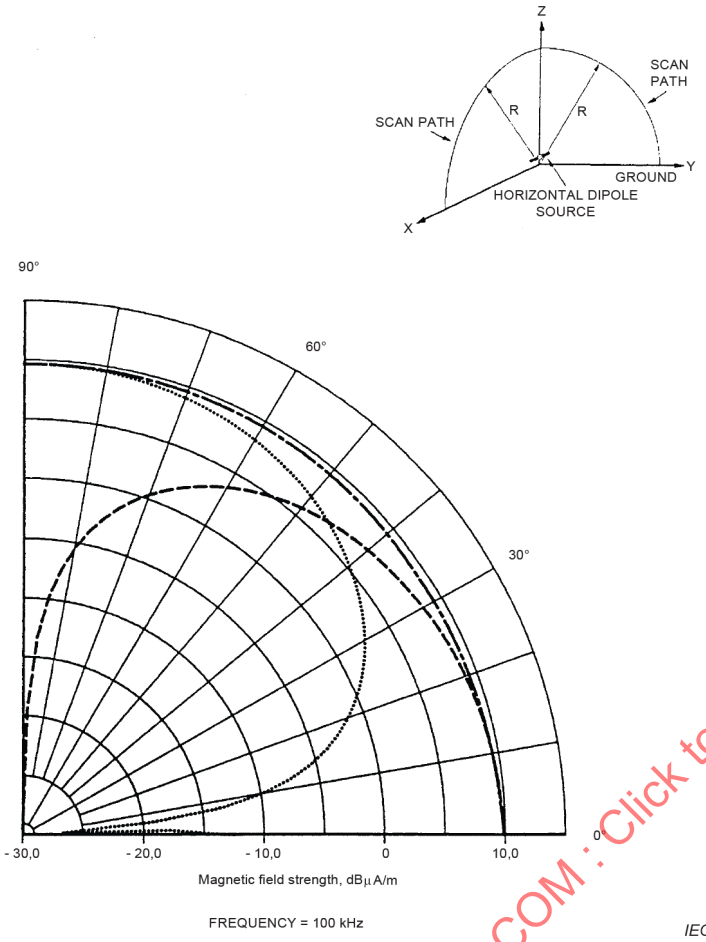
Dipole length 3 m; dipole height above ground of 1 m; dipole moment 1 A·m. Dashed line curve – horizontally oriented $H_y$ at a scan distance of 30 m in the Z-X plane. Dotted line curve – horizontally oriented $H_y$ at a scan distance of 30 m in the Y-Z plane. Solid line curve – vertically oriented $H_z$ at a scan distance of 30 m in the Y-Z plane. Dash-dot line curve – horizontally oriented $H_y$ at a scan distance of 30 m in the Z-X plane. Electrical constants of the ground: $\sigma$ = 1 mS/m, $\varepsilon_r$ = 15. Perfectly conducting ground.

**Figure 61 – Vertical radiation patterns of the *H*-fields emitted by a small horizontal electric dipole located close to the ground**

Dipole length 3 m; dipole height above ground of 1 m; dipole moment 1 A·m. $H_y$ at a scan distance of 30 m in the Z-X plane. Dash-dot line curve – ground constants are $\sigma$ = 0,1 mS/m, $\varepsilon_r$ = 3. Dashed line curve – ground constants are $\sigma$ = 1 mS/m, $\varepsilon_r$ = 15. Dotted line curve – ground constants are $\sigma$ = 10 mS/m, $\varepsilon_r$ = 30. Electrical constants of the ground: $\sigma$ = 1 mS/m, $\varepsilon_r$ = 15. Perfectly conducting ground.

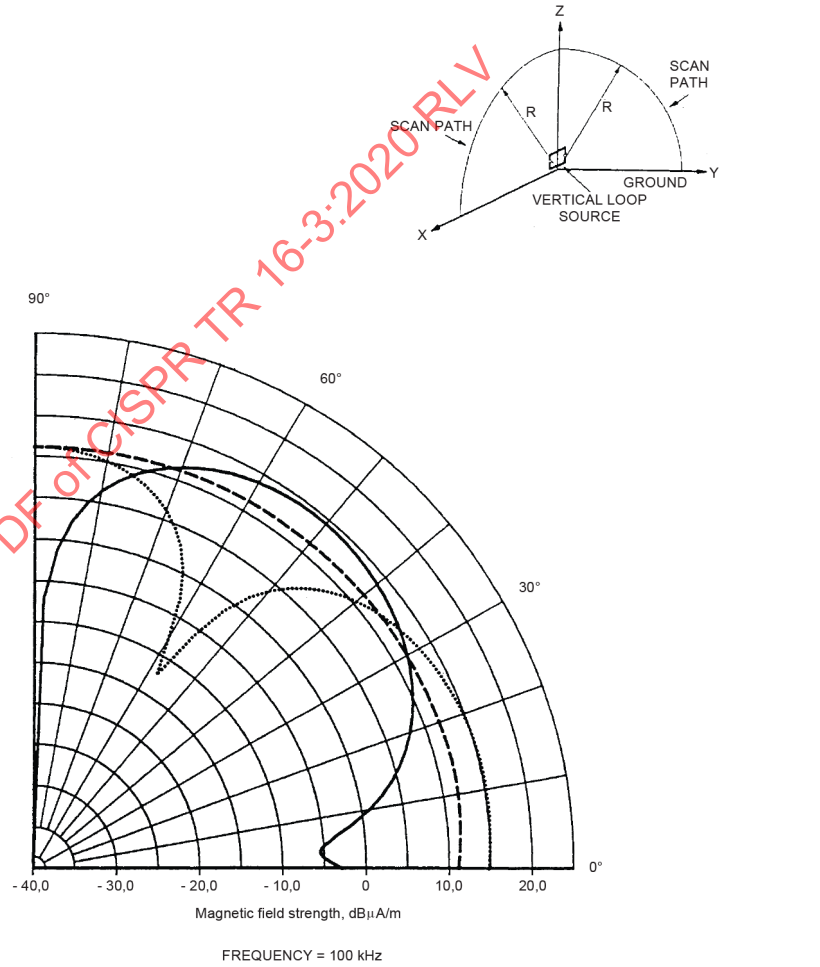
**Figure 62 – Influence of a wide range of values of the electrical constants of the ground on the vertical radiation patterns of the horizontally oriented *H*-fields emitted by a small horizontal electric dipole located close to the ground**

IECNORM.COM : Click to view the full PDF of CISPR TR 16-3:2020 RLV




Dipole length 3 m; dipole height above ground of 1 m; dipole moment 1 A·m. Dashed line curve – $H_y$ at a scan distance of 300 m in the Z-X plane. Dotted line curve – $H_y$ at a scan distance of 3 000 m in the Z-X plane. Electrical constants of the ground $\sigma$ = 1 mS/m, $\varepsilon_r$ = 15.

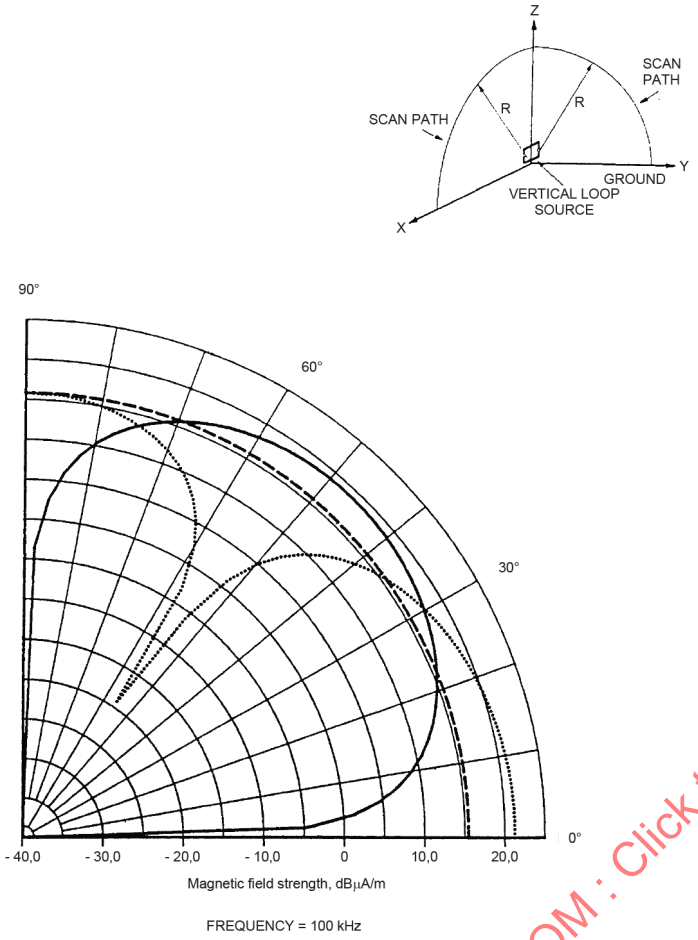
**Figure 63 – Vertical radiation patterns of the horizontally oriented *H*-fields emitted by a small horizontal electric dipole located close to the ground**




Dipole length 3 m; dipole height above ground of 1 m; dipole moment 1 A·m. Dashed line curve – vertically oriented $E_z$ at a scan distance of 30 m in the Z-X plane. Dotted line curve – horizontally oriented $E_x$ at a scan distance of 30 m in the Z-X plane. Electrical constants of the ground $\sigma$ = 1 mS/m, $\varepsilon_r$ = 15.

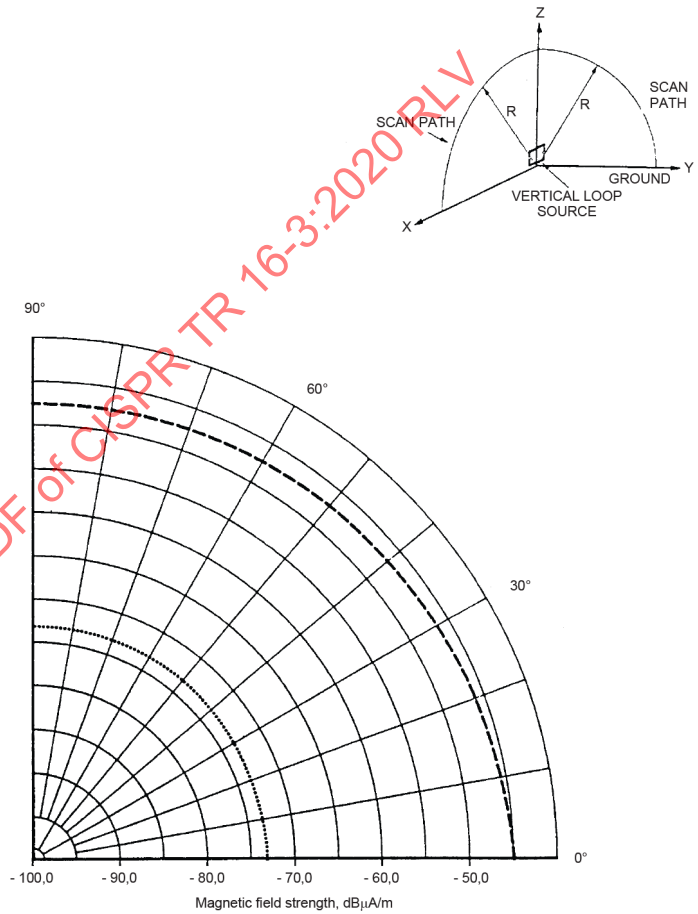
**Figure 64 – Vertical radiation patterns of the *E*-fields emitted by a small horizontal electric dipole located close to the ground**

IECNORM.COM : Click to view the full PDF of CISPR TR 16-3:2020 RLV




Dipole length 3 m; dipole height above ground of 1 m; dipole moment 1 A·m. Dashed line curve – vertically oriented $E_z$ at a scan distance of 3 000 m in the Z-X plane. Dotted line curve – horizontally oriented $E_x$ at a scan distance of 3 000 m in the Z-X plane. Dash-dot line curve – total vector/phasor sum of $E_z$ and $E_x$ at a scan distance of 3 000 m in the Z-X plane, the vertically polarized $E$-field. Electrical constants of the ground $\sigma$ = 1 mS/m, $\varepsilon_r$ = 15.

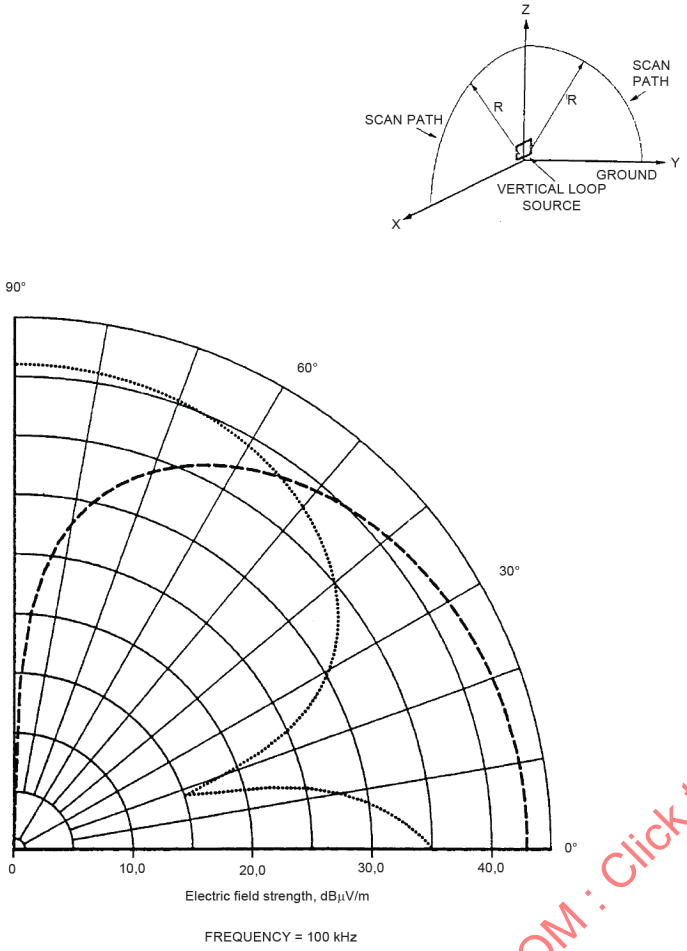
**Figure 65 – Vertical radiation patterns of the $E$-fields emitted by a small horizontal electric dipole located close to the ground**




Square loop 3 m by 3 m. Loop base height above the ground 1 m. Dipole moment 1 A·m$^2$. Dashed line curve – horizontally oriented $H_y$ at a scan distance of 30 m in the Z-X plane. Dotted line curve – horizontally oriented $H_y$ at a scan distance of 30 m in the Y-Z plane. Solid line curve – vertically oriented $H_z$ at a scan distance of 30 m in the Y-Z plane. Electrical constants of the ground $\sigma$ = 1 mS/m, $\varepsilon_r$ = 15.

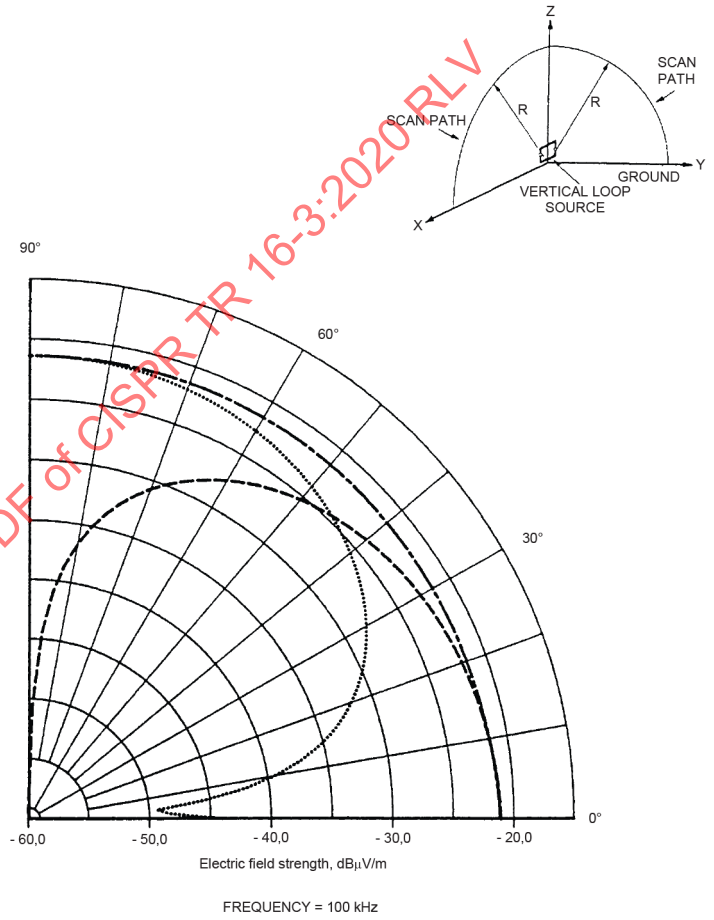
**Figure 66 – Vertical radiation patterns of $H$-fields emitted by small horizontal magnetic dipole (vertical loop) located close to ground**

IECNORM.COM : Click to view the full PDF of CISPR TR 16-3:2020 RLV




Square loop 3 m by 3 m. Loop base height above the ground 1 m. Dipole moment 1 A·m$^2$. Dashed line curve – horizontally oriented $H_y$ at a scan distance of 30 m in the Z-X plane. Dotted line curve – horizontally oriented $H_y$ at a scan distance of 30 m in the Y-Z plane. Solid line curve – vertically oriented $H_z$ at a scan distance of 30 m in the Y-Z plane. Perfectly conducting ground.

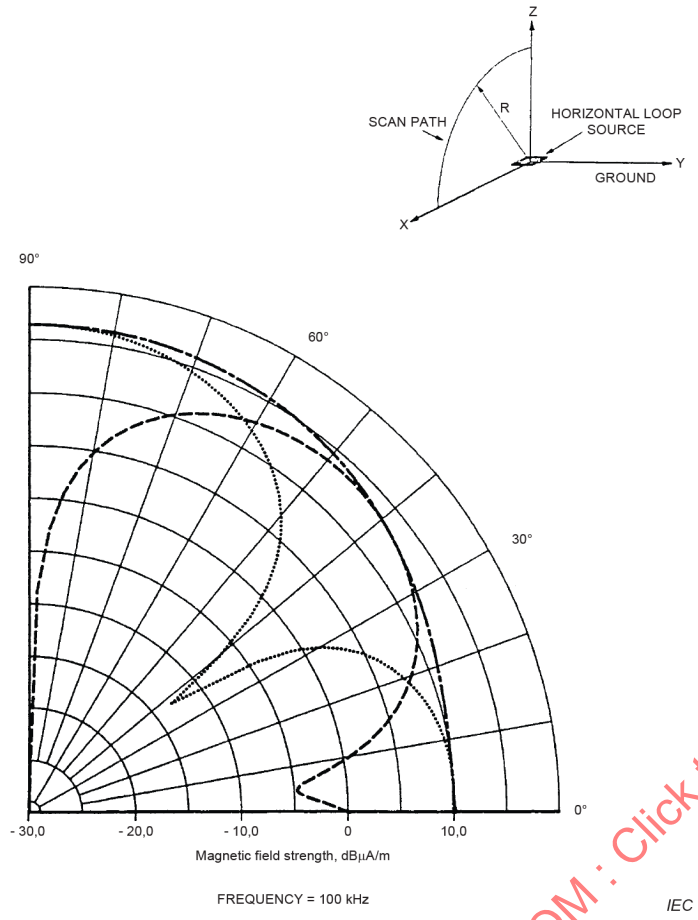
**Figure 67 – Vertical radiation patterns of the horizontally oriented *H*-fields emitted by a small horizontal magnetic dipole (vertical loop) located close to the ground**




Square loop 3 m by 3 m. Loop base height above the ground 1 m. Dipole moment 1 A·m$^2$. Dashed line curve – $H_y$ at a scan distance of 300 m in the Z-X plane. Dotted line curve – $H_y$ at a scan distance of 3 000 m in the Z-X plane. Electrical constants of the ground $\sigma$ = 1 mS/m, $\varepsilon_r$ = 15.

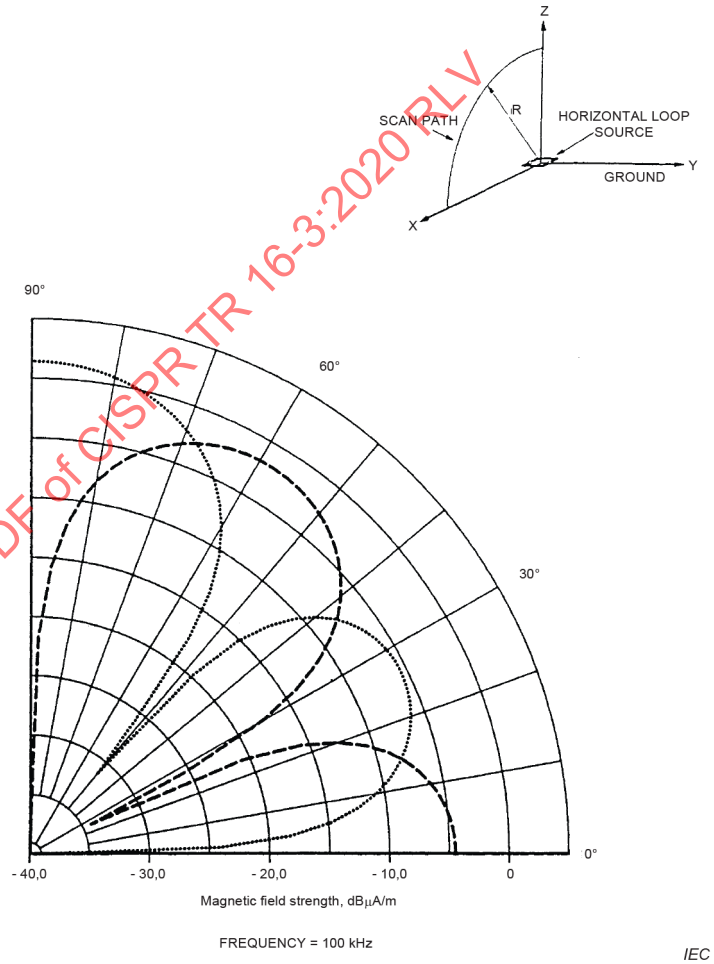
**Figure 68 – Vertical radiation patterns of the horizontally oriented *H*-fields emitted by a small horizontal magnetic dipole (vertical loop) located close to the ground**

IECNORM.COM : Click to view the full PDF of CISPR TR 16-3:2020 RLV




Square loop 3 m by 3 m. Loop base height above the ground 1 m. Dipole moment 1 A·m$^2$. Dashed line curve – vertically oriented $E_z$ at a scan distance of 30 m in the Z-X plane. Dotted line curve – horizontally oriented $E_x$ at a scan distance of 30 m in the Z-X plane. Electrical constants of the ground $\sigma$ = 1 mS/m, $\varepsilon_r$ = 15.

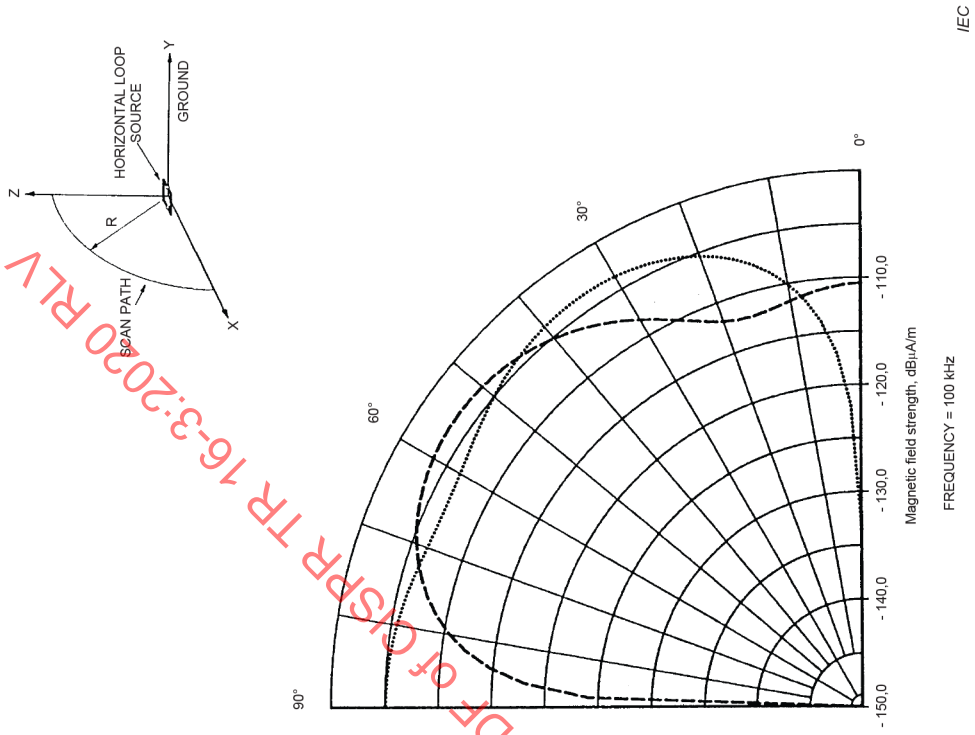
**Figure 69 – Vertical radiation patterns of the $E$-fields emitted by a small horizontal magnetic dipole (vertical loop) located close to the ground**

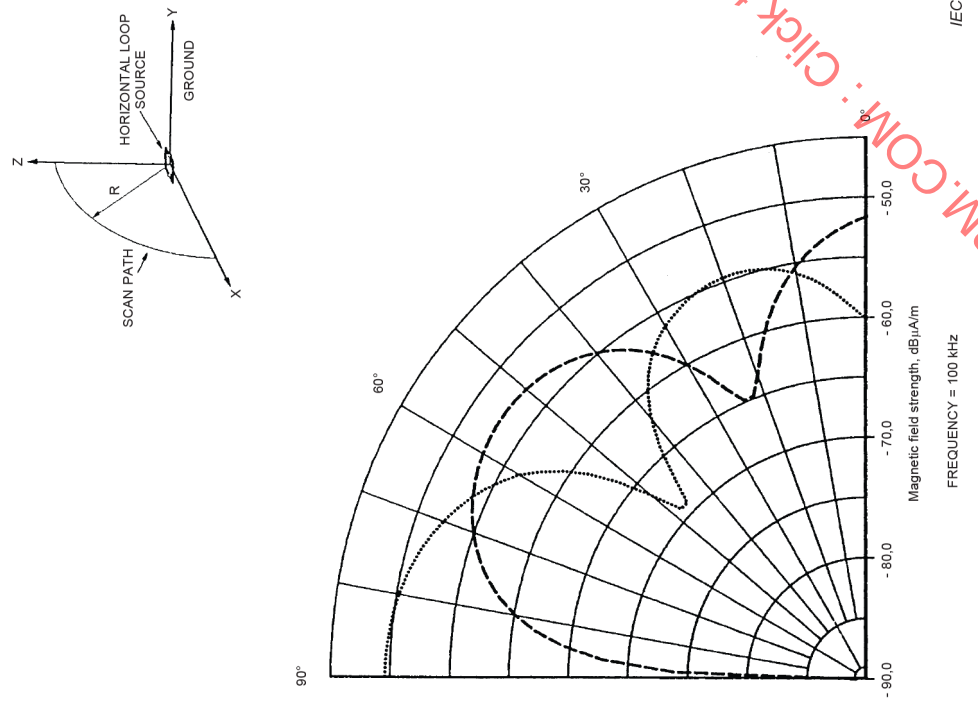



Square loop 3 m by 3 m. Loop base height above the ground 1 m. Dipole moment 1 A·m$^2$. Dashed line curve – vertically oriented $E_z$ at a scan distance of 3 000 m in the Z-X plane. Dotted line curve – horizontally oriented $E_x$ at a scan distance of 3 000 m in the Z-X plane. Dash-dot line curve – total vector/phasor sum of $E_z$ and $E_x$ at a scan distance of 3 000 m in the Z-X plane, the vertically polarized $E$-field. Electrical constants of the ground $\sigma$ = 1 mS/m, $\varepsilon_r$ = 15.

**Figure 70 – Vertical radiation patterns of the $E$-fields emitted by a small horizontal magnetic dipole (vertical loop) located close to the ground**

IECNORM.COM : Click to view the full PDF of CISPR TR 16-3:2020 RLV




IECNORM.COM : Click to view the full PDF of CISPR TR 16-3:2020 RLV

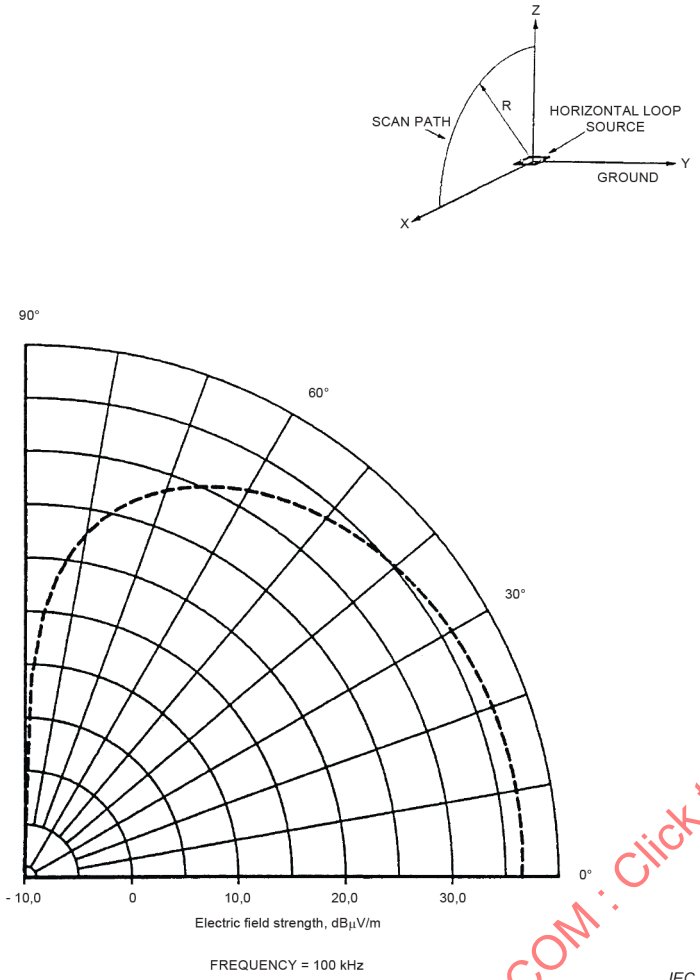
Square loop 3 m by 3 m. Loop base height above the ground 1 m. Dipole moment 1 A·m$^2$. Dashed line curve – horizontally oriented $H_x$ at a scan distance of 30 m. Dotted line curve – horizontally oriented $H_z$ at a scan distance of 30 m. Dash-dot line curve – total vector/phasor sum of $H_x$ and $H_z$ at a scan distance of 30 m, the total $H$-field component of the horizontally polarized radiation. Electrical constants of the ground $\sigma$ = 1 mS/m, $\varepsilon_r$ = 15.

**Figure 71 – Vertical radiation patterns of the $H$-fields emitted by a small vertical magnetic dipole (horizontal loop) located close to the ground**

Square loop 3 m by 3 m. Loop base height above the ground 1 m. Dipole moment 1 A·m$^2$. Dashed line curve – horizontally oriented $H_x$ at a scan distance of 30 m. Dotted line curve – vertically oriented $H_z$ at a scan distance of 30 m. Perfectly conducting ground.

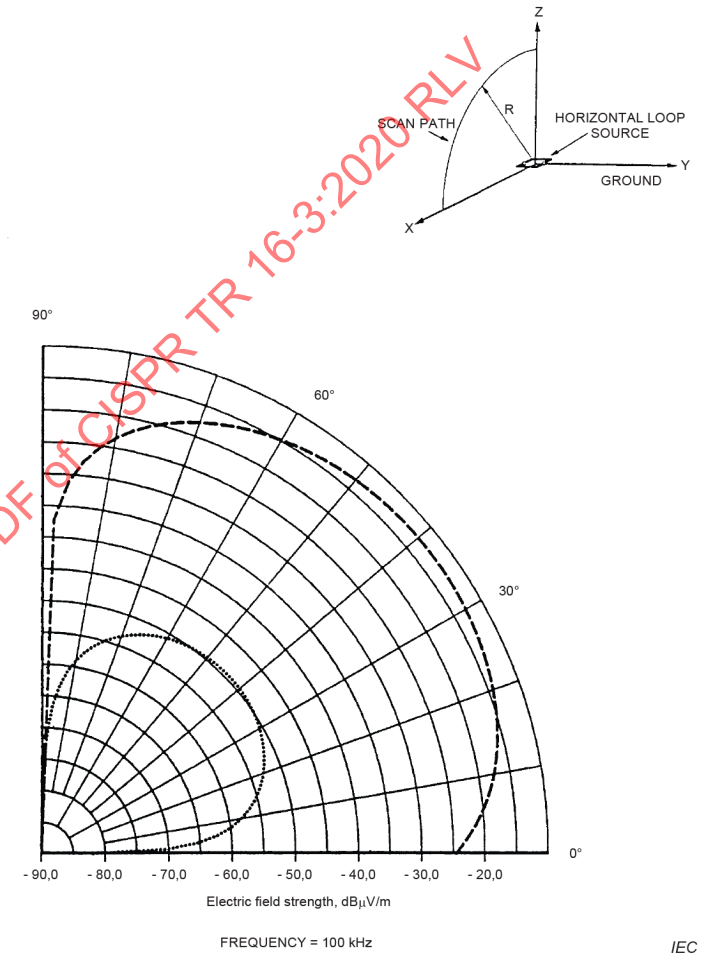
**Figure 72 – Vertical radiation patterns of the $H$-fields emitted by a small vertical magnetic dipole (horizontal loop) located close to the ground**

IECNORM.COM : Click to view the full PDF of CISPR TR 16-3:2020 RLV




Square loop 3 m by 3 m. Loop base height above the ground 1 m. Dipole moment 1 A·m$^2$. Dashed line curve – horizontally oriented $H_x$ at a scan distance of 300 m. Dotted line curve – vertically oriented $H_z$ at a scan distance of 300 m. Electrical constants of the ground $\sigma$ = 1 mS/m, $\varepsilon_r$ = 15.

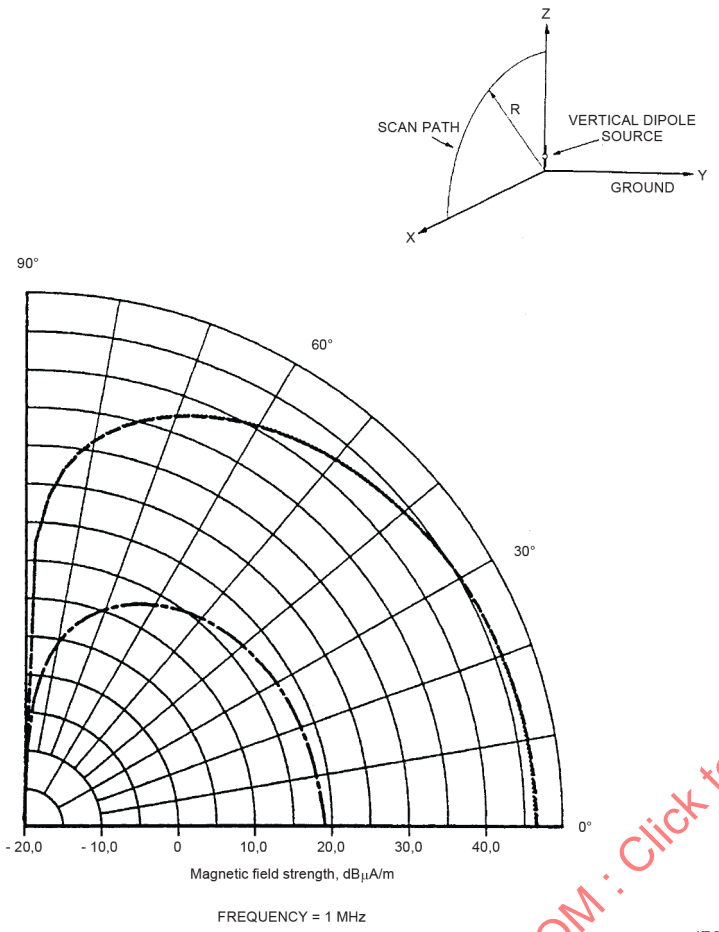
**Figure 73 – Vertical radiation patterns of the *H*-fields emitted by a small vertical magnetic dipole (horizontal loop) located close to the ground**




Square loop 3 m by 3 m. Loop base height above the ground 1 m. Dipole moment 1 A·m$^2$. Dashed line curve – horizontally oriented $H_x$ at a scan distance of 3 000 m. Dotted line curve – vertically oriented $H_z$ at a scan distance of 3 000 m. Electrical constants of the ground $\sigma$ = 1 mS/m, $\varepsilon_r$ = 15.

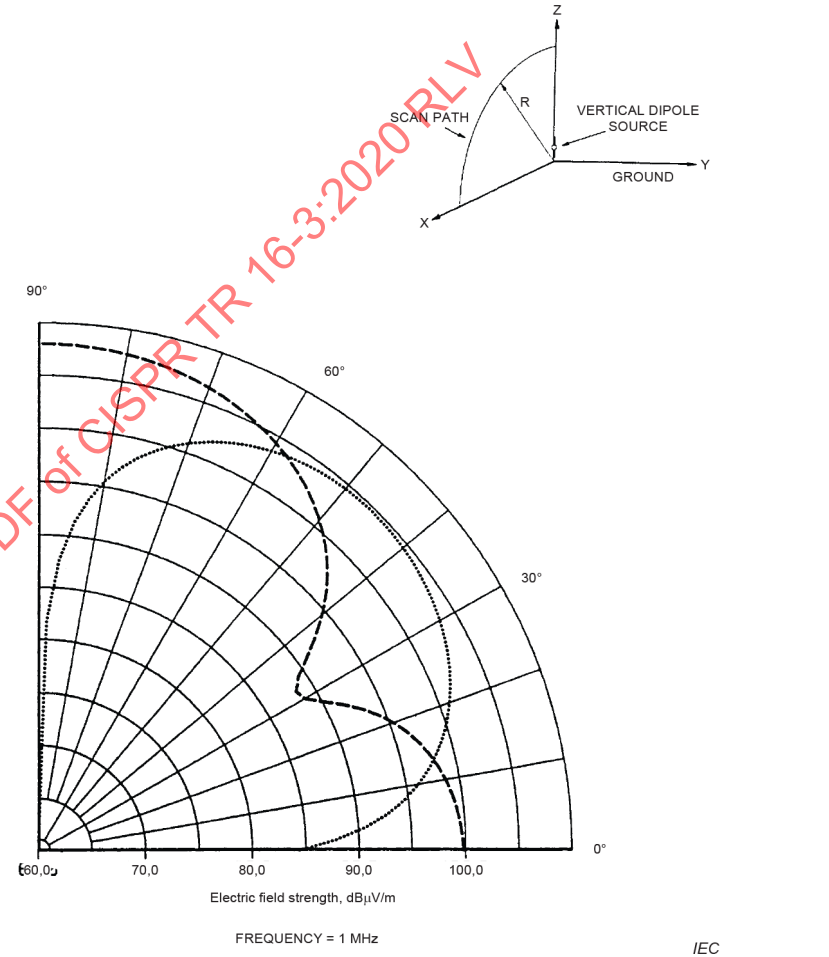
**Figure 74 – Vertical radiation patterns of the *H*-fields emitted by a small vertical magnetic dipole (horizontal loop) located close to the ground**

IECNORM.COM : Click to view the full PDF of CISPR TR 16-3:2020 RLV




Square loop 3 m by 3 m. Loop base height above the ground 1 m. Dipole moment 1 A·m$^2$. Dashed line curve – horizontally oriented $E_y$ at a scan distance of 30 m. Electrical constants of the ground $\sigma$ = 1 mS/m, $\varepsilon_r$ = 15.

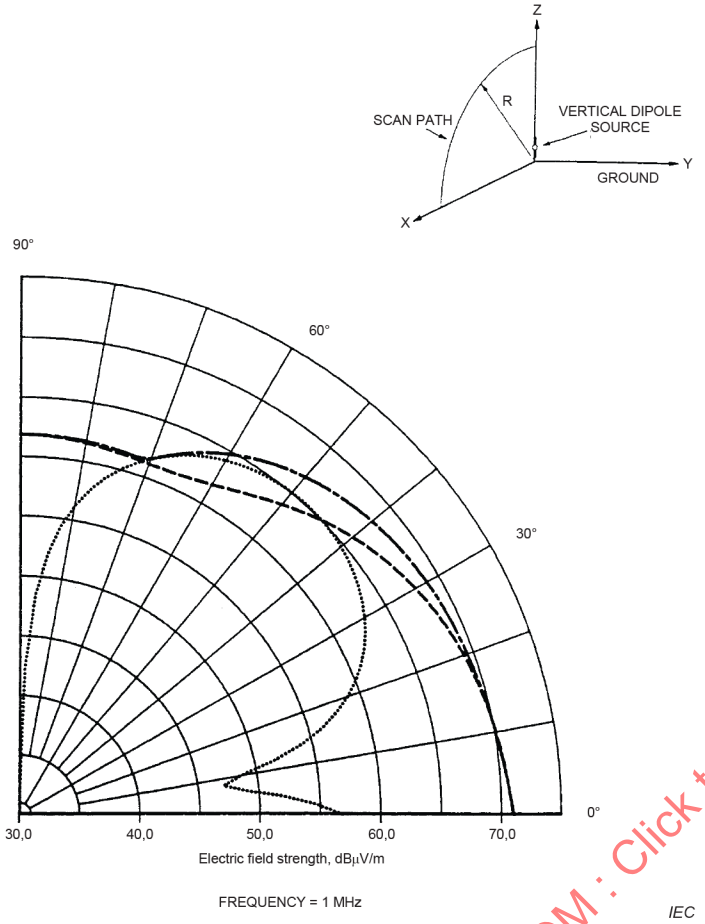
**Figure 75 – Vertical radiation pattern of the *E*-field emitted by a small vertical magnetic dipole (horizontal loop) located close to the ground**




Square loop 3 m by 3 m. Loop base height above the ground 1 m. Dipole moment 1 A·m$^2$. Dashed line curve – horizontally oriented $E_y$ at a scan distance of 300 m. Dotted line curve – horizontally oriented $E_y$ at a scan distance of 3 000 m. Electrical constants of the ground $\sigma$ = 1 mS/m, $\varepsilon_r$ = 15.

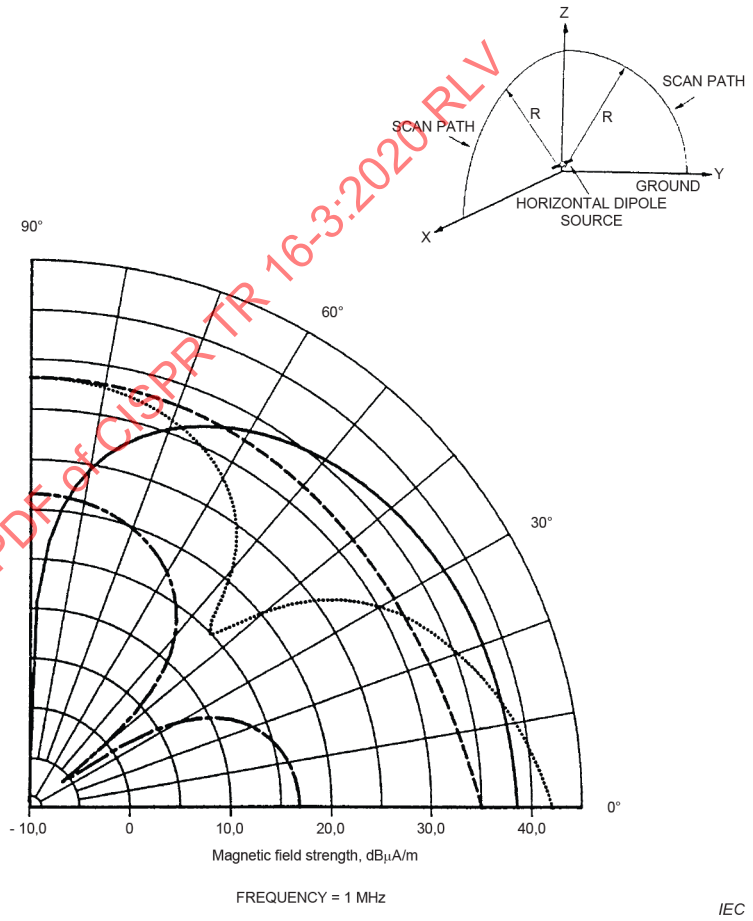
**Figure 76 – Vertical radiation patterns of the *E*-fields emitted by a small vertical magnetic dipole (horizontal loop) located close to the ground**

IECNORM.COM : Click to view the full PDF of CISPR TR 16-3:2020 RLV




Dipole length 3 m. Dipole base at a height above ground of 0,15 m. Dipole moment 1 A·m. Dashed line curve – $H_y$ at a scan distance of 30 m. Dotted line curve – $H_y$ at a scan distance of 30 m. Dash-dot line curve – $H_y$ at a scan distance of 300 m. Electrical constants of the ground $\sigma$ = 1 mS/m, $\varepsilon_r$ = 15. Perfectly conducting ground.

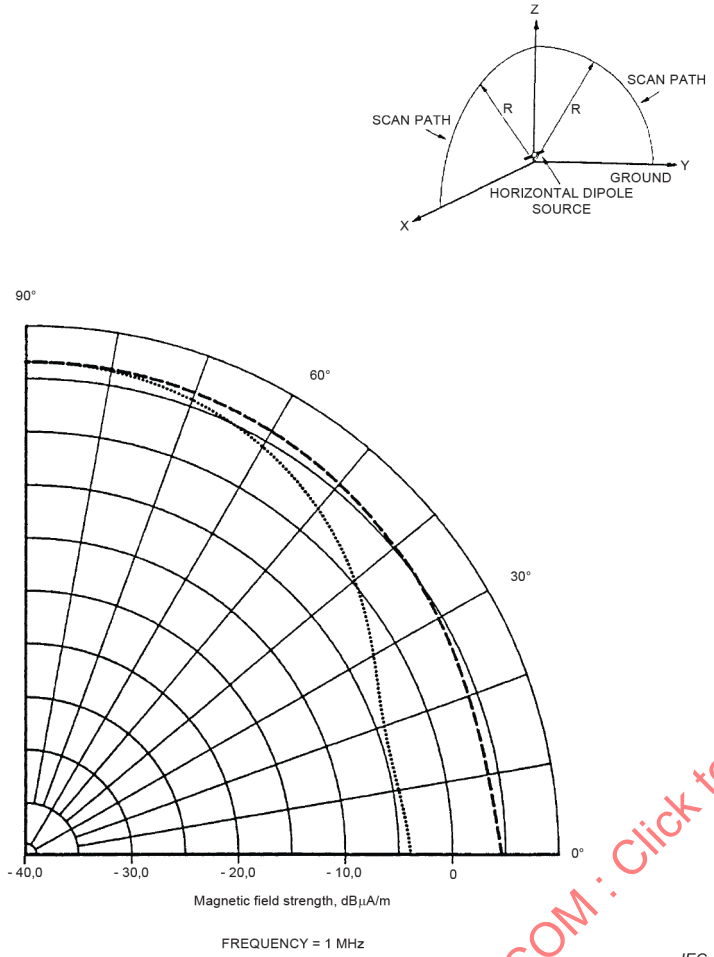
**Figure 77 – Vertical radiation patterns of the horizontally oriented *H*-fields emitted by a small vertical electric dipole located close to the ground**




Dipole length 3 m. Dipole base at a height above ground of 0,15 m. Dipole moment 1 A·m. Dashed line curve – vertically oriented $E_z$ at a scan distance of 30 m. Dotted line curve – horizontally oriented $E_x$ at a scan distance of 30 m. Electrical constants of the ground $\sigma$ = 1 mS/m, $\varepsilon_r$ = 15.

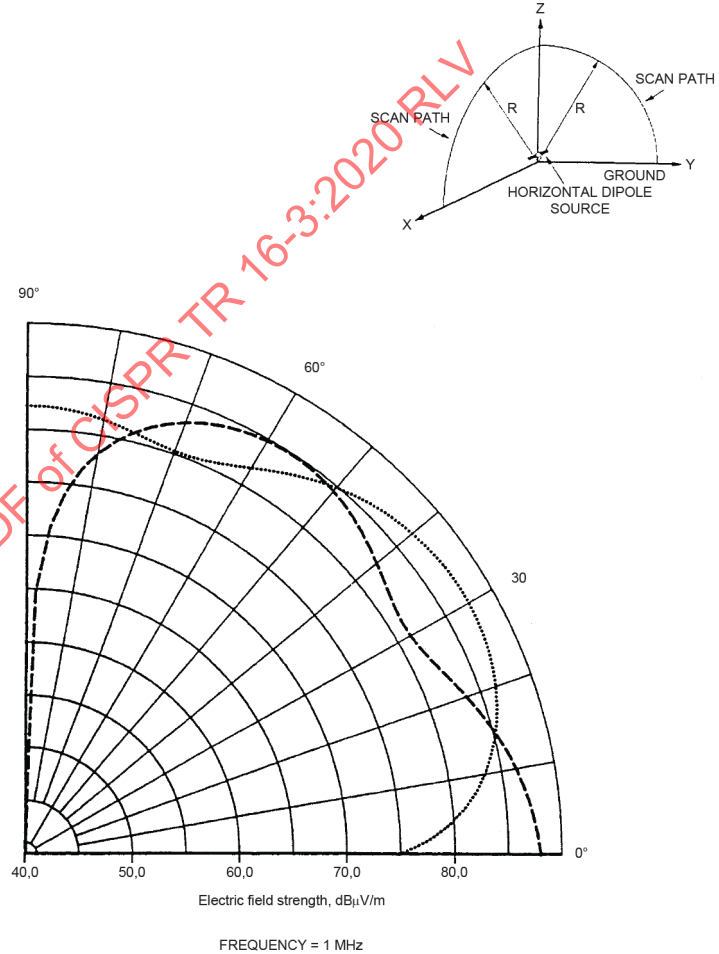
**Figure 78 – Vertical radiation patterns of the *E*-fields emitted by a small vertical electric dipole located close to the ground**

IECNORM.COM : Click to view the full PDF of CISPR TR 16-3:2020 RLV




Dipole length 3 m. Dipole base at a height above ground of 0,15 m. Dipole moment 1 A·m. Dashed line curve – vertically oriented $E_z$ at a scan distance of 300 m. Dotted line curve– horizontally oriented $E_x$ at a scan distance of 300 m. Dash-dot line curve – total vector/phasor sum of $E_z$ and $E_x$ at a scan distance of 300 m, the vertically polarized $E$-field. Electrical constants of the ground $\sigma$ = 1 mS/m, $\varepsilon_r$ = 15.

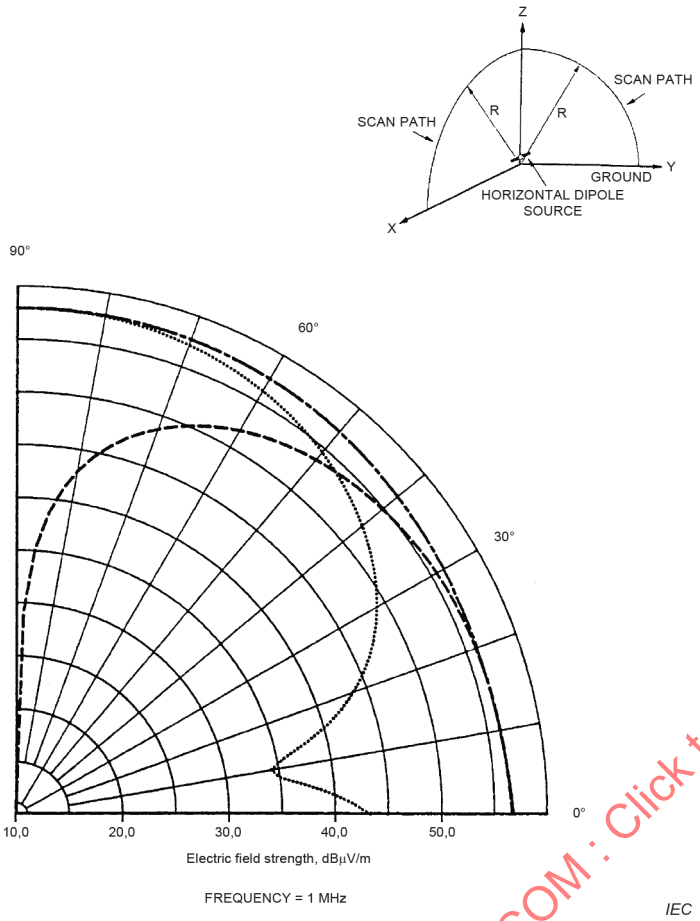
**Figure 79 – Vertical radiation patterns of the *E*-fields emitted by a small vertical electric dipole located close to the ground**




Dipole length 3 m. Dipole height above ground 1 m. Dipole moment 1 A·m. Dashed line curve – horizontally oriented $H_y$ at a scan distance of 30 m in the Z-X plane. Dotted line curve – horizontally oriented $H_y$ at a scan distance of 30 m in the Y-Z plane. Dash-dot line curve – horizontally oriented $H_y$ at a scan distance of 30 m in the Z-X plane. Solid line curve – vertically oriented $H_z$ at a scan distance of 30 m in the Y-Z plane. Electrical constants of the ground $\sigma$ = 1 mS/m, $\varepsilon_r$ = 15. Perfectly conducting ground.

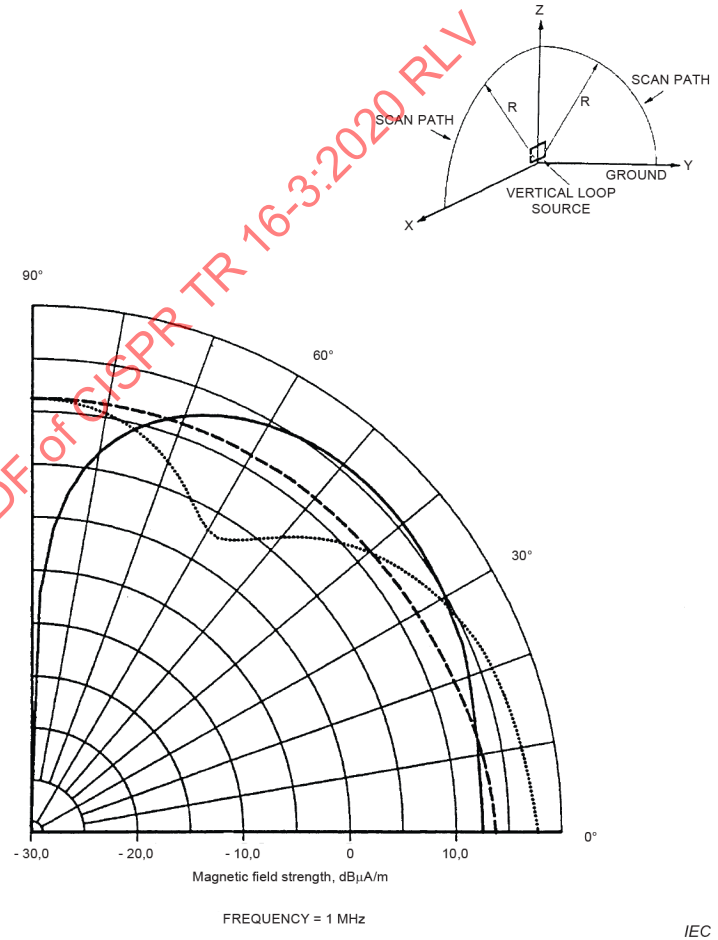
**Figure 80 – Vertical radiation patterns of the *H*-fields emitted by a small horizontal electric dipole located close to the ground**

IECNORM.COM : Click to view the full PDF of CISPR TR 16-3:2020 RLV




Dipole length 3 m. Dipole height above ground 1 m. Dipole moment 1 A·m. Dashed line curve – $H_y$ at a scan distance of 300 m in the Z-X plane. Dotted line curve – $H_y$ at a scan distance of 300 m in the Y-Z plane. Electrical constants of the ground $\sigma$ = 1 mS/m, $\varepsilon_r$ = 15.

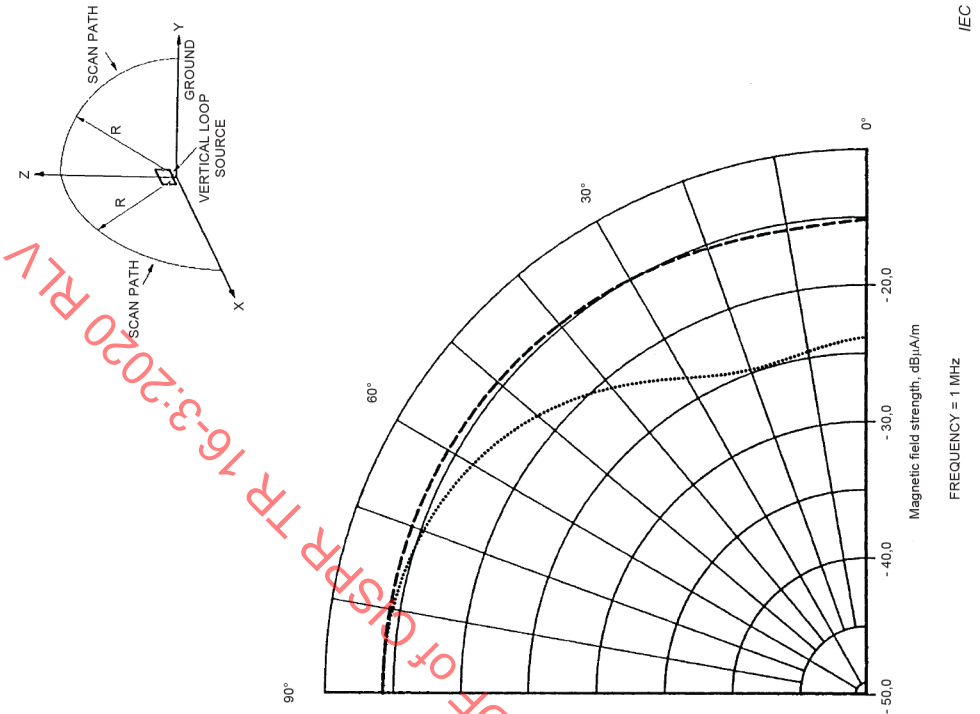
**Figure 81 – Vertical radiation patterns of the horizontally oriented *H*-fields emitted by a small horizontal electric dipole located close to the ground**

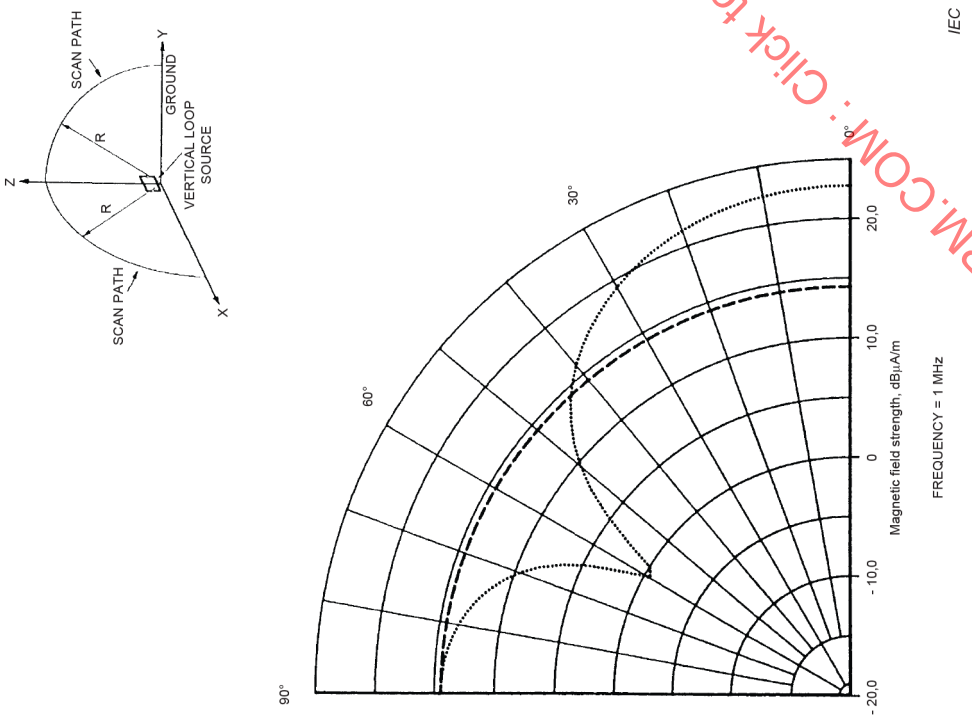



Dipole length 3 m. Dipole height above ground 1 m. Dipole moment 1 A·m. Dashed line curve – vertically oriented $E_z$ at a scan distance of 30 m in the Z-X plane. Dotted line curve – horizontally oriented $E_x$ at a scan distance of 30 m in the Z-X plane. Electrical constants of the ground $\sigma$ = 1 mS/m, $\varepsilon_r$ = 15.

**Figure 82 – Vertical radiation patterns of the *E*-fields emitted by a small horizontal electric dipole located close to the ground**

IECNORM.COM : Click to view the full PDF of CISPR TR 16-3:2020 RLV




IECNORM.COM : Click to view the full PDF of CISPR TR 16-3:2020 RLV

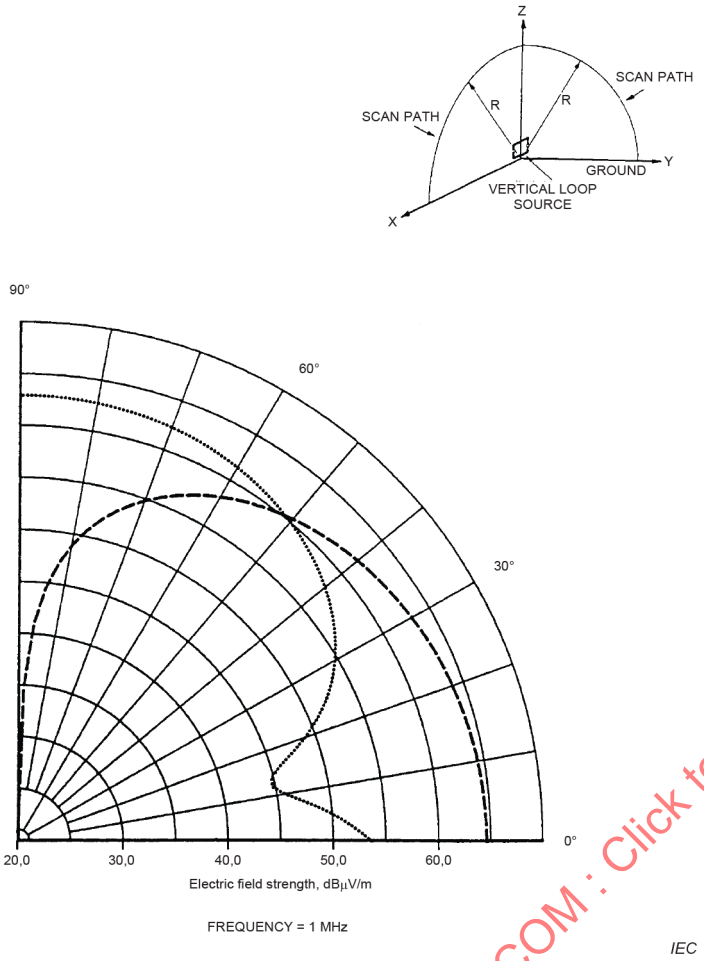
Dipole length 3 m. Dipole height above ground 1 m. Dipole moment 1 A·m. Dashed line curve – vertically oriented $E_z$ at a scan distance of 300 m in the Z-X plane. Dotted line curve – horizontally oriented $E_x$ at a scan distance of 300 m in the Z-X plane. Dash-dot line curve – total vector/phasor sum of $E_z$ and $E_x$ at a scan distance of 300 m in the Z-X plane, the vertically polarized $E$-field. Electrical constants of the ground $\sigma$ = 1 mS/m, $\varepsilon_r$ = 15.

**Figure 83 – Vertical radiation patterns of the $E$-fields emitted by a small horizontal electric dipole located close to the ground**

Square loop 3 m × 3 m. Loop base height above ground 0,15 m. Dipole moment 1 A·m$^2$. Dashed line curve – horizontally oriented $H_y$ at a scan distance of 30 m in the Z-X plane. Dotted line curve – horizontally oriented $H_y$ at a scan distance of 30 m in the Y-Z plane. Solid line curve – vertically oriented $H_z$ at a scan distance of 30 m in the Y-Z plane. Electrical constants of the ground $\sigma$ = 1 mS/m, $\varepsilon_r$ = 15.

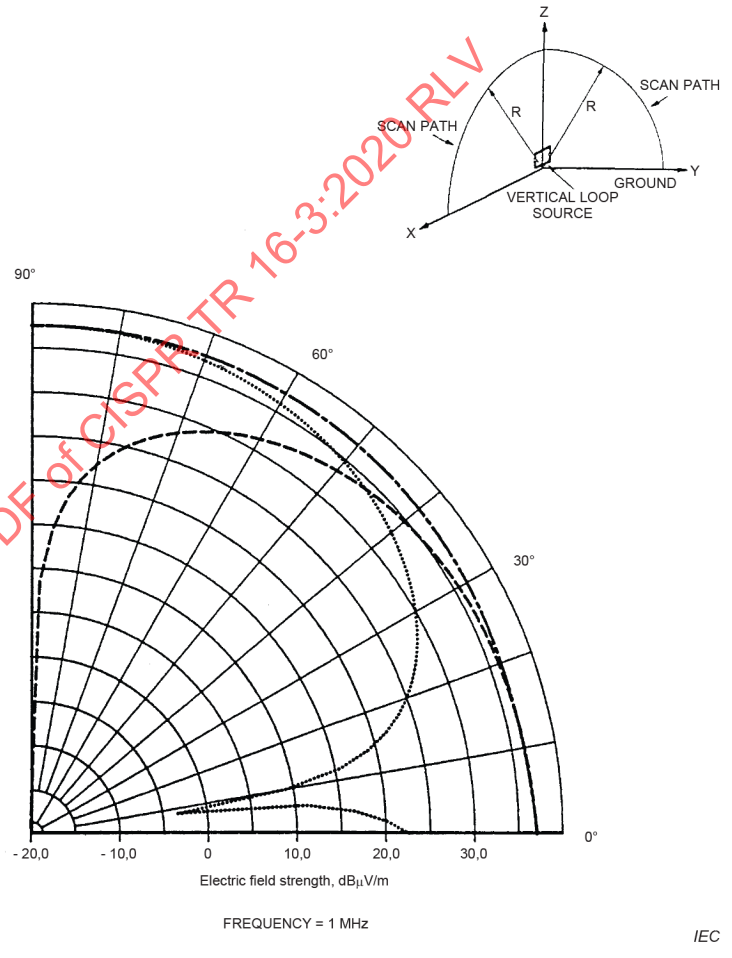
**Figure 84 – Vertical radiation patterns of the $H$-fields emitted by a small horizontal magnetic dipole (vertical loop) located close to the ground**

IECNORM.COM : Click to view the full PDF of CISPR TR 16-3:2020 RLV




Square loop 3 m × 3 m. Loop base height above ground 0,15 m. Dipole moment 1 A·m$^2$. Dashed line curve – $H_y$ at a scan distance of 30 m in the Z-X plane. Dotted line curve – $H_y$ at a scan distance of 30 m in the Y-Z plane. Perfectly conducting ground.

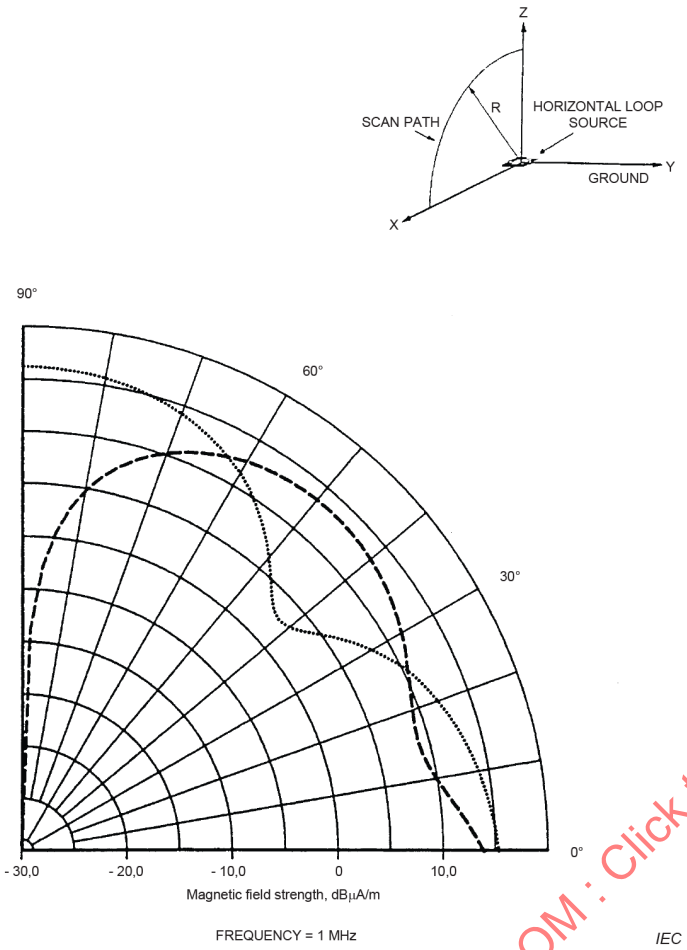
**Figure 85 – Vertical radiation patterns of the horizontally oriented *H*-fields emitted by a small horizontal magnetic dipole (vertical loop) located close to the ground**




Square loop 3 m × 3 m. Loop base height above ground 0,15 m. Dipole moment 1 A·m$^2$. Dashed line curve – $H_y$ at a scan distance of 300 m in the Z-X plane. Dotted line curve – $H_y$ at a scan distance of 300 m in the Y-Z plane. Electrical constants of the ground $\sigma$ = 1 mS/m, $\varepsilon_r$ = 15.

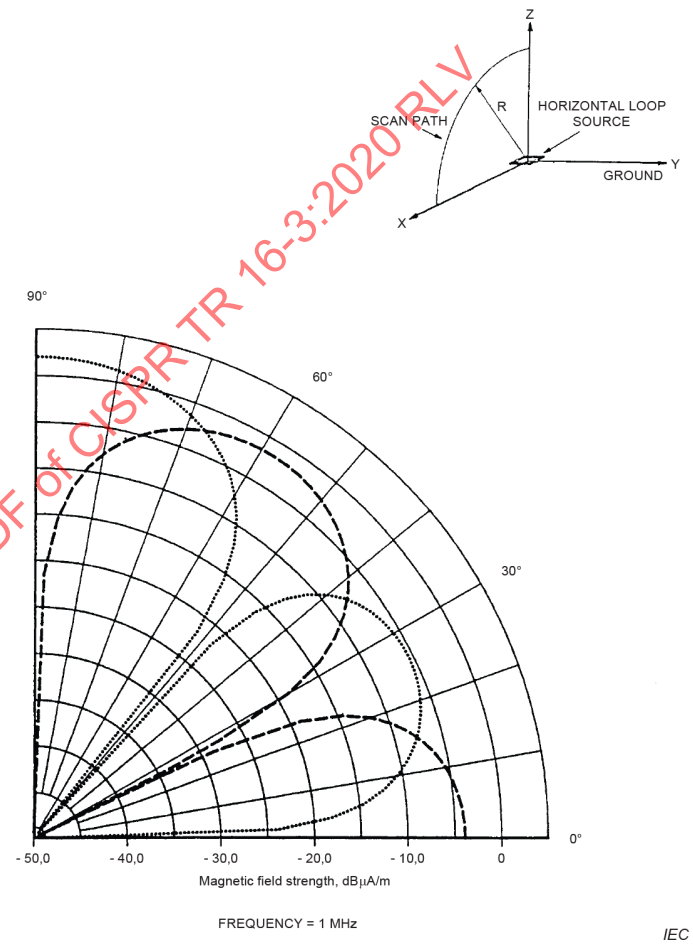
**Figure 86 – Vertical radiation patterns of the horizontally oriented *H*-fields emitted by a small horizontal magnetic dipole (vertical loop) located close to the ground**

IECNORM.COM : Click to view the full PDF of CISPR TR 16-3:2020 RLV




Square loop 3 m × 3 m. Loop base height above ground 0,15 m. Dipole moment 1 A·m$^2$. Dashed line curve – vertically oriented $E_z$ at a scan distance of 30 m in the Z-X plane. Dotted line curve – horizontally oriented $E_x$ at a scan distance of 30 m in the Z-X plane. Electrical constants of the ground $\sigma$ = 1 mS/m, $\varepsilon_r$ = 15.

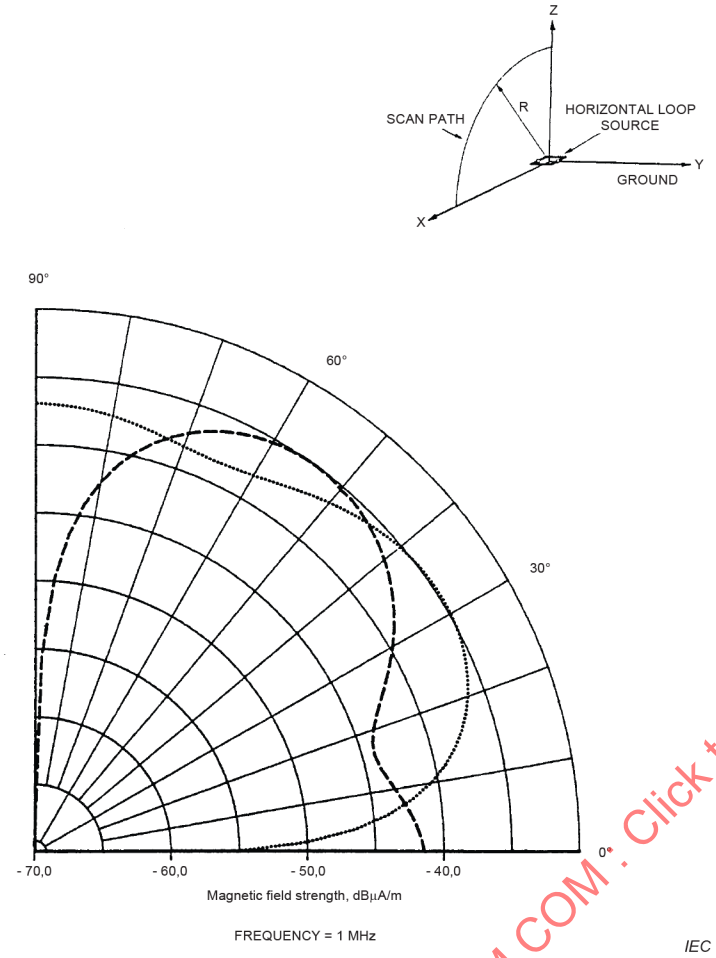
**Figure 87 – Vertical radiation patterns of the $E$-fields emitted by a small horizontal magnetic dipole (vertical loop) located close to the ground**




Square loop 3 m × 3 m. Loop base height above ground 0,15 m. Dipole moment 1 A·m$^2$. Dashed line curve – vertically oriented $E_z$ at a scan distance of 300 m in the Z-X plane. Dotted line curve – horizontally oriented $E_x$ at a scan distance of 300 m in the Z-X plane. Dash-dot line curve – total vector/phasor sum of $E_z$ and $E_x$ at a scan distance of 300 m in the Z-X plane, the vertically polarized $E$-field. Electrical constants of the ground $\sigma$ = 1 mS/m, $\varepsilon_r$ = 15.

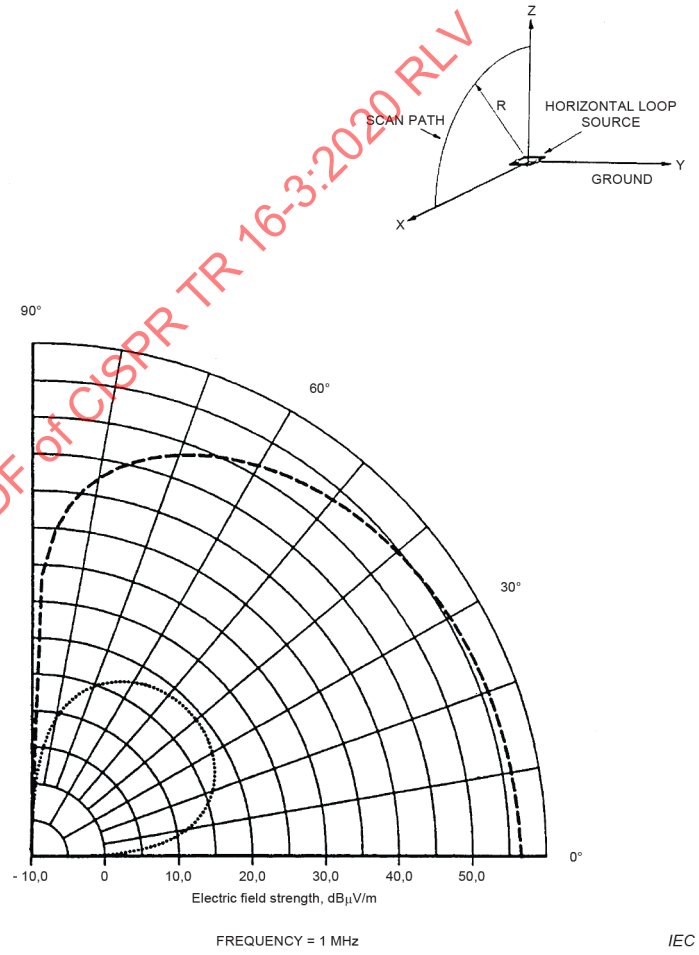
**Figure 88 – Vertical radiation patterns of the $E$-fields emitted by a small horizontal magnetic dipole (vertical loop) located close to the ground**

IECNORM.COM : Click to view the full PDF of CISPR TR 16-3:2020 RLV




Square loop 3 m × 3 m. Loop height above ground 1 m. Dipole moment 1 A·m$^2$.Dashed line curve – horizontally oriented $H_x$ at a scan distance of 30 m. Dotted line curve – vertically oriented $H_z$ at a scan distance of 30 m. Electrical constants of the ground $\sigma$ = 1 mS/m, $\varepsilon_r$ = 15.

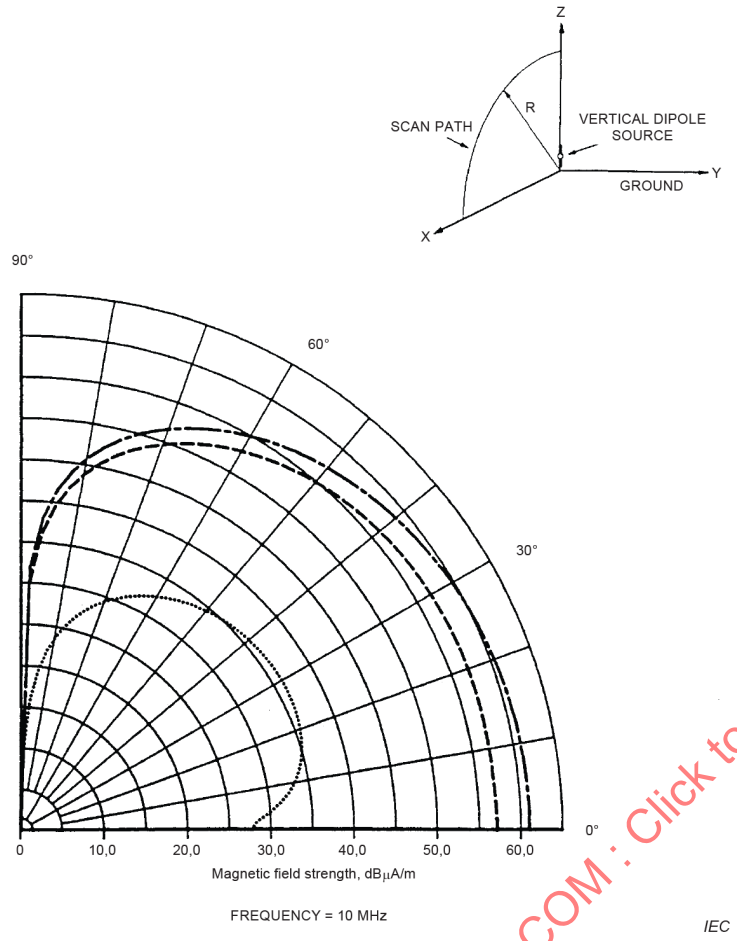
**Figure 89 – Vertical radiation patterns of the *H*-fields emitted by a small vertical magnetic dipole (horizontal loop) located close to the ground**




Square loop 3 m × 3 m. Loop height above ground 1 m. Dipole moment 1 A·m$^2$. Dashed line curve – horizontally oriented $H_x$ at a scan distance of 30 m. Dotted line curve – vertically oriented $H_z$ at a scan distance of 30 m. Perfectly conducting ground.

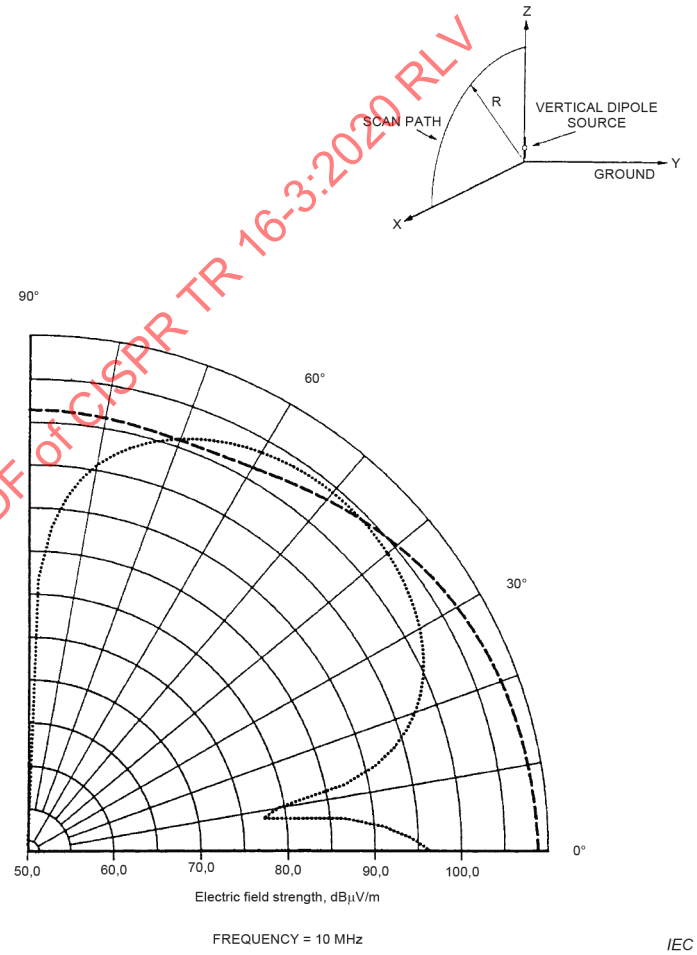
**Figure 90 – Vertical radiation patterns of the *H*-fields emitted by a small vertical magnetic dipole (horizontal loop) located close to the ground**

IECNORM.COM : Click to view the full PDF of CISPR TR 16-3:2020 RLV




Square loop 3 m × 3 m. Loop height above ground 1 m. Dipole moment 1 A·m$^2$. Dashed line curve – horizontally oriented $H_x$ at a scan distance of 300 m. Dotted line curve – vertically oriented $H_z$ at a scan distance of 300 m. Electrical constants of the ground $\sigma$ = 1 mS/m, $\varepsilon_r$ = 15.

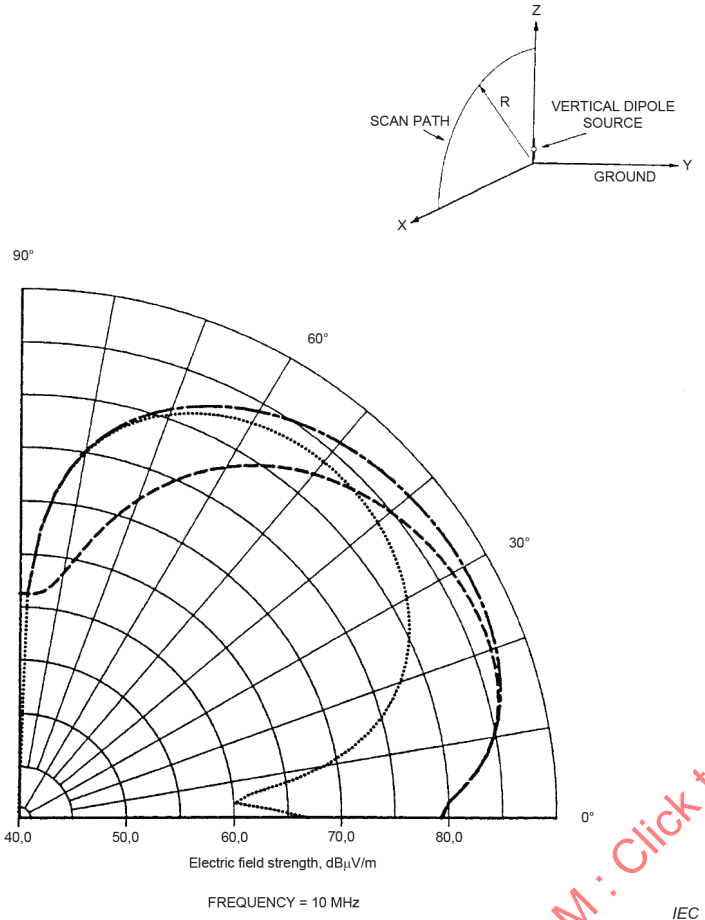
**Figure 91 – Vertical radiation patterns of the *H*-fields emitted by a small vertical magnetic dipole (horizontal loop) located close to the ground**




Square loop 3 m × 3 m. Loop height above ground 1 m. Dipole moment 1 A·m$^2$. Dashed line curve – horizontally oriented $E_y$ at a scan distance of 30 m. Dotted line curve – horizontally oriented $E_y$ at a scan distance of 300 m. Electrical constants of the ground $\sigma$ = 1 mS/m, $\varepsilon_r$ = 15.

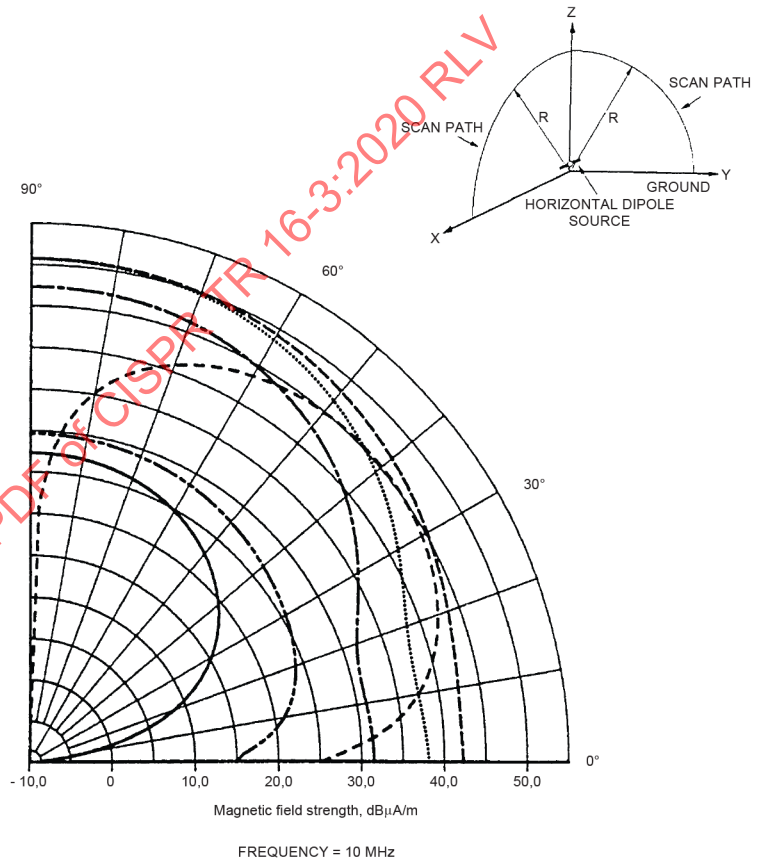
**Figure 92 – Vertical radiation patterns of the *E*-fields emitted by a small vertical magnetic dipole (horizontal loop) located close to the ground**

IECNORM.COM : Click to view the full PDF of CISPR TR 16-3:2020 RLV




Dipole length 1 m. Dipole base at a height above ground of 0,15 m. Dipole moment 1 A·m. Dashed line curve – $H_y$ at a scan distance of 30 m. Dotted line curve – $H_y$ at a scan distance of 300 m. Dash-dot line curve – $H_y$ at a scan distance of 30 m. Electrical constants of the ground $\sigma$ = 1 mS/m, $\varepsilon_r$ = 15. Perfectly conducting ground.

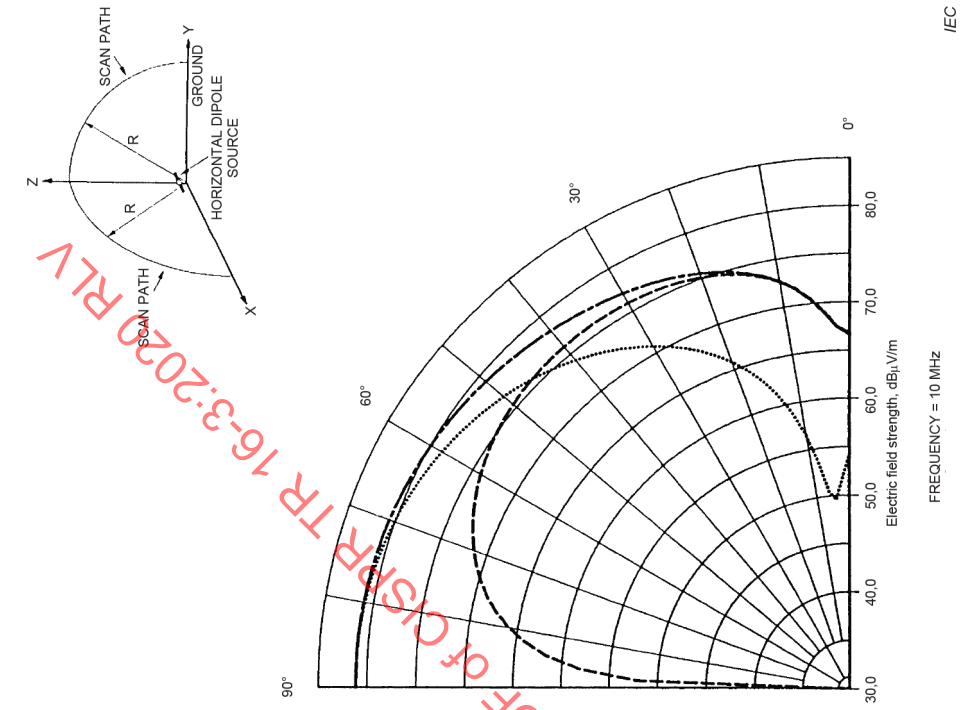
**Figure 93 – Vertical radiation patterns of the horizontally oriented *H*-fields emitted by a small vertical electric dipole located close to the ground**

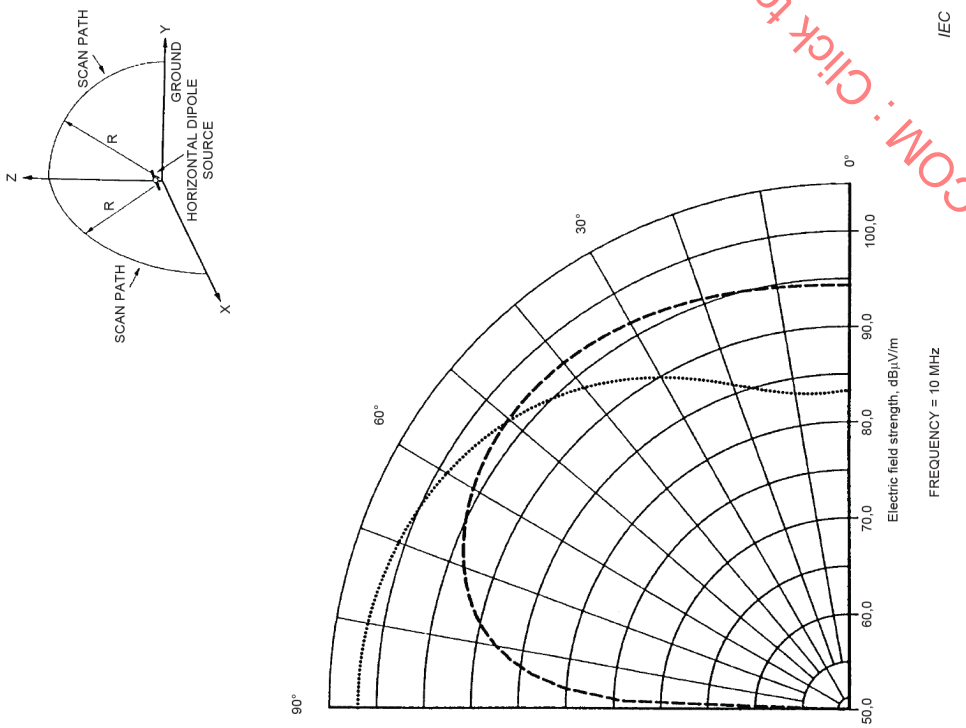



Dipole length 1 m. Dipole base at a height above ground of 0,15 m. Dipole moment 1 A·m. Dashed line curve – vertically oriented $E_z$ at a scan distance of 30 m. Dotted line curve – horizontally oriented $E_x$ at a scan distance of 30 m. Electrical constants of the ground $\sigma$ = 1 mS/m, $\varepsilon_r$ = 15.

**Figure 94 – Vertical radiation patterns of the *E*-fields emitted by a small vertical electric dipole located close to the ground**

IECNORM.COM : Click to view the full PDF of CISPR TR 16-3:2020 RLV




IECNORM.COM : Click to view the full PDF of CISPR TR 16-3:2020 RLV

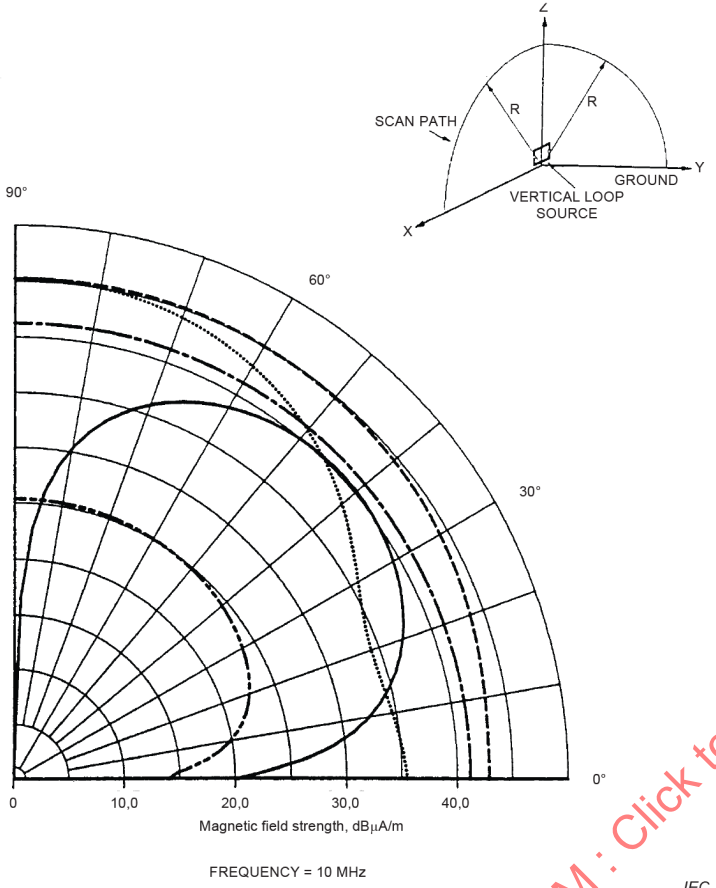
Dipole length 1 m. Dipole base at a height above ground of 0,15 m. Dipole moment 1 A·m. Dashed line curve – vertically oriented $E_z$ at a scan distance of 300 m. Dotted line curve – horizontally oriented $E_x$ at a scan distance of 300 m. Dash-dot line curve – total vector/phasor sum of $E_z$ and $E_x$ at a scan distance of 300 m, the vertically polarized $E$-field. Electrical constants of the ground $\sigma$ = 1 mS/m, $\varepsilon_r$ = 15.

**Figure 95 – Vertical radiation patterns of the $E$-fields emitted by a small vertical electric dipole located close to the ground**

Dipole length 1 m. Dipole height above ground 1 m. Dipole moment 1 A·m. Long-dash line curve – horizontally oriented $H_y$ at a scan distance of 30 m in the Z-X plane. Short-dash line curve – vertically oriented $H_z$ at a scan distance of 30 m in the Y-Z plane. Dotted line curve – horizontally oriented $H_y$ at a scan distance of 30 m in the Y-Z plane. Dash-double-dot curve – horizontally oriented $H_y$ at a scan distance of 300 m in the Z-X plane. Dash-dot line curve – horizontally oriented $H_y$ at a scan distance of 30 m in the Z-X plane. Solid line curve – horizontally oriented $H_y$ at a scan distance of 300 m in the Z-X plane. Electrical constants of the ground $\sigma$ = 1 mS/m, $\varepsilon_r$ = 15. Perfectly conducting ground.

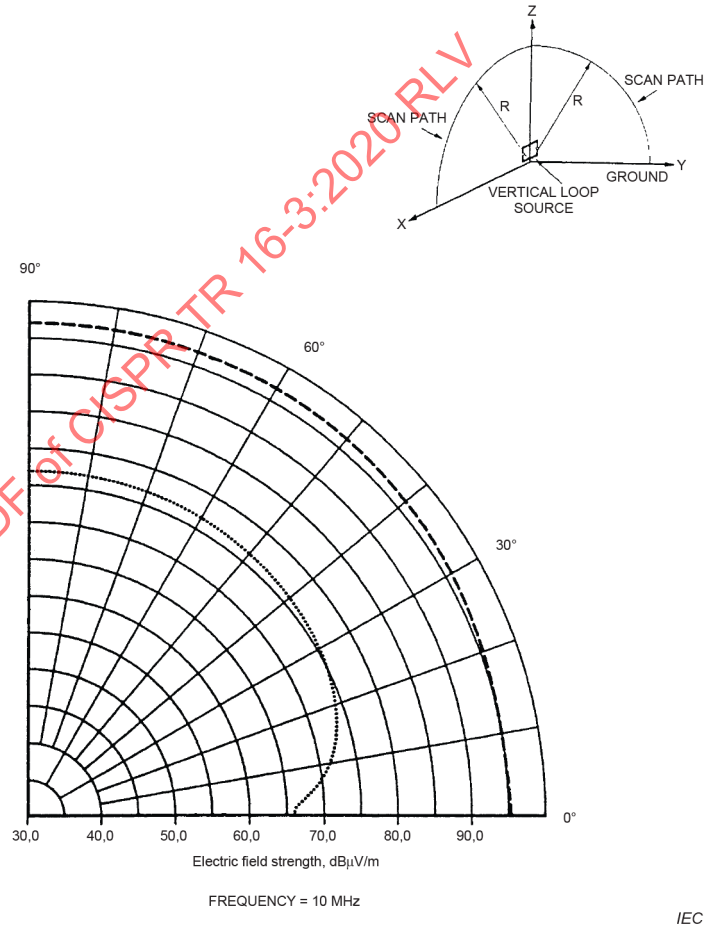
**Figure 96 – Vertical radiation patterns of the $H$-fields emitted by a small horizontal electric dipole located close to the ground**

IECNORM.COM : Click to view the full PDF of CISPR TR 16-3:2020 RLV




Dipole length 1 m. Dipole height above ground 1 m. Dipole moment 1 A·m. Dashed line curve – vertically oriented $E_z$ at a scan distance of 30 m in the Z-X plane. Dotted line curve – horizontally oriented $E_x$ at a scan distance of 30 m in the Z-X plane. Electrical constants of the ground $\sigma$ = 1 mS/m, $\varepsilon_r$ = 15.

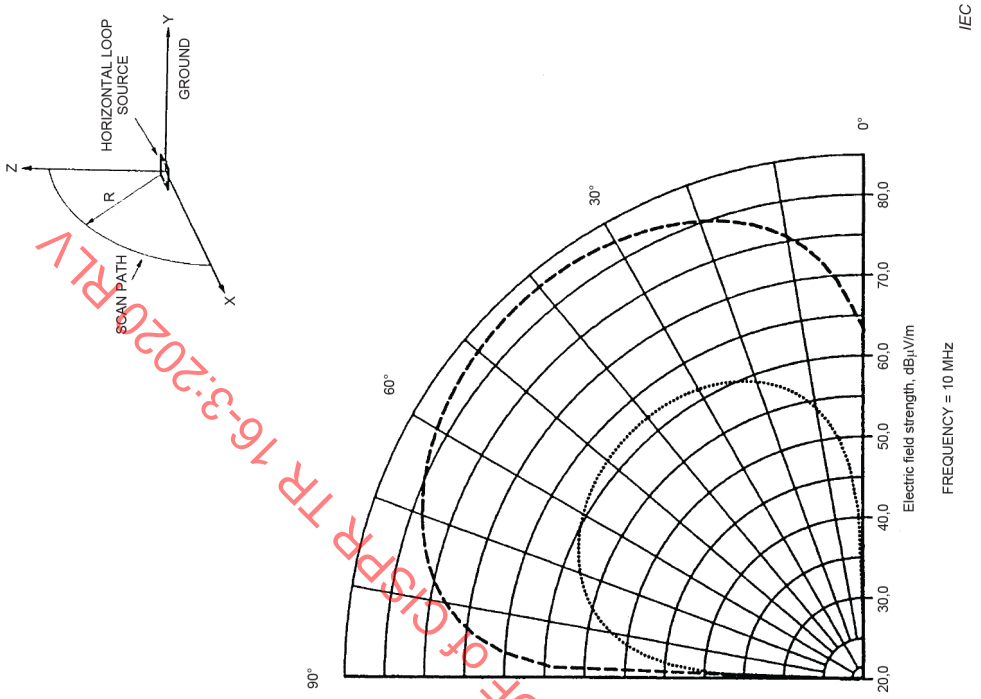
**Figure 97 – Vertical radiation patterns of the $E$-fields emitted by a small horizontal electric dipole located close to the ground**

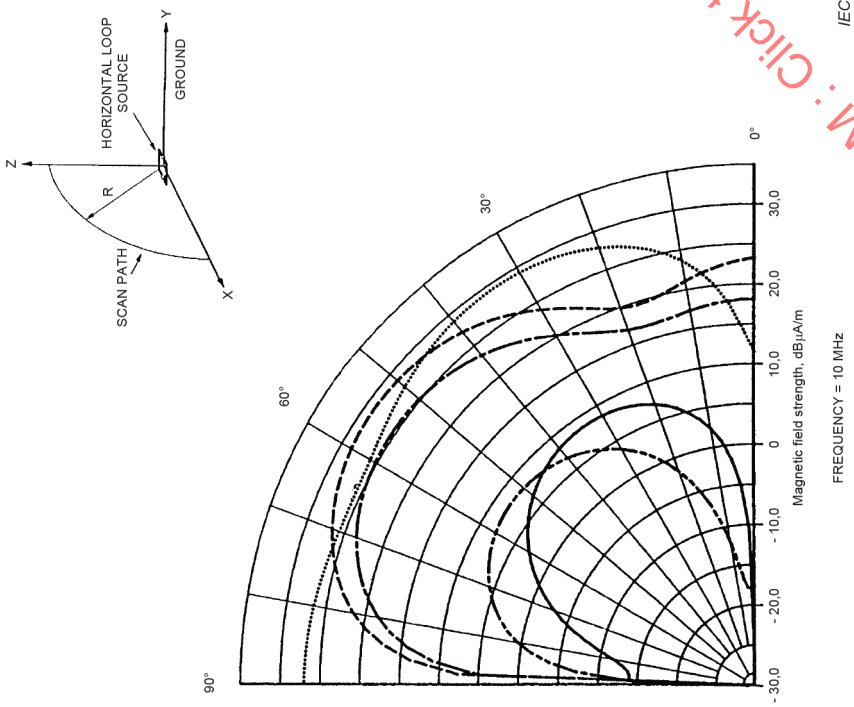



Dipole length 1 m. Dipole height above ground 1 m. Dipole moment 1 A·m. Dashed line curve – vertically oriented $E_z$ at a scan distance of 300 m in the Z-X plane. Dotted line curve – horizontally oriented $E_x$ at a scan distance of 300 m in the Z-X plane. Dash-dot line curve – total vector/phasor sum of $E_z$ and $E_x$ at a scan distance of 300 m in the Z-X plane, the vertically polarized $E$-field. Electrical constants of the ground $\sigma$ = 1 mS/m, $\varepsilon_r$ = 15.

**Figure 98 – Vertical radiation patterns of the $E$-fields emitted by a small horizontal electric dipole located close to the ground**

IECNORM.COM : Click to view the full PDF of CISPR TR 16-3:2020 RLV




IECNORM.COM : Click to view the full PDF of CISPR TR 16-3:2020 RLV

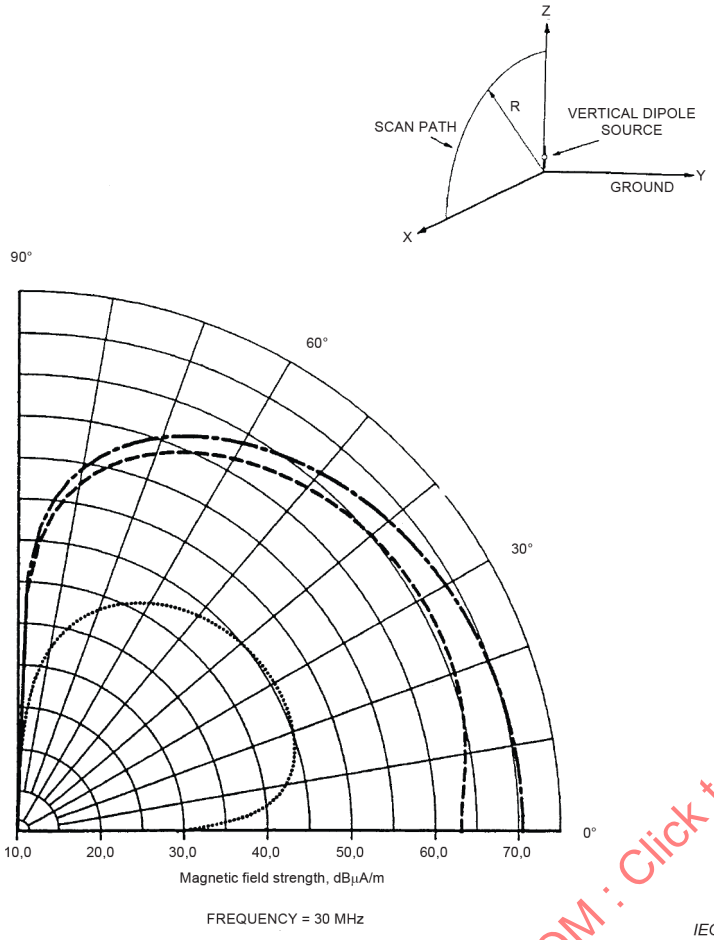
Square loop 0,6 m × 0,6 m. Loop base height above ground 0,07 m. Dipole moment 1 A·m$^2$. Dashed line curve – horizontally oriented $H_y$ at a scan distance of 30 m in the Z-X plane. Dotted line curve – horizontally oriented $H_y$ at a scan distance of 30 m in the Y-Z plane. Solid line curve – vertically oriented $H_z$ at a scan distance of 30 m in the Y-Z plane. Dash-double-dot curve – horizontally oriented $H_y$ at a scan distance of 300 m in the Z-X plane. Dash-dot line curve – horizontally oriented $H_y$ at a scan distance of 30 m in the Z-X plane. Electrical constants of the ground $\sigma$ = 1 mS/m, $\varepsilon_r$ = 15. Perfectly conducting ground.

**Figure 99 – Vertical radiation patterns of the *H*-field emitted by a small horizontal magnetic dipole (vertical loop) located close to the ground**

Square loop 0,6 m × 0,6 m. Loop base height above ground 0,07 m. Dipole moment 1 A·m$^2$. Dashed line curve – total vector/phasor sum of $E_z$ and $E_x$ at a scan distance of 30 m in the Z-X plane, the vertically polarized $E$-field. Dotted line curve – total vector/phasor sum of $E_z$ and $E_x$ at a scan distance of 300 m in the Z-X plane, the vertically polarized $E$-field. Electrical constants of the ground $\sigma$ = 1 mS/m, $\varepsilon_r$ = 15.

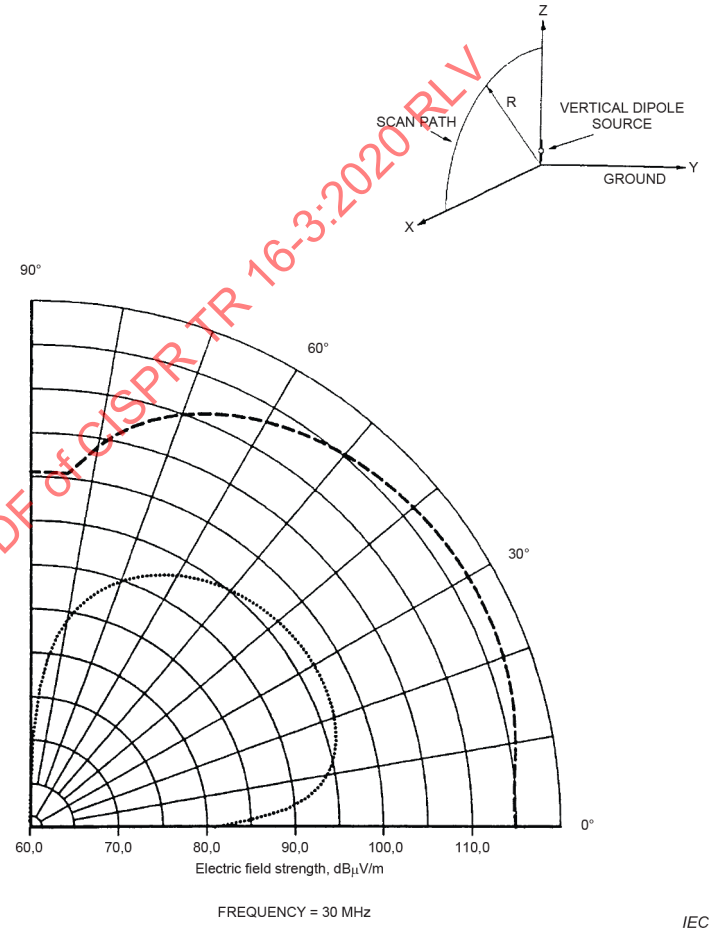
**Figure 100 – Vertical radiation patterns of the vertically polarized *E*-fields emitted by a small horizontal magnetic dipole (vertical loop) located close to the ground**

IECNORM.COM : Click to view the full PDF of CISPR TR 16-3:2020 RLV




Square loop 0,2 m × 0,2 m. Loop height above ground 1 m. Dipole moment 1 A·m$^2$. Dashed line curve – horizontally oriented $H_x$ at a scan distance of 30 m. Dotted line curve – vertically oriented $H_z$ at a scan distance of 30 m. Dash-double-dot curve – horizontally oriented $H_x$ at a scan distance of 300 m. Dash-dot line curve – horizontally oriented $H_x$ at a scan distance of 30 m. Solid line curve – vertically oriented $H_z$ at a scan distance of 300 m. Electrical constants of the ground $\sigma$ = 1 mS/m, $\varepsilon_r$ = 15. Perfectly conducting ground.

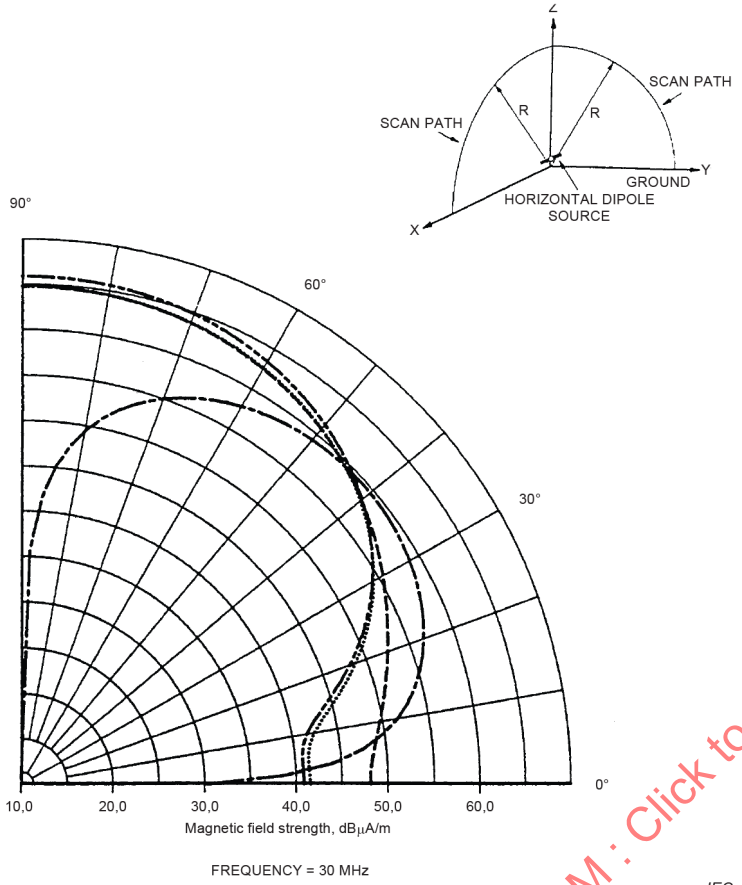
**Figure 101 – Vertical radiation patterns of the $H$-field emitted by a small vertical magnetic dipole (horizontal loop) located close to the ground**




Square loop 0,2 m × 0,2 m. Loop height above ground 1 m. Dipole moment 1 A·m$^2$. Dashed line curve – horizontally oriented $E_y$ at a scan distance of 30 m. Dotted line curve – horizontally oriented $E_y$ at a scan distance of 300 m. Electrical constants of the ground $\sigma$ = 1 mS/m, $\varepsilon_r$ = 15.

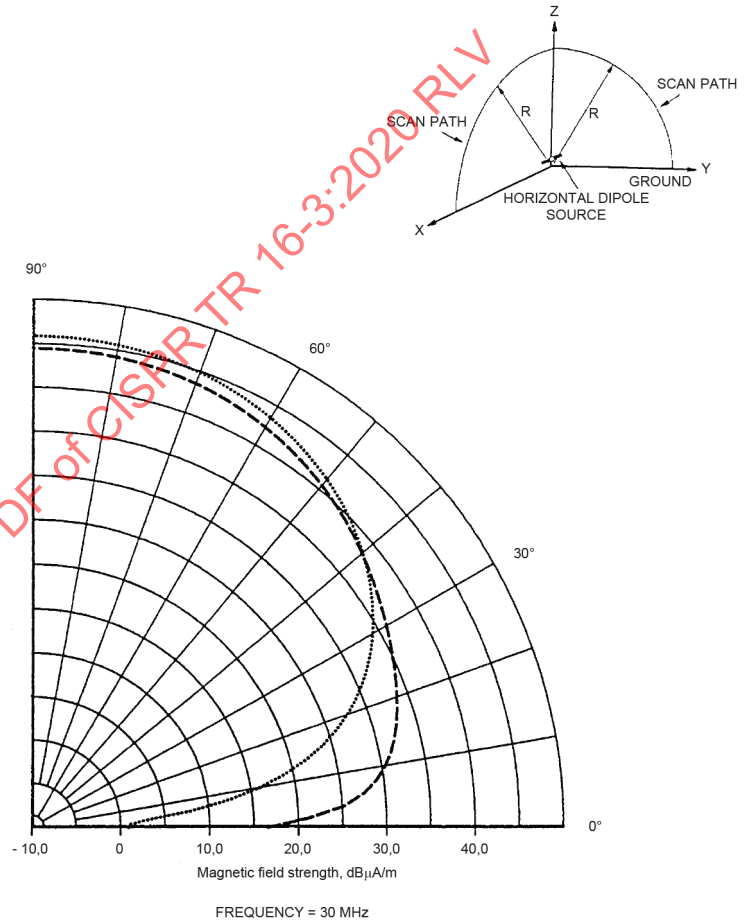
**Figure 102 – Vertical radiation patterns of the $E$-fields emitted by a small vertical magnetic dipole (horizontal loop) located close to the ground**

IECNORM.COM : Click to view the full PDF of CISPR TR 16-3:2020 RLV




Dipole length 1 m. Dipole base at a height above ground of 0,15 m. Dipole moment 1 A·m. Dashed line curve – $H_y$ at a scan distance of 30 m. Dotted line curve – $H_y$ at a scan distance of 300 m. Dash-dot line curve – $H_y$ at a scan distance of 30 m. Electrical constants of the ground $\sigma$ = 1 mS/m, $\varepsilon_r$ = 15. Perfectly conducting ground.

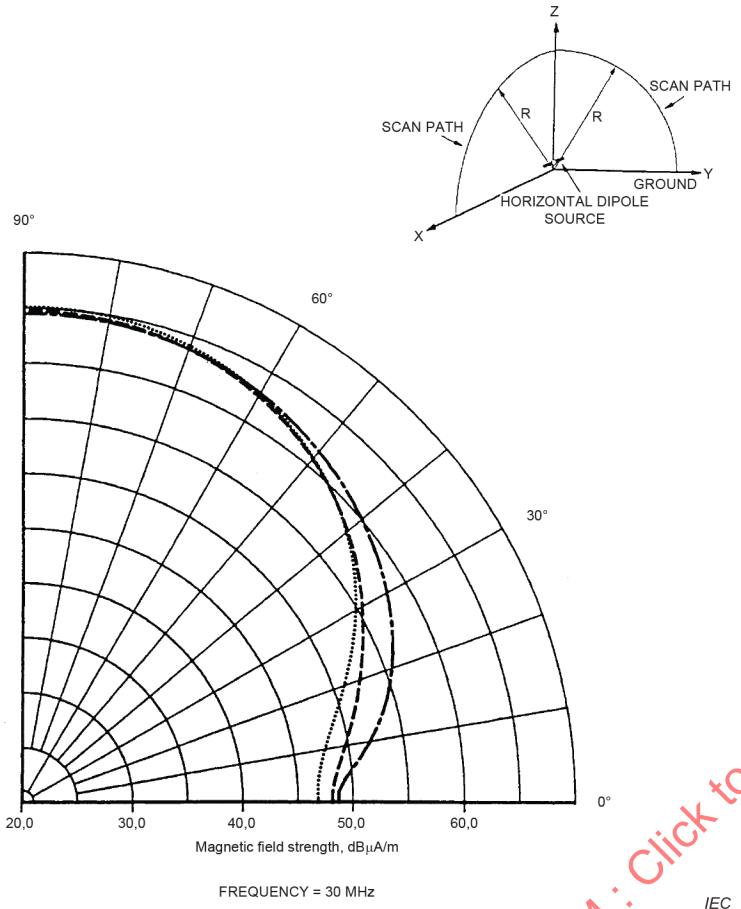
**Figure 103 – Vertical radiation patterns of the horizontally oriented *H*-fields emitted by a small vertical electric dipole located close to the ground**




Dipole length 1 m. Dipole base at a height above ground of 0,15 m. Dipole moment 1 A·m. Dashed line curve – total vector/phasor sum of $E_z$ and $E_x$ at a scan distance of 30 m in the Z-X plane, the vertically polarized $E$-field. Dotted line curve – total vector/phasor sum of $E_z$ and $E_x$ at a scan distance of 300 m in the Z-X plane, the vertically polarized $E$-field. Electrical constants of the ground $\sigma$ = 1 mS/m, $\varepsilon_r$ = 15.

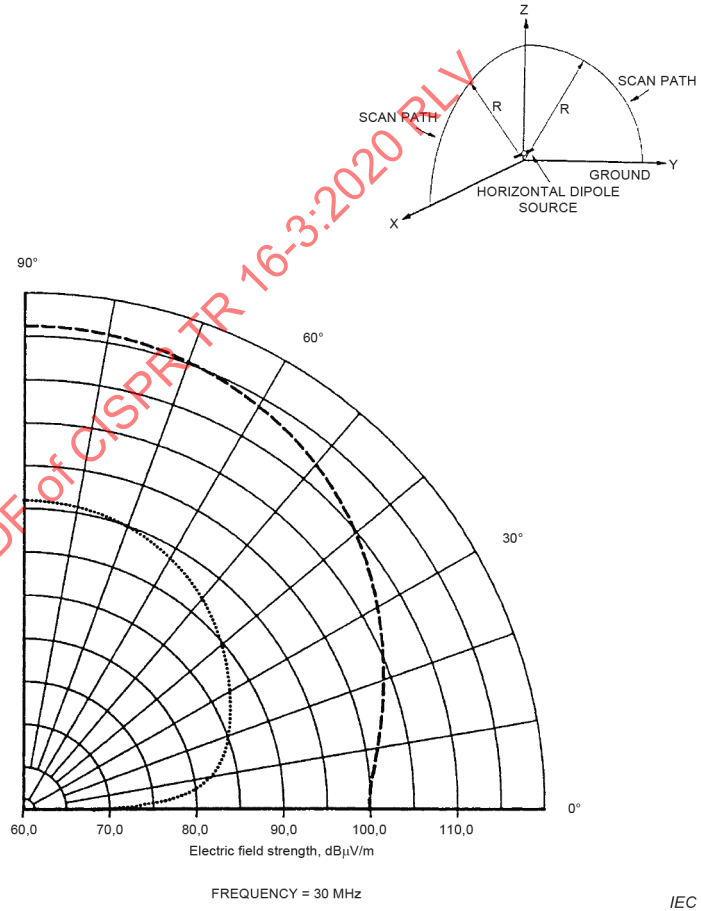
**Figure 104 – Vertical radiation patterns of the vertically polarized *E*-fields emitted by a small vertical electric dipole located close to the ground**

IECNORM.COM : Click to view the full PDF of CISPR TR 16-3:2020 RLV




Dipole length 1 m. Dipole height above ground 1 m. Dipole moment 1 A·m. Dashed line curve – horizontally oriented $H_y$ at a scan distance of 30 m in the Z-X plane. Dotted line curve – horizontally oriented $H_y$ at a scan distance of 30 m in the Y-Z plane. Dash-dot line curve – vertically oriented $H_z$ at a scan distance of 30 m in the Y-Z plane. Dash-double-dot curve – horizontally oriented $H_y$ at a scan distance of 30 m in the Z-X plane. Electrical constants of the ground $\sigma$ = 1 mS/m, $\varepsilon_r$ = 15. Perfectly conducting ground.

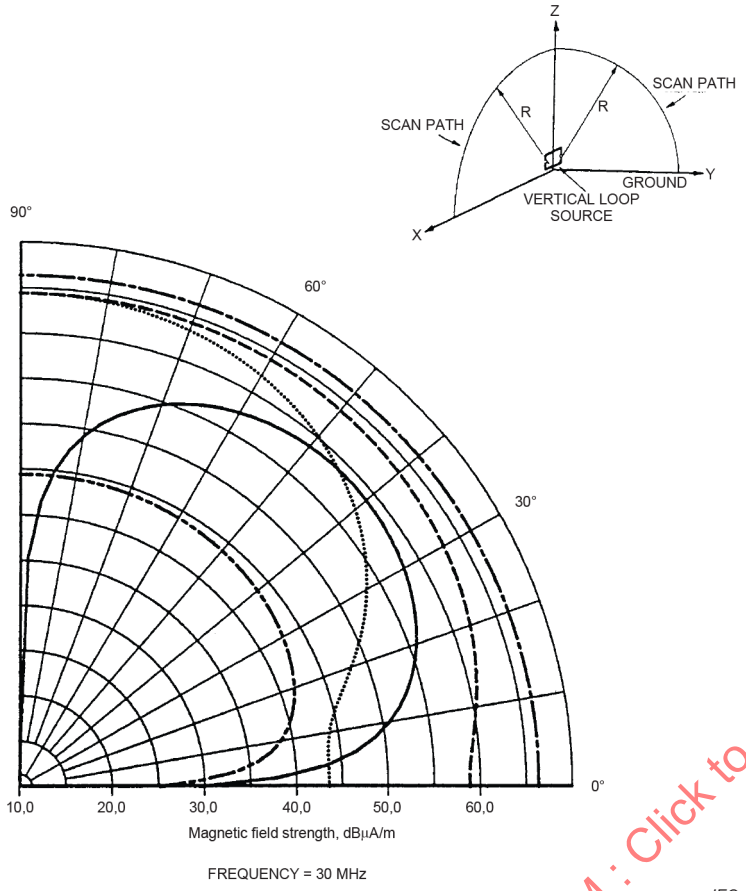
**Figure 105 – Vertical radiation patterns of the *H*-fields emitted by a small horizontal electric dipole located close to the ground**




Dipole length 1 m. Dipole height above ground 1 m. Dipole moment 1 A·m. Dashed line curve – $H_y$ at a scan distance of 300 m in the Z-X plane. Dotted line curve – $H_y$ at a scan distance of 300 m in the Z-X plane. Electrical constants of the ground $\sigma$ = 1 mS/m, $\varepsilon_r$ = 15. Perfectly conducting ground.

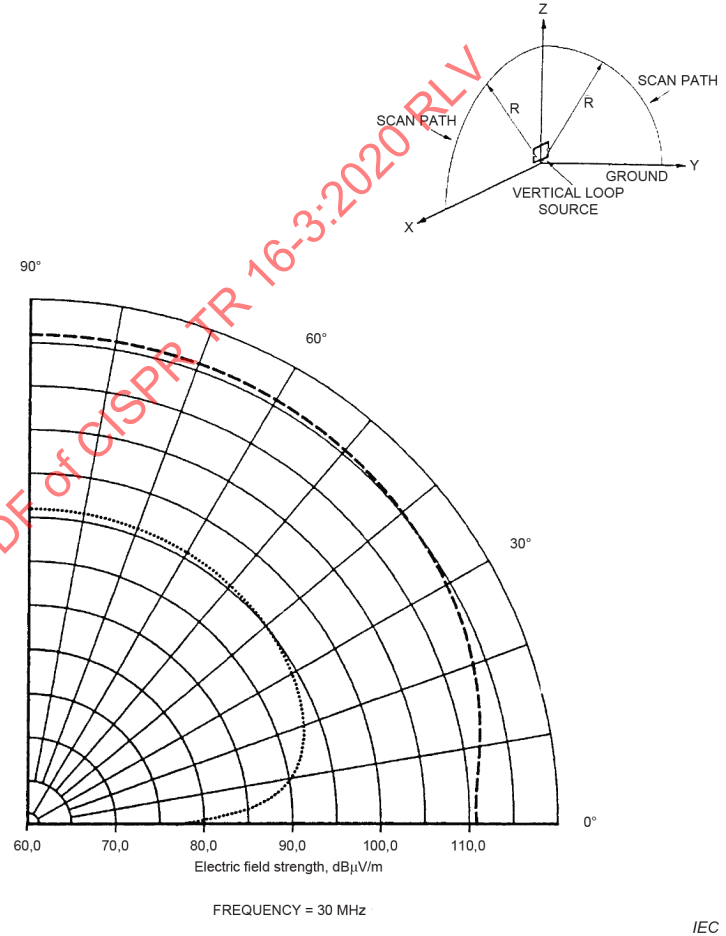
**Figure 106 – Vertical radiation patterns of the horizontally oriented *H*-fields emitted by a small horizontal electric dipole located close to the ground**

IECNORM.COM : Click to view the full PDF of CISPR TR 16-3:2020 RLV




Dipole length 1 m. Dipole height above ground 1 m. Dipole moment 1 A·m. $H_y$ at a scan distance of 30 m in the Z-X plane. Dash-dot line curve – ground constants are $\sigma$ = 0,1 mS/m, $\varepsilon_r$ = 3. Dashed line curve – ground constants are $\sigma$ = 1 mS/m, $\varepsilon_r$ = 15. Dotted line curve – ground constants are $\sigma$ = 10 mS/m, $\varepsilon_r$ = 30.

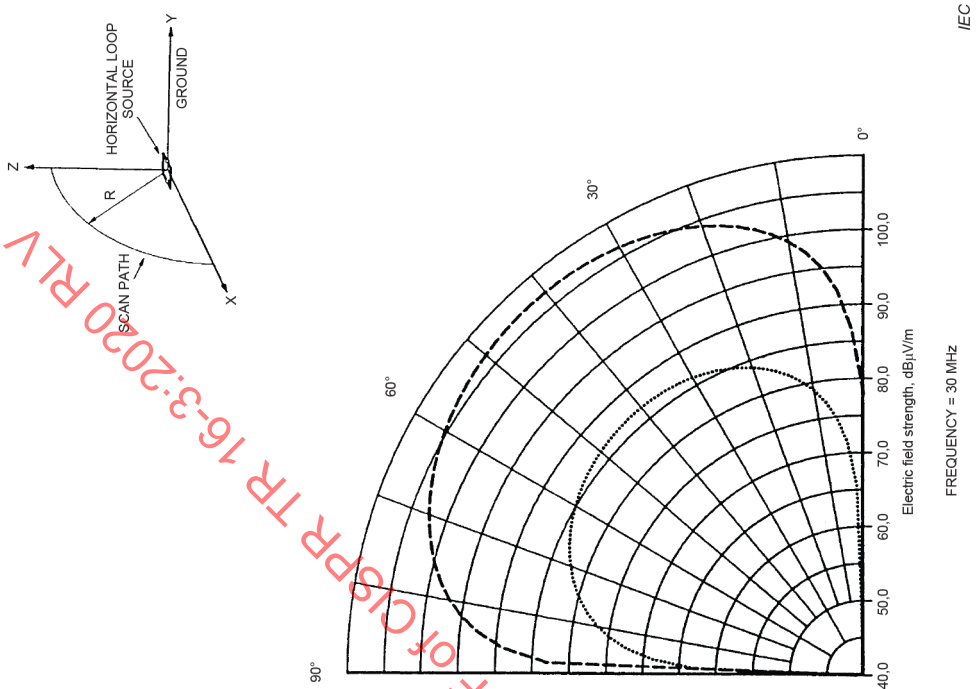
**Figure 107 – Influence of a wide range of values of the electrical constants of the ground on the vertical radiation patterns of the horizontally oriented *H*-fields emitted by a small horizontal electric dipole located close to the ground**

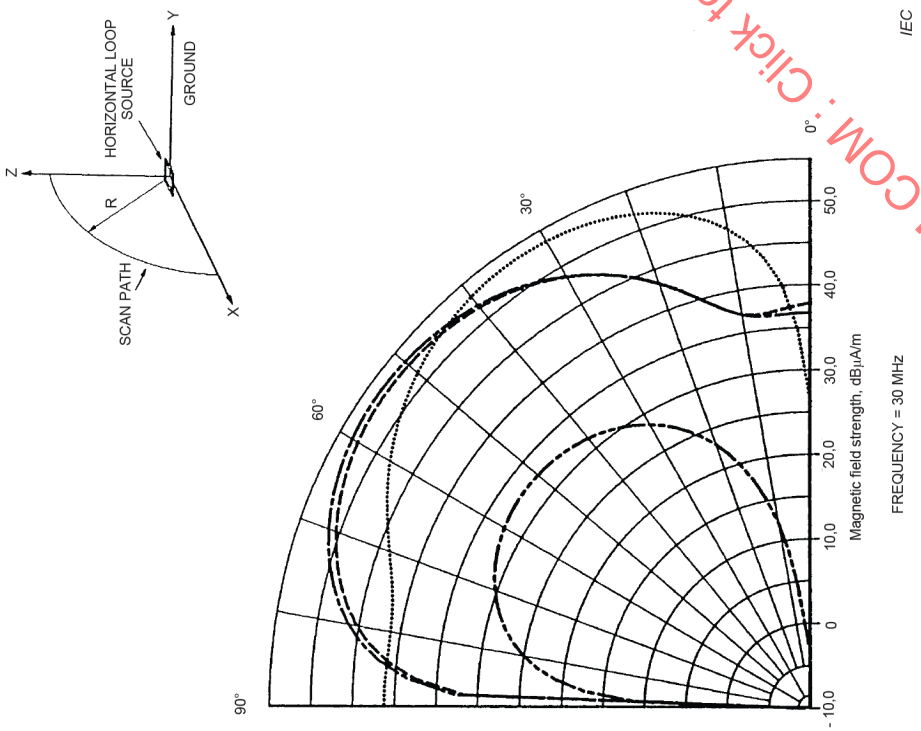



Dipole length 1 m. Dipole height above ground 1 m. Dipole moment 1 A·m. Dashed line curve – total vector/phasor sum of $E_z$ and $E_x$ at a scan distance of 30 m in the Z-X plane, the vertically polarized $E$-field. Dotted line curve – total vector/phasor sum of $E_z$ and $E_x$ at a scan distance of 300 m in the Z-X plane, the vertically polarized $E$-field. Electrical constants of the ground $\sigma$ = 1 mS/m, $\varepsilon_r$ = 15.

**Figure 108 – Vertical radiation patterns of the vertically polarized *E*-fields emitted by a small horizontal electric dipole located close to the ground**

IECNORM.COM : Click to view the full PDF of CISPR TR 16-3:2020 RLV




IECNORM.COM : Click to view the full PDF of CISPR TR 16-3:2020 RLV

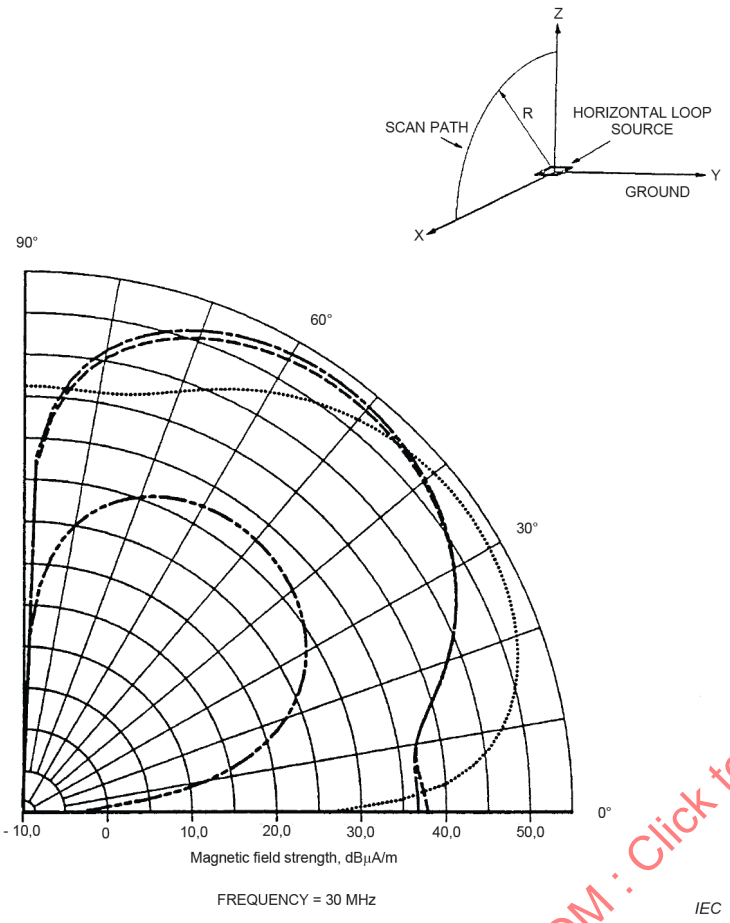
Square loop 0,1 m × 0,1 m. Loop base height above ground 0,07 m. Dipole moment 1 A·m$^2$. Dashed line curve – horizontally oriented $H_y$ at a scan distance of 30 m in the Z-X plane. Dotted line curve – horizontally oriented $H_y$ at a scan distance of 30 m in the Y-Z plane. Solid line curve – vertically oriented $H_z$ at a scan distance of 30 m in the Y-Z plane. Dash-double-dot curve – horizontally oriented $H_y$ at a scan distance of 300 m in the Z-X plane. Dash-dot line curve – horizontally oriented $H_y$ at a scan distance of 30 m in the Z-X plane Electrical constants of the ground $\sigma$ = 1 mS/m, $\varepsilon_r$ = 15. Perfectly conducting ground.

**Figure 109 – Vertical radiation patterns of the $H$-fields emitted by a small horizontal magnetic dipole (vertical loop) located close to the ground**

Square loop 0,1 m × 0,1 m. Loop base height above ground 0,07 m. Dipole moment 1 A·m$^2$. Dashed line curve – total vector/phasor sum of $E_z$ and $E_x$ at a scan distance of 30 m in the Z-X plane, the vertically polarized $E$-field. Dotted line curve – total vector/phasor sum of $E_z$ and $E_x$ at a scan distance of 300 m in the Z-X plane, the vertically polarized $E$-field. Electrical constants of the ground $\sigma$ = 1 mS/m, $\varepsilon_r$ = 15.

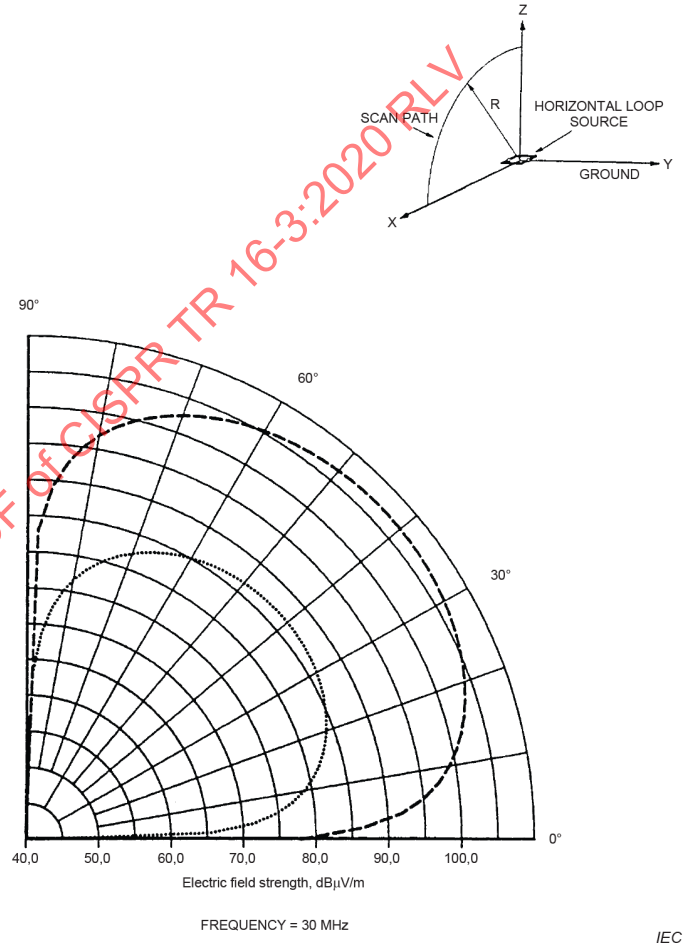
**Figure 110 – Vertical radiation patterns of the vertically polarized $E$-fields emitted by a small horizontal magnetic dipole (vertical loop) located close to the ground**

IECNORM.COM : Click to view the full PDF of CISPR TR 16-3:2020 RLV




Square loop 0,1 m × 0,1 m. Loop height above ground 1 m. Dipole moment 1 A·m$^2$. Dashed line curve – horizontally oriented $H_x$ at a scan distance of 30 m. Dotted line curve – vertically oriented $H_z$ at a scan distance of 30 m. Dash-double-dot curve – horizontally oriented $H_x$ at a scan distance of 300 m. Dash-dot line curve – horizontally oriented $H_x$ at a scan distance of 30 m. Electrical constants of the ground $\sigma$ = 1 mS/m, $\varepsilon_r$ = 15. Perfectly conducting ground.

**Figure 111 – Vertical radiation patterns of the $H$-fields emitted by a small vertical magnetic dipole (horizontal loop) located close to the ground**




Square loop 0,1 m by 0,1 m. Loop height above ground 1 m. Dipole moment 1 A·m$^2$. Dashed line curve – horizontally oriented $E_y$ at a scan distance of 30 m. Dotted line curve – horizontally oriented $E_y$ at a scan distance of 300 m. Electrical constants of the ground $\sigma$ = 1 mS/m, $\varepsilon_r$ = 15.

**Figure 112 – Vertical radiation patterns of the $E$-fields emitted by a small vertical magnetic dipole (horizontal loop) located close to the ground**

IECNORM.COM : Click to view the full PDF of CISPR TR 16-3:2020 RLV

## 4.7 Correlation between amplitude probability distribution (APD) characteristics of disturbance and performance of digital communication systems

### 4.7.1 General

The relationship between the degradation in quality of digital communication systems and APD of disturbance is shown in the following experimental results. Actual microwave ovens (MWO), such as the transformer and the inverter types, and a noise simulator, were used as a noise source in the following experiment. Bit Error Rate without error correction was basically used as a parameter of communication system performance (e.g. W-CDMA and PHS). Throughput is used if error correction could not be removed (e.g. W-LAN, Bluetooth and PHS).

Quantitative correlation between noise parameters and system performance is shown in 4.7.6 and 4.7.7 by using measured and simulated results.

These results show that APD measurement of disturbance is suitable for evaluating its interference potential on digital communication systems. Therefore APD measurement may be applicable to the compliance test of some products or product families, such as microwave ovens.

### 4.7.2 Influence on a wireless LAN system

The set-up for measuring communication quality degradation is shown in Figure 113, and measurement conditions are shown in Table 23. Throughput was chosen as a measure for communication quality evaluation. It was calculated from the time taken to transmit and time to receive data of a fixed size.

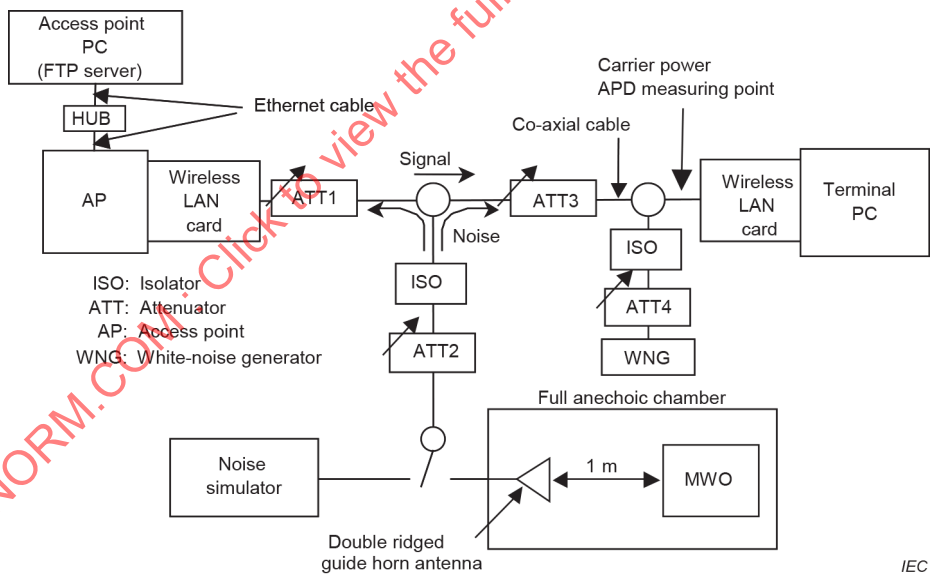



**Figure 113 – Set-up for measuring communication quality degradation of a wireless LAN**

IECNORM.COM : Click to view the full PDF of CISPR TR 16-3:2020 RLV

**Table 23 – Conditions for measuring communication quality degradation**

| | | |
|---|---|---|
| **Wireless LAN** | Frequency (channel number) | 2 462 MHz (channel 11) |
| | Transmission data | 20 MB |
| | Protocol | FTP (GET command from terminal PC) |
| | Transmission mode | Packet transmission |
| **Others** | Noise power density (dBm/Hz) | –154 dBm/Hz (set by ATT4) |

The APDs of disturbance are shown in Figure 114. The horizontal axis shows the level of radiated noise normalized by $N_0$, which has been approximated as the noise level from the white noise generator. The main frequency for measuring APD was 2 462 MHz. The average and root-mean-square (RMS) values of the noise level normalized by $N_0$ derived from APD of the MWO noise and noise simulator noise are shown in Table 24.

APD of the noise simulator at ATT2 = 0 dB was in good agreement with APD of the inverter type MWO at ATT2 = 10 dB.

IECNORM.COM : Click to view the full PDF of CISPR TR 16-3:2020 RLV

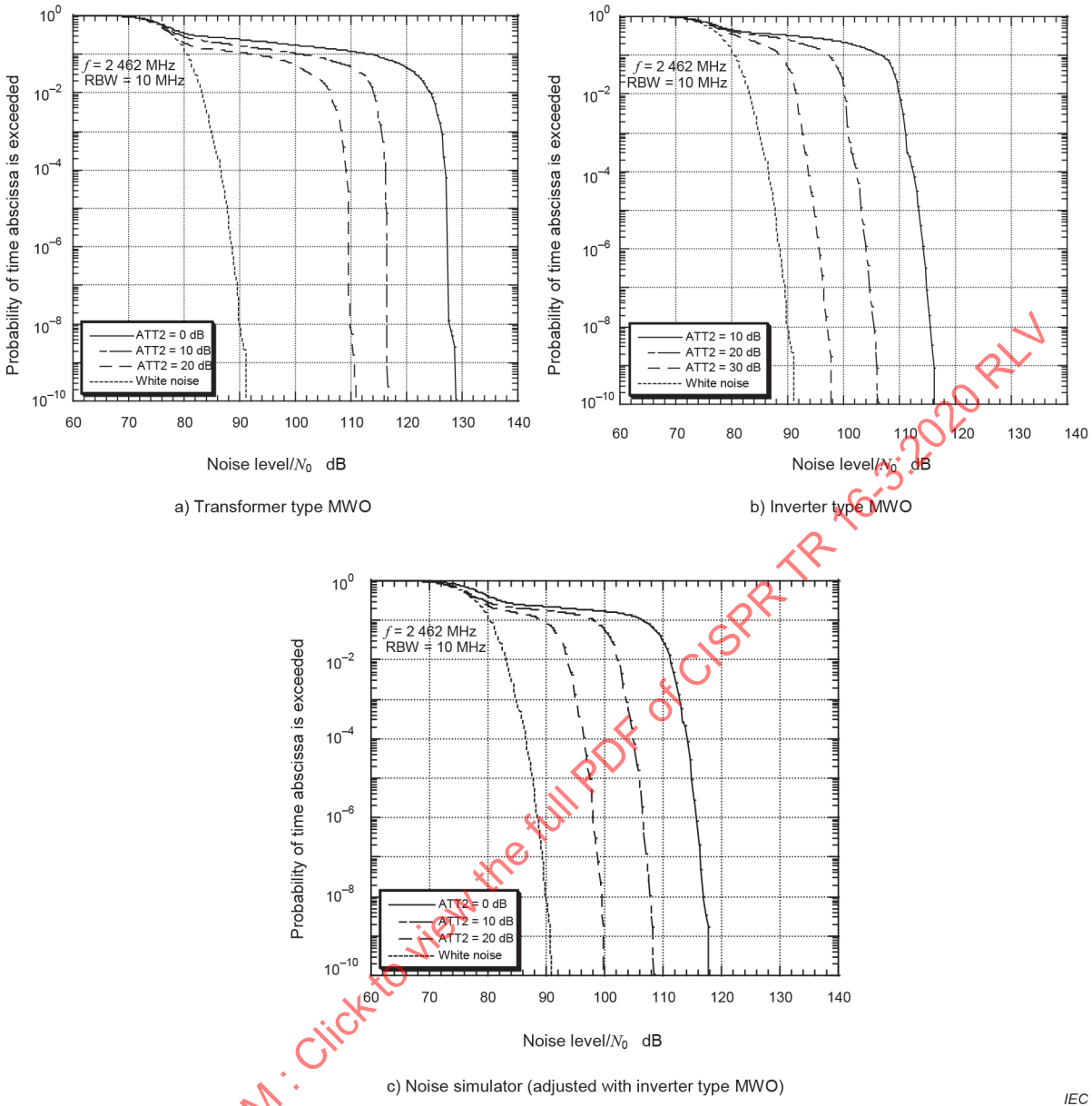



**Figure 114 – APD characteristics of disturbance**

**Table 24 – Average and RMS values of noise level normalized by $N_0$**

| | | ATT2 | | | | White noise |
|---|---|---|---|---|---|---|
| | | 0 dB | 10 dB | 20 dB | 30 dB | |
| **Transformer type MWO** | Average (dB) | 111,2 | 101,0 | 92,6 | | 77,6 |
| | RMS (dB) | 117,1 | 107,0 | 98,8 | | 78,7 |
| **Inverter type MWO** | Average (dB) | | 100,6 | 91,4 | 83,4 | 77,6 |
| | RMS (dB) | | 104,4 | 94,8 | 86,2 | 78,7 |
| **Noise simulator** | Average (dB) | 100,6 | 91,9 | 83,8 | | 77,5 |
| | RMS (dB) | 105,1 | 96,2 | 87,6 | | 78,6 |

The measured communication quality degradation for various amounts of attenuation of injected noise is shown in Figure 115. The horizontal axis shows $C/N_0$, where $C$ is the sub-carrier power and $N_0$ is the noise power density.

IECNORM.COM : Click to view the full PDF of CISPR TR 16-3:2020 RLV

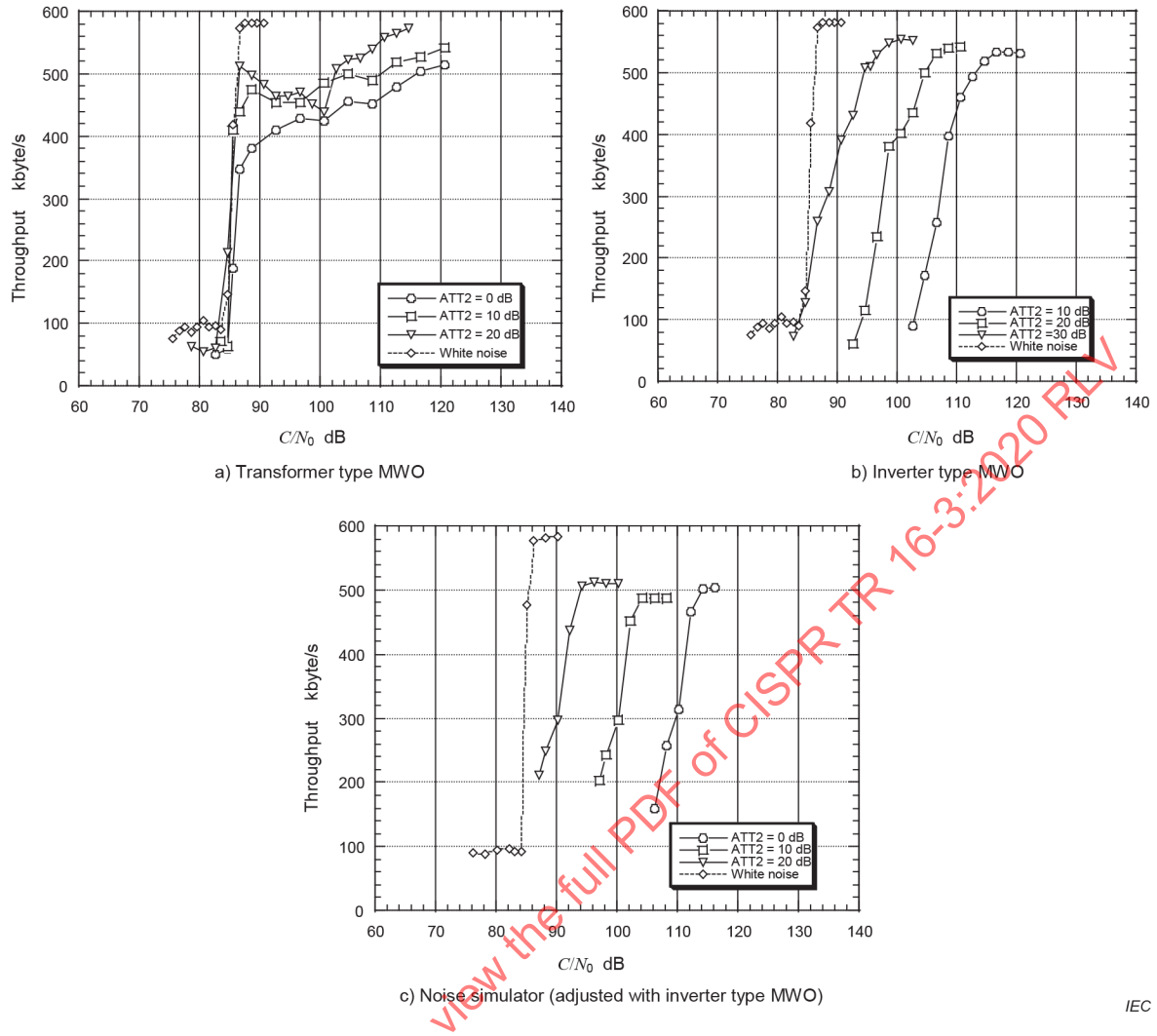



**Figure 115 – Wireless LAN throughput influenced by noise**

The throughput influenced by a transformer type MWO is 400 kbytes/s or more when $C/N_0$ is 90 dB or more, and decreases rapidly when $C/N_0$ is below 90 dB. This tendency is almost the same irrespective of the noise level. On the other hand, the throughput influenced by an inverter type MWO decreases almost in proportion to the noise level. The throughput influenced by a noise simulator has almost the same degradation characteristics as that for an inverter type MWO.

### 4.7.3 Influence on a Bluetooth system

The set-up for measuring communication quality degradation is shown in Figure 116, and measurement conditions are shown in Table 25.

Throughput was chosen as the measure for communication quality evaluation.

IECNORM.COM : Click to view the full PDF of CISPR TR 16-3:2020 RLV

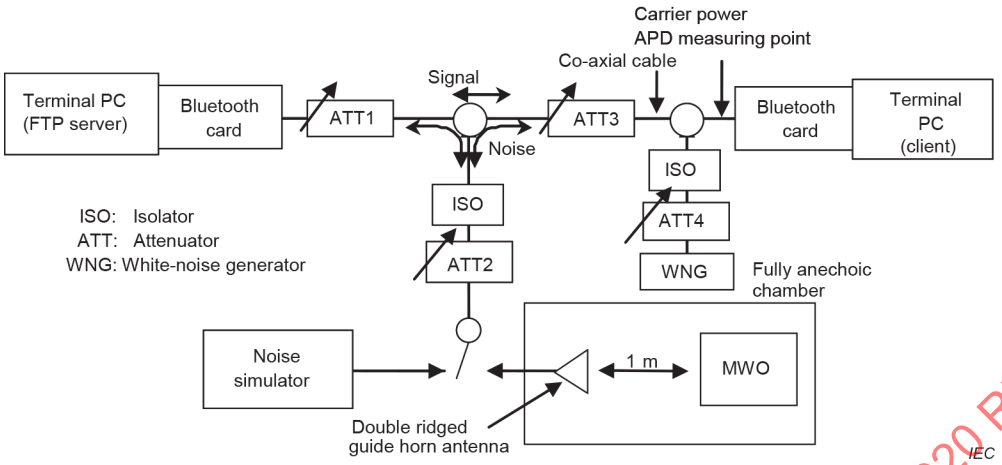



**Figure 116 – Set-up for measuring the communication quality degradation of Bluetooth**

**Table 25 – Conditions for measuring communication quality degradation of Bluetooth**

| | | |
|---|---|---|
| **Bluetooth** | Frequency | 2 400 MHz to 2 483,5 MHz |
| | Transmission data | 2,5 MB |
| | Protocol | FTP (GET command from terminal PC) |
| | Transmission mode | Packet exchange data transmission mode |
| **Others** | Noise power density (dBm/Hz) | -148 dBm/Hz (set by ATT4) |

The APDs at a frequency of 2 441 MHz are shown in Figure 117, and the average and RMS values of noise level normalized by $N_0$ are shown in Table 26.

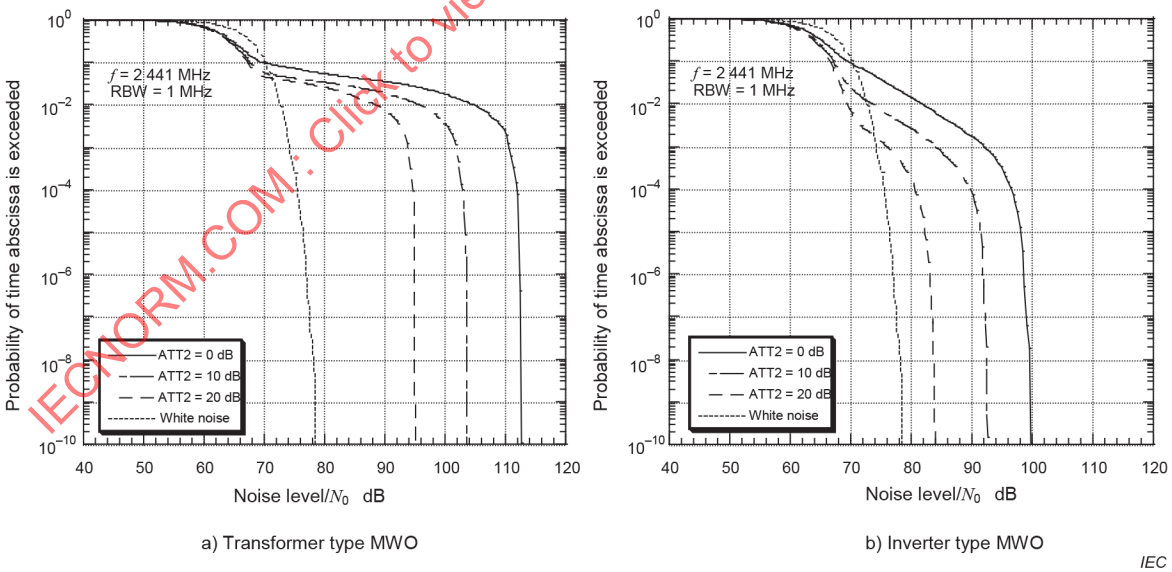


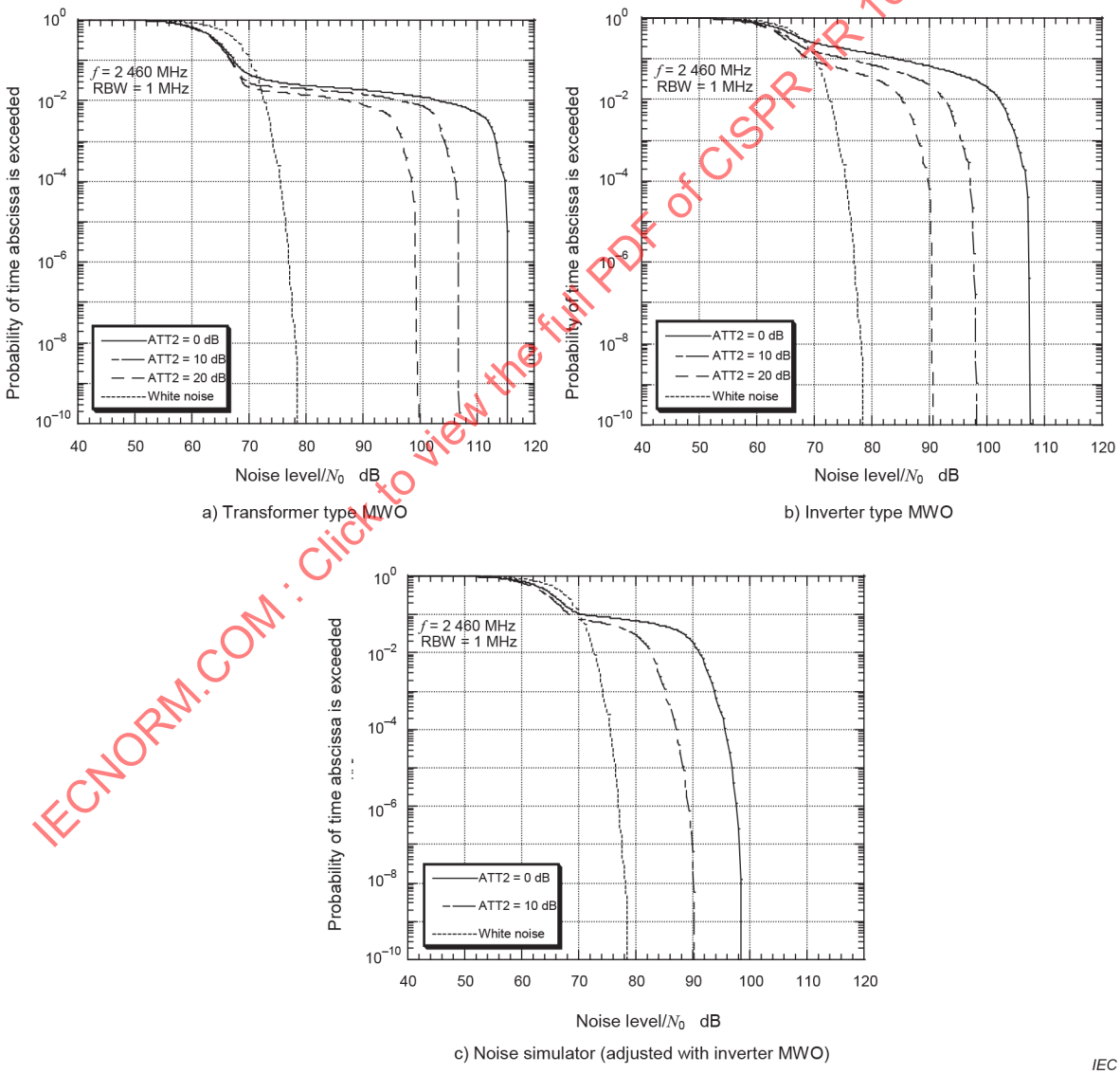

**Figure 117 – APD of disturbance of actual MWO (2 441MHz)**

IECNORM.COM : Click to view the full PDF of CISPR TR 16-3:2020 RLV

**Table 26 – Average and RMS values of noise level normalized by $N_0$**

| | | ATT2 | | | | White noise |
|---|---|---|---|---|---|---|
| | | 0 dB | 10 dB | 20 dB | 30 dB | |
| **Transformer type MWO** | Average (dB) | 89,8 | 80,8 | 73,7 | | 67,1 |
| | RMS (dB) | 99,2 | 90,2 | 82,5 | | 68,3 |
| **Inverter type MWO** | Average (dB) | 70,7 | 65,4 | 63,5 | | 67,1 |
| | RMS (dB) | 80,6 | 73,3 | 66,0 | | 68,3 |

The APDs measured at 2 460 MHz, where the noise level of an MWO is at maximum, are shown in Figure 118, and the average and RMS values of noise normalized by $N_0$ are shown in Table 27. The noise level is about 10 dB larger than that at the frequency of 2 441 MHz. The APD of the noise simulator at ATT2 = 0 dB is in good agreement with that of the inverter type MWO at ATT2 = 10 dB.




IECNORM.COM : Click to view the full PDF of CISPR TR 16-3:2020 RLV

**Figure 118 – APD characteristics of disturbance (2 460 MHz)**

**Table 27 – Average and RMS values of noise level normalized by $N_0$**

| | | ATT2 | | | | White noise |
|---|---|---|---|---|---|---|
| | | 0 dB | 10 dB | 20 dB | 30 dB | |
| **Transformer type MWO** | Average (dB) | 87,8 | 78,4 | 71,4 | | 67,1 |
| | RMS (dB) | 94,9 | 85,4 | 78,0 | | 68,3 |
| **Inverter type MWO** | Average (dB) | 70,7 | 65,4 | 63,5 | | 67,1 |
| | RMS (dB) | 80,6 | 73,3 | 66,0 | | 68,3 |
| **Noise simulator** | Average (dB) | 77,6 | 69,8 | | | 67,1 |
| | RMS (dB) | 84,1 | 75,5 | | | 68,3 |

The measured communication quality degradation for various amounts of attenuation of injected noise is shown in Figure 119.

There is only a minor difference in degradation caused by the level of noise between a transformer and an inverter type MWO. This is because Bluetooth performs frequency hopping, and is hard to be influenced by noise continuously. Furthermore, there is almost no difference in communication quality degradation for a noise simulator.

IECNORM.COM : Click to view the full PDF of CISPR TR 16-3:2020 RLV

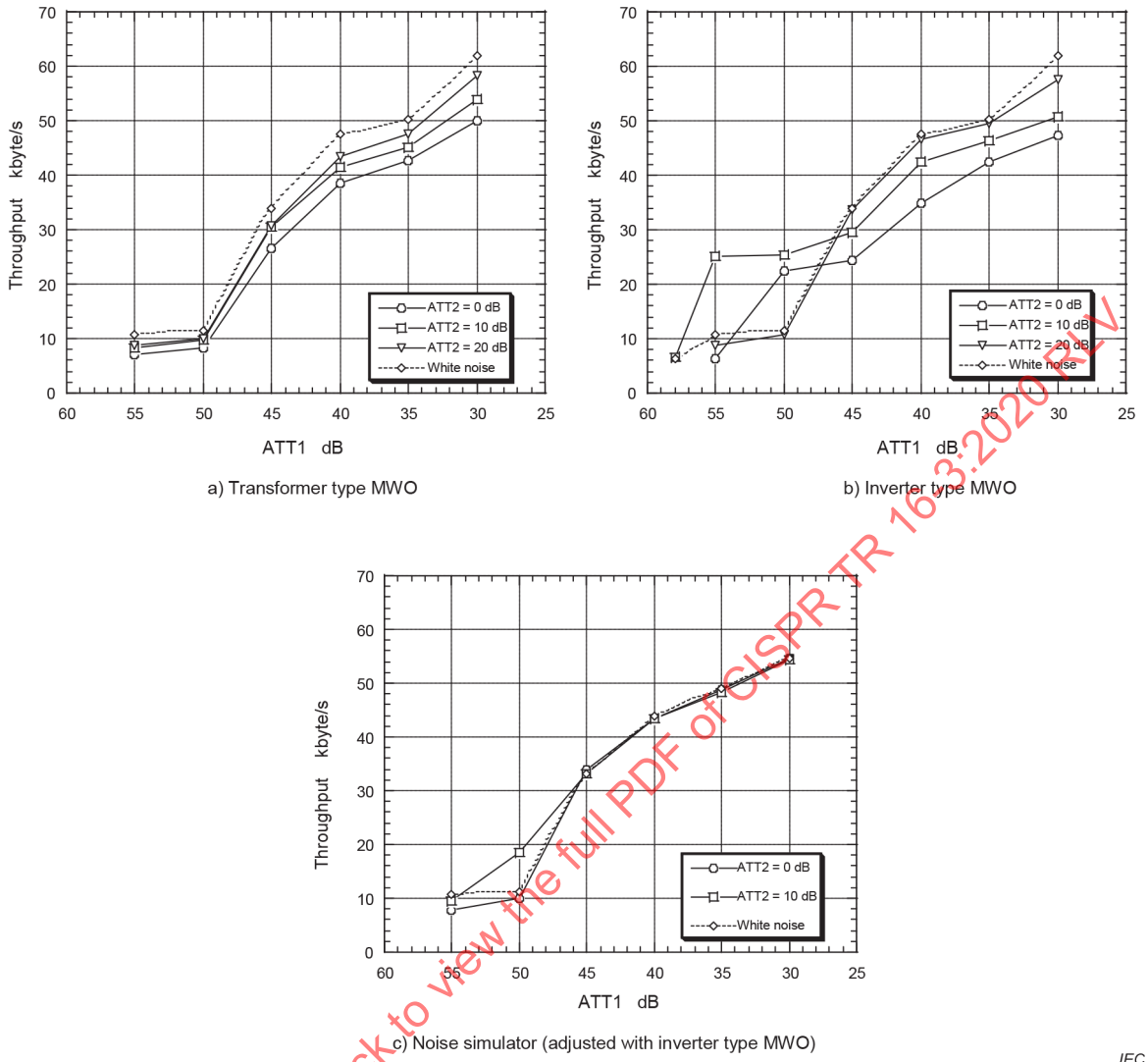



**Figure 119 – Throughput of Bluetooth influenced by noise**

According to the specifications, Bluetooth controls the transmission power automatically depending on the communication situation. The sub-carrier power at the reception point cannot be obtained uniquely since transmission power may change when ATT1 is changed. The horizontal axis in this figure shows the attenuation of signal power.

### 4.7.4 Influence on a W-CDMA system

The set-up for measuring communication quality degradation is shown in Figure 120, and measurement conditions are shown in Table 28.

Bit error rate (BER) was chosen as the measure for communication quality evaluation.

IECNORM.COM : Click to view the full PDF of CISPR TR 16-3:2020 RLV

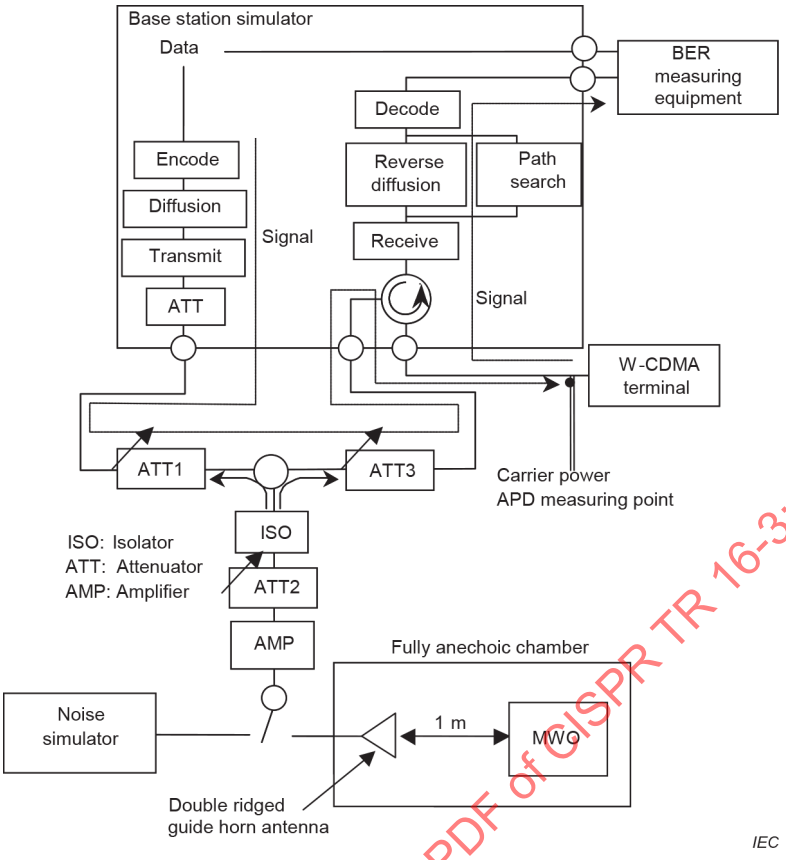



**Figure 120 – Set-up for measuring the BER of W-CDMA**

**Table 28 – Conditions for measuring communication quality degradation of W-CDMA**

| | | |
|---|---|---|
| **Baseband simulator** | Frequency | 2 137,6 MHz (downlink) |
| | Chip rate | 3,84 Mc/s |
| | Spread rate | Uplink: DPDCH 64 / downlink: DPCH 128 |
| | Data rate | 12,2 kb/s (acoustic) |
| | Transmission data | 6 Mb |
| | Transmission mode | RMC communication test (UE turn)<br>3GPP TS34.121 [84] |

The measured APDs of the noise are shown in Figure 121, and the average and RMS values of the noise level normalized by $N_0$ are shown in Table 29. The APD of the noise simulator at ATT2 = 0 dB is in good agreement with the APD of the inverter type MWO at ATT2 = 10 dB.

IECNORM.COM : Click to view the full PDF of CISPR TR 16-3:2020 RLV

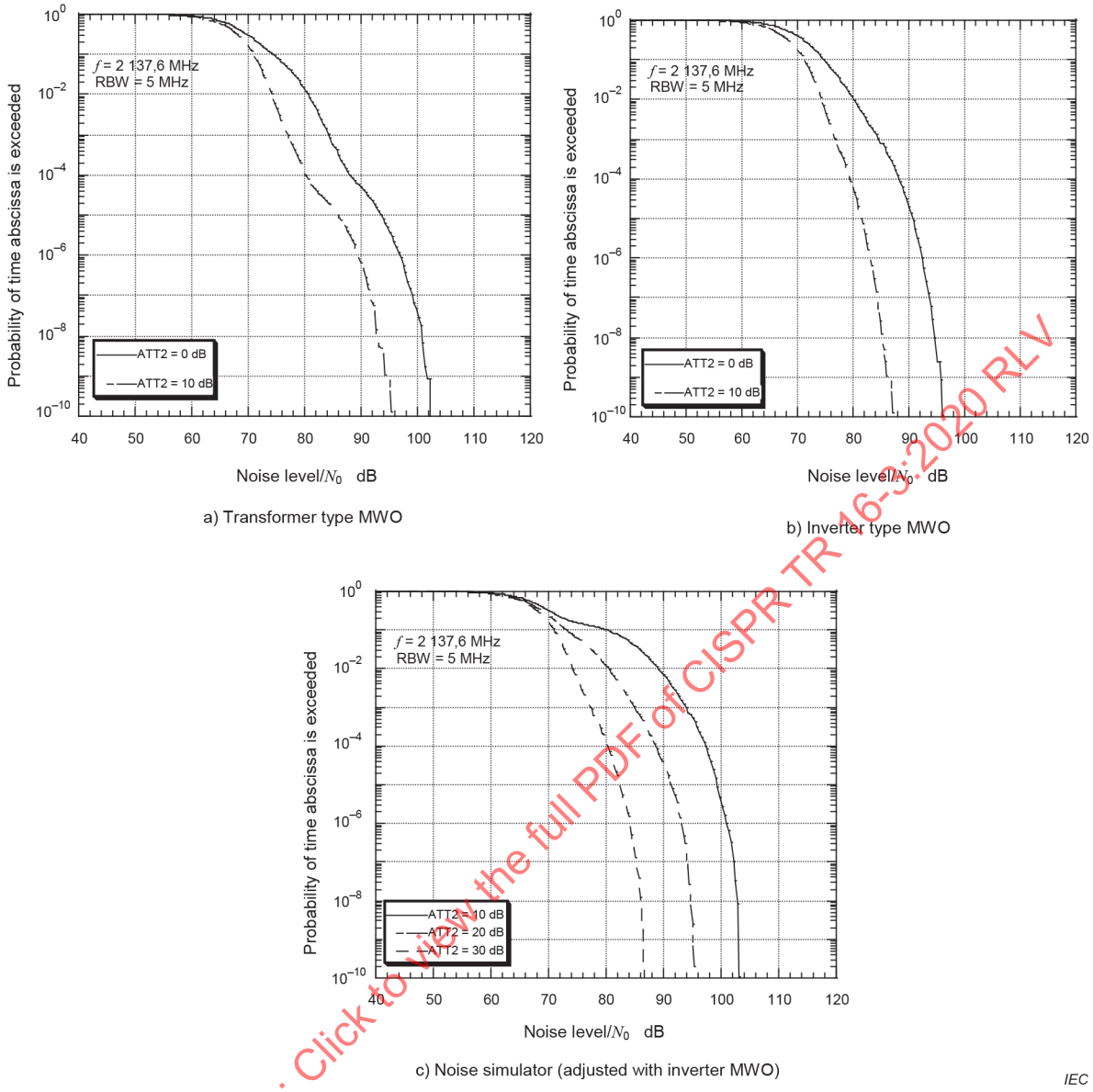



**Figure 121 – APD characteristics of disturbance**

**Table 29 – Average and RMS values of noise level normalized by $N_0$**

| | | ATT2 | | | | Receiver noise |
|---|---|---|---|---|---|---|
| | | 0 dB | 10 dB | 20 dB | 30 dB | |
| **Transformer type MWO** | Average (dB) | 71,1 | 67,7 | | | 67,2 |
| | RMS (dB) | 75,1 | 69,4 | | | 68,6 |
| **Inverter type MWO** | Average (dB) | 71,6 | 68,0 | | | 67,2 |
| | RMS (dB) | 74,7 | 69,4 | | | 68,6 |
| **Noise simulator** | Average (dB) | | 77,1 | 70,4 | 67,7 | 67,2 |
| | RMS (dB) | | 83,3 | 74,7 | 69,3 | 68,6 |

The measured communication quality degradation for various amounts of attenuation of injected noise is shown in Figure 122.

IECNORM.COM : Click to view the full PDF of CISPR TR 16-3:2020 RLV

For both types of MWO, the BER was degraded by several dB after a 10 dB change in noise level. Moreover, BER characteristics influenced by the noise simulator are in good agreement in these measurement results.

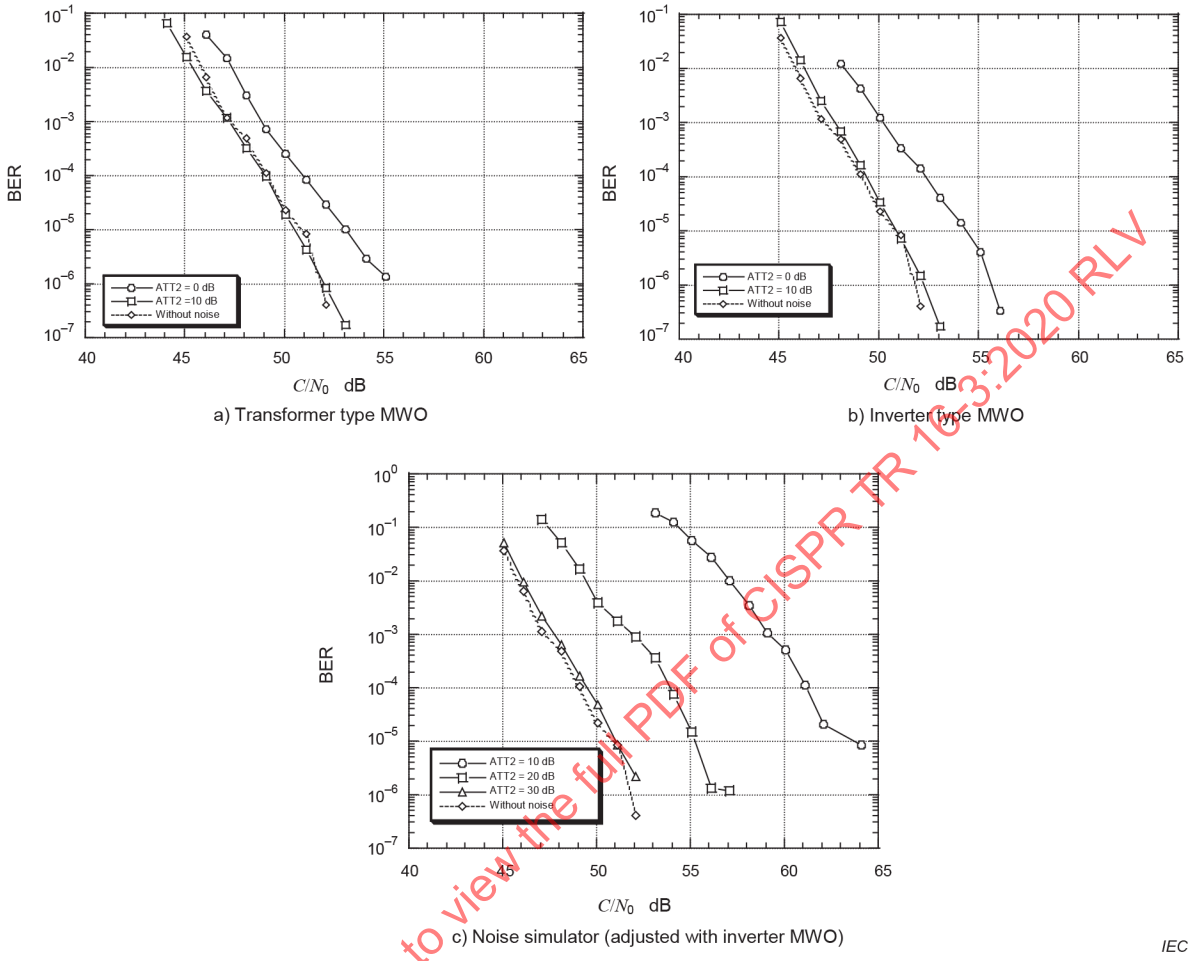



**Figure 122 – BER of W-CDMA caused by radiation noise**

### 4.7.5 Influence on Personal Handy Phone System (PHS)

The set-ups for measuring communication quality degradation are shown in Figure 123 and Figure 124, and conditions for measuring throughput and BER are shown in Table 30 and Table 31.

Throughput and BER were chosen as measures for evaluating the communication quality of PHS.

The measured APDs are shown in Figure 125, and the average and RMS values of noise normalized by $N_0$ are shown in Table 32.

IECNORM.COM : Click to view the full PDF of CISPR TR 16-3:2020 RLV

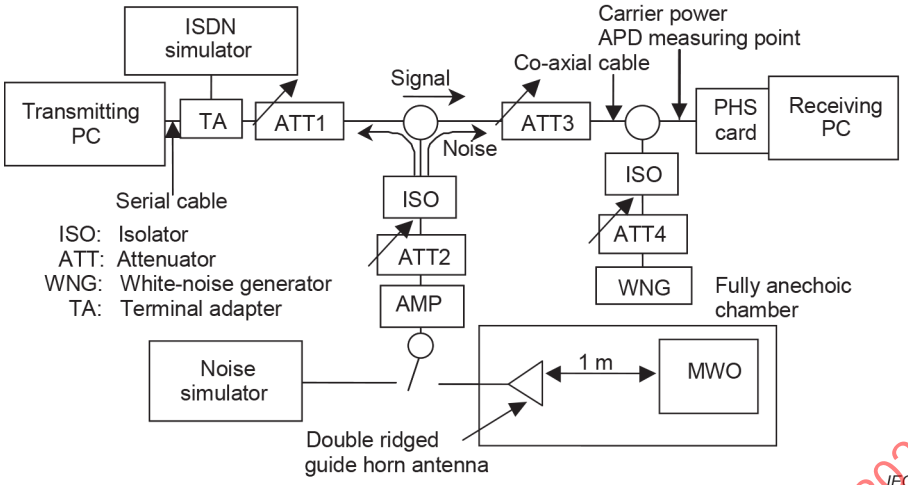



**Figure 123 – Set-up for measuring the PHS throughput**

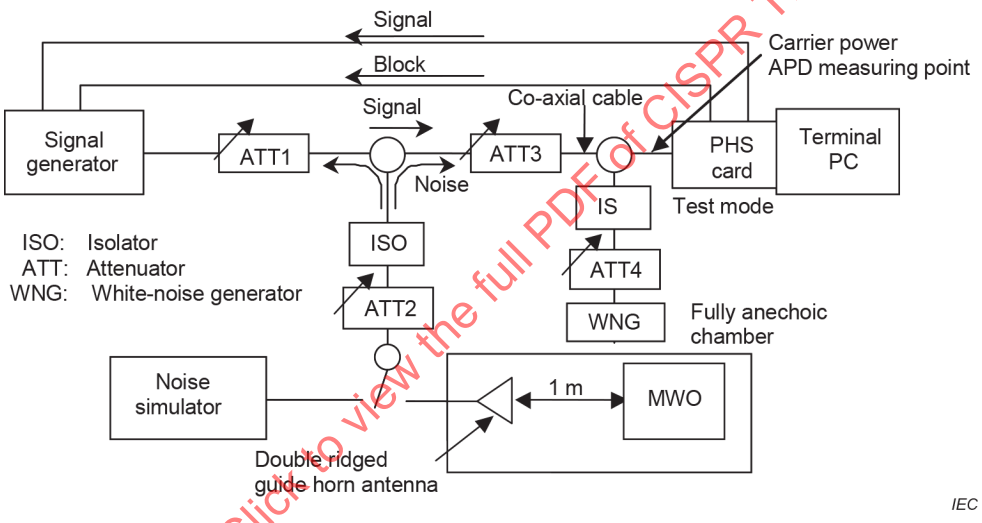



**Figure 124 – Set-up for measuring the BER of PHS**

**Table 30 – Conditions for measuring the PHS throughput**

| | | |
|---|---|---|
| **PHS** | Transmission data | About 376 kB data |
| | Transmission system | Non protocol |
| | Transmission mode | 32 kb/s real time data transmission |
| **Others** | Noise power density $N$ (dBm/Hz) | –160 dBm/Hz (set by ATT4) |

**Table 31 – Conditions for measuring the BER of PHS**

| | | |
|---|---|---|
| **PHS** | Frequency (channel number) | 1 907,15 MHz (channel 41) |
| | Transmission data | 5 Mb PN9 |
| | Data rate | 32 kb/s |
| **Others** | Noise power density (dBm/Hz) | –160 /Hz (set by ATT4) |

IECNORM.COM : Click to view the full PDF of CISPR TR 16-3:2020 RLV

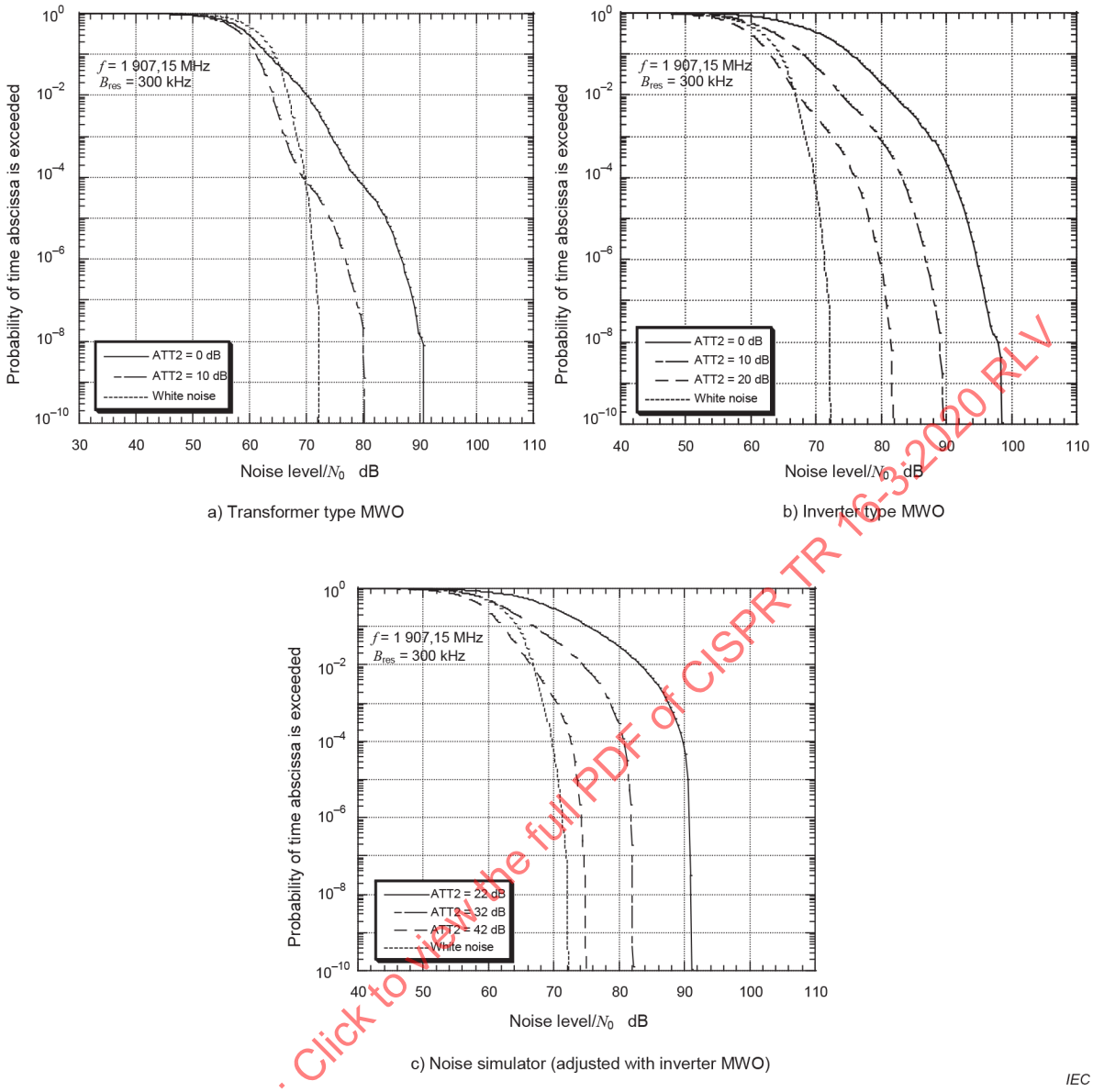



**Figure 125 – APD characteristics of disturbance**

**Table 32 – Average and RMS values of noise level normalized by $N_0$**

| | | ATT2 | | | | White noise |
|---|---|---|---|---|---|---|
| | | 0 dB | 10 dB | 20 dB | 30 dB | |
| **Transformer type MWO** | Average (dB) | 60,6 | 58,1 | | | 61,2 |
| | RMS (dB) | 64,9 | 59,4 | | | 62,4 |
| **Inverter type MWO** | Average (dB) | 72,6 | 64,9 | 59,9 | 58,0 | 61,2 |
| | RMS (dB) | 76,7 | 68,9 | 62,5 | 59,3 | 62,4 |
| **Noise simulator** | Average (dB) | 72,3 | 64,2 | 59,1 | 57,8 | 61,2 |
| | RMS (dB) | 77,0 | 68,2 | 61,1 | 59,0 | 62,4 |
| NOTE The values of ATT2 are 22 dB, 32 dB, 42 dB and 52 dB, respectively for the noise simulator. | | | | | | |

The measured throughput for various amounts of attenuation of injected noise is shown in Figure 126.

IECNORM.COM : Click to view the full PDF of CISPR TR 16-3:2020 RLV

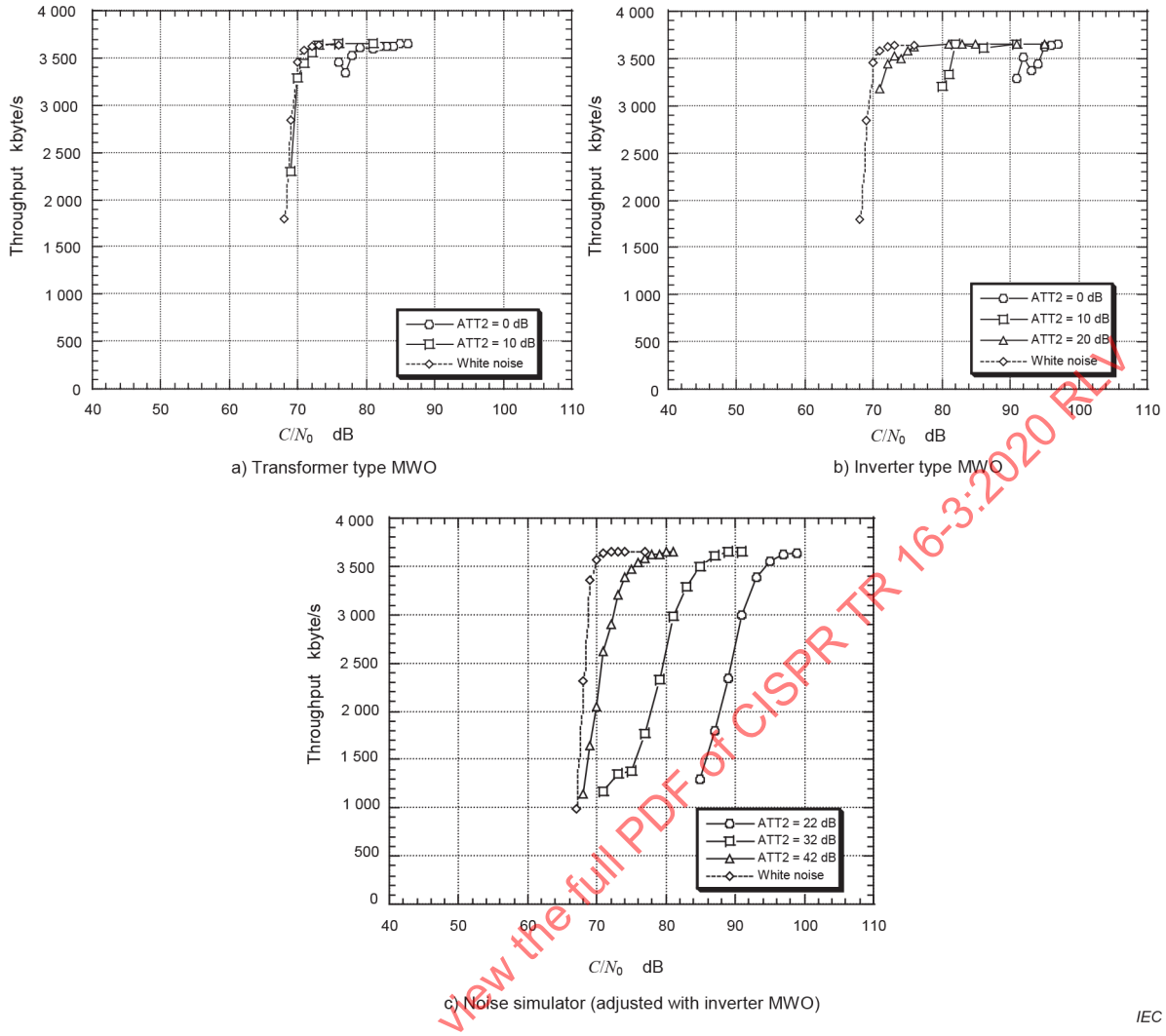



**Figure 126 – PHS throughput caused by radiation**

Similarly, the measured BER is shown in Figure 127. The BER characteristics caused by the noise simulator were in good agreement in the measurement results of the inverter-type MWO.

IECNORM.COM : Click to view the full PDF of CISPR TR 16-3:2020 RLV

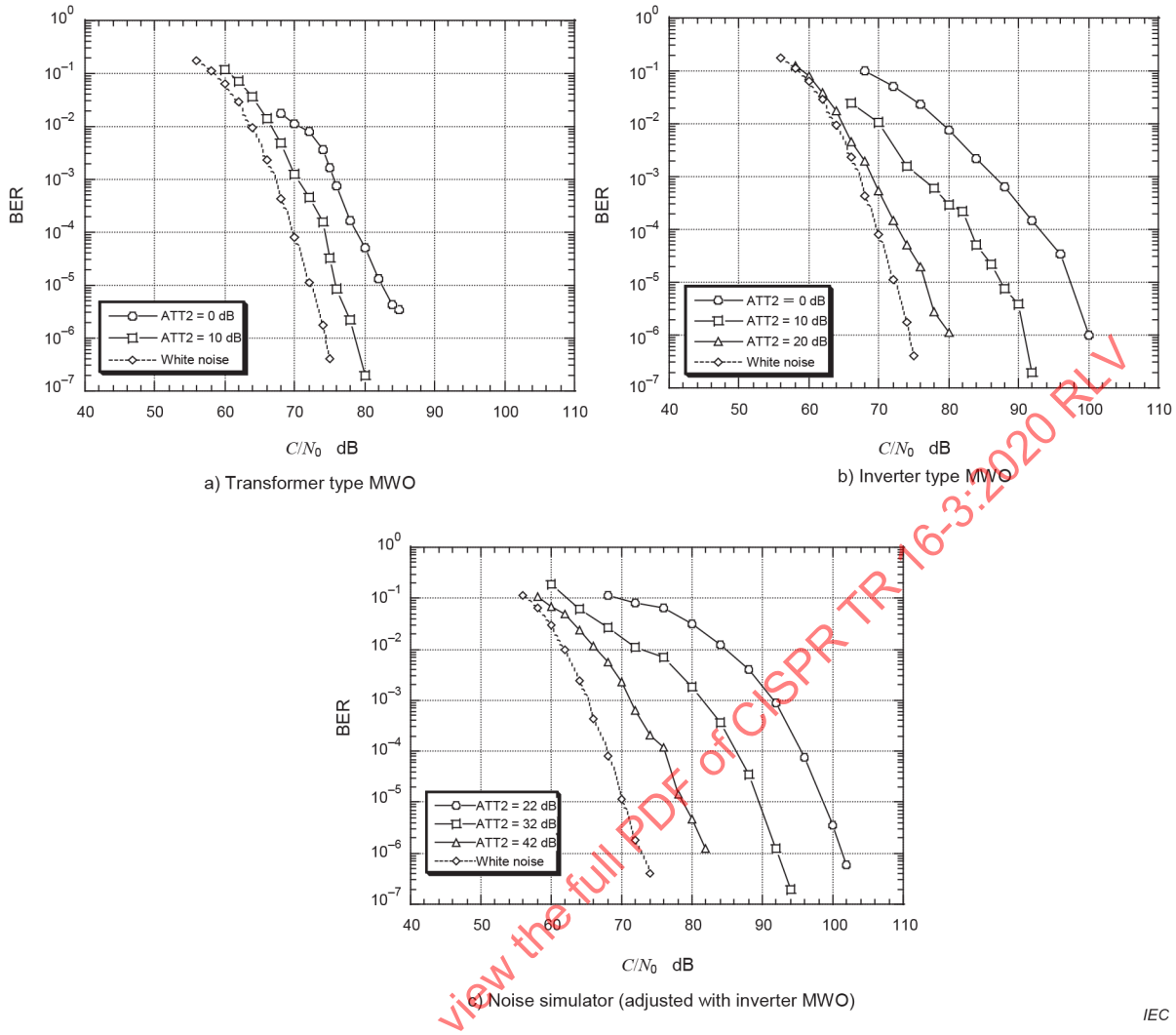



**Figure 127 – BER of PHS caused by radiation noise**

IECNORM.COM : Click to view the full PDF of CISPR TR 16-3:2020 RLV

### 4.7.6 Quantitative correlation between noise parameters and system performance

#### 4.7.6.1 General

Correlations between the noise parameter of the disturbance (levels of disturbance correspond to certain probability that is derived from APD) and degradation of system performance (throughput and/or bit error rate) are evaluated for the communication systems described in 4.7.2 to 4.7.5.

#### 4.7.6.2 Wireless LAN (throughput)

From Figure 114 a) and Figure 114 b), the disturbance voltage for each probability, e.g. $10^{-1}$, $10^{-2}$, $10^{-3}$, $10^{-4}$, was read. $C/N_0$ values that are necessary to assure the throughput of 500 kByte/s under microwave oven disturbance were obtained from Figure 115 a) and Figure 115 b). The correlation between the disturbance voltages and the $C/N_0$ values is plotted in Figure 128 a) and Figure 128 b) for a transformer type oven and inverter type oven, respectively.

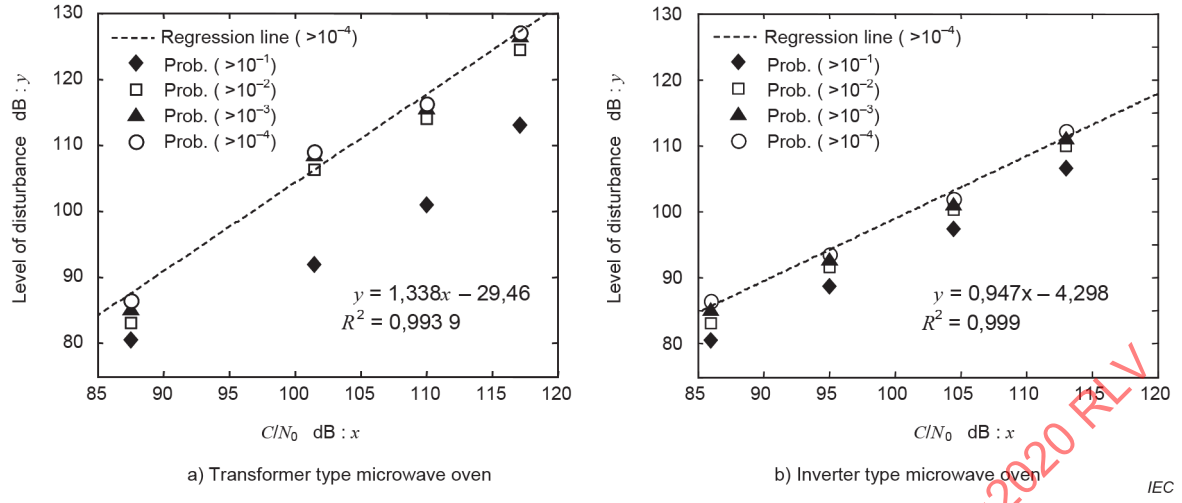



**Figure 128 – Correlation of the disturbance voltages with the system performance ($C/N_0$)**

In Figure 128, the linear regression line by using the values for $10^{-4}$ probability is also plotted with the equation and correlation coefficients $R$. It is found that $10^{-4}$ probability values are well correlated to the $C/N_0$ and thus these values are suitable for the noise parameters to estimate the degradation of the system performance.

#### 4.7.6.3 Bluetooth (throughput)

From Figure 118 a) and Figure 118 b), the disturbance voltage for each probability was read. As shown in Figure 116, not only MWO disturbance but also white noise was injected to the communication link. Then, disturbance voltages are meaningful only when MWO disturbance exceeds the white noise. Therefore, probability of $10^{-1}$ value was ignored and probability of $10^{-2}$, $10^{-3}$ and $10^{-4}$ values were used in the evaluation below.

Relative $C/N_0$ values that are necessary to assure the throughput of 40 kByte/s under microwave oven disturbance were obtained from Figure 119 a) and Figure 119 b) (relative $C/N_0$ = dB corresponds to ATT1 = 43 dB). The correlation between the disturbance voltages and the relative $C/N_0$ values are plotted in Figure 129 a) and Figure 129 b) for a transformer type oven and inverter type oven, respectively.

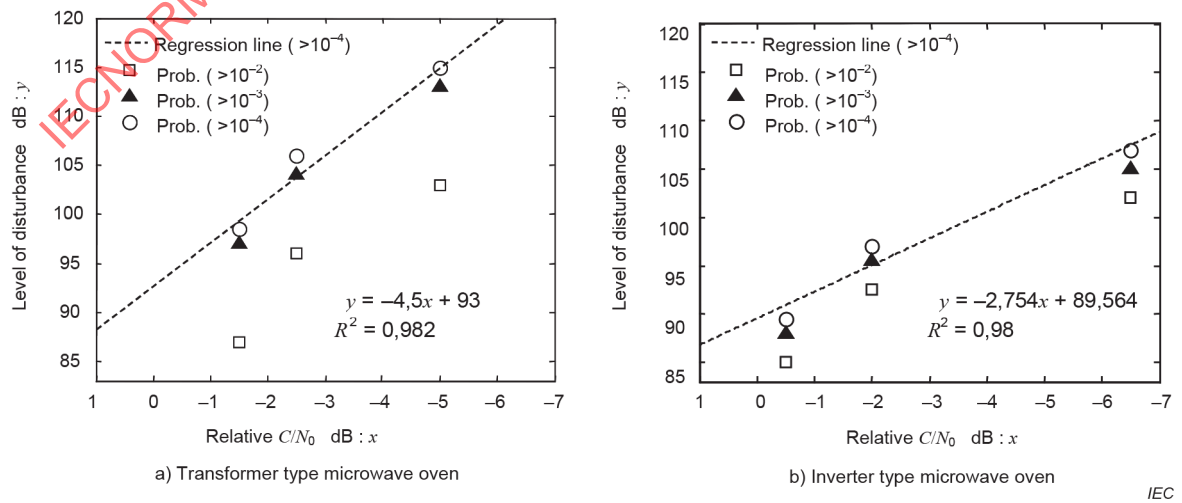



**Figure 129 – Correlation of the disturbance voltages with the system performance**

IECNORM.COM : Click to view the full PDF of CISPR TR 16-3:2020 RLV

In Figure 129, the linear regression line by using the values for $10^{-4}$ probability is also plotted with the equations and correlation coefficients. The same results were obtained as in 4.7.6.1.

#### 4.7.6.4 W-CDMA (BER)

From Figure 121 a) and Figure 121 b), disturbance voltages for each probability, e.g. $10^{-2}$, $10^{-3}$, $10^{-4}$ were read. $C/N_0$ values that are necessary to assure the BER of $10^{-4}$ under microwave oven disturbance were obtained from Figure 130 a) and Figure 130 b). Because only two curves available are in the APD and BER, regression analyses were not performed.

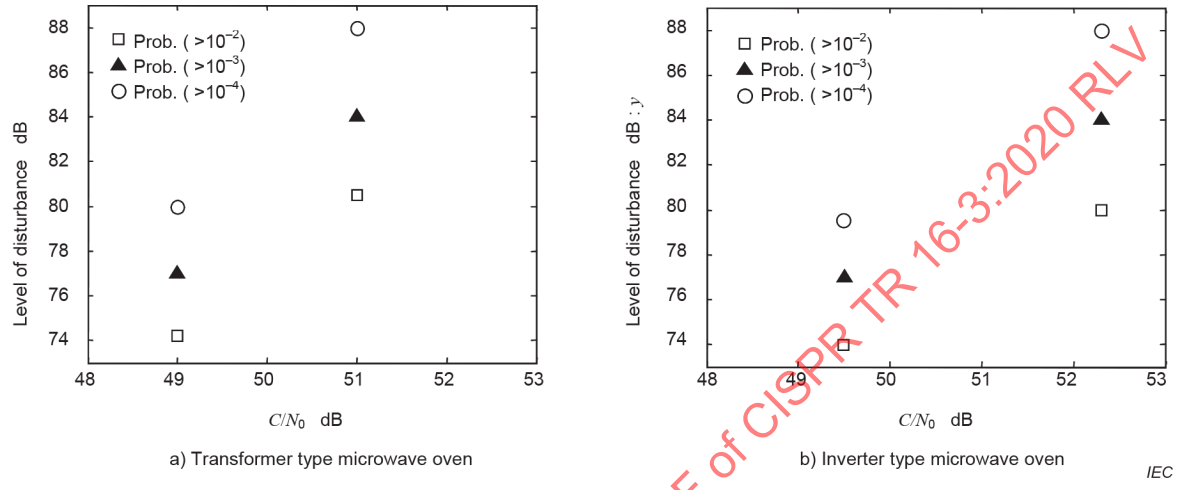



**Figure 130 – Correlation of the disturbance voltages with the system performance**

#### 4.7.6.5 PHS (BER and throughput)

Same analyses were performed on PHS data. $C/N_0$ values correspond to the signal input that is necessary to assure the BER of $10^{-4}$ under microwave oven disturbance. The correlation between the disturbance level and the $C/N_0$ values is plotted in Figure 131 a) and Figure 131 b) for a transformer type oven and inverter type oven, respectively.

Because only one set of data was usable in the APD and BER for the transformer type oven, regression analysis was not performed. On the other hand, excellent correlation was confirmed in the case of inverter type oven.

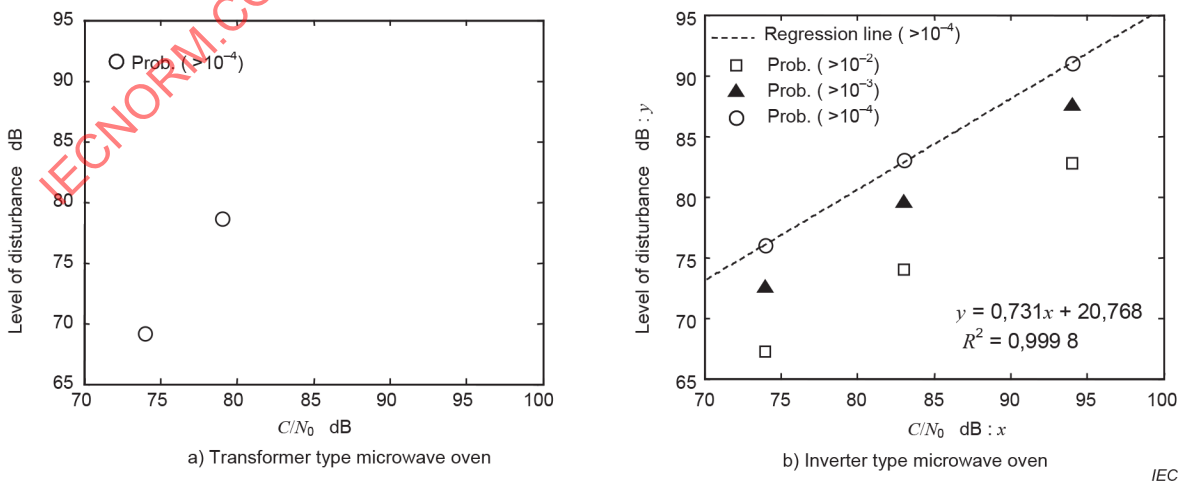



**Figure 131 – Correlation of the disturbance voltages with the system performance ($C/N_0$)**

IECNORM.COM : Click to view the full PDF of CISPR TR 16-3:2020 RLV

Additional analyses were performed on PHS data. From Figure 125 a) and Figure 125 b), disturbance voltages for each probability were read. $C/N_0$ values corresponding to the signal input that was necessary to assure the throughput of 3,5 kByte/s under microwave oven disturbance were read from Figure 115 a) and Figure 115 b). The correlation between the disturbance level and the $C/N_0$ values are plotted in Figure 132 a) and Figure 132 b) for a transformer type oven and inverter type oven, respectively. The same results were obtained as for the correlation with BER.

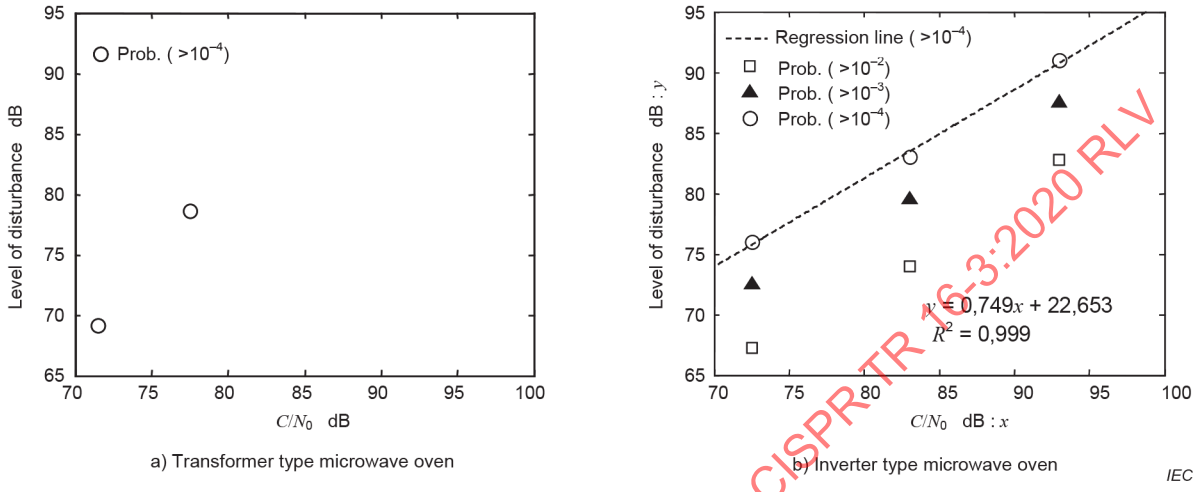



**Figure 132 – Correlation of the disturbance voltages with the system performance ($C/N_0$)**

### 4.7.7 Quantitative correlation between noise parameters of repetition pulse and system performance of PHS and W-CDMA (BER)

Correlations between APD of repetition pulse noise and communication quality degradation of PHS and W-CDMA are obtained by the following additional experiment and simulation. The experimental set-up for measuring communication quality degradation of the PHS or W-CDMA is shown in Figure 133. Repetition pulses combined with Gaussian noise are used as a disturbance. The Gaussian noise level is adjusted to the same noise floor level of vector signal analyzer for BER measurement and spectrum analyzer for APD measurement. Concerning repetition pulses, the pulse width is constant (100 μs) and the repetition frequency is variable. Figure 134 shows a block-diagram of numerical simulation for estimating communication quality degradation. In this simulation, the same noise parameters are used as for the experiment.

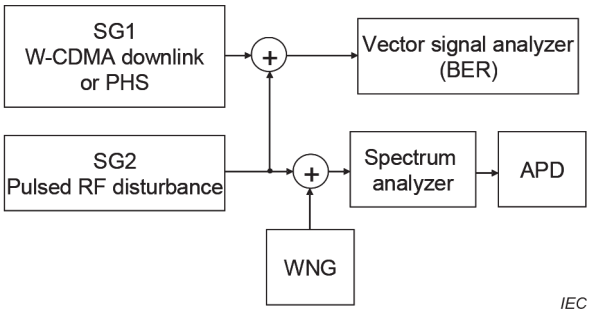



**Figure 133 – Experimental set-up for measuring communication quality degradation of a PHS or W-CDMA**

IECNORM.COM : Click to view the full PDF of CISPR TR 16-3:2020 RLV

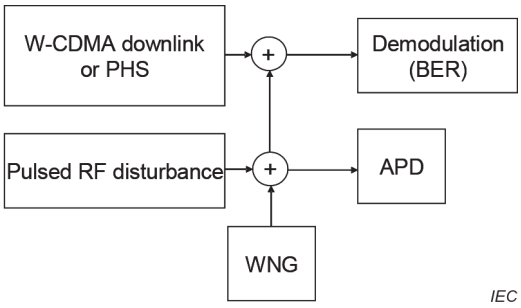



**Figure 134 – Simulation set-up for estimating communication quality degradation of a PHS or W-CDMA**

Measured APD are shown in Figure 135. Marker type represents the duty cycle of the pulse disturbance, i.e. circle, inverted triangle, triangle, diamond, square and star indicate 40 %, 10 %, 4 %, 1 %, 0,4 %, respectively. The dashed line shows the APD of Gaussian noise without repetition pulse.

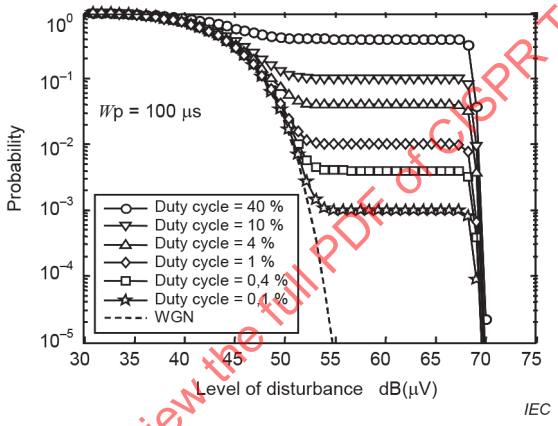



**Figure 135 – APD of pulse disturbance**

Measured BER and estimated BER by numerical simulations are shown in Figure 136 a) and Figure 136 b) for PHS system and W-CDMA system, respectively. Measured BER can be verified by the numerical simulation results. In the case of PHS results, simulation results do not show full agreement at high signal level since the simulation model of receiver is simplified as $\pi/4$ QPSK with a synchronized detector that is different from the experimental setup.

IECNORM.COM : Click to view the full PDF of CISPR TR 16-3:2020 RLV

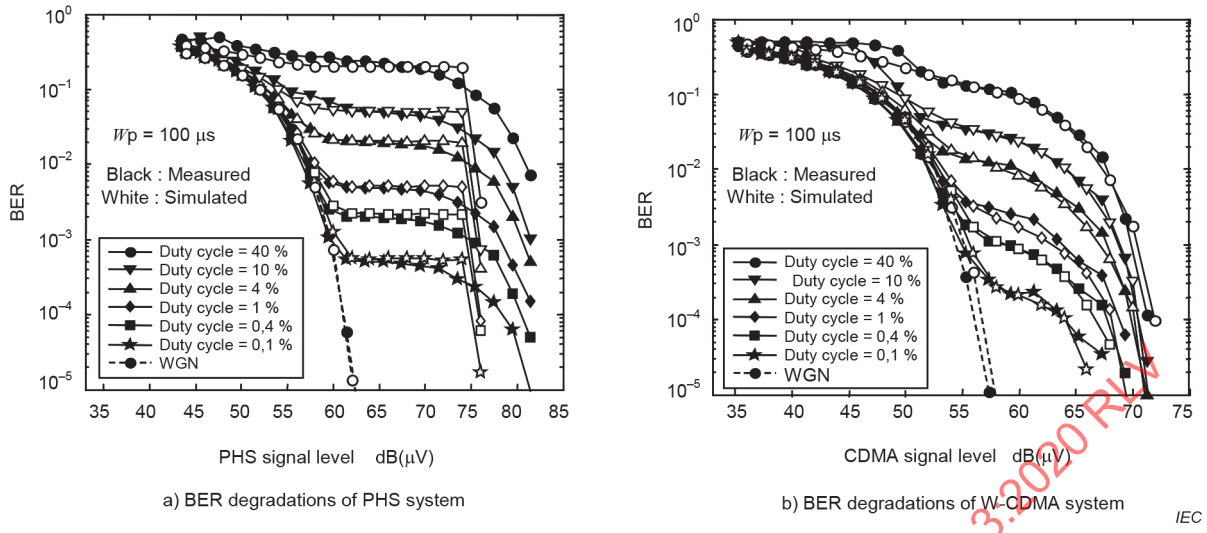



**Figure 136 – BER degradation of PHS and W-CDMA caused by repetition pulse (Carrier power, –35 dBm)**

Figure 137 explains the evaluation method for quantitative correlation between BER and APD. For the level comparison, $\Delta L_{BER}$ and $\Delta L_{APD}$ can be defined as disturbance effects on BER and APD. They are measured by the difference of level between Gaussian noise (without repetition pulse) and disturbance (with repetition pulse) at a certain rate of BER and at a certain probability of APD, respectively. Similarly, $p_{BER}$ and $p_{APD}$ are defined as the probabilities caused by disturbance on BER and APD, respectively.

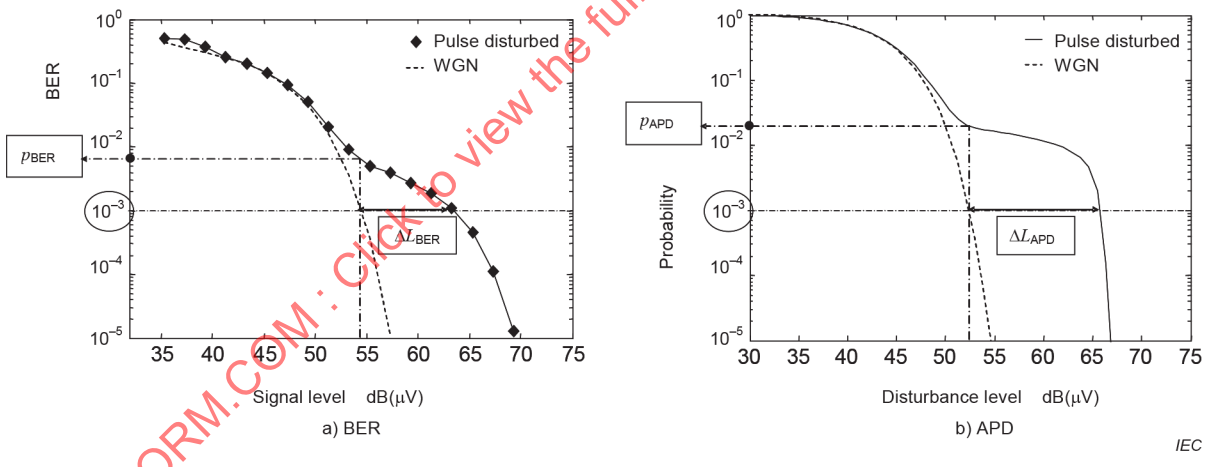



**Figure 137 – Evaluation method of the correlation between BER and APD**

Correlation between measured $\Delta L_{BER}$ and $\Delta L_{APD}$ for several pulse amplitudes are shown in Figure 138 where the pulse has constant duty cycle (10 %, pulse width: 100 µs). The disturbance is generated by modulating a carrier with the repetition pulse. The carrier power is set from –45 dBm to –35 dBm with 2 dB step. Black mark and white mark show the characteristics of W-CDMA and PHS, respectively. BER and probability values ($BER_0$, $APD_0$) selected for these evaluations are (a) $10^{-2}$, (b) $10^{-3}$ and (c) $10^{-4}$.

IECNORM.COM : Click to view the full PDF of CISPR TR 16-3:2020 RLV

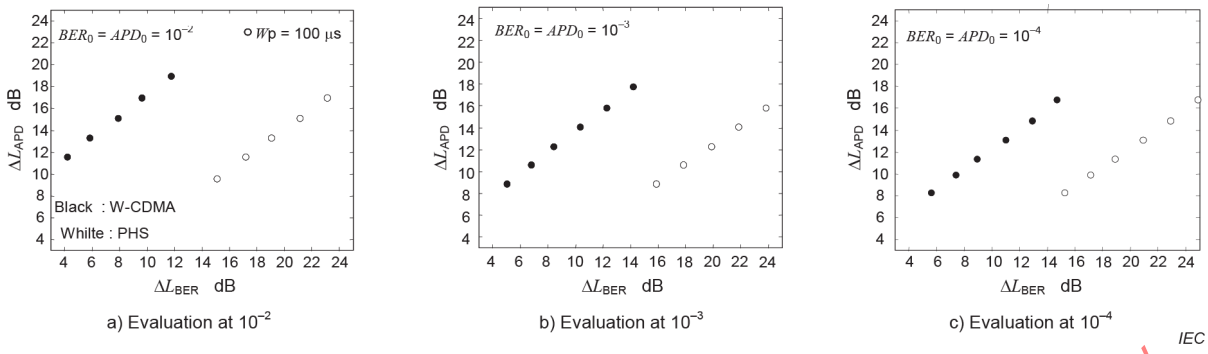



**Figure 138 – Correlation between measured $\Delta L_{BER}$ and $\Delta L_{APD}$**

Correlation between measured $p_{BER}$ and $p_{APD}$ for several duty cycles of the pulse disturbance are also shown in Figure 139, where the disturbance has constant carrier power (-35 dBm). The duty cycle is changed as 40 %, 10 %, 4 %, 1 %, 0,4 % and 0,1 %. Black mark and white mark show the characteristics of W-CDMA and PHS respectively. Diamond, circle, triangle and square marks indicate the results for the pulse width 1 000 µs, 100 µs, 10 µs and 1 µs respectively. BER and probability values ($BER_0$, $APD_0$) selected for these evaluations are (a) $10^{-2}$, (b) $10^{-3}$ and (c) $10^{-4}$.

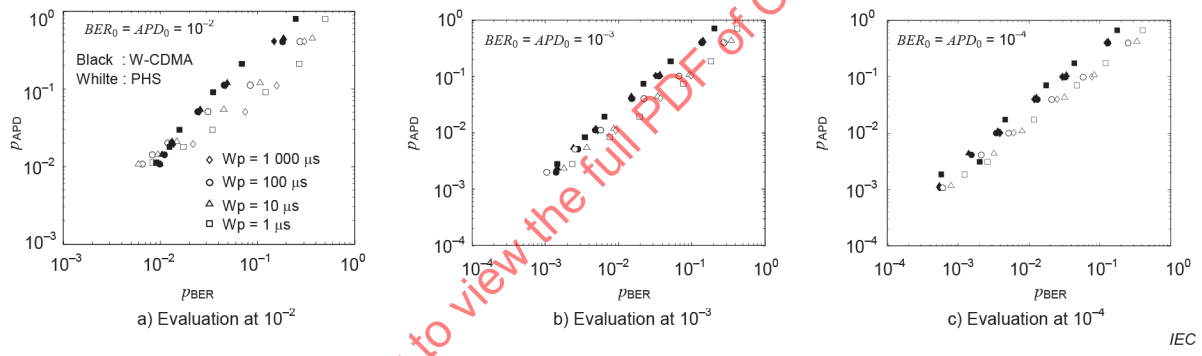



**Figure 139 – Correlation between measured $p_{BER}$ and $p_{APD}$**

In all cases, APD indices ($\Delta L_{APD}$, $p_{APD}$) have close correlation with BER degradation indices ($\Delta L_{BER}$, $p_{BER}$), respectively. It is therefore concluded that APD measurement of the disturbance is one of the most effective methods for evaluating the interference potential on digital communication systems.

## 4.8 Background material on the definition of the RMS-average weighting detector for measuring receivers

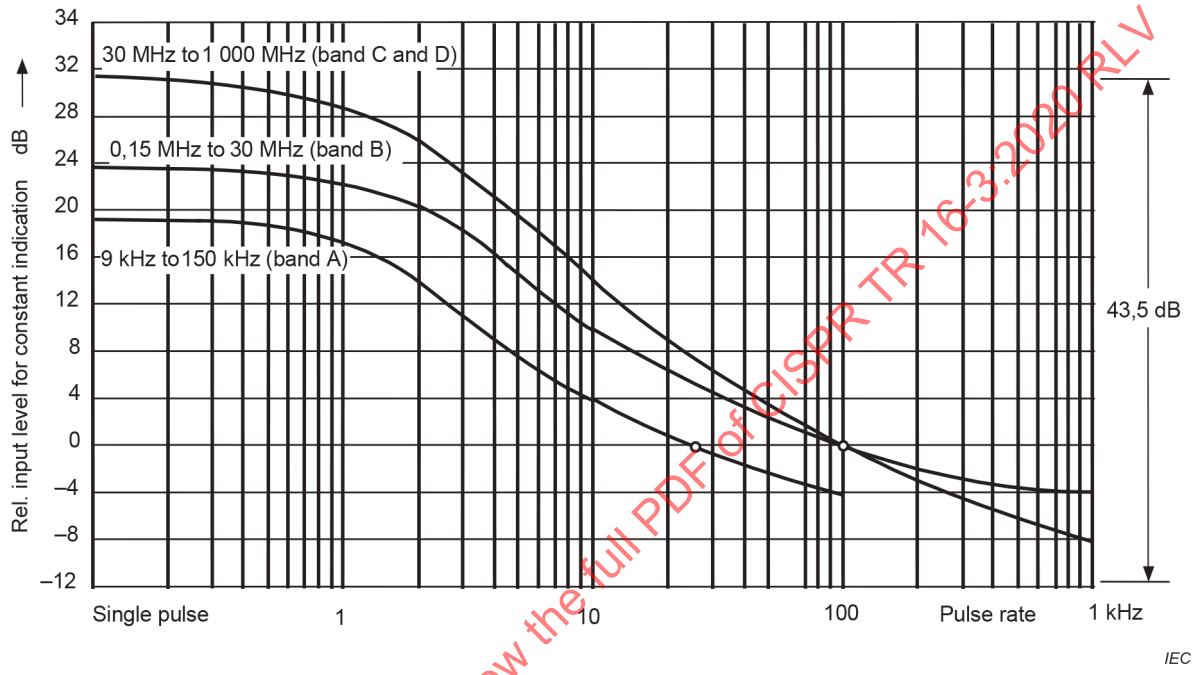
### 4.8.1 General – purpose of weighted measurement of disturbance

Generally, a weighted measurement of impulsive disturbance serves the purpose of minimizing the cost of disturbance suppression, while keeping an agreed level of radio protection. The weighting of a disturbance for its effect on modern digital radiocommunication services is important for the definition of emission limits that protect these services. CISPR 16-1-1 defines a detector that is a combination of an RMS and an average detector. The selection of the type of detector and of the transition between these detector functions is based on measurements and theoretical investigations.

IECNORM.COM : Click to view the full PDF of CISPR TR 16-3:2020 RLV

### 4.8.2 General principle of weighting – the CISPR quasi-peak detector

The effect on radiocommunication services depends on the type of interference (e.g. broadband or narrowband, pulse rate etc.) and on the type of service itself. The effect of the pulse rate was recognized a short time after CISPR was founded in 1933. As a result, the quasi-peak weighting receiver for the frequency range of 150 kHz to 1 605 kHz was defined as shown for band B in Figure 140. However in CISPR 1 [1] it was already accepted that "Subsequent experience has shown that the RMS voltmeter might give a more accurate assessment" but the quasi-peak type of voltmeter has been retained for certain reasons – mainly for continuity.




NOTE The weighting factor is shown relative to a reference pulse rate (25 Hz or 100 Hz).

**Figure 140 – Weighting curves of quasi-peak measuring receivers for the different frequency ranges as defined in CISPR 16-1-1**

### 4.8.3 Other detectors defined in CISPR 16-1-1

#### 4.8.3.1 Peak detector

The peak detector follows the signal at the output of the IF envelope detector and holds the maximum value during the measurement time (also called dwell time) until its discharge is forced. This indication is independent of the pulse repetition frequency (PRF).

#### 4.8.3.2 Average detector

The average detector determines the linear average of the signal at the output of the IF envelope detector. It should be kept in mind that for low PRFs, CISPR 16-1-1 specifies the average detector measurement result as the maximum scale deflection of a meter with a time constant specified for the quasi-peak detector. This is necessary to avoid reduced level indication for a pulse modulated disturbance by using long measurement times. The weighting function varies with 20 dB per decade of the PRF (see Figure 141).

IECNORM.COM : Click to view the full PDF of CISPR TR 16-3:2020 RLV

#### 4.8.3.3 RMS detector

The RMS detector determines the RMS value of the signal at the output of the IF envelope detector. Despite being mentioned in [1] and being described in CISPR 16-1-1, at the time of writing of this subclause it has not been put to practical use in CISPR product standards. The weighting function varies with 10 dB per decade of the PRF (see Figure 141). Up to now, no meter time constant applies for the RMS detector for intermittent, unsteady and drifting narrowband disturbances.

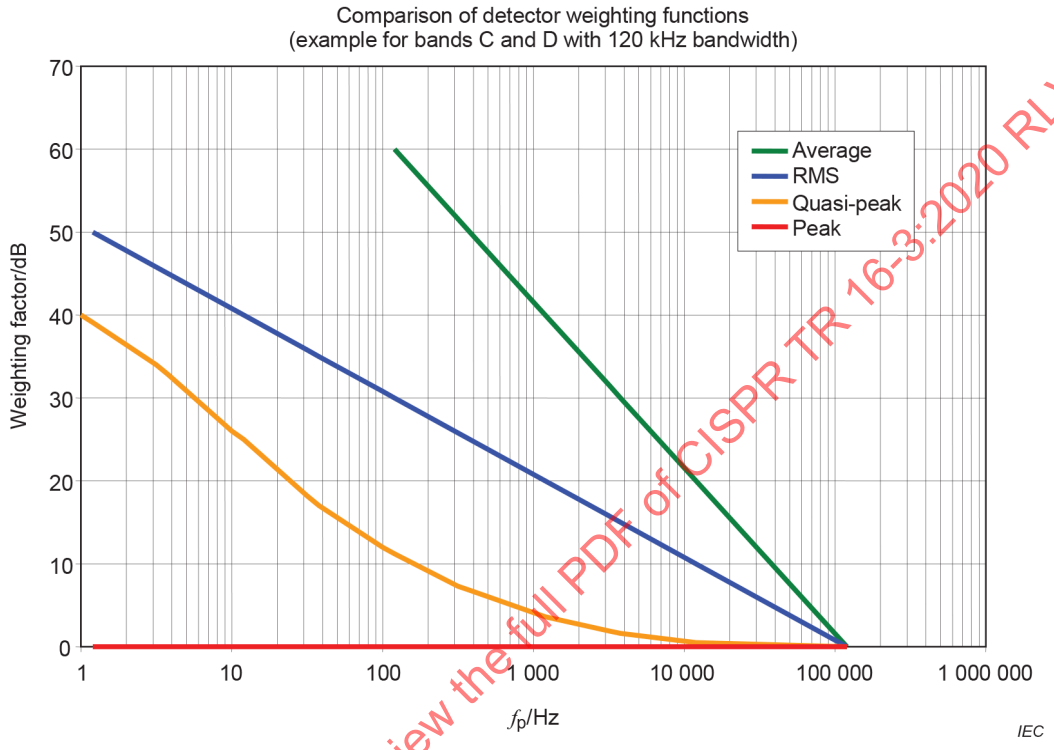



**Figure 141 – Weighting curves for peak, quasi-peak, RMS and linear average detectors for CISPR bands C and D**

### 4.8.4 Procedures for measuring pulse weighting characteristics of digital radiocommunications services

#### 4.8.4.1 General

All modern radio services use digital modulation schemes. This is not only true for mobile radio but also for audio and TV. Procedures for data compression and processing of analog signals (voice and picture) are used together with data redundancy for error correction. Usually, up to a certain critical bit-error ratio (BER) the system can correct errors so that perfect reception occurs.

Whereas analog radio systems require signal-to-noise ratios of as much as 50 dB for satisfactory operation, in general, digital radio communication systems allow error-free operation down to signal-to-noise ratios of approximately 10 dB. However the transition region from error-free operation to malfunction is small. Therefore planning guidelines for digital radio are based on almost 100 % coverage. When a digital radio receiver operates at low input levels, the susceptibility to radio disturbance is important. In mobile radio reception, the susceptibility to radio disturbance is combined with the problem of multi-path propagation.

IECNORM.COM : Click to view the full PDF of CISPR TR 16-3:2020 RLV

#### 4.8.4.2 Principles of measurement

The significance of the weighting curve for band B is as follows: to a listener the degradation of reception quality, caused by a 100-Hz pulse, is equivalent to the degradation from a 10-Hz pulse, if the pulse level is increased by an amount of 10 dB. In analogy to the above, an interference source with certain characteristics will produce a certain BER, e.g. $10^{-3}$ in a digital radiocommunication system, when the interfering signal is received in addition to the radio signal. The BER will depend e.g. on the pulse repetition frequency (PRF) and the level of the interfering signal. In order to keep the BER constant, the level of the interfering signal will have to be readjusted while the PRF is varied. This level variation versus PRF determines the weighting characteristics. Measurement systems with BER indication are needed to determine the required level of the interfering signal for a constant BER as e.g. shown in Figure 142.

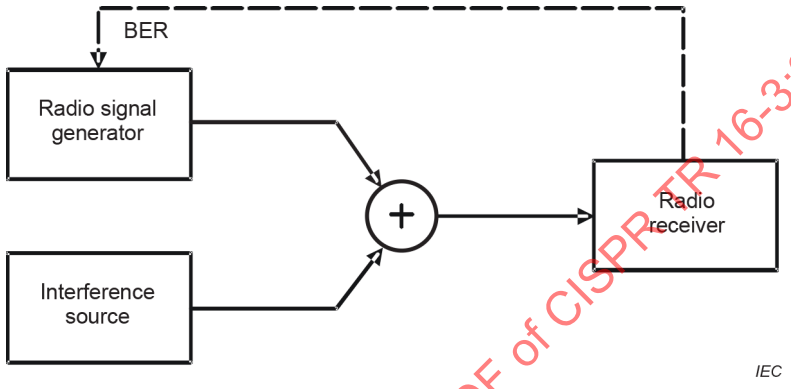



**Figure 142 – Test setup for the measurement of the pulse weighting characteristics of a digital radiocommunication system**

The test set-up shown in Figure 142 consists of a radio signal generator that transmits the wanted radio signal to the receiver. For the determination of the BER, the radio receiver either has to know the original bit sequence for comparison with the detected bit sequence or the latter shall be looped back to the radio signal generator for comparison with the original. Both systems are available and have been used for tests. Mobile radio testers, e.g. apply the loop-back principle.

#### 4.8.4.3 Generation of the interference signal

A signal generator with pulse-modulation capability can be used to generate the interference signal. For correct measurements, the pulse modulator requires a high ON/OFF ratio of more than 60 dB. Using the appropriate pulse width, the interference spectrum can be broadband or narrowband, where the definition of broadband and narrowband is relative to the communication channel bandwidth. Figure 143 gives an example of an interference spectrum used for the determination of weighting characteristics.

IECNORM.COM : Click to view the full PDF of CISPR TR 16-3:2020 RLV

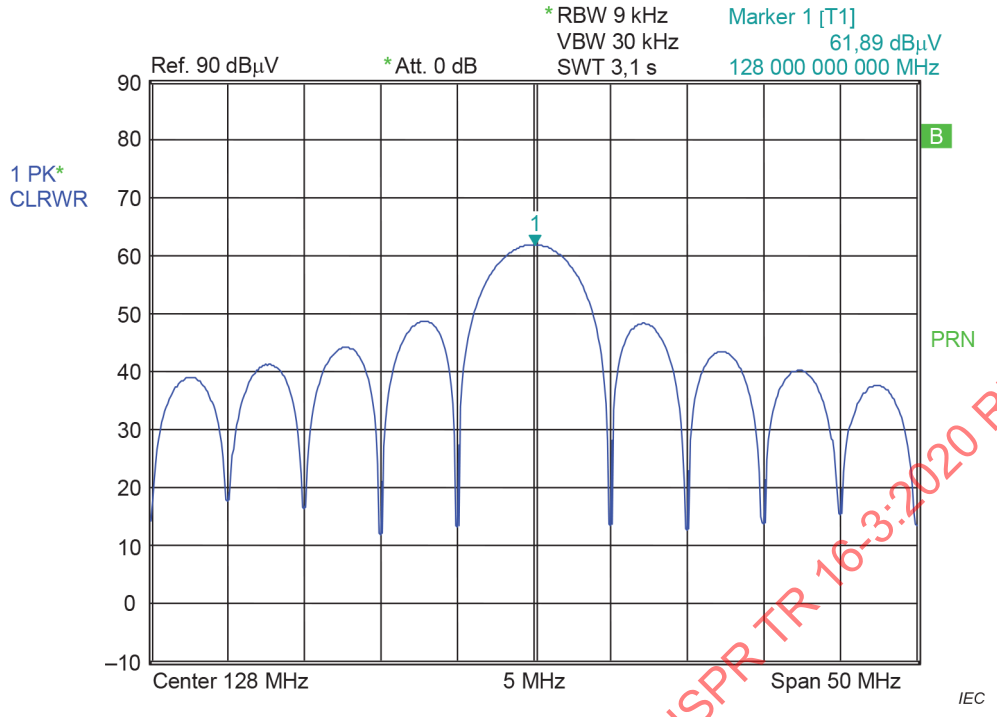



**Figure 143 – Example of an interference spectrum: pulse modulated carrier with a pulse duration of 0,2 µs and a PRF < 10 kHz**

With increasing pulse duration, the main lobe of the spectrum becomes narrower. This is also used to study the effect of narrowband pulses on radiocommunication systems. The advantage of using a band-limited pulse spectrum instead of a broadband pulse generator is to avoid overloading the receiver under test. Otherwise non-linearity effects could cause deterioration of the weighting characteristics. In addition to pulse-modulated carriers, unmodulated carriers can be used to determine the sensitivity of different systems to narrowband (CW signal) EMI.

Extensive measurements have also been presented in [49] with on/off-keying of a QPSK-modulated signal, thus keeping the spectrum width wider than the system bandwidth even with longer pulse durations. Since actual receivers do not provide BER indication, the method described in ITU Recommendation 1368 [59] was used as the failure criteria: DVB-T reception was regarded as distorted when more than one visible erroneous block was shown on the screen within an observation period of 20 s. Alternatively, any picture-freeze, also for short periods, was regarded as a failure. For DRM, the reception was considered as distorted when the system showed more than one dropout in a 20 s observation time.

Further measurements have been made with spread-spectrum modulated carriers in order to study the effect of spread-spectrum clock interference on wideband radiocommunication services (see [50] and [51]). Refer to Table 33.

**Table 33 – Overview of types of interference used in the experimental study of weighting characteristics**

| Interference signals | Pulse-modulated | On/Off-keyed QPSK-modulated | Spread-spectrum modulated |
|---|---|---|---|
| Pulse width in relation to signal bandwidth | $T < 1/B$ to $100/B$ | $T < 1/B$ to $100/B$ | Continuous |
| $T$ = pulse width, $B$ = radio signal bandwidth | | | |

IECNORM.COM : Click to view the full PDF of CISPR TR 16-3:2020 RLV

#### 4.8.4.4 Other principles of measurement

The receiver under test should receive a signal that is just sufficient to give quasi error-free reception (e.g. a BER = $10^{-7}$ or a factor of $10^{-3}$ lower than the critical BER). Thus the receiver operates like a receiver at the edge of a coverage area, where a disturbance above the emission limit can easily cause interference.

For radio telephone systems, where the downlink (base station to mobile) and uplink (mobile to base station) frequencies are in different bands, the use of a pulse modulated carrier helps to concentrate the interference on the mobile receiver and thus avoids interference with the loop-back connection.

### 4.8.5 Theoretical studies

The work of developing measurement procedures considering a digital radio receiver as a disturbance victim, is a very complex problem because there are many different modulation and coding schemes to consider as digital communication services are undergoing rapid development. The results of theoretical studies for radio systems using error correction are presented for example in [52] and [53]. These studies are based on the same fundamental assumptions that are explained above:

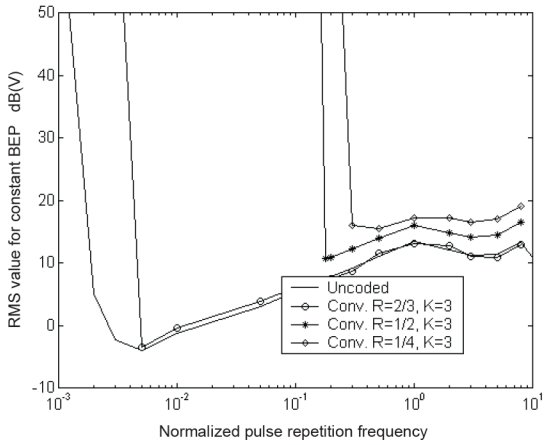
- the BER is the performance parameter of interest for the digital communication system;
- the repetitive pulsed disturbance is the waveform of particular interest;
- the disturbance pulses have a pulse duration that is short compared to the digital symbols transmitted.

Results for some selected convolutional codes include the following – for more details, see [52].

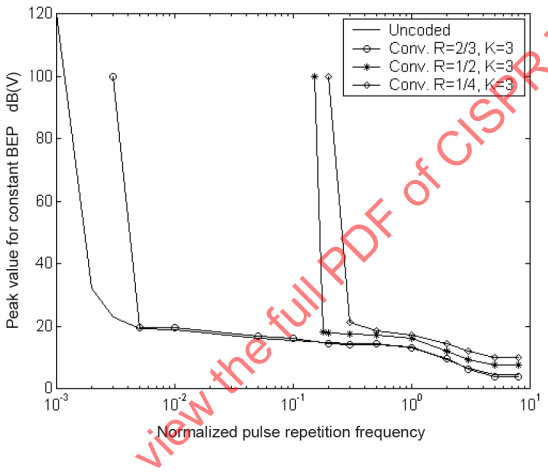
A convolutional code is generated by passing the information sequence through a linear finite-state shift register. In general, the shift register consists of $K$ stages and $n$ algebraic function generators. The input data to the channel encoder is shifted into and along the shift register $k$ bits at a time. The number of output bits for each $k$-input sequence is $n$ bits. The rate $R$ of the code is defined as $n/k$. The parameter $K$ is called the constraint length of the convolutional code. In Figure 144 a) and b) as well as Figure 145 a) and b) the RMS and peak values corresponding to a constant BER of $10^{-3}$ are shown for different convolutional codes and *binary phase shift keying* (BPSK) modulation. These results have been simulated with ACOLADE© (Advanced Communication Link Analysis and Design Environment). In the graphs, the pulse repetition frequency of the disturbance is presented as related (normalized) to the gross-bit rate (or symbol rate) $R_s$ of the communication system. The simulation is done in the band-pass domain. This means that the results can be transformed to an arbitrary carrier frequency. The disturbance pulse width is 10 % of the bit duration time. For the lowest rate $R$ = ¼, the RMS value is approximately constant down to the critical point where it increases rapidly. Thus, for a well-protected system, the RMS value corresponding to a constant BER is constant with respect to the pulse repetition frequency of the repetitive pulsed disturbance.

NOTE ACOLADE© is an example of a suitable product available commercially. This information is given for the convenience of users of this document and does not constitute an endorsement by IEC of this product.

IECNORM.COM : Click to view the full PDF of CISPR TR 16-3:2020 RLV



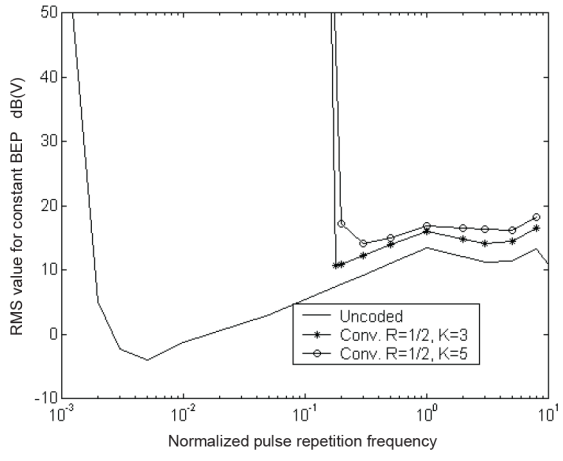

**a) The RMS level**



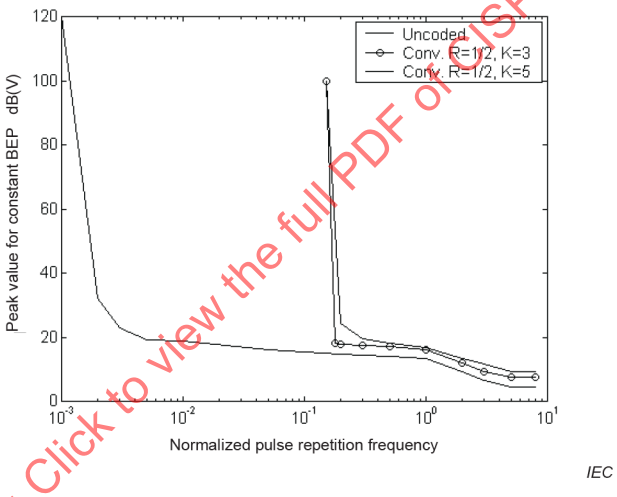

**b) The peak level**

**Figure 144 – The RMS and peak levels for constant BEP for three $K$ = 3, convolutional codes of different rate**

IECNORM.COM : Click to view the full PDF of CISPR TR 16-3:2020 RLV




**a) The RMS level**




**b) The peak level**

**Figure 145 – The RMS and peak levels for constant BEP for two rate ½, convolutional code**

The results in Figure 144 show the following: above the symbol rate $R_s$, the weighting characteristic follows the RMS value of the impulsive signal that causes the interference. Below $R_s$, the weighting characteristic depends on the amount of coding; for the uncoded signal, the peak value increases with less than 10 dB per decade as the PRF decreases. With better coding, the part of the weighting characteristic with flat response becomes shorter. Therefore, it is important to characterize real radiocommunication systems in order to obtain meaningful results.

### 4.8.6 Experimental results

#### 4.8.6.1 General

The methods described in 4.8.4 have been used for the measurement results in this part. The test signals are described where necessary.

IECNORM.COM : Click to view the full PDF of CISPR TR 16-3:2020 RLV

#### 4.8.6.2 Weighting in band A

For band A, i.e. below 150 kHz, no measurement results of digital radiocommunication systems are available.

NOTE Weighting of radio disturbance generally requires a consideration of intermittent, unsteady and drifting narrowband disturbances. Therefore the concept of defining a corner frequency, below which the average detector becomes effective has been applied to band A as well, using the corner frequency proposed for band B, because the original CISPR specification of the RMS detector does not apply a meter time constant.

#### 4.8.6.3 Weighting in band B

**Weighting of interference to the Digital Radio Mondiale (DRM) Broadcast System**

At the World Radio Conference (WRC) in June 2003, the new Digital Radio Mondiale was officially started. During the four-week duration of the conference, a great number of special DRM transmissions became available from many radio stations. The measurement results reported below were acquired on 8 July 2003, when a great number of transmissions were still available.

DRM uses OFDM (orthogonal frequency division multiplex) with 200 carriers. The occupied bandwidth of each transmission is 10 kHz. In addition to the digitized audio signal, a certain amount of data (radio station information, etc.) is transmitted. A conventional AM receiver can be used to downconvert the signal to an IF of 12 kHz, which is then decoded using a digital signal processor and a special DRM software radio.

During the time of measurement, the radio stations in Table 34 were received at the station near Munich, Germany, using amateur-radio dipole antennas mounted on a rooftop with a higher receive input voltage (50 dBμV to 60 dBμV) than required for the experiment.

**Table 34 – DRM radio stations received for the measurement of the weighting characteristics**

| Frequency kHz | Beam[a,b] | Target[c] | Average DRM power kW | Program | Transmit site |
|---|---|---|---|---|---|
| 5 975 | 060 | W Europe | 40 | T-Systems Media Broadcast | Jülich |
| 6 095 | ND | Europe | 35 | RTL/music and short announcements | Junglinster, Luxembourg |
| 6 140 | ND | W and C Europe | 40 | DW English | Jülich |
| 7 320 | 105 | W and C Europe | 33 | BBCWS | Rampisham |
| 13 605 | 037 | C Europe | 6 | IBB/R. Sawa | Morocco |
| 15 440 | 040 | W and C Europe | 80 | DW English | Sines |

[a] ND is non-directional (omnidirectional).

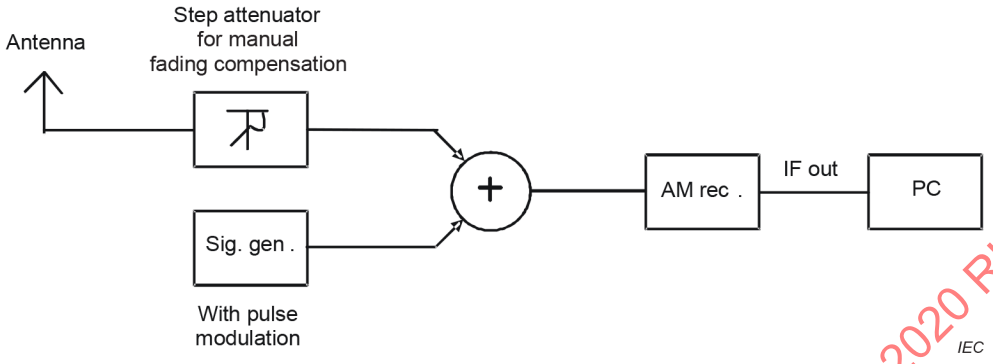
[b] "Beam" indicates antenna beam direction in terms of angle measured clockwise from 0° = north. For example 090 is east, 180 is south, 270 is west. Thus, 105 is approximately east-south-east.

[c] W is west and C is central.

The various transmissions were available for 1 h or 2 h. The measurement results (weighting characteristics) were essentially the same for all frequencies, even if the amount of data transmitted in addition to the audio signal was not the same. Time-dependent fading of the input signal had to be manually compensated using a step attenuator that was inserted in the antenna connection (see Figure 146).

IECNORM.COM : Click to view the full PDF of CISPR TR 16-3:2020 RLV

Principally the same type of interference signal was generated as in Figure 132. However, for a signal with an occupied bandwidth of 10 kHz, it is possible to use a longer pulse duration (10 μs or more).



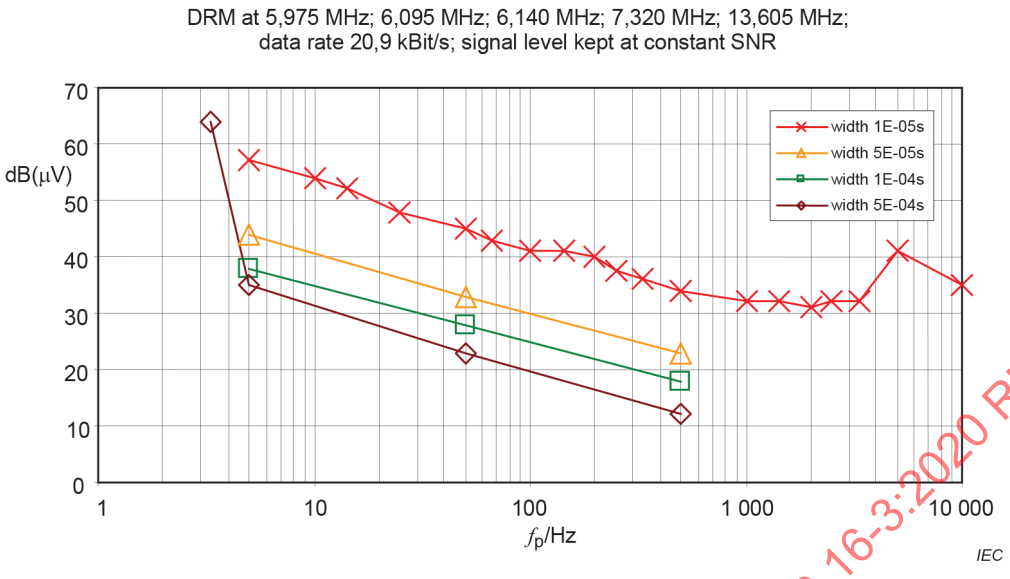

NOTE The received signal is downconverted to an IF of 12 kHz for decoding by special hardware and software in a personal computer (PC).

**Figure 146 – Test setup for the measurement of weighting curves for Digital Radio Mondiale (DRM)**

Because no indication of BER was available, the “Audio” status indication on the PC (DRM software radio display) was used as a criterion. As soon as the interference becomes too high, the “Audio” status indication will turn from green to red.

As explained earlier, the signal level is attenuated so that the reception quality is to be the minimum sufficient. The weighting characteristic (see Figure 147) shows a 10 dB/decade increase of the interference signal for PRFs between 1 kHz and 5 Hz. The non-linearities are mainly due to uncompensated fading of the input signal. A detailed weighting curve is shown for a pulse width of 10 μs. For higher pulse widths, the weighting curve was measured only at three (respectively, four) points to verify the 10 dB/decade behaviour. Below a PRF of 5 Hz, the weighting curve rises suddenly. And below about 2 Hz, the signal cannot be disturbed by the pulse width of 500 μs. However lightning strokes are reported to generate longer dropouts, which indicates that longer clicks might cause such dropouts as well.

IECNORM.COM : Click to view the full PDF of CISPR TR 16-3:2020 RLV




NOTE Because the DRM signals are actual radio signals, the exact modulation scheme is not known.

**Figure 147 – Weighting characteristics for DRM signals for various pulse widths of the pulse-modulated carrier**

The report [49] describes the following DRM signals and two receiver types for the measurements:

- Mode B, Modulation 16/64 QAM, Interleave 2 s, protection level 1 / 0
- Mode B, Modulation 16/64 QAM, Interleave 2 s, protection level 0 / 0

The interference signal for Figure 148 and Figure 149 is a pulse-modulated carrier with additional QPSK modulation, in order to generate a wide bandwidth of the interference spectrum as explained in 4.8.4.2.

IECNORM.COM : Click to view the full PDF of CISPR TR 16-3:2020 RLV

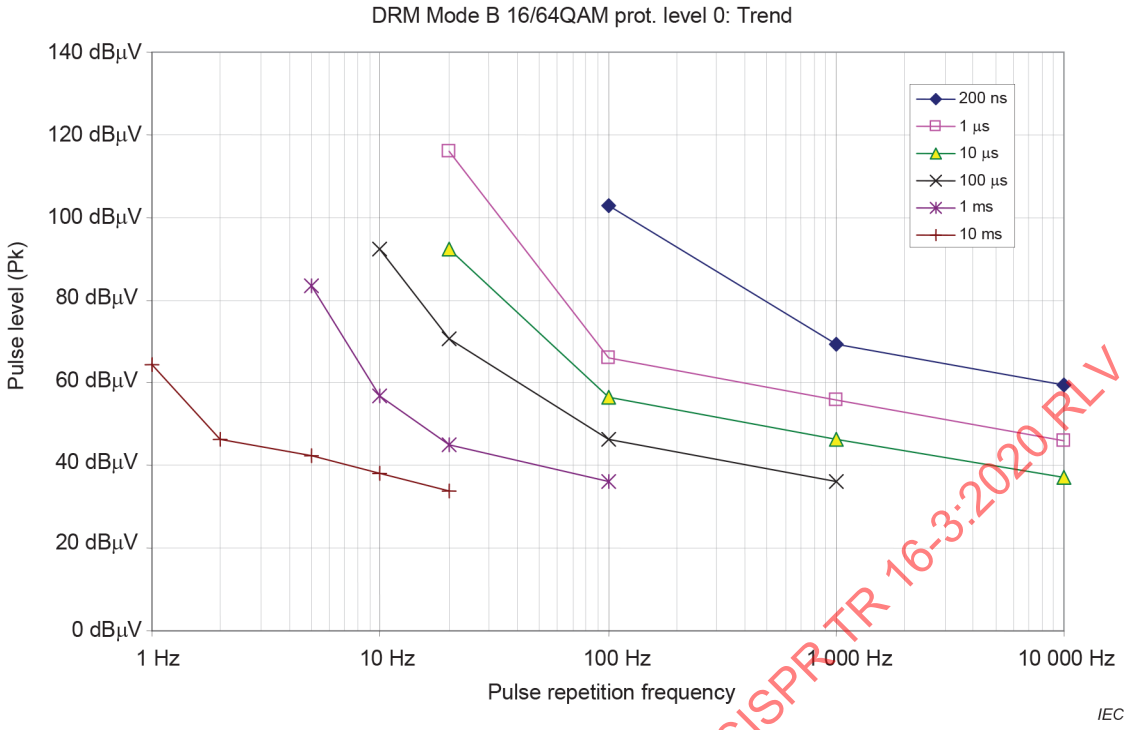



**Figure 148 – Weighting characteristics for DRM protection level 0: average of results for two receivers**

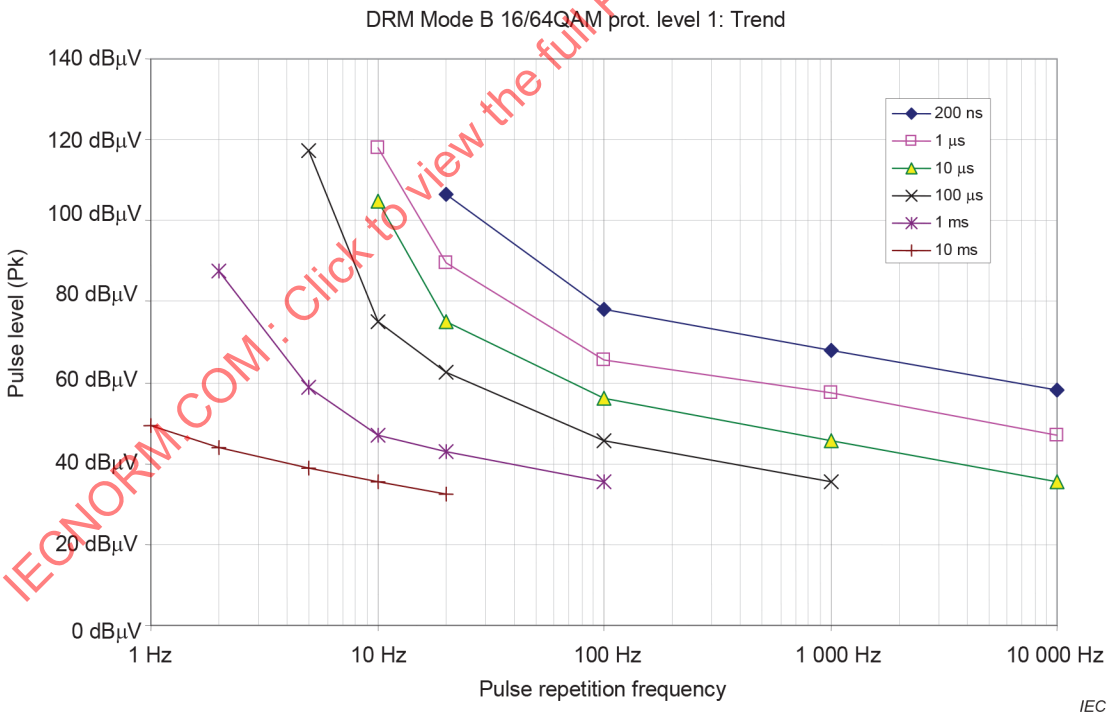



**Figure 149 – Weighting characteristics for DRM protection level 1: average of results for two receivers**

The weighting characteristics in Figure 148 and Figure 149 show a 10 dB/decade slope down to approximately 100 Hz. Because there is no other digital radio system in band B, the corner frequency of the proposed RMS/AV detector between RMS and linear average detection for this frequency band can only be based on the results of DRM (see 4.8.7). A corner frequency of 10 Hz is therefore proposed for band B as a compromise between the two results.

IECNORM.COM : Click to view the full PDF of CISPR TR 16-3:2020 RLV

#### 4.8.6.4 Weighting in bands C/D

##### 4.8.6.4.1 Weighting of impulsive interference to Digital Video Broadcast Terrestrial (DVB-T)

###### 4.8.6.4.1.1 Test setup

One test setup for DVB-T consists of a DVB-T signal generator and a DVB-T measuring receiver. The components are connected via coaxial cables. The interference signal (a pulse-modulated carrier, see Figure 132 for an example of the spectrum) is fed into the signalling connection via a combiner.

The parameters used are detailed in the following paragraphs.

DVB-T uses COFDM (coded orthogonal frequency division multiplex) with 6 817 (8k) or 1 705 (2k) carriers. The OFDM carriers may be modulated either with QPSK (Quadrature Phase Shift Keying) or with 64 QAM (quadrature amplitude modulation), respectively 16 QAM. QAM is preferred to QPSK as QAM allows higher data transfer rates. The transmission code rate $CR$ is defined by $CR$ = number of information bits/(number of information bits + error protection bits). Values of $CR$ = 2/3 and 3/4 are used in actual systems. Each COFDM symbol is followed by a guard interval $GI$ which is $GI$ = 1/8 in actual systems.

The DVB-T modulation and coding system allows many combinations, of which only a few are relevant. Therefore the parameters used in systems operating in some European countries have been selected. These allow transmission rates between 14,745 Mb/s and 24,88 Mb/s (see Table 36) depending on modulation and code rate. Different coders and decoders are used in the system. The bit-error ratio (BER) reading can be taken before the Viterbi decoder as well as before and after the Reed Solomon decoder of the measuring receiver. A comparison is given in Table 35. The transmission level is set so that the BER after the Reed Solomon decoder without interference is just below $10^{-8}$. This produces different signal levels depending on the system parameters. The interference levels have then been adjusted to a critical value of BER = $2{,}0 \times 10^{-4}$ before the Reed Solomon decoder.

For the BER measurement, the modulator generates a Pseudo Random Binary Sequence (PRBS) as a data stream. The evaluation of the data stream is done in the receiver in two different procedures. The BER before Viterbi and before Reed-Solomon is evaluated by correlation. Flags in the bit stream are used to determine the BER after Reed-Solomon. If the decoder does not recognize a flag as correct, the following bit combination is determined to be false.

The relationship in Table 35 was found experimentally between the bit error ratios before and after the Viterbi and Reed Solomon decoders for two pulse rates.

**Table 35 – Comparison of BER values for the same interference level**

| **Pulse rate** Hz | **10 k** | **500 k** |
|---|---|---|
| BER before Viterbi decoder | $1{,}5 \times 10^{-2}$ | $4{,}4 \times 10^{-3}$ |
| BER before Reed Solomon | $2{,}0 \times 10^{-4}$ | $2{,}0 \times 10^{-4}$ |
| BER after Reed Solomon | $1{,}0 \times 10^{-6}$ | $1{,}0 \times 10^{-8}$ |

So, the results with BER measured before Reed Solomon (with $2{,}0 \times 10^{-4}$) and after Reed Solomon (with $1{,}0 \times 10^{-6}$) are roughly comparable.

IECNORM.COM : Click to view the full PDF of CISPR TR 16-3:2020 RLV

**Table 36 – Transmission parameters of DVB-T systems used in various countries**

| Country | Modulation | Code rate | Guard interval | Transfer rate |
|---|---|---|---|---|
| France/UK | 64 QAM 2k | 3/4 | 1/8 | 24,88 Mb/s |
| Spain | 64 QAM 8k | 3/4 | 1/8 | 24,88 Mb/s |
| Germany | 16 QAM 8k | 2/3 | 1/8 | 14,745 Mb/s |

The measurement results are presented in Figure 150, Figure 151 and Figure 152. In all tests, the interference signal leading to these results are pulse-modulated carriers.

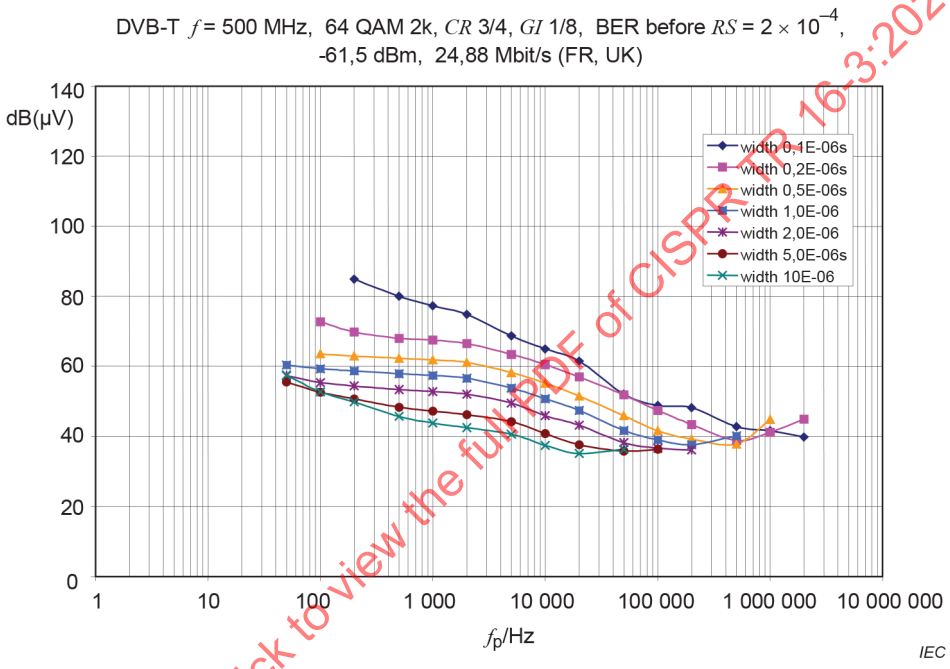



**Figure 150 – Weighting characteristics for DVB-T with 64 QAM 2k, $CR$ 3/4 (as used in France and UK)**

IECNORM.COM : Click to view the full PDF of CISPR TR 16-3:2020 RLV

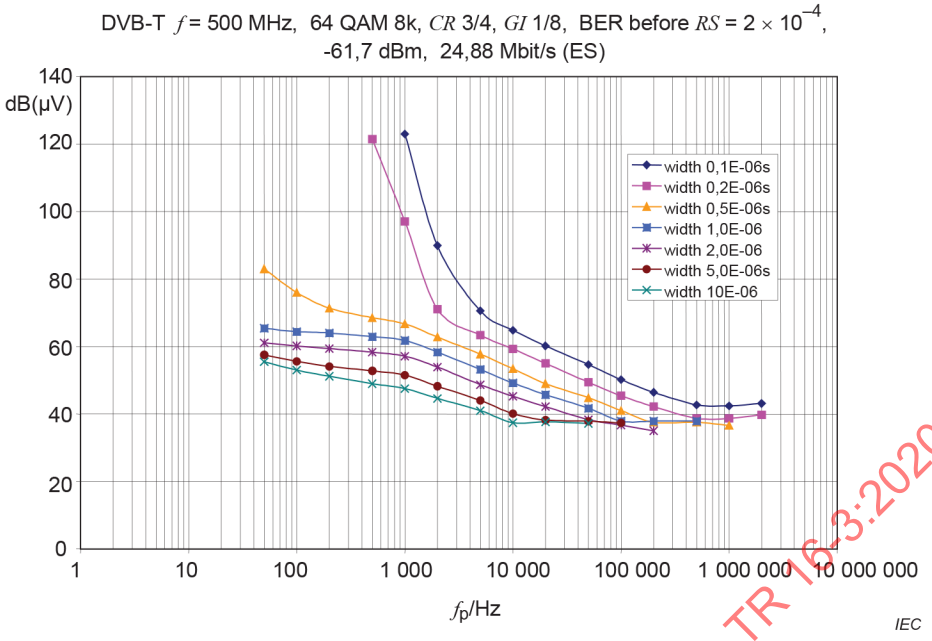



**Figure 151 – Weighting characteristics for DVB-T with 64 QAM 8k, *CR* 3/4 (as used in Spain)**

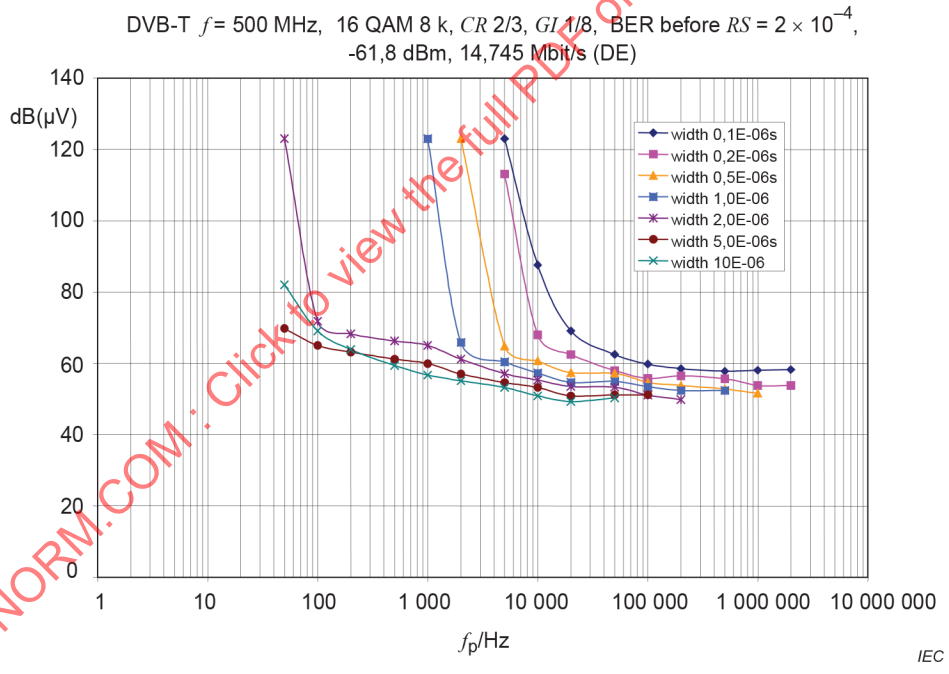



**Figure 152 – Weighting characteristics for DVB-T with 16 QAM 8k, *CR* 2/3 (as used in Germany)**

Six different receiver types were tested in report [49] for DVB-T with 16QAM 8k, $CR$ 2/3 and for DVB-T with 64QAM 8k, $CR$ 2/3. To get receiver independent results, the individual characteristics were combined using average values inside the range where all receivers offered a result. Excluded were two receivers in PRF ranges, where they showed a non-typical behavior. These combined results are shown in the “trend” characteristics in Figure 153 and Figure 154. The interference signal for both figures is a pulse-modulated carrier with additional QPSK modulation in order to generate bandwidth of the interference spectrum at least as wide as the DVB-T signal spectrum as explained in 4.8.4.2.

IECNORM.COM : Click to view the full PDF of CISPR TR 16-3:2020 RLV

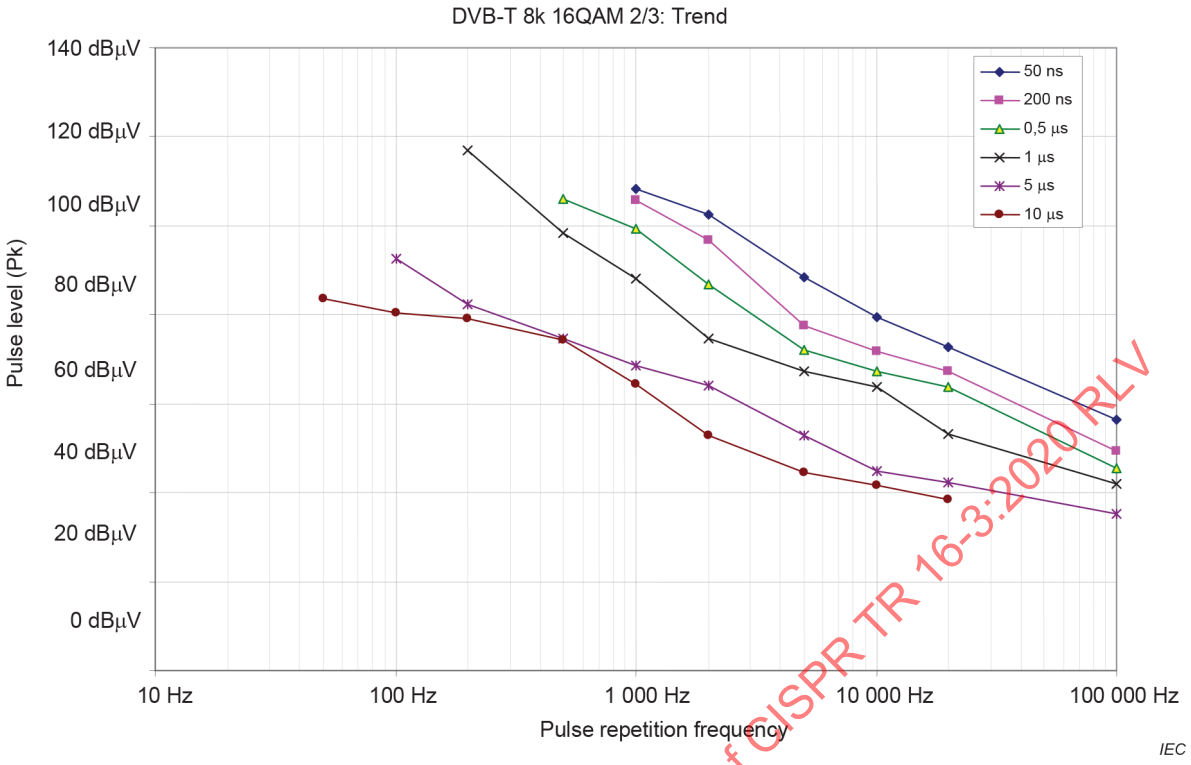



**Figure 153 – Average weighting characteristics of 6 receiver types for DVB-T with 16QAM**

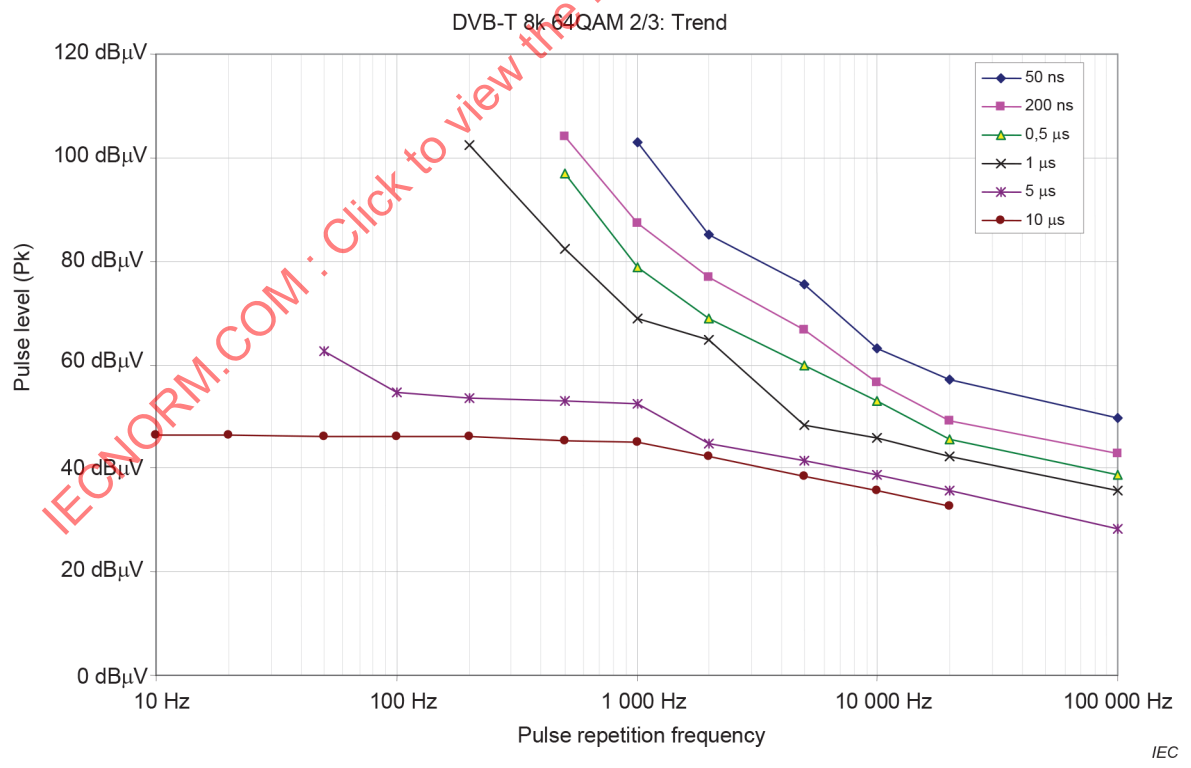



**Figure 154 – Average weighting characteristics of 6 receiver types for DVB-T with 64QAM**

IECNORM.COM : Click to view the full PDF of CISPR TR 16-3:2020 RLV

#### 4.8.6.4.1.2 Interpretation of the results

In Figure 150, the corner frequency can only be assumed to be approximatively 100 Hz, whereas in Figure 151 and Figure 152, the corner frequencies can clearly be seen. They however depend on the interference pulse width as in Figure 150 and Figure 152. Since all weighting curves are given for the shortest pulse (see Figure 140), also for the corner frequency, the shortest pulse is always relevant. The system used in Germany shows the most robust performance against impulsive interference due to its lower code rate and 16QAM 8k modulation.

### 4.8.6.4.2 Weighting of impulsive interference to other digital radiocommunication systems operating in CISPR bands C and D

#### 4.8.6.4.2.1 Digital audio broadcasting (DAB)

DAB operates in the VHF (174 MHz to 230 MHz) and the L (1 452 MHz to 1 492 MHz) bands with a bandwidth of 1,5 MHz per channel using Coded Orthogonal Frequency Division Multiplex (COFDM) to minimise multipath fading. The audio signal data rate is reduced by MUSICAM (a masking pattern adapted for Universal Coding and Multiplexing), which is a part of the MPEG-2 (Moving Picture Expert Group) standard. The total transmitted bit rate is 2,4 Mb/s. The 1 500 subcarriers are modulated using Differential QPSK (DQPSK). The weighting characteristics in Figure 144 were measured using a test version of a DAB receiver. Weighting characteristics of commercial DAB receivers have been presented in report [49].

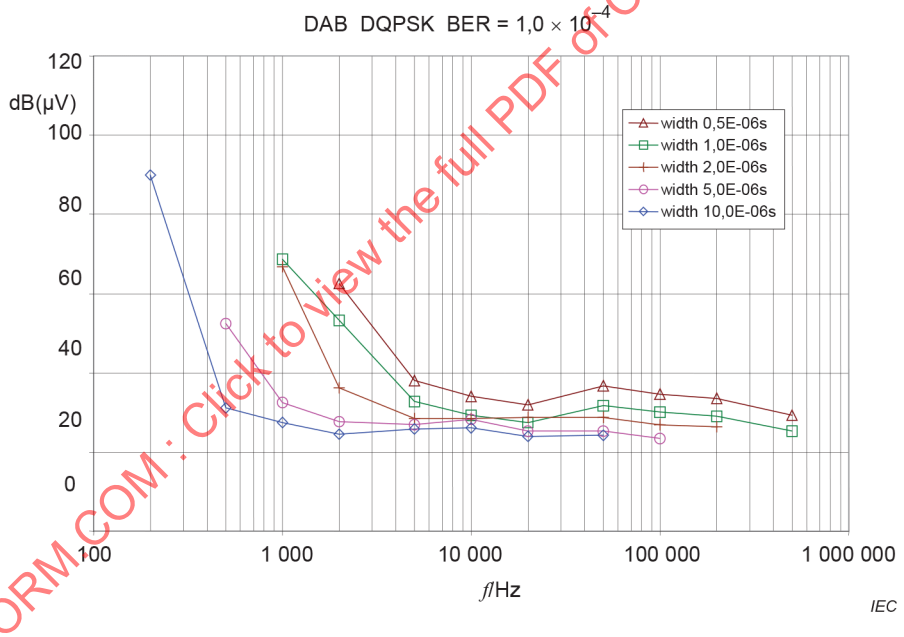



**Figure 155 – Weighting characteristics for DAB (signal level -71 dBm) with a flat response down to approximately 1 kHz**

IECNORM.COM : Click to view the full PDF of CISPR TR 16-3:2020 RLV

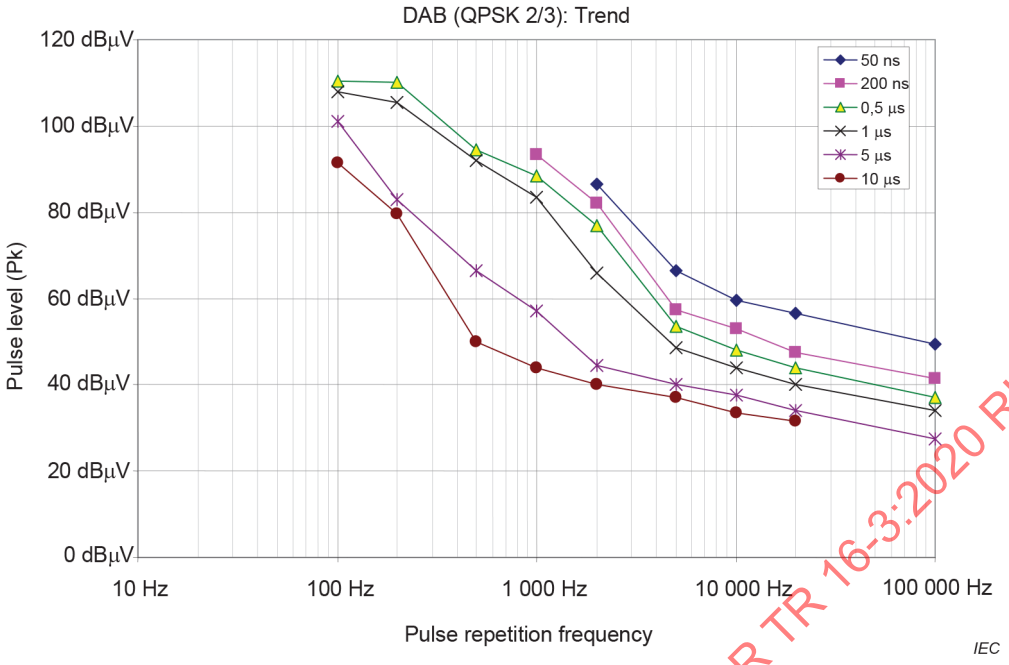



**Figure 156 – Weighting characteristics for DAB: average of two different commercial receiver types**

The differences between the results in Figure 155 and Figure 156 are possibly due to the different types of the impulsive signal: for Figure 155 a simple pulse-modulated carrier was used, whereas for Figure 156 an on/off-keyed QPSK-modulated signal was used.

#### 4.8.6.4.2.2 Terrestrial trunked radio (TETRA) system

TETRA is used in workshops, the building and construction industries, airports, transportation/trucking and safety services. It operates in the frequency range 380 MHz to 520 MHz (in some areas also in 870 MHz to 990 MHz) with a data rate of 36 kb/s per carrier, an occupied bandwidth of ≈ 25 kHz and channel separations of 12,5 kHz, 20 kHz or 25 kHz. Speech data reduction is done using Algebraic Code Excited Linear Prediction (ACELP) to 4,8 kb/s per traffic channel. Up to four traffic channels are normally transmitted on one carrier. The error protection may be high or low, depending on the code rate. The modulation procedure is $\pi$/4-DQPSK. Figure 157 shows the measured weighting characteristics for a high code rate = 1 (low error protection).

IECNORM.COM : Click to view the full PDF of CISPR TR 16-3:2020 RLV

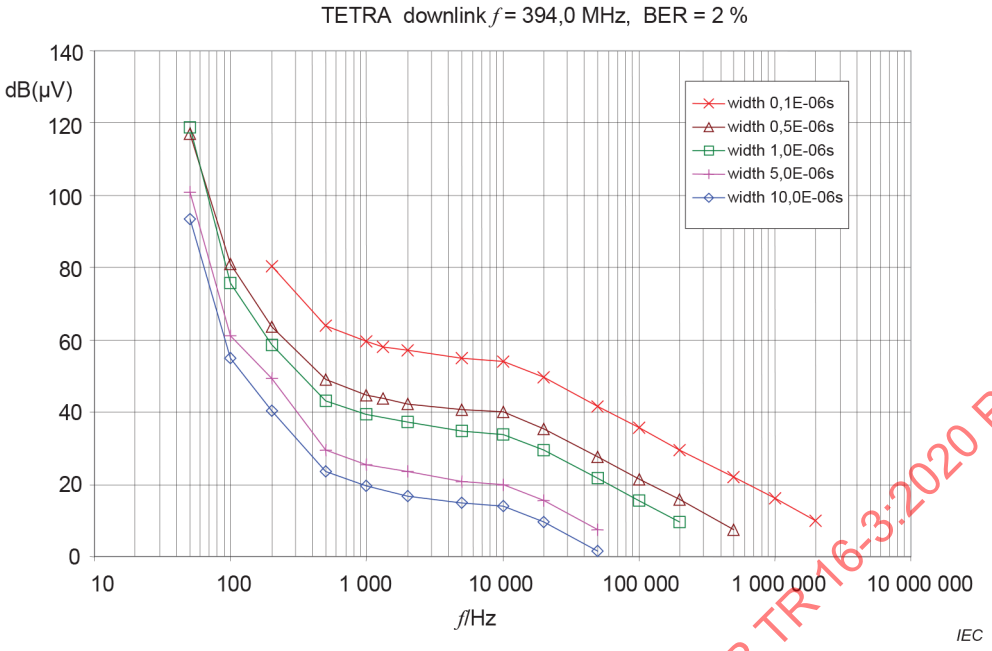



**Figure 157 – Weighting characteristics for TETRA (signal level – 80 dBm) for a code rate of 1**

Since the pulse spectrum is much wider than the channel bandwidth, all weighting characteristics are separated by the PRF ratio in dB. Above a PRF of 10 kHz, the slope of curves is 20 dB/decade, corresponding to the increase of the voltage of the centreline of the interference spectrum. Therefore the weighting characteristics below 10 kHz PRF should be regarded as relevant.

#### 4.8.6.4.2.3 Global system for mobile communication (GSM)

This digital cellular telecommunication system operates in the 900 MHz (GSM 900) and 1 800 MHz (GSM 1800) frequency bands (outside the US). The offset between uplink (mobile to base station) and downlink is 45 MHz (GSM 900) and 95 MHz (GSM 1800) respectively. The occupied bandwidth is 300 kHz and channel spacing is 200 kHz. Modulation for constant spectrum envelope is achieved with Gaussian Minimum Shift Keying (GMSK). The error correction mechanisms applied are different for traffic channels (1b bit) and other bits (Class 2 bits). Therefore different bit error rates apply: BER, RBER 1b and 2 (residual BER) and FER (Frame error rates). The test set-up and signals of Figure 129 and Figure 130 have been used, with a mobile communication tester as a signal source.

IECNORM.COM : Click to view the full PDF of CISPR TR 16-3:2020 RLV

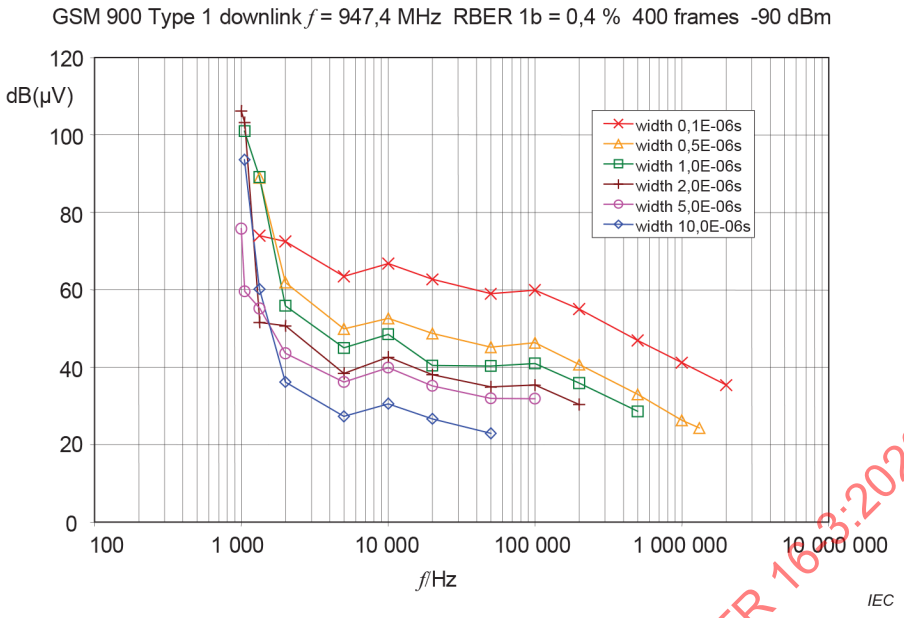



**Figure 158 – Weighting characteristics for RBER 1b of GSM (signal level –90 dBm)**

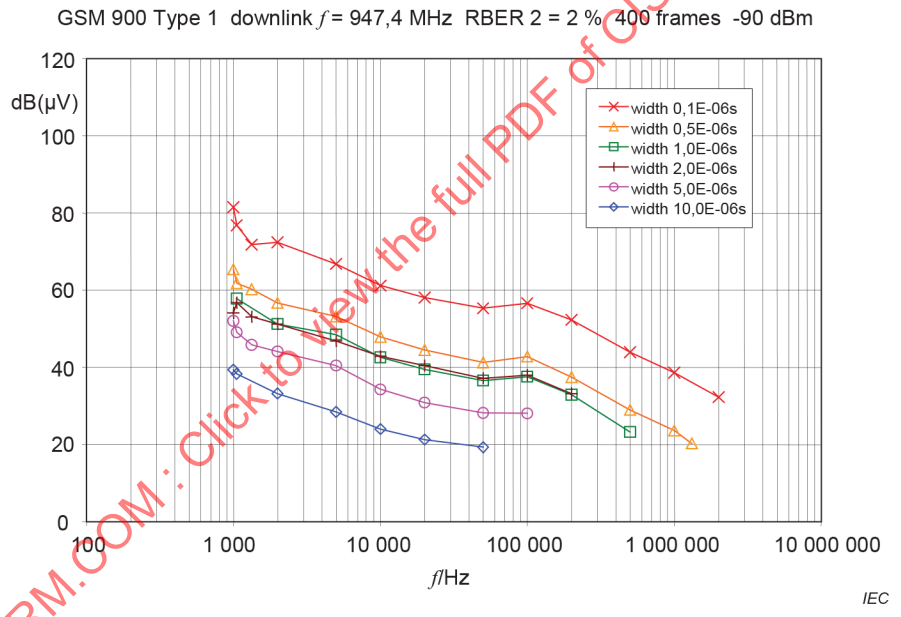



**Figure 159 – Weighting characteristics for RBER 2 of GSM**

IECNORM.COM : Click to view the full PDF of CISPR TR 16-3:2020 RLV

The characteristics typically rise at 10 dB/decade between 100 kHz and 2 kHz with a steeper slope below about 2 kHz PRF. Unfortunately measurements below a PRF of 1 kHz were not possible due to instability of the test system. The results shown in Figure 158 and Figure 159 are very similar to the BER and RBER 1b curves of Figure 160 similar to those published in [54] and [55] using the simulation software COSSAP. The values obtained in Figure 160 have been calculated assuming a pulse-modulated carrier with a pulse duration of 2 µs as the interference signal.

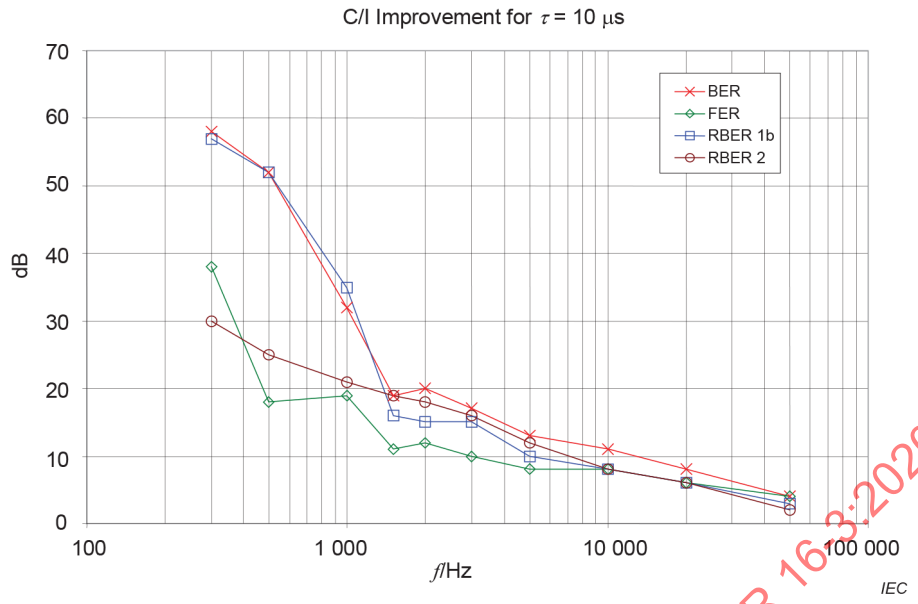



**Figure 160 – Carrier-to-interference improvements with decreasing PRF in dB computed for GSM using COSSAP**

#### 4.8.6.4.2.4 Frequency modulation (FM) broadcast system

Based on the assumption that FM broadcast will survive past the transition from analog to digital radio systems for some time, measurements have been made based on the methods of report [49] resulting in Figure 161. The FM signal contained a pilot carrier only; the increase of noise due to the interference was measured in the demodulated signal. The interference signal is a pulse-modulated carrier with additional QPSK modulation in order to generate bandwidth of the interference spectrum at least as wide as the FM signal spectrum as explained in 4.8.4.2.

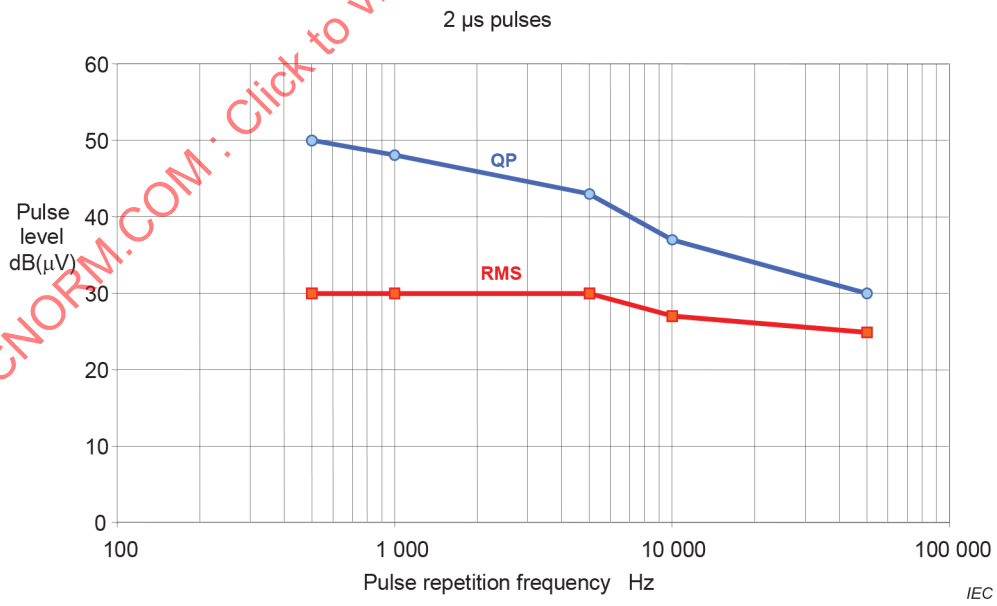



**Figure 161 – RMS and quasi-peak values of pulse level for constant effect on FM radio reception**

Figure 161 is not a weighting characteristic! It shows that the RMS value of the pulse level with 2 µs width is closer to being constant than the quasi-peak value. This has been shown for other pulse widths as well but is not presented here for reasons of space.

IECNORM.COM : Click to view the full PDF of CISPR TR 16-3:2020 RLV

#### 4.8.6.5 Weighting for band E (1 GHz through 18 GHz)

##### 4.8.6.5.1 GSM system

The weighting characteristics found for a mobile operating in the 1 800 MHz (GSM 1 800) frequency band is very similar to the system operating in the 900 MHz (GSM 900) frequency band (compare Figure 162 with Figure 158 through Figure 160). The offset between uplink (mobile to base station) and downlink is 95 MHz for GSM 1 800. As in Figure 158 through Figure 160, the curves are rising below 2 kHz PRF with a slope of more than 20 dB/decade. See Figure 162.

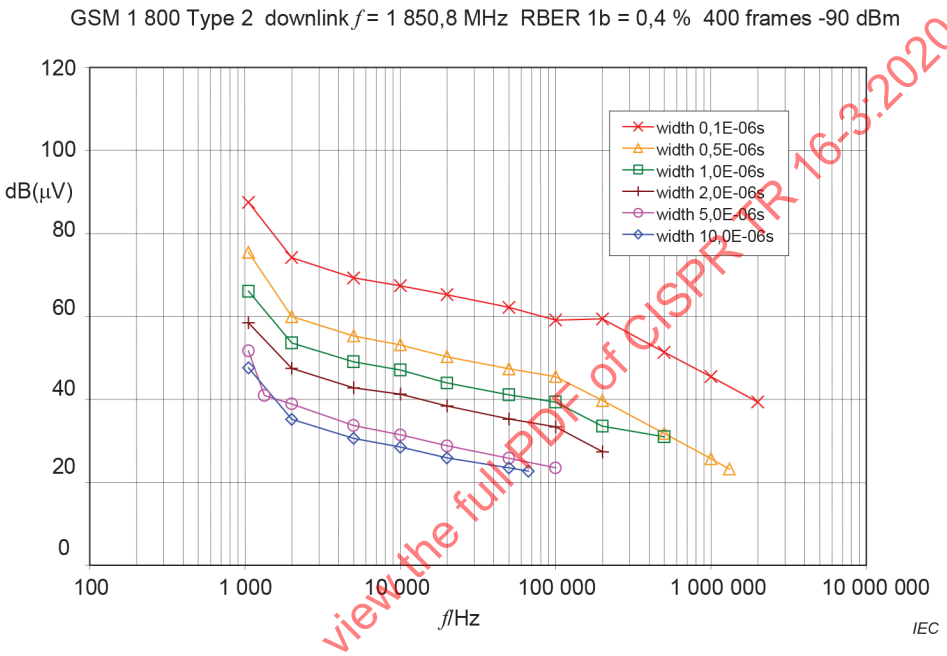



**Figure 162 – Weighting characteristics for RBER 1b of GSM (signal level –90 dBm)**

##### 4.8.6.5.2 Digitally Enhanced Cordless Telephone (DECT) system

DECT is used in homes and offices for distances up to 300 m (in picocells). It provides 10 channels spaced 1,728 MHz apart in the frequency range 1,88 to 1,90 GHz. The occupied bandwidth is ≈ 1,5 MHz. For speech data reduction Adaptive Differential Pulse Code Modulation (ADPCM) is used. Modulation is done with Gaussian Mean Shift Keying (GMSK). The data stream for testing is Pseudo Random Binary Sequence (PRBS). See Figure 163.

IECNORM.COM : Click to view the full PDF of CISPR TR 16-3:2020 RLV

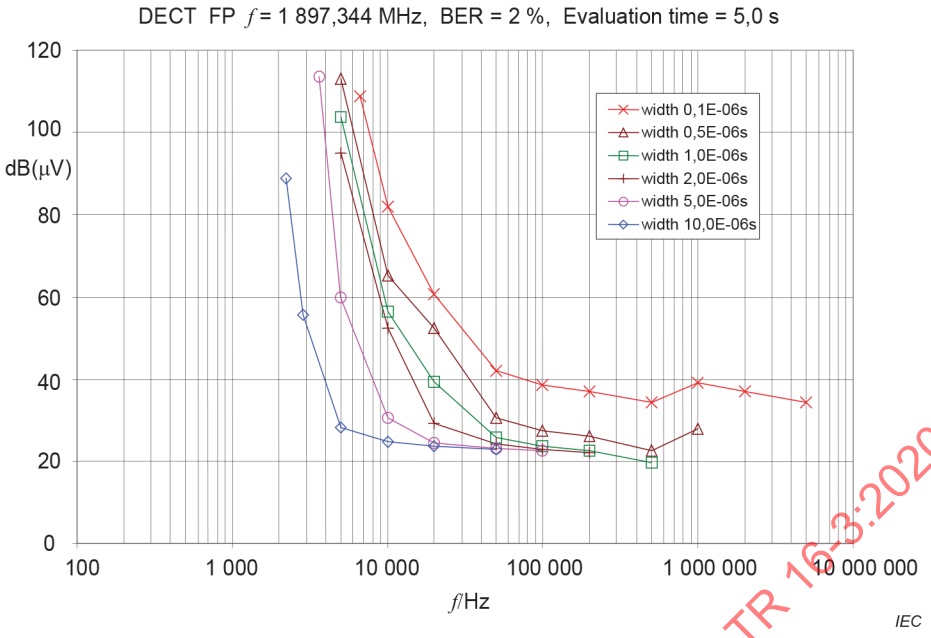



**Figure 163 – Weighting characteristics for DECT (signal level –83 dBm)**

The weighting characteristics for DECT show a response near 10 dB/decade in the range between 50 kHz and 500 kHz PRF in the upper PRF areas for narrow pulses and a steep slope below about 10 kHz PRF. Only for longer pulse widths, the weighting characteristic is flat.

#### 4.8.6.5.3 Code Division Multiple Access (CDMA) systems IS-95 and J-STD 008

IS-95/J-STD 008 have been specified by TIA (US Telecommunications Industry Association) and are used in the frequency ranges 825 MHz to 900 MHz (IS-95) and 1,8 GHz to 2,0 GHz. The occupied bandwidth is ≈ 1,4 MHz (3 dB: 1,23 MHz). The modulation is done with Quadrature Phase Shift Keying (QPSK). For the uplink (mobile to base station) the optimum setting of the receive power at the base station is controlled via power control bits. See Figure 164 and Figure 165.

IECNORM.COM : Click to view the full PDF of CISPR TR 16-3:2020 RLV

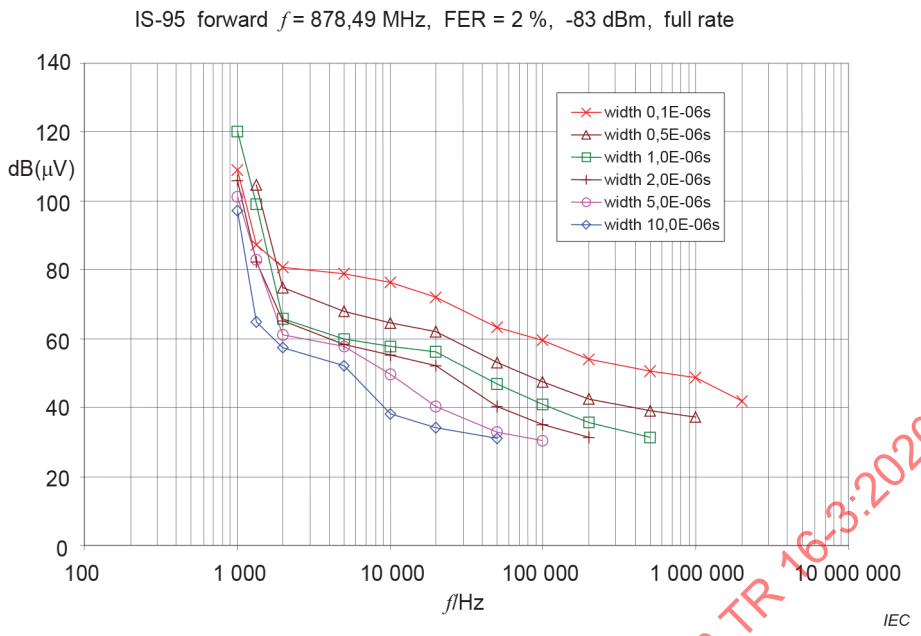
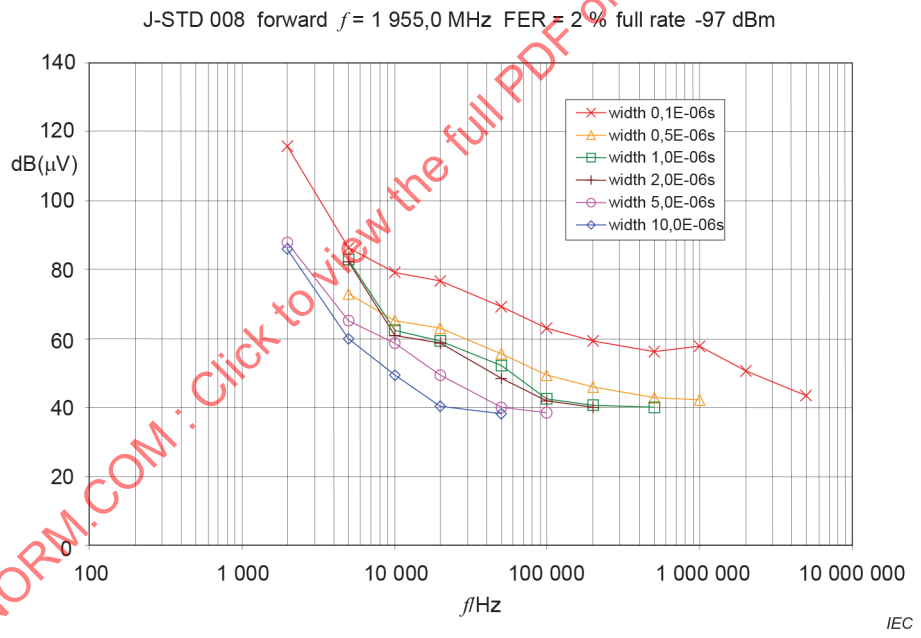



**Figure 164 – Weighting characteristics for IS-95 (signal level -97 dBm) with comparatively high immunity to interference**




IECNORM.COM : Click to view the full PDF of CISPR TR 16-3:2020 RLV

**Figure 165 – Weighting characteristics for J-STD 008 (signal level –97 dBm)**

#### 4.8.6.5.4 Third generation digital radiocommunication systems

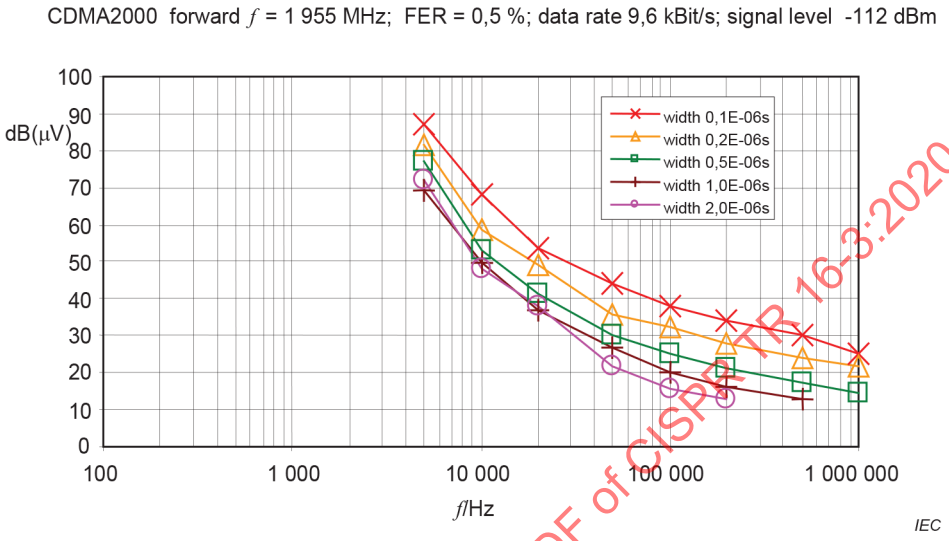
Two different systems have been investigated:

– wideband CDMA (W-CDMA), which is going to be deployed in Europe, and

– CDMA2000, which is mainly going to be applied in North America and some other areas.

Tests have been made on both systems. However at the time of testing, available mobile phones for W-CDMA did not give stable BER results in the test setup (loop back) with the mobile testers. So, only results for CDMA2000 are available now. Results for W-CDMA will certainly become available at a later date. They have been used later with success for evaluating the interference effect to spread-spectrum clock signals (see [50] and [51]).

CDMA2000 as described by Third Generation Partnership 2 (3GPP2) is an access method intended for use in the IMT-2000 proposal for Third Generation (3G) cellular telephone systems. The system is based on spread-spectrum codes and provides high and variable data rates. It is an evolutionary development of IS-95 (cdmaOne) which is also based on Code Domain Multiple Access (CDMA) to the air interface. This means that the individual channels are separated from each other by individual codes. The basic chip rate is 1,228 8 MHz. All IMT-2000 compatible systems feature transmitted bit rates of up to 384 kb/s up to a cruising speed of 500 km/h, in urban areas up to 120 km/h. See Figure 166 and Figure 167.




NOTE The curves are rising increasingly fast at lower PRFs .

**Figure 166 – Weighting characteristics for the Frame Error Ratio (FER) of CDMA2000 (measured at a receive signal level of –112 dBm) for a low data rate of 9,6 kb/s**

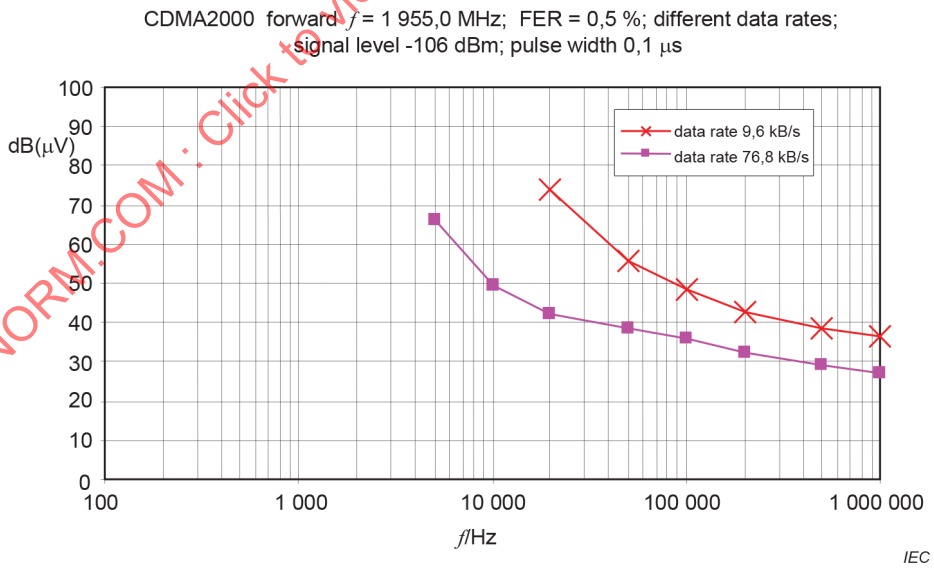



**Figure 167 – Weighting characteristics for the Frame Error Ratio (FER) of CDMA2000 (measured at a receive signal level of –106 dBm) for two different data rates (9,6 kb/s and 76,8 kb/s)**

For higher data rates (e.g. 384 kb/s, which was not available for the test), the system would still be more susceptible to impulsive disturbance. For the higher data rates, the faster rising knee (corner frequency) is shifted to lower PRFs but remains high compared to 1 kHz.

IECNORM.COM : Click to view the full PDF of CISPR TR 16-3:2020 RLV

### 4.8.7 Effects of spread-spectrum clock interference on wideband radiocommunication signal reception

It was argued that the classical impulsive (i.e. broadband) and unmodulated or pulse-modulated narrowband interference may not completely reflect today's sources of interference. In this context, the question on the effect of spread-spectrum-clock signals came up. This type of emission has in the recent past raised the concern of spectrum regulators and some studies have been published. Spread-spectrum clocking reduces the measured emission level of computer clocks, but what is the effect of spread-spectrum clocking on victim radiocommunication systems? Spread-spectrum clock interference was expected to have an especially severe effect on wideband radiocommunication services. Therefore DVB-T and W-CDMA as well as CDMA2000 were selected for tests and presented in [50] and [51].

The application of frequency modulation or other spread spectrum modulation to the clock signal distributes the clock power over a frequency band wider than the EMI measurement bandwidth and thus reduces the emission level, when measured with a bandwidth as narrow as e.g. 120 kHz. In Table 37 measurements are shown for a frequency-modulated clock signal spectrum and of the corresponding unmodulated clock signal with $f_{centre}$ = 500 MHz, $f_{mod}$ = 30 kHz (sinewave), spread amount $\delta$ = 3,5 MHz (i.e. the spectrum width due to modulation) and a peak level reduction Δ = 5,0 dB.

**Table 37 – Example of measurement results in dB(µV) of unmodulated and FM modulated carriers for various detectors (bandwidth 120 kHz)**

| Detector | Unmodulated carrier | FM modulated carrier for highest peak | FM modulated carrier for centre frequency |
|---|---|---|---|
| Pk in dB(µV) | 55,6 | 50,39 | 44,3 |
| Qp in dB(µV) | 55,4 | 49,30 | 43,16 |
| Av in dB(µV) | 55,38 | 38,38 | 37,12 |
| RMS in dB(µV) | 55,38 | 42,50 | 38,87 |

Using the measurement bandwidth of 1 MHz at 2 GHz (with a proportionally higher spread amount) reduces the differences between unmodulated and FM modulated carriers to 1,2 dB for the peak detector, 17 dB for the average detector and to 11 dB for the RMS detector.

The measurement results in [50] and [51] show that the high immunity of the DVB-T and W-CDMA systems to unmodulated carriers (i.e. clock signals) is lost to frequency modulation. Considering

– that due to a lower measured emission level, the interference level may be increased by the amount of Δ (e.g. 6 dB) to reach the same emission limit and
– that frequency modulation causes a reduction of up to 25 dB of the original immunity of the system to clock signals,

frequency modulation causes a total increase of possible interference effect of up to 25 dB + 6 dB = 31 dB.

It is agreed that some digital modulation systems have been especially designed to suppress unmodulated interference. In general, however it shall be pointed out that the EMI measurement bandwidth should match the bandwidth of possible victim radiocommunication receivers. It might therefore be an advantage to describe the detector function for various measurement bandwidths. If an RMS detector is used for the measurement of spread-spectrum modulated emissions, the measured value will be proportional to the square-root of the measurement bandwidth. For the frequency range of CISPR bands C and D, the radiocommunication signal bandwidths have always had a wide range of values. Narrowband FM with as few as 7,5 kHz on the one hand and the amplitude-modulated TV signal spectrum including the residual sideband with as much as 6 MHz on the other were in use until recently

IECNORM.COM : Click to view the full PDF of CISPR TR 16-3:2020 RLV

and the 120 kHz was used as the measurement bandwidth. This situation has not changed very much with the introduction of TETRA (bandwidth approximately 25 kHz) and DVB-T [bandwidth 6,6 MHz (VHF) and 7,6 MHz (UHF)].

### 4.8.8 Analysis of the various weighting characteristics and proposal of a weighting detector

Looking at various results of weighting characteristics in the subclauses above, we can see that above a certain corner frequency, the weighting function decreases with approximately 10 dB per decade of pulse repetition frequency. A decrease of 10 dB per decade corresponds to the weighting function of an RMS detector (see Figure 130). Below this corner frequency, the weighting function decreases with a higher rate. A higher rate of decrease (20 dB/decade) can be achieved using the linear average detector function. This behaviour can be approximated by a combination of two detectors, the RMS and the linear average detector. The average detector applies the meter time constant as described in CISPR 16-1-1 for intermittent, unsteady and drifting narrowband disturbances. Figure 168 serves to understand the meaning of the corner frequency. It is not possible to satisfy the protection requirements of all services with the same perfection, therefore the selection of the various corner frequencies between the proposed average and RMS weighting functions in each band can be regarded as a compromise. Where corner frequencies for different pulse widths are different, the corner frequency for the shorter pulse widths apply, as the detector weighting always applies to the shortest possible pulse width, which is determined by the measurement bandwidth. It is proposed to keep the measurement bandwidths specified in CISPR 16-1-1 for CISPR bands A through E.

**Table 38 – Survey of the corner frequencies found in the various measurement results**

| System | Bibliographic references | $f_c$ [a] kHz | Comment |
|---|---|---|---|
| DRM | 49, 57 | 0,1/0,005 | 10 Hz chosen for feasibility |
| DVB-T | 49, 58 | 0,1 to 10 | $f_c$ depending on $w_p$ [b], modulation and coding |
| DAB | 49, 56 | 5 | $f_c$ partially depending on $w_p$ |
| TETRA | 56 | 0,5 | narrowband system, mainly used below 1 GHz |
| GSM 900 | 52, 55, 56 | 1,5 | above $f_c$:very close to RMS |
| FM | 49 | < 0,5 | weighting characteristics follows RMS down to 0,5 kHz |
| GSM 1800 | 52, 55, 56 | 1,5 | above $f_c$:very close to RMS |
| DECT | 57 | 50 | above $f_c$: flatter than RMS |
| IS-95 | 57 | 2 | very similar to J-STD 008; above $f_c$ close to RMS |
| J-STD 008 | 57 | 5 | very similar to IS-95; above $f_c$ close to RMS |
| CDMA2000 | 57 | 50 | data rate 9,6 kb/s; above $f_c$, curves are very close to RMS |
| CDMA2000 | 57 | 10 | data rate 76,8 kb/s; above $f_c$, curves are very close to RMS |

[a] $f_c$ is the corner frequency.

[b] $w_p$ is the pulse width.

As a result of the values found in Table 38, the following corner frequencies were selected:

IECNORM.COM : Click to view the full PDF of CISPR TR 16-3:2020 RLV

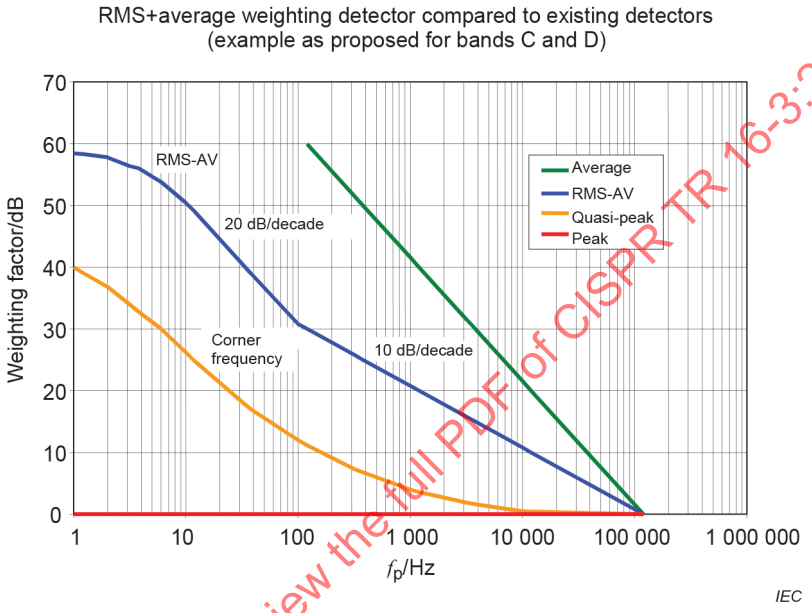
Band A: 10 Hz (same as Band B)

Band B: 10 Hz

Band C/D: 100 Hz

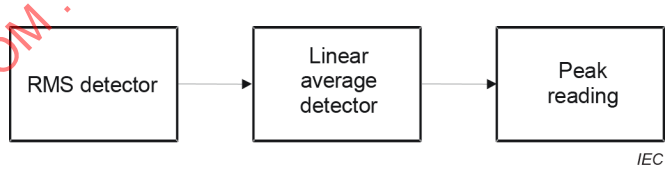
Band E: 1 000 Hz

NOTE The corner frequency of 10 Hz was selected for Band A, in order to give the RMS detector a function similar to the one of band B and in addition to allow the use of the meter time constant in order to provide an asymptote for the purpose of measuring intermittent, unsteady and drifting narrowband disturbances with the RMS detector.




The asymptote of 58,7 dB near 1 Hz is due to the average detector meter time constant.

**Figure 168 – The proposed RMS-average detector for CISPR Bands C and D with a corner frequency of 100 Hz**




The linear average detector has an inherent meter time constant.
The maximum output of the average detector is taken using a peak reading function.

**Figure 169 – RMS-average detector function by using an RMS detector followed by a linear average detector and peak reading**

In Figure 169 a digital RMS detector with RMS computing times of 10 ms, followed by a digital linear average detector results in the RMS-average weighting curve of Figure 168 for the shortest pulse width allowed by the measurement bandwidth of 120 kHz. RMS computing times of 10 ms will give RMS values of the disturbance signal within 10 ms. The 10-ms packets are then weighted using a linear average function. The peak reading function after a meter time constant of 100 ms is effective then for low repetition pulses ($f_p$ below 10 Hz), which causes the weighting curve to approximate the asymptote of 58,7 dB.

Conclusion: it has been shown experimentally and partly numerically that some detector functions that are currently in use in CISPR product standards

IECNORM.COM : Click to view the full PDF of CISPR TR 16-3:2020 RLV

– either indicate a higher interference potential of impulsive disturbance than the interferer actually represents (i.e. they overweigh the disturbance) if “peak” and “quasi-peak” detectors are used, or

– indicate a lower interference potential of impulsive disturbance than the interferer really represents (i.e. underweigh or de-emphasize the disturbance) for the “average” detector with respect to the possible interference effect on digital radiocommunication systems, whereas using the RMS-average detector represents the interference effect rather well.

### 4.8.9 Properties of the RMS-average weighting detector

For CISPR weighting functions, the pulse width is always assumed to be defined as the inverse of the measurement bandwidth, corresponding to the response to the Dirac pulse. Therefore the weighting functions of the RMS-average detector are shown in Figure 170 for the shortest pulse widths allowed by the bandwidths specified.

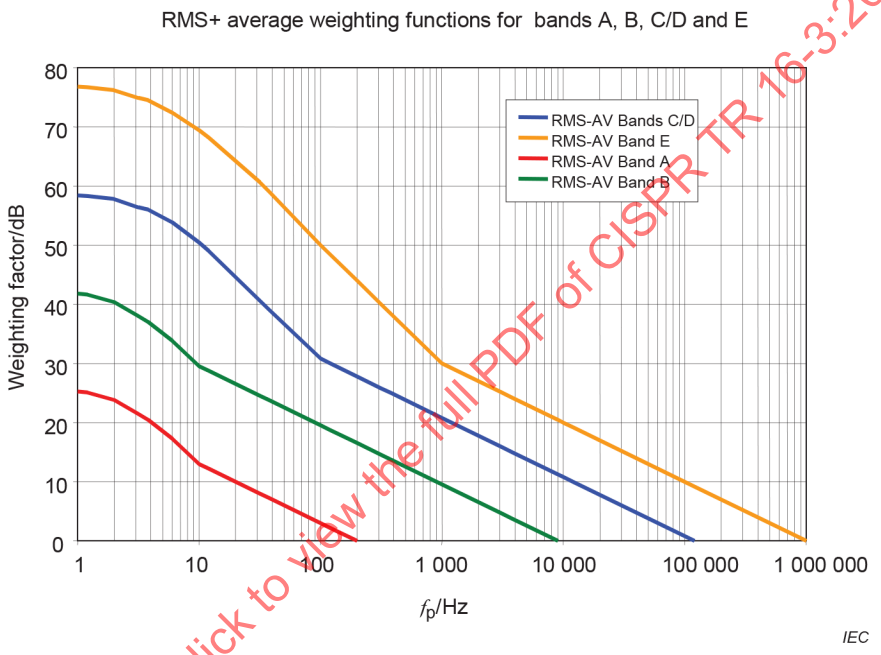



**Figure 170 – RMS-average weighting functions for CISPR Bands A, B, C/D and E for the shortest pulse widths allowed by the measurement bandwidths**

Figure 170 shows theoretical weighting curves. In practice, the weighting factors apply up to values of approximately 40 dB for broadband emissions. If wider pulse widths, e.g. pulse-modulated carriers are measured, then the weighting function will change depending on the pulse width. If e.g. the pulse width is 10 times the shortest pulse width, this will shift the weighting curve by an amount of 10 dB, if the PRF is above the corner frequency, and by 20 dB, if PRF and reciprocal of pulse width are below the corner frequency.

If the RMS-average weighting detector is used with a wider measurement bandwidth than the one specified, then the weighting curve will be shifted due to the shorter pulse width as shown in Figure 171.

IECNORM.COM : Click to view the full PDF of CISPR TR 16-3:2020 RLV

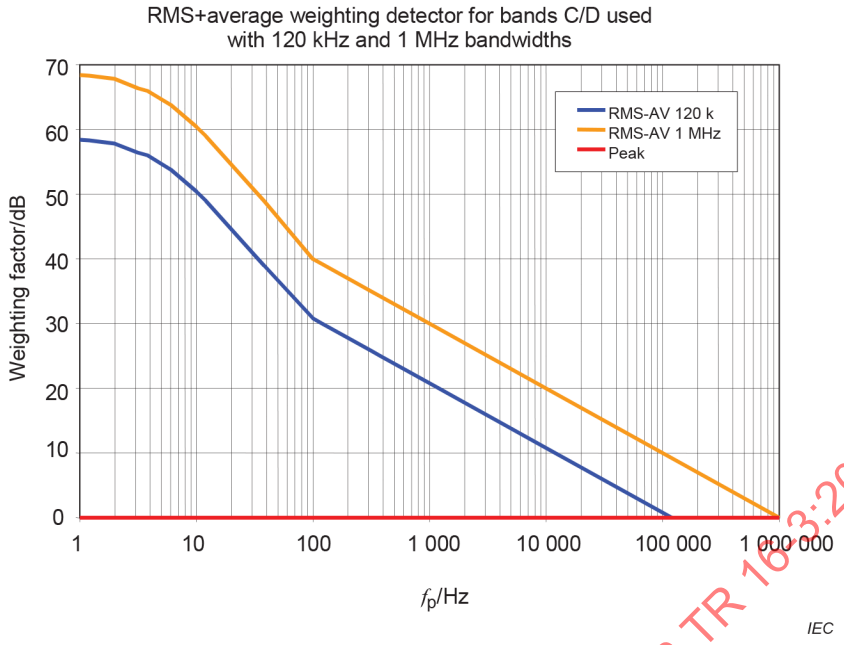



**Figure 171 – Shift of the RMS-average weighting function for CISPR band C/D by using a bandwidth of 1 MHz instead of 120 kHz, if the shortest possible pulse widths are applied**

Measurement speeds: Measurement times and scan rates for the RMS-average measuring receiver can be made similar to those of measuring receivers using the average detector (see CISPR 16-2-1, CISPR 16-2-2 and CISPR 16-2-3), i.e. measurements can be made substantially faster than with the quasi-peak measuring receiver. The definition of measurement times will have to take the characteristics of the disturbance into account.

The process of defining limits that are based on the RMS-average detector has to take into account the effects of different types of disturbances on digital communication systems. For unmodulated sinewave signals, all detectors will yield the same result. For Gaussian noise, the RMS-average measuring receiver will indicate a level approximately 1 dB higher than the average detector level, 6 dB lower than the quasi-peak detector (for bands C and D) level and 10 dB lower than the peak detector indication. Measurements of impulsive noise will result in levels between the average detector level and the quasi-peak detector or peak detector indications. In general, the RMS-average detector is applicable for all types of continuous disturbance.

Table 39 shows examples of measurement results for some broadband disturbance sources, measured with the average, RMS-average and quasi-peak detectors at frequencies in bands B and C. The measurements were taken in a small round-robin test, conducted in Germany in 2004.

IECNORM.COM : Click to view the full PDF of CISPR TR 16-3:2020 RLV

**Table 39 – Measurement results for broadband disturbance sources (measurements with RMS-average and quasi-peak detectors are normalized to average detector values)**

| EUT | $f$ MHz | Average value dB(μV) | RMS-average minus average dB | Quasi-peak minus average dB |
|---|---|---|---|---|
| Hairdryer | 1,0 | 32,75 | +3,39 | +11,81 |
| Hairdryer | 35 | 33,80 | +8,49 | +26,84 |
| Washing machine 1 | 0,768 | 20,67 | +4,74 | +21,79 |
| Washing machine 1 | 124 | 13,68 | +3,80 | +19,91 |
| Washing machine 2 | 0,71 | 26,98 | +1,71 | +9,22 |
| Washing machine 2 | 116 | 18,90 | +3,92 | +22,04 |

Taking into account that the RMS-average measuring receiver addresses disturbance effects of all types of continuous emissions, it is possible to define one limit only, i.e. a single limit could be used and the limits for average and quasi-peak (or peak) detectors could be merged into one single limit, except for cases of discontinuous disturbances and disturbances like microwave oven emissions. However, this decision is ultimately to be made by product committees i.e. the committees responsible for the definition of emission limits. The application of the RMS-average detector for measurements of discontinuous disturbances is to be discussed.

## 4.9 Common mode absorption devices (CMAD)

### 4.9.1 General

#### 4.9.1.1 Purpose and application of CMAD

Common mode absorption devices (CMAD) are applied on cables leaving the test volume during radiated disturbance tests at a test site. The purpose of this part of CISPR 16 is to define the common mode (CM) impedance at the point where the cable leaves the test volume.

Figure 172 shows an example of an EUT in a radiated emission measurement test set-up for table-top equipment. The cables (e.g. the power supply cable, telecom cables, or other external connections used to exercise the EUT during the test) leave the test volume at the centre of the turntable. Radiation at frequencies between 30 MHz and about 200 MHz is from the cable acting as an antenna. The EUT together with the cable and the ground plane of the test site behave like a “top-loaded monopole antenna.” The radiation of such an antenna depends on the HF source (at the EUT connection of the cable), on the current distribution (CM current on the cable), and length of this unintended antenna. The current distribution depends upon the CM impedance at both ends of the antenna.

IECNORM.COM : Click to view the full PDF of CISPR TR 16-3:2020 RLV

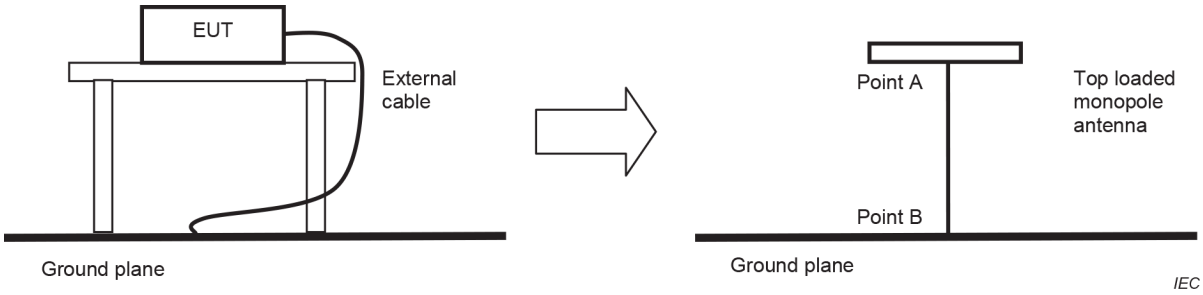



**Figure 172 – Example of a simple EUT model**

The CM impedance is unknown at both ends of the cable (points A and B in Figure 172). The CM impedance at point A is determined by the EUT and can have any value. For a given EUT, the value is fixed whenever the test is performed with an identical EUT. However, the CM impedance at point B ($Z_{apparent}$) may vary at each test laboratory, and can have any value because actual test procedures give no requirements for the CM impedance at this point. The actual value depends on the construction and layout of the test laboratory outside the test volume. Examples are given in [60].

It has been shown [60] [61] that the variation of the undefined CM impedance at point B can lead to variations as shown in Table 40 for radiated emissions measured from small EUTs. The sizes of these small EUTs were between 20 cm by 10 cm by 10 cm and 50 cm by 30 cm by 30 cm.

**Table 40 – Expected deviations between different laboratories for small EUTs due to variations of the impedance $Z_{apparent}$ at point B**

| Frequency range | Possible maximum deviations of the radiated emission results between different laboratories |
|---|---|
| 30 MHz to 50 MHz | 10 dB to 25 dB |
| 50 MHz to 120 MHz | 5 dB to 15 dB |
| 120 MHz to 200 MHz | 2 dB to 7 dB |

NOTE The variations of the cable layout in the test volume are not considered in this context. Table 40 does not include the variations of the radiation emission results due to variations in the cable layout.

The purpose of a CMAD is to reduce the influence of the CM impedance at point B upon the compliance uncertainty to a negligible amount.

#### 4.9.1.2 Important properties of CMADs

The main purpose of a CMAD is to ensure that the CM impedance $Z_{apparent}$ at the point B of Figure 172 is always the same, independent of the undefined impedance at the cable entrance to the test volume in the different laboratories. Therefore the following two properties are important:

- the cable including the CMAD should have a CM impedance $Z_{apparent}$ (or $S_{11apparent}$) within a specified tolerance;
- the CMAD impedance $Z_{apparent}$ (or $S_{11apparent}$) should be independent of the CM impedance at the other end of the CMAD.

An additional purpose of a CMAD can be to attenuate disturbance signals not produced by the EUT, in order to distinguish between the EUT as a disturbance source and other disturbance sources. For this purpose, the insertion loss $A_{IL}$ of the CMAD can be used as a figure-of-merit.

IECNORM.COM : Click to view the full PDF of CISPR TR 16-3:2020 RLV

NOTE 1 The insertion loss $A_{IL}$ is comprised of two components:

a) loss due to dissipation inside the device, and

b) loss due to mismatch between CMAD and line.

If two CMADs are used in cascade, the resulting insertion loss in general is not the sum of the individual insertion losses.

NOTE 2 The primary function of the absorbing clamp described in Clause 4 and Annex B of CISPR 16-1-3:2004, CISPR 16-1-3:2004/AMD1:2016 and CISPR 16-1-3:2004/AMD2:2020 [6], is for the measurement of interference power. Depending on the ferrite material used, some types of absorbing clamps are suitable as CMAD.

NOTE 3 The EM clamp defined in IEC 61000-4-6 for RF-injection immunity testing is not suitable for use as a CMAD as described herein.

### 4.9.2 CMAD as a two-port device

#### 4.9.2.1 Simple model of a CMAD

Usually CMADs are constructed using multiple ferrite clamps. Ferrite clamps have the advantage of being applicable to any type of cable, within a range of diameters. For measurements of the CMAD characteristics, the test cable is replaced by a well-defined test conductor. In Clause 9 of CISPR 16-1-4:2010 [7] a test conductor of 4 mm diameter is defined, located above a ground plane at the height defined by the dimensions of the CMAD (typically 30 mm). The CMAD (ferrite clamp) along with the test conductor above the ground plane is regarded as a two-port device (see Figure 173).

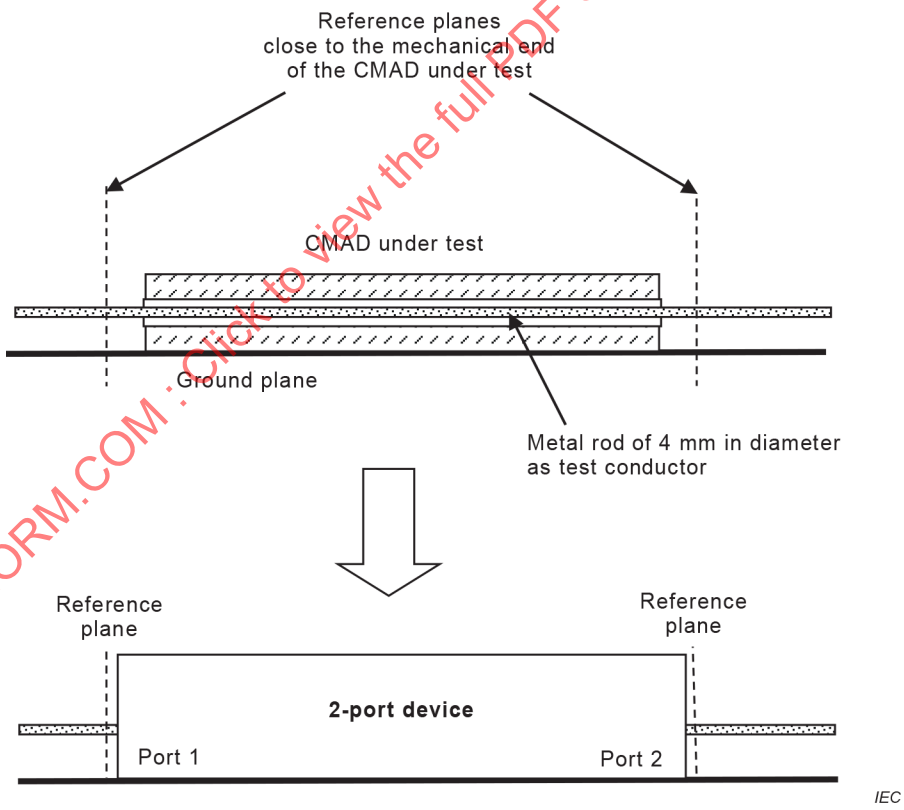



**Figure 173 – Representation of a CMAD as a two-port device**

A two-port device is completely described by the $S$-parameters measured at ports 1 and 2. The $S$-parameters are referenced to the characteristic impedance, $Z_{ref}$, of the test conductor above the ground plane without the CMAD in place, given by

IECNORM.COM : Click to view the full PDF of CISPR TR 16-3:2020 RLV

$$Z_{\text{ref}} = \frac{Z_0}{2\pi}\cosh^{-1}\left(\frac{2h}{d}\right) \text{ in } \Omega \tag{21}$$

where

$Z_0$ is the free-space impedance ($120\pi$) in Ω;

$d$ is the test conductor diameter (defined to be 4 mm);

$h$ is the height of the centre of the test conductor above the ground plane.

EXAMPLE Typical values of $Z_{\text{ref}}$ for various heights $h$:

| $h$ | $Z_{\text{ref}}$ |
|---|---|
| 30 mm | 204 Ω |
| 65 mm | 248 Ω |
| 90 mm | 270 Ω |

Any two-port network may be represented using various sets of parameters; each of these gives a complete characterisation of the two-port device. Examples of two-port parameter sets are:

- $S_{11}$, $S_{21}$, $S_{12}$ and $S_{22}$ – $S$-parameters: four complex numbers, related to a reference impedance $Z_{\text{ref}}$;
- $A$, $B$, $C$, $D$ ($ABCD$ matrix: 4 complex numbers);

Other types of two-port parameter representations are described in the literature, but do not offer any advantages in the present context.

#### 4.9.2.2 Parameters of a CMAD represented as a two-port device

The performance of a CMAD can basically be defined by the four complex $S$-parameters when measured as a two-port device in a test jig. The test conductor in the test jig has a diameter of 4 mm. The height above the ground plane, $h$, is defined by the dimensions of the CMAD. These two parameters define the reference impedance, $Z_{\text{ref}}$, for the $S$-parameter measurements. If the CMAD is symmetrical, $S_{11}$ and $S_{22}$ have the same value. If the device is not symmetrical, the test report shall describe which port was used for the $S_{11}$ test (the end closed to the EUT to be used for radiated emissions measurements), or the results shall be reported for both ports of the CMAD.

#### 4.9.2.3 Conversion between $S$-parameters and $ABCD$-parameters for a two-port network element

The conversion from $S$-parameters to $ABCD$-matrix representation is given by the following equations ($Z_{\text{ref}}$ is the reference impedance to which the $S$-parameters are referred):

$$A = \frac{(1+S_{11})(1-S_{22})+S_{12}S_{21}}{2S_{21}} \tag{22}$$

$$B = \frac{(1+S_{11})(1+S_{22})-S_{12}S_{21}}{2S_{21}} Z_{\text{ref}} \tag{23}$$

$$C = \frac{[(1-S_{11})(1-S_{22})-S_{12}S_{21}]/2S_{21}}{Z_{\text{ref}}C} \tag{24}$$

$$D = \frac{(1-S_{11})(1+S_{22})+S_{12}S_{21}}{2S_{21}} \tag{25}$$

The inverse equations are:

$$S_{21} = \frac{2}{A+B'+C'+D} \tag{26}$$

IECNORM.COM : Click to view the full PDF of CISPR TR 16-3:2020 RLV

$$S_{11} = \frac{A + B' - C' - D}{A + B' + C' + D} \tag{27}$$

$$S_{12} = \frac{2(A \times D - B \times C)}{A + B' + C' + D} \tag{28}$$

$$S_{22} = \frac{-A + B' - C' + D}{A + B' + C' + D} \tag{29}$$

where

$$B' = \frac{B}{Z_{\text{ref}}} \tag{30}$$

$$C' = CZ_{\text{ref}} \tag{31}$$

NOTE All operations in the preceding equations are for complex numbers. All parameters are functions of frequency. The equations are valid at each frequency point.

#### 4.9.2.4 Range of variations for $S_{11}$ due to undefined impedance at the far end of a CMAD

The apparent impedance of a two-port network element characterized by its $ABCD$-parameters is given by:

$$Z_{\text{apparent}} = \frac{AZ_{\text{end}} + B}{CZ_{\text{end}} + D} \tag{32}$$

From this equation the $S_{11}$ parameter can be calculated using:

$$S_{11\text{apparent}} = \frac{Z_{\text{apparent}} - Z_0}{Z_{\text{apparent}} + Z_0} = \frac{(A - CZ_0)Z_{\text{end}} + (B - DZ_0)}{(A + CZ_0)Z_{\text{end}} + (B + DZ_0)} \tag{33}$$

$Z_{\text{apparent}}$ and $S_{11\text{apparent}}$ are the values seen at port 1 if port 2 is connected to an impedance of $Z_{\text{end}}$.

Both quantities $Z_{\text{apparent}}$ and $S_{11\text{apparent}}$ are a conformal mapping of $Z_{\text{end}}$, expressed as:

$$f(Z_{\text{end}}) = \frac{aZ_{\text{end}} + b}{cZ_{\text{end}} + d} \tag{34}$$

The general form of the equation for this type of conformal mapping is:

$$f(z) = \frac{az + b}{cz + d} \tag{35}$$

This type of function has the property that it transforms straight lines and circles in the $z$-plane into either straight lines or circles in the $f$-plane. In particular, if the values of $z$ are restricted to positive real values, the transformation of this half plane results in a circle in the $f$-plane, as shown in Figure 174.

IECNORM.COM : Click to view the full PDF of CISPR TR 16-3:2020 RLV

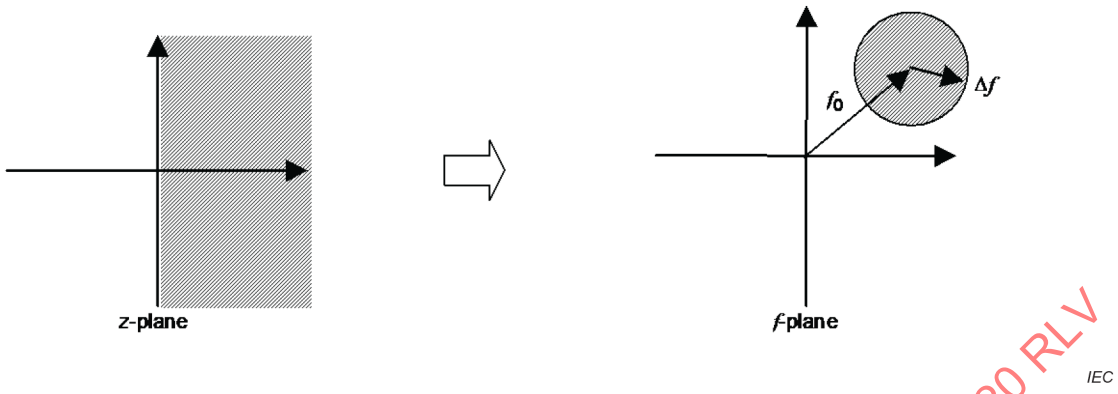



**Figure 174 – Conformal mapping between $z$-plane and $f$-plane**

The centre of this circle is at:

$$f_0 = \frac{bc - ad}{2c^2\,\mathrm{Re}(d/c)} + \frac{a}{c} \quad \text{(complex value)} \tag{36}$$

The radius of this circle is:

$$|\Delta f| = \left| \frac{bc - ad}{2c^2\,\mathrm{Re}(d/c)} \right| \quad \text{(scalar value)} \tag{37}$$

The maximum value of $|f|$ is then:

$$|f|_{\max} = |f_0| + |\Delta f| \quad \text{(scalar value)} \tag{38}$$

The minimum value of $|f|$ is then:

$$|f|_{\min} = |f_0| - |\Delta f| \quad \text{if } |f_0| > |\Delta f| \quad \text{else} \quad |f|_{\min} = 0 \tag{39}$$

Using these relations for $Z_{\text{apparent}}$ gives the following parameters:

Position of the centre of the circle:

$$Z_{\text{apparent centre}} = \frac{BC - AD}{2C^2\,\mathrm{Re}(D/C)} + \frac{A}{C} \quad \text{(complex value)} \tag{40}$$

Radius of the circle:

$$|\Delta Z_{\text{apparent}}| = \frac{BC - AD}{2C^2\,\mathrm{Re}(D/C)} \quad \text{(scalar value)} \tag{41}$$

Maximum value of $Z_{\text{apparent}}$:

$$|Z_{\text{apparent}}|_{\max} = |Z_{\text{apparent centre}}| + |\Delta Z_{\text{apparent}}| \tag{42}$$

IECNORM.COM : Click to view the full PDF of CISPR TR 16-3:2020 RLV

Minimum value of $Z_{\text{apparent}}$:

$$\left|Z_{\text{apparent}}\right|_{\text{min}} = \left|Z_{\text{apparent/center}}\right| - \left|\Delta Z_{\text{apparent}}\right| \quad \text{if} \quad \left|Z_{\text{apparent centre}}\right| > \left|\Delta Z_{\text{apparent}}\right| \quad \text{else} \quad \left|Z_{\text{apparent}}\right|_{\text{min}} = 0 \tag{43}$$

For $S_{11}$ the relevant parameters are given by:

Position of the centre of the circle:

$$S_{11\text{centre}} = \frac{(BC - AD)Z_0}{(A + CZ_0)^2 \,\text{Re}\left(\frac{B + DZ_0}{A + CZ_0}\right)} + \frac{A - CZ_0}{A + CZ_0} \tag{44}$$

Radius of the circle:

$$\left|\Delta S_{11}\right| = \left|\frac{(BC - AD)Z_0}{(A + CZ_0)^2 \,\text{Re}\left(\frac{B + DZ_0}{A + CZ_0}\right)}\right| \tag{45}$$

Maximum value of $\left|S_{11\text{apparent}}\right|$:

$$\left|S_{11\text{apparent}}\right|_{\text{max}} = \left|S_{11\text{centre}}\right| + \left|\Delta S_{11}\right| \tag{46}$$

Minimum value of $\left|S_{11\text{apparent}}\right|$:

$$\left|S_{11\text{apparent}}\right|_{\text{min}} = \left|S_{11\text{centre}}\right| - \left|\Delta S_{11}\right| \text{ if } \left|S_{11\text{centre}}\right| > \left|\Delta S_{11}\right| \quad \text{else} \quad \left|S_{11\text{apparent}}\right|_{\text{min}} = 0 \tag{47}$$

### 4.9.3 Measurement of CMAD

#### 4.9.3.1 General

The CMAD parameters are defined as parameters of the two-port network measured at the reference planes with the reference impedance $Z_{\text{ref}}$ given by the dimensions of the test jig cross section at the reference plane. Vector network analysers (VNA) used to measure the $S$-parameters operate with coaxial connectors having a characteristic impedance of 50 Ω. Between this 50 Ω coaxial connection and the non-coaxial configuration of the two-port device to be measured, an adaptor is needed to convert the 50 Ω coaxial connector to the geometry of the two-port device to be measured. Figure 175 illustrates the relevant set-up.

IECNORM.COM : Click to view the full PDF of CISPR TR 16-3:2020 RLV

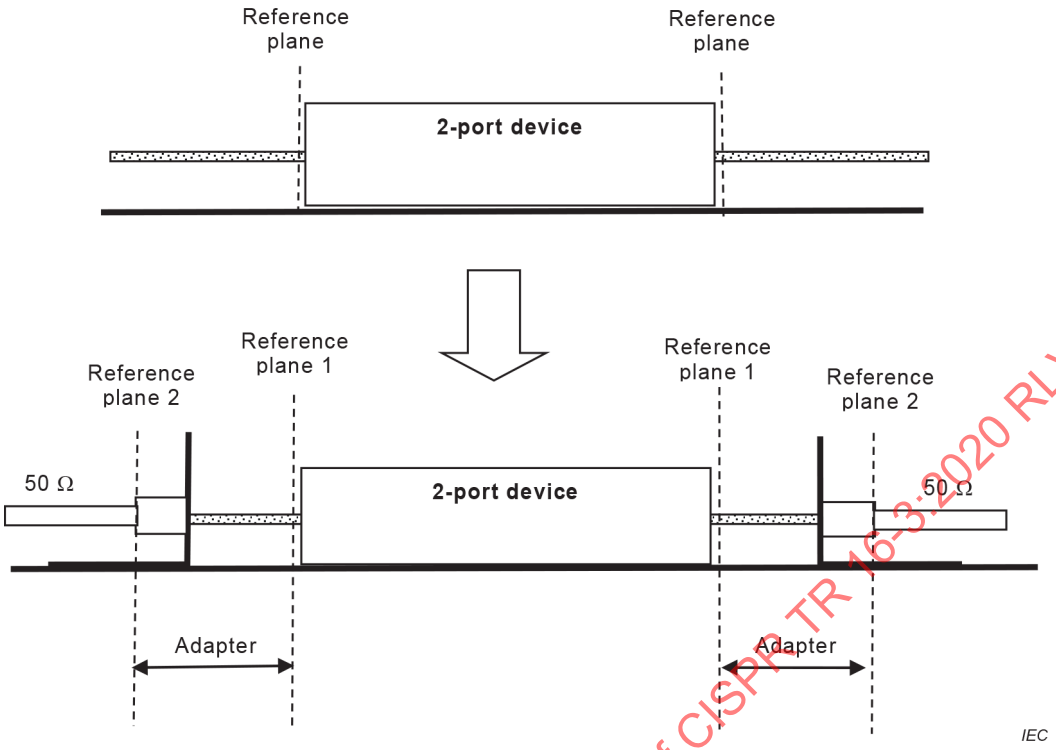



**Figure 175 – Conversion from 50 Ω coaxial system to the geometry of the two-port device-under-test**

If the TRL (through-reflect-line) calibration method is used, it is possible to define calibration at reference plane 1 of Figure 175. The measurement result is directly referred to the connections of the two-port device at reference plane 1, and the measurement result does not include the adaptors. Measurements based on TRL calibrations are therefore recommended for accurate measurements of CMAD characteristics. The details of the TRL calibration method are described in [62], [63].

The classical SOLT (short-open-load-through) calibration method for a VNA is made at the reference plane 2 of Figure 175 for which the necessary calibration kits are commercially available. If this calibration at reference plane 2 is used, the properties of the adaptors are included in the measurement result.

The effect of the adaptors can be compensated partially using other “simplified” methods – two alternative methods are described in 4.9.3.3 and 4.9.3.4:

a) measurement with SOLT calibration and position shifting (matching adaptors);

b) measurement with SOLT calibration and transformation to $Z_{ref}$ (lossless 50 Ω adaptors).

IECNORM.COM : Click to view the full PDF of CISPR TR 16-3:2020 RLV

#### 4.9.3.2 Measurement with TRL calibration method

##### 4.9.3.2.1 General

The TRL calibration method is based on the model shown in Figure 176 [62] [63].

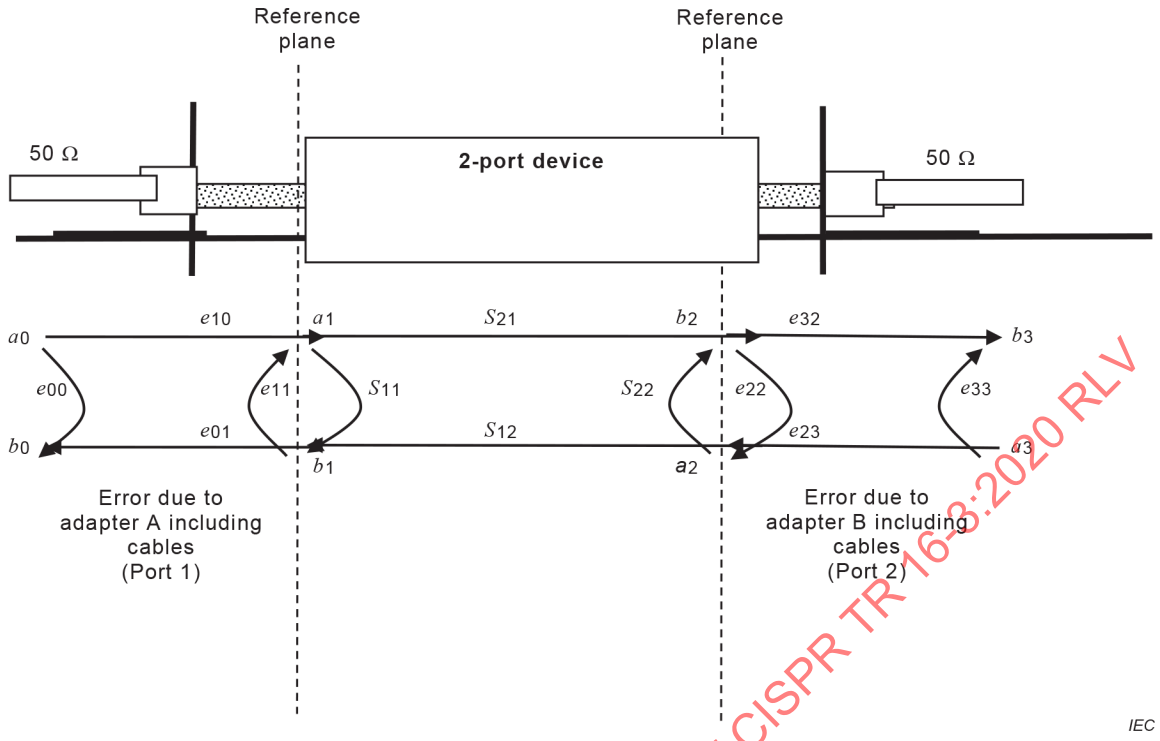



**Figure 176 – Basic model for the TRL calibration**

The four $S$-parameters are the true values of the measured two-port device. The parameters of the two adapters A and B are unknown and need to be derived from the calibration measurements with different external connections.

Four calibration configurations are necessary for the TRL calibration:

a) "reflect" (port 1): measuring the complex value $S_{11}$ of the adaptor section and adapter at port 1 without any other connection (simulating an open) – see Figure 177 a);

b) "reflect" (port 2): measuring the complex value $S_{22}$ of the adapter section and adapter at port 2 without any other connection (simulating an open) – see Figure 177 b);

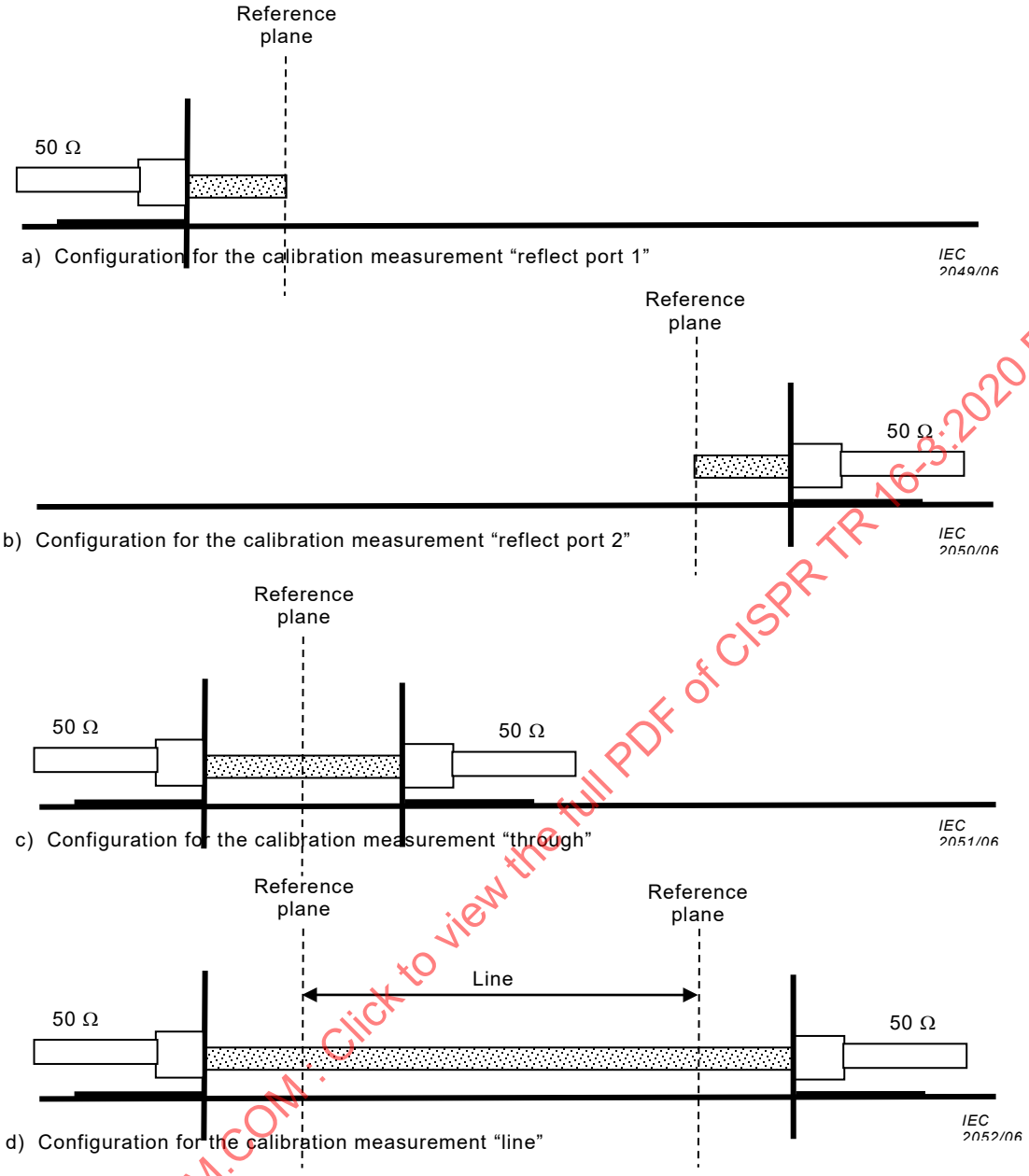
c) "through": measuring the complex values $S_{11}$, $S_{12}$, $S_{21}$, $S_{22}$ with the two adapter sections directly connected together (without the transmission line section in between) – see Figure 177 c);

d) "line": measuring the complex values $S_{11}$, $S_{12}$, $S_{21}$, $S_{22}$ with the transmission line section introduced – see Figure 177 d).

The results of these calibration measurements are 10 complex numbers for each frequency. Many VNAs have firmware for the TRL calibration included. If the VNA includes firmware for TRL calibration, it will use these reference measurements to calculate the proper corrections for the TRL measurement. If the VNA does not support the TRL calibration, the necessary corrections can be made externally according to the procedure described below (4.9.3.2.2 to 4.9.3.2.5).

The characteristic impedance of the "line" section has to be known exactly and is introduced into the calibration data used by the firmware of the VNA. Some firmware also asks for the electrical length of the "line" section, but theoretically only the impedance is needed. The properties of the adaptor section and adaptors outside the calibration plane do not need to be known for the TRL calibration. These properties are measured in the calibration procedure and are compensated directly by the TRL calibration. Any type of adaptors may be used.

IECNORM.COM : Click to view the full PDF of CISPR TR 16-3:2020 RLV




NOTE The length $L$ of the reference line for the calibration needs not to be the same as the length used for the measurement of the CMAD. The length of the reference line for the calibration procedure is selected according to the frequency range needed.

IECNORM.COM : Click to view the full PDF of CISPR TR 16-3:2020 RLV

**Figure 177 – The four calibration configurations necessary for the TRL calibration**

The length of the “line” section during the TRL calibration establishes the frequency range for which the TRL calibration may be used. This limitation results from the mathematical procedure used in the TRL calibration, where for some frequencies a divide-by-zero (or very small values) is possible and shall be avoided.

If the length of the “line” reference is $L$, the frequency range shall be limited to between low and high frequencies $f_L$ and $f_H$ as follows:

$$f_L = 0{,}05\frac{c}{L} \text{ and} \tag{48}$$

$$f_H = 0{,}45\frac{c}{L} \tag{49}$$

where $c$ is 3 × $10^8$ m/s. A "line" length of 0,6 m is appropriate for calibration in the frequency range 30 MHz to 200 MHz. If the measurement has to be extended to higher frequencies, a second "line" calibration is necessary. A second calibration with a "line" length of 0,12 m would be appropriate for the frequency range 150 MHz to 1 000 MHz.

#### 4.9.3.2.2 Measurements

The results of the four calibration measurements shall be recorded in the format shown in Table 41, where the subscript M denotes measured value.

**Table 41 – Calibration measurement results format**

| | |
|---|---|
| Reflect port 1 | $S_{11,M}$ |
| Reflect port 2 | $S_{22,M}$ |
| Through | $T_{Mt} = \begin{bmatrix} T_{11,Mt} & T_{12,Mt} \\ T_{21,Mt} & T_{22,Mt} \end{bmatrix} = \frac{1}{S_{21,Mt}} \begin{bmatrix} S_{12,Mt}S_{21,Mt} - S_{11,Mt}S_{22,Mt} & S_{11,Mt} \\ -S_{22,Mt} & 1 \end{bmatrix}$ |
| Delay | $T_{Md} = \begin{bmatrix} T_{11,Md} & T_{12,Md} \\ T_{21,Md} & T_{22,Md} \end{bmatrix} = \frac{1}{S_{21Md}} \begin{bmatrix} S_{12,Md}S_{21,Md} - S_{11,Md}S_{22,Md} & S_{11,Md} \\ -S_{22,Md} & 1 \end{bmatrix}$ |

The conversion between $T$-parameters and $S$-parameters is given by:

$$\begin{bmatrix} T_{11} & T_{12} \\ T_{21} & T_{22} \end{bmatrix} = \frac{1}{S_{21}} \begin{bmatrix} S_{12}S_{21} - S_{11}S_{22} & S_{11} \\ -S_{22} & 1 \end{bmatrix} \text{ and} \tag{50}$$

$$\begin{bmatrix} S_{11} & S_{12} \\ S_{21} & S_{22} \end{bmatrix} = \frac{1}{T_{22}} \begin{bmatrix} T_{12} & T_{11}T_{22} - T_{12}T_{21} \\ 1 & -T_{21} \end{bmatrix} \tag{51}$$

#### 4.9.3.2.3 Calculation of the conversion parameters

From the calibration measurements, the conversion parameters are derived according to the following procedure:

1) Define the Matrix $M$ as:

$$M = \begin{pmatrix} m_{11} & m_{12} \\ m_{21} & m_{22} \end{pmatrix} \equiv T_{Md}T_{Mt}^{-1} \tag{52}$$

2) Define the Matrix $N$ as:

$$N = \begin{pmatrix} n_{11} & n_{12} \\ n_{21} & n_{22} \end{pmatrix} \equiv T_{Mt}^{-1}T_{Md} \tag{53}$$

3) Solve the preceding equations with respect to $x$:

$$m_{21}x^2 + (m_{22} - m_{11})x - m_{12} = 0 \tag{54}$$

This gives two solutions. Give the two solutions the names $x_1$ and $x_2$ such that $|x_1| > |x_2|$.

4) Solve the equations with respect to $y$:

$$n_{12}y^2 + (n_{22} - n_{11})y - n_{21} = 0 \tag{55}$$

NOTE Take note of the indices – not the same as the previous equation.

IECNORM.COM : Click to view the full PDF of CISPR TR 16-3:2020 RLV

This gives two solutions. Give the two solutions the names $y_1$ and $y_2$ such that $|y_1| > |y_2|$.

5) Define a, b, c, and d as follows:

$$\begin{aligned} a &= x_1 \\ b &= x_2 \\ c &= y_1 \\ d &= y_2 \end{aligned} \tag{56}$$

6) Define also the following variables:

$$\begin{aligned} e_{00} &= b \\ e_{33} &= -d \\ f_1 &= \frac{S_{11,\mathrm{M}} - b}{S_{11,\mathrm{M}} - a} \\ f_2 &= \frac{S_{22,\mathrm{M}} + c}{S_{22,\mathrm{M}} + d} \\ f_3 &= \frac{S_{11,\mathrm{Mt}} - b}{S_{11,\mathrm{Mt}} - a} \end{aligned} \tag{57}$$

7) Now compute the following variables:

$$\begin{aligned} e_{11} &= \sqrt{f_1 f_2 f_3} \\ e_{10}e_{01} &= e_{11}(b - a) \end{aligned} \tag{58}$$

We now have to distinguish which root to take and therefore we compute the real part of the reflection coefficient:

$$\Gamma_{\mathrm{a}} = \frac{1}{e_{11}} \frac{S_{11,\mathrm{M}} - b}{S_{11,\mathrm{M}} - a} \tag{59}$$

It should be near a value of 1 for OPEN and near a value of -1 for SHORT. If not, take the other root for $e_{11}$, and redefine $e_{10}e_{01}$.

8) Perform the further computations:

$$\begin{aligned} e_{22} &= f_3 / e_{11} \\ e_{23}e_{32} &= e_{22}(c - d) \\ e_{10}e_{32} &= S_{21,\mathrm{Mt}}(1 - e_{11}e_{22}) \end{aligned} \tag{60}$$

9) Determine the forward conversion parameters $e_{00}$, $e_{11}$, $e_{22}$, $e_{33}$, as well as:

$$\begin{aligned} \Delta_x &= e_{00}e_{11} - e_{10}e_{01} \\ \Delta_y &= e_{22}e_{33} - e_{32}e_{23} \\ k &= e_{10} / e_{23} = \frac{e_{10}e_{32}}{e_{23}e_{32}} \end{aligned} \tag{61}$$

10) Determine the inverse conversion parameters:

$$\begin{aligned} e_{00}^{\mathrm{inv}} &= e_{00} / \Delta_x \\ e_{11}^{\mathrm{inv}} &= e_{11} / \Delta_x \\ e_{22}^{\mathrm{inv}} &= e_{22} / \Delta_y \\ e_{33}^{\mathrm{inv}} &= e_{33} / \Delta_y \\ \Delta_x^{\mathrm{inv}} &= 1 / \Delta_x \\ \Delta_y^{\mathrm{inv}} &= 1 / \Delta_y \end{aligned} \tag{62}$$

IECNORM.COM : Click to view the full PDF of CISPR TR 16-3:2020 RLV

$$k^{\text{inv}} = \frac{e_{01}\Delta_y}{e_{32}\Delta_x} = \frac{1}{k}\frac{e_{00}e_{11} - \Delta_x}{\Delta_x}\frac{\Delta_y}{e_{22}e_{33} - \Delta_x} = \frac{1}{k}\frac{e_{00}e_{11}/\Delta_x - 1}{e_{22}e_{33}/\Delta_y - 1} \tag{63}$$

#### 4.9.3.2.4 Forward conversion (from $S_{\text{effective}}$ to $S_{\text{measured}}$)

If $S_{ij}$ are the effective $S$-parameters of a network, then the measured $S$-parameters, $M_{ij}$, are computed using:

$$N = (1 - S_{11}e_{11})(1 - S_{22}e_{22}) - S_{21}S_{12}e_{11}e_{22} \tag{64}$$

$$\begin{aligned} M_{11} &= \left[(e_{00} - S_{11}\Delta_x)(1 - S_{22}e_{22}) - S_{21}S_{12}e_{22}\Delta_x\right]/N \\ M_{12} &= (S_{12}/k)(e_{00}e_{11} - \Delta_x)/N \\ M_{21} &= (S_{21}k)(e_{22}e_{33} - \Delta_y)/N \\ M_{22} &= \left[(e_{33} - S_{22}\Delta_y)(1 - S_{11}e_{11}) - S_{12}S_{21}e_{11}\Delta_y\right]/N \end{aligned} \tag{65}$$

#### 4.9.3.2.5 Inverse conversion (from $S_{\text{measured}}$ to $S_{\text{effective}}$)

The effective $S$-parameters $S_{ij}$ are determined from measured $S$-parameters $M_{ij}$ using:

$$N^{\text{inv}} = (1 - M_{11}e_{11}^{\text{inv}})(1 - M_{22}e_{22}^{\text{inv}}) - M_{21}M_{12}e_{11}^{\text{inv}}e_{22}^{\text{inv}} \tag{66}$$

$$\begin{aligned} S_{11} &= \left[(e_{00}^{\text{inv}} - M_{11}\Delta_x^{\text{inv}})(1 - M_{22}e_{22}^{\text{inv}}) - M_{21}M_{12}e_{22}^{\text{inv}}\Delta_x^{\text{inv}}\right]/N^{\text{inv}} \\ S_{12} &= (M_{12}/k^{\text{inv}})(e_{00}^{\text{inv}}e_{11}^{\text{inv}} - \Delta_x^{\text{inv}})/N^{\text{inv}} \\ S_{21} &= (M_{21}k^{\text{inv}})(e_{22}^{\text{inv}}e_{33}^{\text{inv}} - \Delta_y^{\text{inv}})/N^{\text{inv}} \\ S_{22} &= \left[(e_{33}^{\text{inv}} - M_{22}\Delta_y^{\text{inv}})(1 - M_{11}e_{11}^{\text{inv}}) - M_{12}M_{21}e_{11}^{\text{inv}}\Delta_y^{\text{inv}}\right]/N^{\text{inv}} \end{aligned} \tag{67}$$

These four $S$-parameters are the result of measurements using the TRL calibration method.

### 4.9.3.3 Measurement with SOLT calibration and position shifting – simplified method

#### 4.9.3.3.1 General

The SOLT (Short-Open-Load-Through) calibration method is only possible at the reference planes 1 and 6 shown in Figure 178. The influence of the adaptor section (between reference planes 1 and 2 and between reference planes 5 and 6, of Figure 178 and the open length of the test conductor (between reference planes 2 and 3, and between reference planes 4 and 5, of Figure 178 upon the final result may be partially compensated by making two measurements with the CMAD at two different positions inside the jig, then combining results from these two measurements. This compensation is optimal if matching adaptors are used (to match the impedance of the 50 Ω coaxial connection to the reference impedance $Z_{\text{ref}}$ of the test jig). The following simplified method may be applied in the frequency range from 30 MHz to 1 000 MHz.

#### 4.9.3.3.2 Scattering parameter representation

Figure 178 shows a scattering parameter representation of the CMAD measurement. A network analyzer is connected to the reference planes 1 and 6. Hence the measurement can yield only the $S$-parameters, $S_{ij_T}$, of the total system, while the $S$-parameters of a CMAD, $S_{ij_C}$, are to be determined. The total $S$-parameters are express in terms of the $S$-parameters of the various sections as:

IECNORM.COM : Click to view the full PDF of CISPR TR 16-3:2020 RLV

$$\left(S_{11_T}\right)_{CMAD} = S_{11_a} + S_{21_a}S_{12_a}\frac{S_{11_c}e^{(-j2\beta L_A)}(1-Y) + S_{21_c}S_{12_c}S_{11_b}e^{[-j2\beta(L_A+L_B)]}}{(1-X)(1-Y)-Z} \tag{68}$$

$$\approx S_{11_a} + \frac{S_{21_a}S_{12_a}S_{11_c}e^{(-j2\beta L_A)}}{1-X}$$

$$\left(S_{21_T}\right)_{CMAD} = \frac{S_{21_a}S_{21_c}S_{21_b}e^{[-j\beta(L_A+L_B)]}}{(1-X)(1-Y)-Z} \tag{69}$$

$$\approx \frac{S_{21_a}S_{21_c}S_{21_b}e^{[-j\beta(L_A+L_B)]}}{(1-X)(1-Y)}$$

where

$$X \equiv S_{22_a}S_{11_c}e^{(-j2\beta L_A)}$$

$$Y \equiv S_{22_c}S_{11_b}e^{(-j2\beta L_B)} \tag{70}$$

$$Z \equiv S_{22_a}S_{21_c}S_{12_c}S_{11_b}e^{[-j2\beta(L_A+L_B)]}$$

The approximate expressions in the above equations are derived assuming that the insertion loss of a CMAD is relatively large, i.e. $|S_{21_c}|$, $|S_{12_c}| << 1$, because usually the insertion loss is more than 20 dB. Due to the symmetrical structure of a CMAD, the unknown parameters to be determined are $S_{11_c}$ (= $S_{22_c}$) and $S_{21_c}$ (= $S_{12_c}$) only.

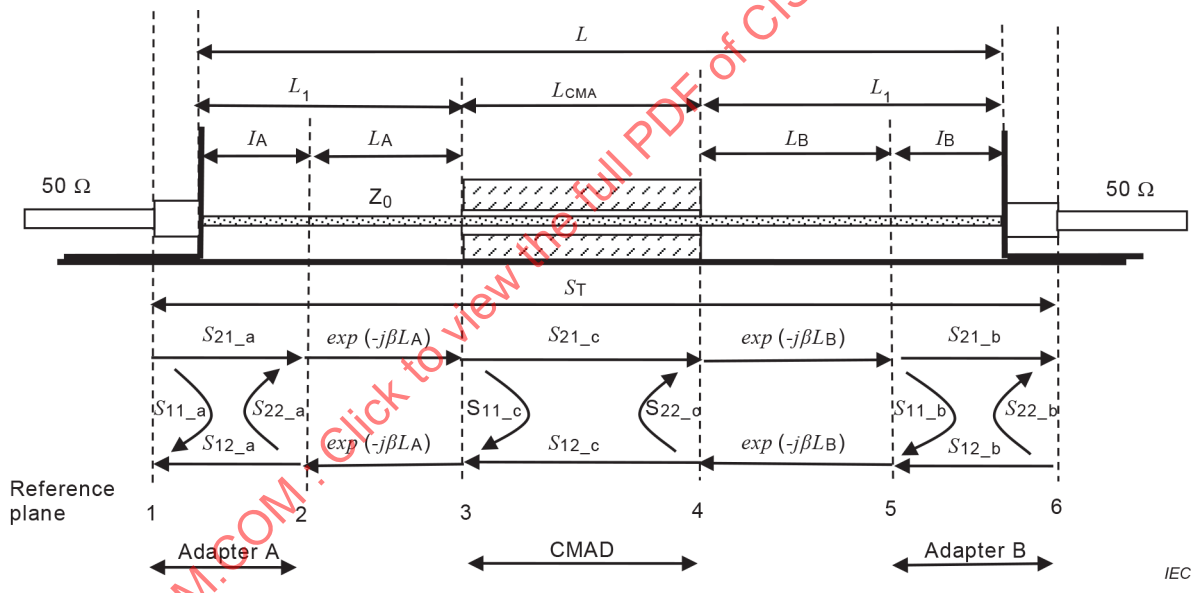



**Figure 178 – Measurement of CMAD characteristics**

IECNORM.COM : Click to view the full PDF of CISPR TR 16-3:2020 RLV

#### 4.9.3.3.3 Estimation of $|S_{21_c}|$

The $|S_{21_c}|$ of a CMAD under test is approximately given by

$$\left|S_{21_c}\right|_{simple} = \frac{\left|S_{21_T}\right|_{CMAD}}{\left|S_{21_T}\right|_{empty}} \approx \tag{71}$$

$$\frac{\left|1-(S_{22_a})^2e^{[-j2\beta(L_A+L_B+L_{CMAD})]}\right|}{\left|\left[1-S_{22_a}S_{11_c}e^{(-j2\beta L_A)}\right]\left[1-S_{22_a}S_{11_c}e^{(-j2\beta L_B)}\right]\right|}\left|S_{21_c}\right|$$

where

$$\left|S_{21_T}\right|_{empty} = \left|\frac{S_{21_a}S_{21_b}e^{(-j\beta\times L)}}{1-S_{22_a}S_{11_b}e^{(-j2\beta\times L)}}\right| = \left|\frac{S_{21_a}S_{21_b}}{1-S_{22_a}S_{11_b}e^{(-j2\beta\times L)}}\right| \tag{72}$$

This equation apparently demonstrates that if the adapters have a good match with the line section (i.e. $S_{22_a}$ = 0), the simplified method may yield an accurate value of $|S_{21_c}|$.

#### 4.9.3.3.4 Estimation of $\Gamma$ (= $|S_{11_c}|$)

The $|S_{11_c}|$ of a CMAD under test is approximately given by

$$\Gamma_{\text{simple}} = \frac{\left[\left(S_{11_T}\right)_1 - \left(S_{11_T}\right)_2\right] e^{(-j\beta L)}}{\left(S_{21_T}\right)_{\text{empty}} \left[e^{(-j2\beta L l_1)} - e^{(-j2\beta L l_2)}\right]} \tag{73}$$

where $(S_{11_T})_1$ and $(S_{11_T})_2$ denote $S_{11_T}$ parameters measured with $L_A = L_{A1}$ and $L_{A2}$, respectively. Both adapters are assumed to be identical, i.e. $|S_{21_b}| = |S_{12_a}|$.

#### 4.9.3.3.5 Uncertainty of $|S_{21_c}|$

Since the adapters may cause mismatch to some extent, uncertainty in the estimated insertion loss $A_{\text{IL_simple}}$ (=1/$|S_{21_c}|_{\text{simple}}$) should be evaluated using the following equation derived from Equation (71) with $L_A$, $L_B << \lambda$ assumed:

$$\frac{\left|1 - 2\left|S_{22_a}\right| \times \left|S_{11_c}\right|\right|}{1 + \left|S_{22_a}\right|^2} < \text{error in } A_{\text{IL_simple}} < \frac{1 + 2\left|S_{22_a}\right| \times \left|S_{11_c}\right|}{1 - \left|S_{22_a}\right|^2} \tag{74}$$

Equation (74) can provide a good estimate for a test set-up having matching adapters. However, it overestimates the uncertainty in the case of simple adapters without matching circuit. Hence, the following expression should apply to a set-up that does not have matching adapters:

$$\frac{\left(1 - \left|S_{22_a}\right| \times \left|S_{11_c}\right|\right)^2}{1 + \left|S_{22_a}\right|^2} < \text{error in } A_{\text{IL_simple}} < \frac{\left(1 + \left|S_{22_a}\right| \times \left|S_{11_c}\right|\right)^2}{1 - \left|S_{22_a}\right|^2} \tag{75}$$

The following preliminary check of the test set-up shall be made with the SOLT calibration before the CMAD measurement:

1) $|S_{21_T}|$ empty is the magnitude of $S_{21_T}$ measured in the test set-up without a CMAD introduced, as shown in Figure 179 a);
2) $|S_{21_T}|$ open is the magnitude of $S_{21_T}$ measured in the test set-up with truncated metal rods as shown in Figure 179 b). The lengths of the rods, $L_1$ and $L_2$, are determined according to Figure 178. The $|S_{21_T}|$ open data provides information about possible adverse effects of direct coupling between the adapters.

During the above measurements, the distance between the flanges, $L$, is the same as in the CMAD measurement.

IECNORM.COM : Click to view the full PDF of CISPR TR 16-3:2020 RLV

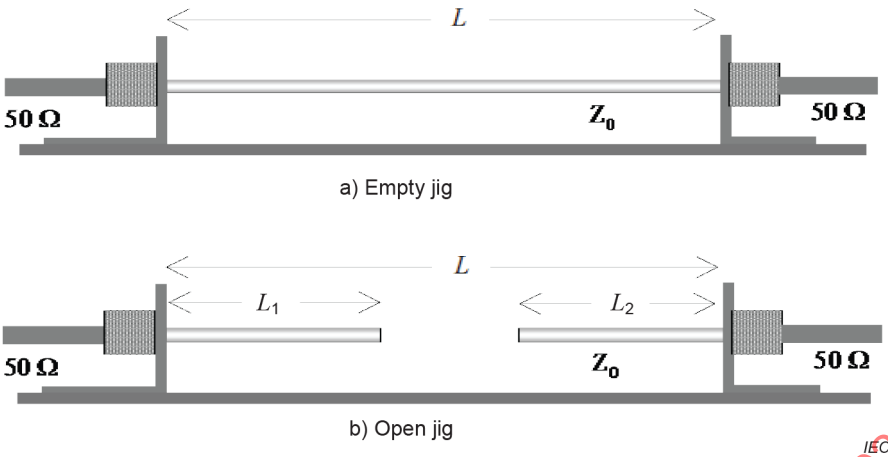



**Figure 179 – Preliminary measurements of the test set-up**

#### 4.9.3.3.6 Uncertainty of $\Gamma$ (= $|S_{11_c}|$)

Equation (74) provides approximations for the uncertainty in the estimated $|\Gamma|$ caused by mismatch. Theoretical and experimental analysis yields the same expressions for the uncertainty as shown in Equation (74) or Equation (75). Estimation of the uncertainty in $|\Gamma_{simple}|$ caused by mismatch is done using Equation (74) or Equation (75), assuming a U-shaped probability distribution.

Another error is introduced by the position of a CMAD during actual measurements. Errors in $|\Gamma_{simple}|$ can be estimated using the equation

$$\text{error in } |\Gamma| = \frac{|\sin(\beta(\Delta L + \delta))|}{|\sin(\beta(\Delta L)|} \tag{76}$$

for the case of an error $\delta$ in $\Delta L$=$|L_{A1}$-$L_{A2}|$. Uncertainty is estimated using Equation (76), assuming a uniform distribution.

#### 4.9.3.3.7 Mismatch of the adapters

The ratio of the maximum and minimum values of $|(S_{21_T})_{empty}|$ may be expressed as

$$\frac{\left|(S_{21_T})_{empty}\right|_{max}}{\left|(S_{21_T})_{empty}\right|_{min}} \cong \frac{1+\left|S_{22_a}\right|^2}{1-\left|S_{22_a}\right|^2} \tag{77}$$

in which the adapters A and B are assumed to be identical. Thus, variations in $|S_{21_T}|_{empty}$ versus frequency gives information about the reflection coefficients of the adapters.

### 4.9.3.4 Measurement with SOLT calibration and $ABCD$ transformation to $Z_{ref}$ level

The SOLT calibration is only possible at the reference planes 1 and 6 shown in Figure 178 and in Figure 180. If lossless 50 Ω adaptors are used, it is possible to measure the two-port parameters at the 50 Ω level then convert the results to the $Z_{ref}$ level by applying the $ABCD$ matrix method described in 4.9.2.3. The reference planes in Figure 180 have slightly different positions to those shown in Figure 178.

IECNORM.COM : Click to view the full PDF of CISPR TR 16-3:2020 RLV

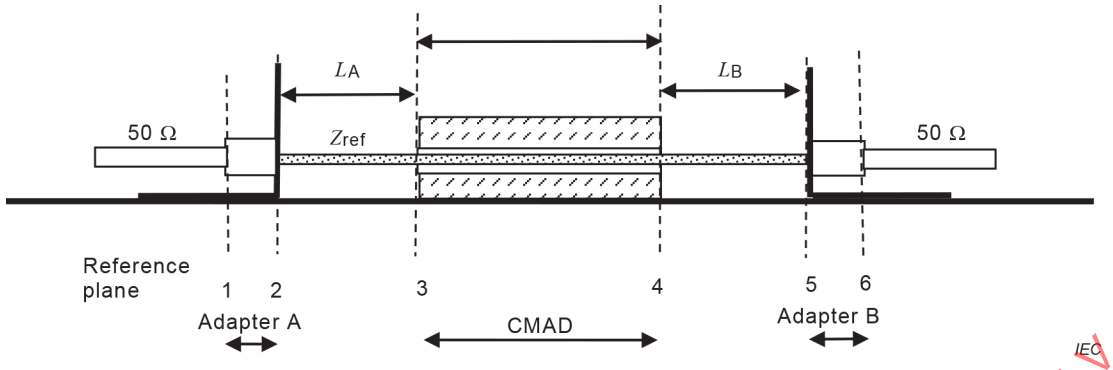



**Figure 180 – Position of the reference planes for the measurement with SOLT calibration and $ABCD$ transformation to $Z_{ref}$ level**

The VNA is calibrated at reference planes 1 and 6. The $S$-parameters of interest are the $S$-parameters at reference planes 3 and 4. The error due to this difference of reference shall be kept as small as possible, considering the following. If a lossless 50 Ω adapter is used, and if the construction of the adapter is such that the 50 Ω impedance is maintained in the section between reference planes 1 and 2, it is possible to compensate the electrical delay between the two reference planes. Most VNAs allow an internal compensation for an electrical delay. The length may be determined by calculation, or by measurement of the $S_{11}$ with the open adaptor and adjusting the delay by observing the Smith chart until the result approaches the result of an open circuit. The $S$-parameters measured by the VNA with electrical delay adjusted and activated are then the $S$-parameters at reference planes 2 and 5.

Using the Equations (22) to (25) with $Z_{ref}$ = 50 Ω, the $ABCD$ parameters of the two-port network between reference planes 2 and 5 are obtained. Equations (25) to (30) are used to transform the $ABCD$ parameters back to $S$-parameters, as referred to a new $Z_{ref}$ (for example 204 Ω for typical CMAD dimensions). These $S$-parameters are the values referred to the reference planes 2 and 5. If the lengths $L_A$ and $L_B$, between the reference planes 2 and 3 and the reference planes 4 and 5, are small (for example less than 30 mm for typical CMAD dimensions), the influence of the line elements $L_A$ and $L_B$ may be neglected (at least for frequencies up to about 300 MHz).

The most significant contributions to the uncertainty in this measurement are:

- tolerance of the calibration kit used for the calibration at the reference plane 1 and 6;
- tolerance of the mechanical dimensions of the test jig;
- impedance value of the adapter section between reference plane 1 and 2 or 5 and 6;
- electrical length of the adapter section between reference plane 1 and 2 or 5 and 6;
- tolerance of the delay compensation for the adapter section between reference plane 1 and 2 or 5 and 6;
- distance between adaptor and CMAD ($L_A$ and $L_B$).

### 4.10 Background on the definition of the FFT-based receiver

#### 4.10.1 General

In this subclause the following nomenclature is used:

a) upper case letters such as $X$ are used to describe signals in the frequency domain;

b) lower case letters such as $x$ are used for signals in the time domain;

IECNORM.COM : Click to view the full PDF of CISPR TR 16-3:2020 RLV

c) gapless non-sampled signals are written with round brackets $x(t)$;

d) square brackets such as $x[n]$ describe sampled signals;

e) two dimensional signals (arrays) are described with two indices e.g. $Z[n,m]$ and in upper case letters.

### 4.10.2 Tuned selective voltmeters and spectrum analyzers

Initially, tunable selective voltmeters were used to carry out emission measurements. This type of instrument routes the received signal through a preselector using a band-pass filter, then downconverts and weights it with a detector, e.g. a quasi-peak detector. Technical improvements to instrumentation then offered the possibility of performing stepped scans. Such instruments are referred to as EMI receivers.

For pre-compliance and compliance measurements, spectrum analyzers are also used, which usually perform a swept scan. The disadvantage of tuned selective voltmeters is the rather long time it takes to complete a scan across an entire frequency band of interest (e.g. Bands C and D). Such scans can take considerable time, especially when an intermittent signal is to be measured or when the quasi-peak detector is used. Spectrum analyzers usually have sweep times shorter than the scan time of a stepped scan. However such instruments may have a lower dynamic range than EMI receivers. Spectrum analyzers and EMI receivers have the disadvantage that the measurement can only be performed at a single frequency at any point in time.

Research and development activities on signal processing methods offered the possibility to replace analogue filters and detectors in EMI measurement equipment. Modern EMI receivers and spectrum analyzers have digital filters at the intermediate frequency and digital circuits to simulate detectors such as the quasi-peak detector. The implementation of digital technology in these instruments improved their accuracy, stability and reliability.

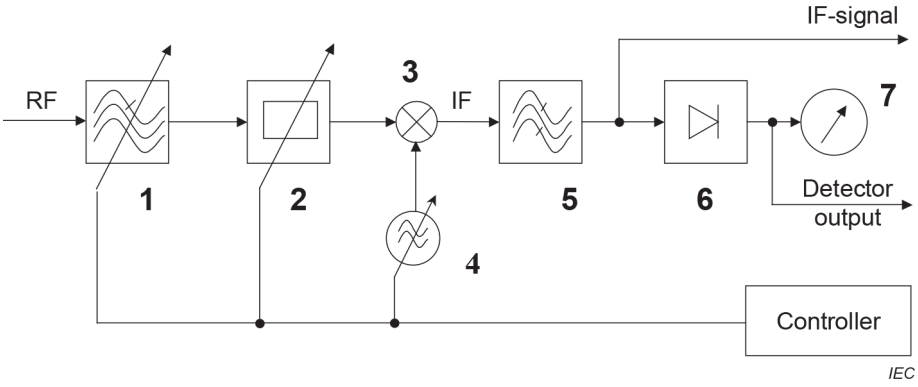
With availability of fast digital circuits and high-speed analogue-to-digital converters (ADC), systems can be implemented that calculate the spectrum at several thousand frequencies. The discrete Fourier transform (DFT) is a numerical mathematical method that calculates the spectrum for a periodic signal. Methods with a reduced number of multiplications are applied by the fast Fourier transform (FFT) that uses decimation in frequency (DIF) and decimation in time (DIT) [68].

However, a single FFT calculation will not yield the same result as measurements with a tuned selective voltmeter. Thus FFT analyzers are not suitable for use in emission measurements. Similar results can be obtained only if the IF filters and the detectors are modelled such that they do meet the requirements in CISPR 16-1-1. Research has been performed on this topic and it has been proven theoretically and through experiments that an FFT-based measurement system can be implemented that will provide the same result within the given measurement uncertainty as a tuned selective voltmeter. Its advantage is the significantly reduced scan time that is achieved by the parallel calculation at several frequencies [69]. Such instruments are called FFT-based receivers.

### 4.10.3 General principle of a tuned selective voltmeter

EMI receivers measure emissions in the frequency domain. The measurement for a given set of frequencies is performed sequentially. Modern EMI receivers are based on the superheterodyne principle. The block diagram of a conventional superheterodyne receiver is shown in Figure 181.

IECNORM.COM : Click to view the full PDF of CISPR TR 16-3:2020 RLV




**Key**

| | | | |
|---|---|---|---|
| 1 | Preselector | 5 | IF filter |
| 2 | Attenuator | 6 | Detector |
| 3 | Mixer | 7 | Meter |
| 4 | Local oscillator | | |

**Figure 181 – Superheterodyne EMI receiver**

The preselection filter suppresses signals that are far outside the frequency range of interest. This filtering process improves the dynamic range of the instrument for measurements of impulsive signals. A selectable input attenuator allows the control of the amplitude level at the mixer to avoid overload and thus ensure linear operation. A mixer and a local oscillator perform a downconversion of the signal to an intermediate frequency (IF). The signal is filtered by an IF band-pass filter. CISPR 16-1-1 defines certain IF bandwidths for each CISPR band. Each IF filter has to meet the requirements defined by a mask. The IF signal $S_{IF}(t)$ is made available as an analogue output signal.

The analogue output signal $S_{IF}$ is described in the frequency domain by:

$$S_{IF}(f) = S(f - f_{sel} + f_{IF}) H_{IF}(f) \quad (78)$$

where

$f_{sel}$ is the selected frequency,

$f_{IF}$ is the intermediate frequency, and

$H_{IF}(f)$ is the amplitude response of the IF filter.

The measured signal is shifted to the intermediate frequency $f_{IF}$ and multiplied by the frequency response of the IF filter. The output signal is weighted with the peak, average, RMS-average or quasi-peak detectors for the selected dwell time.

### 4.10.4 FFT-based receivers – digital signal processing

#### 4.10.4.1 Fast Fourier transform

Digital spectral estimation is achieved by the discrete Fourier transform (DFT). Algorithms for DFT computations that exploit symmetry and repetition properties of the DFT are defined as FFT. The DFT formulation that considers periodic repetition of the signal in the time-domain is defined as follows:

$$X[k] = \sum_{n=0}^{N-1} x[n] \times e^{-j2\pi kn/N} \quad (79)$$

IECNORM.COM : Click to view the full PDF of CISPR TR 16-3:2020 RLV

where

$x[n]$ is the sampled signal in the time domain; and

$X[k]$ is the discretized amplitude spectrum;

$n$ is an integer ranging from 0 to ($N$-1) that stores the element number of the signal in the frequency domain;

$k$ is an integer ranging from 0 to ($N$-1) that stores the element number of the signal in the frequency domain.

The properties of the Fourier series have been described by J. B. Fourier [82]. The exact mathematical proof was performed by Dirichlet [83]. DFT uses signals that consist of a series with a fixed number in time and frequency domains. These signals are equidistantly sampled in time domain, as well as in frequency domain [70].

#### 4.10.4.2 Short-time FFT

In general, EMI signals include both periodic and transient signals as well as noise, so the EMI receiver cannot be modelled with a single FFT calculation. In order to model the exact behavior of an EMI receiver, the short-time FFT (STFFT) is used. With the use of a Gaussian window function the IF filter is modeled according to its impulse bandwidth, noise-bandwidth and the filter masks as defined in CISPR 16-1-1. A spectrogram is calculated by applying STFFT [70]. This spectrogram shows a discretization in both the frequency and time domains. The resolution in the frequency domain is described by the bin width, $\Delta f$; the resolution in the time domain is described by a time step, $T_{\text{sbb}}$. The inverse of the time-step is called the baseband sampling rate, $f_{\text{sbb}}$.

The STFFT, $Z[m,k]$, is calculated as follows:

$$Z[m,k] = \sum_{n=0}^{N-1} x[n-m] \times w[n] \times \mathrm{e}^{-j2\pi kn/N} \tag{80}$$

where

$x[n\text{-}m]$ is the sampled signal in the time domain;

$w[n]$ is the discretized window function in the time domain, which is real, positive and symmetrical;

$N$ is the length of a single DFT calculation;

$n$ is an integer ranging from 0 to ($N$-1);

$k$ is an integer ranging from 0 to ($N$-1) that stores the element number of the spectrogram $Z[m,k]$ in the frequency domain;

$m$ is an integer ranging from 0 to ($N$-1) that stores the element number of the spectrogram $Z[m,k]$ in the time-domain.

and where $w[n]$ is the Gaussian window function that models the IF filter of an EMI receiver [71]. The result is a spectrogram at discrete points in both the time and frequency domains illustrated in Figure 182. Further, $m$ is the integer index for the discrete steps in the time-domain and $k$ is the integer index for the discrete steps in the frequency domain of the spectrogram.

IECNORM.COM : Click to view the full PDF of CISPR TR 16-3:2020 RLV

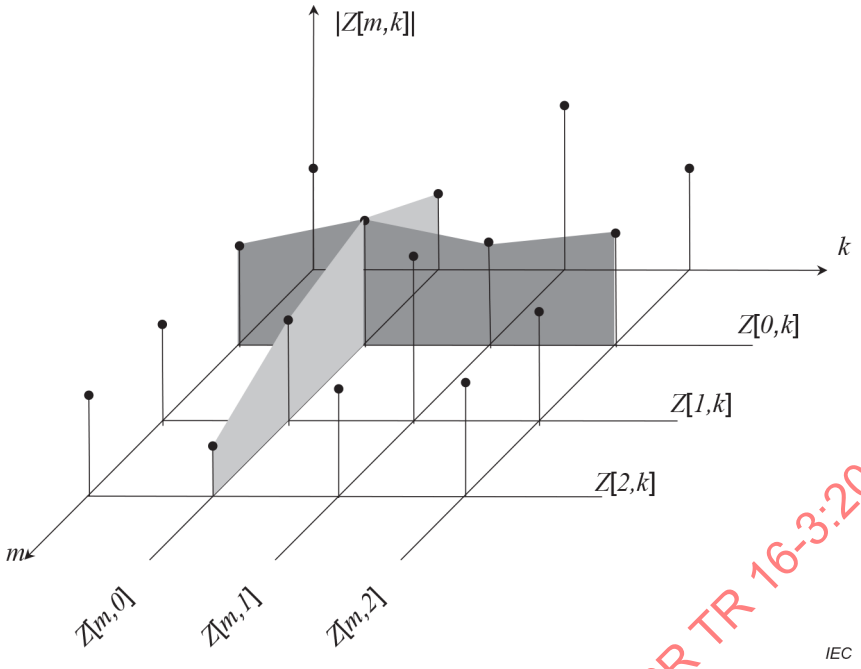



**Figure 182 – An example spectrogram *Z*[*m*,*k*]**

The relationship between the samples that are processed by a single FFT, and the number of samples where shifting in the time domain is performed, is described by the overlap factor $F_{ol}$. The shifting in the time-domain is performed, to get a series of FFT spectra over the complete dwell time, which compose the spectrogram $Z[m,k]$. The time interval of $N$ samples is typically much smaller than the dwell time. The index $m$ is shifted by a number which is a fraction of $N$. The number of FFT calculations, $N_O$, that have to be performed for $N$ samples is described by:

$$N_o = \frac{1}{1 - F_{ol}} = \frac{f_{sbb}}{\Delta f} \tag{81}$$

#### 4.10.4.3 Window function

The window function determines the IF filter response of an FFT-based measuring receiver. The multiplication in the time-domain is described according to:

$$z[n] = x[n] \times w[n] \tag{82}$$

where

$w[n]$ is the sampled window function; and
$x[n]$ is the sampled input signal;
$n$ is an integer ranging from 0 to ($N$-1).

In the frequency domain, the multiplication presented in Equation (82) becomes a convolution according to:

$$Z[k] = X[k] \times W[k] \tag{83}$$

where $W[k]$ is the IF filter response discretized in the frequency domain. A Gaussian window function is preferable, because this will yield a Gaussian IF filter in the frequency domain. In order to obtain the same result as with a tuned voltmeter, its equivalent noise bandwidth as well as impulse bandwidth shall be same as the IF filter bandwidth of the FFT-based measuring receiver. The filter shall also meet the selectivity criteria called out in CISPR 16-1-1. Derivation of the Gaussian window from the 6-dB bandwidth specification in CISPR 16-1-1 is outlined with the following equations.

IECNORM.COM : Click to view the full PDF of CISPR TR 16-3:2020 RLV

For a continuous (non-sampled) signal, the window function is used to create an IF filter bandwidth $B_{IF}$ (6 dB). It is calculated according to:

$$w(t)' = \left(\frac{1}{2}\sqrt{\frac{\pi}{\ln 2}}\right) B_{IF} e^{\left(-\pi^2 / 4\ln 2\right) B_{IF}^2 t^2} \tag{84}$$

In the frequency domain, the following transfer function is obtained:

$$W(f)' = e^{-f^2\left(2B_{IF}^2 / 8\ln 2\right)} \tag{85}$$

Sampling the input signal with sampling intervals of $T_s$, the discretized window function $w[n]$ is derived:

$$w[n]' = \frac{1}{g_c(NT_s)N} e^{(-1/2)\left[\left(\pi / \sqrt{2\ln 2}\right) B_{IF} T_s n\right]^2} \qquad n = -\frac{N}{2}..0..+\frac{N}{2} \tag{86}$$

where $g_c$ is called coherent gain. The coherent gain is defined by:

$$g_c = \frac{1}{N}\sum_{n=0}^{N-1} w[n]' \tag{87}$$

The output result for sinusoidal signals is independent of the window function and the number of samples $N$ used during the FFT when divided by the coherent gain:

$$w(n) = \frac{w[n]'}{Ng_c} \tag{88}$$

The equivalent noise bandwidth is calculated numerically by:

$$B_{ENBW} = f_s \sum_{n=0}^{N} w[n]^2 \tag{89}$$

where $f_s$ is the sampling rate. The impulse bandwidth $B_{IMP}$ of the filter is determined according to:

$$B_{IMP} = \frac{f_s}{Ng_c} \tag{90}$$

#### 4.10.4.4 Comparison to EMI receiver – mathematical equivalence

The mathematical equivalence between a superheterodyne receiver and an STFFT-based receiver is shown below. A comparison of the virtual IF signal at a single frequency, $f_{sel}$, that can be extracted from the output of the STFFT and the analogue output signal of an EMI receiver is used for this determination.

At a single frequency, Equation (80) is taken and $f_{sel} = kn / Nf_s$. The output of the STFFT at a single frequency is obtained as follows:

$$s_{bb,f,sel}[m] = \sum_{n=0}^{N-1} x[n-m] \times w[n] \times e^{-j2\pi f_{sel}} = x[m] \times w[m] \times e^{-j2\pi f_{sel} t} \tag{91}$$

The convolution between $x[m]$ and $w[m]$ in the time domain is a multiplication in the frequency domain. The factor $e^{-j2\pi f_{sel}}$ describes a frequency shift by the selected frequency. The signal $s_{bb,f,sel}$ $[m]$ shows a discretization in time that is the inverse of the baseband sampling rate $f_{sbb}$. The baseband signal for a non-sampled signal is described in the frequency domain by:

$$S_{bb,f,sel}(f) = W(f)X(f - f_{sel}) \tag{92}$$

IECNORM.COM : Click to view the full PDF of CISPR TR 16-3:2020 RLV

### 4.10.5 Measurement errors specific to FFT processing

#### 4.10.5.1 Measurement error for sinusoidal signals

The calculated spectrum shows a frequency step that is dependent on the number of frequency points and the sampling rate. If the sampled signal is sinusoidal, but at a frequency that does not align exactly with a calculated frequency point, the calculated amplitude shows an amplitude error. Such effects are described in [70]. For FFT calculations the term 'picket fence effect' is generally used to describe this error. Sequential measurements with a stepped frequency scan performed with a tuned selective voltmeter show also an amplitude error that is dependent on the frequency step as well as on the shape of the IF Filter. In order to decrease the step size in the frequency domain, the number of samples for FFT calculation can be increased. A further method to increase the number of frequency bins is to combine digital I-Q Mixing with FFT as shown in [72].

#### 4.10.5.2 Numerical behavior of the window function

Due to the finite number, $N$, of samples, the first and the last value of the vector $w(n)$ are not exactly zero. The results are sidelobes. These sidelobes should be suppressed by at least 40 dB. A detailed description on such effects for a Gaussian window function as well as other window functions, e.g. the Kaiser window is shown in [73]. An example of such an effect is shown in Figure 183.

IECNORM.COM : Click to view the full PDF of CISPR TR 16-3:2020 RLV

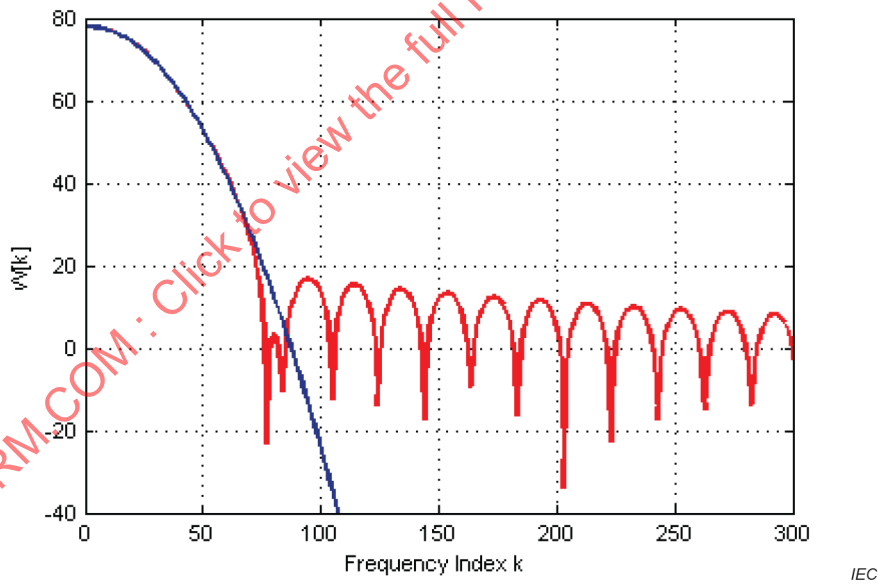



**Figure 183 – Sidelobe effect due to the finite length of window**

#### 4.10.5.3 Measurement error for an isolated pulse

The baseband sampling rate $f_{sbb}$ has to be high enough to fulfill the Nyquist criterion. FFT-based receivers show a measurement uncertainty for single pulses that is dependent on the overlapping factor $F_{ol}$. With a very low overlapping factor, the number of overlapping FFT calculations is reduced, however the measurement accuracy for single pulses is reduced. The effect is shown in Figure 184.

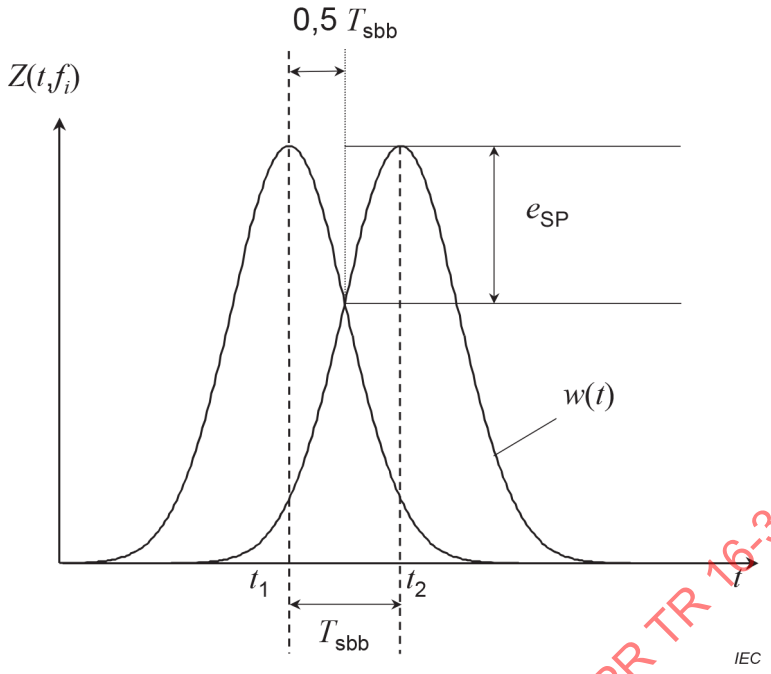



**Figure 184 – Measurement error for a single pulse**

$$f_{sbb} = \frac{1}{T_{sbb}} \tag{93}$$

The dependence of the maximum measurement error for the measurement of an isolated pulse in the peak detector mode, $e_{SP}$ ("SP" for single pulse), described by using an IF filter of the Gaussian filter type:

$$e_{SP} = e^{\left(\pi^2 / 4 \ln 2\right)\left(B_{IF} f_{sbb}\right)^2} \tag{94}$$

where $B_{IF}$ is the 6 dB bandwidth of the IF filter. The baseband sampling rate $f_{sbb}$ is normalized to the 6 dB bandwidth of the IF filter:

$$f_{sbb\,/\,B_{IF}} = \frac{f_{sbb}}{B_{IF}} \tag{95}$$

The maximum error of the measurement of an isolated impulse is calculated in dB according to:

$$e_{SP,dB} = \frac{10\pi}{(\ln 10)\sqrt{8 \ln 2}} \left( \frac{1}{f^2_{sbb/B_{IF}}} \right) \text{dB} \approx 5{,}79 \left( \frac{1}{f^2_{sbb/B_{IF}}} \right) \text{dB} \tag{96}$$

For EMI measurements, FFT-based measuring instruments shall sample and evaluate the signal gapless during the measurement time.

#### 4.10.5.4 Measurement error for a sequence of pulses

The maximum measurement error that may occur for an isolated impulse can be calculated according to Equation (96). However this effect is not limited to isolated pulses. During the measurement of a sequence of pulses, a measurement error may occur that is always smaller than the measurement error calculated by Equation (96). An example of the recalculated IF Signal for different overlapping factors is shown in Figure 185. A detailed description and evaluation of this effect using the histogram method has been described in [74].

IECNORM.COM : Click to view the full PDF of CISPR TR 16-3:2020 RLV

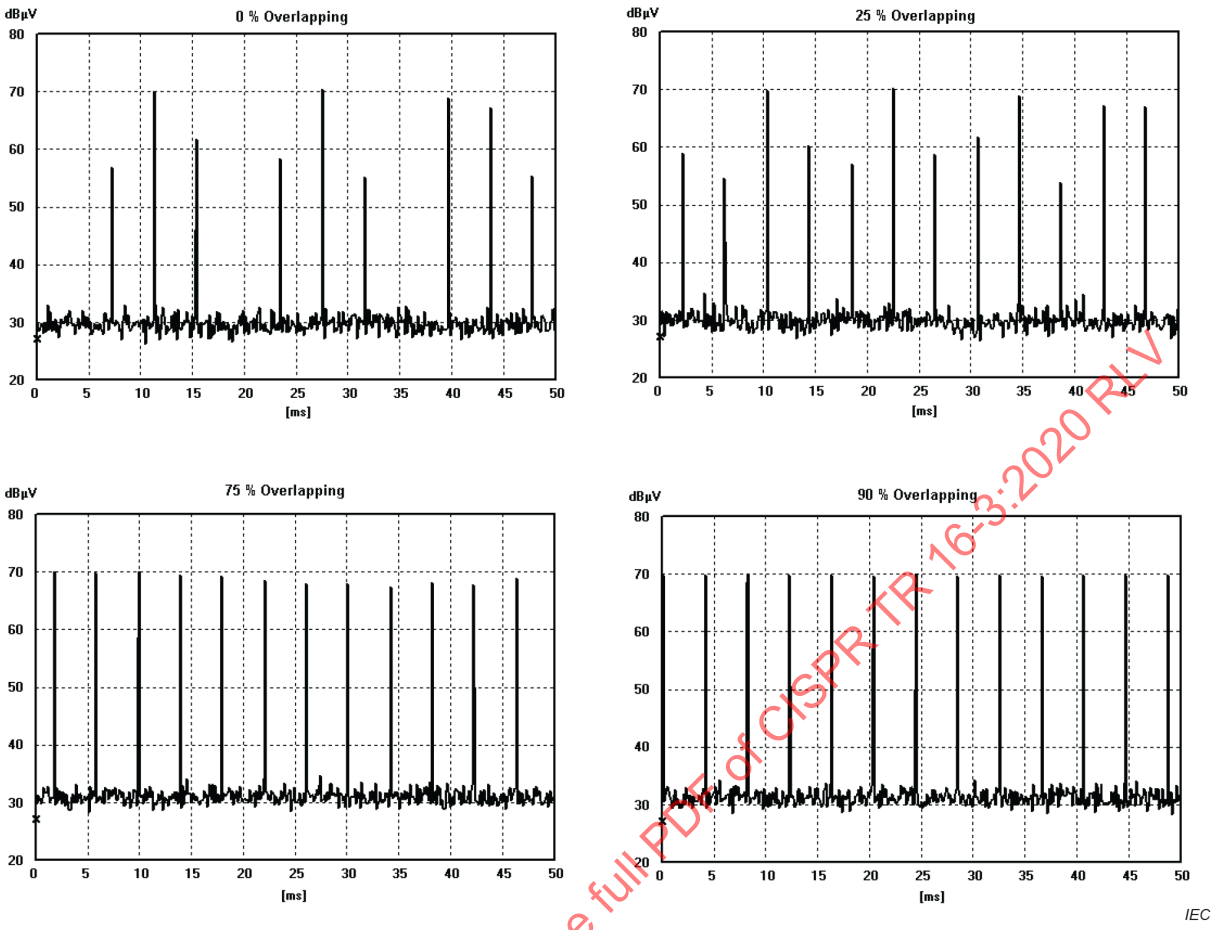



**Figure 185 – IF signal for different overlapping factors for the same sequence of pulses**

### 4.10.6 FFT-based receivers – examples

#### 4.10.6.1 General

Two different types of FFT-based measuring instruments are available:

1) those that digitize the signal in the baseband; and
2) those that digitize the IF of a superheterodyne receiver.

For both types the digitized signal is processed digitally by STFFT.

#### 4.10.6.2 FFT-based baseband systems

##### 4.10.6.2.1 Overview

FFT-based baseband systems digitize the input signal in the time domain with an ADC. Spectral calculations are performed using FFT algorithms. The block diagram of such a system is shown in Figure 186.

IECNORM.COM : Click to view the full PDF of CISPR TR 16-3:2020 RLV

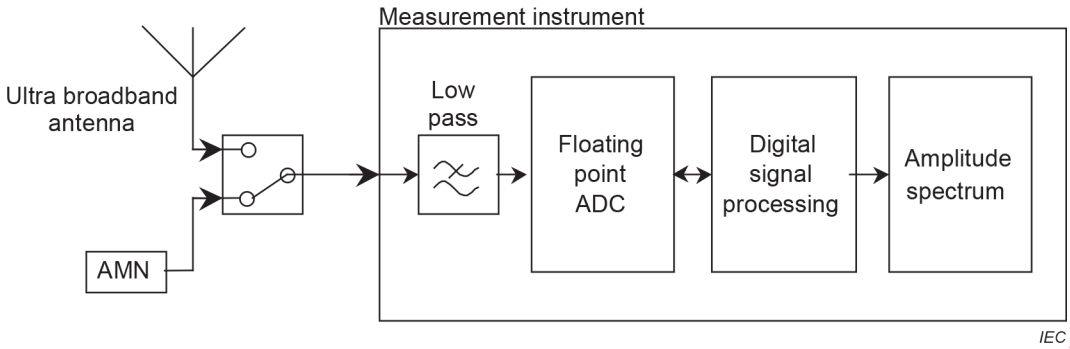



**Figure 186 – FFT-based baseband system**

The EMI signal is fed into the receiver input via a transducer [e.g. broadband antenna or artificial mains network (AMN)]. The low-pass filter shown in Figure 186 is used to suppress aliasing.

A multi-resolution ADC system performs a floating-point conversion [75]. A multi-resolution system consists of several ADCs with different gains to support a higher dynamic range of the input signal. Such a system improves the dynamic range, especially for measurements of broadband signals (i.e. impulsive signals). The baseband system does not use pre-selection filters. The digitized EMI signal is further processed by digital signal processing and the amplitude spectrum is displayed. An algorithm that allows measurements in the peak, average and RMS detector modes to be simulated has been presented in [69]. One of the first baseband measuring instruments was based on a digital storage oscilloscope and used FFT as presented by C. Keller [76]. An algorithm for the quasi-peak detector mode has been presented in [77]. With both algorithms almost all requirements that are called out in CISPR 16-1-1 can be met except the gapless processing. However, gapless processing is mandatory in order to provide the mandatory IF-signal and quasi-peak response [71], [78], [79].

A solution for the implementation of gapless processing is real-time processing. Due to the real-time operation, the system can emulate the complete behavior of an EMI receiver. The EMI signal is digitized by an ADC system. The frequency range of the EMI signal considered during the emissions measurement is subdivided into several sub-bands. The sub-bands are measured sequentially. Each sub-band is down-converted into its baseband by a digital down-conversion (DDC) unit. The down-converted signal is down-sampled and processed by STFFT. STFFT generates a spectrogram that shows a discretization in time and frequency domains as shown in Figure 182. At each calculated discrete frequency the evaluation is performed by a digital detector.

#### 4.10.6.2.2 Real-time digital signal processing

An overview of the digital signal processing system elements is presented in Figure 187.

IECNORM.COM : Click to view the full PDF of CISPR TR 16-3:2020 RLV

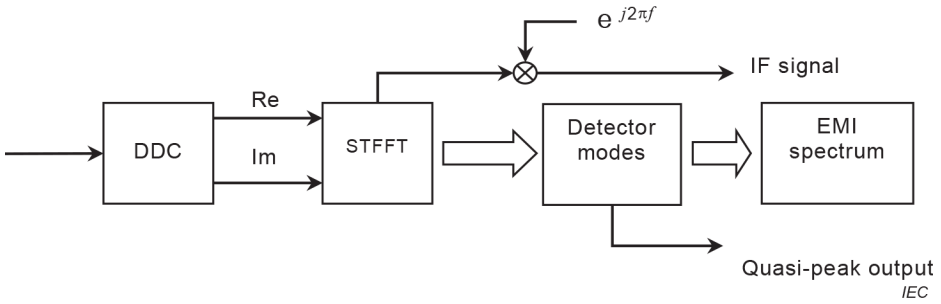



**Figure 187 – Real-time FFT-based measuring instrument**

In order to perform measurements in the frequency range 30 MHz to 1 GHz, the sampling rate $f_S$ has to be at least 2 GSa/s (giga-samples per second) to meet the Nyquist criterion. Because of the limited processing speed of the digital real-time signal-processing unit, the input of the digital down-conversion (DDC) is subdivided into eight parallel inputs with at least 250 MSa/s per channel. As a consequence the maximum frequency has to be reduced by a factor of 8. Thus, the frequency range 0 GHz to 1 GHz is subdivided into eight bands. The spectrum of each band is processed separately by DDC, STFFT and the digital detectors. After selection and measurement of each band one by one, the complete spectrum is composed of those eight subparts.

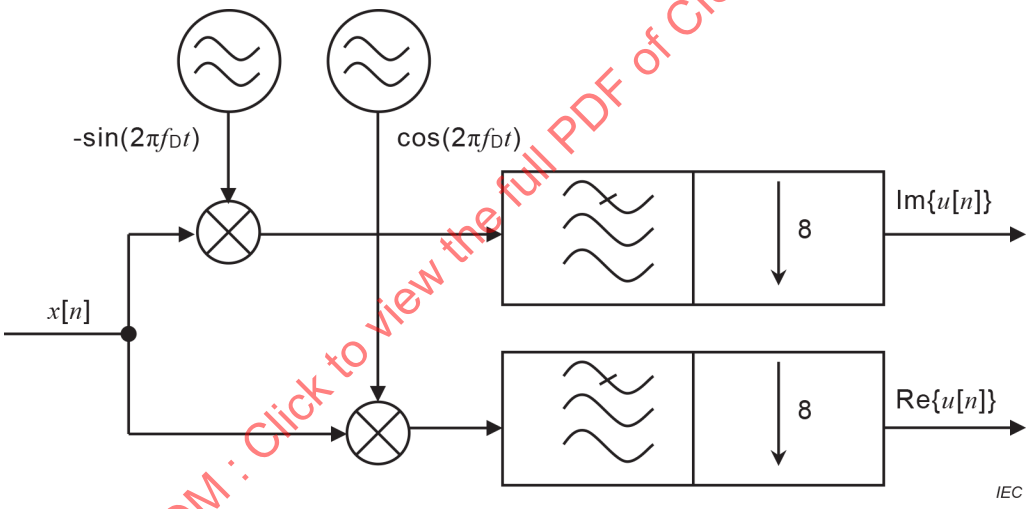



**Figure 188 – Digital down-converter**

Figure 188 shows the block diagram of the DDC unit; $f_{Di}$ is the centre frequency of band $i$. The signal $x[n]$ is the sampled signal of at least 2 GSa/s. The selected band is shifted into baseband. This is done in order to process the output signal by the STFFT.

The real part is obtained by multiplication with a cosine signal. The imaginary part is calculated by multiplication with a sinusoidal signal. In this way the complete spectrum is shifted by $f_D$. In order to get the signal of a single frequency band, two identical polyphase decimators [80] are used.

#### 4.10.6.2.3 Short time fast Fourier transform

Overlapping is achieved by three cascaded shift registers. A block diagram is illustrated in Figure 189. Alternately, decimation in frequency (DIF) [76] can be used to calculate only a fraction of the discrete spectral values, resulting in an increase in the measurement time by a factor of 4.

IECNORM.COM : Click to view the full PDF of CISPR TR 16-3:2020 RLV

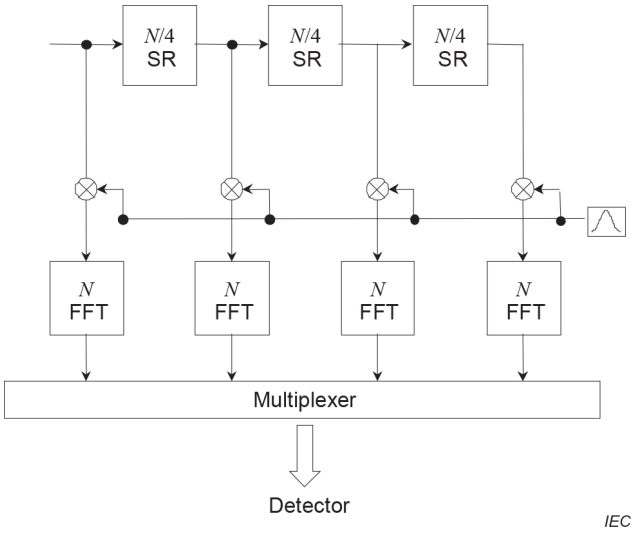



**Figure 189 – Short time fast Fourier transform – An example of implementation**

#### 4.10.6.2.4 Multi-resolution ADC

Figure 190 provides the block diagram of an ADC system. The input signal is distributed through a power splitter as three channels. Each channel consists of a limiter, a low noise amplifier, and an ADC. While the upper channel digitizes the amplitude range from 0 mV to 1,8 mV, the lower channel digitizes the amplitude range from 0 V to 5 V. The middle channel is used to digitize the intermediate amplitude range from 0 mV to 200 mV. The signal is recorded at all three channels simultaneously. A signal digitized in high resolution is reconstructed by extracting each sampled value from the ADC where the signal shows the maximum nonclipped value.

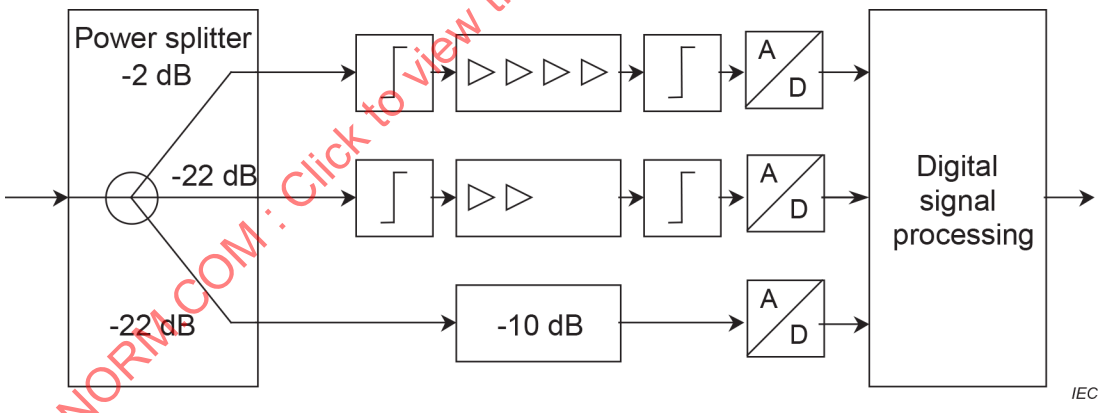



**Figure 190 – Floating-point analogue-to-digital conversion**

#### 4.10.6.2.5 Dynamic range

The dynamic range of a broadband system strongly depends on the linearity of the system, and the number of bits of the ADC. Multi-resolution systems allow enhancement of the dynamic range for pulses and bursts. With the development of the technology, ADCs with a larger number of bits will be available. With a single ADC more than 16 bits are required to fulfil the requirements of CISPR 16-1-1. With multi-resolution at least three ADCs with 8 bits are required. For higher dynamic range additional pre-selection may have to be used.

By using a Gaussian window function, which is equivalent to the use of a Gaussian IF filter, the requirements to the selectivity masks are fulfilled.

IECNORM.COM : Click to view the full PDF of CISPR TR 16-3:2020 RLV

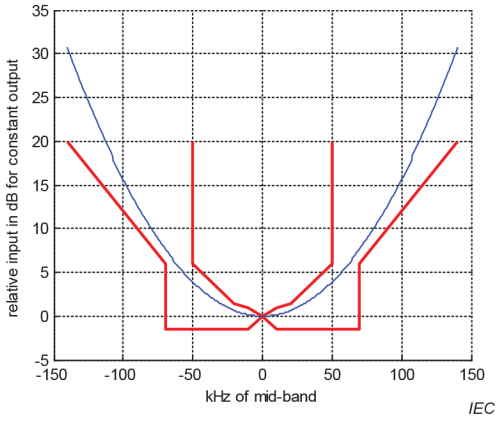



**Figure 191 – Example of a 120 kHz Gaussian filter**

In Figure 191 the measured transfer function of an IF-Filter of an FFT-based measuring instrument is shown.

#### 4.10.6.2.6 Scan times

Typical scan times for quasi-peak measurements with a dwell time of 3 s (at each individual frequency of the band) are provided in Table 42.

**Table 42 – Scan times**

| Band | $N_{seg}$ | fstep FFT | $f_{step\ final}$ | Scan time, approximate |
|---|---|---|---|---|
| Band A | 1 | 248 Hz | 62 Hz | 12 s |
| Band B | 1 | 36 kHz | 4,9 kHz | 12 s |
| Band C | 2 | 159 kHz | 3,97 kHz | 24 s |
| Band C+ D | 7 | 159 kHz | 3,97 kHz | 84 s |

The realtime STFFT calculation unit as well as the realtime detectors can calculate the result at the frequencies for a segment with the resolution of $f_{step\ FFT}$. However in order to avoid the picket fence effect during the measurement, a higher frequency resolution ($f_{step\ final}$) is preferred. Thus the scan time takes the dwell time multiplied by the ratio of $f_{step\ FFT}$ to $f_{step\ final}$. Because the presented system splits the range into eight subbands, several subbands also exist. The total scan time has to be additionally multiplied by the number of subbands where the measurement has been performed during the scan.

#### 4.10.6.3 Heterodyne receivers with FFT applied to the wideband IF signal

#### 4.10.6.3.1 General

Generally, heterodyne receivers with FFT applied to the wideband IF signal offer the following advantages:

- high dynamic range by limited bandwidth and high resolution ADC, e.g. 14-bit;
- frequency range not limited by the Nyquist criterion, but by the maximum receiver frequency;
- long maximum dwell time by low sampling rate;
- use of receiver preselection, preamplifier, RF-attenuation;
- receiver can be used in the standard receiver mode.

IECNORM.COM : Click to view the full PDF of CISPR TR 16-3:2020 RLV

#### 4.10.6.3.2 System type 1 based on a receiver with wideband IF

##### 4.10.6.3.2.1 General

The measurement system consists of a measuring receiver with preselector. Figure 192 shows a schematic diagram of the essential parts of the system. An ADC with up to 81,6 MHz sampling rate converts the IF signal with a spectrum width of up to 7 MHz at a time. The restriction to 7 MHz is due to the built-in analogue IF filter, which precedes ADC. The ADC has 14-bit resolution, which in combination with the preselector ensures a higher dynamic range than many other available FFT analyzers where 8-bit ADCs are used.

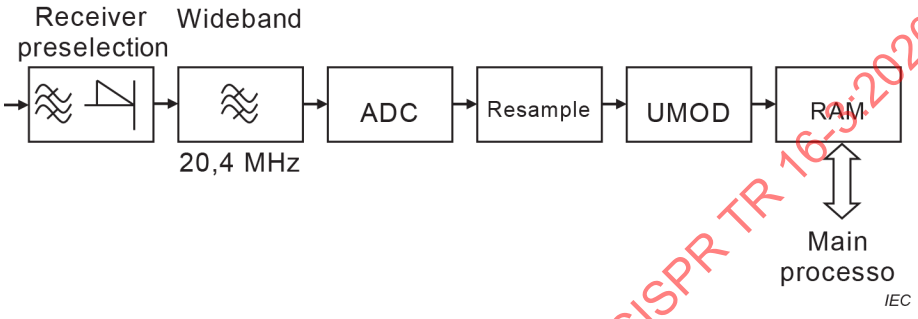



**Figure 192 – Essential parts of an FFT-based heterodyne receiver**

The resampler provides data reduction where needed, avoiding unnecessary oversampling at narrower IF bandwidths, which saves processing time. The universal digital module (UMOD) saves the data in the 16 M-words RAM for measurement times up to 3 s without any gap. The main processor accesses the RAM, applies a Gaussian window to the time domain signal (to avoid leakage effects) and calculates the FFT for the frequency segment around the receive frequency. For a resolution bandwidth of 120 kHz this results in an acceleration of the measurement speed by a factor of 15 and by a factor of up to 150 with a 9 kHz resolution bandwidth.

To avoid any picket fence effect, the frequency step of the FFT is $B_{IF}/4$, where $B_{IF}$ is the resolution bandwidth. In order to provide an overview of the emission spectrum over a wide frequency range, the system applies a combination of receiver frequency steps in segments of the FFT span, called time domain scan (TD SCAN).

The system applies FFT to the IF time domain signal and not to the baseband signal. This also allows digitizing very high frequencies (here up to 40 GHz) with a rather low sampling rate without violation of the Nyquist criterion, and reduces the throughput of data. The inherent level errors appearing at the border of the frequency range provided by the FFT calculation are minimized by means of a corresponding pre-correction of the analogue IF filters.

The filtering and band-limitation (preselector) is performed with the same circuitry that the measuring receiver is using for the conventional stepped frequency scan. This reduces the risk of overloading by strong out-of-band signals to a minimum.

In order to avoid missing impulsive signals, several FFTs with a certain overlap are applied to the time-domain signal. The system provides a rather high degree of overlap (90 %), which ensures that even very short impulsive signals at the border of the time domain window are calculated without significant amplitude error.

IECNORM.COM : Click to view the full PDF of CISPR TR 16-3:2020 RLV

#### 4.10.6.3.2.2 Application of the system to prescan and final measurements

The prescan is used to get a detailed overview of the emission spectrum [81]. With conventional EMI receivers this measurement may take up the major part of the overall measurement time.

The prescan result is then analyzed and the critical frequencies can be determined. At the critical frequencies, the signal can be reconstructed in order to calculate the weighted measurement results using [81] or, if further maximization with antenna mast and turntable movement is needed, the receiver can be used in its conventional measurement function for final measurements with quasi-peak and/or average detection to provide a measurement result which complies with CISPR 16-1-1 even for the single pulse. So, the system combines the conventional receiver with FFT-based measuring receiver functions.

#### 4.10.6.3.2.3 Dynamic range for broadband emissions

For EMI measurements, the dynamic range for broadband emissions is of importance. Dynamic range may be measured with a CISPR pulse generator in the time-domain scan. In order to see the difference between the maximum pulse level and noise, the pulse generator is switched to a pulse repetition frequency (PRF) of 40 Hz whereas the measurement time is 10 ms (see Figure 193). This results in a display where one FFT segment catches a pulse whereas the neighboring segment presents the noise level at a time when no pulse is present.

The dynamic range is significantly reduced by the bandwidth ratio $B_{WIF} / B_{IF}$ for broadband pulses, which determines the overload factor $F_{ol}$ according to:

$$F_{ol} = 20 \log \frac{B_{WIF}}{B_{IF}} \tag{97}$$

where

$B_{WIF}$ is the bandwidth of the wideband IF Filter, that serves as a preselection,

$B_{IF}$ is the bandwidth of the by window function modelled IF Filter, and

$F_{ol}$ is the overload factor.

For $B_{WIF}$ = 10 MHz and $B_{IF}$ = 120 kHz, the reduction is 38,4 dB. For a $B_{IF}$ of 9 kHz $F_{ol}$ becomes 60,9 dB, resulting in further reduction of the dynamic range.

IECNORM.COM : Click to view the full PDF of CISPR TR 16-3:2020 RLV

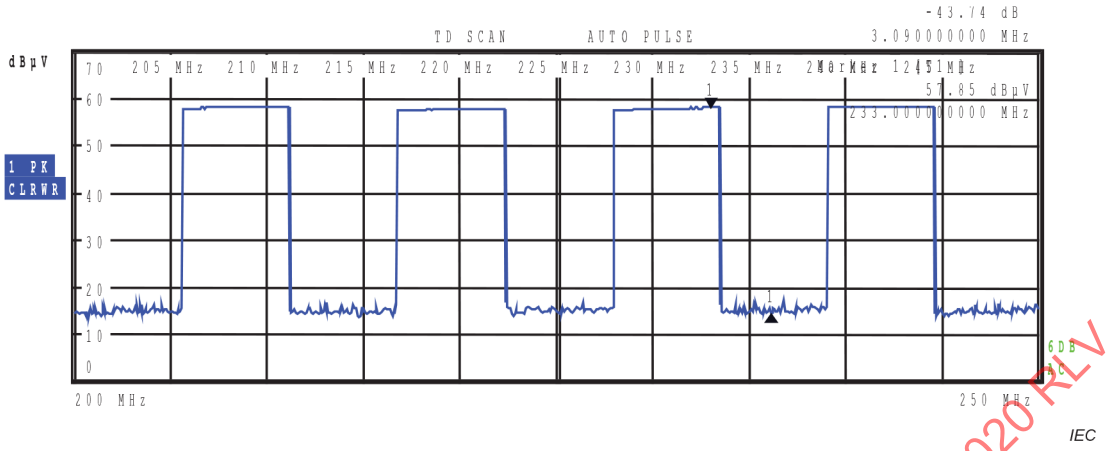



**Figure 193 – Dynamic range for broadband emission as measured with the peak detector**

#### 4.10.6.3.3 System type 2 based on a receiver with wideband IF

##### 4.10.6.3.3.1 General

In this system the broadband IF-output of an EMI receiver is digitized, stored and processed by STFFT. The EMI receiver-specific parts such as preselection, preamplifier, RF-attenuation and IF-bandwidth are more or less identical with system type 1. Digitizing and signal processing are performed using an external PC with commercially available digitizer card and control software. See Figure 194.

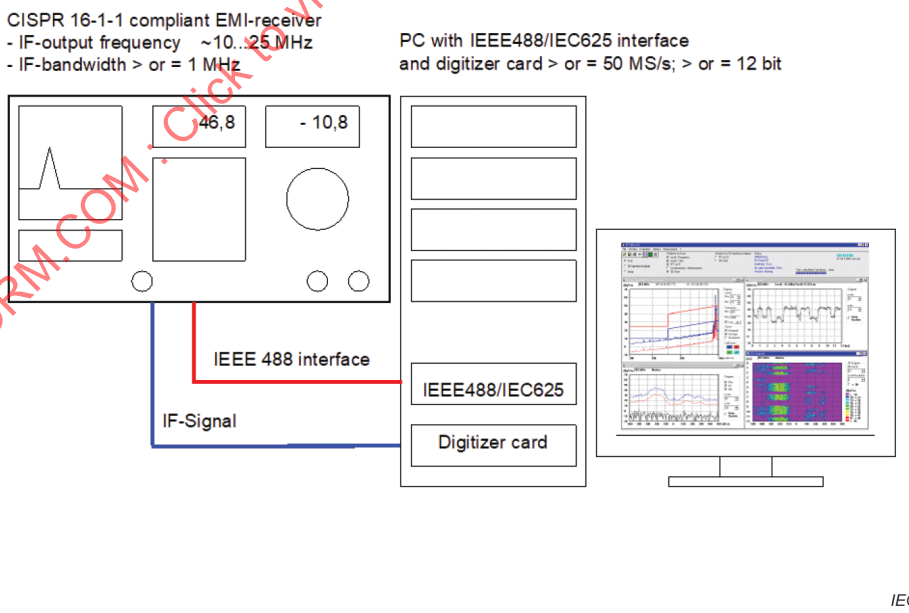



**Figure 194 – Set-up of FFT-based system type 2**

IECNORM.COM : Click to view the full PDF of CISPR TR 16-3:2020 RLV

The complete frequency range is split into frequency intervals according to the bandwidth of the down converter. Usually, the wideband bandwidth $B_{WIF}$ is 1 MHz. The signal is sampled and the weighted spectrum (peak, quasi-peak, average and RMS) is calculated for the specific band. The whole band is calculated by merging of consecutive spectra. The measurement step size depends on the frequency and the available maximum IF-BW of the receiver:

up to ~ 300 kHz: $B_{WIF}$ = 9 kHz
up to ~ 2 MHz: $B_{WIF}$ = 120 kHz
above 2 MHz: $B_{WIF}$ = 1 MHz
above 30 MHz: $B_{WIF}$ = 10 MHz (depending on the receiver)

For increased operating range each single measurement is auto-ranged. As a result, the operating range for disturbances outside the calculated frequency band is increased.

#### 4.10.6.3.3.2 FFT parameter settings

In the first step the software determines the optimum sampling rate. Parameters are IF output frequency, down-converter bandwidth and the bandwidth for -40 dB spurious-free signal detection.

The relationship between the wideband IF bandwidth $B_{WIF}$ and the sampling rate $f_s$ is shown in Table 43. Possible sampling rates are integer divisions of the digitizer basic sampling rate.

**Table 43 – Sampling rates for different $B_{WIF}$**

| $B_{WIF}$ | $f_s$ |
|---|---|
| 10 MHz | 100 MSa/s |
| 1 MHz | 4,76 MSa/s to 7,69 MSa/s depending on receiver IF filter shape |
| 120 kHz | 1 MSa/s |
| 9 kHz | 200 kSa/s |

The total number of recorded samples is given by:

$$N_{total} = f_s t_{dwell} \quad (98)$$

The frequency step is given by:

$$f_{step} = \frac{f_s}{N} \quad (99)$$

A radix-2 FFT processor is used; thus the step is given by:

$$N = 2^n \quad (100)$$

where $n$ is a natural number (starting with 1).

The IF bandwidth $B_{IF}$ is given by:

$$B_{IF} = f_{step} k_w \quad (101)$$

where $k_w$ is between 1,8 and 3,6 depending on the window function.

IECNORM.COM : Click to view the full PDF of CISPR TR 16-3:2020 RLV

The frequency step size can be set as a factor of 2. Finer adjustment for the resulting IF bandwidth is accomplished by using different window functions. For getting exact values of IF bandwidth a variable $k_W$ factor will be necessary, which can be done by zero padding [70] or using a variable window function.

A Kaiser window is used, which has a shape calculated with Bessel functions. Its shape is close to the Gaussian window, but gives a significant improvement in selectivity. An advantage is the variation of the value $k_W$, which is used to adapt the window for different step sizes and sampling rates.

#### 4.10.6.3.3.3 Results

An overview of the comparison for typical scan times between the system type 2 (using "FFTemi" software) and a scan performed with a tuned selective voltmeter ("receiver") is shown in Table 44.

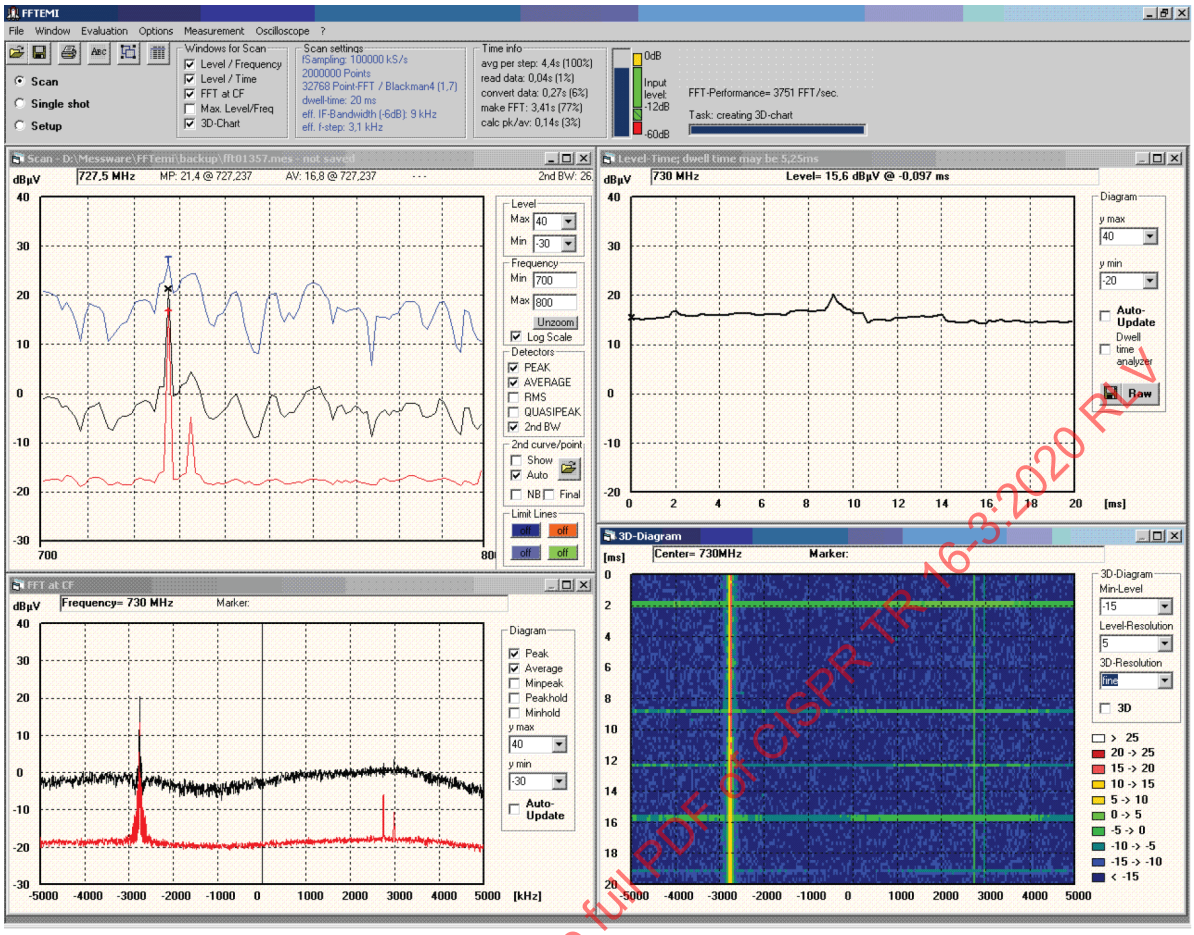
**Table 44 – Scan times for a scan 30 MHz to 1 GHz**

| Dwell time | $B_{IF}$ = 120 kHz | | $B_{IF}$ = 9 kHz | |
|---|---|---|---|---|
| ms | Receiver | "FFTemi" | Receiver | "FFTemi" |
| 10 | < 3 min | < 3 min | 32 min | < 3 min |
| 50 | > 13 min | < 3 min | > 160 min | < 3 min |
| 1 000 | ~4,5 h | < 0,5 h | ~ 50 h | < 0,5 h |

For short dwell times the scan time is limited by speed of data transfer. For longer dwell times a reduction of the scan time by up to two orders of magnitude is achieved.

Figure 195 shows an example measurement. The displayed signal is received in the FM frequency range at 105 MHz. The 3D view allows viewing the disturbance at time and frequency in one graph and direct relationship, which can help to decide if broadband or narrowband noise is present, and to find the noise source.

IECNORM.COM : Click to view the full PDF of CISPR TR 16-3:2020 RLV




IEC

Left-top: The entire frequency scan (black and red – different detectors; blue – different IF-bandwidth)

Right-top: Level versus time at the marker frequency

Left-bottom: Detailed frequency domain at marker frequency (black and red – different detectors)

Right-bottom: 3D view of the signal at marker frequency

X-axis = frequency (CF ± half down converter-BW

Y-axis = time from 0 to top to $t_{dwell}$ on bottom

Colour = level of signal

**Figure 195 – FFT Software ("FFTemi") screen shot**

IECNORM.COM : Click to view the full PDF of CISPR TR 16-3:2020 RLV

#### 4.10.6.3.3.4 Dynamic range

In addition to the dynamic range, the system provides an improvement of the indication range via autoranging of the individual measured spectra. Especially, signals that show a different level over the frequency range require additional indication range. An example of such a phenomena is shown in Figure 196.

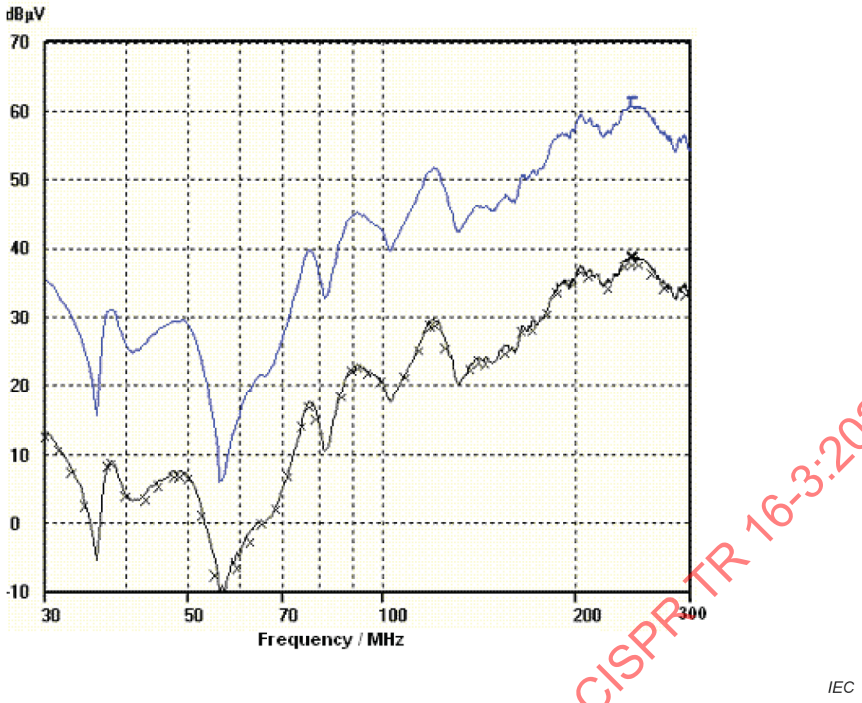



**Figure 196 – Example of pulse generator measurement with antenna**

Both curves are a measurement performed with FFTemi. The upper curve is a measurement with $B_{IF}$ = 120 kHz and the lower curve is a measurement with $B_{IF}$ = 9 kHz. The marks are comparison measurements performed with a tuned selective voltmeter.

In this case the additional indication range by the frequency response is approximately 50 dB. Systems without auto-ranging or full broadband FFT solutions may not be able to evaluate such phenomena even if CISPR 16-1-1 compliant.

#### 4.10.6.4 Applications

##### 4.10.6.4.1 Measurement of intermittent signals

The measurements of intermittent signals are difficult with an EMI receiver. The dwell time shall be kept to a minimum level in order to make the measurement feasible. On the other hand a large dwell time is required for a reproducible measurement.

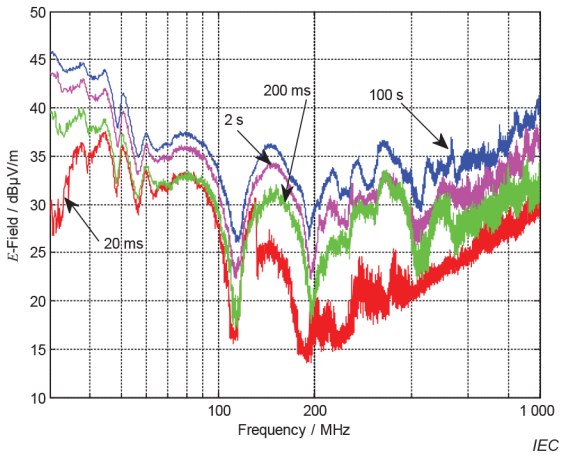



**Figure 197 – Radiated emission measurement of a motor – peak detector**

IECNORM.COM : Click to view the full PDF of CISPR TR 16-3:2020 RLV

FFT-based instruments have the advantage that scans are faster by several orders of magnitude. Thus longer dwell times can be selected which reduces the measurement uncertainty. In Figure 197 the radiated emission of a motor was investigated. The measurement was performed with the peak detector. A dwell time of 100 s gives a very accurate result. A pre-scan with 20 ms dwell time results in measurement errors up to 15 dB.

#### 4.10.6.4.2 Azimuth characterization of an EUT

Figure 198 shows the result of a full characterization with quasi-peak detection of a partially opened personal computer enclosure. Such a measurement can be used to enhance the quality of emission measurements.

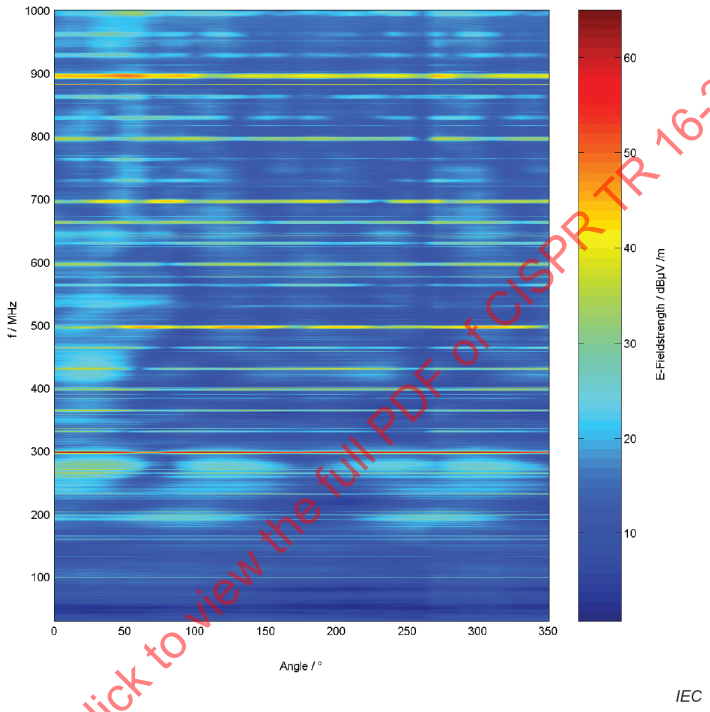



**Figure 198 – Angular characterization of a PC**

#### 4.10.6.4.3 Using FFT for IF analysis

Previously, IF analysis required extra hardware in order to give the user an overview of the spectrum adjacent to the signal within the IF resolution bandwidth when using the tune-and-listen function on an OATS (open area test site). Now, the extra hardware can be replaced by FFT analysis. As a result the user can see the level display, listen to the demodulated signal (e.g. with AM or FM demodulator) and see the spectrum display with sufficient span. An example is provided in Figure 199, with trace averaging used in the FM frequency range and where two FM signals are adjacent to the signal to be measured, the level display shows results with three detectors and $B_{IF}$ is 120 kHz.

IECNORM.COM: Click to view the full PDF of CISPR TR 16-3:2020 RLV

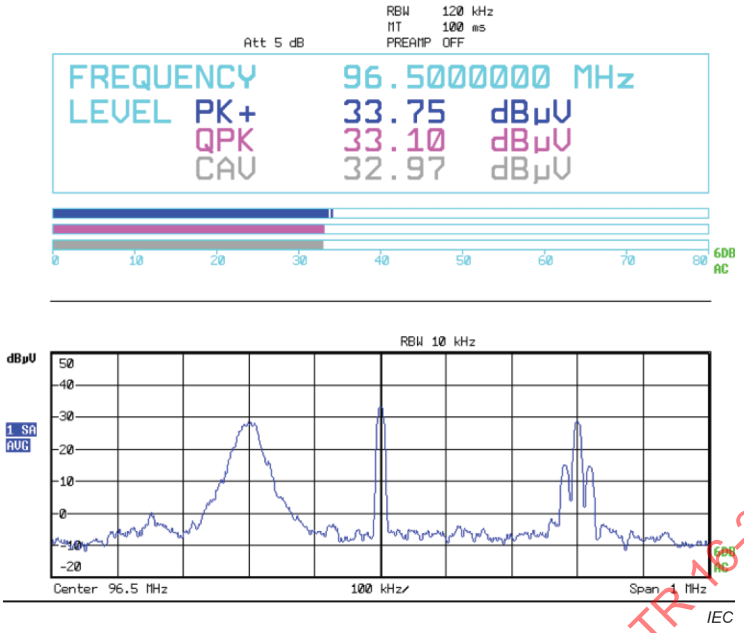



**Figure 199 – Example FFT IF analysis display**

## 4.11 Parameters of signals at telecommunication ports

### 4.11.1 General

The maximum signal levels that can be present at telecommunication ports in differential mode are dependent upon, and are limited by, the electrical balance or LCL [85], [86], of the telecommunication ports and the cables or networks to which they are intended to be connected, if the wanted signals are not to appear as unacceptable disturbances across the common mode impedance to ground.

The LCL of a signal port, cable or network causes a portion of any differential mode signals on that port, cable or network to be converted to common mode disturbances, for which a product standard has defined limits [87], [88], [89]. Common mode disturbances (also called antenna mode disturbances, because they are a source of radiated disturbances to the environment) should be limited if interference with the reception of radio signals of all kinds is to be minimized. Common mode disturbances created at a nominally balanced signal port or transmission medium, for example a twisted copper pair, should be controlled and limited, whether or not the port or medium is provided with an overall shield. If a shielded medium is used, deficiencies in the shield itself as well as in the shield connectors, leading perhaps to significant electrical discontinuities, will allow a portion of the common mode disturbances created within the shield environment to appear outside the shield.

The worst-case values for balance and LCL quoted in many network specifications are based upon the desired signal transmission and crosstalk performance of the networks, and do not necessarily have regard for the control of the common mode disturbances considered in the product standard.

To ensure that the physical layer specifications for telecommunication networks do not inadvertently lead to the generation of unacceptable electromagnetic disturbances, it is essential that the EMC implications of the specifications for some critical parameters be considered early in the development of the network standards.

To achieve EMC of telecommunication networks employing twisted pair media, the most important parameters to consider are the:

- levels specified for the wanted transverse or differential mode electrical signals;

IECNORM.COM : Click to view the full PDF of CISPR TR 16-3:2020 RLV

- spectral characteristics of the line codes specified for the wanted differential mode signals;
- design of the protocol of the wanted differential mode signals;
- expected electrical balance or LCL of the physical copper media, *in situ*, on which the wanted electrical signals will be conveyed;
- electrical balance or LCL of the telecommunication signal ports that will be connected to the physical media;
- differential mode and the common mode impedances expected for the physical media on which the wanted differential mode signals will be conveyed;
- differential mode and the common mode impedances specified at the telecommunication signal ports on which the wanted differential mode signals will appear;
- shielding effectiveness expected of connectors and shields, if shielded media are to be used.

The influence of the absolute levels of the wanted differential mode signals on the resultant common mode disturbance levels needs little elaboration. In the absence of nonlinearities, the levels of the common mode disturbances produced by differential mode to common mode conversion, due to electrical unbalance of the telecommunication ports or the physical media, will be directly proportional to the levels of the wanted differential mode signals. The spectral characteristics and the protocols specified for the wanted differential mode signals will also have a major influence on the levels of the common mode disturbances appearing on the physical media.

For a given data rate, a differential mode signal employing line coding, designed to spread the signal power across a wide range of frequencies, is less likely to create unacceptable common mode disturbances than is a differential mode signal line code that concentrates the power into a narrow spectral band or bands.

Selection of the signal protocols can significantly influence the spectral characteristics of the differential mode signals. The formats of start and end delimiters, framing and synchronization bit patterns, the bit patterns of tokens, and ultimately the design of the access control protocols, will have a significant influence on how much concentration of differential mode signal power into narrow spectral bands takes place during the various operating states (i.e. high traffic periods, low traffic periods, idle periods) of telecommunication networks. The creation of highly periodic waveforms that persist for lengthy periods of time should be avoided, if the levels of common mode disturbances, created from the differential mode signals on the network, are to be minimized.

### 4.11.2 Estimation of common mode disturbance levels

Estimations can be made of the levels of common mode disturbances that will be created by differential mode to common mode conversion of the wanted differential mode signals, if the relationships between the important electrical and spectral parameters are known. In particular, estimations can be made of the maximum allowed levels for differential mode signals, if the common mode disturbances created from those are not to exceed the common mode disturbance limits.

Consider two devices connected together in a LAN, for example a nominally balanced telecommunication signal port connected to a nominally balanced unshielded twisted pair terminated in its characteristic impedance. Assume that the electrical unbalance of the combination of these two devices is dominated by the electrical unbalance of the device that exhibits the worst (lowest) LCL. The strength of the common mode disturbances produced by differential mode to common mode conversion through the LCL of that device can be estimated approximately from the equation

IECNORM.COM : Click to view the full PDF of CISPR TR 16-3:2020 RLV

$$I_{cm} \approx V_T - a_{LCL} - 20\lg\left|2Z_{dm} \times \frac{Z_{cm} + Z_{ct}}{Z_{dm} + 4Z_{cm}}\right| \quad (102)$$

when estimating the common mode current $I_{cm}$,in dB(μA), caused by the differential mode signal voltage, and the equation

$$V_{cm} \approx V_T - a_{LCL} - 20\lg\left|\frac{2Z_{dm}}{Z_{cm}} \times \frac{Z_{cm} + Z_{ct}}{Z_{dm} + 4Z_{cm}}\right| \quad (103)$$

when estimating the common mode voltage $V_{cm}$, in dB(μV), caused by the differential mode signal voltage $V_T$, in dB(μV), where

$a_{LCL}$ is the LCL, in dB;

$Z_{cm}$ is the common mode impedance presented by the item having the worst (lowest) LCL, in Ω;

$Z_{ct}$ is the common mode impedance presented by the item with the higher LCL, in Ω, and

$Z_{dm}$ is the transverse or differential mode impedance at the telecommunication signal port, in Ω.

The above expressions, which have been derived from relationships developed in [90], implicitly assume that both of the devices in the combination present a transverse or differential mode impedance of $Z_{dm}$.

By setting the common mode disturbance levels in Equations (102) and (103) equal to the common mode disturbance limits, the maximum allowable transverse or differential mode signal levels can be estimated.

When making use of Equations (102) and (103), it should be recalled that a common mode disturbance limit is a quantity that is specified for comparison with disturbances measured in a defined bandwidth (e.g. 9 kHz), using a specified detector function (quasi-peak or average). Therefore, for the given LCL the maximum allowed differential mode signal levels estimated using these Equations (102) and (103) are those that are allowed to appear in the same bandwidth when measured differentially with the same detector functions.

## 4.12 Background on CDNE equipment and measurement method

### 4.12.1 General

The CDN measurement method was originally developed for assessment of radiated disturbances of lighting equipment from 30 MHz to 300 MHz. In October 2006 the CDN method was adopted by a first amendment of Edition 7 of CISPR 15, published in 2006 [91].

A CISPR joint Task Force between CISPR SC/A and CISPR SC/F on the 'CDN measurement method of radio frequency disturbances for lighting equipment in the frequency range 30 MHz to 300 MHz' (CDNE JTF A/F) was established in 2008, and tasked with transferring the CDN method of emission measurement in the frequency range 30 MHz to 300 MHz to the CISPR 16 series. This was to give the method a more generic status and enable use for other types of equipment. An additional aim was to improve the CDN method uncertainties.

The CDNE JTF developed specifications and measurement methods for a CDNE, which is the CDN for emission measurement. Between 2008 and 2014 the CDNE specification, the associated measurement method, the measurement instrumentation uncertainties and the correlation with the classical radiated measurement method were implemented in respectively CISPR 16-1-2 [95], CISPR 16-2-1 [8], CISPR 16-4-2 [96] and CISPR 16-4-5 [97].

IECNORM.COM : Click to view the full PDF of CISPR TR 16-3:2020 RLV

The following subclauses give background information and rationales on the CDN and the CDNE equipment and measurement method.

### 4.12.2 Historical overview

#### 4.12.2.1 Situation around 1996

Before the first amendment to Edition 7, lighting products were subject to conducted and radiated RF disturbance measurements according to CISPR 15 [98] in the frequency range below 30 MHz. Radiated disturbance measurements above 30 MHz according to CISPR 22 [99] were carried out on a voluntary basis to assure quality and to avoid complaints in specific environments. Generally the emission levels of lighting products with bipolar circuit technology were negligible for frequencies above 30 MHz.

In 1996, within the EMC group of Philips Research in Eindhoven, the Netherlands, an investigation was started on possible workbench methods as an alternative for the radiated tests in the frequency range 30 MHz to 300 MHz. The CDN, which is known from RF immunity tests in the range of 150 kHz to 80 MHz according to IEC 61000-4-6 [15], seemed a suitable candidate for application to measurement of RF disturbances as well. Therefore, a method using the CDN for disturbance measurements was developed and investigated. Especially the relationship with the established radiated disturbance measurement method in a SAC was explored.

It is generally accepted that correlation between two test methods only makes sense when both methods have good reproducibility and low uncertainty. The established radiated RF disturbance measurement method has a fairly large compliance uncertainty (7 dB) due to variability in cable layout and termination, while the CDN method has a moderate compliance uncertainty (4 dB) provided that the EUT is small and the cable length between the CDN and EUT is limited. Still, a reasonable correlation between the CDN method and the 3-m and 10-m radiated method was demonstrated for luminaires of different sizes.

#### 4.12.2.2 CDN concept for disturbance measurements introduced in 1999

The feasibility and concept of the CDN method was presented in a paper at the 1999 Zurich EMC conference by Stef Worm [93]. In that paper, the radiated disturbance measurement method in a 3 m SAC and the CDN method (refer to Figure 200) are compared. It is demonstrated by modelling that the CM current in a cable (single wire – see NOTE 1) connected to the EUT is a good metric for the E-field measured using the 3 m SAC/OATS method.

NOTE 1 The single wire and its impedance is the model of a cable with one or more wires including the protective earth wire. The CM impedance mentioned in the report represents the “total” CM impedance of the cable.

NOTE 2 At the time of this investigation the 3 m SAC/OATS was used as reference. Later it was agreed more formally (see CISPR 16-4-5 [97] ) that the 10 m SAC/OATS is the reference, called the established test method.

Note that the cable does not necessarily need to be a mains cable and is not connected to a network. The E-field/CM-current ratio depends on the termination impedance. Measurement results [92] have shown (see Figure 201) that the response is reasonably flat if the termination impedance of the cable (single wire) equals 150 Ω. Also the impact of cable layout and set-up of the EUT and CDN has been investigated. The 150-Ω impedance also provides a good match with the disturbance source, which prevents standing waves. Different options for the 150-Ω impedance have been compared in [93], where it was concluded that the best candidate for the 150-Ω termination impedance was the existing CDN used for immunity tests.

So, in the original and basic concept of the CDN method, the purpose of the CM impedance of 150 Ω is to enable a good match (no standing waves) with the disturbance source. With this property, a relatively simple relation between the E-field limit and the limit applicable for the CDN method could be derived and implemented in Table B.1 of CISPR 15:2013 [98]. It has

IECNORM.COM : Click to view the full PDF of CISPR TR 16-3:2020 RLV

not been the intention that the CDN emulates the CM impedance and LCL − or whatever other property of the network to which the (mains) cable could be connected.

The CDNE method is an alternative method to assess radiated disturbance of a product in the frequency range of 30 MHz to 300 MHz, under specific limitations of the product characteristics. Hence it addresses the radiation coming from the enclosure port of the EUT. Another example of a radiated disturbance assessment method is the absorbing clamp method in the frequency range between 30 MHz and 1 000 MHz.

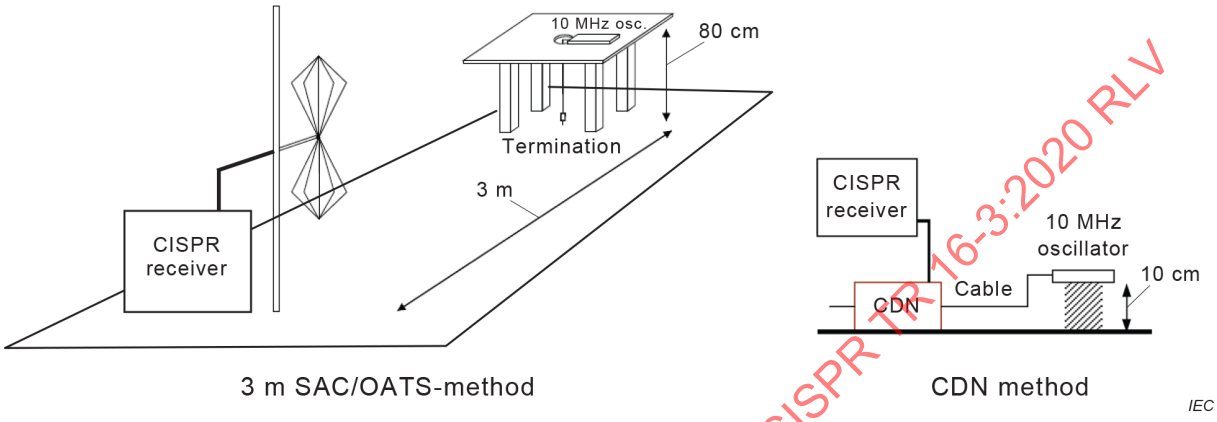
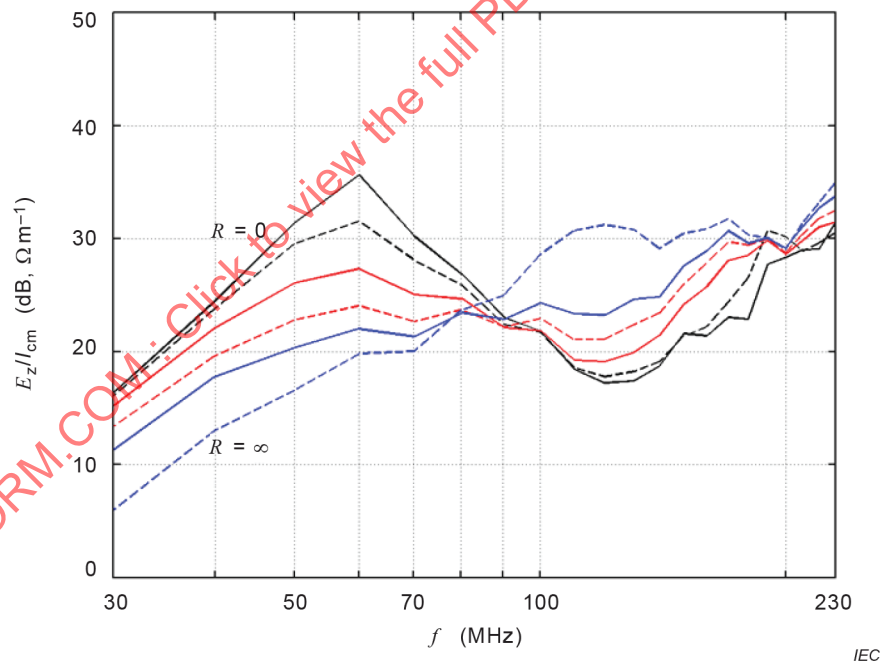



**Figure 200 – Equivalent radiated measurement methods (30 MHz to 300 MHz)**




The red curve is the 150-Ω termination.

**Figure 201 – Measured relationship between field strength $E_z$ and CM current $I_{cm}$ for various termination resistances $R$**

#### 4.12.2.3 Derivation of the CDN limit

The asymptotic curve given in Figure 202 (using the equations given in [92]; matched case $\Gamma$ = 0), is used to translate the limit levels $E_{Rad}^{Lim,3\,m}$ of the existing 3 m (see NOTE 2 of

IECNORM.COM : Click to view the full PDF of CISPR TR 16-3:2020 RLV

4.12.2.2) radiated disturbance limits to the limit $I_{\mathrm{CDN}}^{\mathrm{Lim}}$ for the CM current of the CDN test method limit with the following equation:

$$I_{\mathrm{CDN}}^{\mathrm{Lim}} = \frac{E_{\mathrm{Rad}}^{\mathrm{Lim,3m}}}{E/I \text{ ratio}} \tag{104}$$

where the $E/I$ ratio is the average relationship between field strength and CM current for various CM-impedance terminations, i.e. the black straight dashed line shown in Figure 202.

The CDN current limit is expressed in terms of terminal voltage limit across a 150-Ω impedance ($V_{\mathrm{CDN}}^{\mathrm{Lim}}$), so

$$V_{\mathrm{CDN}}^{\mathrm{Lim}} = 150\,\Omega \times \frac{E_{\mathrm{Rad}}^{\mathrm{Lim,3\,m}}}{E/I \text{ ratio}} \tag{105}$$

For example, a radiated disturbance limit of 40 dB(μV/m) at 3 m and 100 MHz translates to a terminal voltage limit of 20 lg (150) + 40 − 30 = 54 dB(μV). The CISPR 15 radiated limits translate in this way to the values given in Table B.1 of CISPR 15:2013 [98]; see also Figure 203.

Note that the voltage division factor $F_{\mathrm{CDNE}}$ (in dB) and the value of the attenuator external to the CDN are added to achieve the CM-terminal voltage across 150 Ω, i.e. -20 lg(50/150) + dB-value of the external attenuator (6 dB):

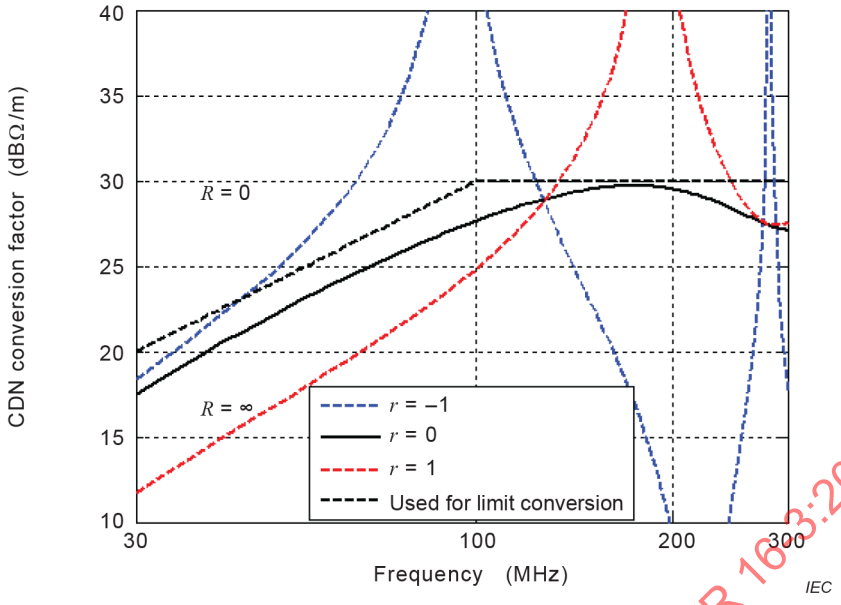
$$F_{\mathrm{CDNE}} = -20 \text{ lg } (50/150) + 6 \tag{106}$$

The CDNE-disturbance level $V_{\mathrm{CDNE}}$, then can be calculated as follows:

$$V_{\mathrm{CDNE}} = V_{\mathrm{meas}} + F_{\mathrm{CDNE}} \tag{107}$$

where $V_{\mathrm{CDNE}}$ and $V_{\mathrm{meas}}$ are in dB(μV).

IECNORM.COM : Click to view the full PDF of CISPR TR 16-3:2020 RLV




The black straight dashed lines are an asymptotic boundary curve used for translation of the limit.

**Figure 202 – Modelled relationship between field strength $E_z$ and CM current $I_{cm}$ using EUT height 0,8 m, measurement distance 3 m, receive antenna height 1 m**

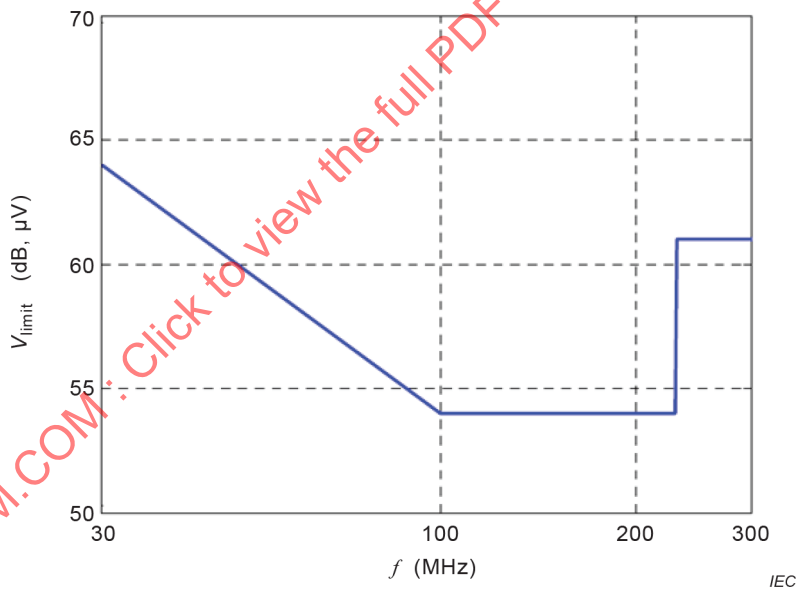



**Figure 203 – Limit for the terminal voltage at the CDN**

IECNORM.COM : Click to view the full PDF of CISPR TR 16-3:2020 RLV

#### 4.12.2.4 2006: first implementation of the CDN method in CISPR 15

In October 2006 the CDN method was adopted in the first amendment of Edition 7 of CISPR 15 [91] published in 2006 [91].

The CDN measurement method, the CDN specification and the CDN limits were included in a separate normative Annex B of CISPR 15:2005/AMD1:2006.

Basically, the CDN should satisfy the specifications of IEC 61000-4-6 [15], and the specification of the CM-impedance of 150 Ω was extended to 300 MHz.

The limit given in CISPR 15 is the same as given in Figure 203.

### 4.12.3 From CDN to CDNE

#### 4.12.3.1 Shortcomings

After applying the CDN method for testing of lighting equipment for a few years, a number of shortcomings of the CDN method were found, including:

– lack of reproducibility of tests when using CDNs from different manufacturers;
– no restrictions on the size of the EUT;
– absence of an uncertainty budget;
– specification to only 230 MHz − CISPR 15 specified the CDN for measurements to 300 MHz;
– no documented correlation between the CDN method and the classical radiated method.

As an example, Figure 204 gives the results of an RRT. CDN measurement results from 11 laboratories within Philips were obtained using class 1 and class 2 artificial EUTs consisting of a comb generator and a coupling unit that launches both DM and CM disturbances. Each laboratory applied its own CDN from different manufacturers. The results of the class 1 EUT (CDN-M3) exhibited an especially large spread due to the variation in the performance of the CDNs. More in-depth investigations revealed that the main reason for the large spread was the absence of a DM-impedance specification of the CDN, large tolerances of the CM impedance, the absence of impedance specification above 230 MHz and the absence of phase angle tolerance of the CM impedance.

#### 4.12.3.2 CISPR A/F JTF

A joint task force between CISPR/A and CISPR/F was formed on the ‘CDN measurement method of radio frequency disturbances for lighting equipment in the frequency range 30 MHz to 300 MHz’ (CDNE JTF A/F). That JTF was established in 2008 and tasked with transferring the CDN method of emission measurement in the frequency range 30 MHz to 300 MHz to the CISPR 16 series. An additional aim was to improve the reproducibility of the CDN method. Also in view of the EMC-standardization debate on the subject of ‘alternative test methods’ there was a need to consolidate the relationship between the CDN method and the classical radiated test method in CISPR 16-4-5 [97].

The JTF work included the following projects:

– adding CDNE specifications and validation methods in CISPR 16-1-2 [95];
– adding measurement set-up and method in CISPR 16-2-1 [8];
– adding background and rationale in CISPR TR 16-3 (this subclause);
– adding uncertainty aspects in CISPR 16-4-2 [96];
– adding conditions for alternative methods in CISPR TR 16-4-5 [97].

IECNORM.COM : Click to view the full PDF of CISPR TR 16-3:2020 RLV

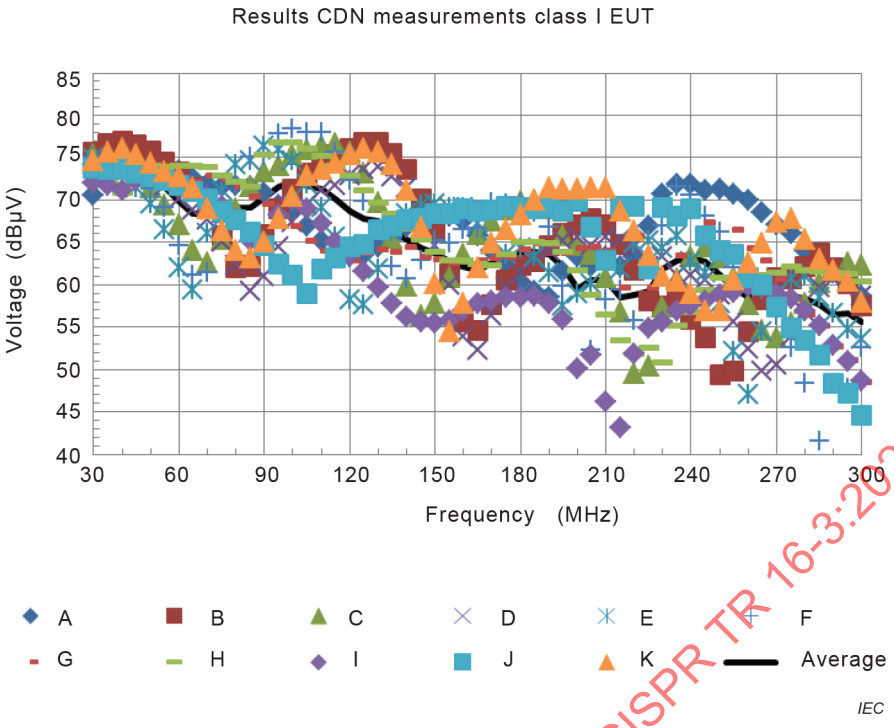



**Figure 204 – Results of a Philips 11-lab internal CDN RRT using an artificial class 1 EUT – expanded uncertainty nearly 10 dB**

#### 4.12.3.3 Improvements of the CDNE

The main function of the CDNE has not changed compared with the CDN, i.e. the CDNE couples asymmetric (CM) disturbance voltage from the EUT into the input lead of the measuring receiver, and decouples that lead from any emissions or influences present in the test environment. It measures the CM disturbance in a short cable connected to the EUT (often AC mains but not absolutely necessary) through a nominal impedance of 150 Ω (see 4.12.2.2).

The most important changes in the CDNE specification are as follows (see CISPR 16-1-2 [95]).

a) A specification for the phase tolerance of the CM impedance has been added: 0° ± 25°;

b) The tolerance of the magnitude of the CM impedance of the CDNE (150 Ω) has been reduced to +10 Ω/–20 Ω;

c) A specification and tolerance of the DM impedance at the EUT port has been added, i.e. 100 Ω ± 20 Ω. Any symmetric (DM) disturbance coming from the EUT is loaded either by a symmetric impedance of 100 Ω at the EUT mains port (CDNE-M2 and CDNE-M3), or by the external symmetric load at the AE port of the CDNE-S$x$. The value of 100 Ω equals the DM impedance of a mains network/LISN. However, the main reason of the CDNE JTF to specify the 100 Ω DM impedance was based on the fact that the reproducibility of test results was improved when this 100 Ω DM impedance was applied;

d) Instead of a separate external attenuator of 6 dB, a fixed internal attenuator of at least 6 dB is applied. This avoids mistakes in setting up the test method without an external attenuator at the receiver port;

e) A tolerance of the voltage division factor has been added: ± 1,5 dB;

NOTE This tolerance refers to the theoretical voltage division factor given in Equation (106). Normally the actual voltage division factor of a CDNE obtained during calibration is applied during a measurement. Then the value of ±1,5 dB is not used as the basis for the uncertainty contribution. The basis is the uncertainty of the voltage division factor calibration which is typically much lower; see CISPR 16-4-2 [96].

IECNORM.COM : Click to view the full PDF of CISPR TR 16-3:2020 RLV

f) A decoupling attenuation of at least 30 dB has been added to decouple disturbances coming from the AE or mains port towards the measuring receiver. Thereby the measured CM current is also insensitive for variations of the CM/DM impedances of the network connected to the AE/mains port;

g) A longitudinal conversion loss (LCL) of at least 20 dB is specified for the CDNE-M2 and CDNE-M3. For EUTs that apply the CDNE to the mains port, in general above 30 MHz, the level of asymmetric disturbance voltage is much higher than the level of symmetric disturbance voltage. Therefore a minimum LCL value of 20 dB is adequate to prevent any influences of the symmetric voltage on the measurement results. In contrast, the assessment of EUTs using the DM for communication on unscreened leads requires specific LCL values (minimum and maximum value) of the CDNE;

h) A more detailed validation/verification procedure for each of the above specifications has been added.

#### 4.12.3.4 Improvements of CDNE test method

The test method has changed significantly as follows (set-up and procedure specified in CISPR 16-2-1 [8]; see Figure 205):

a) tighter specification for the distance of the EUT to any other metallic object; the distance is ≥ 0,8 m; for a shorter distance, but not less than 0,4 m, an additional uncertainty of 0,2 dB is added;

b) more elaborate specifications for CDNE tests where two CDNEs are applied;

c) a more detailed measurement procedure.

Furthermore the limitations for application are given more explicitly, i.e.:

a) the CDNE cannot be used for applications on a mains network with intentional DM signals, e.g. where transmitting of a wanted differential signal would require a specific LCL, minimum and maximum value, to take the network quality into account;

b) when the largest dimension of the EUT enclosure is larger than a quarter wavelength at the highest frequency of measurement, unless otherwise specified by the product committee;

c) the rated supply voltage should not exceed 600 V;

d) the EUT should not have more than two cables.

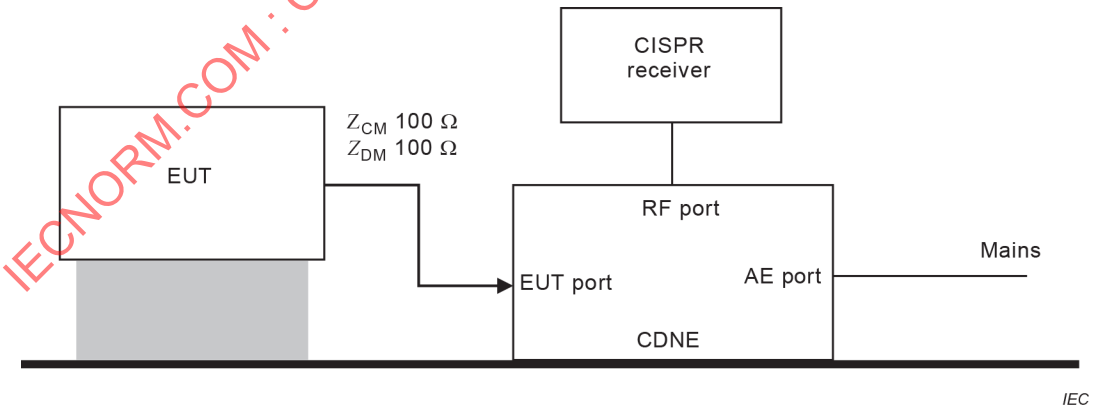



**Figure 205 – Block diagram for CDNE-measurement method**

#### 4.12.3.5 Reduced measurement uncertainty

An aim of all the changes in the CDNE-specification and test method is to reduce the measurement instrumentation uncertainty. The uncertainty budget published in CISPR 16-4-2 [96]) gives an expanded uncertainty value of $U$(V) = 2$u_c$(V) = 3,79 dB.

IECNORM.COM : Click to view the full PDF of CISPR TR 16-3:2020 RLV

#### 4.12.3.6 Conversion of limits

The factor for conversion of the established 10-m SAC/OATS limit to the CDNE limit is reported in CISPR TR 16-4-5 [97]. In this case the conversion factor is determined using the procedure for measurement results given in Clause 7 of CISPR TR 16-4-5:2006/AMD1:2014 [97].

### 4.13 Background on LLAS, validation and measurement method

#### 4.13.1 General

The large loop antenna system (LLAS) and its associated measurement method was originally developed for assessment of magnetic field strength disturbances from 9 kHz to 30 MHz of lighting equipment as an alternative for applying an electrically-screened magnetic-field loop antenna at a certain distance from an EUT both located above a ground plane. An LLAS has a high sensitivity and it is insensitive to external high ambient signals from radio sources.

The following subclauses give detailed background information on an LLAS, its measurement method in general and on the models and equations that apply to calculate the reference validation factor and conversion factor curves that are given in CISPR 16-1-4:2019, CISPR 16-1-4:2019/AMD1:2020 and CISPR 16-1-4:2019/AMD2:20—[102].

#### 4.13.2 Historical overview

##### 4.13.2.1 Development of the LLAS measurement method

The large-loop antenna system (LLAS) and its measurement method is based on the 1989 EMC Zurich conference paper by Bergervoet and Van Veen [103]. Bergervoet and Van Veen are the inventors of the LLAS, also called the loop antenna system (LAS). At that time, the term *large* has been used in LLAS and LLA, to distinguish this antenna system from the generally smaller (typically 60 cm diameter) single loop antennas used for magnetic-field strength measurement at a certain distance from an EUT. They started the development of the LLAS method in 1987 as a more convenient alternative method for magnetic field strength measurements below 30 MHz. In the period between 1987 and 1993, Goedbloed and others submitted various proposals [104], [105], [106], [107], [108] in CISPR for adoption of the LLAS method in CISPR 16. Also, in 1993 Shinozuka et al. published a review paper [110] including a rigorous analysis of the LLAS method.

##### 4.13.2.2 First adoption in CISPR publications

In 1993, the LLAS method was included for the first time in the first edition of CISPR 16-1. In 1989, the LLAS method was proposed for introduction in CISPR 15:1985 for disturbance measurement of lighting equipment [109]. In 1992, the LLAS method and limits were implemented in the fourth edition of CISPR 15.

Subsequently, the LLAS method was also included in the product standards CISPR 14-1 and CISPR 11 for testing induction cooking appliances for domestic use.

##### 4.13.2.3 Maintenance and further adoption in CISPR publications

In 2014, CISPR/F requested that CISPR/A [111] start a maintenance project for adding an uncertainty budget in CISPR 16-4-2 for the LLAS measurement method. At that time, it was also recognized that there would be an increasing need for radiated disturbance measurements in the frequency range of 9 kHz to 30 MHz because of widespread introduction of inductive power transfer technologies. The LLAS method is also convenient for disturbance testing of such equipment.

IECNORM.COM : Click to view the full PDF of CISPR TR 16-3:2020 RLV

In 2014, during the CISPR A meeting in Frankfurt, it was decided to start working on the establishment of an uncertainty budget of the LLAS measurement method. Furthermore, on request of the Japanese NC it was decided to add tabular values of the various curves given in Figure C.8, Figure C.10 and Figure C.11 of CISPR 16-1-4:2010 and CISPR 16-1-4:2010/AMD1:2012 [102] for magnetic field strength conversion and for the validation factor. Availability of tabular numerical values as a function of frequency avoids the introduction of inaccuracies when laboratories shall extract values from these curves for LLAS validation and applications. Preparatory work was undertaken in 2014 to 2017 [100], [101]. In the same period, papers of Midori et al. [117] and Mc. Lean et al. [113] identified an inaccuracy in the original calculation of the mutual inductance between the loops of the LLAS and the calibration dipole that is used for calculating the validation factor.

During the 2015 CISPR A meeting in Stresa it was decided to start a maintenance project on the LLAS validation method of CISPR 16-1-4 including the following:

a) To upgrade the model of the LLAS validation method by applying the more accurate value of the mutual inductance and to achieve a better match of the validation factor in practice;

b) To recalculate the curves and tabular values of the reference validation factor;

c) To change the tolerance of the measured validation factor from ±2 dB to ±3 dB.

As a result of the various LLAS-related maintenance activities for CISPR 16-1-4 and CISPR 16-4-2, it was also decided to consolidate the background, rationale and underlying details in new subclauses of this document CISPR TR 16-3.

#### 4.13.3 Models and equations for the LLAS method

Annex G describes the models and equations that are needed to determine the LLAS reference validation factor curves and the magnetic field conversion factor curves given in CISPR 16-1-4:2019, CISPR 16-1-4:2019/AMD1:2020 and CISPR 16-1-4:2019/AMD2:20— [102].

Matlab scripts for calculating the values of the reference validation factors and the magnetic field strength conversion factors are available through the Matlab Central File Exchange [120].

## 5 Background and history of CISPR

### 5.1 The history of CISPR

#### 5.1.1 The early years: 1934-1984

An *ad hoc* conference of interested international organizations was held in 1933 in Paris to decide how the subject of radio interference should be dealt with internationally. There was general agreement that the most urgent international problem was to secure some uniformity in the method of measurement and stipulation of limits to avoid difficulties in the exchange of goods and services.

The result of this meeting was to form the Comité International Spécial des Perturbations Radioélectriques (CISPR) or in English, International Special Committee on Radio Interference. The first meeting was held in 1934. The first Chairman was Sir Clifford Patterson and members were appointed by their national committees. In 1935, the specification for the measuring set including the Mains Network (in the US known as LISN) was drafted. After this specification was finalized, it was found that the measuring sets produced by different countries, produced different data. Consequently, the Belgian Electrotechnical Committee took on the task to construct the standard CISPR measuring set. In 1939, twelve copies of this set were delivered to different countries.

IECNORM.COM : Click to view the full PDF of CISPR TR 16-3:2020 RLV

The work with interference limits progressed slowly. At the first CISPR meeting the lowest protected field strength was set at 1 mV/m (60 dB(μV/m)) with a modulation index of 80 %. The lowest protection ratio was to be 100 (40 dB). Various limits were proposed but none even came close to (the then required) 20 dB(μV/m). There was no agreement on limits before WW II. Agreement was reached on the antenna height to be used for measurement and for the model for coupling from the mains to the antenna. This proved valuable for future work. The requirements for the electrical parameters of interference-suppression capacitors were also established.

During WW II no meetings were held. The work started again in 1946 under the then CISPR Chairman: Dr. S. Whitehead. During WW II many individual countries had set up services for the suppression of interference to aid the war effort. A significant unifying effort was based on the 12 measuring sets delivered to different national committees by the Belgian Electrotechnical Committee at the brink of WW II. On the basis of this set, the frequency range was extended to 30 MHz to give coverage from 150 kHz to 30 MHz with the quasi-peak detector that was also in the Belgian set. This measuring set specification was approved in The Hague in 1958. The specification was considerably improved over the 1935 version and the building of a simple prototype was no longer necessary. Further work led to the approval of the ISM specification in 1965 and the artificial hand specification in 1968. These specifications were merged into one specification in 1972 with an amendment issued in 1975.

CISPR measuring set specifications were extended from 30 MHz to 300 MHz in 1958 with an amendment for ISM in 1965. The same year, the measuring set specifications was extended from 300 MHz to 1 000 MHz. Mr. Meyer de Stadelhofen's absorbing clamp appeared in 1966 and was added to the specification in 1970.

New editions of the measuring set specifications appeared as follows:

CISPR 1 (1972), 0,15 MHz to 30 MHz

CISPR 2 (1985), 30 MHz to 300 MHz

CISPR 4 (1967), 300 MHz to 1 000 MHz

In addition several supplements were released until 1993 when CISPR 16-1 merged all specifications into one document.

Limits were first proposed in 1950 for the 150 kHz to 285 kHz and the 150 kHz to 1 605 kHz frequency ranges for domestic, industrial and commercial appliances up to 1 kW and for connection to the low-voltage power network. The adopted limits were reduced or increased at every CISPR meeting. The frequency range was extended to 25 MHz and abolished again at the whim of the delegates. For some years, a voltage range was given as the limit since agreement could not be reached for a specific value. Until 1964, when higher limits were specified for motor-operated appliances for domestic and similar use and for portable tools. The permissible voltages were measured with the 150 Ω V-network between each line and ground. The limits were amended again in 1973. The working conditions of the appliances were specified in 1961 and amended in 1967, 1970 and 1973. The limits of interference power radiated from the power cord from 30 MHz to 300 MHz and as measured with the MDS absorbing clamp were agreed upon in 1970 and amended in 1973.

Interference from low repetition transient events was first controlled in 1961 and limits for regulating controls incorporating semiconductors and for thermostatically controlled appliances were specified in 1970. Limits for program-controlled appliances were set in 1967. In 1973, the limits for the transient events were combined into one document: Rules for the Evaluation of Radio Noise Produced by Switching Operations in Appliances for Household and similar purposes in the 0,15 MHz to 300 MHz frequency range.

Limits for radiation from sound and TV broadcast receivers were specified in 1961 with amendments issued in 1964, 1967 and 1970. Limits for the mains interference immunity factor for long- and medium-wave receivers were given in 1961 with amendments in 1964 and 1967.

IECNORM.COM : Click to view the full PDF of CISPR TR 16-3:2020 RLV

Limits for ISM-frequencies were requested by the ITU WARC in 1959. CISPR published limits for out-of-band frequencies in 1961 with amendments in 1964, 1967 and 1973

Limits for ignition systems in the automotive field were given in 1961 with amendments given in 1964, 1970 and 1973.

The limits for fluorescent lighting fixtures for the long and medium waves were specified in 1964 with amendments in 1967, 1970 and 1973.

The characteristics of spectrum analyzers required for interference measurements from 0,3 GHz to 18 GHz of microwave equipments for heating and medical purposes were released in 1973.

Methods for estimation of compliance with limits for appliances in large-scale production were agreed upon in 1961 and 1964. The “Significance of a CISPR Limit” rule was established in 1970.

The safety aspects of filters and capacitors used for suppression on the power mains was discussed since before WW II. The initial discussions were extensive throughout the 1950s, but then subsided since CISPR interests concentrated on suppression of higher frequencies that required smaller values of capacitance.

The first standard on industrial, scientific and medical (ISM) equipment was published in 1973. Five further publications were released in 1975 on the general topic of “Limits and Methods of Measurement” for:

a) ISM equipment excluding surgical diathermy apparatus;
b) vehicles, motorboats and devices that utilized ignition systems;
c) sound and television receivers;
d) household electrical appliances, portable tools and similar devices;
e) fluorescent lamps and luminaries.

Subsequent work continuously updated these documents.

#### 5.1.2 The division of work

In 1973 it became apparent that the work of CISPR needed to be subdivided and organized along major product families. The following subcommittees were established:

CISPR/A defines the instrumentation and the measurement methods;

CISPR/B is concerned with the interference from industrial, scientific and medical equipment (ISM);

CISPR/C is concerned with the interference from overhead power lines, high-voltage equipment and traction systems;

CISPR/D is concerned with the interference from motor vehicles and internal combustion engines;

CISPR/E is concerned with the interference from and to TV and broadcast receivers;

CISPR/F is concerned with the interference from and to household appliances, motor-operated equipment, lighting apparatus and similar equipment;

CISPR/G is concerned with the interference from and to computers and information technology equipment (ITE).

IECNORM.COM : Click to view the full PDF of CISPR TR 16-3:2020 RLV

### 5.1.3 The computer years: 1984 to 1998

Since 1984, much attention has been concerned with refining the measurements methods and the limits for information technology equipment. In principle, this is any equipment that uses a microprocessor and switching frequencies or clocks above 9 kHz. CISPR work was and still is primarily concerned with refining the Open-Area Test Site (OATS) requirements, as well as replacing the OATS with anechoic room, TEM and GTEM test sites. In addition, much effort has been expended on CISPR Publication 16, “The CISPR Handbook,” which contains all instrument specifications and measurement methods.

CISPR work since 1984 is best described by the number of documents that were produced. The titles are reduced to the keywords and the number and year identifying each publication:

| | |
|---|---|
| 10 (1990) | Rules and procedures of CISPR |
| 11 (1990) | Limits and measurement methods, ISM |
| 12 (1990) | Automobiles and ignition systems |
| 13 (1996) | Sound and TV receivers |
| 14 (1993) | Household appliances and electric tools |
| 15 (1993) | Fluorescent and RF lighting fixtures |
| 16-1 (1993) | Specification for EMC measurement equipment |
| 16-2 (1996) | Methods of EMC measurements |
| 17 (1981) | Specification for filters |
| 18-1 (1982) | Overhead power line, phenomena |
| 18-2 (1986) | Overhead power line, limits and methods |
| 18-3 (1986) | Overhead power line, suppression |
| 19 (1983) | Microwave oven substitution measurements |
| 20 (1996) | Immunity of sound and RV receivers |
| 21 (1985) | Reception of radio in the presence of noise |
| 22 (1993), (1997) | Information technology equipment |
| 23 (1987) | Determination of ISM limits |
| 24 (1997) | Immunity of ITE |
| 25 (1995) | Emission limits to protect radios in cars |

The future is unknown. However, the work of CISPR will go on to address any problem that may occur because of the new technologies proposed.

### 5.1.4 The people in CISPR

As in any organization it takes dedication and perseverance in the task at hand. Some of the key people in CISPR were and are as follows:

Chairmen of CISPR

| | |
|---|---|
| Sir C.C. Patterson (UK) | Paris 1934 |
| Prof. A.F. Enström (SE) | Berlin 1935 |
| Mr. R. Braillard (BE) | 1934-1939 |
| Dr. S. Whitehead (UK) | 1946-1953 |
| Mr. O.W. Humphreys (BG) | 1953-1961 |

IECNORM.COM : Click to view the full PDF of CISPR TR 16-3:2020 RLV

| | |
|---|---|
| Prof. L. Morren (BE) | 1961-1967 |
| Prof. F.L. Stumpers (NL) | 1967-1973 |
| Mr. J. Meyer de Stadelhofen (CH) | 1973-1977 |
| Mr. P. Akerlind (SE) | 1977-1979 |
| Prof. R.M. Showers (USA) | 1979-1985 |
| Mr. G.A. Jackson (UK) | 1985-1991 |
| Prof. A. Warner (DE) | 1991-1994 |
| Mr. P. Kerry (UK) | 1995-2007 |
| Mr. D. Heirman (USA) | 2007-present |

## 5.2 Historical background to the method of measurement of the interference power produced by electrical household and similar appliances in the VHF range

### 5.2.1 Historical detail

Measurement of field strength is, in theory, most suitable for determining the interference capability of all types of appliances at frequencies higher than 30 MHz. However, the methods involved together with the precautions to be taken prove troublesome in application. Consequently, engineers have for a long time used the terminal voltage method, while waiting for something more satisfactory. Several methods have been explained to replace those involving electro-magnetic field measurements on an OATS by radiation measurements in the laboratory. Among the most interesting are the stop filter method and the earth current method. These are substitution methods, in which a slotted coaxial filter with negligible losses is used to adjust the radiating length of the supply lead of the source of interference to obtain maximum radiation. In these methods, the interference capability of an appliance is defined as the power which a standard generator shall inject into a simple antenna of known characteristics in order to obtain the same effect on an antenna connected to the measuring receivers as that produced by the source of interference. Several more convenient methods have been developed from those just mentioned.

The measurement of terminal voltages has been considerably improved by replacing the artificial mains V-network by a Y-network so as to obtain the true asymmetric voltage produced by the source of interference. A similar method using a reactive slotted coaxial filter was developed. A method for measuring the power that the source of interference may inject into the supply lead has also been proposed. This method is based on the measurement of the current at the input of an absorbent coaxial device.

The advantage of the latter over the terminal voltage method is that it is not necessary to disconnect the supply lead. It indicates values of the interference power corresponding closely with those obtained by the methods in which the radiation of the supply lead is measured in the resonant condition.

Although, through their ease of operation, the terminal voltage and the absorbing coaxial device methods were preferable to the stop filter and the earth current methods, it remained to be shown that the results which they gave conformed with those obtained in practice.

Statistical measurements on the interference sources have shown that the interference measured by the stop filter method agrees, more closely than that measured by the terminal voltage method, with the effect of the same sources measured at the input of receivers located in the same building. Measurements made by the absorbent device method gave results intermediate between the two previous ones. Other methods have been compared.

IECNORM.COM : Click to view the full PDF of CISPR TR 16-3:2020 RLV

### 5.2.2 Development of the method

In the stop filter method, a value directly related to the current at the centre of a resonant half-way dipole antenna is measured. The most important factor is not the radiating system itself but the power that the source of interference is capable of coupling into the radiating system. The same principle applies to the earth current method. If it were possible to measure this power without measuring the field-strength, all the disadvantages arising from the influence of surrounding objects on the propagation between the radiating element and the receiving aerial would be removed. The attempt to replace the coaxial stop filter by a ferrite tube showed that a large part of the energy produced by the source of interference was dissipated in this tube. It was then thought that the measurements of the current at the input of the ferrite tube might replace, at least in part, the measurement of the field by the stop filter method. This gave rise to the device described in Clause 7 of CISPR 16-2-2:2010.

The following question was then studied: how do the different methods of measurement compare in the particular case of a shielded source of interference of given available power, with a purely resistive internal impedance and transmitting all its interference energy to the supply lead in the asymmetrical mode when the size of this source is varied? Experimental investigations showed the remarkable fact that the new device gave results which were practically independent of the dimensions of those obtained by the other methods.

In fact, one can reduce the absorbing device measuring system to the following circuit: a source of interference of internal impedance $Z_s$ supplying a load $Z_c$ through a low-loss line of characteristic impedance $Z_L$. If the length of the line is varied from zero, the power absorbed by the load $Z_c$ passes (when $Z_c$ is different from $Z_L$) through maxima and minima corresponding to resonance and anti-resonance of the system.

Neglecting the radiation and other losses of the line and discussing the case in which the load is located at a distance corresponding to the first maximum, we consider the point in the line at which the source and the load appear as pure resistances $R_s$ and $R_c$. It can thus be shown that if $P_d$ is the available power of the source, $P_c$ the power absorbed by the load and

$$m = \frac{R_s}{R_c} \qquad (\text{~~102~~}108)$$

then:

$$\frac{P_c}{P_d} = \frac{4m}{(m+1)^2} \qquad (\text{~~103~~}109)$$

This gives for:

| $m$ = | 0,1 | 0,2 | 0,5 | 1 | 2 | 5 | 10 | 20 | 30 |
|---|---|---|---|---|---|---|---|---|---|
| $M = 10\log\frac{P_c}{P_d}$ = | 4,8 | 2,5 | 0,5 | 0 | 0,5 | 2,5 | 4,8 | 7,4 | 9 |

where $M$ is in dB.

It will be seen that the matching of the source of the lead is not very critical and that if an absorbent clamp is used to constitute a load, for example of the order of 200 Ω, the results obtained will not be very different from those obtained if a load is applied to the output of the source of interference in the form of a line brought to resonance by means of a coaxial stop filter.

IECNORM.COM : Click to view the full PDF of CISPR TR 16-3:2020 RLV

It can therefore be concluded that this device, developed primarily in order to avoid the disadvantage of the test site for measuring the radiation, and the necessity to interrupt or disconnect the lead supplying the source of interference, has technical qualities that justify its adoption for the measurement of the interference produced by domestic and similar electrical appliances.

IECNORM.COM : Click to view the full PDF of CISPR TR 16-3:2020 RLV

# Annex A
(informative)

## Derivation of the formula

Consider the general case of a lossless antenna with gain $g$ and input power $p$. At distance $d$ in the direction of maximum radiation, the field strength $e$ is given by the well-known formula:

$$e = \frac{(30pg)^{1/2}}{d} \tag{A.1}$$

Thus, for two antennas, with gains $g_1$ and $g_2$ and input powers $p_1$ and $p_2$ producing the same field strength at a point at the same distance in the direction of maximum radiation

$$p_1 g_1 = p_2 g_2 \text{ or, in log form } P_1 + G_1 = P_2 + G_2 \tag{A.2}$$

and, in the case given in 4.3.2, $P_1$ = $P_t$ and $G_1$ = $G$; $P_2$ = $P_q$ and $G_2$ = 2; therefore the relationship is

$$P_t + G = P_q + 2 \tag{A.3}$$

Sample results are plotted in Figure A.1 and Figure A.2.

IECNORM.COM : Click to view the full PDF of CISPR TR 16-3:2020 RLV

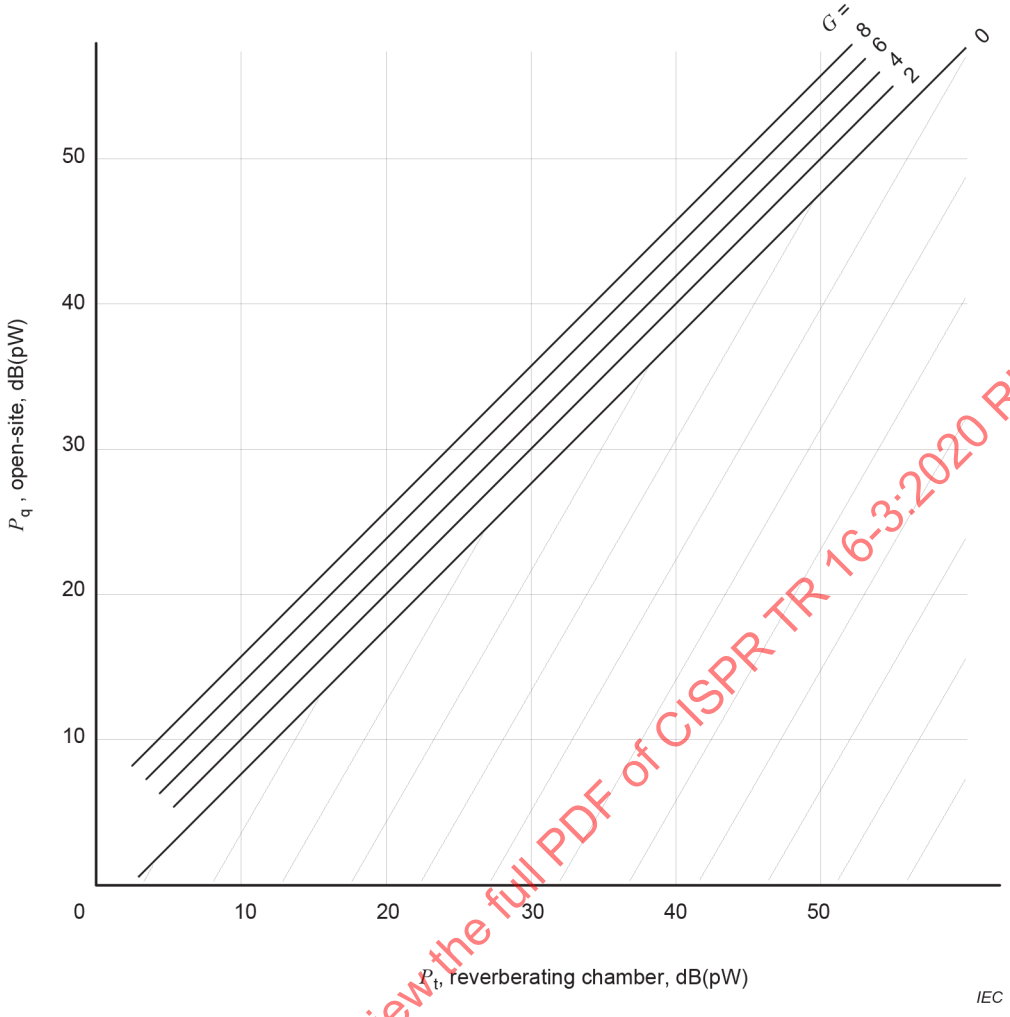
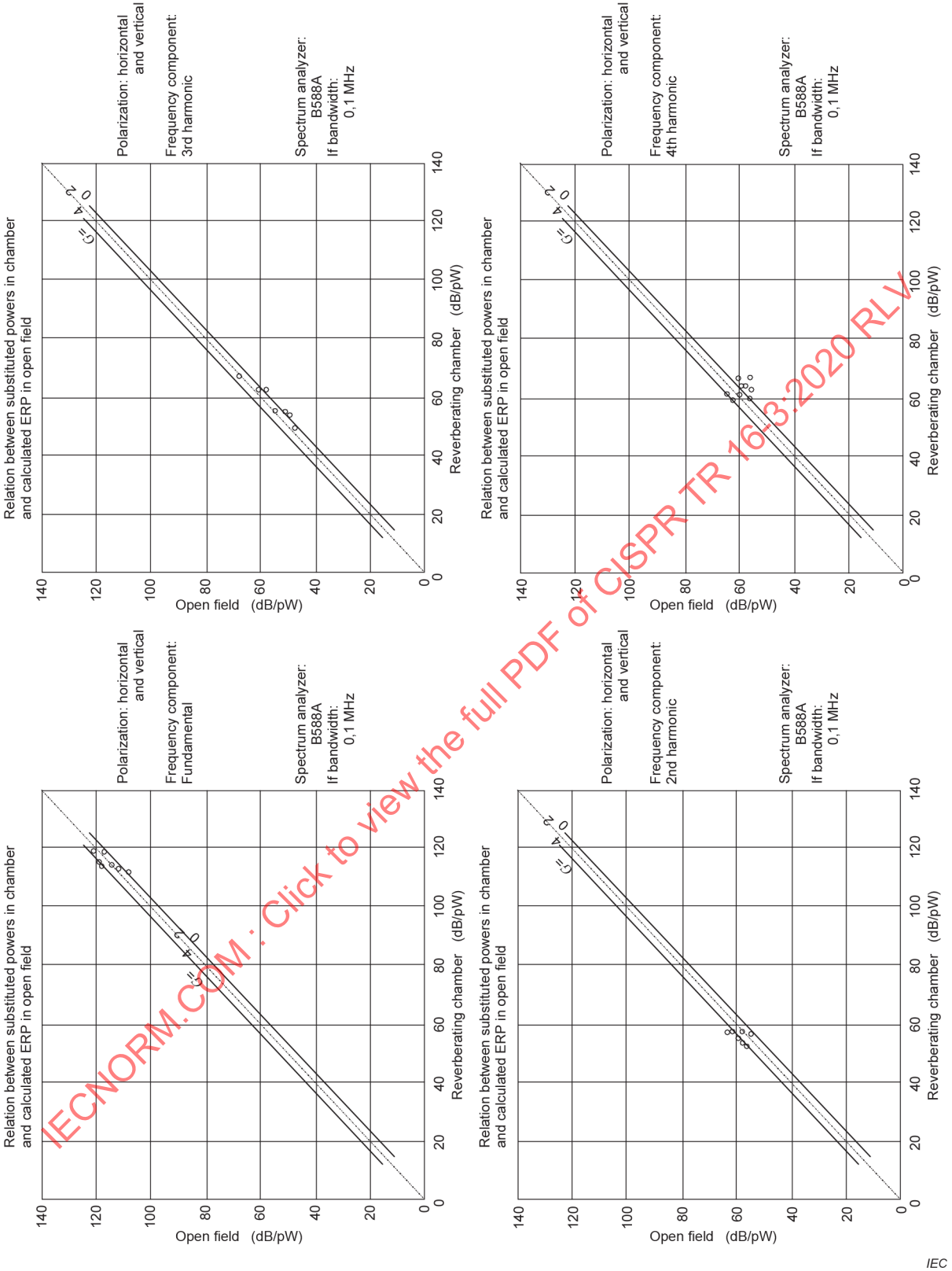
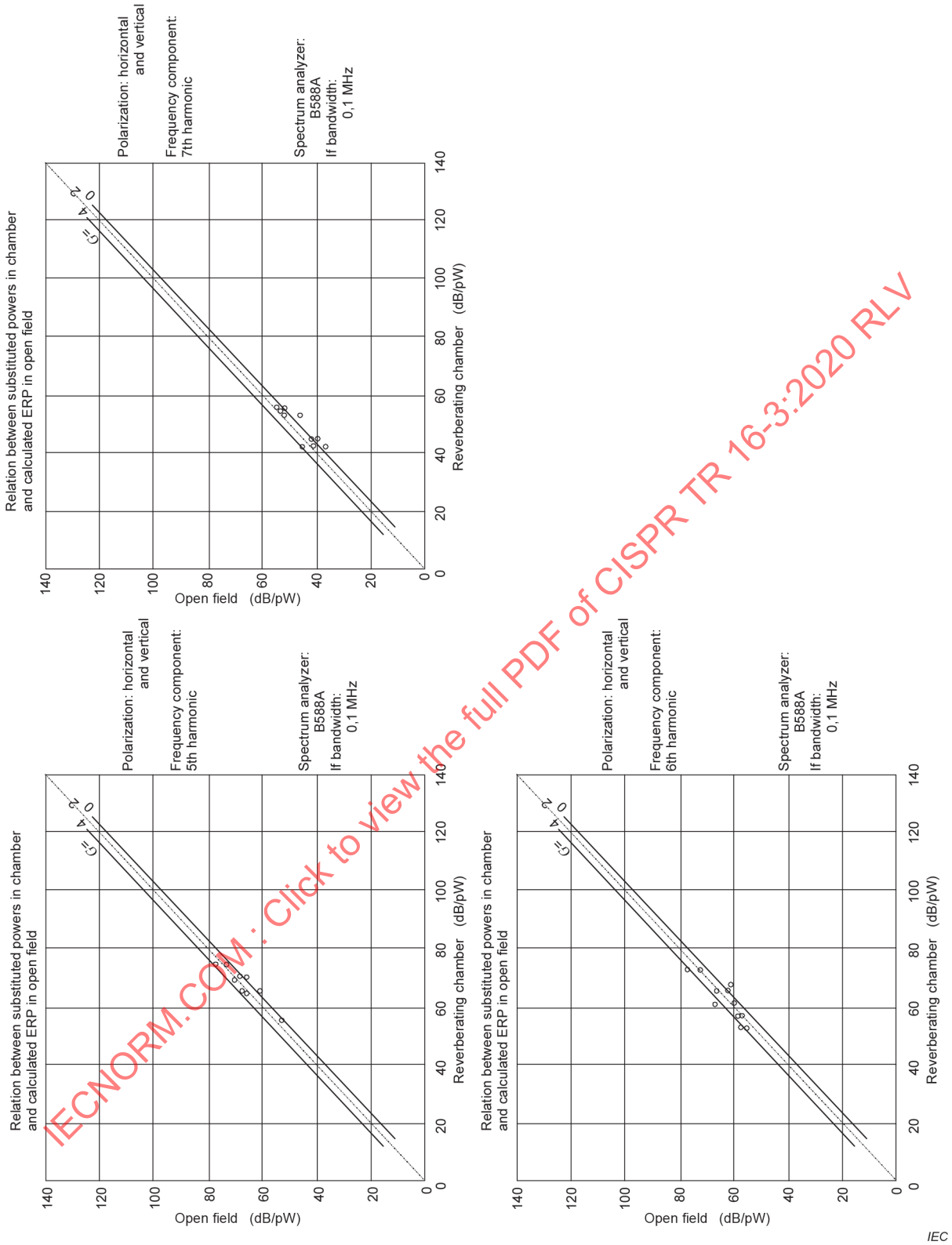



**Figure A.1 – Example plot using the expression** $P_t + G = P_q + 2$

IECNORM.COM : Click to view the full PDF of CISPR TR 16-3:2020 RLV




IECNORM.COM : Click to view the full PDF of CISPR TR 16-3:2020 RLV




IECNORM.COM : Click to view the full PDF of CISPR TR 16-3:2020 RLV

**Figure A.2 – Examples of a number of microwaves measured for $P_q$ and $P_t$**

# Annex B
(informative)

# The field-strength distribution

## B.1 General

Further to 4.4, this annex considers the probability $pr\{H_o \geq T_L\}$ that in a ring-shaped area around a transmitter the outdoor magnetic field strength $H_o$ is equal to or larger than a given field strength $H_L$. The magnetic field strength has been chosen because the experimental data presented in 4.4.2 are based on magnetic-field-strength measurements. At the end of this annex expressions will be given based on the outdoor electric field strength $E_o$, assuming that the far-field condition is fulfilled.

## B.2 $H_o$-field expressions

Recalling the results given in 4.4.2, it is assumed that $H_o$ can be written as

$$H_o = \frac{k\sqrt{P}}{rZ_0} \text{ for } (r \geq R_{min}) \tag{B.1}$$

where

$k$ is a constant;

$r$ is the distance between the transmitter and the point of observation;

$P$ is the transmitter power, and

$Z_0$ the free-space wave impedance.

The condition $r \geq R_{min}$ is needed to indicate that Equation (B.1) is not valid close to the transmitter, i.e. in the near-field region.

Using Equation (B.1), it follows that:

$$pr\{H_o \geq H_L\} = pr\left\{\frac{1}{r} \geq \frac{1}{R_L}\right\} = pr\{r \leq R_L\} \text{ for } (R_L \leq R_{max}) \tag{B.2}$$

where $R_L = (k/P) / (H_L Z_0)$. The latter probability is equal to the area of the ring determined by $R_L$ and $R_{min}$, see Figure B.1, normalized to the area of the total ring, i.e. the ring determined by $R_{min}$ and $R_{max}$. A finite outer boundary $R_{max}$ has to be specified, as an infinitely extended region around the transmitter would create an infinitely large region with field strength zero, thus meaning that $pr\{H_o \geq H_L\}$ would be approaching zero for all values of $H_L$ with $R_L > R_{min}$.

IECNORM.COM : Click to view the full PDF of CISPR TR 16-3:2020 RLV

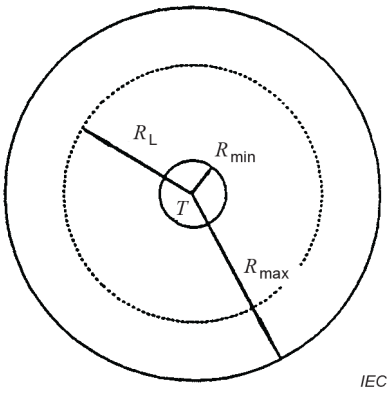



**Figure B.1 – Definition of the ring-shaped area round the transmitter *T***

The probability can now be written as

$$pr\{H_o \geq H_L\} = \frac{\pi\left(R_L^2 - R_{min}^2\right)}{\pi\left(R_{max}^2 - R_{min}^2\right)} = \frac{H_L^{-2} - H_{max}^{-2}}{H_{min}^{-2} - H_{max}^{-2}} \tag{B.3}$$

or as

$$pr\{H_o \geq H_L\} = \frac{\left(H_{max}^2 - H_L^2\right)H_{min}^2}{\left(H_{max}^2 - H_{min}^2\right)H_L^2} \tag{B.4}$$

where $H_{min}$ = $(k/P)$ / $(R_{max}Z_0)$ and $H_{max}$ = $(k/P)/(R_{min}Z_0)$, i.e. $H_{max}$ and $H_{min}$ are the field strength at the inner boundary and the outer boundary of the ring-shaped area. In the case where $H_{max} >> \{H_L, H_{min}\}$ Equation (B.4) reduces to

$$pr\{H_o \geq H_L\} \approx \frac{H_{min}^2}{H_L^2} \tag{B.5}$$

which means that $pr\{H_o \geq H_L\}$ is no longer a function of $H_{max}$. By definition $pr\{H_o \geq H_{max}\} = 0$ and $pr\{H_o \geq H_{min}\} = 1$ so that $H_L$ is not an explicit function of the distance $r$. Consequently, the choice of $H_{min}$ is very important.

In Annex C and Annex D the distribution function $f(H_o)$ has to be known. Because the cumulative distribution $F(H_o) = pr\{H_o \leq H_L\} = 1 - pr\{H_o \geq H_L\}$ and, by definition, $f(H_o)$ is the derivative of $F(H_o)$ with respect to the field strength, the normalized distribution function $f_n(H_o)$ can be calculated using Equation (B.4), yielding

$$f_n(H_o) = \frac{\partial}{\partial H} pr\{H_o \leq H\} = \frac{-2}{H_o^3\left(1/H_{max}^2 - 1/H_{min}^2\right)} = \frac{-C_{ho}}{H_o^3} = -C_{Ho} f(H_o) \tag{B.6}$$

Hence the distribution function $f(H_o)$ = $1/H^3$. The constant of proportionality $C_{Ho}nf_n(H_o) = C_{Ho}f(H_o)$ arose from normalizing $f(H_o)$. The constant $C_{Ho}$ can formally be written as

$$C_{Ho}^{-1} = \int_{H_{min}}^{H_{max}} \frac{dH_o}{H_o^3} \tag{B.7}$$

The relation $f_n(H_o) = -C_{Ho}/H^3$ is applicable in all cases where the field strength varies in inverse proportion to that distance and no specification of the transmitter power $P$ is needed. Of course, $H_o$ is an implicit function of $r$ and $P$.

Finally, $pr\{H_o \geq H_L\}$ can be written formally as

IECNORM.COM : Click to view the full PDF of CISPR TR 16-3:2020 RLV

$$pr\{H_o \geq H_L\} = \frac{\int_{R_L}^{H_{max}} f(H_o)dH_o}{\int_{H_{min}}^{H_{max}} f(H_o)dH_o} \tag{B.8}$$

## B.3 $H_i$ field expressions

For the indoor field $H_i$ no direct model is available as it is for the outdoor field $H_o$. Therefore the distribution $f(H_i)$ has to be derived from $f(H_o)$ and the distribution $f(A_b)$ of the building effect.

Assuming $f(H_o)$ and $f(A_b)$ to be independent, the joint distribution $f(H_o,A_b) = f(H_o)f(A_b)$. The latter distribution represents the distribution of locations where the outdoor field strength equals $H_o$ and, simultaneously, the building effect amounts $A_b$. By carrying out the transformation $H_i = H_o/A_b$ the joint distribution $f(H_i,A_b)$ is known. Since

$$f(H_i, A_b)dH_i = f(A_b)f(H_o)dH_o \quad \text{or} \quad f(H_i, A_b) = \frac{f(H_o)f(A_b)}{dH_i / dH_o} = A_b f(H_o)f(A_b) \tag{B.9}$$

and $f(H_o) = 1/H_o^3$ it follows that

$$pf\{H_i \leq H_L\} = \int_{H_i} dH_i \int_{A_b} dA_b \frac{f(A_b)}{A_b^2 H_i^3} = E[A_b^{-2}] \int_{H_i} \frac{dH_i}{H_i^3} \tag{B.10}$$

where $E[A_b^{-2}]$ is the expectation of $A_b^{-2}$. Using the truncated distribution of $A_b$ with truncation factor $\alpha_{tA}$, see 4.4.2.2 and 4.4.2.3.4, $E[A_b^{-2}]$ is given by

$$E[A_b^{-2}] = \int_{A_{bl}}^{A_{bu}} \frac{f(A_b)dA_b}{A_b^2} = \frac{\alpha_{tA}}{2}\{erf(Z_u) - erf(z_i)\}e^{-2\pi_A + 2\sigma_A^2} \tag{B.11}$$

where $A_{bu}$ and $A_{bl}$ are the upper and lower boundary of the range of experimental $A_b$ data, as explained in 4.4.2.3.4, $\mu_A = M_a \ln(10)/20$ and $\sigma_A = S_a \ln(10)/20$ with $M_A$ and $S_A$ being the average value and the standard deviation of the lognormal distribution of $A_b$. In Equation (B.11) "*erf*" denotes the error function, see Annex E, while $z_u$ and $z_i$ are given by

$$z_u = \frac{\ln(A_{bu}) - \mu_A}{\sigma_A\sqrt{2}} + \sigma_A\sqrt{2}\ ,\ z_i = \frac{\ln(A_{bl}) - \mu_A}{\sigma_A\sqrt{2}} + \sigma_A\sqrt{2} \tag{B.12}$$

By definition $f(H_i)$ is the derivative of $F(H_i)$ with respect to the field strength. Hence, the normalized distribution $f_n(H_i)$ reads

$$f_n(H_i) = \frac{C_{Hi}}{H_i^3} \quad \text{with} \quad C_{Hi}^{-1} = E\left\{A_b^{-2}\right\} \int_{H_{i,min}}^{H_{i,max}} \frac{dH_i}{H_i^3} \tag{B.13}$$

where $H_{i,min} = H_{min}/A_u$ and $H_{i,max} = H_{max}/A_t$ and $H_{min}$ and $H_{max}$ are the minimum and maximum outdoor field strength, respectively.

IECNORM.COM : Click to view the full PDF of CISPR TR 16-3:2020 RLV

## B.4 $E_o$-field expressions

Assuming far-field conditions, the outdoor magnetic field component $H_o$ and the outdoor electric field component $E_o$ have a constant ratio, i.e. $E_o = H_o Z_0$. If $E_{min}$ and $E_{max}$ are the field strength at the inner and outer boundary of the ring-shaped area, the probability that $E_o \geq E_L$ can be written as

$$pr\{E_o \geq E_L\} = \frac{\left(E_{max}^2 - E_L^2\right)E_{min}^2}{\left(E_{max}^2 - E_{min}^2\right)E_L^2} \tag{B.14}$$

In the classification of the field strength carried out in 4.4.3.2, use has been made of Equation (B.9) to determine the boundaries between the field-strength classes. In that application Equation (B.9) was rewritten as

$$E_L = \frac{E_{min}}{\sqrt{pr\{E_o \geq E_L\}\left\{1-(E_{min}/E_{max})^2\right\}+(E_{min}/E_{max})^2}} \approx \frac{E_{min}}{\sqrt{pr\{E_o \geq E_L\}}} \tag{B.15}$$

which follows directly from Equation (B.6), while the approximation is valid in the case where $E_{max} >> \{E_{min}, E_L\}$. In the latter case $E_L$ is independent of $E_{max}$.

Similar to (B.~~1~~13) in the case of $f(H_o)$, the distribution function $f(E_o)$ is given by

$$f_n(E_o) = \frac{-C_E}{E_o^3} = -C_E f(E_o) \quad \text{with} \quad C_E^{-1} = \int_{E_{min}}^{E_{max}} \frac{dE_o}{E_o^3} \tag{B.16}$$

and $pr\{E_o \geq E_L\}$ is given by

$$pr\{E_o \geq E_L\} = \frac{\int_{E_L}^{E_{max}} f(E_o)dE_o}{\int_{E_{min}}^{E_{max}} f(E_o)dE_o} \tag{B.17}$$

The constants $C_{Eo}$ and $C_{Ho}$ are related via $C_{Eo} = C_{Ho} Z_0^2$.

Of course, in a similar way also $f(H_i)$ and $f_n(H_i)$ can be converted into $f(E_i)$ and $f_n(E_i)$.

IECNORM.COM : Click to view the full PDF of CISPR TR 16-3:2020 RLV

# Annex C
(informative)

# The induced asymmetrical open-circuit voltage distribution

## C.1 General

Further to 4.4, in this annex the distribution function $f(U_h)$ of the induced asymmetrical open-circuit voltage $U_h$ is derived by combining the distribution function of the field strength (see Annex B) and that of the $G$ factors or the $L$ factors. After that, the probability $pr\{U_h \geq U_L\}$ that $U_h$ is equal to or larger than a given value $U_L$ is calculated. Results of this calculation have been used in 4.4.3.3.

As in Annex B, it is assumed that the outdoor magnetic field strength $H_o$ can be written as $H_o = (k/P) / rZ_0$) or $E_o = (k/P)/r$, where $k$ is a constant, $P$ the transmitter power, $Z_0$ the free-space wave impedance and $r$ the distance between the transmitter and the point of observation. As in Annex B, it is also assumed that the transmitter causing the field $H_o$ or $E_o$ is in the centre of a ring-shaped area with an inner radius $R_{min}$ and an outer radius $R_{max}$. The field strength as the inner boundary is $H_{max}$ or $E_{max}$, and that at the outer boundary $H_{min}$ or $E_{min}$. The need for these boundaries has been explained in Annex B, where it was also explained that the derivation of the relations will start from the magnetic field strength, i.e. use is made of the $G$ factors defined by $U_h = G_o H$. Electric-field-strength relations using the $L$ factors defined by $U_h = L_E$ will be addressed in Clause B.2.

## C.2 *H*-field-based relations

Assuming the field distribution $f_n(H_o)$ and the $G$ factor distribution $f(G_o)$ to be independent, the joint distribution $f(H_o,G_o)$ $f_n(H_o)f(G_o)$. This joint distribution gives the distribution of the locations where the outdoor field strength equals $H_o$ and, simultaneously, the outdoor $G$ factor equals $G_o$. Then, by carrying out the transformation $U_h = G_o H_o$, the distribution is found of the situations where simultaneously the asymmetrical voltage equals $U_h$ and the $G$ factor equals $G_o$. Since

$$f(U_h)dU_h = f_n(H_o)dH_o \quad \text{or} \quad f(U_h) = \frac{f_n(H_o)}{dU_h / dH_o} = \frac{f_n(H_o)}{G_o} \tag{C.1}$$

it follows that

$$f(U_h, G_o) = \frac{f_n(U_h / G_o) f(G_o)}{G_o} = \frac{C_{Ho} G_o^2 f(G_o)}{U_h^3} \tag{C.2}$$

where the right-hand part of this equation is valid if the distribution derived in Annex B is used, i.e. when it is assumed that $f_n(H_o) = C_{Ho} / H_o^3$, see Equation (B.6). If $f(G_i)$ is used, the building effect $A_b$ has to be taken into account and, hence, $f_n(H_i)$ should be used as discussed in B.2.

By integrating the joint distribution over the permissible ranges of $U_h$ and $G_o$, the probability $pr\{U_h \geq U_L\}$ can be calculated from

$$pr\{U_h \geq U_L\} = \int_{U_h} dU \int_{G_o} dG \frac{C_{Ho} G_o^2 f(G_o)}{U_h^3} = \frac{C_{Ho}}{2} \int_{G_o} \left\{ \frac{G_o^2}{U_{h1}^2} - \frac{G_o^2}{U_{h2}^2} \right\} f(G_o) dG \tag{C.3}$$

where $U_{h1}$ and $U_{h2}$ are relevant boundaries. To find the relevant ranges and boundaries of $U_h$ and $G$, consider Figure C.1 showing the $U_h$-$G$ plane. As the field strength ranges between $H_{min}$ and $H_{max}$ the voltage satisfies the relation $H_{min}G \leq U_h \leq H_{max}G$. Using a truncated lognormal distribution of the $G$ factors (see 4.4.2.3.2), we have $G_L \leq G \leq G_u$.

IECNORM.COM : Click to view the full PDF of CISPR TR 16-3:2020 RLV

If $U_L$ has the value indicated in Figure C.1, $pr\{U_h \geq U_L\}$ is found by integrating the joint distribution over the range of $U_h$ and $G$ values indicated by the shaded area in Figure C.1. From that figure it will be clear that $U_L$ can only have values between $U_a = H_{min}G_L$ and $U_d = H_{max}G_U$. The voltages $U_b$ and $U_c$ are defined by $U_b = H_{max}G_L$ and $U_c = H_{min}G_U$, respectively.

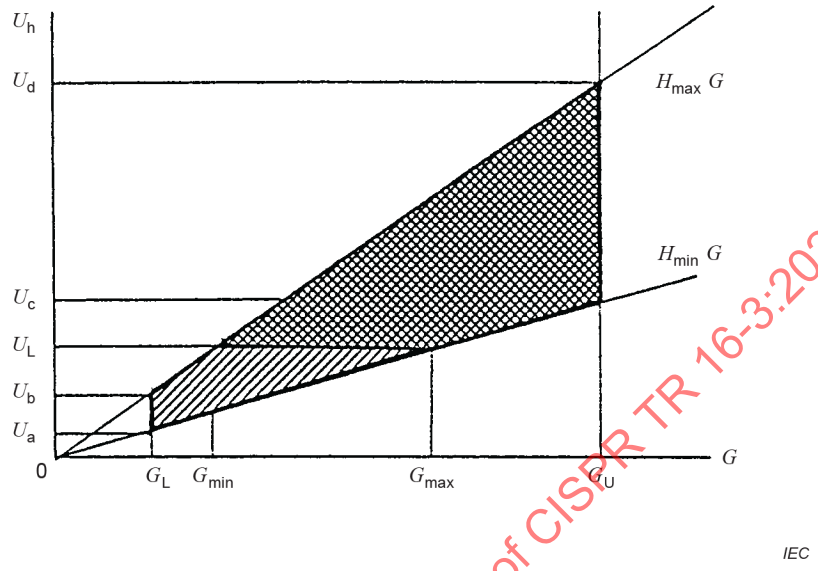



**Figure C.1 – The permissible ranges of $U_h$ and $G$ are within the polygon $\{G_L,U_a\}$, $\{G_L,U_b\}$, $\{G_U,U_d\}$, $\{G_l,U_c\}$ and $\{G_L,U_a\}$. For the given value $U_L$ the double-shaded area represents $pr\{U_h \geq U_L\}$**

After straightforward calculations it follows from Equation (C.3) that $pr\{U_h,U_L\}$ is given by

$$pr\{I_h \geq U_L\} = \frac{\alpha_{tG}C_{Ho}}{4}\left\{\delta_U \frac{erf(x_u)-erf(x_i)}{H_{min}^2} - \frac{erf(y_i)-erf(y_i)}{H_{max}^2} + e^{2\mu_G+2\sigma_G^2}\frac{erf(z_u)-erf(z_i)}{U_L^2}\right\} \quad \text{(C.4)}$$

where $\mu_G = M_G \times \ln(10)/20$ and $\sigma_G = S_G \times \ln(10)/20$, $M_G$ and $S_G$ being the average value and the standard deviation of the relevant truncated lognormal $G$ factor distribution with truncation factor $\alpha_{tG}$. The variables $x_u$ and $x_i$ are given in Equation (C.5), while $y_u$, $y_i$, $z_u$, $z_i$ and $\delta$, which depend on the value of $U_L$, are given by Equations (C.6) through (C.11).

$$x_u = \frac{\ln(G_u)-\mu_G}{\sigma_G\sqrt{2}},\quad x_i = \frac{\ln(U_L/H_{min})-\mu_G}{\sigma_G\sqrt{2}} \quad \text{(C.5)}$$

a) $U_a \leq U_L < U_b$: $\delta_U = 1$,

$$y_u = \frac{\ln(G_u)-\mu_G}{\sigma_G\sqrt{2}},\quad y_i = \frac{\ln(G_L)-\mu_G}{\sigma_G\sqrt{2}} \quad \text{(C.6)}$$

$$z_u = \frac{\ln(U_L/H_{min})-\mu_G-2\sigma_G^2}{\sigma_G\sqrt{2}},\quad z_l = \frac{\ln(G_L)-\mu_G-2\sigma_G^2}{\sigma_G\sqrt{2}} \quad \text{(C.7)}$$

b) $U_b \leq U_L < U_c$: $\delta_U = 1$

$$y_u = \frac{\ln(G_U)-\mu_G}{\sigma_G\sqrt{2}},\quad y_i = \frac{\ln(U_L/H_{max})-\mu_G}{\sigma_G\sqrt{2}} \quad \text{(C.8)}$$

IECNORM.COM : Click to view the full PDF of CISPR TR 16-3:2020 RLV

$$z_{\mathrm{u}} = \frac{\ln(U_{\mathrm{L}} / H_{\mathrm{min}}) - \mu_G - 2\sigma_G^2}{\sigma_G\sqrt{2}}, \quad z_{\mathrm{i}} = \frac{\ln(U_{\mathrm{L}} / H_{\mathrm{max}}) - \mu_G - 2\sigma_G^2}{\sigma_G\sqrt{2}} \tag{C.9}$$

c) $U_{\mathrm{c}} \leq U_{\mathrm{L}} < U_{\mathrm{d}}$: $\delta_U = 0$

$$y_{\mathrm{u}} = \frac{\ln(G_U) - \mu_G}{\sigma_G\sqrt{2}}, \quad y_{\mathrm{i}} = \frac{\ln(U_{\mathrm{L}} / H_{\mathrm{max}}) - \mu_G}{\sigma_G\sqrt{2}} \tag{C.10}$$

$$z_{\mathrm{u}} = \frac{\ln(G_U) - \mu_G - 2\sigma_G^2}{\sigma_G\sqrt{2}}, \quad z_{\mathrm{i}} = \frac{\ln(U_{\mathrm{L}} / H_{\mathrm{max}}) - \mu_G - 2\sigma_G^2}{\sigma_G\sqrt{2}} \tag{C.11}$$

In the case where the $G_{\mathrm{i}}$ factors are used, Equation (C.4) is applicable provided that $C_{Ho}$ is replaced by $E\left[A_{\mathrm{b}}^{-2}\right]C_{Hi}$, and $H_{\mathrm{min}}$ and $H_{\mathrm{max}}$ by $H_{\mathrm{i,min}}$ and $H_{\mathrm{i,max}}$, respectively (see B.3).

Equations (C.4) to (C.11) have been used to calculate the data summarized in Table 10 and to calculate the results displayed in Figure 16 and Figure 17.

## C.3 *E*-field-based relations

Assuming far-field conditions the outdoor electric field strength may be used to calculate $pr\{U_{\mathrm{h}} \geq U_{\mathrm{L}}\}$ in connection with the $L_{\mathrm{o}}$ factors, see 4.4.2.3.3. In that case Equations (C.4) to (C.11) can be used, provided that $C_{Ho}$ is replaced by $C_{Eo}$, $H_{\mathrm{max}}$ by $E_{\mathrm{max}}$, $H_{\mathrm{min}}$ by $E_{\mathrm{min}}$, $G_{\mathrm{o}}$ by $L_{\mathrm{o}}$, and $M_G$ and $S_G$ by $M_{\mathrm{L}}$ and $S_{\mathrm{L}}$. In other words, Equations (C.4) to (C.11) can be used, provided that all magnetic-field-related quantities are replaced by the corresponding electric-field quantities.

Similar remarks are valid in the case where $L_{\mathrm{i}}$ factors are to be used, but see NOTE 3 at the end of 4.4.4.2.

IECNORM.COM : Click to view the full PDF of CISPR TR 16-3:2020 RLV

# Annex D
(informative)

# The outlet-voltage distribution

## D.1 General

This annex considers the number of outlets $N_o(U_h \geq U_L)$ showing an induced open-circuit voltage $U_h$ equal to or larger than a given voltage $U_L$. This quantity is derived in a number of steps. First, the probability density $n(H_o)$ giving the density of outlets experiencing a certain field strength $H_o$ is considered. Use will be made of the simple models with the ring-shaped area (RSA) already discussed in Annex B and Annex C, and of the $G_o$ factors, which give $U_h$ normalized to the magnetic field strength. After that it is possible to calculate the joint distribution $n(H_o,G_o)$ along the lines described in Annex C, and $N_o(U_h \geq U_L)$ follows after integration of the joint distribution factor over the permissible values of the parameters concerned. When using the $G_i$ factors in combination with the building effect $A_b$ the same procedure can be followed as in Annex C.

## D.2 *H*-field-based relations

Assuming a homogeneous density of $\mu$ outlets per square metre around the transmitter in question, the number $dn(r)$ of outlets in an elementary ring-shaped area between $r$ and $r + dr$ is given by

$$dn(r) = \mu 2\pi r dr \tag{D.1}$$

Using $H_o = (k/P)/(rZ_0)$ (see Annex B), it follows from Equation (D.1) that the number of outlets $dn(H_o)$ in the area determined by the field-strength range $H_o(r)$ to $H_o(r + dr)$, is given by

$$dn(H_o) = 2\pi\mu \frac{k^2 P}{H_o^3 Z_0^2} dH_o \tag{D.2}$$

In the case of $N$ transmitters, where the $j$-th transmitter is characterized by $\{k_j,P_j\}$ and the density of outlets around that transmitter is $\mu_j$, $dn(H_o)$ can be written as

$$dn(H_o) = \sum_{j=1}^{N} 2\pi\mu_j \frac{k_j^2 P_j}{Z_0^2} \frac{d_{Ho}}{H_o^3} = \frac{d_{Ho}}{Z_0^2 H_o^3} = \sum_{j=1}^{N} 2\pi\mu_j k_j^2 P_j = \frac{C_{Ho}}{H_o^3} dH_o \tag{D.3}$$

Hence, in this model the normalized distribution $n(H_o)$ is given by

$$n(H_o) = \frac{dn(H_o)}{dH_o} = \frac{C_{Ho}}{H_o^3} \tag{D.4}$$

$$\text{with } C_{Ho} = \frac{2\pi}{Z_o^2} \sum_{j=1}^{N} \mu_j k_j^2 P_j \tag{D.5}$$

As had to be expected, the distribution $n(H_o)$ is equal to $f_n(H_o)$ discussed in Annex B.

If $N_T$ is the total number of outlets in the RSA and if $H_{max}$ and $H_{min}$ determine the boundaries of that RSA, the following relation has to be satisfied

$$N_T = \int_{H_{min}}^{H_{max}} n(H) dH \tag{D.6}$$

or, after substitution of Equation (D.4):

IECNORM.COM : Click to view the full PDF of CISPR TR 16-3:2020 RLV

$$N_T = \frac{C_{Ho}}{2}\left\{\frac{1}{H_{min}^2} - \frac{1}{H_{max}^2}\right\} \quad (D.7)$$

If the connection between $N_T$ and $C_{Ho}$ is made via Equations (D.4) and (D.5), the expression for the number of outlets $N_o(H_u \geq U_L)$ showing an induced open-circuit voltage $U_h \geq U_L$ is identical to that for $pr\{U_h \geq U_L\}$ as derived in Annex C, Equation (C.4). So $N_o(U_h \geq U_L)$ reads

$$N_o\{U_h \geq U_L\} = \frac{\alpha_{tG} C_{Ho}}{4}\left\{\delta_U \frac{erf(x_u) - erf(x_l)}{H_{min}^2} - \frac{erf(y_u) - erf(Y_l)}{H_{max}^2} + e^{2\mu_G + 2\sigma_G^2} \frac{erf(z_u) - erf(z_l)}{U_L^2}\right\} \quad (D.8)$$

The parameters needed in Equation (D.6) have been explained in Equations (C.4) to (C.11). In Annex C it has also been explained how to change Equation (D.6) to make a calculation using $G_i$ factors possible.

When it is assumed that $N_T$ is known and $H_{max}$ has been chosen there remain two "unknowns" in Equation (D.7): $C_{Ho}$ and $H_{min}$. If $C_{Ho}$ is calculated for a certain geographical region from Equation (D.5), then $H_{min}$ is known, so that all parameters in Equation (D.8) are known. As discussed in 4.4.4, another possibility is to determine $H_{min}$ in that region and $C_{Ho}$ can be calculated by using Equation (D.7).

## D.3 *E*-field-based relations

Assuming far-field conditions, the outdoor electric field strength together with the $L$ factors may be used to calculate $N_o\{U_h \geq U_L\}$. In that case Equation (D.8) can be used, provided that $C_{Ho}$ is replaced by $C_{Eo}$, $H_{max}$ by $E_{max}$, $H_{min}$ by $E_{min}$, $G_o$ by $L_o$ and $M_G$ and $S_G$ by $M_L$ and $S_L$. In other words Equation (D.8) can be used, provided that all magnetic-field-related quantities are replaced by the corresponding electric-field quantities.

If $E_o = (k/P)/r$ the equivalent of Equations (D.4) and (D.5) read

$$n(E) = \frac{dN(E)}{dE} = -\frac{C_{Eo}}{E^3} \quad (D.9)$$

$$\text{with } C_{Eo} = 2\pi \sum_{j=1}^{N} \mu_j k_j^2 P_j \quad (D.10)$$

and the equivalent of Equation (D.4) reads

$$N_T = \frac{C_{Eo}}{2}\left\{\frac{1}{E_{min}^2} - \frac{1}{E_{max}^2}\right\} \quad (D.11)$$

See Annex C about how to change the various relations to make calculations using $L_i$ factors possible.

IECNORM.COM : Click to view the full PDF of CISPR TR 16-3:2020 RLV

# Annex E
(informative)

# Some mathematical relations

## E.1 General

Further to 4.4, in this annex a number of mathematical relations involving the so-called Error Function, as used in Annexes C and D, are summarized. In E.2 a series expansion of the error function is also given which is sufficiently accurate to be used in computer calculations based on the analytical expressions presented in Annexes C and D. Subclause E.3 summarizes some mathematical relations involving the lognormal distribution and the error function. Refer also to [66] and [67].

## E.2 The error function

By definition $erf(x)$, the error function of $x$, is given by Equation (E.1)

$$erf(x) = \frac{2}{\sqrt{\pi}} \int_0^x e^{-\alpha^2} d\alpha \tag{E.1}$$

The error function has the following properties

$$erf(0) = 0 \tag{E.2}$$

$$erf(\infty) = 1 \tag{E.3}$$

$$erf(-x) = erf(x) \tag{E.4}$$

A useful series expansion of $erf(x)$ is the following Equation (E.5)

$$erf(s) = 1 - \left(a_1 t + a_2 t^2 + a_3 t^3 + a_4 t^4 + a_5 t^5\right) e^{-x^2} + \varepsilon(x) \tag{E.5}$$

$$t = \frac{1}{1 + px}, |\varepsilon(x)| \leq 1{,}5 \times 10^{-7} \tag{E.6}$$

where

$p$ = 0,284 496 736

$a_1$ = 0,254 829 592

$a_2$ = 0,284 496 736

$a_3$ = 1,421 413 741

$a_4$ = –1,453 152 027

$a_5$ = 1,061 405 429

IECNORM.COM : Click to view the full PDF of CISPR TR 16-3:2020 RLV

## E.3 Application to the lognormal distribution

A quantity $x$ has a lognormal distribution when the logarithm of $x$ has a normal distribution. In mathematical form the lognormal distribution of $x$ reads

$$f(x)dx = \frac{1}{x\sigma\sqrt{2\pi}}\,\mathrm{e}^{-(\ln(x)-\mu)^2/2\sigma^2}\,dx \tag{E.7}$$

where $\mu$ is the average value of $\ln(x)$ and $\sigma$ the associated standard deviation. If the latter parameters are known in dB and $M$(dB...) is the average value and $S$(dB) is the associated standard deviation, $\mu = M \times \ln(10)/20$ and $\sigma = S \times \ln(10)/20$. The distribution function given in Equation (E.7) has the property that the integral of this function over all values of $x$ = 1 if $-\infty \le x \le \infty$. This means that $f(x)$ given in Equation (E.7) is properly normalized. If $f_t(x)$ is the truncated lognormal distribution of $x$, such that $x_l \le x \le x_u$, the distribution has to be normalized again. In that case $f_t(x)$ can formally be written as $f_t(x) = \alpha_t \times f(x)$ with

$$\alpha_t^{-1} = \int_{x_l}^{x_u} \frac{1}{x\sigma\sqrt{2\pi}}\,\mathrm{e}^{-(\ln(x)-\mu)^2/2\sigma^2}\,dx = \frac{1}{\sqrt{\pi}}\int_{-\infty}^{y_u} e^{-y^2}\,dy - \frac{1}{\sqrt{\pi}}\int_{-\infty}^{y_l} e^{-y^2}\,dy \tag{E.8}$$

so that

$$\alpha_t = \frac{erf(y_u) - erf(y_l)}{2} \tag{E.9}$$

where

$$y = \frac{\ln(x)-\mu}{\sigma\sqrt{2}} \tag{E.10}$$

$$y_u = \frac{\ln(x_u)-\mu}{\sigma\sqrt{2}} \tag{E.11}$$

$$y_l = \frac{\ln(x_l)-\mu}{\sigma\sqrt{2}} \tag{E.12}$$

When carrying out the integrations in Annex C, use has been made of the following integral solutions, which can easily be verified using the above relations.

In the case of Equation (C.4) leading to Equation (C.8), use was made of

$$\int_{x_l}^{x_u} x^2 f_t(x)dx = \alpha_t \frac{\mathrm{e}^{2\mu+2\sigma^2}}{2}\{erf(z_u) - erf(z_l)\} \tag{E.13}$$

where

$$z_u = y_u - \sigma\sqrt{2} \quad \text{and} \quad z_l = y_l - \sigma\sqrt{2} \tag{E.14}$$

and in the derivation of Equation (C.5) use was made of

$$\int_{x_l}^{x_u} x^{-2} f_t(x)dx = \alpha_t \frac{e^{-2\mu+2\sigma^2}}{2}\{erf(z_u) - erf(z_l)\} \tag{E.15}$$

where

$$z_u = y_u + \sigma\sqrt{2} \quad \text{and} \quad z_l = y_l + \sigma\sqrt{2} \tag{E.16}$$

IECNORM.COM : Click to view the full PDF of CISPR TR 16-3:2020 RLV

# Annex F
(informative)

## Harmonic fields radiated at elevated angles from 27 MHz ISM equipment over real ground

Further to 4.5, a close match can be achieved between vertical radiation patterns calculated for simple electrically small electric dipoles and loops over real ground and the vertical radiation patterns created by real ISM equipment. This can be shown using airborne data, measured by Ohio University, of the harmonic field strengths from four different 27 MHz ISM machines positioned at ground level on an earthen open field site [33]. Each ISM machine was a RF plastics sealer, identified by a letter symbol A, B, C or D. Fundamental operating powers ranged from 2 kW to 27 kW. In [34], the horizontally polarized fourth harmonic field-strength data at approximately 109 MHz, collected by an aircraft flying at constant height and varying slant range, were converted to field strengths in vertical polar radiation patterns at a constant radial distance of 300 m, at elevation angles varying from approximately 4° up to 90°. The resultant far-field vertical radiation patterns were then compared with vertical radiation patterns calculated at the same distance from small electric dipoles and loops over real ground. The objective was to meet a tolerance of fit that was arbitrarily chosen as ±10 dB. The comparisons show that the vertical radiation patterns of harmonic radiation from ISM equipment, at 109 MHz in the aeronautical ILS localizer band, closely resemble the patterns calculated for simple dipoles and loops.

The in-flight field strength data gathered at varying slant distances from the ISM equipment were converted to vertical radiation patterns using the simple inverse distance law of attenuation in Equation (F.1)

$$E_{300} = E_d + 20\log\left(\frac{d_s}{300}\right) \quad \text{(F.1)}$$

where

$E_d$ is the field strength measured at the aircraft at a particular elevation angle, in dB(μV/m);

$d_s$ is the slant distance to the aircraft at that elevation angle, in m; and

$E_{300}$ is the calculated field strength at 300 m radial distance at the same elevation angle, in dB(μV/m).

The values of $E_{300}$ have been plotted against elevation angle to create two vertical radiation patterns for each flight. One vertical radiation pattern has been created for that part of the flight which took place to the south of the ISM device and another for that part of the flight which took place to the north of the ISM device. Each pattern therefore extends up to an elevation angle of 90°, which locates the common field point between the two patterns.

Sommerfeld-Norton surface wave contributions to the horizontally polarized fields at very low elevation angles have also been considered inasmuch as their presence might have complicated the adjustment with distance of the measured field strengths at those low angles. Surface waves at frequencies above 30 MHz have been studied in [40]. In [40] it is shown that at the distances and heights over ground at which the in-flight data were gathered, the contributions of surface waves are insignificant.

Figure F.1 illustrates vertical patterns of horizontally polarized fourth harmonic radiation from ISM Machine A (a 25 kW RF plastic sealer) with its RF shields removed, calculated from the data in [33] using Equation (F.1) and shown as solid line curves, compared with vertical patterns of horizontally polarized radiation calculated at 109 MHz for two electrically small horizontal electric dipoles (dashed curves). The in-flight field strength data were obtained at a flight altitude of 152 m (500 feet) and plotted in Figure A.4, page 54 of [33].

IECNORM.COM : Click to view the full PDF of CISPR TR 16-3:2020 RLV

The sharp step in the field strength from Machine A close to the elevation angle of 5° in Figure F.1 b) corresponds with the switch-on of the ISM equipment. Note that, to match the patterns of the fields measured to the south of the ISM equipment, the dipole current moment $I.dl$, the dipole height above ground, and the radiated power required from the small electric dipole, are all different from those required to match the fields measured to the north.

Figure F.2 uses in-flight data for ISM Machine B operated with RF shields in place, collected at an altitude of 152 m. In Figure F.2 b) the noise floor of the measurements is visible in the solid curve for elevation angles between 12° and 20°. Switch-on of the ISM equipment occurred near the elevation angle of 20°. Note that the horizontally polarized vertical field patterns created broadside to two electrically small vertical loops were used to provide the matching patterns in Figure F.2. The dipole moments required were the same, but the source height and therefore the radiated power required to match the patterns to the north were different from those required to match the patterns to the south.

Figure F.3 compares the radiation at 109 MHz emitted from Machine C (a 3 kW RF plastics sealer), derived from in-flight data measured at an altitude of 152 m, with the calculated horizontally polarized field patterns for two small horizontal electric dipoles. Machine C was operated with its RF shields in place. The sharp step in the Machine C field strength close to the elevation angle of 20° in Figure F.3 b) corresponds with the switch-on of the ISM equipment. The match in Figure F.3 a) was obtained with a small horizontal electric dipole at a height of 2,7 m, slightly higher than the 2 m maximum source height considered elsewhere in this annex.

Examples of pattern matching for ISM Machine D (a 2 kW RF plastic sealer), with its RF shields in place, are shown in Figure F.4. In this example the horizontally polarized fields emitted broadside from two small vertical loops were used to provide the matching patterns. The match in Figure F.4 a) was obtained using an electrically small vertical loop at a centre height of 0,85 m, slightly lower than the 1 m minimum source height considered elsewhere in this paper. Switch-off of the ISM equipment is shown by the field strength step near the elevation angle of 5° in Figure F.4 a).

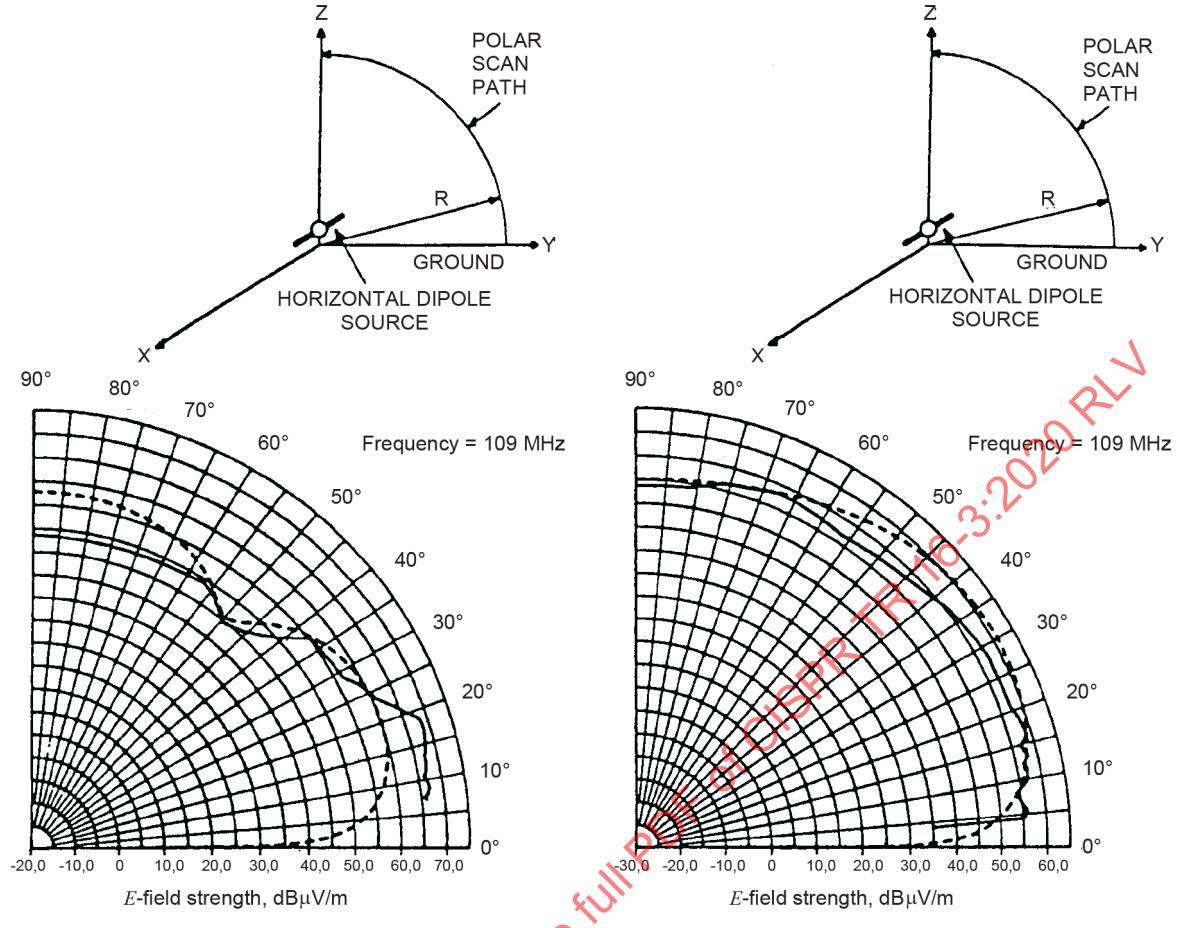
The figures all show how variable the field strengths of the disturbances radiated from ISM equipment can be during short periods of time. Each data gathering flight took place at an air speed of approximately 135 knots [34], from north to south over the ISM equipment. Only one ISM equipment operating cycle of approximately 1 min duration occurred during each flight.

However, after examination of the vertical radiation patterns, it can be concluded – in spite of the field strength fluctuations – that the horizontally polarized field distribution encountered by an aircraft at elevated angles, during any single flight pass over the ISM equipment, can be reasonably well matched (within ≈ ±10 dB) with field distributions created at elevated angles by simple electric or magnetic dipole sources. Given the relatively good match of the simple model patterns with the measured fields at angles above about 4°, and the boundary conditions which reduce the strength of the horizontally polarized fields near the ground, the patterns of the fields of the simple models calculated near the ground will be similar to the patterns of the real fields if they were measured at elevation angles below 4° (see [40]). These results support the belief that the predictability of far field radiation emitted at elevated angles by ISM equipment *in situ* can be judged by considering the vertical patterns of radiation emitted by simple electric and magnetic dipoles near the ground.

Moreover, there seems to be no obvious reason why vertically polarized fields emitted by typical ISM equipment should behave differently from the vertically polarized fields emitted over ground by small dipoles. Such small dipole models should also serve to indicate the predictability of vertically polarized fields.

More detailed studies of the measurements reported by the Avionics Engineering Center at Ohio University [33], and many more examples of matching the measured data with vertical patterns calculated for electrically small electric or magnetic dipole sources, have been described in [34]. Figure F.1 to Figure F.4 are adapted from figures in [34].

IECNORM.COM : Click to view the full PDF of CISPR TR 16-3:2020 RLV




a) Flight data measured south of the ISM equipment.

b) Flight data measured north of the ISM equipment.

IEC

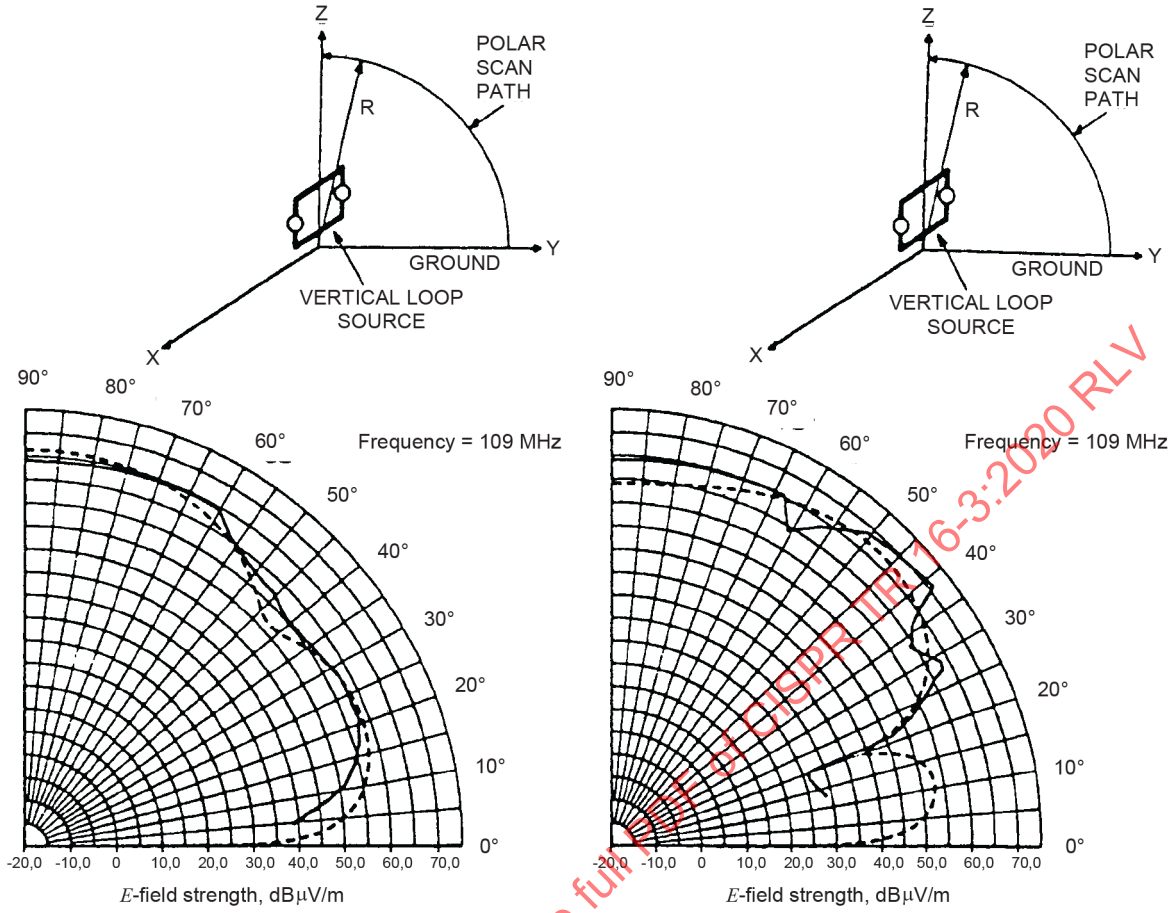
Solid curves: Machine A (fundamental RF power 25 kW), 180° azimuth, flight altitude 152 m, RF shields removed, derived from in-flight field strength data in Figure A-4 at page 54 in [33].

a) Dashed curve: Source = horizontal electric dipole, centre height above ground 1,8 m, dipole (current) moment $I.dl \approx 2{,}51$ mA·m, radiated power ≈ 704 μW.

b) Dashed curve Source = horizontal electric dipole, centre height above ground 1,3 m, dipole (current) moment $I.dl \approx 2{,}82$ mA·m, radiated power ≈ 996 μW.

**Figure F.1 – Vertical radiation patterns of horizontally polarized fields, 109 MHz, 300 m scan radius (adapted from [34])**

IECNORM.COM : Click to view the full PDF of CISPR TR 16-3:2020 RLV




a) Flight data measured south of the ISM equipment.

b) Flight data measured north of the ISM equipment.

IEC

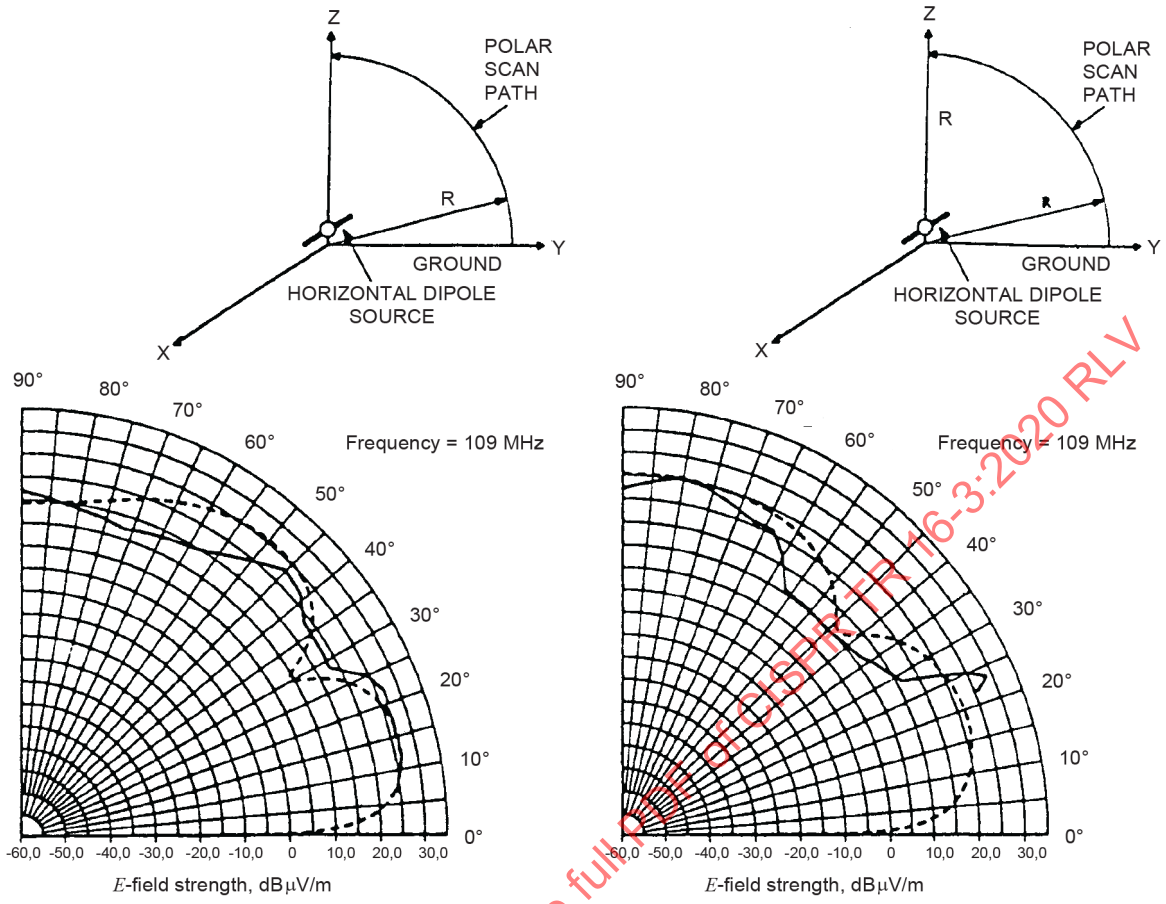
Solid curves: Machine B (fundamental RF power 2 kW), 0° azimuth, flight altitude 152 m, RF shields in place, derived from in-flight field strength data in Figure A.11 at page 62 in [33].

a) Dashed curve: Source = small vertical loop, centre height above ground 1 m, dipole moment $I.dA \approx$ 3,6 mA·m$^2$, radiated power ≈ 6,56 mW.

b) Dashed curve Source = small vertical loop, centre height above ground 2 m, dipole moment $I.dA \approx$ 3,6 mA·m$^2$, radiated power ≈ 8,33 mW.

**Figure F.2 – Vertical radiation patterns of horizontally polarized fields, 109 MHz, 300 m scan radius (adapted from [34])**

IECNORM.COM : Click to view the full PDF of CISPR TR 16-3:2020 RLV




a) Flight data measured south of the ISM equipment.

b) Flight data measured north of the ISM equipment.

*IEC*

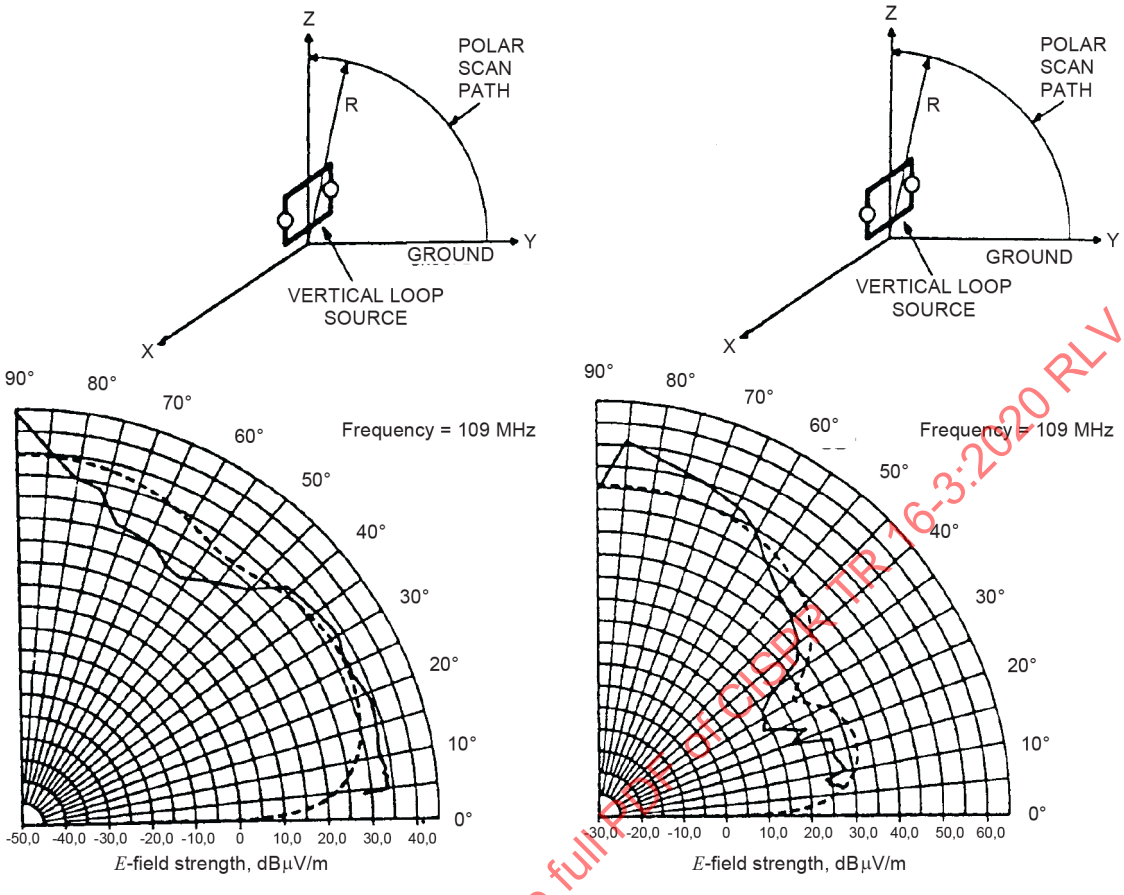
Solid curves: Machine C (fundamental RF power 3 kW), 20° azimuth, flight altitude 152 m, RF shields in place, derived from in-flight field strength data in Figure A-13 at page 65 in [33].

a) Dashed curve: Source = horizontal electric dipole, centre height above ground 2,7 m, dipole (current) moment $I.dl \approx 50{,}1$ μA·m, radiated power ≈ 0,31 μW.

b) Dashed curve Source = horizontal electric dipole, centre height above ground 2 m, dipole (current) moment $I.dl \approx 28{,}2$ μA·m, radiated power ≈ 0,096 μW.

**Figure F.3 – Vertical radiation patterns of horizontally polarized fields, 109 MHz, 300 m scan radius (adapted from [34])**

IECNORM.COM : Click to view the full PDF of CISPR TR 16-3:2020 RLV




a) Flight data measured south of the ISM equipment.

b) Flight data measured north of the ISM equipment.

Solid curves: Machine D (fundamental RF power 2 kW), 20° azimuth, flight altitude 152 m, RF shields in place, derived from in-flight field strength data in Figure A-19 at page 72 in [33].

a) Dashed curve: Source = small vertical loop, centre height above ground 0,85 m, dipole moment $I.dA \approx$ 0,14 mA·m$^2$, radiated power ≈ 10,4 μW.

b) Dashed curve Source = small vertical loop, centre height above ground 2 m, dipole moment $I.dA \approx$ 0,23 mA·m$^2$, radiated power ≈ 42,0 μW.

**Figure F.4 – Vertical radiation patterns of horizontally polarized fields, 109 MHz, 300 m scan radius (adapted from [34])**

IECNORM.COM : Click to view the full PDF of CISPR TR 16-3:2020 RLV

# Annex G
(informative)

# Models and equations associated with the LLAS method

## G.1 General

In connection with 4.13, this annex describes the models and equations of the Large Loop Antenna System (LLAS) that are needed to determine the reference validation factor curves given in CISPR 16-1-4:2019, CISPR 16-1-4:2019/AMD1:2020 and CISPR 16-1-4:2019/AMD2:20— [102].

Also, G.4 of this annex gives the models and equations for calculating the conversion factors of the magnetic field strength from the current measured by an LLAS for a certain EUT at specified distances; see CISPR 16-1-4:2019, CISPR 16-1-4:2019/AMD1:2020 and CISPR 16-1-4:2019/AMD2:20— [102].

Finally, the justification for changing the LLAS validation criterion from ±2 dB to ±3 dB is given in G.5.

## G.2 Response of an LAS to a magnetic field dipole

### G.2.1 Magnetic field strength model of a disturbance source

Equipment under test (EUT) that contains a magnetic field disturbance source is represented by a circular loop with radius $R$ (diameter $D = 2R$) that carries a sinusoidal varying current $I$ (frequency $\nu$). See Figure G.1.

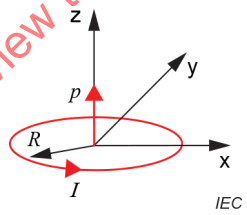



**Figure G.1 – Geometry and coordination system for a single magnetic field dipole**

The magnetic field strength disturbance source can be represented by its magnetic field dipole moment $p$ as follows:

$$p = S \times I = \pi R^2 I \quad \text{(in Am}^2\text{)} \tag{G.1}$$

where

$S$ is the surface area of the disturbance loop of the EUT (in m$^2$);

$I$ is the disturbance current through loop of the EUT (in A).

IECNORM.COM : Click to view the full PDF of CISPR TR 16-3:2020 RLV

### G.2.2 Response of an LAS to a magnetic field dipole

#### G.2.2.1 Relation of LLA current and EUT current using the transformer model

The configuration of an EUT in the center of an LLA is depicted in Figure G.2. The detailed specification of the LLA and its coaxial cable construction with the two opposite slits and the current probe are given in CISPR 16-1-4. The magnetic field strength disturbance source of the EUT is represented by its magnetic field dipole moment $p_{EUT}$; see Equation (G.1). In the remainder of this annex it is assumed that the loop of the disturbance source of the EUT and the LLA are coaxially positioned in the same plane. The current measured in an LLA is proportional with the magnetic field dipole moment of an EUT. Theoretical details are given in the paper of Bergervoet and Van Veen [103]. Also papers of McLean et al [112][113], give the models and equations of the LLAS measurement method.

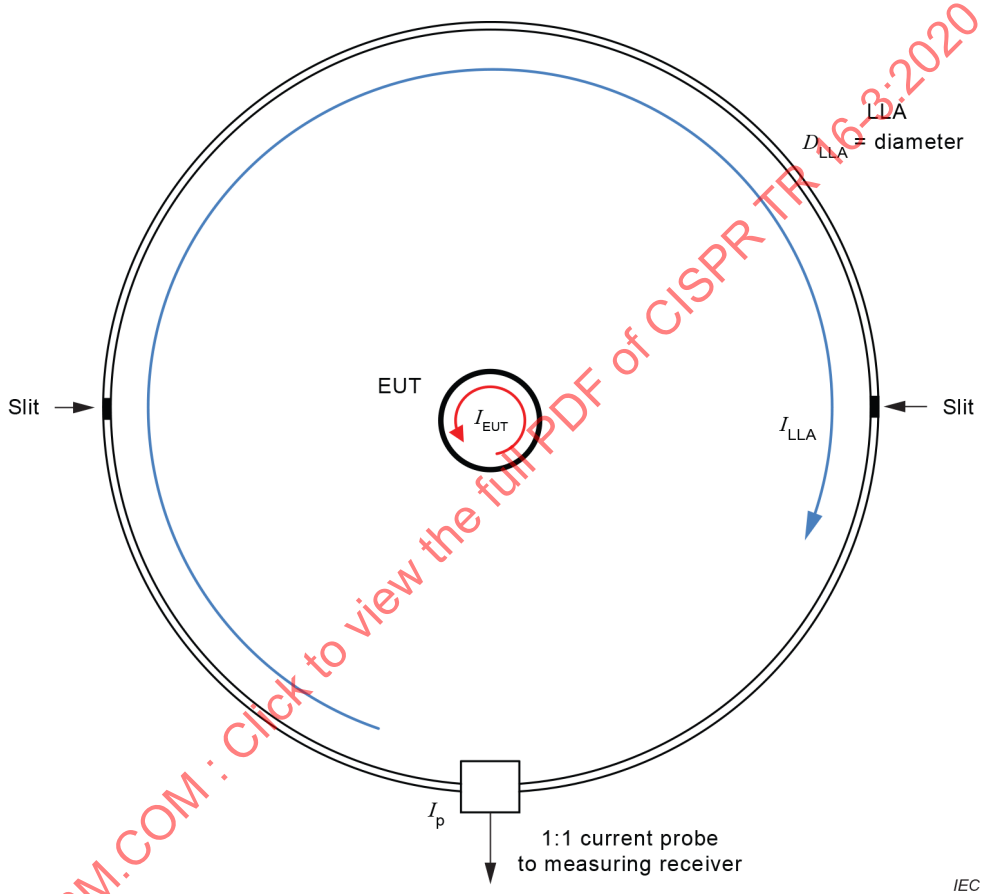



**Figure G.2 – Configuration of measurement of an EUT in an LLA with two slits**

The configuration of Figure G.2 can be considered as a loosely coupled loop transformer. The current $I_{LLA}$ in a short-circuited LLA corresponds with the magnetic field dipole moment $p_{EUT}$ of the EUT as given in Equation (G.2) (which is Equation (2) of [103]):

$$I_{LLA} = \frac{\mu_0}{D_{LLA} L_{LLA}} \times p_{EUT} \qquad \text{(G.2)}$$

where

$\mu_0$ is the permeability of free space; $\mu_0 = 4\pi \cdot 10^{-7}$ H/m,

$D_{LLA}$ is the diameter of an LLA (in m),

IECNORM.COM : Click to view the full PDF of CISPR TR 16-3:2020 RLV

$L_{LLA}$ is the inductance of an LLA (in H).

The inductance of an LLA is given by the following equation (see Equation (3) of [103]):

$$L_{LLA} = \frac{\mu_0}{2} \cdot D_{LLA} \left\{ \ln\left( \frac{8 D_{LLA}}{d_{LLA}} \right) - 2 \right\} \tag{G.3}$$

where $d_{LLA}$ is the diameter of the cross-section of an LLA-loop wire in meters.

For an LLA, this relates to the outer diameter of the shield of the coaxial cable. In case of RG-223/U, $d_{LLA}$ = 3,96 mm (0,003 96 m).

For a 2 m LLA constructed with RG-223/U coaxial cable, the inductance $L_{LLA}$ is given by Equation (G.4):

$$L_{LLA} \text{ (2 m LLA)} = 7{,}92 \text{ µH}. \tag{G.4}$$

As mentioned before, the two coupled loops can be represented by a loosely coupled loop transformer. The network can be represented as shown in Figure G.3. This gives the following ratio (absolute value) of the LLA current and the disturbance current; see Equation (G.5) or Equation (1) of [113]:

$$\frac{I_{LLA}}{I_{EUT}} = \frac{M}{L_{LLA}}, \tag{G.5}$$

where $M$ is the mutual inductance between the two circular concentric coplanar loops. The mutual inductance $M$ is simply determined by the sizes of the two loops and is given by Equation (G.6) (Equation (5) of [113]):

$$M = \frac{\mu_0 S}{D_{LLA}} = \frac{\mu_0 \pi R^2}{D_{LLA}}. \tag{G.6}$$

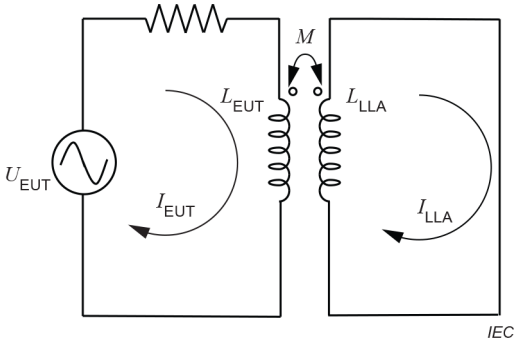



**Figure G.3 – Transformer model representation of a disturbance source inside an LLA**

IECNORM.COM : Click to view the full PDF of CISPR TR 16-3:2020 RLV

#### G.2.2.2 Relation of LLA current and measured signal by the 1 V/A current probe

The current in the LLA is measured using a 1 V/A current probe as specified in CISPR 16-1-4. The LLA as specified in CISPR 16-1-4, is not a typical single short-circuited loop. Each LLA consists of two semi-circles of coaxial cable with specified interconnections and terminations. In this case the LLA can be modelled as two parallel coaxial cables terminated with 50 Ω resistors (two 100 Ω resistors in parallel). This two-slit configuration gives a flat frequency response over the frequency range of interest (9 kHz through 30 MHz) and provides shielding against electric fields. The transfer function giving the EUT magnetic dipole moment current $I_p$ measured by the 1 V/A current probe in terms of the loop current is given by Equation (G.7) (see also Equation (11) of [103]). The Equation (G.7) is also given in [112].

$$f_c(\omega) = \frac{I_p}{I_{LLA}} = j\left[\frac{R_c}{R_T}\sin\left(\frac{k_c \pi R_{LLA}}{2}\right) - j\cos\left(\frac{k_c \pi R_{LLA}}{2}\right) - j\frac{R_c}{R_A}\frac{\sin\left(\frac{k_c \pi R_{LLA}}{2}\right)}{\tan\left(\frac{k \pi R_{LLA}}{2}\right)}\right]^{-1} \quad \text{(G.7)}$$

where

$j$ is the imaginary unit (time dependence $e^{j\omega t}$ is used);

$\omega$ is the angular frequency $2\pi\nu$;

$k$ is the free-space wave number = $\frac{2\pi}{\lambda}$ and $\lambda$ is the free-space wavelength;

$R_{LLA}$ is the radius of an LLA;

$k_c$ is the wave number inside the dielectric of the coaxial cable = $\frac{2\pi}{\lambda_c} = \frac{k}{V_c}$, where $V_c = 1/\sqrt{\varepsilon_r}$ is the signal speed inside the coaxial cable relative to the speed of light in vacuum ($c = 1/\sqrt{\varepsilon_0 \mu_0}$); $V_c$ = 0,67 for PTFE dielectric of an RG-223/U cable, $\varepsilon_r$ is the relative permittivity and $\lambda_c$ is the wavelength inside the dielectric of the coaxial cable;

$R_c$ is the characteristic impedance (resistance) of the LLAS-coaxial cable = 50 Ω (RG-223/U);

$R_T$ is the termination resistance of the LLAS-coaxial cable = 50 Ω (two 100 Ω in parallel);

$R_A$ is the per-unit length inductance of the LLAS-coaxial cable times speed of light given in Equation (G.8):

$$R_A = L_{LLA}\frac{c}{2\pi R_{LLA}} = \frac{\mu_0 c}{2\pi} \times \left\{\ln\left(\frac{8D_{LLA}}{d_{LLA}}\right) - 2\right\} \quad \text{(G.8)}$$

Hence, combining the Equations (G.2) and (G.7) gives the measured current given by the following Equation (G.9):

$$I_p = \frac{\mu_0}{D_{LLA} L_{LLA}} \times f_c(\omega) \times p_{EUT} \quad \text{(G.9)}$$

In Figure G.4 the transfer function $f_c(\omega)$ is shown as a function of frequency for a 2 m LLAS.

The transfer function is constant for a large part of the frequency range of interest. For low frequencies the transfer function becomes Equation (G.10):

IECNORM.COM : Click to view the full PDF of CISPR TR 16-3:2020 RLV

$$\lim_{\omega \to 0} f_c(\omega) = \frac{R_A}{R_A + R_C / V_c} = 0{,}835 \tag{G.10}$$

Expressed in dB the value of the low-frequency approximation of the transfer function is -1,57 dB.

#### G.2.2.3 Electric-field effect

The influence of the electric field of the disturbance source requires an additional correction factor to Equation (G.9). In the original paper of Bergervoet [103], the influence of the near field of the disturbance source is taken into account by an additional transfer function $g_c(\omega)$ that applies for an LLA and EUT in free-space:

$$I_p = \frac{\mu_0}{D_{LLA} L_{LLA}} \times f_c(\omega) \times g_c(\omega) \times p_{EUT}\,, \tag{G.11}$$

where $g_c(\omega)$ is given by the following Equation (G.12):

$$g_c(\omega) = 1 - jkD_{LLA} / 2\,. \tag{G.12}$$

NOTE In the original paper of Bergervoet [103] an error is present in Equation (16) of the paper, i.e. the radius of the LLA is missing in the second term of the equation.

Equation (G.11) can be simplified by using Equations (G.1) and (G.6):

$$\frac{I_p}{I_{EUT}} = \frac{M}{L_{LLA}} \times f_c(\omega) \times g_c(\omega) \tag{G.13}$$

Figure G.4 shows the transfer function $g_c(\omega)$ as a function of frequency for a 2 m LLAS. Also, the product $f_c(\omega) \times g_c(\omega)$ is shown in Figure G.4.

IECNORM.COM : Click to view the full PDF of CISPR TR 16-3:2020 RLV

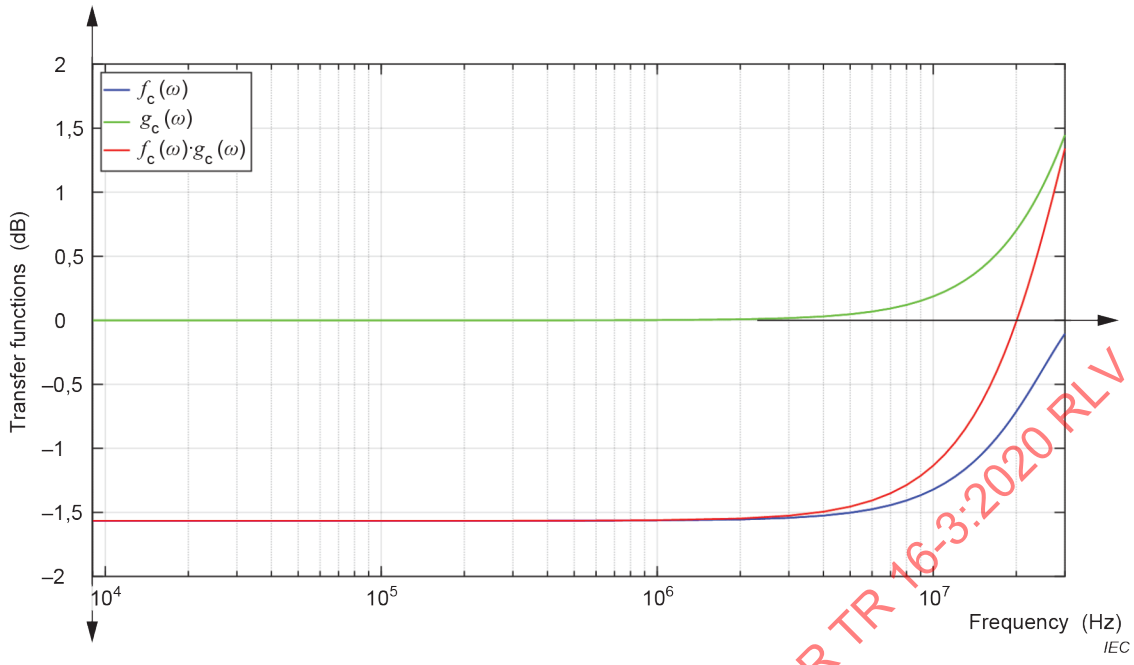



**Figure G.4 – Transfer functions $f_c(\omega)$, $g_c(\omega)$ and their product (expressed in dB) as a function of frequency for a 2 m LLAS**

### G.2.2.4 Low-frequency approximations

For low-frequencies (the flat region of the frequency response), the inductance of the 2 m LLA is $L_{LLA}$ = 7,92 µH (Equation (G.3)).

Equation (G.11) becomes Equation (G.14):

$$I_p = 0{,}079\,3 \times f_c(\omega) \times g_c(\omega) \times p_{EUT} \approx 0{,}066 \times p_{EUT} \quad \text{(G.14)}$$

or expressed in dB it can be written as Equation (G.15):

$$I_p \text{ dB(µA)} = -23{,}6 \text{ dB(1/m}^2\text{)} + p_{EUT} \text{ dB(µAm}^2\text{)} \quad \text{(G.15)}$$

### G.2.3 Sensitivity of an LLAS for different diameters

Equation (G.11) has been calculated for the different diameters of an LLAS given in Figure C.10 of CISPR 16-1-4:2019 [102] (Figure C.11 of CISPR 16-1-4:2010 and CISPR 16-1-4:2010/AMD1:2012 [102]). If the 2 m LLAS is taken as the reference, the relative sensitivity can be calculated that replicates the results of Figure C.11 of CISPR 16-1-4:2010 [102]. The result of this replication is given in Figure G.5. Tabular values of this Figure G.5 are also given in CISPR 16-1-4:2019 [102].

IECNORM.COM : Click to view the full PDF of CISPR TR 16-3:2020 RLV

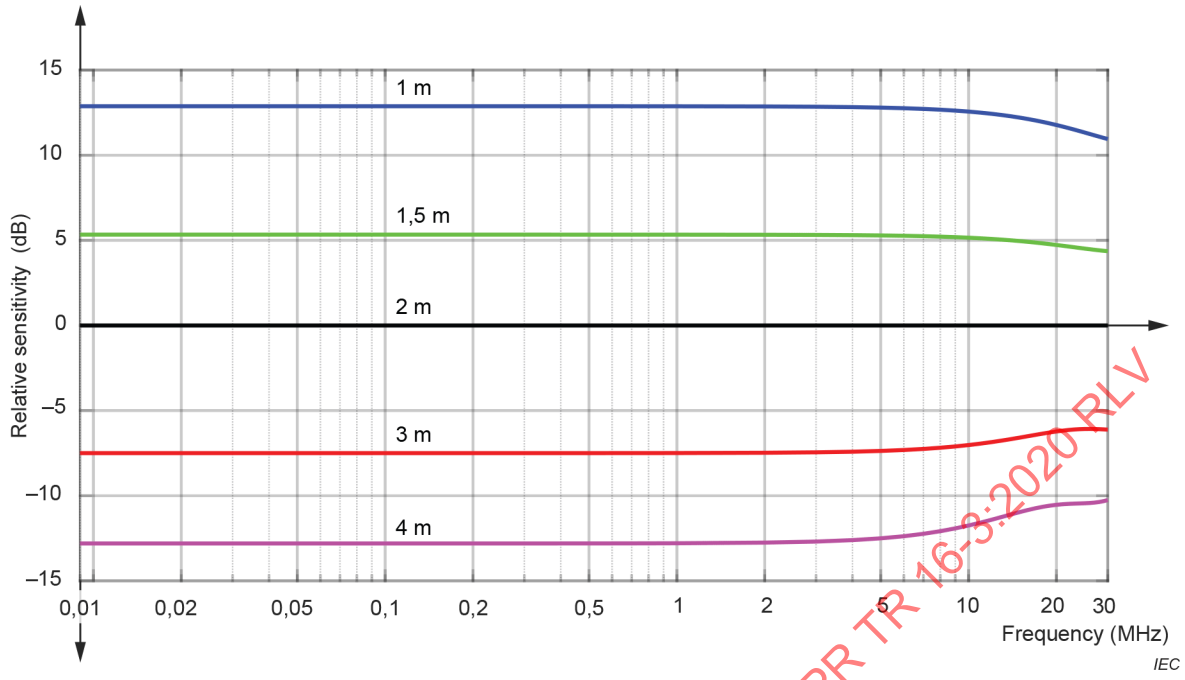



**Figure G.5 – Sensitivity $S_D$ of an LLAS with diameter $D$ relative to an LLAS with 2 m diameter (Figure C.11 of CISPR 16-1-4:2019 [102])**

### G.2.4 Limitation of application of the relative sensitivity curves

Initially, the relative sensitivity curves of Figure C.11 of CISPR 16-1-4:2019 were used in CISPR 16-1-4:2010 [102] for two purposes:

1) To calculate the induced current or magnetic field strength of an EUT in the center of an LLA if an LLA is used with a different diameter than the standard diameter $D_{\text{LLA}}$ = 2 m, or;
2) To calculate the reference validation factor of an LLAS having a different diameter than the standard diameter $D_{\text{LLA}}$ = 2 m.

The second application is invalid for the following reasons:

– this Figure C.11 of CISPR 16-1-4:2019 is only valid for small-sized EUTs, not for large EUTs like the LLAS verification dipole (previously called the ‘balun-dipole’);
– in the case of an LLA with diameter of 3 m or 4 m, the reference validation factor shall be calculated using the method given in G.3, and using the Neumann integral for calculating the mutual inductance (see G.3.6 for details). In this way the specific structure of the LLAS verification dipole is accounted for and a more accurate reference validation factor is obtained;
– in the case of an LLAS with diameters of 1 m or 1,5 m, the LLAS verification dipole (with a maximum dimension of 1,5 m) cannot be applied. Hence, for such LLAS systems no formal validation factor can be measured using the LLAS verification dipole. Therefore, those LLASs with diameters less than 2 m, cannot be used to perform formal compliance measurements.

As a result, in CISPR 16-1-4:2019, CISPR 16-1-4:2019/AMD1:2020 and CISPR 16-1-4:2019/AMD2:20— [102], the following additional changes are included:

a) Deletion of the usage of the relative sensitivity (Figure C.11 of CISPR 16-1-4:2010 [102]) curves to determine the reference validation factor for other than 2 m LLAS diameters;
b) Addition of the reference validation factor curves and tables specifically for LLAS having the standard diameters of 3 m and 4 m;

IECNORM.COM : Click to view the full PDF of CISPR TR 16-3:2020 RLV

c) Making it explicitly clear that an LLA with diameter 1 m and 1,5 m cannot be validated using the LLAS verification dipole;

d) Making it clear that the relative sensitivity curves only apply for relatively small-sized EUTs.

## G.3 Response of LLAS to the LLAS verification dipole

### G.3.1 Relation of LLA current and voltage applied to the LLAS verification dipole

The validation of an LLAS is carried out by measuring the current $I_{ver}$ induced in an LLAS by the LLAS verification dipole (previously called the 'balun dipole') specified in CISPR 16-1-4:2019, CISPR 16-1-4:2019/AMD1:2020 and CISPR 16-1-4:2019/AMD2:20— [102] (see Figure G.6). The LLAS verification dipole of width $w$ and height $s$ is fed with an RF generator with an open circuit voltage $U_{go}$. The validation factor $Z^{LLAS}$ is defined in the following Equation (G.16):

$$Z^{LLAS} = 20\log\frac{U_{go}}{I_{ver}} \quad \text{(G.16)}$$

The measured validation factor shall not deviate more than ±3 dB from the reference validation factor $Z_{ref}^{LLAS}$ given in Figure C.8 of CISPR 16-1-4:2019 and CISPR 16-1-4:2019/AMD1:2020 [102]. See G.5.

NOTE Initially the single term 'validation factor' was applied. However, in order to distinguish between the theoretical reference of the validation factor and the measured validation factor, in CISPR 16-1-4:2019 [102] the term 'reference validation factor' is introduced for the theoretical reference value.

In this subclause, the equation for the reference validation factor $Z_{ref}^{LLAS}$ is derived.

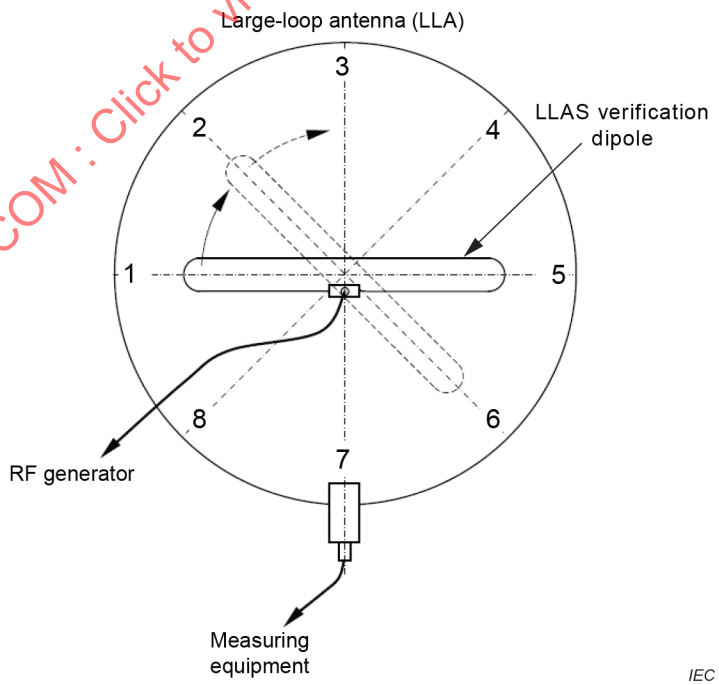



**Figure G.6 – Setup of the LLAS verification dipole for verification of an LLAS**

IECNORM.COM : Click to view the full PDF of CISPR TR 16-3:2020 RLV

### G.3.2 Calculation of mutual inductance: the original method

The LLAS verification dipole is a folded dipole with semicircular ends. The mutual inductance $M_{bd}$ between the LLAS verification dipole and an LLA can be calculated using Equation (G.6). It gives the following Equation (G.17):

$$M_{bd} = \frac{\mu_0 S_{bd}}{D_{LLA}}, \tag{G.17}$$

where the surface area $S_{bd}$ of the LLAS verification dipole is given by Equation (G.18):

$$S_{bd} = 1{,}4 \text{ m} \times 0{,}1 \text{ m} + (\pi \times 0{,}05^2) \text{ m}^2 = 0{,}147\ 9 \text{ m}^2. \tag{G.18}$$

The details of the construction of the LLAS verification dipole are given in Figure C.9 of CISPR 16-1-4:2019 and CISPR 16-1-4:2019/AMD1:2020 [102].

For a 2 m LLAS, the mutual inductance $M_{bd}$ of the LLAS verification dipole is:

$$M_{bd} \text{ (2 m LLAS)} = 92{,}9 \text{ nH}. \tag{G.19}$$

This value of $M_{bd}$ was used in the original paper by Bergervoet [103] to calculate the reference validation factor curve. The same value was also applied in the first versions of the CISPR 16 publications where the LLAS method was introduced (preceding CISPR 16-1-4:2019 and CISPR 16-1-4:2019/AMD1:2020 [102]).

### G.3.3 Calculation of mutual inductance: the improved method

The mutual inductance between the LLAS verification dipole and an LLA can be computed more rigorously using the Neumann integral [113]:

$$M_{bd} = \frac{\mu_0}{4\pi} \oint_{C1} \oint_{C2} \frac{\vec{dl}_1 \times \vec{dl}_2}{R_{12}}, \tag{G.20}$$

where $R_{12}$ is the distance between the source point on the LLAS verification dipole and the observation point on an LLA, and $\vec{dl}_1$ and $\vec{dl}_2$ are the differential path vectors as shown in Figure G.7.

When applying Equation (G.20) for a 2 m LLA, the mutual inductance $M_{bd}$ between the LLAS verification dipole and the LLA is given by Equation (G.21) [117]:

$$M_{bd} \text{ (2 m LLA)} = 112{,}2 \text{ nH}. \tag{G.21}$$

### G.3.4 Derivation of the equation for the reference validation factor

In this subclause, the analytical equation for the reference validation factor is replicated using the method given in [103], [112], [113]. In this method, the system comprising the LLA and the LLAS verification dipole is considered as a loosely coupled transformer.

IECNORM.COM : Click to view the full PDF of CISPR TR 16-3:2020 RLV

The two halves of the folded dipole may be represented by two pieces of short-circuited transmission line of length $W/2$ in series (Figure G.8). The transmission line is comprised of two conductors with spacing $s$ = 0,1 m. The total impedance of the two transmission lines can be approximated by Equation (G.22) [115]:

$$Z_{\text{bd}} \approx j2Z_0 \tan(kW/2), \tag{G.22}$$

where $Z_0$ is the characteristic impedance of the two-wire transmission line given by Equation (G.23):

$$Z_0 \approx 120 \cosh^{-1}(s/d_{\text{bd}}), \tag{G.23}$$

where $d_{\text{bd}}$ is the outer diameter of the coaxial cable of the LLAS verification dipole. For a two-wire transmission line with the centers of the wires with spacing $s$ = 0,1 m and for a diameter of each wire $d_{\text{bd}}$ = 3,96 mm for RG-223/U, the characteristic impedance becomes $Z_0 \approx$ 470 Ω.

As mentioned before, these two coupled loops can be represented by a loosely coupled loop transformer. The total network representation of the generator, the LLAS verification dipole and a single LLA then can be represented as in Figure G.9. From this figure we see that the reference validation factor can be calculated using the following Equation (G.24):

$$Z_{\text{ref}}^{\text{LLAS}} = 20 \log\left\{\frac{U_{\text{go}}}{I_{\text{bd}}} \cdot \frac{I_{\text{bd}}}{I_{\text{ver}}}\right\}. \tag{G.24}$$

The ratio of the generator open circuit voltage $U_{\text{go}}$ and the current in the LLAS verification dipole $I_{\text{bd}}$ can be calculated using the following Equation (G.25):

$$\frac{U_{\text{go}}}{I_{\text{bd}}} = R_{\text{g}} + Z_{\text{bd}} - \frac{j\omega M_{\text{bd}}^2}{L_{\text{LLA}}} \tag{G.25}$$

The ratio of the LLAS verification dipole current $I_{\text{bd}}$ and the measured LLA current $I_{\text{ver}}$ can be derived from the following Equation (G.26):

$$\frac{I_{\text{bd}}}{I_{\text{ver}}} = \frac{L_{\text{LLA}}}{M_{\text{bd}} \times f_{\text{c}}(\omega) \times g_{\text{c}}(\omega)} \tag{G.26}$$

The reference validation factor defined in Equation (G.24) then becomes Equation (G.27):

$$Z_{\text{ref}}^{\text{LLAS}} = 20 \log\left\{\frac{L_{\text{LLA}}\left\{R_{\text{g}} + Z_{\text{bd}} - \frac{j\omega M_{\text{bd}}^2}{L_{\text{LLA}}}\right\}}{M_{\text{bd}} \times f_{\text{c}}(\omega) \times g_{\text{c}}(\omega)}\right\} \tag{G.27}$$

IECNORM.COM : Click to view the full PDF of CISPR TR 16-3:2020 RLV

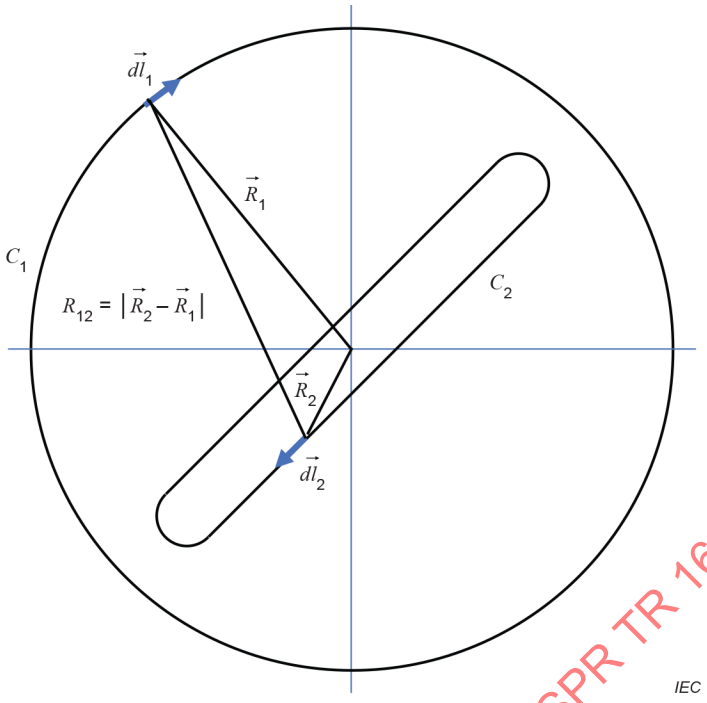
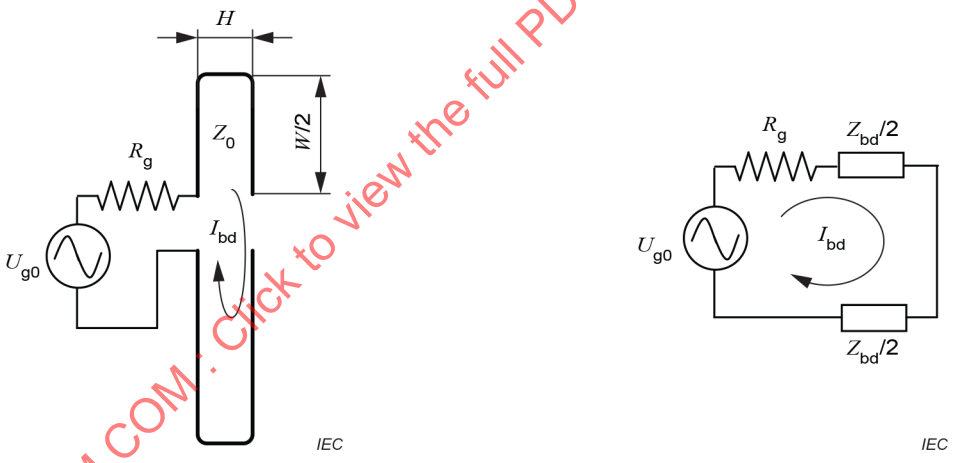



**Figure G.7 – Geometry model of LLA for numerical computation of Neumann integral [113]**




a) Geometrical topology

b) Circuit representation

**Figure G.8 – LLAS verification dipole excluding the coupling effect from the LLAS loops**

IECNORM.COM : Click to view the full PDF of CISPR TR 16-3:2020 RLV

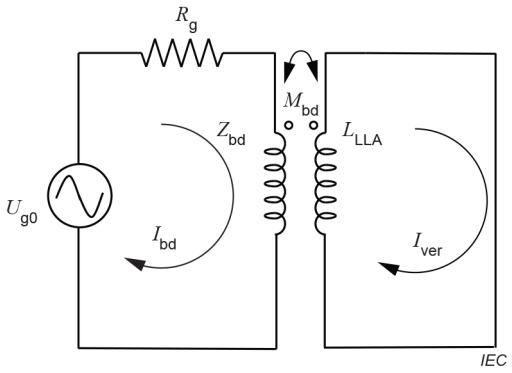



**Figure G.9 – Network model representation of the LLAS verification dipole fed by a generator source and the LLA**

### G.3.5 Replication of the original version of the reference validation factor

The reference validation factor has been calculated for an LLA of 2 m diameter using Equation (G.27) and the value of $M_{bd}$ given in Equation (G.19). The result is shown in Figure G.10. This figure gives the same result as Figure C.8 of CISPR 16-1-4:2010 [102].

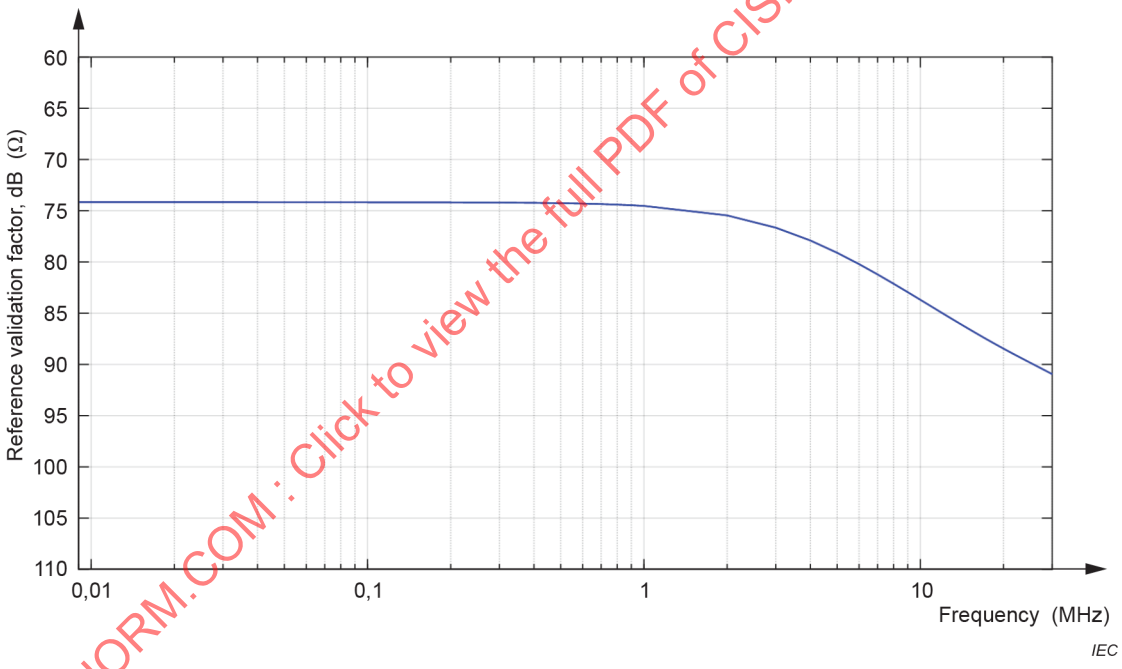



**Figure G.10 – First version of the reference validation factor for an LLA of 2 m diameter (Figure C.8 of CISPR 16-1-4:2010 [102])**

IECNORM.COM : Click to view the full PDF of CISPR TR 16-3:2020 RLV

### G.3.6 Calculation of the improved reference validation factor

The new improved reference validation factor has been calculated for an LLA of 2 m diameter using Equation (G.27) and using the more precise value of $M_{bd}$ derived from the Neumann integral given in Equation (G.21). The result is shown in Figure G.11. This figure shows an adjustment of the curve by -1,64 dB with respect to the curve in Figure G.10.

NOTE The vertical axis of Figure G.11 has been reversed w.r.t. the vertical axis of Figure G.10 (Figure C.8 of CISPR 16-1-4:2019 [102]), as this is a more common representation of a vertical scale.

The same calculation method is also applied for an LLA with the standard diameters of 3 m and 4 m (see G.2.4 for the reason). The values of $M_{bd}$ derived from Equation (G.20) for these LLA diameters are respectively 66,3 nH and 48,2 nH.

Tabular values of the new reference validation factor curves given in Figure G.11 are also given in CISPR 16-1-4:2019, CISPR 16-1-4:2019/AMD1:2020 and CISPR 16-1-4:2019/AMD2:20— [102].

Figure G.12 shows the relative response of an LLA to the LLAS verification dipole for different diameters of the LLA. This Figure G.12 shows that the relative sensitivities calculated from the LLAS verification dipole model are slightly different from the relative sensitivities that were obtained through the generic loosely-coupled loop transformer model of a small concentric coplanar loop outlined in G.2.2 (see Figure G.5). This demonstrates also that the relative sensitivity curves of Figure C.11 of CISPR 16-1-4:2010 [102] (Figure G.5 in this document) cannot be applied for deriving the reference validation factors for an LLA with diameters of 3 m or 4 m. See also the considerations in G.2.4.

The low-frequency asymptotic value of the new reference validation factor is given by Equation (G.28):

$$\lim_{\omega \to 0} \left| Z_{\text{ref}}^{\text{LLAS}} \right| = 20 \log \left\{ \frac{L_{\text{LLA}} R_{\text{g}}}{M_{\text{bd}} \times \left( \frac{R_{\text{A}}}{R_{\text{A}} + \frac{R_{\text{C}}}{V_{\text{c}}}} \right)} \right\} = 72{,}52 \text{ dB}(\Omega) \qquad \text{(G.28)}$$

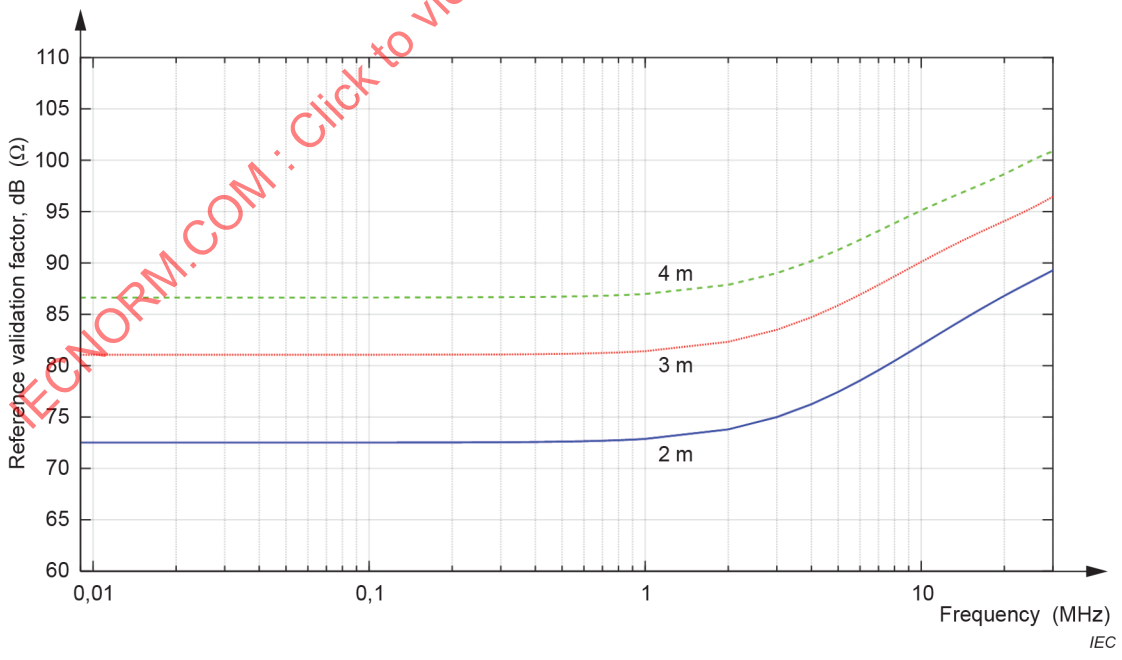



**Figure G.11 – Reference validation factors for an LLA of 2 m, 3 m and 4 m diameter (Figure C.8 of CISPR 16-1-4:2019 and CISPR 16-1-4:2019/AMD1:2020 [102])**

IECNORM.COM : Click to view the full PDF of CISPR TR 16-3:2020 RLV

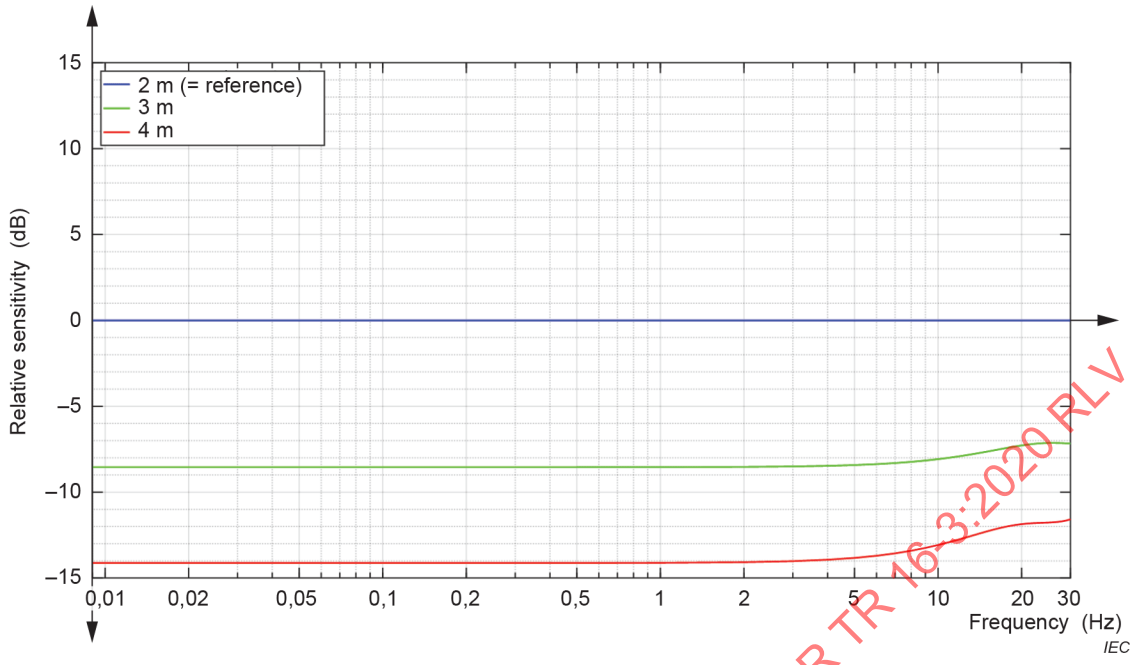



**Figure G.12 – Relative sensitivities of the LLAS verification dipole for an LLAS with different diameters (relative to an LLAS of 2 m diameter)**

### G.3.7 NEC2 method

In [117] a numerical method using NEC2 modelling has been applied, which gives slightly different results above 5 MHz because at upper frequencies, the current distribution is not uniform anymore. It is acknowledged that the results between 5 MHz and 30 MHz are more accurate using the NEC2 method. The maximum differences occur in the region between 5 MHz and 30 MHz and are 0,13 dB, 0,30 dB and 0,47 dB for LLA diameters of respectively 2 m, 3 m and 4 m (see Figure G.13). For the purpose of standardization, it is preferred to apply the analytical Equation of (G.27) that can readily be applied without the need for NEC2.

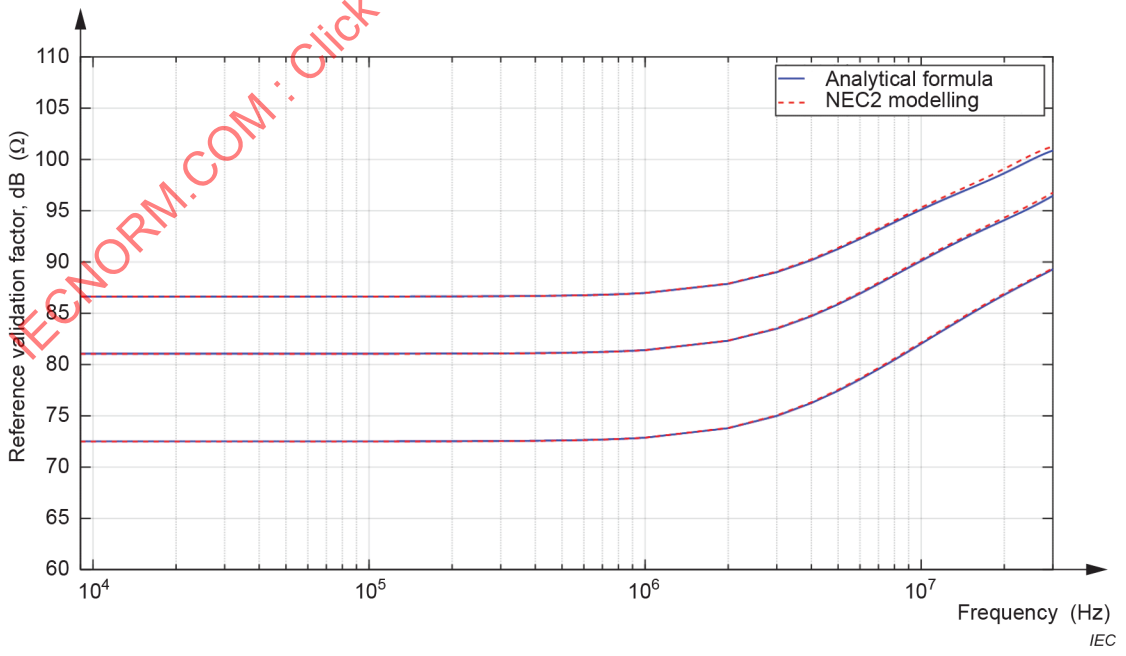



**Figure G.13 – Comparison of analytical and numerical (NEC2) calculations of the reference validation factors**

IECNORM.COM : Click to view the full PDF of CISPR TR 16-3:2020 RLV

## G.4 Magnetic field strength of a magnetic field dipole above a ground plane

### G.4.1 Model

Figure C.10 of CISPR 16-1-4:2010 [102] gives conversion factors for calculating the magnetic field from the current measured by an LLAS for a certain EUT at specified distances. The conversion factors given in Figure C.10 are taken over from the paper of Bergervoet [103]. In this subclause the equations for these conversion factors are given.

For the calculations the analytical equation for the magnetic field strength resulting from a magnetic field dipole is used. Generally, the magnetic field strength vector $\boldsymbol{H}$ consists of three components $H_x$, $H_y$ and $H_z$. It is assumed that the disturbance source in the EUT is represented by a magnetic field dipole moment vector $\boldsymbol{p}$, whose magnitude is given by Equation (G.1). See Figure G.14.

The direction of this vector $\boldsymbol{p}$ is normal to the plane of the loop of the source current. In free space, the magnetic field strength vector $\boldsymbol{H}$ would be according to Equation (G.29) [114]:

$$\boldsymbol{H} = \frac{1}{4\pi}\left[k^2(\boldsymbol{n}\times\boldsymbol{p})\times\boldsymbol{n}\frac{e^{-jkr}}{r} + \left[3\boldsymbol{n}(\boldsymbol{n}\cdot\boldsymbol{p}) - \boldsymbol{p}\right]\cdot\left(\frac{1}{r^3} + \frac{jk}{r^2}\right)e^{-jkr}\right], \tag{G.29}$$

where

$\boldsymbol{n}$ is the unit vector from the source to the observation point;

$r$ is the absolute value of the distance between the EUT, the center of the loop (or the source), and the observation point.

Equation (G.29) is the exact analytical description in free space and contains the far-field part ($1/r$ - term) and the near-field and intermediate-field terms.

The position of the EUT at a height $h$ above the ground plane and the associated x-y-z-coordinate system is depicted in Figure G.15. The three possible orientations of the magnetic field dipole inside the EUT are also given in Figure G.15. It is assumed that the magnetic field dipole is located above an ideally conductive ground plane (SAC or OATS). For calculating the total magnetic field strength, an additional image source shall be considered. Two examples of the way the direct source adds to the image source are given in Figure G.16. In case of a horizontal x- or y-directed magnetic field dipole, the dipole moment of the image has the same direction, which means that the image field adds to the direct field. The total field can be calculated by applying Equation (G.29) twice, giving Equation (G.30):

$$\boldsymbol{H}_{\text{total}} = \boldsymbol{H}_{\text{direct}} + \boldsymbol{H}_{\text{image}} \tag{G.30}$$

For a vertical z-directed magnetic field dipole (caused by a horizontal current loop) the image source has an opposite direction, which means that the direct field is weakened by its image field.

In this way the total magnetic field strength at a certain horizontal measurement distance $r_{\text{m}}$ of a magnetic field dipole above a ground plane can be calculated e.g. using Matlab.

IECNORM.COM : Click to view the full PDF of CISPR TR 16-3:2020 RLV

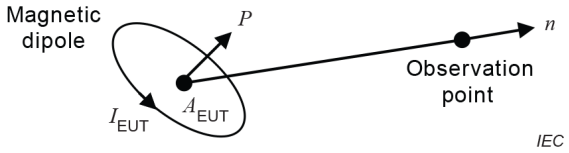



**Figure G.14 – Magnetic field dipole moment of a small loop radiator in free space**

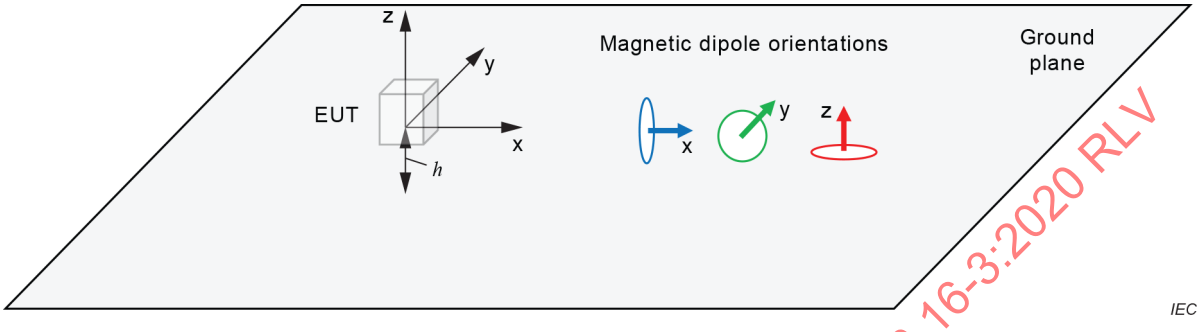
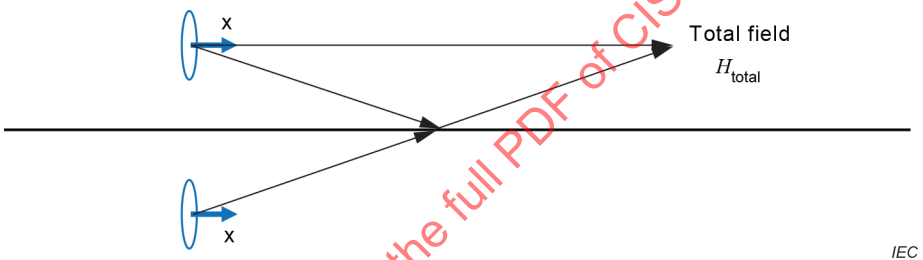
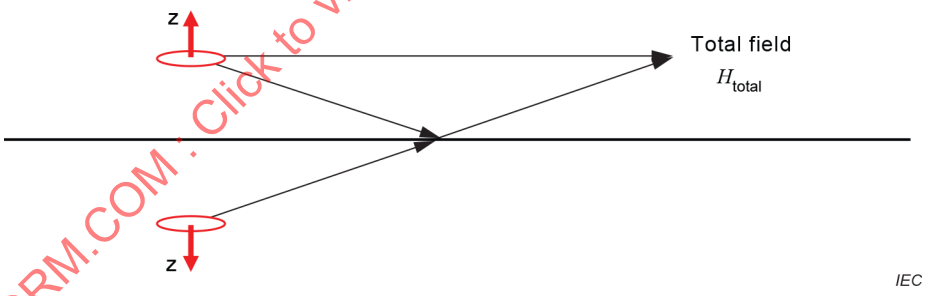



**Figure G.15 – EUT above a ground plane and the coordinate system and possible magnetic field dipole orientations**




**x-directed magnetic field dipole**




**z-directed magnetic field dipole**

**Figure G.16 – Magnetic field strength resulting from a source and its image below the ground plane (side view)**

IECNORM.COM : Click to view the full PDF of CISPR TR 16-3:2020 RLV

### G.4.2 Replication of Figure C.10

The three components $H_x, H_y$ and $H_z$ of the magnetic field strength of respectively three orthogonally oriented magnetic field dipoles have been calculated for three horizontal distances. In order to replicate Figure C.10 of CISPR 16-1-4:2010 [102], the parameters of the configuration that have been published in [103] have been gathered from a Philips internal Technical Note [116]. These parameters are as follows:

– horizontal measurement distance $r_m$ = 3 m, 10 m and 30 m,

– height of the center of the magnetic field dipoles above the ground plane $h$ = 1,3 m,

– height at which the magnetic field strength is calculated = 1,3 m,

– diameter of the magnetic field dipole $D$ = 0,4 m,

– current in the magnetic field dipole loop $I$ = 100 dB(µA).

The results shown in Figure G.17 give the magnetic field strength expressed in terms of dB(µA/m). Note that the colors of the curves given in Figure G.17 correspond with the colors of the magnetic field dipoles shown in Figure G.15. From these results we see that the levels of either the $H_x$ or $H_y$ component of respectively the x- and y-directed magnetic field dipole will always be larger than the levels of the $H_z$ component. Therefore, the maximum value of the $H_x$ or $H_y$ components are only of interest and have been determined [103]. These maximum values are related to the current that would be measured by a 2 m LLA for the same magnetic field dipole. This current is calculated using Equation (G.13). The ratio between these maximum levels of magnetic field strength in dB(µA/m) measured at a distance $r_m$ and the LLA current $I_{LLA}$ in dB(µA) gives the conversion factor in dB(1/m). The results are shown in Figure G.18. This Figure G.18 is the same as Figure C.10 of CISPR 16-1-4:2010 [102] with the exception that also the conversion factor for 30 m distance is given. Tabular values of the curves presented in Figure G.18 are given in CISPR 16-1-4:2019 and CISPR 16-1-4:2019/AMD1:2020 [102].

In Figure C.10 of CISPR 16-1-4:2019 [102], the magnetic field strength is converted into electric field strength expressed in terms of dB(µV/m), simply by assuming that the free-space impedance relation applies (which is generally not the case). The electric field strength in dB(µV/m) can be obtained by adding the free-space impedance value dB(Ω) given by the following Equation (G.31):

$$Z_{fs} = 20\log(120\pi) = 51{,}5 \text{ dB}(\Omega). \quad \text{(G.31)}$$

IECNORM.COM : Click to view the full PDF of CISPR TR 16-3:2020 RLV

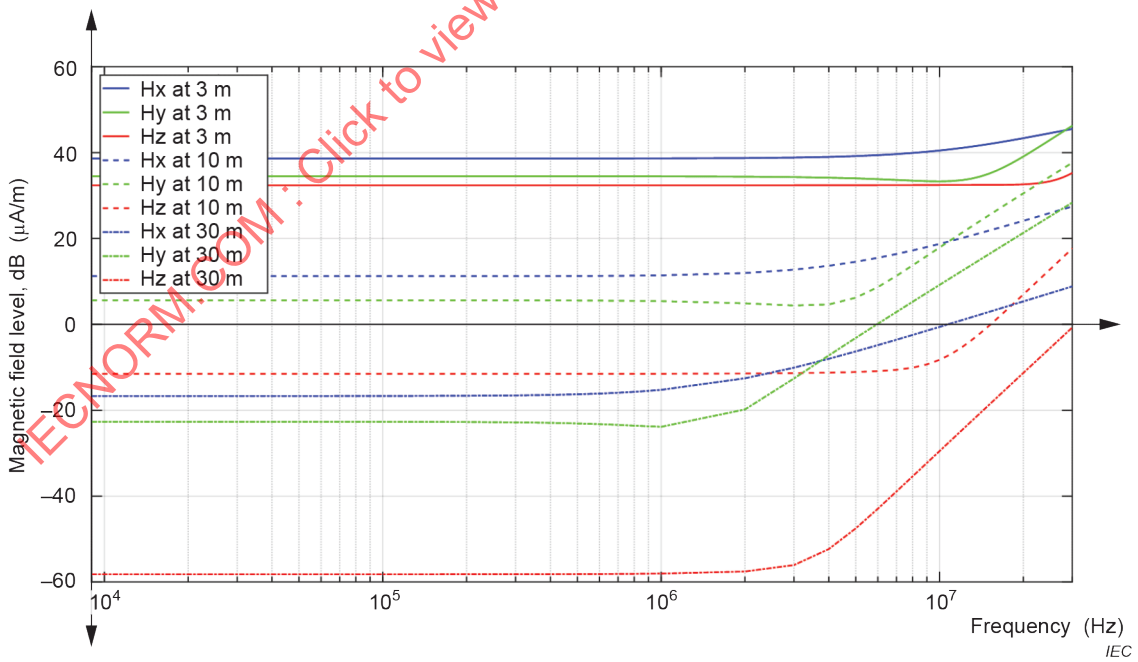



**Figure G.17 – Magnetic field strength expressed in dB(µA/m) of three magnetic field dipole orientations at three distances**

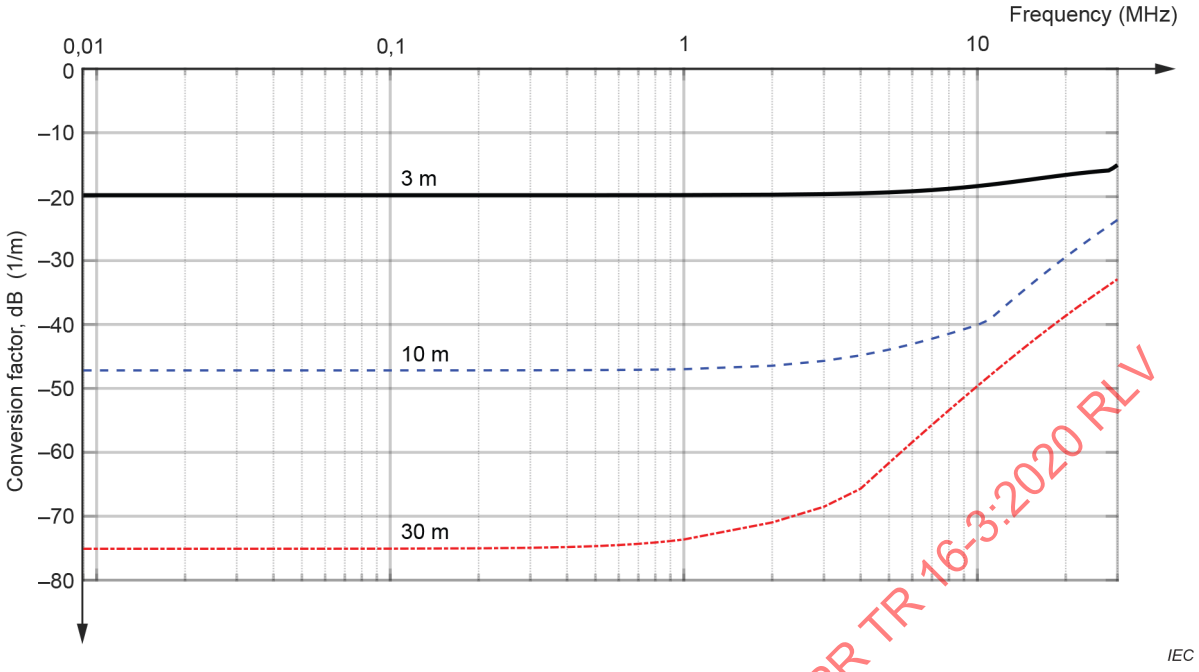



**Figure G.18 – Conversion factors $C_{dA}$ [for conversion into dB(µA/m)] for three standard measurement distances $d$ (replicated Figure C.10 of CISPR 16-1-4:2010; exclusive the 30 m curve [102])**

### G.4.3 Conversion factors for calculating magnetic field strength at other distances

The result shown in Figure G.18 can be used also to calculate conversion factors for calculating the magnetic field strength at different distances. For instance, if the magnetic field strength value is available at 3 m distance, the field at 10 m or 30 m can be obtained using the curves given in Figure G.19.

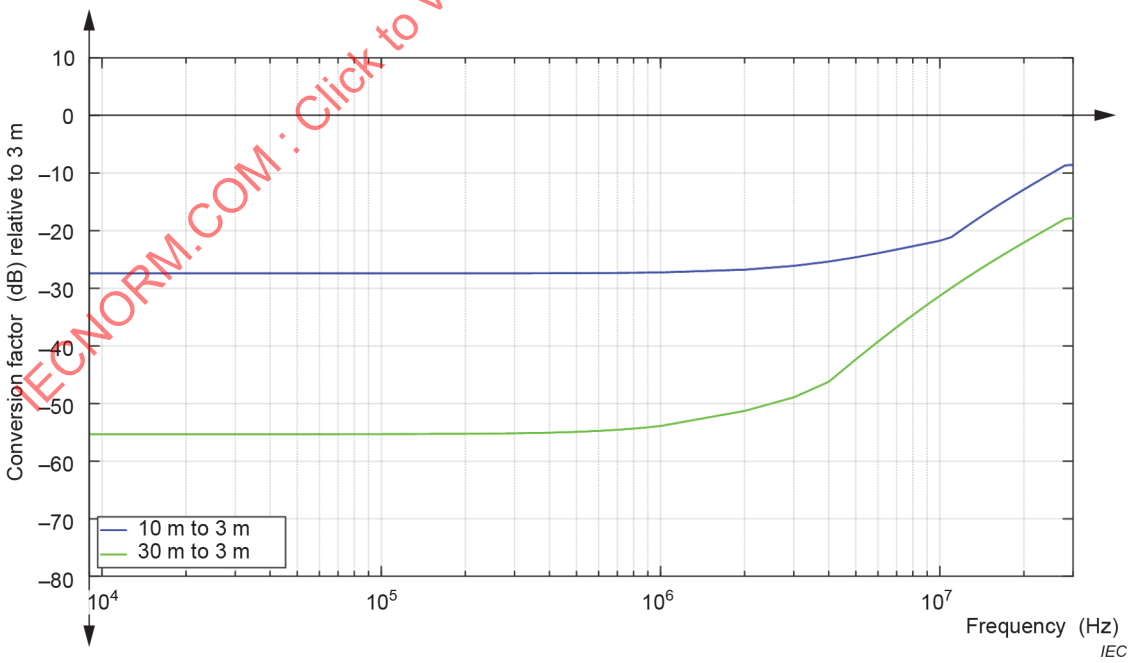



**Figure G.19 – Conversion factors for calculating magnetic field strength at 10 m or 30 m**

IECNORM.COM : Click to view the full PDF of CISPR TR 16-3:2020 RLV

## G.5 LLAS validation criterion

In CISPR 16-1-4:2010 [102], the acceptance criterion for the LLAS validation was a maximum deviation of the measured validation factor ±2 dB with respect to the reference validation factor.

To assess the impact of the improved reference validation factor, several verification measurements have been executed. Verification measurement results have been reported at the CISPR A WG1 meeting in Stresa by Midori et al. [117] and by Schwarzbeck [118].

Midori et al. [117] reported verification test results using five existing LLAS systems in the market. It was shown that the validation criterion of ±2 dB in CISPR 16-1-4:2019 [102] is very tight due to design and manufacturing tolerances for an LLAS and due to the influence of the surrounding (floor) during the test.

In Schwarzbeck's paper [118], the average reference validation factor of 24 LLAS units is shown. The 24 LLAS units were exactly constructed according to the CISPR 16-1-4:2010 [102] specification. The resulting average value was approximately between the former and the new reference validation factor curves given in respectively CISPR 16-1-4: 2010 [102] and CISPR 16-1-4:2019 [102]. Verification results reported by Midori et al. in a later paper [119] shows that improved reference validation curve with the 1,64 dB shift (see G.3.6) provides a better match with verification measurements of actual LLAS units in the field (in the Japanese market). From these verification tests, it was also concluded that the LLAS validation acceptance criterion of ±2 dB given in CISPR 16-1-4:2010 [102] is difficult to meet in practice. Midori et al. showed in [119] that the measurement uncertainty of the LLAS validation test is 1,9 dB (expanded uncertainty). The uncertainty due to construction tolerances and probe sensitivity variations is 0,8 dB. Hence, the LLAS acceptance criterion of ±2 dB specified in CISPR 16-1-4:2010 [102] is extremely tight.

From these practical findings and the above considerations, CISPR/A decided to change the acceptance criterion for the LLAS validation test from ±2 dB to ±3 dB.

IECNORM.COM : Click to view the full PDF of CISPR TR 16-3:2020 RLV

# Bibliography

[1] CISPR 1:1972, *Specification for CISPR radio interference measuring apparatus for the frequency range 0,15 MHz to 30 MHz*[3]

[2] CISPR 2:1975, *Specification for CISPR. radio interference measuring apparatus for the frequency range 25 MHz to 300 MHz*[4]

[3] CISPR 7:1969, *Recommendations of the CISPR.*[5]

[4] CISPR 8:1969, *Report and study questions of the CISPR.*[6]

[5] CISPR 11:2003, *Industrial, scientific and medical (ISM) radio-frequency equipment – Electromagnetic disturbance characteristics – Limits and methods of measurement* [7]
CISPR 11:2003/AMD1:2004
CISPR 11:2003/AMD2:2006

[6] CISPR 16-1-3:2004, *Specification for radio disturbance and immunity measuring apparatus and methods – Part 1-3: Radio disturbance and immunity measuring apparatus – Ancillary equipment – Disturbance power*
CISPR 16-1-3:2004/AMD1:2004
CISPR 16-1-3:2004/AMD2:2020

[7] CISPR 16-1-4:2010, *Specification for radio disturbance and immunity measuring apparatus and methods – Part 1-4: Radio disturbance and immunity measuring apparatus – Antennas and test sites for radiated disturbance measurements*[8]
CISPR 16-1-4:2010/AMD1:2012
CISPR 16-1-4:2010/AMD2:2017

[8] CISPR 16-2-1, *Specification for radio disturbance and immunity measuring apparatus and methods – Part 2-1: Methods of measurement of disturbances and immunity – Conducted disturbance measurements*

[9] CISPR 16-2-2:2010, *Specification for radio disturbance and immunity measuring apparatus and methods – Part 2-2: Methods of measurement of disturbances and immunity – Measurement of disturbance power*

[10] CISPR 16-2-3, *Specification for radio disturbance and immunity measuring apparatus and methods – Part 2-3: Methods of measurement of disturbances and immunity – Radiated disturbance measurements*

[11] CISPR TR 16-4-1:2009, *Specification for radio disturbance and immunity measuring apparatus and methods – Part 4-1: Uncertainties, statistics and limit modelling – Uncertainties in standardized EMC tests*

IECNORM.COM : Click to view the full PDF of CISPR TR 16-3:2020 RLV

3 This publication was withdrawn and replaced by CISPR 16-1:1993.

4 This publication was withdrawn and replaced by CISPR 16-1:1993.

5 This publication was withdrawn and replaced by CISPR 11:1975.

6 This publication was withdrawn and replaced by CISPR 11:1975.

7 This publication was withdrawn and replaced by CISPR 11:2009.

8 This publication was withdrawn and replaced by CISPR 16-1-4:2019.

[12] CISPR TR 16-4-3, *Specification for radio disturbance and immunity measuring apparatus and methods – Part 4-3: Uncertainties, statistics and limit modelling – Statistical considerations in the determination of EMC compliance of mass-produced products*

[13] CISPR TR 16-4-4:2007, *Specification for radio disturbance and immunity measuring apparatus and methods – Part 4-4: Uncertainties, statistics and limit modelling – Statistics of complaints and a model for the calculation of limits for the protection of radio services*

[14] CISPR 20:2006, *Sound and television broadcast receivers and associated equipment – Immunity characteristics – Limits and methods of measurement*

[15] IEC 61000-4-6, *Electromagnetic compatibility (EMC) – Part 4-6: Testing and measurement techniques – Immunity to conducted disturbances, induced by radio-frequency fields*

[16] Whalen, J.J., "Determining EMI in microelectronics – A review of the past decade," *Proceedings of International Symposium on Electromagnetic Compatibility*, Zurich, Switzerland, March 1995, p 337-344

[17] Larson, C.E. and Roe, J.M., "A modified Ebers-Moll transistor model for RF interference analysis," *IEEE Transactions on Electromagnetic Compatibility*, November 1979, vol. EMC-21, p 283-290

[18] Liu, K. and Whalen, J.J., "The combined effects of internal noise and electromagnetic interference in CMOS VLSI circuits", *Procedures of the 6th International Symposium on Electromagnetic Compatibility,* York, United Kingdom, September 1988, p 303

[19] Demoulin, B., Lardé, C. and Degauge, P., "Interference effects in CMOS and TTL integrated circuits", *Proceedings of International Symposium on Electromagnetic Compatibility,* Zurich, Switzerland, March 1989, p 543-546

[20] *EMI problems associated with non-linear device characteristics, Proceedings of 1st International Symposium on Electromagnetic Compatibility*, Madrid, Spain, Nov 1990

[21] EMC Working Group of the ZVEI (Union of Electrotechnical Industries), P.O. Box 700969, 6000 Frankfurt/Main 70, Germany

[22] ~~Doedbloed~~ Goedbloed, J.J. and Jeschar, G., "RF disturbances on telephone-subscriber lines induced by AM broadcasting transmitters", *Proceedings of International Symposium on Electromagnetic Compatibility*, Zurich, Switzerland, March 1989, p 537-542

[23] Goedbloed, J.J. and Pasmooij, W.A., "Characterization of transient and CW disturbances induced in telephone-subscriber lines", *Proceedings of International Symposium on Electromagnetic Compatibility*, York, August 1990, United Kingdom, p 211-218

[24] DIN/VDE 0878, Funk-Entstörung von Anlagen und Geräten der Fernmelde Technik, Part 1/12.86, December 1986

[25] CISPR/A(Secretariat)98, *Amendment of Publication 16, Part 1, Clause 20: T-type networks*, March 1989

[26] *World Radio and TV Handbook*, 1986

IECNORM.COM : Click to view the full PDF of CISPR TR 16-3:2020 RLV

[27] Hattori, M., Ohtsuki, F., Motomitsu, T. and Koga, H., “IEEE Radio broadcast induction voltage and pair unbalance in subscriber cable”, *Proceedings on International Symposium on Electromagnetic Compatibility*, 1984, p 884-889

[28] ITU-T Recommendation K.18, *Calculation of voltage induced into telecommunication lines from radio stations broadcasts and method of reducing interference*

[29] ITU-R Recommendation BS.468-4, *Measurement of audio-frequency noise voltage level in sound broadcasting*

[30] Hattori, M., and Ideguchi, T., “Electromagnetic interference and countermeasures on metallic lines for ISDN”, *IECEE Transactions on Communications*, Jan 1992, vol. E75-B, no. 1

[31] ITU-R Recommendation 527-1, *Electrical Characteristics of the Surface of the Earth*, International Consultative Committee on Radio (CCIR), International Telecommunication Union, Geneva, 1982

[32] ITU-R Report 879-1, *Methods for Estimating Effective Electrical Characteristics of the Surface of the Earth*, International Consultative Committee on Radio (CCIR), International Telecommunication Union, Geneva, 1986

[33] Nickum, J.D., and Drury, W., “Measurement of RF Fields Associated With ISM Equipment as it Relates to Aeronautical Services”, Report No. OU/AEC/EER 67-1, Avionics Engineering Center, Department of Electrical and Computer Engineering, Ohio University, Athens, Ohio 45701, USA; and “Final report to the US Federal Aviation Administration, Systems Engineering Service”, Washington, DC 20591, Report No. DOT/FAA/ES-84/2, May 1985; documents disseminated under sponsorship of the US Department of Transportation, publicly available through the National Technical Information Service, Springfield, Virginia 22161, USA

[34] Macfarlane, I.P., “Harmonic Fields Radiated at Elevated Angles from 27 MHz ISM Apparatus Over Real Ground”, *Telstra Research Laboratories Report 8347*, 1995, Telstra Research Laboratories, 770 Blackburn Road, Clayton, Victoria 3168, Australia

[35] Burke, G.J. and Poggio, A.J., *Numerical Electromagnetics Code* (NEC) – “Method of Moments”, Naval Ocean Systems Center – NOSC Technical Document 116, 1981, San Diego, CA 92152,USA (Numerical Electromagnetics Code (NEC2) developed at Lawrence Livermore National Laboratory, Livermore, California, File Created 4/11/80, Double Precision 6/4/85)

[36] Sommerfeld, translated by Straus, "Partial Differential Equations in Physics", *Lectures on Theoretical Physics*, vol.VI, chapter VI, Academic Press, New York, 1964

[37] Stutzman, W.L. and Thiele, G.A., *Antenna Theory and Design*, p 123, John Wiley & Sons, New York, 1981

[38] *Radio Regulations, Edition 1990*, International Telecommunication Union (ITU), General Secretariat, Geneva

[39] Macfarlane, I.P., “Predictability of Electromagnetic Radiation in the Vertical Plane Over Real Ground at Frequencies Above 30 MHz”, *Telstra Research Laboratories Report 8331*, 1995, Telstra Research Laboratories, 770 Blackburn Road, Clayton, Victoria 3168, Australia

IECNORM.COM : Click to view the full PDF of CISPR TR 16-3:2020 RLV

[40] Macfarlane. I.P., “Surface Waves and Near Fields Over Ground Planes at Frequencies Above 30 MHz”, *Telstra Research Laboratories Report 8329*, 1995, Telstra Research Laboratories, 770 Blackburn Road, Clayton, Victoria 3168, Australia

[41] Jordon, E.C. and Balmain, K.G., *Electromagnetic Waves and Radiating Systems*, Chapter 16, Prentice-Hall, Inc., Second Edition, 1968,

[42] US Code of Federal Regulations (CFR), Chapter I – *Federal Communications Commission (FCC), Title 47, Part 18, Industrial, scientific and medical equipment*, US Government Printing Office, issue of October 1992. Measurement techniques to determine compliance as set out in FCC/OST Measurement Procedure MP-5 (1986), *Methods of Measurement of Radio Noise Emissions from Industrial, Scientific and Medical Equipment*, US Department of Commerce, National Technical Information Service, Springfield, VA 22161, February 1986

[43] ITU-R Recommendation 527-1, *Electrical Characteristics of the Surface of the Earth*, International Telecommunication Union, Geneva, 1982

[44] ITU-R Report 879-1, *Methods of Estimating Effective Electrical Characteristics of the Surface of the Earth*, International Telecommunication Union, Geneva, 1986

[45] Macfarlane, I.P., “Error in the Numerical Electromagnetic Code (NEC2) Calculation of Magnetic Field Strength Near Ground”, *Australian telecommunication Research (ATR),* 1990, vol. 24, No.1

[46] Macfarlane, I.P., Fleming, A.H.J., Iskra, S. and Haack, G., “Pilgrims' Progress – Learning to Use the Numerical Electromagnetics Code (NEC) to Calculate Magnetic Field Strength Close to a Sommerfeld Ground”, *Applied Computational Electromagnetics Society (ACES) Journal*, Winter 1990, vol. 5, no. 2

[47] Macfarlane, I.P., addendum to: “Error in the Numerical Electromagnetics Code (NEC2). Calculation of Magnetic Field Strength Near Ground”, *Australian Telecommunication Research (ATR)*, 1990, vol. 24, no. 2

[48] Haack, G.R. and Fleming, A.H.J., “Using the Numerical Electromagnetics Code (NEC) to Calculate Magnetic Field Strength Close to a Sommerfeld Ground”, *Proceedings of the Seventh Annual Review of Progress in Applied Computational Electromagnetics*, Monterey, California, USA, March 18-22, 1991, p 493-506 (Managing Editor: Richard W. Adler, U.S. Naval Postgraduate School, Code EC/AB, Monterey, CA 93943, USA)

[49] CISPR/A/WG1(Hasenpusch/Dunker)04-01, “Investigations of broadcast radio services in Germany”

[50] CISPR/A/WG12(Ad hoc Weight Convenor)05-01, “Possible Effects of Spread-Spectrum-Clock Interference on Wideband Radiocommunication Services”

[51] STECHER, M., “Possible Effects of Spread-Spectrum-Clock Interference on Wideband Radiocommunication Services”, *Proceedings of IEEE Electromagnetic Compatibility Symposium,* Chicago, USA, 2005

[52] CISPR/A/WG1(Stecher-Stenumgaard)03-01, “Weighting of interference according to its effect on digital communication services – results for convolutional codes”

[53] STENUMGAARD, P., “A Promising Solution of How to Evolve Present Radiated Emission Standards in Order to Protect Digital Communication Services”, *Proceeding of IEEE International Symposium on Electromagnetic Compatibility*, Istanbul, Turkey, May 2003

IECNORM.COM : Click to view the full PDF of CISPR TR 16-3:2020 RLV

[54] CISPR/A/WG1(Stecher/Neibig)01-01, “Weighting of Disturbance taking the Effect on Digital Radiocommunication Systems into account, Example: The Effect on GSM-900”

[55] Neibig, U., “Störempfindlichkeit digitaler Mobilfunkempfänger am Beispiel von GSM-900” (Susceptibility of digital mobile receivers for the example of GSM 900)”, *Frequenz*, 2000, no. 54, p 257–262

[56] CISPR/A/WG1(Stecher)00-1, measurement results

[57] CISPR/A/WG1(Stecher)03-1, measurement results

[58] CISPR/A/WG1(Stecher)04-1, measurement results

[59] ITU Recommendation BT.1368, *Planning criteria for digital terrestrial television services in the VHF/UHF bands*, International Telecommunication Union, Geneva

[60] Ryser, H., “Using ferrite clamps on the cables leaving the turntable”, *CISPR/G/WG1(Ryser)96-1*, September 1996

[61] Osabe, K. et al., “A correlation test among measurement sites for radiated EMI using an actual machine and a stabilized power line impedance”, *Zurich EMC Symposium*, 2001

[62] Gronau, G., "TRL Kalibrierung, “*Höchstfrequenztechnik*, Springer Verlag 2001, chapter 8.1.4.3, p 389–408, ISBN 3-540-41790-7

[63] Engen, G.F. and Hoer, C.A., “Thru-Reflect-Line: an improved technique for calibrating the dual six-port automatic network analyser”, *IEEE Transactions on Microwave Theory and Techniques*, 1979, vol. 27, p 987-998

[64] Pozar, D.M., *Microwave Engineering*, 2nd ed., John Wiley & Sons, Inc., New York, 1998, pp. 217-221

[65] Yeo, S.P. and Cheng, M., “Network analyzer calibration for measurements near waveguide cutoff frequency”, *Microwave Journal*, March 1999, p 134-142

[66] Abramowitz M., and Stegun, I.A., *Handbook of mathematical functions*, Dover Publications inc., New York, 1972

[67] Hastings Jr., C., *Approximations for digital computers*, Princeton University Press, Princeton, N.J., 1959

[68] Cooley, JW. and Tukey, JW., An Algorithm for the Machine Calculation of Complex Fourier Series, *Math. Computation*, 1965, vol. 19, p. 297-301

[69] Krug, F. and Russer P., Ultra-fast broadband EMI measurement in time domain using FFT and Periodogram, *IEEE International Symposium On Electromagnetic Compatibility*, 2002, p. 577-582

[70] Oppenheim, AV. and Schafer RW., *Discrete Time Signal Processing*, Prentice-Hall, 1999, ISBN 0-13-214107-8

[71] Braun, S., Aidam, M. and Russer, P., Development of a Multiresolution Time-Domain EMI Measurement System that Fulfills CISPR 16-1, *IEEE International Symposium On Electromagnetic Compatibility*, Chicago, USA, 2005, p. 388-393

IECNORM.COM : Click to view the full PDF of CISPR TR 16-3:2020 RLV

[72] Braun, S., Schneider, R. and Russer, P., A Novel Ultra-fast High Resolution Time-domain EMI Measurement System based on Field Programmable Gate Arrays, EMC Europe 2006, Barcelona, Spain, vol. 1, September 2006, p. 701-705

[73] Harris, FJ., On the Use of Windows for Harmonic Analysis with the Discrete Fourier Transform, Proceedings of the IEEE, January 1978, vol 66, no. 1, p. 51-83

[74] Braun, S., Frech, A., Russer, P., CISPR specification and measurement uncertainty of the time-domain EMI measurement system, *IEEE International Symposium on Electromagnetic Compatibility*, August 2008

[75] Braun, S. and Russer, P., A Low-Noise Multiresolution High-Dynamic Ultra-Broad-Band Time-Domain EMI Measurement System, *IEEE Transactions on Microwave Theory and Techniques*, November 2005, vol. 53, no. 11, p. 3354-3363

[76] Keller, C. and Feser, K., Fast Emission Measurement in Time Domain, *IEEE Transactions on Electromagnetic Compatibility*, November 2007, vol. 49, issue 4, p. 816-824

[77] Krug, F., Braun, S., Kishida, Y. and Russer, P., A novel Digital Quasi-Peak Detector for Time-Domain Measurements, 33rd European Microwave Conference, Munich, Germany, October 2003, p. 1027-1030

[78] Boss, H., Development of a Novel Digital Quasi-Peak Detector for EMI Measurements, Proceedings on EMC Symposium 2001, Zurich, Switzerland

[79] Ristau, D. and Hansen, D., Modulation impact on quasi-peak detector response, IEEE International Symposium On Electromagnetic Compatibility, Austin, TX, USA, August 1997, p. 90-95

[80] Braun, S., Donauer, T. and Russer, P., A real-time time-domain EMI Measurement System for Full Compliance Measurements according to CISPR 16-1-1, IEEE Transactions on Electromagnetic Compatibility, May 2008, vol. 50, issue 2, p. 259-267

[81] Stecher, M., Automated Measurements of Emissions from Equipment and Systems, Proceedings of IEEE EMC Symposium 2002, Minneapolis, USA

[82] J. B. J. Fourier, Theorie analytique de la chaleur, Firmin Didot, 1822

[83] P. L. Dirichlet, Sur la convergence des séries trigonométriques qui servent à représenter une fonction arbitraire entre des limites données, Journal für die reine und angewandte Mathematik 4, p. 157-169, 1829

[84] 3GPP TS 34.121 V3.14.0 (2003-09), 3rd Generation Partnership Project; Technical Specification Group Terminals; Terminal conformance specification; Radio transmission and reception (FDD) (Release 1999), 3GPP Organization Partners

[85] ITU-T Recommendation G.117:1996, *Transmission aspects of unbalance about earth*

[86] ITU-T Recommendation O.9:1999, *Measuring arrangements to assess the degree of unbalance about earth*

[87] DANEFFEL, H.R. and RYSER, H., Problem on the ISDN subscriber S and U interface, International Symposium on Services and Local Access 86, 1986, p. 145-149

IECNORM.COM : Click to view the full PDF of CISPR TR 16-3:2020 RLV

[88] DAVIES, W.S., MACFARLANE, I.P. and BEN-MEIR, D., Potential EMI from ISDN basic access systems, Electronics Letters, Vol. 24, No. 9, April 1988, p. 533-534

[89] KUWABARA, N., AMEMIYA, F. and IDEGUCHI, T., Interference field emission due to unbalance in telecommunication lines, IEEE International Symposium on Electromagnetic Compatibility, Nagoya, Japan, September 1989, p. 487-492

[90] VAN MAURIK, R.M., Potential Common Mode Currents On The ISDN S And T-Interface Caused By Cable Unbalance, IEE Eighth International Conference on Electromagnetic Compatibility, Edinburgh, Scotland, September 21-24 1992, IEE Conference Publication No. 362, p. 202-206

[91] CISPR 15:2005, *Limits and methods of measurement of radio disturbance characteristics of electrical lighting and similar equipment* [9]
CISPR 15:2005/AMD1:2006
CISPR 15:2005/AMD2:2008

[92] S. B. Worm, On the relation between radiated and conducted RF emission tests, *Proceedings 13th International Zurich Symposium on Electromagnetic Compatibility*, February 1999

[93] S.B. Worm, Modeling and experimental investigations of the alternative CDN emission measurement method in CISPR15, *Workshop on Alternative & reference test methods in EMC applications*, 20th Int. Zurich Symposium on EMC, 2009

[94] CISPR/A-F/JTF CDNE(Seoul-Beeckman)11-02, *Results Philips CDNE-RRT*, 2011-10-05

[95] CISPR 16-1-2:2014, *Specification for radio disturbance and immunity measuring apparatus and methods – Part 1-2: Radio disturbance and immunity measuring apparatus – Coupling devices for conducted disturbance measurements*

[96] CISPR 16-4-2:2011, *Specification for radio disturbance and immunity measuring apparatus and methods – Part 4-2: Uncertainties, statistics and limit modelling – Measurement instrumentation uncertainty*
CISPR 16-4-2:2011/AMD1:2014
CISPR 16-4-2:2011/AMD2:2018

[97] CISPR TR 16-4-5:2006, *Specification for radio disturbance and immunity measuring apparatus and methods – Part 4-5: Uncertainties, statistics and limit modelling – Conditions for the use of alternative test methods*
CISPR TR 16-4-5:2006/AMD1:2014

[98] CISPR 15:2013, *Limits and methods of measurement of radio disturbance characteristics of electrical lighting and similar equipment* [10]
CISPR 15:2013/AMD1:2015

[99] CISPR 22:2008, *Information technology equipment – Radio disturbance characteristics – Limits and methods of measurement* [11]

[100] CISPR/A/WG1 LAS tables (Beeckman)15-01, *LAS model and tabular values of LLA figures in Annex C of CISPR 16-1-4*, 2015-01-21

9 This publication was withdrawn and replaced by CISPR 15:2018.

10 This publication was withdrawn and replaced by CISPR 15:2018.

11 This publication was withdrawn and replaced by CISPR 32:2015.

IECNORM.COM : Click to view the full PDF of CISPR TR 16-3:2020 RLV

[101] CISPR/A/WG1 LLAS tables (Beeckman)16-01A, *Updated LLAS model and amended figures and tabular values of LLAS figures in Annex C of CISPR 16-1-4*, 2016-08-18

[102] CISPR 16-1-4:2010, *Specification for radio disturbance and immunity measuring apparatus and methods – Part 1-4: Radio disturbance and immunity measuring apparatus – Antennas and test sites for radiated disturbance measurements*[12]
CISPR 16-1-4:2010/AMD1:2012
CISPR 16-1-4:2010/AMD2:2017

CISPR 16-1-4:2019, *Specification for radio disturbance and immunity measuring apparatus and methods – Part 1-4: Radio disturbance and immunity measuring apparatus – Antennas and test sites for radiated disturbance measurements*
CISPR 16-1-4:2019/AMD1:2020
CISPR 16-1-4:2019/AMD2:20—[13]

[103] J.R. Bergervoet, H. van Veen, *A Large-Loop Antenna for Magnetic Field Measurements*, Proceedings of the 8th International Zürich Symposium on Electromagnetic Compatibility, March 1989, ETH Zentrum – IKT, 8092 Zürich, Switzerland, p. 29-34

[104] CISPR/A/WG1(Goedbloed/van Veen)1, *Proposal for an alternative measuring method of magnetic fields*, November 1987

[105] CISPR/A/WG1(Goedbloed/van Veen)2, *Extension proposal for an alternative measuring method for magnetic fields*, May 1988

[106] CISPR/A/WG1(Campinas/Goedbloed), *Alternative measuring method for magnetic fields – Addendum to CISPR/A/WG1(Goedbloed/van Veen)2*, July 1988

[107] CISPR/A/WG1(Goedbloed/van Veen)3, *Measuring Method for Magnetic Fields in the Frequency Range 9 kHz – 30 MHz, using the Large-Loop Antenna System*, March 1989

[108] CISPR/A/WG1(Goedbloed/Rotterdam), *Conversion of LAS induced current data in H-field data*, September 1993

[109] CISPR/F/WG2(Vrolijk/van Veen)89-03, *Draft-Modification of CISPR 15 (1985); Introduction of radiated field measurements in CISPR 15, Measuring Method*, January 1989

[110] T. Shinozuka, A. Sugiura, A. Nishikata, *Rigorous analysis of a loop antenna system for magnetic interference measurement*, IEICE Trans. Commun., vol. E76-B, no. 1, January 1993

[111] CISPR/F/641/INF, *Request of CISPR F to CISPR A for the development of an uncertainty budget for the loop antenna measurement method in CISPR 16-4-2*, 2014-07-11

[112] J. McLean, H. Sako, A. Medina, R. Sutton, *Operation of the Van Veen Loop in a shielded chamber*, Instrumentation and Measurement Technology Conference (I2MTC), May 2013

IECNORM.COM : Click to view the full PDF of CISPR TR 16-3:2020 RLV

12 This publication was withdrawn and replaced by CISPR 16-1-4:2019.

13 Under preparation. Stage at the time of publication: CISPR CDM 16-1-4:2020.

[113] J. McLean, K. Takizawa, M. Midori, H. Kurihara, R. Sutton, *The Effects of Asymmetry on the operation of the Van Veen Loop*, Proc. of the 2014 International Symposium on Electromagnetic Compatibility (EMC Europe 2014), Gothenburg, Sweden, September 1-4, 2014

[114] J.P. Jackson, *Classical electrodynamics*, John Wiley & Sons, 3rd edition

[115] S. Ramo, J.R. Whinnery, T. Van Duzer, *Fields and Waves in Communication Electronics*, Wiley

[116] H. van Veen, *Correlation between maximum magnetic field strengths and transmitter distances*, Philips Lighting Central Development Laboratories Technical Note VLc TM 2037/87, 1987-08-21

[117] CISPR/A/WG1 LAS Tables (Midori-McLean-Kurihara-Fujii-Shinozuka)15-02, *Proposal of tabular values of validation factor and conversion factor for LAS*, August 2015

[118] CISPR A WG1 paper Schwarzbeck (Stresa meeting 2015), *Loop Antenna System CISPR 16-1-4 Ed. 3*

[119] CISPR/A/WG1 LAS Tables (Midori-Kurihara-Fujii-Shinozuka)15-04, *Verification of the calculation model of validation factor and the tolerance of validation factor for LAS*, January 2016

[120] Matlab Central File Exchange, *Large-loop antenna system toolbox*, https://nl.mathworks.com/matlabcentral/fileexchange/65858-large-loop-antenna-system-toolbox?s_tid=srchtitle

[121] CISPR 16-1:1993, *Specification for radio disturbance and immunity measuring apparatus and methods – Part 1: Radio disturbance and immunity measuring apparatus*[14]

[122] CISPR 15:1985, *Limits and methods of measurement of radio interference characteristics of fluorescent lamps and luminaires*[15]

[123] CISPR 15:1992, *Limits and methods of measurement of radio disturbance characteristics of electrical lighting and similar equipment*[16]

[124] CISPR TR 16-3:2000, *Specification for radio disturbance and immunity measuring apparatus and methods – Part 3: Reports and recommendations of CISPR*
CISPR TR 16-3:2010/AMD1:2002[17]

IECNORM.COM : Click to view the full PDF of CISPR TR 16-3:2020 RLV

14 This publication was withdrawn.

15 This publication was withdrawn.

16 This publication was withdrawn.

17 1st edition (2000). This 1st edition has been replaced in 2020 by the current 4th Edition CISPR TR 16-3, Specification for radio disturbance and immunity measuring apparatus and methods – Part 3: CISPR technical reports.

# CISPR TR 16-3

Edition 4.0 2020-10

# TECHNICAL REPORT

IECNORM.COM : Click to view the full PDF of CISPR TR 16-3:2020 RLV

colour inside

INTERNATIONAL SPECIAL COMMITTEE ON RADIO INTERFERENCE

## Specification for radio disturbance and immunity measuring apparatus and methods –
## Part 3: CISPR technical reports



# CONTENTS

FOREWORD ..... 16
1 Scope ..... 18
2 Normative references ..... 18
3 Terms, definitions and abbreviated terms ..... 19
3.1 Terms and definitions ..... 19
3.2 Abbreviated terms ..... 22
4 Technical reports ..... 23
4.1 Correlation between measurements made with apparatus having characteristics differing from CISPR characteristics and measurements made with CISPR apparatus ..... 23
4.1.1 General ..... 23
4.1.2 Critical interference-measuring instrument parameters ..... 23
4.1.3 Impulse interference – correlation factors ..... 25
4.1.4 Random noise ..... 27
4.1.5 The root mean square (RMS) detector ..... 27
4.1.6 Discussion ..... 27
4.1.7 Application to typical noise sources ..... 27
4.1.8 Conclusions ..... 28
4.2 Interference simulators ..... 29
4.2.1 General ..... 29
4.2.2 Types of interference signals ..... 29
4.2.3 Circuits for simulating broadband interference ..... 30
4.3 Relationship between limits for open-area test site and the reverberation chamber ..... 34
4.3.1 General ..... 34
4.3.2 Correlation between measurement results of the reverberation chamber and OATS ..... 34
4.3.3 Limits for use with the reverberation chamber method ..... 35
4.3.4 Procedure for the determination of the reverberation chamber limit ..... 35
4.4 Characterization and classification of the asymmetrical disturbance source induced in telephone subscriber lines by AM broadcasting transmitters in the LW, MW and SW bands ..... 36
4.4.1 General ..... 36
4.4.2 Experimental characterization ..... 36
4.4.3 Prediction models and classification ..... 46
4.4.4 Characterization of the immunity-test disturbance source ..... 50
4.5 Predictability of radiation in vertical directions at frequencies above 30 MHz ..... 57
4.5.1 Summary ..... 57
4.5.2 Range of application ..... 58
4.5.3 General ..... 58
4.5.4 Method used to calculate field patterns in the vertical plane ..... 60
4.5.5 Limitations of predictability of radiation at elevated angles ..... 61
4.5.6 Differences between the fields over a real ground and the fields over a perfect conductor ..... 89
4.5.7 Uncertainty ranges ..... 95
4.5.8 Conclusions ..... 97

IECNORM.COM : Click to view the full PDF of CISPR TR 16-3:2020 RLV

4.6 The predictability of radiation in vertical directions at frequencies up to 30 MHz ..... 98
4.6.1 Range of application ..... 98
4.6.2 General ..... 99
4.6.3 Method of calculation of the vertical radiation patterns ..... 100
4.6.4 The source models ..... 100
4.6.5 Electrical constants of the ground ..... 102
4.6.6 Predictability of radiation in vertical directions ..... 102
4.6.7 Conclusions ..... 110
4.6.8 Figures associated with predictability of radiation in vertical directions ..... 111
4.7 Correlation between amplitude probability distribution (APD) characteristics of disturbance and performance of digital communication systems ..... 146
4.7.1 General ..... 146
4.7.2 Influence on a wireless LAN system ..... 146
4.7.3 Influence on a Bluetooth system ..... 149
4.7.4 Influence on a W-CDMA system ..... 153
4.7.5 Influence on Personal Handy Phone System (PHS) ..... 156
4.7.6 Quantitative correlation between noise parameters and system performance ..... 160
4.7.7 Quantitative correlation between noise parameters of repetition pulse and system performance of PHS and W-CDMA (BER) ..... 163
4.8 Background material on the definition of the RMS-average weighting detector for measuring receivers ..... 166
4.8.1 General – purpose of weighted measurement of disturbance ..... 166
4.8.2 General principle of weighting – the CISPR quasi-peak detector ..... 167
4.8.3 Other detectors defined in CISPR 16-1-1 ..... 167
4.8.4 Procedures for measuring pulse weighting characteristics of digital radiocommunications services ..... 168
4.8.5 Theoretical studies ..... 171
4.8.6 Experimental results ..... 173
4.8.7 Effects of spread-spectrum clock interference on wideband radiocommunication signal reception ..... 191
4.8.8 Analysis of the various weighting characteristics and proposal of a weighting detector ..... 192
4.8.9 Properties of the RMS-average weighting detector ..... 194
4.9 Common mode absorption devices (CMAD) ..... 196
4.9.1 General ..... 196
4.9.2 CMAD as a two-port device ..... 198
4.9.3 Measurement of CMAD ..... 202
4.10 Background on the definition of the FFT-based receiver ..... 212
4.10.1 General ..... 212
4.10.2 Tuned selective voltmeters and spectrum analyzers ..... 213
4.10.3 General principle of a tuned selective voltmeter ..... 213
4.10.4 FFT-based receivers – digital signal processing ..... 214
4.10.5 Measurement errors specific to FFT processing ..... 218
4.10.6 FFT-based receivers – examples ..... 220
4.11 Parameters of signals at telecommunication ports ..... 233
4.11.1 General ..... 233
4.11.2 Estimation of common mode disturbance levels ..... 234
4.12 Background on CDNE equipment and measurement method ..... 235

IECNORM.COM : Click to view the full PDF of CISPR TR 16-3:2020 RLV

4.12.1 General ..... 235
4.12.2 Historical overview ..... 236
4.12.3 From CDN to CDNE ..... 240
4.13 Background on LLAS, validation and measurement method ..... 243
4.13.1 General ..... 243
4.13.2 Historical overview ..... 243
4.13.3 Models and equations for the LLAS method ..... 244
5 Background and history of CISPR ..... 244
5.1 The history of CISPR ..... 244
5.1.1 The early years: 1934-1984 ..... 244
5.1.2 The division of work ..... 246
5.1.3 The computer years: 1984 to 1998 ..... 247
5.1.4 The people in CISPR ..... 247
5.2 Historical background to the method of measurement of the interference power produced by electrical household and similar appliances in the VHF range ..... 248
5.2.1 Historical detail ..... 248
5.2.2 Development of the method ..... 249
Annex A (informative) Derivation of the formula ..... 251
Annex B (informative) The field-strength distribution ..... 255
B.1 General ..... 255
B.2 $H_o$-field expressions ..... 255
B.3 $H_i$ field expressions ..... 257
B.4 $E_o$-field expressions ..... 258
Annex C (informative) The induced asymmetrical open-circuit voltage distribution ..... 259
C.1 General ..... 259
C.2 $H$-field-based relations ..... 259
C.3 $E$-field-based relations ..... 261
Annex D (informative) The outlet-voltage distribution ..... 262
D.1 General ..... 262
D.2 $H$-field-based relations ..... 262
D.3 $E$-field-based relations ..... 263
Annex E (informative) Some mathematical relations ..... 264
E.1 General ..... 264
E.2 The error function ..... 264
E.3 Application to the lognormal distribution ..... 265
Annex F (informative) Harmonic fields radiated at elevated angles from 27 MHz ISM equipment over real ground ..... 266
Annex G (informative) Models and equations associated with the LLAS method ..... 272
G.1 General ..... 272
G.2 Response of an LAS to a magnetic field dipole ..... 272
G.2.1 Magnetic field strength model of a disturbance source ..... 272
G.2.2 Response of an LAS to a magnetic field dipole ..... 273
G.2.3 Sensitivity of an LLAS for different diameters ..... 277
G.2.4 Limitation of application of the relative sensitivity curves ..... 278
G.3 Response of LLAS to the LLAS verification dipole ..... 279
G.3.1 Relation of LLA current and voltage applied to the LLAS verification dipole ..... 279

IECNORM.COM : Click to view the full PDF of CISPR TR 16-3:2020 RLV

G.3.2 Calculation of mutual inductance: the original method ..... 280
G.3.3 Calculation of mutual inductance: the improved method ..... 280
G.3.4 Derivation of the equation for the reference validation factor ..... 280
G.3.5 Replication of the original version of the reference validation factor ..... 283
G.3.6 Calculation of the improved reference validation factor ..... 283
G.3.7 NEC2 method ..... 285
G.4 Magnetic field strength of a magnetic field dipole above a ground plane ..... 286
G.4.1 Model ..... 286
G.4.2 Replication of Figure C.10 ..... 287
G.4.3 Conversion factors for calculating magnetic field strength at other distances ..... 289
G.5 LLAS validation criterion ..... 290
Bibliography ..... 291

Figure 1 – Relative response of various detectors to impulse interference ..... 24
Figure 2 – Pulse rectification coefficient $P(\alpha)$ ..... 25
Figure 3 – Pulse repetition frequency ..... 26
Figure 4 – Block diagram and waveforms of a simulator generating noise bursts ..... 32
Figure 5 – Block diagram of a simulator generating noise bursts according to the pulse principle ..... 33
Figure 6 – Details of a typical output stage ..... 34
Figure 7 – Scatter plot of the measured outdoor magnetic field strength $H_o$ (dBμA/m) versus the calculated outdoor magnetic field strength $H_c$ dB(μA/m) ..... 38
Figure 8 – Measured outdoor magnetic versus distance, and probability of the building-effect parameter ..... 39
Figure 9 – Normal probability plot of the building-effect parameter $A_b$ dB ..... 40
Figure 10 – Scatter plot of the outdoor antenna factor $G_o$ dB(Ωm) versus the indoor antenna factor $G_i$ ..... 41
Figure 11 – Normal probability plots of the antenna factors ..... 42
Figure 12 – Normal probability plot of the equivalent asymmetrical resistance $R_a$ dB(Ω) ..... 45
Figure 13 – Examples of the frequency dependence of some parameters ..... 46
Figure 14 – Example of the frequency histogram $\Delta N(E_o,\Delta E_o)$ ..... 51
Figure 15 – Example of $n_m(E_o)$, i.e. the distribution of the outlets experiencing a maximum field strength $E_o$ resulting from a given number of transmitters in (or near) the respective geographical region ..... 52
Figure 16 – Example of the number of outlets with an induced asymmetrical open-circuit voltage $U_L \leq U_h \leq U_{max}$ = 79 V (see Table 10) ..... 54
Figure 17 – Examples of number (left-hand scale) and relative number (right-hand scale) of outlets with $U_L \leq U_h \leq U_{max}$ ..... 55
Figure 18 – Vertical polar patterns of horizontally polarized $E_x$ field strengths emitted around small vertical loop (horizontal magnetic dipole) over three different types of real ground ..... 63
Figure 19 – Height scan patterns of vertically oriented $E_z$ field strengths emitted from small vertical loop (horizontal magnetic dipole) over three different types of real ground ..... 63
Figure 20 – Vertical polar patterns of horizontally polarized $E_x$ field strengths emitted around small vertical loop (horizontal magnetic dipole), over three different types of real ground ..... 65

IECNORM.COM : Click to view the full PDF of CISPR TR 16-3:2020 RLV

Figure 21 – Vertical polar patterns of vertically oriented $E_z$ field strengths emitted around small vertical loop (horizontal magnetic dipole) over three different types of real ground ..... 65

Figure 22 – Height scan patterns of vertically oriented $E_z$ field strengths emitted at 1 000 MHz from the small vertical loop (horizontal magnetic dipole), at horizontal distance of 10 m, 30 m and 300 m in the Z-X plane over three different types of real ground ..... 66

Figure 23 – Vertical polar patterns of horizontally polarized $E_x$ and vertically oriented $E_z$ field strengths emitted around small horizontal electric dipole, in Y-Z and Z-X planes respectively ..... 68

Figure 24 – Height scan patterns of horizontally polarized $E_x$ field strengths emitted from small horizontal electric dipole ..... 68

Figure 25 – Vertical polar patterns of horizontally polarized $E_x$ and vertically oriented $E_z$ field strengths emitted around small horizontal electric dipole in Y-Z and Z-X planes respectively ..... 71

Figure 26 – Height scan patterns of horizontally polarized $E_x$ field strengths emitted small horizontal electric dipole ..... 71

Figure 27 – Vertical polar patterns of horizontally polarized $E_x$ and vertically oriented $E_z$ field strengths emitted around small vertical loop (horizontal magnetic dipole) in Y-Z and Z-X planes respectively ..... 72

Figure 28 – Height scan patterns of vertically oriented $E_z$ and horizontally oriented $E_x$ field strengths emitted from small vertical loop (horizontal magnetic dipole) ..... 72

Figure 29 – Vertical polar patterns of vertically oriented $E_z$ and horizontally oriented $E_x$ field strengths emitted around small vertical electric dipole ..... 75

Figure 30 – Height scan patterns of vertically oriented $E_z$ and horizontally oriented $E_x$ field strengths emitted from small vertical electric dipole ..... 75

Figure 31 – Vertical polar patterns of horizontally polarized $E_x$ and vertically oriented $E_z$ field strengths emitted around small vertical loop (horizontal magnetic dipole) in Y-Z and Z-X planes respectively ..... 76

Figure 32 – Height scan patterns of vertically oriented $E_z$ and horizontally oriented $E_x$ field strengths emitted from small vertical loop (horizontal magnetic dipole) ..... 76

Figure 33 – Vertical polar patterns of horizontally polarized $E$-field strength emitted around small horizontal loop (vertical magnetic dipole) ..... 77

Figure 34 – Height scan patterns of horizontally polarized $E$-field strength emitted from small horizontal loop (vertical magnetic dipole) ..... 77

Figure 35 – Vertical polar patterns of vertically oriented $E_z$ and horizontally oriented $E_x$ field strengths emitted around small vertical electric dipole ..... 80

Figure 36 – Height scan patterns of vertically oriented $E_z$ and horizontally oriented $E_x$ field strengths emitted from the small vertical electric dipole ..... 80

Figure 37 – Vertical polar patterns of horizontally polarized $E_x$ and vertically oriented $E_z$ field strengths emitted around small vertical loop (horizontal magnetic dipole) in Y-Z and Z-X planes respectively ..... 81

Figure 38 – Height scan patterns of vertically oriented $E_z$ and horizontally oriented $E_x$ field strengths emitted from small vertical loop (horizontal magnetic dipole) ..... 81

Figure 39 – Vertical polar patterns of horizontally polarized $E$-field strength emitted around small horizontal loop (vertical magnetic dipole) ..... 82

Figure 40 – Height scan patterns of horizontally polarized $E$-field strength emitted from small horizontal loop (vertical magnetic dipole) ..... 82

Figure 41 – Vertical polar patterns of horizontally polarized $E$-field strength emitted around the small horizontal loop (vertical magnetic dipole) ..... 85

Figure 42 – Height scan patterns of horizontally polarized $E$-field strength emitted from small horizontal loop (vertical magnetic dipole) ..... 85

IECNORM.COM : Click to view the full PDF of CISPR TR 16-3:2020 RLV

Figure 43 – Height scan patterns of horizontally polarized $E$-field strength emitted from small horizontal loop (vertical magnetic dipole) ..... 89
Figure 44 – Height scan patterns of the vertical component of the $E$-fields emitted from a small vertical electric dipole ..... 92
Figure 45 – Height scan patterns of the vertical component of the $E$-fields emitted from a small vertical electric dipole ..... 92
Figure 46 – Height scan patterns of the horizontally polarized $E$-fields emitted in the vertical plane normal to the axis of a small horizontal electric dipole ..... 94
Figure 47 – Height scan patterns of the horizontally polarized $E$-fields emitted in the vertical plane normal to the axis of a small horizontal electric dipole ..... 94
Figure 48 – Ranges of uncertainties in the predictability of radiation in vertical directions from electrically small sources located at a height of 1 m or 2 m above ground ..... 96
Figure 49 – Ranges of uncertainties in the predictability of radiation in vertical directions from electrically small sources located at a height of 1 m or 2 m above ground ..... 96
Figure 50 – Ranges of uncertainties in the predictability of radiation in vertical directions from electrically small sources located at a height of 1 m or 2 m above ground ..... 97
Figure 51 – Geometry of the small vertical electric dipole model ..... 101
Figure 52 – Geometry of the small horizontal electrical dipole model ..... 101
Figure 53 – Geometry of the small horizontal magnetic dipole model (small vertical loop) ..... 101
Figure 54 – Geometry of the small vertical magnetic dipole model (small horizontal loop) ..... 101
Figure 55 – Ranges of errors in the predictability of radiation in vertical directions from electrically small sources located close to the ground, based on measurements of the horizontally oriented $H$-field near ground at a distance of 30 m from the sources ..... 109
Figure 56 – Ranges of errors in the predictability of radiation in vertical directions from electrically small sources located close to the ground, based on measurements of the horizontally oriented $H$-field at the ground supplemented with measurements of the vertically oriented $H$-field in a height scan up to 6 m at a distance of 30 m from the sources ..... 110
Figure 57 – Vertical radiation patterns of horizontally oriented $H$-fields emitted by a small vertical electric dipole located close to the ground ..... 112
Figure 58 – Vertical radiation patterns of horizontally oriented $H$-fields emitted by a small vertical electric dipole located close to the ground ..... 112
Figure 59 – Vertical radiation patterns of $E$-fields emitted by a small vertical electric dipole located close to the ground ..... 113
Figure 60 – Vertical radiation patterns of the $E$-fields emitted by a small vertical electric dipole located close to the ground ..... 113
Figure 61 – Vertical radiation patterns of the $H$-fields emitted by a small horizontal electric dipole located close to the ground ..... 115
Figure 62 – Influence of a wide range of values of the electrical constants of the ground on the vertical radiation patterns of the horizontally oriented $H$-fields emitted by a small horizontal electric dipole located close to the ground ..... 115
Figure 63 – Vertical radiation patterns of the horizontally oriented $H$-fields emitted by a small horizontal electric dipole located close to the ground ..... 116
Figure 64 – Vertical radiation patterns of the $E$-fields emitted by a small horizontal electric dipole located close to the ground ..... 116

IECNORM.COM : Click to view the full PDF of CISPR TR 16-3:2020 RLV

Figure 65 – Vertical radiation patterns of the $E$-fields emitted by a small horizontal electric dipole located close to the ground ..... 117
Figure 66 – Vertical radiation patterns of $H$-fields emitted by small horizontal magnetic dipole (vertical loop) located close to ground ..... 117
Figure 67 – Vertical radiation patterns of the horizontally oriented $H$-fields emitted by a small horizontal magnetic dipole (vertical loop) located close to the ground ..... 118
Figure 68 – Vertical radiation patterns of the horizontally oriented $H$-fields emitted by a small horizontal magnetic dipole (vertical loop) located close to the ground ..... 118
Figure 69 – Vertical radiation patterns of the $E$-fields emitted by a small horizontal magnetic dipole (vertical loop) located close to the ground ..... 119
Figure 70 – Vertical radiation patterns of the $E$-fields emitted by a small horizontal magnetic dipole (vertical loop) located close to the ground ..... 119
Figure 71 – Vertical radiation patterns of the $H$-fields emitted by a small vertical magnetic dipole (horizontal loop) located close to the ground ..... 121
Figure 72 – Vertical radiation patterns of the $H$-fields emitted by a small vertical magnetic dipole (horizontal loop) located close to the ground ..... 121
Figure 73 – Vertical radiation patterns of the $H$-fields emitted by a small vertical magnetic dipole (horizontal loop) located close to the ground ..... 122
Figure 74 – Vertical radiation patterns of the $H$-fields emitted by a small vertical magnetic dipole (horizontal loop) located close to the ground ..... 122
Figure 75 – Vertical radiation pattern of the $E$-field emitted by a small vertical magnetic dipole (horizontal loop) located close to the ground ..... 123
Figure 76 – Vertical radiation patterns of the $E$-fields emitted by a small vertical magnetic dipole (horizontal loop) located close to the ground ..... 123
Figure 77 – Vertical radiation patterns of the horizontally oriented $H$-fields emitted by a small vertical electric dipole located close to the ground ..... 124
Figure 78 – Vertical radiation patterns of the $E$-fields emitted by a small vertical electric dipole located close to the ground ..... 124
Figure 79 – Vertical radiation patterns of the $E$-fields emitted by a small vertical electric dipole located close to the ground ..... 125
Figure 80 – Vertical radiation patterns of the $H$-fields emitted by a small horizontal electric dipole located close to the ground ..... 125
Figure 81 – Vertical radiation patterns of the horizontally oriented $H$-fields emitted by a small horizontal electric dipole located close to the ground ..... 126
Figure 82 – Vertical radiation patterns of the $E$-fields emitted by a small horizontal electric dipole located close to the ground ..... 126
Figure 83 – Vertical radiation patterns of the $E$-fields emitted by a small horizontal electric dipole located close to the ground ..... 128
Figure 84 – Vertical radiation patterns of the $H$-fields emitted by a small horizontal magnetic dipole (vertical loop) located close to the ground ..... 128
Figure 85 – Vertical radiation patterns of the horizontally oriented $H$-fields emitted by a small horizontal magnetic dipole (vertical loop) located close to the ground ..... 129
Figure 86 – Vertical radiation patterns of the horizontally oriented $H$-fields emitted by a small horizontal magnetic dipole (vertical loop) located close to the ground ..... 129
Figure 87 – Vertical radiation patterns of the $E$-fields emitted by a small horizontal magnetic dipole (vertical loop) located close to the ground ..... 130
Figure 88 – Vertical radiation patterns of the $E$-fields emitted by a small horizontal magnetic dipole (vertical loop) located close to the ground ..... 130
Figure 89 – Vertical radiation patterns of the $H$-fields emitted by a small vertical magnetic dipole (horizontal loop) located close to the ground ..... 131

IECNORM.COM : Click to view the full PDF of CISPR TR 16-3:2020 RLV

Figure 90 – Vertical radiation patterns of the $H$-fields emitted by a small vertical magnetic dipole (horizontal loop) located close to the ground ..... 131
Figure 91 – Vertical radiation patterns of the $H$-fields emitted by a small vertical magnetic dipole (horizontal loop) located close to the ground ..... 132
Figure 92 – Vertical radiation patterns of the $E$-fields emitted by a small vertical magnetic dipole (horizontal loop) located close to the ground ..... 132
Figure 93 – Vertical radiation patterns of the horizontally oriented $H$-fields emitted by a small vertical electric dipole located close to the ground ..... 133
Figure 94 – Vertical radiation patterns of the $E$-fields emitted by a small vertical electric dipole located close to the ground ..... 133
Figure 95 – Vertical radiation patterns of the $E$-fields emitted by a small vertical electric dipole located close to the ground ..... 135
Figure 96 – Vertical radiation patterns of the $H$-fields emitted by a small horizontal electric dipole located close to the ground ..... 135
Figure 97 – Vertical radiation patterns of the $E$-fields emitted by a small horizontal electric dipole located close to the ground ..... 136
Figure 98 – Vertical radiation patterns of the $E$-fields emitted by a small horizontal electric dipole located close to the ground ..... 136
Figure 99 – Vertical radiation patterns of the $H$-field emitted by a small horizontal magnetic dipole (vertical loop) located close to the ground ..... 138
Figure 100 – Vertical radiation patterns of the vertically polarized $E$-fields emitted by a small horizontal magnetic dipole (vertical loop) located close to the ground ..... 138
Figure 101 – Vertical radiation patterns of the $H$-field emitted by a small vertical magnetic dipole (horizontal loop) located close to the ground ..... 139
Figure 102 – Vertical radiation patterns of the $E$-fields emitted by a small vertical magnetic dipole (horizontal loop) located close to the ground ..... 139
Figure 103 – Vertical radiation patterns of the horizontally oriented $H$-fields emitted by a small vertical electric dipole located close to the ground ..... 140
Figure 104 – Vertical radiation patterns of the vertically polarized $E$-fields emitted by a small vertical electric dipole located close to the ground ..... 140
Figure 105 – Vertical radiation patterns of the $H$-fields emitted by a small horizontal electric dipole located close to the ground ..... 141
Figure 106 – Vertical radiation patterns of the horizontally oriented $H$-fields emitted by a small horizontal electric dipole located close to the ground ..... 141
Figure 107 – Influence of a wide range of values of the electrical constants of the ground on the vertical radiation patterns of the horizontally oriented $H$-fields emitted by a small horizontal electric dipole located close to the ground ..... 142
Figure 108 – Vertical radiation patterns of the vertically polarized $E$-fields emitted by a small horizontal electric dipole located close to the ground ..... 142
Figure 109 – Vertical radiation patterns of the $H$-fields emitted by a small horizontal magnetic dipole (vertical loop) located close to the ground ..... 144
Figure 110 – Vertical radiation patterns of the vertically polarized $E$-fields emitted by a small horizontal magnetic dipole (vertical loop) located close to the ground ..... 144
Figure 111 – Vertical radiation patterns of the $H$-fields emitted by a small vertical magnetic dipole (horizontal loop) located close to the ground ..... 145
Figure 112 – Vertical radiation patterns of the $E$-fields emitted by a small vertical magnetic dipole (horizontal loop) located close to the ground ..... 145
Figure 113 – Set-up for measuring communication quality degradation of a wireless LAN .. 146
Figure 114 – APD characteristics of disturbance ..... 148
Figure 115 – Wireless LAN throughput influenced by noise ..... 149

IECNORM.COM : Click to view the full PDF of CISPR TR 16-3:2020 RLV

Figure 116 – Set-up for measuring the communication quality degradation of Bluetooth ..... 150
Figure 117 – APD of disturbance of actual MWO (2 441MHz) ..... 150
Figure 118 – APD characteristics of disturbance (2 460 MHz) ..... 151
Figure 119 – Throughput of Bluetooth influenced by noise ..... 153
Figure 120 – Set-up for measuring the BER of W-CDMA ..... 154
Figure 121 – APD characteristics of disturbance ..... 155
Figure 122 – BER of W-CDMA caused by radiation noise ..... 156
Figure 123 – Set-up for measuring the PHS throughput ..... 157
Figure 124 – Set-up for measuring the BER of PHS ..... 157
Figure 125 – APD characteristics of disturbance ..... 158
Figure 126 – PHS throughput caused by radiation ..... 159
Figure 127 – BER of PHS caused by radiation noise ..... 160
Figure 128 – Correlation of the disturbance voltages with the system performance ($C/N_0$) ..... 161
Figure 129 – Correlation of the disturbance voltages with the system performance ..... 161
Figure 130 – Correlation of the disturbance voltages with the system performance ..... 162
Figure 131 – Correlation of the disturbance voltages with the system performance ($C/N_0$) ..... 162
Figure 132 – Correlation of the disturbance voltages with the system performance ($C/N_0$) ..... 163
Figure 133 – Experimental set-up for measuring communication quality degradation of a PHS or W-CDMA ..... 163
Figure 134 – Simulation set-up for estimating communication quality degradation of a PHS or W-CDMA ..... 164
Figure 135 – APD of pulse disturbance ..... 164
Figure 136 – BER degradation of PHS and W-CDMA caused by repetition pulse (Carrier power, –35 dBm) ..... 165
Figure 137 – Evaluation method of the correlation between BER and APD ..... 165
Figure 138 – Correlation between measured $\Delta L_{BER}$ and $\Delta L_{APD}$ ..... 166
Figure 139 – Correlation between measured $p_{BER}$ and $p_{APD}$ ..... 166
Figure 140 – Weighting curves of quasi-peak measuring receivers for the different frequency ranges as defined in CISPR 16-1-1 ..... 167
Figure 141 – Weighting curves for peak, quasi-peak, RMS and linear average detectors for CISPR bands C and D ..... 168
Figure 142 – Test setup for the measurement of the pulse weighting characteristics of a digital radiocommunication system ..... 169
Figure 143 – Example of an interference spectrum: pulse modulated carrier with a pulse duration of 0,2 μs and a PRF < 10 kHz ..... 170
Figure 144 – The RMS and peak levels for constant BEP for three $K$ = 3, convolutional codes of different rate ..... 172
Figure 145 – The RMS and peak levels for constant BEP for two rate ½, convolutional code ..... 173
Figure 146 – Test setup for the measurement of weighting curves for Digital Radio Mondiale (DRM) ..... 175
Figure 147 – Weighting characteristics for DRM signals for various pulse widths of the pulse-modulated carrier ..... 176

IECNORM.COM : Click to view the full PDF of CISPR TR 16-3:2020 RLV

Figure 148 – Weighting characteristics for DRM protection level 0: average of results for two receivers ..... 177
Figure 149 – Weighting characteristics for DRM protection level 1: average of results for two receivers ..... 177
Figure 150 – Weighting characteristics for DVB-T with 64 QAM 2k, $CR$ 3/4 (as used in France and UK) ..... 179
Figure 151 – Weighting characteristics for DVB-T with 64 QAM 8k, $CR$ 3/4 (as used in Spain) ..... 180
Figure 152 – Weighting characteristics for DVB-T with 16 QAM 8k, $CR$ 2/3 (as used in Germany) ..... 180
Figure 153 – Average weighting characteristics of 6 receiver types for DVB-T with 16QAM ..... 181
Figure 154 – Average weighting characteristics of 6 receiver types for DVB-T with 64QAM ..... 181
Figure 155 – Weighting characteristics for DAB (signal level -71 dBm) with a flat response down to approximately 1 kHz ..... 182
Figure 156 – Weighting characteristics for DAB: average of two different commercial receiver types ..... 183
Figure 157 – Weighting characteristics for TETRA (signal level –80 dBm) for a code rate of 1 ..... 184
Figure 158 – Weighting characteristics for RBER 1b of GSM (signal level –90 dBm) ..... 185
Figure 159 – Weighting characteristics for RBER 2 of GSM ..... 185
Figure 160 – Carrier-to-interference improvements with decreasing PRF in dB computed for GSM using COSSAP ..... 186
Figure 161 – RMS and quasi-peak values of pulse level for constant effect on FM radio reception ..... 186
Figure 162 – Weighting characteristics for RBER 1b of GSM (signal level –90 dBm) ..... 187
Figure 163 – Weighting characteristics for DECT (signal level –83 dBm) ..... 188
Figure 164 – Weighting characteristics for IS-95 (signal level -97 dBm) with comparatively high immunity to interference ..... 189
Figure 165 – Weighting characteristics for J-STD 008 (signal level –97 dBm) ..... 189
Figure 166 – Weighting characteristics for the Frame Error Ratio (FER) of CDMA2000 (measured at a receive signal level of –112 dBm) for a low data rate of 9,6 kb/s ..... 190
Figure 167 – Weighting characteristics for the Frame Error Ratio (FER) of CDMA2000 (measured at a receive signal level of –106 dBm) for two different data rates (9,6 kb/s and 76,8 kb/s) ..... 190
Figure 168 – The proposed RMS-average detector for CISPR Bands C and D with a corner frequency of 100 Hz ..... 193
Figure 169 – RMS-average detector function by using an RMS detector followed by a linear average detector and peak reading ..... 193
Figure 170 – RMS-average weighting functions for CISPR Bands A, B, C/D and E for the shortest pulse widths allowed by the measurement bandwidths ..... 194
Figure 171 – Shift of the RMS-average weighting function for CISPR band C/D by using a bandwidth of 1 MHz instead of 120 kHz, if the shortest possible pulse widths are applied ..... 195
Figure 172 – Example of a simple EUT model ..... 197
Figure 173 – Representation of a CMAD as a two-port device ..... 198
Figure 174 – Conformal mapping between $z$-plane and $f$-plane ..... 201

IECNORM.COM : Click to view the full PDF of CISPR TR 16-3:2020 RLV

Figure 175 – Conversion from 50 Ω coaxial system to the geometry of the two-port device-under-test ..... 203
Figure 176 – Basic model for the TRL calibration ..... 204
Figure 177 – The four calibration configurations necessary for the TRL calibration ..... 205
Figure 178 – Measurement of CMAD characteristics ..... 209
Figure 179 – Preliminary measurements of the test set-up ..... 211
Figure 180 – Position of the reference planes for the measurement with SOLT calibration and $ABCD$ transformation to $Z_{ref}$ level ..... 212
Figure 181 – Superheterodyne EMI receiver ..... 214
Figure 182 – An example spectrogram $Z[m,k]$ ..... 216
Figure 183 – Sidelobe effect due to the finite length of window ..... 218
Figure 184 – Measurement error for a single pulse ..... 219
Figure 185 – IF signal for different overlapping factors for the same sequence of pulses ..... 220
Figure 186 – FFT-based baseband system ..... 221
Figure 187 – Real-time FFT-based measuring instrument ..... 222
Figure 188 – Digital down-converter ..... 222
Figure 189 – Short time fast Fourier transform – An example of implementation ..... 223
Figure 190 – Floating-point analogue-to-digital conversion ..... 223
Figure 191 – Example of a 120 kHz Gaussian filter ..... 224
Figure 192 – Essential parts of an FFT-based heterodyne receiver ..... 225
Figure 193 – Dynamic range for broadband emission as measured with the peak detector ..... 227
Figure 194 – Set-up of FFT-based system type 2 ..... 227
Figure 195 – FFT Software (“FFTemi”) screen shot ..... 230
Figure 196 – Example of pulse generator measurement with antenna ..... 231
Figure 197 – Radiated emission measurement of a motor – peak detector ..... 231
Figure 198 – Angular characterization of a PC ..... 232
Figure 199 – Example FFT IF analysis display ..... 233
Figure 200 – Equivalent radiated measurement methods (30 MHz to 300 MHz) ..... 237
Figure 201 – Measured relationship between field strength $E_z$ and CM current $I_{cm}$ for various termination resistances $R$ ..... 237
Figure 202 – Modelled relationship between field strength $E_z$ and CM current $I_{cm}$ using EUT height 0,8 m, measurement distance 3 m, receive antenna height 1 m ..... 239
Figure 203 – Limit for the terminal voltage at the CDN ..... 239
Figure 204 – Results of a Philips 11-lab internal CDN RRT using an artificial class 1 EUT – expanded uncertainty nearly 10 dB ..... 241
Figure 205 – Block diagram for CDNE-measurement method ..... 242
Figure A.1 – Example plot using the expression $P_t + G = P_q + 2$ ..... 252
Figure A.2 – Examples of a number of microwaves measured for $P_q$ and $P_t$ ..... 254
Figure B.1 – Definition of the ring-shaped area round the transmitter $T$ ..... 256
Figure C.1 – The permissible ranges of $U_h$ and $G$ are within the polygon $\{G_L,U_a\}$, $\{G_L,U_b\}$, $\{G_U,U_d\}$, $\{G_l,U_c\}$ and $\{G_L,U_a\}$. For the given value $U_L$ the double-shaded area represents $pr\{U_h \geq U_L\}$ ..... 260

IECNORM.COM : Click to view the full PDF of CISPR TR 16-3:2020 RLV

Figure F.1 – Vertical radiation patterns of horizontally polarized fields, 109 MHz, 300 m scan radius (adapted from [34]) ..... 268
Figure F.2 – Vertical radiation patterns of horizontally polarized fields, 109 MHz, 300 m scan radius (adapted from [34]) ..... 269
Figure F.3 – Vertical radiation patterns of horizontally polarized fields, 109 MHz, 300 m scan radius (adapted from [34]) ..... 270
Figure F.4 – Vertical radiation patterns of horizontally polarized fields, 109 MHz, 300 m scan radius (adapted from [34]) ..... 271
Figure G.1 – Geometry and coordination system for a single magnetic field dipole ..... 272
Figure G.2 – Configuration of measurement of an EUT in an LLA with two slits ..... 273
Figure G.3 – Transformer model representation of a disturbance source inside an LLA ..... 274
Figure G.4 – Transfer functions $f_c(\omega)$, $g_c(\omega)$ and their product (expressed in dB) as a function of frequency for a 2 m LLAS ..... 277
Figure G.5 – Sensitivity $S_D$ of an LLAS with diameter $D$ relative to an LLAS with 2 m diameter (Figure C.11 of CISPR 16-1-4:2019 [102]) ..... 278
Figure G.6 – Setup of the LLAS verification dipole for verification of an LLAS ..... 279
Figure G.7 – Geometry model of LLA for numerical computation of Neumann integral [113] ..... 282
Figure G.8 – LLAS verification dipole excluding the coupling effect from the LLAS loops ..... 282
Figure G.9 – Network model representation of the LLAS verification dipole fed by a generator source and the LLA ..... 283
Figure G.10 – First version of the reference validation factor for an LLA of 2 m diameter (Figure C.8 of CISPR 16-1-4:2010 [102]) ..... 283
Figure G.11 – Reference validation factors for an LLA of 2 m, 3 m and 4 m diameter (Figure C.8 of CISPR 16-1-4:2019 and CISPR 16-1-4:2019/AMD1:2020 [102]) ..... 284
Figure G.12 – Relative sensitivities of the LLAS verification dipole for an LLAS with different diameters (relative to an LLAS of 2 m diameter) ..... 285
Figure G.13 – Comparison of analytical and numerical (NEC2) calculations of the reference validation factors ..... 285
Figure G.14 – Magnetic field dipole moment of a small loop radiator in free space ..... 287
Figure G.15 – EUT above a ground plane and the coordinate system and possible magnetic field dipole orientations ..... 287
Figure G.16 – Magnetic field strength resulting from a source and its image below the ground plane (side view) ..... 287
Figure G.17 – Magnetic field strength expressed in dB(µA/m) of three magnetic field dipole orientations at three distances ..... 288
Figure G.18 – Conversion factors $C_{dA}$ [for conversion into dB(µA/m)] for three standard measurement distances $d$ (replicated Figure C.10 of CISPR 16-1-4:2010; exclusive the 30 m curve [102]) ..... 289
Figure G.19 – Conversion factors for calculating magnetic field strength at 10 m or 30 m ..... 289

Table 1 – Comparative response of slideback peak, quasi-peak and average detectors to sine wave, periodic pulse and Gaussian waveform ..... 24
Table 2 – Characteristics of gate generator and modulator to simulate various types of broadband interference ..... 30
Table 3 – Summary results of building-effect, $A_b$, analysis ..... 40
Table 4 – Summary of results of $G$-factor analysis ..... 43
Table 5 – Summary of $L_o$ factors (far-field) ..... 43

IECNORM.COM : Click to view the full PDF of CISPR TR 16-3:2020 RLV

Table 6 – Summary of truncation parameters of $f(G)$ ..... 44
Table 7 – Summary results of equivalent-resistance analysis ..... 45
Table 8 – Example of field-strength classification ..... 48
Table 9 – Example of voltage classification assuming for the outdoor field strength: $E_{max}$ = 60 V/m and $E_{min}$ = 0,01 V/m ..... 49
Table 10 – Summary of the parameters used in the numerical examples presented in Figure 16 and Figure 17 ..... 53
Table 11 – Frequencies of interest in ITU designated bands from Table 9 of CISPR 11:2009 ..... 60
Table 12 – Electrical constants for “medium dry ground” [31] (CCIR: medium dry ground; rocks; sand; medium sized towns[32]) ..... 61
Table 13 – Electrical constants for “wet ground” [31] (CCIR: marshes (fresh water); cultivated land [24]) and “very dry ground” [31] (CCIR: very dry ground; granite mountains in cold regions; industrial areas [32]) ..... 61
Table 14 – Estimates of the errors in prediction of radiation in vertical directions based on a measurement height scan from 1 m to 4 m at known distances, $d$; frequency = 75 MHz (adapted from [39]) ..... 69
Table 15 – Estimates of the errors in prediction of radiation in vertical directions based on a measurement height scan from 1 m to 4 m at known distances, $d$; frequency = 110 MHz (adapted from [39]) ..... 73
Table 16 – Estimates of the errors in prediction of radiation in vertical directions based on a measurement height scan from 1 m to 4 m at known distances, $d$; frequency = 243 MHz (adapted from [39]) ..... 78
Table 17 – Estimates of the errors in prediction of radiation in vertical directions based on a measurement height scan from 1 m to 4 m at known distances, $d$; frequency = 330 MHz (adapted from [39]) ..... 83
Table 18 – Estimates of the errors in prediction of radiation in vertical directions based on a measurement height scan from 1 m to 4 m at known distances, $d$; frequency = 1 000 MHz (adapted from [39]) ..... 86
Table 19 – Predictability of radiation in vertical directions at 100 kHz, using ground-based measurements of horizontally oriented $H$-field at distances up to 3 km from the source (figures are located in 4.6.8) ..... 103
Table 20 – Predictability of radiation in vertical directions at 1 MHz, using ground-based measurements of horizontally oriented $H$-field at distances up to 300 m from the source (figures are located in 4.6.8) ..... 104
Table 21 – Predictability of radiation in vertical directions at 10 MHz, using ground-based measurements of horizontally oriented $H$-field at distances up to 300 m from the source (figures are located in 4.6.8) ..... 105
Table 22 – Predictability of radiation in vertical directions at 30 MHz, using ground-based measurements of horizontally oriented $H$-field at distances up to 300 m from the source (figures are located in 4.6.8) ..... 106
Table 23 – Conditions for measuring communication quality degradation ..... 147
Table 24 – Average and RMS values of noise level normalized by $N_0$ ..... 148
Table 25 – Conditions for measuring communication quality degradation of Bluetooth ..... 150
Table 26 – Average and RMS values of noise level normalized by $N_0$ ..... 151
Table 27 – Average and RMS values of noise level normalized by $N_0$ ..... 152
Table 28 – Conditions for measuring communication quality degradation of W-CDMA ..... 154
Table 29 – Average and RMS values of noise level normalized by $N_0$ ..... 155
Table 30 – Conditions for measuring the PHS throughput ..... 157
Table 31 – Conditions for measuring the BER of PHS ..... 157

IECNORM.COM : Click to view the full PDF of CISPR TR 16-3:2020 RLV

Table 32 – Average and RMS values of noise level normalized by $N_0$ ..... 158
Table 33 – Overview of types of interference used in the experimental study of weighting characteristics ..... 170
Table 34 – DRM radio stations received for the measurement of the weighting characteristics ..... 174
Table 35 – Comparison of BER values for the same interference level ..... 178
Table 36 – Transmission parameters of DVB-T systems used in various countries ..... 179
Table 37 – Example of measurement results in dB(μV) of unmodulated and FM modulated carriers for various detectors (bandwidth 120 kHz) ..... 191
Table 38 – Survey of the corner frequencies found in the various measurement results ..... 192
Table 39 – Measurement results for broadband disturbance sources (measurements with RMS-average and quasi-peak detectors are normalized to average detector values) ..... 196
Table 40 – Expected deviations between different laboratories for small EUTs due to variations of the impedance $Z_{apparent}$ at point B ..... 197
Table 41 – Calibration measurement results format ..... 206
Table 42 – Scan times ..... 224
Table 43 – Sampling rates for different $B_{WIF}$ ..... 228
Table 44 – Scan times for a scan 30 MHz to 1 GHz ..... 229

IECNORM.COM : Click to view the full PDF of CISPR TR 16-3:2020 RLV

INTERNATIONAL ELECTROTECHNICAL COMMISSION

_____

# SPECIFICATION FOR RADIO DISTURBANCE AND IMMUNITY MEASURING APPARATUS AND METHODS –

## Part 3: CISPR technical reports

## FOREWORD

1) The International Electrotechnical Commission (IEC) is a worldwide organization for standardization comprising all national electrotechnical committees (IEC National Committees). The object of IEC is to promote international co-operation on all questions concerning standardization in the electrical and electronic fields. To this end and in addition to other activities, IEC publishes International Standards, Technical Specifications, Technical Reports, Publicly Available Specifications (PAS) and Guides (hereafter referred to as "IEC Publication(s)"). Their preparation is entrusted to technical committees; any IEC National Committee interested in the subject dealt with may participate in this preparatory work. International, governmental and non-governmental organizations liaising with the IEC also participate in this preparation. IEC collaborates closely with the International Organization for Standardization (ISO) in accordance with conditions determined by agreement between the two organizations.
2) The formal decisions or agreements of IEC on technical matters express, as nearly as possible, an international consensus of opinion on the relevant subjects since each technical committee has representation from all interested IEC National Committees.
3) IEC Publications have the form of recommendations for international use and are accepted by IEC National Committees in that sense. While all reasonable efforts are made to ensure that the technical content of IEC Publications is accurate, IEC cannot be held responsible for the way in which they are used or for any misinterpretation by any end user.
4) In order to promote international uniformity, IEC National Committees undertake to apply IEC Publications transparently to the maximum extent possible in their national and regional publications. Any divergence between any IEC Publication and the corresponding national or regional publication shall be clearly indicated in the latter.
5) IEC itself does not provide any attestation of conformity. Independent certification bodies provide conformity assessment services and, in some areas, access to IEC marks of conformity. IEC is not responsible for any services carried out by independent certification bodies.
6) All users should ensure that they have the latest edition of this publication.
7) No liability shall attach to IEC or its directors, employees, servants or agents including individual experts and members of its technical committees and IEC National Committees for any personal injury, property damage or other damage of any nature whatsoever, whether direct or indirect, or for costs (including legal fees) and expenses arising out of the publication, use of, or reliance upon, this IEC Publication or any other IEC Publications.
8) Attention is drawn to the Normative references cited in this publication. Use of the referenced publications is indispensable for the correct application of this publication.
9) Attention is drawn to the possibility that some of the elements of this IEC Publication may be the subject of patent rights. IEC shall not be held responsible for identifying any or all such patent rights.

IECNORM.COM : Click to view the full PDF of CISPR TR 16-3:2020 RLV

The main task of IEC technical committees is to prepare International Standards. However, a technical committee may propose the publication of a technical report when it has collected data of a different kind from that which is normally published as an International Standard, for example "state of the art."

CISPR 16-3, which is a Technical Report, has been prepared by CISPR subcommittee A: Radio-interference measurements and statistical methods.

This fourth edition cancels and replaces the third edition published in 2015. This edition constitutes a technical revision.

The main technical change with respect to the previous edition consists of the addition of detailed background information on the large loop antenna system (LLAS) and its measurement method in general and on the models and equations which apply to calculate the reference validation factor and conversion factor curves.

The text of this Technical Report is based on the following documents:

| Draft TR | Report on voting |
|---|---|
| CIS/A/1298/DTR | CIS/A/1310/RVDTR |

Full information on the voting for the approval of this Technical Report can be found in the report on voting indicated in the above table.

This publication has been drafted in accordance with the ISO/IEC Directives, Part 2.

A list of all parts of the CISPR 16 series can be found, under the general title *Specification for radio disturbance and immunity measuring apparatus and methods*, on the IEC website.

The committee has decided that the contents of the base publication and its amendments will remain unchanged until the stability date indicated on the IEC web site under "http://webstore.iec.ch" in the data related to the specific publication. At this date, the publication will be

- reconfirmed,
- withdrawn,
- replaced by a revised edition, or
- amended.

**IMPORTANT – The 'colour inside' logo on the cover page of this publication indicates that it contains colours which are considered to be useful for the correct understanding of its contents. Users should therefore print this document using a colour printer.**

IECNORM.COM : Click to view the full PDF of CISPR TR 16-3:2020 RLV

# SPECIFICATION FOR RADIO DISTURBANCE AND IMMUNITY MEASURING APPARATUS AND METHODS –

## Part 3: CISPR technical reports

## 1 Scope

This part of CISPR 16 is a collection of technical reports (Clause 4) that serve as background and supporting information for the various other standards and technical reports in CISPR 16 series. In addition, background information is provided on the history of CISPR, as well as a historical reference on the measurement of interference power from household and similar appliances in the VHF range (Clause 5).

Over the years, CISPR prepared a number of recommendations and reports that have significant technical merit but were not generally available. Reports and recommendations were for some time published in CISPR 7 and CISPR 8.

At its meeting in Campinas, Brazil, in 1988, CISPR subcommittee A agreed on the table of contents of CISPR 16-3, and to publish the reports for posterity by giving the reports a permanent place in CISPR 16-3.

With the reorganization of CISPR 16 in 2003, the significance of CISPR limits material was moved to CISPR 16-4-3, whereas recommendations on statistics of disturbance complaints and on the report on the determination of limits were moved to CISPR 16-4-4:2007. The contents of Amendment 1 (2002) of CISPR 16-3:2000 were moved to CISPR 16-4-1.

NOTE As a consolidated collection of independent technical reports, this document can contain symbols that have differing meanings from one clause to the next. Attempts have been made to minimize this to the extent possible at the time of editing.

## 2 Normative references

The following documents are referred to in the text in such a way that some or all of their content constitutes requirements of this document. For dated references, only the edition cited applies. For undated references, the latest edition of the referenced document (including any amendments) applies.

CISPR 11:2009, *Industrial, scientific and medical equipment – Radio-frequency disturbance characteristics – Limits and methods of measurement*[1]

CISPR 16-1-1, *Specification for radio disturbance and immunity measuring apparatus and methods – Part 1-1: Radio disturbance and immunity measuring apparatus – Measuring apparatus*

IEC 60050-161:1990, *International Electrotechnical Vocabulary (IEV) – Part 161: Electromagnetic compatibility*

IECNORM.COM : Click to view the full PDF of CISPR TR 16-3:2020 RLV

1 5th edition (2009). This 5th edition has been replaced in 2016 by a 6th Edition CISPR 11, Industrial, scientific and medical equipment – Radio-frequency disturbance characteristics – Limits and methods of measurement.

IEC 60050-300:2001, *International Electrotechnical Vocabulary (IEV) – Electrical and electronic measurements and measuring instruments – Part 311: General terms relating to measurements – Part 312: General terms relating to electrical measurements – Part 313: Types of electrical measuring instruments – Part 314: Specific terms according to the type of instrument*

ISO/IEC Guide 99:2007, *International vocabulary of metrology – Basic and general concepts and associated terms (VIM)*

## 3 Terms, definitions and abbreviated terms

### 3.1 Terms and definitions

For the purposes of this document, the terms and definitions given in IEC 60050-161, IEC 60050-300, ISO/IEC Guide 99, as well as the following apply.

NOTE While the symbol $U$ is commonly used in CISPR publications to represent uncertainty, in this technical report the symbols $U$ and $V$ are used interchangeably to represent "voltage" in order to accommodate the legacy diagrams contained herein.

**3.1.1**
**asymmetric voltage**
radio-frequency disturbance voltage appearing between the electrical mid-point of the mains terminals and earth

Note 1 to entry: It is sometimes called the common-mode voltage and is half the vector sum of $V_a$ and $V_b$, i.e. $(V_a + V_b)/2$

Note 2 to entry: $V_a$ is the vector voltage between one of the mains terminals and earth, and $V_b$ is the vector voltage between the other mains terminal and earth.

**3.1.2**
**bandwidth**
$B_n$
width of the overall selectivity curve of the receiver between two points at a stated attenuation, below the mid-band response

Note 1 to entry: The bandwidth is represented by the symbol $B_n$, where $n$ is the stated attenuation in decibels.

**3.1.3**
**electrical charge time constant**
$T_C$
time needed after the instantaneous application of a constant sine-wave voltage to the stage immediately preceding the input of the detector for the output voltage of the detector to reach 63 % of its final value

Note 1 to entry: This time constant is determined as follows. A sine-wave signal of constant amplitude and having a frequency equal to the mid-band frequency of the IF amplifier is applied to the input of the stage immediately preceding the detector. The indication $\alpha_{max}$ of an instrument having no inertia (for example, a cathode-ray oscilloscope) connected to a terminal in the DC amplifier circuit so as not to affect the behaviour of the detector, is noted. The level of the signal is chosen such that the response of the stages concerned remains within the linear operating range. A sine-wave signal of this level, applied for a limited time only and having a wave train of rectangular envelope is gated such that the deflection registered is $0{,}63\alpha_{max}$. The duration of this signal is equal to the charge time of the detector.

**3.1.4**
**electrical discharge time constant**
$T_D$
time needed after the instantaneous removal of a constant sine-wave voltage applied to the stage immediately preceding the input of the detector for the output of the detector to fall to 37 % of its initial value

IECNORM.COM : Click to view the full PDF of CISPR TR 16-3:2020 RLV

Note 1 to entry: The method of measurement is analogous to that for the charge time constant, but instead of a signal being applied for a limited time, the signal is interrupted for a definite time. The time taken for the deflection to fall to 0,37$D$ is the discharge time constant of the detector.

**3.1.5**
**impulse bandwidth**
$B_{imp}$

$$B_{imp} = \frac{A(t)_{max}}{2G_o \times A_{imp}} \quad (1)$$

where

$A(t)_{max}$ is the peak of the envelope at the IF output of the receiver with an impulse area $A_{imp}$ applied at the receiver input;

$G_o$ is the gain of the circuit at the centre frequency;

specifically, for two critically coupled tuned transformers,

$$B_{imp} = 1{,}05 \times B_6 = 1{,}31 \times B_3 \quad (2)$$

where $B_6$ and $B_3$ are respectively the bandwidths at the –6 dB and –3 dB points (see CISPR 16-1-1 for further information)

**3.1.6**
**impulse area**
impulse strength
$A_{imp}$
voltage-time area of a pulse defined by the integral:

$$A_{imp} = \int_{-\infty}^{+\infty} V(t)dt \text{ expressed in } \mu Vs \text{ or } dB(\mu Vs) \quad (3)$$

Note 1 to entry: Spectral density $D$ is related to impulse area and is expressed in μV/MHz or dB(μV)/MHz. For rectangular impulses of pulse duration $T$ at frequencies $f << 1/T$, the relationship $D = 2 \times 10^6 / A_{imp}$ applies because $D$ is calibrated in RMS values of a corresponding sine wave.

**3.1.7**
**mechanical time constant of a critically damped indicating instrument**
$T_M$

$$T_M = \frac{T_L}{2\pi} \quad (4)$$

where $T_L$ is the period of free oscillation of the instrument with all damping removed

Note 1 to entry: For a critically damped instrument, the equation of motion of the system may be written as

$$T_M^2\left(\frac{d^2\alpha}{dt^2}\right) + 2T_M\frac{d\alpha}{dt} + \alpha = ki \quad (5)$$

where

$\alpha$ is the deflection;

$i$ is the current through the instrument;

$k$ is a constant.

It can be deduced from this relation that this time constant is also equal to the duration of a rectangular pulse (of constant amplitude) that produces a deflection equal to 35 % of the steady deflection produced by a continuous current having the same amplitude as that of the rectangular pulse.

IECNORM.COM : Click to view the full PDF of CISPR TR 16-3:2020 RLV

Note 2 to entry: The methods of measurement and adjustment are deduced from one of the following:

a) The period of free oscillation having been adjusted to $2\pi T_M$, damping is added so that $\alpha_{TM}$ = 0,35 $\alpha_{max}$.

b) When the period of oscillation cannot be measured, the damping is adjusted to be just below critical such that the over-swing is not greater than 5 % and the moment of inertia of the movement is such that $\alpha_{TM}$ = 0,35 $\alpha_{max}$.

**3.1.8**
**overload factor**
ratio of the level that corresponds to the range of practical linear function of a circuit (or a group of circuits) to the level that corresponds to full-scale deflection of the indicating instrument

Note 1 to entry: The maximum level at which the steady-state response of a circuit (or group of circuits) does not depart by more than 1 dB from ideal linearity defines the range of practical linear function of the circuit (or group of circuits).

**3.1.9**
**symmetric voltage**
radio-frequency disturbance voltage appearing between the wires of a two-wire circuit, such as a single-phase mains supply

Note 1 to entry: Symmetric voltage is sometimes called the differential mode voltage and is the vector difference between $V_a$ and $V_b$, i.e. ($V_a$ – $V_b$). Refer to the NOTE in 3.1.1 for definition of $V_a$ and $V_b$.

**3.1.10**
**unsymmetric voltage**
amplitude of the vector voltage, $V_a$ or $V_b$

Note 1 to entry: Unsymmetric voltage is the voltage measured by the use of an artificial mains V-network. Refer to the NOTE in 3.1.1 for definition of $V_a$ and $V_b$.

**3.1.11**
**weighting** (of e.g. impulsive disturbance)
pulse-repetition-frequency (PRF) dependent conversion (mostly reduction) of a peak-detected impulse voltage level to an indication that corresponds to the interference effect on radio reception

Note 1 to entry: For the analogue receiver, the psychophysical annoyance of the interference is a subjective quantity (audible or visual, usually not a certain number of misunderstandings of a spoken text).

Note 2 to entry: For the digital receiver, the interference effect is an objective quantity that may be defined by the critical bit error ratio (BER) or bit error probability (BEP) for which perfect error correction can still occur, or by another objective and reproducible parameter.

**3.1.11.1**
**weighted disturbance measurement**
measurement of disturbance using a weighting detector

**3.1.11.2**
**weighting characteristic**
peak voltage level as a function of PRF for a constant effect on a specific radiocommunication system, i.e. the disturbance is weighted by the radiocommunication system itself

**3.1.11.3**
**weighting detector**
detector which provides an agreed weighting function

**3.1.11.4**
**weighting factor**
value of the weighting function relative to a reference PRF or relative to the peak value

Note 1 to entry: Weighting factor is expressed in dB.

IECNORM.COM : Click to view the full PDF of CISPR TR 16-3:2020 RLV

**3.1.11.5**
**weighting function**
**weighting curve**
relationship between input peak voltage level and PRF for constant level indication of a measuring receiver with a weighting detector, i.e. the curve of response of a measuring receiver to repeated pulses

## 3.2 Abbreviated terms

| | |
|---|---|
| ADPCM | Adaptive differential pulse code modulation |
| AGC | Automatic gain control |
| AM | Amplitude modulation |
| AMN | Artificial mains network |
| APD | Amplitude probability distribution |
| BEP | Bit error probability |
| BER | Bit error rate |
| CDN | Coupling decoupling network |
| CDNE | CDN for emission measurement |
| CM | Common mode |
| CMAD | Common mode absorption device |
| COFDM | Coded orthogonal frequency division multiplex |
| DAB | Digital audio broadcasting |
| DDC | Digital down-conversion |
| DECT | Digitally enhanced cordless telephone |
| DIF | Decimated in frequency |
| DIT | Decimated in time |
| DM | Differential mode |
| DPCH | Dedicated physical channel |
| DPDCH | Dedicated physical data channel |
| DQPSK | Digital QPSK |
| DRM | Digital radio mondiale |
| DVB-T | Digital video broadcasting – terrestrial |
| EMC | Electromagnetic compatibility |
| EMI | Electromagnetic emissions |
| ERP | Equivalent radiating power |
| EUT | Equipment under test |
| FER | Frame error rate |
| FFT | Fast Fourier transform |
| FM | Frequency modulation |
| GSM | Global system for mobile communications |
| GMSK | Gaussian minimum shift keying |
| GTEM | Gighertz TEM |
| IF | Intermediate frequency |
| ILS | Instrument landing system |
| ISM | Industrial, scientific and medical |
| ITU | International Telecommunications Union |
| LAN | Local area network |
| LAS | Loop antenna system |
| LCL | Longitudinal conversion loss |
| LISN | Line-impedance stabilization network |
| LLA | Large loop antenna |
| LLAS | Large loop antenna system |
| LW | Long wave |
| MPEG | Moving picture expert group |
| MW | Medium wave |
| MWO | Microwave oven |
| OATS | Open-area test site |
| OFDM | Orthogonal frequency division multiplex |
| PC | Personal computer |
| PHS | Personal handy phone system |
| PRBS | Pseudo random binary sequence |
| PRF | Pulse-repetition frequency |
| QAM | Quadrature amplitude modulation |
| QPSK | Quadrature phase-shift keying |
| RAM | Random access memory |
| RBER | Residual bit error rate |
| RF | Radio frequency |
| RMS | Root-mean square |
| RRT | Round robin test |
| RSA | Ring-shaped area |
| SAC | Semi-anechoic chamber |
| SOLT | Short-open-load-through |
| STFFT | Short-time FFT |
| SW | Short wave |
| TEM | Transverse electromagnetic |
| TETRA | Terrestrial trunked radio |
| TRL | Through-reflect-line |
| TTE | Telephone terminal equipment |
| VNA | Vector network analyzer |
| W-CDMA | Wideband code division multiple access |

IECNORM.COM : Click to view the full PDF of CISPR TR 16-3:2020 RLV

# 4 Technical reports

## 4.1 Correlation between measurements made with apparatus having characteristics differing from CISPR characteristics and measurements made with CISPR apparatus

### 4.1.1 General

CISPR standards for instrumentation and methods of measurement have been established to provide a common basis for controlling radio interference from electrical and electronic equipment in international trade.

The basis for establishing limits is that of providing a reasonably good correlation between measured values of the interference and the degradation it produces in a given communications system. The acceptable value of signal-to-noise ratio in any given communication system is a function of its parameters, including bandwidth, type of modulation, and other design factors. As a consequence, various types of measurements are used in the laboratory in research and development work in order to carry out the required investigations.

The purpose of this subclause is to analyse the dependence of the measured values on the parameters of the measuring equipment and on the waveform of the measured interference.

### 4.1.2 Critical interference-measuring instrument parameters

The most critical factors in determining the response of an instrument for measuring interference are the following: the bandwidth, the detector, and the type of interference being measured. Considered to be of secondary importance, but, nevertheless, quite significant in correlating instruments under particular circumstances, are: overload factor, AGC design (if used), image and other spurious responses, and meter time constant and damping.

For purposes of discussion, reference is made to three fundamental types of radio noise: impulse, random and sine wave. The dependence of the response to each of these on the bandwidth and the type of detector is given in Table 1. In Table 1, $\delta$ is the magnitude of the impulse strength, $\Delta f_{\text{imp}}$ is the impulse bandwidth, $\Delta f_{\text{rn}}$ is the random noise bandwidth, $P(\alpha)$ is the pulse response for the quasi-peak detector, $f_{\text{PR}}$ is the pulse repetition frequency, and $E'$ is the spectral amplitude of the random noise. The relative responses of various detectors to impulse interference for one instrument are shown in Figure 1.

Table 1 shows that the dependence of the noise meter response on bandwidth is different for all three types of interference. If the waveform being measured can be defined as being any of the three types listed in Table 1, and if a standard source provides that type of waveform, then by using the substitution method, a satisfactory calibration can be obtained for any instrument with adequate overload factor independent of its bandwidth. Thus, with a purely random interference or a purely impulsive interference of known repetition rate, calibration can be made using a corresponding source, or a correlation factor calculated on the basis of known circuit parameters.

If a particular interference waveform is of an intermediate type between these three types, then the correction or correlation factors will also be intermediate. In any given case, it will be necessary to classify the noise waveform in such a manner that a significant correlation factor can be established. Hence, in order to develop this subject to any significant extent, it will be necessary to examine typical interference sources and to determine the extent to which they are of impulsive, random, or sine-wave type.

If an interference measuring set with several types of detectors is available, for example, peak, quasi-peak and average, the type of interference can be assessed by measuring the ratios of the readings obtained with these detectors. These ratios will, of course, depend upon the bandwidth and other characteristics of the instrument being used for the measurement.

IECNORM.COM : Click to view the full PDF of CISPR TR 16-3:2020 RLV

**Table 1 – Comparative response of slideback peak, quasi-peak and average detectors to sine wave, periodic pulse and Gaussian waveform**

| Input waveform | Detector type | | | |
|---|---|---|---|---|
| | Slideback peak (sb) | Quasi-peak:1/600 (qp) | Field intensity (average) | RMS |
| CW sine wave | $e$ | $e$ | $e$ | $e$ |
| Periodic pulse (no overlap) | $1{,}41\ \delta\ \Delta f_{imp}$ | $1{,}41\ \delta\ \Delta f_{imp}\ P(\alpha)$ | $1{,}41\ \delta f_{PR}$ | $1{,}41\ \delta\ \sqrt{f_{PR}\Delta f_{imp}}$ |
| Random | – | $1{,}85\ \sqrt{\Delta f_{rn} E'}$ | $0{,}88\ \sqrt{\Delta f_{rn} E'}$ | $\sqrt{\Delta f_{rn} E'}$ |

**Key**

$e$ is the RMS value of the applied sine wave.

$P(\alpha)$ is given in Figure 2.

$E'$ is the spectral strength in RMS V/Hz bandwidth.

$\delta$ is the impulse strength. It is assumed the instrument is calibrated in terms of the RMS value of a sine wave. It is assumed that characteristics of the envelope are measured by the detector on random noise.

$\Delta f_{imp}$ is the impulse bandwidth.

$\Delta f_{rn}$ is the random noise bandwidth.

$f_{PR}$ is the pulse repetition frequency.

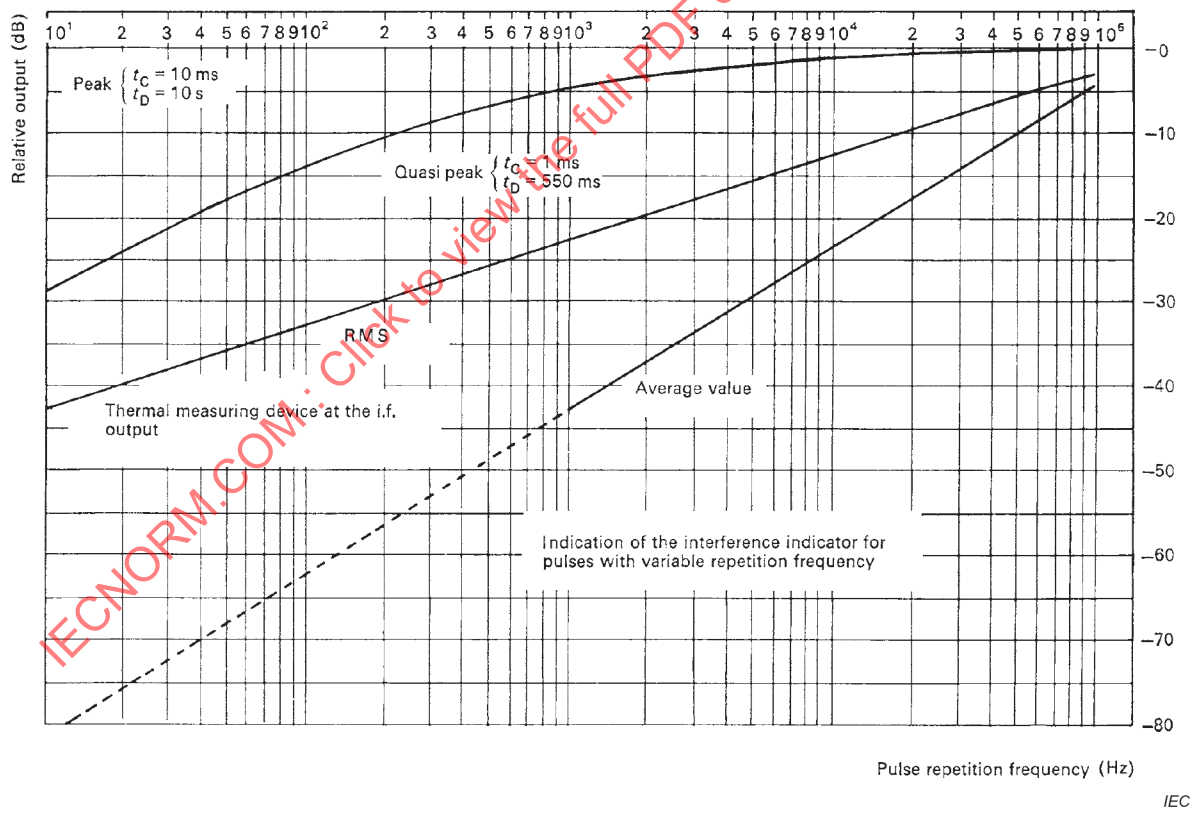


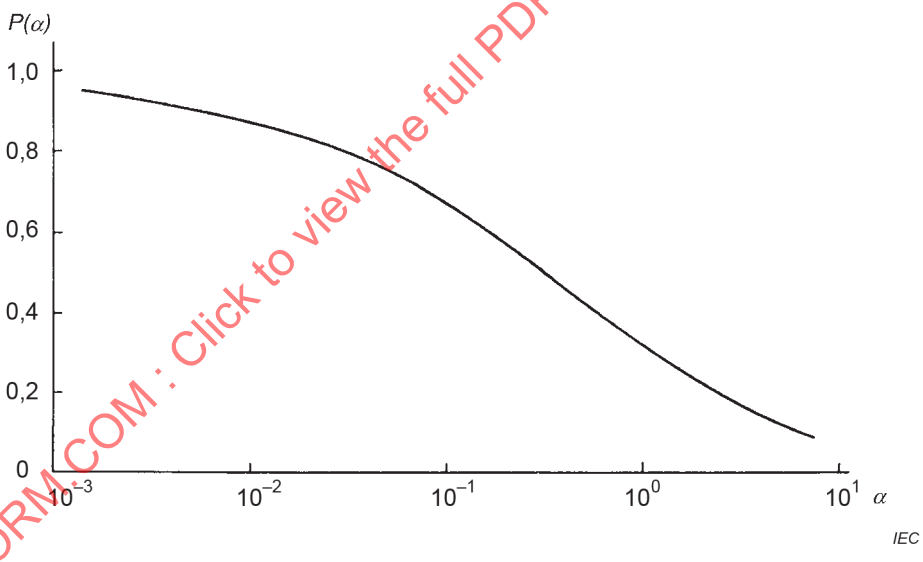

**Figure 1 – Relative response of various detectors to impulse interference**

IECNORM.COM : Click to view the full PDF of CISPR TR 16-3:2020 RLV

### 4.1.3 Impulse interference – correlation factors

The quasi-peak detector response of any interference measuring set to regularly repeated impulses of uniform amplitude can be determined by the use of the "pulse response curve" which is shown in Figure 2. This figure shows the response of the detector in percentage of peak response for any given bandwidth and value of charge resistance and discharge resistance. Applying this curve, it should be noted that the peak itself is dependent upon the bandwidth, so that as the bandwidth increases, the peak value increases, but the percentage of peak, which is read by the detector, decreases; over a narrow range of bandwidth, these effects tend to counteract each other. The bandwidth used in this curve is the 6 dB bandwidth, which for the passband characteristics typical of most interference measuring equipment, is about 5 % less than the so-called impulse bandwidth. A theoretical comparison of instruments having various bandwidths and detector parameters with the CISPR instrument is shown in Figure 3.

The response of the average detector to impulsive noise is an interesting case. The reading of an average detector for impulsive noise is independent of the bandwidth of the pre-detector stages. It is, of course, directly proportional to the repetition rate. In most cases, the reading obtained with an average detector for impulsive noise is so low as to be of no practical value unless the noise meter bandwidth is exceedingly narrow, such as of the order of a few hundred hertz. For a repetition rate of 100 Hz and a bandwidth of the order of 10 kHz, the average value would be approximately 1 % of the peak value. Such a value is too low to measure with any degree of precision. Furthermore, for many communication systems, the annoyance effect may be well above the reading obtained with the average meter. This, of course, is one of the justifications for the use of the quasi-peak instrument.



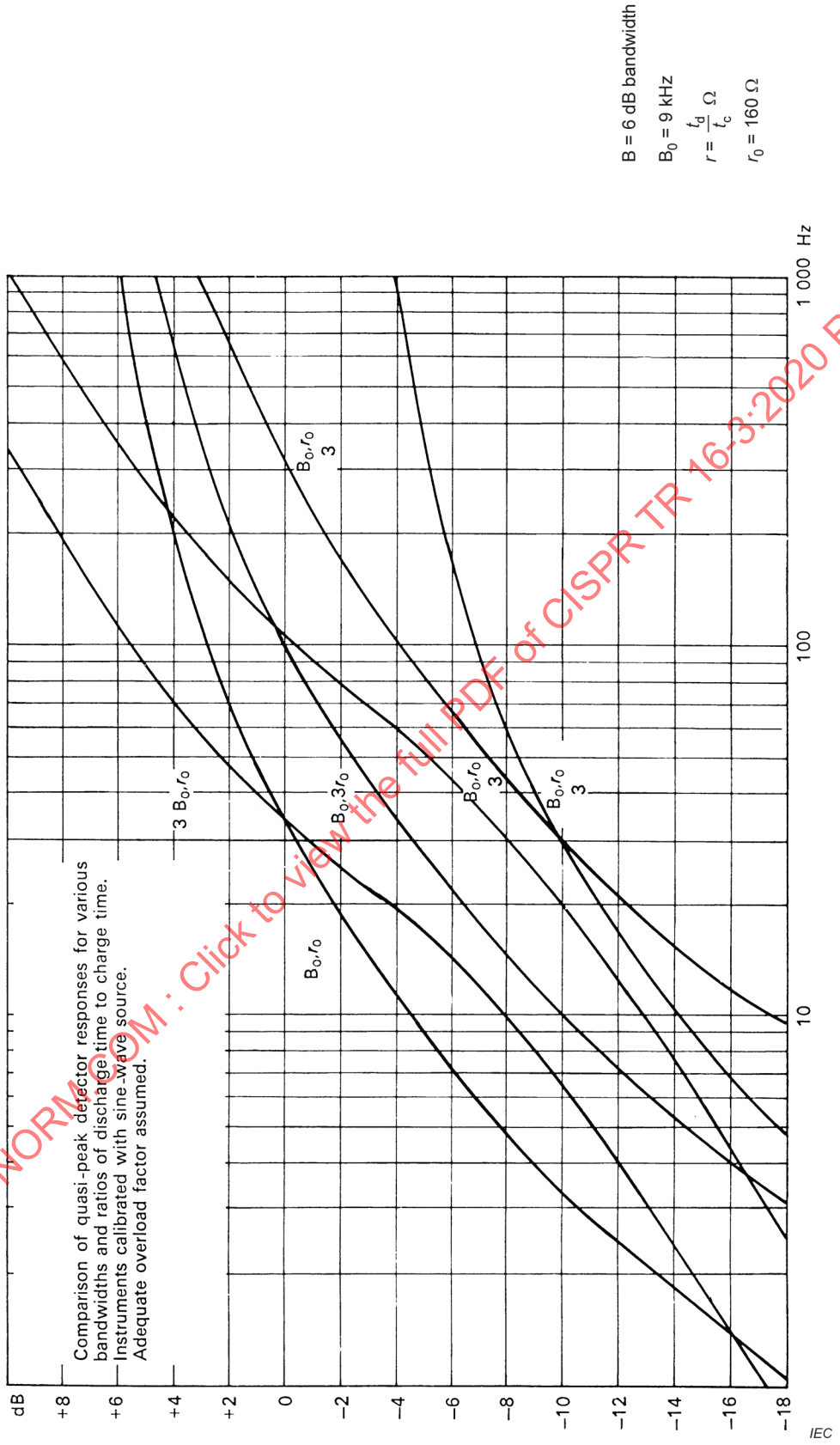

$$\alpha = \frac{(\pi R_c \Delta F)}{(R_d f_{PR})}$$

**Key**

| | |
|---|---|
| $R_c$ | charging resistance, in Ω |
| $R_d$ | discharging resistance, in Ω |
| $\Delta F$ | 6 dB bandwidth, in Hz |
| $f_{PR}$ | pulse repetition frequency, in Hz |

**Figure 2 – Pulse rectification coefficient $P(\alpha)$**

IECNORM.COM : Click to view the full PDF of CISPR TR 16-3:2020 RLV




IECNORM.COM : Click to view the full PDF of CISPR TR 16-3:2020 RLV

**Figure 3 – Pulse repetition frequency**

#### 4.1.4 Random noise

The response of a noise meter to random noise is proportional to the square root of the bandwidth. This result is independent of the type of detector used. The ratio of the random noise bandwidth to the 3-dB bandwidth is a function of the type of filter circuit. On the other hand, it has been shown that for many circuits typical of those used in interference measuring equipment, a value of about 1,04 for the ratio of effective random noise bandwidth to the 3 dB bandwidth is a reasonable figure.

#### 4.1.5 The root mean square (RMS) detector

One of the advantages of the RMS detector in correlation work is that for broadband noise the output obtained from it will be proportional to the square root of the bandwidth, i.e. the noise power is directly proportional to the bandwidth. This feature makes the RMS detector particularly desirable and is one of the main reasons for adopting the RMS detector to measure atmospheric noise. Another advantage is that the RMS detector makes a correct addition of the noise power produced by different sources, for example, impulsive noise and random noise, thus for instance allowing a high degree of background noise.

The RMS values of noise often give a good assessment of the subjective effect of interference to AM sound and television reception. However, the very wide dynamic range needed when using very wide-band instruments for measuring impulsive noise, limits the use of RMS detectors to narrow-band instruments.

#### 4.1.6 Discussion

The preceding paragraphs have indicated the theoretical basis for comparing measurements obtained with different instruments. As mentioned previously, the possibility of establishing significant correlation factors depends upon the extent to which noise can be classified and identified so that the proper correlation factors may be used. In many frequency ranges, impulsive interference appears to be the most serious; however, for power lines where corona interference is the primary concern, random interference would be expected to be more characteristic. Additional quantitative data are needed on typical interference characteristics. Another important parameter is the overload factor.

#### 4.1.7 Application to typical noise sources

##### 4.1.7.1 Commutator motors

The noise generated by commutator motors is usually a combination of impulse and random noise. The random noise originates in the varying brush contact resistance, while the impulse noise is generated from the switching action at the commutator bars. For optimum adjustment of commutation, the impulse noise can be minimized. However, where variable loading is possible, measurements have confirmed that for the peak and quasi-peak detectors, the dominant noise is of impulse type and the random component may be neglected. While the repetition rate may be of the order of 4 kHz, the effective rate is lower because the amplitude of the impulses is usually modulated at twice the line frequency. Hence, experimental results have shown that quasi-peak readings are consistent with bandwidth variations if the repetition rate of the impulse is assumed to be twice the line frequency.

Peak measurements show fluctuating levels on such noise because of the irregular nature of the commutator switching action.

The quasi-peak to average ratio is lower than would be obtained for pure impulse noise for two reasons:

1) the modulation of the commutator switching transients by line frequency produces many pulses below the measured quasi-peak level. These pulses do not contribute to the quasi-peak value but do contribute to the average.

IECNORM.COM : Click to view the full PDF of CISPR TR 16-3:2020 RLV

2) the relatively low level, but continuous, random noise can likewise contribute substantially only to the average value. Experimental values of quasi-peak to average ratio ranged from 13 dB to 23 dB with the highest ratios for the widest bandwidths (120 kHz).

#### 4.1.7.2 Impulsive sources

Tests on an ignition model, commutator motor appliances, and appliances using vibrating regulators showed reasonable agreement on instruments with the same nominal bandwidth, but with time constant ratios of the order of 3:1 on restricted portions of the output indicator scale. Deviations at higher scale values are without explanation. Relatively poor correlation was obtained on sources producing very low repetition rate pulses.

#### 4.1.7.3 Ignition interference

"CISPR Recommendation 35" recognizes that correlation between quasi-peak and peak detectors can be established as a practical matter. The conversion factor of 20 dB is explained partly on the basis of theory for uniform repeated impulses, and partly on the basis of the actual irregularity of the amplitude and wave shape of such impulses.

NOTE "CISPR Recommendation 35", from CISPR 7:1969, *Recommendations of the CISPR*, is quoted for reference:

" RECOMMENDATION No. 35
THE CORRELATION BETWEEN PEAK AND QUASI-PEAK MEASUREMENTS OF INTERFERENCE FROM IGNITION SYSTEMS
(This Recommendation closes Study Question No. 45 of 1961)
(Stockholm, 1964)

The C.I.S.P.R.,
CONSIDERING
that for the measurement of interference from the ignition systems of internal combustion engines there will, in general, be two types of detector, namely, peak and quasi-peak;

RECOMMENDS
that a correlation factor of 20 dB between peak and quasi-peak measurements of interference from ignition systems be adopted for frequencies in the range covered by C.I.S.P.R. Publication 2, i.e. when peak measurements are made the acceptable limits are 20 dB above the corresponding quasi-peak measurements; for peak measurements the engine may be operated at any speed above idling speed but for quasi-peak measurements the speed should be set as near as possible to 1 500 rev/min for multi-cylinder engines and 2 500 rev/min for single cylinder engines."

#### 4.1.7.4 Dependence on bandwidth

Comparisons of measurements made in the UK with two instruments having bandwidths of 90 kHz and 9 kHz respectively have been reported to show that for most interference sources, the values obtained are in the ratio 14 dB to 18 dB. This figure is consistent with the concept that the interference is dominated by impulse type noise but that some random components are present.

### 4.1.8 Conclusions

Analysis of data comparing the responses of various instruments shows that, in almost every case, it is possible to explain the differences in measured values on the basis of theoretical and practical considerations. In many instances, it is indicated that waveform characteristics are known to predict correlation factors adequately with an accuracy of 2 dB to 4 dB.

Further studies are needed:

a) to characterize in some detail the waveforms of various sources of interference, and

b) to correlate these waveform characteristics with measured values and the instrument parameters.

IECNORM.COM : Click to view the full PDF of CISPR TR 16-3:2020 RLV

## 4.2 Interference simulators

### 4.2.1 General

Interference simulators can be used for various applications, in particular to study signal processing in systems and equipment in the presence of interference (for example, overloading of receivers, synchronization of TV receivers, error rate of data signals, etc.) and for assessment of the annoyance caused by disturbances in broadcast and communication services.

A simulator should produce a stable and reproducible output signal, which requirement is normally not fulfilled by an actual interference source, and the simulator output waveform should show a good resemblance to the actual interference signal.

### 4.2.2 Types of interference signals

The following interference sources can be simulated.

a) Narrowband interference sources generating sine-wave signals, for example receiver oscillators and ISM equipment. An appropriate RF standard signal generator can be used to simulate these sources. ISM interference is often modulated by the mains voltage, which can be simulated by modulating the RF signal with a full-wave rectified mains signal.

b) Broadband interference sources producing continuous broadband noise, for example, gaseous discharges and corona. For simulating purposes a standard broadband noise source (saturated vacuum tube diode, zener diode or gas tube followed by a suitable broadband amplifier) can be used. In mains-fed sources of this type, mains modulation is present, but because of the non-linear behaviour of gaseous discharges the envelope of the actual noise signal can deviate appreciably from the normal full-wave rectified mains waveform. In this case, gating the noise of the simulator at a repetition frequency of twice the mains frequency can yield a good correspondence with the actual interference signal.

c) Thyristor controlled regulators with phase control generate narrow pulses of constant amplitude in an RF-channel at a repetition frequency equal to twice the mains frequency. Standard pulse generators with narrow output pulses ($10^{-7}$ s to $10^{-9}$ s width) of the same repetition frequency can be used to easily simulate these sources.

d) Ignition systems, mechanical contacts and commutator motors generate short periods (bursts) of quasi-impulsive noise. This type of noise is caused by very short pulses of regular or irregular height at random time intervals; if the average interval between adjacent pulses is less than the reciprocal of the channel bandwidth under test ($\tau_{av} < 1/B$), the pulses overlap, and because of the random phase conditions, a random fluctuating output signal (noise) results. Therefore, bursts of quasi-impulsive interference of this type can be simulated by a gated broadband noise signal.

The duration and the repetition frequency of the bursts depend on the type of interference source (see Table 2).

Ignition interference is characterized by burst durations between 20 μs and 200 μs and repetition frequencies between 30 bursts/s and 300 bursts/s depending on the number of cylinders and revolutions/min of the engine.

Mechanical contacts produce bursts (clicks) which can vary between some milliseconds (snap-off switches) and more than 200 ms. In the case of a contact device in a mains-fed circuit, the noise during the burst is modulated with the full-wave rectified mains voltage.

Commutator motors produce much shorter bursts with durations between 20 μs and 200 μs at repetition frequencies between $10^3$ bursts/s and $10^4$ bursts/s, depending on the number of commutator bars and revolutions per minute of the rotor. Also in this case, the mains supply causes a similar envelope modulation of the noise bursts.

IECNORM.COM : Click to view the full PDF of CISPR TR 16-3:2020 RLV

### 4.2.3 Circuits for simulating broadband interference

Simulators of this type should generate gated noise bursts with or without mains modulation according to the characteristics specified in Table 2. Figure 4 shows a straightforward design with a noise source followed by an appropriate amplifier of 70 dB to 80 dB gain, a gating circuit to simulate the bursts, a mains envelope modulator and an output attenuator to adjust the required output level.

**Table 2 – Characteristics of gate generator and modulator to simulate various types of broadband interference**

| Simulator signal | Burst duration | Burst repetition frequency | Mains modulation [a] |
|---|---|---|---|
| Gaseous discharge | | Continuous | Yes/no [b] |
| Ignition | 20 μs to 200 μs | 30 bursts/s to 300 bursts/s | No |
| Switches | 5 ms to 500 ms | 0,2 bursts/min to 30 bursts/min, or single | Yes/no |
| Commutator motors | 30 μs to 300 μs | $10^3$ bursts/s to $10^4$ bursts/s | Yes/no |

[a] Depending on AC or DC supply.

[b] In the case of mains modulation, gating at a repetition frequency $2f_{mains}$ and gate width of 1 ms to 2 ms may be more appropriate.

The disadvantage of this layout is that a wide usable frequency range requires a broad bandwidth for the entire circuit between noise source and output terminal. The most critical part in this respect is the high-gain amplifier. For applications in a wide frequency range (for example, 0 MHz to 1 000 MHz) such a range can be split up in several smaller ranges or a tunable amplifier may be used. Such a design complicates the construction of the simulator appreciably.

Another way to produce a gated wideband noise signal is given in the diagram of Figure 5. In this design, nanosecond pulses are generated in the output stage, for example, a step recovery diode or similar device. These pulses of constant height are triggered at random time intervals and at a sufficiently high repetition rate to cause overlap in the RF channel under test in order to result in quasi-impulsive noise in the output of the channel. Average repetition rates of a few megahertz are required for measurements in a TV channel of at least 100 kHz for measurements in an FM channel and of at least 10 kHz in an AM channel. The random occurrence of the trigger pulses is obtained from the zero crossings of a broadband signal. For this purpose the output of a noise source is fed to an appropriate amplifier which is followed by a gating circuit for burst simulation. The gated noise signal is fed to a bistable multivibrator which converts the zero crossings into pulses of random varying width from which narrow trigger pulses at random distances are generated by the monostable multivibrator.

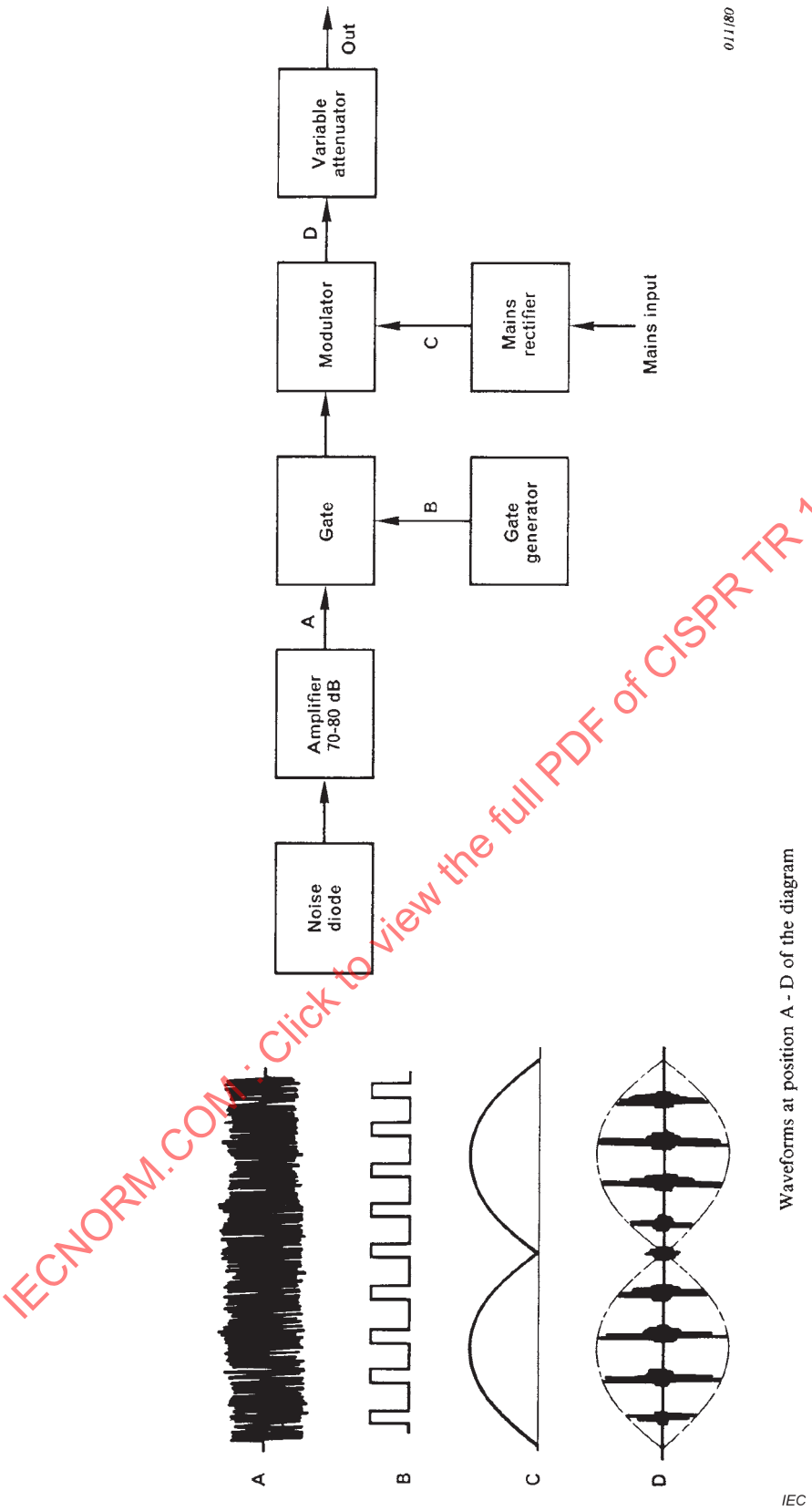
The advantage of this system over the circuit of Figure 4 is that the usable frequency range is determined by the output pulses of the step-recovery diode only. An example of such a circuit is given in Figure 6, in which circuit output pulses are generated by the step recovery diode HP0102, the pulse width is determined by the length of a short-circuited coaxial cable $L$. Ringing effects are suppressed by the fast switch diode HP2301, and mains modulation can be effected simply by modulating the supply voltage of the step recovery diode with a full-wave rectified mains voltage. Pulses of 1 ns duration and 5 V amplitude are generated and offer an output spectrum flat to about 500 MHz. Such a single pulse causes a 50 mV pulse in a TV channel and a 1 mV pulse in an FM channel; overlapping pulses add up, and the peak and quasi-peak value of the resulting signal is considerably higher.

IECNORM.COM : Click to view the full PDF of CISPR TR 16-3:2020 RLV

The bandwidth of the preceding stages which generate the trigger signal (noise source, amplifier and gating circuit) should be sufficient for the required pulse repetition rate, so for measurements in a TV channel a bandwidth of 5 MHz to 10 MHz is quite satisfactory. Moreover, the linearity of these stages is not critical because only the position of the zero crossings is important. The multivibrators have to generate steep pulses of short duration (about 0,1 μs) to drive the step-recovery diode.

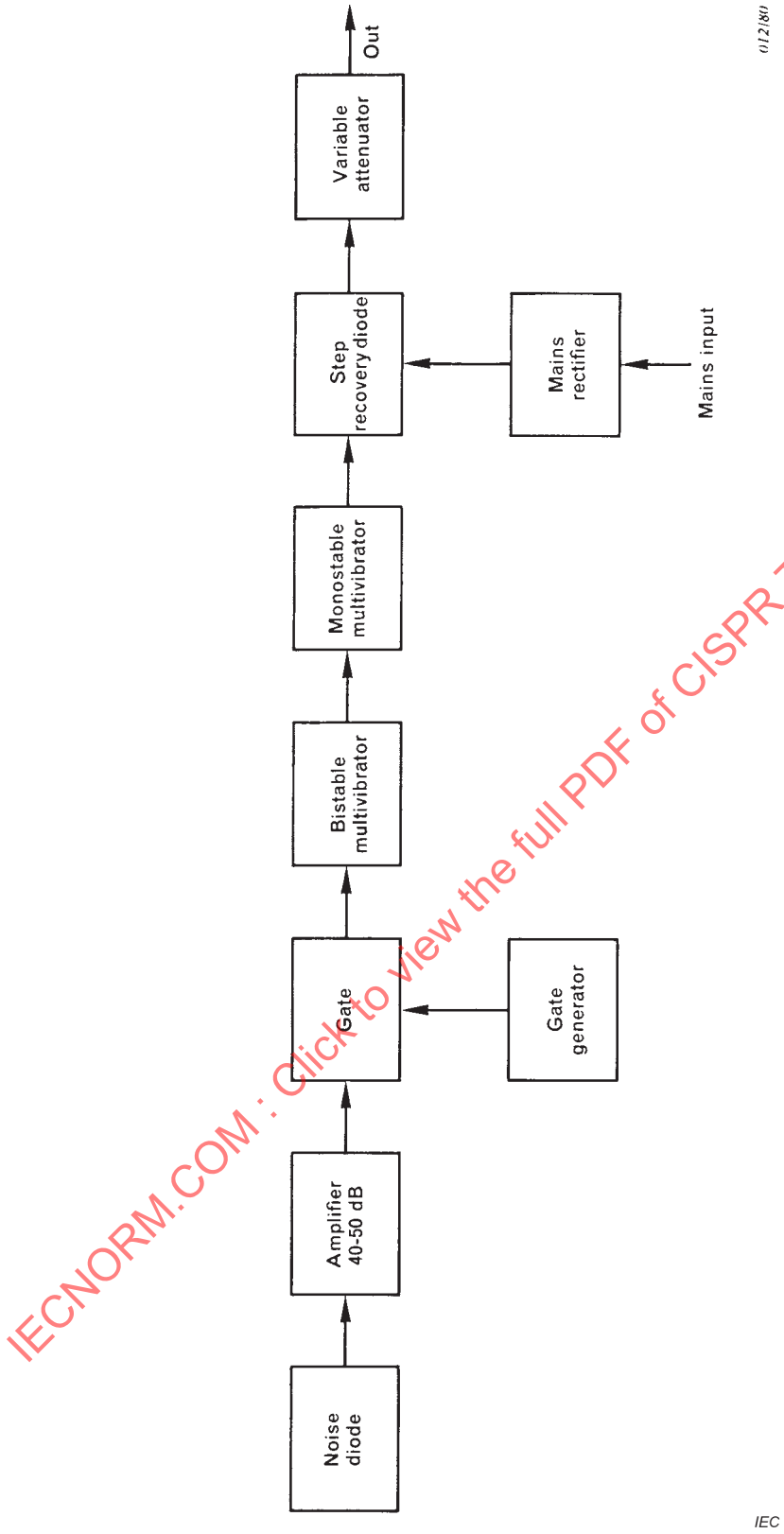
In summary, the circuit according to Figure 4 is very useful for broadband interference simulators to be operated in a limited frequency range, whereas the circuit of Figure 5 is more suitable for simulators intended for wideband use.

IECNORM.COM : Click to view the full PDF of CISPR TR 16-3:2020 RLV




IECNORM.COM : Click to view the full PDF of CISPR TR 16-3:2020 RLV

**Figure 4 – Block diagram and waveforms of a simulator generating noise bursts**




IECNORM.COM : Click to view the full PDF of CISPR TR 16-3:2020 RLV

**Figure 5 – Block diagram of a simulator generating noise bursts according to the pulse principle**

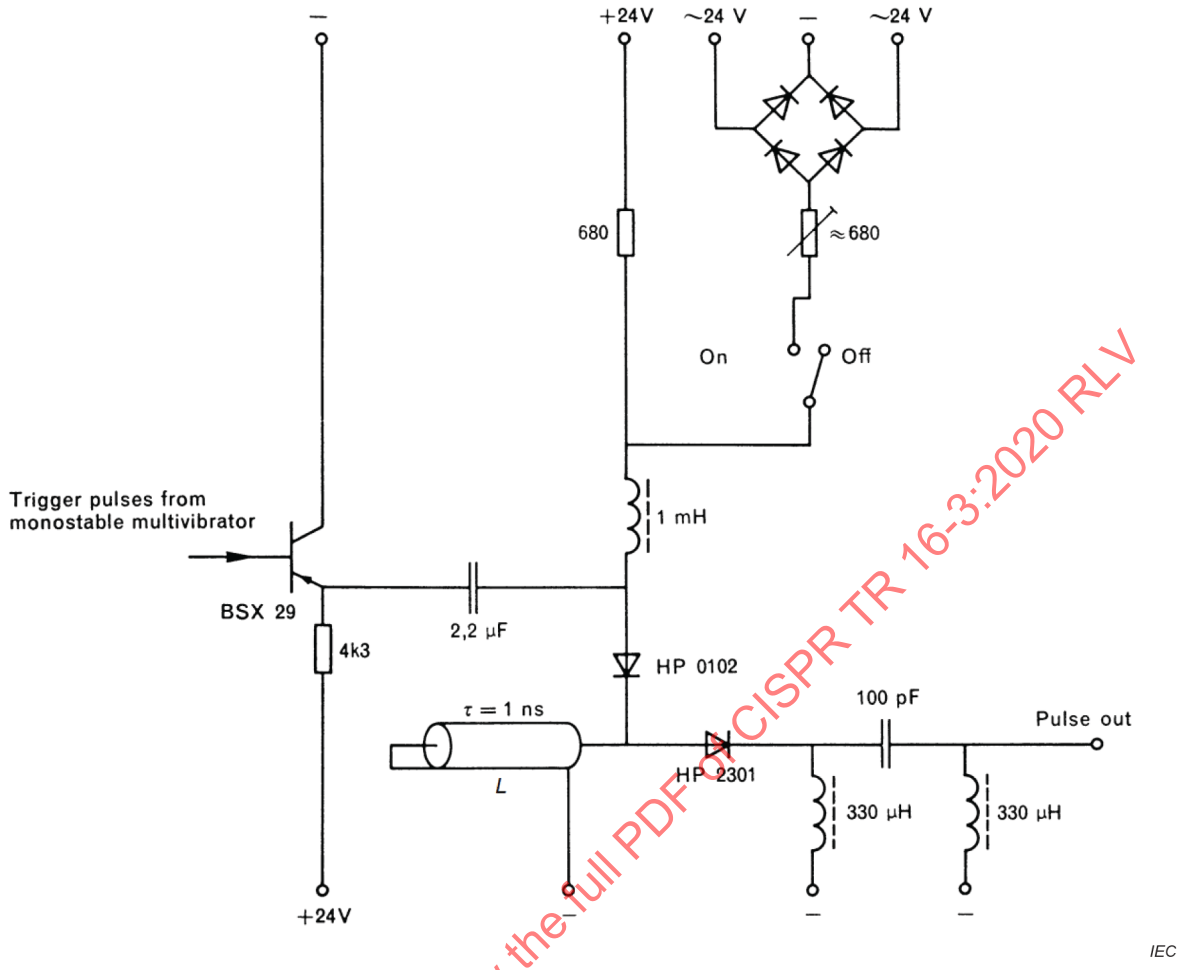



**Figure 6 – Details of a typical output stage**

## 4.3 Relationship between limits for open-area test site and the reverberation chamber

### 4.3.1 General

At present there are limits for use with the open-area test site method of measurement specified in several CISPR publications. For equipment that can be measured using the reverberation chamber method, a procedure is required to relate the limit to be used with that of the open-area test site (OATS) limit. The procedure is described in this subclause.

### 4.3.2 Correlation between measurement results of the reverberation chamber and OATS

The OATS measurement sets out to find the maximum level of radiation of an EUT (equipment under test). Whether the measurement is of the field strength or of power density at the measurement antenna, or of the power into an antenna in substitution of an EUT, the measured results can be expressed in terms of the equivalent radiated power from a half-wave dipole. Let this equivalent radiated power be $P_q$ in dB(pW).

The reverberation chamber measures the total radiated power of the EUT. Let the measured power be $P_t$ in dB(pW).

The two measurements are related to each other by the gain of the EUT as a radiator with respect to an isotropic radiator. Let this EUT gain be $G$ in dB. The relationship is given by Equation (6). The equation is derived in Annex A.

IECNORM.COM : Click to view the full PDF of CISPR TR 16-3:2020 RLV

$$P_t + G = P_q + 2 \quad (6)$$

#### 4.3.3 Limits for use with the reverberation chamber method

Consider the case of an EUT which is exactly on the limit, $L_o$, when measured in the open area test site, i.e. $P_q = L_o$.

This EUT should also be exactly on the corresponding limit, $L_r$, when it is measured in the reverberating chamber, i.e. $P_t = L_r$.

From Equation (6), we can relate the two limits as in Equation (7).

$$L_r = L_o + 2 - G \quad (7)$$

The value of $L_r$ is dependent not only on $L_o$, but also on $G$. Because $G$ will not be the same for all EUTs, it is not possible to set $L_r$ to treat all EUTs in a manner identical to the effect of $L_o$. If say $L_r = L_o$, then it is correct only for EUTs with $G = 2$. EUTs with a $G$ greater than 2 will find it easier to pass the reverberation chamber limit, and vice versa.

It is necessary to determine the value of $G$. This can be done from measurements of $P_q$ and $P_t$. Figure A.1 shows the curves of $P_q$ versus $P_t$ for various values of $G$. The shaded region is for negative values of $G$. (Experimental points appearing in this region are caused by failure to locate the maximum open-site radiation, probably due to the maximum radiation lying outside of the horizontal plane).

An example is given in Figure A.2. A number of microwave ovens were measured for $P_q$ and $P_t$. It can be seen that:

– for points lying in the positive $G$ region, the majority have values around 2;

– more points lying in the positive $G$ region as the frequency goes up, indicating that the radiation pattern is becoming more directional in the vertical direction.

Based on this evidence, the reverberation chamber results can be related to those of an OATS. In fact, use of a reverberation chamber appears to be a more effective method in the ability to measure a quantity representative of the maximum radiation.

#### 4.3.4 Procedure for the determination of the reverberation chamber limit

The procedure to determine the reverberation chamber limit is as follows.

i) Measure a sample of equipment for the maximum radiation on an OATS. Convert the measured quantities to the equivalent power from a half-wave dipole. Call this quantity $P_q$, in dB(pW).

ii) Measure the same sample in the reverberating chamber for total radiated power. Call this quantity $P_t$, in dB(pW).

iii) The relationship between the reverberation chamber limit and the OATS limit can be found by the graphical method of Figure A.1, or by calculating the gain of each equipment, obtaining a representative value of $G$ for the equivalent type using statistical methods, and applying Equation (7).

IECNORM.COM : Click to view the full PDF of CISPR TR 16-3:2020 RLV

## 4.4 Characterization and classification of the asymmetrical disturbance source induced in telephone subscriber lines by AM broadcasting transmitters in the LW, MW and SW bands

### 4.4.1 General

The use of semiconductor devices in telephone terminal equipment (TTE) has created the need to verify the immunity to RF fields of this equipment, as non-linear semiconductor devices demodulate the induced RF signals [1], [17], [18], [19], [20].[2] The latter effect gives rise to a DC shift which may alter the operating point of such a device, thus, for example, reducing the noise margin of digital devices. In the case of amplitude-modulated RF fields, the non-linearity gives rise to a baseband signal that may become audible in the telephony system. AM broadcasting transmitters in the LW, MW and SW bands form an important class of RF-field sources.

Because of the relatively small dimensions of TTE (compared to the wavelength of the disturbance signal) the asymmetrical (common-mode) source induced in telecommunication lines is expected to be the dominant disturbance source. Therefore, a conducted-immunity test (current-injection test) is relevant for this equipment. In this test, the disturbance signal is applied via the telecommunication lines. As a consequence, this subclause deals with the characterization of the unwanted antenna properties of telecommunication lines and with prediction models supplying information about the probability that certain parameter values will be met in practice. Moreover, it discusses the parameters that are of relevance when specifying the disturbance source used in the immunity test. The various considerations will be limited to parameters relevant at the subscriber end of the telephone lines.

In 4.4.2 the antenna properties will be expressed in terms of an antenna factor of the subscriber lines i.e. the induced asymmetrical open-circuit voltage normalized to the RF field strength, and an equivalent resistance of the induced asymmetrical source. The prediction models are needed in the classification of the RF fields and the induced asymmetrical disturbances, i.e. 4.4.3, and when setting immunity limits, i.e. 4.4.4. This subclause takes the view that the disturbance source in the immunity test is to be specified by an open-circuit voltage and a source impedance.

All mathematical relations associated with the derivation of the models and those needed by the user of this subclause when applying the models to the respective geographical area are given in Annex B, Annex C, Annex D, and Annex E.

This subclause is based on results of experimental investigations carried out on buried telephone-subscriber lines in Germany [21], [22] and in the Netherlands [23]. In these investigations induced-voltage and current data and magnetic-field-strength data were recorded at a large number of locations, permitting a statistical evaluation of the parameter values. A statistical approach was needed, because the telephone lines have random routing in the buildings and, consequently, random orientation with respect to the RF field makes for random coupling with nearby metal objects, while the buildings cause a random scattering of the RF fields.

It is to be expected that the contents of this subclause will also be applicable to other types of lines running through buildings in a similar manner to telephone-subscriber lines, for example, bus-system lines and signal and control lines.

### 4.4.2 Experimental characterization

#### 4.4.2.1 General

A full description of the experimental characterization is presented in [22] and [23]. Therefore, this subclause contains only a summary of this method with regard to the parameters needed.

---

2 Numbers in square brackets refer to the bibliography.

IECNORM.COM : Click to view the full PDF of CISPR TR 16-3:2020 RLV

The induced asymmetrical voltage was measured at the outlet of a telephone-subscriber line using a modified T-network [24] and [25]. As a result of this modification, a voltage $U_h$ could be measured across a 10 kΩ resistor and a voltage $U_l$ across a 150 Ω resistor. The investigations showed that $U_h$ could be considered as the induced open-circuit voltage. In practice, the reference for this voltage is generally unknown. During the measurements that reference was a special metal measuring cart connected via a copper strap to the central heating system. The equivalent resistance $R_a$ of the induced source is estimated from data pairs $\{U_h, U_l\}$.

At each location two magnetic-field-strength data of the broadcasting transmitter were measured using a loop antenna positioned in a vertical plane and rotated about its vertical axis to find the maximum reading. One datum, $H_i$, was measured near the outlet under investigation inside the building, and one datum, $H_o$, was measured outside the building at a distance of about 10 m from that building. In order to obtain a sufficiently high induced-signal-to-ambient-noise ratio, the measurements were carried out in areas with a relatively high value of the RF field strength. This is not expected to influence the applicability of the results, as the presence of a broadcasting transmitter is not taken into account in the layout of telephone-subscriber lines. Moreover, as mentioned in 4.4.1, the induced voltage will be normalized to the field strength and the resulting "antenna factor" will represent a property of the subscriber lines measured.

#### 4.4.2.2 Field strength and building effect

Although the RF field is not a characteristic of the subscriber lines, it forms the origin of the induced disturbances. Two aspects of the RF field will be considered in this subclause:

a) The measured field strength $H_o$ outside the buildings compared to the field strength $H_c$ calculated from the simple far-field relation for a half-wave dipole (in its main direction):

$$H_c = \frac{7\sqrt{P}}{Z_0 r} \tag{8}$$

where

$P$ is the transmitter power;

$Z_0$ is free-space wave impedance (377 Ω) and

$r$ the distance between the transmitter and the point of observation.

In the calculations, the values of $P$ as given in [28] are used.

NOTE Although broadcast transmitter antennas usually are monopoles (in the frequencies of interest), the half-wave dipole formula in Equation (8) has been used for convenience.

b) The effect of the building on the field strength, which can be expressed in a building-effect parameter $A_b$ defined by:

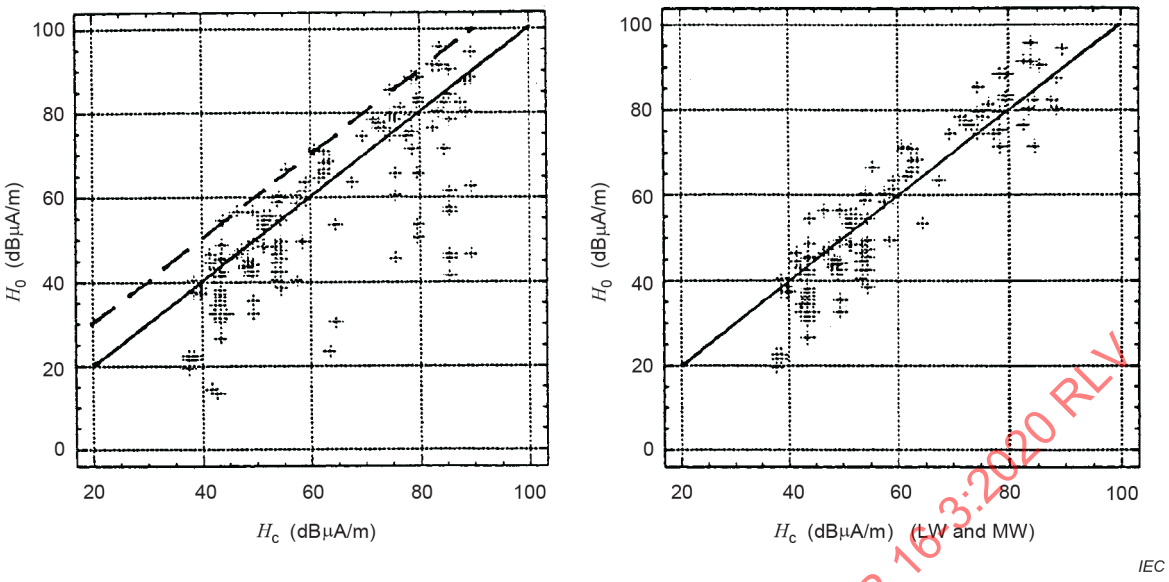
$$A_b = H_o - H_i \tag{9}$$

where $H_o$ and $H_i$ are in dB(μA/m).

This factor is often called the building attenuation. However, this factor not only depends on the attenuation properties of the building material itself, but also on the re-radiation properties of metallic structures in and near the building, and on the height above ground at which $H_o$ and $H_i$ were measured. Therefore the term building effect is used in this subclause.

A consideration of these two aspects is needed in view of the antenna factors to be discussed in 4.4.2.3 and in view of the prediction models to be discussed in 4.4.2.4.

IECNORM.COM : Click to view the full PDF of CISPR TR 16-3:2020 RLV



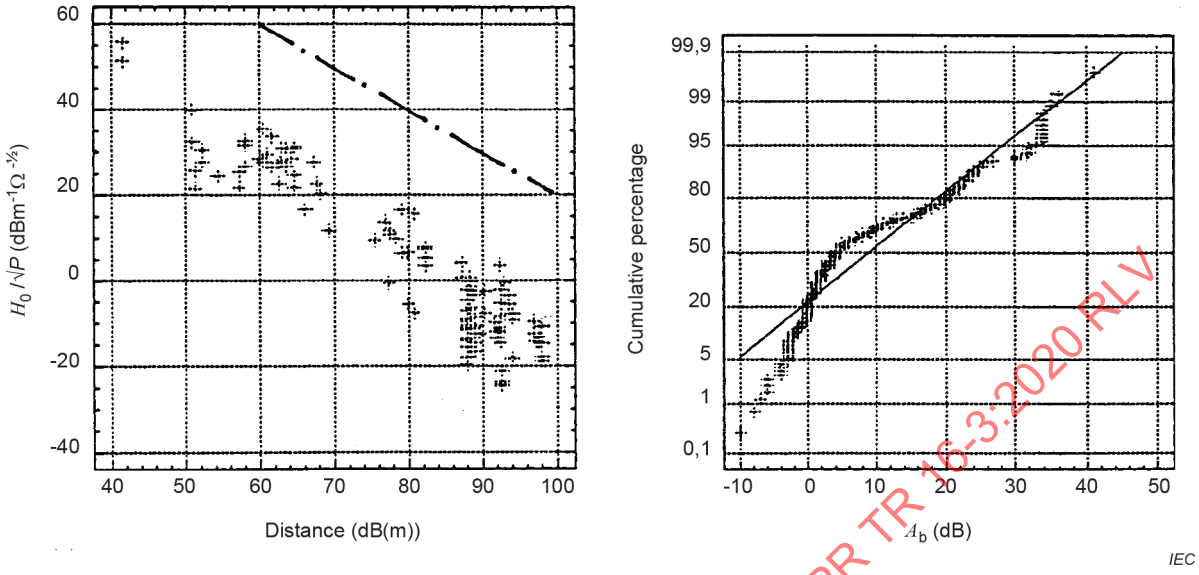

a) All data

b) Data of SW transmitters rejected

**Figure 7 – Scatter plot of the measured outdoor magnetic field strength $H_o$ (dBμA/m) versus the calculated outdoor magnetic field strength $H_c$ dB(μA/m)**

The results of $H_o(H_c)$ given in Figure 7a) show that large deviations from $H_o = H_c$ are possible (solid line), but that $H_o \leq (H_c + 10)$ dB(μA/m) (dashed line), hence the measured value is at most a factor of 3 higher than the value calculated from Equation (8). The largest deviations concern data of SW transmitters. This is understandable, because SW transmitters normally have a beamed antenna pattern, whereas the antenna patterns of the LW and MW transmitters are generally close to circular. Figure 7b) gives the scatter plot $H_o(H_c)$ after rejection of the SW transmitter data.

IECNORM.COM : Click to view the full PDF of CISPR TR 16-3:2020 RLV




**a) Scatter plot of the measured outdoor magnetic field strength $H_o$ normalized to the square root of the reported power [26] versus the distance $d$ (m) to the transmitter**

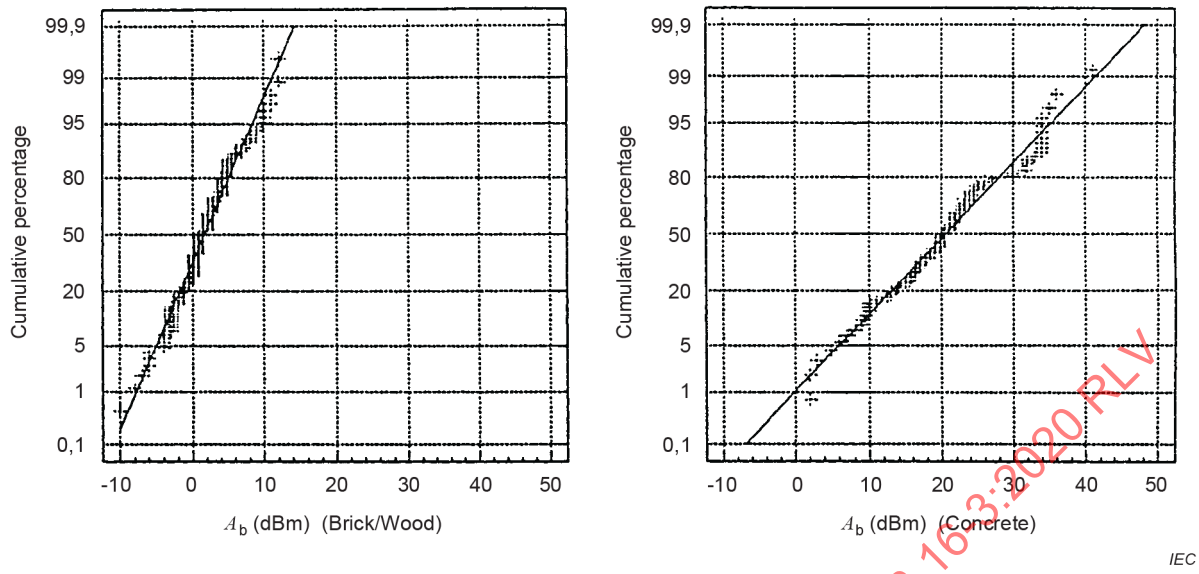
**b) Normal probability plot of the building-effect parameter $A_b$ dB, all data**

**Figure 8 – Measured outdoor magnetic versus distance, and probability of the building-effect parameter**

Figure 8a) shows the ratio $H_o/\sqrt{P}$ versus the distance between the point of observation and the transmitter, and the dash-dot line indicates a slope –1. It can be concluded that, on average, the data follow this slope fairly well. The associated intercept is higher than that expected from Equation (8), which is in agreement with the ($H_c$ + 10) dBμA/m limit observed in Figure 7.

Figure 8b) shows the normal probability plot of all building-effect data. If these data were normally distributed, a straight line would have resulted. This is not the case, and the data suggest that, in a first-order approximation, two distributions are superimposed. The two distributions are found when distinguishing between data associated with buildings constructed from brick and/or wood (B/W) and data associated with buildings constructed from reinforced concrete (C). The normal probability plots of these distributions are given in Figure 9a) and Figure 9b). The negative values of $A_b$ predominantly stem from measurements where $H_i$ was measured on an upper floor of the building, whereas $H_o$ was already measured at about 1,5 m above ground level outside the building. Effects of re-radiation also influence the actual field-strength data.

IECNORM.COM : Click to view the full PDF of CISPR TR 16-3:2020 RLV




**a) Buildings constructed from brick and/or wood**

**b) Buildings constructed from reinforced concrete**

**Figure 9 – Normal probability plot of the building-effect parameter $A_b$ dB**

The numerical results have been summarized in Table 3. No clear frequency dependence of the $A_b$ data could be observed (see 4.4.2.5).

**Table 3 – Summary results of building-effect, $A_b$, analysis**

| Building material | Average<br>dB | Standard deviation<br>dB | Median<br>dB | Number of data |
|---|---|---|---|---|
| Brick and/or wood | 1,6 | 4,0 | 1,0 | 138 |
| Reinforced concrete | 20,6 | 8,7 | 20,1 | 84 |

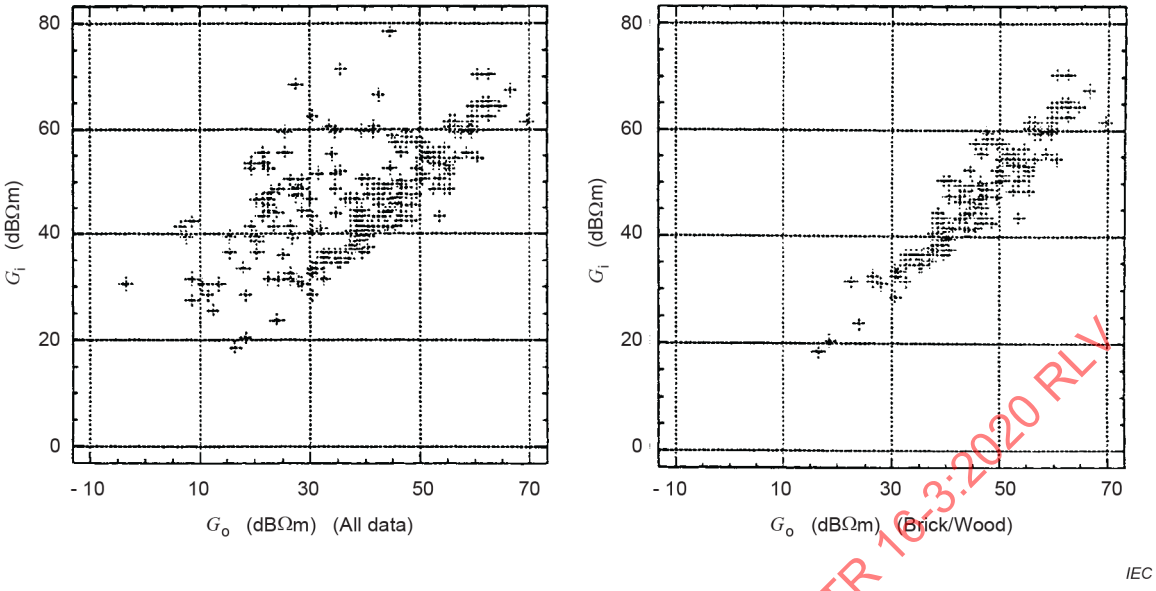
#### 4.4.2.3 The asymmetrical open-circuit voltage normalized to the field strength

##### 4.4.2.3.1 General

The interface for the voltage measurements was the outlet to which the telephone set was connected during the measurements. The investigations showed that the influence on the measured voltages of the telephone set and its standard lead (4 m long) could be neglected.

The measured voltage will be normalized to the measured magnetic field strength in 4.4.2.3.2, and assuming far-field conditions, to the electric field strength in 4.4.2.3.3. After that, 4.4.2.3.4 deals with truncation of the distributions found in 4.4.2.3.2 and 4.4.2.3.3.

IECNORM.COM : Click to view the full PDF of CISPR TR 16-3:2020 RLV




**a) All data**

**b) Data associated with buildings constructed from brick and/or wood**

**Figure 10 – Scatter plot of the outdoor antenna factor $G_o$ dB(Ωm) versus the indoor antenna factor $G_i$**

#### 4.4.2.3.2 *G* factors

To obtain an antenna property of the subscriber lines, the open-circuit voltage $U_h$ is normalized to the field strength ($H_i$ or $H_o$), yielding the antenna factors $G_i$ and $G_o$ defined by

$$G_{i,o} = \frac{U_h}{H_{ino}} \tag{10}$$

where

$G_{i,o}$ is in Ωm,

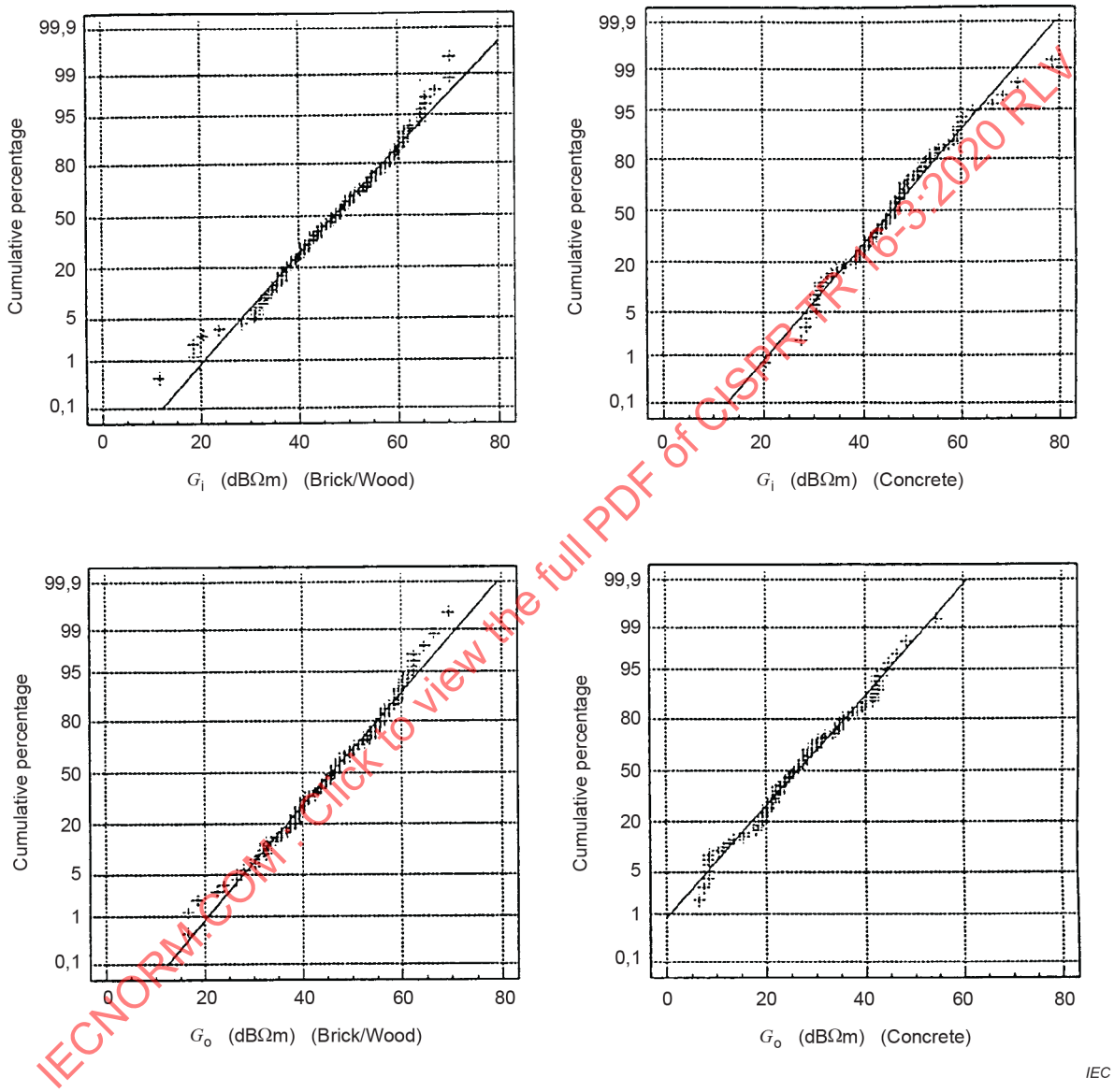
$U_h$ is in μV, and

$H_{ino}$ is in μA/m.

Figure 10a) shows the scatter plot $G_i(G_o)$ using all data. The plot suggests that there is one dominant "cloud" of data with a limited scattering and a second "cloud" with much more scattering. Further investigation revealed that the first cloud stems from data measured in buildings constructed from brick and/or wood, see Figure 10b), while the other cloud is associated with buildings constructed (predominantly) from reinforced concrete. Consequently, the building effect discussed in 4.4.2.2 is of importance.

IECNORM.COM : Click to view the full PDF of CISPR TR 16-3:2020 RLV

The normal probability plots of $G_i$ dB(Ωm) and $G_o$ dB(Ωm) associated with the two types of building material considered, are given in Figure 11. It can be concluded that the data follow a normal distribution, which means lognormal distributions of the $G$ factors in Ωm. The numerical results have been summarized in Table 4, where $G_U$ and $G_L$ are the upper and lower limit of the range of experimental $G$ data (see 4.4.2.3.4). The differences between $G_i$ and $G_o$ of the two classes of building material considered are consistent with the building-effect data for these buildings (see Table 3). No clear frequency dependence could be observed (see 4.4.2.5).




**a) $G_i$ dB(Ωm) and c) $G_o$ dB(Ωm), associated with buildings constructed from brick and/or wood**

**b) $G_i$ dB(Ωm) and d) $G_o$ dB(Ωm), associated with buildings constructed from reinforced concrete**

**Figure 11 – Normal probability plots of the antenna factors**

IECNORM.COM : Click to view the full PDF of CISPR TR 16-3:2020 RLV

**Table 4 – Summary of results of $G$-factor analysis**

| $G$ factor | Building material | Average<br>dB(Ωm) | Standard deviation<br>dB | Median<br>dB(Ωm) | Number of data points |
|---|---|---|---|---|---|
| $G_i$ | B/W | 47,3 | 11,2 | 47,5 | 135 |
| $G_i$ | C | 45,9 | 10,5 | 46,5 | 88 |
| $G_o$ | B/W | 45,8 | 10,6 | 46,4 | 134 |
| $G_o$ | C | 26,5 | 10,9 | 26,0 | 90 |

#### 4.4.2.3.3 $L$ factors

In 4.4.2.3.2, $U_h$ was normalized to the measured magnetic field strength, thus yielding the $G$ factors. Assuming far-field conditions, the electric field strength follows from $E = Hz_0$ with $Z_0 = 377\ \Omega$. If the outdoor field strength is considered, this assumption seems to be reasonable and the $G_o$ factor can be converted into an $L_o$ factor defined by

$$L_o = \frac{G_o}{Z_0} = \frac{U_h}{H_o Z_0} = \frac{U_h}{E_o} \tag{11}$$

where $U_h$ is in µV and $E_o$ is in µV/m.

The $L$ factor can be considered as the effective length or effective height of the subscriber line acting as an antenna. The results for $L_o$ have been summarized in Table 5, where $L_U$ and $L_L$ are the upper and lower limit of the range of experimental $L$ factors (see 4.4.2.3.4).

**Table 5 – Summary of $L_o$ factors (far-field)**

| $L$ factor | Building material | Average[a]<br>dB(m) | Standard deviation<br>dB | $L_U$<br>dB(m) | $L_L$<br>dB(m) |
|---|---|---|---|---|---|
| $L_o$ | B/W | –5,7 | 10,6 | 18,0 | –35,0 |
| $L_o$ | C | –25,0 | 10,9 | 3,0 | –55,0 |

[a] Note that dB(m) refers to dB with respect to 1 m.

In the literature an $L$ factor of –3,0 dB(m) average (standard deviation 10 dB, number of data points = 10) has been reported [27] for a cable running 1 300 m underground and 1 000 m to 3 000 m overhead (aerial cable) towards the subscriber. Broadcasting frequencies were 594 kHz and 1 242 kHz. No details were given about the field-strength measurements, the reference for the asymmetrical voltage and the properties of the building material. The results reported in [27] are in line with the results for $L_o$ (B/W), as given in Table 5. However, more recent investigations by the same team [29] indicate an average $L$-factor of 0 dB(m).

$L_i$ factors might be derived from the $G_i$ factors in a similar way as the $L_o$ factors. However, it is to be expected that inside the buildings the far-field conditions are not satisfied and it has to be decided which wave impedance has to be taken. Therefore, no $L_i$ data have been presented in Table 5. See also NOTE 2 at the end of 4.4.4.2.

#### 4.4.2.3.4 Truncation

In 4.4.2.3.2 it was concluded that the distribution $f(G)$ of the $G$ factors (antenna factors) is lognormal or in mathematical form

IECNORM.COM : Click to view the full PDF of CISPR TR 16-3:2020 RLV

$$f(g)dG = \frac{1}{G\sigma\sqrt{2\pi}} e^{(\ln G-\mu)/2\sigma^2}\, dG \tag{12}$$

However, by adopting this lognormal distribution it is automatically assumed that a $G$ factor may range from zero to infinitely large. In practice, infinitely large will never occur as wavelength effects and effects of coupling with nearby structures create an upper limit ($G_U$ or $L_U$) of the antenna factors [28]. Consequently, for correct use in the prediction models (4.4.3 and 4.4.4) $f(G)$ has to be truncated. Similarly, truncation has to be applied to the distribution of the building-effect parameters.

Unfortunately, no theoretical study is known which predicts the upper limit of $G$ (or $L$) of an actual telephone-subscriber line taking into account the length and the routing of a line inside the building and, buried, outside the building. However, it has to be expected that such a limit exists and the best approach is to use the experimental upper limit ($G_U$ or $L_U$).

In addition to the upper limit, one may also consider a lower limit ($G_L$ or $L_L$) and truncate $f(G)$ at the lower end. It is found that in the range of parameter values to be considered in 4.4.3 and 4.4.4, the influence of $G_L$ (or $L_L$) is negligible.

The truncated probability density function reads

$$f_t(G)dG = \frac{f(G)dG}{\int_{G_L}^{G_U} f(G)dG} = \frac{f(G)dG}{F(G_U) - F(G_L)} = \alpha_t f(G)dG \tag{13}$$

The mathematical form of the cumulative distributions $F(G_U)$ and $F(G_L)$ is given in Annex E. Table 6 summarizes the truncation data of the $G$ factors and the building-effect parameter $A_b$. Note that $\alpha t$ differs very little from 1, that is from the value of $\alpha t$ if $-\infty \le G$ dB(Ωm) $\le \infty$ or $-\infty \le A_b$ (dB) $\le \infty$ because $F(\infty) = 0{,}5$ and $F(-\infty) = -0{,}5$. The upper and lower limit in dB(m) of the $L$ factor range are found by subtracting 51,5 dB(Ω) from the corresponding $G$ factors in dB(Ωm).

**Table 6 – Summary of truncation parameters of $f(G)$**

| $G$ factor or $A_b$ | Building material | $G_U$ dB(Ωm) $A_{bu}$ (dB) | $G_L$ dB(Ωm) $A_{bl}$ (dB) | $F(G_U)$ $F(A_{bu})$ | $F(G_L)$ $F(A_{bl})$ | $\alpha t_G$ $\alpha t_A$ |
|---|---|---|---|---|---|---|
| $G_i$ | B/W | 70,5 | 11,5 | 0,480 5 | –0,499 3 | 1,021 |
| $G_i$ | C | 78,5 | 20,5 | 0,498 5 | –0,492 2 | 1,009 |
| $G_o$ | B/W | 69,5 | 16,5 | 0,487 3 | –0,497 1 | 1,016 |
| $G_o$ | C | 54,5 | –3,5 | 0,495 0 | –0,497 1 | 1,008 |
| $A_b$ | B/W | 12,0 | –10,0 | 0,495 3 | –0,498 1 | 1,007 |
| $A_b$ | C | 41,0 | 2,0 | 0,490 5 | –0,483 7 | 1,026 |

#### 4.4.2.4 The equivalent asymmetrical-source resistance

The equivalent resistance of the induced asymmetrical source can be determined from data pairs $\{U_h, U_l\}$, where $U_h$ is the open-circuit voltage and $U_l$ the voltage measured across 150 Ω, using the simple relation:

IECNORM.COM : Click to view the full PDF of CISPR TR 16-3:2020 RLV

$$R_a = \frac{U_h - U_l}{U_l} 150\ (\Omega) \tag{14}$$

The normal probability plot of $R_a$ dB(Ω) is given in Figure 12. It can be concluded that $R_a$ in dB(Ω) follows a normal distribution and, hence, $R_a$ in Ω follows a lognormal distribution. The numerical results have been summarized in Table 7. The average value found is close to the value 150 Ω used in existing immunity tests [24], [14]. In Table 7, $R_{au}$ and $R_{al}$ are the upper and lower limit of the range of experimental $R_a$ data. The relatively large and small values of $R_{au}$ and $R_{al}$ compared to the average value of $R_a$ stem from resonances and anti-resonances in the common mode circuit of the subscriber line. No clear frequency dependence of $R_a$ could be observed (see 4.4.2.5), and no influence of the building material was observed.

**Table 7 – Summary results of equivalent-resistance analysis**

| $R_a$ (average) | Standard deviation | Median | $R_a$ (average) | Number of data points | $R_{au}$ | $R_{al}$ | $R_{au}$ | $R_{al}$ |
|---|---|---|---|---|---|---|---|---|
| dB(Ω) | dB | dB(Ω) | Ω | | dB(Ω) | dB(Ω) | Ω | Ω |
| 44,2 | 6,8 | 43,5 | 162 | 204 | 63,7 | 25,2 | 1 531 | 18 |

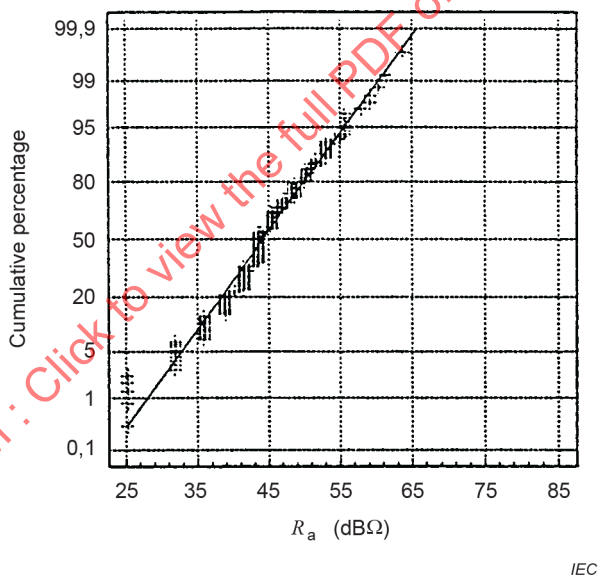


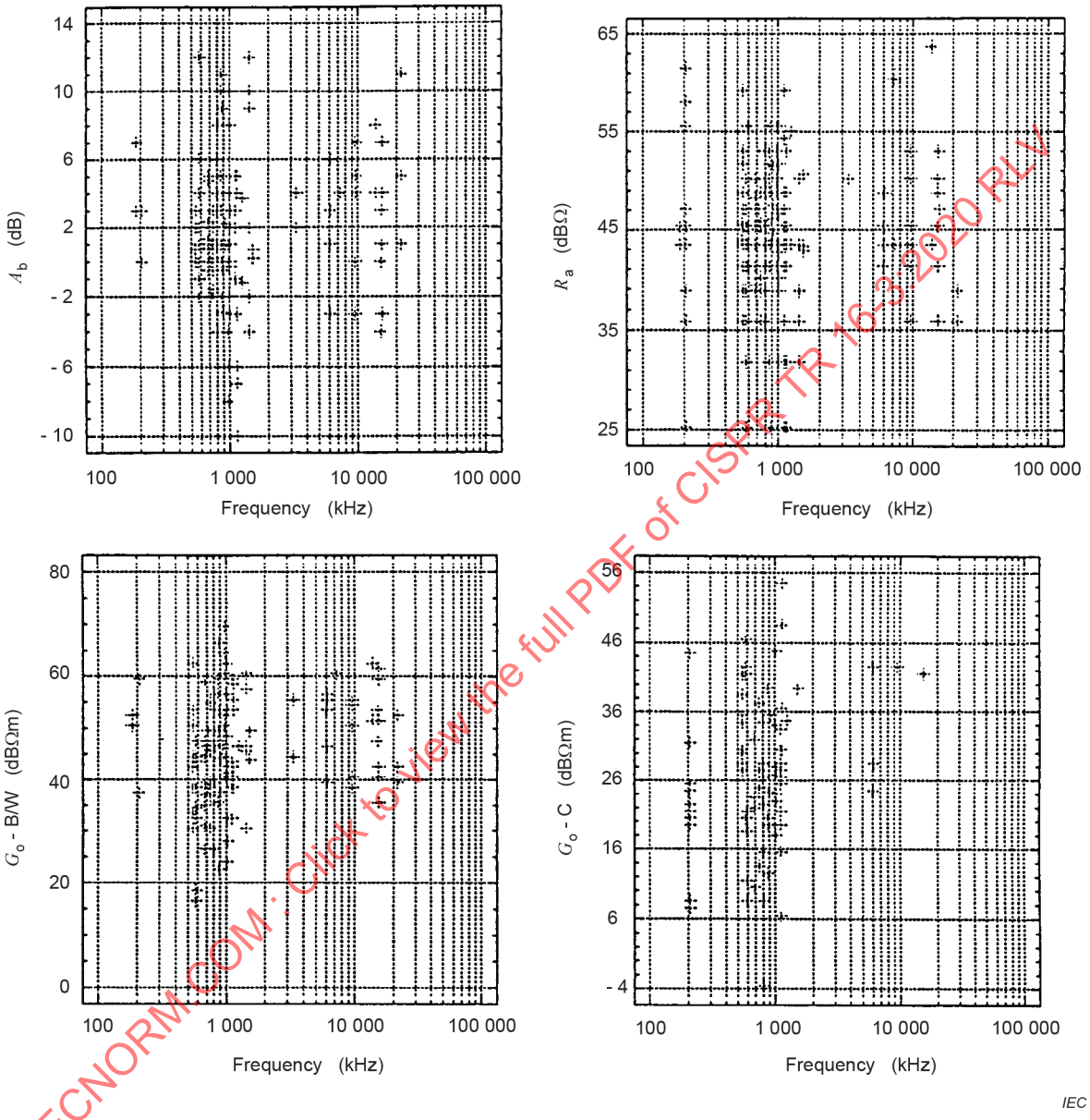

**Figure 12 – Normal probability plot of the equivalent asymmetrical resistance $R_a$ dB(Ω)**

#### 4.4.2.5 Frequency dependence of the parameters

In the frequency range determined by the measurements in the LW, MW and SW bands, no clear frequency dependence of the building effect $A_b$, the $G$ factors $G_o$ and $G_i$, and the equivalent resistance $R_a$ could be observed. This is illustrated in Figure 13a) and Figure 13b) the $A_b$ data for brick/wood buildings, the $R_a$ data, the $G_o$ data for brick/wood buildings, and for reinforced concrete buildings.

IECNORM.COM : Click to view the full PDF of CISPR TR 16-3:2020 RLV

Because no clear frequency dependence of the various quantities could be observed, it will be assumed in 4.4.3 and 4.4.4 that the building effect, the $G$ and the $L$ factors and the equivalent resistance are independent of the frequency in the frequency range of the LW, MW and SW bands. A possible frequency dependence is then incorporated in the standard deviation of the respective distributions.




a) Building effect $A_b$ in the case of brick/wood buildings

b) Equivalent resistance $R_a$

c) $G_o$ factor for brick/wood buildings

d) $G_o$ factor for reinforced concrete buildings

**Figure 13 – Examples of the frequency dependence of some parameters**

### 4.4.3 Prediction models and classification

#### 4.4.3.1 General

This subclause presents some simple prediction models for fields and voltages needed in the process of classification of the electromagnetic environment and when setting immunity limits for the telephone sets to be connected to the subscriber lines.

IECNORM.COM : Click to view the full PDF of CISPR TR 16-3:2020 RLV

Because the measuring locations were not chosen randomly in order to obtain a sufficiently high induced signal-to-ambient noise ratio, the basic data from which the parameters reported in 4.4.2 were derived cannot be used directly because they form a non-random sample from their actual distributions. The models to be discussed permit an estimate to be made of the complete distributions of the field strength and induced voltage. In addition, the complete distributions allow for a classification of these quantities. This subclause gives only the procedure for this classification. The actual class limits are outside its scope.

#### 4.4.3.2 Field-strength classification

As mentioned in 4.4.2.2, the field strength is not a property of the subscriber line. Nevertheless, information about the field strength is needed in order to make a prediction of the induced voltages.

From the results given in 4.4.2.2, it follows that in a first-order approximation the outdoor field strength, to be indicated by $E_o$ and $H_o$ for the electric and magnetic field component respectively, is inversely proportional to the distance $r$ between the point of observation and the transmitter, and proportional to the square root of the transmitter power. From the results summarized in 4.4.2.2 it follows that, in the worst case, the constant of proportionality is a factor of 3 (≡ 10 dB) larger than the constant of proportionality in the case of a half-wave dipole.

A classification of the outdoor electric or magnetic field strength may be based on the probability $pr\{E_o \geq E_L\}$ or $pr\{H_o \geq H_L\}$ that the outdoor field strength is greater than or equal to a given limit value, indicated by the subscript $L$. As explained in Annex B, this probability can be written as

$$pr\{H_o \geq H_L\} = \int_{R_L}^{H_{max}} f_n(H)dH \quad \text{or} \quad pr\{E_o \geq E_L\} = \int_{E_L}^{E_{max}} f_n(E)dH \tag{15}$$

where

$f(H)$ and $f(E)$ are the normalized field-strength distribution, and

$H_{max}$ and $E_{max}$ are the maximum field strength in the geographical region in which the probability has to be estimated.

Under far-field conditions both relations in Equation (15) are equivalent.

Considering a ring-shaped area (RSA) around a transmitter having a circular antenna pattern, it follows (see Annex B) that

$$pr\{E_o \geq E_L\} = \frac{\left(E_{max}^2 - E_L^2\right)E_{min}^2}{\left(E_{max}^2 - E_{min}^2\right)E_L^2} \approx \frac{E_{min}^2}{E_L^2} \tag{16}$$

where

$E_{max}$ is the field strength at the inner boundary of the RSA, and

$E_{min}$ is the field strength at the outer boundary of the RSA.

A similar expression is valid for the magnetic field strength (see Annex B).

IECNORM.COM : Click to view the full PDF of CISPR TR 16-3:2020 RLV

The inner boundary of the RSA has to be specified, as the relation between $E_o$ and $r$ derived from the measuring data will not be valid arbitrarily close to the transmitter, i.e. in the near-field region of the transmitter. A non-zero outer boundary field strength is needed, as $E_{min}$ = 0 would mean that $pr\{E_o \geq E_L\}$ = 0 for all values of $E_L$. Note that by definition $pr\{E_o \geq E_L\}$ = 0 and that $pr\{E_o \geq E_{min}\}$ = 1 (= 100 %). The approximation given in Equation (16) is valid if $E_{max} >> \{E_{min}, E_L\}$, which is normally the case. Hence, it can be concluded that in the present model the value of $E_{min}$ to be specified is very important. The choice of $E_{min}$ and $E_{max}$ will be discussed further in 4.4.4.

As an example, Table 8 gives the values of $E_L$ for a number of probability values, assuming $E_{max}$ = 60 V/m, which is an example of a radiation-hazard limit in the MW band of frequencies, and $E_{min}$ = 0,01 V/m [= 80 dB(μV/m)]. The latter value is of the order of magnitude of the minimum field strength in the service area of a broadcasting transmitter. Note that the probability values are almost completely determined by $E_{min}$.

**Table 8 – Example of field-strength classification**

| $pr\{E_o \geq E_L\}$ | $E_L$ | $\frac{E_{min}}{\sqrt{pr\{E_o \geq E_L\}}}$ | $P$ = 500 kW | |
|---|---|---|---|---|
| | | | $k$ = 7<br>$R_L$ | $k$ = 22<br>$R_L$ |
| % | V/m | | m | m |
| 0 | 60 | – | (80) | (260) |
| 100 | 0,01 | – | 495 000 | 1 550 000 |
| $10^{-1}$ | 0,32 | 0,33 | 15 652 | 49 193 |
| $10^{-2}$ | 1,00 | 1,00 | 4 950 | 11 556 |
| $10^{-3}$ | 3,16 | 3,16 | 1 565 | 4 919 |
| $10^{-4}$ | 9,86 | 10,00 | 495 | 1 556 |

By expressing the RSA boundaries in terms of a field strength, and not, for example, in terms of the distance between the transmitter and the point of observation, Equation (15) is applicable to any transmitter producing a field strength which is inversely proportional to the distance. However, after the classes have been established, a certain transmitter will have a certain value of the constant of proportionality $k$. Then class boundaries can be associated with distances $R_L = (k/P)/E_L$ between transmitter and point of observation. In Table 8 examples of $R_L$ are given, assuming $k$ = 7 (as in the case of a half-wave dipole) and $k$ = 22 (the worst-case value found in 4.4.2.2), while the transmitter power $P$ = 500 kW. The $R_L$ values for $E_L$ = 60 V/m have been put in between brackets, because, in the considered frequency range, the far-field condition is not valid at these distances.

The advantage of choosing the field-strength boundaries first is that the classes are the same for all kinds of transmitter, while the choice of a class is then determined by the probability that victim equipment will be at a certain distance from the chosen class of transmitters. In general, an estimate of the latter probability is easier than an estimate of the field-strength probability.

#### 4.4.3.3 Asymmetrical-voltage classification

A classification of the induced open-circuit common-mode voltage $U_h$ may be based on the probability $pr\{U_h \geq U_L\}$ that $U_h$ is equal to or larger than a given limit value $U_L$. If $f_t(G)$ describes the truncated distribution of $G$ factors (see 4.4.2.3.4), $f_n(H_o)$ the normalized field-strength distribution and use is made of the relation $U_h = G_o \times H_o$, in Annex C it is shown that this probability can formally be written as

IECNORM.COM : Click to view the full PDF of CISPR TR 16-3:2020 RLV

$$pr\{U_h \geq U_L\} = \int_{G_1}^{G_2} dG_o \int_{U_1}^{U_2} dU_h \frac{1}{G_o} f\left(\frac{U_h}{G_o}\right) f_t(G_o) \quad (17)$$

where $G_1$, $G_2$, $U_1$ and $U_2$ are suitably chosen boundaries (see Annex C). In Equation (17) the product of the two distributions, i.e. the joint distribution, is needed because $pr\{U_h \geq U_L\}$ depends on simultaneously meeting a certain field-strength value $H_o = (U_h/G_o)$ and a certain value of $G_o$. In Equation (17) the factor $1/G_o$ stems from the transformation of $f(H_o)$ into $f(U_h/G_o)$.

Note that Equation (17) is not an explicit function of the distance between the transmitter and the point of observation as a consequence of the fact that the boundaries of the RSA have been defined by field-strength values. A similar remark was made in connection with Equation (15), and similar conclusions are possible here.

Considering again the ring-shaped area as introduced in 4.4.3.2, examples of the classification of $U_h$, i.e. $U_L$ values corresponding with chosen values $pr\{U_h \geq U_L\}$, are given in classification of Table 9. The relations used can be found in Annex C. As in 4.4.3.1, it was assumed that the outdoor field strengths $E_{max}$ = 60 V/m ($H_{max}$ = 0,16 A/m) and $E_{min}$ = 0,01 V/m ($H_{min}$ = 27 µA/m) have been specified. When using $G_i$ and specifying the outdoor field strength, the building effect has to be taken into account, as is explained in Annex C.

**Table 9 – Example of voltage classification assuming for the outdoor field strength: $E_{max}$ = 60 V/m and $E_{min}$ = 0,01 V/m**

| | | $G_i$ | | $G_o$ | |
|---|---|---|---|---|---|
| **Building material** | | **B/W** | **C** | **B/W** | **C** |
| $A_b$ | dB | 1,6 | 20,6 | – | – |
| $S_b$ | dB | 4,0 | 8,7 | – | – |
| $A_{bu}$ | dB | 12,0 | 41,0 | – | – |
| $A_{bl}$ | dB | –10,0 | 2,0 | – | – |
| $G_{i,o}$ | dB(Ωm) | 47,3 | 45,9 | 45,8 | 26,5 |
| $S$ | dB | 11,2 | 10,5 | 10,6 | 10,9 |
| $G_U$ | dB(Ωm) | 70,5 | 78,5 | 69,5 | 54,5 |
| $G_L$ | dB(Ωm) | 11,5 | 20,5 | 16,5 | –3,5 |
| $pr\{U_h \geq U_L\}$ | | $U_L$ dB(µV) | $U_L$ dB(µV) | $U_L$ dB(µV) | $U_L$ dB(µV) |
| $10^{-1}$ | | 115 | 101 | 114 | 96 |
| $10^{-2}$ | | 125 | 111 | 124 | 106 |
| $10^{-3}$ | | 135 | 121 | 134 | 116 |
| $19^{-4}$ | | 145 | 131 | 143 | 125 |

**Key**

B/W is brick and/or wood

C is concrete

IECNORM.COM : Click to view the full PDF of CISPR TR 16-3:2020 RLV

### 4.4.4 Characterization of the immunity-test disturbance source

#### 4.4.4.1 General

The results presented in 4.4.2 and 4.4.3 may be used to specify the open-circuit voltage and the internal impedance of the disturbance source in a conducted-immunity test that would be needed to achieve a sufficiently high probability that TTE to be connected to the subscriber lines will be electromagnetically compatible.

The specification of the open-circuit voltage $U_h$ should be based on the distribution of the voltages over all telephone outlets to be considered. Therefore, this distribution is calculated first, using models and parameter values derived in the preceding subclauses. Once the distribution is known it is possible to calculate $N_o(U_h \geq U_L)$, i.e. the number of outlets in the respective geographical region showing a voltage $U_h \geq U_L$, where $U_L$ may be considered as the open-circuit voltage in the immunity test. The internal impedance may be chosen directly using the results given in Table 5. After that, the relevant parameters for the specification of the disturbance source in the immunity test will be summarized in 4.4.4.3.

This subclause gives only the procedures to arrive at a specification of the parameters needed. The assignment of actual values is the prerogative of the Product Committees.

#### 4.4.4.2 Outlet-voltage distribution

The derivation of the outlet-voltage distribution is described in detail in Annex C and Annex D. In this derivation, the following steps have been taken.

(1) Determine the total probability density $n(H_o)$ of the telephone outlets experiencing an outdoor magnetic field strength $H_o$ in ring-shaped areas around the $N$ transmitters to be considered, where the inner boundary of the areas is specified by a maximum field strength $H_{max}$ and the outer boundary by a minimum field strength $H_{min}$.

(Again, the magnetic field strength is considered first, because this field strength was measured in the experimental characterization procedure. If far-field conditions are valid, so that the magnetic and electric field strength have a constant ratio, the results can be converted directly in terms of the electric field strength.)

(2) Determine the joint probability density $f(H_o,G_o) = f(H_o) \times f(G_o)$ describing the density of outlets where the field strength has a magnitude $H_o$ and, simultaneously, the antenna factor of the subscriber lines has the magnitude $G_o$, then and convert the result into the joint probability density $f(U_h,G_o)$, by using the relation $U_h = H_o G_o$.

(3) Calculate the probability $pr\{U_h \geq U_L\}$. If $N_T$ is the total number of outlets in the respective geographical region, and the boundary conditions are taken into account such that $N_o(U_h \geq U_L) \leq N_T$ (or = 0) if $pf\{U_h \geq U_L\} = 1$ (or = 0), then the number of outlets $N_o(U_h \geq U_L)$ equals $N_T \times pr\{U_h \geq U_L\}$.

It is the prerogative of a product committee to choose a value of $N_o$ $(U_h \geq U_L)$ from which $U_L$ follows, and hence the open-circuit voltage of the disturbance source in the immunity test.

Assuming the field strength to be inversely proportional to the distance between the outlet and the transmitter, and assuming constant densities of outlets around the transmitters, it is shown in Annex D that the field-strength distribution $n(H_o)$ can be written as

$$n(H_o) = \frac{2\pi \sum_{j=1}^{N} \mu_j k_j^2 P_j}{E_o^3} = \frac{-C_{Eo}}{E_o^3} \tag{18}$$

IECNORM.COM : Click to view the full PDF of CISPR TR 16-3:2020 RLV

where

$\mu_j$ is the outlet density,

$k_j$ is the constant of proportionality of the $j$-th transmitter and

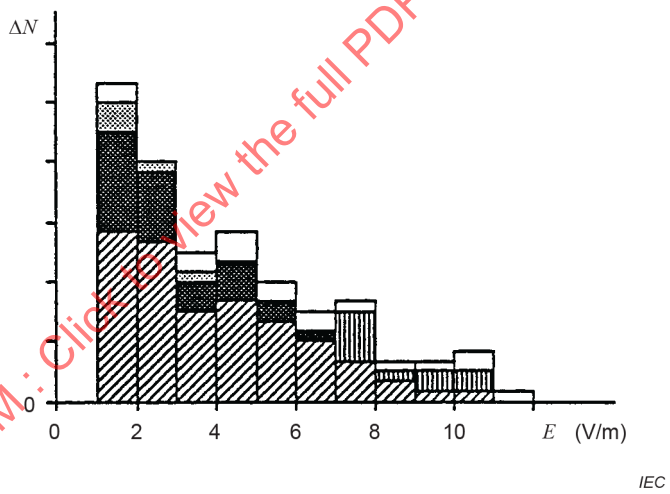
$N$ is the total number of transmitters considered.

If the density $\mu$ is the same around all transmitters and all transmitters have the same constant of proportionality $k$, $CH_o$ is simply a constant times the sum over all transistor powers.

When considering the electric field strength $E_o = (k/P)/r$, the distribution $n(E_o)$ reads

$$n(E_o) = \frac{2\pi \sum_{j=1}^{N} \mu_j k_j^2 P_j}{E_o^3} = \frac{-C_{Eo}}{E_o^3} \tag{19}$$

so that $C_{Eo} = C_{Ho} Z_o^2$. In Annex B and Annex C it is explained how the various relations change when the indoor field strength $H_i$ or $E_i$ is to be used.




NOTE The various shadings indicate schematically the contributions from various transmitters and non-homogeneous outlet densities; in this example the field-strength increment is $\Delta E_o$ = 1 V/m.

**Figure 14 – Example of the frequency histogram $\Delta N(E_o,\Delta E_o)$**

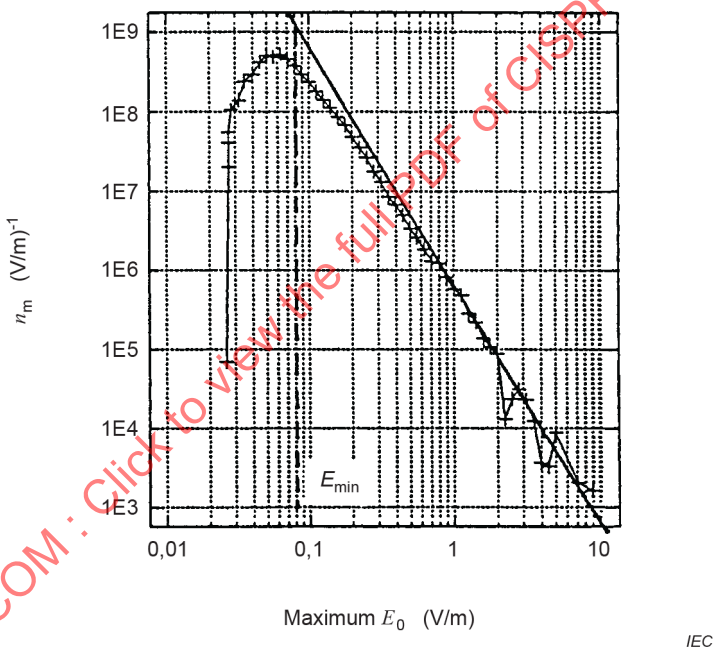
The outlet density, in general, will not be homogeneous around a transmitter. To derive $n(H_o)$ in that case, a possible procedure is to determine a frequency histogram $\Delta N(H_o,\Delta H_o)$ so that $n(H_o)$ is approximated by $n(H_o) = \Delta N(H_o,\Delta H_o) / \Delta H_o$.

In practice, the magnitude of the electric field strength is mostly considered, so $n(E_o)$ may be determined first, after which $n(H_o)$ follows after assuming far-field conditions. An example of $\Delta N(E_o,\Delta E_o)$ is given in Figure 14, where the different shadings indicate the various contributions resulting from various transmitters and non-homogeneous outlet densities around these transmitters.

IECNORM.COM : Click to view the full PDF of CISPR TR 16-3:2020 RLV

A drawback of the method leading to Figure 14 and a drawback of the model leading to Equations (18) and (19), is that the fields of the various transmitters overlap, particularly in the lower field strength regions. As a result, the same outlets in these regions are counted more than once if no discrimination is made with respect to the broadcast frequency. In 4.4.2.5 it was explained that no real frequency dependence could be observed, so this discrimination is not possible, which leads to an over-estimate of $\Delta N(E_o,\Delta E_o)$ at the lower field-strength values.

A procedure which might be followed is then to determine $n_m(E_o)$, i.e. the distribution of the maximum field strength in the respective geographical region resulting from the $N$ relevant transmitters in (and in the direct vicinity of) that region. An example of such a distribution is given in Figure 15. This distribution is a result for a part of Germany (having an area of 2,5 × $10^5$ km and 42 × $10^6$ outlets) by calculating the maximum field strength in each node at a 1 km by 1 km grid over this region as caused by one of the seventy-nine actual broadcasting transmitters in the respective frequency range, with a total ERP of 12,2 MW. The resolution of the field strength, i.e. $\Delta E_o$ was taken to be 0,1 dB(μV/m). It was assumed that the density $\mu$ was a constant (42 × $10^6$/2,5 × $10^5$ = 168 $km^{-2}$) throughout the region. When performing these calculations it was found that $n_m(E_o)$ does not vary much beyond a certain number (fifty in this case, with a total power of 7,5 MW) of transmitters taken into account.




NOTE The solid line represents $n(E_o) = -C_{Eo}/E_o^3$ with $n(E_o$ = 1 V/m) = $n_m(E_o$ = 1 V/m) × $E_{min}$ chosen such that the integral over the field strength of $n_m(E_o)$ and $n(E_o)$ both yield the total number of outlets in that region.

**Figure 15 – Example of $n_m(E_o)$, i.e. the distribution of the outlets experiencing a maximum field strength $E_o$ resulting from a given number of transmitters in (or near) the respective geographical region**

The solid line in Figure 15 represents $n(E_o) = -C_{Eo}/E_o^3$ with $C_{Eo}$ taken such that $n_m(E_o) = n(E_o)$ when $E_o$ = 1 V/m. This value is somewhat smaller than $C_{Eo}$ calculated from Equation (19), due to the aforementioned fact that $n_m(E_o)$ seems to "saturate" when the number of transmitters is increased.

When integrating the distributions over the entire respective region, the total number of outlets $N_T$ shall follow the equation

IECNORM.COM : Click to view the full PDF of CISPR TR 16-3:2020 RLV

$$N_T = \int_{E\,\min}^{E\,\max} n(E_o)\,d_{Eo} = \frac{C_{Eo}}{2}\left\{\frac{1}{E_{\min}^2} - \frac{1}{E_{\max}^2}\right\} \quad (20)$$

where the right-hand side of Equation (20) follows when Equation (19) is used. Equation (20) indicates that for a given or agreed maximum field strength $E_{max}$, the value of $E_{min}$ follows when $C_{Eo}$ is given or that $C_{Eo}$ follows when $E_{min}$ is given. The former approach was used to calculate $E_{min}$ = 0,08 V/m, as indicated in Figure 15, assuming $n_m(E_o$ = 1 V/m) = $C_{Eo}/E_o^3$ = $C_{Eo}$) 5,4 × $10^5$ $V^2/m^2$.

**Table 10 – Summary of the parameters used in the numerical examples presented in Figure 16 and Figure 17**

| Figure | | 16 | 17 a) | | | 17 b) | | |
|---|---|---|---|---|---|---|---|---|
| Curve | | – | 1 | 3 | 4 | 2 | 3 | 4 |
| *L*-factor | | $L_o$ | $L_o$ | $L_o$ | $L_o$ | $L_i$ [a] | $L_o$ | $L_i$ [a] |
| Building material | | B/W | B/W | B/W | B/W | B/W | C | C |
| $M_L$ | dB(m) | –5,7 | –5,7 | –5,7 | –5,7 | –4,2 | –25,0 | –5,6 |
| $S_L$ | dB | 10,6 | 10,6 | 10,6 | 10,6 | 11,2 | 10,9 | 10,5 |
| $L_u$ | dB(m) | 18,0 | +∞ | 18,0 | 18,0 | 19,0 | 3,0 | 27,0 |
| $L_u$ | m | 7,9 | +∞ | 7,9 | 7,9 | 8,9 | 1,4 | 22,4 |
| $L_i$ | dB(m) | –35,0 | –∞ | –35,0 | –35,0 | –40,0 | –55,0 | –31,0 |
| $L_i$ | m | 0,02 | –∞ | 0,02 | 0,02 | 0,01 | 0,002 | 0,03 |
| $M_A$ | dB | – | – | – | – | 1,6 | – | 20,6 |
| $S_A$ | dB | – | – | – | – | 4,0 | – | 8,7 |
| $A_{bu}$ | dB | – | – | – | – | 12,0 | – | 41,0 |
| $A_{bl}$ | dB | – | – | – | – | –10,0 | – | 0,0 |
| $N_T$ | millions | 42 | 42 | 42 | 42 | 42 | 42 | 42 |
| $C_{Eo}$ | $V^2/m^2$ | 5,4 × $10^5$ | 5,4 × $10^5$ | 5,4 × $10^5$ | 5,4 × $10^5$ | – | 5,4 × $10^5$ | – |
| $C_{Ei}$ | $V^2/m^2$ | – | – | – | – | 3,3 × $10^4$ | – | – |
| $E_{max}$ | V/m | 10,0 | 10,0 | 3,0 | 10,0 | 3,0 | 3,0 | 3,0 |
| $E_{i,max}$ | V/m | – | – | – | – | 9,5 | – | 2,4 |
| $E_{min}$ | V/m | 0,08 | 0,08 | 0,08 | 0,008 | 0,08 | 0,08 | 0,08 |
| $E_{i,min}$ | V/m | – | – | – | – | 0,02 | – | 0,000 7 |
| $U_{max}$ | V | 79 | +∞ | 24 | 79 | 85 | 42 | 53 |

[a] See NOTE 3 at the end of 4.4.4.2.

NOTE Some curves have the same parameter values: Figure 17 a) curve 2 and Figure 16, and Figure 17 b) curve 1 and Figure 17 a) curve 3.

**Key**

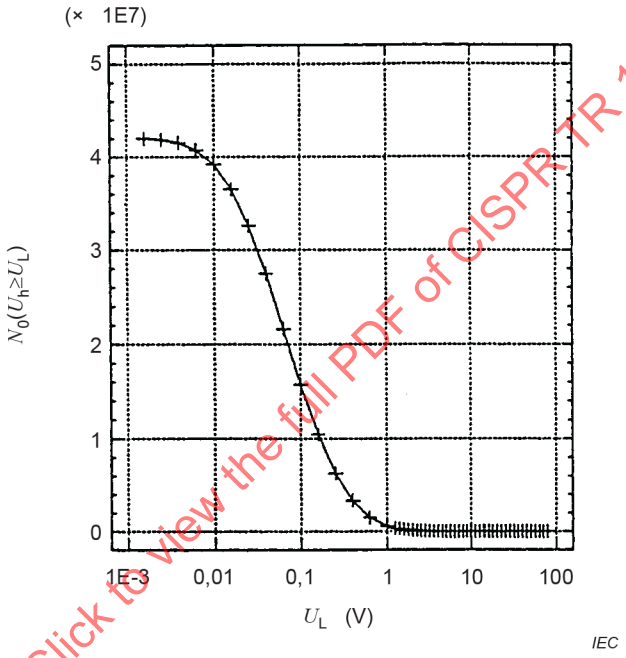
B/W is brick and/or wood

C is concrete

IECNORM.COM : Click to view the full PDF of CISPR TR 16-3:2020 RLV

This subclause is concluded by giving several numerical examples of $N_o(U_h \geq U_L)$, i.e. of the number of outlets in the respective geographical region showing an induced open-circuit voltage $U_h \geq U_L$, where $U_L$ may be considered as the open-circuit voltage in the immunity test. The region in these examples is the aforementioned part of Germany. The relations used in the calculation of $N_o(U_h \geq U_L)$ can be found in Annex C and Annex D. The values of the various parameters used in these calculations are summarized in Table 10.

Figure 15 shows an example of $N_o(U_h \geq U_L)$ in the voltage range $U_L \leq U_{max}$ = 79 V, based on $L_o$ data for buildings constructed from brick and/or wood (B/W) and assuming that all 42 million outlets are in these types of building. $U_{max}$ (see also Table 10) is given by $U_{max} = E_{max} L_U$, where $E_{max}$ is the maximum outdoor field strength in the respective geographical region, and $L_U$ the upper limit of the range of $L_o$(B/W) data (see 4.4.2.3.3). $U_{max}$ is quite large in this case. The maximum value measured in the experimental investigations is 22 V.




NOTE The total number of outlets $N_T = 42 \times 10^6$ .

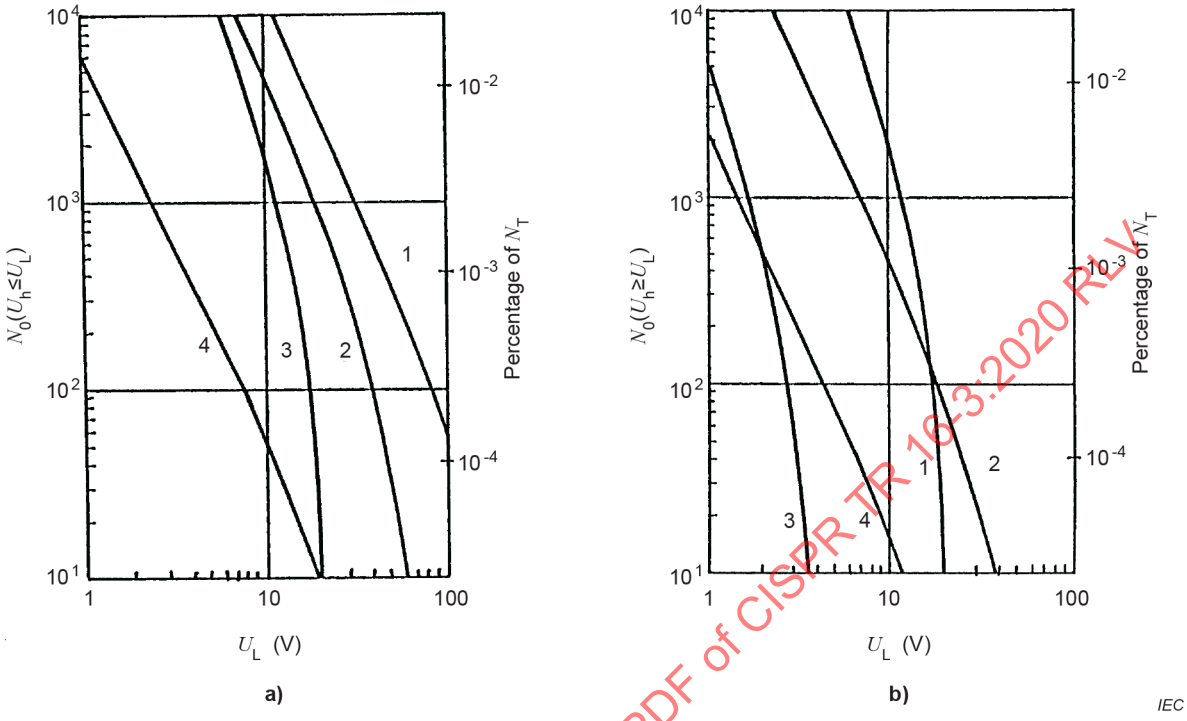
**Figure 16 – Example of the number of outlets with an induced asymmetrical open-circuit voltage $U_L \leq U_h \leq U_{max}$ = 79 V (see Table 10)**

To set the specifications for an immunity test, the higher range of $U_L$ values is of interest. Therefore, the results given in Figure 16 have been replotted as curve 2 in Figure 17a). Curve 1 in Figure 17a) gives $N_o(U_h \geq U_L)$ for the same situation as in Figure 16 but neglecting the truncation of the $L$ factor distribution. In that case $U_{max}$ is infinitely large, which is not very realistic. Curve 3 in Figure 17a) demonstrates how the results represented by curve 2 are modified when $E_{max}$ is reduced from 10 V/m to 3 V/m; then $U_{max}$ = 24 V. Finally, curve 4 in Figure 17a demonstrates how the results represented by curve 2 are modified when $E_{min}$ is reduced from 0,08 V/m to 0,008 V/m. The latter curve clearly demonstrates the importance of the minimum field strength in the geographical region.

In Figure 17b) the influence of the building material (B/W or reinforced concrete, C) and the choice of $L$ factor ($L_o$ or $L_i$) on the results can be observed. Curve 1 in that figure is identical to curve 3 in Figure 17 a), so it concerns $L_o$ data for B/W-buildings. When using $L_i$ data the building effect has to be taken into account because there is no direct model to predict the indoor field-strength distribution. By doing so, the results represented by curve 2 are found. As for curve 1 the maximum outdoor field-strength $E_{max}$ = 3 V/m, but due to the building effect the maximum indoor field strength $E_{i,max} = E_{max} A_{bi}$, where $A_{bi}$ is the lowest building effect as

IECNORM.COM : Click to view the full PDF of CISPR TR 16-3:2020 RLV

determined from the experimental data. In this case $A_{bi}$ = −10 dB, so that $E_{i,max}$ = 9,5 V/m, hence there is an amplification of the outdoor field strength.




NOTE See Table 10 for the various parameter values used, and below for key. Total number of outlets 42 × 106, homogeneous density of the outlets: $\mu$ = 168 km$^{-2}$.

**Figure 17 – Examples of number (left-hand scale) and relative number (right-hand scale) of outlets with $U_L \leq U_h \leq U_{max}$**

Key to Figure 17 curves:

a) B/W buildings

| | | | |
|---|---|---|---|
| Curve 1: | nontruncated $L_o$ factor, | $E_{max}$ = 10 V/m, | $E_{min}$ = 0,08 V/m |
| Curve 2: | truncated $L_o$ factor, | $E_{max}$ = 10 V/m, | $E_{min}$ = 0,08 V/m |
| Curve 3: | truncated $L_o$ factor, | $E_{max}$ = 3 V/m, | $E_{min}$ = 0,008 V/m |
| Curve 4: | truncated $L_o$ factor, | $E_{max}$ = 10 V/m, | $E_{min}$ = 0,08 V/m |

b) Truncated $L$ factors, maximum outdoor field strength 3 V/m

| | |
|---|---|
| Curve 1: | B/W buildings, $L_o$ factor |
| Curve 2: | B/W buildings, $L_i$ factor |
| Curve 1: | C buildings, $L_o$ factor |
| Curve 2: | C buildings, $L_i$ factor |

One might argue that a negative value of $A_{bi}$ is not realistic. As mentioned in 4.4.2.2, the negative values predominantly originated from measurements where the indoor field strength was measured at an upper floor of the building, and the outdoor field strength at 1,5 m above ground level. Furthermore, re-radiation effects also influenced the actual field-strength data. One may decide to truncate the building-effect distribution at the lower end at 0 dB. In that case, $E_{i,max}$ and $U_{max}$ reduce from 85 V to $L_u E_{max}$ = 8,9 × 3 = 27 V.

IECNORM.COM : Click to view the full PDF of CISPR TR 16-3:2020 RLV

Assuming that all 42 million outlets are located in reinforced concrete buildings, the results represented by curve 1 in Figure 17 b) are modified into those represented by curve 3, while curve 4 follows if the $L_i$ data are used. In practice, the outlets will be distributed over the B/W and C buildings. Then $N_T$ in the calculations is the total number of outlets in a given type of building, and the results for both types of building have to be added.

NOTE 1 Although the number of outlets $N_o(U_h \geq U_L)$ as given in Figure 17 may have non-negligible values, the relative number is very low. This stresses the importance of the "tails" of the various distributions used and of the applied truncation. In addition, if the analytical expressions given in the annexes are not used, but a full-numerical calculation is made [for example, one starting with $n_m(E_o)$], care has to be taken that the accuracy of the numerical calculations is sufficiently high. The very low values of the relative number $N_o(U_h \geq U_L)/N_T$ form an indication of the accuracy needed. The relative number is identical to $pr\{U_h \geq U_L\}$ in %.

NOTE 2 In all calculations the density of the outlets $\mu$ was considered to be a constant over the entire respective region. The results can be improved, for example, when the calculations leading to $n_m(E_o)$ (see Figure 15), take a location-dependent $\mu$ into account.

NOTE 3 Curves 2 and 4 in Figure 17b) are based on $L_i$ and $A_b$ data, and a warning has to be given here. As mentioned in 4.4.2, it is not very likely that inside the buildings the far-field condition will be satisfied and, formally speaking $L_i$ cannot be derived from $G_i$. In addition, $A_b$ was determined from magnetic field-strength data and $A_b$ for the electric field need not be the same. In the calculations leading to curves 2 and 4, it was tacitly assumed that $L_i = G_i/Z_0$ ($Z_0$ = 377 Ω). However, the same curves for $N_o(U_h \geq U_L)$ would have been found when correctly using the $G_i$ and $A_b$, but quoting rows 15 and 16 of Table 10 means the magnetic field quantities $H_{max} = E_{max}/Z_0$ etc., and replacing $C_{Ei}$ by $C_{Hi} = C_{Ei}/Z_0^2$ (see B.4).

#### 4.4.4.3 Summary of disturbance source parameters

##### 4.4.4.3.1 General

Assuming that the disturbance source in the conducted-immunity test is sufficiently described by an open-circuit voltage and internal impedance, the following parameters are of importance.

##### 4.4.4.3.2 The internal impedance

The internal impedance may be specified as a purely resistive quantity, for which the magnitude is chosen on the basis of the results for the equivalent asymmetrical resistance $R_a$, as given in 4.4.2.4. The choice depends on the reference for the asymmetrical disturbance source considered to be relevant in the situations where interference problems have to be prevented. An often used value is $R_a$ = 150 Ω [24], [25], [14] which is not in conflict with the $R_a$ results presented in 4.4.2.4.

##### 4.4.4.3.3 The open-circuit voltage

Because the induced asymmetrical voltage has been measured at non-random locations in order to have a sufficiently large induced-signal-to-ambient-noise ratio, the raw $U_h$ data cannot be used and the procedure described in 4.4.4.2 has to be followed. From that procedure, described in more detail in Annex C and Annex D, it can be concluded that the following parameters have to be considered (see also Table 10).

a) $N_T$ — The total number of outlets in the geographical region (country) to be considered. $N_T$ is either the grand total of outlets or the total number of outlets in a certain type of building (brick/wood or reinforced concrete).

b) $M_G$ or $M_L$ — The average value of the $G$ or $L$ factor, in dB(Ωm) or dB(m) (see Table 4 and Table 5). If the $G_i$ or $L_i$ factors are used, the following building effect parameters shall be known (see Table 3 and Table 6):

$M_A$: the average building effect $A_b$ in dB

$S_A$: the standard deviation of $A_b$ in dB

$A_{bu}$: the maximum building effect

IECNORM.COM : Click to view the full PDF of CISPR TR 16-3:2020 RLV

$A_{BI}$: the minimum building effect

c) $S_G$ or $S_L$ The standard deviation (in dB) associated with $M_G$ or $M_L$

d) $G_U$, $G_L$ The upper and lower limit of the $G$-factor range or the $L$-factor range

$L_U$, $L_L$

e) $H_{max}$ or $E_{max}$ The upper boundary of the outdoor field strength, in A/m or V/m, which determines the inner boundary of the areas around the transmitters to be considered.

This value may be chosen after considering radiation hazards. However, in particular in the case of mass-produced appliances, the following consideration seems to be relevant. Choose (or agree on) a maximum field strength of $X$ (A/m or V/m) such that there is a high probability that all equipment will be electromagnetically compatible when the field strength is equal to or smaller than $X$ (A/m or V/m), and agree that special EMC hardening measures are to be taken in that part of the region where the field strength is larger than $X$ (A/m or V/m) and (simultaneously) a complaint occurs.

f) $H_{min}$ or $E_{min}$ The minimum field strength determining the outer boundary of the areas around the transmitters (see 4.4.4.2).

This value needs to be chosen only when the field-strength distribution $n(H)$ or $n(E)$ is unknown. If this distribution is known, $H_{min}$ or $E_{min}$ is calculated from an equation like Equation (20).

g) $n(H)$ or $n(E)$ The field-strength distribution, as discussed in 4.4.4.2 and Annex B.

## 4.5 Predictability of radiation in vertical directions at frequencies above 30 MHz

### 4.5.1 Summary

CISPR 11 sets limits for the electromagnetic disturbances emitted *in situ* near the ground from industrial, scientific and medical (ISM) radio-frequency equipment. In CISPR 11:2003 with Amendment 1 (2004) [5], referring to protection of safety of life services, it was stated, "Many aeronautical communications require the limitation of vertically radiated electromagnetic disturbances. Work is continuing to determine what provisions may be necessary to provide protection for such systems."

This subclause considers the calculated vertical radiation patterns of the $E$-field which will be emitted at frequencies above 30 MHz from electrically small sources physically located close to the surface of real homogeneous plane ground. Its purpose is the study of the predictability of radiation in vertical directions based on *in situ* measurements of the strength of the $E$-field near the ground. The sources considered are electrically small balanced electric and magnetic dipoles excited in the frequency range from 30 MHz to 1 000 MHz.

The effects on the vertical radiation patterns caused by a wide range of the electrical properties of the ground, varying from wet ground to very dry ground – and the special case of a ground that behaves like a near-perfect conductor – have also been considered.

These studies show the limitations of the predictability of radiation at elevated angles when based on measurements near the ground. The subclause identifies some of the factors to be considered when developing and specifying limits of radiated electromagnetic disturbances and methods of measurement which are intended to protect aeronautical radionavigation and communication systems operating at frequencies above 30 MHz. For example, it shows that vertical patterns of the fields over good conductors do not represent the field patterns over real grounds. Moreover, the subclause shows that for good predictability of the field strengths at elevated angles, the *in situ* measurements near the ground shall not be made at fixed heights but instead they shall use height scans and, in particular shall be made at a known distance from the equipment which is the source of the radiation.

IECNORM.COM : Click to view the full PDF of CISPR TR 16-3:2020 RLV

### 4.5.2 Range of application

This subclause considers the predictability of radiation in vertical directions based on measurements of the strength of the electric ($E$) fields emitted by electrical equipment near the ground. It is intended to give guidance about the predictability of radiation emitted at elevated angles by electrical equipment *in situ*, in particular industrial, scientific, and medical (ISM) radio-frequency equipment. For that purpose, it studies the calculated vertical radiation patterns of the $E$-fields which will be emitted at frequencies above 30 MHz from electrically small sources located close to the surface of real homogeneous plane ground.

The vertical radiation patterns of the horizontally and vertically polarized $E$-fields, including the surface waves, have been calculated at distances of 10 m, 30 m and 300 m from various electrically small sources, so that the field variations with distance can be quantified. In this way, a general knowledge has been obtained of the shapes of the vertical radiation patterns, showing the magnitudes of the $E$-field strengths near ground compared with the magnitudes of the $E$-field components at elevated angles, and the ways in which the relative magnitudes can be expected to vary with distance over a plane ground.

The sources considered were electrically small balanced electric and magnetic dipoles excited in the frequency range from 30 MHz to 1 000 MHz. For the purposes of the study, an electrically small source is defined as one whose largest linear dimension is one-tenth or less of the free-space wavelength at the frequency of interest.

Subclause 4.5 also considers the effects on the vertical radiation patterns caused by a range of electrical properties of the ground, varying from electrical conductivities and dielectric constants of wet ground to those of very dry ground [31], [32], and the special case of a ground that behaves like a near-perfect conductor.

The effects on wave propagation near the ground of walls, buildings, terrain irregularities, watercourses, vegetation cover, and so on, are not within the scope of this subclause. It is important to note, therefore, that the additional uncertainties in wave propagation caused by the presence of such discontinuities, and their effects on predictability based on measurements *in situ*, have not been considered.

### 4.5.3 General

Table E.1 of CISPR 11:2009 provides radiation limits for the protection of specific safety-related radio services. The limits apply to ground level measurements of the electromagnetic disturbances emitted by ISM radio-frequency (RF) equipment *in situ*, not on a test site. Above 30 MHz the five frequency bands listed in Table E.1 of CISPR 11:2009 are all used for aeronautical services, including the instrument landing system (ILS) or instrument low-approach system marker beacon, localizer, and glide path frequencies, as well as a survival frequency and other radio-navigation and communication frequencies bands.

The *in situ* measuring distance specified in Table E.1 of CISPR 11:2009, for all five frequency bands above 30 MHz, is 10 m "from the outer face of the exterior wall outside the building in which the equipment is situated." It is important to note that the precise measuring distance from the ISM apparatus itself is not specified.

IECNORM.COM : Click to view the full PDF of CISPR TR 16-3:2020 RLV

The heights at which measurements of horizontally and vertically polarized $E$-fields in the frequency range from 30 MHz to 1 000 MHz are made using a balanced dipole, and are specified in 7.3.4 of CISPR 11:2009. “The nearest point of the antenna to ground shall be not less than 0,2 m. For measurements *in situ* the centre of the antenna shall be fixed at 2,0 m ± 0,2 m height above the ground. For measurements on a test site the centre of the antenna shall be varied between 1 m and 4 m height for maximum indication at each test frequency”. CISPR 11:2009 specifies that “Class A equipment may be measured on a test site or *in situ*, as preferred by the manufacturer” and notes that “Due to size, complexity or operating conditions, some equipment may have to be measured *in situ* in order to show compliance with the radiation disturbance limits”. It goes on to say that “Class B equipment shall be measured on a test site.”

After considering the methods of specifying *in situ* measurement distance and measuring antenna height in CISPR 11, it is useful to address the following questions:

a) How well do measurements of the vertically and horizontally polarized $E$-fields, in a height scan of 1 m to 4 m at a horizontal distance of 10 m from the source over real ground, predict the field strengths emitted at elevated angles? (See 4.5.5.2)

b) How predictable are the field strengths at elevated angles when the horizontal measuring distance is greater than 10 m but, beyond that fact, the actual distance is not known (not specified)? (See 4.5.5.3)

c) How is the predictability affected when the height above ground to the centre of the measuring antenna is fixed, for example at a nominal 3 m? (See 4.5.5.4)

d) What errors in judgement of the predictability of the vertical patterns may arise if calculations are made using the common approximation that the influence of the real ground can be simulated by replacing it with a perfect conductor? (See 4.5.6)

To provide some answers, in the frequency range 30 MHz to 1 000 MHz a number of vertical polar patterns and linear height scan patterns have been calculated for the $E$-field radiation emitted by four kinds of electrically small sources located close to the surface of real homogeneous plane ground. Predictability has been assessed by judging how well, or how badly, the calculated patterns show that ground-based measurements of the vertically and horizontally polarized $E$-fields emitted from the various sources will correlate with the maximum strengths of either vertically or horizontally polarized $E$-fields (whichever are greater) at elevated angles. The patterns have been calculated for the simplest of sources radiating into the half-space above ground. If these patterns identify problems of predictability, it is unlikely that predictability will be improved when real ISM devices, like plastics welders or RF diathermy machines, are the sources.

Vertical polar patterns and linear height scan patterns have also been calculated for the $E$-field radiation emitted from the small sources over a copper ground plane. A copper ground plane provides boundary conditions which distinguish, in effect, a perfect conductor from a real ground, and allows identification of the differences between the vertical radiation patterns that will exist close to the surface of a real ground when compared with those calculated close to the surface of a perfect conductor. The differences determine how large the errors will be if predictability is judged by considering vertical patterns calculated over a perfectly conducting ground plane.

The four kinds of sources considered were electrically small vertical and horizontal balanced electric and magnetic dipoles. There is justification for the use of small dipole sources as models in the study of the predictability of radiation at elevated angles from real ISM equipment. Airborne measurements of the fourth harmonic field radiated from 27 MHz ISM apparatus over real ground reported in [33] have been studied further in [34]. In [34] it is shown that the vertical distribution of horizontally polarized fields at approximately 109 MHz, encountered by an aircraft during any single flight pass over the ISM apparatus, can be well matched with a field distribution produced at elevated angles by a simple small electric or magnetic dipole source. Some of the work in [34] is summarized in Annex F.

IECNORM.COM : Click to view the full PDF of CISPR TR 16-3:2020 RLV

### 4.5.4 Method used to calculate field patterns in the vertical plane

#### 4.5.4.1 General

The $E$-field vertical polar patterns and linear height scan patterns have been calculated using a double precision version of the method of moments computer code known as the Numerical Electromagnetics Code (NEC) [35]. NEC2 with the companion code SOMNEC allows the Sommerfeld integral evaluation of the field interactions at the air-ground interface [36], and so includes the contribution of the Sommerfeld-Norton surface wave when calculating the total $E$-fields above real grounds (discussed in 4.5.6.4). The near fields were also included in the calculations for results in this subclause.

The small vertical and horizontal balanced electric dipoles, and vertical and horizontal balanced loops (magnetic dipoles) used as the models for the calculations each had a unit dipole moment [i.e. a dipole (current) moment of 1 A·m for the electric dipoles and a dipole moment of 1 A·m$^2$ for the loops]. All were positioned with their centres at a height above ground of either 1 m or 2 m in order to show the effects of variations in the source height on the vertical radiation patterns. The effects include the appearance of additional major lobes of radiation – called grating lobes – as the spacing between the source and its image in the ground increases beyond $\lambda/2$ with increasing frequency [37].

The geometries of the models, and the paths of the scans in vertical planes at constant radius about each source for the vertical polar pattern computations, are shown in the top right corner of each polar pattern plot.

The planes in which the linear height scan patterns were calculated are shown in the diagrams accompanying each linear height scan pattern plot.

#### 4.5.4.2 Frequencies of interest and the electrical constants of the ground

The five frequencies of interest at which the models were excited, in the five ITU designated bands [38] listed in Table E.1 of CISPR 11:2009, are shown here in Table 11.

**Table 11 – Frequencies of interest in ITU designated bands from Table 9 of CISPR 11:2009**

| Excitation frequency MHz | ITU designated bands |
|---|---|
| 75 | 74,8 MHz to 75,2 MHz, Aeronautical Radionavigation (Instrument Landing System (ILS) marker beacons, horizontal polarization) |
| 110 | 108 MHz to 137 MHz, Aeronautical Radionavigation and Aeronautical Mobile (R) (including ILS localizers (108 MHz to 112 MHz), horizontal polarization) |
| 243 | 243 MHz is for use by survival craft stations and equipment used for survival purposes |
| 330 | 328,6 MHz to 335,4 MHz, limited to ILS (glide path, horizontal polarization) |
| 1 000 | 960 MHz to 1 215 MHz, reserved on a worldwide basis for the use and development of airborne electronic aids to air navigation |

Most attention has been devoted to the small sources placed above a “medium dry ground” [31] (CCIR: medium dry ground; rocks; sand; medium sized towns [32]). The electrical constants, the relative permittivity $\varepsilon_r$ and the conductivity $\sigma$ (mS/m), for “medium dry ground” at 30 MHz and the other five frequencies of interest are listed in Table 12.

IECNORM.COM : Click to view the full PDF of CISPR TR 16-3:2020 RLV

**Table 12 – Electrical constants for "medium dry ground" [31] (CCIR: medium dry ground; rocks; sand; medium sized towns[32])**

| Frequency<br>MHz | $\varepsilon_r$ | $\sigma$<br>mS/m |
|---|---|---|
| 30 | 15 | 1 |
| 75 | 15 | 1,5 |
| 110 | 15 | 2 |
| 243 | 15 | 4,5 |
| 330 | 15 | 7,5 |
| 1 000 | 15 | 35 |

Near the lower and upper ends of the frequency range, at frequencies of 75 MHz and 1 000 MHz, examples of two other types of grounds have been used with the electrically small vertical loop model (horizontal magnetic dipole) to illustrate the influence of differing values of the ground constants on the vertical radiation patterns (see 4.5.6.2). The electrical constants for "wet ground" and "very dry ground" at 30 MHz, 75 MHz and 1 000 MHz, are listed in Table 13.

**Table 13 – Electrical constants for "wet ground" [31] (CCIR: marshes (fresh water); cultivated land [24]) and "very dry ground" [31] (CCIR: very dry ground; granite mountains in cold regions; industrial areas [32])**

| Frequency<br>MHz | Wet ground | | Very dry ground | |
|---|---|---|---|---|
| | $\varepsilon_r$ | $\sigma$<br>mS/m | $\varepsilon_r$ | $\sigma$<br>mS/m |
| 30 | 30 | 10 | 3 | 0,1 |
| 75 | 30 | 13 | 3 | 0,1 |
| 1 000 | 30 | 140 | 3 | 0,15 |

### 4.5.5 Limitations of predictability of radiation at elevated angles

#### 4.5.5.1 Influence of the electrical constants of the ground

##### 4.5.5.1.1 General

It is useful to observe the relatively small influence of widely differing values of the ground constants on the predictability of the field strengths at elevated angles. A small vertical loop (horizontal magnetic dipole) at a centre height of 2 m above ground was chosen as the source model. The geometry of the model is shown in Figure 18. For this source, the best predictability is obtained when the vertical $E_z$ field component is measured near the ground to estimate the maximum strength of either the horizontally oriented $E_x$ field or the vertically oriented $E_z$ field at elevated angles.

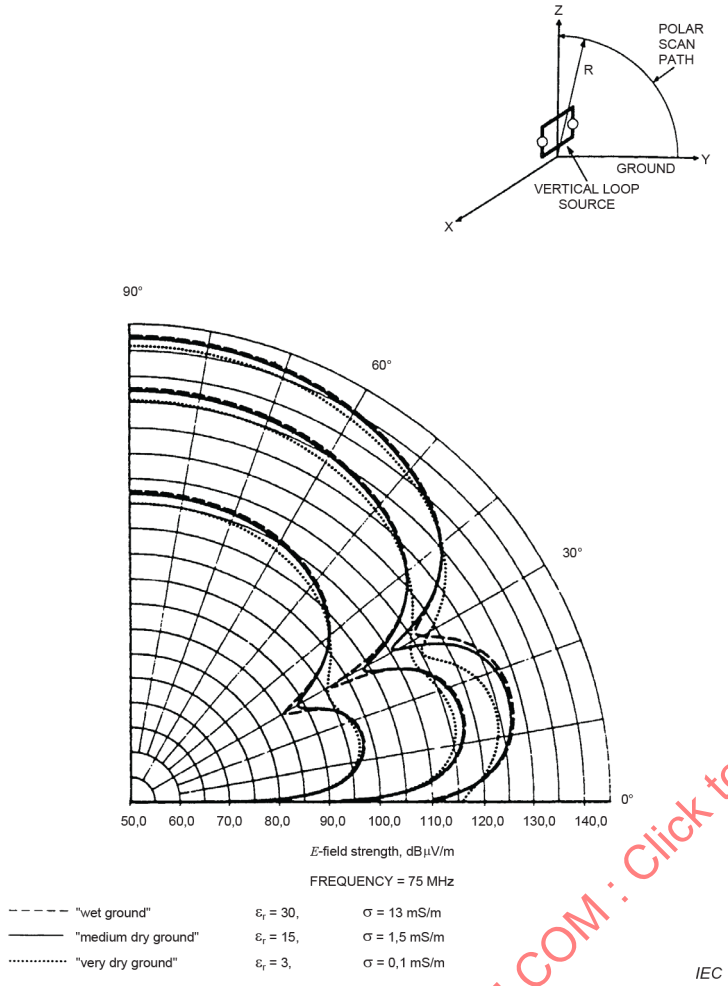
##### 4.5.5.1.2 Influence of the ground constants at 75 MHz

In Figure 18, the vertical polar patterns at 75 MHz show the horizontally polarized $E_x$ field strengths in the Y-Z plane at scan radii $R$ of 10 m, 30 m, and 300 m, over real grounds having the electrical constants in Table 12 and Table 13. It can be seen that at each of the three scan radii, the total *spread* in the maximum $E_x$ fields in the vertical direction is less than 3 dB.

IECNORM.COM : Click to view the full PDF of CISPR TR 16-3:2020 RLV

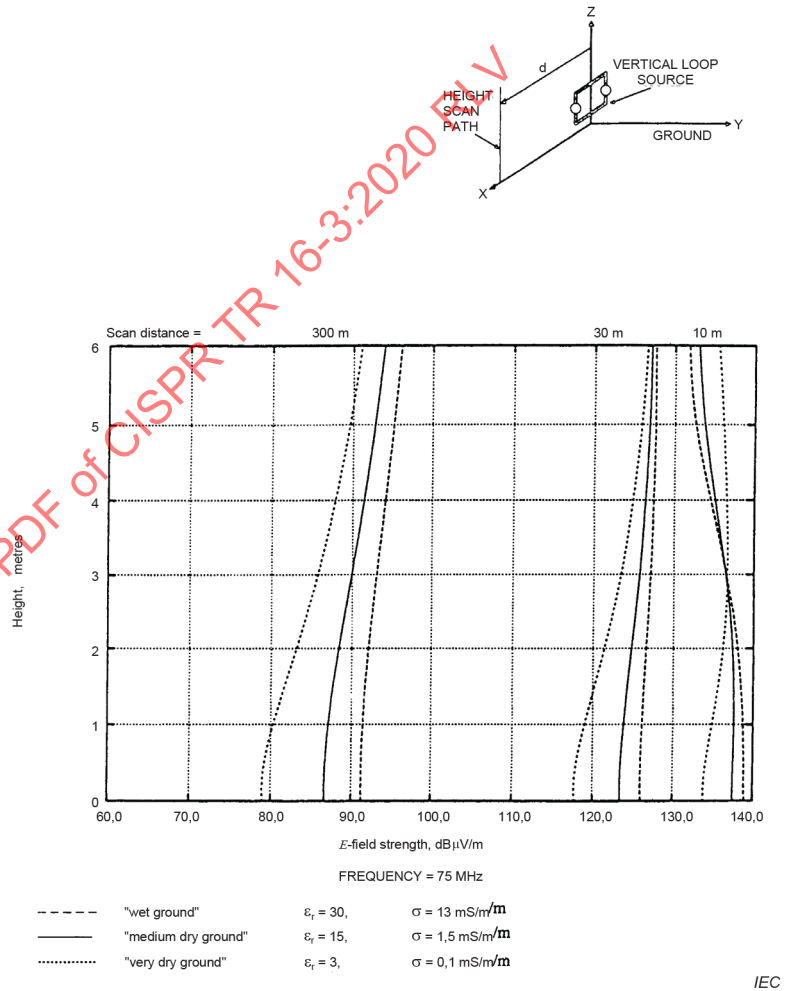
In Figure 19, the height scan patterns calculated up to a height of 6 m at 75 MHz show the $E_z$ field strengths in the Z-X plane at the three corresponding horizontal distances over the same three types of real ground. It can be seen that the *spread* in magnitudes of the $E_z$ field strengths at ground level for the three ground types is much greater than 3 dB. However, if measurements of $E_z$ are made at heights from 1 m to 4 m, then at a horizontal distance of 10 m the underestimates of the maximum $E_x$ field strengths in the vertical direction vary from about 3,9 dB to about 4,7 dB (a *spread* of only 0,8 dB), at a horizontal distance of 30 m, the underestimates vary from about 5,1 dB to about 5,7 dB (a *spread* of only 0,6 dB), and at 300 m, the underestimates vary from about 18,4 dB to about 22,1 dB (a *spread* of 3,7 dB). Thus, for the range of values of the ground constants and measuring distances considered here, the worst case *spread* or *variation* in the underestimates of maximum field strengths in the vertical direction is only 3,7 dB, and this occurs at the largest measuring distance of 300 m.

IECNORM.COM : Click to view the full PDF of CISPR TR 16-3:2020 RLV




NOTE Loop dimensions 0,1 m × 0,1 m; loop centre height 2 m; dipole moment 1 A·m$^2$; scan radii of 10 m, 30 m and 300 m; 75 MHz; Y-Z plane (Reproduced from [39]).

**Figure 18 – Vertical polar patterns of horizontally polarized $E_x$ field strengths emitted around small vertical loop (horizontal magnetic dipole) over three different types of real ground**




NOTE Loop dimensions 0,1 m × 0,1 m; loop centre height 2 m; dipole moment 1 A·m$^2$; horizontal distances 10 m, 30 m and 300 m; 75 MHz; Z-X plane (Reproduced from [39]).

**Figure 19 – Height scan patterns of vertically oriented $E_z$ field strengths emitted from small vertical loop (horizontal magnetic dipole) over three different types of real ground**

IECNORM.COM : Click to view the full PDF of CISPR TR 16-3:2020 FULV

#### 4.5.5.1.3 Influence of the ground constants at 1 000 MHz

In Figure 20, the vertical polar patterns at 1 000 MHz show the horizontally polarized $E_x$ field strength in the Y-Z plane at the same three scan radii $R$ around the small vertical loop over the same three types of real ground with the electrical constants at 1 000 MHz given in Table 12 and Table 13. It can be seen that for a source height of 2 m at this frequency, multiple grating lobes are established.

Figure 21 shows the vertical polar patterns of the vertically oriented $E_z$ field strengths in the Z-X plane, and Figure 22 shows the height scan patterns of the $E_z$ field strengths calculated up to a height of 6 m in the Z-X plane, at the three scan distances and over the three types of real ground.

Figure 20 shows that the maximum strength of the $E_x$ field occurs at an elevation angle between 77° and 78° at all three scan radii. A comparison of Figure 21 with Figure 20 also shows, in the case of a "very dry ground", that the maximum field strength is contributed by $E_z$ at the scan radii of 30 m and 300 m at an elevation angle of 2° (that is, at heights of approximately 1,1 m and 10,5 m at the two radii respectively).

Inspection of Figure 20 through Figure 22 reveals the following information. If a vertically polarized antenna measures maximum $E_z$ in height scans from 1 m to 4 m, then at 10 m horizontal distance the resulting underestimates of the maximum $E_x$ field strengths range from about 1,8 dB to about 3,2 dB, a *spread* of only 1,4 dB. At 30 m horizontal distance, with "medium dry ground" or "wet ground," a 1 m to 4 m $E_z$ height scan measurement underestimates the maximum $E_x$ field strengths by about 1,4 dB ("medium dry ground") or about 2,9 dB ("wet ground"), a *spread* of only 1,5 dB. Over "very dry ground," the maximum field strength, $E_z$, is reached at a height of about 1,1 m, and will therefore be measured within the height scan from 1 m to 4 m.

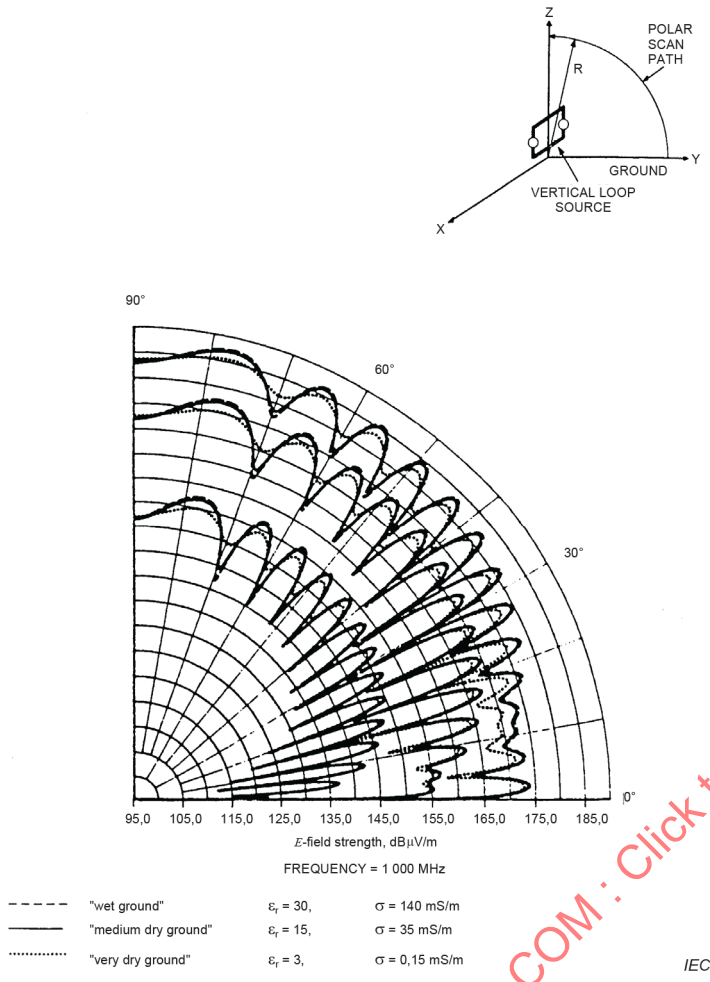
At 300 m horizontal distance, over "medium dry ground" and "wet ground", a 1 m to 4 m height scan of $E_z$ underestimates the maximum $E_x$ field strengths (at about 77° elevation) by about 4,4 dB ("medium dry ground") or about 5,2 dB ("wet ground") a *spread* of only 0,8 dB. Over "very dry ground" a measurement of $E_z$ at a height of 4 m underestimates the maximum field strength (maximum $E_z$ at an elevation angle of 2°, height approximately 10,5 m) by about 5,1 dB. The overall *spread* in the underestimates at 300 m distance therefore remains only 0,8 dB.

Thus, at 1 000 MHz, the calculations show that the differing values of the electrical constants of the ground we have considered here produce a worst-case *variation* or *spread* of only 1,5 dB in the underestimates of the maximum $E$-field strengths at elevated angles, when the estimates are based on 1 m to 4 m height scan measurements of $E_z$ at horizontal distances ranging from 10 m to 300 m.

#### 4.5.5.1.4 Predictability estimated over a "medium dry ground"

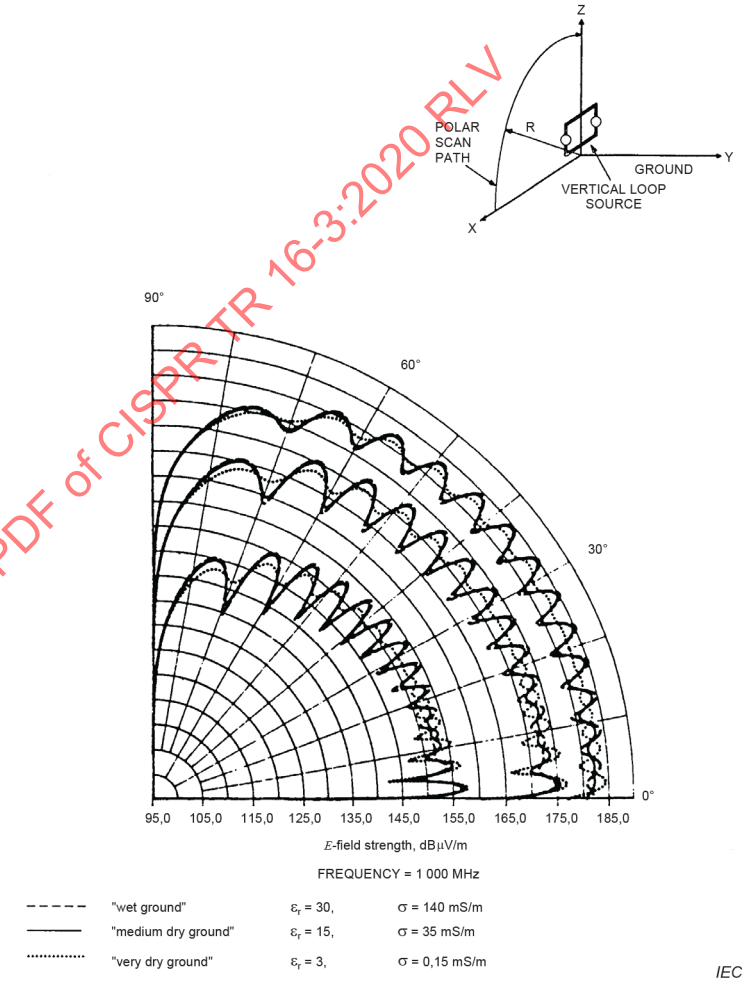
The foregoing shows that in the frequency range from 75 MHz to 1 000 MHz it is justifiable to make general judgements of the predictability of the strength of radiation in vertical directions above ground by considering the $E$-field patterns calculated over a real ground having the electrical constants of a "medium dry ground."

IECNORM.COM : Click to view the full PDF of CISPR TR 16-3:2020 RLV




NOTE Loop dimensions 0,02 m × 0,02 m; loop centre height 2 m; dipole moment 1 A·m$^2$; scan radii of 10 m, 30 m and 300 m; 1 000 MHz; Y-Z plane (Reproduced from [39]).

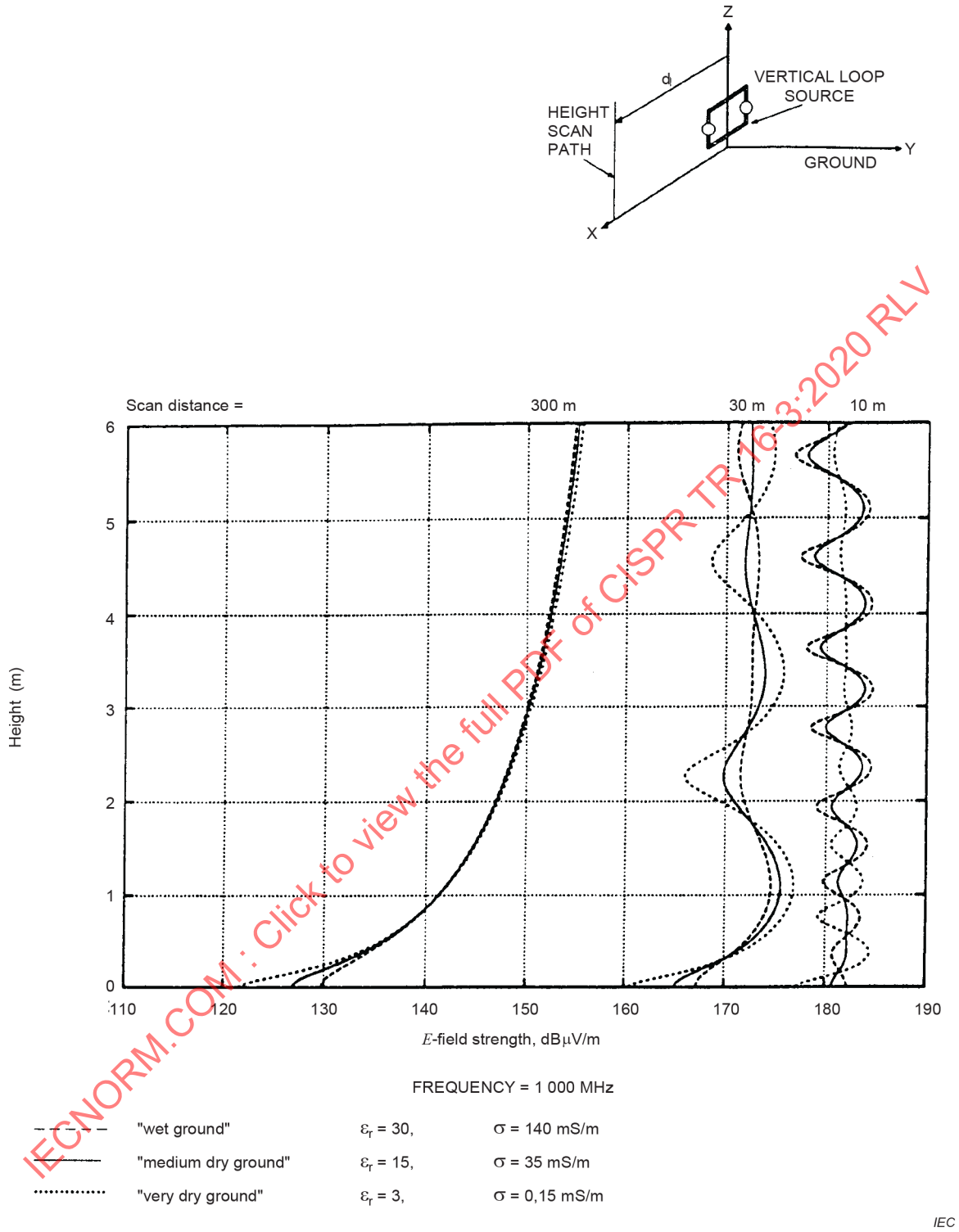
**Figure 20 – Vertical polar patterns of horizontally polarized $E_x$ field strengths emitted around small vertical loop (horizontal magnetic dipole), over three different types of real ground**




NOTE Loop dimensions 0,02 m × 0,02 m; loop centre height 2 m; dipole moment 1 A·m$^2$; scan radii of 10 m, 30 m and 300 m; 75 MHz; Z-X plane (Reproduced from [39]).

**Figure 21 – Vertical polar patterns of vertically oriented $E_z$ field strengths emitted around small vertical loop (horizontal magnetic dipole) over three different types of real ground**

IECNORM.COM : Click to view the full PDF of CISPR TR 16-3:2020 RLV




IECNORM.COM : Click to view the full PDF of CISPR TR 16-3:2020 RLV

NOTE Loop dimensions 0,02 m × 0,02 m. Loop centre height 2 m. Dipole moment 1 A·m$^2$. (Reproduced from [39]).

**Figure 22 – Height scan patterns of vertically oriented $E_z$ field strengths emitted at 1 000 MHz from the small vertical loop (horizontal magnetic dipole), at horizontal distance of 10 m, 30 m and 300 m in the Z-X plane over three different types of real ground**

#### 4.5.5.2 Predictability based on height scan measurements near real ground at 10 m distance from the source

##### 4.5.5.2.1 General

Here we can provide an answer to the first question raised in 4.5.3.

In summary, the answer is that the predictability of the maximum $E$-field strengths at elevated angles by means of 1 m to 4 m height scan measurements at a horizontal distance of 10 m, for all four types of sources placed either 1 m or 2 m above a “medium dry ground” is very good. Underestimates at all five of the frequencies used for aeronautical services are less than 6 dB.

At the two lower frequencies of 75 MHz and 110 MHz, the larger underestimates occur when the source is either a small horizontal electric dipole 1 m above the ground or a small vertical loop (horizontal magnetic dipole) with a centre height 2 m above ground.

At the frequencies of 243 MHz and 330 MHz, the larger underestimates occur when the source is either a small vertical electric dipole or a small vertical loop with a centre height 1 m above ground.

At 1 000 MHz, the larger underestimate occurs when the source is a small vertical loop with a centre height 2 m above ground.

##### 4.5.5.2.2 Predictability at 75 MHz

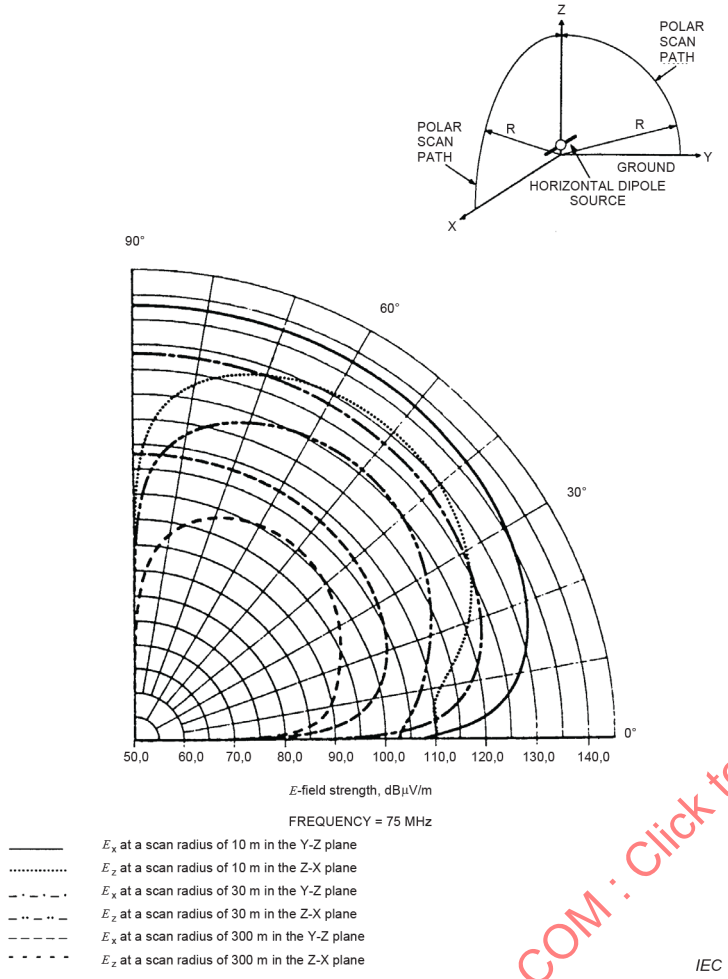
Figure 23 shows polar plots of $E_x$ in the Y-Z plane and $E_z$ in the Z-X plane, at 75 MHz, around the horizontal electric dipole placed 1 m above ground. At a scan radius of 10 m, $E_x$ reaches maximum field strength of almost 138 dBμV/m at an elevation angle near 73°. The polar plots of $E_z$ in the Z-X plane – the vertically polarized radiation emitted from the tips of a horizontal electric dipole over real ground [36] – show that vertically polarized measurements near the ground do not give the best predictions of field strength at high elevation angles. Therefore, Figure 24 shows the height scan calculations of horizontally polarized $E_x$ in the Y-Z plane, reaching an $E_x$ magnitude of almost 133 dB(μV/m) at a horizontal distance of 10 m and a height of 4 m. In consequence, 1 m to 4 m height scan measurements of $E_x$ at a distance of 10 m will underestimate the maximum $E_x$ at 73° elevation by almost 5 dB.

The vertical polar plots in Figure 18 show that measurement of $E_x$ at a distance of 10 m near the ground will not give a good prediction of the maximum field strength emitted at 75 MHz by a small vertical loop placed at a height of 2 m above a “medium dry ground.”

$E_x$ field strength reaches a maximum of over 142 dB(μV/m) in the vertical Y-Z plane. The calculated height scan patterns in Figure 19 show that a vertically polarized measurement of $E_z$ at a horizontal distance of 10 m in the Z-X plane will reach a maximum of almost 138 dB(μV/m) at 1,2 m height. This underestimates by less than 5 dB the maximum strength of the radiation in the vertical direction.

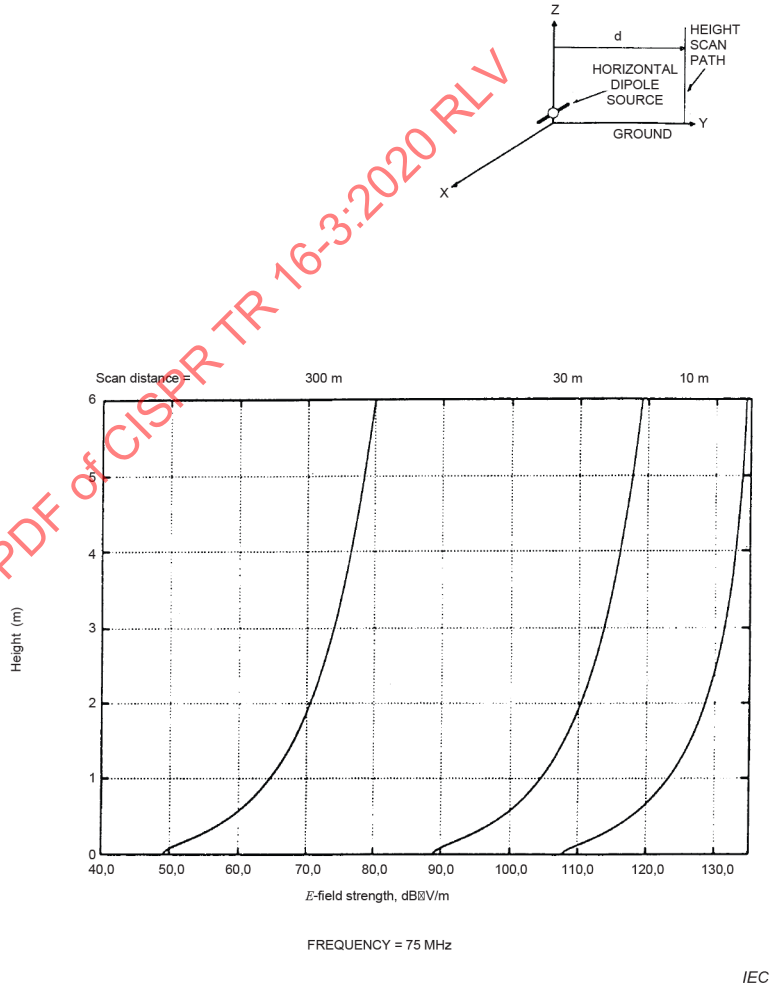
Column (4) of Table 14 summarizes the estimated errors to be expected in the predictability of radiation in vertical directions when based on measurements in height scans from 1 m to 4 m at a horizontal distance of 10 m from each of the four sources operating at 75 MHz. Column (1) lists the radiation sources and their heights. Column (2) lists the field components that contribute the maximum field strengths in the vertical polar patterns, and the elevation angles at which the maximum field strengths occur. Column (3) lists the field component that should be measured in a linear height scan at a horizontal distance of 10 m to provide the best estimates of the maximum field strengths.

IECNORM.COM : Click to view the full PDF of CISPR TR 16-3:2020 RLV




NOTE Dipole length 0,2 m; dipole height 1 m; dipole moment 1 A·m; scan radii of 10 m, 30 m and 300 m; 75 MHz; ground constants: $\varepsilon_r$ = 15, $\sigma$ = 1,5 mS/m (Reproduced from [39]).

**Figure 23 – Vertical polar patterns of horizontally polarized $E_x$ and vertically oriented $E_z$ field strengths emitted around small horizontal electric dipole, in Y-Z and Z-X planes respectively**




NOTE Dipole length 0,2 m; dipole height 1 m; dipole moment 1 A·m; horizontal distances 10 m, 30 m and 300 m; 75 MHz; ground constants: $\varepsilon_r$ = 15, $\sigma$ = 1,5 mS/m, Y-Z plane (Reproduced from [39]).

**Figure 24 – Height scan patterns of horizontally polarized $E_x$ field strengths emitted from small horizontal electric dipole**

IECNORM.COM : Click to view the full PDF of CISPR TR 16-3:2020 RLV

**Table 14 – Estimates of the errors in prediction of radiation in vertical directions based on a measurement height scan from 1 m to 4 m at known distances, $d$; frequency = 75 MHz (adapted from [39])**

| (1) Source of radiation at height | (2) Max. $E$, at angle, in 10 m polar plot | (3) At hor. $d$ = 10 m, measure this field | (4) Estimated prediction error, at $d$ = 10 m | (5) Max. $E$, at angle, in 30 m polar plot | (6) At hor. $d$ = 30 m, measure this field | (7) Estimated prediction error, at $d$ = 30 m | (8) Max. $E$, at angle, in 300 m polar plot | (9) At hor. $d$ = 300 m, measure this field | (10) Estimated prediction error, at $d$ = 300 m |
|---|---|---|---|---|---|---|---|---|---|
| Vertical electric dipole at 1 m | $E_z$ at 15,25° | $E_z$ $z$ | 0 dB | $E_z$ at 17,75° | $E_z$ | –2 dB | $E_z$ at 18° | $E_z$ | –17,5 dB |
| Vertical electric dipole at 2 m | $E_z$ at 8° | $E_z$ | 0 dB | $E_z$ at 12,75° | $E_z$ | –1 dB | $E_z$ at 13° | $E_z$ | –16 dB |
| Horizontal electric dipole at 1 m | $E_x$ at 72,5° in Y-Z plane | $E_y$ in Y-Z plane | –5 dB | $E_x$ at 67,5° in Y-Z plane | $E_y$ in Y-Z plane | –12 dB | $E_x$ at 66° in Y-Z plane | $E_y$ in Y-Z plane | –31,5 dB |
| Horizontal electric dipole at 2 m | $E_x$ at 30° in Y-Z plane | $E_y$ in Y-Z plane | –1,5 dB | $E_x$ at 28,75° in Y-Z plane | $E_y$ in Y-Z plane | –7 dB | $E_x$ at 28,5° in Y-Z plane | $E_y$ in Y-Z plane | –26,5 dB |
| Vertical loop (horizontal magnetic dipole) at 1 m | $E_z$ at 17,5° in Z-X plane | $E_z$ in Z-X plane | –0,5 dB | $E_z$ at 19,75° in Z-X plane | $E_z$ in Z-X plane | –2,5 dB | $E_z$ at 20° in Z-X plane | $E_z$ in Z-X plane | –18 dB |
| Vertical loop (horizontal magnetic dipole at 2 m | $E_x$ at 90° | $E_x$ in Z-X plane | –4,5 dB | $E_x$ at 90° | $E_z$ in X-Z plane | –5,5 dB | $E_x$ at 90° | $E_z$ in Z-X plane | –20,5 dB |
| Horizontal loop (vertical magnetic dipole at 1 m | $E_y$ at 37,5° in Z-X plane | $E_y$ in Z-X plane | –2,5 dB | $E_y$ at 36,75° in Z-X plane | $E_y$ in Z-X plane | –9 dB | $E_y$ at 36,5° in Z-X plane | $E_y$ in Z-X plane | –28,5 dB |
| Horizontal loop (vertical magnetic dipole) at 2 m | $E_y$ at 27° in Z-X plane | $E_y$ in Z-X plane | –1 dB | $E_y$ at 25,5° in Z-X plane | $E_y$ in Z-X plane | –6,5 dB | $E_y$ at 25° in Z-X plane | $E_y$ in Z-X plane | –25,5 dB |

IECNORM.COM : Click to view the full PDF of CISPR TR 16-3:2020 RLV

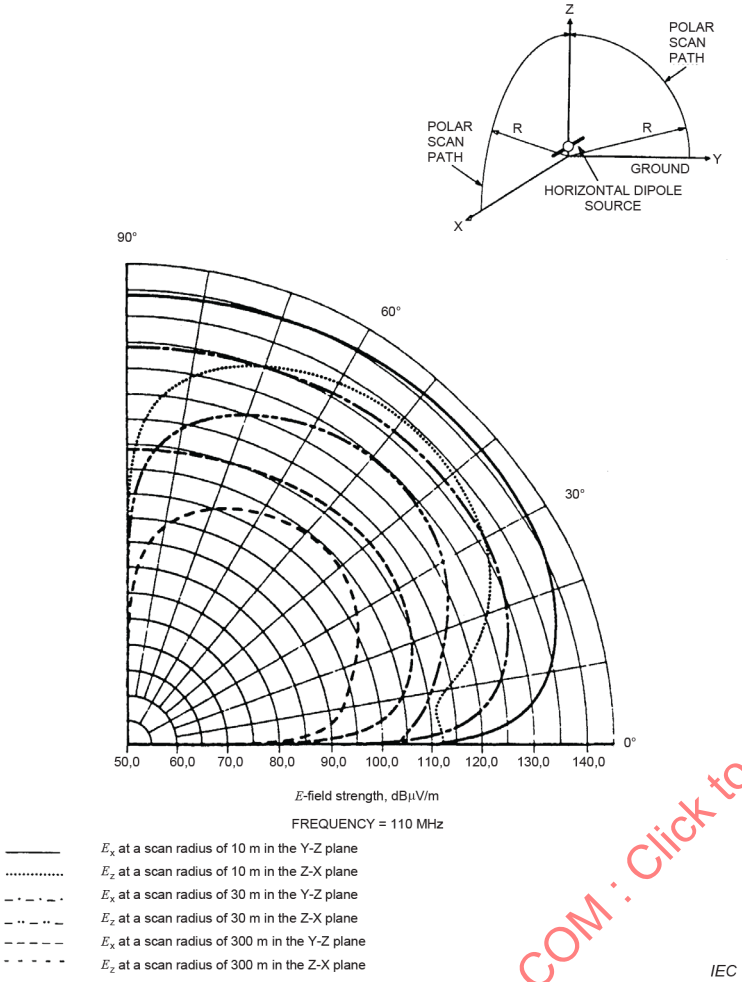
#### 4.5.5.2.3 Predictability at 110 MHz

Figure 25 shows vertical polar plots of $E_x$ in the Y-Z plane and $E_z$ in the Z-X plane, at 110 MHz, around a small horizontal electric dipole placed 1 m above the ground. At a scan radius of 10 m, $E_x$ reaches a maximum field strength of over 141 dB(μV/m) at an elevation angle of 41°. The polar plots of $E_z$ in the Z-X plane show that vertically polarized measurements near the ground will not give good guidance to high-angle field strength. Figure 26 shows height scan calculations of $E_x$ in the Y-Z plane. At a horizontal distance of 10 m the magnitude of $E_x$ reaches almost 139 dB(μV/m) at a height of 4 m, and a height scan measurement of horizontally polarized $E_x$ therefore underestimates the maximum strength of $E_x$ at 41° elevation by less than 3 dB.

Figure 27 shows vertical polar plots of $E_x$ in the Y-Z plane and $E_z$ in the Z-X plane, around a small vertical loop (horizontal magnetic dipole) placed at a centre height of 2 m above ground and excited at 110 MHz. The maximum field strength reached at a scan radius of 10 m is the vertical $E_z$ component, 146 dB(μV/m) at an elevation angle of 40°. The height scan plots of $E_z$ in Figure 28 show that at a horizontal distance of 10 m the magnitude of $E_z$ is almost 144 dB(μV/m) at a height of 1 m, which underestimates the strength of $E_z$ at 40° elevation by less than 2,5 dB.

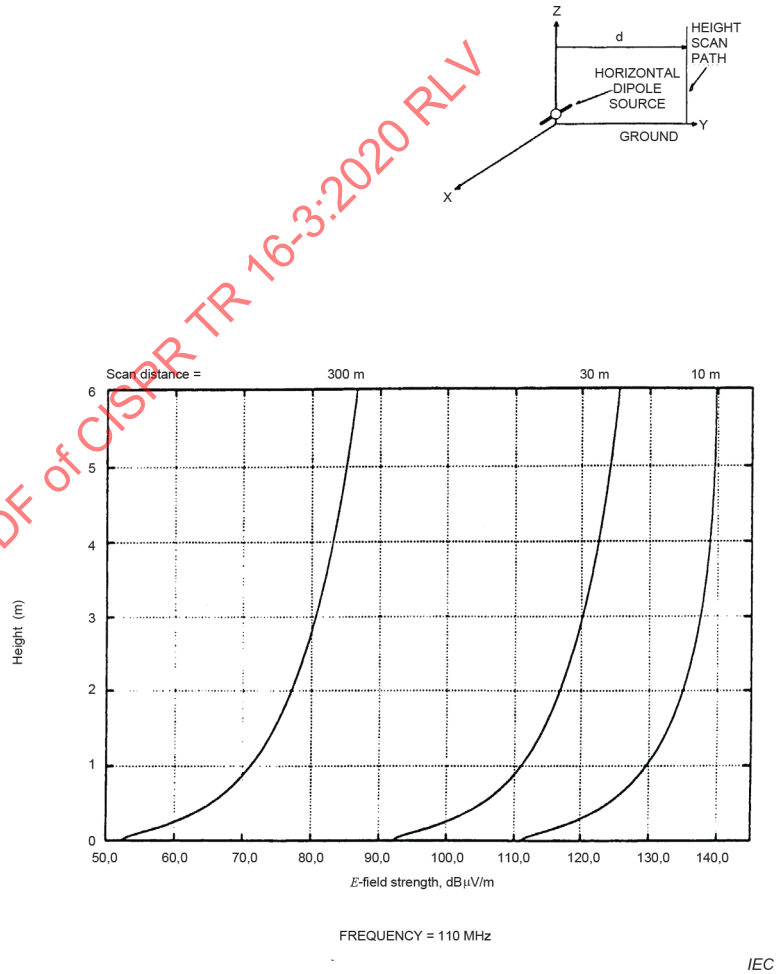
Column (4) of Table 15 summarizes the errors expected in the predictability of radiation in vertical directions based on measurements in height scans from 1 m to 4 m at a horizontal distance of 10 m from each of the four sources operating at 110 MHz.

IECNORM.COM : Click to view the full PDF of CISPR TR 16-3:2020 RLV




NOTE Dipole length 0,2 m; dipole height 1 m; dipole moment 1 A·m; scan radii of 10 m, 30 m and 300 m; 110 MHz; ground constants: $\varepsilon_r$ = 15, $\sigma$ = 2 mS/m (Reproduced from [39]).

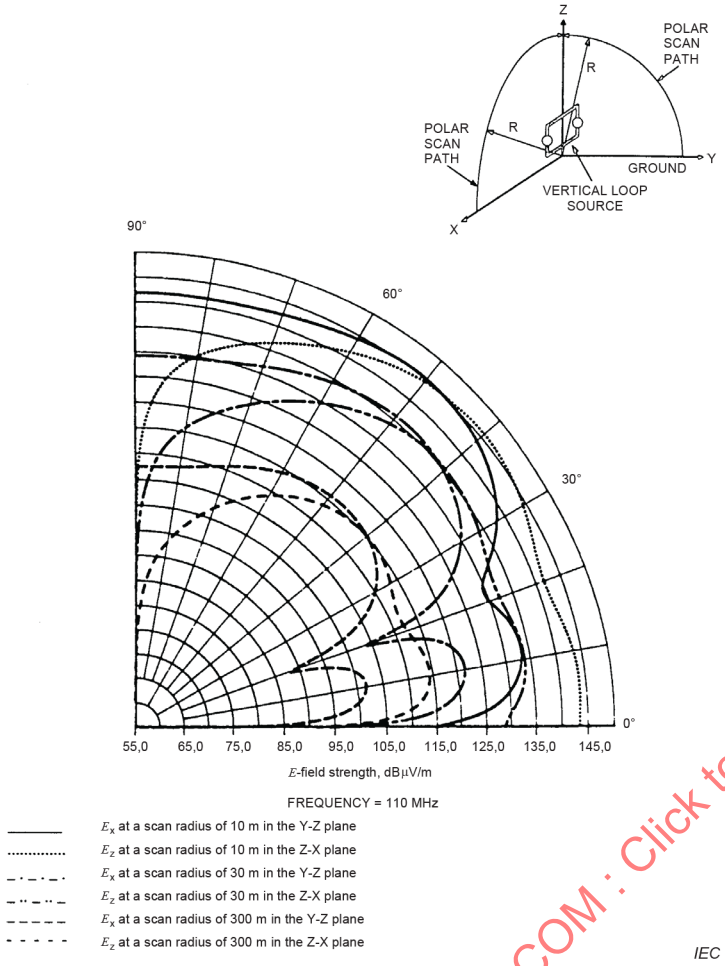
**Figure 25 – Vertical polar patterns of horizontally polarized $E_x$ and vertically oriented $E_z$ field strengths emitted around small horizontal electric dipole in Y-Z and Z-X planes respectively**




NOTE Dipole length 0,2 m; dipole height 1 m; dipole moment 1 A·m; horizontal distances 10 m, 30 m and 300 m; 110 MHz; ground constants: $\varepsilon_r$ = 15, $\sigma$ = 2 mS/m, Y-Z plane (Reproduced from [39]).

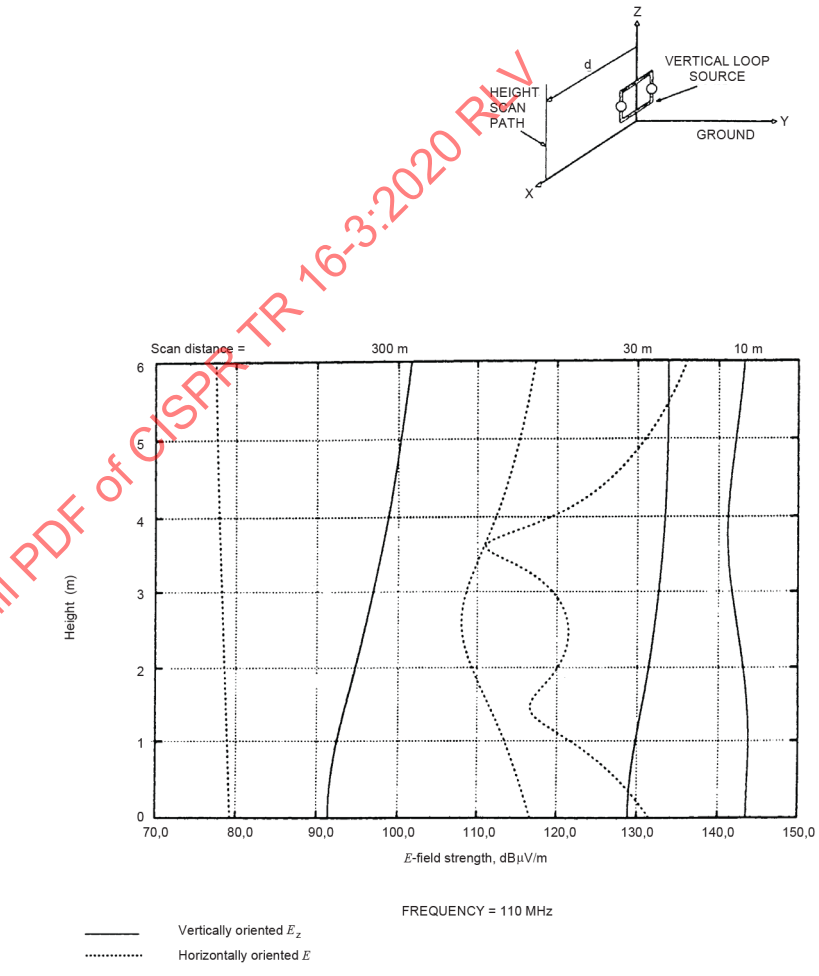
**Figure 26 – Height scan patterns of horizontally polarized $E_x$ field strengths emitted small horizontal electric dipole**

IECNORM.COM : Click to view the full PDF of CISPR TR 16-3:2020 RLV




NOTE Loop dimensions 0,1 m × 0,1 m; loop centre height 2 m; dipole moment 1 A·m$^2$; scan radii of 10 m, 30 m and 300 m; 110 MHz; ground constants: $\varepsilon_r$ = 15, $\sigma$ = 2 mS/m (Reproduced from [39]).

**Figure 27 – Vertical polar patterns of horizontally polarized $E_x$ and vertically oriented $E_z$ field strengths emitted around small vertical loop (horizontal magnetic dipole) in Y-Z and Z-X planes respectively**




NOTE Loop dimensions 0,1 m × 0,1 m; loop centre height 2 m; dipole moment 1 A·m$^2$; horizontal distances 10 m, 30 m and 300 m; ground constants: $\varepsilon_r$ = 15, $\sigma$ = 2 mS/m; 110 MHz; Z-X plane (Reproduced from [39]).

**Figure 28 – Height scan patterns of vertically oriented $E_z$ and horizontally oriented $E_x$ field strengths emitted from small vertical loop (horizontal magnetic dipole)**

IECNORM.COM : Click to view the full PDF of CISPR TR 16-3:2020 RLV

**Table 15 – Estimates of the errors in prediction of radiation in vertical directions based on a measurement height scan from 1 m to 4 m at known distances, $d$; frequency = 110 MHz (adapted from [39])**

| (1) Source of radiation at height | (2) Max. $E$, at angle, in 10 m polar plot | (3) At hor. $d$ = 10 m, measure this field | (4) Estimated prediction error, at $d$ = 10 m | (5) Max. $E$, at angle, in 30 m polar plot | (6) At hor. $d$ = 30 m, measure this field | (7) Estimated prediction error, at $d$ = 30 m | (8) Max. $E$, at angle, in 300 m polar plot | (9) At hor. $d$ = 300 m, measure this field | (10) Estimated prediction error, at $d$ = 300 m |
|---|---|---|---|---|---|---|---|---|---|
| Vertical electric dipole at 1 m | $E_z$ at 13,5° | $E_z$ | 0 dB | $E_z$ at 15,25° | $E_z$ | –1,5 dB | $E_z$ at 15,25° | $E_z$ | –17,5 dB |
| Vertical electric dipole at 2 m | $E_z$ at 36,5° | *1* | –1 dB | $E_z$ at 10,75° | $E_z$ | –0,5 dB | $E_z$ at 11° | $E_z$ | –15,5 dB |
| Horizontal electric dipole at 1 m | $E_x$ at 41° in Y-Z plane | $E_y$ in Y-Z plane | –2,5 dB | $E_x$ at 40° in Y-Z plane | $E_y$ in Y-Z plane | –9,5 dB | $E_x$ at 39,75° in Y-Z plane | $E_y$ in Y-Z plane | –29 dB |
| Horizontal electric dipole at 2 m | $E_x$ at 20° in Y-Z plane | $E_y$ in Y-Z plane | –0,5 dB | $E_x$ at 19,25° in Y-Z plane | $E_y$ in Y-Z plane | –4,5 dB | $E_x$ at 19,25° in Y-z plane | $E_y$ in Y-Z plane | –23,5 dB |
| Vertical loop (horizontal magnetic dipole) at 1 m | $E_x$ at 90° | $E_z$ in Z-X plane | –2 dB | $E_y$ at 90° | $E_z$ in Z-X plane | –3,5 dB | $E_y$ at 90° | $E_z$ in Z-X plane | –19 dB |
| Vertical loop (horizontal magnetic dipole) at 2 m | $E_y$ at 40° in Z-X plane | $E_z$ in Z-X plane | –2,5 dB | $E_x$ at 48° in Y-Z plane | $E_z$ in Z-X plane | –2,5 dB | $E_x$ at 47,5° in Y-Z plane | $E_z$ in Z-X plane | –17,5 dB |
| Horizontal loop (vertical magnetic dipole) at 1 m | $E_y$ at 31,75° in Z-X plane | $E_y$ in Z-X plane | –1,5 dB | $E_y$ at 31° in Z-X plane | $E_y$ in Z-X plane | –8 dB | $E_y$ at 31° in Z-X plane | $E_y$ in Z-X plane | –27 dB |
| Horizontal loop (vertical magnetic dipole) at 2 m | $E_y$ at 19,25° in Z-X plane | $E_y$ in Z-X plane | –0,5 dB | $E_y$ at 18,5° in Z-X plane | $E_y$ in Z-X plane | –4 dB | $E_y$ at 18,25° in Z-X plane | $E_y$ in Z-X plane | –23 dB |

IECNORM.COM : Click to view the full PDF of CISPR TR 16-3:2020 RLV

#### 4.5.5.2.4 Predictability at 243 MHz

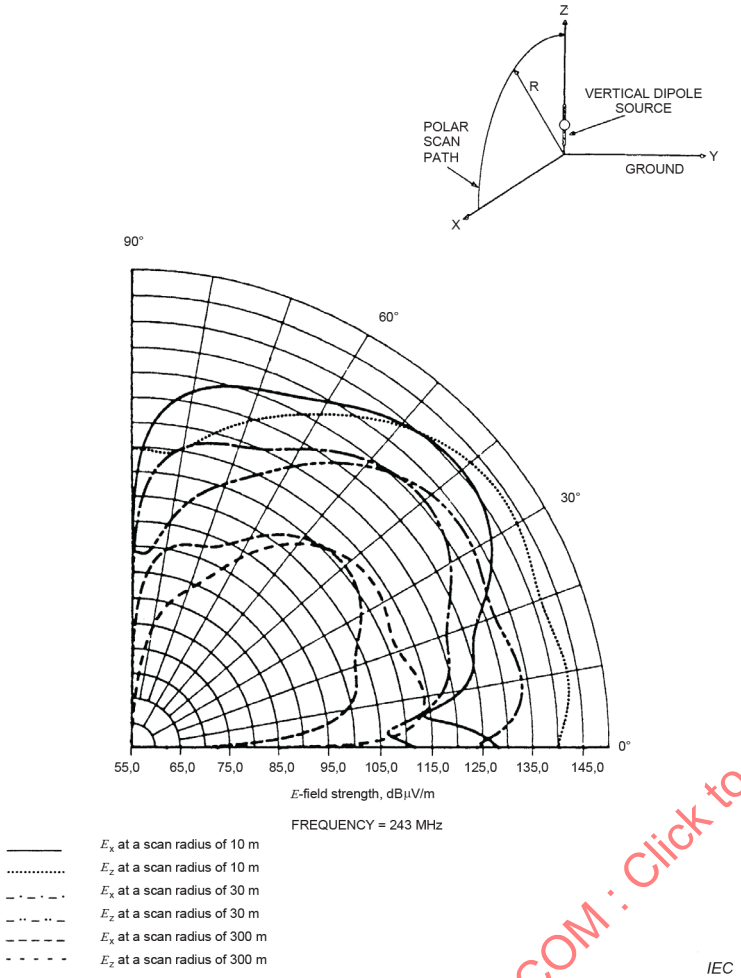
Figure 29 shows vertical polar plots of $E_z$ and $E_x$ in the Z-X plane, at 243 MHz, around the small vertical electric dipole placed at a centre height of 1 m above ground. At a scan radius of 10 m the maximum field strength of almost 144 dB(μV/m) is contributed by $E_z$ at an elevation angle of 33,75°. Calculations of the vertical field component $E_z$ in a height scan from 1 m to 4 m at a horizontal distance of 10 m produce a peak magnitude of almost 143 dB(μV/m) at a measuring height of 1,65 m, as shown in Figure 30. This underestimates the maximum field strength by only 1 dB.

Figure 31 shows vertical polar plots of $E_x$ in the Y-Z plane and $E_z$ in the Z-X plane, around the small vertical loop placed at a centre height of 1 m above a "medium dry ground." It can be seen that, at a scan radius of 10 m, the maximum field strength of more than 159 dB(μV/m) is reached by $E_z$ at an elevation angle of 36,25° in the Z-X plane. The calculated $E_z$ height scan patterns shown in Figure 32 produce a peak field strength of 157 dB(μV/m), at 10 m horizontal distance and a height of 1,65 m. This underestimates the maximum $E_z$ by approximately 2,5 dB.

The vertical polar plots of horizontally polarized $E$-field emitted at 243 MHz by a small horizontal loop placed at a height of 1 m above a “medium dry ground” are shown in Figure 33. The peak of the major lobe, nearest the ground, occurs at an elevation angle of 17° and is therefore reached at a height of 2,9 m at a horizontal distance of 10 m. The height scan plot at a horizontal distance of 10 m in Figure 34, which is of $E_y$ in the Z-X plane in this example, underestimates the maximum field strength in a vertical polar scan by less than 0,5 dB.

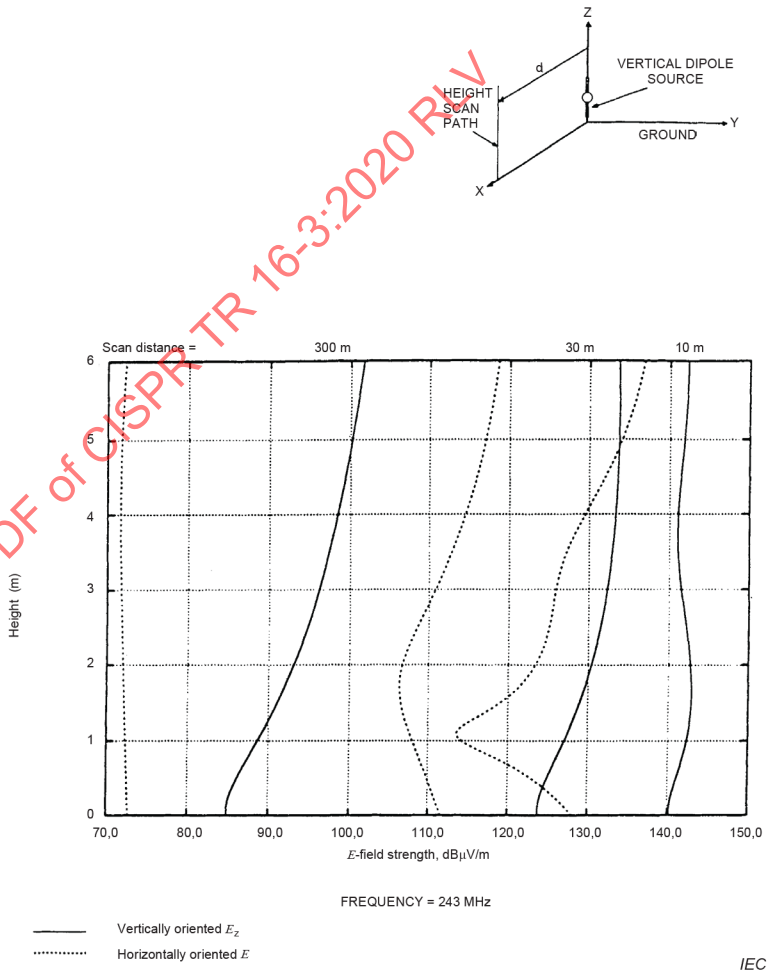
Column (4) of Table 16 summarizes the errors expected in the predictability of radiation in vertical directions based on measurements in height scans from 1 m to 4 m at a horizontal distance of 10 m from each of the four sources operating at 243 MHz.

IECNORM.COM : Click to view the full PDF of CISPR TR 16-3:2020 RLV




NOTE Dipole length 0,05 m; dipole centre height 1 m; dipole moment 1 A·m; scan radii of 10 m, 30 m and 300 m; 243 MHz; ground constants: $\varepsilon_r$ = 15, $\sigma$ = 4,5 mS/m; Z-X plane (Reproduced from [39]).

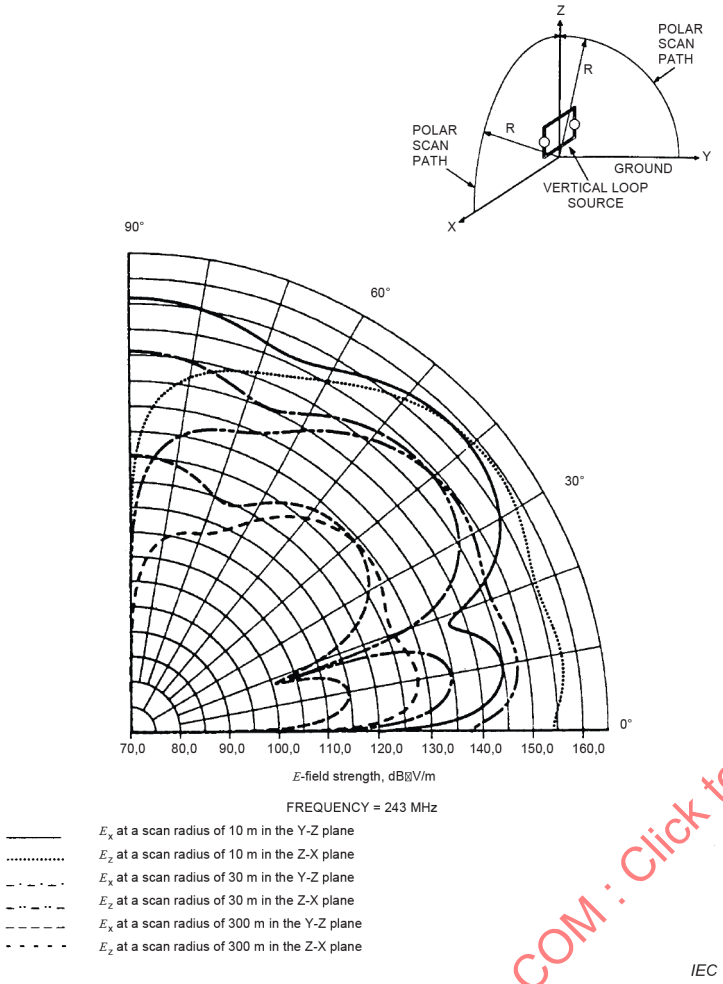
**Figure 29 – Vertical polar patterns of vertically oriented $E_z$ and horizontally oriented $E_x$ field strengths emitted around small vertical electric dipole**




NOTE Dipole length 0,05 m; dipole centre height 1 m; dipole moment 1 A·m; horizontal distance 10 m, 30 m and 300 m; 243 MHz; ground constants: $\varepsilon_r$ = 15, $\sigma$ = 4,5 mS/m; Z-X plane (Reproduced from [39]).

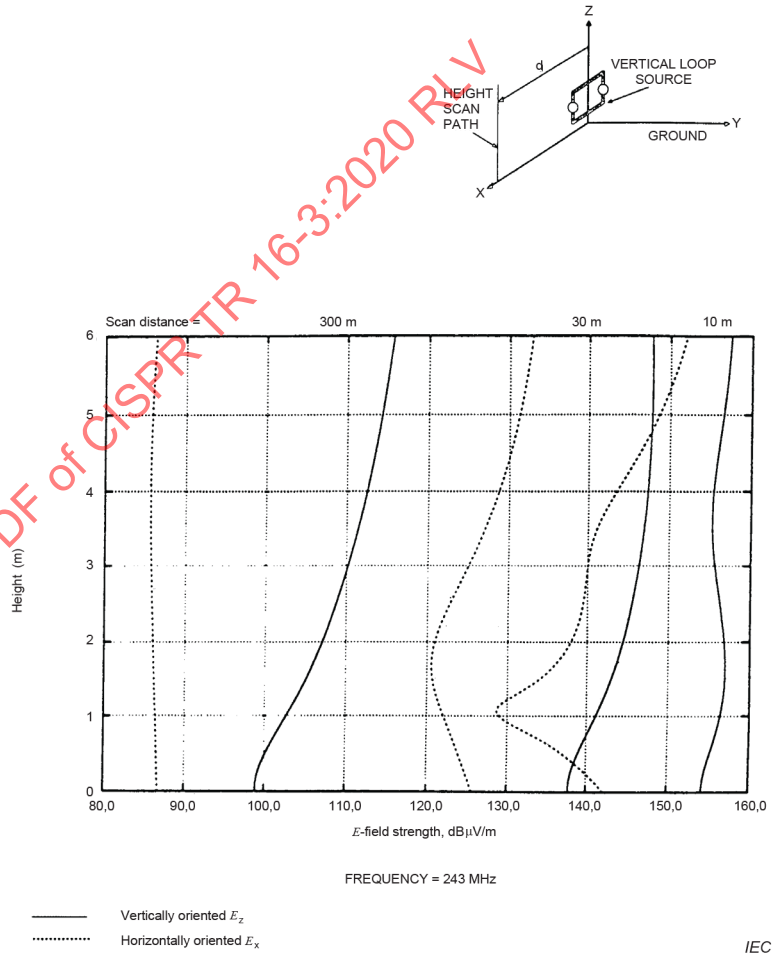
**Figure 30 – Height scan patterns of vertically oriented $E_z$ and horizontally oriented $E_x$ field strengths emitted from small vertical electric dipole**

IECNORM.COM : Click to view the full PDF of CISPR TR 16-3:2020 RLV




NOTE Loop dimensions 0,05 m × 0,05 m; loop centre height 1 m; dipole moment 1 A·m$^2$; scan radii of 10 m, 30 m and 300 m; 243 MHz; ground constants: $\varepsilon_r$ = 15, $\sigma$ = 4,5 mS/m (Reproduced from [39]).

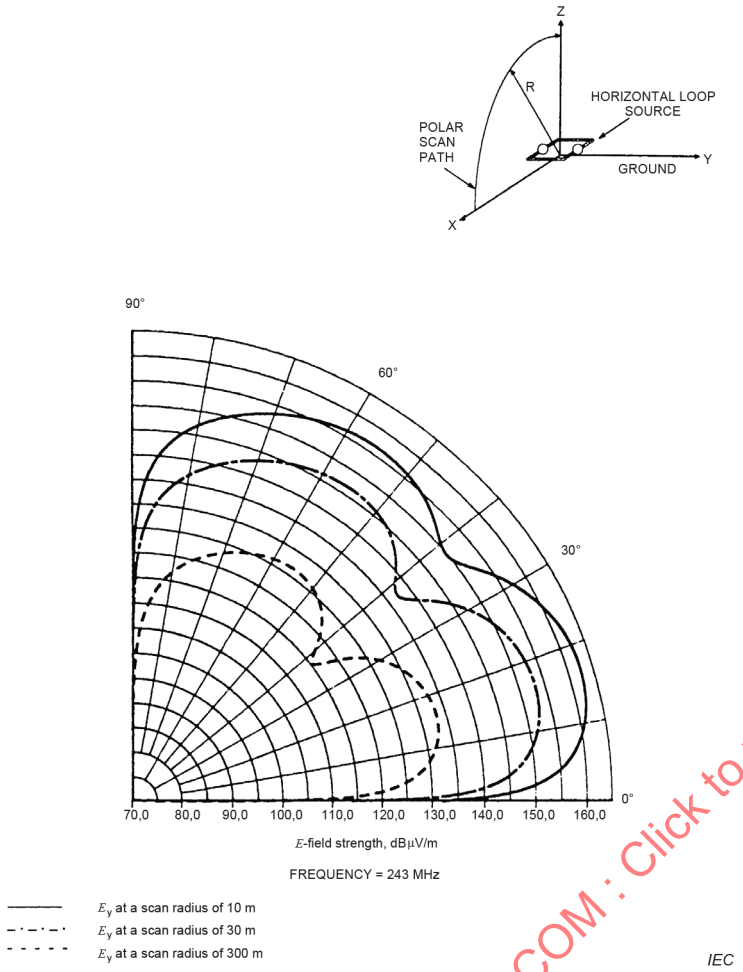
**Figure 31 – Vertical polar patterns of horizontally polarized $E_x$ and vertically oriented $E_z$ field strengths emitted around small vertical loop (horizontal magnetic dipole) in Y-Z and Z-X planes respectively**




NOTE Loop dimensions 0,05 m × 0,05 m; loop centre height 1 m; dipole moment 1 A·m$^2$; horizontal distance 10 m, 30 m and 300 m; 243 MHz; ground constants: $\varepsilon_r$ = 15, $\sigma$ = 4,5 mS/m; Z-X plane (Reproduced from [39]).

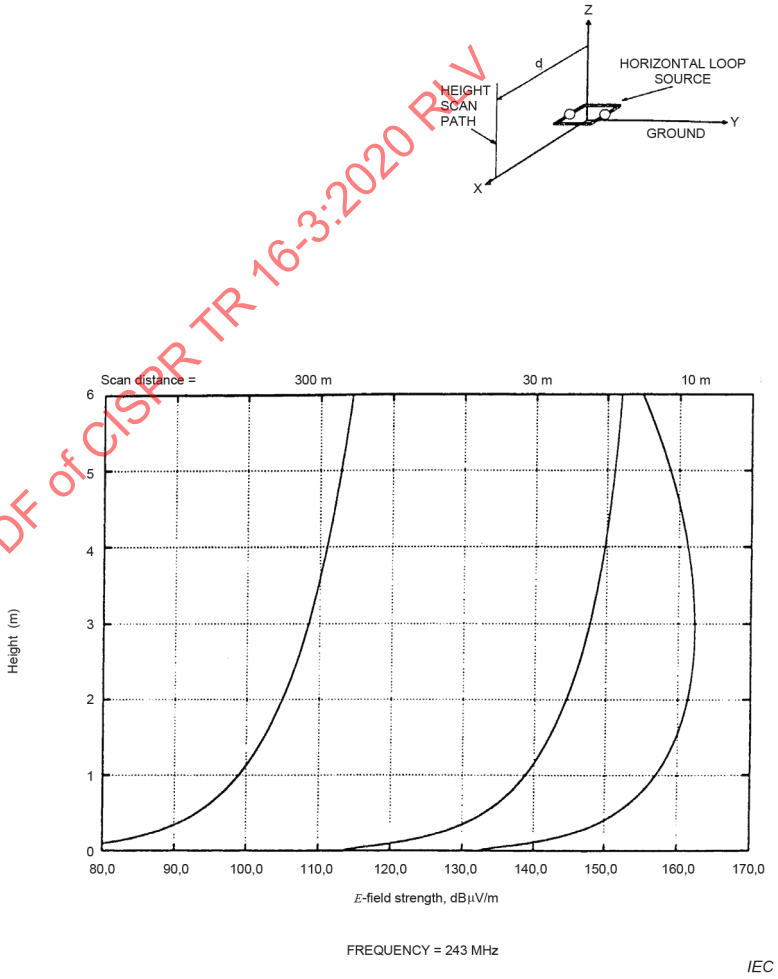
**Figure 32 – Height scan patterns of vertically oriented $E_z$ and horizontally oriented $E_x$ field strengths emitted from small vertical loop (horizontal magnetic dipole)**

IECNORM.COM : Click to view the full PDF of CISPR TR 16-3:2020 RLV




NOTE Loop dimensions 0,05 m × 0,05 m; loop height 1 m; dipole moment 1 A·m$^2$; scan radii of 10 m, 30 m and 300 m; 243 MHz; ground constants: $\varepsilon_r$ = 15, $\sigma$ = 4,5 mS/m; Z-X plane (Reproduced from [39]).

**Figure 33 – Vertical polar patterns of horizontally polarized *E*-field strength emitted around small horizontal loop (vertical magnetic dipole)**




NOTE Loop dimensions 0,05 m × 0,05 m; loop height 1 m; dipole moment 1 A·m$^2$; horizontal distance 10 m, 30 m and 300 m; 243 MHz; ground constants: $\varepsilon_r$ = 15, $\sigma$ = 4,5 mS/m; Z-X plane (Reproduced from [39]).

**Figure 34 – Height scan patterns of horizontally polarized *E*-field strength emitted from small horizontal loop (vertical magnetic dipole)**

IECNORM.COM : Click to view the full PDF of CISPR TR 16-3:2020 RLV

**Table 16 – Estimates of the errors in prediction of radiation in vertical directions based on a measurement height scan from 1 m to 4 m at known distances, $d$; frequency = 243 MHz (adapted from [39])**

| (1) Source of radiation at height | (2) Max. $E$, at angle, in 10 m polar plot | (3) At hor. $d$ = 10 m, measure this field | (4) Estimated prediction error, at $d$ = 10 m | (5) Max. $E$, at angle, in 30 m polar plot | (6) At hor. $d$ = 30 m, measure this field | (7) Estimated prediction error, at $d$ = 30 m | (8) Max. $E$, at angle, in 300 m polar plot | (9) At hor. $d$ = 300 m, measure this field | (10) Estimated prediction error, at $d$ = 300 m |
|---|---|---|---|---|---|---|---|---|---|
| Vertical electric dipole at 1 m | $E_z$ at 33,75° | $E_z$ | –1 dB | $E_z$ at 10,5° | $E_z$ | –0,5 dB | $E_z$ at 10,5° | $E_z$ | –16 dB |
| Vertical electric dipole at 2 m | $E_z$ at 18,25° | $E_z$ | –0,5 dB | $E_z$ at 18,25° | $E_z$ | –0,5 dB | $E_z$ at 7° | $E_z$ | –13 dB |
| Horizontal electric dipole at 1 m | $E_x$ at 17,5° in Y-Z plane | $E_x$ in Y-Z plane | –0,5 dB | $E_x$ at 17,5° in Y-Z plane | $E_x$ in Y-Z plane | –4 dB | $E_x$ at 17,5° in Y-Z plane | $E_x$ in Y-Z plane | –22,5 dB |
| Horizontal electric dipole at 2 m | $E_x$ at 9° in Y-Z plane | $E_x$ in Y-Z plane | 0 dB | $E_x$ at 8,75° in Y-Z plane | $E_x$ in Y-Z plane | –0,5 dB | $E_x$ at 8,75° in Y-Z plane | $E_x$ in Y-Z plane | –17 dB |
| Vertical loop (horizontal magnetic dipole) at 1 m | $E_z$ at 36,25° in Z-X plane | $E_z$ in Z-X plane | –2,5 dB | $E_z$ at 36,5° in Z-X plane | $E_z$ in Z-X plane | –2 dB | $E_z$ at 36,5° in Z-X plane | $E_z$ in Z-X plane | –17 dB |
| Vertical loop (horizontal magnetic dipole at 2 m | $E_x$ at 70,5° in Y-Z plane | $E_z$ in Z-X plane | –2,5 dB | $E_x$ at 69,25° in Y-Z plane | $E_z$ in Z-X plane | –3 dB | $E_x$ at 69° in Y-Z plane | $E_z$ in Z-X plane | –15 dB |
| Horizontal loop (vertical magnetic dipole) at 1 m | $E_y$ at 17° in Z-X plane | $E_y$ in Z-X plane | –0,5 dB | $E_y$ at 16,75° in Z-X plane | $E_y$ in Z-X plane | –3,5 dB | $E_y$ at 16,75° in Z-X plane | $E_y$ in Z-X plane | –22,5 dB |
| Horizontal loop (vertical magnetic dipole) at 2 m | $E_y$ at 9° in Z-X plane | $E_y$ in Z-X plane | 0 dB | $E_y$ at 8,75° in Z-X plane | $E_y$ in Z-X plane | 0 dB | $E_y$ at 8,75° in Z-X plane | $E_y$ in Z-X plane | –17 dB |

IECNORM.COM : Click to view the full PDF of CISPR TR 16-3:2020 RLV

#### 4.5.5.2.5 Predictability at 330 MHz

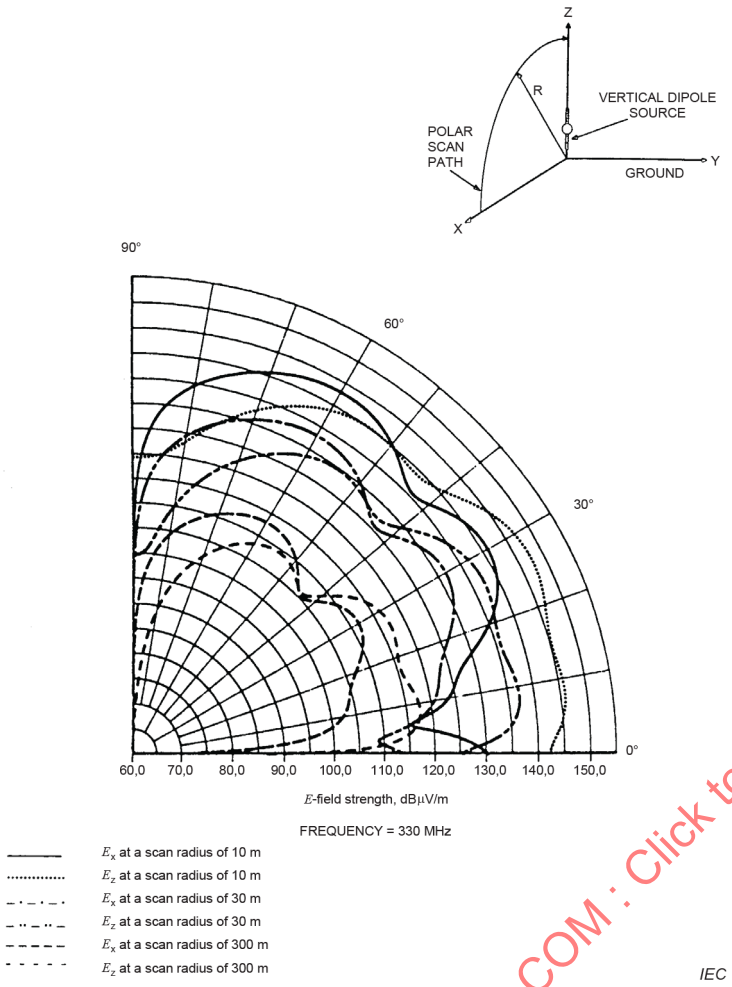
Figure 35 shows vertical polar plots of $E_z$ and $E_x$ in the Z-X plane, at 330 MHz, around the small vertical electric dipole placed at a centre height of 1 m above ground. At a scan radius of 10 m the maximum field strength of almost 148 dB(μV/m) is contributed by $E_z$ at an elevation angle of 26°. Calculations of the vertically oriented $E_z$ field in a height scan from 1 m to 4 m at 10 m horizontal distance produce a peak magnitude of almost 146 dB(μV/m) at a measuring height of 1,45 m, as shown in Figure 36. This underestimates the maximum field strength by less than 2 dB.

Figure 37 shows vertical polar plots of $E_x$ in the Y-Z plane and $E_z$ in the Z-X plane, around the small vertical loop placed at a centre height of 1 m above a “medium dry ground.” It can be seen that, at a scan radius of 10 m, the maximum field strength of almost 167 dB(μV/m) is reached by $E_x$ at an elevation angle of 69° in the Y-Z plane. The calculated $E_z$ height scan patterns in the Z-X plane shown in Figure 38 produce a peak magnitude greater than 162 dB(μV/m) at 10 m horizontal distance, measured at a height of 1,45 m. A height scan measurement of the vertical $E_z$ field therefore underestimates the maximum strength of the radiation in vertical directions, the horizontal polarized $E_x$ at an elevation angle of 69°, by approximately 4,5 dB.

It is interesting to observe the vertical polar plots of horizontally polarized $E$-field emitted at 330 MHz by a small horizontal loop placed at a height of 1 m above a “medium dry ground,” shown in Figure 39. The peak of the major lobe, nearest the ground, occurs at an elevation angle of only 12,75°. It is therefore measured at a height of only 2,2 m at a horizontal distance of 10 m, see Figure 40. Thus, there is virtually no error in this example of the estimation of maximum field strength at elevated angles.

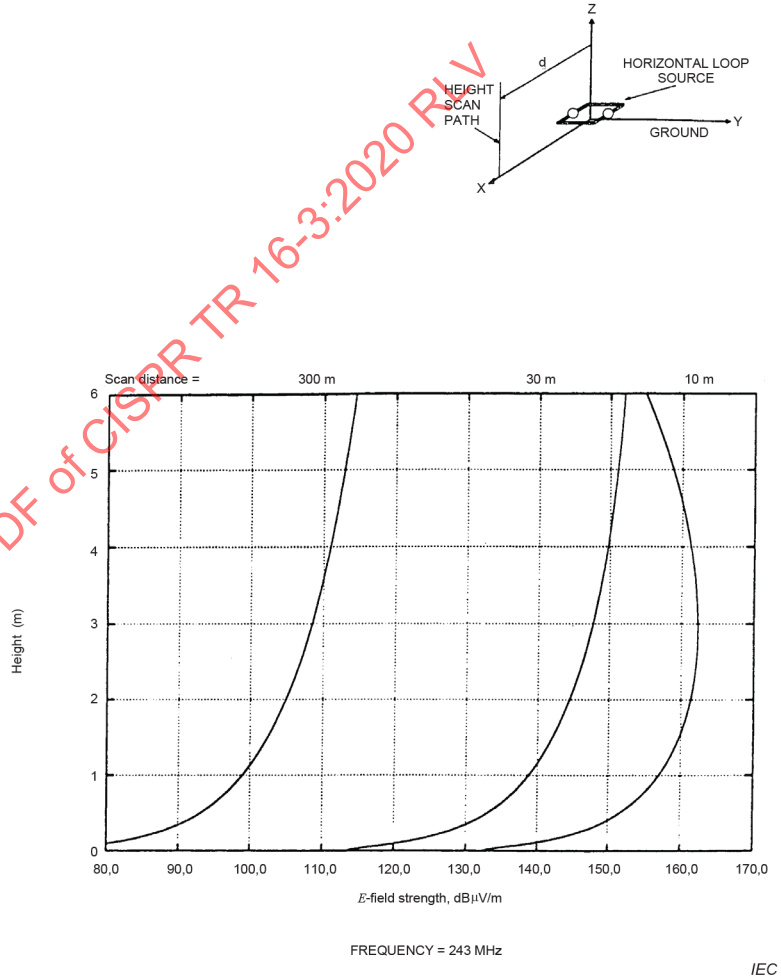
Column (4) of Table 17 summarizes the estimated errors in the predictability of radiation in vertical directions based on measurements in height scans from 1 m to 4 m at a horizontal distance of 10 m from each of the four sources operating at 330 MHz.

IECNORM.COM : Click to view the full PDF of CISPR TR 16-3:2020 RLV




NOTE Dipole length 0,05 m; dipole centre height 1 m; dipole moment 1 A·m; scan radii of 10 m, 30 m and 300 m; 330 MHz; ground constants: $\varepsilon_r$ = 15, $\sigma$ = 7,5 mS/m; Z-X plane (Reproduced from [39]).

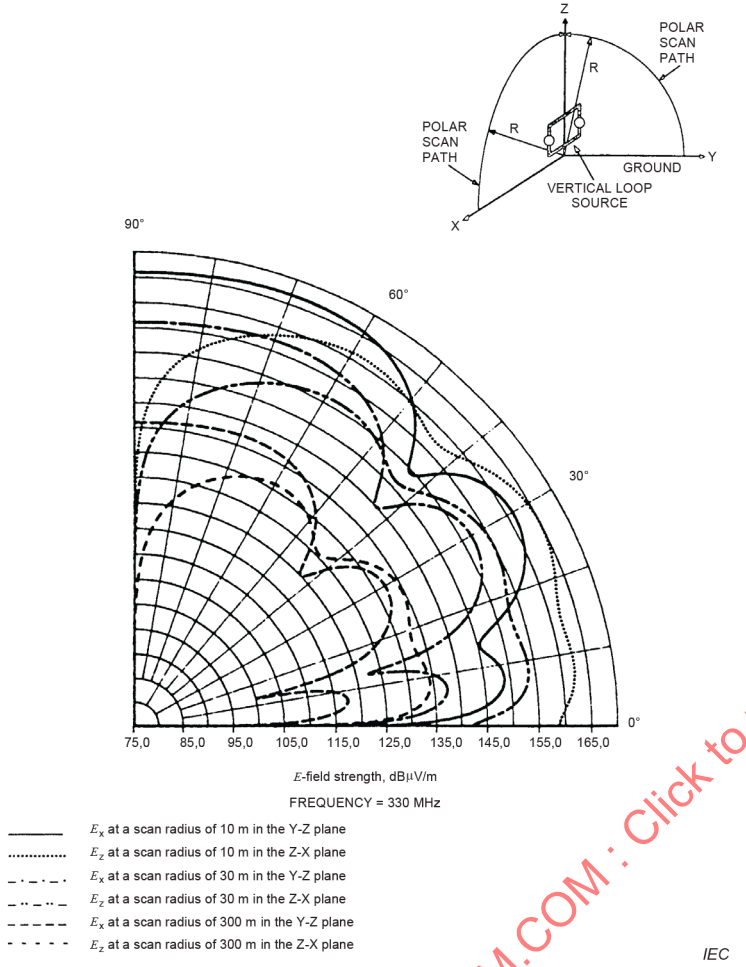
**Figure 35 – Vertical polar patterns of vertically oriented $E_z$ and horizontally oriented $E_x$ field strengths emitted around small vertical electric dipole**




NOTE Loop dimensions 0,05 m × 0,05 m; loop height 1 m; dipole moment 1 A·m$^2$; horizontal distance 10 m, 30 m and 300 m; 243 MHz; ground constants: $\varepsilon_r$ = 15, $\sigma$ = 4,5 mS/m; Z-X plane (Reproduced from [39]).

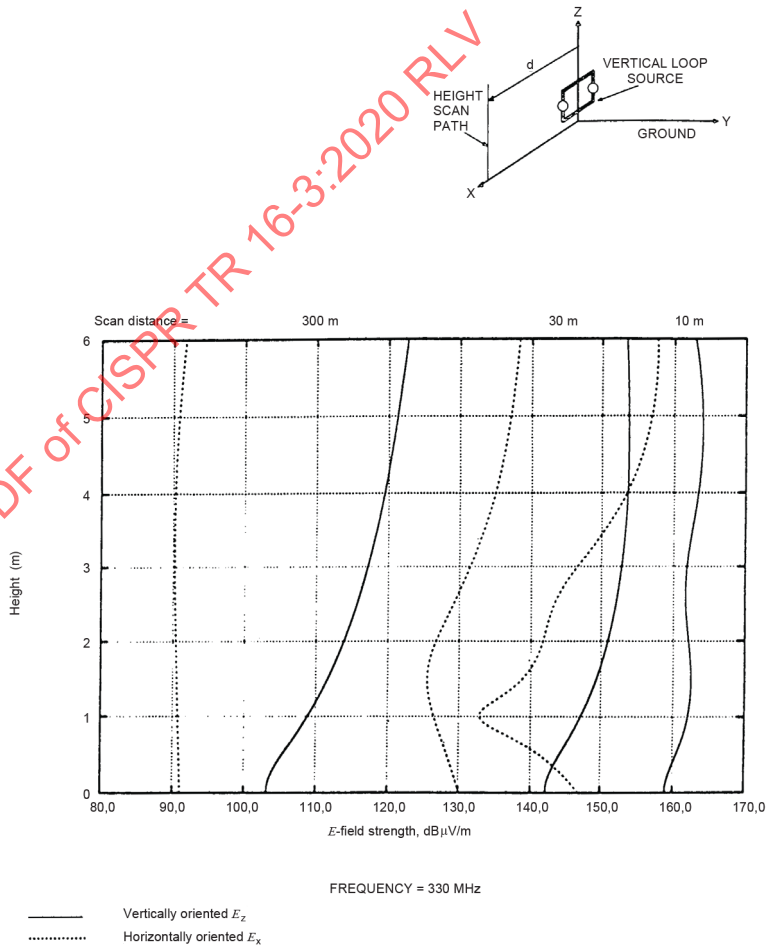
**Figure 36 – Height scan patterns of vertically oriented $E_z$ and horizontally oriented $E_x$ field strengths emitted from the small vertical electric dipole**

IECNORM.COM : Click to view the full PDF of CISPR TR 16-3:2020 RLV




NOTE Loop dimensions 0,05 m × 0,05 m; loop centre height 1 m; dipole moment 1 A·m$^2$; scan radii of 10 m, 30 m and 300 m; 330 MHz; ground constants: $\varepsilon_r$ = 15, $\sigma$ = 7,5 mS/m (Reproduced from [39]).

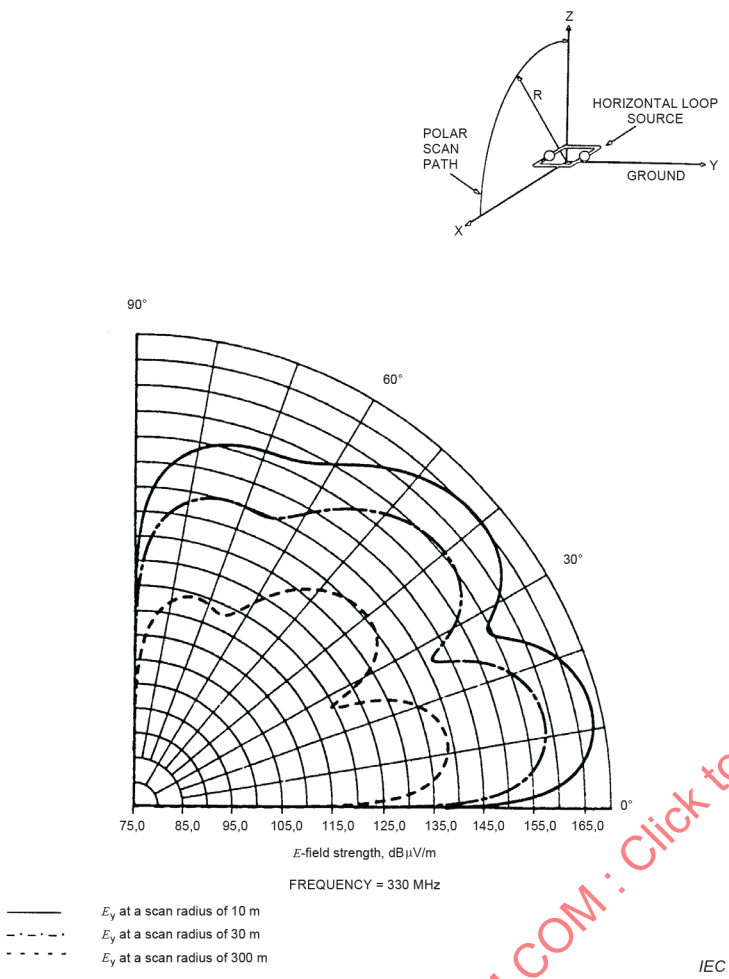
**Figure 37 – Vertical polar patterns of horizontally polarized $E_x$ and vertically oriented $E_z$ field strengths emitted around small vertical loop (horizontal magnetic dipole) in Y-Z and Z-X planes respectively**




NOTE Loop dimensions 0,05 m × 0,05 m; loop centre height 1 m; dipole moment 1 A·m$^2$; horizontal distance 10 m, 30 m and 300 m; 330 MHz; ground constants: $\varepsilon_r$ = 15, $\sigma$ = 7,5 mS/m; Z-X plane (Reproduced from [39]).

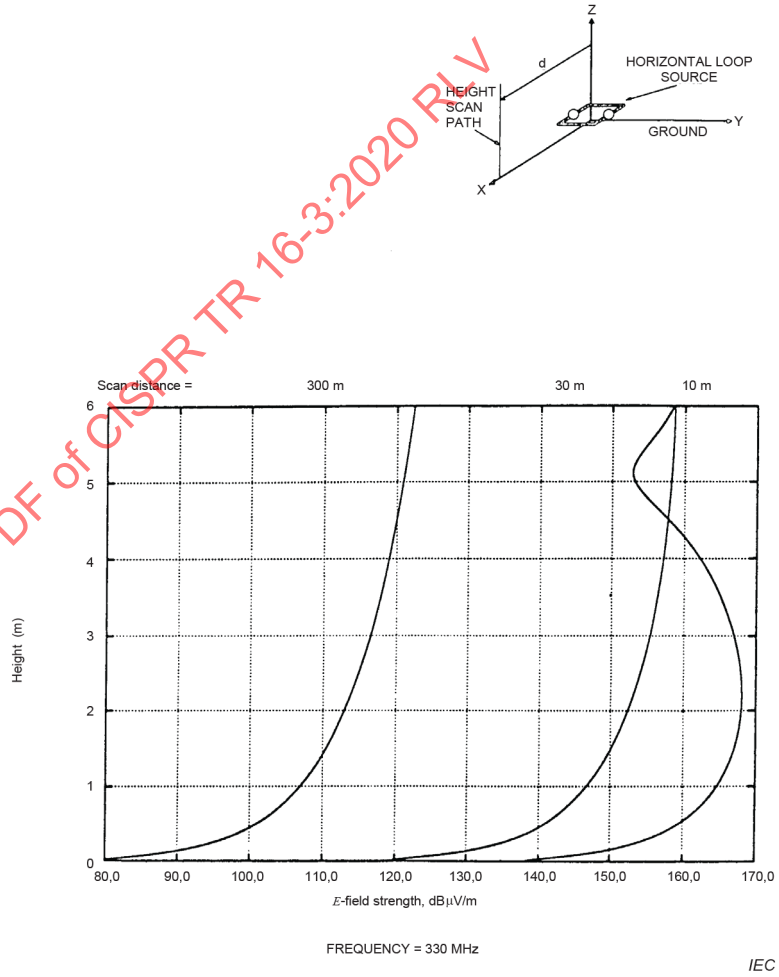
**Figure 38 – Height scan patterns of vertically oriented $E_z$ and horizontally oriented $E_x$ field strengths emitted from small vertical loop (horizontal magnetic dipole)**

IECNORM.COM : Click to view the full PDF of CISPR TR 16-3:2020 RLV




NOTE Loop dimensions 0,05 m × 0,05 m; loop height 1 m; dipole moment 1 A·m$^2$; scan radii of 10 m, 30 m and 300 m; 330 MHz; ground constants: $\varepsilon_r$ = 15, $\sigma$ = 7,5 mS/m; Z-X plane (Reproduced from [39]).

**Figure 39 – Vertical polar patterns of horizontally polarized *E*-field strength emitted around small horizontal loop (vertical magnetic dipole)**




NOTE Loop dimensions 0,05 m × 0,05 m; loop height 1 m; dipole moment 1 A·m$^2$; horizontal distance 10 m, 30 m and 300 m; 330 MHz; ground constants: $\varepsilon_r$ = 15, $\sigma$ = 4,5 mS/m; Z-X plane (Reproduced from [39]).

**Figure 40 – Height scan patterns of horizontally polarized *E*-field strength emitted from small horizontal loop (vertical magnetic dipole)**

IECNORM.COM : Click to view the full PDF of CISPR TR 16-3:2020 RLV

**Table 17 – Estimates of the errors in prediction of radiation in vertical directions based on a measurement height scan from 1 m to 4 m at known distances, $d$; frequency = 330 MHz (adapted from [39])**

| (1) Source of radiation at height | (2) Max. $E$, at angle, in 10 m polar plot | (3) At hor. $d$ = 10 m, measure this field | (4) Estimated prediction error, at $d$ = 10 m | (5) Max. $E$, at angle, in 30 m polar plot | (6) At hor. $d$ = 30 m, measure this field | (7) Estimated prediction error, at $d$ = 30 m | (8) Max. $E$, at angle, in 300 m polar plot | (9) At hor. $d$ = 300 m, measure this field | (10) Estimated prediction error, at $d$ = 300 m |
|---|---|---|---|---|---|---|---|---|---|
| Vertical electric dipole at 1 m | $E_z$ at 26° | $E_z$ | –2 dB | $E_z$ at 26° | $E_z$ | –0,5 dB | $E_z$ at 9° | $E_z$ | –15 dB |
| Vertical electric dipole at 2 m | $E_z$ at 27,25° | $E_z$ | –0,5 dB | $E_z$ at 5,75° | $E_z$ | 0 dB | $E_z$ at 5,5° | $E_z$ | –11,5 dB |
| Horizontal electric dipole at 1 m | $E_x$ at 13° in Y-Z plane | $E_y$ in Y-Z plane | 0 dB | $E_x$ at 12,75° in Y-Z plane | $E_y$ in Y-Z plane | –2 dB | $E_x$ at 12,75° in Y-Z plane | $E_y$ in Y-Z plane | –20 dB |
| Horizontal electric dipole at 2 m | $E_x$ at 6,5° in Y-Z plane | $E_y$ in Y-Z plane | 0 dB | $E_x$ at 6,5° in Y-Z plane | $E_y$ in Y-Z plane | 0 dB | $E_x$ at 6,5° in Y-Z plane | $E_y$ in Y-Z plane | –14,5 dB |
| Vertical loop (horizontal magnetic dipole) at 1 m | $E_x$ at 69° in Y-Z plane | $E_z$ in Z-X plane | –4,5 dB | $E_x$ at 68,25° in Y-Z plane | $E_z$ in Z-X plane | –3,5 dB | $E_x$ at 68° in Y-Z plane | $E_z$ in Z-X plane | –17,5dB |
| Vertical loop (horizontal magnetic dipole) at 2 m | $E_x$ at 66,75° in Y-Z plane | $E_z$ in Z-X plane | –2,5 dB | $E_x$ at 66° in Y-Z plane | $E_z$ in Z-X plane | –2,5 dB | $E_x$ at 66° in Y-Z plane | $E_z$ in Z-X plane | –12,5 dB |
| Horizontal loop (vertical magnetic dipole) at 1 m | $E_y$ at 12,75° in Z-X plane | $E_y$ in Z-X plane | 0 dB | $E_y$ at 12,5° in Z-X plane | $E_y$ in Z-X plane | –2 dB | $E_y$ at 12,5° in Z-X plane | $E_y$ in Z-X plane | –20 dB |
| Horizontal loop (vertical magnetic dipole) at 2 m | $E_y$ at 6,5° in Z-X plane | $E_y$ in Z-X plane | 0 dB | $E_y$ at 6,5° in Z-X plane | $E_y$ in Z-X plane | 0 dB | $E_y$ at 6,5° in Z-X plane | $E_y$ in Z-X plane | –14,5 dB |

IECNORM.COM : Click to view the full PDF of CISPR TR 16-3:2020 RLV

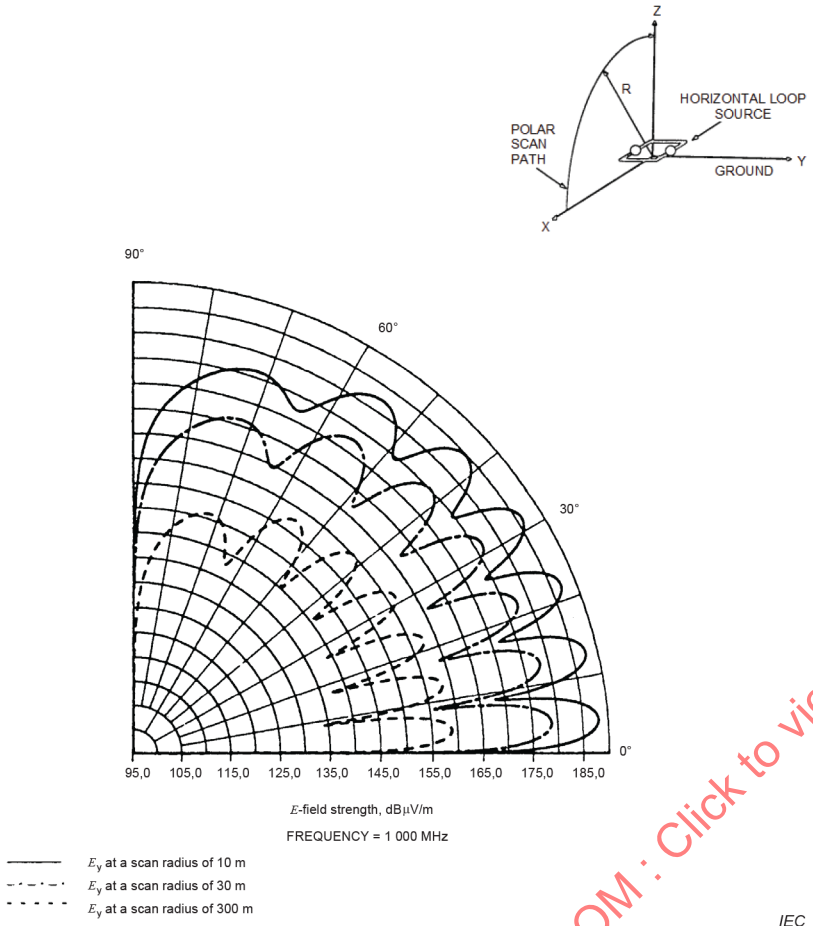
#### 4.5.5.2.6 Predictability at 1 000 MHz

Figure 20 to Figure 22 show vertical polar plots of $E_z$ and $E_x$, at 1 000 MHz, around a small vertical loop placed at a centre height of 2 m above ground. At a scan radius of 10 m over a "medium dry ground" the maximum field strength of 187 dB(μV/m) is contributed by the horizontally polarized $E_x$ at an elevation angle of 77,5° in the Y-Z plane. Calculations of the vertically oriented $E_z$ field in a height scan from 1 m to 4 m at 10 m horizontal distance in the Z-X plane produce a peak field of almost 184 dB(μV/m) at a height of 3,2 m, as shown in Figure 22. A vertically polarized height scan measurement therefore underestimates the maximum field strength by approximately 3 dB.

It is interesting to observe the vertical polar plots of horizontally polarized $E$-field emitted at 1 000 MHz by a small horizontal loop placed at a height of 1 m above a “medium dry ground,” shown in Figure 41. The peak of the major lobe, nearest the ground, occurs at an elevation angle of only 4,25°. Shown again in Figure 42, it occurs at a height of 0,74 m at a horizontal distance of 10 m, and therefore will *not* be measured in a 1 m to 4 m height scan measurement. The next grating lobe is encountered at a height of 2,3 m, and its measurement contributes to an underestimate of less than 0,5 dB to the prediction of maximum field strength of the major (lower) lobe.

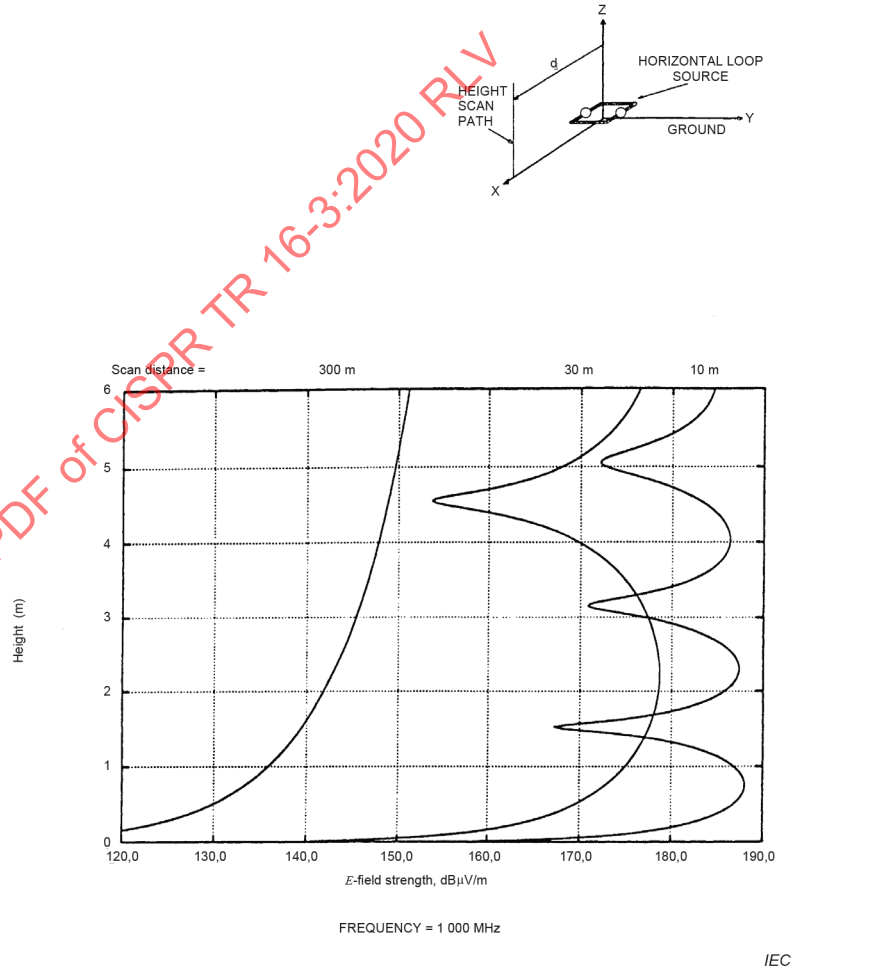
Column (4) of Table 18 summarizes the errors estimated for the predictability of radiation in vertical directions based on measurements in height scans from 1 m to 4 m at a horizontal distance of 10 m from each of the four sources operating at 1 000 MHz.

IECNORM.COM : Click to view the full PDF of CISPR TR 16-3:2020 RLV




NOTE Loop dimensions 0,02 m × 0,02 m; loop height 1 m; dipole moment 1 A·m$^2$; scan radii of 10 m, 30 m and 300 m; 1 000 MHz; ground constants: $\varepsilon_r$ = 15, $\sigma$ = 35 mS/m; Z-X plane (Reproduced from [39]).

**Figure 41 – Vertical polar patterns of horizontally polarized *E*-field strength emitted around the small horizontal loop (vertical magnetic dipole)**




NOTE Loop dimensions 0,02 m × 0,02 m; loop height 1 m; dipole moment 1 A·m$^2$; horizontal distance 10 m, 30 m and 300 m; 1 000 MHz; ground constants: $\varepsilon_r$ = 15, $\sigma$ = 35 mS/m; Z-X plane (Reproduced from [39]).

**Figure 42 – Height scan patterns of horizontally polarized *E*-field strength emitted from small horizontal loop (vertical magnetic dipole)**

IECNORM.COM : Click to view the full PDF of CISPR TR 16-3:2020 RLV

**Table 18 – Estimates of the errors in prediction of radiation in vertical directions based on a measurement height scan from 1 m to 4 m at known distances, $d$; frequency = 1 000 MHz (adapted from [39])**

| (1) Source of radiation at height | (2) Max. $E$, at angle, in 10 m polar plot | (3) At hor. $d$ = 10 m, measure this field | (4) Estimated prediction error, at $d$ = 10 m | (5) Max. $E$, at angle, in 30 m polar plot | (6) At hor. $d$ = 30 m, measure this field | (7) Estimated prediction error, at $d$ = 30 m | (8) Max. $E$, at angle, in 300 m polar plot | (9) At hor. $d$ = 300 m, measure this field | (10) Estimated prediction error, at $d$ = 300 m |
|---|---|---|---|---|---|---|---|---|---|
| Vertical electric dipole at 1 m | $E_z$ at 17,5° | $E_z$ | –0,5 dB | $E_z$ at 4° | $E_z$ | 0 dB | $E_z$ at 3,75° | $E_z$ | –9,5 dB |
| Vertical electric dipole at 2 m | $E_z$ at 17,75° | $E_z$ | –0,5 dB | $E_z$ at 2° | $E_z$ | 0 dB | $E_z$ at 2° | $E_z$ | –5 dB |
| Horizontal electric dipole at 1 m | $E_x$ at 4,25° in Y-Z plane | $E_y$ in Y-Z plane | –0,5 dB | $E_x$ at 4,25° in Y-Z plane | $E_y$ in Y-Z plane | 0 dB | $E_x$ at 4,25° in Y-Z plane | $E_y$ in Y-Z plane | –11 dB |
| Horizontal electric dipole at 2 m | $E_x$ at 2,25° in Y-Z plane | $E_y$ in Y-Z plane | 0 dB | $E_x$ at 2,25° in Y-Z plane | $E_y$ in Y-Z plane | 0 dB | $E_x$ at 2,25° in Y-Z plane | $E_y$ in Y-Z plane | –5,5 dB |
| Vertical loop (horizontal magnetic dipole) at 1 m | $E_x$ at 64,5° in Y-Z plane | $E_z$ in Z-X plane | –2,5 dB | $E_x$ at 64,25° in Y-Z plane | $E_z$ in Z-X plane | –1 dB | $E_z$ at 4° in Z-X plane | $E_z$ in Z-X plane | –9,5 dB |
| Vertical loop (horizontal magnetic dipole) at 2 m | $E_x$ at 77,5° in Y-Z plane | $E_z$ in Z-X plane | –3 dB | $E_x$ at 77,25° in Y-Z plane | $E_z$ in Z-X plane | –1,5 dB | $E_z$ at 2° in Z-X plane | $E_z$ in Z-X plane | –5 dB |
| Horizontal loop (vertical magnetic dipole) at 1 m | $E_y$ at 4,25° in Z-X plane | $E_y$ in Z-X plane | –0,5 dB | $E_y$ at 4,25° in Z-X plane | $E_y$ in Z-X plane | 0 dB | $E_y$ at 4,25° in Z-X plane | $E_y$ in Z-X plane | –11 dB |
| Horizontal loop (vertical magnetic dipole) at 2 m | $E_y$ at 2,25° in Z-X plane | $E_y$ in Z-X plane | 0 dB | $E_y$ at 2,25° in Z-X plane | $E_y$ in Z-X plane | 0 dB | $E_y$ at 2,25° in Z-X plane | $E_y$ in Z-X plane | –5,5 dB |

IECNORM.COM : Click to view the full PDF of CISPR TR 16-3:2020 RLV

#### 4.5.5.3 Predictability based on height scan measurements near real ground at an unknown distance, greater than 10 m, from the radiation source

Here we can answer the second question posed in 4.5.3. This measurement situation is analogous to making measurements *in situ* at a distance of 10 m from the wall outside a building containing ISM equipment that is located at an unknown distance inside the building. As mentioned earlier, we do not consider here the attenuation that may be introduced by intervening building materials.

Calculations have been made of vertical polar patterns and linear height scan patterns at distances of 30 m and 300 m. The reader will have already seen that patterns for those distances have also been included in the figures.

The figures, together with the comprehensive summaries presented in columns (7) and (10) of Table 14 to Table 18, show that the predictability of fields at elevated angles based on height scan measurements near real ground becomes more prone to underestimation as the horizontal measuring distance increases beyond 10 m, especially at the lower frequencies. Underestimation can become very large at a distance of 300 m. At the lower frequencies underestimates can reach more than 30 dB at that distance when the source behaves as a small horizontal electric dipole. The underestimates for both horizontally and vertically polarized fields occur in spite of the significant contributions that can be made by surface waves at the lower frequencies near 30 MHz [40]. Predictability improves as the frequency increases, primarily because at higher frequencies, the surface wave contributions decrease and the maximum field strength measured in the height scan is created by the sum of the direct and reflected space wave components (the sum is sometimes called, somewhat misleadingly, the “ground wave”). The contributions of the space wave signals increase at lower elevation angles as more grating lobes form with increasing frequency.

It is particularly important to recognize that, at horizontal distances of 30 m and more, the worst-case underestimations of the maximum levels of field strengths at elevated angles will generally occur when the fields are horizontally polarized. This is very unfortunate, because the signals for the ILS (marker beacons, localizer, and glide path, see Table 11) are all horizontally polarized transmissions and therefore require the maximum protection from horizontally polarized disturbances.

The figures also provide guidance to the rates of change of the fields with distance. Calculations and measurements made at a constant height, avoiding nulls, show that the maximum rate of change of the fields with distance can approach a rate that is inversely proportional to distance squared. When surface wave contributions are negligible, then for grazing incidence in the far field a field strength inversely proportional to distance squared is to be expected at a constant measuring height [40], [41]. However, the space wave field strengths along radial paths at constant elevation angles vary in simple proportion with inverse distance, which is to be expected of such far fields propagating freely in space. Therefore, it is to be expected that the fields measured near the ground (the so-called “ground waves”), in general, will attenuate more rapidly with increasing distance than do the fields from the same source which are propagating radially up into space.

If the horizontal distances at which height scan measurements are made *in situ* are not known, very large errors can arise – all of them underestimates – in the predictability of the strength of radiation in vertical directions from all four types of source and at all frequencies from 75 MHz to 1 000 MHz.

#### 4.5.5.4 Predictability based on measurement at a fixed height

In its measurement procedures relating to the ways in which measuring antennas are to be used, CISPR 11 does not distinguish between measurements made *in situ* for the protection of specific safety-related radio services and those made for the protection of other services. Thus, if a measurement of emissions is made *in situ* from a Group 2 Class A ISM equipment in accordance with the specification, the measuring antenna is placed at a height of 2,0 m ± 0,2 m (7.3.4 of CISPR 11:2009); no height scan is specified.

The obvious risk with fixed height measurements is that a measurement will be made at a null in the field strength pattern. The risk of this happening is increased if the electrical height above ground of the radiation centre of the source increases – for example with increasing frequency – which contributes to the formation of an increasing number of grating lobes, and hence nulls. A few examples of the effects these nulls can have on a measurement made at a height near 3 m (or any other *fixed* height) are shown in several of the figures.

IECNORM.COM : Click to view the full PDF of CISPR TR 16-3:2020 RLV

For example, Figure 22 shows that, depending on the type of ground over which the measurements are made, at a horizontal distance of 10 m from a small vertical loop source located at a height of 2 m, the measured vertically polarized field strength at 1 000 MHz might vary by more than 6 dB for measurements made somewhere in the height tolerance range of 2,8 m to 3,2 m, and that at 30 m horizontal distance a measurement made at 3 m height is also close to a null.

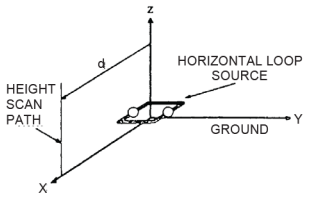
Figure 40 shows that a horizontal distance of 10 m from a small horizontal loop source located 1 m above ground with the measured horizontally polarized field strength at 1 000 MHz might vary by more than 12 dB in the CISPR measurement height tolerance range from 2,8 m to 3,2 m. It also shows how the field strength can vary with distance in an apparently anomalous manner when measurements are made at a fixed height. Note that at a height of 3 m, the field strength at 30 m distance is the same as the field strength at 10 m distance. At other heights, the field strength at 30 m distance becomes greater than that at 10 m distance.

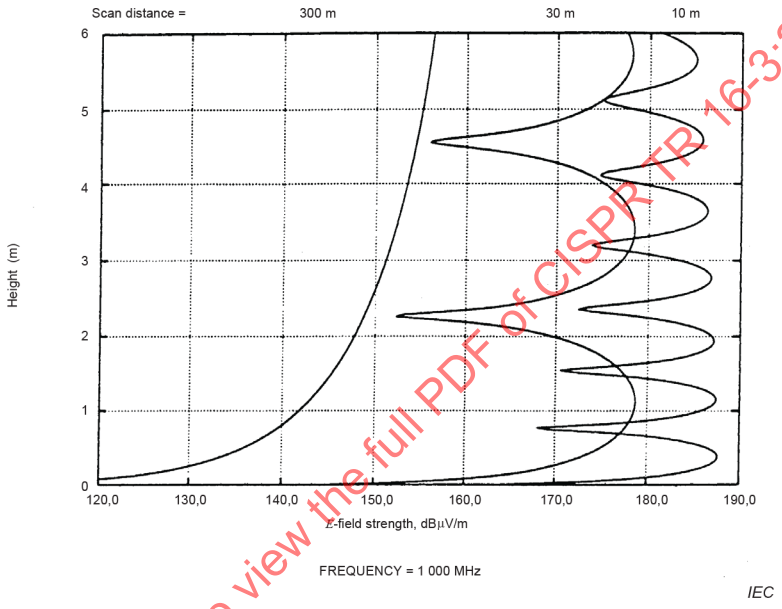
Comparison of the height scan curves in Figure 43 with those in Figure 40, at 1 000 MHz, shows that as the small horizontal loop source height varies between 1 m and 2 m, deep nulls will pass through the measuring height of 3 m at horizontal measuring distance of 10 m and 30 m. These effects can be encountered at *greater horizontal measuring distances* and *lower frequencies* if the height of the radiating source is increased.

We are now in a position to answer the third question posed in 4.5.3. The answer is that predictability is degraded by fixed height measurements. Measurements at a fixed height should not be permitted, especially if they are being made to determine protection for specific safety services.

Height scans shall be specified or, for measuring convenience, the measuring height *in situ* could be specified in the manner of [42], so that at a horizontal distance of 10 m, the measuring height would be specified as 4 m above the immediate terrain *or at such lower height at which the field strengths may exceed that at 4 m.*

IECNORM.COM : Click to view the full PDF of CISPR TR 16-3:2020 RLV




NOTE Loop dimensions 0,02 m × 0,02 m; loop height 2 m; dipole moment 1 A·m$^2$; horizontal distance 10 m, 30 m and 300 m; 1 000 MHz; ground constants: $\varepsilon_r$ = 15, $\sigma$ = 35 mS/m; Z-X plane (Reproduced from [39]).

**Figure 43 – Height scan patterns of horizontally polarized $E$-field strength emitted from small horizontal loop (vertical magnetic dipole)**

IECNORM.COM : Click to view the full PDF of CISPR TR 16-3:2020 RLV

### 4.5.6 Differences between the fields over a real ground and the fields over a perfect conductor

#### 4.5.6.1 General

There are significant differences between the field distributions above a real earth plane and over a perfect conductor. There are several reasons for the differences, not the least being that the reflection factors for both polarizations over a perfect conductor always have a magnitude of unity at all angles of incidence, whereas over real ground they have a magnitude less than unity except at grazing incidence. In addition, for vertically polarized waves over a perfect conductor there is no Brewster's angle, or expressed in another way, at all reflection angles a vertically polarized image in a perfect conductor is always in phase with the vertically polarized source above the conductor. This contrasts with the situation of vertically polarized waves impinging upon a lossy dielectric such as real ground, where reflections taking place below Brewster's angle experience a large phase change, and the image can be visualized as being in approximate anti-phase with the source. It should also be observed that the reflection factor for a vertically polarized wave reflecting at Brewster's angle has a very small magnitude for most types of real ground encountered in practice.

The behaviour of the fields above a metal ground plane compared with the fields over an earthen ground plane is discussed at length in [40]. The brief discussion below, derived from [40], serves to provide an answer to the fourth question posed in 4.5.3.

#### 4.5.6.2 Vertically polarized fields over a perfect conductor

The contribution of the vertically polarized surface wave over real ground can be significant. However, it cannot increase the total field strength created by a small vertical electric dipole over real ground to equal the strength of the fields created by the same vertical dipole moment over a perfect conductor. Figure 44 displays the vertical components of the fields emitted at 30 MHz from a small vertical electric dipole situated 1 m above a “medium dry ground,” calculated using NEC and SOMNEC to include the surface wave, compared with the fields calculated over an almost perfect conductor (in this case annealed copper).

Comparisons of the fields over real ground with those over the good conductor show why vertically polarized measurements at 30 MHz on a measuring site with a metal ground plane are not comparable with measurements made on sites with earthen ground planes. Specifically, they show why measurements of vertically polarized disturbances made on a metal ground place for comparison with field strength disturbance limits developed for earth sites may penalize the equipment under test (EUT). The fields measured over a metal ground plane can exceed the limits, even when the fields from the same EUT over an earthen ground plane are comfortably below the limits. The comparisons also show why calculations of the vertically polarized fields created at 30 MHz over a perfect conductor or a metal ground plane, for a given dipole moment, are a bad guide to the predictability achievable for the fields created at elevated angles by that dipole moment over a real ground. If the fields over the good conductor are mistakenly believed to resemble those over a real ground, they will encourage a false sense of confidence that ground based measurements over real ground will give good guidance to the field strengths to be expected at elevated angles.

In Figure 45, the height scan patterns of the vertical components of the $E$-fields emitted from the small vertical dipole show that at 1 000 MHz, just as was the case at 30 MHz, the vertically polarized fields developed near a metal ground plane at 1 000 MHz are much stronger than those developed near a “medium dry ground.” The same conclusions which were reached at a frequency of 30 MHz regarding the possible penalties imposed on an EUT, when the disturbances measured on a metal ground plane site are compared with field strength disturbance limits developed for earth sites, also apply at a frequency of 1 000 MHz. Similarly, it can be seen in Figure 45 that at 1 000 MHz the patterns of the vertically polarized fields over a metal ground plane are a bad guide to the predictability of the fields created at elevated angles by the same dipole moment over a real ground.

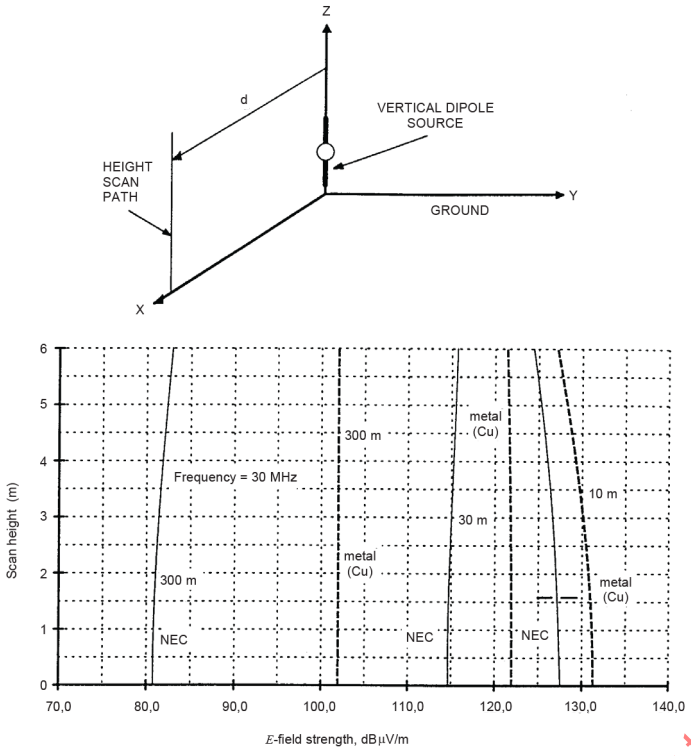
The height scan patterns in Figure 45 also clearly illustrate the effect of the phase reversal of the vertical dipole image in a lossy dielectric when reflection take place below Brewster's angle. The dashed horizontal line across the height scan pattern for 10 m distance shows the height to the field point, approximately 1,6 m, which corresponds with a reflection taking place at Brewster's angle when the source is 1 m above the “medium dry ground.”

In Figure 45 it is quite clear that at 10 m distance the field nulls and maxima at heights greater than 1,6 m above both the copper ground plane and the “medium dry ground” are in phase, signifying that the images in the two kinds of ground planes have similar phases when reflection from the real ground takes place at elevation angles above Brewster's angle. However, it is also quite clear that vertically polarized waves reflected below Brewster's angle over the “medium dry ground” are reversed in phase with respect to the corresponding reflected waves over the copper ground plane. In other words, the vertical image in the lossy dielectric is reversed, producing destructive interference (a null) at the surface of the “medium dry ground” whereas constructive interference (a maximum) occurs at the surface of the copper ground plane (the direct and reflected path lengths being the same in both cases). With the vertical dipole source at a height of 1 m, a maximum occurs in the field at 10 m distance at a height of 0,75 m above the “medium dry ground”, whereas a very deep null occurs at that height over the copper ground plane (the direct and reflected path lengths differ by $\lambda/2$ in both cases).

IECNORM.COM : Click to view the full PDF of CISPR TR 16-3:2020 RLV

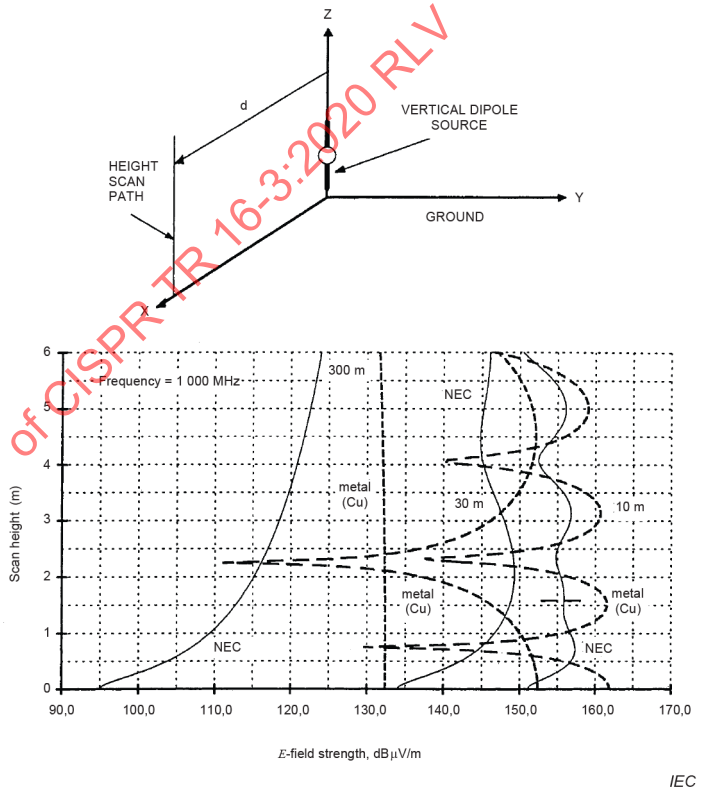
The height scans at 30 m and 300 m, up to a height of 6 m, take place below Brewster's angle. Maxima in the height-scanned fields over the metal ground plane therefore coincide with minima in the fields over real ground in both those height scans. This is largely the reason why it shall not be believed that the height scanned vertically polarized fields calculated over a good conductor will resemble those over real ground, especially at the larger horizontal distances. Such a belief will create false confidence that measurements made near real ground, without regard for the horizontal distance from the source, can give good guidance to the field strengths to be expected at elevated angles.

IECNORM.COM : Click to view the full PDF of CISPR TR 16-3:2020 RLV




NOTE NEC dipole length 0,2 m; dipole centre height 1 m; dipole moment 1 A·m; horizontal distance 10 m, 30 m and 300 m; 30 MHz; ground constants: real ground ("medium dry ground") $\varepsilon_r$ = 15, $\sigma$ = 1 mS/m, copper $\varepsilon_r$ = 1, $\sigma$ = 5,81 × $10^7$ S/m; Z-X plane (Adapted from [40]). Fields calculated in NEC (solid lines) include the surface wave over real ground. The dashed curves were calculated geometrically to include the direct and reflected space waves from an infinitesimal vertical electric dipole over a metal (copper) ground plane.

**Figure 44 – Height scan patterns of the vertical component of the *E*-fields emitted from a small vertical electric dipole**




NOTE NEC dipole length 0,02 m; dipole centre height 1 m; dipole moment 1 A·m; horizontal distance 10 m, 30 m and 300 m; 30 MHz; ground constants: real ground $\varepsilon_r$ = 15, $\sigma$ = 35 mS/m, copper $\varepsilon_r$ = 1, $\sigma$ = 5,81 × $10^7$ S/m; Z-X plane (Adapted from [40]). Fields calculated in NEC (solid lines) include the surface wave over real ground. The dashed curves were calculated geometrically to include the direct and reflected space waves from an infinitesimal vertical electric dipole over a metal (copper) ground plane.

**Figure 45 – Height scan patterns of the vertical component of the *E*-fields emitted from a small vertical electric dipole**

IECNORM.COM : Click to view the full PDF of CISPR TR 16-3:2020 RLV

#### 4.5.6.3 Horizontally polarized fields over a perfect conductor

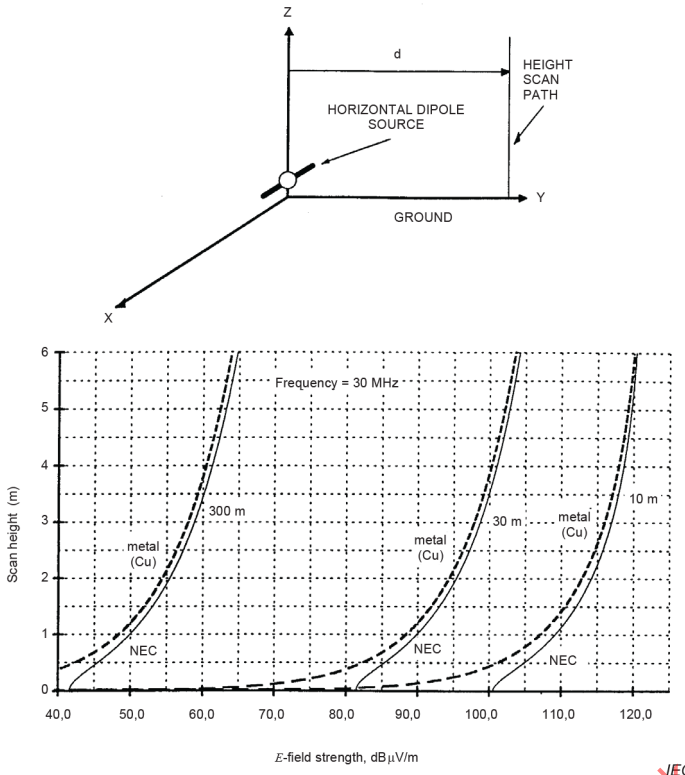
Although the contribution of the horizontally polarized surface wave over real ground at 30 MHz is small, nevertheless the height scan patterns in Figure 46 show that the horizontally polarized fields near the “medium dry ground” are stronger in this case than the corresponding fields near the copper ground plane.

In both cases a null is required in the vertical field pattern at the ground, to satisfy the boundary conditions, and the null is deeper in the copper ground plane example. This example shows, in contrast with vertically polarized measurements, that it is possible that measurements of horizontally polarized fields made on a metal ground plane for comparison with radiated disturbance limits developed for earth sites may slightly favour the EUT when measuring for compliance with the limits.

In Figure 47, the height scan patterns of the horizontally polarized $E$-fields emitted at 1 000 MHz from the small horizontal electric dipole show that at height scan distance of 30 m and more, with no useful contribution from the surface wave, the maximum horizontally polarized fields over a “medium dry ground” are very similar to those over a copper ground plane. The similarity of magnitude in regions of constructive interference is caused by the similar reflection factors (magnitudes close to unity) over both surfaces at low angles of reflection. At higher reflection angles, and a shorter measurement distance of 10 m, the maximum horizontally polarized fields over a metal ground plane exceed those over an earthen ground plane because the magnitude of the reflection factor over the earth plane becomes significantly less than unity. The reflected wave then contributes less to the constructive interference occurring at the field maxima.

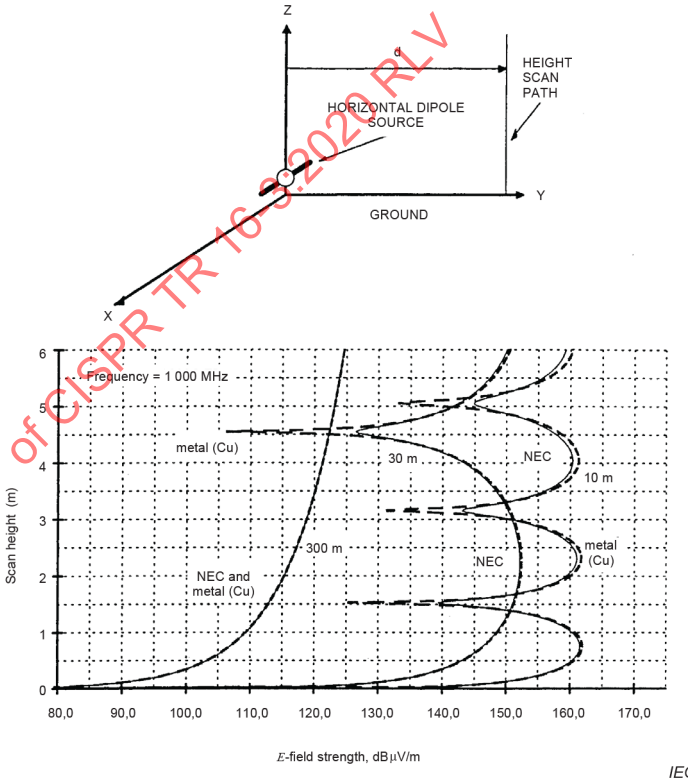
The behaviour of the horizontally polarized fields over an earthen ground plane is not complicated by a Brewster's angle phenomenon. In general, at frequencies of 30 MHz and above, the horizontally polarized field patterns over a real ground resemble the shapes of the corresponding patterns over a metal ground plane. Some small differences in field strengths are created over real ground compared with those over a metal ground plane at the lower frequencies by the presence of the surface wave over a real ground. Differences are also created at short horizontal distances, and higher frequencies at which the surface wave is insignificant, because the magnitude of the horizontal reflection factor decreases below unity as the waves reflect at higher angles from the earth plane.

IECNORM.COM : Click to view the full PDF of CISPR TR 16-3:2020 RLV




NOTE NEC dipole length 0,2 m; dipole height 1 m; dipole moment 1 A·m; horizontal distance 10 m, 30 m and 300 m; 30 MHz; ground constants: real ground ("medium dry ground") $\varepsilon_r$ = 15, $\sigma$ = 1 mS/m, copper $\varepsilon_r$ = 1, $\sigma$ = 5,81 × $10^7$ S/m; Z-X plane. Fields calculated in NEC (solid lines) include the surface wave over real ground. The dashed curves were calculated geometrically to include the direct and reflected space waves from an infinitesimal horizontal electric dipole over a metal (copper) ground plane. (Adapted from [40])

**Figure 46 – Height scan patterns of the horizontally polarized *E*-fields emitted in the vertical plane normal to the axis of a small horizontal electric dipole**




NOTE NEC dipole length 0,02 m; dipole height 1 m; dipole moment 1 A·m; horizontal distance 10 m, 30 m and 300 m; 1 000 MHz; ground constants: real ground ("medium dry ground") $\varepsilon_r$ = 15, $\sigma$ = 35 mS/m, copper $\varepsilon_r$ = 1, $\sigma$ = 5,81 × $10^7$ S/m; Z-X plane. Fields calculated in NEC (solid lines) include the surface wave over real ground. The dashed curves were calculated geometrically to include the direct and reflected space waves from an infinitesimal horizontal electric dipole over a metal (copper) ground plane. (Adapted from [40])

**Figure 47 – Height scan patterns of the horizontally polarized *E*-fields emitted in the vertical plane normal to the axis of a small horizontal electric dipole**

IECNORM.COM : Click to view the full PDF of CISPR TR 16-3:2020 RLV

#### 4.5.6.4 Fields over a perfect conductor as guides to the fields over real ground

We can now answer the fourth question raised in 4.5.3.

In summary, the horizontal polarized field patterns created over real ground at frequencies of 30 MHz and above resemble the corresponding patterns over a metal ground plane. There are some differences of a few decibels in field magnitudes. At the lower frequencies some small differences are also created by the existence of the surface wave over a real ground. At the higher frequencies, the field strength differences at short measuring distances are caused by the decrease below unity of the magnitude of the horizontal reflection factor for real ground when reflection takes place at angles significantly above grazing incidence. Constructive interference of direct and reflected waves over real ground then produces field strength maxima of somewhat smaller magnitudes than those produced over a good conductor which has a reflection factor close to unity at all reflection angles.

However, very large differences are found when comparing the patterns of vertically polarized fields over a metal ground plane with those over a real ground. The differences are primarily created by the existence of Brewster's angle for the reflections of vertically polarized waves from a lossy dielectric like real ground. When reflections from real ground take place below Brewster's angle the minima in the fields occur at the same heights at which the maxima are produced with the same measuring geometry over the metal ground plane, most notably at the surface of the ground plane. This contrapositioning of minima and maxima is the main reason why the height scanned vertically polarized fields calculated over a good conductor shall not be assumed to resemble those over real ground, especially at the larger horizontal distances when reflection takes place near grazing incidence. An assumption that there is a resemblance encourages false confidence that measurements near real ground, without regard for the horizontal distance from the source, can give good guidance to the field strengths to be expected at elevated angles.

Vertically polarized field patterns over a metal ground plane do not resemble the shapes and magnitudes of the vertically polarized field patterns to be expected from the same sources over a real ground.

### 4.5.7 Uncertainty ranges

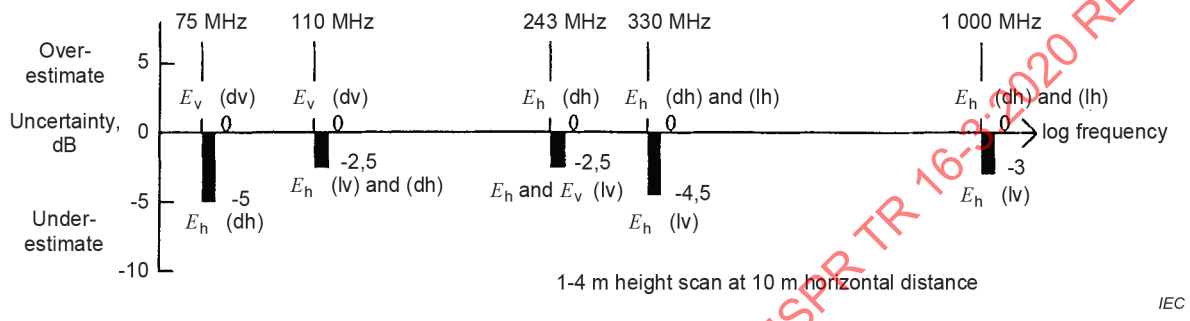
The information summarized in Table 14 to Table 18 can also be used to show pictorially the ranges of uncertainties in the predictability of the radiation emitted at elevated angles at frequencies above 30 MHz. The information has been used to construct bar charts illustrating the uncertainties for electrically small sources located 1 m or 2 m above ground when predictions of the field strengths at elevated angles are based on $E$-field measurements in 1 m to 4 m height scans at horizontal distances of 10 m, 30 m and 300 m.

Figure 48 illustrates the uncertainties in predictability based on measurements made at a horizontal distance of 10 m. The bar for the uncertainty range at 330 MHz shows that the best predictability at 330 MHz is obtained when the source behaves as either a small horizontal dipole (dh) or as a small horizontal loop (lh). There is nominally zero error predicting the maximum strength of the horizontally polarized $E_{\mathrm{h}}$ fields. The poorest predictability at 330 MHz results in an underestimate of approximately 4,5 dB for the maximum horizontally polarized field $E_{\mathrm{h}}$ emitted at elevated angles from a small vertical loop (lv).

When measurements are made in a height scan at a horizontal distance of 30 m, the bar for the uncertainty range at 110 MHz in Figure 49 shows that the best predictability at 110 MHz occurs when the source behaves as a small vertical dipole (dv). There is a negligible underestimate, by 0,5 dB, predicting the $E_z$ vertical component of the vertically polarized field. The poorest predictability at 110 MHz produces a greater underestimate, by 9,5 dB, of the horizontally polarized $E_{\mathrm{h}}$ field emitted at elevated angles from a small horizontal dipole source (dh).

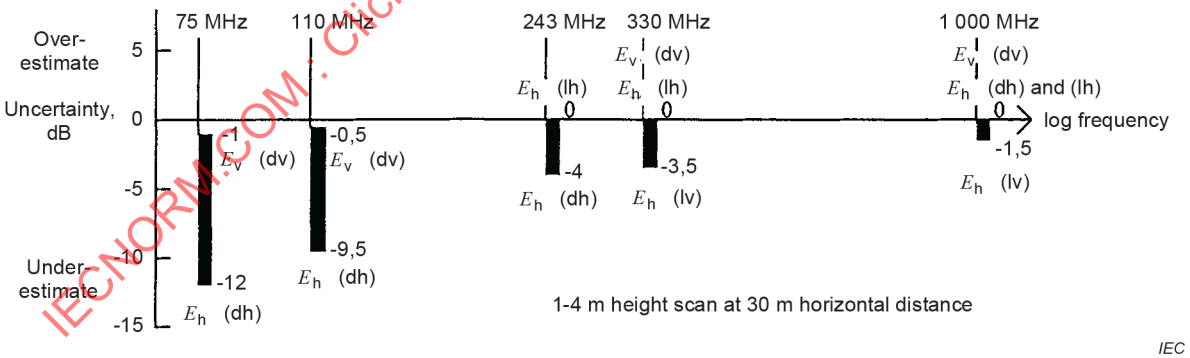
IECNORM.COM : Click to view the full PDF of CISPR TR 16-3:2020 RLV

Figure 50 graphically illustrates the very large uncertainties in predictability that occur if the horizontal measuring distance is as great as 300 m. At 243 MHz, the bar illustrating the uncertainty range shows that the poorest predictability at 243 MHz introduces a very large underestimate by 22,5 dB for the horizontally polarized $E_h$ fields emitted at elevated angles from a small horizontal dipole (dh) and from a small horizontal loop (lh). The best predictability at 243 MHz also produces a large underestimate, by 13 dB, of the vertical $E_z$ component of the vertically polarized field emitted at elevated angles from a small vertical dipole (dv). Figure 49 and Figure 50, in particular, graphically illustrate the very large underestimates which can occur when attempts are made to predict the strength of radiation in vertical directions based on measurements near the ground at unknown horizontal distances greater than 10 m from the sources.




NOTE The predictability is based on measurements of the horizontally and vertically polarized $E$-fields in a height scan from 1 m to 4 m at a horizontal distance of 10 m from the sources. The following example shows how the bar chart can be interpreted. At 243 MHz, the bar shows that the best predictability, with nominally zero error, is obtained when estimating the maximum strength of the horizontally polarized $E_h$ field emitted at elevated angles from a source behaving as a small horizontal dipole (dh). The poorest predictability at 243 MHz, an underestimate by as much as 2,5 dB, can occur when predicting the maximum strengths of the horizontally polarized $E_h$ fields and the $E_z$ vertical component of the vertically polarized fields emitted at elevated angles from a source behaving as a small vertical loop (lv). (Reproduced from [39])

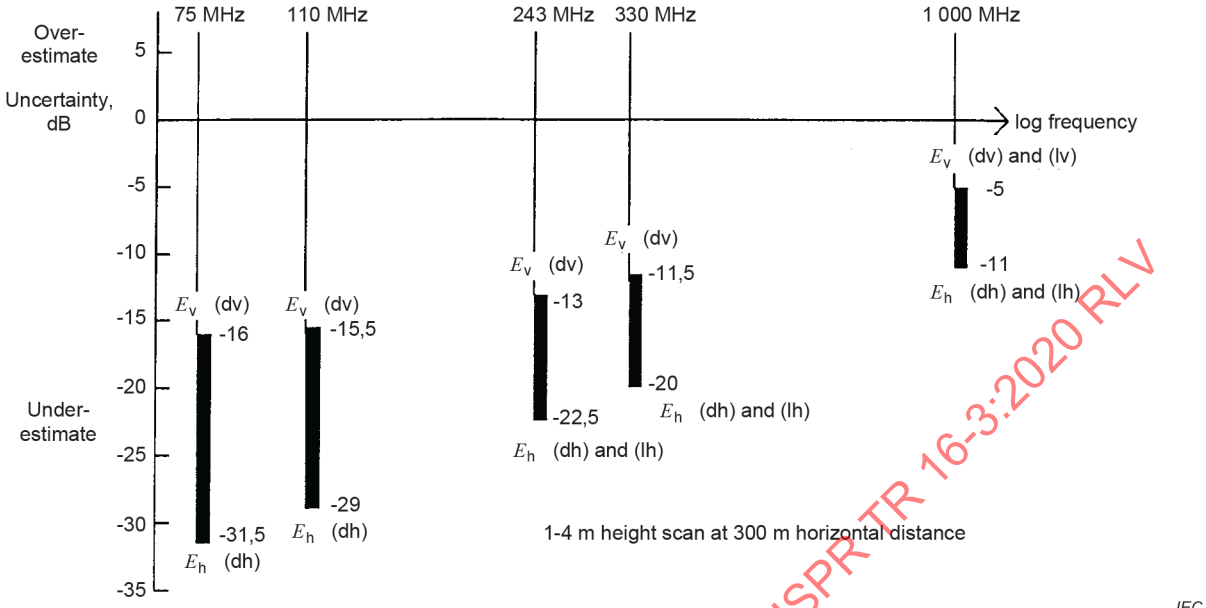
**Figure 48 – Ranges of uncertainties in the predictability of radiation in vertical directions from electrically small sources located at a height of 1 m or 2 m above ground**




NOTE The predictability is based on measurements of the horizontally and vertically polarized $E$-fields in a height scan from 1 m to 4 m at a horizontal distance of 30 m from the sources. The following example shows how the bar chart can be interpreted. At 330 MHz, the bar shows that the best predictability, with nominally zero error, is obtained when estimating the maximum strength of either the horizontally polarized $E_h$ field emitted at elevated angles from a small horizontal loop (lh) or the $E_z$ vertical component of the vertically polarized field emitted at elevated angles from a small vertical dipole (dv). But at 330 MHz the height scan measurements can provide an underestimate by as much as 3,5 dB when predicting the strength of the horizontally polarized $E_h$ field, which is the maximum field emitted at elevated angles from a source behaving as a small vertical loop (lv) (Reproduced from [39])

**Figure 49 – Ranges of uncertainties in the predictability of radiation in vertical directions from electrically small sources located at a height of 1 m or 2 m above ground**

IECNORM.COM : Click to view the full PDF of CISPR TR 16-3:2020 RLV




NOTE The predictability is based on measurements of the horizontally and vertically polarized $E$-fields in a height scan from 1 m to 4 m at a horizontal distance of 300 m from the sources. The following example shows how the bar chart can be interpreted. The bar at 1 000 MHz shows that the best predictability at that frequency, which is an underestimate by as much as 5 dB, will be obtained when predicting the maximum strength of the $E_z$ vertical component of the vertically polarized field emitted at elevated angles from a source behaving as a small vertical loop (lv) or a small vertical dipole (dv). However, an underestimate by as much as 11 dB can occur at 1 000 MHz when predicting the maximum strength of the horizontally polarized $E_h$ field emitted at elevated angles from a source behaving as a small horizontal loop (lh) or a small horizontal dipole (dh). (Reproduced from [39])

**Figure 50 – Ranges of uncertainties in the predictability of radiation in vertical directions from electrically small sources located at a height of 1 m or 2 m above ground**

### 4.5.8 Conclusions

The *in situ* measurement procedures at frequencies above 30 MHz which are specified in CISPR 11 can lead to significant underestimates of the field strengths emitted at elevated angles from ISM equipment. The underestimates can arise due to the ill-defined measurement distance; the measuring distance from the radiating ISM equipment is not defined.

The largest underestimates of the fields at elevated angles will generally occur for horizontally polarized fields. This is a cause for concern, because the aeronautical safety of life services requiring greatest protection from disturbances originating at the ground are those provided by the horizontally polarized marker beacon, localizer, and glide path signals of the aeronautical ILS.

Under some conditions, measurements are specified in CISPR 11 at a fixed height of 2,0 m. Measurements at a fixed height should not be specified if they are being made to determine protection for specific safety services. There is a risk that fixed height measurements will be made in, or close to, a null. The risk increases at the higher frequencies and when the height to the radiation centre of the source is unknown. Fixed height measurements can seriously underestimate the true field strength near the ground and, in consequence, the maximum field strength at elevated angles.

IECNORM.COM : Click to view the full PDF of CISPR TR 16-3:2020 RLV

Calculations or measurements of the field strength patterns of vertically polarized fields over a perfect conductor or metal ground plane do not provide good guidance to the fields to be expected over a real ground. At reflection angles below Brewster's angle over real ground the field minima and maxima are contraposed with those created by the same source over a metal ground plane.

To provide protection for aeronautical safety of life services, and other communication systems, height scan measurements and limits for radiated disturbances from *in situ* ISM equipment located near the ground shall be *specified at a known horizontal distance from the equipment*. Height scan measurements at a horizontal distance of 10 m from an ISM equipment *in situ* allow accurate estimates to be made of the fields emitted at elevated angles. If for practical reasons the *in situ* measurements shall be made at a distance greater than 10 m from the equipment which is the source of the radiation then the limits at the larger distance, particularly if it is more than 30 m, shall be derived from the 10 m limits by adjusting them in inverse proportion with increasing distance squared. This shall be so in order to prevent relaxation of the protection when limits are intended to provide for communication or radionavigation systems that are operated high above ground.

### 4.6 The predictability of radiation in vertical directions at frequencies up to 30 MHz

#### 4.6.1 Range of application

This subclause considers the vertical radiation patterns of the magnetic ($H$) fields and electric ($E$) fields emitted at frequencies up to 30 MHz from electrically small sources located close to the surface of real homogeneous plane ground, for the purpose of studying the predictability of radiation in vertical directions based on measurements of the strength of the $H$-field near the ground.

The vertical radiation patterns of the fields have been calculated at a distance of 30 m from various electrically small sources, and then the patterns of the fields at greater distances have been calculated so that the field variations with distance can be quantified. In this way, a general knowledge has been obtained of the shapes of the vertical radiation patterns, showing the magnitudes of the field strengths near ground compared with the magnitudes of the field components at elevated angles, and the ways in which the relative magnitudes can be expected to vary with distance over a plane ground.

The sources considered are electrically small balanced electric and magnetic dipoles excited in the frequency range 100 kHz to 30 MHz. For the purposes of the subclause, an electrically small source is defined as one whose largest linear dimension is one-tenth or less of the free space wavelength at the frequency of interest.

This subclause also considers the effects on the vertical radiation patterns of locating the electrically small sources close to real grounds having several different values of electrical conductivity and dielectric constants [43], [44], and includes the special case of a ground that behaves as a perfect conductor.

The possible effects on the vertical radiation patterns produced by walls, buildings, reinforced concrete structures, and the like, in the vicinity of the sources, and the effects on wave propagation near the ground that could be produced by changes with distance of the electrical constants of the ground, caused by intervening roads, watercourses, buried metallic pipes, and so on, are not within the scope of this subclause. It is important to note, therefore, that the errors in predictability that may be produced by such effects have not been considered.

IECNORM.COM : Click to view the full PDF of CISPR TR 16-3:2020 RLV

### 4.6.2 General

CISPR 11 sets limits for the electromagnetic disturbances emitted near the ground from industrial, scientific and medical (ISM) radio-frequency equipment. The limits are intended to provide protection of the reception of radio services. At frequencies below 30 MHz the limits apply to the horizontally oriented components of the $H$-fields emitted by the ISM apparatus. For measurements on a test site, the limits apply at a distance of 30 m from the source. When measurements are made *in situ* the distance to the measurement point is defined as 30 m from the exterior wall outside the building in which the ISM equipment is situated; the distance from the source is not defined. Measurements are to be made with a vertically oriented loop, the base of which shall be 1 m above the ground.

It is acknowledged in CISPR 11 that many aeronautical communications require the limitation of vertically radiated electromagnetic disturbances, and that work is necessary to determine what provisions may be required to provide protection of such systems.

The aeronautical radio services to be protected may be either horizontally or vertically polarized transmissions. Thus, the field components at elevated angles, emitted from potential interference sources located near the ground, that are of interest in a study of field strength predictability include the vertically and horizontally oriented $H$- and $E$-field components.

In this subclause the judgements of predictability of radiation in vertical directions are based on the accuracy with which ground-based measurements of the horizontally oriented $H$-fields emitted from a variety of sources will indicate the maximum strengths of the horizontally or vertically oriented $H$-fields at elevated angles.

As might be expected, at a distance of 30 m from an electrically small source there are significant changes in the field behaviour with changing wavelength as the frequency is varied from 100 kHz to 30 MHz. The subclause, therefore, concentrates attention at four frequencies, namely 100 kHz, 1 MHz, 10 MHz and 30 MHz. At 100 kHz the distance of 30 m lies well within the electrostatic or inductive near-field region close to the source. At 1 MHz the distance of 30 m is within $\lambda/10$ of an electrically small source, and places the measurement position in what might be called the radiating near-field region. At 10 MHz, a distance of 30 m represents approximately one wavelength from the source, a region where the far field has become established. At 30 MHz, a distance of 30 m represents approximately three wavelengths from the source and places the measurement position well into the far field.

In addition to the variations in field behaviour produced by changes from near-field to far-field conditions as the wavelength is varied, in the frequency range 100 kHz to 30 MHz the electrical behaviour of real ground varies. In general, real ground has the characteristics of a lossy conductor at low frequencies, and the characteristics of a lossy dielectric at the higher frequencies. Moreover, the values of the electrical constants of real ground can vary widely; they may range typically from a conductivity of $10^{-4}$ S/m and relative permittivity of 3 to a conductivity of $10^{-2}$ S/m and relative permittivity of 30 [43], [44]. Even this wide range of values of the ground constants does not encompass all of the values that may be encountered in some localities.

The subclause shows the limitations of the predictability of radiation in vertical directions. In particular, it identifies the critical importance of a knowledge of the precise measurement distance – the actual distance between the source and the field measuring point near the ground – if it is to be possible to make predictions of the radiated field strengths at elevated angles with a known margin of error.

IECNORM.COM : Click to view the full PDF of CISPR TR 16-3:2020 RLV

Subclause 4.6 indicates the ranges of magnitude of the significant errors in predictability that can still occur when the precise measurement distance over real ground is 30 m from the sources, and the large errors that can arise from the approximation that the influence of real ground can be determined by assuming it behaves like a perfect conductor. It also shows how magnitudes of the errors in predictability above real ground may be reduced, although they remain significant, by supplementing measurements of horizontally oriented $H$-fields near ground with height scan measurements of vertically oriented $H$-fields at heights up to 6 m, when the measurements are made at a distance of 30 m from the sources.

### 4.6.3 Method of calculation of the vertical radiation patterns

The $H$- and $E$-field vertical radiation patterns in this subclause were calculated using a Method of Moments computer code known as the Numerical Electromagnetics Code (NEC) [35]. A double precision version, NEC2D, with the companion code SOMNEC2D, was used. NEC with SOMNEC allows the Sommerfeld integral evaluation of the field interactions at the air-ground interface [36] to be included in the determination of the $E$-fields above real grounds.

In the version of the NEC codes that were first released for public use, a section of code for calculation of the near $H$-field in the presence of real ground was omitted, which can lead to large errors in the $H$-field calculations [45], [46]. In the version of NEC2D used to calculate the radiation patterns in this subclause the missing code has been restored, allowing calculation of all the $H$-field components close to the surface of a real ground. The restored section of code calculates the $H$-field components by using a six-point finite-difference approximation of the curl of the $E$-field obtained by the Sommerfeld method.

The spatial sampling interval used in the finite-difference calculation of $H$-field in NEC is normally fixed at $10^{-3}\ \lambda$. For the $H$-field radiation patterns calculated at the frequencies of 100 kHz and 1 MHz the spatial sampling interval has to be altered to $10^{-5}\ \lambda$ and $10^{-4}\ \lambda$, respectively, in order to obtain accurate calculations of the near $H$-field [46], [47].

Some remaining problems of numerical stability, arising from the finite-difference approximation of the $H$-fields from $E$-fields, which in some cases have components whose curl is mathematically zero but which have become numerically non-zero due to small numerical inaccuracies [48], have required smoothing of some of the calculated $H$-field radiation patterns.

### 4.6.4 The source models

The electrically small sources that form the basis of this subclause consist of small vertical and horizontal balanced electric dipoles, and vertical and horizontal balanced magnetic dipoles (horizontally and vertically oriented loops respectively), each having a unit dipole moment [i.e. a dipole (current) moment of 1 A·m for the electric dipoles and a dipole moment of 1 A·m$^2$ for the magnetic dipoles]. All were located very close electrically to the air-ground interface (within a small fraction of a wavelength); the height above ground of the base of each dipole was varied between either 7 cm or 15 cm and a maximum of 1 m to determine the sensitivity of the shape of the field-strength patterns to changes in the source height. The patterns considered in this subclause are those that exhibited the greatest variation in shape with height.

The geometries of the models used for the field-pattern computations are shown in Figure 51 to Figure 52, including the paths of the radial scans about each source; advantage has been taken of the verified azimuthal symmetry of the fields around the vertical magnetic and vertical electric dipoles to confine attention to the radial scans around those sources in only the Z-X plane.

IECNORM.COM : Click to view the full PDF of CISPR TR 16-3:2020 RLV

It is seen in Figure 53 and Figure 54 that two generators drive each loop. Although the loops used in the models were electrically small, it was found that when driven by one generator only, each displayed sufficient current asymmetry to produce a significant electric dipole contribution to the electromagnetic fields – because of their finite size the small loops did not behave as electrically infinitesimal magnetic dipole sources. In the models used here, therefore, each loop was driven by two identical aiding generators located as shown, and the electric dipole contribution produced by current asymmetry arising from the use of a single generator was reduced to insignificance. Of course, in the case of the horizontal magnetic dipole (vertical loop), there is always a loop current asymmetry (and a resultant electric dipole moment) caused by proximity to the ground and this effect also occurs in the models used in this subclause.

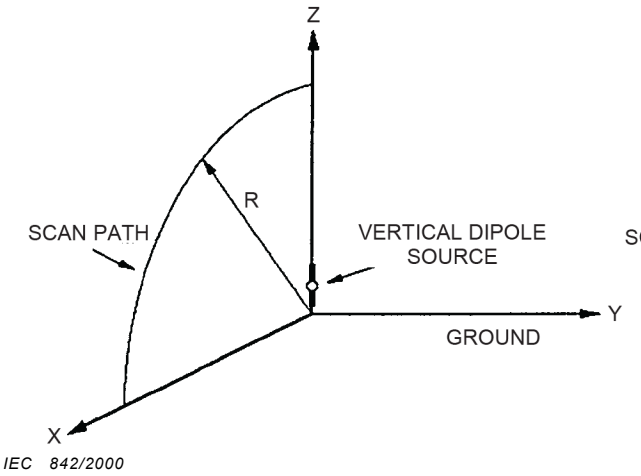



**Figure 51 – Geometry of the small vertical electric dipole model**

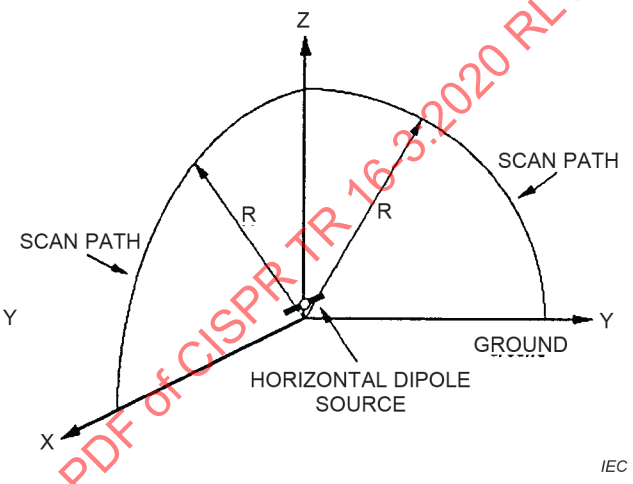



**Figure 52 – Geometry of the small horizontal electrical dipole model**

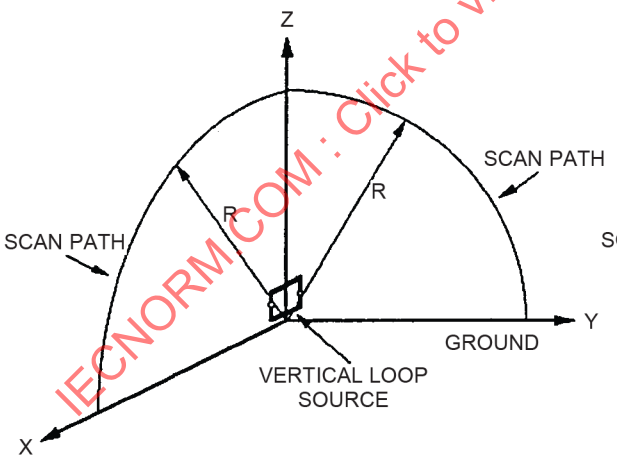



**Figure 53 – Geometry of the small horizontal magnetic dipole model (small vertical loop)**

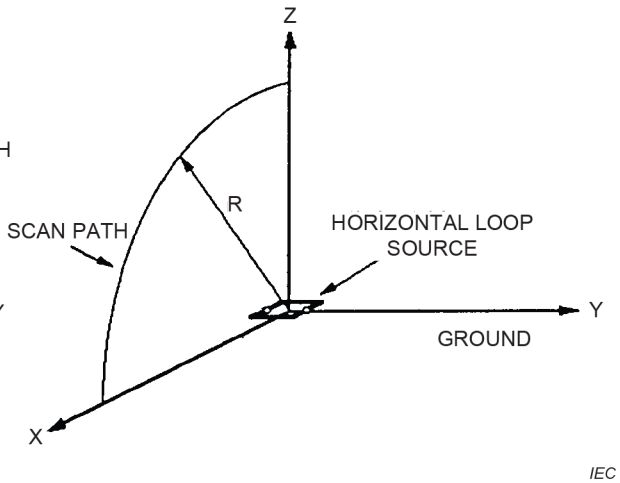



**Figure 54 – Geometry of the small vertical magnetic dipole model (small horizontal loop)**

IECNORM.COM : Click to view the full PDF of CISPR TR 16-3:2020 RLV

#### 4.6.5 Electrical constants of the ground

Most attention in this subclause has been devoted to radiation sources located close to a ground having a conductivity, $\sigma$ = $10^{-3}$ S/m and a relative dielectric constant, $\varepsilon_r$ of 15; these electrical constants are in the CCIR category of a medium dry ground [43], [44].

At the upper and lower extremes of the frequency range, i.e. 30 MHz and 100 kHz, examples of two other sets of values of ground constants were used with the small horizontal electric dipole model to illustrate the influence of differing values of the ground constants on the vertical radiation patterns. The electrical constants mentioned in 4.6.2, with the numerical values of $\sigma$ = $10^{-2}$ S/m and $\varepsilon_r$ = 30 (ITU-R – cultivated land and fresh water marshes) and $\sigma$ = $10^{-4}$ S/m and $\varepsilon_r$ = 3 (ITU-R – very dry ground and granite mountains in cold regions), were chosen as the examples [43], [44].

For each type of source, the field patterns above a perfectly conducting ground were also been compared with the patterns generated above real grounds, to identify the errors that can arise from the approximation which is sometimes made so that the influence of real ground can be determined by assuming it behaves as a perfect conductor.

In general, it is necessary to recall that specific boundary conditions apply to the fields at the surface of a perfect conductor that do not necessarily apply at the surface of a real ground. In particular, the $H$-field component normal to the surface of a perfect conductor shall go to zero at the surface, as shall the tangential $E$-field component at the surface, and it will be recalled that this is why a horizontally polarized surface wave cannot exist at the surface of a perfect conductor. Further, a vertically polarized surface wave travelling on a perfectly conducting ground plane experiences no ohmic loss – it merely attenuates with distance at the free space rate. Those boundary conditions, however, certainly do not apply at the surface of a real ground; thus the boundary conditions identify the most general set of differences between the vertical radiation patterns that will exist close to the surface of a real ground when compared with those calculated close to the surface of a perfectly conducting ground.

#### 4.6.6 Predictability of radiation in vertical directions

##### 4.6.6.1 Tabular summaries of predictability

The vertical radiation patterns on which the judgements of predictability are based are presented in Figure 55 to Figure 112 (see 4.6.8), which are polar patterns showing field strength plotted against elevation angle above the ground. To summarize the information presented in those figures, the summary information of Table 19 through Table 22 were prepared, one for each frequency considered in this subclause.

IECNORM.COM : Click to view the full PDF of CISPR TR 16-3:2020 RLV

**Table 19 – Predictability of radiation in vertical directions at 100 kHz, using ground-based measurements of horizontally oriented *H*-field at distances up to 3 km from the source (figures are located in 4.6.8)**

| Type of source | Predictability based on measurements near real ground at 30 m distance from the source | Predictability based on *in situ* measurements near real ground when the measurement distance from the source is not precisely known | Predictability based on vertical radiation patterns calculated at a known distance from the source, assuming the ground behaves as a perfect conductor |
|---|---|---|---|
| Electrically small vertical electric dipole | Excellent (see Figure 57, Figure 59) | Excellent (see Figure 57 to Figure 60) | Excellent (see Figure 57) |
| Electrically small horizontal electric dipole | Excellent (see Figure 61 to Figure 63) Notes 1, 2 | Very good (see Figure 49, Figure 63 to Figure 65) | Poor (see Figure 61) Note 3 |
| Electrically small horizontal magnetic dipole (vertical loop) | Excellent (see Figure 66, Figure 68) Note 4 | Very good (see Figure 66, Figure 68 to Figure 70) | Very good (see Figure 66, Figure 67) Note 5 |
| Electrically small vertical magnetic dipole (horizontal loop) | Poor (see Figure 71, Figure 81) Note 6 | Impossible (see Figure 71, Figure 73 to Figure 76) Note 7 | Impossible (see Figure 71, Figure 72) Note 8 |

NOTE 1 The measurement of the horizontally oriented $H$-field emitted by the small horizontal electric dipole near the ground can overestimate the maximum vertically oriented $H$-field strength emitted at an elevated angle by approximately 1 dB (see Figure 61). Note, however, that the measurement overestimates the strength of the horizontally oriented $H$-field emitted in the vertical direction by 5 dB.

NOTE 2 The small influence exerted on the small horizontal electric dipole vertical radiation patterns at 100 kHz by a wide range of the electrical constants of the ground is shown in Figure 62.

NOTE 3 The horizontal electric dipole's $H$-field pattern calculated assuming a perfectly conducting ground shows that such an assumption causes an underestimate of more than 20 dB in the absolute field strength, and falsely indicates that the ground-based measurement underestimates the maximum field strength by 6 dB (refer to NOTE 1) (see Figure 61).

NOTE 4 The measurement of horizontally oriented $H$-field emitted by the small horizontal magnetic dipole (vertical loop) near the ground can overestimate the maximum vertically oriented $H$-field strength at elevated angles by less than 1 dB (see Figure 66). Note, however, that the measurement overestimates the strength of the horizontally oriented $H$-field emitted in the vertical direction by more than 3 dB.

NOTE 5 Vertical patterns of the horizontally oriented $H$-fields emitted by the small horizontal magnetic dipole (vertical loop), calculated assuming a perfectly conducting ground, can overestimate absolute values of field strength over real ground by 6 dB, but the shapes of the patterns are a good guide to those over real ground. However, boundary conditions are such that the vertically oriented $H$-field goes to zero at the surface of the perfectly conducting ground which is not the case at the surface of a real ground. See Figure 66 and Figure 67.

NOTE 6 The measurement of horizontally oriented $H$-field emitted by the small vertical magnetic dipole (horizontal loop) near the ground at a distance of 30 m underestimates the $H$-field strengths at elevated angles by more than 16 dB (see Figure 71). However, measurement of the vertically oriented $H$-field, in Hz, near the ground improves predictability; it provides an underestimate of the vertically oriented $H$-field emitted in the vertical direction by approximately 6 dB, and an underestimate of the maximum horizontally oriented $H$-field emitted at elevated angles by about 3 dB.

NOTE 7 The relative magnitudes of the $H$-field components near the ground and at elevated angles are strongly dependent on the actual distance from the small horizontal loop. See Figure 71, Figure 73 and Figure 74.

NOTE 8 The small horizontal loop field patterns calculated close to the ground assuming a perfectly conducting ground have no resemblance, in shape and absolute magnitude, to the field patterns calculated close to a real ground. See Figure 71 and Figure 72.

IECNORM.COM : Click to view the full PDF of CISPR TR 16-3:2020 RLV

**Table 20 – Predictability of radiation in vertical directions at 1 MHz, using ground-based measurements of horizontally oriented *H*-field at distances up to 300 m from the source (figures are located in 4.6.8)**

| Type of source | Predictability based on measurements near real ground at 30 m distance from the source | Predictability based on *in situ* measurements near real ground when the measurement distance from the source is not precisely known | Predictability based on vertical radiation patterns calculated at a known distance from the source, assuming the ground behaves as a perfect conductor |
|---|---|---|---|
| Electrically small vertical electric dipole | Excellent (see Figure 77, Figure 78) | Excellent (see Figure 77 to Figure 79) | Excellent (see Figure 77) |
| Electrically small horizontal electric dipole | Very good (see Figure 80, Figure 82) Note 1 | Good (see Figure 80 to Figure 83) | Poor (see Figure 80) Note 2 |
| Electrically small horizontal magnetic dipole (vertical loop) | Excellent (see Figure 82, Figure 87) Note 3 | Good (see Figure 82, Figure 86 to Figure 88) | Fair (see Figure 84, Figure 85) Note 4 |
| Electrically small vertical magnetic dipole (horizontal loop) | Excellent (see Figure 89, Figure 92) Note 5 | Impossible (see Figure 89, Figure 91 to Figure 92) Note 6 | Poor (see Figure 90) Note 7 |

NOTE 1 The measurement of the horizontally oriented $H$-field emitted by the horizontal electric dipole near the ground can overestimate the maximum vertically oriented $H$-field strength emitted at elevated angles by approximately 3 dB (see Figure 80). Note, however, that the measurement can overestimate the strength of the horizontally oriented $H$-field emitted in the vertical direction by more than 9 dB.

NOTE 2 The $H$-field patterns calculated at a distance of 30 m from the horizontal electric dipole assuming a perfectly conducting ground show that such an assumption causes an underestimate of 20 dB in the absolute field strength at 1 MHz, and falsely indicates that the ground-based measurement underestimates the maximum field strength emitted in vertical directions by 5 dB. See Figure 80.

NOTE 3 The measurement of the horizontally oriented $H$-field emitted by the small vertical loop near the ground can overestimate the maximum field strength emitted at elevated angles by less than 3 dB (see Figure 84).

NOTE 4 The patterns of horizontally oriented $H$-field calculated at 30 m from the small vertical loop assuming perfectly conducting ground are very similar to the $H$-field patterns over a real ground. See Figure 84 and Figure 85.

NOTE 5 The measurement of the horizontally oriented $H$-field emitted by the small horizontal loop near the ground at 30 m distance can underestimate the maximum vertically oriented $H$-field strength emitted in the vertical direction by more than 2 dB, and the maximum horizontally oriented $H$-field emitted at elevated angles by less than 1 dB (see Figure 89). A measurement of the vertically oriented $H$-field, Hz, near ground reduces the underestimate of the strength of the vertically oriented $H$-field emitted in the vertical direction to about 1 dB, and overestimates the maximum horizontally oriented $H$-field strength by more than 1 dB.

NOTE 6 The relative magnitudes of the $H$-field components near the ground and at elevated angles are strongly dependent on the actual distance from the horizontal loop source. The horizontally oriented $H$-field near the ground is a radially directed component which attenuates more rapidly with increasing distance than does the horizontally oriented $H$-field at elevated angles. The vertically oriented $H$-field near the ground is a component of the horizontally polarized ground wave launched by the horizontal loop and attenuates very rapidly with increasing distance from the source at 1 MHz. See Figure 89 and Figure 91.

NOTE 7 At 1 MHz, the vertical radiation pattern of the horizontally oriented $H$-field emitted by the small horizontal loop above a perfectly conducting ground has an absolute value more than 15 dB less than the field strength calculated above a real ground. The shape of the vertical pattern of the vertically oriented $H$-field calculated close to a perfectly conducting ground bears no resemblance to the vertical pattern calculated close to the real ground. Compare Figure 89 and Figure 90. In general, the boundary condition which requires the vertically oriented $H$-field strength to be zero at the surface of a perfectly conducting ground means that the pattern of vertically oriented $H$-field at the real ground, which is non-zero, does not resemble the corresponding pattern at the perfect ground.

IECNORM.COM : Click to view the full PDF of CISPR TR 16-3:2020 RLV

**Table 21 – Predictability of radiation in vertical directions at 10 MHz, using ground-based measurements of horizontally oriented *H*-field at distances up to 300 m from the source (figures are located in 4.6.8)** *(1 of 2)*

| Type of source | Predictability based on measurements near real ground at 30 m distance from the source | Predictability based on *in situ* measurements near real ground when the measurement distance from the source is not precisely known | Predictability based on vertical radiation patterns calculated at a known distance from the source, assuming the ground behaves as a perfect conductor |
|---|---|---|---|
| Electrically small vertical electric dipole | Excellent (see Figure 93, Figure 94) | Excellent (see Figure 93 to Figure 95) Note 1 | Impossible (see Figure 93) Note 2 |
| Electrically small horizontal electric dipole | Poor (see Figure 96, Figure 97) Note 3 | Good (see Figure 96 to Figure 98) Note 4 | Impossible (see Figure 96) Note 5 |
| Electrically small horizontal magnetic dipole (vertical loop) | Very good (see Figure 99, Figure 100) Note 6 | Impossible (see Figure 99, Figure 100) Note 7 | Impossible (see Figure 99) Note 8 |
| Electrically small vertical magnetic dipole (horizontal loop) | Poor (see Figure 101, Figure 102) Note 9 | Impossible (see Figure 101, Figure 102) Note 10 | Fair (see Figure 101) Note 11 |

NOTE 1 The horizontally oriented $H$-field near the ground is a component of the vertically polarized ground wave emitted from the vertical electric dipole. At 10 MHz the vertically polarized wave near the ground attenuates rapidly with increasing distance, such that there is an excess 8 dB ground-wave attenuation in addition to the 20 dB sky-wave attenuation over the distance from 30 m to 300 m. See Figure 93.

NOTE 2 At a distance of 30 m from the vertical electric dipole over a perfectly conducting ground the vertical radiation pattern of the horizontally oriented $H$-field is within about 3 dB of the pattern of the $H$-field over a real ground. However, the vertically polarized wave near a perfectly conducting ground attenuates with increasing distance at the free space rate and therefore does not attenuate with distance in the way it does over a real ground at 10 MHz (see NOTE 11). It is thus misleading as a guide to the vertical radiation patterns over real ground at distances much beyond 30 m.

NOTE 3 The measurement of the horizontally oriented $H$-field near the real ground at 30 m from the small horizontal electric dipole can underestimate the field strength of the horizontally oriented $H$-field emitted in the vertical direction by approximately 8 dB, and the vertically oriented $H$-field strength emitted at elevated angles by about 3 dB. Measurements of vertically oriented Hz near ground cannot improve the predictability in this case. See Figure 96.

NOTE 4 At 10 MHz, the horizontally oriented $H$-field components near real ground attenuate more rapidly with increasing distance from the horizontal electric dipole than do the sky-wave components. The excess attenuation is approximately 7 dB over the distance from 30 m to 300 m. See Figure 96.

NOTE 5 The horizontally oriented $H$-field near a perfectly conducting ground attenuates by 40 dB as the distance from the small horizontal electric dipole increases from 30 m to 300 m, an excess attenuation of 20 dB more than the sky-wave attenuation over the same distance. Near a real ground the excess attenuation is about 7 dB over the same distance at 10 MHz. The vertical radiation patterns over real and perfectly conducting grounds therefore differ significantly in that range of measuring distances. See Figure 96.

NOTE 6 The measurement of the horizontally oriented $H$-field near the real ground at 30 m distance from the small vertical loop can underestimate the horizontally oriented $H$-field strength emitted in the vertical direction by less than 3 dB, but it overestimates the strength of the vertically oriented $H$-field emitted at elevated angles by approximately 3 dB. See Figure 99.

NOTE 7 The horizontally oriented $H$-field components near real ground attenuate much more rapidly with increasing distance from the small vertical loop than do the sky-wave components, at 10 MHz. The excess attenuation is approximately 8 dB over the distance from 30 m to 300 m. See Figure 99.

NOTE 8 At a distance of 30 m from the small vertical loop over a perfectly conducting ground the vertical radiation pattern of the horizontally oriented $H$-field is within about 4 dB of the pattern of the $H$-field over a real ground. However, the vertically polarized wave near a perfectly conducting ground attenuates with increasing distance at the free space rate, unlike a vertically polarized wave over a real ground which attenuates more rapidly with distance at 10 MHz – see NOTE 11 and Figure 99 and Figure 100. Vertical radiation patterns calculated over a perfectly conducting ground can therefore be very misleading as guidance to the patterns to be expected over real ground at distances much beyond 30 m at 10 MHz.

IECNORM.COM : Click to view the full PDF of CISPR TR 16-3:2020 RLV

**Table 21** *(2 of 2)*

NOTE 9 The measurement of the horizontally oriented $H$-field components near the real ground at 30 m distance from the small horizontal loop can underestimate the maximum horizontally and vertically oriented $H$-field strengths at elevated angles by more than 6 dB. Note, however, that a measurement of the vertically oriented $H$-field, Hz, at a height of 6 m underestimates the maximum $H$-field, the vertically oriented $H$-field, at elevated angles by approximately 5 dB at 10 MHz. See Figure 101.

NOTE 10 The relative magnitudes of the $H$-field components near the ground and at elevated angles are strongly dependent on the actual distance from the horizontal loop source at 10 MHz. The horizontally oriented $H$-field near the ground is a radially directed component which attenuates more rapidly with increasing distance than does the horizontally oriented $H$-field at elevated angles. The vertically oriented $H$-field near the ground is a component of the horizontally polarized ground wave launched by the horizontal loop and attenuates very rapidly with increasing distance from the source. See Figure 101.

NOTE 11 The shape of the vertical radiation pattern of the horizontally oriented $H$-field calculated at a distance of 30 m from the small horizontal loop over perfectly conducting ground is very similar to that calculated over a real ground at 10 MHz. The absolute value of the field strength calculated over perfectly conducting ground is about 5 dB less than the field strength calculated over real ground. Both calculated vertical radiation patterns at 30 m distance indicate that ground-based measurement of horizontally oriented $H$-field underestimates the maximum field strength at elevated angles by more than 6 dB. The measurable horizontally oriented $H$-field components near the ground in both cases are the remnants of radially directed near-field components, not a part of propagating waves, and they attenuate more rapidly with increasing distance from the source than do the fields at elevated angles. See Figure 101. In general, the boundary condition which requires the vertically oriented $H$-field strength to be zero at the surface of a perfectly conducting ground means that at all frequencies up to 30 MHz the patterns of vertically oriented $H$-field which are non-zero at the real ground do not resemble the corresponding vertically oriented $H$-field patterns which go to zero at the perfectly conducting ground.

**Table 22 – Predictability of radiation in vertical directions at 30 MHz, using ground-based measurements of horizontally oriented $H$-field at distances up to 300 m from the source (figures are located in 4.6.8)** *(1 of 3)*

| Type of source | Predictability based on measurements near real ground at 30 m distance from the source | Predictability based on *in situ* measurements near real ground when the measurement distance from the source is not precisely known | Predictability based on vertical radiation patterns calculated at a known distance from the source, assuming the ground behaves as a perfect conductor |
|---|---|---|---|
| Electrically small vertical electric dipole | Very good (see Figure 103, Figure 104) Note 1 | Impossible (see Figure 103, Figure 104) Note 2 | Impossible (see Figure 103) Note 3 |
| Electrically small horizontal electric dipole | Poor (see Figure 105, Figure 106, Figure 108) Notes 4, 5 | Impossible (see Figure 105, Figure 106, Figure 108) Note 6 | Impossible (see Figure 105, Figure 106) Note 7 |
| Electrically small horizontal magnetic dipole (vertical loop) | Good (see Figure 109, Figure 110) Note 8 | Impossible (see Figure 109, Figure 110) Note 9 | Impossible (see Figure 109) Note 10 |
| Electrically small vertical magnetic dipole (horizontal loop) | Poor (see Figure 111, Figure 112) Note 11 | Impossible (see Figure 111, Figure 112) Note 12 | Good (see Figure 111) Note 13 |

NOTE 1 The measurement of the horizontally oriented $H$-field near the real ground at 30 m distance from the small vertical electric dipole underestimates the maximum field strength at elevated angles by about 3 dB at 30 MHz.

NOTE 2 The horizontally oriented $H$-field near ground is a component of the vertically polarized ground wave emitted from the vertical electric dipole. At 30 MHz the vertically polarized wave attenuates rapidly with increasing distance near ground, such that there is an excess 13 dB attenuation of the ground wave in addition to the 20 dB sky-wave attenuation over the distance from 30 m to 300 m. See Figure 103 and Figure 105.

IECNORM.COM : Click to view the full PDF of CISPR TR 16-3:2020 RLV

**Table 22** *(2 of 3)*

NOTE 3 At a distance of 30 m from the small vertical electric dipole over a perfectly conducting ground, the vertical radiation pattern of the horizontally oriented $H$-field is within about 8 dB of the pattern of the $H$-field over real ground. However, the very high rate of attenuation with a distance of a vertically polarized ground wave over real ground at 30 MHz is apparent even at the short range of 30 m (see Figure 103). Moreover, at 30 MHz there is an excess 13 dB attenuation of the ground wave in addition to the 20 dB sky-wave attenuation over the distance from 30 m to 300 m. Over a perfectly conducting ground the excess ground-wave attenuation does not occur, so that the vertical radiation patterns over perfectly conducting ground cannot give guidance to the patterns over real ground at the distances from the small vertical electric dipole that are considered in this subclause.

NOTE 4 The measurement of horizontally oriented $H$-field emitted by the small horizontal electric dipole near the ground can underestimate the maximum horizontally oriented $H$-field strength in the vertical direction by more than 16 dB at 30 MHz (see Figure 105). Note, however, that a measurement of the vertically oriented $H$-field, Hz, at a height of 6 m improves predictability and underestimates the magnitude of the horizontally oriented $H$-field in the vertical direction by approximately 12 dB. The height scan measurement of Hz underestimates the magnitude of the vertically oriented $H$-field at elevated angles by approximately 7 dB.

NOTE 5 The small influence exerted by a wide range of the electrical constants of the real ground on the shape and magnitude of the small horizontal electric dipole vertical radiation pattern at 30 MHz is shown in Figure 107.

NOTE 6 Excess attenuation of the horizontally oriented $H$-field component of the vertically polarized ground wave emitted by the small horizontal electric dipole at the real ground is almost 12 dB more than the sky-wave attenuation over the distance from 30 m to 300 m from the source. If the true measurement distance is not known, the amount of excess attenuation suffered by the ground wave cannot be known when making predictions of the strength of radiation in vertical directions based on measurements at the ground.

NOTE 7 The horizontally oriented $H$-field near a perfectly conducting ground attenuates by 40 dB as the distance from the small horizontal electric dipole increases from 30 m to 300 m, an excess attenuation of 20 dB more than the sky-wave attenuation, as the far-field radiation pattern becomes established over that distance. On the other hand, the excess attenuation of the $H$-field component of the vertically polarized ground wave is about 12 dB near a real ground over the 30 m to 300 m distance. The vertical radiation patterns over real and perfectly conducting grounds therefore differ significantly at 30 MHz in that range of measuring distances. See Figure 105 and Figure 106.

NOTE 8 Measurement of the horizontally oriented $H$-field near real ground at 30 m distance from the small vertical loop can underestimate the maximum horizontally oriented $H$-field strength emitted in the vertical direction by less than 6 dB. It gives an exact indication of the strength of the vertically oriented $H$-field emitted at elevated angles. See Figure 109.

NOTE 9 The horizontally oriented $H$-field components near real ground attenuate more rapidly with increasing distance from the small vertical loop than do the sky-wave components, at 30 MHz. The excess attenuation is approximately 13 dB over the distance from 30 m to 300 m. See Figure 109.

NOTE 10 At a distance of 30 m from the small vertical loop over a perfectly conducting ground the vertical radiation pattern of the horizontally oriented $H$-field is within about 8 dB of the pattern of the $H$-field over a real ground. However, the vertically polarized wave near a perfectly conducting ground attenuates with distance at the free space rate, unlike the vertically polarized wave over a real ground which attenuates more rapidly with distance at 30 MHz (see Figure 109 and Figure 110). Vertical radiation patterns calculated over a perfectly conducting ground can therefore be very misleading as guidance to the patterns over real ground at a distance of 30 m and beyond.

NOTE 11 Measurement of the horizontally oriented $H$-field components near the real ground at 30 m distance from the small horizontal loop can underestimate the $H$-field strengths emitted at elevated angles by more than 16 dB. Note, however, that a measurement of the vertically oriented $H$-field, in Hz, at a height of 6 m underestimates the maximum $H$-field strengths at elevated angles by less than 6 dB. See Figure 111.

NOTE 12 The relative magnitudes of the $H$-field components near the ground and at elevated angles are strongly dependent on the actual distance from the horizontal loop source. The horizontally oriented $H$-field near the ground is a radially directed component which attenuates more rapidly with increasing distance than does the horizontally oriented $H$-field at elevated angles. The vertically oriented $H$-field near the ground is a component of the horizontally polarized ground wave launched by the horizontal loop and at 30 MHz it attenuates very rapidly with increasing distance from the source. See Figure 111 and Figure 112.

IECNORM.COM : Click to view the full PDF of CISPR TR 16-3:2020 RLV

**Table 22** *(3 of 3)*

| |
|---|
| NOTE 13 The shape and magnitude of the vertical radiation pattern of the horizontally oriented $H$-field calculated at a distance of 30 m from the small horizontal loop over perfectly conducting ground at 30 MHz are very similar to the shape and magnitude of the pattern calculated over real ground. Both the calculated patterns indicate that ground-based measurement of horizontally oriented $H$-field will underestimate the maximum field strength at elevated angles by 16 dB or 17 dB. However, the measurable horizontally oriented $H$-field components near the ground in both cases are the remnants of radially directed near-field components, not a part of propagating waves, and they attenuate more rapidly with increasing distance from the small horizontal loop than do the fields at elevated angles. See Figure 100. In general, the boundary condition which requires the vertically oriented $H$-field strength to be zero at the surface of a perfectly conducting ground means that at all frequencies up to 30 MHz the patterns of vertically oriented $H$-field which are non-zero at the real ground do not resemble the corresponding vertically oriented $H$-field patterns which go to zero at the perfectly conducting ground. |

#### 4.6.6.2 Error ranges

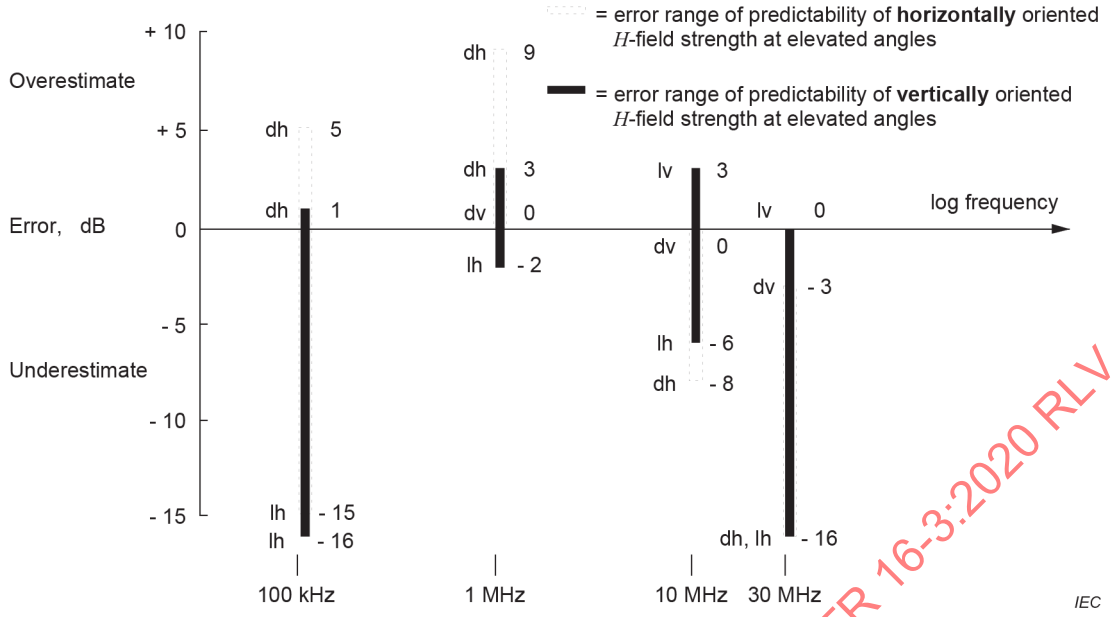
It is possible to present pictorially the ranges of errors of the predictability of radiation in vertical directions at different frequencies, when the precise horizontal measurement distance from the sources is known to be 30 m. Figure 55 and Figure 56 show in bar chart form the error ranges to be expected; Figure 55 is for measurements of the horizontally oriented $H$-field near the ground at 30 m distance from the sources, and Figure 56 is for the measurements of horizontally oriented $H$-field supplemented with measurements of vertically oriented $H$-field in a 6 m height scan near the ground at 30 m distance from the sources.

The error range bar charts summarize the information presented in the various notes to the tables and in the radiation pattern diagrams. The following examples serve to illustrate the ways in which the error range bar charts can be interpreted.

In Figure 55, which is used when predictability of radiation in vertical directions is to be based only on measurements near ground of the horizontally oriented $H$-field components at 30 m horizontal distance from the sources, the charts show that at 100 kHz the largest over-estimation of the strength of radiation in vertical directions occurs in the case of a source behaving as a small horizontal electric dipole, and the error is an overestimate by 5 dB of the maximum strength of the horizontally oriented $H$-field. The largest error in overestimating the maximum vertically oriented $H$-field strength at 100 kHz is an overestimate of only 1 dB, as indicated in the chart by the solid bar, again for the case of a source behaving as a small horizontal electric dipole. At 100 kHz, Figure 55 shows that the largest error in prediction of the strength of radiation in vertical directions occurs in the case of a source behaving as a small vertical magnetic dipole (horizontal loop) and the error is an underestimate by 16 dB of the maximum vertically oriented $H$-field. The largest error at 100 kHz in predicting the maximum horizontally oriented $H$-field strength emitted in vertical directions is an under-estimate by 15 dB, again in the case of a source behaving as a small vertical magnetic dipole (horizontal loop).

In Figure 56, which is used when predictability of radiation in vertical directions is to be based on measurements near ground of the horizontally oriented $H$-field components supplemented with 6 m height-scan measurements of the vertically oriented $H$-field components at 30 m distance, the charts show that at 100 kHz the worst error in the prediction of the strength of radiation in vertical directions still occurs for the vertically oriented $H$-field components emitted from a source behaving as a small vertical magnetic dipole (horizontal loop), but that the magnitude of the error has been reduced to an underestimate by 6 dB (solid bar). The magnitude of the largest underestimate at 100 kHz of the maximum strength of the horizontally oriented $H$-field emitted in vertical directions has been reduced to 3 dB, and this also occurs for the case of a source behaving as a small vertical magnetic dipole (horizontal loop).

IECNORM.COM : Click to view the full PDF of CISPR TR 16-3:2020 RLV




Electrical constants of the ground: $\sigma$ = 1 mS/m, $\varepsilon_r$ = 15.

Source identification:

dh = horizontal electric dipole

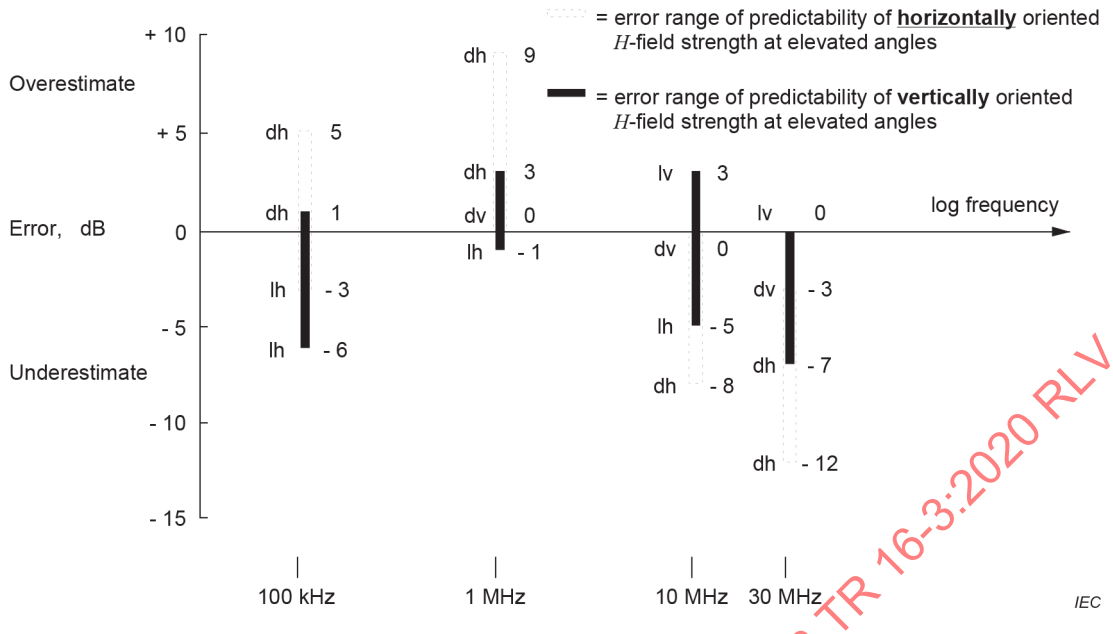
dv = vertical electric dipole

lh = vertical magnetic dipole (horizontal loop)

lv = horizontal magnetic dipole (vertical loop)

**Figure 55 – Ranges of errors in the predictability of radiation in vertical directions from electrically small sources located close to the ground, based on measurements of the horizontally oriented *H*-field near ground at a distance of 30 m from the sources**

IECNORM.COM : Click to view the full PDF of CISPR TR 16-3:2020 RLV




Electrical constants of the ground: $\sigma$ = 1 mS/m, $\varepsilon_r$ = 15.

Source identification:

dh = horizontal electric dipole

dv = vertical electric dipole

lh = vertical magnetic dipole (horizontal loop)

lv = horizontal magnetic dipole (vertical loop)

**Figure 56 – Ranges of errors in the predictability of radiation in vertical directions from electrically small sources located close to the ground, based on measurements of the horizontally oriented *H*-field at the ground supplemented with measurements of the vertically oriented *H*-field in a height scan up to 6 m at a distance of 30 m from the sources**

### 4.6.7 Conclusions

Vertical radiation patterns have been calculated for electrically small sources located close to real homogeneous plane ground, ignoring the possible contributions to pattern distortion that might arise from the presence of nearby buildings or other field disturbing objects, or from discontinuities in the electrical constants of the ground. Nevertheless, even with such a simplification, the studies still show that in the case of solitary electrically small sources located close to a plane homogeneous ground the predictability of radiation in vertical directions can be subject to large errors, when the predictions are to be based on measurements of the strength of the horizontally oriented *H*-field at the ground in the manner presently described in CISPR 11.

In particular, this subclause has identified many examples of the impossibility of making predictions of field strength at elevated angles with a known margin of error, using ground-based measurements, when the measuring distances from the sources are not precisely known. The limits and methods of measurement of radiation *in situ* for which the precise measurement distance from the ISM equipment is not defined in CISPR 11 cannot provide a known level of protection of aeronautical communication services. For example, this limitation applies over the entire frequency range from 100 kHz to 30 MHz if the radiation source behaves like an electrically small vertical magnetic dipole (horizontal loop).

IECNORM.COM : Click to view the full PDF of CISPR TR 16-3:2020 RLV

The large errors in calculation of the vertical radiation patterns that can arise from the approximation, which is sometimes made, that the influence of real ground can be determined by assuming it behaves like a perfect conductor have also been indicated. Apart from the more complex interaction between the source and its image in a real ground, two more obvious reasons for the errors are: that the boundary condition that requires the vertically oriented $H$-field strength and the horizontally oriented $E$-field strength to be zero at the surface of a perfectly conducting ground does not apply at the surface of a real ground, and the vertically polarized ground wave attenuation with distance over real ground is greater than the attenuation with distance over a perfectly conducting ground, especially at the higher frequencies.

Subclause 4.6 has also shown, even when the measurement distance over real ground is precisely known, that predictability of the strength of radiation in vertical directions based on measurements near the ground at a distance of 30 m remains subject to significant errors.

Figure 55 depicts the error ranges that can apply when predictability is based solely on measurement of the horizontally oriented $H$-field near ground at 30 m distance. It can be seen that over the frequency range from 100 kHz to 30 MHz the margin for error can be as much as +9 dB (overestimate) at 1 MHz, or as much as –16 dB (underestimate) at the extremes of the frequency range, i.e. 100 kHz and 30 MHz.

Figure 56 illustrates the reduced error ranges obtained for predictability of radiation in vertical directions when measurements of horizontally oriented $H$-field near the ground are supplemented with measurements of vertically oriented $H$-field at heights up to 6 m above the ground. It can be seen that the potential overestimate of 9 dB at 1 MHz remains a possibility, but the potential underestimate of 16 dB at 100 kHz and 30 MHz has become a possible underestimate of 6 dB at 100 kHz and of 12 dB at 30 MHz.

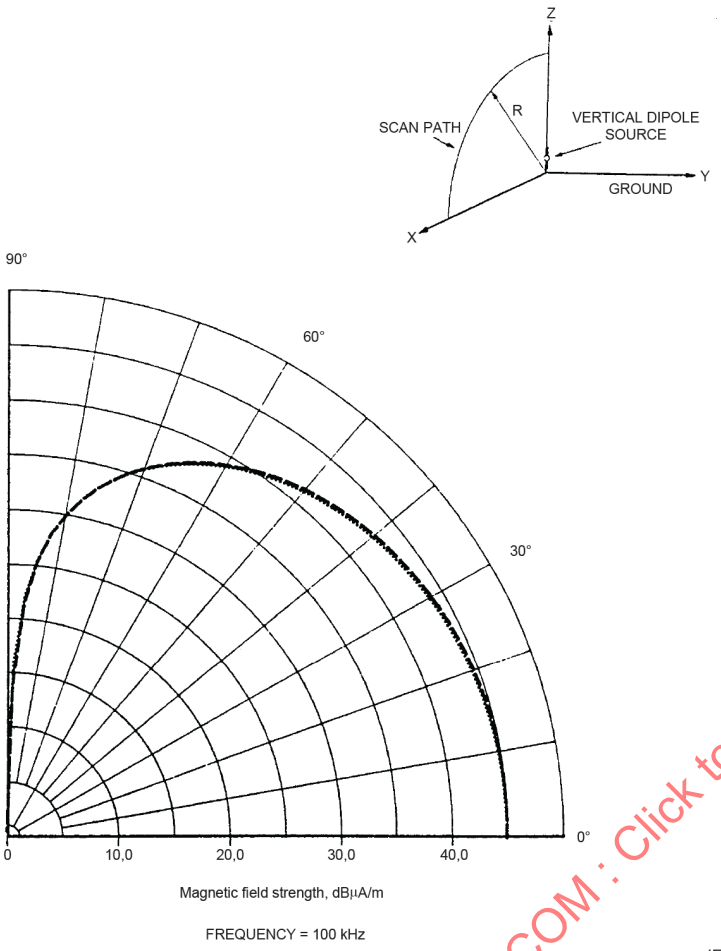
The studies described in 4.6 have identified some of the factors that shall be taken into account when determining limits and methods of measurement of radiated electromagnetic disturbances from ISM apparatus to ensure the protection of aeronautical communication services operating below 30 MHz.

In addition, the comparisons of the vertical radiation patterns over real ground with those over perfectly conducting ground have also shown the large differences that can occur in the assessments of the potential for interference made by measurements on a test site having a conducting metal ground plane compared with assessments using measurements made on a test site having a real ground reference plane.

### 4.6.8 Figures associated with predictability of radiation in vertical directions

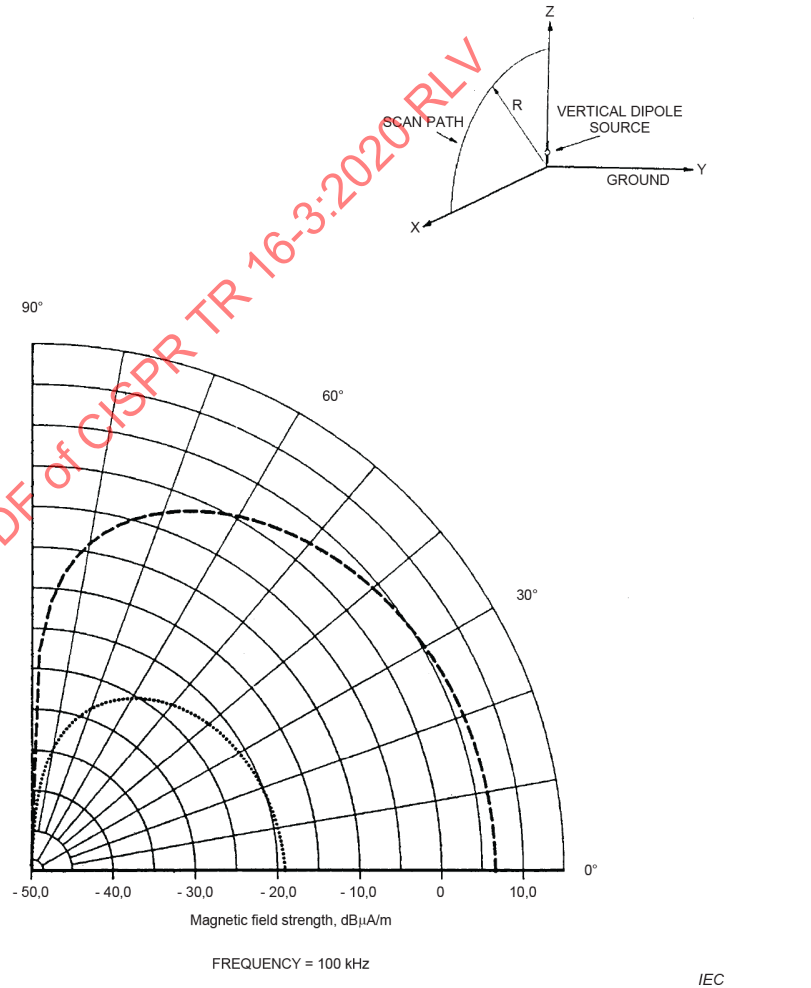
Figures referenced in 4.6.6.1 are provided in this subclause.

IECNORM.COM : Click to view the full PDF of CISPR TR 16-3:2020 RLV




Dipole length 3 m; dipole base at a height above ground of 0,15 m; dipole moment 1 A·m. Dashed line curve – $H_y$ at a scan distance of 30 m. Dotted line curve – $H_y$ at a scan distance of 30 m. Electrical constants of the ground: $\sigma$ = 1 mS/m, $\varepsilon_r$ = 15. Perfectly conducting ground.

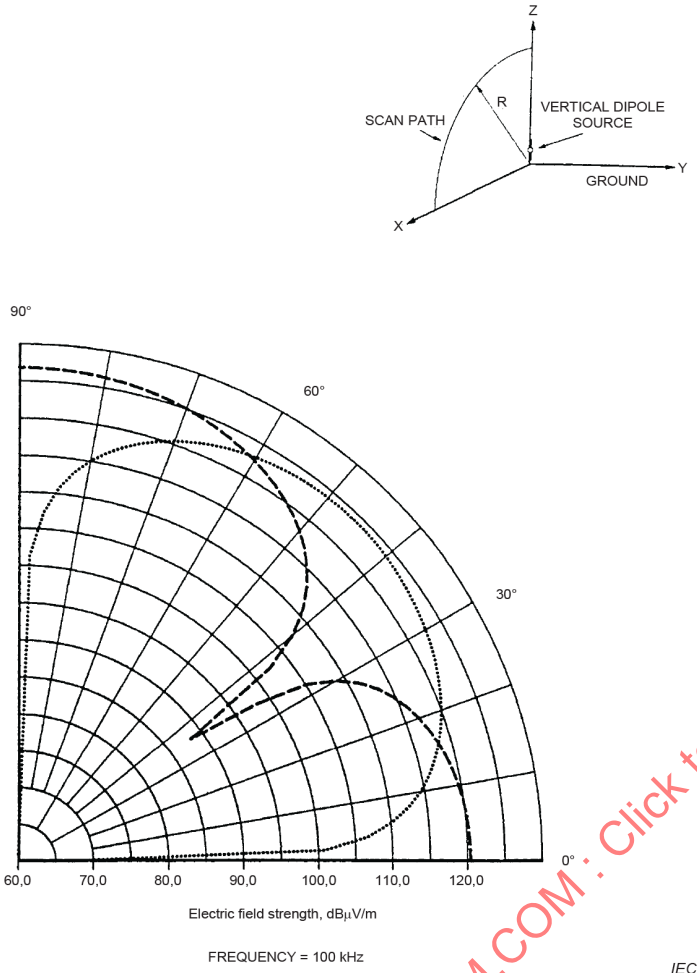
**Figure 57 – Vertical radiation patterns of horizontally oriented *H*-fields emitted by a small vertical electric dipole located close to the ground**




Dipole length 3 m; dipole base at a height above ground of 0,15 m; dipole moment 1 A·m. Dashed line curve – $H_y$ at a scan distance of 300 m. Dotted line curve – $H_y$ at a scan distance of 3 000 m. Electrical constants of the ground: $\sigma$ = 1 mS/m, $\varepsilon_r$ = 15.

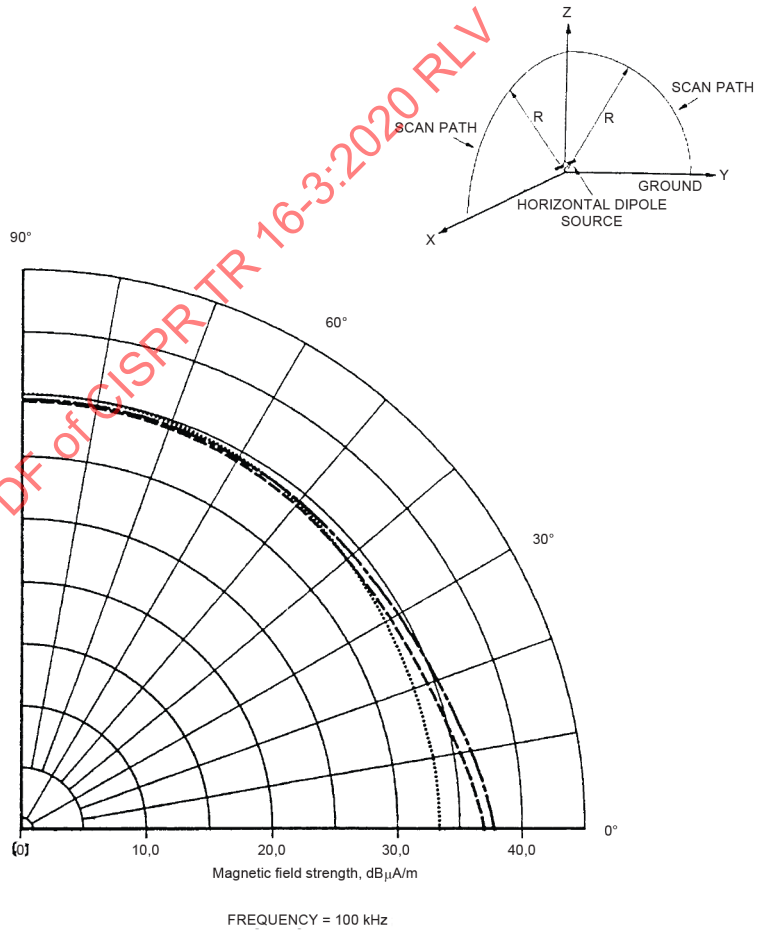
**Figure 58 – Vertical radiation patterns of horizontally oriented *H*-fields emitted by a small vertical electric dipole located close to the ground**

IECNORM.COM : Click to view the full PDF of CISPR TR 16-3:2020 RLV




Dipole length 3 m; dipole base at a height above ground of 0,15 m; dipole moment 1 A·m. Dashed line curve – vertically oriented $E_z$ at a scan distance of 30 m. Dotted line curve – horizontally oriented $E_x$ at a scan distance of 30 m. Electrical constants of the ground: $\sigma$ = 1 mS/m, $\varepsilon_r$ = 15.

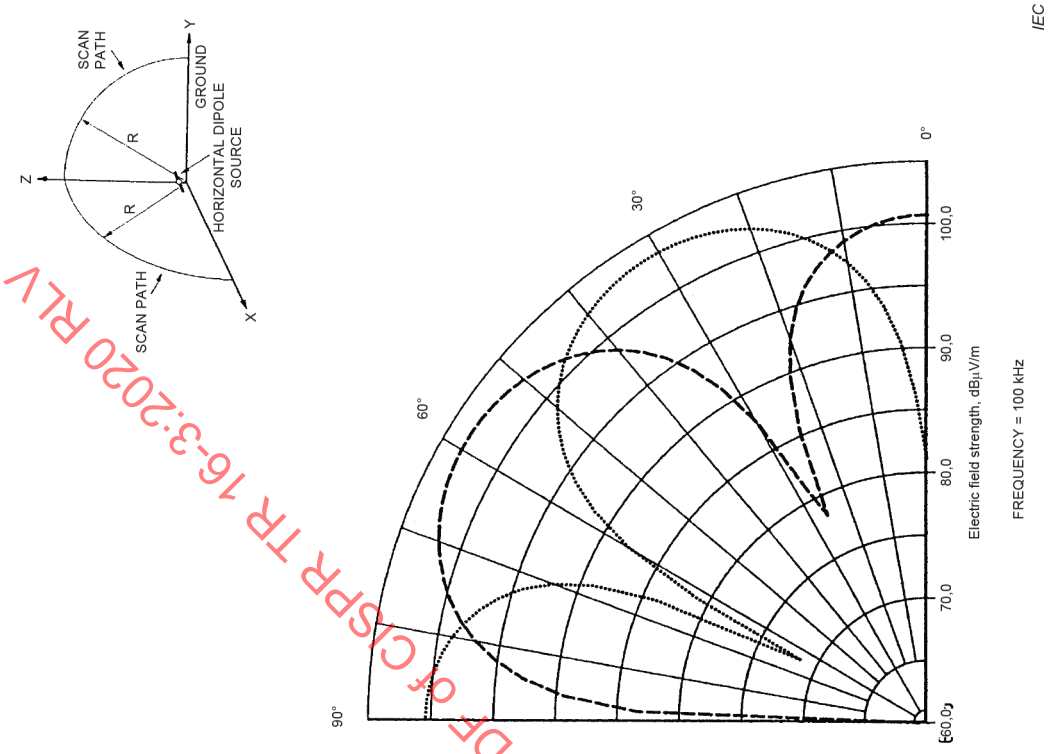
**Figure 59 – Vertical radiation patterns of *E*-fields emitted by a small vertical electric dipole located close to the ground**

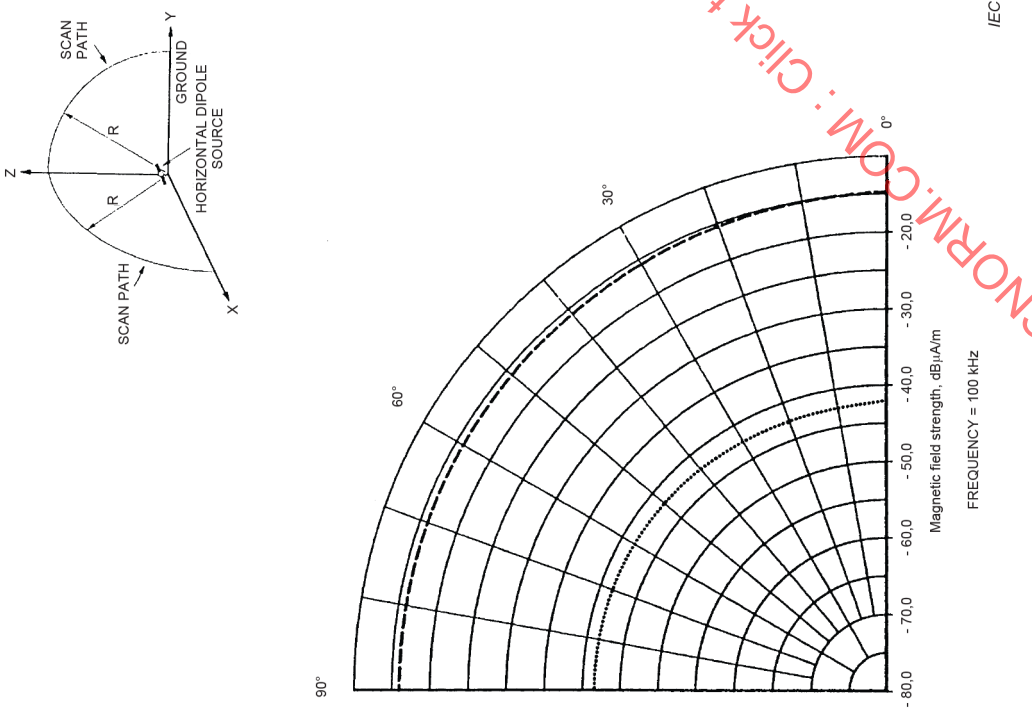



Dipole length 3 m; dipole base at a height above ground of 0,15 m; dipole moment 1 A·m. Dashed line curve – vertically oriented $E_z$ at a scan distance of 3 000 m. Dotted line curve – horizontally oriented $E_x$ at a scan distance of 3 000 m. Dash-dot line curve – total vector/phasor sum of $E_z$ and $E_x$ at a scan distance of 3 000 m, the vertically polarized $E$-field. Electrical constants of the ground: $\sigma$ = 1 mS/m, $\varepsilon_r$ = 15.

**Figure 60 – Vertical radiation patterns of the *E*-fields emitted by a small vertical electric dipole located close to the ground**

IECNORM.COM : Click to view the full PDF of CISPR TR 16-3:2020 RLV




IECNORM.COM : Click to view the full PDF of CISPR TR 16-3:2020 RLV

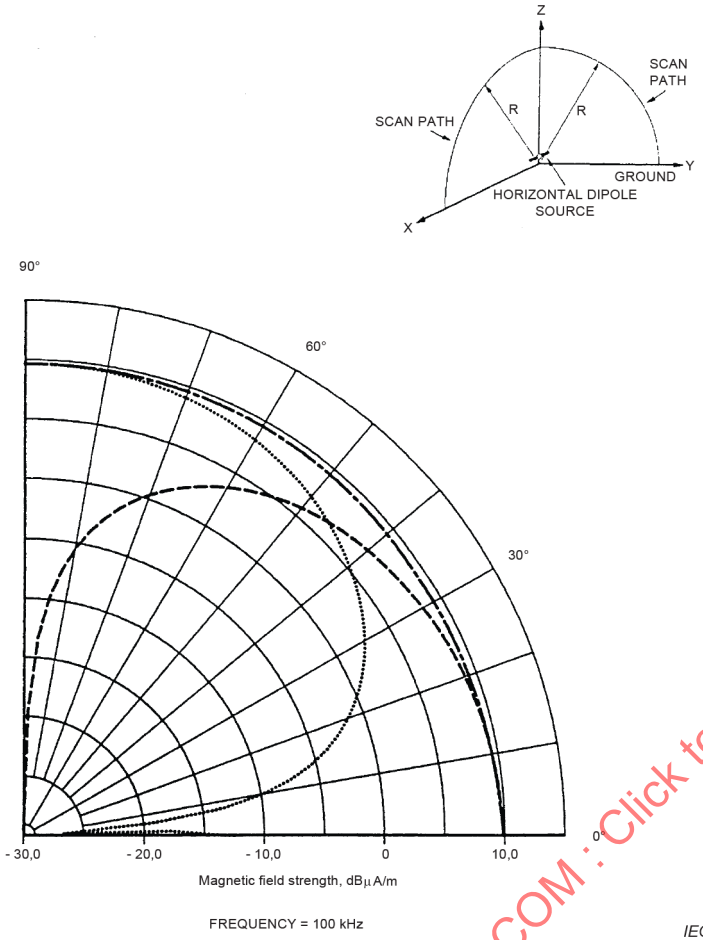
Dipole length 3 m; dipole height above ground of 1 m; dipole moment 1 A·m. Dashed line curve – horizontally oriented $H_y$ at a scan distance of 30 m in the Z-X plane. Dotted line curve – horizontally oriented $H_y$ at a scan distance of 30 m in the Y-Z plane. Solid line curve – vertically oriented $H_z$ at a scan distance of 30 m in the Y-Z plane. Dash-dot line curve – horizontally oriented $H_y$ at a scan distance of 30 m in the Z-X plane. Electrical constants of the ground: $\sigma$ = 1 mS/m, $\varepsilon_r$ = 15. Perfectly conducting ground.

**Figure 61 – Vertical radiation patterns of the *H*-fields emitted by a small horizontal electric dipole located close to the ground**

Dipole length 3 m; dipole height above ground of 1 m; dipole moment 1 A·m. $H_y$ at a scan distance of 30 m in the Z-X plane. Dash-dot line curve – ground constants are $\sigma$ = 0,1 mS/m, $\varepsilon_r$ = 3. Dashed line curve – ground constants are $\sigma$ = 1 mS/m, $\varepsilon_r$ = 15. Dotted line curve – ground constants are $\sigma$ = 10 mS/m, $\varepsilon_r$ = 30. Electrical constants of the ground: $\sigma$ = 1 mS/m, $\varepsilon_r$ = 15. Perfectly conducting ground.

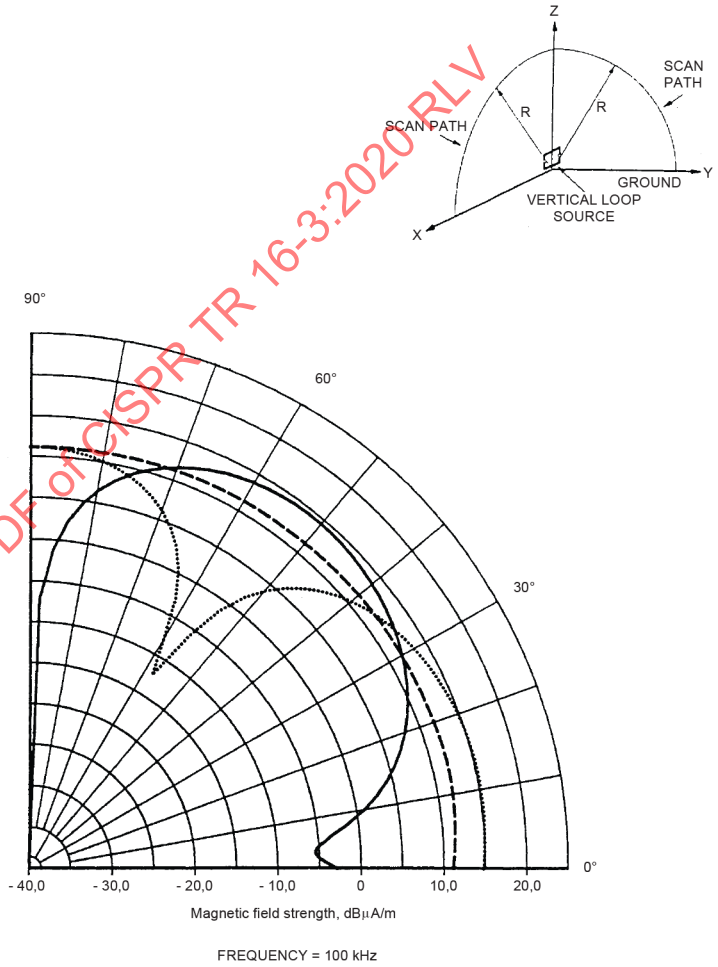
**Figure 62 – Influence of a wide range of values of the electrical constants of the ground on the vertical radiation patterns of the horizontally oriented *H*-fields emitted by a small horizontal electric dipole located close to the ground**

IECNORM.COM : Click to view the full PDF of CISPR TR 16-3:2020 RLV




Dipole length 3 m; dipole height above ground of 1 m; dipole moment 1 A·m. Dashed line curve – $H_y$ at a scan distance of 300 m in the Z-X plane. Dotted line curve – $H_y$ at a scan distance of 3 000 m in the Z-X plane. Electrical constants of the ground $\sigma$ = 1 mS/m, $\varepsilon_r$ = 15.

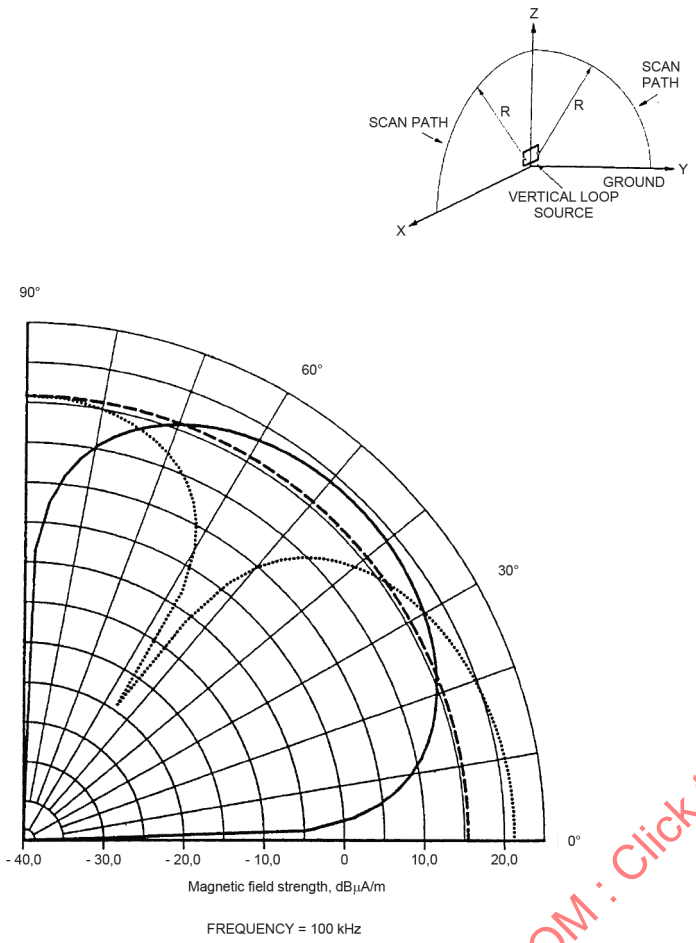
**Figure 63 – Vertical radiation patterns of the horizontally oriented *H*-fields emitted by a small horizontal electric dipole located close to the ground**




Dipole length 3 m; dipole height above ground of 1 m; dipole moment 1 A·m. Dashed line curve – vertically oriented $E_z$ at a scan distance of 30 m in the Z-X plane. Dotted line curve – horizontally oriented $E_x$ at a scan distance of 30 m in the Z-X plane. Electrical constants of the ground $\sigma$ = 1 mS/m, $\varepsilon_r$ = 15.

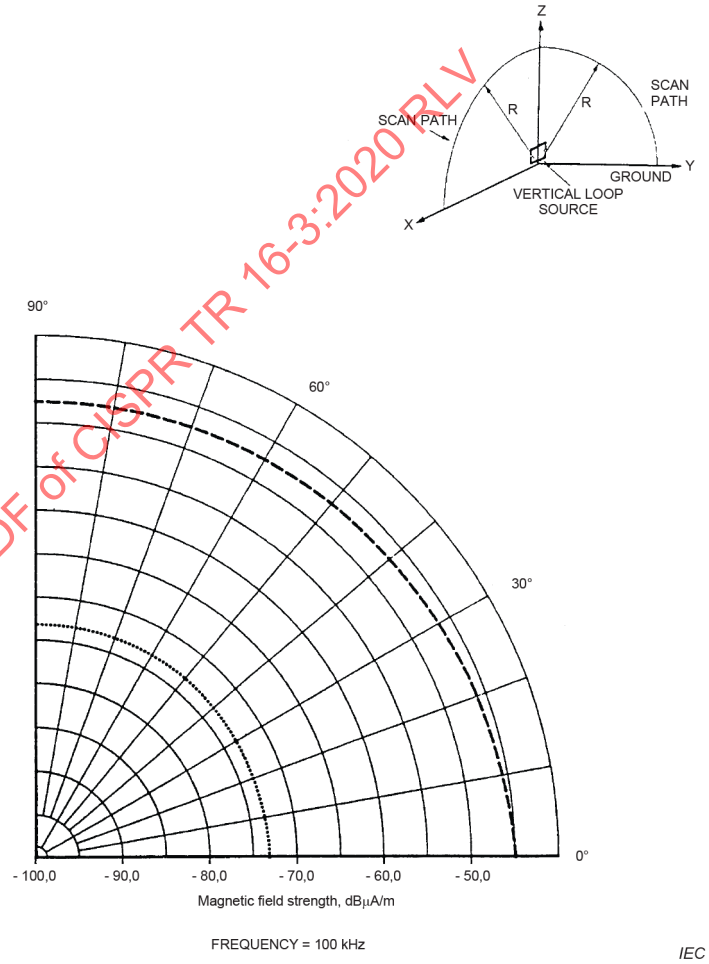
**Figure 64 – Vertical radiation patterns of the *E*-fields emitted by a small horizontal electric dipole located close to the ground**

IECNORM.COM : Click to view the full PDF of CISPR TR 16-3:2020 RLV




Dipole length 3 m; dipole height above ground of 1 m; dipole moment 1 A·m. Dashed line curve – vertically oriented $E_z$ at a scan distance of 3 000 m in the Z-X plane. Dotted line curve – horizontally oriented $E_x$ at a scan distance of 3 000 m in the Z-X plane. Dash-dot line curve – total vector/phasor sum of $E_z$ and $E_x$ at a scan distance of 3 000 m in the Z-X plane, the vertically polarized $E$-field. Electrical constants of the ground $\sigma$ = 1 mS/m, $\varepsilon_r$ = 15.

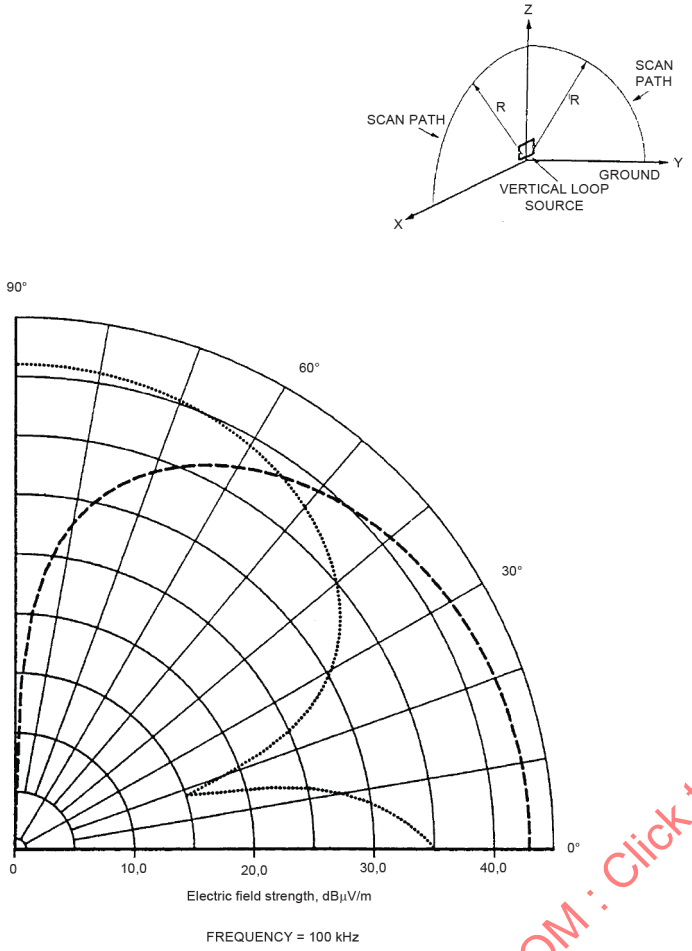
**Figure 65 – Vertical radiation patterns of the $E$-fields emitted by a small horizontal electric dipole located close to the ground**




Square loop 3 m by 3 m. Loop base height above the ground 1 m. Dipole moment 1 A·m$^2$. Dashed line curve – horizontally oriented $H_y$ at a scan distance of 30 m in the Z-X plane. Dotted line curve – horizontally oriented $H_y$ at a scan distance of 30 m in the Y-Z plane. Solid line curve – vertically oriented $H_z$ at a scan distance of 30 m in the Y-Z plane. Electrical constants of the ground $\sigma$ = 1 mS/m, $\varepsilon_r$ = 15.

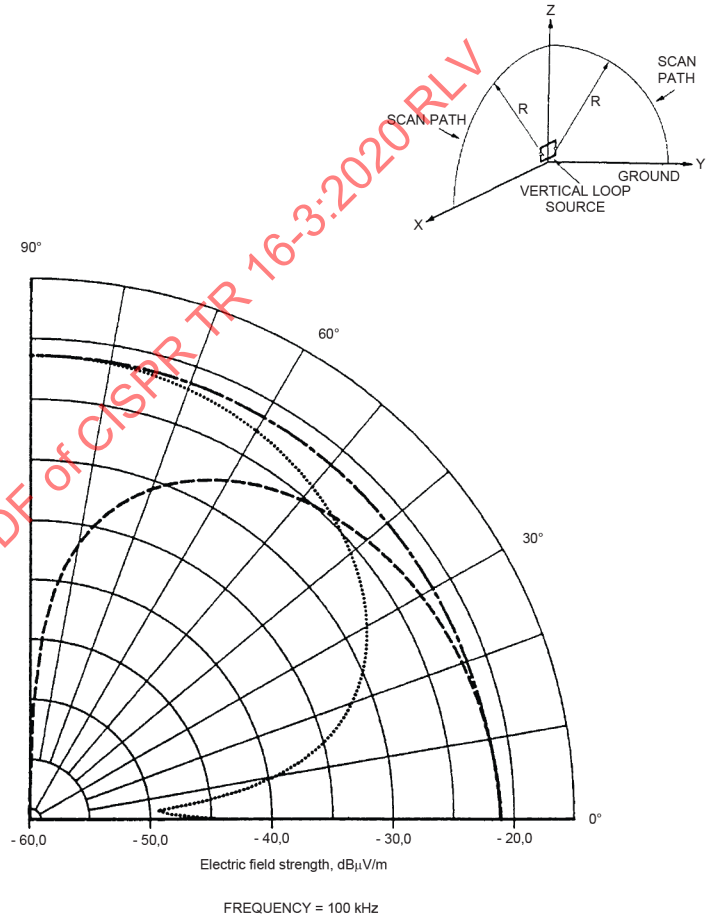
**Figure 66 – Vertical radiation patterns of $H$-fields emitted by small horizontal magnetic dipole (vertical loop) located close to ground**

IECNORM.COM : Click to view the full PDF of CISPR TR 16-3:2020 RLV




Square loop 3 m by 3 m. Loop base height above the ground 1 m. Dipole moment 1 A·m$^2$. Dashed line curve – horizontally oriented $H_y$ at a scan distance of 30 m in the Z-X plane. Dotted line curve – horizontally oriented $H_y$ at a scan distance of 30 m in the Y-Z plane. Solid line curve – vertically oriented $H_z$ at a scan distance of 30 m in the Y-Z plane. Perfectly conducting ground.

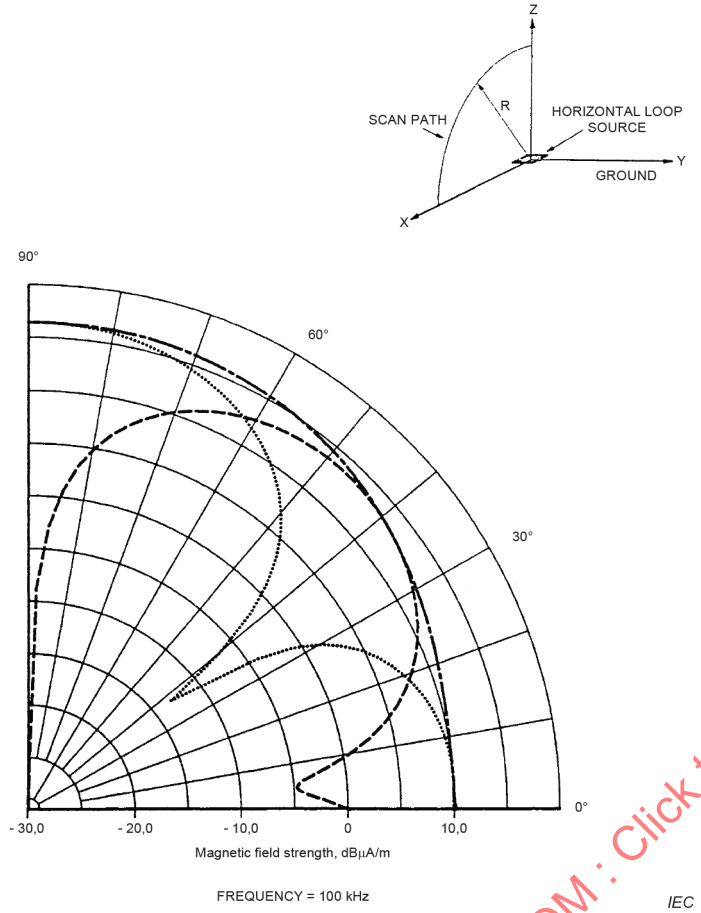
**Figure 67 – Vertical radiation patterns of the horizontally oriented *H*-fields emitted by a small horizontal magnetic dipole (vertical loop) located close to the ground**




Square loop 3 m by 3 m. Loop base height above the ground 1 m. Dipole moment 1 A·m$^2$. Dashed line curve – $H_y$ at a scan distance of 300 m in the Z-X plane. Dotted line curve – $H_y$ at a scan distance of 3 000 m in the Z-X plane. Electrical constants of the ground $\sigma$ = 1 mS/m, $\varepsilon_r$ = 15.

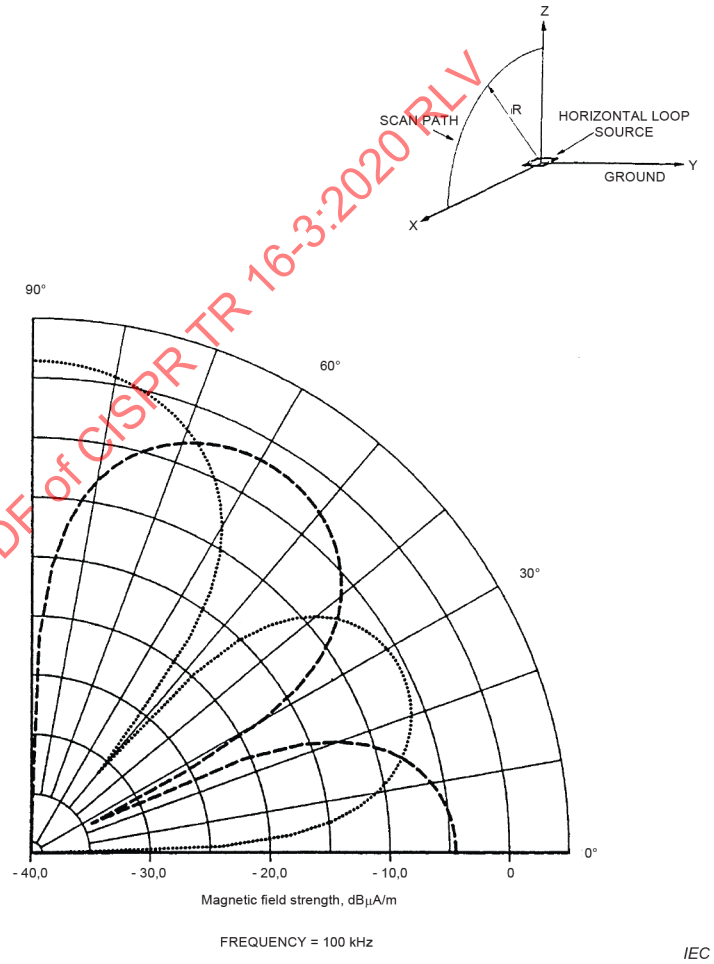
**Figure 68 – Vertical radiation patterns of the horizontally oriented *H*-fields emitted by a small horizontal magnetic dipole (vertical loop) located close to the ground**

IECNORM.COM : Click to view the full PDF of CISPR TR 16-3:2020 RLV




Square loop 3 m by 3 m. Loop base height above the ground 1 m. Dipole moment 1 A·m$^2$. Dashed line curve – vertically oriented $E_z$ at a scan distance of 30 m in the Z-X plane. Dotted line curve – horizontally oriented $E_x$ at a scan distance of 30 m in the Z-X plane. Electrical constants of the ground $\sigma$ = 1 mS/m, $\varepsilon_r$ = 15.

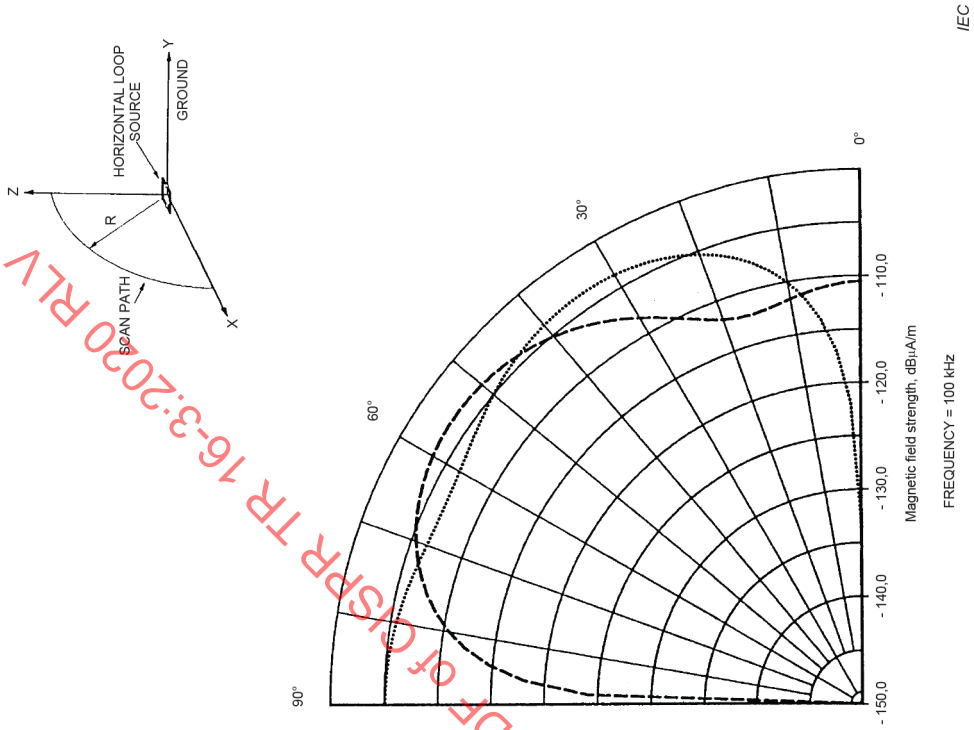
**Figure 69 – Vertical radiation patterns of the *E*-fields emitted by a small horizontal magnetic dipole (vertical loop) located close to the ground**

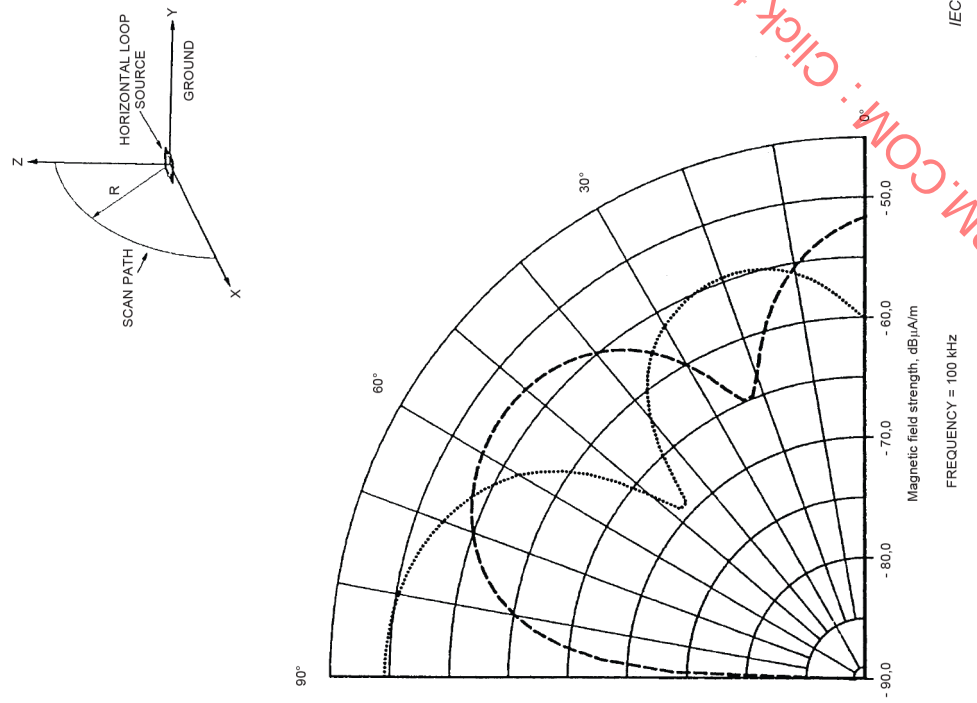



Square loop 3 m by 3 m. Loop base height above the ground 1 m. Dipole moment 1 A·m$^2$. Dashed line curve – vertically oriented $E_z$ at a scan distance of 3 000 m in the Z-X plane. Dotted line curve – horizontally oriented $E_x$ at a scan distance of 3 000 m in the Z-X plane. Dash-dot line curve – total vector/phasor sum of $E_z$ and $E_x$ at a scan distance of 3 000 m in the Z-X plane, the vertically polarized $E$-field. Electrical constants of the ground $\sigma$ = 1 mS/m, $\varepsilon_r$ = 15.

**Figure 70 – Vertical radiation patterns of the *E*-fields emitted by a small horizontal magnetic dipole (vertical loop) located close to the ground**

IECNORM.COM : Click to view the full PDF of CISPR TR 16-3:2020 RLV




IECNORM.COM : Click to view the full PDF of CISPR TR 16-3:2020 RLV

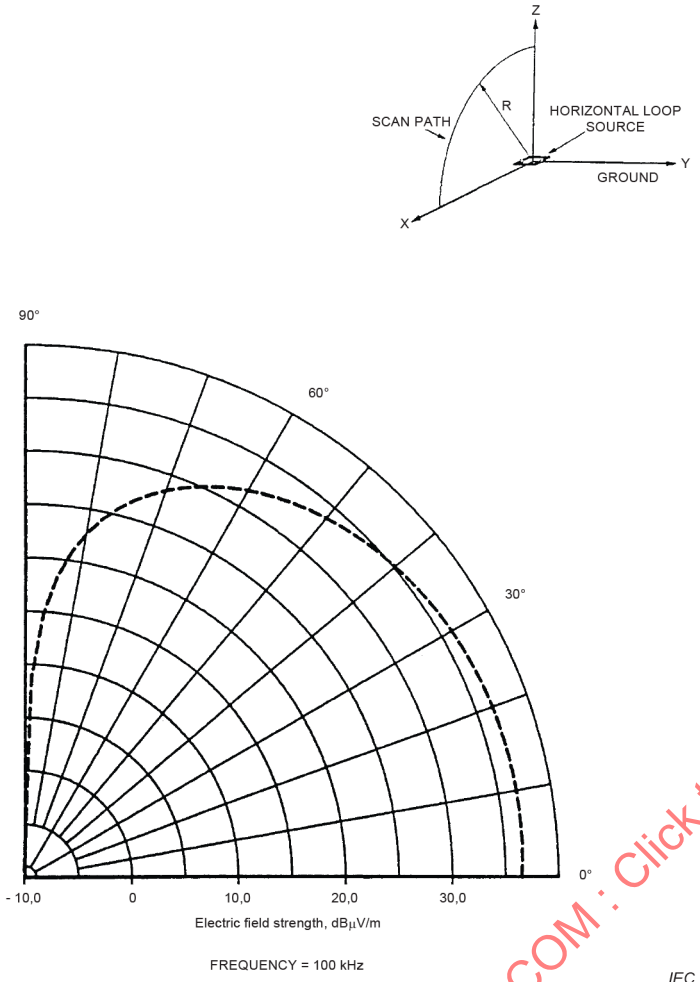
Square loop 3 m by 3 m. Loop base height above the ground 1 m. Dipole moment 1 A·m$^2$. Dashed line curve – horizontally oriented $H_x$ at a scan distance of 30 m. Dotted line curve – horizontally oriented $H_z$ at a scan distance of 30 m. Dash-dot line curve – total vector/phasor sum of $H_x$ and $H_z$ at a scan distance of 30 m, the total $H$-field component of the horizontally polarized radiation. Electrical constants of the ground $\sigma$ = 1 mS/m, $\varepsilon_r$ = 15.

**Figure 71 – Vertical radiation patterns of the $H$-fields emitted by a small vertical magnetic dipole (horizontal loop) located close to the ground**

Square loop 3 m by 3 m. Loop base height above the ground 1 m. Dipole moment 1 A·m$^2$. Dashed line curve – horizontally oriented $H_x$ at a scan distance of 30 m. Dotted line curve – vertically oriented $H_z$ at a scan distance of 30 m. Perfectly conducting ground.

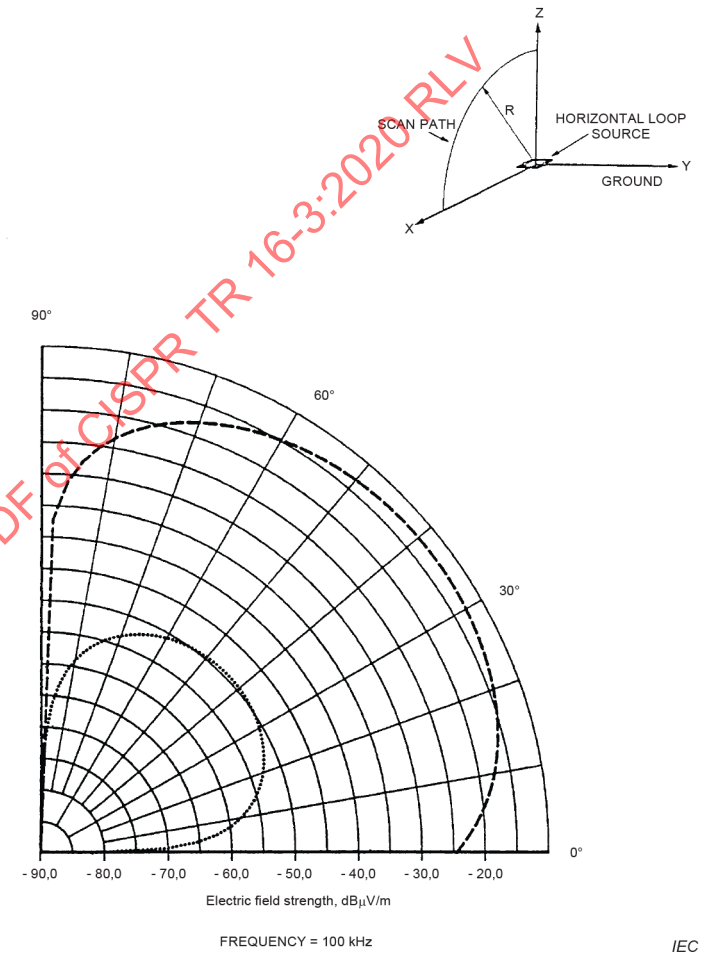
**Figure 72 – Vertical radiation patterns of the $H$-fields emitted by a small vertical magnetic dipole (horizontal loop) located close to the ground**

IECNORM.COM : Click to view the full PDF of CISPR TR 16-3:2020 RLV




Square loop 3 m by 3 m. Loop base height above the ground 1 m. Dipole moment 1 A·m$^2$. Dashed line curve – horizontally oriented $H_x$ at a scan distance of 300 m. Dotted line curve – vertically oriented $H_z$ at a scan distance of 300 m. Electrical constants of the ground $\sigma$ = 1 mS/m, $\varepsilon_r$ = 15.

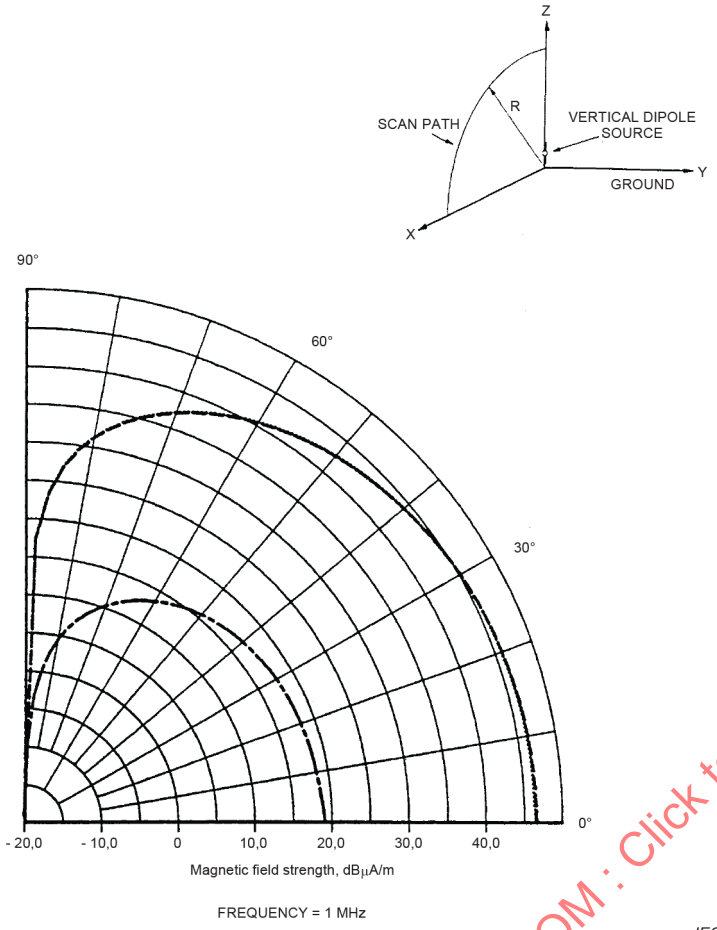
**Figure 73 – Vertical radiation patterns of the *H*-fields emitted by a small vertical magnetic dipole (horizontal loop) located close to the ground**




Square loop 3 m by 3 m. Loop base height above the ground 1 m. Dipole moment 1 A·m$^2$. Dashed line curve – horizontally oriented $H_x$ at a scan distance of 3 000 m. Dotted line curve – vertically oriented $H_z$ at a scan distance of 3 000 m. Electrical constants of the ground $\sigma$ = 1 mS/m, $\varepsilon_r$ = 15.

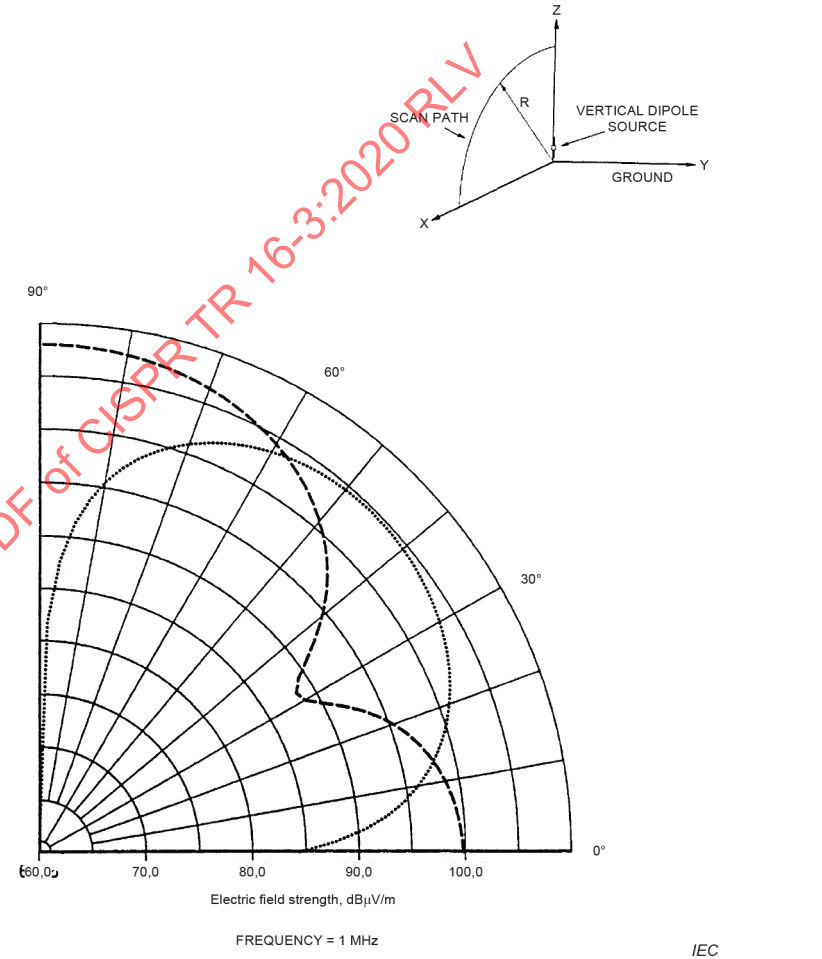
**Figure 74 – Vertical radiation patterns of the *H*-fields emitted by a small vertical magnetic dipole (horizontal loop) located close to the ground**

IECNORM.COM : Click to view the full PDF of CISPR TR 16-3:2020 RLV




Square loop 3 m by 3 m. Loop base height above the ground 1 m. Dipole moment 1 A·m$^2$. Dashed line curve – horizontally oriented $E_y$ at a scan distance of 30 m. Electrical constants of the ground $\sigma$ = 1 mS/m, $\varepsilon_r$ = 15.

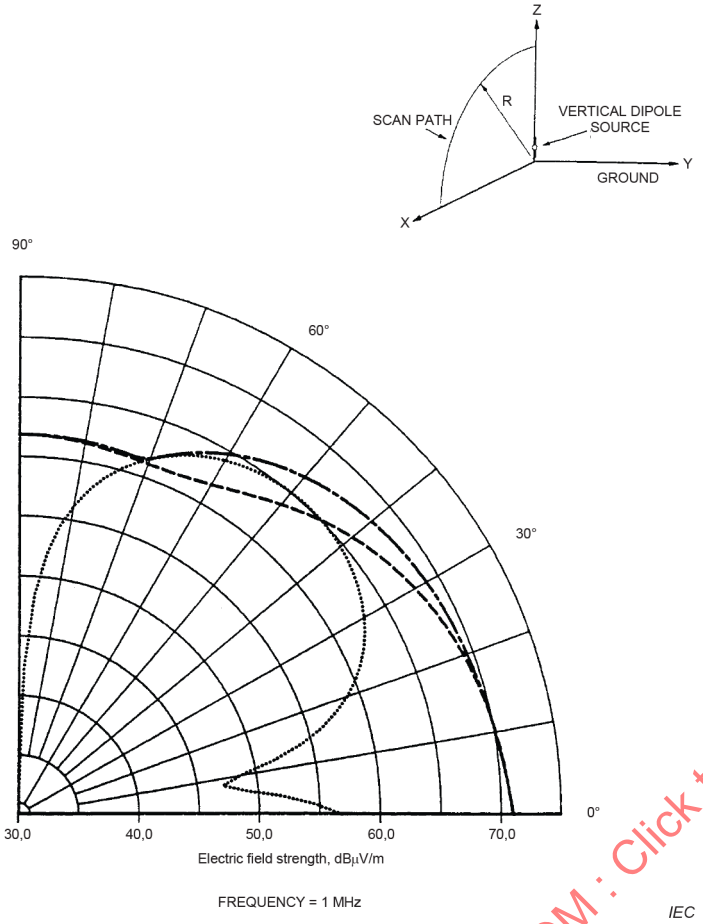
**Figure 75 – Vertical radiation pattern of the $E$-field emitted by a small vertical magnetic dipole (horizontal loop) located close to the ground**




Square loop 3 m by 3 m. Loop base height above the ground 1 m. Dipole moment 1 A·m$^2$. Dashed line curve – horizontally oriented $E_y$ at a scan distance of 300 m. Dotted line curve – horizontally oriented $E_y$ at a scan distance of 3 000 m. Electrical constants of the ground $\sigma$ = 1 mS/m, $\varepsilon_r$ = 15.

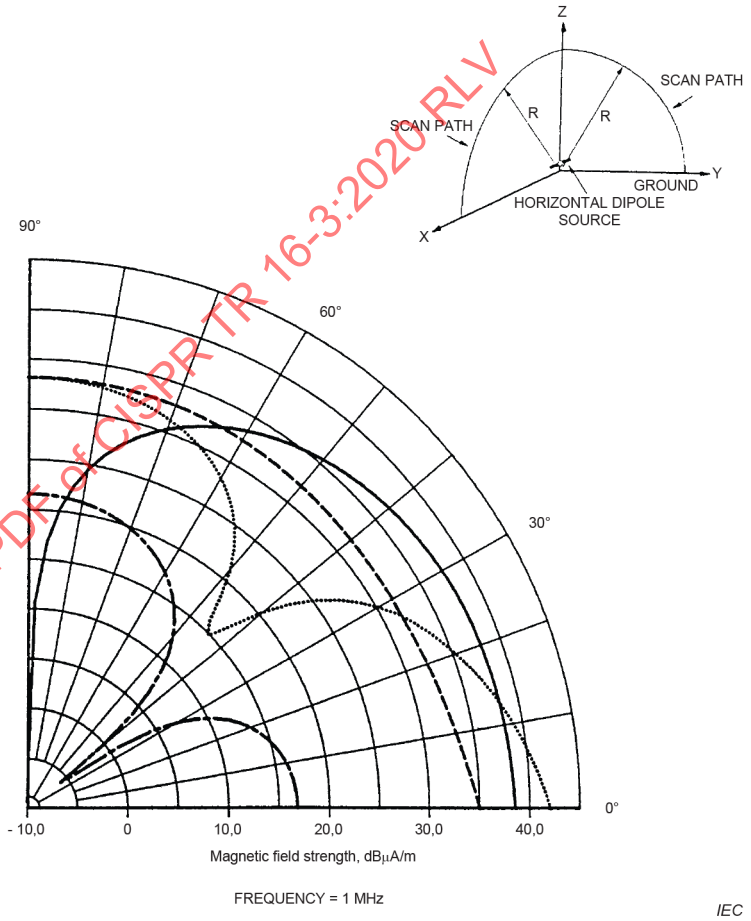
**Figure 76 – Vertical radiation patterns of the $E$-fields emitted by a small vertical magnetic dipole (horizontal loop) located close to the ground**

IECNORM.COM : Click to view the full PDF of CISPR TR 16-3:2020 RLV




Dipole length 3 m. Dipole base at a height above ground of 0,15 m. Dipole moment 1 A·m. Dashed line curve – $H_y$ at a scan distance of 30 m. Dotted line curve – $H_y$ at a scan distance of 30 m. Dash-dot line curve – $H_y$ at a scan distance of 300 m. Electrical constants of the ground $\sigma$ = 1 mS/m, $\varepsilon_r$ = 15. Perfectly conducting ground.

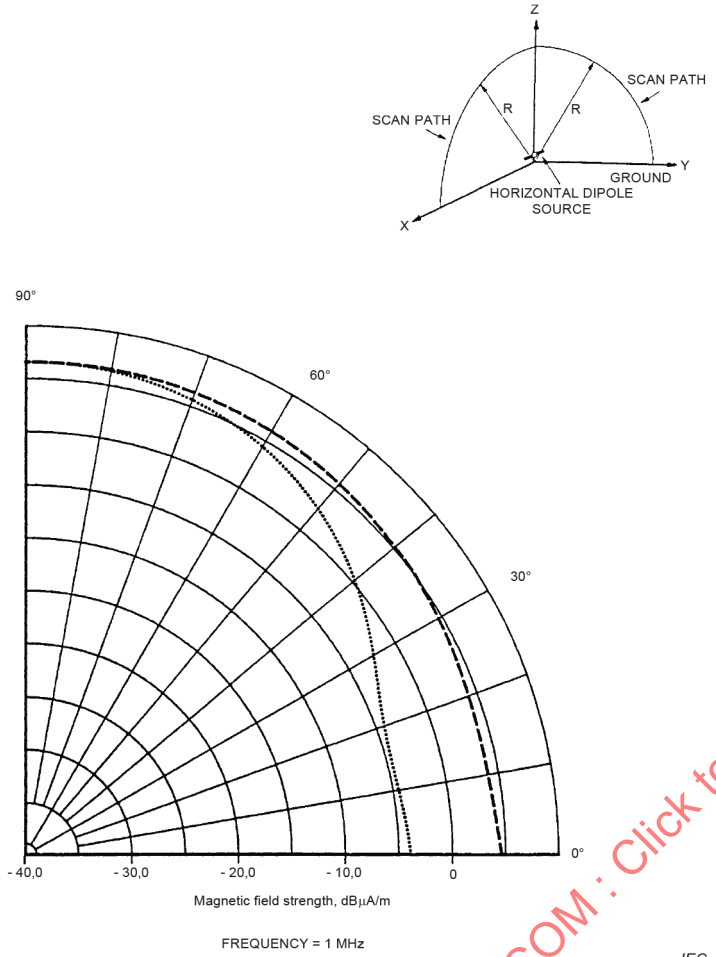
**Figure 77 – Vertical radiation patterns of the horizontally oriented *H*-fields emitted by a small vertical electric dipole located close to the ground**




Dipole length 3 m. Dipole base at a height above ground of 0,15 m. Dipole moment 1 A·m. Dashed line curve – vertically oriented $E_z$ at a scan distance of 30 m. Dotted line curve – horizontally oriented $E_x$ at a scan distance of 30 m. Electrical constants of the ground $\sigma$ = 1 mS/m, $\varepsilon_r$ = 15.

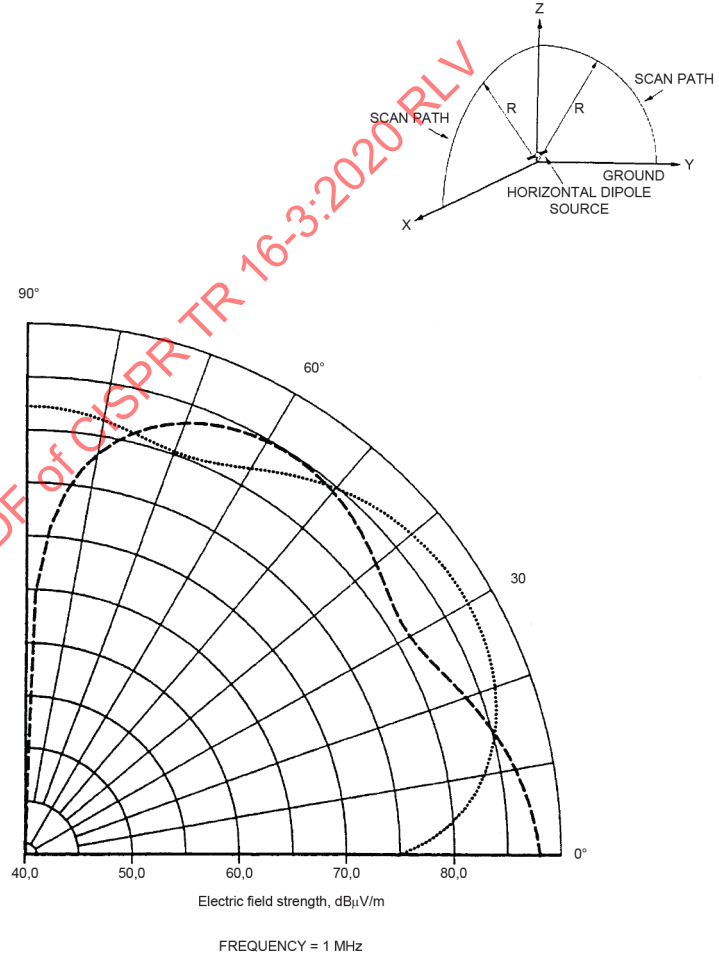
**Figure 78 – Vertical radiation patterns of the *E*-fields emitted by a small vertical electric dipole located close to the ground**

IECNORM.COM : Click to view the full PDF of CISPR TR 16-3:2020 RLV




Dipole length 3 m. Dipole base at a height above ground of 0,15 m. Dipole moment 1 A·m. Dashed line curve – vertically oriented $E_z$ at a scan distance of 300 m. Dotted line curve– horizontally oriented $E_x$ at a scan distance of 300 m. Dash-dot line curve – total vector/phasor sum of $E_z$ and $E_x$ at a scan distance of 300 m, the vertically polarized $E$-field. Electrical constants of the ground $\sigma$ = 1 mS/m, $\varepsilon_r$ = 15.

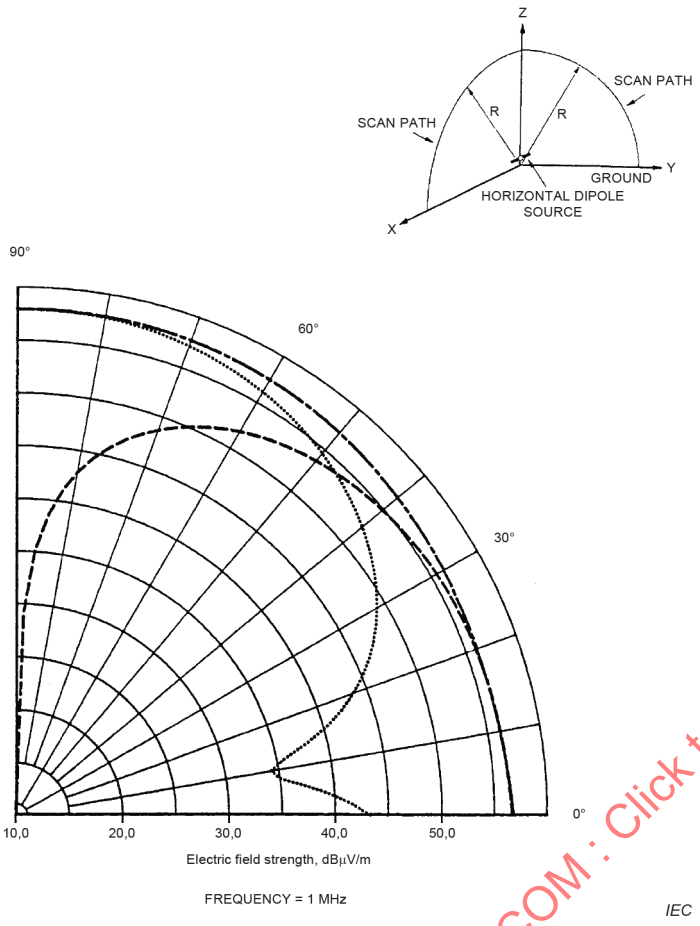
**Figure 79 – Vertical radiation patterns of the $E$-fields emitted by a small vertical electric dipole located close to the ground**




Dipole length 3 m. Dipole height above ground 1 m. Dipole moment 1 A·m. Dashed line curve – horizontally oriented $H_y$ at a scan distance of 30 m in the Z-X plane. Dotted line curve – horizontally oriented $H_y$ at a scan distance of 30 m in the Y-Z plane. Dash-dot line curve – horizontally oriented $H_y$ at a scan distance of 30 m in the Z-X plane. Solid line curve – vertically oriented $H_z$ at a scan distance of 30 m in the Y-Z plane. Electrical constants of the ground $\sigma$ = 1 mS/m, $\varepsilon_r$ = 15. Perfectly conducting ground.

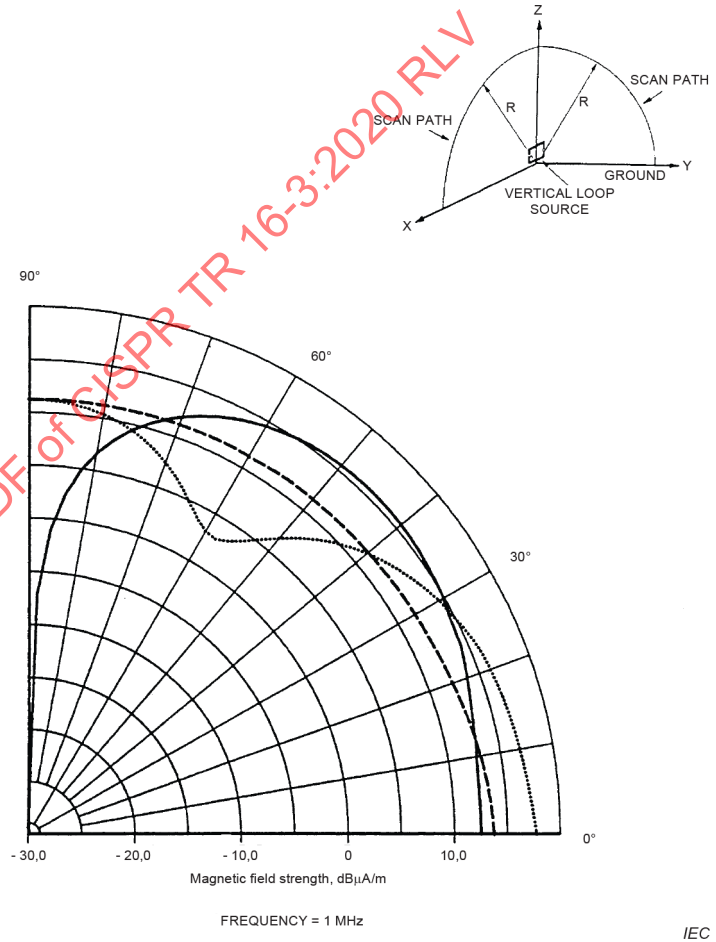
**Figure 80 – Vertical radiation patterns of the $H$-fields emitted by a small horizontal electric dipole located close to the ground**

IECNORM.COM : Click to view the full PDF of CISPR TR 16-3:2020 RLV




Dipole length 3 m. Dipole height above ground 1 m. Dipole moment 1 A·m. Dashed line curve – $H_y$ at a scan distance of 300 m in the Z-X plane. Dotted line curve – $H_y$ at a scan distance of 300 m in the Y-Z plane. Electrical constants of the ground $\sigma$ = 1 mS/m, $\varepsilon_r$ = 15.

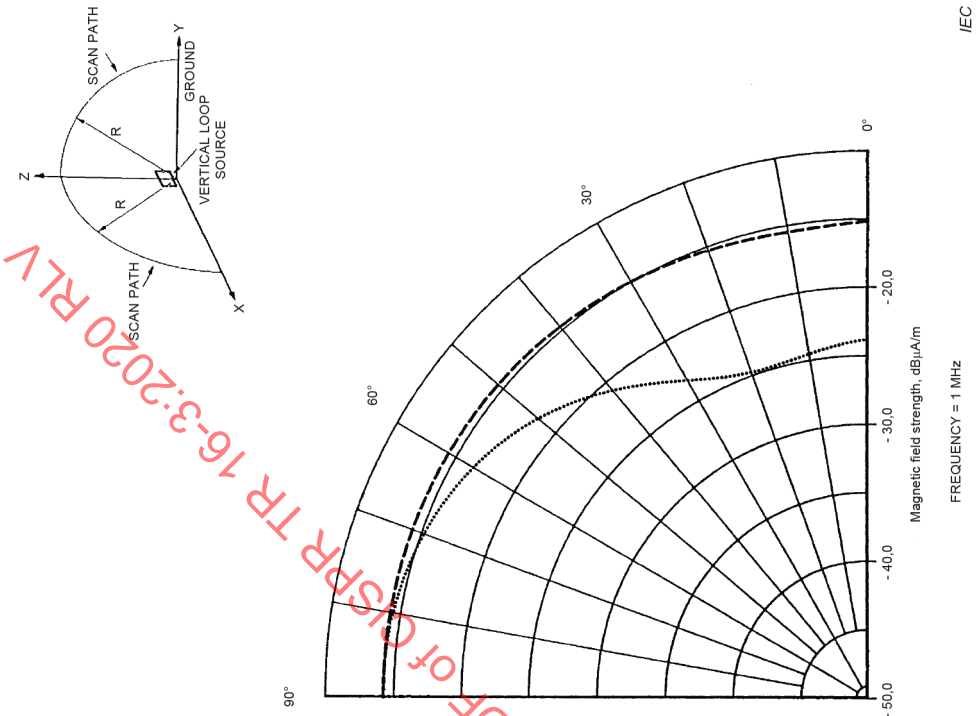
**Figure 81 – Vertical radiation patterns of the horizontally oriented *H*-fields emitted by a small horizontal electric dipole located close to the ground**

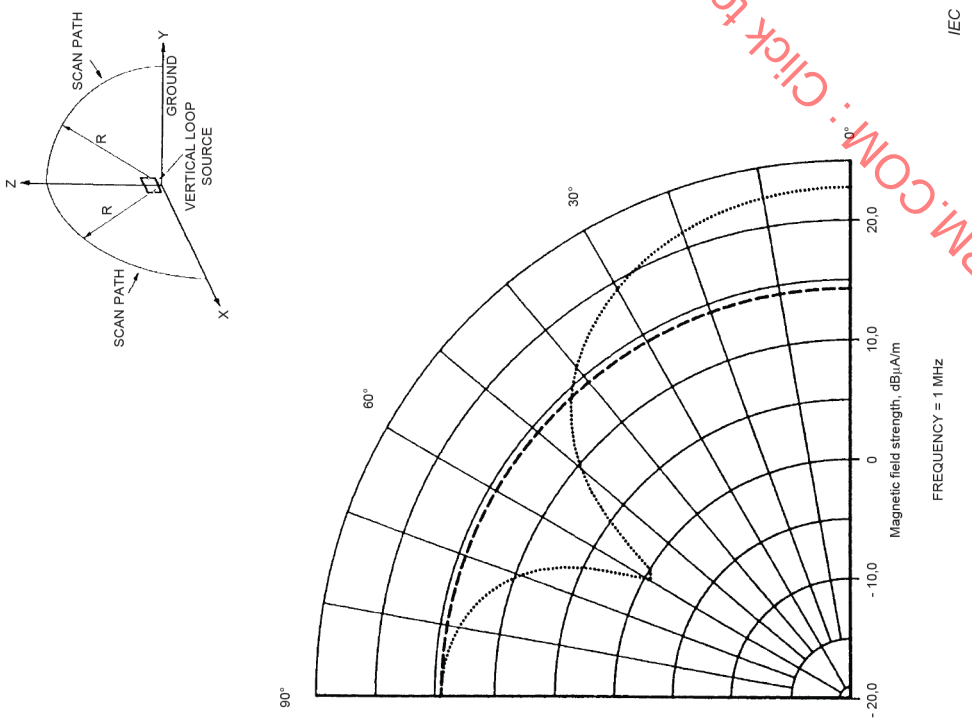



Dipole length 3 m. Dipole height above ground 1 m. Dipole moment 1 A·m. Dashed line curve – vertically oriented $E_z$ at a scan distance of 30 m in the Z-X plane. Dotted line curve – horizontally oriented $E_x$ at a scan distance of 30 m in the Z-X plane. Electrical constants of the ground $\sigma$ = 1 mS/m, $\varepsilon_r$ = 15.

**Figure 82 – Vertical radiation patterns of the *E*-fields emitted by a small horizontal electric dipole located close to the ground**

IECNORM.COM : Click to view the full PDF of CISPR TR 16-3:2020 RLV




IECNORM.COM : Click to view the full PDF of CISPR TR 16-3:2020 RLV

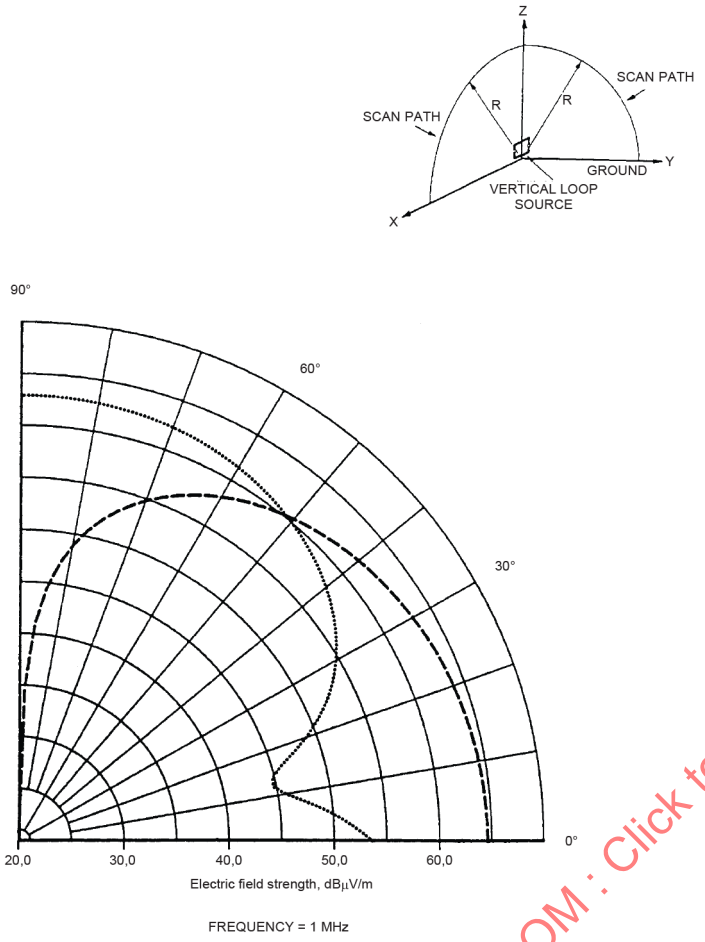
Dipole length 3 m. Dipole height above ground 1 m. Dipole moment 1 A·m. Dashed line curve – vertically oriented $E_z$ at a scan distance of 300 m in the Z-X plane. Dotted line curve – horizontally oriented $E_x$ at a scan distance of 300 m in the Z-X plane. Dash-dot line curve – total vector/phasor sum of $E_z$ and $E_x$ at a scan distance of 300 m in the Z-X plane, the vertically polarized $E$-field. Electrical constants of the ground $\sigma$ = 1 mS/m, $\varepsilon_r$ = 15.

**Figure 83 – Vertical radiation patterns of the $E$-fields emitted by a small horizontal electric dipole located close to the ground**

Square loop 3 m × 3 m. Loop base height above ground 0,15 m. Dipole moment 1 A·m$^2$. Dashed line curve – horizontally oriented $H_y$ at a scan distance of 30 m in the Z-X plane. Dotted line curve – horizontally oriented $H_y$ at a scan distance of 30 m in the Y-Z plane. Solid line curve – vertically oriented $H_z$ at a scan distance of 30 m in the Y-Z plane. Electrical constants of the ground $\sigma$ = 1 mS/m, $\varepsilon_r$ = 15.

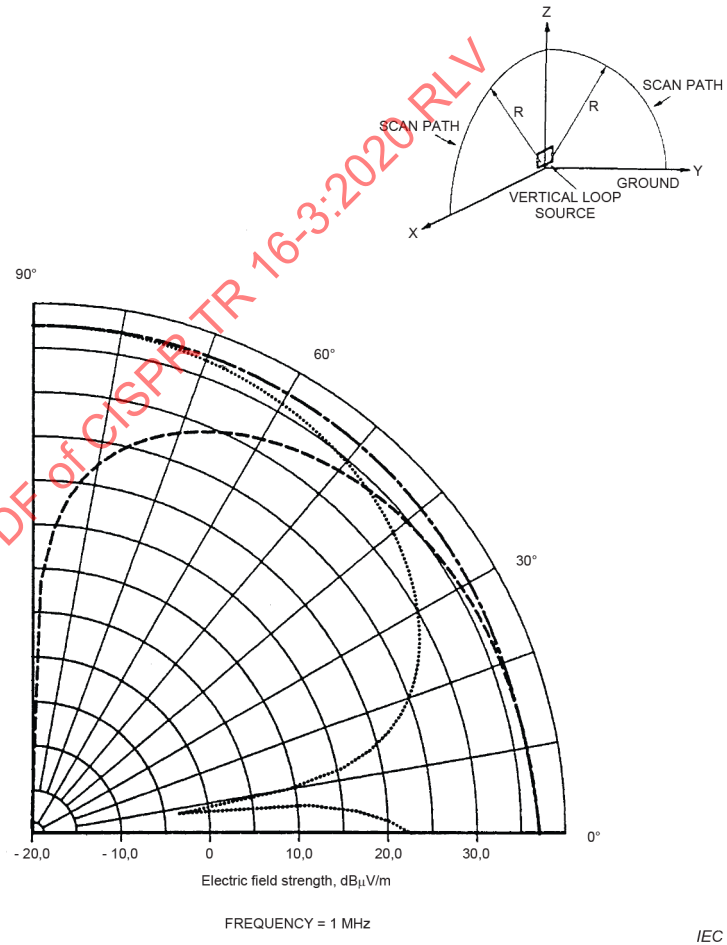
**Figure 84 – Vertical radiation patterns of the $H$-fields emitted by a small horizontal magnetic dipole (vertical loop) located close to the ground**

IECNORM.COM : Click to view the full PDF of CISPR TR 16-3:2020 RLV




Square loop 3 m × 3 m. Loop base height above ground 0,15 m. Dipole moment 1 A·m$^2$. Dashed line curve – $H_y$ at a scan distance of 30 m in the Z-X plane. Dotted line curve – $H_y$ at a scan distance of 30 m in the Y-Z plane. Perfectly conducting ground.

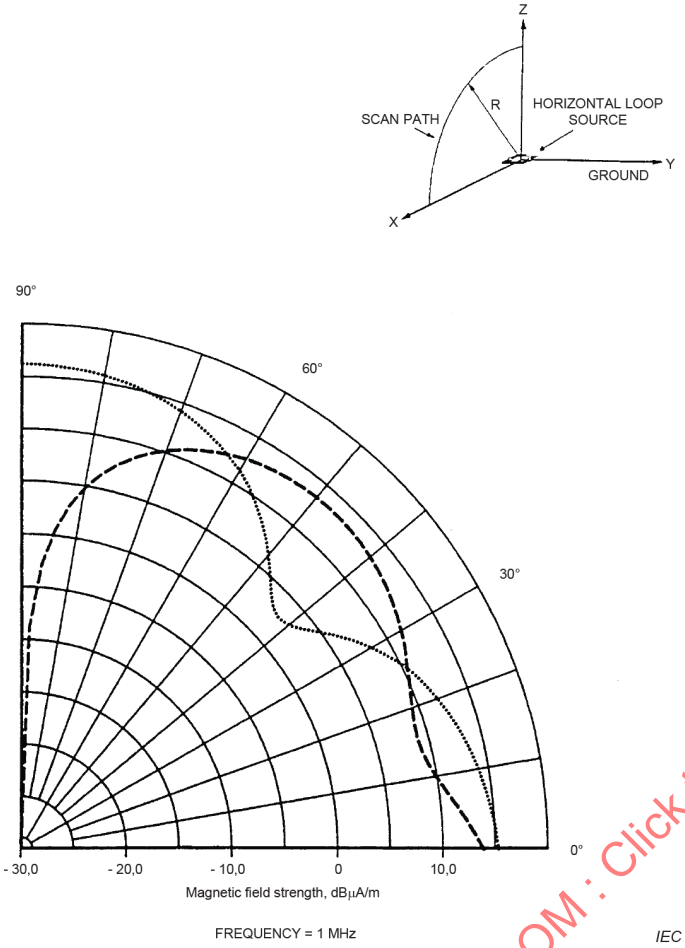
**Figure 85 – Vertical radiation patterns of the horizontally oriented *H*-fields emitted by a small horizontal magnetic dipole (vertical loop) located close to the ground**




Square loop 3 m × 3 m. Loop base height above ground 0,15 m. Dipole moment 1 A·m$^2$. Dashed line curve – $H_y$ at a scan distance of 300 m in the Z-X plane. Dotted line curve – $H_y$ at a scan distance of 300 m in the Y-Z plane. Electrical constants of the ground $\sigma$ = 1 mS/m, $\varepsilon_r$ = 15.

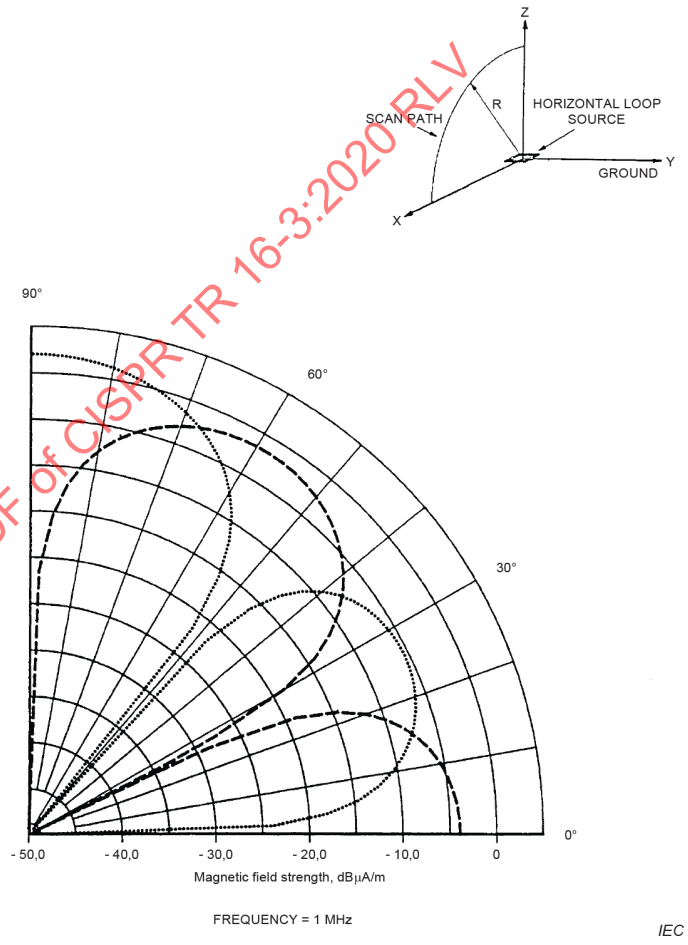
**Figure 86 – Vertical radiation patterns of the horizontally oriented *H*-fields emitted by a small horizontal magnetic dipole (vertical loop) located close to the ground**

IECNORM.COM : Click to view the full PDF of CISPR TR 16-3:2020 RLV




Square loop 3 m × 3 m. Loop base height above ground 0,15 m. Dipole moment 1 A·m$^2$. Dashed line curve – vertically oriented $E_z$ at a scan distance of 30 m in the Z-X plane. Dotted line curve – horizontally oriented $E_x$ at a scan distance of 30 m in the Z-X plane. Electrical constants of the ground $\sigma$ = 1 mS/m, $\varepsilon_r$ = 15.

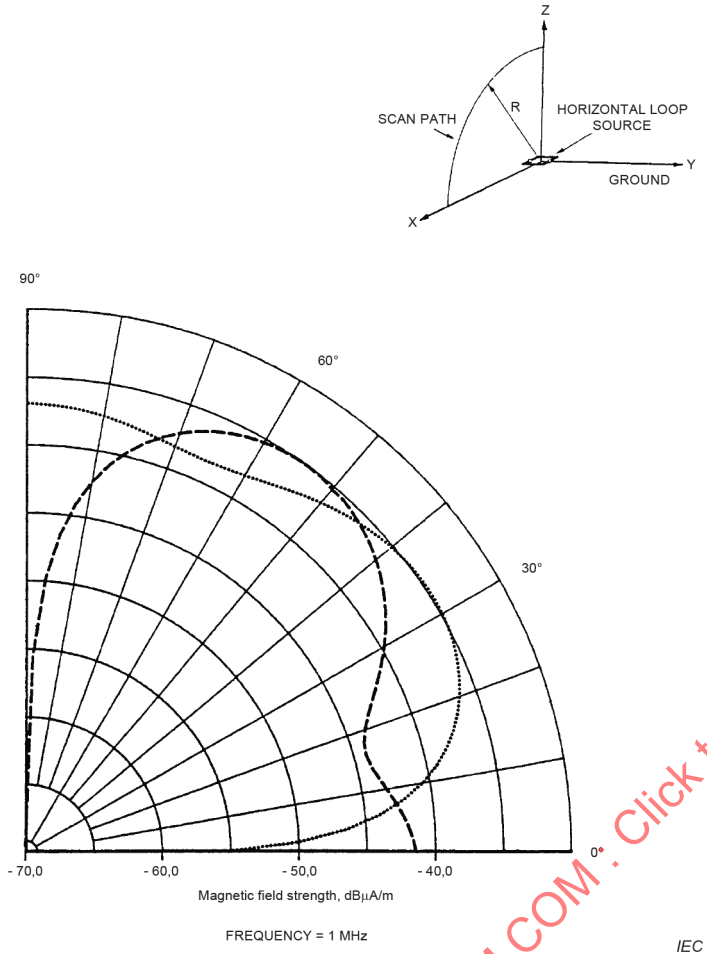
**Figure 87 – Vertical radiation patterns of the *E*-fields emitted by a small horizontal magnetic dipole (vertical loop) located close to the ground**




Square loop 3 m × 3 m. Loop base height above ground 0,15 m. Dipole moment 1 A·m$^2$. Dashed line curve – vertically oriented $E_z$ at a scan distance of 300 m in the Z-X plane. Dotted line curve – horizontally oriented $E_x$ at a scan distance of 300 m in the Z-X plane. Dash-dot line curve – total vector/phasor sum of $E_z$ and $E_x$ at a scan distance of 300 m in the Z-X plane, the vertically polarized $E$-field. Electrical constants of the ground $\sigma$ = 1 mS/m, $\varepsilon_r$ = 15.

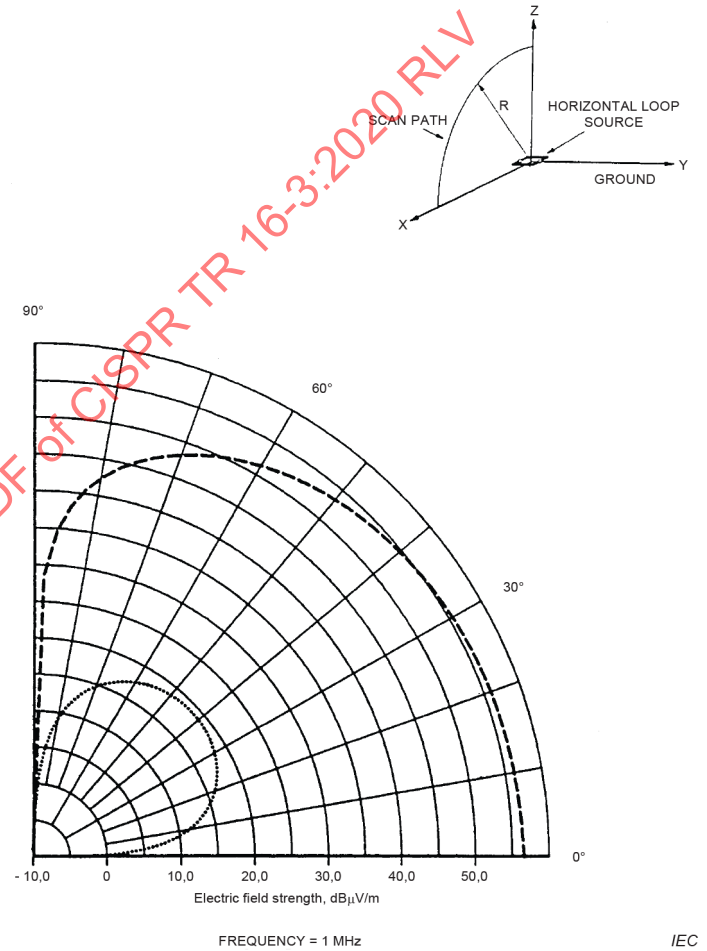
**Figure 88 – Vertical radiation patterns of the *E*-fields emitted by a small horizontal magnetic dipole (vertical loop) located close to the ground**

IECNORM.COM : Click to view the full PDF of CISPR TR 16-3:2020 RLV




Square loop 3 m × 3 m. Loop height above ground 1 m. Dipole moment 1 A·m$^2$.Dashed line curve – horizontally oriented $H_x$ at a scan distance of 30 m. Dotted line curve – vertically oriented $H_z$ at a scan distance of 30 m. Electrical constants of the ground $\sigma$ = 1 mS/m, $\varepsilon_r$ = 15.

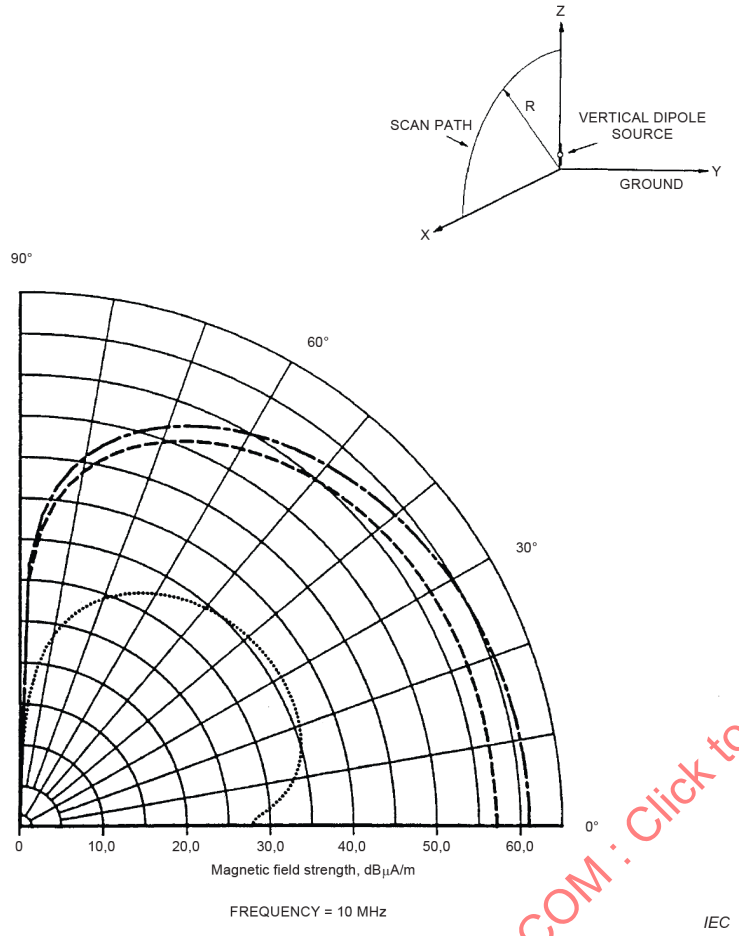
**Figure 89 – Vertical radiation patterns of the *H*-fields emitted by a small vertical magnetic dipole (horizontal loop) located close to the ground**




Square loop 3 m × 3 m. Loop height above ground 1 m. Dipole moment 1 A·m$^2$. Dashed line curve – horizontally oriented $H_x$ at a scan distance of 30 m. Dotted line curve – vertically oriented $H_z$ at a scan distance of 30 m. Perfectly conducting ground.

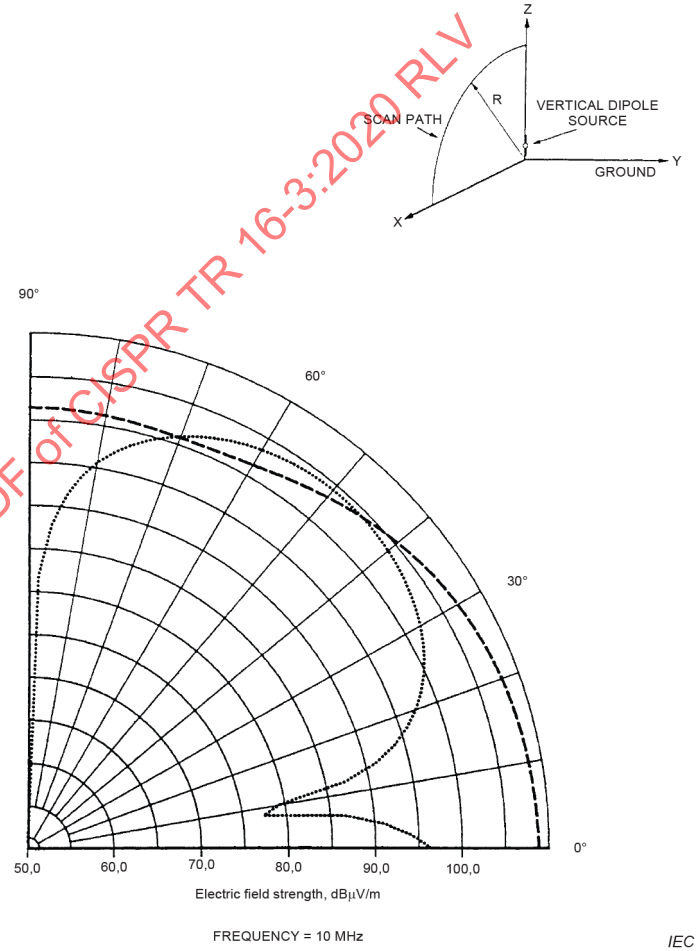
**Figure 90 – Vertical radiation patterns of the *H*-fields emitted by a small vertical magnetic dipole (horizontal loop) located close to the ground**

IECNORM.COM : Click to view the full PDF of CISPR TR 16-3:2020 RLV




Square loop 3 m × 3 m. Loop height above ground 1 m. Dipole moment 1 A·m$^2$. Dashed line curve – horizontally oriented $H_x$ at a scan distance of 300 m. Dotted line curve – vertically oriented $H_z$ at a scan distance of 300 m. Electrical constants of the ground $\sigma$ = 1 mS/m, $\varepsilon_r$ = 15.

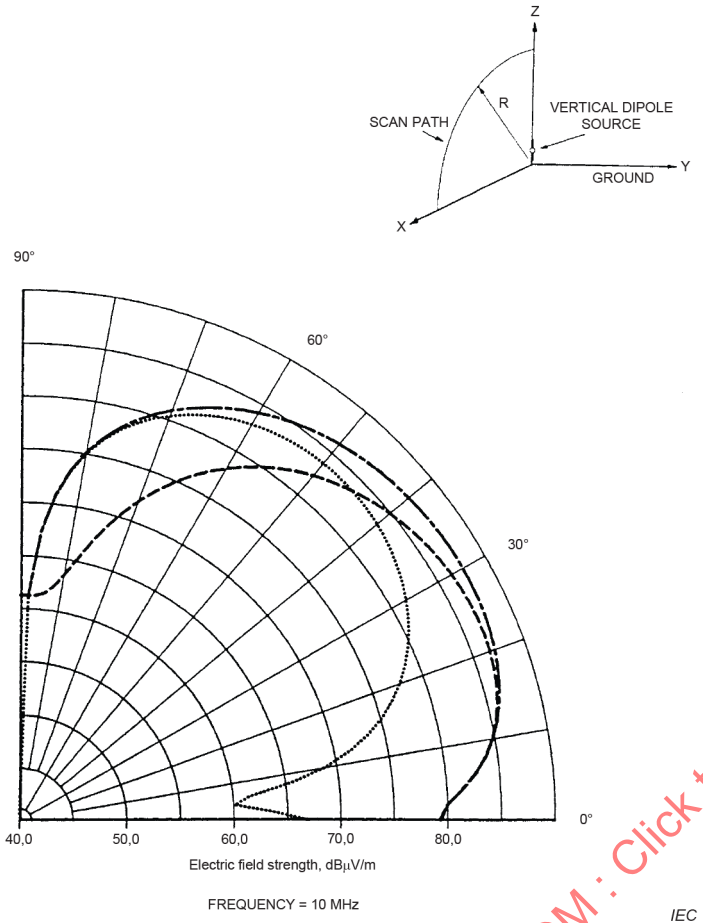
**Figure 91 – Vertical radiation patterns of the *H*-fields emitted by a small vertical magnetic dipole (horizontal loop) located close to the ground**




Square loop 3 m × 3 m. Loop height above ground 1 m. Dipole moment 1 A·m$^2$. Dashed line curve – horizontally oriented $E_y$ at a scan distance of 30 m. Dotted line curve – horizontally oriented $E_y$ at a scan distance of 300 m. Electrical constants of the ground $\sigma$ = 1 mS/m, $\varepsilon_r$ = 15.

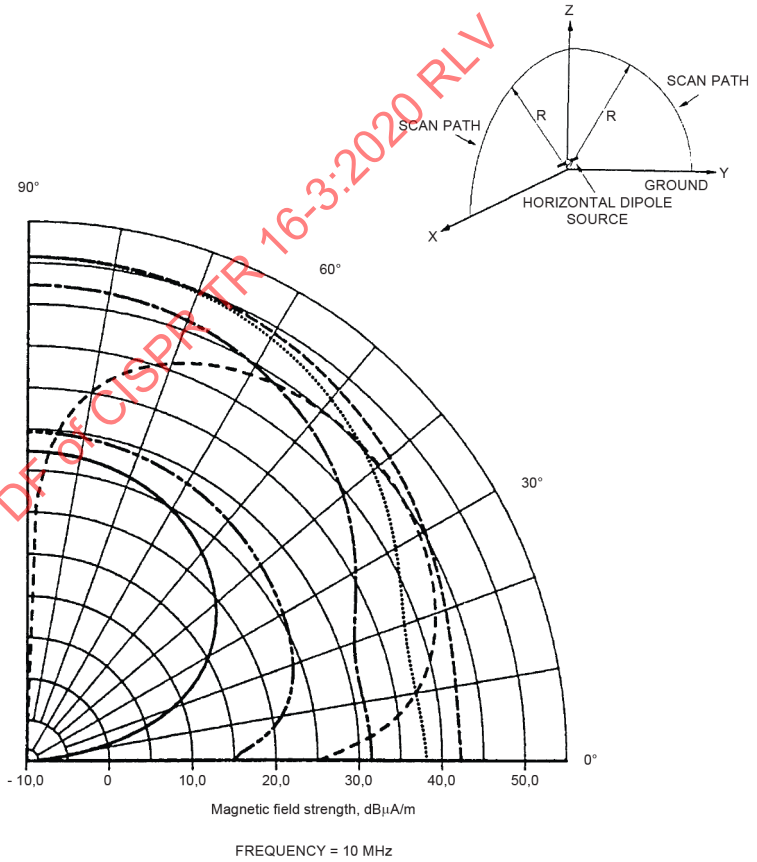
**Figure 92 – Vertical radiation patterns of the *E*-fields emitted by a small vertical magnetic dipole (horizontal loop) located close to the ground**

IECNORM.COM : Click to view the full PDF of CISPR TR 16-3:2020 RLV




Dipole length 1 m. Dipole base at a height above ground of 0,15 m. Dipole moment 1 A·m. Dashed line curve – $H_y$ at a scan distance of 30 m. Dotted line curve – $H_y$ at a scan distance of 300 m. Dash-dot line curve – $H_y$ at a scan distance of 30 m. Electrical constants of the ground $\sigma$ = 1 mS/m, $\varepsilon_r$ = 15. Perfectly conducting ground.

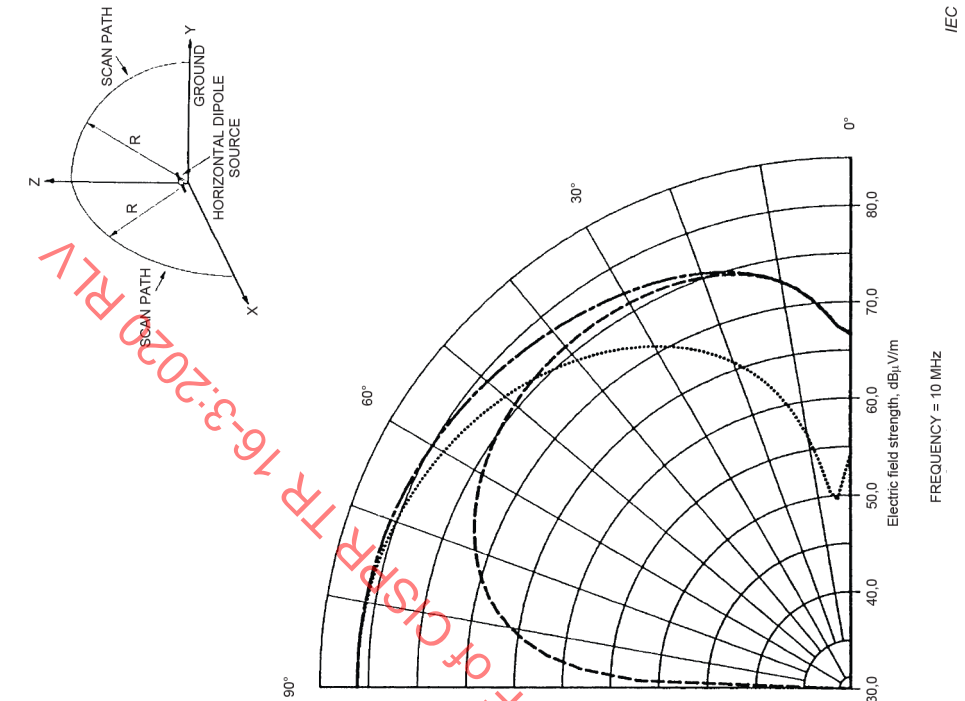
**Figure 93 – Vertical radiation patterns of the horizontally oriented *H*-fields emitted by a small vertical electric dipole located close to the ground**

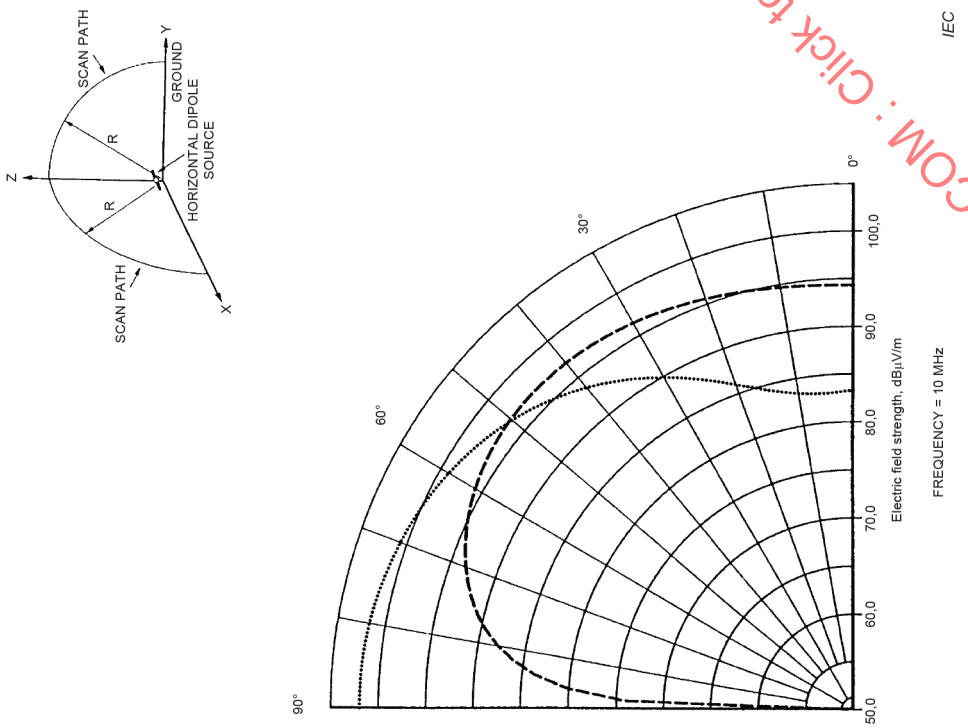



Dipole length 1 m. Dipole base at a height above ground of 0,15 m. Dipole moment 1 A·m. Dashed line curve – vertically oriented $E_z$ at a scan distance of 30 m. Dotted line curve – horizontally oriented $E_x$ at a scan distance of 30 m. Electrical constants of the ground $\sigma$ = 1 mS/m, $\varepsilon_r$ = 15.

**Figure 94 – Vertical radiation patterns of the *E*-fields emitted by a small vertical electric dipole located close to the ground**

IECNORM.COM : Click to view the full PDF of CISPR TR 16-3:2020 RLV




IECNORM.COM : Click to view the full PDF of CISPR TR 16-3:2020 RLV

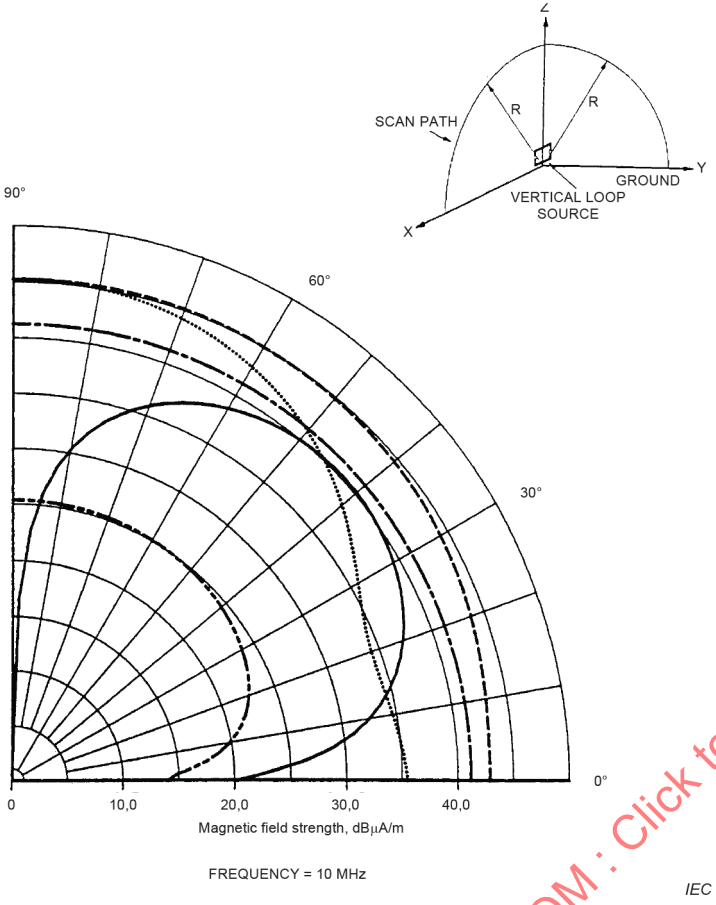
Dipole length 1 m. Dipole base at a height above ground of 0,15 m. Dipole moment 1 A·m. Dashed line curve – vertically oriented $E_z$ at a scan distance of 300 m. Dotted line curve – horizontally oriented $E_x$ at a scan distance of 300 m. Dash-dot line curve – total vector/phasor sum of $E_z$ and $E_x$ at a scan distance of 300 m, the vertically polarized $E$-field. Electrical constants of the ground $\sigma$ = 1 mS/m, $\varepsilon_r$ = 15.

**Figure 95 – Vertical radiation patterns of the $E$-fields emitted by a small vertical electric dipole located close to the ground**

Dipole length 1 m. Dipole height above ground 1 m. Dipole moment 1 A·m. Long-dash line curve – horizontally oriented $H_y$ at a scan distance of 30 m in the Z-X plane. Short-dash line curve – vertically oriented $H_z$ at a scan distance of 30 m in the Y-Z plane. Dotted line curve – horizontally oriented $H_y$ at a scan distance of 30 m in the Y-Z plane. Dash-double-dot curve – horizontally oriented $H_y$ at a scan distance of 300 m in the Z-X plane. Dash-dot line curve – horizontally oriented $H_y$ at a scan distance of 30 m in the Z-X plane. Solid line curve – horizontally oriented $H_y$ at a scan distance of 300 m in the Z-X plane. Electrical constants of the ground $\sigma$ = 1 mS/m, $\varepsilon_r$ = 15. Perfectly conducting ground.

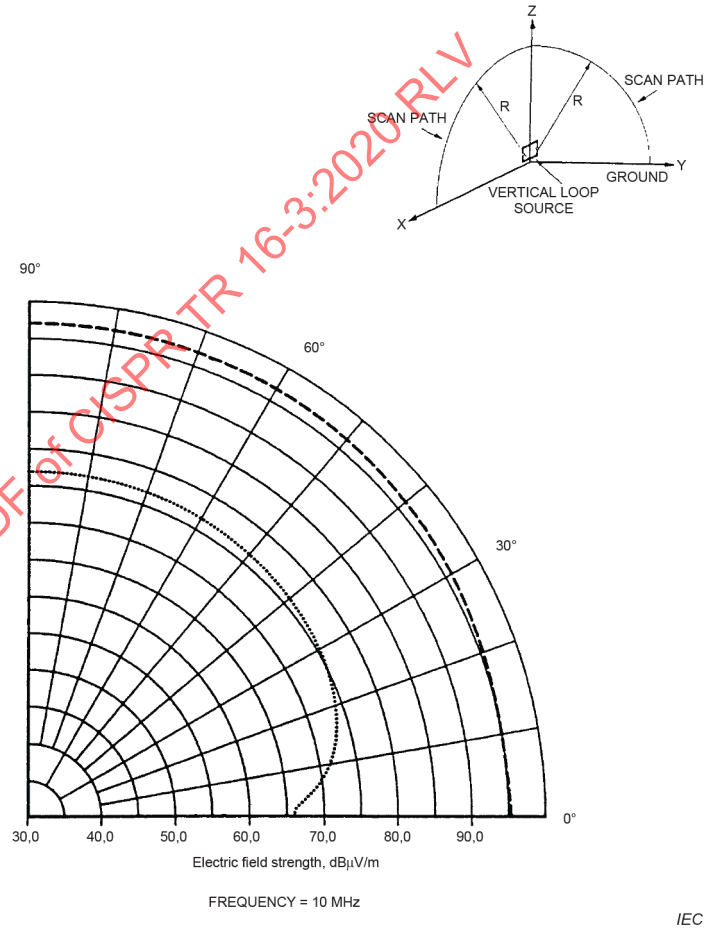
**Figure 96 – Vertical radiation patterns of the $H$-fields emitted by a small horizontal electric dipole located close to the ground**

IECNORM.COM : Click to view the full PDF of CISPR TR 16-3:2020 RLV




Dipole length 1 m. Dipole height above ground 1 m. Dipole moment 1 A·m. Dashed line curve – vertically oriented $E_z$ at a scan distance of 30 m in the Z-X plane. Dotted line curve – horizontally oriented $E_x$ at a scan distance of 30 m in the Z-X plane. Electrical constants of the ground $\sigma$ = 1 mS/m, $\varepsilon_r$ = 15.

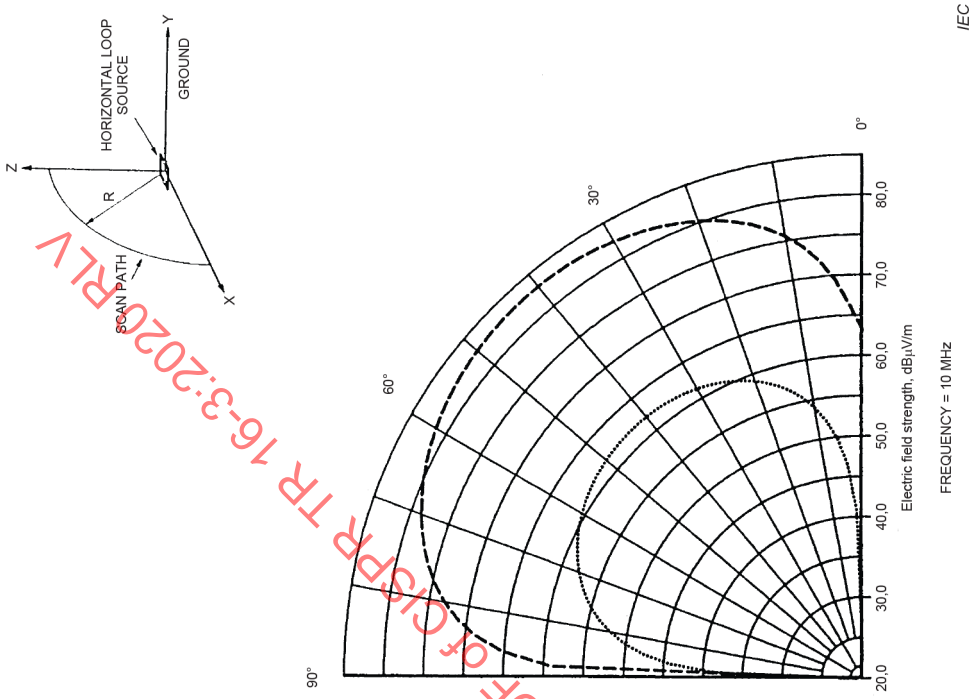
**Figure 97 – Vertical radiation patterns of the *E*-fields emitted by a small horizontal electric dipole located close to the ground**

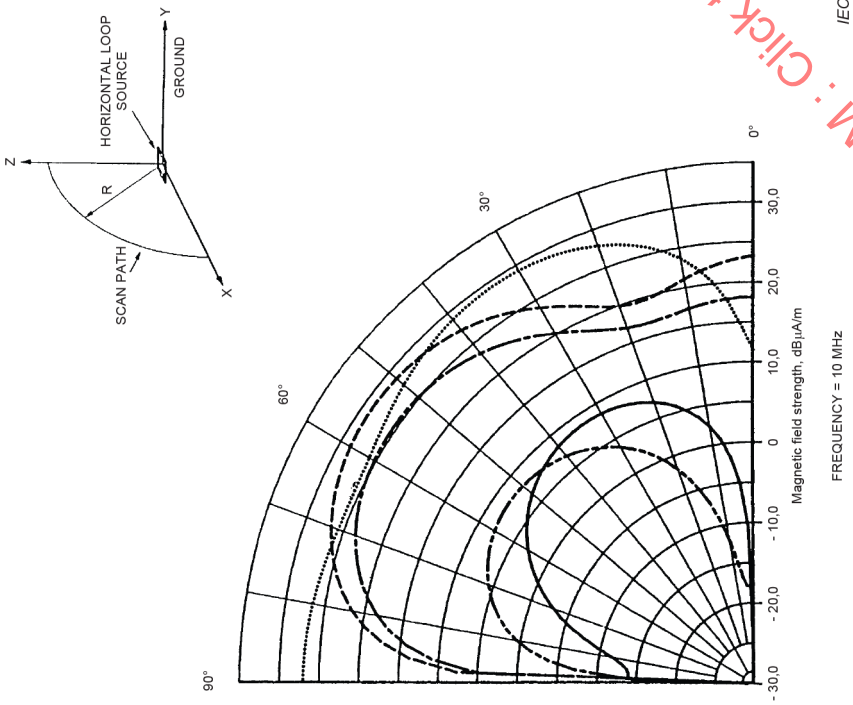



Dipole length 1 m. Dipole height above ground 1 m. Dipole moment 1 A·m. Dashed line curve – vertically oriented $E_z$ at a scan distance of 300 m in the Z-X plane. Dotted line curve – horizontally oriented $E_x$ at a scan distance of 300 m in the Z-X plane. Dash-dot line curve – total vector/phasor sum of $E_z$ and $E_x$ at a scan distance of 300 m in the Z-X plane, the vertically polarized $E$-field. Electrical constants of the ground $\sigma$ = 1 mS/m, $\varepsilon_r$ = 15.

**Figure 98 – Vertical radiation patterns of the *E*-fields emitted by a small horizontal electric dipole located close to the ground**

IECNORM.COM : Click to view the full PDF of CISPR TR 16-3:2020 RLV




IECNORM.COM : Click to view the full PDF of CISPR TR 16-3:2020 RLV

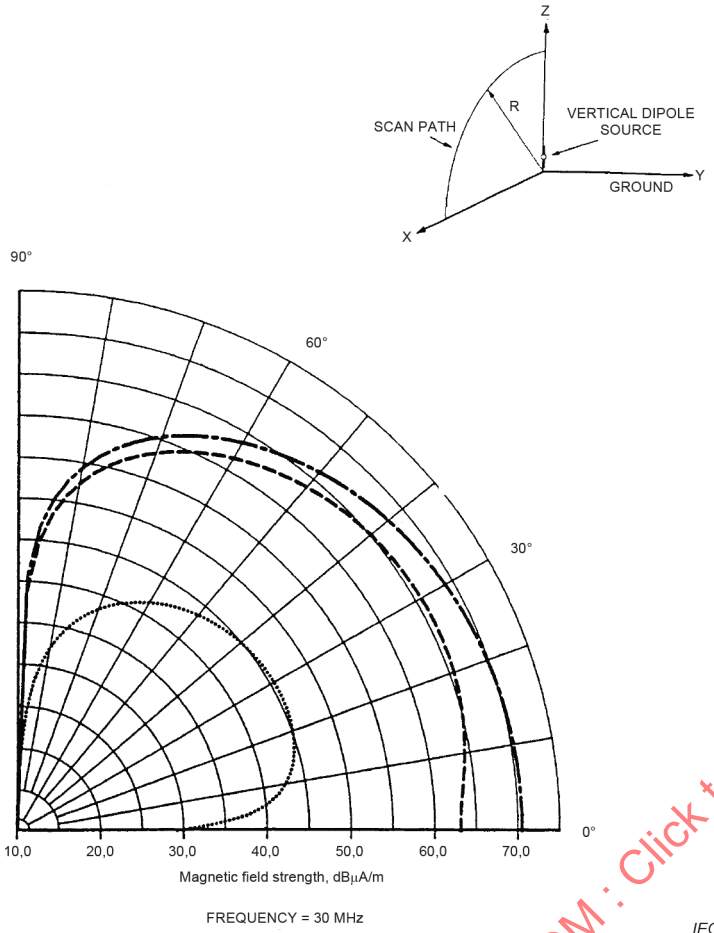
Square loop 0,6 m × 0,6 m. Loop base height above ground 0,07 m. Dipole moment 1 A·m$^2$. Dashed line curve – horizontally oriented $H_y$ at a scan distance of 30 m in the Z-X plane. Dotted line curve – horizontally oriented $H_y$ at a scan distance of 30 m in the Y-Z plane. Solid line curve – vertically oriented $H_z$ at a scan distance of 30 m in the Y-Z plane. Dash-double-dot curve – horizontally oriented $H_y$ at a scan distance of 300 m in the Z-X plane. Dash-dot line curve – horizontally oriented $H_y$ at a scan distance of 30 m in the Z-X plane. Electrical constants of the ground $\sigma$ = 1 mS/m, $\varepsilon_r$ = 15. Perfectly conducting ground.

**Figure 99 – Vertical radiation patterns of the *H*-field emitted by a small horizontal magnetic dipole (vertical loop) located close to the ground**

Square loop 0,6 m × 0,6 m. Loop base height above ground 0,07 m. Dipole moment 1 A·m$^2$. Dashed line curve – total vector/phasor sum of $E_z$ and $E_x$ at a scan distance of 30 m in the Z-X plane, the vertically polarized $E$-field. Dotted line curve – total vector/phasor sum of $E_z$ and $E_x$ at a scan distance of 300 m in the Z-X plane, the vertically polarized $E$-field. Electrical constants of the ground $\sigma$ = 1 mS/m, $\varepsilon_r$ = 15.

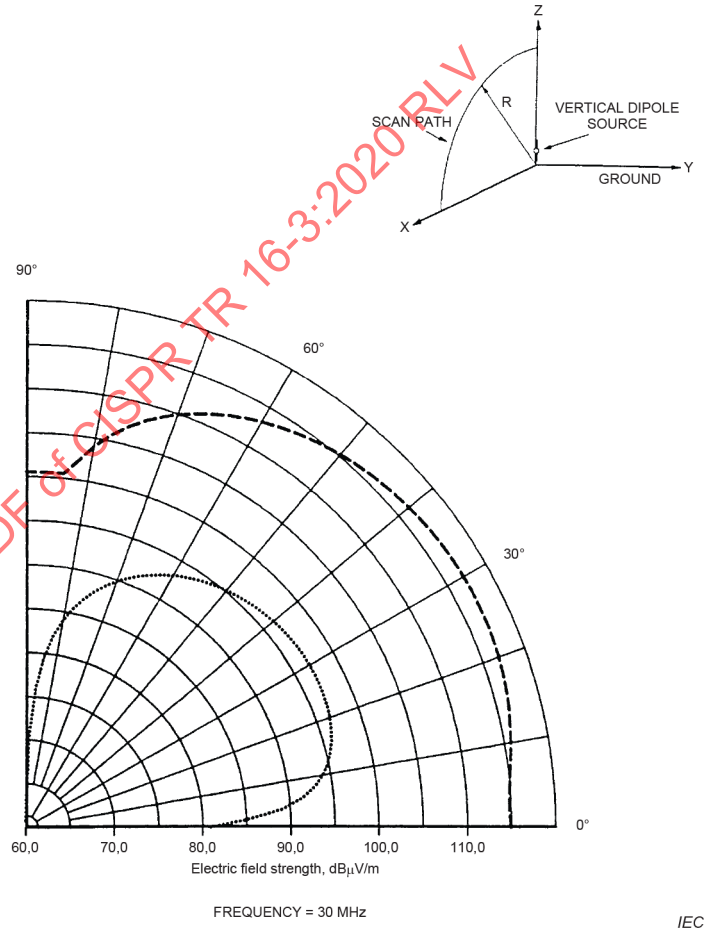
**Figure 100 – Vertical radiation patterns of the vertically polarized *E*-fields emitted by a small horizontal magnetic dipole (vertical loop) located close to the ground**

IECNORM.COM : Click to view the full PDF of CISPR TR 16-3:2020 RLV




Square loop 0,2 m × 0,2 m. Loop height above ground 1 m. Dipole moment 1 A·m$^2$. Dashed line curve – horizontally oriented $H_x$ at a scan distance of 30 m. Dotted line curve – vertically oriented $H_z$ at a scan distance of 30 m. Dash-double-dot curve – horizontally oriented $H_x$ at a scan distance of 300 m. Dash-dot line curve – horizontally oriented $H_x$ at a scan distance of 30 m. Solid line curve – vertically oriented $H_z$ at a scan distance of 300 m. Electrical constants of the ground $\sigma$ = 1 mS/m, $\varepsilon_r$ = 15. Perfectly conducting ground.

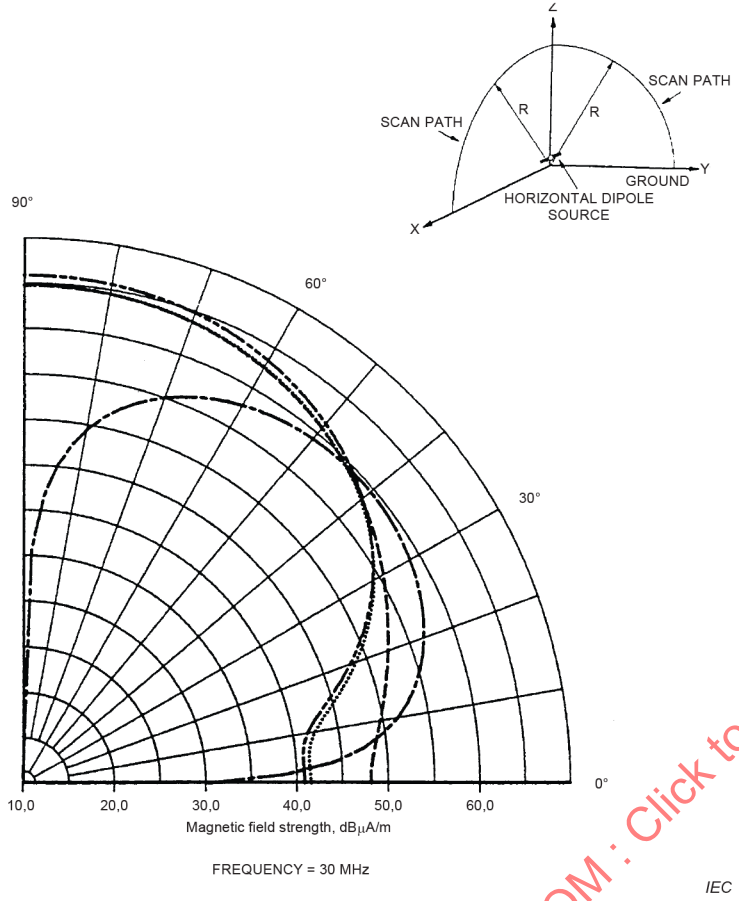
**Figure 101 – Vertical radiation patterns of the $H$-field emitted by a small vertical magnetic dipole (horizontal loop) located close to the ground**




Square loop 0,2 m × 0,2 m. Loop height above ground 1 m. Dipole moment 1 A·m$^2$. Dashed line curve – horizontally oriented $E_y$ at a scan distance of 30 m. Dotted line curve – horizontally oriented $E_y$ at a scan distance of 300 m. Electrical constants of the ground $\sigma$ = 1 mS/m, $\varepsilon_r$ = 15.

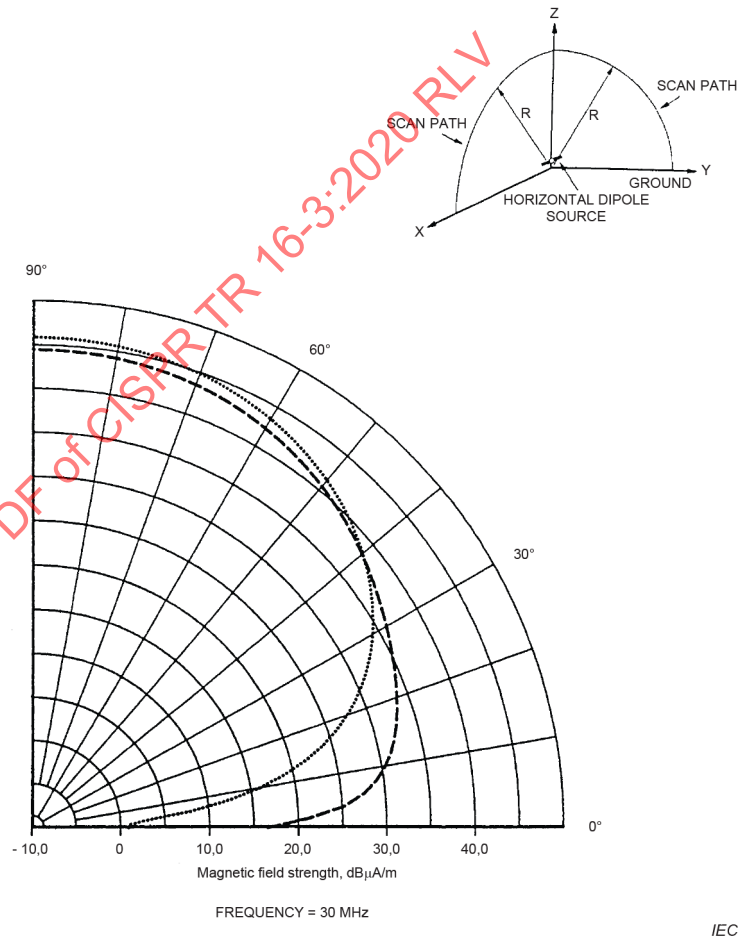
**Figure 102 – Vertical radiation patterns of the $E$-fields emitted by a small vertical magnetic dipole (horizontal loop) located close to the ground**

IECNORM.COM : Click to view the full PDF of CISPR TR 16-3:2020 RLV




Dipole length 1 m. Dipole base at a height above ground of 0,15 m. Dipole moment 1 A·m. Dashed line curve – $H_y$ at a scan distance of 30 m. Dotted line curve – $H_y$ at a scan distance of 300 m. Dash-dot line curve – $H_y$ at a scan distance of 30 m. Electrical constants of the ground $\sigma$ = 1 mS/m, $\varepsilon_r$ = 15. Perfectly conducting ground.

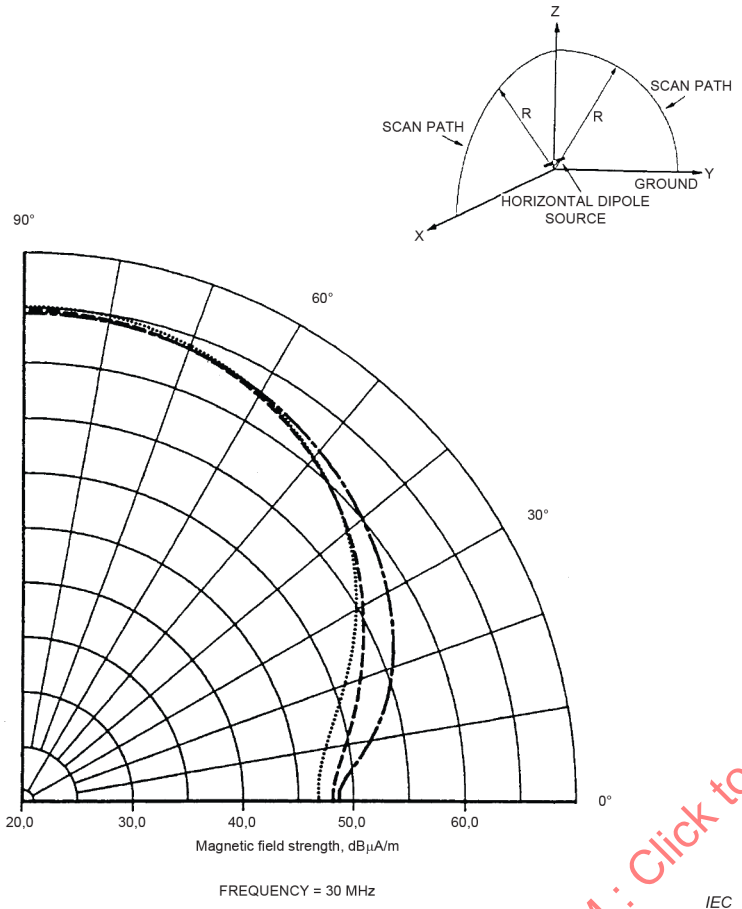
**Figure 103 – Vertical radiation patterns of the horizontally oriented *H*-fields emitted by a small vertical electric dipole located close to the ground**




Dipole length 1 m. Dipole base at a height above ground of 0,15 m. Dipole moment 1 A·m. Dashed line curve – total vector/phasor sum of $E_z$ and $E_x$ at a scan distance of 30 m in the Z-X plane, the vertically polarized $E$-field. Dotted line curve – total vector/phasor sum of $E_z$ and $E_x$ at a scan distance of 300 m in the Z-X plane, the vertically polarized $E$-field. Electrical constants of the ground $\sigma$ = 1 mS/m, $\varepsilon_r$ = 15.

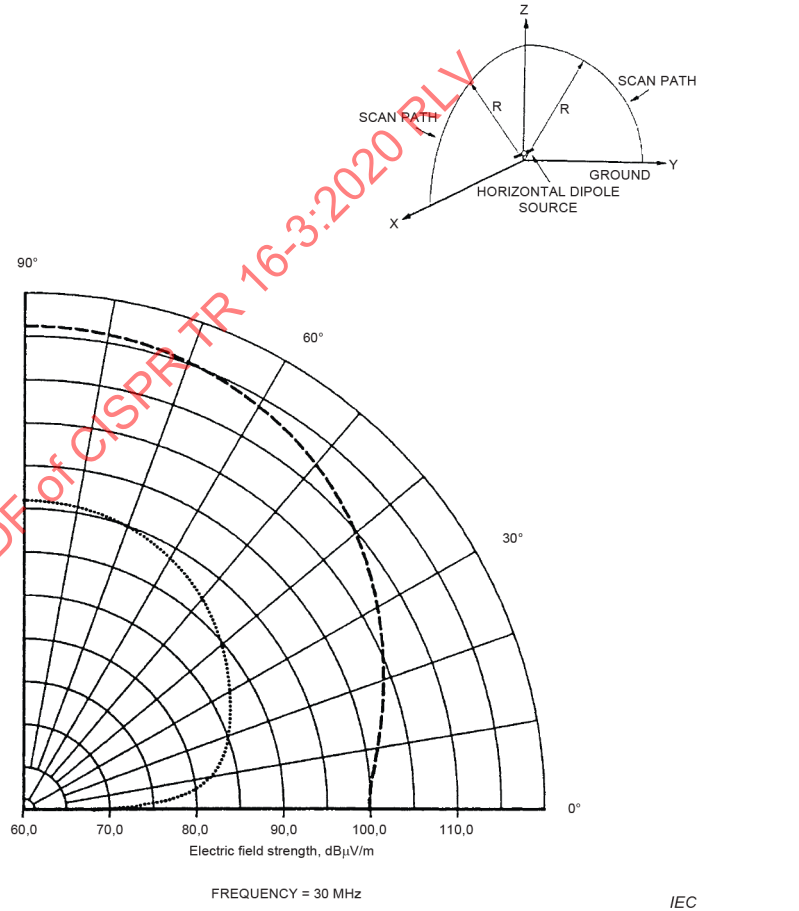
**Figure 104 – Vertical radiation patterns of the vertically polarized *E*-fields emitted by a small vertical electric dipole located close to the ground**

IECNORM.COM : Click to view the full PDF of CISPR TR 16-3:2020 RLV




Dipole length 1 m. Dipole height above ground 1 m. Dipole moment 1 A·m. Dashed line curve – horizontally oriented $H_y$ at a scan distance of 30 m in the Z-X plane. Dotted line curve – horizontally oriented $H_y$ at a scan distance of 30 m in the Y-Z plane. Dash-dot line curve – vertically oriented $H_z$ at a scan distance of 30 m in the Y-Z plane. Dash-double-dot curve – horizontally oriented $H_y$ at a scan distance of 30 m in the Z-X plane. Electrical constants of the ground $\sigma$ = 1 mS/m, $\varepsilon_r$ = 15. Perfectly conducting ground.

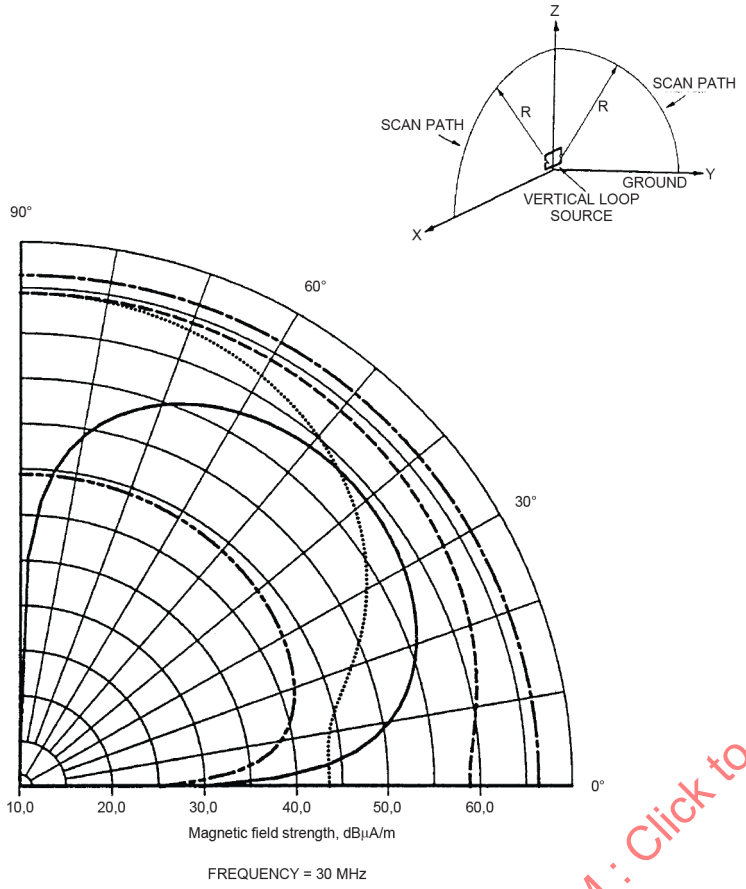
**Figure 105 – Vertical radiation patterns of the *H*-fields emitted by a small horizontal electric dipole located close to the ground**




Dipole length 1 m. Dipole height above ground 1 m. Dipole moment 1 A·m. Dashed line curve – $H_y$ at a scan distance of 300 m in the Z-X plane. Dotted line curve – $H_y$ at a scan distance of 300 m in the Z-X plane. Electrical constants of the ground $\sigma$ = 1 mS/m, $\varepsilon_r$ = 15. Perfectly conducting ground.

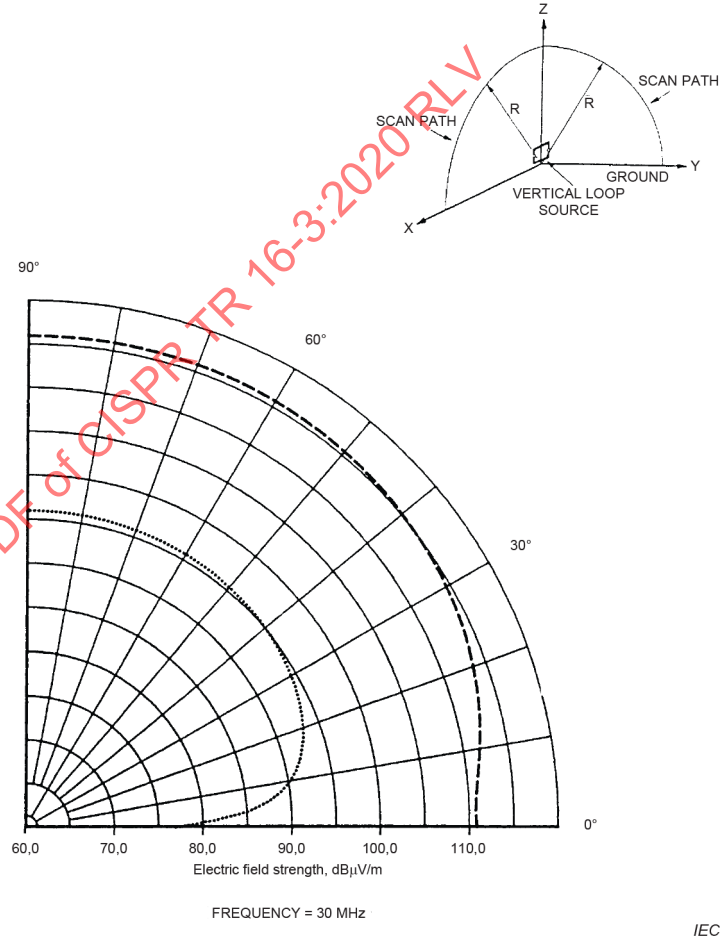
**Figure 106 – Vertical radiation patterns of the horizontally oriented *H*-fields emitted by a small horizontal electric dipole located close to the ground**

IECNORM.COM : Click to view the full PDF of CISPR TR 16-3:2020 RLV




Dipole length 1 m. Dipole height above ground 1 m. Dipole moment 1 A·m. $H_y$ at a scan distance of 30 m in the Z-X plane. Dash-dot line curve – ground constants are $\sigma$ = 0,1 mS/m, $\varepsilon_r$ = 3. Dashed line curve – ground constants are $\sigma$ = 1 mS/m, $\varepsilon_r$ = 15. Dotted line curve – ground constants are $\sigma$ = 10 mS/m, $\varepsilon_r$ = 30.

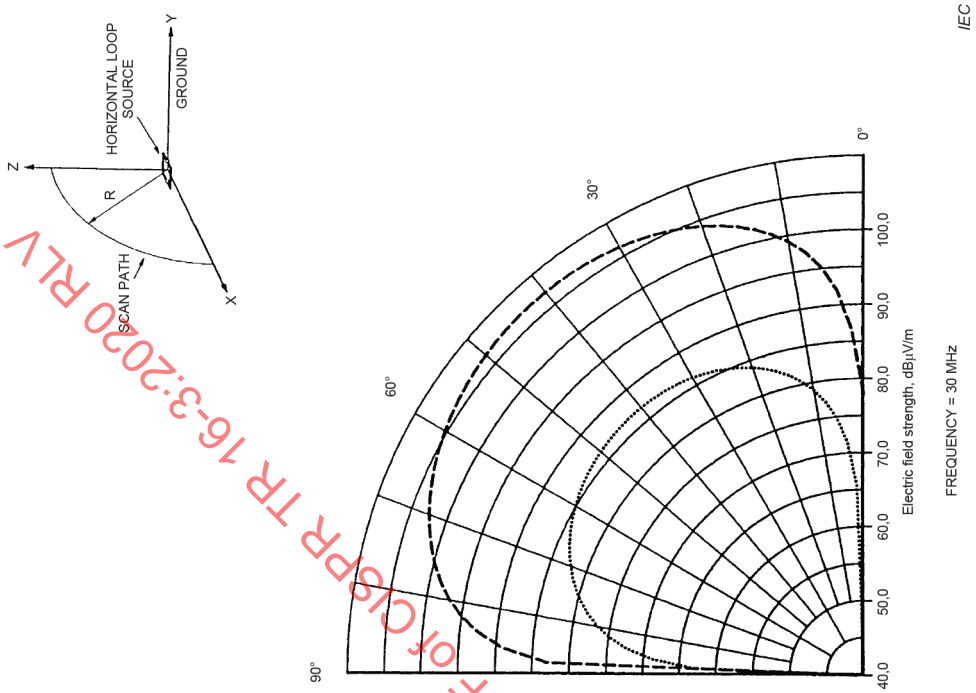
**Figure 107 – Influence of a wide range of values of the electrical constants of the ground on the vertical radiation patterns of the horizontally oriented *H*-fields emitted by a small horizontal electric dipole located close to the ground**

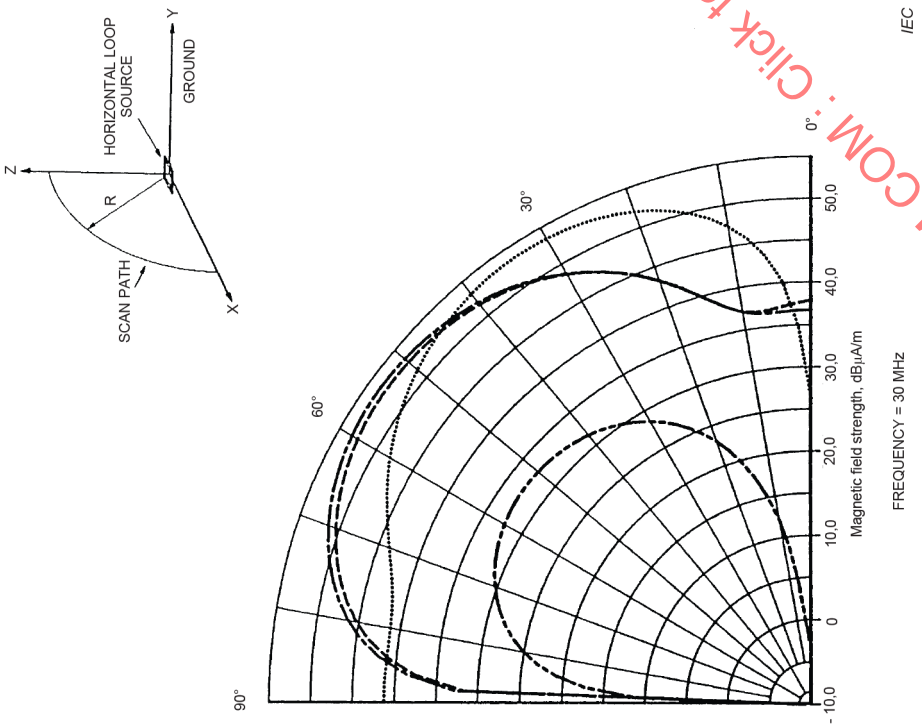



Dipole length 1 m. Dipole height above ground 1 m. Dipole moment 1 A·m. Dashed line curve – total vector/phasor sum of $E_z$ and $E_x$ at a scan distance of 30 m in the Z-X plane, the vertically polarized $E$-field. Dotted line curve – total vector/phasor sum of $E_z$ and $E_x$ at a scan distance of 300 m in the Z-X plane, the vertically polarized $E$-field. Electrical constants of the ground $\sigma$ = 1 mS/m, $\varepsilon_r$ = 15.

**Figure 108 – Vertical radiation patterns of the vertically polarized *E*-fields emitted by a small horizontal electric dipole located close to the ground**

IECNORM.COM : Click to view the full PDF of CISPR TR 16-3:2020 RLV




IECNORM.COM : Click to view the full PDF of CISPR TR 16-3:2020 RLV

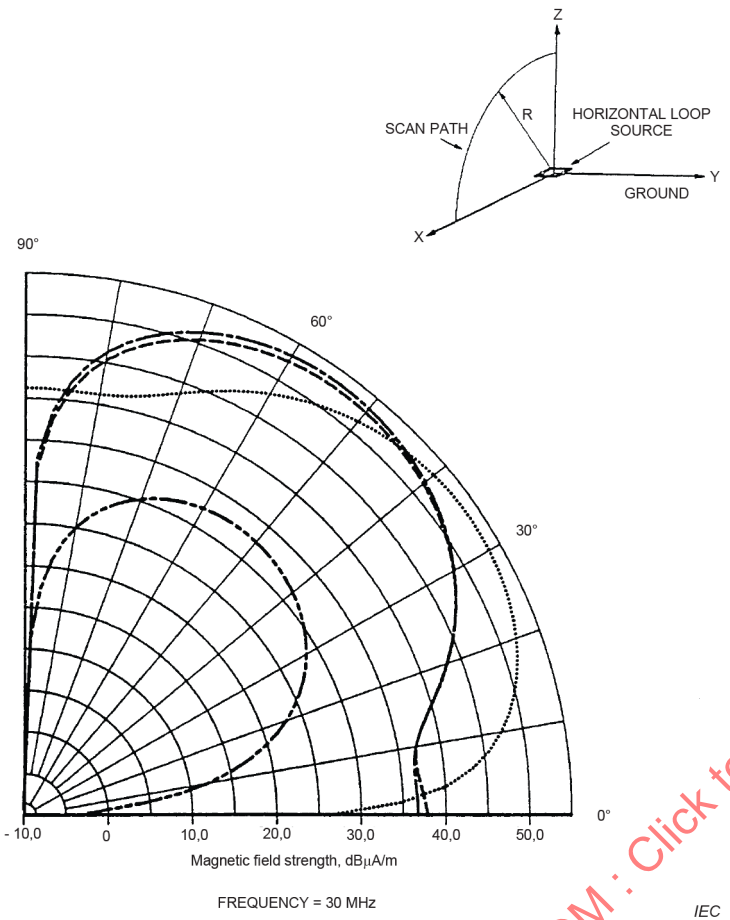
Square loop 0,1 m × 0,1 m. Loop base height above ground 0,07 m. Dipole moment 1 A·m$^2$. Dashed line curve – horizontally oriented $H_y$ at a scan distance of 30 m in the Z-X plane. Dotted line curve – horizontally oriented $H_y$ at a scan distance of 30 m in the Y-Z plane. Solid line curve – vertically oriented $H_z$ at a scan distance of 30 m in the Y-Z plane. Dash-double-dot curve – horizontally oriented $H_y$ at a scan distance of 300 m in the Z-X plane. Dash-dot line curve – horizontally oriented $H_y$ at a scan distance of 30 m in the Z-X plane Electrical constants of the ground $\sigma$ = 1 mS/m, $\varepsilon_r$ = 15. Perfectly conducting ground.

**Figure 109 – Vertical radiation patterns of the $H$-fields emitted by a small horizontal magnetic dipole (vertical loop) located close to the ground**

Square loop 0,1 m × 0,1 m. Loop base height above ground 0,07 m. Dipole moment 1 A·m$^2$. Dashed line curve – total vector/phasor sum of $E_z$ and $E_x$ at a scan distance of 30 m in the Z-X plane, the vertically polarized $E$-field. Dotted line curve – total vector/phasor sum of $E_z$ and $E_x$ at a scan distance of 300 m in the Z-X plane, the vertically polarized $E$-field. Electrical constants of the ground $\sigma$ = 1 mS/m, $\varepsilon_r$ = 15.

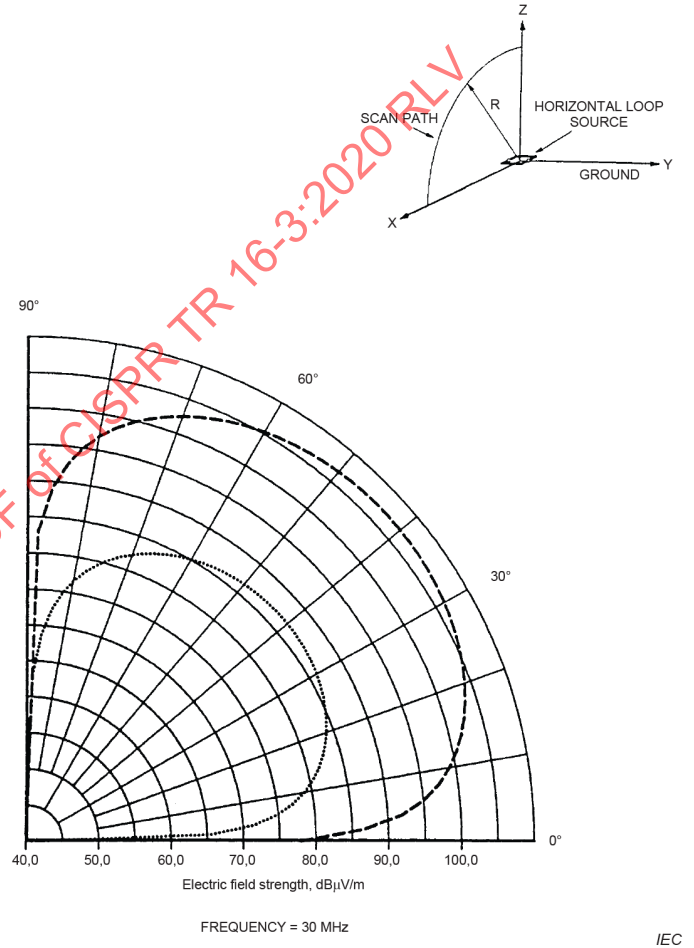
**Figure 110 – Vertical radiation patterns of the vertically polarized $E$-fields emitted by a small horizontal magnetic dipole (vertical loop) located close to the ground**

IECNORM.COM : Click to view the full PDF of CISPR TR 16-3:2020 RLV




Square loop 0,1 m × 0,1 m. Loop height above ground 1 m. Dipole moment 1 A·m$^2$. Dashed line curve – horizontally oriented $H_x$ at a scan distance of 30 m. Dotted line curve – vertically oriented $H_z$ at a scan distance of 30 m. Dash-double-dot curve – horizontally oriented $H_x$ at a scan distance of 300 m. Dash-dot line curve – horizontally oriented $H_x$ at a scan distance of 30 m. Electrical constants of the ground $\sigma$ = 1 mS/m, $\varepsilon_r$ = 15. Perfectly conducting ground.

**Figure 111 – Vertical radiation patterns of the $H$-fields emitted by a small vertical magnetic dipole (horizontal loop) located close to the ground**




Square loop 0,1 m by 0,1 m. Loop height above ground 1 m. Dipole moment 1 A·m$^2$. Dashed line curve – horizontally oriented $E_y$ at a scan distance of 30 m. Dotted line curve – horizontally oriented $E_y$ at a scan distance of 300 m. Electrical constants of the ground $\sigma$ = 1 mS/m, $\varepsilon_r$ = 15.

**Figure 112 – Vertical radiation patterns of the $E$-fields emitted by a small vertical magnetic dipole (horizontal loop) located close to the ground**

IECNORM.COM : Click to view the full PDF of CISPR TR 16-3:2020 RLV

## 4.7 Correlation between amplitude probability distribution (APD) characteristics of disturbance and performance of digital communication systems

### 4.7.1 General

The relationship between the degradation in quality of digital communication systems and APD of disturbance is shown in the following experimental results. Actual microwave ovens (MWO), such as the transformer and the inverter types, and a noise simulator, were used as a noise source in the following experiment. Bit Error Rate without error correction was basically used as a parameter of communication system performance (e.g. W-CDMA and PHS). Throughput is used if error correction could not be removed (e.g. W-LAN, Bluetooth and PHS).

Quantitative correlation between noise parameters and system performance is shown in 4.7.6 and 4.7.7 by using measured and simulated results.

These results show that APD measurement of disturbance is suitable for evaluating its interference potential on digital communication systems. Therefore APD measurement may be applicable to the compliance test of some products or product families, such as microwave ovens.

### 4.7.2 Influence on a wireless LAN system

The set-up for measuring communication quality degradation is shown in Figure 113, and measurement conditions are shown in Table 23. Throughput was chosen as a measure for communication quality evaluation. It was calculated from the time taken to transmit and time to receive data of a fixed size.

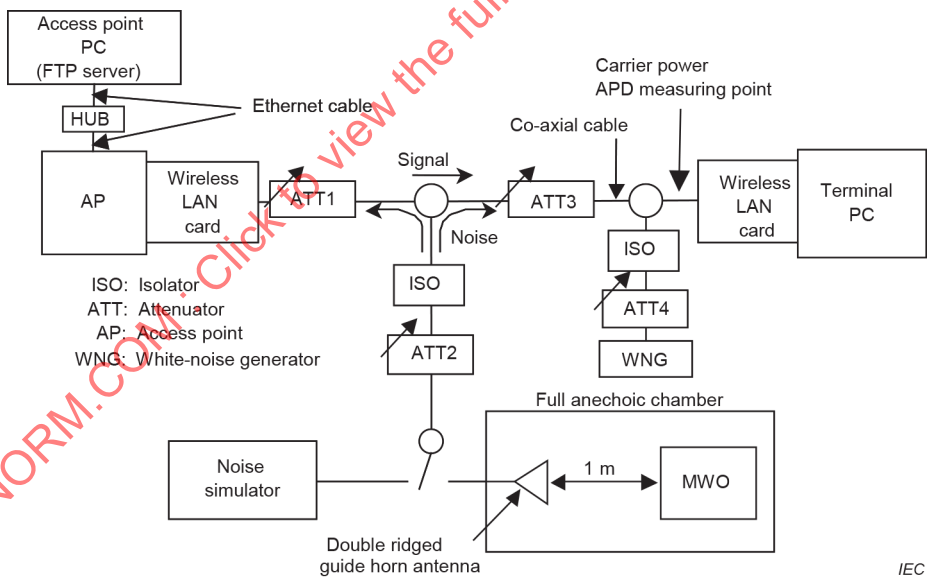



**Figure 113 – Set-up for measuring communication quality degradation of a wireless LAN**

IECNORM.COM : Click to view the full PDF of CISPR TR 16-3:2020 RLV

**Table 23 – Conditions for measuring communication quality degradation**

| | | |
|---|---|---|
| **Wireless LAN** | Frequency (channel number) | 2 462 MHz (channel 11) |
| | Transmission data | 20 MB |
| | Protocol | FTP (GET command from terminal PC) |
| | Transmission mode | Packet transmission |
| **Others** | Noise power density (dBm/Hz) | –154 dBm/Hz (set by ATT4) |

The APDs of disturbance are shown in Figure 114. The horizontal axis shows the level of radiated noise normalized by $N_0$, which has been approximated as the noise level from the white noise generator. The main frequency for measuring APD was 2 462 MHz. The average and root-mean-square (RMS) values of the noise level normalized by $N_0$ derived from APD of the MWO noise and noise simulator noise are shown in Table 24.

APD of the noise simulator at ATT2 = 0 dB was in good agreement with APD of the inverter type MWO at ATT2 = 10 dB.

IECNORM.COM : Click to view the full PDF of CISPR TR 16-3:2020 RLV

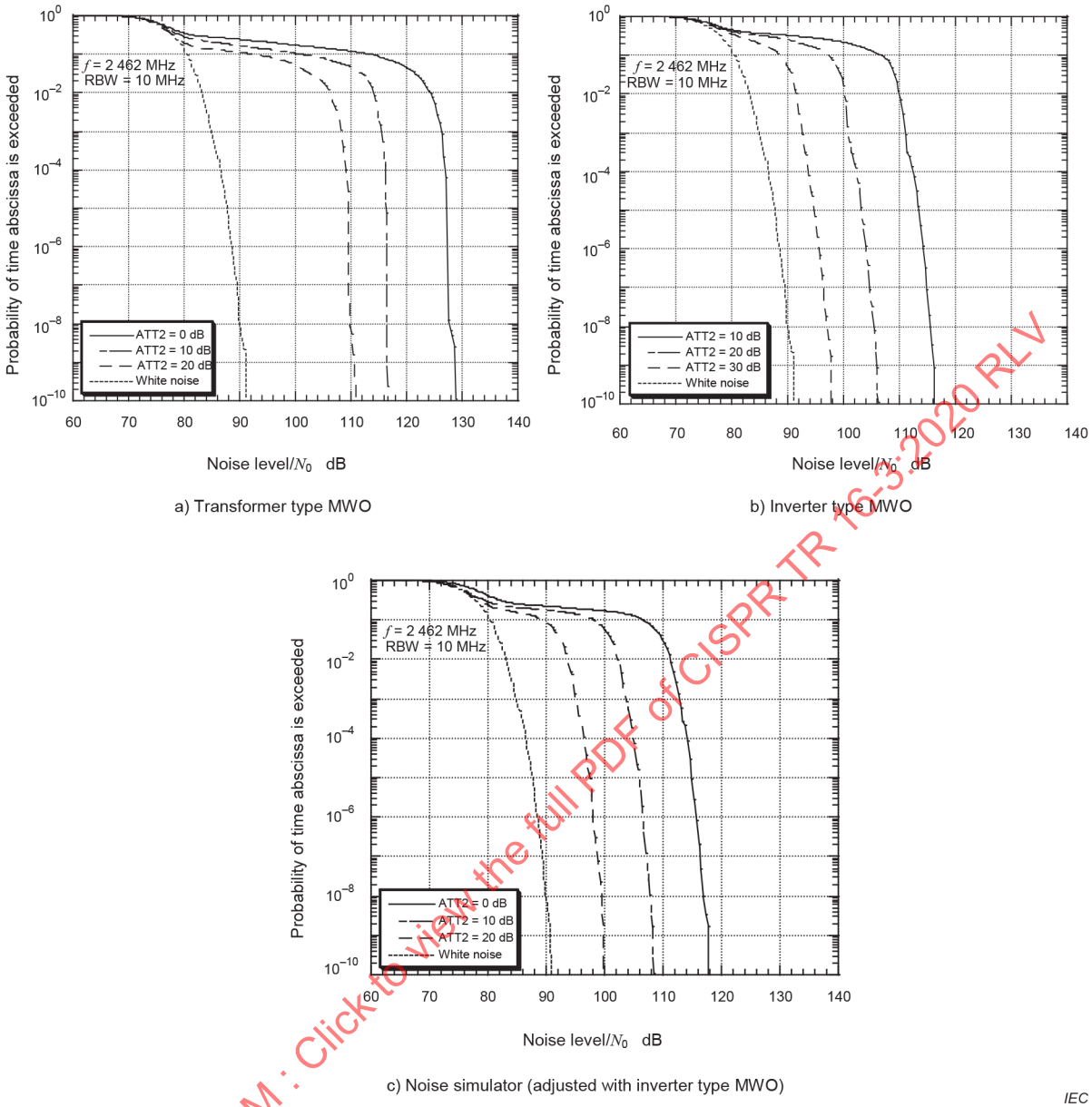



**Figure 114 – APD characteristics of disturbance**

**Table 24 – Average and RMS values of noise level normalized by $N_0$**

| | | ATT2 | | | | White noise |
|---|---|---|---|---|---|---|
| | | 0 dB | 10 dB | 20 dB | 30 dB | |
| **Transformer type MWO** | Average (dB) | 111,2 | 101,0 | 92,6 | | 77,6 |
| | RMS (dB) | 117,1 | 107,0 | 98,8 | | 78,7 |
| **Inverter type MWO** | Average (dB) | | 100,6 | 91,4 | 83,4 | 77,6 |
| | RMS (dB) | | 104,4 | 94,8 | 86,2 | 78,7 |
| **Noise simulator** | Average (dB) | 100,6 | 91,9 | 83,8 | | 77,5 |
| | RMS (dB) | 105,1 | 96,2 | 87,6 | | 78,6 |

The measured communication quality degradation for various amounts of attenuation of injected noise is shown in Figure 115. The horizontal axis shows $C/N_0$, where $C$ is the sub-carrier power and $N_0$ is the noise power density.

IECNORM.COM : Click to view the full PDF of CISPR TR 16-3:2020 RLV

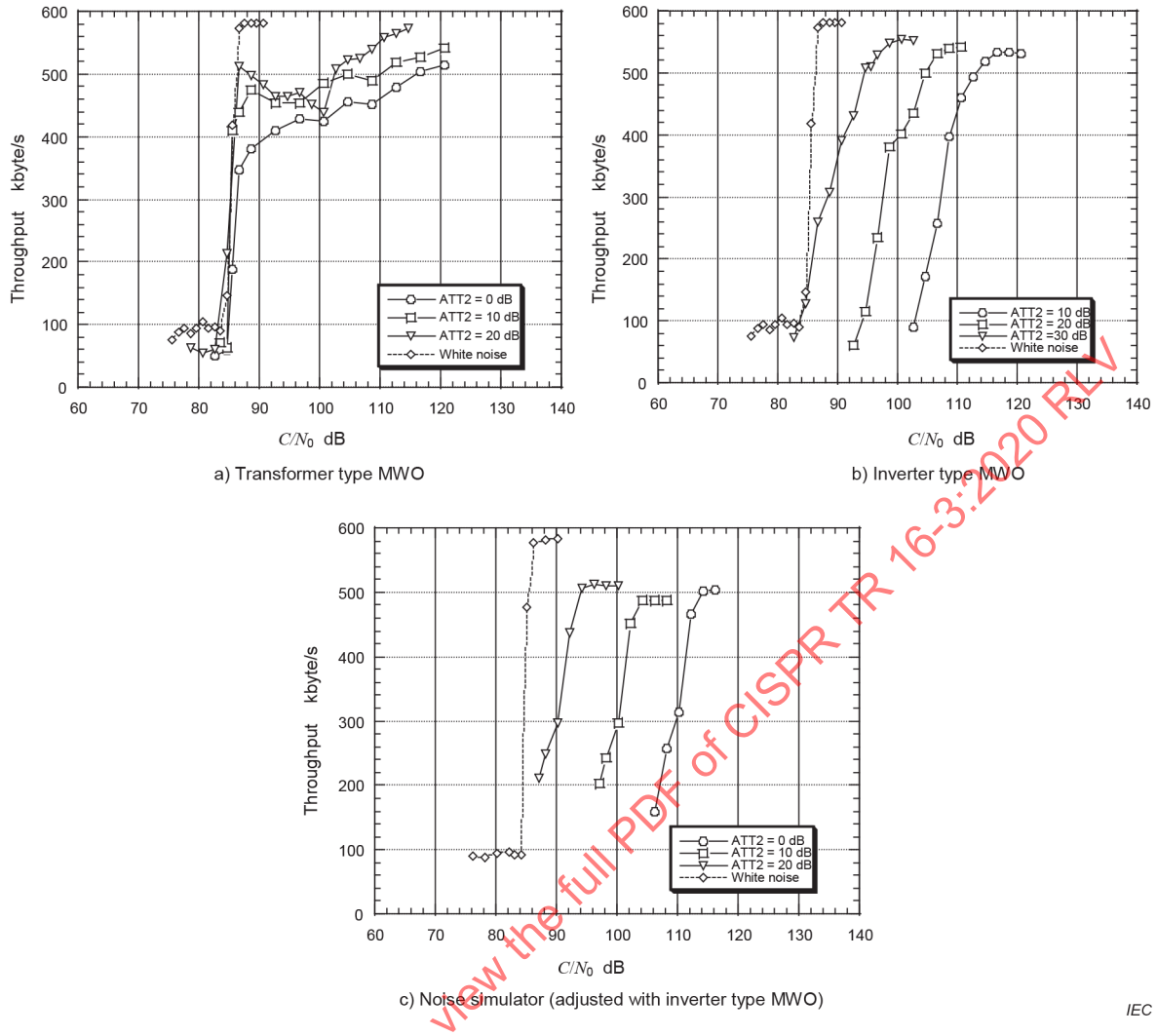



**Figure 115 – Wireless LAN throughput influenced by noise**

The throughput influenced by a transformer type MWO is 400 kbytes/s or more when $C/N_0$ is 90 dB or more, and decreases rapidly when $C/N_0$ is below 90 dB. This tendency is almost the same irrespective of the noise level. On the other hand, the throughput influenced by an inverter type MWO decreases almost in proportion to the noise level. The throughput influenced by a noise simulator has almost the same degradation characteristics as that for an inverter type MWO.

### 4.7.3 Influence on a Bluetooth system

The set-up for measuring communication quality degradation is shown in Figure 116, and measurement conditions are shown in Table 25.

Throughput was chosen as the measure for communication quality evaluation.

IECNORM.COM : Click to view the full PDF of CISPR TR 16-3:2020 RLV

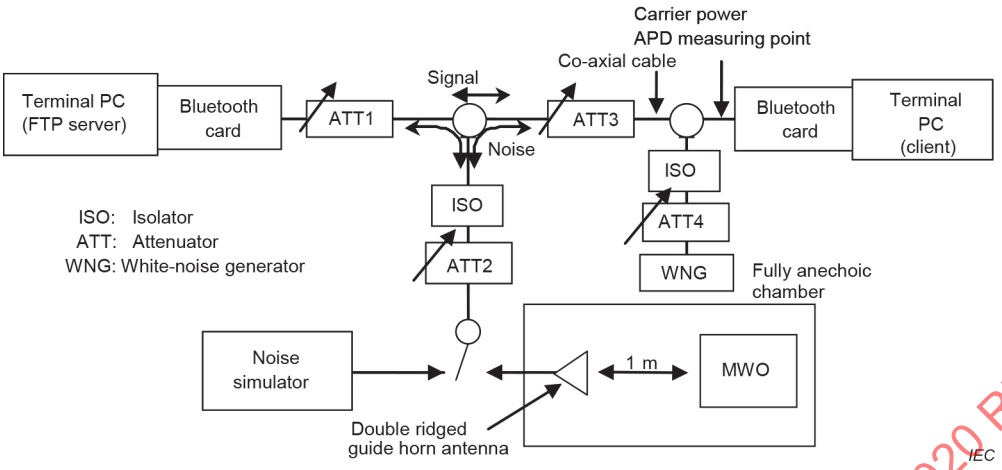



**Figure 116 – Set-up for measuring the communication quality degradation of Bluetooth**

**Table 25 – Conditions for measuring communication quality degradation of Bluetooth**

| | | |
|---|---|---|
| **Bluetooth** | Frequency | 2 400 MHz to 2 483,5 MHz |
| | Transmission data | 2,5 MB |
| | Protocol | FTP (GET command from terminal PC) |
| | Transmission mode | Packet exchange data transmission mode |
| **Others** | Noise power density (dBm/Hz) | -148 dBm/Hz (set by ATT4) |

The APDs at a frequency of 2 441 MHz are shown in Figure 117, and the average and RMS values of noise level normalized by $N_0$ are shown in Table 26.

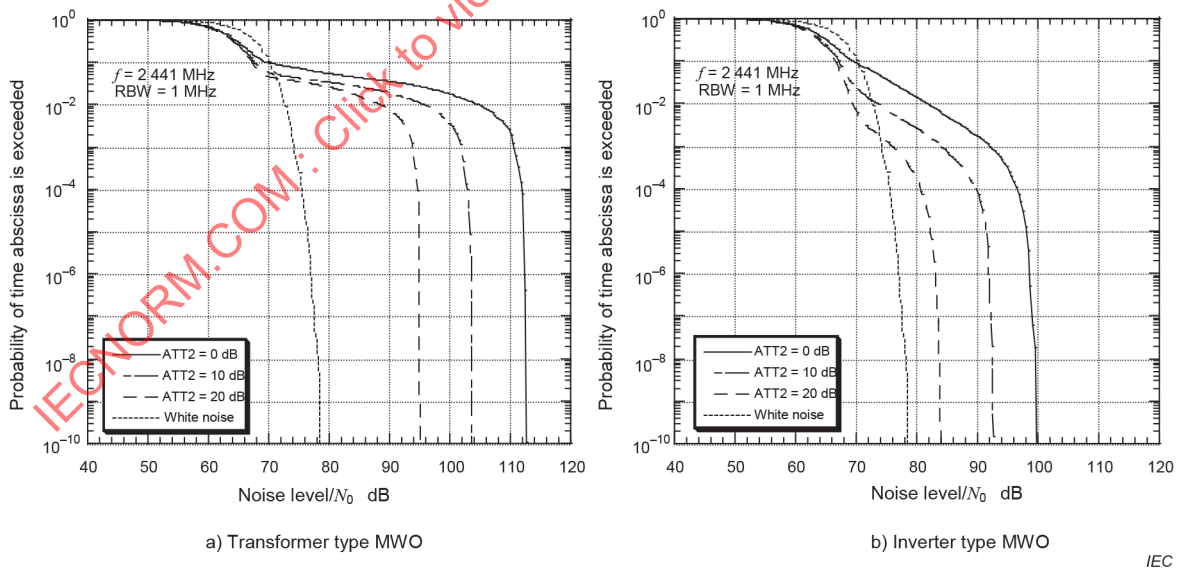


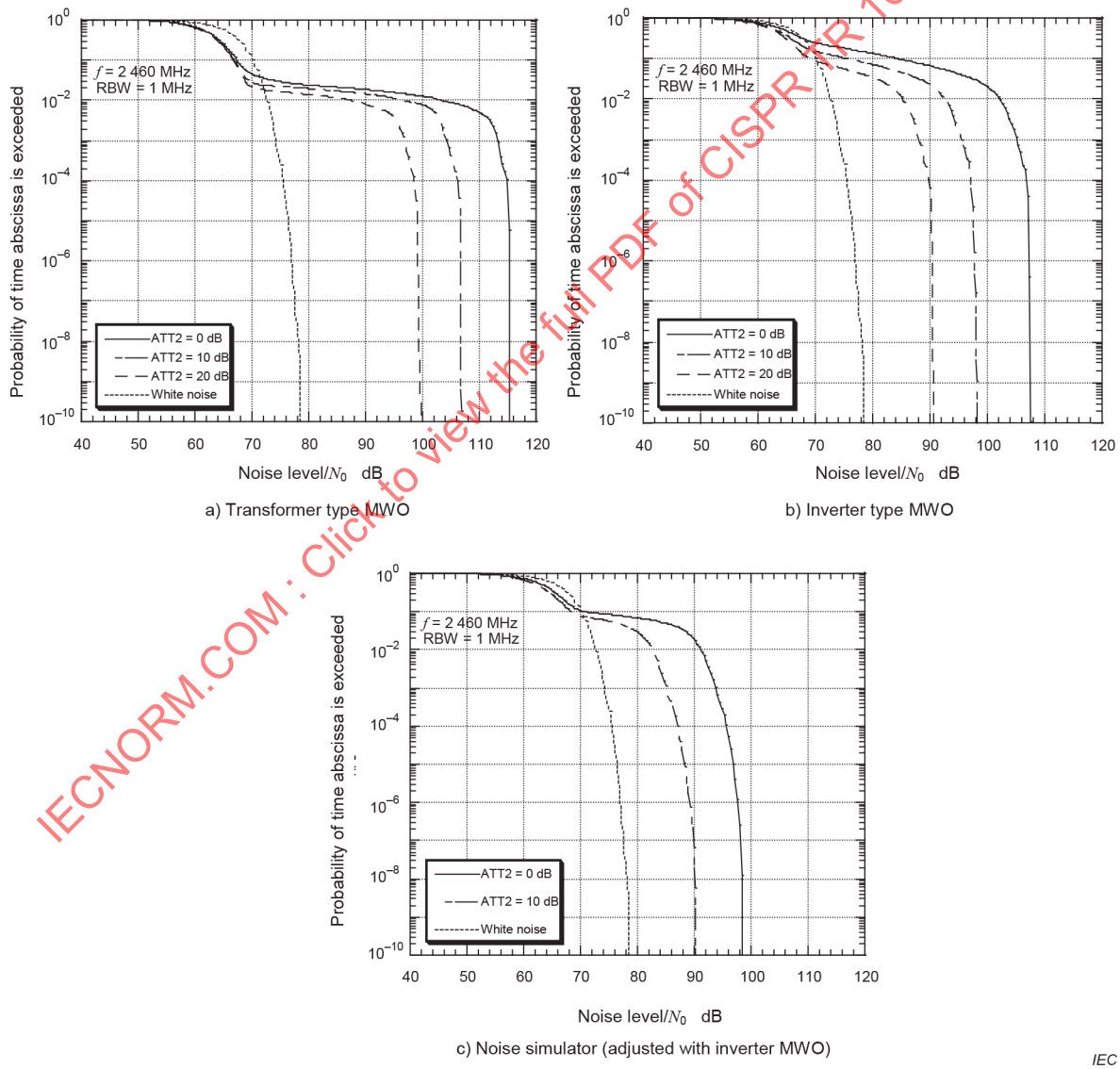

**Figure 117 – APD of disturbance of actual MWO (2 441MHz)**

IECNORM.COM : Click to view the full PDF of CISPR TR 16-3:2020 RLV

**Table 26 – Average and RMS values of noise level normalized by $N_0$**

| | | ATT2 | | | | White noise |
|---|---|---|---|---|---|---|
| | | 0 dB | 10 dB | 20 dB | 30 dB | |
| **Transformer type MWO** | Average (dB) | 89,8 | 80,8 | 73,7 | | 67,1 |
| | RMS (dB) | 99,2 | 90,2 | 82,5 | | 68,3 |
| **Inverter type MWO** | Average (dB) | 70,7 | 65,4 | 63,5 | | 67,1 |
| | RMS (dB) | 80,6 | 73,3 | 66,0 | | 68,3 |

The APDs measured at 2 460 MHz, where the noise level of an MWO is at maximum, are shown in Figure 118, and the average and RMS values of noise normalized by $N_0$ are shown in Table 27. The noise level is about 10 dB larger than that at the frequency of 2 441 MHz. The APD of the noise simulator at ATT2 = 0 dB is in good agreement with that of the inverter type MWO at ATT2 = 10 dB.




IECNORM.COM : Click to view the full PDF of CISPR TR 16-3:2020 RLV

**Figure 118 – APD characteristics of disturbance (2 460 MHz)**

**Table 27 – Average and RMS values of noise level normalized by $N_0$**

| | | ATT2 | | | | White noise |
|---|---|---|---|---|---|---|
| | | 0 dB | 10 dB | 20 dB | 30 dB | |
| **Transformer type MWO** | Average (dB) | 87,8 | 78,4 | 71,4 | | 67,1 |
| | RMS (dB) | 94,9 | 85,4 | 78,0 | | 68,3 |
| **Inverter type MWO** | Average (dB) | 70,7 | 65,4 | 63,5 | | 67,1 |
| | RMS (dB) | 80,6 | 73,3 | 66,0 | | 68,3 |
| **Noise simulator** | Average (dB) | 77,6 | 69,8 | | | 67,1 |
| | RMS (dB) | 84,1 | 75,5 | | | 68,3 |

The measured communication quality degradation for various amounts of attenuation of injected noise is shown in Figure 119.

There is only a minor difference in degradation caused by the level of noise between a transformer and an inverter type MWO. This is because Bluetooth performs frequency hopping, and is hard to be influenced by noise continuously. Furthermore, there is almost no difference in communication quality degradation for a noise simulator.

IECNORM.COM : Click to view the full PDF of CISPR TR 16-3:2020 RLV

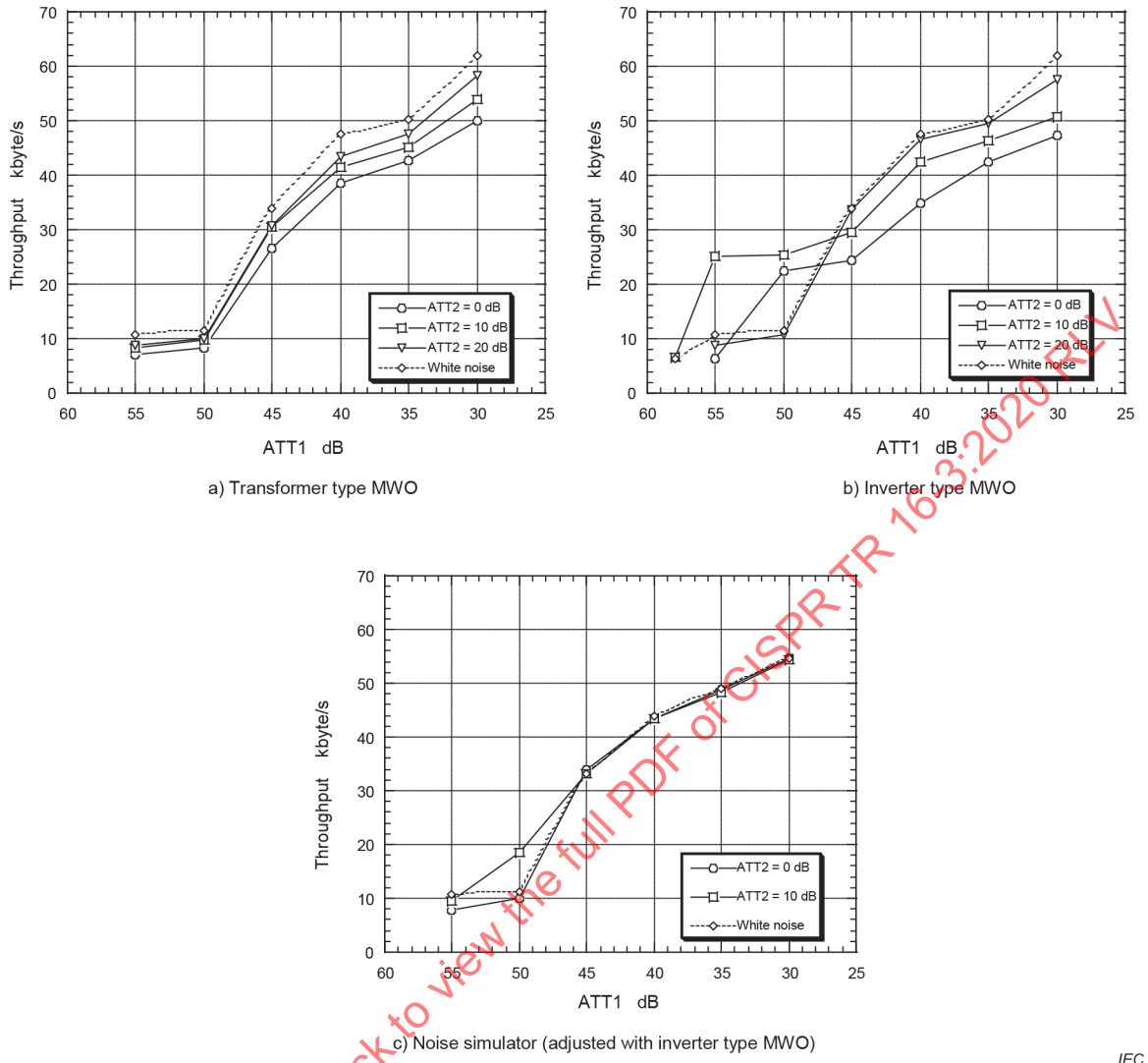



**Figure 119 – Throughput of Bluetooth influenced by noise**

IECNORM.COM : Click to view the full PDF of CISPR TR 16-3:2020 CLV

According to the specifications, Bluetooth controls the transmission power automatically depending on the communication situation. The sub-carrier power at the reception point cannot be obtained uniquely since transmission power may change when ATT1 is changed. The horizontal axis in this figure shows the attenuation of signal power.

### 4.7.4 Influence on a W-CDMA system

The set-up for measuring communication quality degradation is shown in Figure 120, and measurement conditions are shown in Table 28.

Bit error rate (BER) was chosen as the measure for communication quality evaluation.

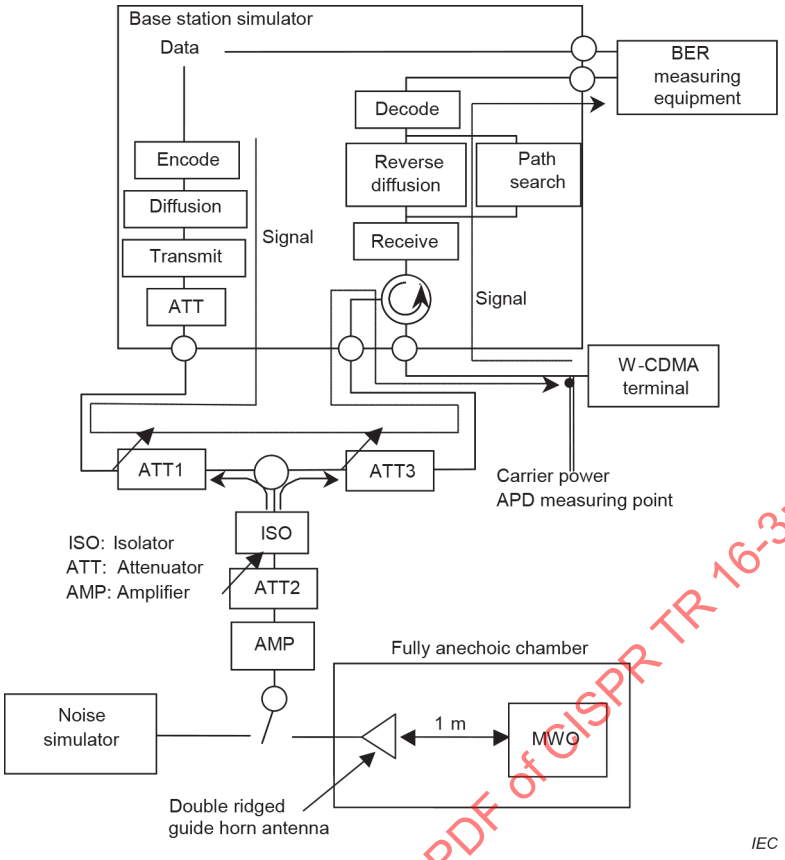



**Figure 120 – Set-up for measuring the BER of W-CDMA**

**Table 28 – Conditions for measuring communication quality degradation of W-CDMA**

| | | |
|---|---|---|
| **Baseband simulator** | Frequency | 2 137,6 MHz (downlink) |
| | Chip rate | 3,84 Mc/s |
| | Spread rate | Uplink: DPDCH 64 / downlink: DPCH 128 |
| | Data rate | 12,2 kb/s (acoustic) |
| | Transmission data | 6 Mb |
| | Transmission mode | RMC communication test (UE turn)<br>3GPP TS34.121 [84] |

The measured APDs of the noise are shown in Figure 121, and the average and RMS values of the noise level normalized by $N_0$ are shown in Table 29. The APD of the noise simulator at ATT2 = 0 dB is in good agreement with the APD of the inverter type MWO at ATT2 = 10 dB.

IECNORM.COM : Click to view the full PDF of CISPR TR 16-3:2020 RLV

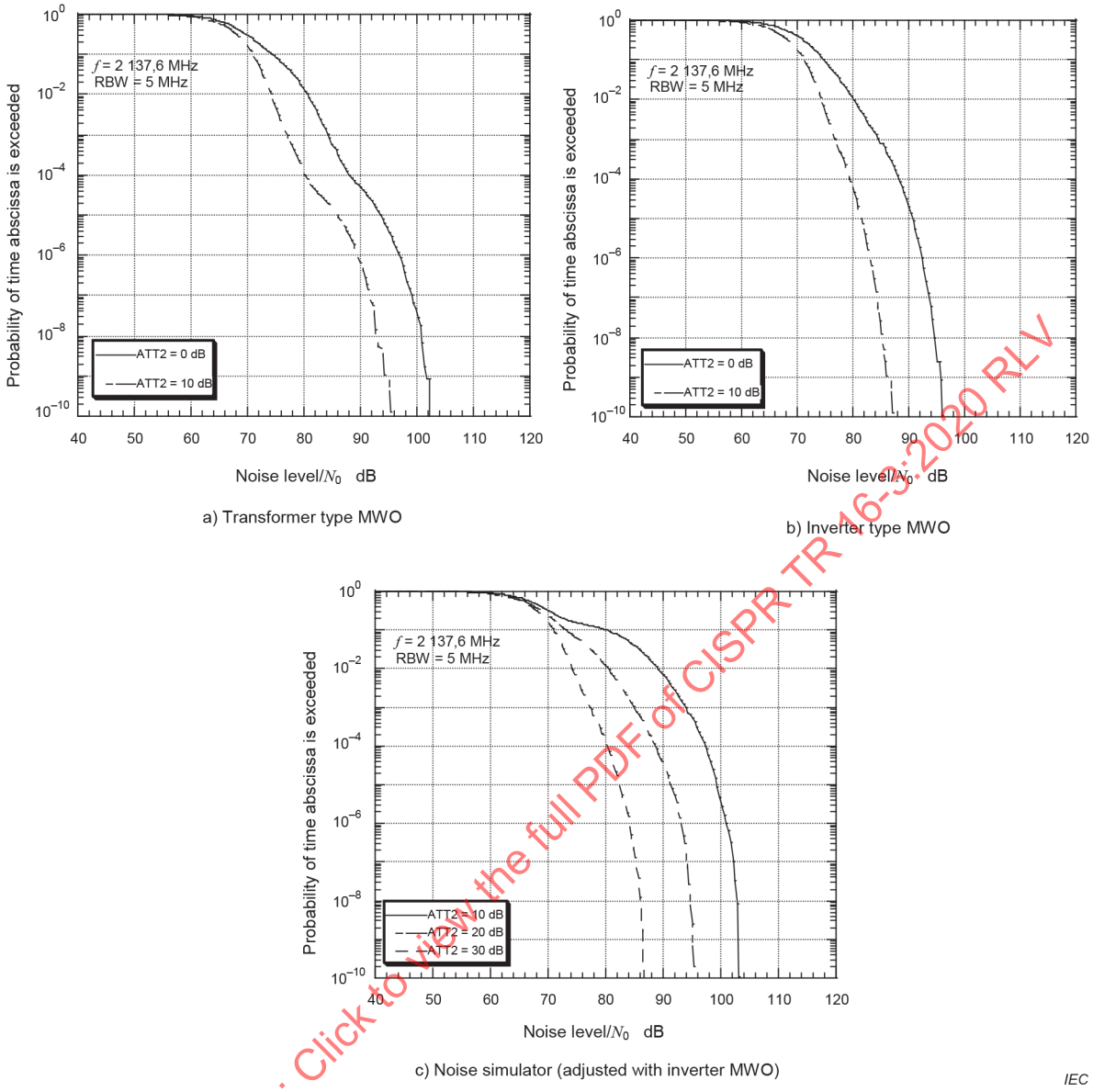



**Figure 121 – APD characteristics of disturbance**

**Table 29 – Average and RMS values of noise level normalized by $N_0$**

| | | ATT2 | | | | Receiver noise |
|---|---|---|---|---|---|---|
| | | 0 dB | 10 dB | 20 dB | 30 dB | |
| **Transformer type MWO** | Average (dB) | 71,1 | 67,7 | | | 67,2 |
| | RMS (dB) | 75,1 | 69,4 | | | 68,6 |
| **Inverter type MWO** | Average (dB) | 71,6 | 68,0 | | | 67,2 |
| | RMS (dB) | 74,7 | 69,4 | | | 68,6 |
| **Noise simulator** | Average (dB) | | 77,1 | 70,4 | 67,7 | 67,2 |
| | RMS (dB) | | 83,3 | 74,7 | 69,3 | 68,6 |

The measured communication quality degradation for various amounts of attenuation of injected noise is shown in Figure 122.

IECNORM.COM : Click to view the full PDF of CISPR TR 16-3:2020 RLV

For both types of MWO, the BER was degraded by several dB after a 10 dB change in noise level. Moreover, BER characteristics influenced by the noise simulator are in good agreement in these measurement results.

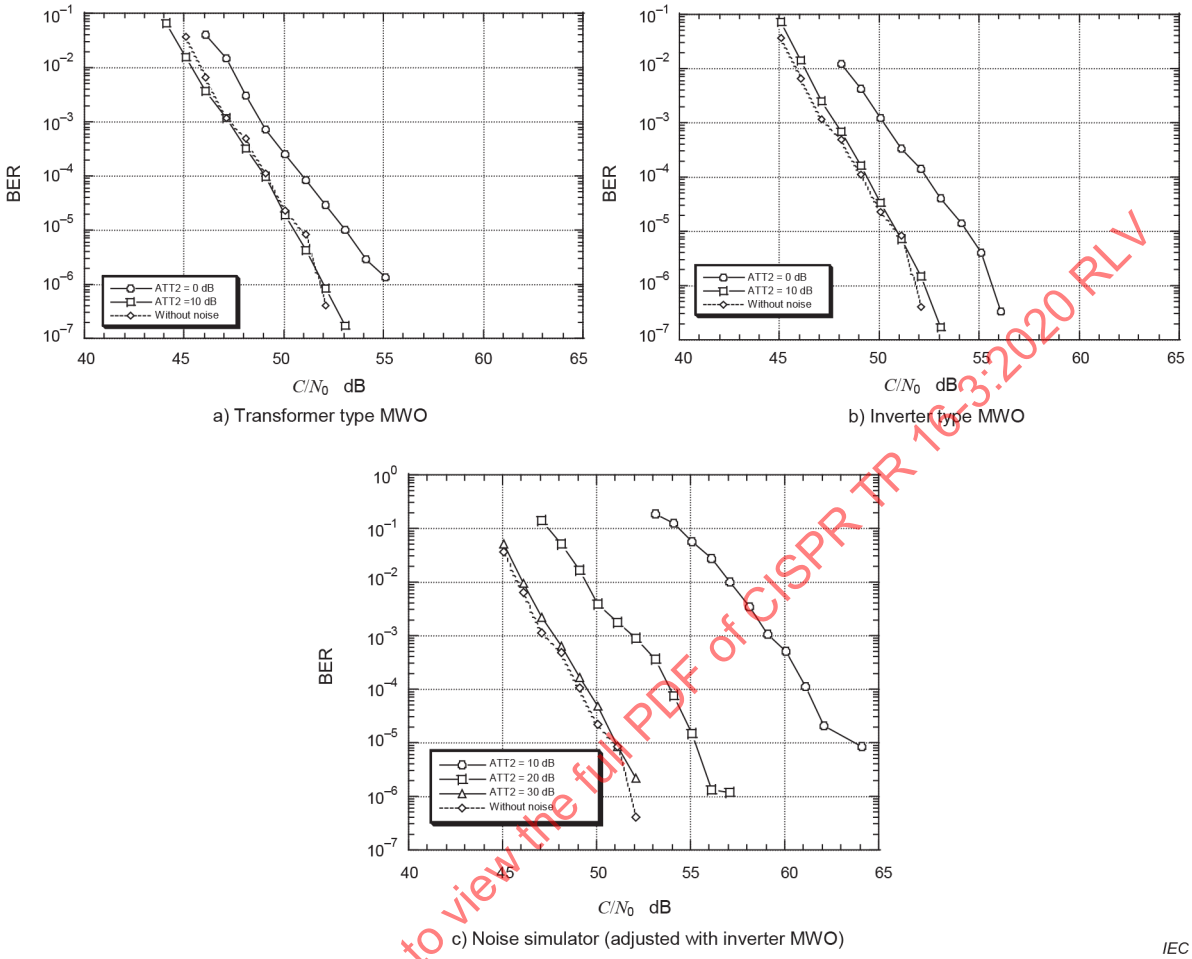



**Figure 122 – BER of W-CDMA caused by radiation noise**

### 4.7.5 Influence on Personal Handy Phone System (PHS)

The set-ups for measuring communication quality degradation are shown in Figure 123 and Figure 124, and conditions for measuring throughput and BER are shown in Table 30 and Table 31.

Throughput and BER were chosen as measures for evaluating the communication quality of PHS.

The measured APDs are shown in Figure 125, and the average and RMS values of noise normalized by $N_0$ are shown in Table 32.

IECNORM.COM : Click to view the full PDF of CISPR TR 16-3:2020 RLV

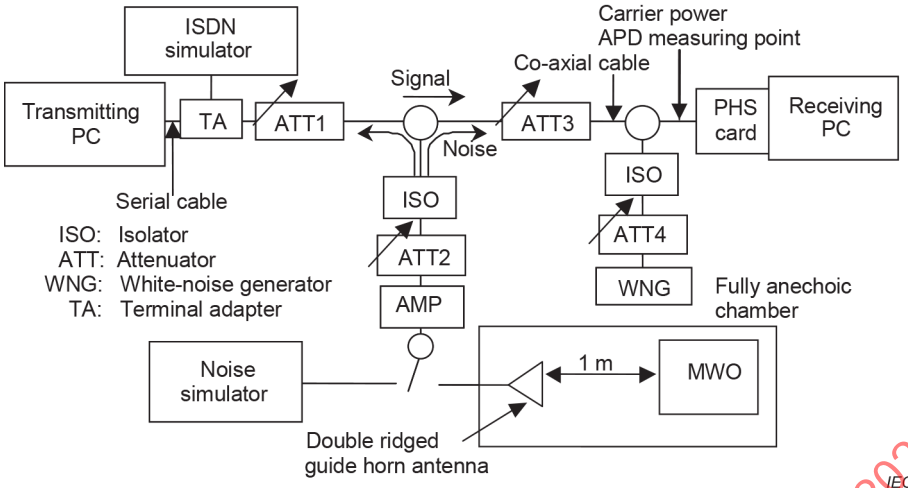



**Figure 123 – Set-up for measuring the PHS throughput**

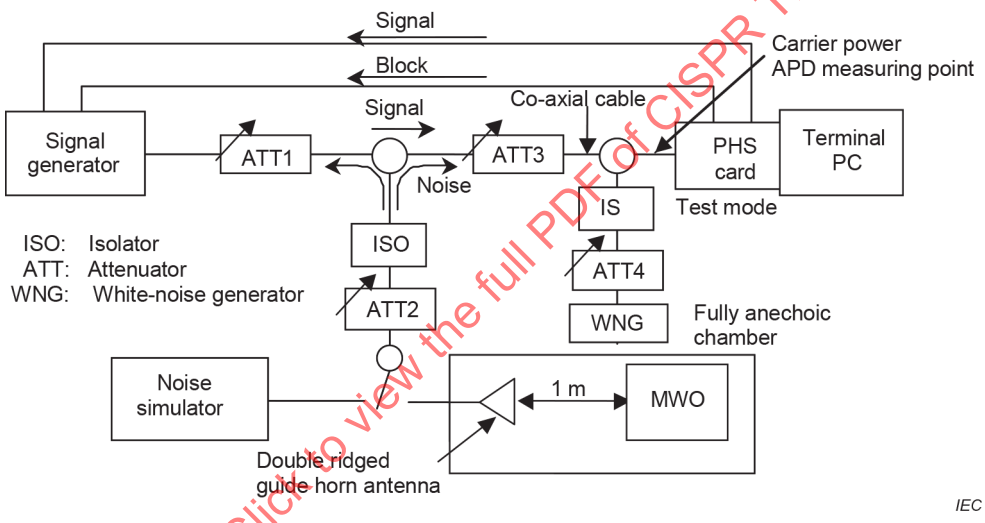



**Figure 124 – Set-up for measuring the BER of PHS**

**Table 30 – Conditions for measuring the PHS throughput**

| | | |
|---|---|---|
| **PHS** | Transmission data | About 376 kB data |
| | Transmission system | Non protocol |
| | Transmission mode | 32 kb/s real time data transmission |
| **Others** | Noise power density $N$ (dBm/Hz) | –160 dBm/Hz (set by ATT4) |

**Table 31 – Conditions for measuring the BER of PHS**

| | | |
|---|---|---|
| **PHS** | Frequency (channel number) | 1 907,15 MHz (channel 41) |
| | Transmission data | 5 Mb PN9 |
| | Data rate | 32 kb/s |
| **Others** | Noise power density (dBm/Hz) | –160 /Hz (set by ATT4) |

IECNORM.COM : Click to view the full PDF of CISPR TR 16-3:2020 RLV

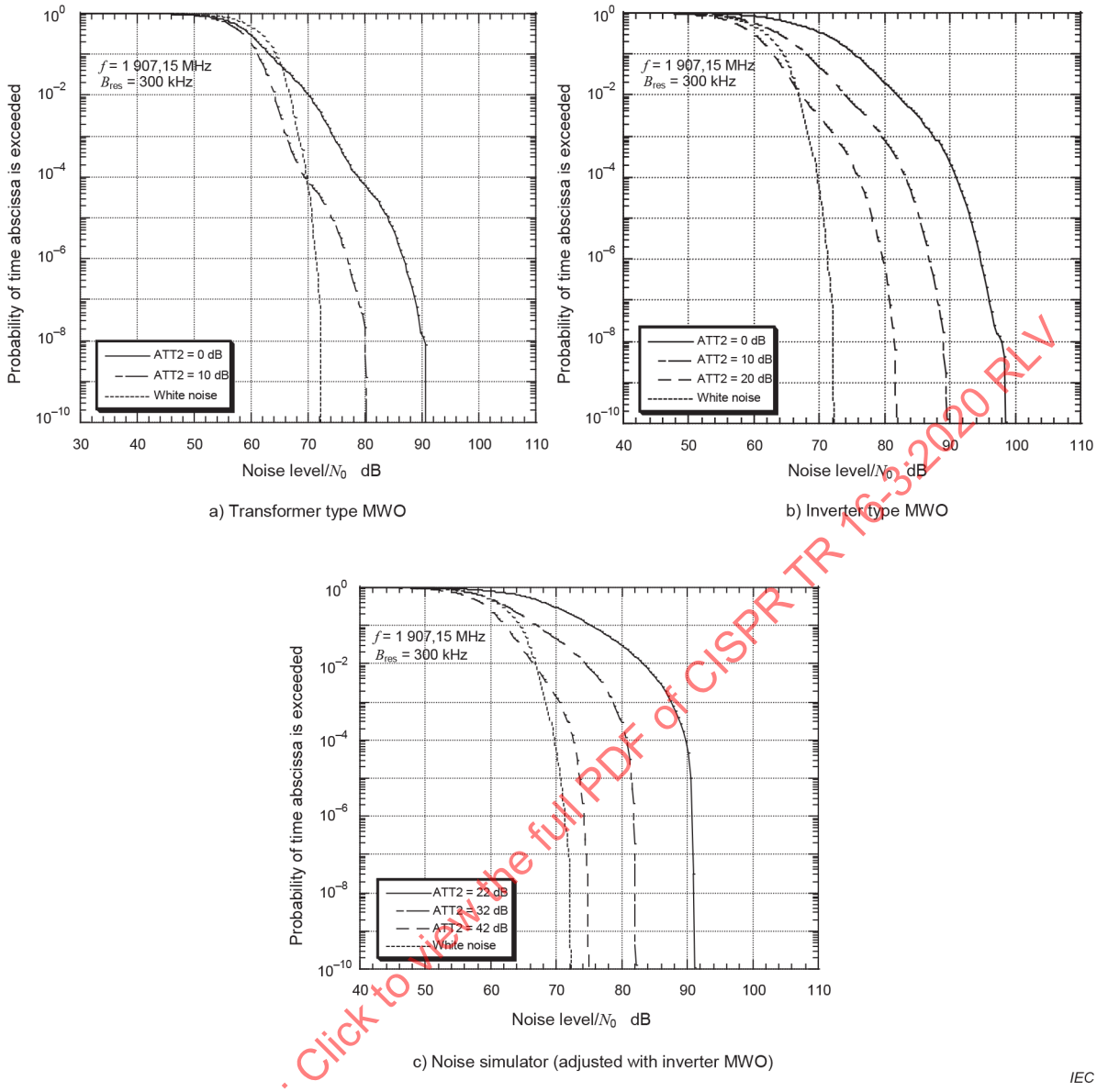



**Figure 125 – APD characteristics of disturbance**

**Table 32 – Average and RMS values of noise level normalized by $N_0$**

| | | ATT2 | | | | White noise |
|---|---|---|---|---|---|---|
| | | 0 dB | 10 dB | 20 dB | 30 dB | |
| **Transformer type MWO** | Average (dB) | 60,6 | 58,1 | | | 61,2 |
| | RMS (dB) | 64,9 | 59,4 | | | 62,4 |
| **Inverter type MWO** | Average (dB) | 72,6 | 64,9 | 59,9 | 58,0 | 61,2 |
| | RMS (dB) | 76,7 | 68,9 | 62,5 | 59,3 | 62,4 |
| **Noise simulator** | Average (dB) | 72,3 | 64,2 | 59,1 | 57,8 | 61,2 |
| | RMS (dB) | 77,0 | 68,2 | 61,1 | 59,0 | 62,4 |
| NOTE The values of ATT2 are 22 dB, 32 dB, 42 dB and 52 dB, respectively for the noise simulator. | | | | | | |

The measured throughput for various amounts of attenuation of injected noise is shown in Figure 126.

IECNORM.COM : Click to view the full PDF of CISPR TR 16-3:2020 RLV

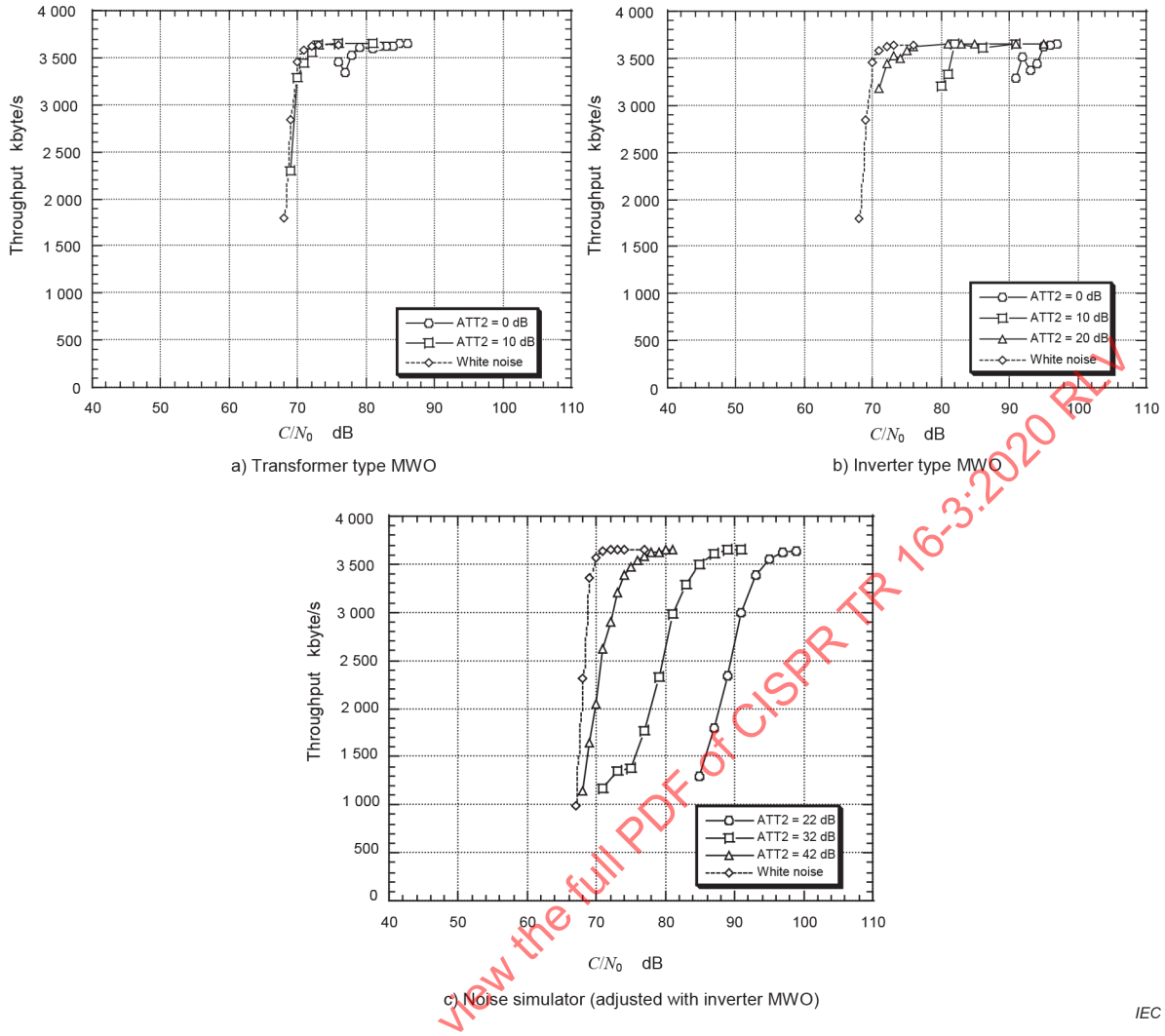



**Figure 126 – PHS throughput caused by radiation**

Similarly, the measured BER is shown in Figure 127. The BER characteristics caused by the noise simulator were in good agreement in the measurement results of the inverter-type MWO.

IECNORM.COM : Click to view the full PDF of CISPR TR 16-3:2020 RLV

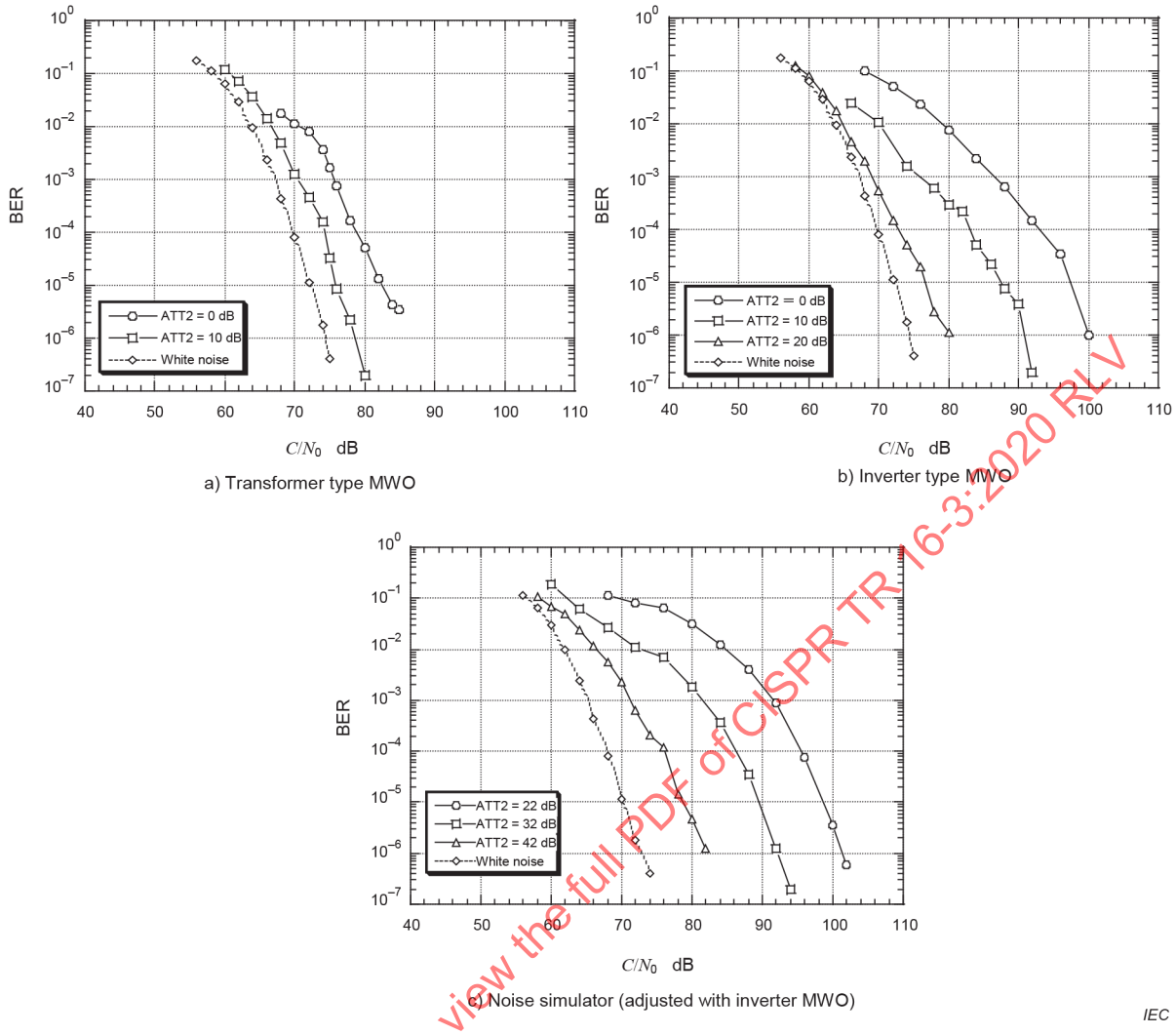



**Figure 127 – BER of PHS caused by radiation noise**

### 4.7.6 Quantitative correlation between noise parameters and system performance

#### 4.7.6.1 General

Correlations between the noise parameter of the disturbance (levels of disturbance correspond to certain probability that is derived from APD) and degradation of system performance (throughput and/or bit error rate) are evaluated for the communication systems described in 4.7.2 to 4.7.5.

#### 4.7.6.2 Wireless LAN (throughput)

From Figure 114 a) and Figure 114 b), the disturbance voltage for each probability, e.g. $10^{-1}$, $10^{-2}$, $10^{-3}$, $10^{-4}$, was read. $C/N_0$ values that are necessary to assure the throughput of 500 kByte/s under microwave oven disturbance were obtained from Figure 115 a) and Figure 115 b). The correlation between the disturbance voltages and the $C/N_0$ values is plotted in Figure 128 a) and Figure 128 b) for a transformer type oven and inverter type oven, respectively.

IECNORM.COM : Click to view the full PDF of CISPR TR 16-3:2020 RLV

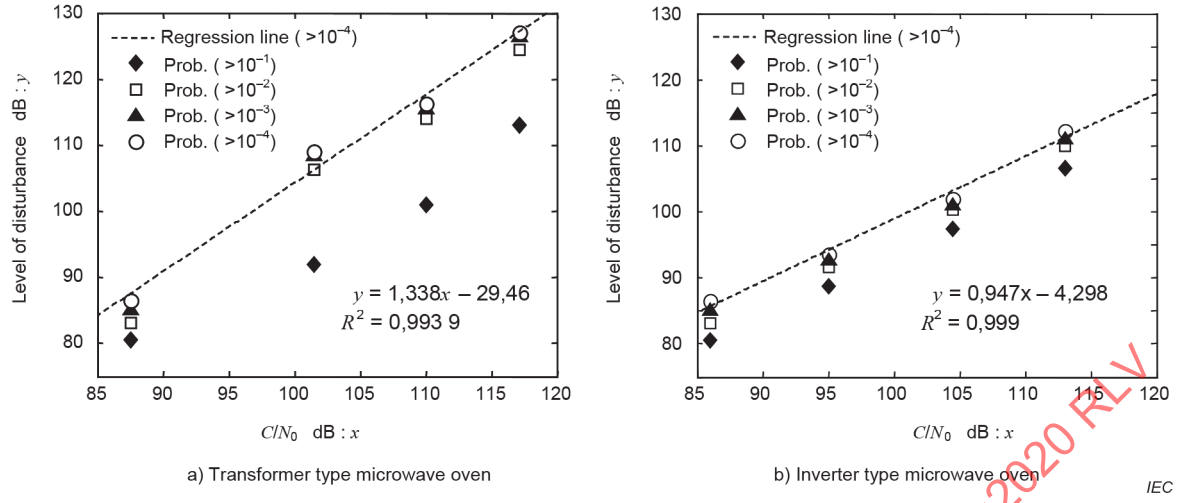



**Figure 128 – Correlation of the disturbance voltages with the system performance ($C/N_0$)**

In Figure 128, the linear regression line by using the values for $10^{-4}$ probability is also plotted with the equation and correlation coefficients $R$. It is found that $10^{-4}$ probability values are well correlated to the $C/N_0$ and thus these values are suitable for the noise parameters to estimate the degradation of the system performance.

#### 4.7.6.3 Bluetooth (throughput)

From Figure 118 a) and Figure 118 b), the disturbance voltage for each probability was read. As shown in Figure 116, not only MWO disturbance but also white noise was injected to the communication link. Then, disturbance voltages are meaningful only when MWO disturbance exceeds the white noise. Therefore, probability of $10^{-1}$ value was ignored and probability of $10^{-2}$, $10^{-3}$ and $10^{-4}$ values were used in the evaluation below.

Relative $C/N_0$ values that are necessary to assure the throughput of 40 kByte/s under microwave oven disturbance were obtained from Figure 119 a) and Figure 119 b) (relative $C/N_0$ = dB corresponds to ATT1 = 43 dB). The correlation between the disturbance voltages and the relative $C/N_0$ values are plotted in Figure 129 a) and Figure 129 b) for a transformer type oven and inverter type oven, respectively.

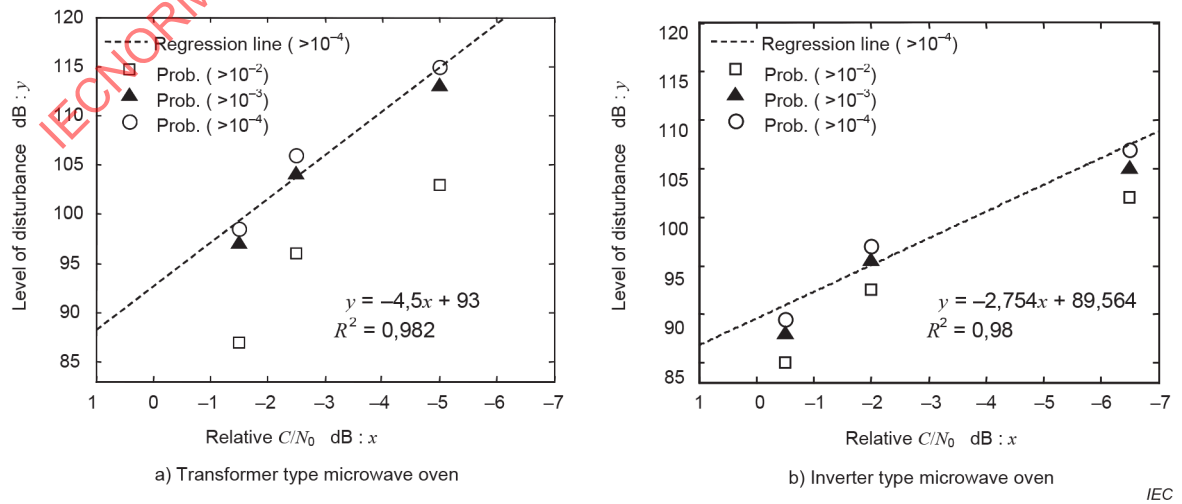



**Figure 129 – Correlation of the disturbance voltages with the system performance**

IECNORM.COM : Click to view the full PDF of CISPR TR 16-3:2020 RLV

In Figure 129, the linear regression line by using the values for $10^{-4}$ probability is also plotted with the equations and correlation coefficients. The same results were obtained as in 4.7.6.1.

#### 4.7.6.4 W-CDMA (BER)

From Figure 121 a) and Figure 121 b), disturbance voltages for each probability, e.g. $10^{-2}$, $10^{-3}$, $10^{-4}$ were read. $C/N_0$ values that are necessary to assure the BER of $10^{-4}$ under microwave oven disturbance were obtained from Figure 130 a) and Figure 130 b). Because only two curves available are in the APD and BER, regression analyses were not performed.

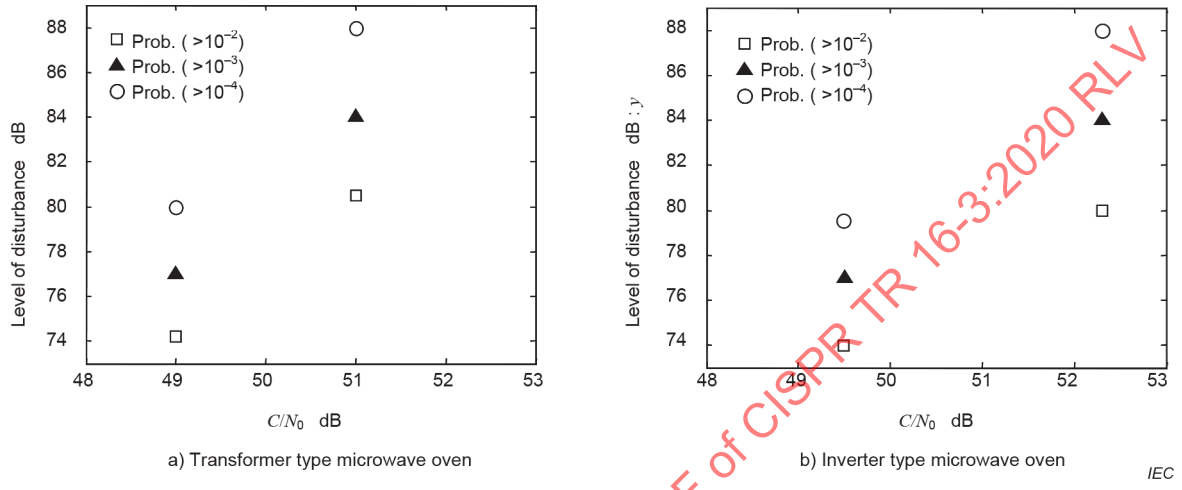



**Figure 130 – Correlation of the disturbance voltages with the system performance**

#### 4.7.6.5 PHS (BER and throughput)

Same analyses were performed on PHS data. $C/N_0$ values correspond to the signal input that is necessary to assure the BER of $10^{-4}$ under microwave oven disturbance. The correlation between the disturbance level and the $C/N_0$ values is plotted in Figure 131 a) and Figure 131 b) for a transformer type oven and inverter type oven, respectively.

Because only one set of data was usable in the APD and BER for the transformer type oven, regression analysis was not performed. On the other hand, excellent correlation was confirmed in the case of inverter type oven.

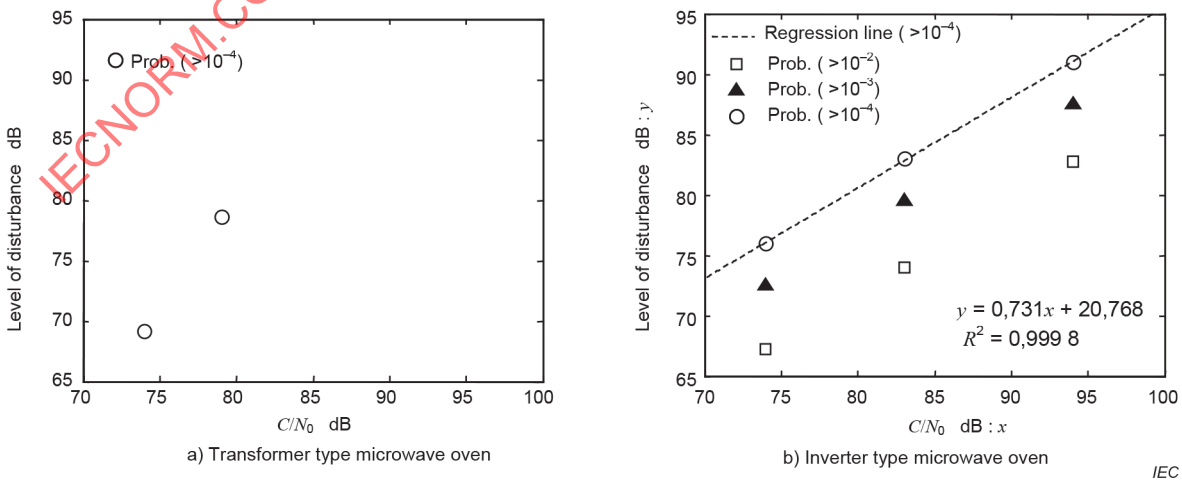



**Figure 131 – Correlation of the disturbance voltages with the system performance ($C/N_0$)**

IECNORM.COM : Click to view the full PDF of CISPR TR 16-3:2020 RLV

Additional analyses were performed on PHS data. From Figure 125 a) and Figure 125 b), disturbance voltages for each probability were read. $C/N_0$ values corresponding to the signal input that was necessary to assure the throughput of 3,5 kByte/s under microwave oven disturbance were read from Figure 115 a) and Figure 115 b). The correlation between the disturbance level and the $C/N_0$ values are plotted in Figure 132 a) and Figure 132 b) for a transformer type oven and inverter type oven, respectively. The same results were obtained as for the correlation with BER.

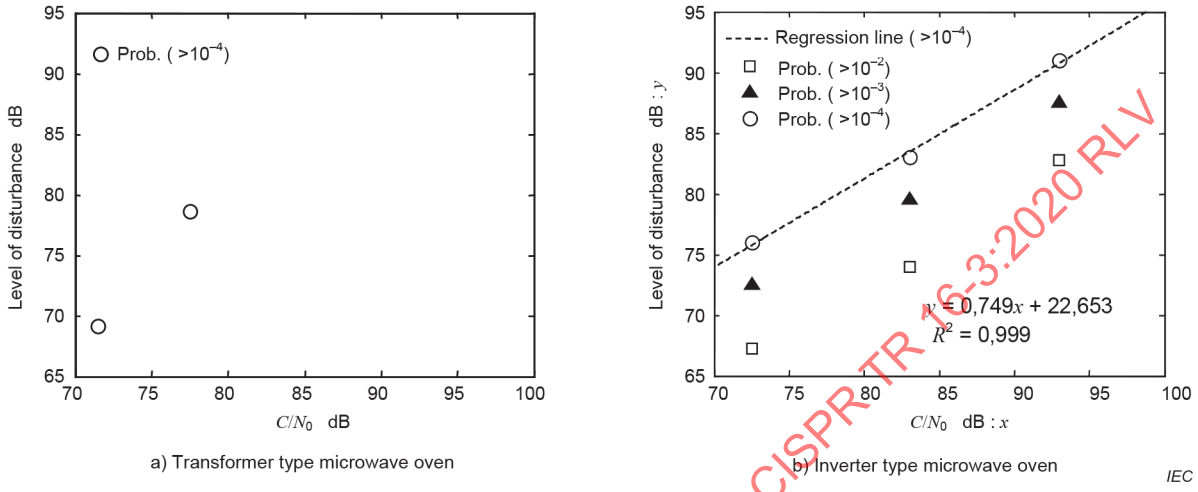



**Figure 132 – Correlation of the disturbance voltages with the system performance ($C/N_0$)**

### 4.7.7 Quantitative correlation between noise parameters of repetition pulse and system performance of PHS and W-CDMA (BER)

Correlations between APD of repetition pulse noise and communication quality degradation of PHS and W-CDMA are obtained by the following additional experiment and simulation. The experimental set-up for measuring communication quality degradation of the PHS or W-CDMA is shown in Figure 133. Repetition pulses combined with Gaussian noise are used as a disturbance. The Gaussian noise level is adjusted to the same noise floor level of vector signal analyzer for BER measurement and spectrum analyzer for APD measurement. Concerning repetition pulses, the pulse width is constant (100 µs) and the repetition frequency is variable. Figure 134 shows a block-diagram of numerical simulation for estimating communication quality degradation. In this simulation, the same noise parameters are used as for the experiment.

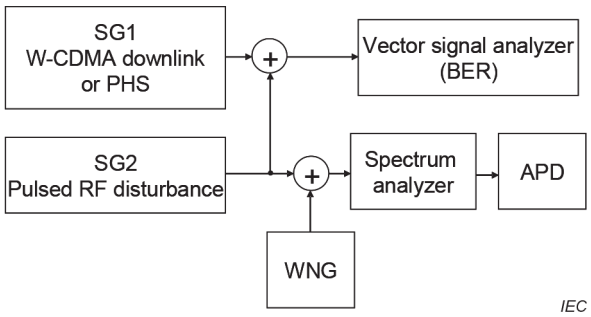



**Figure 133 – Experimental set-up for measuring communication quality degradation of a PHS or W-CDMA**

IECNORM.COM : Click to view the full PDF of CISPR TR 16-3:2020 RLV

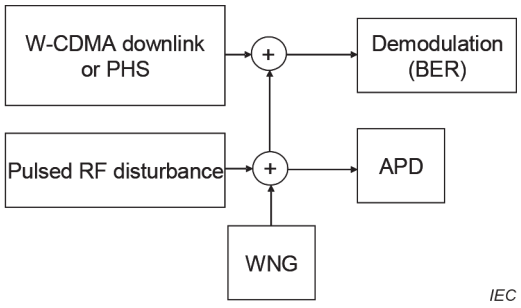



**Figure 134 – Simulation set-up for estimating communication quality degradation of a PHS or W-CDMA**

Measured APD are shown in Figure 135. Marker type represents the duty cycle of the pulse disturbance, i.e. circle, inverted triangle, triangle, diamond, square and star indicate 40 %, 10 %, 4 %, 1 %, 0,4 %, respectively. The dashed line shows the APD of Gaussian noise without repetition pulse.

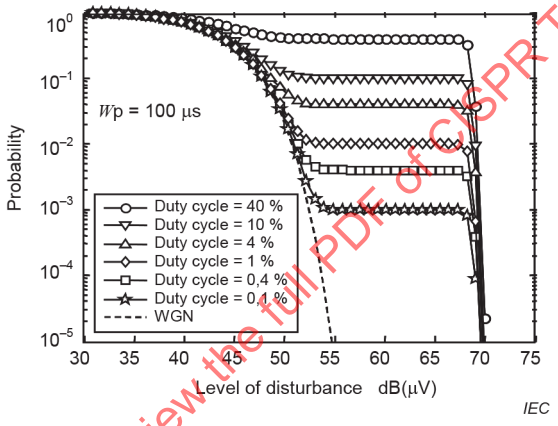



**Figure 135 – APD of pulse disturbance**

Measured BER and estimated BER by numerical simulations are shown in Figure 136 a) and Figure 136 b) for PHS system and W-CDMA system, respectively. Measured BER can be verified by the numerical simulation results. In the case of PHS results, simulation results do not show full agreement at high signal level since the simulation model of receiver is simplified as $\pi/4$ QPSK with a synchronized detector that is different from the experimental setup.

IECNORM.COM : Click to view the full PDF of CISPR TR 16-3:2020 RLV

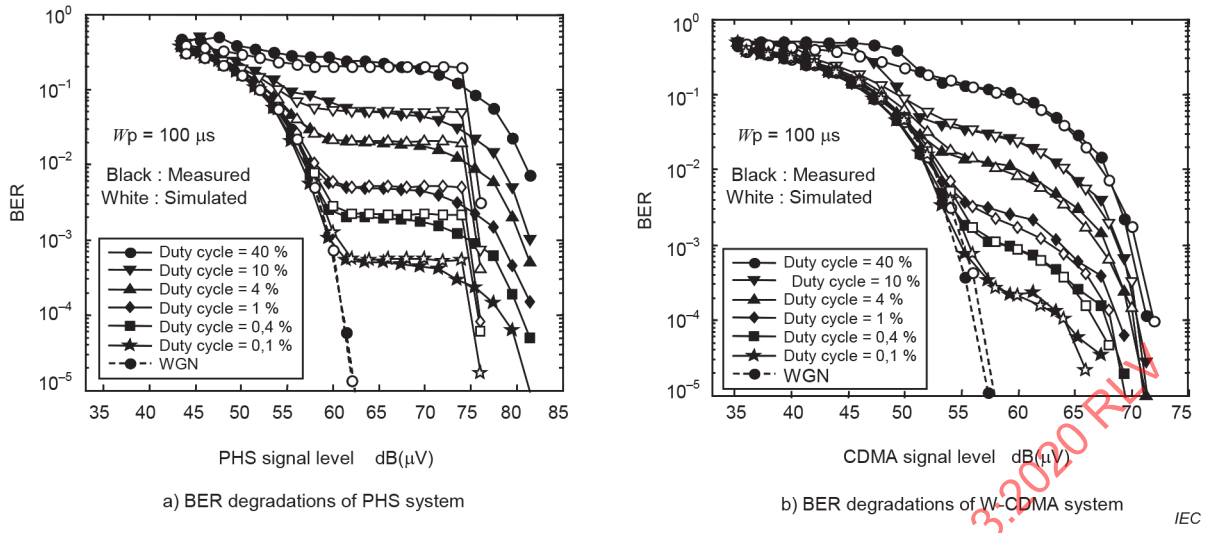



**Figure 136 – BER degradation of PHS and W-CDMA caused by repetition pulse (Carrier power, –35 dBm)**

Figure 137 explains the evaluation method for quantitative correlation between BER and APD. For the level comparison, $\Delta L_{BER}$ and $\Delta L_{APD}$ can be defined as disturbance effects on BER and APD. They are measured by the difference of level between Gaussian noise (without repetition pulse) and disturbance (with repetition pulse) at a certain rate of BER and at a certain probability of APD, respectively. Similarly, $p_{BER}$ and $p_{APD}$ are defined as the probabilities caused by disturbance on BER and APD, respectively.

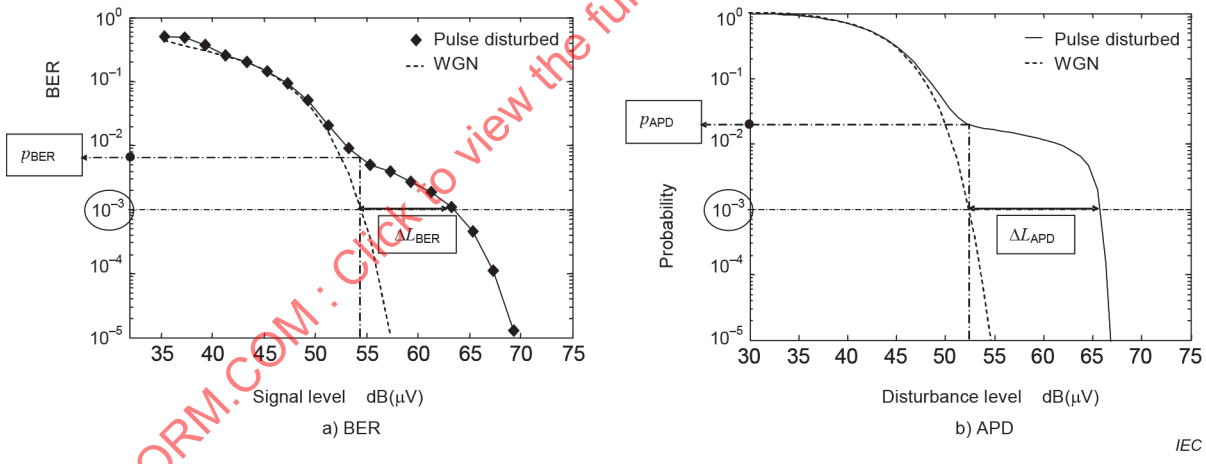



**Figure 137 – Evaluation method of the correlation between BER and APD**

Correlation between measured $\Delta L_{BER}$ and $\Delta L_{APD}$ for several pulse amplitudes are shown in Figure 138 where the pulse has constant duty cycle (10 %, pulse width: 100 µs). The disturbance is generated by modulating a carrier with the repetition pulse. The carrier power is set from –45 dBm to –35 dBm with 2 dB step. Black mark and white mark show the characteristics of W-CDMA and PHS, respectively. BER and probability values ($BER_0$, $APD_0$) selected for these evaluations are (a) $10^{-2}$, (b) $10^{-3}$ and (c) $10^{-4}$.

IECNORM.COM : Click to view the full PDF of CISPR TR 16-3:2020 RLV

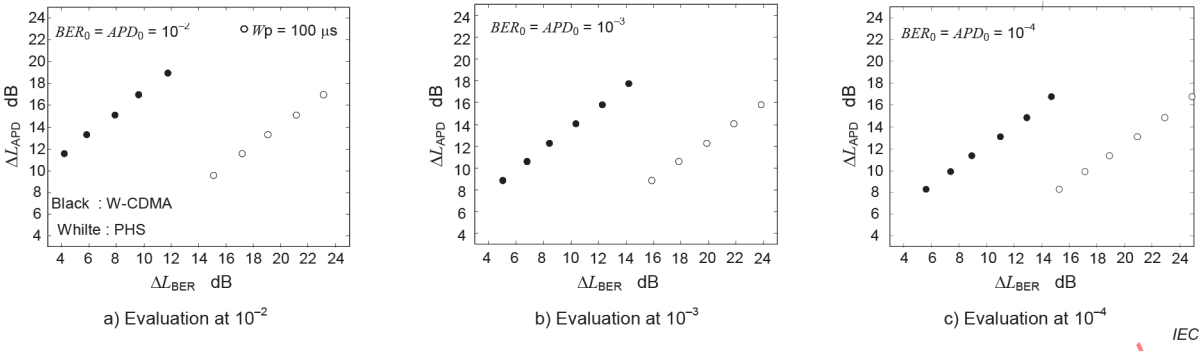



**Figure 138 – Correlation between measured $\Delta L_{BER}$ and $\Delta L_{APD}$**

Correlation between measured $p_{BER}$ and $p_{APD}$ for several duty cycles of the pulse disturbance are also shown in Figure 139, where the disturbance has constant carrier power (-35 dBm). The duty cycle is changed as 40 %, 10 %, 4 %, 1 %, 0,4 % and 0,1 %. Black mark and white mark show the characteristics of W-CDMA and PHS respectively. Diamond, circle, triangle and square marks indicate the results for the pulse width 1 000 µs, 100 µs, 10 µs and 1 µs respectively. BER and probability values ($BER_0$, $APD_0$) selected for these evaluations are (a) $10^{-2}$, (b) $10^{-3}$ and (c) $10^{-4}$.

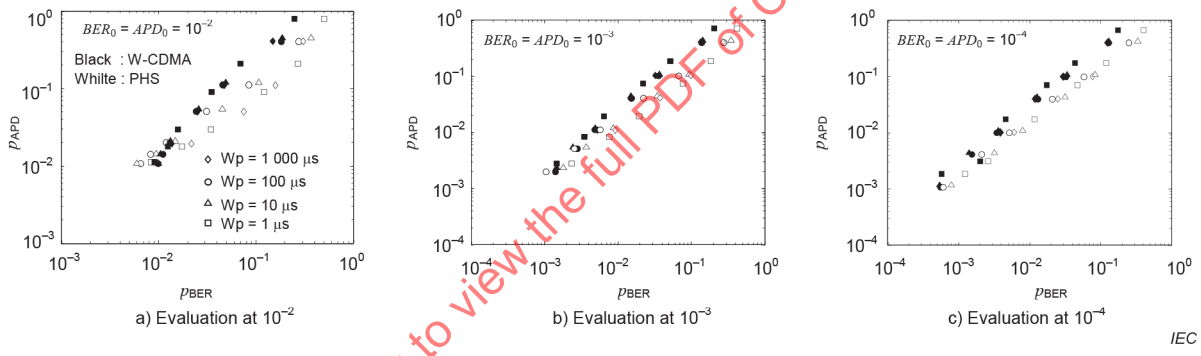



**Figure 139 – Correlation between measured $p_{BER}$ and $p_{APD}$**

In all cases, APD indices ($\Delta L_{APD}$, $p_{APD}$) have close correlation with BER degradation indices ($\Delta L_{BER}$, $p_{BER}$), respectively. It is therefore concluded that APD measurement of the disturbance is one of the most effective methods for evaluating the interference potential on digital communication systems.

## 4.8 Background material on the definition of the RMS-average weighting detector for measuring receivers

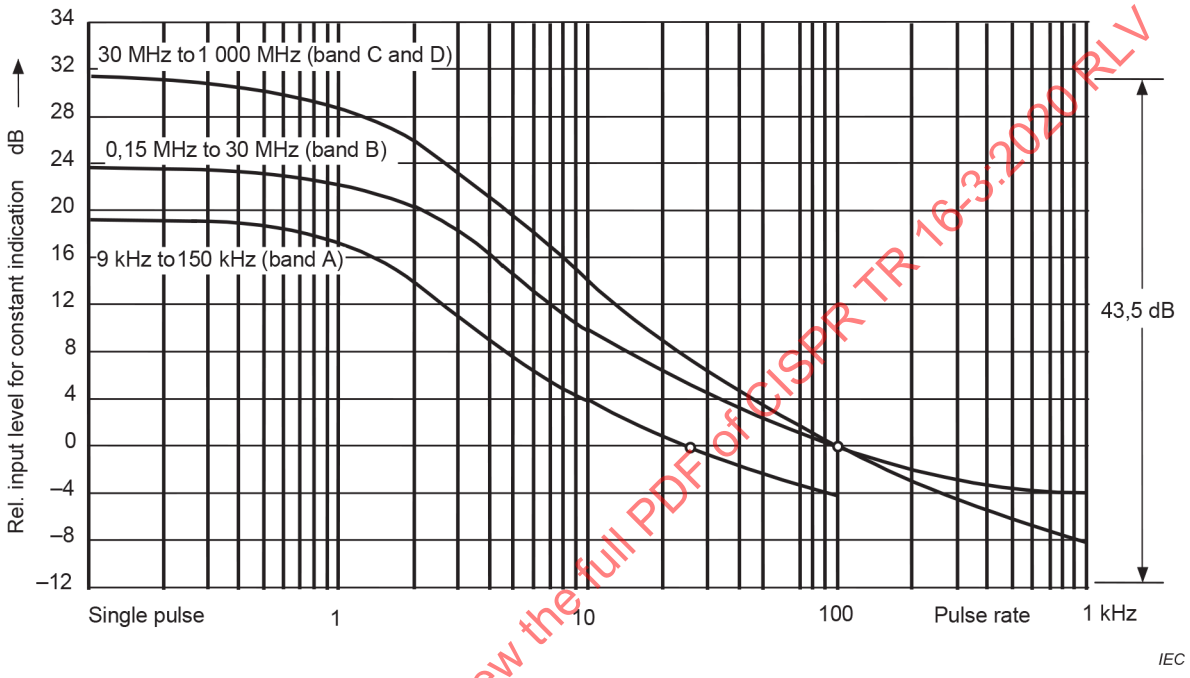
### 4.8.1 General – purpose of weighted measurement of disturbance

Generally, a weighted measurement of impulsive disturbance serves the purpose of minimizing the cost of disturbance suppression, while keeping an agreed level of radio protection. The weighting of a disturbance for its effect on modern digital radiocommunication services is important for the definition of emission limits that protect these services. CISPR 16-1-1 defines a detector that is a combination of an RMS and an average detector. The selection of the type of detector and of the transition between these detector functions is based on measurements and theoretical investigations.

IECNORM.COM : Click to view the full PDF of CISPR TR 16-3:2020 RLV

### 4.8.2 General principle of weighting – the CISPR quasi-peak detector

The effect on radiocommunication services depends on the type of interference (e.g. broadband or narrowband, pulse rate etc.) and on the type of service itself. The effect of the pulse rate was recognized a short time after CISPR was founded in 1933. As a result, the quasi-peak weighting receiver for the frequency range of 150 kHz to 1 605 kHz was defined as shown for band B in Figure 140. However in CISPR 1 [1] it was already accepted that "Subsequent experience has shown that the RMS voltmeter might give a more accurate assessment" but the quasi-peak type of voltmeter has been retained for certain reasons – mainly for continuity.




NOTE The weighting factor is shown relative to a reference pulse rate (25 Hz or 100 Hz).

**Figure 140 – Weighting curves of quasi-peak measuring receivers for the different frequency ranges as defined in CISPR 16-1-1**

### 4.8.3 Other detectors defined in CISPR 16-1-1

#### 4.8.3.1 Peak detector

The peak detector follows the signal at the output of the IF envelope detector and holds the maximum value during the measurement time (also called dwell time) until its discharge is forced. This indication is independent of the pulse repetition frequency (PRF).

#### 4.8.3.2 Average detector

The average detector determines the linear average of the signal at the output of the IF envelope detector. It should be kept in mind that for low PRFs, CISPR 16-1-1 specifies the average detector measurement result as the maximum scale deflection of a meter with a time constant specified for the quasi-peak detector. This is necessary to avoid reduced level indication for a pulse modulated disturbance by using long measurement times. The weighting function varies with 20 dB per decade of the PRF (see Figure 141).

IECNORM.COM : Click to view the full PDF of CISPR TR 16-3:2020 RLV

#### 4.8.3.3 RMS detector

The RMS detector determines the RMS value of the signal at the output of the IF envelope detector. Despite being mentioned in [1] and being described in CISPR 16-1-1, at the time of writing of this subclause it has not been put to practical use in CISPR product standards. The weighting function varies with 10 dB per decade of the PRF (see Figure 141). Up to now, no meter time constant applies for the RMS detector for intermittent, unsteady and drifting narrowband disturbances.

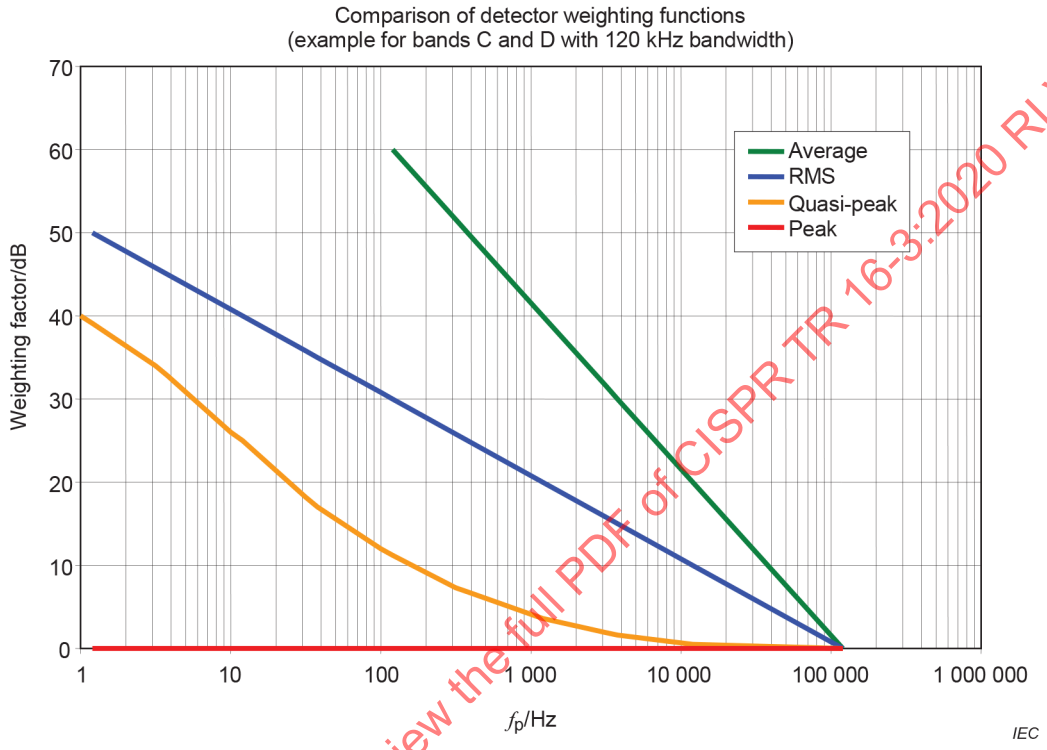



**Figure 141 – Weighting curves for peak, quasi-peak, RMS and linear average detectors for CISPR bands C and D**

IECNORM.COM : Click to view the full PDF of CISPR TR 16-3:2020 RLV

### 4.8.4 Procedures for measuring pulse weighting characteristics of digital radiocommunications services

#### 4.8.4.1 General

All modern radio services use digital modulation schemes. This is not only true for mobile radio but also for audio and TV. Procedures for data compression and processing of analog signals (voice and picture) are used together with data redundancy for error correction. Usually, up to a certain critical bit-error ratio (BER) the system can correct errors so that perfect reception occurs.

Whereas analog radio systems require signal-to-noise ratios of as much as 50 dB for satisfactory operation, in general, digital radio communication systems allow error-free operation down to signal-to-noise ratios of approximately 10 dB. However the transition region from error-free operation to malfunction is small. Therefore planning guidelines for digital radio are based on almost 100 % coverage. When a digital radio receiver operates at low input levels, the susceptibility to radio disturbance is important. In mobile radio reception, the susceptibility to radio disturbance is combined with the problem of multi-path propagation.

#### 4.8.4.2 Principles of measurement

The significance of the weighting curve for band B is as follows: to a listener the degradation of reception quality, caused by a 100-Hz pulse, is equivalent to the degradation from a 10-Hz pulse, if the pulse level is increased by an amount of 10 dB. In analogy to the above, an interference source with certain characteristics will produce a certain BER, e.g. $10^{-3}$ in a digital radiocommunication system, when the interfering signal is received in addition to the radio signal. The BER will depend e.g. on the pulse repetition frequency (PRF) and the level of the interfering signal. In order to keep the BER constant, the level of the interfering signal will have to be readjusted while the PRF is varied. This level variation versus PRF determines the weighting characteristics. Measurement systems with BER indication are needed to determine the required level of the interfering signal for a constant BER as e.g. shown in Figure 142.

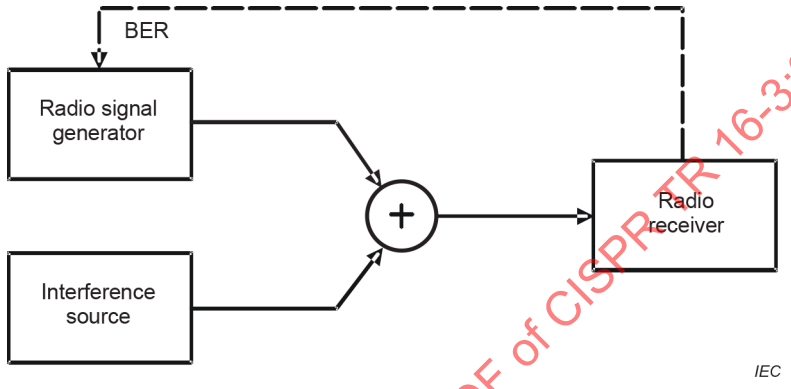



**Figure 142 – Test setup for the measurement of the pulse weighting characteristics of a digital radiocommunication system**

The test set-up shown in Figure 142 consists of a radio signal generator that transmits the wanted radio signal to the receiver. For the determination of the BER, the radio receiver either has to know the original bit sequence for comparison with the detected bit sequence or the latter shall be looped back to the radio signal generator for comparison with the original. Both systems are available and have been used for tests. Mobile radio testers, e.g. apply the loop-back principle.

#### 4.8.4.3 Generation of the interference signal

A signal generator with pulse-modulation capability can be used to generate the interference signal. For correct measurements, the pulse modulator requires a high ON/OFF ratio of more than 60 dB. Using the appropriate pulse width, the interference spectrum can be broadband or narrowband, where the definition of broadband and narrowband is relative to the communication channel bandwidth. Figure 143 gives an example of an interference spectrum used for the determination of weighting characteristics.

IECNORM.COM : Click to view the full PDF of CISPR TR 16-3:2020 RLV

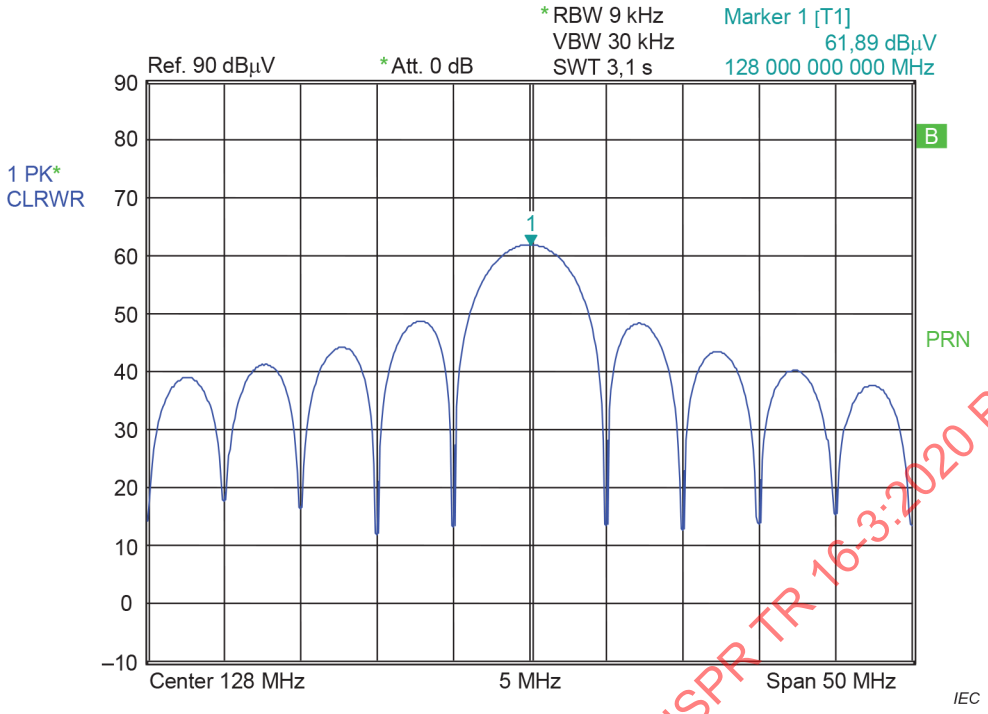



**Figure 143 – Example of an interference spectrum: pulse modulated carrier with a pulse duration of 0,2 µs and a PRF < 10 kHz**

With increasing pulse duration, the main lobe of the spectrum becomes narrower. This is also used to study the effect of narrowband pulses on radiocommunication systems. The advantage of using a band-limited pulse spectrum instead of a broadband pulse generator is to avoid overloading the receiver under test. Otherwise non-linearity effects could cause deterioration of the weighting characteristics. In addition to pulse-modulated carriers, unmodulated carriers can be used to determine the sensitivity of different systems to narrowband (CW signal) EMI.

Extensive measurements have also been presented in [49] with on/off-keying of a QPSK-modulated signal, thus keeping the spectrum width wider than the system bandwidth even with longer pulse durations. Since actual receivers do not provide BER indication, the method described in ITU Recommendation 1368 [59] was used as the failure criteria: DVB-T reception was regarded as distorted when more than one visible erroneous block was shown on the screen within an observation period of 20 s. Alternatively, any picture-freeze, also for short periods, was regarded as a failure. For DRM, the reception was considered as distorted when the system showed more than one dropout in a 20 s observation time.

Further measurements have been made with spread-spectrum modulated carriers in order to study the effect of spread-spectrum clock interference on wideband radiocommunication services (see [50] and [51]). Refer to Table 33.

**Table 33 – Overview of types of interference used in the experimental study of weighting characteristics**

| Interference signals | Pulse-modulated | On/Off-keyed QPSK-modulated | Spread-spectrum modulated |
|---|---|---|---|
| Pulse width in relation to signal bandwidth | $T < 1/B$ to $100/B$ | $T < 1/B$ to $100/B$ | Continuous |
| $T$ = pulse width, $B$ = radio signal bandwidth | | | |

IECNORM.COM : Click to view the full PDF of CISPR TR 16-3:2020 RLV

#### 4.8.4.4 Other principles of measurement

The receiver under test should receive a signal that is just sufficient to give quasi error-free reception (e.g. a BER = $10^{-7}$ or a factor of $10^{-3}$ lower than the critical BER). Thus the receiver operates like a receiver at the edge of a coverage area, where a disturbance above the emission limit can easily cause interference.

For radio telephone systems, where the downlink (base station to mobile) and uplink (mobile to base station) frequencies are in different bands, the use of a pulse modulated carrier helps to concentrate the interference on the mobile receiver and thus avoids interference with the loop-back connection.

### 4.8.5 Theoretical studies

The work of developing measurement procedures considering a digital radio receiver as a disturbance victim, is a very complex problem because there are many different modulation and coding schemes to consider as digital communication services are undergoing rapid development. The results of theoretical studies for radio systems using error correction are presented for example in [52] and [53]. These studies are based on the same fundamental assumptions that are explained above:

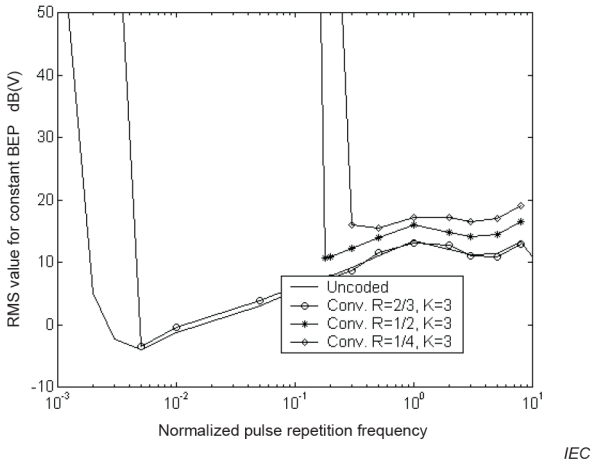
- the BER is the performance parameter of interest for the digital communication system;
- the repetitive pulsed disturbance is the waveform of particular interest;
- the disturbance pulses have a pulse duration that is short compared to the digital symbols transmitted.

Results for some selected convolutional codes include the following – for more details, see [52].

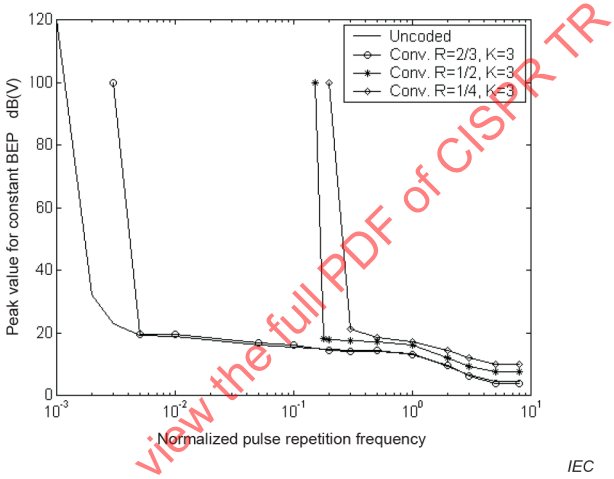
A convolutional code is generated by passing the information sequence through a linear finite-state shift register. In general, the shift register consists of $K$ stages and $n$ algebraic function generators. The input data to the channel encoder is shifted into and along the shift register $k$ bits at a time. The number of output bits for each $k$-input sequence is $n$ bits. The rate $R$ of the code is defined as $n/k$. The parameter $K$ is called the constraint length of the convolutional code. In Figure 144 a) and b) as well as Figure 145 a) and b) the RMS and peak values corresponding to a constant BER of $10^{-3}$ are shown for different convolutional codes and *binary phase shift keying* (BPSK) modulation. These results have been simulated with ACOLADE© (Advanced Communication Link Analysis and Design Environment). In the graphs, the pulse repetition frequency of the disturbance is presented as related (normalized) to the gross-bit rate (or symbol rate) $R_s$ of the communication system. The simulation is done in the band-pass domain. This means that the results can be transformed to an arbitrary carrier frequency. The disturbance pulse width is 10 % of the bit duration time. For the lowest rate $R$ = ¼, the RMS value is approximately constant down to the critical point where it increases rapidly. Thus, for a well-protected system, the RMS value corresponding to a constant BER is constant with respect to the pulse repetition frequency of the repetitive pulsed disturbance.

NOTE ACOLADE© is an example of a suitable product available commercially. This information is given for the convenience of users of this document and does not constitute an endorsement by IEC of this product.

IECNORM.COM : Click to view the full PDF of CISPR TR 16-3:2020 RLV



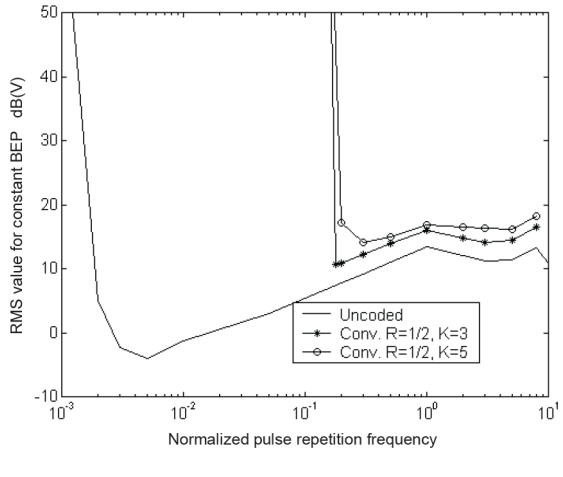

**a) The RMS level**



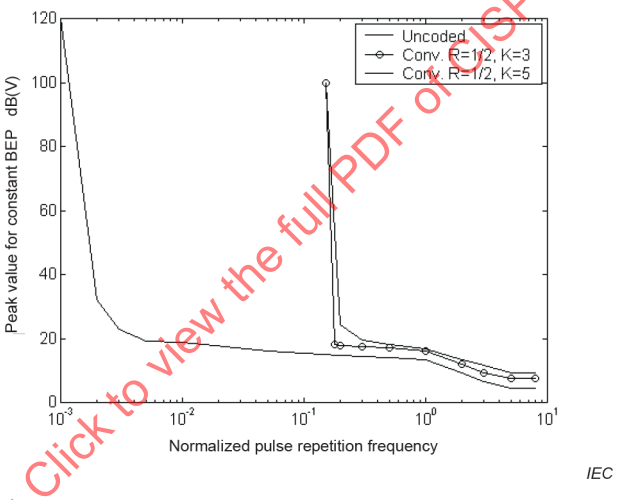

**b) The peak level**

**Figure 144 – The RMS and peak levels for constant BEP for three $K$ = 3, convolutional codes of different rate**

IECNORM.COM : Click to view the full PDF of CISPR TR 16-3:2020 RLV




a) The RMS level




b) The peak level

**Figure 145 – The RMS and peak levels for constant BEP for two rate ½, convolutional code**

IECNORM.COM : Click to view the full PDF of CISPR TR 16-3:2020 RLV

The results in Figure 144 show the following: above the symbol rate $R_s$, the weighting characteristic follows the RMS value of the impulsive signal that causes the interference. Below $R_s$, the weighting characteristic depends on the amount of coding; for the uncoded signal, the peak value increases with less than 10 dB per decade as the PRF decreases. With better coding, the part of the weighting characteristic with flat response becomes shorter. Therefore, it is important to characterize real radiocommunication systems in order to obtain meaningful results.

### 4.8.6 Experimental results

#### 4.8.6.1 General

The methods described in 4.8.4 have been used for the measurement results in this part. The test signals are described where necessary.

#### 4.8.6.2 Weighting in band A

For band A, i.e. below 150 kHz, no measurement results of digital radiocommunication systems are available.

NOTE Weighting of radio disturbance generally requires a consideration of intermittent, unsteady and drifting narrowband disturbances. Therefore the concept of defining a corner frequency, below which the average detector becomes effective has been applied to band A as well, using the corner frequency proposed for band B, because the original CISPR specification of the RMS detector does not apply a meter time constant.

#### 4.8.6.3 Weighting in band B

**Weighting of interference to the Digital Radio Mondiale (DRM) Broadcast System**

At the World Radio Conference (WRC) in June 2003, the new Digital Radio Mondiale was officially started. During the four-week duration of the conference, a great number of special DRM transmissions became available from many radio stations. The measurement results reported below were acquired on 8 July 2003, when a great number of transmissions were still available.

DRM uses OFDM (orthogonal frequency division multiplex) with 200 carriers. The occupied bandwidth of each transmission is 10 kHz. In addition to the digitized audio signal, a certain amount of data (radio station information, etc.) is transmitted. A conventional AM receiver can be used to downconvert the signal to an IF of 12 kHz, which is then decoded using a digital signal processor and a special DRM software radio.

During the time of measurement, the radio stations in Table 34 were received at the station near Munich, Germany, using amateur-radio dipole antennas mounted on a rooftop with a higher receive input voltage (50 dBμV to 60 dBμV) than required for the experiment.

**Table 34 – DRM radio stations received for the measurement of the weighting characteristics**

| Frequency kHz | Beam[a,b] | Target[c] | Average DRM power kW | Program | Transmit site |
|---|---|---|---|---|---|
| 5 975 | 060 | W Europe | 40 | T-Systems Media Broadcast | Jülich |
| 6 095 | ND | Europe | 35 | RTL/music and short announcements | Junglinster, Luxembourg |
| 6 140 | ND | W and C Europe | 40 | DW English | Jülich |
| 7 320 | 105 | W and C Europe | 33 | BBCWS | Rampisham |
| 13 605 | 037 | C Europe | 6 | IBB/R. Sawa | Morocco |
| 15 440 | 040 | W and C Europe | 80 | DW English | Sines |

[a] ND is non-directional (omnidirectional).

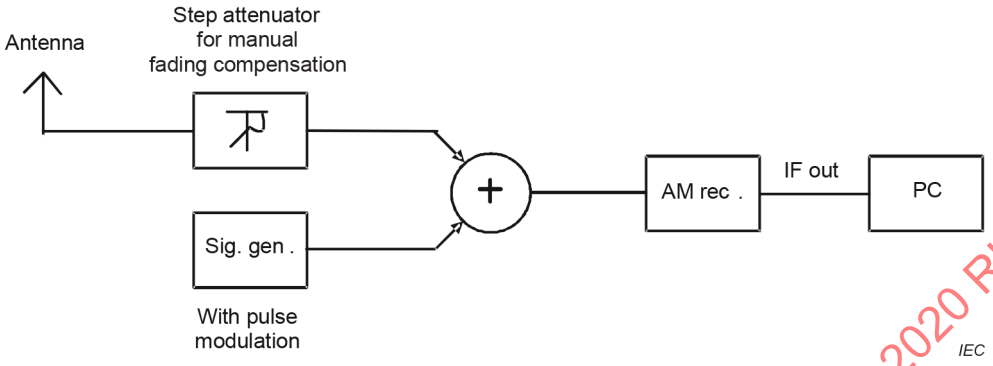
[b] “Beam” indicates antenna beam direction in terms of angle measured clockwise from 0° = north. For example 090 is east, 180 is south, 270 is west. Thus, 105 is approximately east-south-east.

[c] W is west and C is central.

The various transmissions were available for 1 h or 2 h. The measurement results (weighting characteristics) were essentially the same for all frequencies, even if the amount of data transmitted in addition to the audio signal was not the same. Time-dependent fading of the input signal had to be manually compensated using a step attenuator that was inserted in the antenna connection (see Figure 146).

IECNORM.COM : Click to view the full PDF of CISPR TR 16-3:2020 RLV

Principally the same type of interference signal was generated as in Figure 132. However, for a signal with an occupied bandwidth of 10 kHz, it is possible to use a longer pulse duration (10 μs or more).



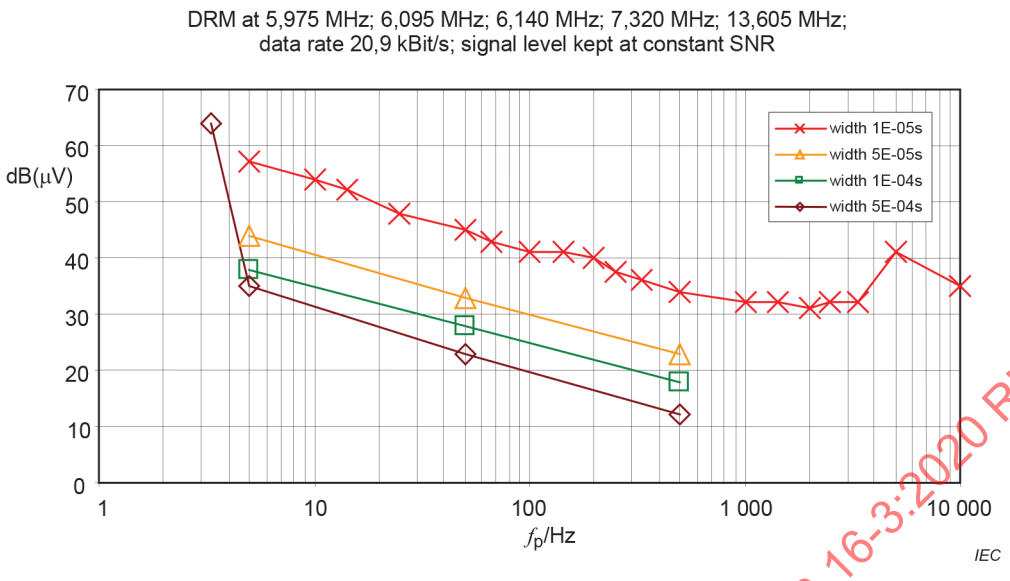

NOTE The received signal is downconverted to an IF of 12 kHz for decoding by special hardware and software in a personal computer (PC).

**Figure 146 – Test setup for the measurement of weighting curves for Digital Radio Mondiale (DRM)**

Because no indication of BER was available, the “Audio” status indication on the PC (DRM software radio display) was used as a criterion. As soon as the interference becomes too high, the “Audio” status indication will turn from green to red.

As explained earlier, the signal level is attenuated so that the reception quality is to be the minimum sufficient. The weighting characteristic (see Figure 147) shows a 10 dB/decade increase of the interference signal for PRFs between 1 kHz and 5 Hz. The non-linearities are mainly due to uncompensated fading of the input signal. A detailed weighting curve is shown for a pulse width of 10 μs. For higher pulse widths, the weighting curve was measured only at three (respectively, four) points to verify the 10 dB/decade behaviour. Below a PRF of 5 Hz, the weighting curve rises suddenly. And below about 2 Hz, the signal cannot be disturbed by the pulse width of 500 μs. However lightning strokes are reported to generate longer dropouts, which indicates that longer clicks might cause such dropouts as well.

IECNORM.COM : Click to view the full PDF of CISPR TR 16-3:2020 RLV




NOTE Because the DRM signals are actual radio signals, the exact modulation scheme is not known.

**Figure 147 – Weighting characteristics for DRM signals for various pulse widths of the pulse-modulated carrier**

The report [49] describes the following DRM signals and two receiver types for the measurements:

- Mode B, Modulation 16/64 QAM, Interleave 2 s, protection level 1 / 0
- Mode B, Modulation 16/64 QAM, Interleave 2 s, protection level 0 / 0

The interference signal for Figure 148 and Figure 149 is a pulse-modulated carrier with additional QPSK modulation, in order to generate a wide bandwidth of the interference spectrum as explained in 4.8.4.2.

IECNORM.COM : Click to view the full PDF of CISPR TR 16-3:2020 RLV

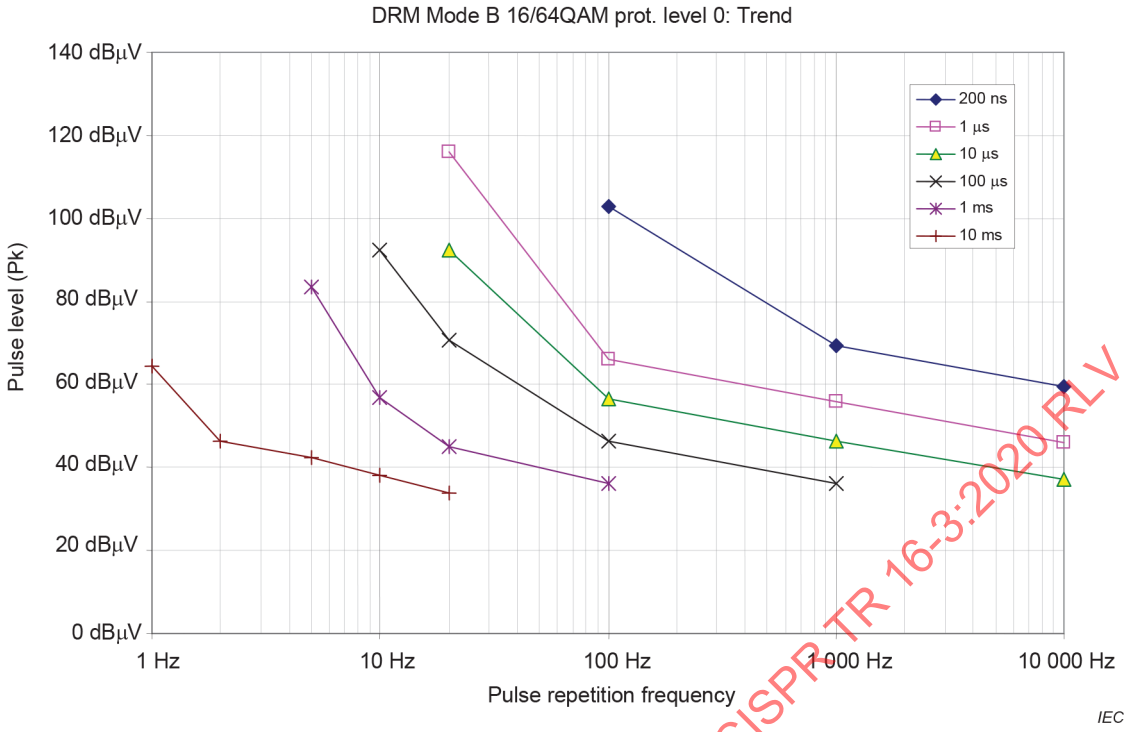



**Figure 148 – Weighting characteristics for DRM protection level 0: average of results for two receivers**

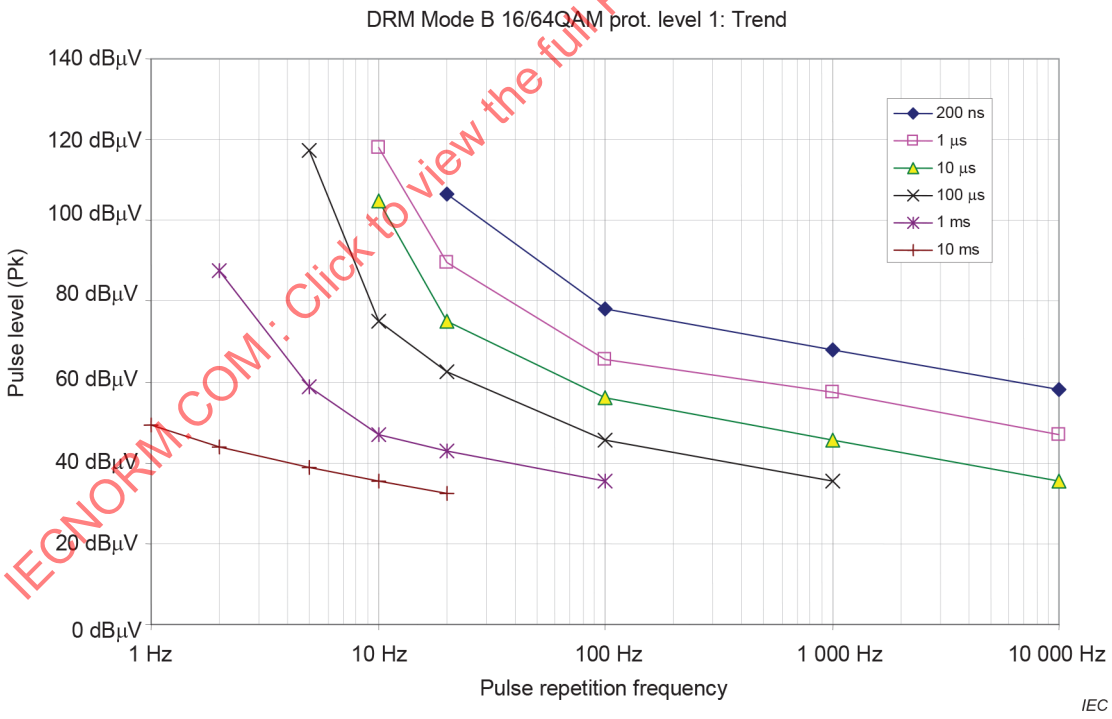



**Figure 149 – Weighting characteristics for DRM protection level 1: average of results for two receivers**

The weighting characteristics in Figure 148 and Figure 149 show a 10 dB/decade slope down to approximately 100 Hz. Because there is no other digital radio system in band B, the corner frequency of the proposed RMS/AV detector between RMS and linear average detection for this frequency band can only be based on the results of DRM (see 4.8.7). A corner frequency of 10 Hz is therefore proposed for band B as a compromise between the two results.

IECNORM.COM : Click to view the full PDF of CISPR TR 16-3:2020 RLV

#### 4.8.6.4 Weighting in bands C/D

##### 4.8.6.4.1 Weighting of impulsive interference to Digital Video Broadcast Terrestrial (DVB-T)

###### 4.8.6.4.1.1 Test setup

One test setup for DVB-T consists of a DVB-T signal generator and a DVB-T measuring receiver. The components are connected via coaxial cables. The interference signal (a pulse-modulated carrier, see Figure 132 for an example of the spectrum) is fed into the signalling connection via a combiner.

The parameters used are detailed in the following paragraphs.

DVB-T uses COFDM (coded orthogonal frequency division multiplex) with 6 817 (8k) or 1 705 (2k) carriers. The OFDM carriers may be modulated either with QPSK (Quadrature Phase Shift Keying) or with 64 QAM (quadrature amplitude modulation), respectively 16 QAM. QAM is preferred to QPSK as QAM allows higher data transfer rates. The transmission code rate $CR$ is defined by $CR$ = number of information bits/(number of information bits + error protection bits). Values of $CR$ = 2/3 and 3/4 are used in actual systems. Each COFDM symbol is followed by a guard interval $GI$ which is $GI$ = 1/8 in actual systems.

The DVB-T modulation and coding system allows many combinations, of which only a few are relevant. Therefore the parameters used in systems operating in some European countries have been selected. These allow transmission rates between 14,745 Mb/s and 24,88 Mb/s (see Table 36) depending on modulation and code rate. Different coders and decoders are used in the system. The bit-error ratio (BER) reading can be taken before the Viterbi decoder as well as before and after the Reed Solomon decoder of the measuring receiver. A comparison is given in Table 35. The transmission level is set so that the BER after the Reed Solomon decoder without interference is just below $10^{-8}$. This produces different signal levels depending on the system parameters. The interference levels have then been adjusted to a critical value of BER = $2{,}0 \times 10^{-4}$ before the Reed Solomon decoder.

For the BER measurement, the modulator generates a Pseudo Random Binary Sequence (PRBS) as a data stream. The evaluation of the data stream is done in the receiver in two different procedures. The BER before Viterbi and before Reed-Solomon is evaluated by correlation. Flags in the bit stream are used to determine the BER after Reed-Solomon. If the decoder does not recognize a flag as correct, the following bit combination is determined to be false.

The relationship in Table 35 was found experimentally between the bit error ratios before and after the Viterbi and Reed Solomon decoders for two pulse rates.

**Table 35 – Comparison of BER values for the same interference level**

| **Pulse rate** Hz | **10 k** | **500 k** |
|---|---|---|
| BER before Viterbi decoder | $1{,}5 \times 10^{-2}$ | $4{,}4 \times 10^{-3}$ |
| BER before Reed Solomon | $2{,}0 \times 10^{-4}$ | $2{,}0 \times 10^{-4}$ |
| BER after Reed Solomon | $1{,}0 \times 10^{-6}$ | $1{,}0 \times 10^{-8}$ |

So, the results with BER measured before Reed Solomon (with $2{,}0 \times 10^{-4}$) and after Reed Solomon (with $1{,}0 \times 10^{-6}$) are roughly comparable.

IECNORM.COM : Click to view the full PDF of CISPR TR 16-3:2020 RLV

**Table 36 – Transmission parameters of DVB-T systems used in various countries**

| Country | Modulation | Code rate | Guard interval | Transfer rate |
|---|---|---|---|---|
| France/UK | 64 QAM 2k | 3/4 | 1/8 | 24,88 Mb/s |
| Spain | 64 QAM 8k | 3/4 | 1/8 | 24,88 Mb/s |
| Germany | 16 QAM 8k | 2/3 | 1/8 | 14,745 Mb/s |

The measurement results are presented in Figure 150, Figure 151 and Figure 152. In all tests, the interference signal leading to these results are pulse-modulated carriers.

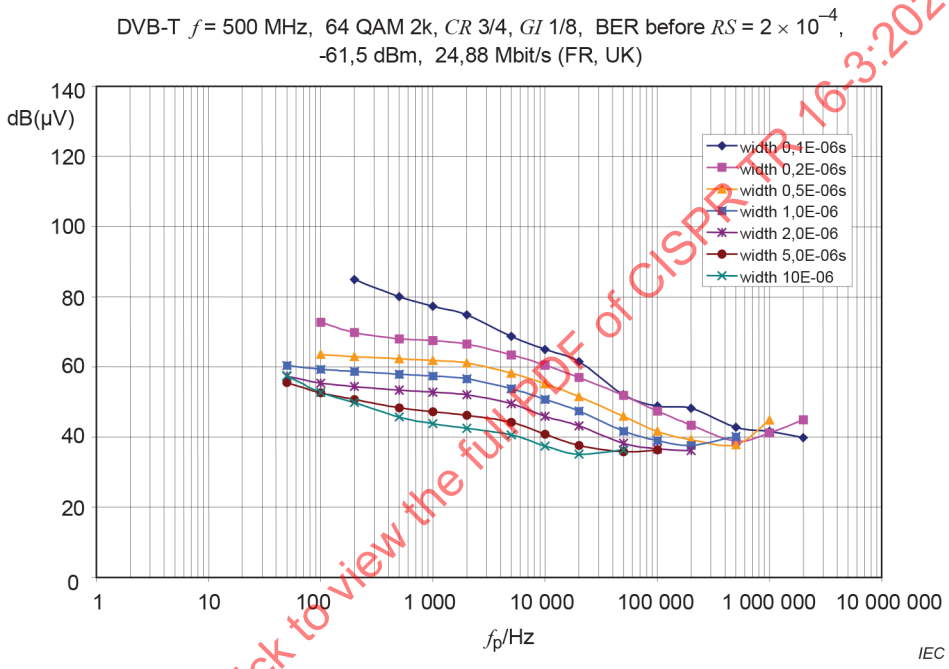



**Figure 150 – Weighting characteristics for DVB-T with 64 QAM 2k, $CR$ 3/4 (as used in France and UK)**

IECNORM.COM : Click to view the full PDF of CISPR TR 16-3:2020 RLV

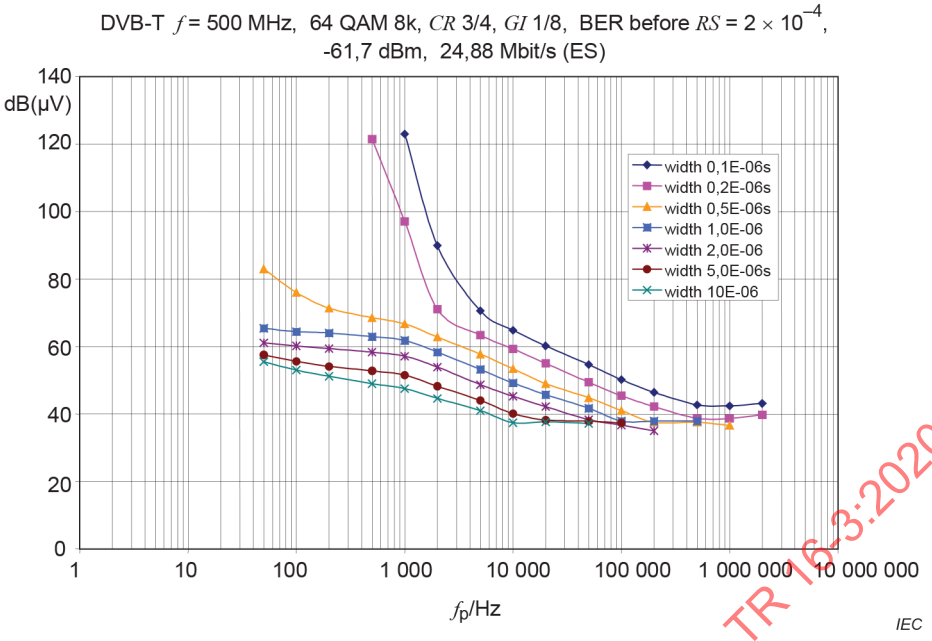



**Figure 151 – Weighting characteristics for DVB-T with 64 QAM 8k, *CR* 3/4 (as used in Spain)**

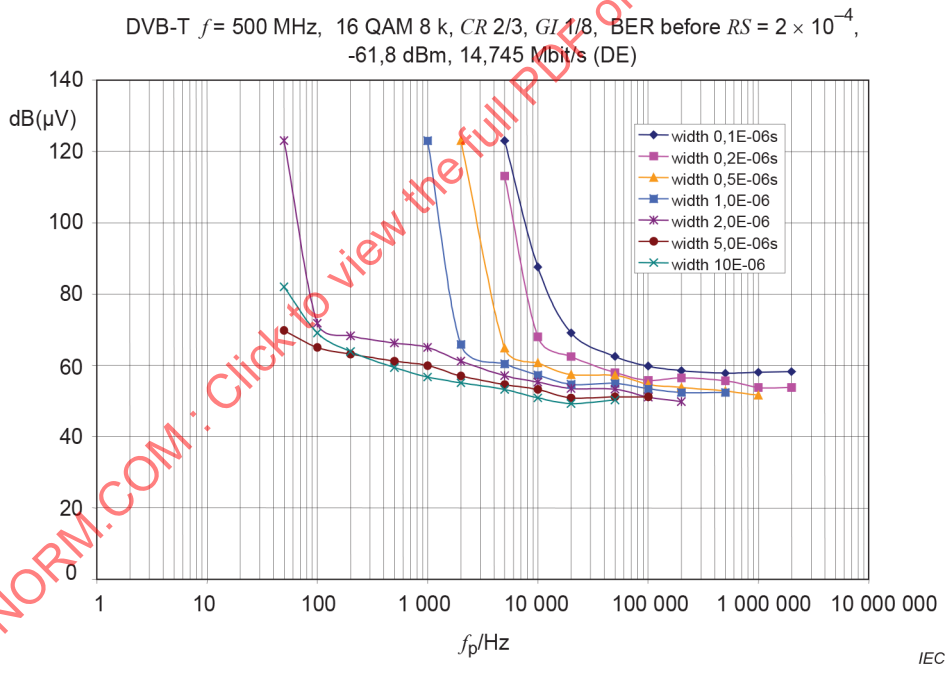



**Figure 152 – Weighting characteristics for DVB-T with 16 QAM 8k, *CR* 2/3 (as used in Germany)**

Six different receiver types were tested in report [49] for DVB-T with 16QAM 8k, $CR$ 2/3 and for DVB-T with 64QAM 8k, $CR$ 2/3. To get receiver independent results, the individual characteristics were combined using average values inside the range where all receivers offered a result. Excluded were two receivers in PRF ranges, where they showed a non-typical behavior. These combined results are shown in the "trend" characteristics in Figure 153 and Figure 154. The interference signal for both figures is a pulse-modulated carrier with additional QPSK modulation in order to generate bandwidth of the interference spectrum at least as wide as the DVB-T signal spectrum as explained in 4.8.4.2.

IECNORM.COM : Click to view the full PDF of CISPR TR 16-3:2020 RLV

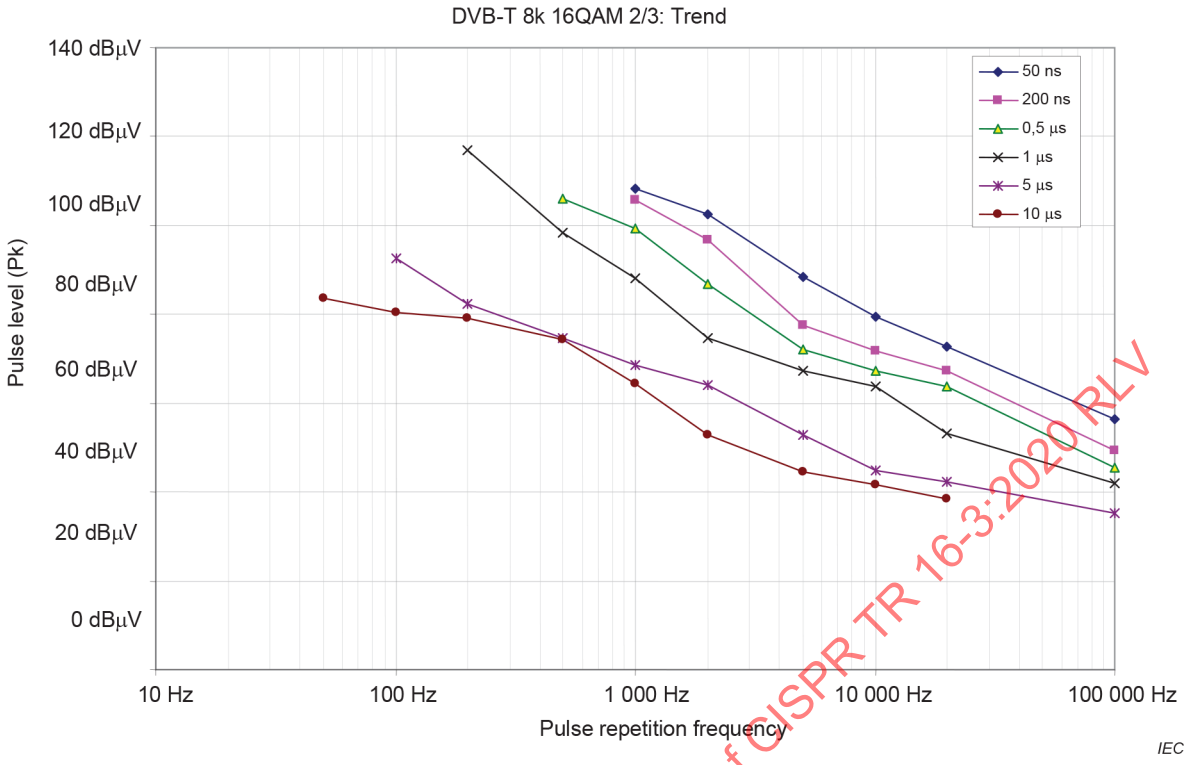



**Figure 153 – Average weighting characteristics of 6 receiver types for DVB-T with 16QAM**

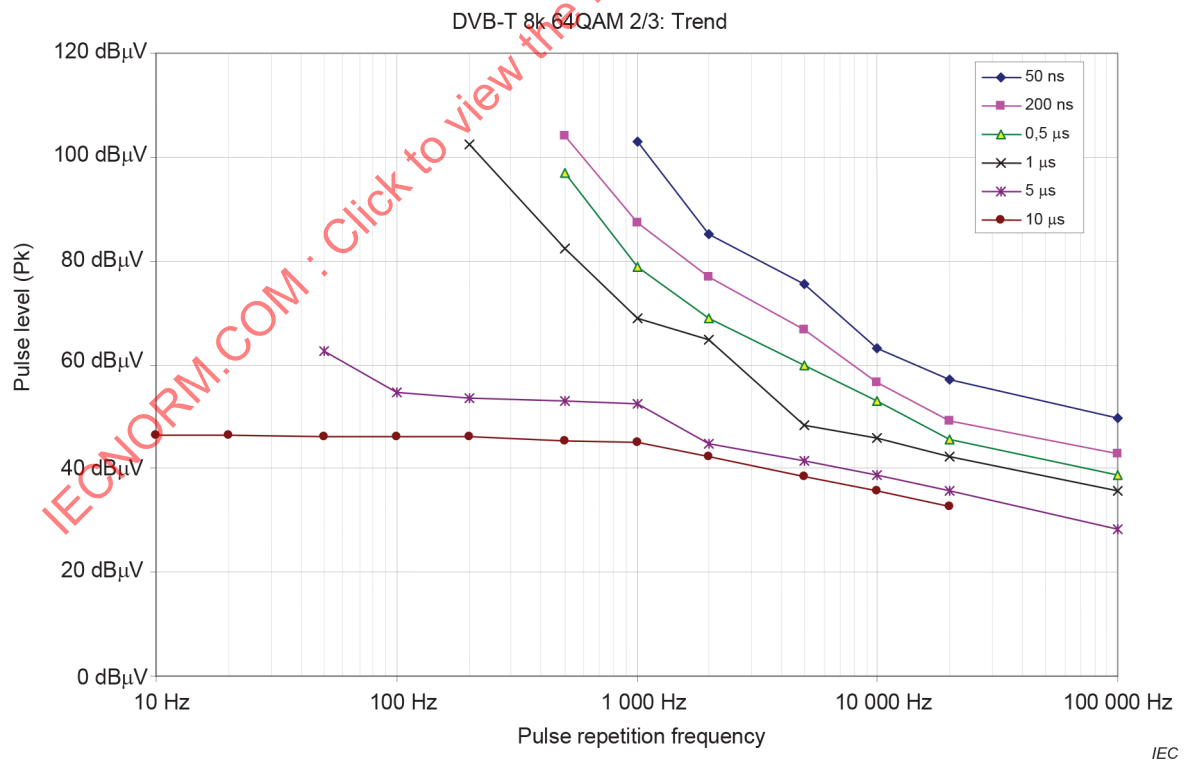



**Figure 154 – Average weighting characteristics of 6 receiver types for DVB-T with 64QAM**

IECNORM.COM : Click to view the full PDF of CISPR TR 16-3:2020 RLV